The Motion of Fine Sand Particles in Turbulent Open Channel Shear Flows over Porous Bed Conditions

A thesis submitted in partial fulfilment of the requirements
for the degree of Doctor of Philosophy by

Alan James Stewart Cuthbertson

Project supervisor: Professor D.A. Ervine
Department of Civil Engineering, University of Glasgow
December 2001

To Katrina; my parents; Lynn and Jill.
For their endless encouragement, patience and support.

Abstract

It is universally accepted that the turbulent flow environment generated within a gravel-bed river will have a crucial role in sedimentation processes. Unfortunately, as the underlying mechanisms are extremely complex, the interactions existing between fine sediment particles and turbulence are as yet poorly understood and researched. Recent visualisation studies have, however, begun to shed light on the primary role near-bed coherent structures play in sediment entrainment and suspension processes. On this basis, the current study aims to investigate the physical mechanisms controlling fine sediment transport within open channel shear flows over porous beds, with particular emphasis on the role of flow turbulence in particle settling and deposition processes.

Preliminary visualisation experiments used a VHS camera to observe the near-bed motion of sand particles and their behaviour within the surface layer of a rhombically-packed bed of uniform spheres. Measurement of near-bed particle trajectories indicate that turbulent particle fall velocities w'_s, are generally larger than fall velocities measured in still water w_s, most notably for finer sand grades. Distinctive modes of particle behaviour observed at the bed interface also suggest that flow-separation eddies, generated within surface interstices, have a primary influence on subsequent particle motion, i.e. deposition or re-entrainment. Similar particle behaviour is also displayed in a natural gravel bed.

A more detailed analysis of sand particle motion in turbulent open channel flow was carried out employing a high-speed camera and particle-tracking technique to record and analyse particle trajectories within different flow regions. The non-dimensional ratio of measured particle fall velocity w'_s and still water fall velocity w_s was used to indicate the relative *enhancement* of vertical particle motion within the turbulent flow conditions. Experiment-averaged values of this ratio reveal that particle fall velocities are generally *enhanced* (i.e. $w'_s/w_s > 1$) in recorded near-bed and intermediate flow regions ($z/H \leq 0.5$) and *hindered* (i.e. $w'_s/w_s < 1$) in a recorded outer flow region ($z/H \geq 0.5$). The ratio w'_s/w_s also reveals a general tendency to increase with decreasing grain size d_i. Vertical profiles of the normalised particle fall velocity w'_s/u_* are shown to be analogous to turbulence intensity distributions (u'_{rms}/u_*

and w'_{rms}/u_*), with the highest values of w'_s/u_* occurring in the near-bed region and coinciding approximately with the regions of highest turbulence activity. This clearly implies the existence of *turbulence-enhanced* particle fall velocities within the flow conditions considered. Application of a quadrant analysis technique reinforces this notion, revealing further similarities between conditioned turbulent fluid fluctuations and particle motions, in particular, the dominance of 'inrush' events (quadrant 4) in the near-bed flow and '*ejection*' events (quadrant 2) away from the bed.

An independent series of experiments employing non-visual techniques verified the main findings from the visualisation experiments. Importantly, they confirmed the existence of turbulence-enhanced particle motion above the bed surface and extended its influence to the deposition of fine to medium sand grades within natural gravel beds, highlighting the importance of other parameters such as Reynolds number, fine sediment input rate, bed material type and shear velocity.

The notion of turbulence-enhanced settling and deposition processes has been identified in previous experimental studies (e.g. Jobson and Sayre 1970; Peloutier 1998). In a numerical study of sediment deposition, Hoyal et al. (1995) used a parameter $w_* = w_s/u_*$ to define the transition between gravity- and turbulence-dominated particle motion. The vast majority of experimental conditions used within the current study are noted to lie within this transitional region ($0.1 \leq w^* \leq 1$) and the levels of enhancement obtained show reasonable agreement with Hoyal's findings.

Further visualisation experiments employing a moving camera system identified distinctive interactions between sand particles and large-scale vortices generated within turbulent flow above a natural gravel bed. Particles are often observed to accumulate in preferential paths around the top of the vortices and form steep trajectories on the downflow side, with enhanced vertical motion outwith the vortex core. Predicted particle trajectories obtained from a zero-order Rankine-vortex model reveal similar behaviour and suggest that '*preferential sweeping*' represents a possible mechanism responsible for the enhanced turbulent fall velocities observed. It is demonstrated that this mechanism is primarily controlled by a sediment trapping parameter Γ and by the relative trapping width X/R within the vortex. The application of the preferential sweeping and vortex trapping mechanisms are demonstrated in relation to sediment deposition processes, while the implications for fine sediment entrainment mechanisms from gravel beds are also investigated.

Acknowledgements

I would like to express my sincere gratitude and appreciation to everyone who assisted me during my three years as Ph.D. research student within the Department and in the subsequent years, including:

My supervisor, **Prof. D. Alan Ervine**, for his invaluable help and support throughout the course of this work and for his continuing encouragement in the years subsequent to my time within the Department.

Prof. Gareth Pender and **Dr. Trevor Hoey** for their useful suggestions and advice on experimental aspects of the project.

Prof. Walter Graf of Laboratoire de Recherches Hydrauliques, Switzerland, for his pertinent suggestions, comments and advice on the content of this thesis.

Dr. Yusuf Kaya, Technical Director with the Babtie Group, for arranging a leave of absence from work, which allowed me to complete a substantial part of the write-up.

Prof. P.A. Davies, Department of Civil Engineering, University of Dundee, for his encouragement and support in allowing me time and resources to complete the thesis.

Tim Montgomery and **Willy Henderson,** laboratory technicians, for their strenuous efforts in developing and constructing the test facilities and equipment.

Dr. Vincent Peloutier, for his useful advice on experimental measurement techniques.

Okko Heinrich, former M.Sc. student, for his valuable assistance with the particle tracking experiments.

Dr. Ron Thomson and **Tim Lucas**, Department of Mechanical Engineering, for allowing access to their high-speed camera equipment and image analysis software.

Kenny McColl for solving all my IT problems and providing invaluable advice on all aspects of computing.

Finally, I would like to thank all my other colleagues within the Department, who were unfortunately too many to name individually, but who each made my study period at Glasgow University immensely enjoyable and a time I look back on with great fondness.

"Rivers are magnets for the imagination, for conscious pondering and subconscious dreams, thrills, fears. People stare into the moving water, captivated, as they are when gazing into a fire. What is it that draws and holds us? The rivers' reflections of our lives and experiences are endless . . ."

Tim Palmer, *Lifelines: The Case for River Conservation*, Dec. 1994.

Table of Contents

List of Figures

List of Tables

Chapter 7 Discussion and Analysis

Notation

Alphabetic Notation

A - cross-sectional flow area (L^2) (m^2).
an - coefficient of turbulence anisotropy.
B - channel width (L) (m).
B_r - integration constant from 'law-of-the-wall' logarithmic velocity profile.
C - sediment concentration ($M.L^{-3}$) ($mg.\ell^{-1}$).
C_0 - initial sediment concentration ($M.L^{-3}$) ($mg.\ell^{-1}$).
C_b - near-bed sediment concentration ($M.L^{-3}$) ($mg.\ell^{-1}$).
C_D - particle-fluid drag coefficient.
c - volumetric concentration of sediment (particle volume/fluid volume).
D - bed material grain size (L) (mm).
d - fine sediment particle/grain size (L) (μm or mm).
d_* - dimensionless particle parameter [$= d(\Delta g/\nu^2)^{1/3}$].
d'_* - dimensionless particle parameter for fluid-sediment mixture [$= d(\Delta' g/\nu'^2)^{1/3}$].
F - Newtonian drag resistance on a sphere ($M.L.T^{-2}$) ($kg.m.s^{-2}$).
F_r - Froude number [$= \bar{U}(gH)^{1/2}$].
f - frequency of vortex shedding (T^{-1}) (s^{-1} or H_z).
f_b - Darcy-Weisbach friction factor for bed material.
g - gravitational acceleration ($L.T^{-2}$) ($m.s^{-2}$).
H - flow depth (L) (m).
H_L - threshold value for detection of fluid ejection and inrush events.
I_R - fine sediment input rate ($M.T^{-1}$) ($g.s^{-1}$).
k_s - Nikuradse equivalent sand roughness height (L) (m).
k_s^+ - non-dimensional roughness Reynolds number ($= k_s u_*/\nu$).
L - sediment deposition length (L) (m).
l - turbulent mixing length (L) (m).
p - probability of particle deposition.
Q - flow rate ($L^3.T^{-1}$) ($m^3.s^{-1}$).
R - characteristic vortex radius (L) (m) and hydraulic radius (L) (m).
R_e - flow Reynolds number ($= 4\bar{U}H/\nu$).
R_{ep} - particle Reynolds number ($= w_s d/\nu$).
R_{e*p} - particle Reynolds number relating to shear velocity u_* ($= u_* d/\nu$).
R_{uw} - correlation coefficient for the Reynolds stress [$= \overline{u'w'}/(u'_{rms}w'_{rms})$].
r - radial distance from vortex centre (L) (m).
S - Strouhal number for vortex shedding ($= fD/U_{max}$).
S_0 - channel bed slope.
SF - triaxial particle shape factor.
S_f - slope of the energy line (~S_0 for steady, uniform flow).
$Sk_{w'}$ - skewness coefficient for vertical fluid velocity fluctuations w'.
S_s - specific density of sediment ($= \rho_s/\rho$).
S_t - particle Stokes number ($= t_d/t_f$).
T - half-life of particle suspension ($\equiv \tilde{L}/\bar{U}$) (T) (s).
T_B - turbulent bursting period (T) (s).

T_D - mean duration of turbulent burst events (T) (s).
T_{LF} - Lagrangian integral time scale for fluid (T) (s).
T_{LS} - Lagrangian integral time scale for sediment particles (T) (s).
$\overline{T}_s$ - time scale for vortex shedding period (T) (s).
t_a - aerodynamic particle response time scale (T) (s).
t_f - characteristic time scale associated with fluid motion (T) (s).
t_s - characteristic time scale associated with particle settling (T) (s).
U, u - mean component of longitudinal flow velocity ($L.T^{-1}$) ($m.s^{-1}$).
U_r - instantaneous vortex circulation velocity ($L.T^{-1}$) ($m.s^{-1}$).
u' - turbulent component of longitudinal flow velocity ($L.T^{-1}$) ($m.s^{-1}$).
u_* - shear velocity ($L.T^{-1}$) ($m.s^{-1}$).
u_s - streamwise particle velocity ($L.T^{-1}$) ($m.s^{-1}$).
u'_s - fluctuating component of streamwise particle velocity ($L.T^{-1}$) ($m.s^{-1}$).
V_T - terminal rise speed of a bubble in still water ($L.T^{-1}$) ($m.s^{-1}$).
v - mean component of lateral fluid velocity ($L.T^{-1}$) ($m.s^{-1}$).
w - mean component of vertical fluid velocity ($L.T^{-1}$) ($m.s^{-1}$).
w' - fluctuating component of vertical fluid velocity ($L.T^{-1}$) ($m.s^{-1}$).
w_* - parameter accounting for relative influence of gravity and turbulence on vertical particle motion ($= w_s H/2\varepsilon_s \sim w_s/u_*$).
w_d - particle deposition velocity ($L.T^{-1}$) ($m.s^{-1}$).
w_s - terminal particle fall velocity in still water ($L.T^{-1}$) ($m.s^{-1}$).
w_{sm} - still water fall velocity for concentration of particles ($L.T^{-1}$) ($m.s^{-1}$).
w'_s - particle fall velocity in turbulent flow ($L.T^{-1}$) ($m.s^{-1}$).
$\overline{w}'_s, \widetilde{w}'_s$ - depth-averaged particle fall velocities in turbulent flow ($L.T^{-1}$) ($m.s^{-1}$).
w''_s - fluctuating component of turbulent particle fall velocity ($L.T^{-1}$) ($m.s^{-1}$).
X - width of particle trapping region within a vortex (L) (m).
x - downstream or streamwise distance (L) (m).
x_+ - streamwise wall units ($= x.u_*/\nu$).
y - lateral distance across width of channel (L) (m).
z - elevation above bed surface (L) (m).
z_+ - vertical wall units ($= z.u_*/\nu$).

Symbols

α - aspect ratio of flow ($= B/H$).
α_3 - mean value of the lognormal distribution.
α_r - particle position relative to vortex centre ($= x/R$).
β - empirical constant relating ε_s to ε_f (i.e. $\varepsilon_s = \beta.\varepsilon_f$).
β_3 - standard deviation of the lognormal distribution.
χ - displacement vector of a particle relative to centre of vortex.
Δ - $(\rho_s - \rho)/\rho$.
Δ' - $(1 - c)\Delta/(1 + c\Delta)$.
Δ_0 - average sediment deposition rate ($M.T^{-1}.L^{-2}$) ($g.s^{-1}.m^{-2}$).
Δ_b - local bed sediment deposition rate ($M.T^{-1}.L^{-2}$) ($g.s^{-1}.m^{-2}$).
Δt - time step (T) (sec.).
Δu - velocity difference across a mixing layer or vortex ($L.T^{-1}$) ($m.s^{-1}$).
δ - mixing or boundary layer thickness (L) (m).
δz - bed reference or 'zero velocity' level (L) (m).
ε_f - transfer coefficient for fluid momentum ($L^2.T^{-1}$) ($m^2.s^{-1}$).

ε_s - sediment diffusion coefficient ($L^2.T^{-1}$) ($m^2.s^{-1}$).
ϕ - characteristic diameter of large-scale vortices (L) (m).
Γ - sediment particle trapping parameter (= $\Delta u/w_s$).
γ - experimentally-determined coefficient relating w'_{rms} and w'_s.
κ - von Karman's constant (= 0.4, assumed).
λ - bed porosity.
μ - dynamic viscosity of fluid ($M.L^{-1}.T^{-1}$) ($kg.m^{-1}.s^{-1}$).
ν - kinematic viscosity of fluid (= μ/ρ) ($L^2.T^{-1}$) ($m^2.s^{-1}$).
ν' - kinematic viscosity of fluid-sediment mixture ($L^2.T^{-1}$) ($m^2.s^{-1}$).
ν_t - turbulent eddy viscosity ($\equiv \varepsilon_f$) ($L^2.T^{-1}$) ($m^2.s^{-1}$).
Π - sediment particle relaxation parameter (= $\Delta u^2/g\delta$).
Π_i - i^{th} non-dimensional group from dimensional analysis.
ρ - density of fluid ($M.L^{-3}$) ($kg.m^{-3}$).
ρ_s - density of sediment ($M.L^{-3}$) ($kg.m^{-3}$).
ρ'_s - submerged density of sediment ($\rho_s - \rho$)($M.L^{-3}$) ($kg.m^{-3}$).
τ - total shear stress ($M.L^{-1}.T^{-2}$) (Pa).
Ω - rotation frequency of large-scale vortices (T^{-1}) (H_z or s^{-1}).
Ω_0 - vorticity or rotation frequency of solid-body vortex (T^{-1}) (H_z or s^{-1}).

Other Variable Subscripts

16,50,84- 16^{th}, 50^{th} and 84^{th} percentile of fine sediment or bed material size (L) (μm or mm).
b - relating to the bed surface.
Cb - relating to near-bed sediment concentration samples (Series 2).
dep - relating to deposited sediment samples (Series 2).
f - variables relating to fluid.
i - fraction size index.
j - centreline sediment trap index (Series 2).
max - maximum value.
min - minimum value.
rms - root-mean-square value.
s - variables relating to fine sediments.
sf - variables relating to free surface.

Special Notation

$\langle x \rangle$ - experiment-averaged value of any variable x.
$\tilde{x}$ - median value of any variable x.
$\bar{x}$ - mean value of any variable x.
$|x|$ - absolute value of any variable x.
$\sigma(x)$ - standard deviation of any variable x.
$\vec{x}$ - variable x displayed in vector form.
$\sim x$ - approximately equal to x.

Convention

Unless otherwise stated, the convention shown schematically below has been adopted in this study. The notable exception to this is vertical particle motions, which are generally described as being positive in the downward direction, i.e. particle fall velocities are positive.

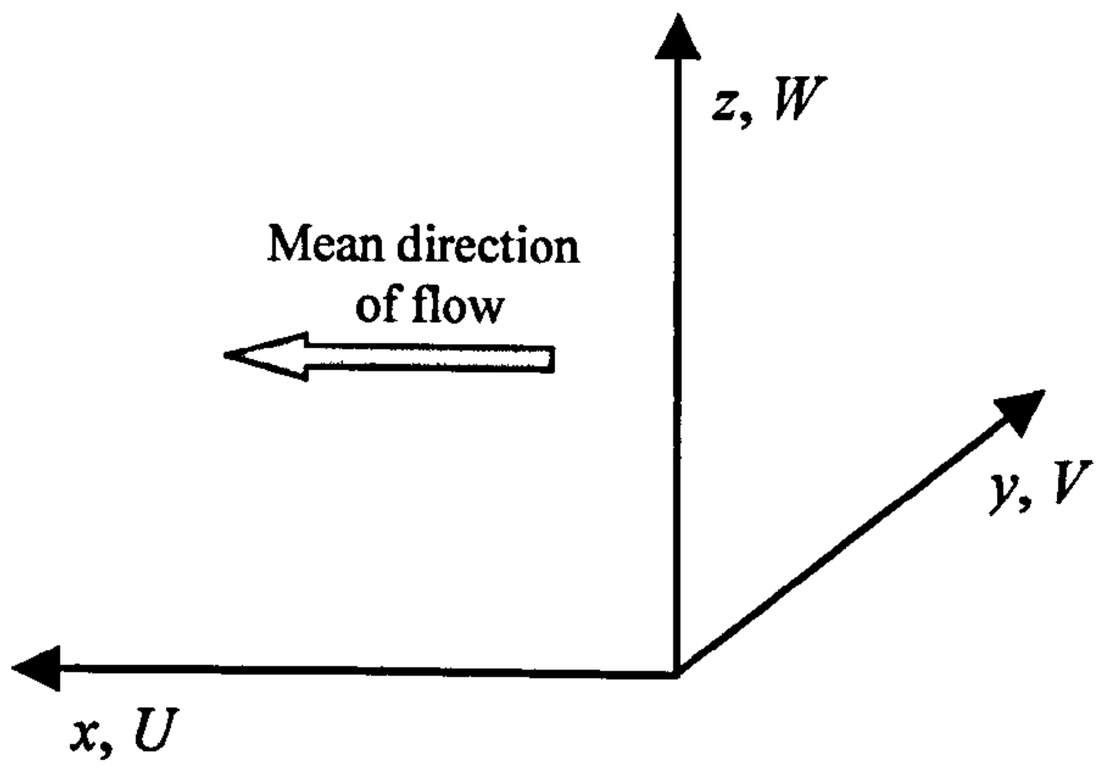

CHAPTER 1

Introduction

1.1 Sedimentation Processes in Gravel-bed Rivers

Rivers and streams can be perceived to represent the main arteries of the hydrological cycle, transporting rainfall and snowmelt from surrounding upland catchment areas in self-formed channels towards lakes, reservoirs and oceans. As a by-product, they also provide the primary medium for the downstream transportation of sediments and solutes, generated through natural weathering processes or as a consequence of human activity within the surrounding catchment. The generic term '*sedimentation*' has been widely used to encompass some or all of the physical processes associated with sediment transport. These processes, having exerted significant influence on the topography and stratification of the earth's surface throughout geological time, continue to control the formation and evolution of rivers, lakes, estuaries and coastal areas (Yalin, 1977).

The sedimentation regime within a gravel-bed river or stream is predominantly governed by the reaction of *intrinsic* controls within the local, in-bank channel environment to changes in *extrinsic* controls such as peak discharge, flood frequency, sediment load and characteristics (Sear, 1992). Steep upland gravel-bed rivers are particularly dynamic environments, reacting quickly to abrupt changes in discharge and/or upstream sediment supply by adjusting the balance between in-bank erosion and deposition processes. On a river reach scale, this balance or equilibrium can have a direct influence on channel morphology, while more locally, it can affect the composition and structure of the gravel bed.

Gravel-bed rivers often display a wide range of grain sizes at any one location (Ashworth and Ferguson, 1989). In many cases, the grain size distribution of fluvial gravels is distinctly bimodal in nature (Kuhnle, 1993), comprising of a primary

coarser gravel mode (referred to as *framework* material, $D > 2$mm) and a secondary finer sediment mode (*matrix* material, $d \leq 2$mm). In general, the framework material provides the main structure of the gravel bed (i.e. *framework* or *clast-supported*), with finer matrix sediment residing within interstitial spaces or voids formed between the framework elements. The source of framework gravels is typically derived from the erosion of existing in-bank fluvial deposits, while a large proportion of the matrix-sized sediments is derived from erosion within the surrounding catchment. The ingress of these fine sediments into gravel-bed rivers and streams as a result of surface run-off is considered to be a significant non-point source pollution problem (Diplas and Parker, 1992) with possible deleterious impacts on the overall ecology of the river. It is therefore of considerable practical importance to understand the exact nature of sedimentation processes determining the transportation and fate of fine sediments within gravel-bed rivers in order to assess their relative impact on the river environment. These processes are shown schematically in Figure 1.1 overleaf.

Following release into the stream flow, an influx of fine sediment can be transported in the mean direction of flow both as suspended load and bedload. The predominant mode of transport will depend on sediment characteristics (i.e. size, shape and density) and on the mean and turbulent characteristics of the river flow (Celik and Rodi, 1988). During this transportation phase, the tendency for suspended sediments to settle towards the bed surface will largely depend on the relative influence of gravitational and flow turbulence effects, which is precisely the main topic of investigation within the current study.

Fine sediments only then become available for deposition on reaching the bed surface. The deposition process represents the vertical transfer of fine sediments between the near-bed flow and the surface interstices within the gravel bed, and is primarily dependent on the bed surface characteristics and near-bed turbulent flow conditions (Peloutier, 1998). Once deposited, the fine sediment particles can infiltrate into deeper subsurface interstices, principally under gravitational settling. The depth to which infiltration can occur is generally accepted to depend on the geometric constraints imposed by the fine sediment grain size to framework pore size ratio (Frostick et al. 1984; Lisle 1989). This infiltration process can give rise to large accumulations of matrix sediments becoming trapped within the gravel bed as their removal through re-entrainment is governed by flow conditions within the river.

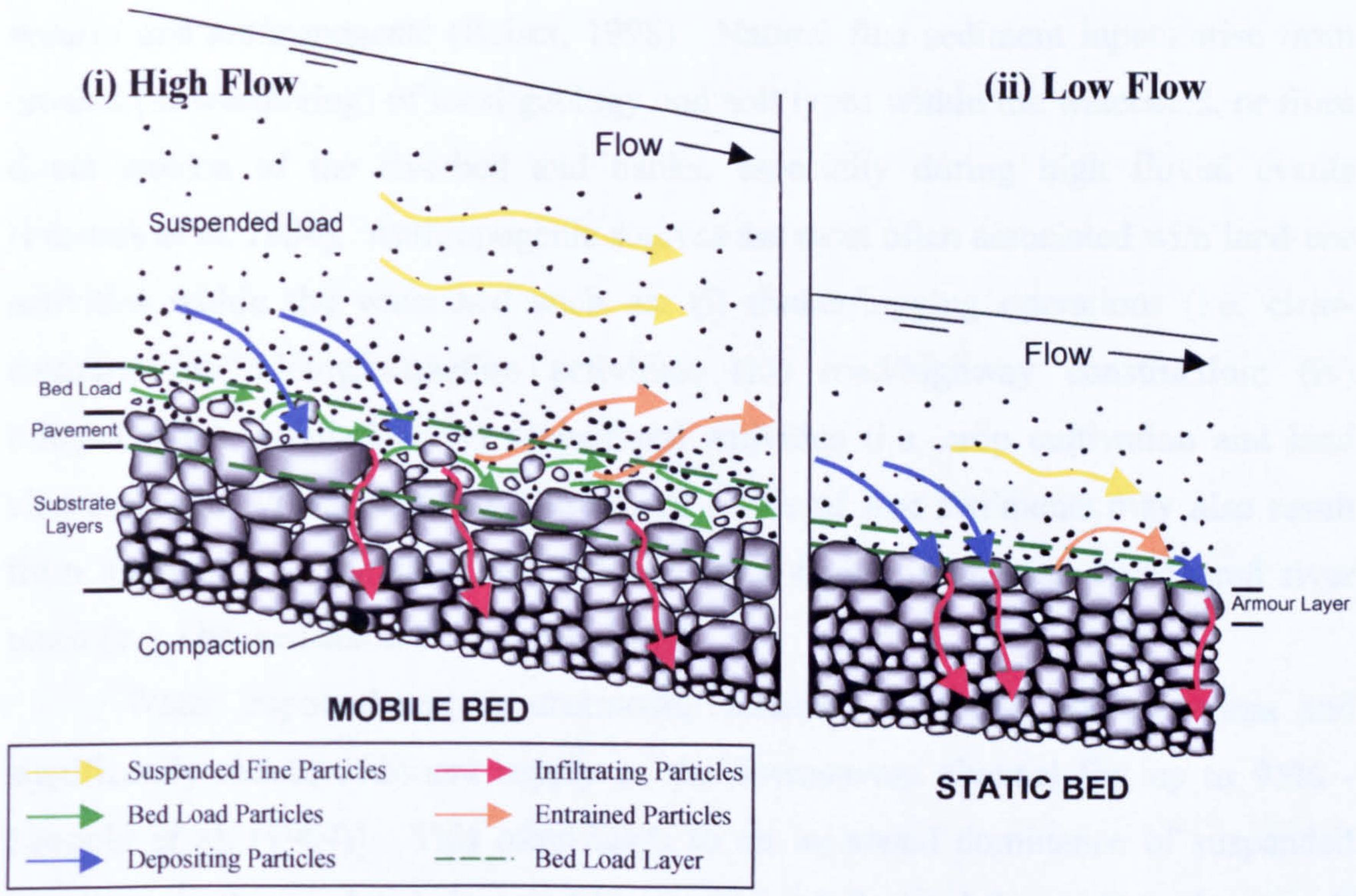

Figure 1.1 – Schematic representation of the sedimentation processes within a framework -supported gravel-bed river for (i) *active* bed conditions; (ii) *static* bed conditions.

Extended periods of low flow conditions (i.e. during the summer months) typically result in the formation of a static or *armoured* pavement layer at the bed surface [Figure 1.1(ii)], which is markedly coarser than the substrate material (Parker et al. 1982). This layer protects the subsurface matrix sediments from erosion and allows large accumulations to develop within the bed. Removal of these matrix sediments requires mobilisation of the pavement layer (Milhous 1973; O'Brien 1987; Diplas and Parker 1992). Under high fluvial flows [Figure 1.1(i)], pavement mobilisation allows virtually all bed grain sizes to be set in motion within an active layer at the bed surface, in a condition commonly referred to as *equal mobility* (Parker et al. 1982). The corresponding entrainment of accumulated matrix sediments from subsurface bed interstices can result in high suspended sediment rates occurring during large fluvial events [observed to range between 75-94% of the total clastic load in field studies by Lisle (1989)].

1.2 Sources of Fine Sediments

Sources of fine sediment inputs can be broadly categorised in two groups: *natural* and *anthropogenic* (Reiser, 1998). Natural fine sediment inputs arise from erosion (or weathering) of local geology and soil types within the watershed, or from direct erosion of the riverbed and banks, especially during high fluvial events (Frostick et al. 1984). Anthropogenic sources are most often associated with land-use activities within the watershed such as: (i) timber/logging operations (i.e. clear-cutting); (ii) mining/extraction activities; (iii) road/highway construction; (iv) bridge/culvert installation; (v) agricultural activities (i.e. crop cultivation and land clearing); and (vi) urbanisation. Increased levels of fine sediments may also result from alterations to the flow and sedimentation regime within an engineered river reach (e.g. channelisation or straightening).

Water impoundment or abstraction schemes eliminate flood maxima and significantly reduce sediment supply to the downstream channel [by up to 95% - Leopold et al. (1964)]. This often leads to an increased dominance of suspended sediments in the regulated river and larger accumulations of fines within the gravel-bed (Sear 1993), particularly downstream of unregulated tributaries (Carling 1988; Petts 1984). The loss of channel competence resulting from the elimination of high fluvial flows also prevents the removal of these accumulated sediments, except from the very surface layer of the gravel bed.

1.3 Environmental and Ecological Implications

In the context of relative ecological impact, anthropogenic derived sources result in significantly higher fine sediment influxes into gravel-bed rivers than natural sources (Diplas and Parker, 1992), with induced erosion rates up to one hundred times higher than those occurring normally (Julien, 1995). While suspended sediment concentrations are relatively low in UK gravel-bed rivers by worldwide standards [<500 $mg.l^{-1}$ generally and rarely >5000 $mg.l^{-1}$ (Walling and Webb, 1987)], their presence may still impact on the streambed habitat; aquatic biota; physical and chemical water quality; and amenity value of the river.

Having evolved around geological, hydrological and sedimentary conditions, aquatic ecosystems provided by gravel-bed rivers and streams are highly sensitive to physical change. For instance, an increased fine sediment influx is generally accepted

to have a detrimental effect on the aquatic habitat and stream biota therein (Carling, 1984), most notably in the spawning success of salmon and other species of fish (Iwamoto et al., 1978). Large accumulations of fines within spawning gravels can reduce bed permeability and inter-gravel flow, essential for the removal of toxic wastes produced by the buried eggs and for the provision of adequate dissolved oxygen levels required for the growth and development of alevin (Diplas and Parker, 1992). They can also reduce the diversity and population of the benthic invertebrates that provide an important food resource for the fish emerging from the inter-gravel environment (Gibbons and Salo, 1973).

High turbidity levels within the river flow can affect the respiratory mechanism of fish species through gill abrasion and clogging. Significant reductions in photosynthesis and organic matter production (e.g. algae and plankton), which are basic food sources for the aquatic environment, can also result from the attenuation of light penetration due to high suspended sediment levels within the river.

Pollutants such as metals, salts, nutrients, pesticides and persistent organic compounds can be introduced into the aquatic environment through adsorption in sediments. Owing to their greater surface area to volume ratio, fine sediment particles will adsorb relatively larger quantities of pollutants than larger sediment particles. A significant and long-term threat to the aquatic habitat is therefore posed from reduced water quality and deep infiltration of contaminated fines in gravel-bed rivers.

The amenity and recreational value of a gravel-bed river may also diminish as a direct result of increased levels of fine sediments, although this is primarily related to their detrimental effect on the aquatic environment as a whole (i.e. through the reduction in fish population and water quality).

1.4 Basis for Current Study

Knowledge of the physical processes governing the behaviour of fine sediments in gravel-bed rivers clearly represents an important area of research for engineers, sedimentologists and biologists alike. The fate of a fine sediment influx into the river environment has been determined to depend on a sequence of four interrelated sedimentation processes, i.e. (i) transportation and settling within the main body of flow; (ii) deposition at the bed surface (iii) deeper infiltration within the gravel bed; and (iv) re-entrainment and re-suspension. The balance between these

processes is controlled by external factors such as mean and turbulent flow characteristics; river channel geometry; fine sediment load; and bed composition and structure.

A significant portion of the total fine sediment load transported in gravel-bed rivers is often carried in suspension at a rate close to the streamflow velocity (Raudkivi, 1990), with an additional downward movement towards the bed as a result of gravitational settling effects (Alonso, 1981). Turbulent fluctuations within the surrounding fluid also affect the motion of the suspended sediment particles.

Knowledge of particle fall velocity within the turbulent flow environment is a clear prerequisite for accurate quantitative analysis of suspended sediment transport processes. However, no substantial body of evidence has yet been presented detailing the influence that turbulent fluctuations within the flow have on the particle fall velocity. Accordingly, it is often assumed that the average fall velocity of sediment particles is unaffected by turbulence and equivalent to the terminal fall velocity in still water conditions, although the validity and limitations of this general assumption are not presently known.

Suspended sediment particles are also diffused as a result of turbulent mixing processes and random molecular motions within the surrounding fluid, though molecular diffusion is usually insignificant in highly turbulent flows and therefore often neglected. Diffusion coefficients are commonly specified to describe these turbulent and molecular mixing processes, with the traditional assumption that the turbulent diffusion of sediment particles is analogous to the momentum transfer of fluid elements within turbulent flow. This analogy allows the turbulent diffusion coefficient for sediment particles to be related to the eddy viscosity through a simple empirical coefficient. It is acknowledged, however, that there are inherent theoretical deficiencies in this analogy (Cao et al. 1996) and that the exact nature of turbulent mixing processes affecting the vertical transfer of suspended sediments are not as yet completely understood.

Near-bed turbulence also has a significant influence on the exchange of fine sediments at the surface interface of a gravel bed, resulting from deposition and entrainment processes. At an interstitial scale, the structure of near-bed turbulence will be affected by spatial variations in the configuration of framework gravels at the bed surface, the influence of which is difficult to determine mathematically (Peloutier,

1998). Additionally, the reworking of surface gravels during periods of high fluvial flow will further complicate this problem. This is reflected in most existing exchange models, which generally take no account of the effect near-bed turbulence has on the deposition and entrainment fluxes. In such cases, these fluxes and the net exchange at the bed surface interface are often defined solely in terms of the products of near-bed and empirically-derived equilibrium concentrations and the terminal fall velocity in still water conditions (e.g. van Rijn 1984; Celik and Rodi 1988). Recent studies by Peloutier (1998) indicated that while the deposition flux was indeed linearly proportional to the near-bed concentration, the transfer rate across the bed surface interface was significantly influenced by near-bed turbulence and often varied considerably from the still water fall velocity.

Overall, it is clear that turbulent fluid motions play a primarily role in sediment particle transport, deposition and entrainment processes within a gravel-bed river. However, the complexity of the particle-turbulence interactions that exist in each case may account for the substantial simplifications and empiricism generally relied upon to describe these processes mathematically. Clearly, any progress in understanding the underlying mechanisms controlling these fine sediment transport processes requires increased awareness of the characteristics of flow turbulence. In this respect, the identification and knowledge of quasi-ordered or coherent structures now known to be present within turbulent open channel flows is essential in advancing the physical understanding of how fine sediments behave in a turbulent flow environment and how they are exchanged at the bed surface. These coherent structures have already been identified to play a central role in particle entrainment in the near-bed flow region (e.g. Sumer and Oguz 1978; Sumer and Deigaard 1981; Kaftori et al. 1995a,b; Niño and Garcia 1996). One of the main aims of this current research is the assessment of how these coherent structures may influence the motion of fine sediment particles during the transport/settling and deposition stages of the overall sedimentation process within an open channel shear flow over a rough, porous bed surface.

1.5 Summary of Main Points and Specific Objectives of Study

The ingress of increased quantities of fine sediments into gravel-bed rivers can have a significant impact on the composition and structure of the bed, as well as on

the fine suspended sediment load, both of which pose significant problems for the ecology of the river. The sedimentation processes by which fine sediments are transported, deposited and entrained within gravel-bed rivers are predominantly controlled by complex interactions between the turbulence and the sediment particles, which are insufficiently understood or researched at present. In respect of the vertical transfer of the fine sediments within turbulent open channel flow conditions, common assumptions made with regards to the influence of turbulence on particle fall velocity require clarification, as does the implied analogy between the turbulent diffusion of sediment particles and the momentum transfer of fluid elements. At the bed surface interface, the deposition process has previously been shown to be primarily dependent on sediment concentration (e.g. Carling 1984; Peloutier 1998). However, sufficient uncertainty remains over the nature of particle-turbulence interactions at the bed surface interface to warrant further investigation and determine how these affect the deposition characteristics of the sediment particles between the near-bed flow and the surface interstices.

Two series of laboratory experiments were carried out in flume facilities situated within the Department of Civil Engineering at the University of Glasgow. These experiments were designed to investigate the motion of fine sediment particles within a turbulent open channel shear flow over a rough, porous bed and their deposition characteristics between the near-bed flow and the surface layers of the bed. The first series of experiments employed various visualisation techniques to record and analyse particle motions within these flow regions (Series 1A and 1B) and subsequently observe typical interactions between the sediment particles and large-scale structures present within the shear flow (Series 1C). In the second series of experiments (Series 2), the processes of fine sediment transport and deposition were studied using more traditional concentration sampling techniques and measurements of deposition rate.

The main aims of the investigation were: (1) to identify the influence of turbulence and other experimental parameters on sediment particle motion and the fall velocity in particular; (2) to determine how this behaviour may be related to observed interactions between the sediment particles and the large-scale turbulent structure of the flow; (3) to establish the mechanisms responsible for the deposition of particles at the bed surface interface; (4) to attempt to present the findings from the two

experimental series in analytical form and show how they may be applied in a numerical modelling framework for fine sediment transport modelling.

This introductory chapter is followed by a wide-ranging review of literature relevant to the current study (Chapter 2). Chapter 3 outlines the experimental work by describing: (i) the two flume facilities in which the experiments were performed; (ii) the development of experimental procedures; (iii) the properties of bed materials and fine sediments tested; and (iv) the instrumentation and equipment used. Chapters 4, 5 and 6 present the main results and findings from the two experimental series. Discussion and analysis of these results is presented in Chapter 7, while Chapter 8 concludes a final summary of the main experimental findings and discusses their wider implications.

CHAPTER 2

Literature Review

2.1 Introduction

The competing effects of turbulent fluid motions and gravity are the predominant control on suspended sediment transport within a turbulent open channel flow. Bagnold (1966) stated that a sediment particle will only remain in suspension when turbulent eddies prevalent in such flows have dominant vertical velocity components which exceed the downward motion of the particle due to gravity. In this context, the terminal fall velocity of sediment particles w_s is evidently an important parameter relating the vertical motion of the particles to the surrounding fluid. The fundamental concepts behind the terminal fall velocity and the factors controlling its magnitude are explored in §2.2.

The underlying physical mechanisms governing suspended sediment transport are, however, far more complex than Bagnold's criterion would suggest, partly realised through an improved understanding of the nature of turbulence. Extensive research over the last three decades or so has identified the existence of quasi-ordered or coherent structures responsible for the generation, maintenance and evolution of turbulence within boundary layer flows. Some of the main contributions to the current knowledge of coherent structures within the near-bed flow region over smooth and rough beds and their association with large-scale outer flow motions are discussed in §2.3.

The complex interactions that exist between discrete particles and coherent structures are acknowledged to exert considerable influence on the suspension and transport processes of fine sediments (Tooby et al. 1977), although knowledge of these particle-turbulence interactions remains predominantly qualitative at present. In particular, recent visualisation studies have revealed the primary role near-bed

coherent structures have in the entrainment and suspension of sediment particles from the near-wall flow (§2.4). Separate experimental investigations have also indicated that particle trapping within coherent vortices or eddies may be a key mechanism in the maintenance of particle suspension, a hypothesis which is investigated in §2.5.

At the bed surface of a gravel-bed river, the net exchange of fine sediment particles between the near-bed flow and surface bed layers is governed by the relative magnitudes of the deposition and entrainment fluxes (e.g. Cao, 1997). Previous experimental investigations of fine sediment deposition and infiltration processes into gravel-beds are described in §2.6, along with the factors controlling the re-entertainment of fine sediments from surface and subsurface interstices within the bed gravels.

In §2.7, the two modelling approaches traditionally employed to describe fine sediment transport and exchange processes at the bed boundary of an open channel flow, namely Eulerian diffusion theory and Lagrangian 'random walk' methods, are described. The implications of the substantial simplifications and assumptions based on empiricism that are traditionally adopted in these modelling techniques are also discussed. Finally, §2.8 summarises the main findings from the detailed literature review in relation to the outline objectives of the current study.

2.2 Sediment Fall Velocity in Quiescent Fluid

The fall velocity is a crucial concept figuring prominently in the quantitative analysis of all sediment transport problems. It describes the influence of gravity on the motion of a sedimentary particle in relation to the surrounding fluid medium.

Within quiescent fluid, the principal physical parameters controlling the fall velocity of a solitary sediment particle are its size, shape and density, as well as the density and viscosity of the fluid. Under such conditions, Stokes (1851) derived an expression for the viscous drag resistance of laminar flow around a sphere from the analytical solution of the simplified Navier-Stokes equations. Falling under the influence of gravity, a spherical particle will reach a *terminal* fall velocity w_s when its drag force balances the submerged weight of the sphere, i.e.

$$3\pi d\mu w_s = \frac{\pi d^3 g}{6}(\rho_s - \rho) \qquad \text{....(2.1)}$$

where d is the particle diameter, ρ_s the particle density, ρ and μ are the fluid density and viscosity, respectively, and g is the gravitational acceleration. By rearranging equation 2.1, an expression for the *terminal* fall velocity w_s, commonly known as the Stokes' Law, can be derived as follows,

$$w_s = \frac{1}{18}\frac{\Delta g d^2}{\nu} \qquad \ldots.(2.2)$$

where $\Delta = (\rho_s-\rho)/\rho$ and $\nu = \mu/\rho$ is the kinematic viscosity. Another common form of the Stokes' law utilises the Newtonian expression for drag resistance in the form,

$$F = C_D \frac{\pi}{4} d^2 \frac{\rho w_s^2}{2} \qquad \ldots.(2.3)$$

where C_D is the drag coefficient. Equating this with the viscous resistance term given in equation 2.1 yields an expression for the drag coefficient,

$$C_D = \frac{24\mu}{w_s d\rho} = \frac{24}{R_{ep}} \qquad \ldots.(2.4)$$

where R_{ep} is the particle Reynolds number ($=\rho w_s d/\mu$ or $w_s d/\nu$). Unfortunately, the resulting linear relationship between C_D and R_{ep} is only valid for $R_{ep} \leq 1$, deviating significantly from experimental data obtained for natural sand and gravel particles (i.e. Engelund and Hansen 1967) for larger R_{ep} values (Figure 2.1). Many researchers have attempted to extend the applicability of equation 2.4 to a wider range of flow conditions (e.g. Oseen 1927; Goldstein 1929; Raudkivi 1990). From consideration of these and other studies, Cheng (1997a) proposed a general non-linear relationship between C_D and R_{ep} for natural sediment particles of the form,

$$C_D = \left[\left(\frac{32}{R_{ep}}\right)^{(1/1.5)} + 1\right]^{1.5} \qquad \ldots.(2.5)$$

Based on this expression, Cheng (1997a) derived an explicit formula for the settling velocity of individual natural sediment particles, applicable within different regimes ranging from Stokes' flow ($R_{ep} \leq 1.0$) to high Reynolds number conditions ($R_{ep} = 10^3 \sim 10^4$);

$$w_s = \frac{\nu}{d}\left(\sqrt{25 + 1.2 d_*^2} - 5\right)^{1.5} \qquad \ldots.(2.6)$$

where d_* is the dimensionless particle parameter [$= d(\Delta g/\nu^2)^{1/3}$]. This equation was shown to have good predictive accuracy with previously published experimental data (US Inter-Agency Committee 1957; Raudkivi 1990). Within the current study, experimental measurements of still water fall velocity, carried out for calibration purposes, are compared with predictions obtained from equation 2.6 (see §4.2.3, pp.96).

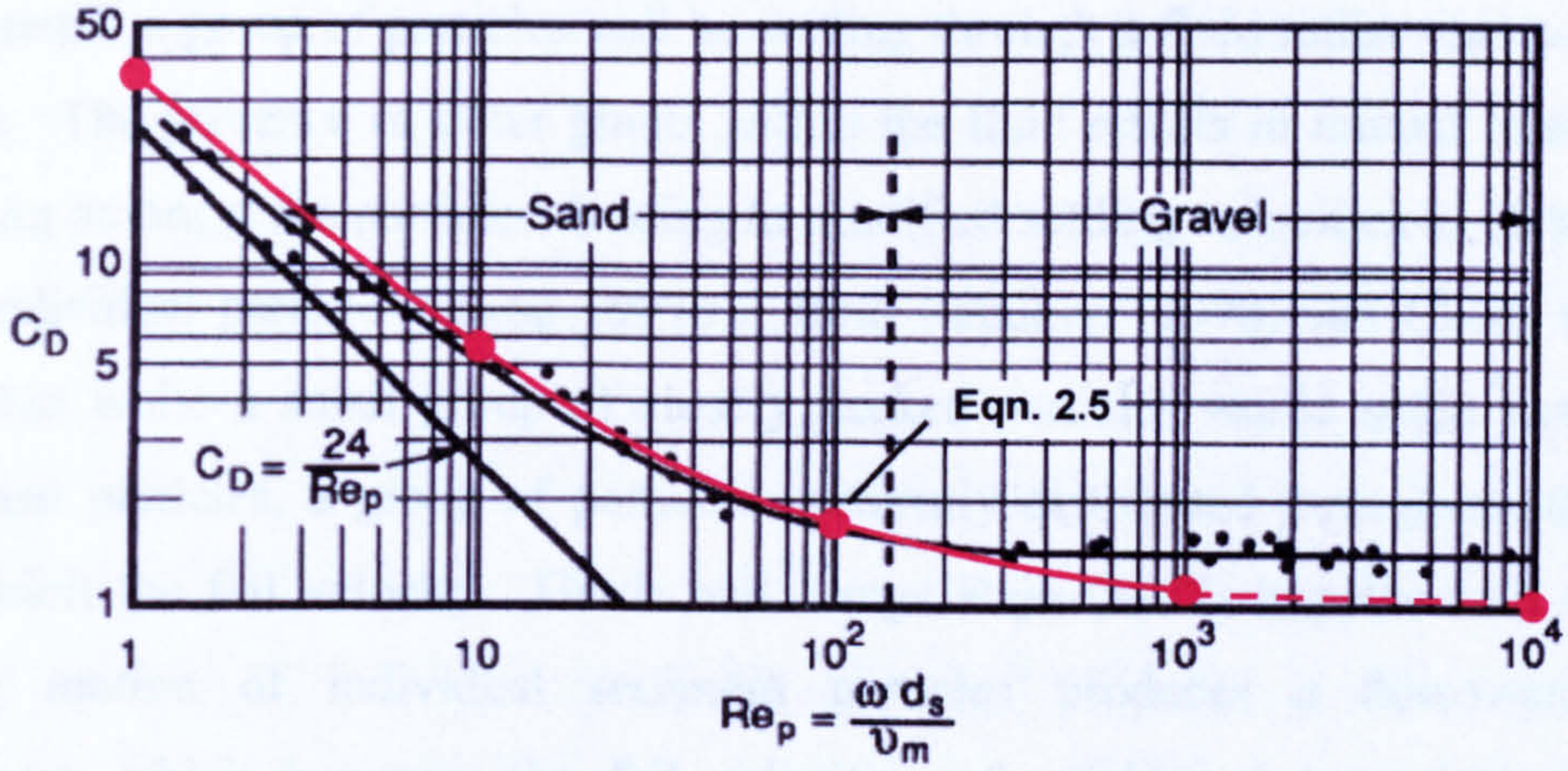

Figure 2.1 - Linear and non-linear drag coefficients for Stokes' solution (spheres) and natural sand and gravel particles (modified from Julien 1995)

2.2.1 Influence of Particle Shape

The influence of particle shape on the fall velocity is known to be dependent on the Reynolds number R_{ep} (Garde and Ranga Raju 1977). Within the Stokes' range, an irregular shaped particle settling in fluid will be stable in any orientation, with the drag coefficient essentially independent of particle shape. At higher Reynolds numbers, however, the particle will tend to settle with its maximum cross-sectional area normal to the direction of motion. At $R_{ep} > \sim 10^3$, oscillatory motions can develop as a result of lift forces acting on the particle, perpendicular to the direction of motion (Raudkivi 1990). A shape factor *SF*, based on the triaxial dimensions of the particle, is commonly used to account for the influence of particle shape on the fall velocity,

$$SF = c/(ab)^{1/2} \qquad \text{....(2.7)}$$

where a, b and c are the longest, intermediate and shortest particle dimensions, respectively. For constant R_{ep} values, particles with small *SF* values will clearly have larger drag coefficients than particles with high *SF* values (i.e. spheres). For naturally

worn sediment particles, typical *SF* values range from 0.6 to 0.7 (Garde and Ranga Raju 1977). It should be noted that equations 2.5 and 2.6 were derived by Cheng (1997a) from data obtained for natural sediment grains with $SF \sim 0.7$.

2.2.2 Influence of Concentration

In most practical applications where the fall velocity of sediment particles is encountered, a group of particles will be settling through a fluid rather than a solitary particle. The presence of other grains within the fluid results in mutual interactions occurring amongst the particles, leading to modified settling velocities in comparison to an individual particle (Cheng 1997b). Both Raudkivi (1990) and Cheng (1997b) noted that while a small group of closely packed particles would settle faster than individual particles, a group of particles uniformly distributed throughout the fluid will inhibit the fall velocity. Garde and Ranga Raju (1977) hypothesised that the settling motion of individual sediment particles produces a downward fluid movement, which increases the fall velocities of neighbouring particles. Some distance away from the particles, a compensatory upward fluid motion exists that can inhibit the settling velocity of particle within this region (Figure 2.2).

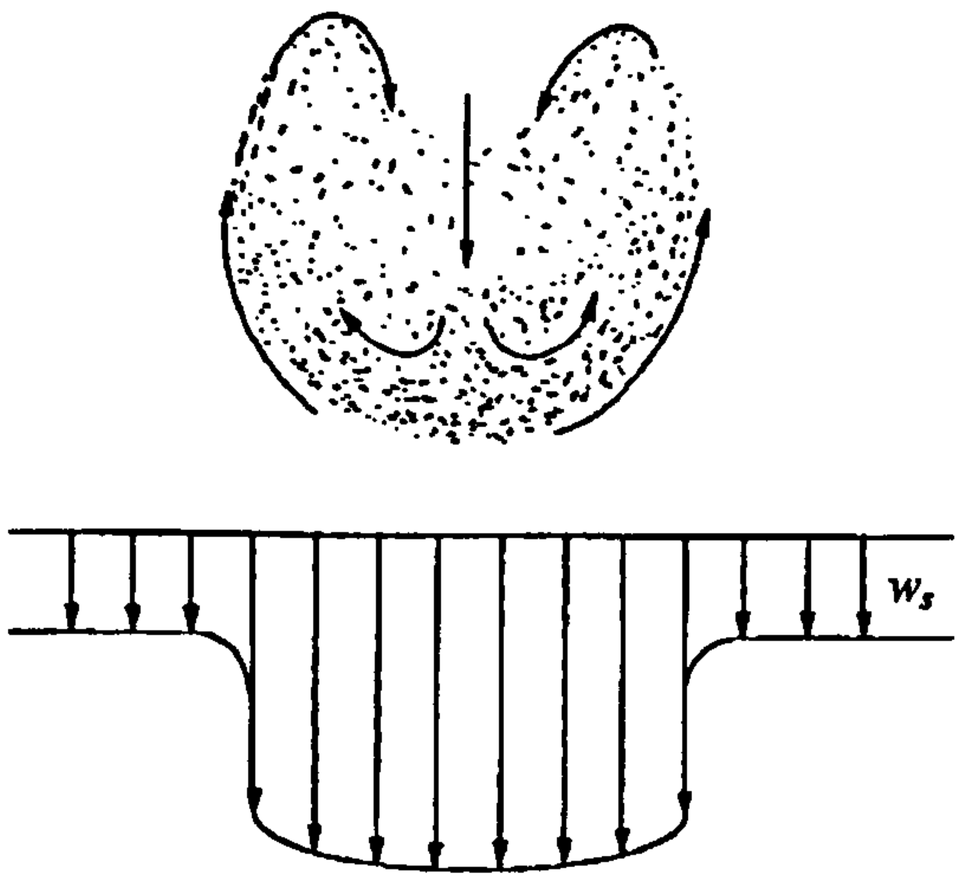

Figure 2.2 - Flow pattern around a group of closely packed grains (from Raudkivi 1990)

McNown and Lin (1952) revealed that increasing sediment concentration within the fluid would result in a reduction of the particles' settling velocity, dependent on the ratio of particle size *d* to the spacing of adjacent particles *s*. They proposed an empirical relationship of the form,

$$\frac{w_s}{w_{sm}} = 1.0 + 1.3\left(\frac{d}{s}\right) \quad \text{....(2.8)}$$

where w_{sm} is the settling velocity of the concentration of particles. For uniform sized particles (d constant), equation 2.8 clearly predicts that the ratio $w_s/w_{sm} \rightarrow 1$ as the spacing between particles increases (i.e. fall velocity approaches that of a single particle). Lewis et al. (1949) and Richardson and Zaki (1954) proposed an expression relating the ratio w_s/w_{sm} to the volumetric concentration c of particles uniformly dispersed within a fluid, which has the general form,

$$\frac{w_{sm}}{w_s} = (1-c)^n \quad \text{....(2.9)}$$

Richardson and Zaki (1954) proposed that exponent n is a function of R_{ep} and tends to different constants at low ($R_{ep} \leq \sim 0.1$) and high ($R_{ep} \geq 10^3$) particle Reynolds numbers. Through theoretical considerations, Cheng (1997b) found that n is also related to the density coefficient Δ [$= (\rho_s-\rho)/\rho$] and the volumetric concentration c. From equation 2.6, Cheng (1997b) derived a similar explicit formula to calculate the settling velocity of sediment particles dispersed in a fluid,

$$w_{sm} = \frac{\nu'}{d}\left(\sqrt{25 + 1.2d_*'^2} - 5\right)^{1.5} \quad \text{....(2.10)}$$

where d'_* is the dimensionless particle parameter for the fluid-sediment mixture [$= (\Delta' g/\nu'^2)^{1/3} d$, where $\Delta' = (1 - c)\Delta/(1 + c\Delta)$] and ν' is the viscosity of the fluid-sediment mixture.

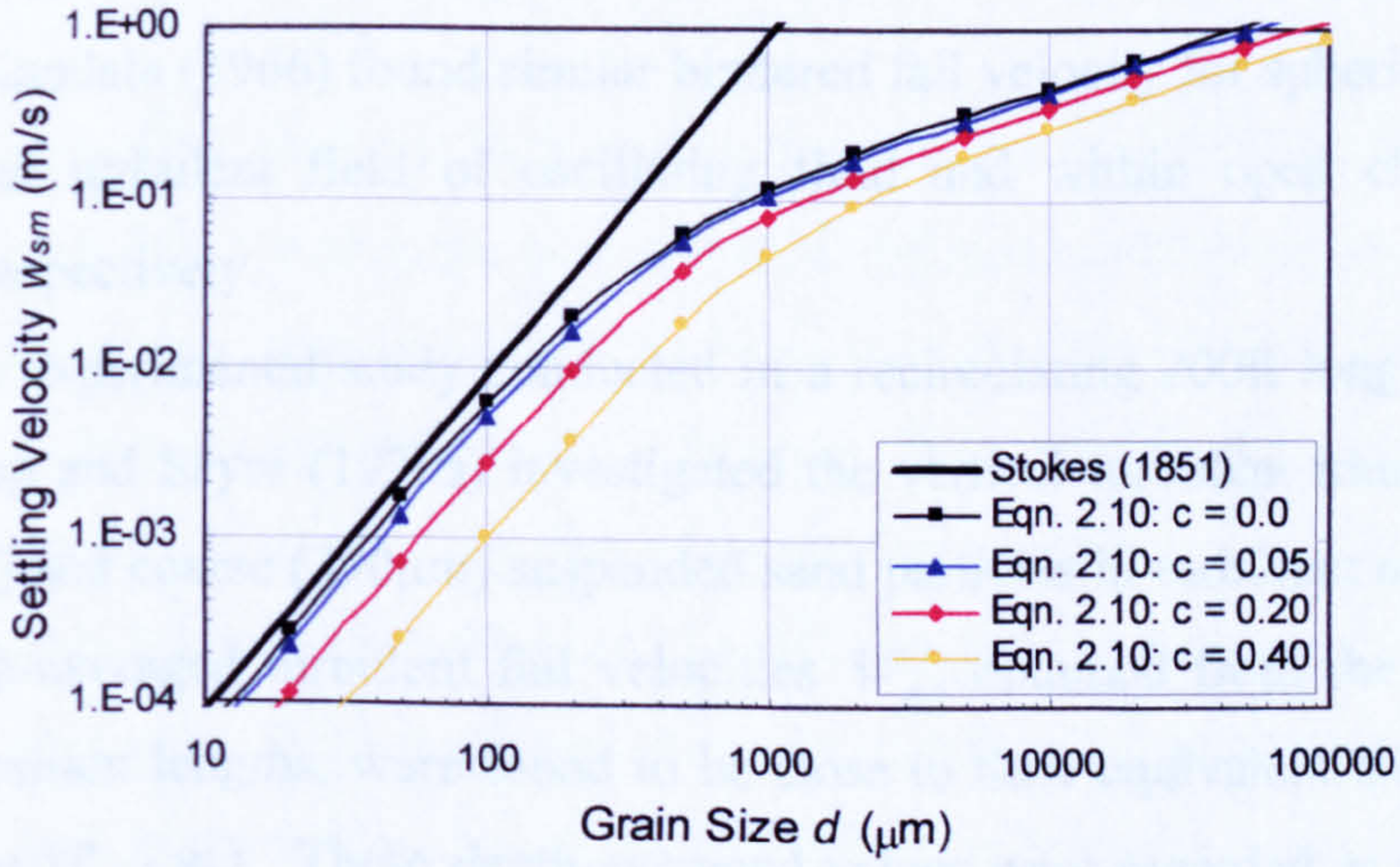

Figure 2.3 - Computed fall velocities from Cheng (1997b) for volumetic concentrations c = 0.0, 0.05, 0.20 and 0.40. Stokes (1851) law shown for comparison purposes

The inhibiting effects of concentration on the particle settling velocity are clearly demonstrated by plotting w_s values calculated from equations 2.6 and 2.10 for various concentrations c and particle sizes d (Figure 2.3 on the previous page). As an example, high concentrations of 100μm particles (i.e. $c = 0.4$) are predicted to settle at about an order of magnitude less than a solitary 100μm particle (i.e. $c = 0.0$)

2.2.3 Influence of Flow Turbulence

The turbulent nature of many of the environments in which sediment particle settling characteristics often require consideration (e.g. rivers, estuaries and coastal waters) brings into question the applicability of relationships derived solely for predicting the sedimentary fall velocity in still fluid conditions. Garde and Ranga Raju (1977) stated that these studies were no more than of general academic interest. While, it is widely acknowledged that flow turbulence will have some influence on the vertical motion of a particle, the nature of this influence (e.g. inhibiting or enhancing fall velocity) remains inconclusive.

Experimental investigations of the vertical motion of sediment particles in turbulent flow conditions are sparse and often inconsistent in their findings. Reynolds et al. (1990) measured the settling rate of Lycopodium spores (d_{50} = 34.6μm) in a recirculating open channel flow and found that their fall velocity w'_s in turbulent flow was only 0.5-0.6 of their equivalent still water fall velocity, generally becoming increasingly retarded with increasing turbulence. As no re-suspension of particles was observed from the channel bed, Reynolds et al. (1990) hypothesised that this retardation resulted from some unquantified feature of the turbulent velocity field. Ho (1964) and Kandala (1966) found similar hindered fall velocity for spherical particles settling in an turbulent field of oscillating fluid and within open channel flow conditions, respectively.

In an experimental study conducted in a recirculating 200ft long rectangular flume, Jobson and Sayre (1970a) investigated the vertical turbulent transfer of both fine (123μm) and coarse (390μm) suspended sand particles in turbulent open channel flow. Depth-averaged turbulent fall velocities $\overline{w}'_s$, obtained from the analysis of median deposition lengths, were found to be close to their equivalent still water fall velocities (i.e. $\overline{w}'_s \sim w_s$). These depth-averaged values were regarded as representing the lower limit of turbulent fall velocities, as the roughened non-porous bed

conditions sanctioned particle movements subsequent to their initial contact with the bed surface.

By contrast, the turbulent fall velocities w'_s calculated from integrated concentration profiles were on average 3-6% higher than the still water fall velocity for the coarser 390μm sand and between 38% and 65% higher for the finer 123μm sand (Figure 2.4). The authors ascribed this apparent enhancement of particle fall velocity to a combination of particle grouping effects resulting from the sediment injection system and to non-specified flow turbulence effects. Unfortunately, neither of these effects could be completely isolated to determine their relative influence.

The authors concluded that the dominant vertical transfer mechanism for the coarse sand grade was gravity, while turbulent diffusion was found to represent the dominant vertical transfer mechanism for the fine sand grade. Flow turbulence was determined, at least in some part, to result in enhanced fall velocities compared with those measured in still water conditions.

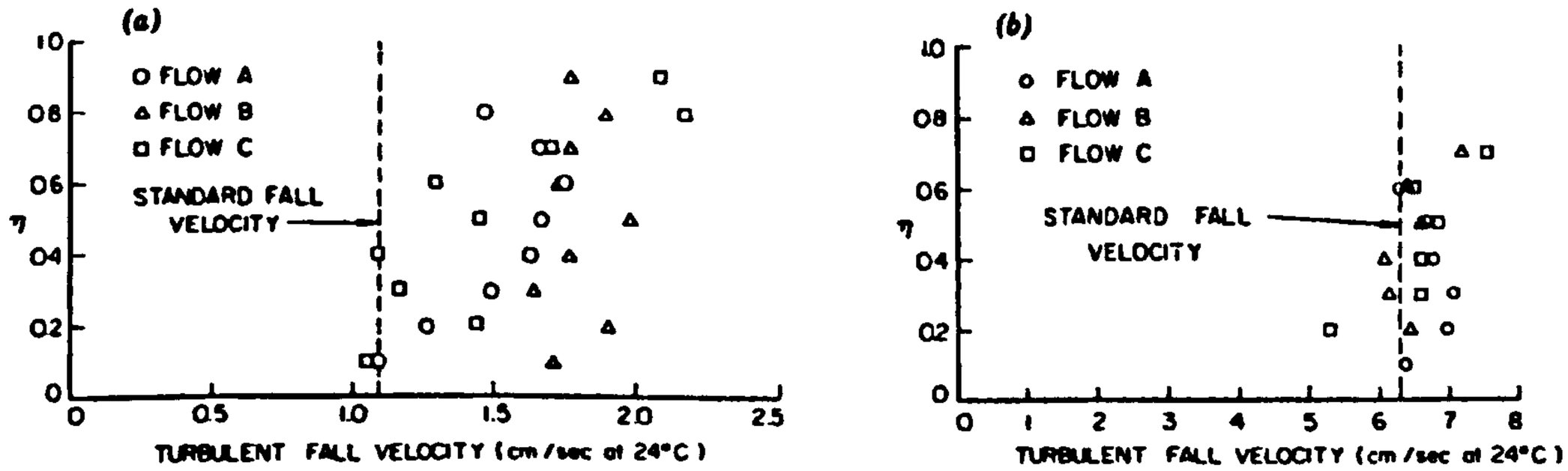

Figure 2.4 - Turbulent fall velocities for sediments settling in open channel flow: (a) fine 123μm sand; (b) coarse 390μm sand (from Jobson and Sayre 1970)

In experiments studying sedimentation processes in settlement tanks, Camp (1943) proposed that the change in suspended sediment concentration, as particle settlement occurs, is a function of a parameter $w_* = w_s H/2\varepsilon_s$ (where H is the flow depth and ε_s is the sediment diffusion coefficient). This variable, a form of the Peclet number, represents the ratio of the characteristic settling rate (w_s/H) to the characteristic rate for turbulent diffusion ($2\varepsilon_s/H^2$) and defines the competing effects of gravity and turbulence. With the assumption that the shear velocity $u_* \approx 2\varepsilon_s/H$ (Hoyal et al. 1995), the parameter w_* is clearly equivalent to the ratio w_s/u_*. Analysis of Camp's sedimentation data led Owen (1969) to define a range of w_* values, i.e. 0.005

$< w_* <$ 5.0, where both gravity and turbulence were found to affect the settling characteristics of sediment particles.

Hoyal et al. (1995) employed a two-dimensional Lagrangian (random walk) model to investigate these competing effects on the vertical transfer of sediment particles to a fully absorbing bed boundary. The results indicated three distinct regions of particle behaviour dependent on the magnitude of w_* (Figure 2.5). For 'heavy' particles with $w_* > 1.0$, the vertical transfer of the sediment particles was dominated by gravity, with the turbulent fall velocity w'_s equal to the still water fall velocity w_s. A transitional region defined by $0.1 < w_* < 1.0$ was determined where both gravity and turbulent diffusion influence the vertical transfer of particles, a condition found to result in enhanced turbulent fall velocities (i.e. $w'_s > w_s$). Finally, the vertical transfer of 'light' particles with $w_* < 0.1$ was dominated by turbulent diffusion and turbulent fall velocities were predicted to be greatly enhanced (i.e. $w'_s >> w_s$).

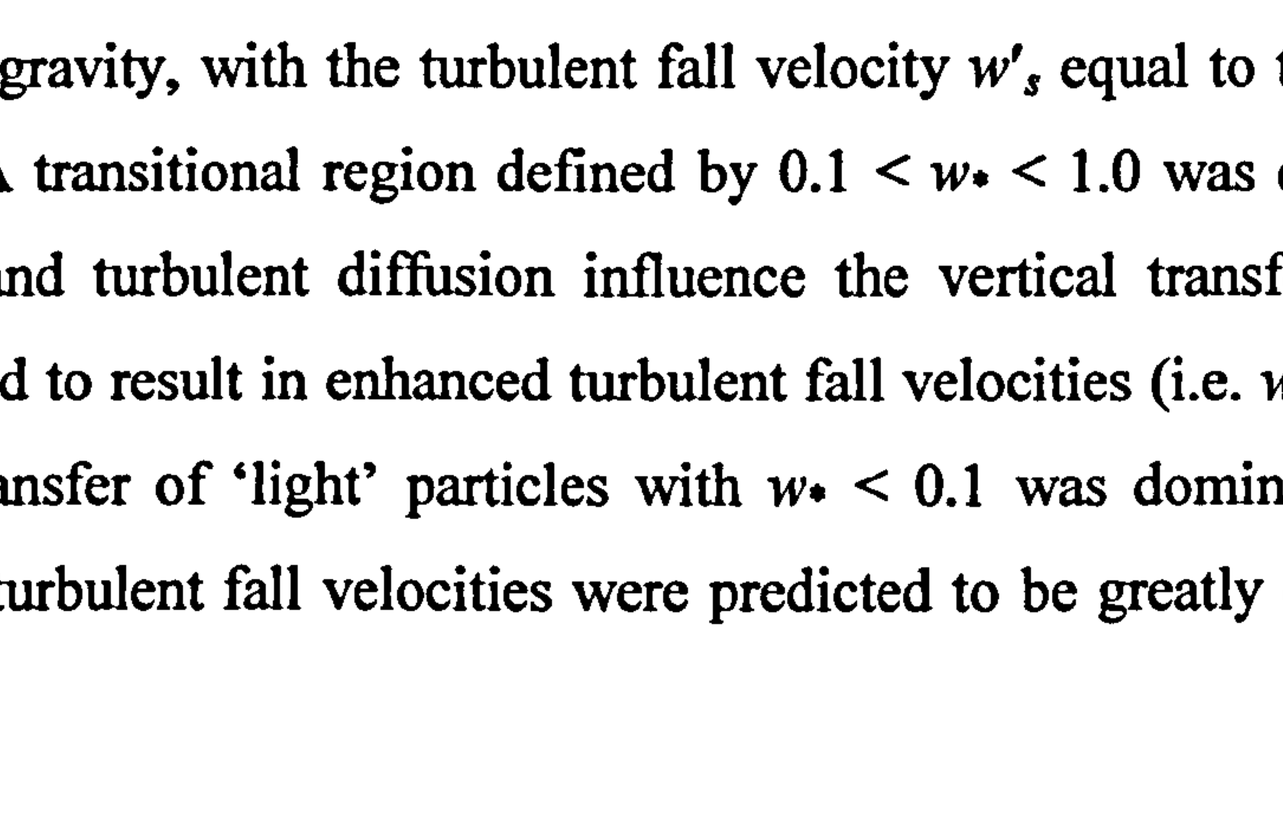

Figure 2.5 - Ratio of mean deposition velocity Vs ($\equiv w'_s$) to still water fall velocity w_s plotted as a function of w_* (from Hoyal et al. 1995)

The increasing levels of enhanced settling predicted by Hoyal et al. (1995) for very small values of w_* (i.e. up to $w'_s/w_s \approx 200$ when $w_* = 0.001$, Figure 2.5) are intuitively erroneous. Clearly, particles close to neutral buoyancy ($w_s/u_* \rightarrow 0$) by definition will have a negligible fall velocity in turbulent flow conditions and would be expected to closely follow the paths of fluid elements (i.e. $\varepsilon_s \approx \varepsilon_f$, where ε_f is the fluid mixing coefficient or eddy viscosity). Even in the event of such particles reaching the bed, it would seem likely that they would be re-suspended, especially

with many criteria for the threshold of sediment suspension being based on critical values of w_* (e.g. Bagnold 1966; van Rijn 1984; Bridge and Bennett 1992). This suggest that Hoyal's assumption of a fully absorbing boundary condition, whereby all particles reaching an elevation close to the bed surface were considered deposited, may be inappropriate for 'light' particles with low w_* values. Wallis and Moores (1996) attributed the enhanced settling characteristics for particles with $w_* < 0.1$ to a combination of this bed boundary condition and the authors' representation of the depth-wise variation of vertical mixing length, which introduced an additional downward motion towards the bed (~10% of the enhancement).

2.2.4 Summary

The fall velocity of an individual sedimentary particle or a concentration of particles can be predicted in quiescent fluid conditions relatively accurately over a large range of particle Reynolds numbers (R_{ep}) using existing equations. Many of these expressions have however been derived from empirical or, at best, quasi-theoretical considerations, and the underlying problem of developing an analytical solution for Reynolds numbers outwith the Stokes' range ($R_{ep} > 0.1$) still remains.

Investigations of the influence of turbulence on the vertical component of sediment particle motion are inconsistent and often conflicting in their findings. While 'heavy' particles [$w_* > 5$ (Owen 1969); $w_* > 1$ (Hoyal et al 1995)] are clearly dominated by gravity and settling close to their still water fall velocity, the role of turbulence in the settling characteristics of 'light' particles [$w_* < 0.1$ (Hoyal et al. (1995)] remains unclear. Sediment particle settling process would also appear to be dependent on the trapping efficiency of the bed boundary, with fully absorbent bed conditions apparently resulting in greatly enhanced settling characteristics (i.e. $w'_s > w_s$). Some experimental data (i.e. Jobson and Sayre 1970) does suggest that enhanced settling conditions may exist over a limited range of w_* values. However, greater understanding of the experimental conditions under which this may occur clearly requires greater consideration of the turbulent structure of the flow and its interaction with discrete sediment particles, as well as the influence of the bed boundary conditions.

2.3 Turbulent Structure of Open Channel Flow

2.3.1 Introduction

As the turbulent motions of the fluid predominantly control the suspended transport of fine sediment particles (Cao et al. 1996), it is important to understand the nature of turbulence within open channel shear flow.

Prior to the late 1950s, turbulent boundary layers were primarily studied through probe measurement techniques such as hot-wire anemometry. During this period, turbulence was generally envisaged to be a stochastic phenomenon arising from the superposition of randomly interacting fluid motions, over a wide range of scales, on the mean flow (Cantwell 1981, Clifford and French 1993). During the 'golden age' of point measurements in the 1960s (Nezu and Nakagawa 1993), hot-wires and pressure transducers were employed to investigate statistical space-time correlations and spectral analysis of turbulent velocity fluctuations.

With the development of dye and hydrogen-bubble flow visualisation techniques in the late 1950s and early 1960s came the realisation of a greater level of organised flow structure within turbulent boundary layer flows than was previously believed (Smith 1996). Most notable were the contributions from Kline et al. (1967), Corino and Brodkey (1969) and Kim et al. (1971) who discovered the existence of coherent fluid motions such as *low-speed steaks*, *outward fluid ejections or* '*bursts*' and *inward fluid inrushes or* '*sweeps*' in the near-wall region of turbulent boundary layers over flat, hydraulically-smooth beds. In an extensive study, Grass (1971) demonstrated that similar coherent turbulent structures also exist in turbulent boundary layers generated over transitionally rough and fully rough walls. The defining characteristics of these turbulent structures are described in §2.3.3.

2.3.2 Statistical Nature of Open Channel Flow Turbulence

2.3.2.1 General Description

Turbulence exists as a conglomeration of eddies varying in diameter l from the smallest *microturbulent* eddies, where $l_{min} \approx \nu/u_*$ (Kolmogorov microscale, ν/u_* represents the viscous length), to the largest *macroturbulent* (or *large-scale*) eddies that scale with the flow depth, i.e. $l_{max} \approx H$ (Yalin 1992). Within a turbulent boundary layer, kinetic energy is extracted from the mean flow and converted into turbulent

fluctuations associated with the generation of large-scale eddies [this is often referred to as the *productive subrange*, Nezu and Nakagawa (1993)]. The disintegration of these large-scale eddies follows, resulting in the transfer of turbulent energy to smaller-scale eddies (i.e. *inertial subrange*) and final dissipation into heat energy by molecular diffusion within the *viscous subrange*. This transfer and dissipation of turbulent energy is often referred to as an *energy-* or *eddy-cascade* process (i.e. Yalin 1992; Nezu and Nakagawa 1993; Kironoto and Graf 1994).

2.3.2.2 Sub-Division of Flow

The turbulent structure of an open channel flow over a hydraulically smooth bed (i.e. $k_s u_*/\nu < 5$) is often sub-divided into two regions (*inner* and *outer* layers) associated with areas of high turbulent energy production G and dissipation ε (Figure 2.6). Kline et al. (1967) demonstrated that about 50% of turbulent energy production occurs within a region very close to the wall (i.e. *laminar or viscous sublayer* and *buffer layer*), while the outer 80% of the boundary layer contributes only 20% to turbulence production.

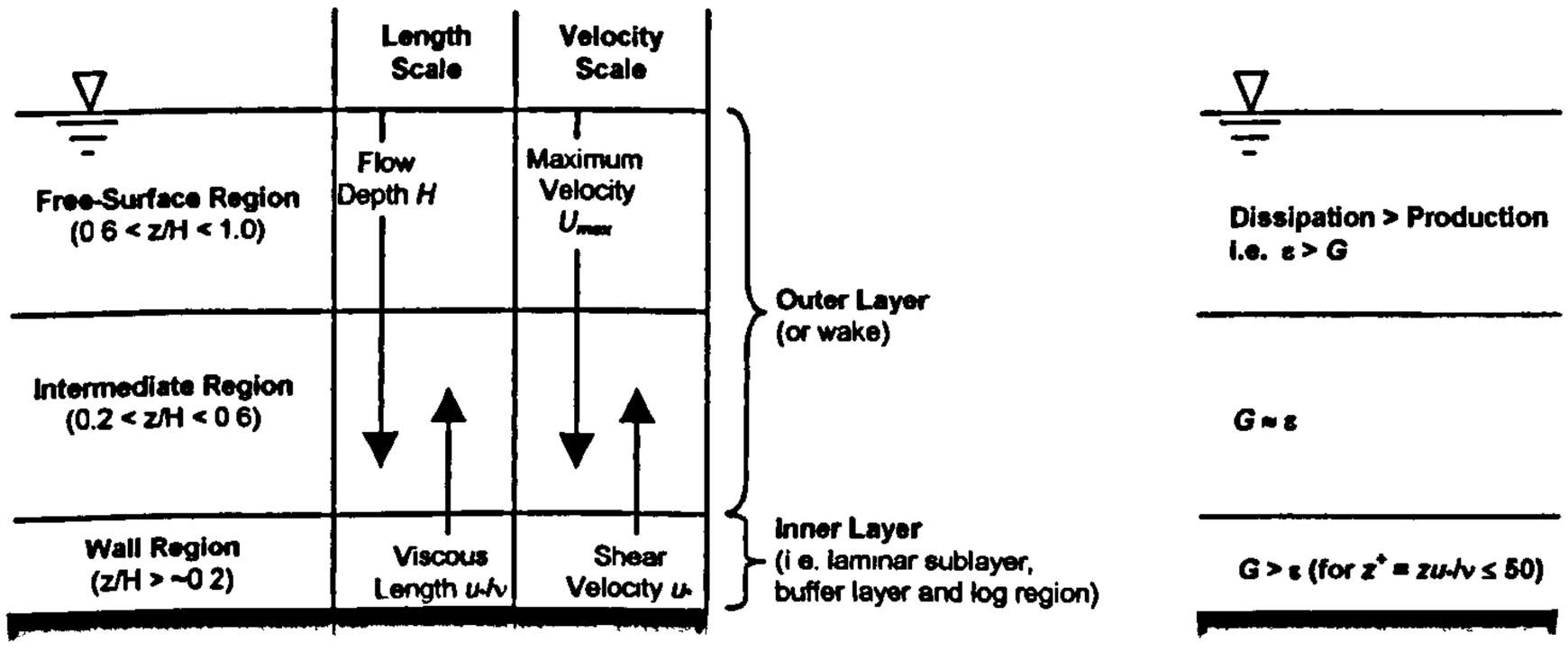

Figure 2.6 - Subdivision of open channel flow field (modified from Nezu and Nakagawa 1993)

In open channel flow over hydraulically rough bed surfaces (i.e. $k_s u_*/\nu > 70$), the viscous sub-layer is diminished through the penetration of the roughness elements into the logarithmic region of the flow. In natural river gravel beds, this roughness is often non-uniform and can result in wake separation and the generation of local boundary layers behind a single protruding bed element or cluster of bed elements (Kirkbride, 1993) (Figure 2.7). Nowell and Church (1979) determined that the structure of the inner flow region was dependent on the density of roughness

elements, with the flow effectively found to '*skim*' over a bed of closely packed roughness elements.

Experimental studies concerned with the turbulent structure of hydraulically rough open channel flow, (i.e. McQuivey and Richardson 1969; Grass 1971; Nowell and Church 1979) have shown that bed roughness does not greatly influence the regions in which high turbulence generation G and dissipation ε rates occur (i.e. within the 'quasi-separated' inner zone and outer zone, respectively, Figure 2.7).

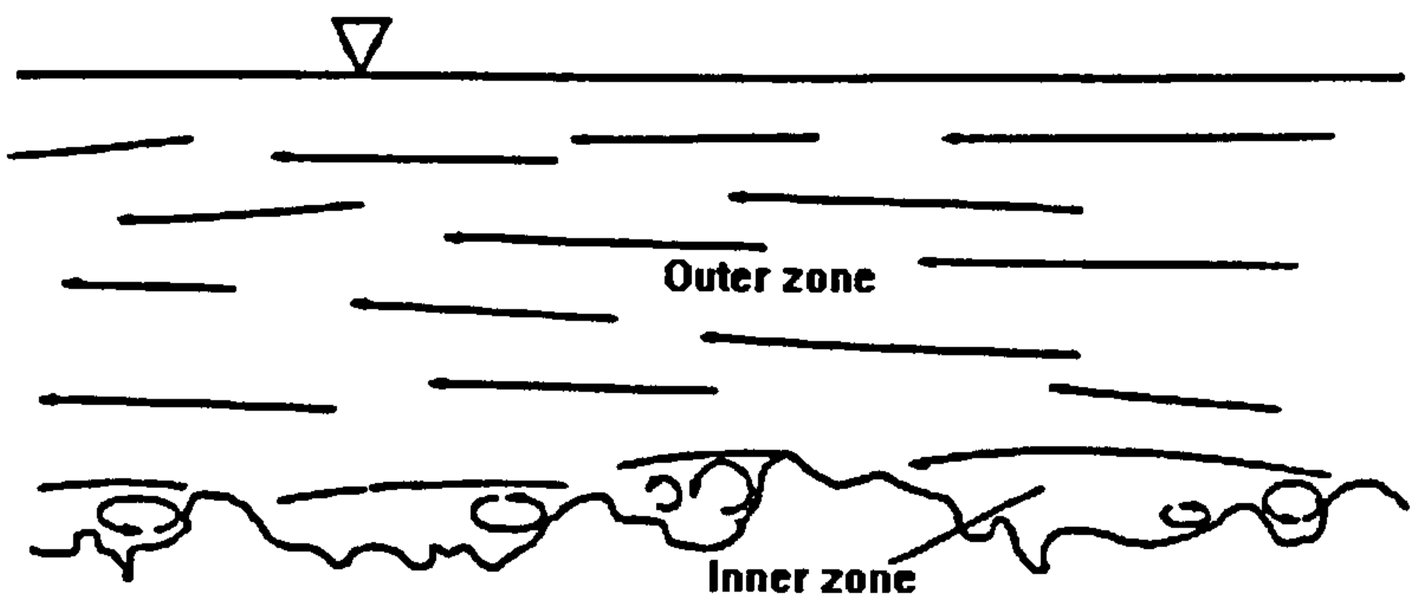

Figure 2.7 - Definition of inner and outer zones within open channel flow over a rough bed (from Kirkbride 1993)

2.3.2.3 Turbulence Intensities and Reynolds Stresses

Measurements of the mean and fluctuating components of flow velocity are clearly essential in determining many statistical characteristics of turbulence including turbulence intensities and Reynolds shear stresses. Universal expressions for longitudinal and vertical turbulence intensity distributions were derived from semi-theoretical considerations and the assumption that turbulent energy is in local equilibrium (i.e. turbulent energy production is approximately in balance with viscous dissipation). These expressions have the general exponential form (Nezu and Rodi, 1986),

$$\frac{u'_{rms}}{u_*} = D_u.exp\left(-\lambda_u \frac{z}{H}\right) \qquad \frac{w'_{rms}}{u_*} = D_w.exp\left(-\lambda_w \frac{z}{H}\right) \qquad ....(2.11)$$

where $u'_{rms} = \sqrt{\overline{u^2}}$ and $w'_{rms} = \sqrt{\overline{w^2}}$ are the root-mean-square longitudinal and vertical velocity fluctuations, respectively, and D_u, D_v, λ_u and λ_v are empirical constants independent of Reynolds and Froude numbers. From curve fitting to extensive experimental hot-wire measurements over mainly smooth boundaries, Nezu and Rodi

(1986) obtained $D_u = 2.26$; $\lambda_u = 0.88$ (shown in Figure 2.8 below) and $D_v = 1.23$; $\lambda_v = 0.67$.

In experiments over rough boundary conditions, Novell and Church (1979) identified three distinct regions in the vertical variation of longitudinal turbulence intensity. (i) For $z/H > 0.35$, turbulence intensities were found to decrease linearly to the free surface ($z/H \rightarrow 1$). (ii) In the region $0.35 > z/H > 0.20$, turbulence intensities were approximately constant with $u'_{rms}/u_* \sim 2$. (iii) For $z/H < 0.20$ turbulence intensities were found to reduce with increasing roughness density (number of roughness elements per unit area of bed). Grass (1971) found that longitudinal turbulence intensity in the near-bed flow region decreased with increasing roughness (smooth → transitional → rough bed conditions), while vertical turbulence intensity increased in this region. By contrast, McQuivey and Richardson (1969) found that longitudinal turbulence intensity over a rough bed increased by up to 50% close to the bed ($z/H = 0.1$) and by 20% at the near surface ($z/H = 0.8$), in comparison with smooth boundary conditions. Vertical turbulence intensity showed an increase of 10% for flows over rough bed conditions.

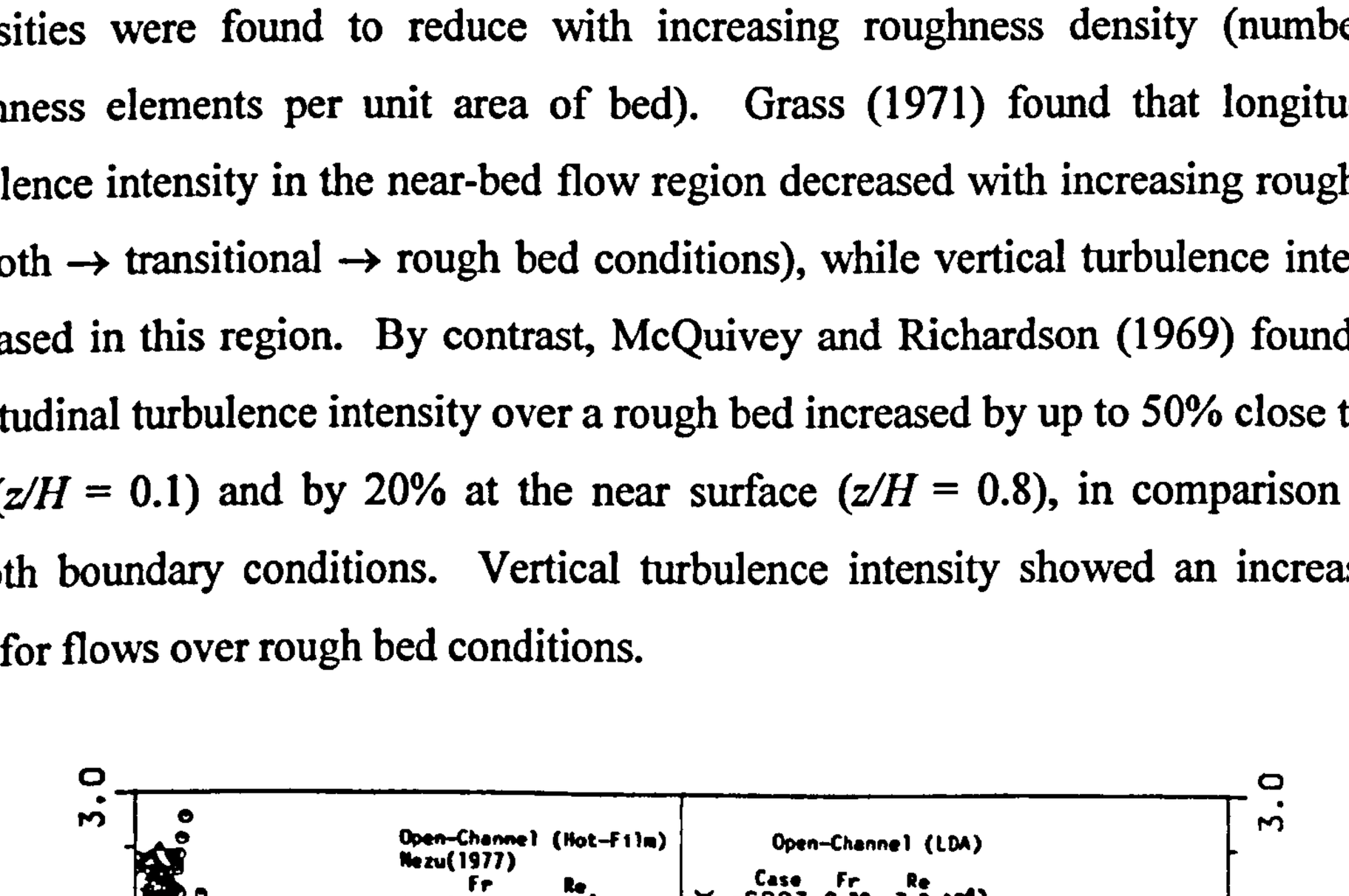

Figure 2.8 - Longitudinal turbulence intensity u'_{rms}/u_* in the intermediate and outer flow regions away from the wall (from Nezu and Rodi 1986)

The total shear stress τ can be determined from the Reynolds equations in 2-D flow as,

$$\tau \equiv -\rho\overline{u'w'} + \rho\nu\frac{\partial U}{\partial z} = \rho u_*^2\left(1-\frac{z}{H}\right) \qquad \text{....(2.12)}$$

where $-\rho\overline{u'w'}$ is the Reynolds stress and $\rho\nu(\partial U/\partial z)$ is the viscous stress. At large Reynolds numbers, the viscous stress term becomes negligible and the total shear stress is well approximated by the Reynolds stress over a wide range of z/H (i.e. $0.05 < z/H < 1$) in both smooth and rough turbulent open channel flows (Kironoto and Graf 1994). At any given location within the flow, the ratio of the Reynolds stress term $\overline{u'w'}$ and the product of the turbulence intensities $u'_{rms}w'_{rms}$ is defined as the correlation coefficient R_{uw} of the Reynolds stress (Schlichting 1968). This coefficient R_{uw} indicates the degree of similarity of turbulence (Nezu and Nakagawa 1993). Experimental results (e.g. Laufer 1954) indicate R_{uw} remains relatively constant, about 0.4-0.5, in the intermediate flow region ($0.2 < z/H < 0.6$), reducing slightly in the near-bed ($z/H < 0.2$) and decreases to zero in the free-surface region ($z/H > 0.6$), as shown in Figure 2.9. Kironto and Graf (1994) derived an equation for R_{uw} from the expressions for turbulence intensities (eqn. 2.11, pp.22) and for the linear Reynolds stress distribution (eqn. 2.12) in the form,

$$-R_{uw} = 0.43\left(1-\frac{z}{H}\right)exp\left(1.73\frac{z}{H}\right) \qquad \text{....(2.13)}$$

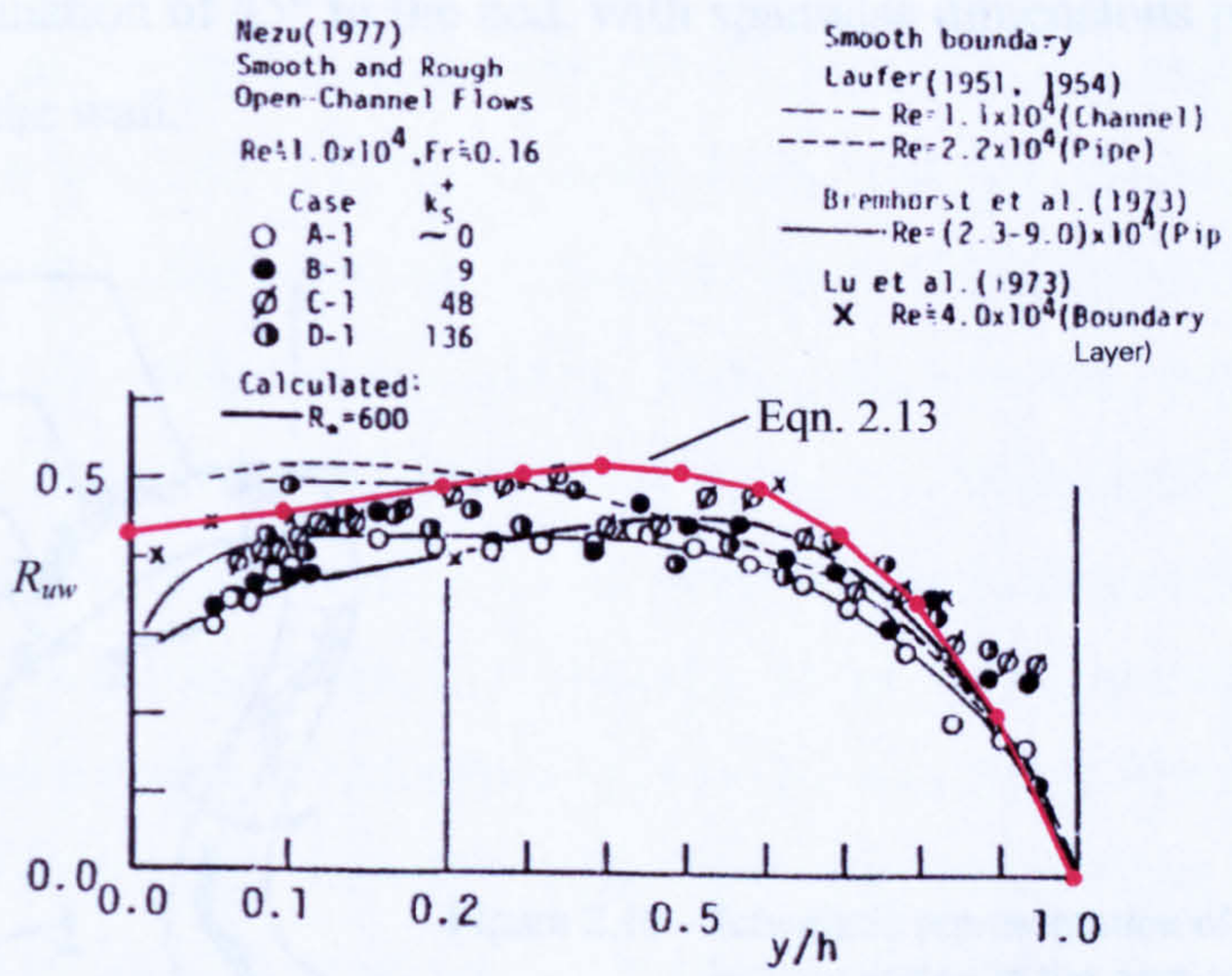

Figure 2.9 - Variation of correlation coefficient R_{uw} with relative depth z/H (modified from Nezu and Nakagawa 1993).

This expression is shown to compare well with previous experimental data (Figure 2.9) and the distribution of R_{uw} would appear to be universal for all flow types (e.g. open channel, boundary layer and pipe flows) and independent of mean flow properties and wall roughness characteristics.

2.3.3 Coherent Structures in Open Channel Flow Turbulence

An inherent disadvantage of most statistical techniques employed to study turbulence in open channel flow is that they ignore quasi-periodic repeating patterns of coherent motion known to exist within the flow (Robinson, 1991). Following the early period in which turbulence was considered to be a stochastic, random phenomenon came the increasing realisation that vortices associated with coherent motions were responsible for sustaining turbulence within a boundary layer flow (i.e. through generation G and dissipation ε) (Smith, 1996).

2.3.3.1 Near-wall Turbulent Structure

Well in advance to the first published observations of near-wall coherent structures, Theodorsen (1955) identified the importance of near-wall flow structure to the generation of turbulence in shear flows. He proposed a simple model of an idealised *horseshoe* or *hairpin* vortex (Figure 2.10) to describe the salient features of instantaneous near-wall turbulent structure. In this model, symmetrical vortical structures were proposed to originate in the low-velocity near-wall fluid, expanding outward at an inclination of 45° to the bed, with spanwise dimensions proportional to the distance from the wall.

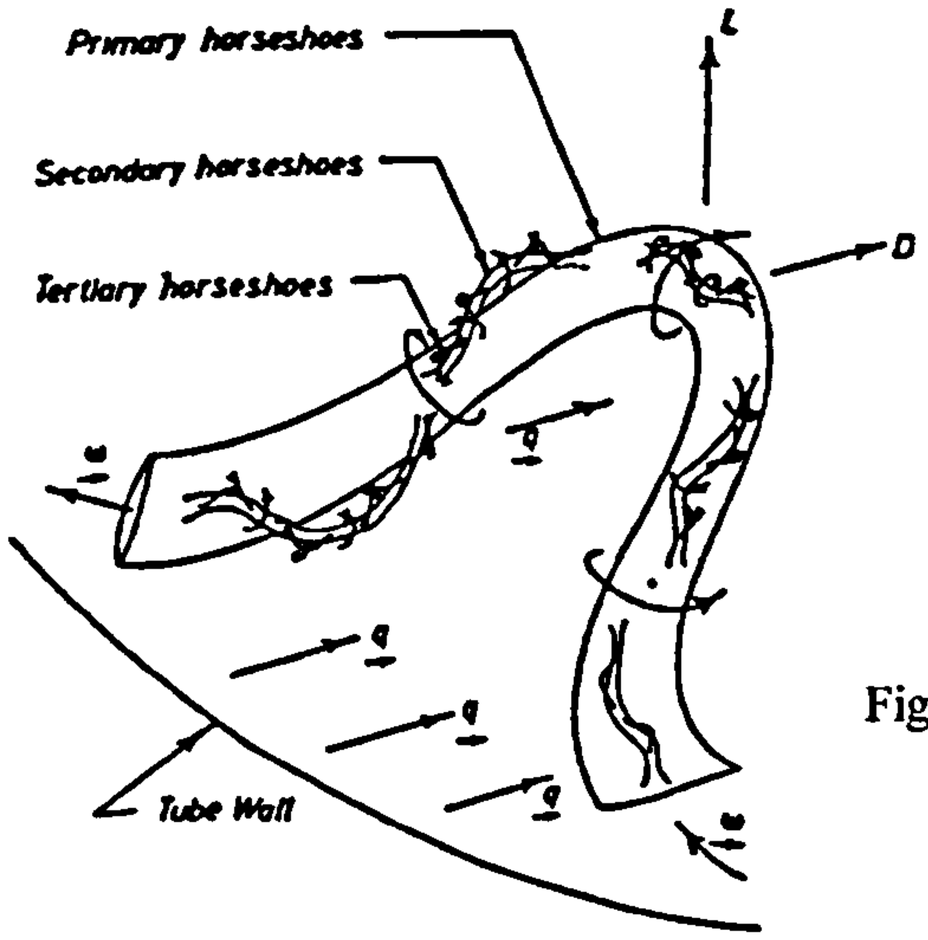

Figure 2.10 - Schematic representation of a *horseshoe* or *hairpin* vortex in the near-wall flow region (after Theodorsen, 1955)

Improved qualitative understanding of the turbulent structure of near-wall flow over smooth boundaries came through the extensive flow visualisation studies carried out by the Stanford group from the late 1950's. This work culminated in the hydrogen-bubble visualisation experiments carried out by Kline et al. (1967), which revealed several new features in the near-wall region of turbulent boundary layer flow. Within the laminar sublayer, hydrogen bubbles released perpendicular to the mean flow direction were found to migrate laterally from high-speed flow regions accumulating in well-defined '*streaks*' in the low-speed flow regions at a pronounced spanwise spacing defined by $\lambda_y^+ = \lambda_y u_*/\nu = 100$ (similar to that shown in Figure 2.11). These '*streaks*' were found to interact intermittently with the outer flow layers in a sequence of four events: (i) slow downstream migration of streak with very slow outward drift; (ii) gradual streak lift-up due to streamwise vorticity within the laminar sublayer ($z_+ = z.u_*/\nu \leq \sim 7$); (iii) sudden instability, characterised by rapid oscillation of the streak ($8 \leq z_+ \leq 12$), resulting in; (iv) break-up of the streak ($10 \leq z_+ \leq 30$). Kline et al. (1967) and Kim et al. (1971) described these sequential events, commonly referred to as the '*bursting process*', in some detail.

This ejection or '*bursting*' phenomenon is known to be closely associated with a subsequent inrush of high-speed outer layer fluid, which penetrates the wall-layer [originally observed by Corino and Brodkey (1969) in fully developed pipe flow]. These high-speed fluid inrushes act to '*sweep*' away the chaotic motion associated with the remnants of the '*burst*' (Smith, 1996). Wallace et al. (1972) and Willmarth and Lu (1972) confirmed the existence of these '*sweeps*' by applying conditional sampling techniques to probe measurements of instantaneous pairs of velocity fluctuations (i.e. u' and w'). These analyses found that the contribution to total Reynolds stress resulting from inward-moving accelerated fluid elements ($u' > 0$, $w' < 0$; i.e. fluid inrush or '*sweep*') was approximately equal to the contribution from outward motion of retarded fluid ($u' < 0$, $w' > 0$; i.e. fluid ejection or '*burst*'). Moreover, these combined ejection and inrush sequences were ascertained to correlate with an extremely high contribution to the total Reynolds stress and hence to the production and maintenance of turbulence in the near-wall flow. These facts clearly suggest that turbulence production is dominated by the intermittent, cyclic process incorporating '*burst*' and '*sweeps*' events (Grass, 1971) (shown schematically in Figure 2.12).

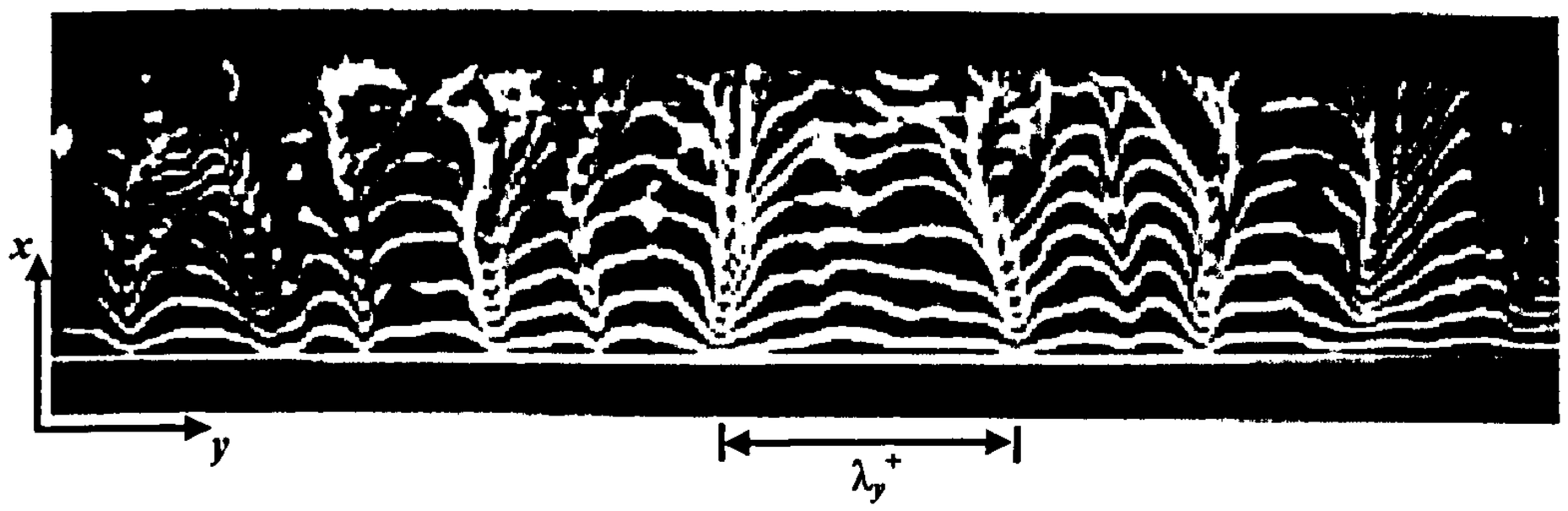

Figure 2.11 - Plan view of near-wall flow structure showing low-speed 'streaks' over a smooth boundary [obtained by Grass et al. (1991) using pulsed hydrogen bubble visualisation technique].

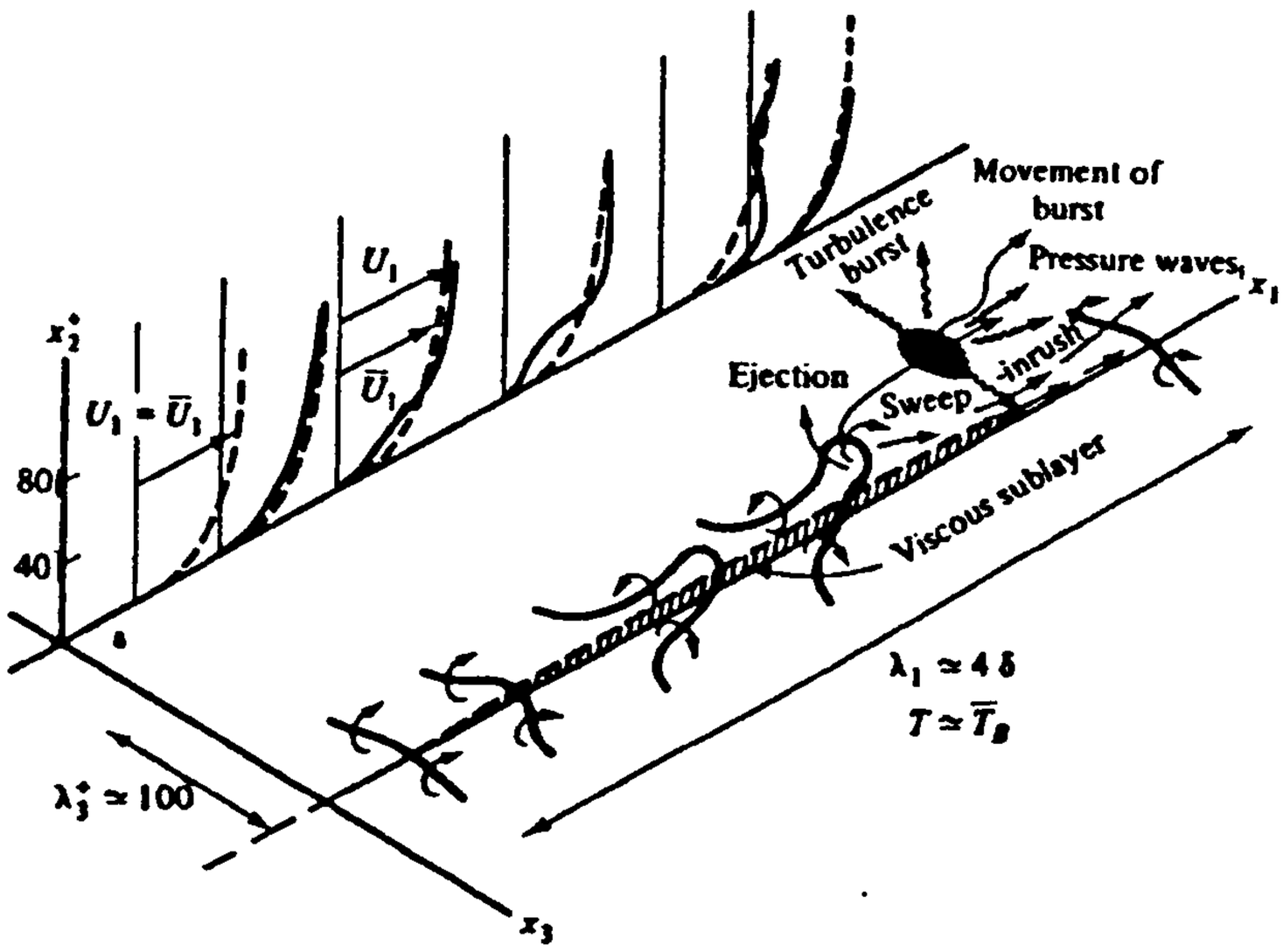

Figure 2.12 - Cyclical processes involved in the production of near-wall turbulence in relation to the generation of hairpin vortices (from Hinze, 1975)

In an extensive experimental study over transitionally rough and fully rough walls, Grass (1971) revealed the existence of '*burst*' and '*sweep*' turbulent coherent structures, similar to those previously reported by Kline et al. (1967) and others for smooth boundary flow, regardless of the boundary roughness. Grass determined that the main differential in the ejection and inrush sequences over rough wall conditions was associated with the origin of the near-wall low-momentum fluid sourced during the '*burst*' sequence. As opposed to the viscous sublayer in smooth-wall boundary flows, in rough boundary flows, the low-momentum fluid was found to be sourced from "passive reservoirs" which exist in the interstices between bed elements as a result of flow separation (shown schematically in Figure 2.7). These observed fluid '*bursts*' in fully rough conditions were also observed to be extremely violent, with the

ejected fluid rising almost vertically from the bed interstices and, on occasion, extending across the entire flow depth. Kirkbride (1993) described two distinct modes of fluid ejection from the interstices of the coarse obstacle clasts (Figure 2.13). The first mechanism relates to an outward expansion of separated low-speed fluid from the bed into a low-pressure zone generated by the impact of high-speed outer fluid on the upstream side of the bed obstacle. Under this condition, the low-speed fluid becomes detached from the bed and is ejected into the outer flow. The second mechanism relates to the evolution of an eddy attached to the lee side of an obstacle. As the eddy increases in both size and vorticity it either decays chaotically or is shed into the outer zone during '*slack*' flow conditions. Both mechanisms were observed to block the upstream high-speed outer flow, which tended to be released and form an inrush back towards the bed following the ejection of the low-speed fluid.

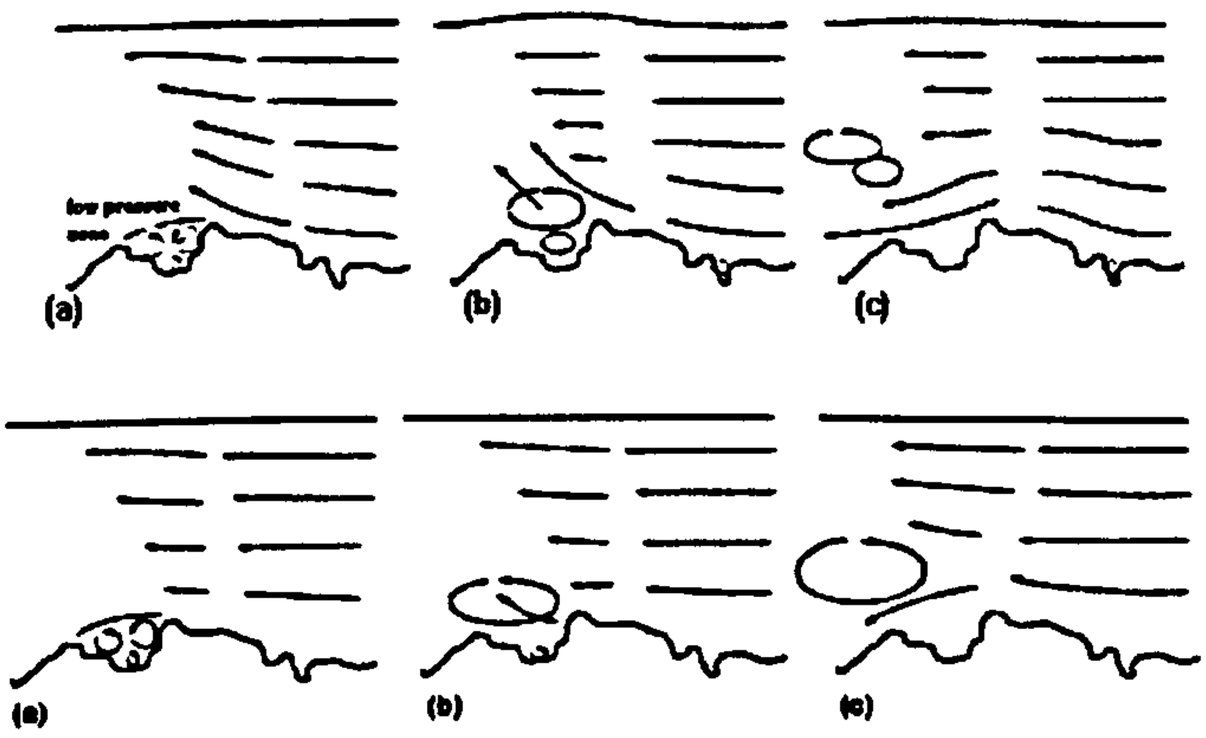

Figure 2.13 - Two distinct modes of low-speed fluid ejection from interstices between obstacle clasts [observed by Kirkbride (1993) for flow over a rough gravel bed]

Other structural features of turbulence such as low-speed '*streaks*' have also been shown to exist in transitional rough and fully rough boundary layer flows (i.e. Defina 1996; Grass et al. 1991) (Figure 2.14). Both investigators found that streak spacing λ_y scaled reasonably well with the bed roughness height k_s (i.e. λ_y/k_s = const. ~ 3.4) within a conceptual thin fluid layer above the roughness elements and for geometrically similar roughness elements and packing arrangements. Grass and Mansour-Tehrani (1996) proposed that streak spacing λ_y within this conceptual layer could be universally scaled in length, regardless of wall roughness k_s, by the ratio of an 'enhanced effective viscosity' ν' to bed shear velocity u_*, such that $\lambda_y = 100\nu'/u_*$.

(Note: for smooth boundaries this length-scale corresponds to the previously defined viscous length, ν/u_*, i.e. $\lambda_y = 100\nu/u_*$).

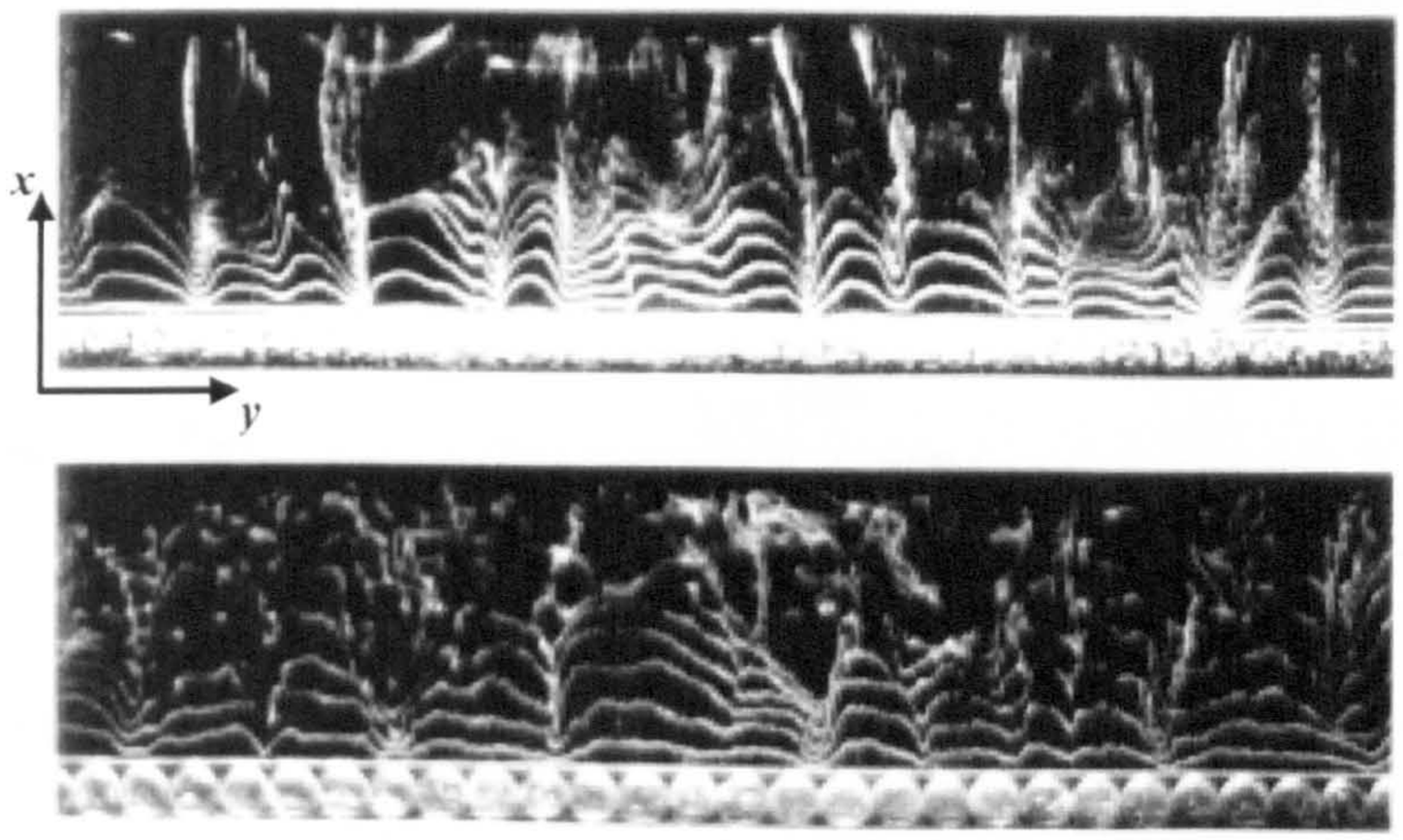

Figure 2.14 - Plan view showing 'streaky' nature of flow structure over transitional rough *(top)* (k_s = 1.15mm) and fully rough *(bottom)* (k_s = 6mm) beds (from Grass et al., 1991).

2.3.3.2 Turbulent Structure of Outer Flow Region

In comparison to the plethora of experimental investigations providing evidence of the organised nature of near-bed turbulent structure, the study of large-scale outer flow structure has received significantly less attention. In addition, hypotheses relating the near-wall flow structure (i.e. bursting phenomenon) with the outer flow structure remain to be well-established (Tamburrino and Gulliver, 1999). Offen and Kline (1974, 1975) attempted to prescribe a kinematic description to this relationship, suggesting that the interactions between burst-type ejections and flow in the logarithmic region resulted in the formation of fluid inrushes towards the bed, which in turn, influenced the generation of fluid ejections or bursts at a location further downstream. Praturi and Brodkey (1978) derived a conceptual model (Figure 2.15) in which an inclined shear-layer interface between the low- and high-speed fluid regions results in the roll-up of large-scale transverse vortices. These vortices associated with the shear layer were hypothesised to induce near-wall ejection events and streamwise vortices, as well as bulges in the outer flow and entrainment of new free-stream fluid. Thomas and Bull (1983) measured wall-pressure variation during to the passage of a burst-sweep cycle and concluded that the regions of characteristic high-pressure result from the passage of inclined shear layers, which traverse most of the boundary layer on the upstream side of the ejection phase (shown in Figure 2.16).

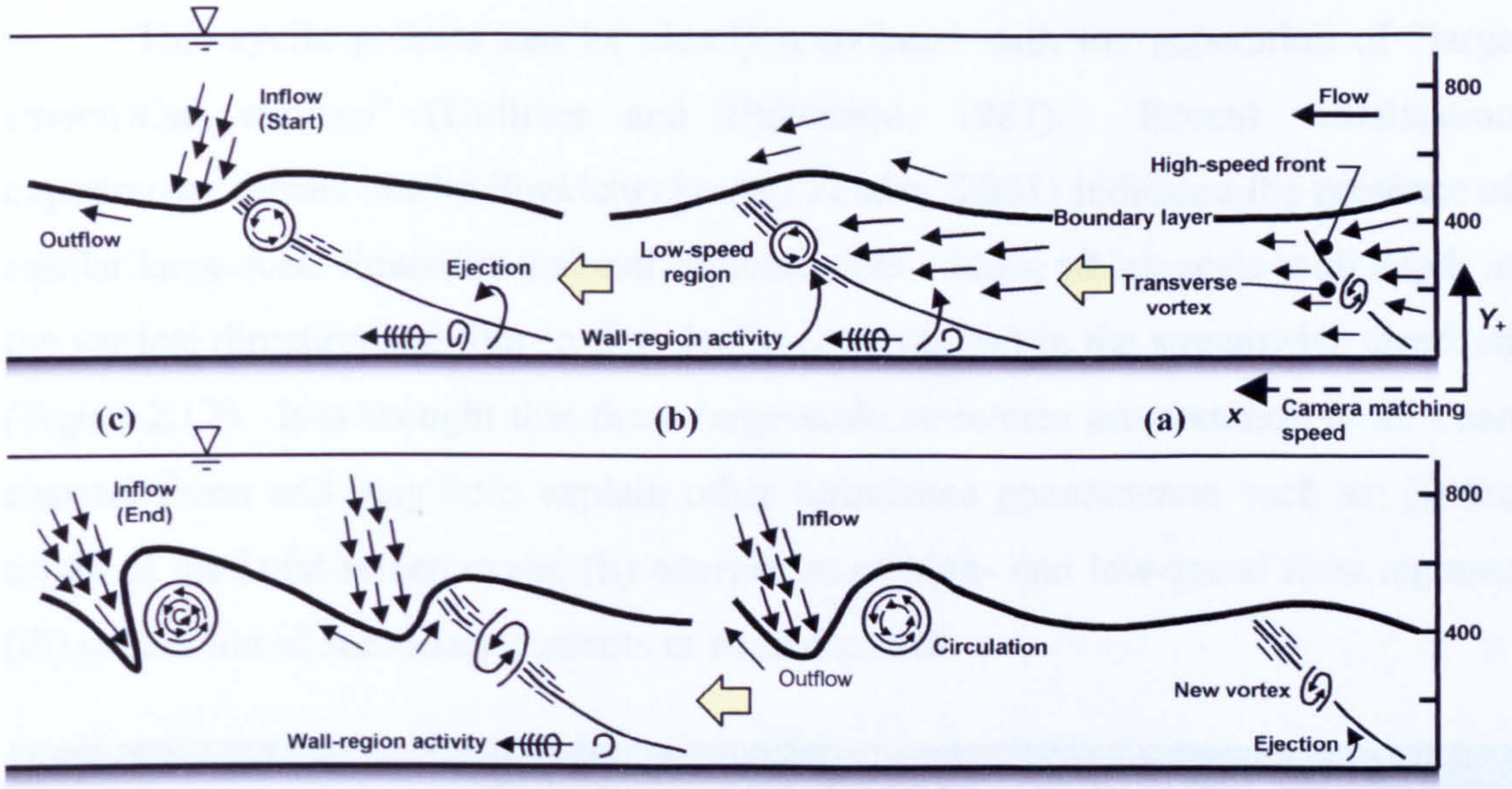

Figure 2.15 - Outer-flow motions and interactions with the wall-region, as shown by a camera moving in the direction of flow (modified from Praturi and Brodkey, 1978).

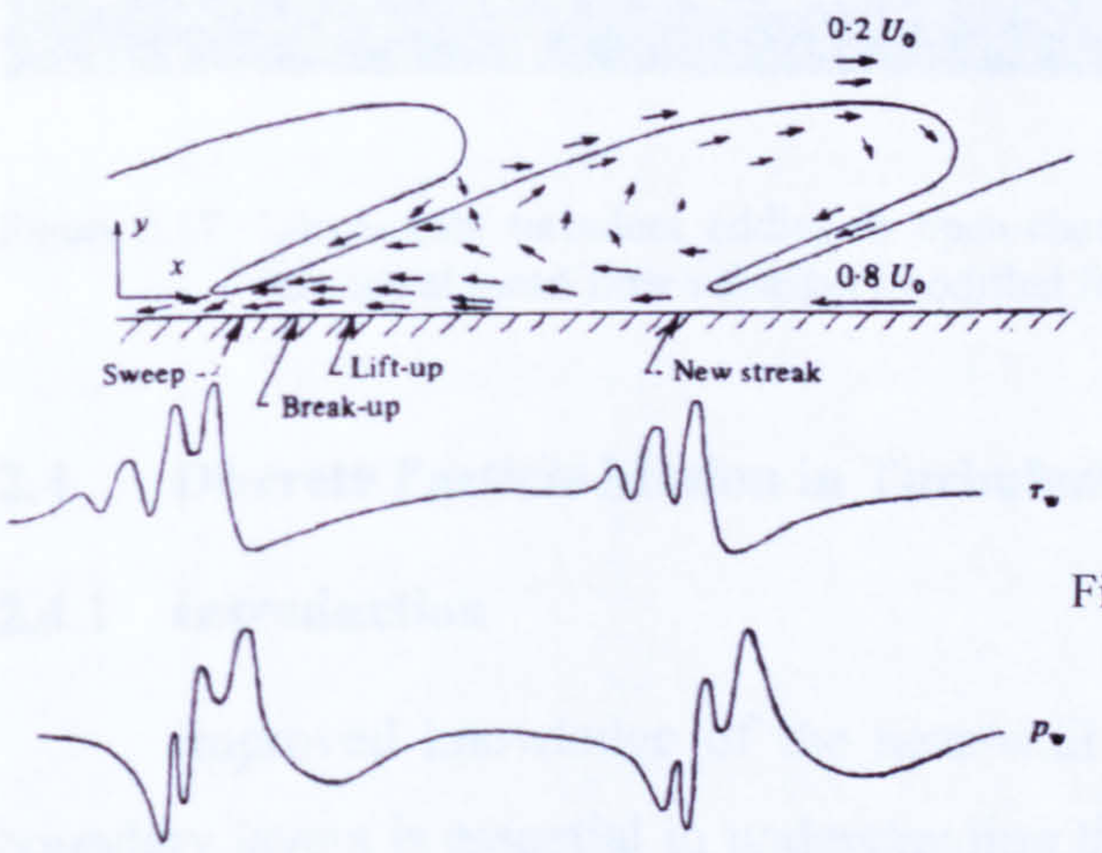

Figure 2.16 - Large-scale structure, associated pressure and shear stress distributions, and position of burst-sweep cycle in a frame of reference moving with the large structure (from Thomas and Bull, 1983).

In fully turbulent open channel flow, some investigators have observed coherent fluid motions, such as bursts and sweeps, to occupy the entire flow depth (e.g. Grass, 1971; Rashidi and Banerjee, 1988; Grass et al., 1991). Rashidi and Banerjee (1988) described a quasi-cyclic process whereby the low streamwise momentum fluid, ejected from the near-wall flow during the bursting process, results in an acceleration of the bulk of fluid towards the free surface. The resulting interaction between ejected fluid and near surface accelerated flow generates a pattern of mixing and rolling which, on reaching the free surface, tends to travel back towards the wall.

This cyclic process can be clearly associated with the generation of "large streamwise vortices" (Gulliver and Halverson, 1987). Recent visualisation experiments carried out by Shvidchenko and Pender (2001) indicated the presence of similar large-scale three-dimensional asymmetrical eddies, which scale with depth in the vertical direction and four to five depths (on average) in the streamwise direction (Figure 2.17). It is thought that these large-scale structures are common to all open channel flows and may help explain other turbulence phenomenon such as: (i) the origin of the burst-sweep cycle; (ii) alternation of high- and low-speed flow regions; (iii) generation of secondary currents in wide channels.

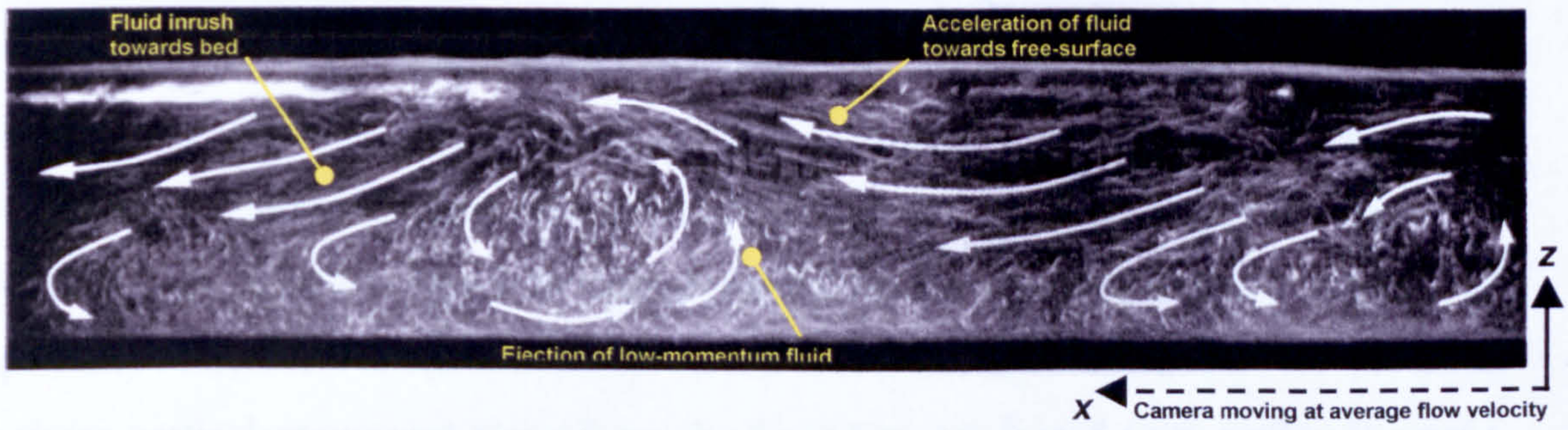

Figure 2.17 - Large-scale turbulent eddies in open-channel flow over a mobile gravel bed (camera moving at mean flow velocity) (modified from Shvidchenko and Pender, 2001).

2.4 Discrete Particle Motion in Turbulent Open Channel Flow

2.4.1 Introduction

Improved knowledge of the near-wall and large-scale structure of turbulent boundary layers is essential in understanding the behaviour of discrete, solid particles in turbulent open channel flow. Clearly, the interactions that may exist between the solid particles and coherent flow structures will have a significant influence on sedimentation processes both within environmental and industrial processes (Kaftori et al., 1995a). However, knowledge relating the mechanics of sediment transport to turbulent processes, such as near-bed bursts and sweeps, remains limited at the present time (Niño and Garcia, 1996).

2.4.2 Particle Motion in Near-Wall Region

The first association between the mechanism controlling sediment particle entrainment and near-wall fluid ejection events (or bursts) occurring in a turbulent boundary layer was most probably put forward by Sutherland (1967). He suggested

that turbulent eddies disrupting the viscous sublayer and impinging down on the sediment bed would result in a localised increase in shear stress over individual sediment grains, resulting in their acceleration and eventual entrainment from the bed. While Sutherland's description is not entirely consistent with current knowledge of the near-bed turbulent structure, it outlines the fundamental interactions between turbulence and individual particles, which have been verified in more recent experimental studies to result in particle entrainment.

Grass (1974) visualised the suspension processes of sand particles from a flat plate in a turbulent boundary layer and revealed that the particles were entrained from the near-wall region and could become suspended through virtually the full boundary layer thickness. Sumer and Oğuz (1978) employed a moving camera system to record the vertical motion of spherical wax particles (d = 2.8 – 4.0mm) near the bottom of a turbulent open-channel flow over a smooth boundary. A separate fixed stroboscopic camera was also employed to obtain the instantaneous longitudinal and vertical particle velocities. Observations of the recorded traces revealed that the particles, whose vertical movement away from the boundary originated from within the near-wall region ($z_+ \leq 50$), generally reached heights z_+ between 100 and 200 before beginning their descent back towards the bed. This downward motion generally continued down to relatively small z_+ values (and on occasion down to the bed boundary) before the particle began another upward excursion. Measurements of the upward vertical velocity of the particles (or "ejection" velocity) revealed consistent trends with previous data obtained by Grass (1974), i.e. low values of ejection velocity close to the bed, generally increasing with z_+ (up to $z_+ \approx 350$). Conditionally averaged streamwise velocity profiles revealed that upward particle motions were associated with lower than average streamwise velocities and descending particle motions were associated with higher than average streamwise velocities. This finding was in remarkable agreement with conditionally averaged streamwise flow velocity profiles obtained during actual burst and sweep events (e.g. Nychas et al., 1973).

Based on their observations and Offen and Kline's (1975) model of the bursting process, Sumer and Oğuz (1978) proposed a mechanism describing particle suspension from the near-wall region of a turbulent boundary layer [shown schematically by Sumer and Deigaard (1981) in Figure 2.18]. They suggested that a particle is lifted away from the boundary as a result of the adverse pressure gradient

imposed on the particle from a burst passing overhead. The upward motion of the particle is then strongly controlled by the ejection of near-wall fluid associated with the bursting process, which expands into the main body of flow as a result of the same adverse pressure gradient. On break-up of this accompanying burst fluid, the upward motion terminates and the particle begins to descend back towards the boundary, where it is expected to encounter a fresh fluid ejection before reaching the bed, or else, in cases where the particle reaches the bed, the particle will be re-entrained by the same mechanism. This results in the particle having another upward motion, thus keeping it in suspension. Sumer and Deigaard (1981) found that this mechanism was also applicable to particle motions in turbulent flows over rough boundary conditions, while both particle ejection velocity and heights reached were noted to increase over the rough bed conditions compared with the smooth wall case. This latter finding is consistent with Grass (1971), in which the bursting process was observed to be significantly more violent in rough-walled turbulent boundary layers than over smooth boundaries. Sumer and Deigaard (1981) also suggested that heavier particles were less likely to remain trapped in the wall fluid ejected during the bursting process, with gravitational effects causing the particle to descend back towards the bed prior to burst break-up (Figure 2.18 - particle 2). This particle, on approaching the bed boundary, was thought to be swept into low-speed wall streaks from which it could be re-entrained by a subsequent bursting mechanism.

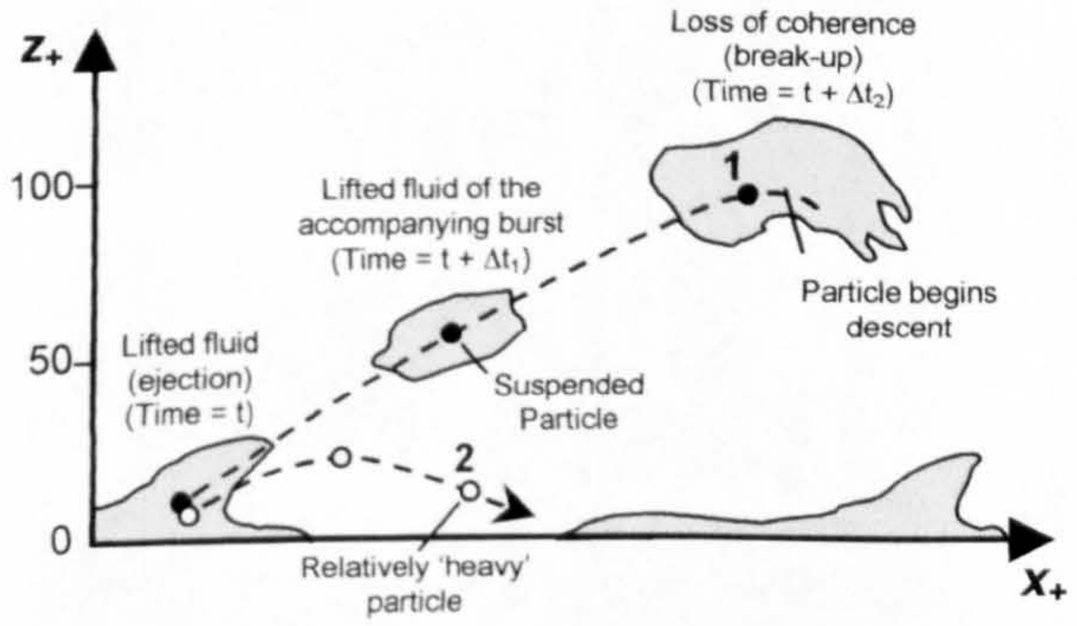

Figure 2.18 - Schematic view of particle-flow ejection interactions. Particle 1 is trapped in intense fluid ejection until flow structure loses coherence (intense ejection event). Particle 2 falls from ejected fluid (weak ejection event). (Adapted from Sumer and Deigaard, 1981)

In a study of near-wall interactions between sediment particles and turbulent structure, Niño and Garcia (1996) observed that particles immersed within the viscous sublayer above a smooth bed did indeed accumulate along low-speed streaks of flow, similar to those observed by Grass et al. (1991) (Figure 2.11, pp. 27). These streaks extended between 1000-2000 wall units in the streamwise direction and had an

average spanwise spacing $\lambda_y^+ = 100$, accepted as the universal value for streak spacing in turbulent boundary layers (Robinson, 1991). No evidence of particle accumulation was obtained over transitionally rough bed conditions, although the authors accepted previous visualisation studies had revealed the formation of wall streaks under such conditions (e.g. Figure 2.14, Grass et al., 1991). They concluded that, in transitionally rough beds, these structures must lack the required coherence, spatial extent and persistence to organise and accumulate heavy sediment particles in low-speed streaks.

In visualisations carried out in the XZ plane (parallel to the flume wall), Niño and Garcia described an apparent link between intense fluid ejections from the near-wall region and frequently observed coherent structures consisting of shear layers of concentrated spanwise vorticity. These were typically inclined at 14° to the bed, occurring between $x_+ = 100$-200 upstream of the fluid ejection (Figure 2.19a). The shear layers were found to interact with particles lying on the bed, such that the downstream fluid ejection induced the pick up of particles away from the boundary. As particles were entrained by the low-speed fluid ejection, their initial relative motion was towards the high-speed fluid immediately upstream of the shear layer (Figure 2.19b).

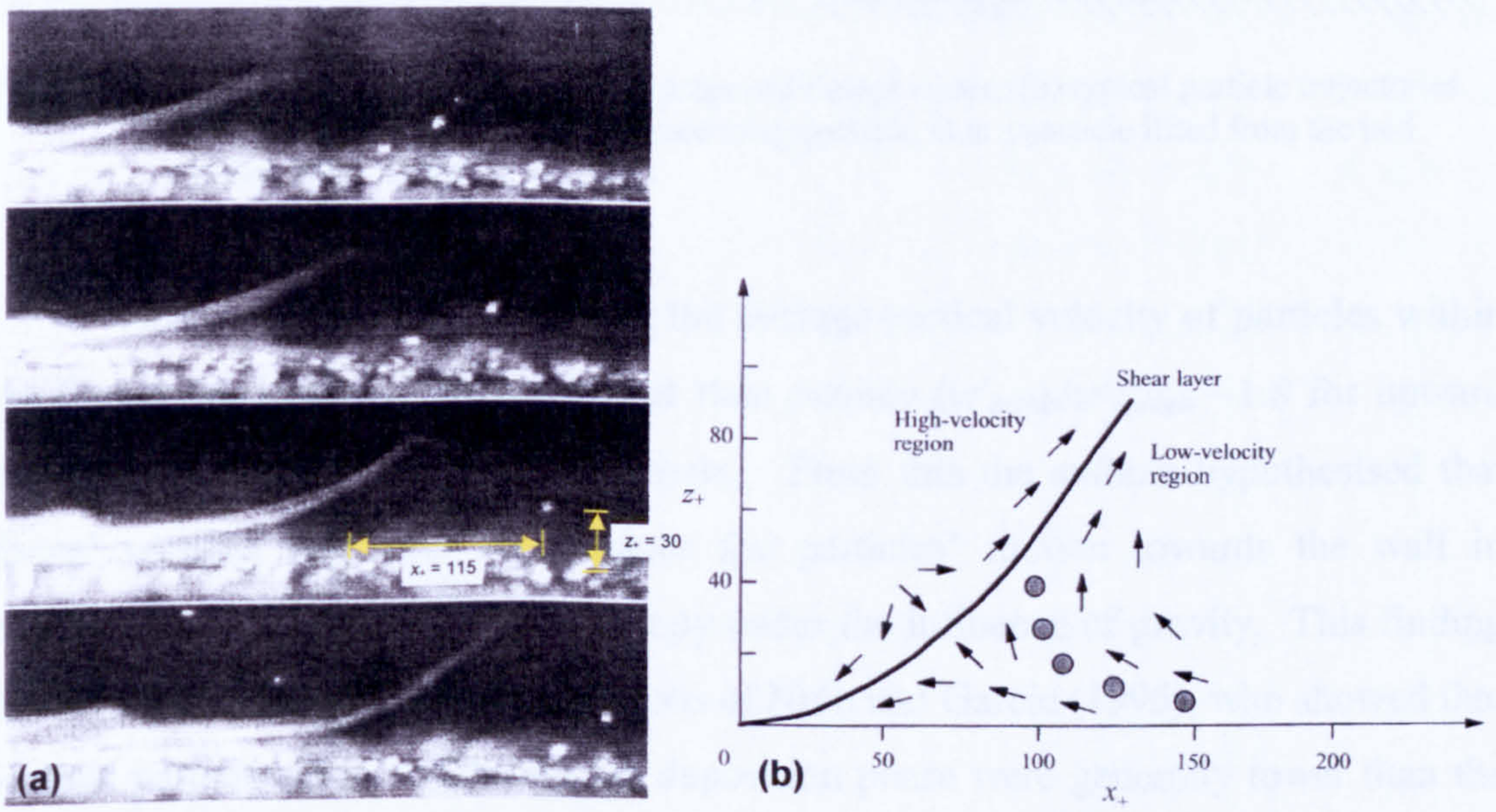

Figure 2.19 - (a) Sequence of images showing particle-shear layer interactions, (b) schematic view of particle motion relative to the downstream movement of the shear layer (both taken from Niño and Garcia, 1996).

In a mechanism similar to that proposed by Sumer and Oğuz (1978), the authors suggest that the particles can become trapped in the core of the coherent structure, continuing to rise within the shear layer until it loses coherence, releasing the particles in the outer regions of the wall-layer. Once released, the particles settled back towards the bed, where they either deposit or are picked up by a new developing ejection event.

Kaftori et al. (1995a) proposed a quasi-streamwise outward-expanding spiral vortex, or *funnel-type* vortex, as the dominant coherent structure within the near-wall region of a turbulent boundary layer (Figure 2.20a). They also proposed that these structures were the primary factor affecting particle motion in the near wall region, including particle entrainment and deposition cycles (similar to those described by Sumer and Oğuz, 1978 and Niño and Garcia, 1996). Particle motion within these funnel vortices was often found to be more quasi-streamwise than the particles' trajectory outwith the vortex (Figure 2.20b), i.e. the vertical motion of the particles appeared to be "delayed" within the vortex.

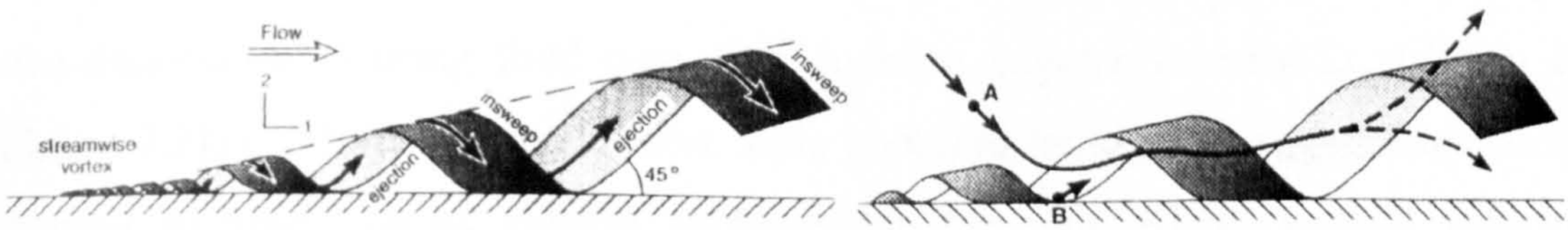

Figure 2.20 - (a) Schematic representation of proposed funnel vortex; (b) typical particle trajectories across a funnel vortex: A is a descending particle, B is a particle lifted from the bed (taken from Kaftori et al. 1995).

However, they also found that the average vertical velocity of particles within the funnel vortices was usually higher than outside ($w'_{inside}/w'_{outside}$ ~1.8 for upward motions and ~1.6 for downward motions). From this the authors hypothesised that funnel vortices may also act enhance the particles' motion towards the wall in comparison to particles settling primarily under the influence of gravity. This finding is not in agreement with the observations of Niño and Garcia (1996), who showed that vertical particle velocities during the deposition phase were generally lower than the settling velocity in still water conditions. Niño and Garcia suggested that this revealed particles to be rarely deposited by high-speed fluid inrushes (or sweeps), but settle back toward the bed following a loss of correlation with the turbulent structures that initially had carried them from the bed.

2.5 Discrete Particle Motion in a Vortex

2.5.1 Introduction

It is well established that the turbulent structure of a turbulent boundary flow consists of eddies and other quasi-ordered coherent structures (i.e. burst-sweep sequence). Whilst the latter have been shown to play a significant role in the entrainment and deposition of discrete sediment particles in the near-bed flow (§2.4), outer flow large-scale coherent eddies or vortex structures are thought to be equally important for suspended sediment transport processes (Nielsen, 1984). In general, these vortices are anisotropic, rotational and often three-dimensional in nature (Tooby et al., 1977), providing conditions under which sediment particles may become trapped and transported considerable distances in suspension.

2.5.2 Particle-Vortex Interactions

Evidence of interactions existing between particles and a turbulent eddy was first presented by Tooby et al. (1977) for the motion of a single particle in a simple two-dimensional rotating fluid core with constant angular velocity Ω_0 (shown in Figure 2.21a). Multi-exposure stroboscopic photographs highlighted particles being trapped in nearly closed circular orbits within the fluid whose vertical velocity opposed to the particles' own gravity (or buoyancy) motions. Tooby et al. showed that the balance of the two dominant forces, Stokes drag force (F_D) and gravity (buoyancy) force (F_g), controlled the formation of these particle orbits (Figure 2.21b). Small second-order perturbing forces, which include the centrifugal buoyancy force (F_p) and a lift force (F_L), were found to control the long-term evolution of the circular orbits (i.e. slow inward or outward spiral).

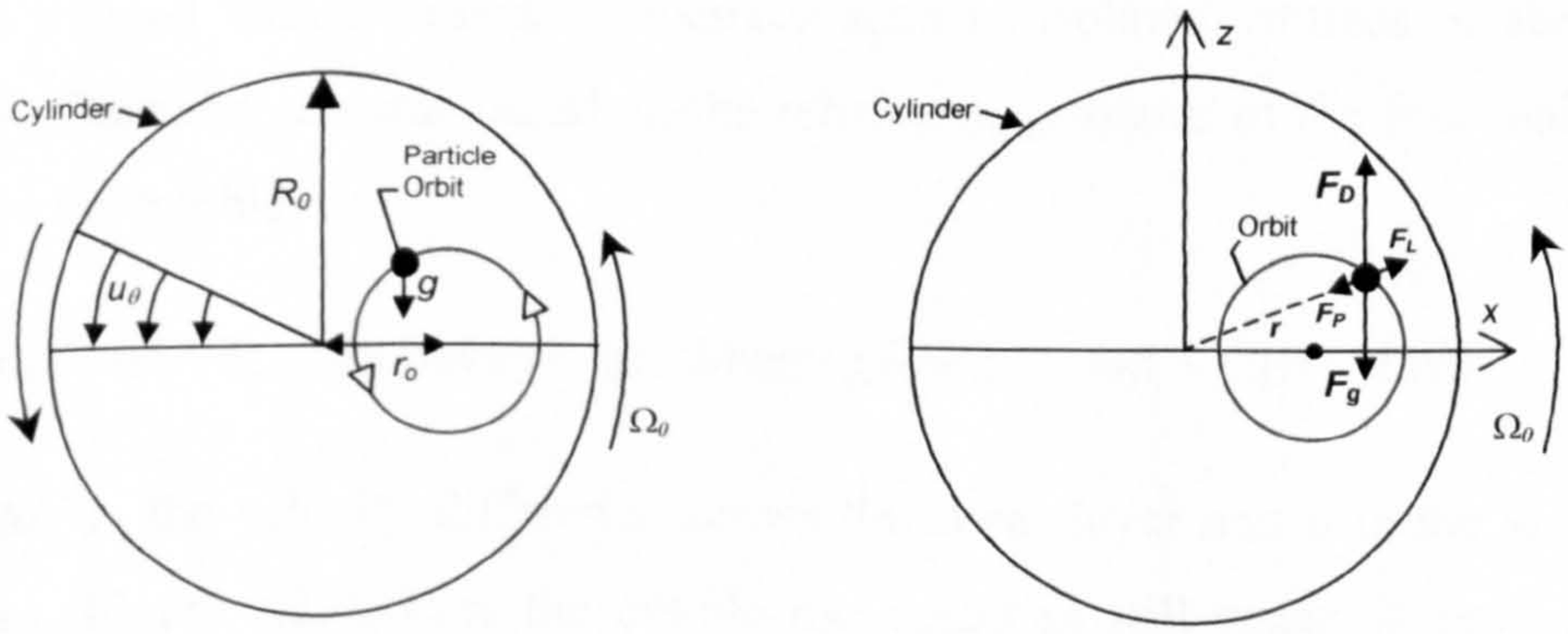

Figure 2.21 - (a) Discrete particle motion in a simulated solid-body vortex; (b) forces acting on a sphere resulting in unstable orbital paths (both modified from Tooby et al., 1977)

Nielsen (1984) adopted an analytical approach to confirm the formation of circular orbits for all sediment particles with fall velocities smaller than the maximum upward velocity within the vortex core. He also proved this trapping mechanism was not restricted to the simplest solid-body vortex flow, considered previously by Tooby et al. (1977), but that closed trajectory paths were in fact a general feature of vortex flow. Nielsen (1984) showed that sediment particles within a free vortex can be theoretically stationary at the two locations where the particle fall velocity is balanced by the upward fluid velocity (Figure 2.22). The circle joining these two points is the locus where particles will have no vertical component of velocity. Particles within this circle will move upward, while particles outwith this circle will have a downward trajectory.

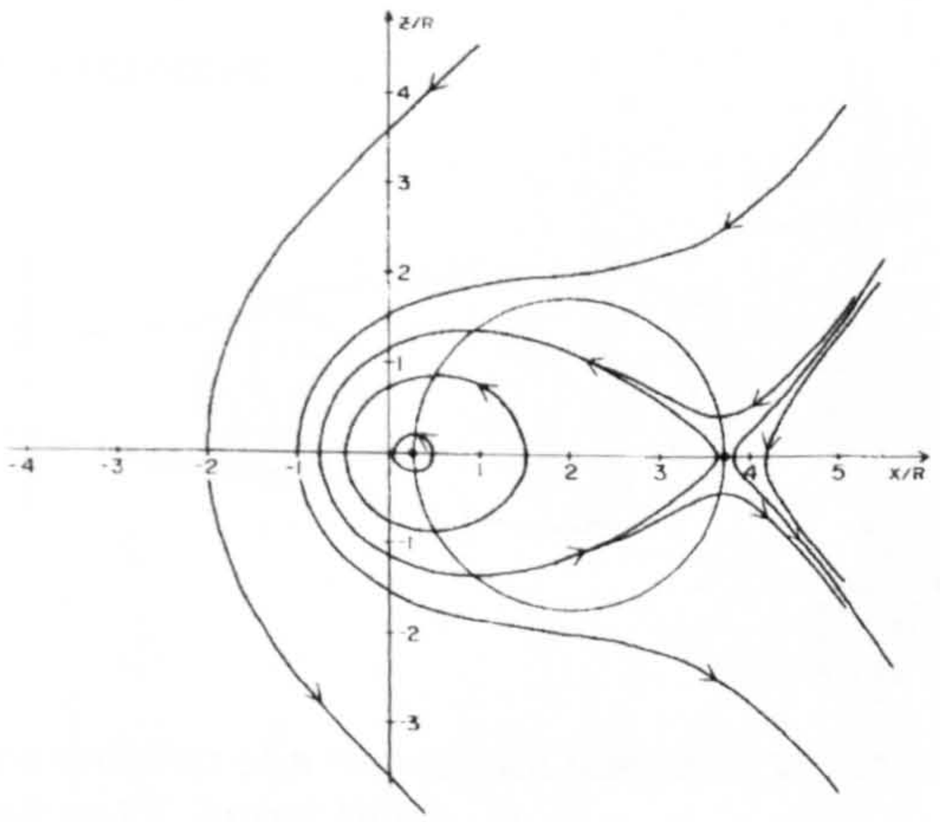

Figure 2.22 - Analytically derived sediment particle trajectories corresponding to $\vec{u}_s = \vec{u}_r + \vec{w}_s$ (taken from Nielsen, 1984).

In a closely related analytical investigation of the forces applied to spherical bubbles within an inhomogeneous and unsteady flow, Sene, Hunt and Thomas (1994) derived two key dimensionless groups which determine whether the bubbles can become trapped within coherent structures such as isolated vortices or shear layer vortices. This analysis was based on the relative magnitudes of the four main forces acting on the bubble, i.e.

$$Inertia \sim \Delta U^2/\delta; \quad Buoyancy \sim g; \quad Drag \sim gW/V_t; \quad Lift \sim C_L W(\Delta U/\delta) \quad \ldots.(2.14)$$

where ΔU is the velocity difference across the shear layer and δ is the shear layer thickness (Figure 2.23), V_t is the bubble rise speed in still water, W represents the bubble slip speed and C_L is the lift coefficient (= 0.5 for spherical bubble).

The first dimensionless group, known as the *relaxation* parameter $\Pi = \Delta U^2/2gx$, represents the ratio of the inertial to buoyancy forces, with the distance from shear layer origin x assumed proportional to δ. The second group, known as the *trapping* parameter $\Gamma = \Delta U/V_t$, effectively represents how well the vortex or shear layer can trap particles. The authors found, for the solid-body forced vortex considered by Tooby et al. (1977), that no bubble trapping occurred when $\Gamma << 1$, i.e. weak shear-generated vorticity or high bubble rise speed. However, when $\Gamma >> 1$ under conditions of strong shear-generated vorticity or small bubble rise speed, bubbles formed closed circular orbits in the downflow side of vortex as a result of buoyancy and drag forces, as previously observed by Tooby et al. (1977) and Nielsen (1984). Inertial and lift forces govern the location within the downflow at which these closed bubble trajectories converge.

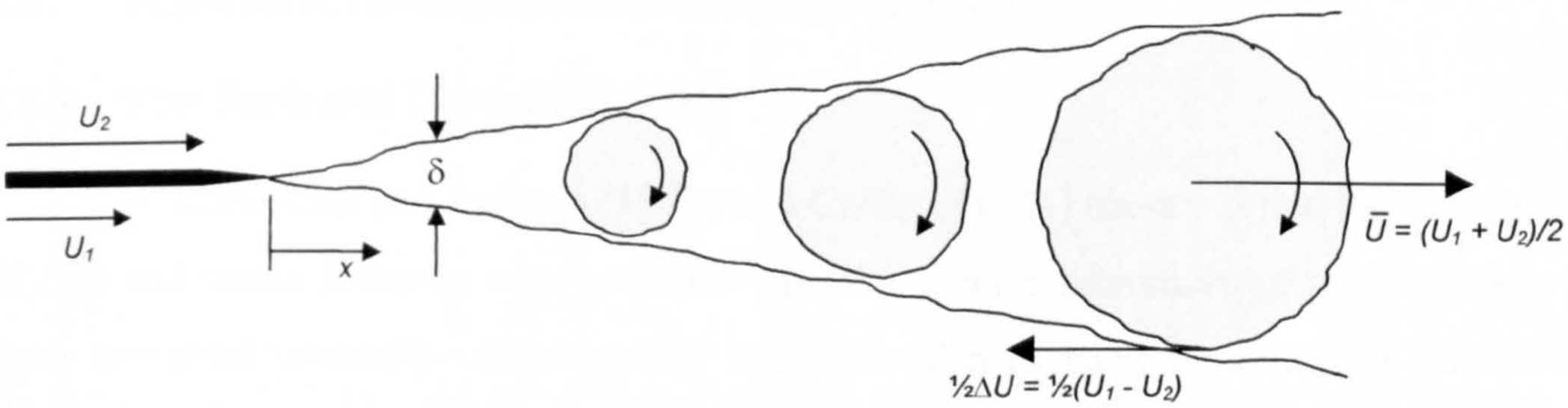

Figure 2.23 - Schematic representation of a two-stream planar shear mixing layer (taken and modified from Sene, Hunt and Thomas, 1994)

Within a horizontal mixing layer (Figure 2.23), the authors found that the critical value of Γ for bubble trapping varied dependent on the relative magnitude of the inertial and buoyancy forces, described by the relaxation parameter Π. For weak inertial forces (i.e. $\Pi \rightarrow 0$), the critical value of Γ is about 10, falling to about 3 when the inertial forces are comparable with buoyancy forces (i.e. $\Pi \rightarrow 0.5$).

In the special case where $\Pi << 1$ (inertia-to-buoyancy ratio) and $\Pi/\Gamma << 1$ (lift-to-drag ratio), inertial and lift forces are negligible in comparison to buoyancy and drag forces. Here, the problem clearly reduces to a simplified case where the relative velocity between the bubble and the fluid is essentially equal to the bubble rise speed in still water. This zero-order solution, where fluid accelerations are negligible compared to gravitational effects, was also determined for sediment particles (Nielsen, 1984), with the particle velocity in a vortex obtained from the vector sum of fluid velocity and still water fall velocity w_s.

2.5.3 Summary

The effect of coherent turbulent structures on the motion of fine particles has been observed within the near-bed region of a turbulent open channel shear flow (§2.4.2, pp. 31) and within a simulated vortex and shear mixing layer (§2.5.2 above). In each case, the observed particle-turbulence interactions are clearly dependent on relative influence of gravity (or buoyancy) and fluid forces on the particle motion. Considering the motion of sediment particles within these flow domains, the motion of large particles is likely to be dominated by gravity, deviating considerably from the flow paths of surrounding fluid elements. By contrast, fluid forces may dominate the motion of smaller particles, leading to a closer association between the trajectories of the particles and surrounding fluid element (i.e. particles tend to follow the fluid).

2.6 Deposition, Infiltration and Flushing Processes

2.6.1 Fine Sediment Deposition Rate

Both Beschta and Jackson (1979) and Carling (1984) observed that the transfer of fine sediments between near-bed flow and the surface interstices of a gravel-bed layer occurred primarily under gravity but were also assisted by turbulent pulses. Peloutier (1998) reported that suspended fine sediments are directly influenced by the near-bed turbulence structure, giving rise to a process referred to as *enhanced deposition* (see below). In general, however, the non-uniform configuration of natural gravel (i.e. grain size, porosity) has meant that knowledge on particle-turbulence interactions that occur within the bed surface interstices and their influence on the deposition of fine sediments remains relatively sparse.

Laboratory investigations of sediment deposition into a static gravel bed have revealed the unequivocal linear relationship between deposition rate and the sediment concentration (i.e. Einstein 1968, Carling 1984 and Peloutier 1998), with the proportionality constant having the dimensions of velocity.

From qualitative observations of the deposition of fine silica flour (3.5-30μm), Einstein (1968) described the deposition process in terms of a conceptual plane or boundary within the surface layers of the bed, below which settling particles were unaffected by turbulence and were not re-entrained back into the flow. From this idealised model, Einstein derived a simple expression for the deposition rate Δ into the bed as,

$$\Delta = C_b w_s \quad \text{....(2.15)}$$

where C_b is the concentration immediately above the conceptual boundary and w_s is the sediment particle fall velocity w_s.

Carling (1984) obtained a high correlation between the initial concentration of fine sands C_0 and their overall deposition rates Δ_{ts} within a test-section of a bed of open-work gravel. The constant of proportionality was defined as representing the average exchange velocity between the flow and the gravel void space. The ratio of this exchange velocity to the average fall velocity of the sand grades used was found to be 0.6, suggesting hindered deposition characteristics, i.e.

$$\Delta_{ts} = 0.6 C_0 w_s \quad \text{....(2.16)}$$

Peloutier (1998) extended the work of Carling (1984) to consider the linear relationship between near-bed fine sediment concentrations (C_b) and local deposition rates (Δ_b) under different hydraulic and sediment conditions. He defined the proportionality coefficient as the deposition velocity w_d, representing the average fall velocity through the bed surface layer. He also defined a non-dimensional ratio of deposition velocity and the still water fall velocity (i.e. $w_d^* = w_d/w_s$) as indicating the effect of the gravel bed surface on the deposition characteristics of the sediment, i.e.

$$\Delta_b = w_d^* C_b w_s = C_b w_d \quad \text{....(2.17)}$$

Deposition velocities w_d were shown to generally increase with grain size d_i, but decreased with increasing bed shear stress and turbulence levels. Most interesting, however, was the observed phenomenon of enhanced deposition (i.e. $w_d^* > 1.0$) for particles finer than about 200 microns in diameter. It was hypothesised that this phenomenon is a result of particle interactions with near-bed turbulent structures. One of the implications of this finding is that observed deposition rates may vary considerably from predicted fluxes, which are commonly assumed to be the product of near-bed concentration C_b and still water fall velocity w_s.

2.6.2 Spatial Distribution of Deposition

Early qualitative experiments by Einstein (1968) revealed size sorting in fine silica flour deposits downstream of the input point, with coarse particles settling out

first, while finer particles remained in suspension for longer periods. Mass continuity principles indicate that this net-deposition of sediment will lead to a decrease in near-bed concentration, and hence deposition rates, with increasing downstream distance. This downstream sorting of sediment is commonly described as an exponential decay function of distance from the point source, e.g. Sundborg equation (Carling, 1984):

$$\Delta = \frac{w_s p}{H} C_0 . e^{-\left(w_s pL/\overline{U}H\right)} \qquad \text{....(2.18)}$$

where p the overall probability of particle deposition, equal to 0.6 (Carling, 1984) or expressed in terms of the excess shear stress as $k\left(1-\tau_b/\tau_{cr}\right)$ (McCave and Swift, 1976); L is the distance from source; and $\overline{U}$ is the mean flow velocity.

From theoretical and experimental considerations, Einstein (1968) described the exponential decay of fine sediment deposition against time through the notion of a half-life T of any particle size to remain in suspension, i.e.

$$T = \frac{0.692H}{w_s \eta} \qquad \text{....(2.19)}$$

where $lnC_0 - ln\frac{1}{2}C_0 = ln2 = 0.692$ represents the half-life concentration; and η is a correction factor for the time spent within the return pipe of the recirculating flume.

Jobson and Sayre (1970a) considered the deposition of fine and coarse sands in open channel flow over an impermeable bed of roughness elements. From the injection point at the free surface, the two grades of sand were found to deposit along the flume bed with a log-normal-type distribution.

2.6.3 Infiltration into a Static Gravel Bed

Once deposited into the surface layers of the stable gravel bed, fine sediments become available for deeper intrusion into the sub-surface layers, a process which has been studied both through laboratory experiments (e.g. Einstein 1968; Beschta and Jackson 1979; Carling 1984; Diplas and Parker 1992; etc.) and field investigations (i.e. Frostick et al. 1984; Lisle 1989; Sear 1993; etc.).

Einstein (1968) observed that deposited fine silica flour settled slowly through the gravel layer to the flume bed, filling the pores from the bottom of the bed layer up, whilst leaving the upper bed layers relatively free from fines. This infiltration pattern is commonly referred to as *siltation* (e.g. Carling, 1984).

Beschta and Jackson (1979) found particle size to be an important variable affecting the amount of fines intrusion into stable gravel beds. While fine (0.2mm) sand was found to fill the gravel voids from the bottom up, in accord with Einstein (1968), coarser (0.5mm) sands clogged the upper layers of the bed, forming a '*seal*' to deeper fines intrusion into the bed gravel. This *sealing* pattern of infiltration forms when the fine sediment particles are large enough to bridge the voids within the framework gravel (Diplas and Parker, 1992). The depth at which this seal forms was found to vary depending on the Froude number and shear stress generated at the bed (Beschta and Jackson, 1979), although these relationships were not fully understood. Typically, however, laboratory and field experiments have revealed the seal formation depth to range between about 2.5 to 5.0D_{90}, where D_{90} refers to the 90-percentile size of the framework gravel (i.e. Beschta and Jackson 1979; Lisle 1989; Diplas and Parker 1992).

From an experimental study of the clogging of a porous column of regularly packed uniform spheres, Sakthivadivel and Einstein (1970) determined the ratio of framework pore size to fine sediment size (D_p/d) to be the critical parameter controlling the infiltration of fines. Tests indicated that fines with $D_p/d \leq 6.35$ were excluded from the framework pores, depositing on top of the spheres and forming a surface mat. This value is comparable with the critical Apollonian ratio of 6.5 for fines infiltrating tight rhombically-packed spheres. When $D_p/d \geq 15.0$, fines passed through the porous spheres with less than 1% of total pore space left occupied by fines (i.e. equivalent to *siltation*). Within the intermediate range $7.0 \leq D_p/d \leq 15.0$, the pore space between the uniform spheres became completely clogged with fines after varying lengths of time (i.e. equivalent to *sealing*).

For naturally graded sediments, Lisle (1989) suggested the ratio of minimum framework size to maximum matrix particle size (i.e. D_{min}/d_{max}) expresses the least potential for fine sediment intrusion into the bed material. Analysis of experimental data revealed that the ratio D/d must be large (> ~60) to allow infiltration below the surface layers of a naturally graded gravel bed and considerably higher than the critical values in a bed of uniform spheres (> ~15). Frostick et al. (1984) also showed that the superimposition of a coarse armour layer on top of a comparatively finer subsurface layer encourages the formation of a seal in the near-surface pores of the bed.

2.6.4 Winnowing and Flushing Processes

While depositing fine sediments can clearly accumulate within the gravel bed, filling the pores from the bottom up or forming a near-surface seal, the surface interstices are often observed to remain relatively clean from fines (e.g. Einstein 1968; Beschta and Jackson 1979; Carling 1984). This bed cleansing process, commonly known as *winnowing*, occurs under static bed conditions and results in the removal of suspendible fines from the bed surface layers. Field experiments revealed the depth to which fines are removed under static bed conditions is generally no greater than a few median bed grain diameters (i.e. Frostick et al. 1984, Lisle 1989). Laboratory experiments indicated only partial cleansing of the surface or pavement layer to a depth approximately equal to the median grain-size of the bed material (Carling, 1984), with the fine sediments deposited within the sub-surface layers remaining intact (Diplas and Parker, 1992).

Beschta and Jackson (1979) suggested that without movement of the bed surface layer (i.e. bedload transport), no mechanism exists to remove infiltrated fine sediments from the sub-surface layers. Other researchers have also emphasised the requirement of bed surface or pavement mobilisation to enable the flushing of fines below the pavement layer (e.g. Milhous 1973; O'Brien 1987). In natural gravel bed reaches, the specification of an appropriate flushing flow to remove fines from gravel bed interstices is complex and has to consider ecological responses as well as the physical changes to the gravel bed composition (Wilcock et al., 1996).

2.7 Mathematical Modelling of Suspended Sediment

2.7.1 Introduction

Analytical models of suspended sediment transport have been extensively used to obtain knowledge of the sediment concentration distribution within turbulent open channel flow and the exchange of fine sediments at the bed boundary. These models can be sub-divided into often overlapping categories: (i) deterministic or theoretical; (ii) probabilistic; and (iii) numerical models.

Deterministic theoretical models are by nature generally restricted to steady-state conditions (i.e. $\partial/\partial t = 0$) (Alonso, 1981). They also assume that sediment concentration is solely a function of elevation above the bed level z, whilst independent of both longitudinal and lateral co-ordinate directions ($\partial/\partial x = \partial/\partial y = 0$)

(Raudkivi, 1990). Consequently, the net flux of sediment across a horizontal plane at any elevation z must by definition be zero, implying that the downward gravitational motion of sediment particles and their upward diffusive motion due to turbulent mixing are in equilibrium. Suspended sediment concentration profiles, derived under the assumption of equilibrium conditions [such as the well-known Rouse equation], have generally limited applicability in natural river environments.

Numerical models have been developed to predict of the time and space distributions of suspended sediment transport that would be observed under non-equilibrium conditions such as exist in gravel-bed rivers. Most commonly, these methods are based on either: (i) the Eulerian solution of a mass-balance equation for suspended sediment within the turbulent flow; or (ii) a probabilistic approach based on the prediction of Lagrangian-type particle trajectories within the flow.

2.7.2 Eulerian Diffusion Approach

Within the Eulerian framework, suspended sediment concentrations are generally computed from the solution of a mass-balance equation representing the advective-diffusive transport of a transferable quantity such as fluid momentum, contaminants or suspended sediment. This equation has the general form (Jobson and Sayre, 1970a),

$$\frac{\partial C}{\partial t}+u_{si}\frac{\partial C}{\partial x_i}-\frac{\partial}{\partial x_i}\left(\varepsilon_{\Gamma i}\frac{\partial C}{\partial x_i}\right)=0 \qquad \ldots.(2.20)$$

in which C is the concentration of the scalar quantity, u_{si} is the advection velocity of the quantity in the ith direction, t is time, x_i is the ith coordinate and $\varepsilon_{\Gamma i}$ represents the turbulent transfer coefficient for the scalar quantity Γ in the ith direction. Under the assumption of steady state conditions ($\partial/\partial t = 0$) and uniform two-dimensional flow, equation 2.20 can be written for suspended sediment in the form,

$$u_s\frac{\partial C}{\partial x}=\varepsilon_{sx}\frac{\partial^2 C}{\partial x^2}+\frac{\partial}{\partial z}\left(\varepsilon_{sz}\frac{\partial C}{\partial z}+w_s C\right) \qquad \ldots.(2.21)$$

where ε_{sx} and ε_{sz} are the sediment turbulent diffusion coefficients in the longitudinal and vertical directions, with u_s and w_s the longitudinal and vertical components of particle velocity in the turbulent flow conditions, respectively.

Within the Fickian diffusion theory invoked in equation 2.21, it is traditionally assumed that the turbulent diffusion coefficient of the sediment ε_s is related to the turbulent eddy viscosity ν_t through an empirical constant β (i.e. $\varepsilon_s = \beta.\nu_t$) (e.g. Jobson and Sayre 1970a, van Rijn 1986). The reciprocal of this empirical constant β equivalent to the proportionality coefficient σ_c known as the Schmidt number (i.e. $\sigma_c = 1/\beta$) (Celik and Rodi, 1988). Jobson and Sayre (1970) summarised that most investigators have concluded that $\varepsilon_s < \nu_t$ (i.e. $\beta < 1$; $\sigma_c > 1$), as particles cannot respond fully to turbulent velocity fluctuations within the flow. Others, however, have reasoned that $\varepsilon_s > \nu_t$ (i.e. $\beta > 1$; $\sigma_c < 1$), as centrifugal forces acting on sediment particles would be greater than those on the fluid elements, resulting in particles being thrown to the outside of the eddies, with a consequent increase in mixing length and diffusion rate. This latter finding appears to be in contradiction to the evidence presented in §2.5 that discrete sediment particles (or bubbles) can become trapped in vortices, forming circular obits in rotational flow regions opposing their gravitational (buoyancy) tendencies (e.g. Tooby et al. 1977; Nielsen 1984; Sene et al. 1994).

Van Rijn (1984) used Coleman's (1970) flume and field data to determine a parabolic-constant distribution for the momentum transfer of fluid elements and computed the empirical constant β relating ε_s to ν_t from,

$$\beta = 1 + 2\left(\frac{w_s}{u_*}\right)^2, \quad \text{for } 0.1 < \frac{w_s}{u_*} < 1 \qquad \ldots.(2.22)$$

Numerous other models have been proposed for ε_s, based on the analogy between the turbulent diffusion of sediment particles and momentum transfer of fluid elements, none of which have been found to provide universally satisfactory results. This results partly from the lack of consensus on the empirical constant β (whether indeed it should remain constant), in addition to the theoretical deficiencies intrinsic in the simplistic analogy (Cao et al. 1996).

Other common assumptions associated with equation 2.22 include the sediment fall velocity w_s being generally taken to be equal to the standard fall velocity in still water conditions and the longitudinal particle velocity u_s assumed to be equal to the mean local streamwise component of fluid velocity U.

2.7.2.1 Boundary Conditions

The boundary conditions at the free surface and bed interface are obtained from integration of equation 2.21. At the free surface, the net vertical flux of sediment across the surface must by definition be equal to zero (Celik and Rodi, 1988), i.e.

$$\varepsilon_s \frac{\partial C}{\partial z} + w_s C = 0 \qquad \text{....(2.23)}$$

At the bed interface, the net flux of sediment is zero only when deposition and entrainment fluxes are equal. Under these equilibrium conditions, it is implicit from equation 2.23 that the downward flux of sediment ($w_s C$) is balanced by an upward flux due to turbulent diffusion ($\varepsilon_s \partial C/\partial z$). Under non-equilibrium conditions, Celik and Rodi (1988) defined the finite flux across the bed boundary as the difference between the deposition and entrainment rates (D and E, respectively), i.e.

$$\varepsilon_s \frac{\partial C}{\partial z} + w_s C = D - E \qquad \text{....(2.24)}$$

The deposition rate D is generally acknowledged to be the product of the sediment deposition velocity (w_d) and near-bed concentration (C_b) (§2.6), with the common assumption that w_d can be taken as the still water fall velocity w_s.

In experiments studying the net-deposition case (i.e. $D > E$), Jobson and Sayre (1970a, b) investigated the relative influence of fall velocities w_s and diffusion coefficients ε_s on the vertical transfer of fine sediments. They suggested the net-deposition rate should also take account of the probability p that particles reaching the bed are deposited there, i.e.

$$\varepsilon_s \frac{\partial C}{\partial z} + p w_s C = D - E \qquad \text{....(2.25)}$$

A general expression for p was proposed by Krone (1962) based on the concept of a critical shear stress for deposition τ_d, and its relative magnitude compared to the bed shear stress, i.e.

$$p = \left(1 - \frac{\tau_b}{\tau_d}\right) \qquad \tau_b \le \tau_d \qquad \text{....(2.26a)}$$

$$p = 0 \qquad \tau_b > \tau_d \qquad \text{....(2.26b)}$$

In comparison to the deposition flux D, an appropriate form for the sediment entrainment rate E is less apparent. Traditionally, a near-bed sediment flux or reference concentration has been prescribed by empirical relationships (Garcia and Parker, 1991). A commonly used approach is to set the near-bed reference concentration C_b to its equilibrium value $C_{b,max,}$. As an alternative to specifying $C_{b,max}$, van Rijn (1986) set the upward entrainment flux equal to its equilibrium value E_{max}, itself calculated from $C_{b,max}$ through $E_{max} = w_s C_{b,max}$. These empirical methods, however, have the disadvantage of being valid only for loose, flat beds of uniform material with unlimited sediment supply (Celik and Rodi, 1988). They also fail to acknowledge the close association between turbulent bursting processes and the entrainment of sediment particles away from the bed (§2.4).

Recently, however, Cao (1997) derived a simple theoretical model relating the entrainment flux E of sediment particles from a flat, loose bed to the averaged turbulent bursting period T_B scaled on inner variables (u_* and ν) and on the spatial extent of the turbulent bursts, i.e.

$$E = \frac{\lambda_b C_0 (\Delta g)^{0.5}}{\nu T_B^+} d_s^{1.5} \left(\frac{F}{f} - 1 \right) F \qquad \text{....(2.27)}$$

where λ_b is the averaged total burst area per unit bed area (estimated from observed burst dimensions); C_0 is the volumetric concentration of the loose bed sediment; T_B^+ is the non-dimensional burst period ($=T_B u_*/\nu$); d_s is the sediment particle size; F is the Shields parameter and f is the critical Shields parameter for the initiation of particle motion. This entrainment flux was found to have generally good agreement with available experimental data and provides a basis for the development of more refined entrainment models based on the turbulent bursting process as opposed to empiricism.

2.7.3 Lagrangian 'Random Walk' Approach

As an alternative to the Eulerian diffusion approach, suspended sediment dispersion, settlement and deposition processes have also be simulated using Lagrangian 'random walk' techniques. This so-called stochastic approach predicts the dispersion of solid particles through applying probabilistic techniques to describe the instantaneous particle motion, based on measured turbulence parameters (Bechteler and Farber 1985). Under the assumption that these turbulence parameters

are realisations of random processes (Hoyal et al. 1995), the vertical and horizontal trajectories of individual particles can be traced within a turbulent velocity field over time (Figure 2.24), i.e.

$$\Delta Z_i = (w' - w_s)\Delta t_i \quad \text{....(2.28)}$$

$$\Delta X_i = (U - u')\Delta t_i \quad \text{....(2.29)}$$

where ΔZ_i and ΔX_i are the i^{th} particle displacements; w' and u' are the random components of fluid velocity; w_s and U are the mean local vertical and streamwise advective velocities, respectively; and Δt_i is the time increment. It is apparent that particle motions, described by equations 2.22 and 2.23, are assumed to mirror the motion of the surrounding fluid, as the particles settle through the fluid with a downward fall velocity w_s (Alonso, 1981). These incremental particle displacements are valid within the full flow region between a reflecting free-surface boundary and a fully absorbing boundary condition at the bed surface, where the particle motion is terminated (Hoyal et al. 1995).

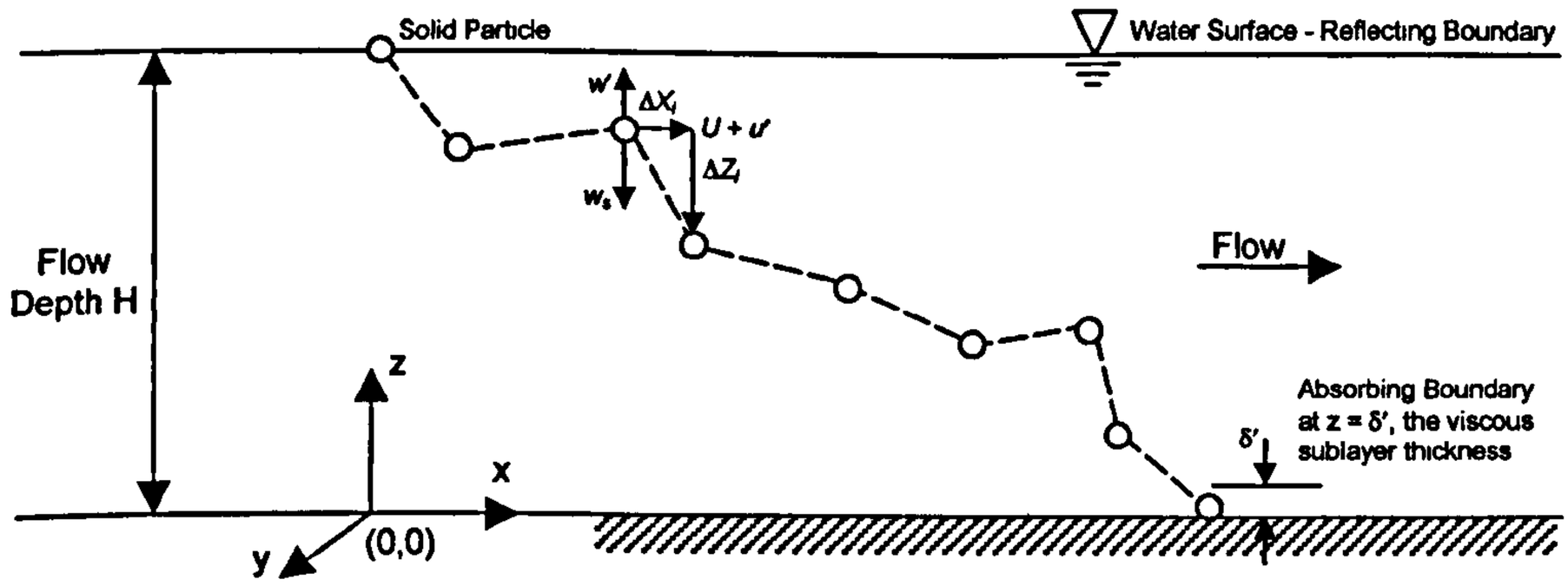

Figure 2.24 - Definition Sketch of Solid Particle Settlement (Lagrangian 'Random Walk' Modelling) (taken and modified from Li and Shen, 1975)

One of the main disadvantages of the Lagrangian approach, like other modelling techniques for suspended sediment transport, is that the fluid is characterised as a highly averaged turbulent flow field with a quiescent near-bed layer which absorbs all particles (Hoyal et al. 1995). This physical representation of the turbulent flow tends to mask the presence of quasi-ordered or coherent turbulent structures (Tooby et al. 1977), and would appear to be most unrepresentative within the near-bed flow region where turbulence is often characterised by violent fluid bursts and sweeps (e.g. Grass, 1971).

In a related discussion, Wallis and Moores (1996) questioned the validity of the fully absorbing bed boundary condition generally employed within Lagrangian 'random walk' modelling, particularly as it assumes all particles reaching the boundary layer are deposited (i.e. no re-entrainment). In reality, the proportion of particles reaching the bed that are deposited will clearly be primarily dependent on the sediment characteristics, mean flow conditions, near-bed turbulence intensities and the bed conditions (e.g. roughness, permeability). Wallis and Moores suggest that a deposition probability term similar to that proposed by Jobson and Sayre (1970a, b) could be used to test the model sensitivity to the 'absorption efficiency' of the bed.

2.7.4 Summary

Of the two modelling approaches traditionally employed to simulate the transport of suspended sediments, Eulerian diffusion theory is employed to a greater extent than the Lagrangian-type trajectory models. Both modelling approaches require significant simplifications to compensate for the lack of knowledge of the physical mechanisms governing the motion of suspended sediment particles.

The principal simplifications employed in the diffusion theory are (i) the assumed analogy between the diffusion of sediment particles and the turbulent transfer of fluid momentum; (ii) the assumption that turbulence has no influence on the sediment fall velocity; and (iii) the assumption of equilibrium transfer conditions at the bed boundary, calculated from empirically derived formulae. Within the Lagrangian framework, while the main difficulties appear to lie in the simulation of turbulence characteristics, the validity of the fully absorbing bed boundary has also been questioned.

2.8 Summary of Key Aspects

The fate of fine sediments transported in suspension within a gravel-bed river is determined by their motion in the turbulent flow conditions and their subsequent behaviour at the bed surface interface. The combined effects of turbulent fluid motions and gravity is the primary control on the vertical motion of suspended sediment, within which, the sedimentary fall velocity is a key parameter determining their relative influence. 'Heavy' particles tend to be relatively unaffected by

turbulence and settle more or less under the primary influence of gravity at their terminal fall velocity. By contrast, turbulent fluid motions dominate the vertical transfer of 'light' particles that lie within the Stokes-range, while an intermediate range of particles exists where their vertical transfer is influenced both by gravity and turbulence. The outstanding issue for the latter two ranges would appear to lie in defining the influence turbulence has on the vertical transfer of particles. Evidence presented from previous studies to date (§2.2.3) appears to be inconclusive, often providing conflicting results.

Improved knowledge of the structure of flow turbulence and in particular the identification of quasi-ordered or coherent structures may improve the understanding of underlying sediment transport mechanisms. The turbulent bursting process has already been shown to play a key role in the suspension of sediment particles from the near-bed flow over both smooth and rough bed surfaces, while vortex trapping has been proposed as a possible mechanism for the maintenance of particle suspension.

The net exchange of sediment across the interface at the gravel-bed surface is controlled by the relative magnitude of the deposition and entrainment fluxes, which in turn controls the composition and structure of the gravel bed. The decision as to whether a sediment particle is deposited appears to be made in the vicinity of the bed surface layer. Deposition rates depend primarily on the near-bed sediment concentration, but can also be affected by other parameters such as bed-shear stress, near-bed turbulent structure and bed surface configuration. Entrainment rates, by contrast, are primarily controlled by the amount of fines stored within the sub-surface gravel pore space and the degree of bed surface mobilisation required for their removal through 'flushing' processes.

In summary, this literature review has attempted to describe the main factors influencing fine sediment transport and its associated sedimentation processes, as well as highlight the deficiencies that remain in the understanding of the underlying mechanisms. These deficiencies are most apparent in the substantial assumptions and simplifications required in modelling techniques employed to describe the motion of fine sediment particles. These tend to be related to the model representation of turbulence and in particular its effect on the vertical motion of sediment particles, both within the main body of flow and across the bed surface boundary. The influence of turbulence and other parameters on particle motion in turbulent flow conditions is the basis on which the current study is undertaken.

CHAPTER 3

Experimental Studies – Apparatus and Procedures

3.1 Introduction

The complexity of studying sediment transport processes in natural river environments has meant that laboratory investigations have often been essential in advancing our knowledge and understanding of the mechanisms governing these processes. The main advantage of laboratory studies is that they are conducted in a controlled environment that allows measurements to be taken with relative ease. This, in turn, facilitates the investigation of individual aspects of sediment transport and allows for single experimental parameters to be varied at any one time, enabling the influence of each individual parameter on the overall process to be isolated. Unfortunately, the sediment transport mechanisms observed within laboratory studies can often differ significantly from those observed in natural river environments. These inconsistencies are most likely to arise from assumptions made in the laboratory to simplify or even isolate the particular physical process under scrutiny or from scaling problems arising between the laboratory model and the river. Nevertheless, the data obtained from laboratory studies can help improve our understanding of the physics behind sediment transport, as well as assisting in the development of numerical models for its prediction.

The experimental investigations reported herein are predominantly concerned with the motion of fine sediments within a turbulent open channel shear flow over static, porous beds consisting of uniform and graded bed material. The typical interactions between the depositing fines and the surface layers of the bed are also investigated. The two measurement techniques employed, namely visualisation and flux measurements, essentially define the two independent series of laboratory flume experiments conducted within the current study.

3.2 Outline of Experimental Studies

Series 1 experiments were carried out in a glass-sided Armfield S5-10 flume (Figure 3.1) employing visualisation techniques to record and analyse the motion of fine sediment particles in the turbulent shear flow conditions. In the absence of expensive state-of-the-art particle image velocimetry (PIV) or particle tracking velocimetry (PTV) equipment, several new visualisation techniques were required to be developed to obtain both qualitative and quantitative data. Series 1 was subdivided into three individual studies (Series 1A, 1B and 1C) relating to the individual techniques employed and the type of observations and measurements made.

Series 1A was conducted as a preliminary set of experiments, primarily aimed at aiding the development of a more sophisticated visualisation technique to enable the detailed quantitative measurement of particle motion with respect to the turbulent flow characteristics. These initial experiments employed a standard VHS camera operating at 25 frames per second (fps) to record predominantly qualitative aspects of fine sediment particle behaviour in the near-bed flow region as well as observed interactions at the bed surface interface and within the surface layers of the porous bed. Ensuing from these preliminary experiments, Series 1B used more sophisticated high-speed motion camera equipment (operating at frame rates up to 600fps) and image capture/analysis software to obtain quantitative data on the motion of the fine sediment within the full depth of flow. The trajectories of individual sediment particles were analysed from sequences of captured frames by a particle tracking technique. The mean and fluctuating components of particle velocity in the XZ plane were calculated from the measured trajectories of a statistically significant number of recorded particles. These were then compared to the mean and turbulent flow characteristics, measured by a three-dimensional acoustic doppler velocimeter (ADV) at specific depth locations. The experiments conducted in Series 1C extended the comparison between the characteristics of fluid and particle motion to consider the specific interactions between sediment particles and local turbulent structures generated within the shear flow conditions. For these experiments a digital video camera was mounted in a frame attached to a mobile trolley system. This allowed the camera to be moved along a 1m section of the flume at the average flow velocity, recording images of typical particle-turbulence interactions at 25 fps. The images captured by the camera were again analysed using image analysis software.

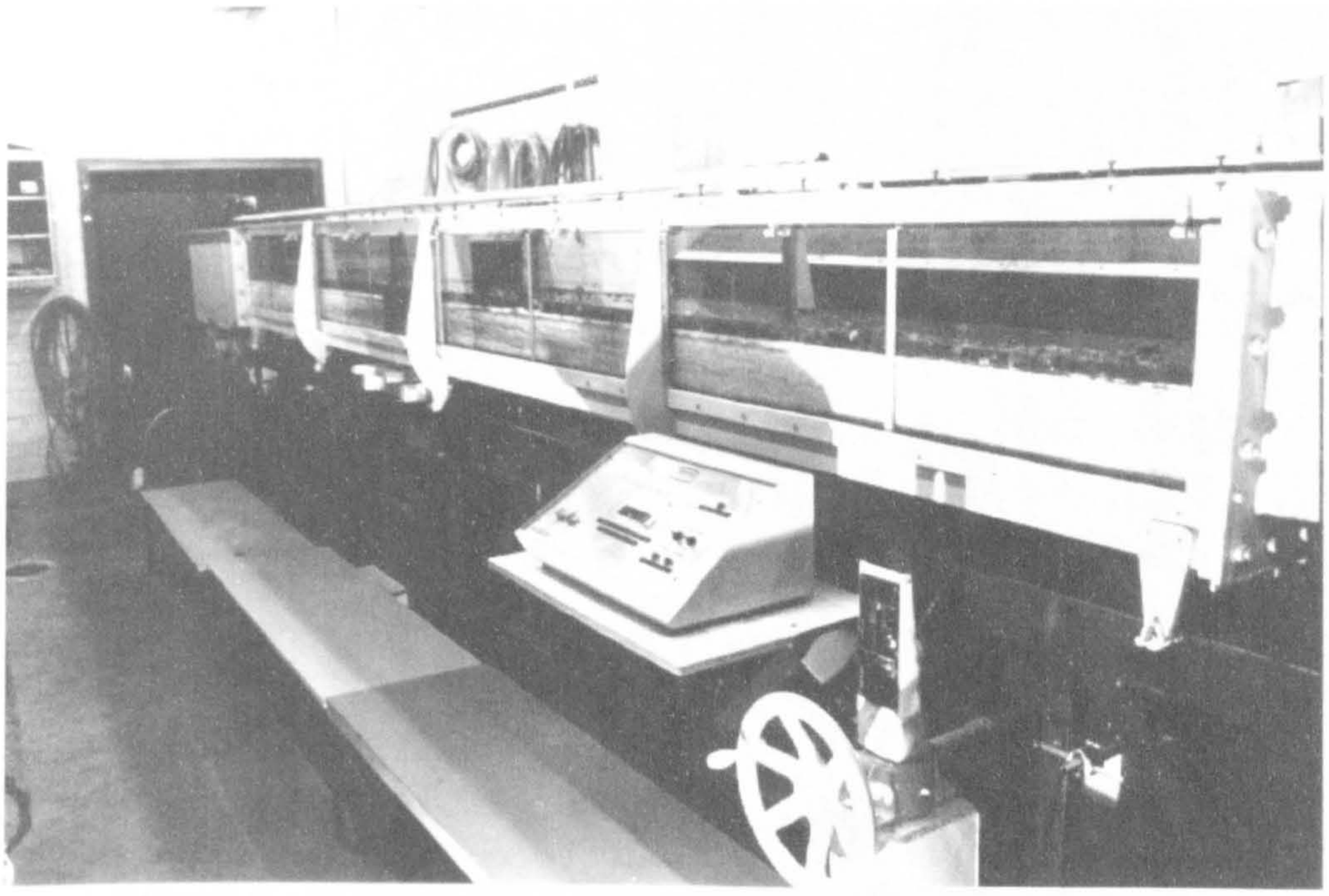

Figure 3.1 - Armfield S5-10 glass-sided laboratory flume used in Series 1 experiments

Series 2 was conducted in a larger rectangular flume facility with non-transparent walls (Figure 3.2), employing more traditional measurement techniques to study fine sediment transport and depositional characteristics in turbulent open-channel flow. One of the primary aims of these experiments was to validate the main findings from the preceding visualisation experiments. A series of sediment traps, running the full length of the flume, was used to collect sediment deposition samples passing through the porous layer of bed material. The deposition samples collected within each trap were sieved to obtain their fractional compositions, which were then used to calculate parameters such as fractional deposition rates, average fractional deposition lengths and depth-averaged turbulent fall velocities. Sediment concentration samples were also taken at specific locations along the flume and at known positions within the water column. When coupled with measured profiles of streamwise flow velocity, these were used to predict vertical profiles of fractional turbulent fall velocities and diffusion coefficients for the fine sediment. Near-bed sediment concentration samples were also related to local deposition rates within underlying traps. A parameter referred to as the *deposition velocity* (Peloutier, 1998), defining the average rate of exchange of fine sediment through the surface bed layers, was calculated from the observed relationship between near-bed concentration and deposition rate.

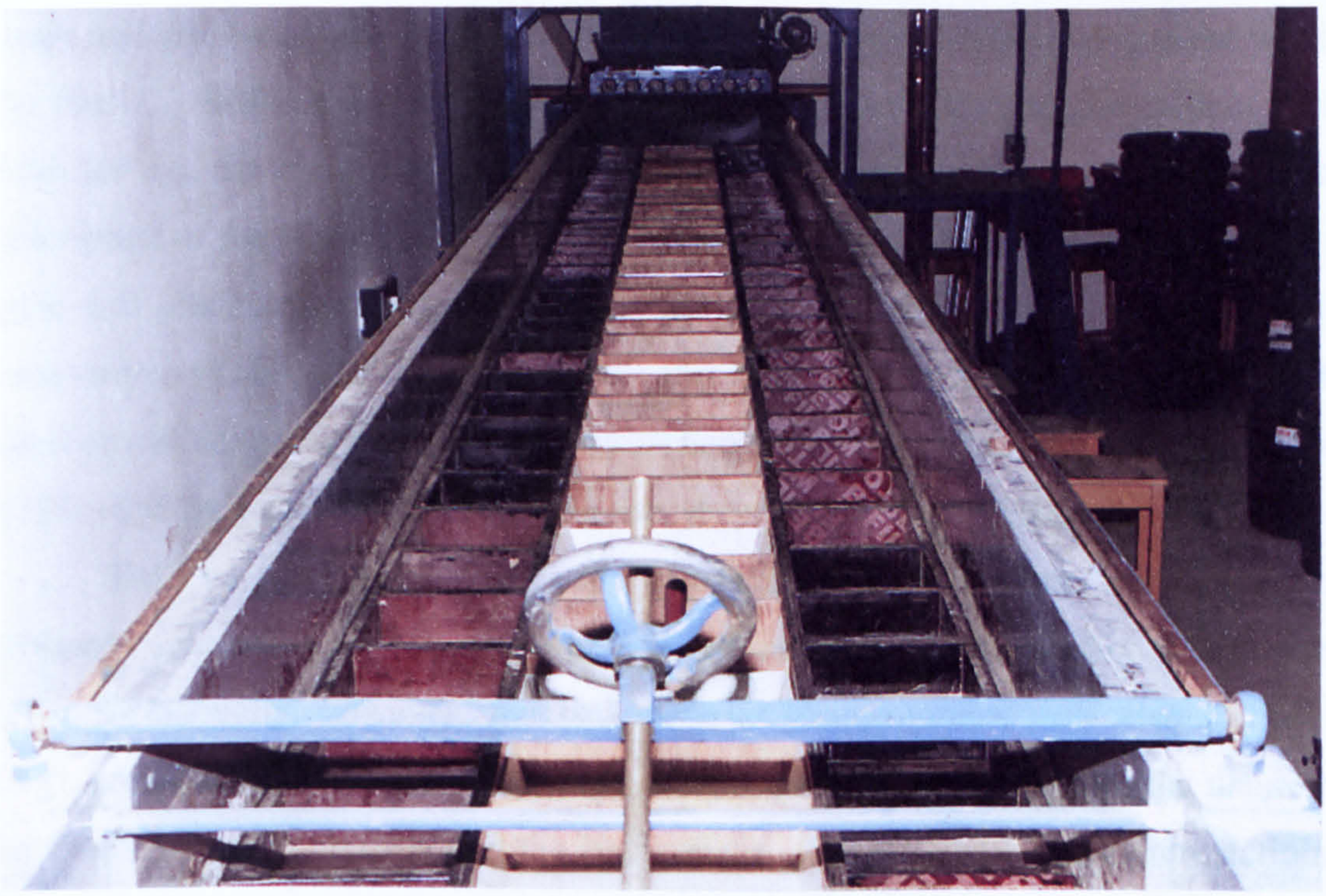

Figure 3.2 - Flume facility used in Series 2 experiments showing sediment bed trap configuration (looking upstream from tailgate weir)

3.3 Determination of Experimental Parameters

Before commencing the experiments, it was necessary to determine which experimental parameters were likely to influence the fine sediment transport, settling and depositional processes under consideration. Mathematically, these processes can be regarded as distinct quantitative variables, defined by a set of n independent or characteristic parameters $a_1, a_2, ..., a_n$ as follows

$$A = f_A(a_1, a_2, a_3, ..., a_n) \qquad ....(3.1)$$

where A is any property of the process under consideration. In the current study, the defining independent parameters a_i can be split into four categories: (a) fluid properties; (b) fine sediment properties; (c) bed material properties, and; (d) prevalent flow conditions. The characteristic parameters defining the fluid are its density ρ and dynamic viscosity μ. While these parameters can be easily measured or calculated for clear water conditions, the presence of fine suspended sediment within the fluid may significantly alter the fluid properties.

The parameters defining the fine sediment properties are its density ρ_s, the representative particle size d, the geometric properties of the sediment (i.e. particle

shape and grain-size distribution), and the sediment concentration at any point within the flow C. With the representative particle size d often taken as the median grain diameter d_{50}, the main problem in defining the fine sediment properties lies in the description of the geometric properties. It has been found that the particle shape and grain-size distribution cannot be adequately described by a finite number of parameters (Yalin, 1977), and have therefore generally been omitted from dimensional analyses. This has the restriction that the functional relation (equation 3.1) is valid only for the specified sediment shape and size distribution.

The bed material properties are especially important when considering the processes controlling the deposition of fine sediment through the surface layers of the bed. Additionally, however, the bed material characteristics may also influence observed particle-turbulence interactions within the flow resulting from the nature of the flow turbulence generated at the bed surface. Characteristic parameters defining the bed properties are the representative size D of the bed material, the porosity λ, and a measure of the bed roughness height, generally taken as the equivalent Nikuradse sand roughness k_s.

The presumption of steady, uniform flow conditions for a given fluid is often used within laboratory experiments when investigating sediment transport processes. For this simplified case, the characteristic parameters defining the mean flow conditions are the flow depth H, the flow width B, the energy line gradient s_f, the vertical distance from the channel bed z, and the gravitational acceleration, g. In general, the energy line gradient s_f is included in the bed shear velocity parameter u_* [$= (g.R.s_f)^{0.5}$, where R is the hydraulic radius of the flow]. In addition to these mean flow parameters, it is expected that the vertical motion and depositional characteristics of the fine sediment will be influenced by turbulence generated within the flow. However, the root-mean-square of the fluctuations in vertical flow velocity w'_{rms} is not included here as an independent variable as it is primarily related to the magnitude of the shear velocity u_* and the relative depth z/H, i.e. $w'_{rms}/u_* \; \alpha \; exp(-z/H)$, where w'_{rms}/u_* is the vertical turbulence intensity.

In summary, thirteen independent variables can be considered to describe the vertical motion of fine sediment within a turbulent open channel flow and its subsequent deposition through a layer of porous bed material. These can be written in the form of equation 3.1 as follows,

$$w'_s = f_{w'_s}(\mu, \rho, \rho_s, d, C, H, B, k_s, g, u_*, z) \quad \ldots.(3.2)$$

$$\Delta_b = f_{\Delta}(\mu, \rho, \rho_s, d, C, D, \lambda, H, k_s, g, u_*) \quad \ldots.(3.3)$$

where w'_s is the turbulent fall velocity of the fine sediment ($L.T^{-1}$) and Δ_b is the deposition rate of the fine sediment through the bed layer ($M.L^{-2}.T^{-1}$).

3.3.1 Dimensional Analysis - Buckingham's Π Theorem

The independent variables defined in equations 3.2 and 3.3 are combinations of the three fundamental quantities: mass M, length L and time T. Applying a dimensional analysis technique known as Buckingham's Π Theorem, these variables can be arranged into non-dimensional groups, which provide clear information on what parameters to vary within the experiments. In this technique $n - m$ non-dimensional Π groups are formed from the n independent variables describing the processes and m fundamental quantities (i.e. M, L and T). In consideration of equation 3.2, $n - m = 12 - 3 = 9\Pi$ groups can be formed. Selecting ρ, u_* and H as repeating variables, the resulting non-dimensional groups can be written:

$$\frac{w'_s}{u_*} = f\left(\frac{u_* H}{\nu}; \frac{\rho_s}{\rho}; \frac{d}{H}; \frac{C}{\rho}; \frac{B}{H}; \frac{k_s}{H}; \frac{u_*}{\sqrt{gH}}; \frac{z}{H}\right) \quad \ldots.(3.4)$$

Π_1 Π_2 Π_3 Π_4 Π_5 Π_6 Π_7 Π_8 Π_9

The turbulent fall velocity w'_s is made into a non-dimensional parameter by the shear velocity u_*, and is referred to herein after as the *non-dimensional turbulent fall velocity*. It is shown to be a function of: (i) the shear Reynolds number (Π_2); (ii) the relative density of the fine sediment (Π_3); (iii) the non-dimensional fine sediment size (Π_4); (iv) the dimensionless sediment concentration (Π_5); (v) the flow aspect ratio (Π_6); (vi) the relative bed roughness height (Π_7); (vii) a form of the Froude number (Π_8); and (viii) the relative depth (Π_9).

Applying the same procedure to equation 3.3 and using ρ, u_* and d as the repeating variables, the resulting 9 non-dimensional Π groups are,

$$\frac{\Delta u_*}{\rho g d} = f\left(\frac{u_* d}{\nu}; \frac{\rho_s}{\rho}; \frac{d}{D}; \frac{C}{\rho}; \lambda; \frac{d}{H}; \frac{k_s}{d}; \frac{u_*}{\sqrt{gd}}\right) \quad \ldots.(3.5)$$

Π_1 Π_2 Π_3 Π_4 Π_5 Π_6 Π_7 Π_8 Π_9

The ratio $u_*/(\rho g d)$ is used to change the deposition rate Δ into a non-dimensional parameter. The dimensionless deposition rate Π_1 is a function of: (i) a form of the Reynolds number relating to fine sediment size (Π_2); (ii) the relative density of the fine sediment (Π_3); (iii) the ratio of the fine sediment to bed material grain size (Π_4); (iv) the dimensionless sediment concentration (Π_5); (v) the bed porosity (Π_6); (vi) the relative size of the fine sediment to flow depth (Π_7) and bed roughness (Π_8); (vii) a form of the Froude number (Π_9).

3.3.2 Scaling Considerations

In conducting a study of sediment transport processes within a laboratory flume, it is important to identify how the relative scales of the flow and sediment parameters vary between the laboratory model and the alluvial river or stream (prototype). It is clearly essential to retain an identical flow regime in the model as would be observed within the river. Under steady, uniform open channel flow conditions, the flow regime can be defined in terms of the flow Reynolds number R_e (i.e. *laminar*, *transitional turbulent* or *fully turbulent*) or the Froude number F_r [i.e. *subcritical* ($F_r < 1$) or *supercritical* ($F_r > 1$)]. However, in maintaining equal flow regime between the model and prototype, it is often not possible to obtain geometric similarity (Novak and Cabelka, 1981), with at least one geometric scale within the model requiring to be distorted, typically the scale of flow depth H.

By contrast, the grain-size distribution and properties of the sediment are often tested at a 1:1 scale to that occurring naturally in alluvial rivers and streams. Previous laboratory investigations of fine sediment deposition and accumulation processes, have generally adopted a 1:1 scaling for the bed gravel and fine sediment (e.g. Beschta and Jackson, 1979; Carling, 1984; Peloutier, 1998), with the exception of Diplas and Parker (1992) who carried out their investigations at a reduced scale. For the current study, the 1:1 scaling of both framework and matrix sediments, in terms of their size distribution and physical properties, has been adopted.

3.3.3 Range of Experimental Variables

The range of the main experimental variables is outlined in Table 3.1 for both the Series 1 and 2 experiments. Comparison values from the previous experimental

investigations carried out by Jobson and Sayre (1970); Beschta and Jackson (1979) and Carling (1984); and Peloutier (1998) are also shown.

The variations in the non-dimensional parameters derived from dimensional analysis in §3.3.1 are also summarised as follows for the Series 1 and 2 experiments. The flow aspect ratios *B/H* within the two flume facilities used were 2.1 - 3.2 and 6.5 - 9.9, respectively. The shear Reynolds number R_{e*} (Π_2 - equation 3.4) ranged between 3.8 10^3 - 7.8 10^3 for Series 1 and 3.0 10^3 - 6.6 10^3 for Series 2. The corresponding Reynolds number related to the fine sediment size (Π_2 - equation 3.5) varied between 7.5 - 26.1 (Series 1) and about 2.3 - 30.2 (Series 2). The two forms of the Froude number (Π_8 in equation 3.4; Π_9 in equation 3.5) were ~0.04 and 0.6 - 1.2 for Series 1 and about 0.03 - 0.08 and 0.7 - 1.6 for Series 2. The submerged particle density ρ_s/ρ for the fines remained constant throughout the study at 2.65. The relative fine sediment size *d/H* varied between 1.27 10^{-3} and 4.97 10^{-3} in Series 1 and between about 7.0 10^{-4} and 6.0 10^{-3} in Series 2. Note the ratio of the fine sediment size to the bed material size *d/D* is discussed separately in §3.4.2.3 (pp.66). The relative bed roughness k_s/H ranged from ~0.16~1.0 and ~0.1~0.3 for Series 1 and 2 experiments, respectively, while the corresponding values of k_s/D were about 1.0 - 5.8 and 1.8 - 3.9. The range of the non-dimensional sediment concentrations C/ρ used in the study can be obtained from dividing the values given in Table 3.1 by the fluid density (assumed 1000kg.m^{-3}). Finally, the relative depth *z/H* ranged from 0 (i.e. bed surface) up to 1 (i.e. free surface), with the notable exception of the ADV probe measurements, which could only be taken up to z/H values between 0.35 and 0.65 due to the probe configuration (§3.4.3.4, pp. 76).

Parameter	Series 1	Series 2	Jobson and Sayre (1970)	Beschta and Jackson (1979)	Carling (1984)	Peloutier (1998)
S_o (%)	0.38 - 0.40	0.10 - 1.0	0.05 - 0 47	1 - 3 (approx.)	1 - 2 (approx.)	0.70 - 1 60
H (m)	0.09 - 0.14	0.08 - 0.12	~0.40	0 06 - 0.14	0 06 - 0.17	0.07 - 0 12
B (m)	0.30	0.76	2.44	0.71	0.81 & 0.98	0 76
Q ($\ell.s^{-1}$)	10 - 29	35 - 55	280 - 870	44 - 96	19 - 117	23 - 54
u_* (m s^{-1})	0.04 - 0.05	0.035 - 0.07	0 04 - 0 13	0.08 - 0.125	0 02 - 0 21	0 07 - 0.12
Froude No. F_r	0.36 - 0.60	0.39 - 0.83	0 26 - 0 81	0 53 - 2.57	0.01 - 1.22	0.28 - 0.77
Reynolds No. R_e	1.4 - 4.2 (10^5)	1.5 - 2.3 (10^5)	4 6 - 14 (10^5)	1 8 - 4 0 (10^5)	0.8 - 5.1 (10^5)	0 8 - 1.9 (10^5)
Bed Material/ Condition	Spheres, Gravel	Gravel	Roughness Strips	Gravel	Gravel	Gravel
D_{50} (Bed) (mm)	15, 17.3	7.0, 17.3	-	15	16, 20	18, 28, 52
λ	0.26, 0.40	0.35, 0.40	-	0.35	0.39	0.42 - 0 46
Matrix Material	Fine/Medium Sand	Fine/Med Sand (2 grades)	Glass Beads/ Coarse Sand	Fine/Coarse Sands	Fine/Coarse Sands	Fine Sands (2 grades)
d_{50} (Fines) (μm)	250	250, 97	123, 390	200, 500	150,190,1400	260, 100
C_o ($mg.\ell^{-1}$)	45 - 210	110 - 590	78 - 213	360 - 4000	38 - 9110	750 - 8200

Table 3.1 - Range of main experimental variables and comparison with previous experimental studies

3.4 Introduction to Series 1 Experiments

This section describes the specifications and geometry of the glass-walled Armfield experimental flume facility used in the study and includes consideration of some important aspects when conducting experiments in open channel flow such as channel aspect ratio and boundary layer development. The flume set-up for the Series 1 experiments is described in detail. The grain size distribution and physical properties of the bed materials and fine sediments used are also outlined. Finally, a comprehensive description of the instrumentation and measurement techniques employed in the visualisation experiments is provided.

3.4.1 Flume Set-up and Operation

3.4.1.1 Description and Operation of Armfield S5-10 Flume

The visualisation experiments in Series 1 were conducted in an Armfield S5-10 type flume (Figure 3.1, pp.53), designed by Armfield Engineering Limited. The walls of the flume are constructed from toughened glass panels, ideally suited for the visualisation techniques employed in these experiments. The bed of the flume is manufactured from a cold rolled steel section. The flume support has a jacking system that allows the working section to be set at a wide range of slopes. The main working parameters of the flume are given below:

Length of working section	-	5.0 m
Cross-sectional shape	-	Rectangular
Width of working section	-	0.305 m
Depth of working section	-	0.305 m
Maximum positive bed slope	-	1:20 (0.05)
Maximum negative bed slope	-	1:100 (0.01)

The necessary volume of water required for feeding the flume is stored in a series of tanks with interconnecting pipe-work. Water is drawn from the sump tank by a recirculating pump designed to deliver flow at a rate of up to 1680 ℓ/min. (28 ℓ/s) against a head of 1.5 m. This flow is then delivered through a flow-regulating valve and a turbine flow meter installed in the delivery pipe to the inlet-stilling tank at the upstream end of the flume. The stilling tank is designed to produce near uniform flow conditions, which allows the maximum length of working section available for the

experimental study. At the downstream end, the flow enters a discharge collecting tank and spills over an adjustable overshot weir, before falling vertically back into the receiving section of the sump tank for re-circulation. A schematic diagram of the Armfield S5-10 flume giving all relevant dimensions is shown in Figure 3.3.

3.4.1.2 Flume Set-up for Series 1

An artificial channel bed was created for the Series 1A and 1B experiments in order to provide a 0.5m long sediment trapping area, located at the test section approximately 3m along the length of the working section (Figure 3.4) and within fully-developed turbulent flow. Bed material comprising uniform spheres and natural gravel were carefully arranged, in turn, within the trap to provide a porous 70-80mm thick bed layer. Upstream and downstream of the test section, a 0.12m thick layer of polystyrene supported a thin layer of similar bed material, placed flush with the bed surface layer within the test section.

Stable open channel flow conditions with minimal free-surface waves were achieved at the flume entrance by the provision of flow straightening tubes and a 1:3 coarse gravel slope (up to the elevated bed level) within the transition between the inlet stilling tank and the flume working section (Figure 3.4 overleaf).

Several modifications were made to the flume prior to the experiments in Series 1C. The length of the flume bed was extended by 1.2m (0.82m at the upstream end and 0.38m at the downstream end), increasing the total length of the working section to 6.2m (Figure 3.3 below). This extension allowed the flow visualisation experiments to be conducted within various 1m long sections of the turbulent open-channel flow along the working section of the flume. The polystyrene layer and trap arrangement for Series 1A and 1B was also replaced with a constant 40-50mm thick layer of natural gravel placed along the length of the extended working section.

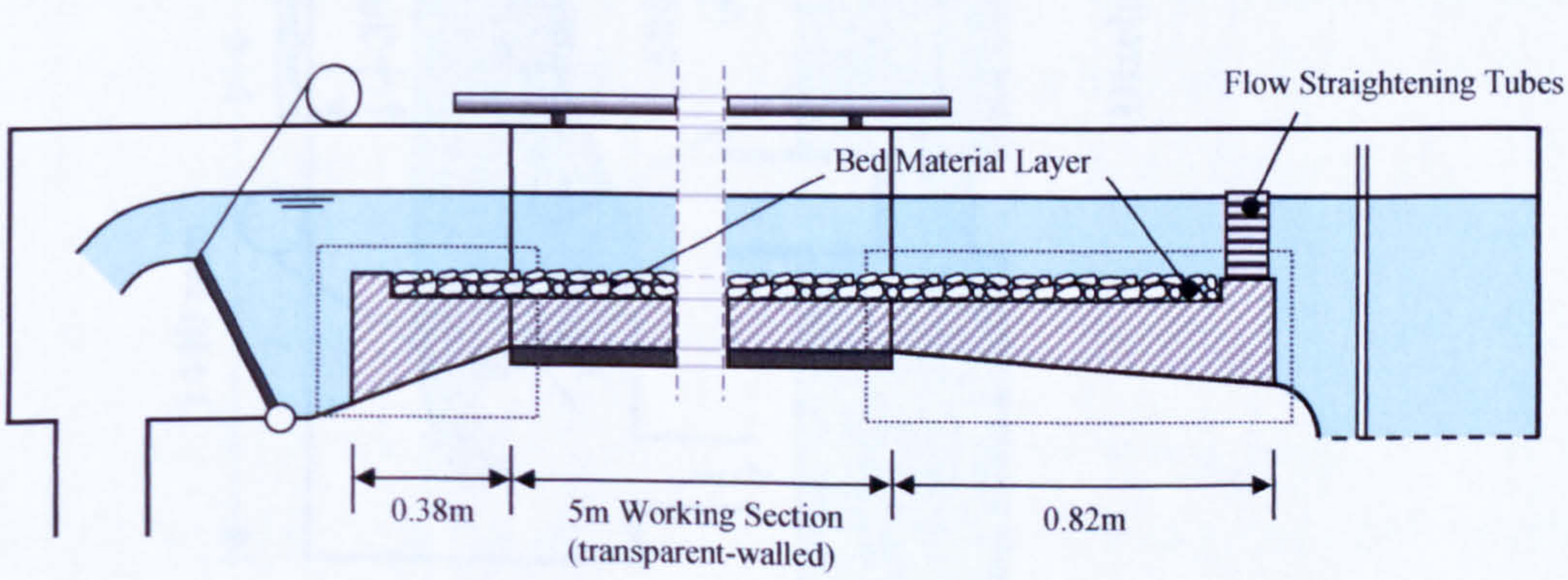

Figure 3.3 - Flume modifications for Series 1C experiments

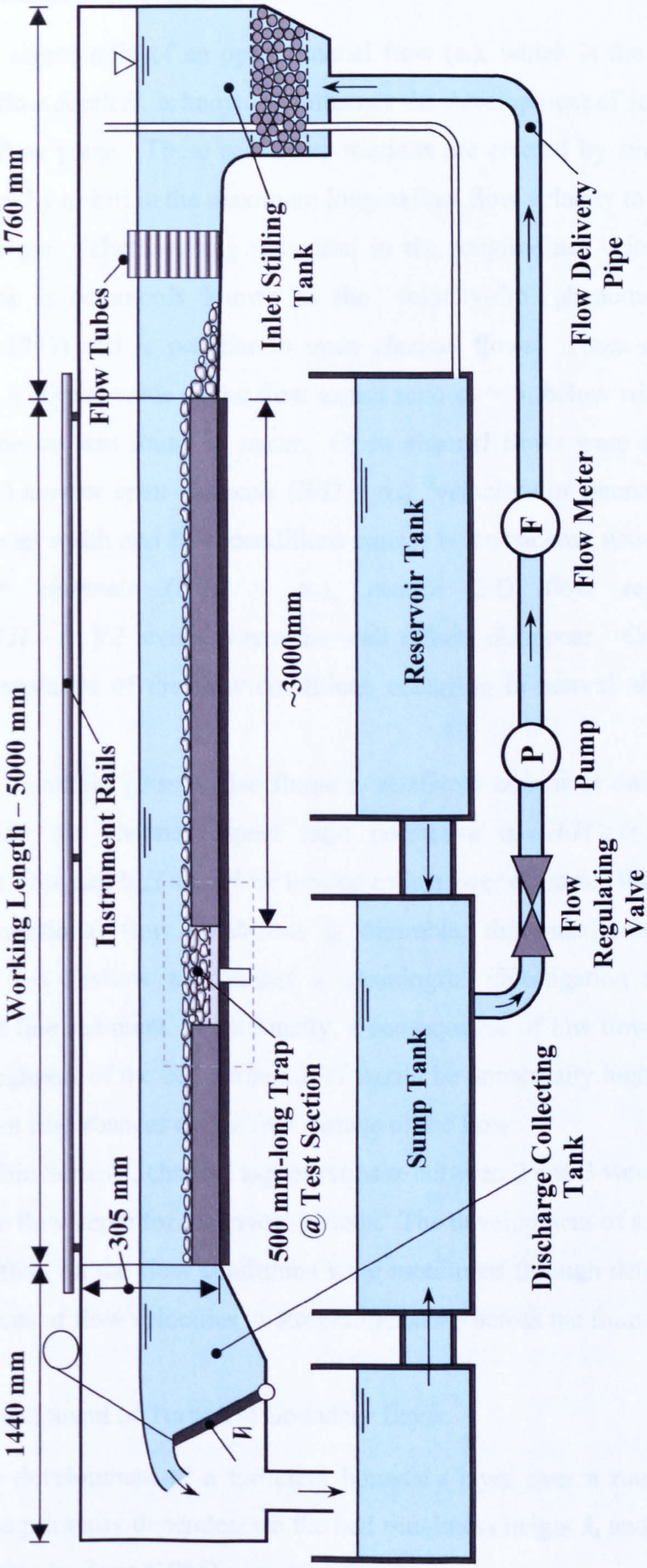

Figure 3.4 - Experimental flume (set-up for Series 1A and 1B)

3.4.1.3 Aspect Ratio of Channel Flow

The aspect ratio of an open channel flow (α), which is the ratio of channel width B to flow depth H, is known to influence the development of secondary currents in the YZ flow plane. These secondary motions are created by strong wall effects, characterised by a shift in the maximum longitudinal flow velocity to a position below the free-surface. The resulting reduction in the longitudinal velocity in the free-surface flow is commonly known as the 'velocity-dip' phenomenon (Nezu and Nakagawa 1993) and is peculiar to open channel flows. Nezu and Rodi (1985) determined a critical value of the flow aspect ratio $\alpha_c = 5$, below which the velocity-dip phenomenon was found to occur. Open channel flows were classified on this basis as: (1) *narrow open channels* ($B/H < \alpha_c$), 'velocity-dip' phenomenon observed across channel width and flow conditions cannot be considered two-dimensional; (2) *wide open channels* ($B/H > \alpha_c$), central 2-D flow region of width $|y/H| < (B/H - \alpha_c)/2$ exists where the wall effects disappear. Case (2) is clearly more representative of the flow conditions occurring in natural alluvial rivers and streams.

The Armfield glass-walled flume is relatively narrow at only 305 mm wide, and applying the channel aspect ratio constraint $\alpha = B/H \geq \alpha_c$, the maximum permissible flow depth H would be limited to just over 60 mm. While the provision of two-dimensional flow conditions is desirable, this maximum flow depth is considered too shallow to conduct a meaningful investigation into the vertical transport of fine sediment. Additionally, a consequence of low flow depth is that the relative roughness of the bed surface k_s/H would be unnaturally high and could result in significant disturbances on the free surface of the flow.

Within Series 1, channel aspect ratios α between 2 and 3 were chosen to allow an adequate flow depth for the investigations. The development of secondary motions and their effect on the flow conditions were monitored through detailed ADV probe measurements of flow velocities in three-dimensions across the flume width.

3.4.1.4 Development of Turbulent Boundary Layer

The development of a turbulent boundary layer over a rough bed has been shown to be primarily dependent on the bed roughness height k_s and can be predicted by an equation by Toso (1986) as follows,

$$\frac{\delta}{x} = \frac{0.233}{(x/k_s)^{0.25}} \qquad \ldots.(3.6)$$

For the range of flow and bed conditions considered in Series 1, assuming the bed roughness height k_s is comparable with the median bed material size D_{50} and the flow is fully developed when $\delta = H$, the development length x ranges from about 1.1 - 2.2m. This estimation does not account for the influence of upstream entry conditions on the turbulent boundary layer development. From previous experience of experiments conducted in short flumes, it was decided to install flow straightening tubes at the upstream end of the flume, which in effect increase the turbulence generation and thus should further reduce the streamwise development length x.

3.4.2 Sediment Details

3.4.2.1 Physical Properties of Bed Material

Two types of bed material were selected for the Series 1 experiments: uniform 15mm glass spheres and well-graded and rounded natural river gravel. The two prerequisite conditions to be satisfied by these bed material grades were: (a) that they should remain stable under the flow conditions set-up in the flume; and (b) they should allow the fine sediment particles to deposit freely within the bed layer.

(1) Uniform Glass Spheres

It is acknowledged that conducting experiments over a bed of uniform spheres does not itself represent any natural bed condition found within alluvial rivers and streams. However, in terms of gaining an initial insight into the typical mechanisms involved in (1) near-bed motion of fine sediment, (2) the turbulent interactions occurring within the surface layers of the bed, and (3) the deposition characteristics of the fine sediment, employing such a regular bed configuration may be advantageous. The uniformity of size and packing arrangement provides a constant bed porosity λ that can be calculated from geometric considerations and thus allows the above processes to be observed independent of the local bed geometry. The regular packing arrangement also ensures constant bed roughness k_s along the working section, which in turn allows the mean flow velocity and turbulence characteristics to be independent of the bed configuration.

Uniform 15mm glass spheres were used as bed material in some of the Series 1A and 1B experiments. The density ρ_s of these spheres was measured and averaged at 2500kg/m^3. The spheres were carefully arranged in a single layer on the artificial bed upstream and downstream of the test section (Figure 3.5a). Within the trapping area, four layers of spheres were packed in a rhombic configuration (Figure 3.5b) with the surface layer flush with the upstream and downstream bed. The porosity λ of this bed arrangement was calculated from geometric considerations to be approximately 26% (by volume) or 0.26 (void to total volume ratio).

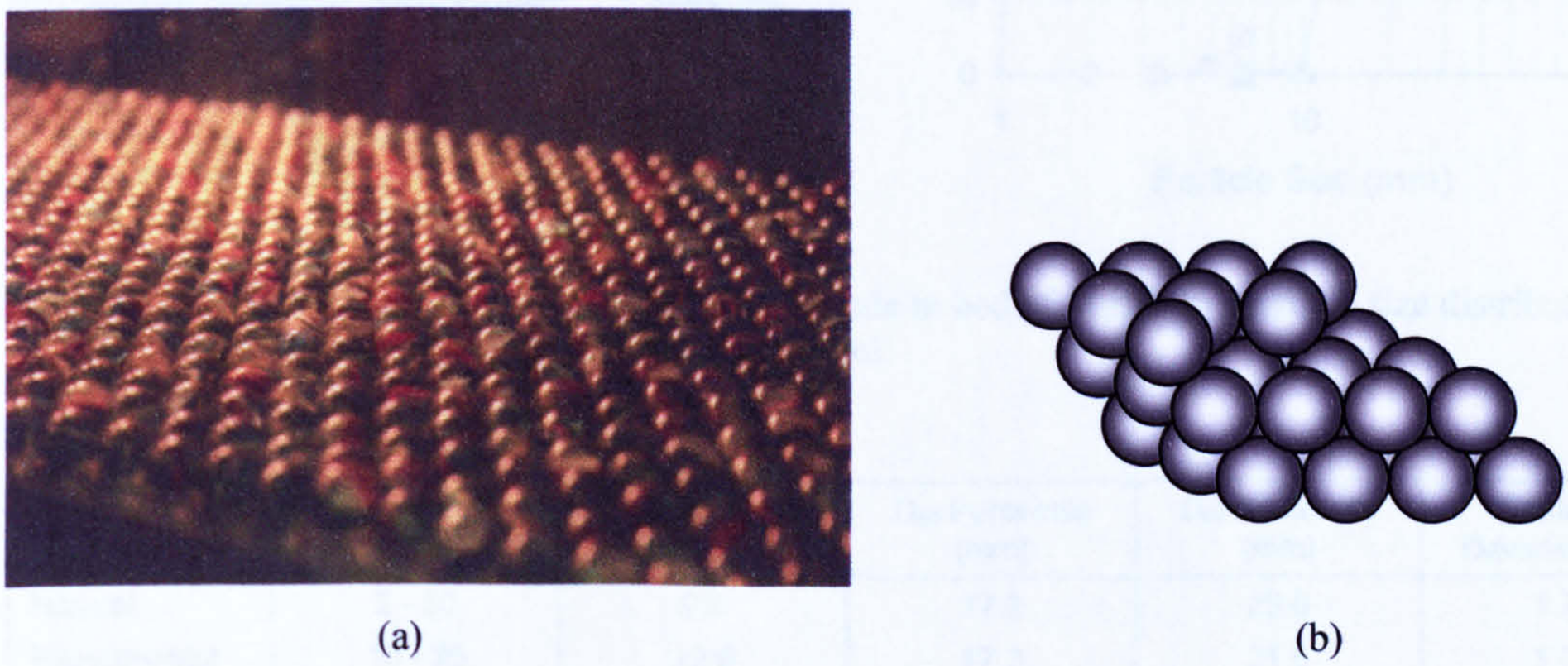

(a) (b)

Figure 3.5 - (a) Single layer packing of spheres on flume bed, (b) 3-D rhombic packing of uniform spheres within trapping area.

(2) Natural River Gravel

Series 1 experiments were also conducted with a more natural gravel bed in place. This gravel was obtained from a lowland river near Drymen, north of Glasgow, and is well-graded in its natural form and well-rounded in shape (Figure 3.6). For the Series 1 experiments, the coarsest and finest fractions (D > 25mm and D < 10mm, respectively) were removed by sieving to obtain a reasonably well-sorted experimental grade. The main reason for removing the finer fractions was to allow the free deposition and infiltration of the fines through the gravel bed, while the coarsest fractions were removed as their size was considered disproportionately high compared with the flow depth. The particle size distribution curves for both the natural and experimental gravel grades are shown in Figure 3.6 overleaf, with the main particle size percentiles and standard deviation for each detailed in Table 3.2. The density ρ_s of the experimental gravel was measured to have average value of 2650kg/m^3, while the bed porosity λ was estimated to be around 0.40.

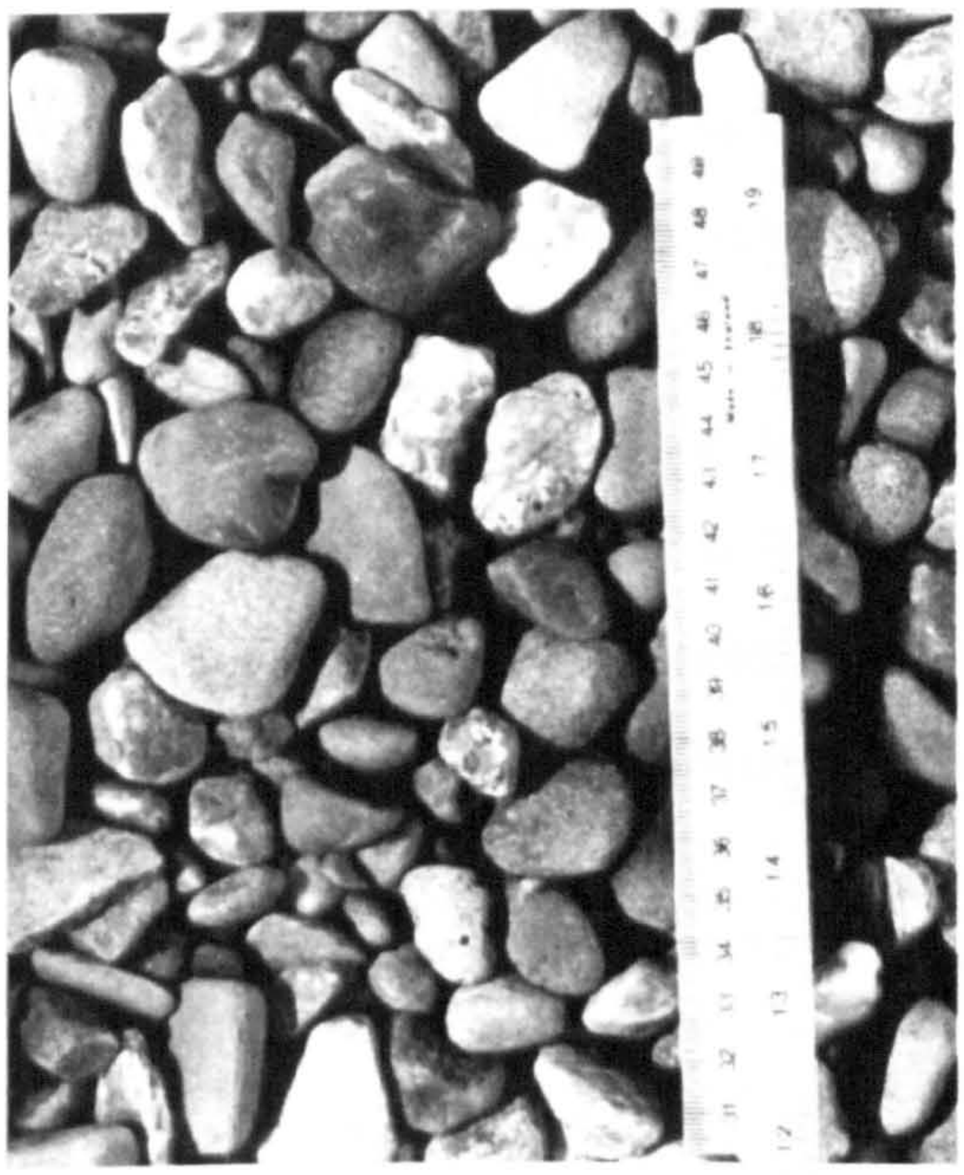

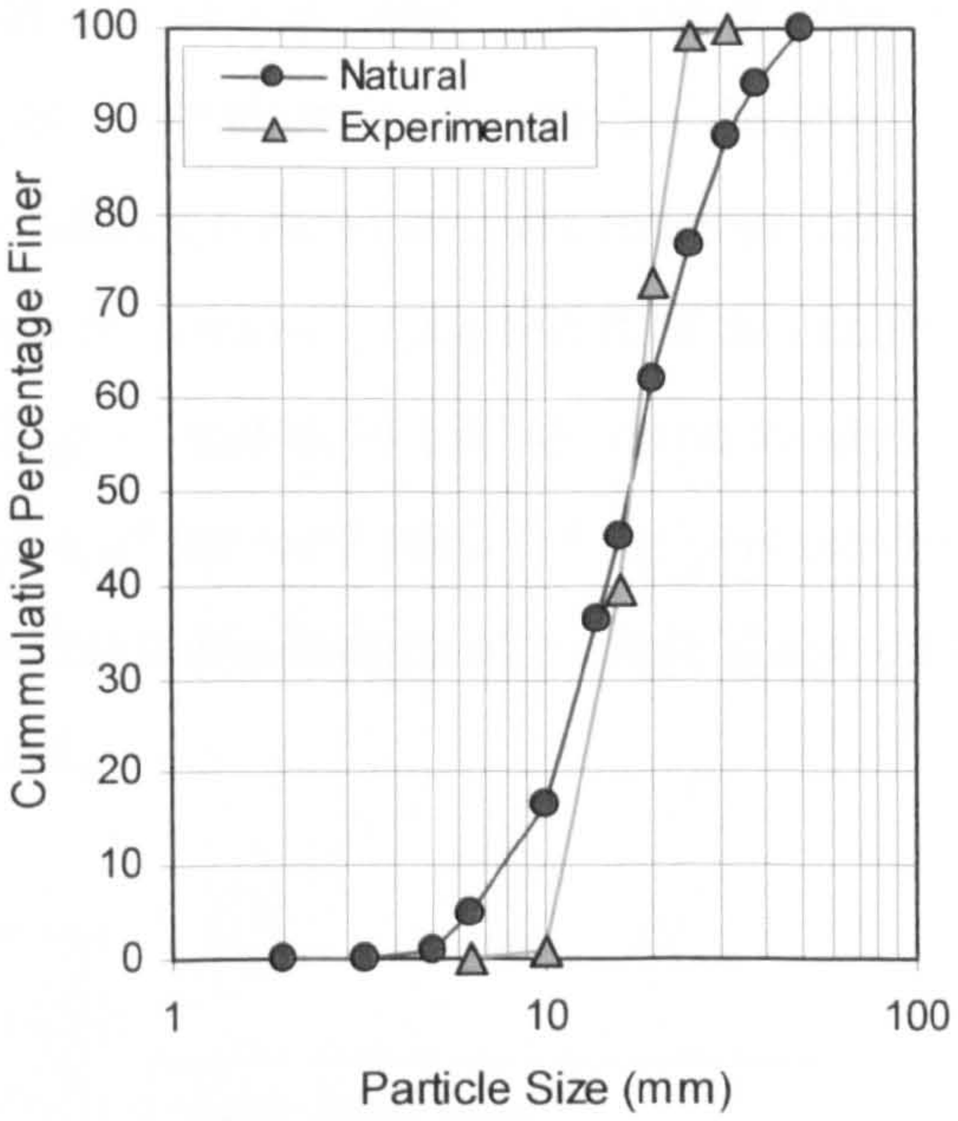

Figure 3.6 - (a) Plan view of experimental gravel grade in bed of flume, (b) particle size distribution of natural and experimental grades of gravel.

	Size Range (mm)	D_{16} Percentile (mm)	D_{50} Percentile (mm)	D_{84} Percentile (mm)	Standard Deviation (σ_g)*
Natural	2 - 50	9.8	17.2	29.0	1.72
Experimental	10 - 25	12.6	17.3	21.6	1.31
* The standard deviation, σ_g, is calculated from the equation $\sigma_g = 0.5[(D_{84}/D_{50})+(D_{50}/D_{16})]$					

Table 3.2 - Calculated particle size percentiles for natural and experimental gravels

For the Series 1A and 1B experiments, the trapping area was carefully packed in layers, each being lightly tamped and levelled to produce uniform gravel surface. Upstream and downstream of the test section, a single layer of bed material was placed flush with the bed surface layer within the trap. For Series 1C, a uniform bed of constant thickness (40-50mm) was placed, tamped and levelled in a similar manner.

3.4.2.2 Physical Properties of Fine Sediment

The matrix grade sediment used in Series 1 was a fine to medium, well-sorted sand obtained from a quarry at Loch Aline, situated north west of Oban. The significant advantages in using this sand grade were its purity and distinct white colour, which was ideal for visualisation and particle tracking experiments. An average particle size distribution (Figure 3.7) was obtained from sieve analysis of a

number of samples taken from different batches of the sand. The main grain size percentiles of this average sand grade are also detailed in Figure 3.7 below. The density ρ_s and porosity λ were estimated by adding a measured dry mass of sand to a known volume of water and noting the change in volume. As a result of this analysis, the average values for ρ_s and λ_s were 2657kg/m^3 and 0.40 (40%), respectively. An additional microscopic examination of samples of the sand revealed the particles to be typically sub-rounded to rounded, indicating that the influence of particle shape on the fall velocity (§2.2.1, pp. 13) would be minimal.

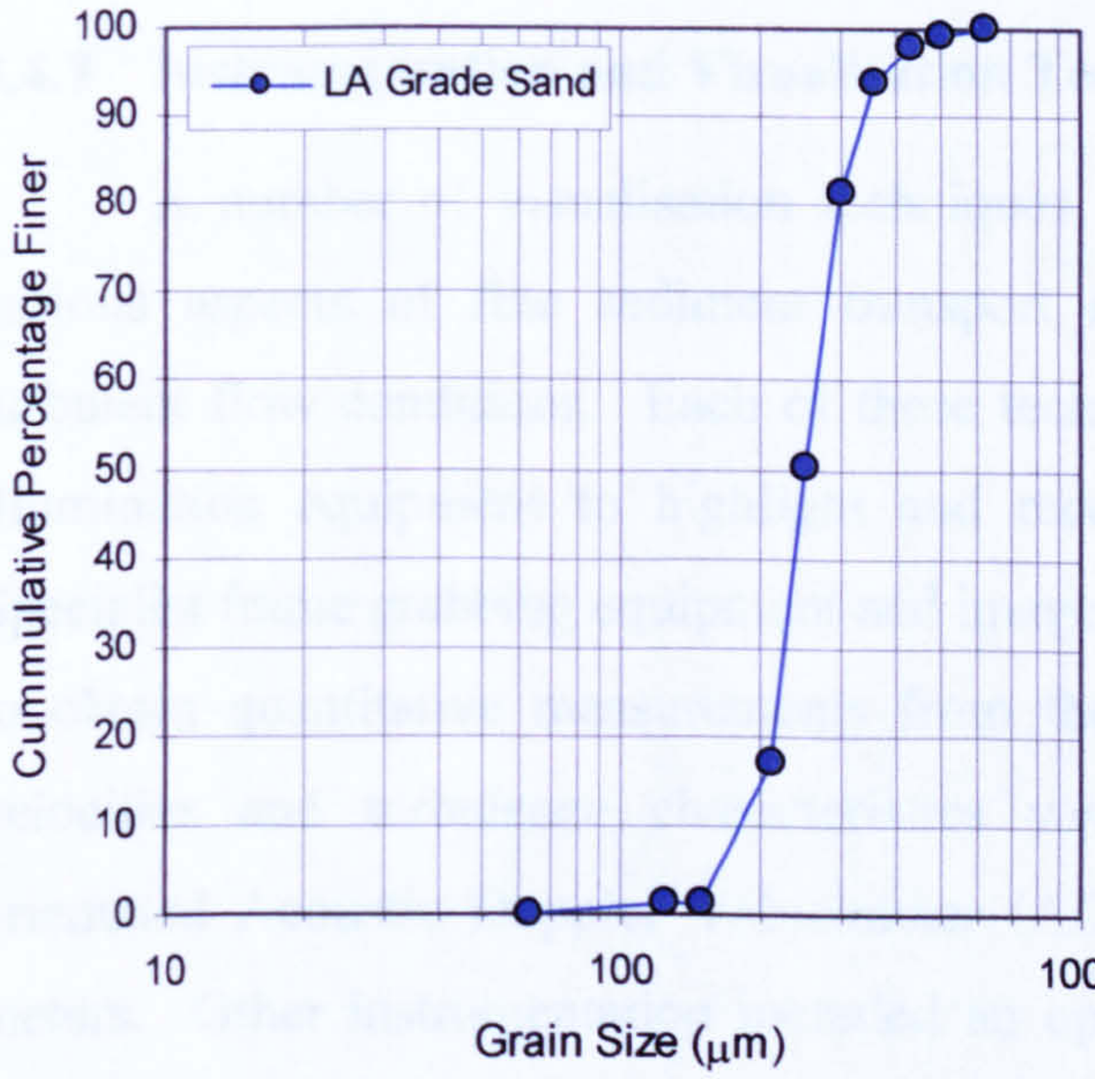

Loch Aline Sand
(LA Grade)

Size Range - 625-125μm

d_{16} Percentile - 209μm

d_{50} Percentile - 250μm

d_{84} Percentile - 306μm

Standard Dev. σ_s - 1.21

Figure 3.7 - Average particle size distribution curve and size properties for Loch Aline sand

3.4.2.3 Size Ratio Comparison of Bed and Fine Sediments

The depth of fine sediment particle intrusion into the coarser bed material is known to dependent on framework to matrix size ratios (§2.6.3, pp. 42). For the two bed grades (uniform spheres and natural gravel) and the LA sand grade used in Series 1, the calculated size ratios are relatively high (Table 3.3), suggesting that the fine sediment will intrude freely and generally deposit at the base of the bed (i.e. siltation).

Bed Material	Median Diameter D_{50} (mm)	Size Ratio D_{50}/d_{50}	Minimum Diameter D_{min} (mm)	Size Ratio D_{min}/d_{max}
15mm Spheres	15.0	60.0	15.0	24.0
Natural Gravel	17.3	69.2	10.0	16.0
For LA Grade Sand: d_{50} = 0.250mm; d_{max} = 0.625mm.				

Table 3.3 - Size ratios of framework (bed) and matrix (fines) materials in Series 1

3.4.2.4 Neutrally Buoyant Seeding Material

In the Series 1C experiments, neutrally buoyant polyamid particles were added to highlight the turbulent structure of the open-channel shear flow. This seeding material, manufactured by Sontek, has a median diameter of 50μm, which is small enough to allow them to follow the local structure of the flow. The particles were introduced into the sump tank at the downstream end of the flume, allowing them to become fully mixed with the fluid to a constant concentration as they re-circulated around the system.

3.4.3 Instrumentation and Visualisation Techniques

A number of visualisation techniques were developed in Series 1 to study various aspects of fine sediment transport and deposition processes within the turbulent flow conditions. Each of these techniques required a motion camera and illumination equipment to highlight and record the observed particle behaviour. Specialist frame grabbing equipment and image analysis software were also employed to obtain quantitative measurements from the recorded images. The mean flow velocities and turbulence characteristics were measured with a 3-D vertically orientated Acoustic Doppler Velocimeter (ADV) probe and mini-propeller current meters. Other instrumentation included an optical level to set the bed layer to the required bed slope, pointer gauges to measure the water surface elevations and a portable feed system to input the fine sediment at a desired feed rate.

3.4.3.1 Visualisation Equipment for Series 1A

These preliminary visualisation experiments used a standard VHS video camcorder [25 frames per second (fps); shutter speed = 0.02sec.] to observe near-bed interactions between the fine sediment particles and the bed surface material within the test section of the flume. The camera was attached to a stable tripod, set perpendicular to the transparent flume wall and levelled prior to each experiment. In recording the particle motion within the flow region immediately adjacent to the near-side flume wall, observations could also be made of the typical interactions occurring within the bed surface interstices and the infiltration paths taken by particles through the upper layers of the bed following deposition.

Illumination of the near-wall flow region within the test section was provided by two fluorescent lights, each set at approximately 45° to the flume wall. Bed elements within the surface layers of the trapping area were painted matt black to enhance their contrast with the fine, white sediment particles. A matt black screen positioned on the opposite flume wall also assisted in highlighting the fine sediment particles by reducing reflections from the bed surface. A schematic diagram of the experimental set-up for Series 1A is shown in Figure 3.8 below.

A macro function on the lens of the video camera allowed it to focus on small, localised areas of the near-bed flow and bed surface layers within the test section, providing recorded images with typical dimensions of 60mm × 45mm, as shown in Figure 3.9. Smaller 40mm x 30mm images were also recorded to observe the motion of the sediment particles within a single interstice at the bed surface.

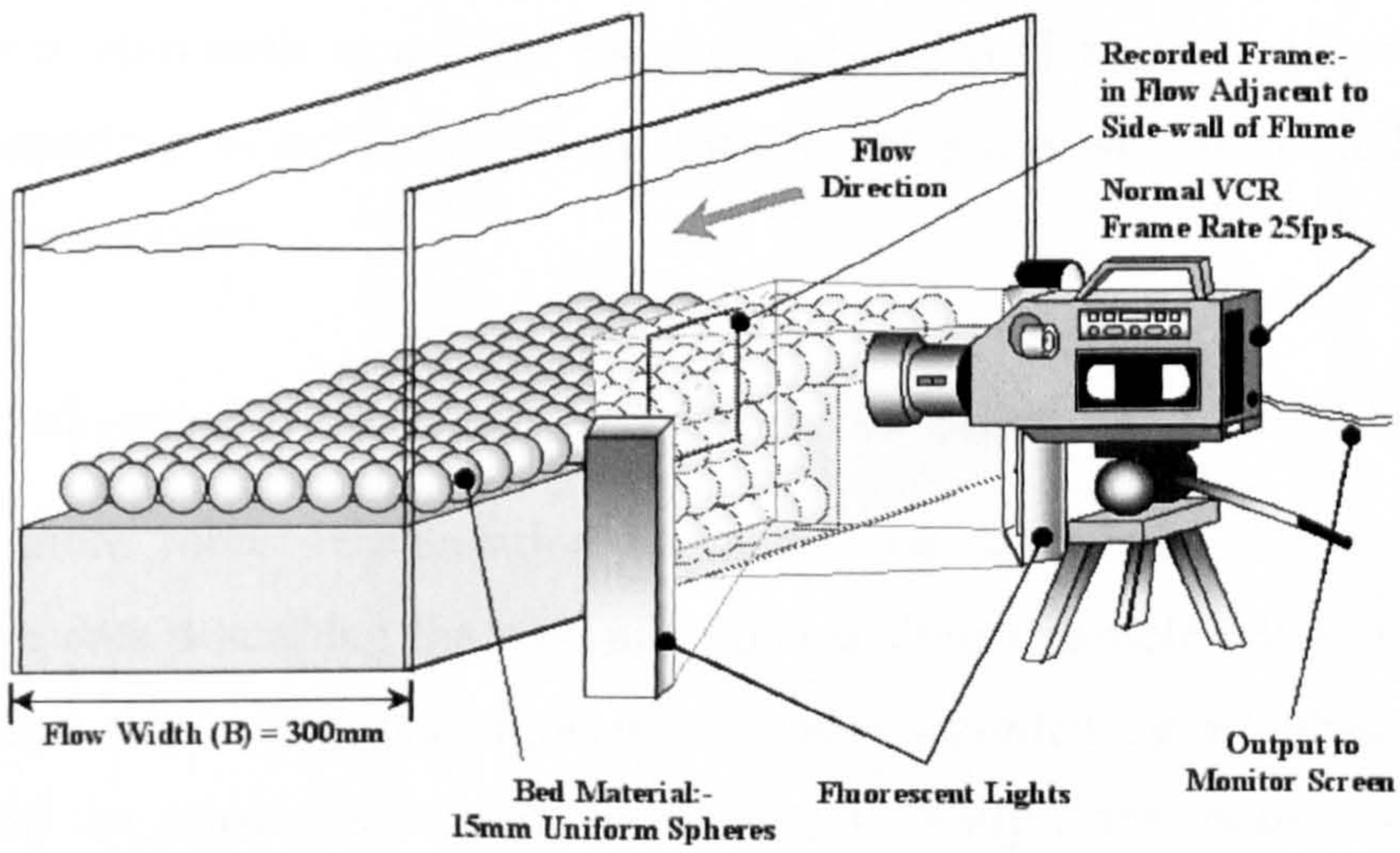

Figure 3.8 - Experimental set-up at the test section for Series 1A

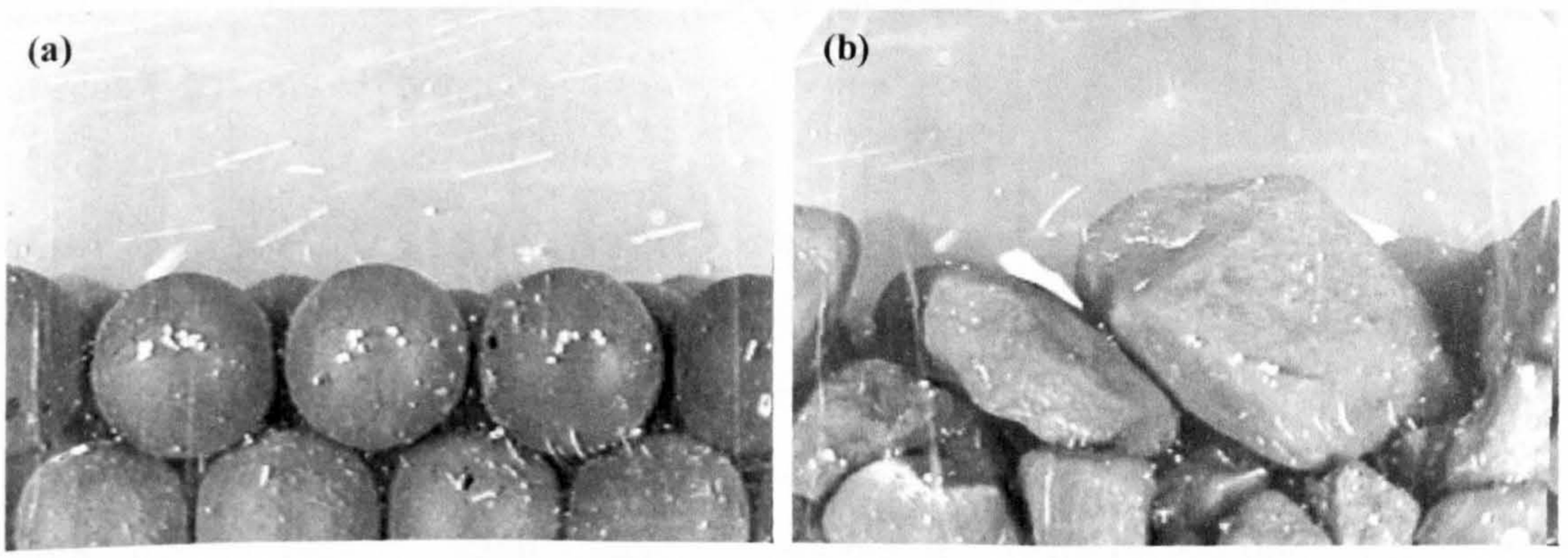

Figure 3.9 - Typical recorded frames obtained from VHS video camera

The video images recorded by the VHS video equipment were of an adequate quality to provide good qualitative observations of particle motion attributes such as: (a) trajectories in near-bed flow; (b) interactions at the bed surface interface; (c) the subsequent deposition within the surface bed layers. In contrast, the amount of quantitative data obtained from these preliminary visualisation experiments regarding the characteristics of particle motion was limited. The low resolution at which recorded images could be transferred from the VHS video camera to a PC (320×250 pixels maximum) diminished the image quality and made the acquisition of accurate measurements from recorded particle trajectories virtually impossible.

Consequently, the limited quantitative measurements made relied on direct analysis of the video recordings. Individual sediment particle trajectories within the near-bed flow and through the bed surface layers were plotted manually on clear acetate sheets using frame by frame advance of the video recordings. Characteristics of particle motion such as average longitudinal and vertical near-bed velocities and average deposition velocity through the surface bed layers were measured from these individual trajectories.

3.4.3.2 Development of Visualisation Technique for Series 1B

A more robust visualisation technique was developed to obtain accurate quantitative data describing the motion of fine sediment particle within the turbulent open channel flow. This technique used images recorded by a high-speed motion camera and the principles of particle tracking to analyse the motion of individual sediment particles within various regions of the flow. The recorded images were captured and digitised on a PC, where they were analysed with specialist image analysis software to identify the relative displacement of the particles between successive captured frames.

Basic Principles of Particle Tracking Techniques

Particle tracking techniques allow information on the motion of particles (e.g. neutrally-buoyant material, sediment) within a two-dimensional, illuminated slice of fluid to be obtained from analysis of recorded sequences of images with a constant time interval between each image. Locating the particle positions within each sequential image allows their Lagrangian paths to be determined, which in turn

provides information on their trajectory, displacement and velocity. As the illuminated particles within each image have similar appearance, each particle has to be carefully tracked frame to frame to ensure the correct displacements are measured. This is generally performed in one of two ways: (a) manually by eye; or (b) applying a matching algorithm, which simply determines the most likely combination between particles in two sequential images. Generally the matching algorithm techniques are more suited to cases where the observed particle displacements between successive frames are small or where the concentration of particles within each image is relatively low. Applying either technique, the instantaneous longitudinal and vertical components of particle velocity (u_s and w'_s) can be obtained from the measured components of particle displacement (Δx and Δz) and the time interval separating the two images (Δt), i.e.

$$u_s(x,t) = \frac{\Delta x(x,t)}{\Delta t}; \quad w'_s(z,t) = \frac{\Delta z(z,t)}{\Delta t} \qquad \text{....(3.7)}$$

where $u_s(x,t)$ and $w'_s(x,t)$ represent the components of particle velocity at a specific location within the flow domain (x,z) at time t.

High-Speed Camera and Flow Illumination

A sophisticated digital high-speed camera, the *KODAK™ MotionCorder Analyser* (Figure 3.10 overleaf) was used in Series 1B. This was capable of recording between 30 and 600 frames per second, with a variable exposure time between 1/30 to 1/10000 seconds. The processor component of the camera has sufficient memory to store up to 29,000 individual images at resolutions up to 640×240 pixels before requiring the images to be downloaded to a PC.

As with Series 1A, the camera was set up at the test section and perpendicular to the transparent flume wall, recording images of particle motion in the XZ flow domain. A slice of illuminated flow approximately 60mm long by 10mm wide, running parallel with the flume walls, was created by a 50-Watt halogen light shining through a narrow slit sited directly above the water surface at the centreline of the flume. The sediment particles within this vertical light sheet were clearly visible and were recorded by the camera in up to three separate flow regions covering the full flow depth. A schematic diagram of the experimental set-up at the test section for Series 1B is shown in Figure 3.11 overleaf.

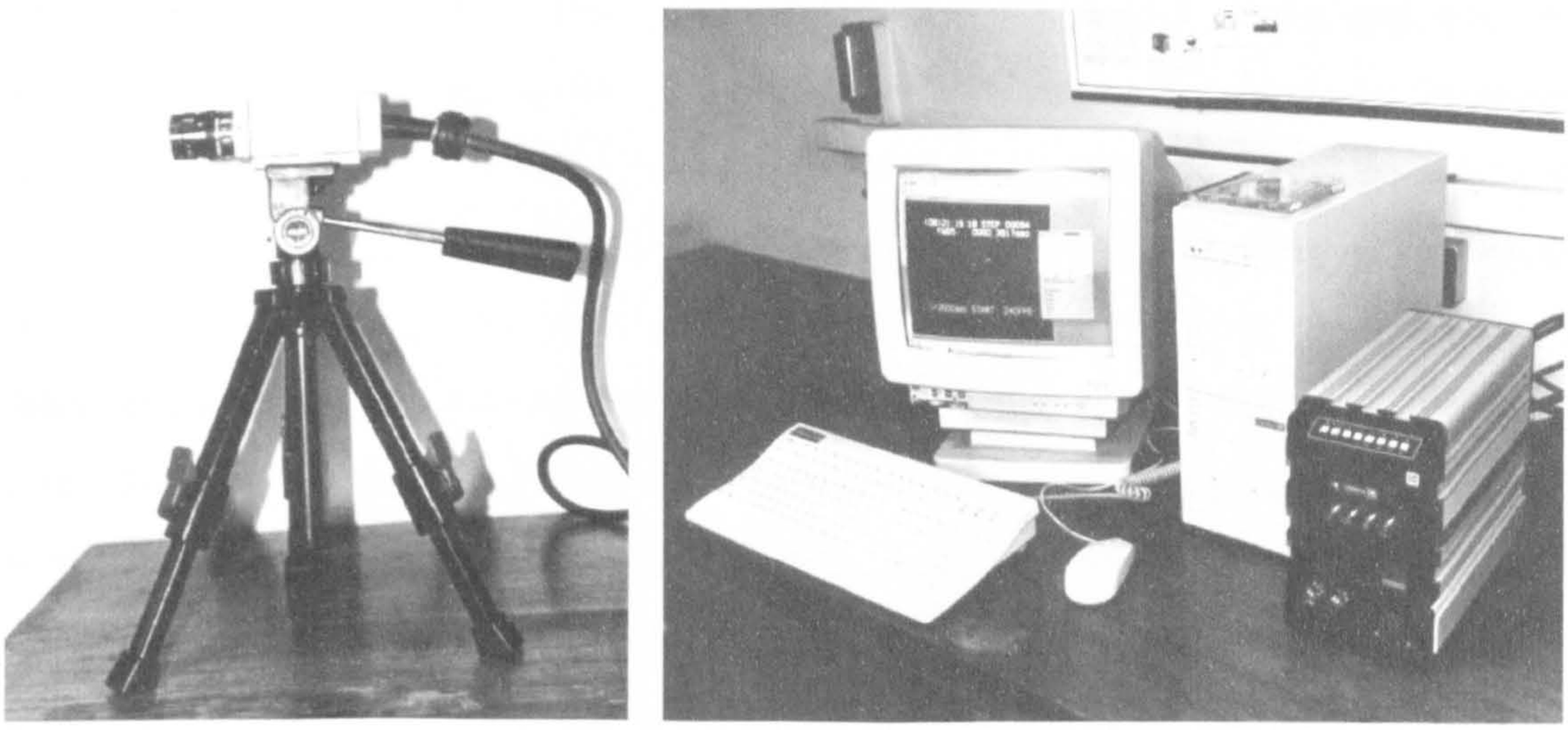

Figure 3.10 - High-speed camera (left) and processing equipment and PC used for image storage and analysis (right)

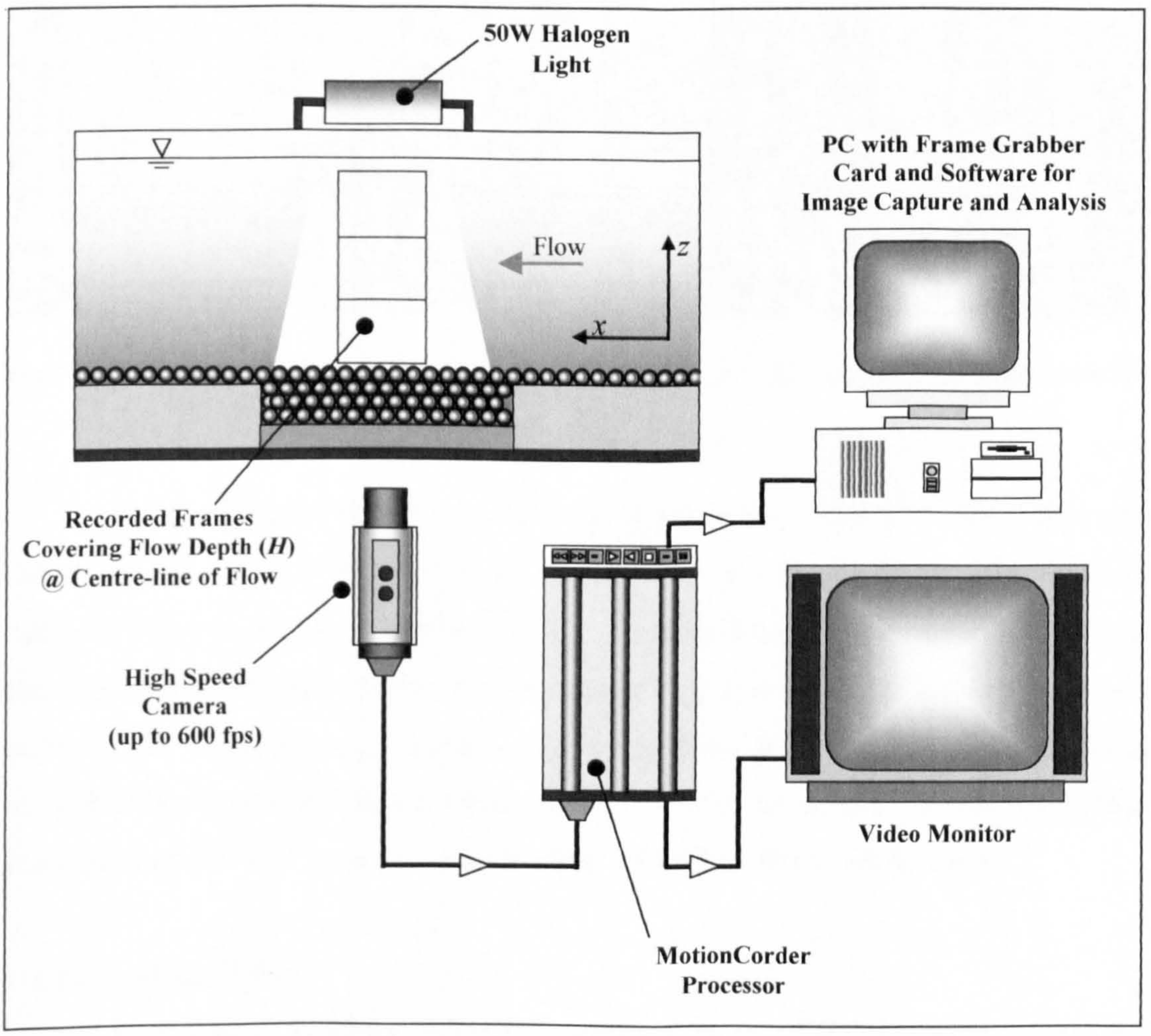

Figure 3.11 - Schematic diagram of experimental set-up for Series 1B

Recording at 240fps was found to provide the optimal temporal resolution for particle tracking. At this frame rate, individual illuminated particles appeared as single 'points' of several pixels in size, and their relative displacement between sequential frames was sufficiently small to allow them to be tracked easily. Figures 3.12(a) and (b) below show two typical images recorded by the high-speed camera at the 240fps setting adopted for the experiments [Note: a 4 frame (or 0.0167sec.) interval exists between the two images shown in Figure 3.12]. The exposure time, controlling the amount of light entering the camera during the capture of each image, was varied through each experiment. Lower shutter speeds of between 1/4000 and 1/8000secs were suitable for recording larger sediment particles, while higher exposure times between 1/1000 and 1/2000secs were required for the finer fractions.

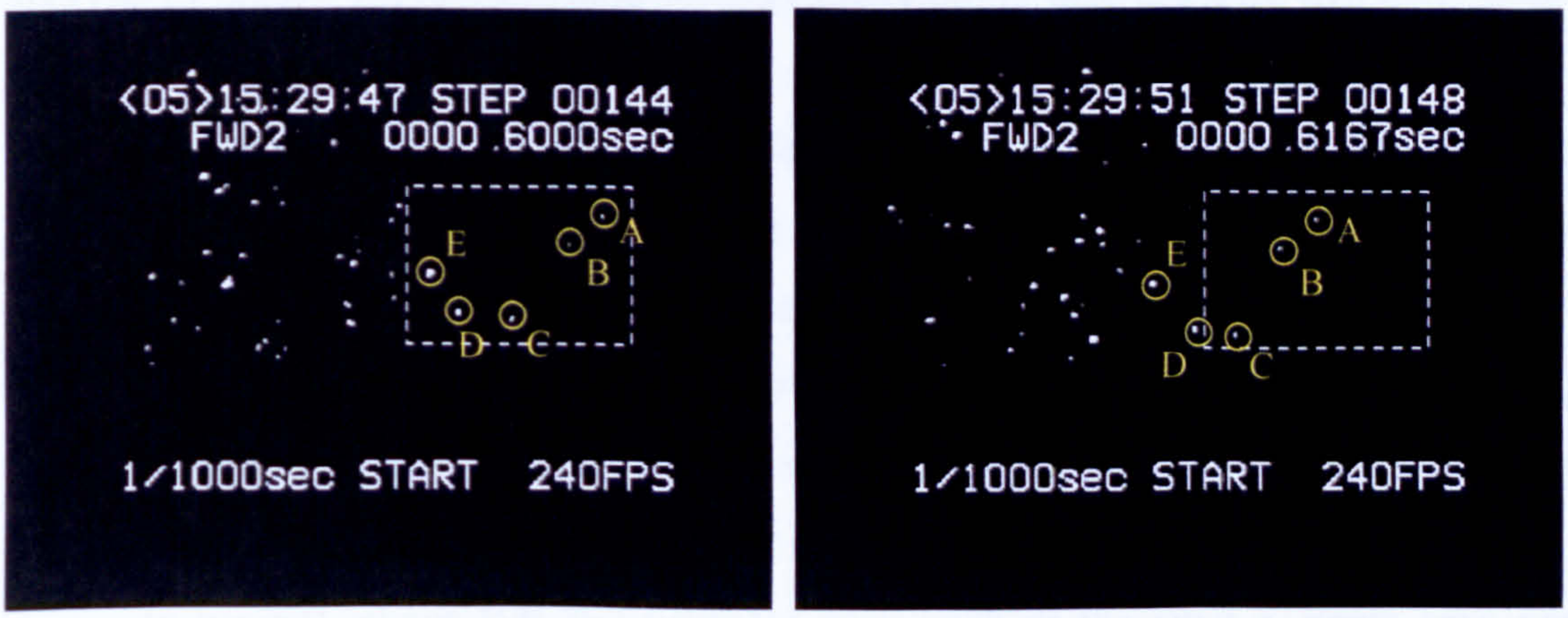

Figure 3.12 - Two typical images recorded by the Kodak MotionCorder showing the relative motion of five tracked sediment particles

Using the camera settings, up to 1963 digital images (about 8 secs real-time) at the maximum display resolution of 640 x 240 pixels could be stored by the *MotionCorder* processor at any one time. As these images were stored in Dynamic Random Access Memory (DRAM), they could be played back via a video monitor or captured for analysis using a frame-grabbing card installed in a PC. Selected blocks of 100-150 sequenced images were captured at the maximum attainable grabbing resolution of 736 x 572 pixels and stored on 100MB media in JPEG format.

Image Analysis Software

Two image analysis software packages were used to obtain quantitative measurements of particle motion from the sequences blocks of images: (a) the

Optimas 6.0 package, included with the camera equipment and; (b) a public domain package called *Scion Image*, developed by the National Institute of Health and the Scion Corporation.

Optimas 6.0 included a procedure for automatic particle tracking based on a standard cross-correlation algorithm for matching particles between successive frames. Unfortunately, tests conducted on the accuracy and reliability of this automated procedure revealed it to have generally low success rates in matching the appropriate particles between sequential frames. This was thought, at least in part, to arise from the observed disappearance and reappearance of particles from the illuminated sheet within the recorded flow region resulting from lateral motions. Consequently, the automatic tracking procedure was deemed too unreliable for the analysis of recordings and consequently, virtually all particle tracking was carried out manually.

Image calibration options available in both software packages allowed each stored image to be scaled by a conversion factor (i.e. pixels per mm, cm or m). The tracked particle positions were then automatically stored as scaled pairs of (x,z) co-ordinates with the (0,0) origin at the top-left corner of each image, thus enabling longitudinal and vertical particle velocities to be calculated from the scaled particle displacements relative to the origin.

In general, about 100-200 particles from each of the six LA grade fractions were tracked from the blocks of sequential images recorded in each of the flow regions covering the flow depth. No specific sampling technique was applied in the selection of the individually tracked particles.

3.4.3.3 Development of Visualisation Technique for Series 1C

When coupled with ADV probe measurements, the captured images of sediment particle trajectories in Series 1B provided an important quantitative comparison between particle motion and statistical aspects of turbulence in the open channel flow. Unfortunately, the combination of point measurements with an ADV probe and recordings with a stationary camera position cannot highlight the spatial extent of turbulent structures or any resulting particle-turbulence interactions within the open channel shear flow. A further series of visualisation experiments was therefore carried out to investigate the nature of these interactions.

Digital Video Camera and Flow Illumination

One of the simplest ways to identify the presence of large-scale turbulent structures within an open-channel flow would be to employ a moving camera technique to record images of the turbulent flow domain as if it were stationary. In other words, a system in which the camera could be moved along an illuminated section of the flume at a constant speed equal to the mean longitudinal flow velocity, recording images of the flow through the glass side-wall of the flume. This moving camera system was developed by attaching the camera to a trolley system that allowed the camera to be moved along a 1m illuminated section of the flume, as shown in Figure 3.13.

The flow illumination unit created a 1m-long light sheet by passing the light emitted from an enclosed 500W halogen source vertically down through a narrow slot. This illuminated a vertical slice of the flow (~5mm wide) extended from the free surface down to the bed boundary. The portability of the unit allowed recordings to be made at four longitudinal positions, located centrally in each of the four glass panels of the transparent side-wall (see Figure 3.1, pp. 53) and at four lateral positions (i.e. $y/B = 0.10$, 0.20, 0.333 and 0.50) across the flume.

A digital video camera was used to record images of the illuminated flow region. This camera operated at 25 frames per second (fps) with a shutter speed of 1/50 seconds. The main reasons for using this camera as opposed to the high-speed motion camera used in Series1B was that it allowed a larger area of flow to be recorded (150×100mm) and a large number of images to be stored on digital videotapes prior to post-processing. All video images acquired were downloaded from the digital tapes onto standard VHS tapes, while selected sequences of images were digitised to a PC using a frame grabber card and subsequently analysed using the *Image* software package.

A number of recording runs (generally 10-20) were made at each longitudinal and lateral position within the flume. During each recording, the camera was manually pulled along the illuminated flow region at a constant speed equal to that of the average flow velocity. In the initial experiments, the flow was seeded solely with 50μm neutrally buoyant particles (§3.4.2.4, pp.67) to identify the presence of turbulent structures within the flow. In subsequent tests, each of the six LA sand fractions were also added to the flow to observe the particle interactions with these

turbulent structures. The sand fractions were introduced to the flow at the free surface at a constant rate of about 1g/s. The noticeable size difference between the neutrally buoyant particles and the sediment made them easy to distinguish.

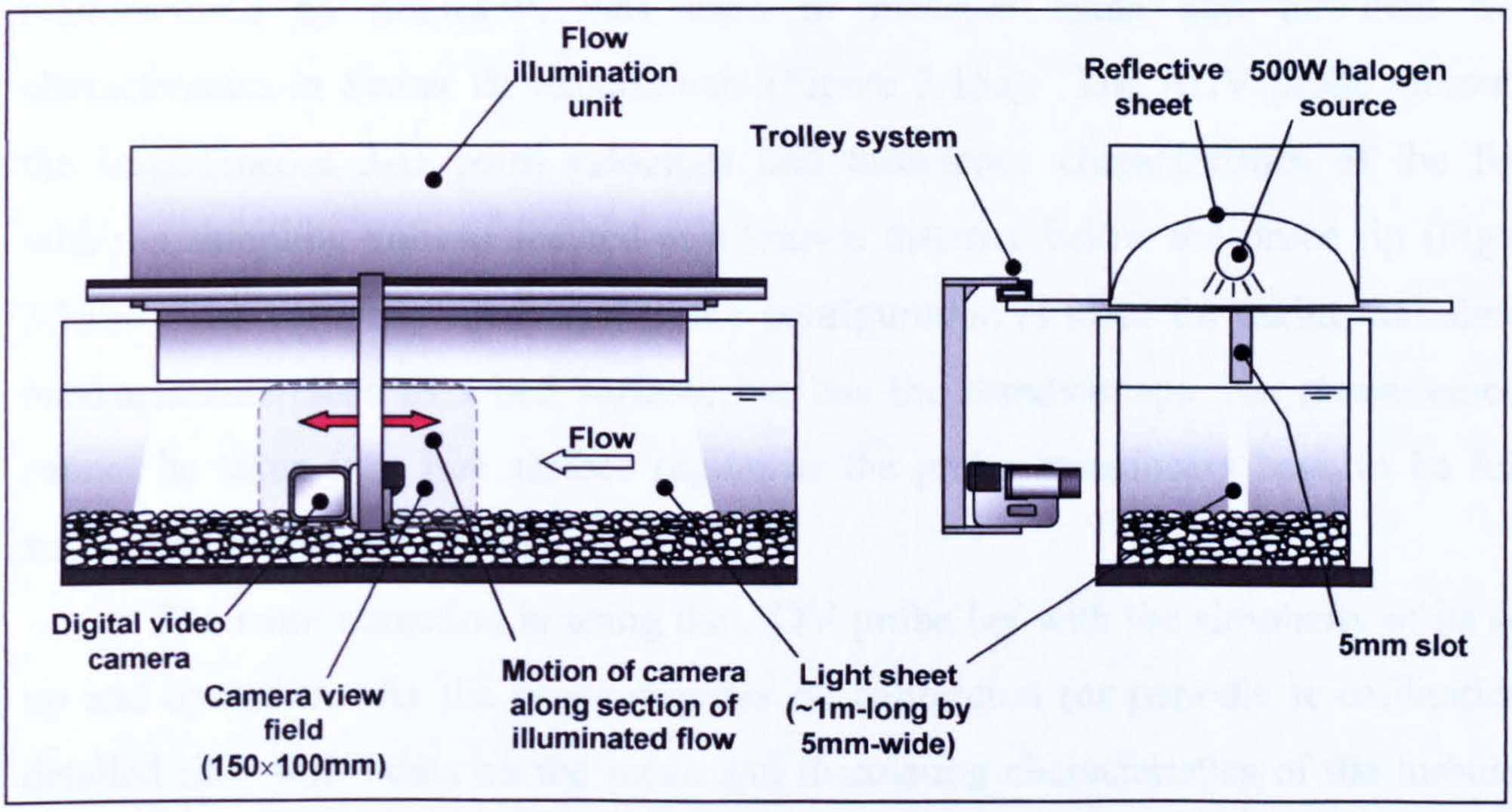

Figure 3.13 - Experimental set-up of moving camera system for Series 1C

Recordings with sediment particles were made through the third glass panel downstream (centred at 3.9m from the flume entrance) at the four lateral positions across the width. Again, about 10-20 recordings were obtained at each position for each size fraction. Sequences of images showing clear interactions between particles and flow structures were digitised to a PC (e.g. Figure 3.14b). A corresponding image obtained with the digital camera set in a static position is shown for comparison in Figure 3.14a. Presentation and discussion of the images obtained from the moving camera system are provided in Chapter 5.

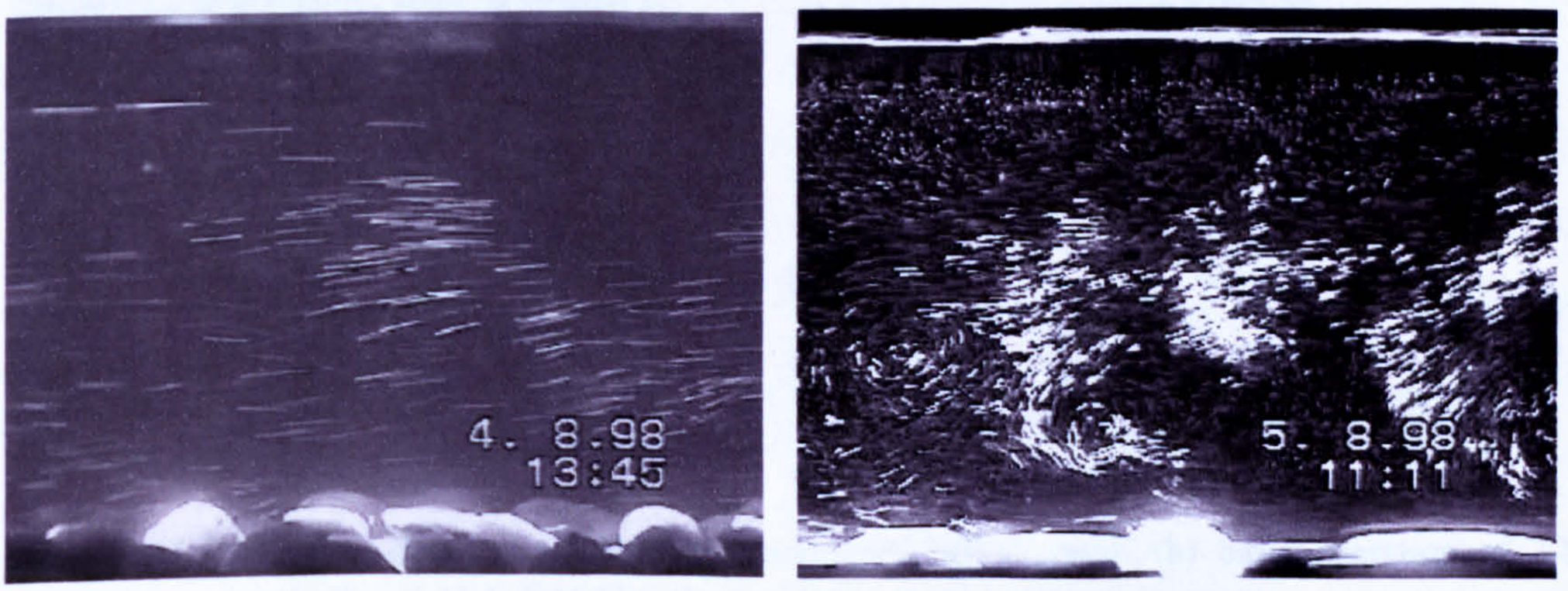

Figure 3.14 - Typical digitised images obtained from: (a) fixed camera position and; (b) moving camera system

3.4.3.4 Other Instrumentation and Apparatus

Acoustic Doppler Velocimeter (ADV)

A vertically orientated 3-D acoustic doppler velocimeter (ADV), manufactured by Sontek™, was used to measure mean and turbulent flow characteristics in Series 1B experiments (Figure 3.15a). The ADV probe measures the instantaneous 3-D point velocities and turbulence characteristics of the flow within a sampling volume located at a known distance below the probe tip (Figure 3.15b). The vertically orientated probe configuration is ideal for taking turbulence measurements close to a bed surface, but has the disadvantage that measurements cannot be taken in a free surface region as the probe transducers have to be fully submerged in order to operate.

The main attraction in using the ADV probe lay with the simplicity of its set-up and operation. As the probe requires no calibration (or periodic re-calibration), detailed time series data on the mean and fluctuating characteristics of the turbulent open-channel flow could be obtained relatively easily prior to each experiment. The post-processing WinADV software also enables significant amounts of velocity data to be processed quickly by executing the direct calculation of the turbulence parameters such as turbulence intensities and Reynolds stresses.

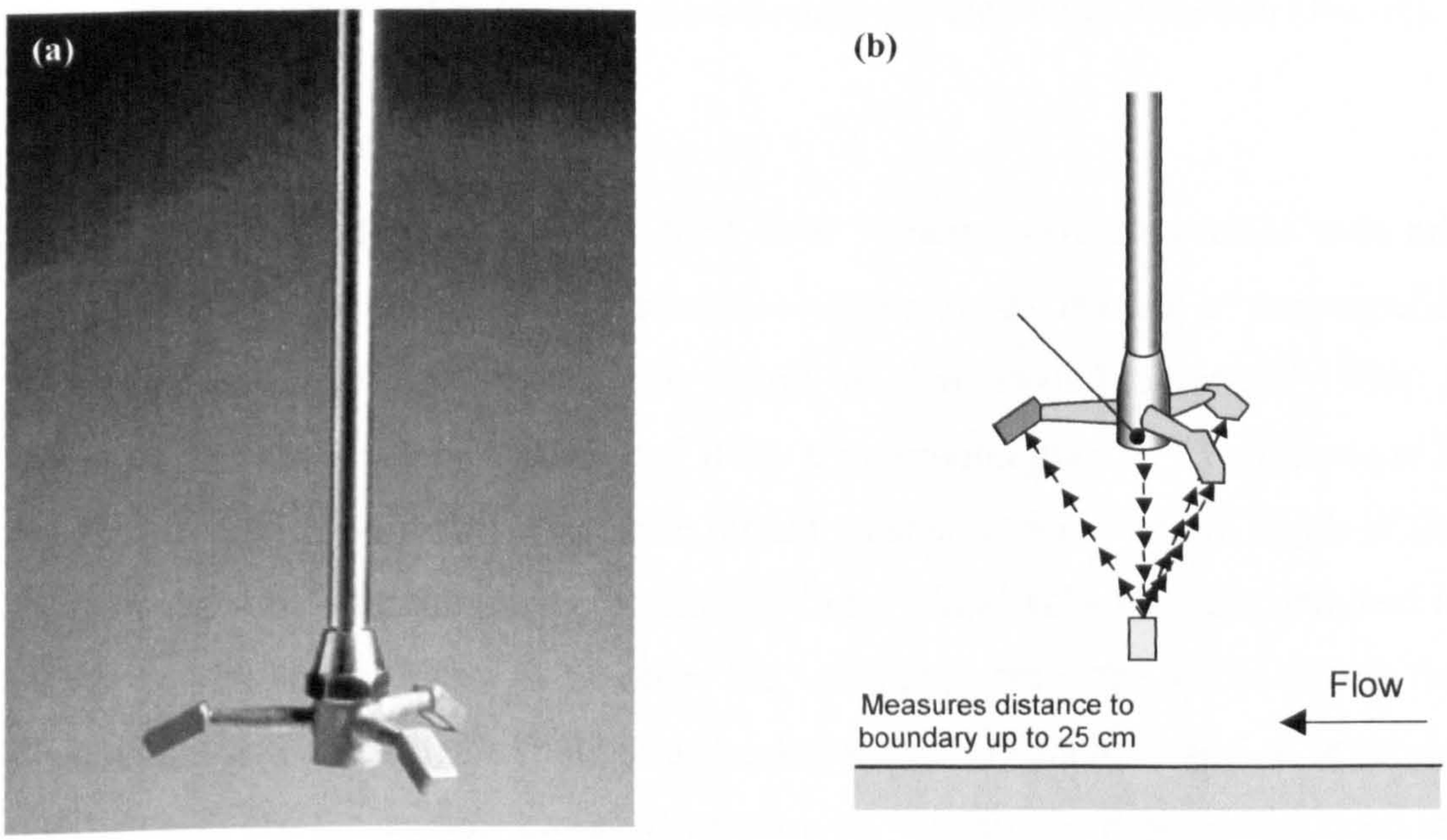

Figure 3.15 - (a) Three-dimensional vertically orientated ADV probe, (b) basic operation of 3-D vertically orientated ADV probe (modified from www.sontek.com).

The ADV probe operates on the principles of the Doppler effect, described in detail in Appendix 3.1, and takes nine measurements from each sample picked up by the three receivers. The three of primary interest are the velocities measured in the X, Y and Z directions. Of the remaining six measurements, three relate to the signal strength (one at each receiver), and three to the correlation values (one at each receiver).

The sampling rate at which velocity measurements were output was generally set at the maximum frequency of 25 Hz. to allow the most detailed measurements of the turbulence characteristics to be obtained. However, it is acknowledged that doubt has been expressed as to whether this frequency provides adequate resolution to capture very small turbulent scales present within the open-channel shear flow. However, this is considered a small disadvantage in comparison to the ease of probe set-up and the acquisition of measurements. The other main user-defined specifications are detailed in Appendix 3.1.

The ADV probe was mounted in a supporting frame, which allowed the sample volume to be positioned accurately at various locations within the flow. In the vertical direction (*Z*-axis), ADV measurements were generally made at incremental steps of between 1mm and 5mm from the bed boundary upwards. The probe was also positioned at various locations across the channel width to assess the variation in mean flow velocities and turbulence characteristics in the lateral direction (*Y*-axis).

Mini-Propeller Current Meters

Measurements of the longitudinal flow velocity were also made with mini-propeller current meters. The current meter output a digital reading of the propeller's frequency of revolution within the flow at two-second intervals, with the corresponding flow velocity calculated from a calibration graph. This technique had the distinct advantage that it could take measurements through the full depth of flow. As with the ADV measurements, profiles of longitudinal velocity were obtained at a number of lateral positions to measure the variation across the width of the flow. These profiles were then used both as a check for the ADV data, as well as to estimate the flow rate and the section-averaged streamwise velocity for experiments conducted in the Armfield flume.

Sediment Feed System

A portable sediment feed system (Figure 3.16) was designed to release a continuous low concentration stream of sediment at the free surface of the flow. This consists of a square-sided perspex funnel mounted in a supporting frame. The sediment is released through a 3mm-diameter hole in the bottom plate of the funnel at a constant rate of between 1.3 $g.s^{-1}$ and 2.1 $g.s^{-1}$ (dependent on particle size *d*). The sediment stream falls vertically onto a sheet of aluminium inclined at an angle of 30 degrees to the horizontal, allowing the it to spread out before entering the flow to reduce the influence of particle grouping effects on the observed sediment particle motion. A further advantage of this feed system was that by releasing the sediment stream down an inclined slope, the vertical distance that the sediment particles fall onto the free surface was minimised. This significantly reduced the vertical component of particle velocity when entering the flow at the free surface, although its effects were not completely diminished. While other methods of sediment feed were also considered (e.g. submerged wet sediment feed), this method was thought to be most reliable in providing a constant low concentration stream of particles with minimal grouping effects.

The feeder position was generally calibrated for each size fraction prior to each experiment. The lateral position of the sediment release could also be varied across the width of the flume (i.e. to correspond with the lateral variations in light sheet position in Series 1C).

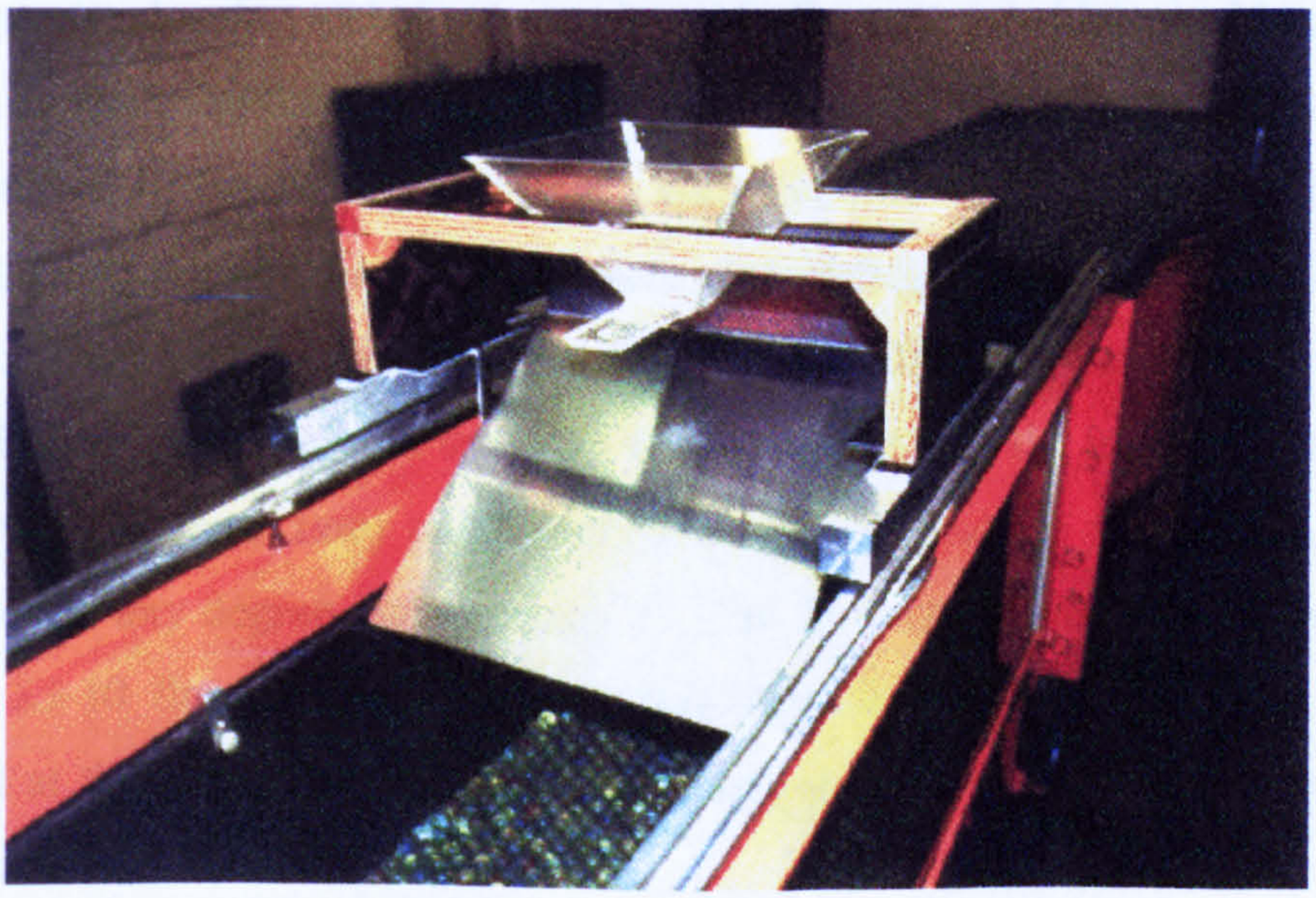

Figure 3.16 - Portable sediment feed system positioned within the Armfield S5-10 flume.

Optical Level and Scale for Bed Slope Measurement

In order to set the bed slope to the required gradient prior to each experiment, an optical level and scale were used to take measurements of the bed elevation at 0.5m increments along the length of the working section. Three measurements were generally taken at each longitudinal position: (i) at the near side wall; (ii) the centreline; and (iii) the far side wall, with the mean bed slope calculated from the average of these three measurements.

Electronic Temperature Probe

An electronic temperature probe was used to monitor the temperature of the water throughout the duration of each experiment. This probe gave a digital readout of the temperature to an accuracy of ±0.1°C.

Pointer Gauges

Conventional pointer gauges were used to measure the water surface elevation and water depths at 0.5m increments along the length of the working section. This allowed the longitudinal water surface profile to be determined which, in turn, ensured that uniform flow conditions were set up in the flume. Full details of the technique employed in setting up uniform flow conditions are given in Appendix 3.2.

3.5 Introduction to Series 2 Experiments

The visualisation techniques employed in Series 1 provide valuable qualitative observations and quantitative data on the processes controlling fine sediment transport and deposition characteristics in turbulent open channel shear flow. Unfortunately, a number of limitations and restrictions were also highlighted with these visualisation techniques, most notably, the requirement of low sediment concentrations to allow recorded images to be analysed successfully. Consequently, the influence of sediment concentration (or input rate) on the characteristics of particle motion could not be investigated to any degree during Series 1. The low aspect ratio of the glass-walled Armfield S5-10 flume also meant that two-dimensional flow conditions were not developed at the centre of the channel and secondary currents may have influenced particle motion.

A second series of experiments was conducted to address these limitations. The opportunity was taken to use a larger flume facility that had been both unavailable and unsuitable for Series 1. As well as having a significantly longer working section (8-9m), the flume was also more than twice the width of the Armfield flume (0.764m). This allowed steady, uniform flow conditions to be established with aspect ratios (α) greater than the critical value of 5, determined by Nezu and Rodi (1985) for the development of two-dimensional flow conditions.

The measurement techniques employed in the Series 2 experiments relied on sampling sediment concentrations within the flow and the collection of deposition samples within traps along the length of the flume. Mean and turbulent flow characteristics were again measured with the vertically orientated ADV probe. The fine sediment was introduced to the flow near the upstream end of the flume at a constant, pre-determined rate from a sediment feeder of a more sophisticated design than employed in Series 1 (§3.4.3.4, pp. 78). The fine sediment was transported a distance along the working section in suspension, from which concentrations were sampled, before gradually depositing into a series of traps under the experimental gravel layer running the length of the flume. The quantity and composition of the deposited material in each trap were analysed to obtain longitudinal distributions of sediment deposition. Analysis of the data obtained from these sampling techniques and from the ADV measurements generated valuable information on the factors influencing fine sediment transport and deposition processes and provided an independent data set on which to compare the main findings from Series 1.

3.5.1 Flume Set-up and Operation

3.5.1.1 Description and Operation of Flume Facility

The flume facility used for the sediment deposition experiments operates as a water re-circulating and sediment feeding system. The walls and bed of the working section of the flume are constructed from wood, with a glass observation window incorporated in the near-side wall about halfway down the length of the flume. The water required for flume operation is stored in the sump and reservoir tanks at the downstream end and the stilling tank at the upstream end. The water is re-circulated through a pump delivering flow rates of up to 55 $\ell.s^{-1}$. The head loss across an orifice plate in the delivery pipe is measured, from which the flow rate can be calculated

from the equation $Q = 1.238\sqrt{H_L}$, where Q is the flow rate (*l*/s) and H_L is the head loss in millimetres. The flow is delivered to the working section of the flume via the upstream stilling tank. At the downstream end of the working section, the flow passes over a tail weir and falls vertically back into the sump/reservoir tanks. A schematic diagram of the facility is shown in Figure 3.17, and its main working parameters outlined below:

Length of working section	-	8.0 m
Cross-sectional shape	-	Rectangular
Width of working section	-	0.764 m
Depth of working section	-	0.270 m
Maximum positive bed slope	-	1:60 (0.0167)

For the flow conditions employed in Series 2, where depth H was varied between about 75 and 120mm, the flow aspect ratios (α) within the flume ranged between about 6.5 and 9.9. The width of the central region in which side-wall effects disappear and two-dimensional flow conditions can be expected to exist can be calculated from the equation $|y/H| < (\alpha - \alpha_c)/2$ (Nezu and Nakagawa, 1993), ranging from 90 to 190mm in width for the given flow conditions.

3.5.1.2 Design and Layout of Sediment Traps

An arrangement of sediment traps was designed to run along the full length of the working section beneath the gravel bed layer, allowing the longitudinal variation in sediment deposition to be assessed. This consisted of a set of twelve galvanised metal trays running along the centreline of the working section and a row of wooden traps running down each side of the flume (Figure 3.18). The centreline trays had dimensions 610mm-long × 305mm-wide × 50mm-deep and are divided into three equally sized compartments, shown schematically in Figure 3.19. In order to define the relative position of each of the centreline trays, they were numbered from the upstream end of the working section, while the three compartments per tray were named a, b and c. Thus, trap 1a was situated at the upstream end and 12c at the downstream end of the working section.

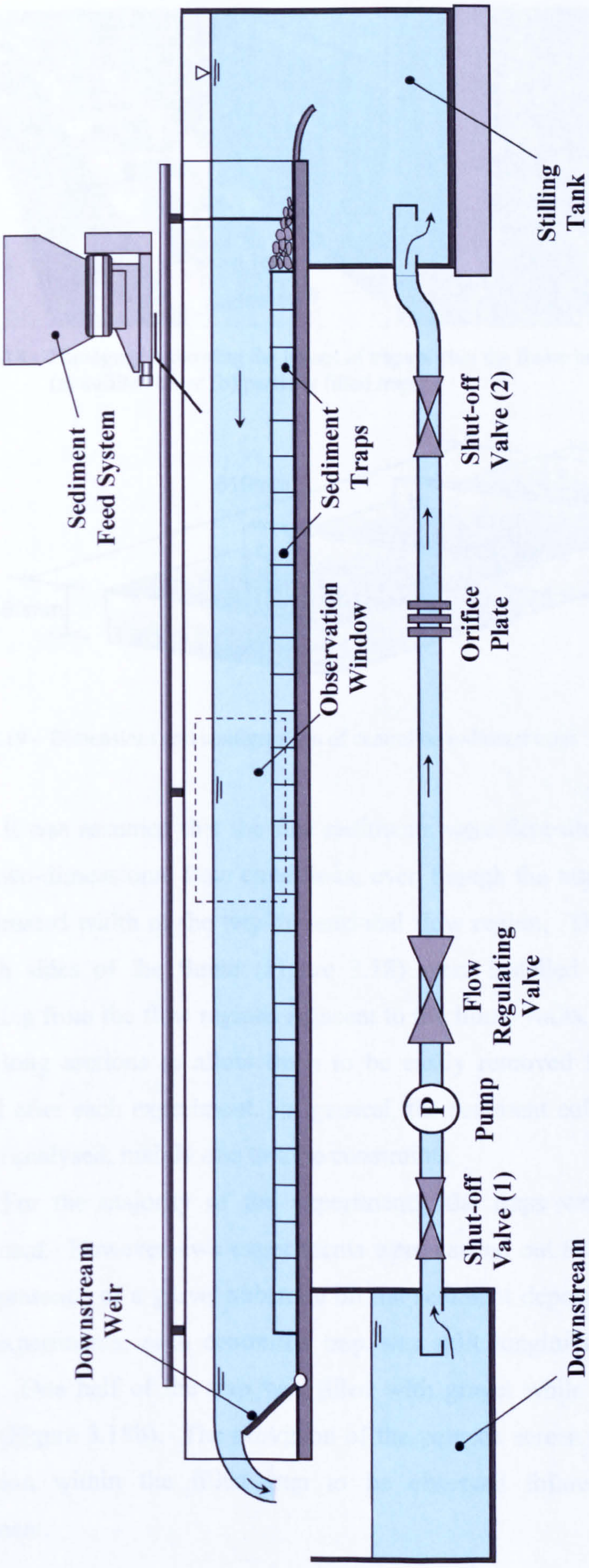

Figur 3.17 - Experimental flume set-up for Series 2

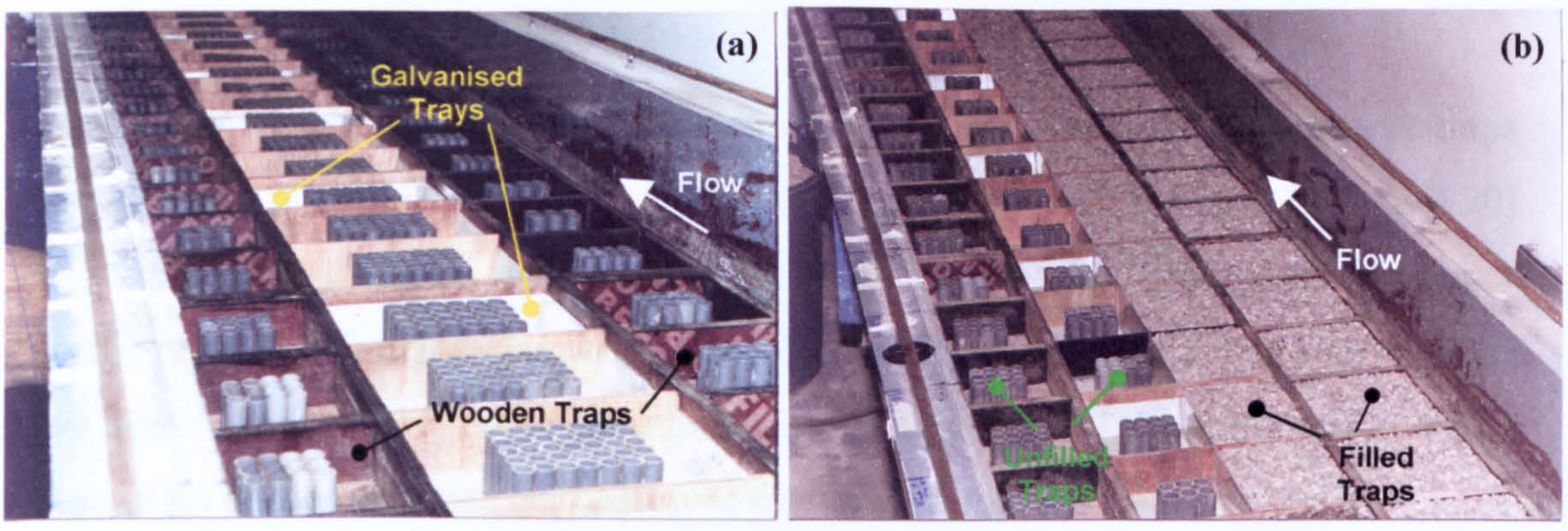

Figure 3.18 - Photographs showing the layout of traps within the flume bed:
(a) unfilled traps; (b) partially filled traps.

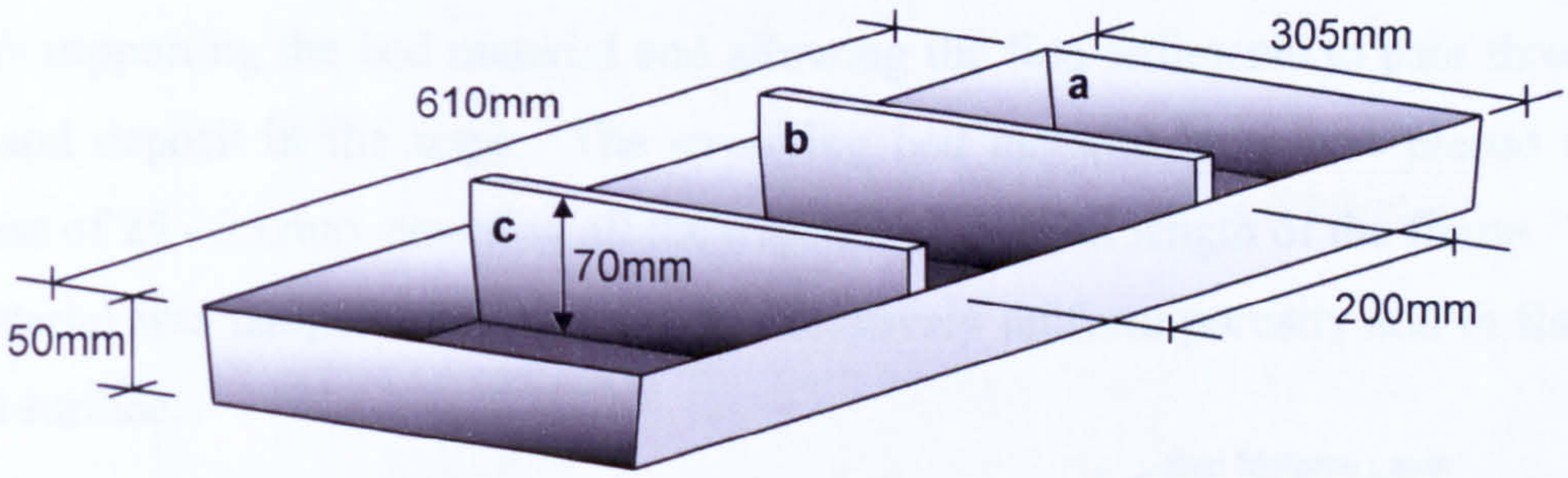

Figure 3.19 - Dimensions and configuration of centreline sediment traps

It was assumed that the fine sediments were deposited in the centreline traps under two-dimensional flow conditions, even though the trap width was greater than the estimated width of the two-dimensional flow region. The wooden traps running up both sides of the flume (Figure 3.18) were installed to collect the sediment depositing from the flow regions adjacent to the flume walls. These were constructed in 1m long sections to allow them to be easily removed from the flume bed and cleaned after each experiment. In general, the sediment collected within these traps was not analysed, mainly due to time constraints.

For the majority of the experiments, the traps were empty prior to each experiment. However, two experiments were carried out to investigate the influence of the presence of a gravel substrate on the sediment deposition characteristics. For these experiments, each centreline trap was split longitudinally by a thin perspex screen. One half of the trap was filled with gravel while the other half remained empty (Figure 3.18b). The provision of the perspex screen allowed for the mode of deposition within the filled trap to be observed following completion of the experiment.

3.5.1.3 Experimental Flume Bed Set-up

The basic arrangement of the bed consisted of the matrix of sediment traps, covered with a coarse mesh and overlain with a layer of bed material (Figure 3.20). The mesh and bed layers were supported above the traps by rectangular sections of plastic tubes positioned in the centre of each trap (Figure 3.18a). It was also expected that these tubes would reduce the circulation of flow within the traps, while having little or no influence on the deposition of the fine sediment.

Eight sections of brass mesh (1 m-long × 0.76 m-wide) were placed on top of the traps and fixed in place. The aperture size of the mesh was 3 mm, a suitable size for both supporting the bed material and allowing the fine sediments to pass through freely and deposit in the traps. The overlying bed material layer was placed to a thickness of 25 - 35 mm, covering all the traps along the full length of the flume. The bed material was tamped to compact it to a relatively uniform porosity and to flatten the bed surface.

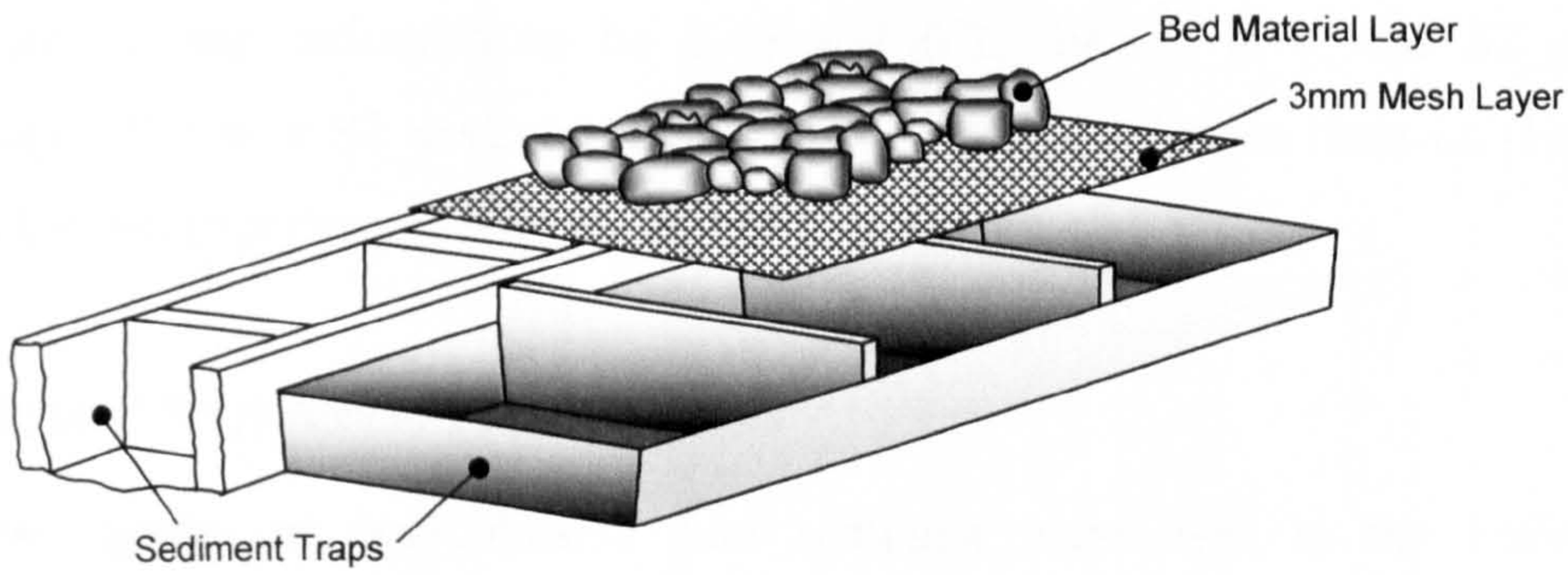

Figure 3.20 - Arrangement of sediment traps, 3mm mesh and bed material

3.5.2 Sediment Details

3.5.2.1 Physical Properties of Bed Material

As for Series 1, the bed material grades were selected to ensure static bed conditions and the free deposition of fine sediment to the underlying traps. Two grades of bed material were used in order to vary the bed conditions (i.e. relative roughness k_s/H, framework to matrix size D/d and bed porosity λ). These are defined as follows: (a) *S2_grv1* - well sorted and rounded 10-25mm natural river gravel with same grading as experimental gravel used in Series 1 (§3.4.2.1, pp.64); (b) *S2_grv2* - well sorted and sub-rounded 5-10mm gravel. The particle size distributions and the main percentiles for the two gravel grades are shown in Figure 3.21 overleaf.

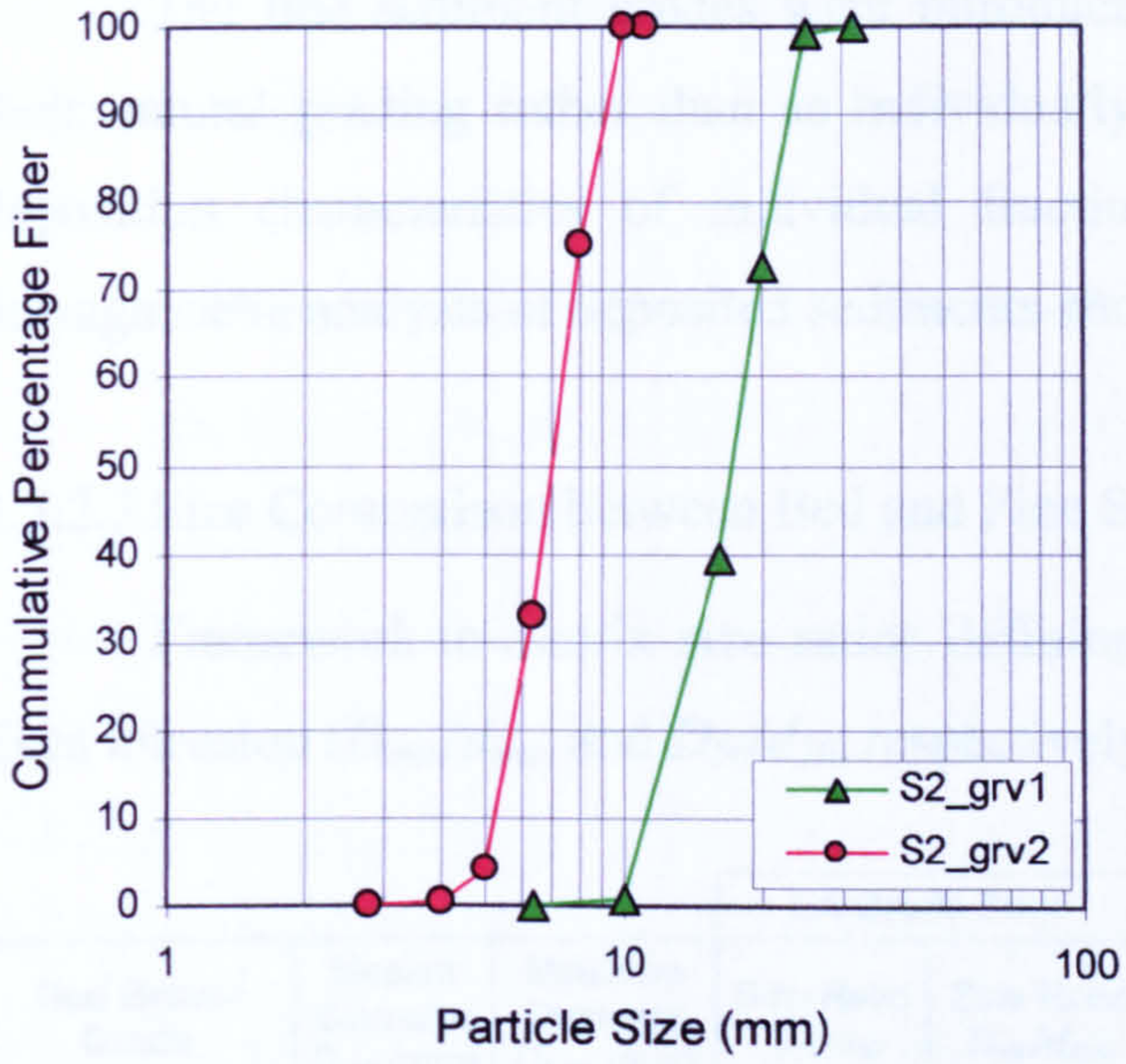

S2_grv1 Gravel

Size Range	- 10-25 mm
D_{16} Percentile	- 12.6 mm
D_{50} Percentile	- 17.3 mm
D_{84} Percentile	- 21.6 mm
Standard Dev.	- 1.31

S2_grv2 Gravel

Size Range	- 5-10 mm
D_{16} Percentile	- 5.62 mm
D_{50} Percentile	- 6.98 mm
D_{84} Percentile	- 8.60 mm
Standard Dev.	- 1.24

Figure 3.21 - Particle size distributions and properties of bed gravels

The density ρ_s of the two gravel grades was approximately 2650 kg.m^{-3}, while the porosity λ was estimated to be 0.40 and 0.35 for S1_grv1 and S2_grv2, respectively. The finer S2_grv2 gravel was also used as a substrate material (Figure 3.18b) in the two experiments with partially filled bed traps.

3.5.2.2 Physical Properties of Fine Sediments

Two grades of non-cohesive fine sediment were used in the Series 2 experiments: (i) Loch Aline sand and (ii) David Ball Fraction E. The particle size distributions and main percentiles for the two grades are shown in Figure 3.22 below,

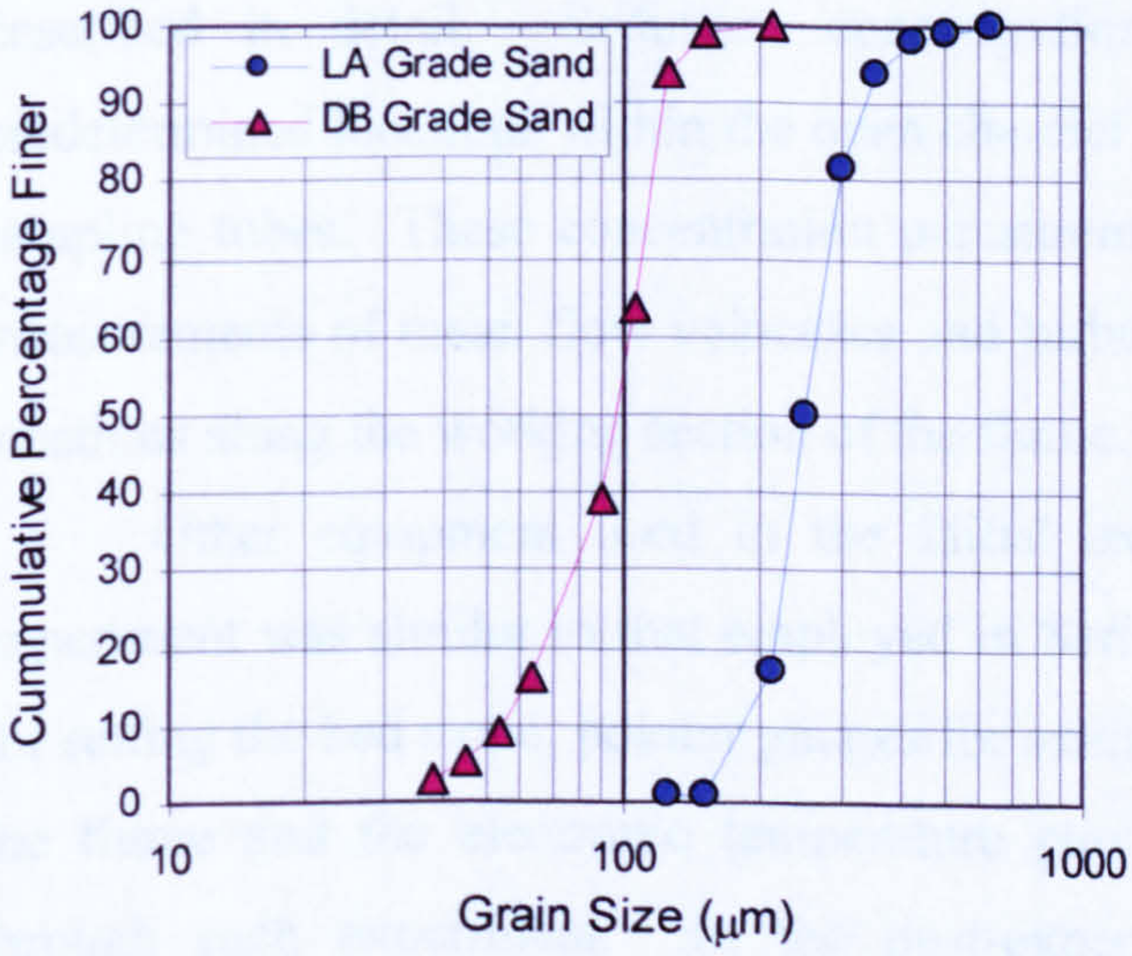

Loch Aline Sand (LA Grade)

Size Range	~ 125-625μm
d_{16} Percentile	- 209μm
d_{50} Percentile	- 250μm
d_{84} Percentile	- 306μm
Standard Dev.	- 1.21

David Ball Sand (DB Grade)

Size Range	~38-212μm
d_{16} Percentile	- 63μm
d_{50} Percentile	- 97μm
d_{84} Percentile	- 119μm
Standard Dev.	- 1.38

Figure 3.22 - Particle size distributions and properties of fine sediments

The fine sediment grades were introduced to the flow at the free-surface in their natural grading rather than as individually sieved fractions, the transport and deposition characteristics of individual fractions being subsequently determined through sieve analysis of deposited sediments and concentration samples.

3.5.2.3 Size Comparison between Bed and Fine Sediments

Framework-to-matrix size ratios defining the least and average potential for fines intrusion (D_{min}/d_{max} and D_{50}/d_{50}, respectively) are shown in Table 3.4 below.

			LA Grade Sand		DB Grade Sand	
Bed Gravel Grade	Median Diameter $D_{f,50}$ (mm)	Minimum Diameter $D_{f,min}$ (mm)	Size Ratio D_{50}/d_{50}	Size Ratio D_{min}/d_{max}	Size Ratio D_{50}/d_{50}	Size Ratio D_{min}/d_{max}
S1_grv1	17.3	10.0	69.2	16.0	178.4	47.2
S2_grv2	6.98	5.0	27.9	8.0	72.0	23.6

Table 3.4 - Size ratios of framework (bed) and matrix (fines) materials in Series 2

In general, the size ratios defined in Table 3.4 should result in the siltation mode of deposition. However, for the combination of LA grade sand and S2_grv2 bed material, the size ratios $D_{min}/d_{max} < 17$ and $D_{50}/d_{50} < 30$ suggest that a sealed layer may form within the experimental bed layer or within the substrate in experiments where S2_grv2 gravel is used as fill material.

3.5.3 Instrumentation and Experimental Procedures

The bed trap arrangement to collect sediment deposition samples has been described in detail. Sediment concentration samples were also collected at predetermined locations within the open channel flow using specially designed siphon sampling tubes. These concentration measurements were coupled with ADV probe measurements of mean flow velocities and turbulence parameters obtained at similar locations along the working section of the flume.

Other equipment used in the initial experimental set-up and during each experiment was similar to that employed in Series 1. This included the optical level for setting the bed slope, pointer gauges for setting up uniform flow conditions within the flume and the electronic temperature gauge to observe temperature variation through each experiment. In the post-experiment analysis, a series of ovens,

electronic scales and sieves were used to dry, weigh and analyse the fractional composition of each concentration and deposition sample collected.

3.5.3.1 Electrically Driven Sediment Feed System

An electrically-driven sediment hopper (Figure 3.23) fed the material into the flow at the free surface in a continuous stream from seven rotating nozzles spaced equally across the width of the channel. The sediment hopper has a variable speed dial, which controls the input rate I_R of sediment from the seven nozzles, ranging from 0 to 500 g/s (about 71g/s per nozzle). The sediment streams fell vertically onto an aluminium sheet inclined at between 30 and 45 degrees to the horizontal. This assisted in spreading out the concentrated streams into a near uniform sediment input across the full flow width, thus reducing the influence of particle grouping effects on transport processes. As in Series 1, it was also found that the provision of the sheet minimised the vertical distance that the sediment particles were required to fall into the free surface of the flow, which significantly reduced the vertical entry velocity of the particles.

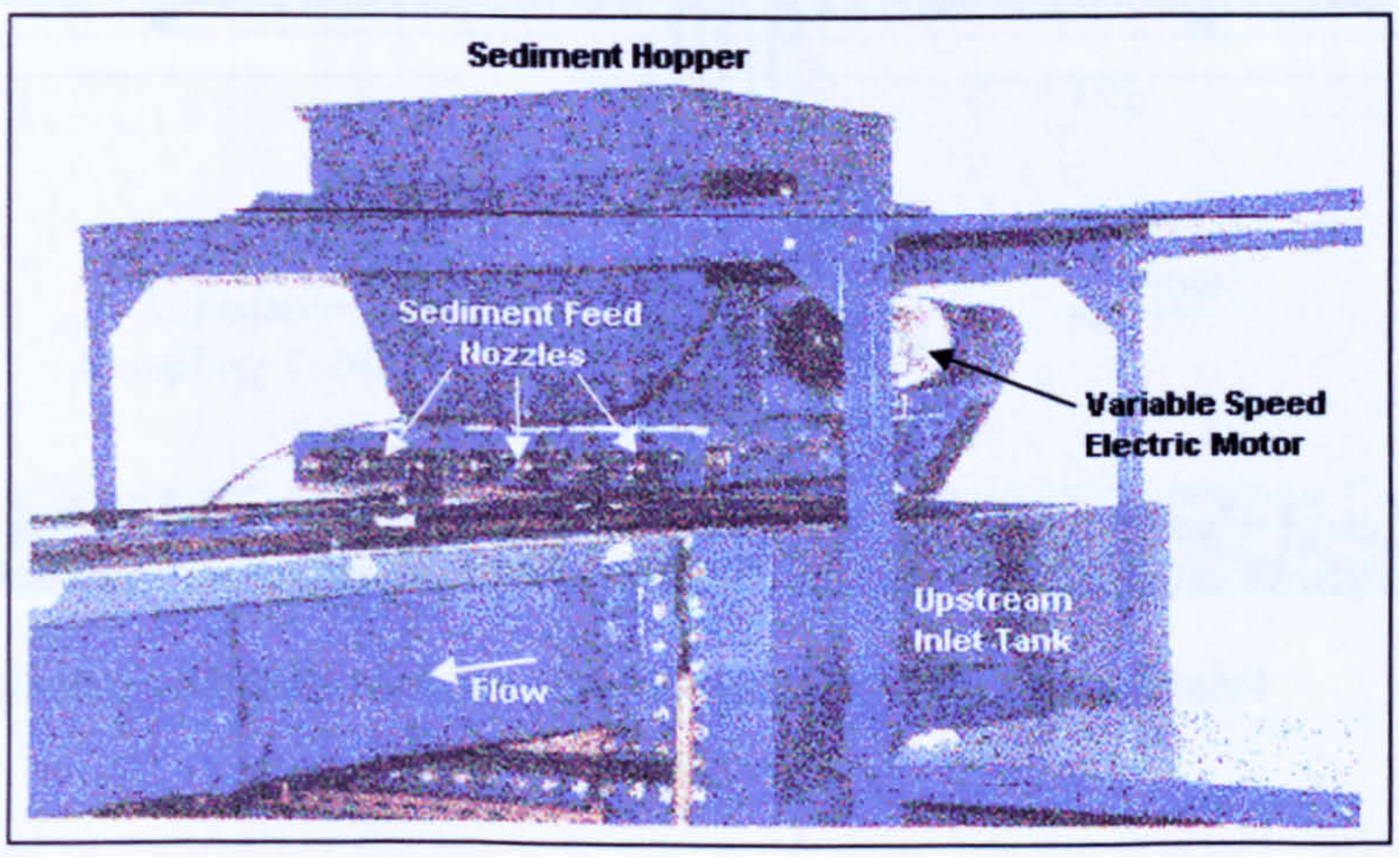

Figure 3.23 - Electrically-driven fine sediment feed system (modified from Peloutier, 1998)

3.5.3.2 Sediment Concentration Sampling Equipment

Sediment concentration samples were taken at five locations along the flume to study the variation in the concentration profiles with increasing distance from the sediment input point. These samples were siphoned from the flow at four elevations through a set of sampling tubes (Figure 3.24). Each tube consisted of a section of 10mm diameter copper pipe (internal diameter = 7mm) with a 90° bend at the end

submerged in the flow. These were each adjusted vertically to their predetermined elevations within the flow. A length of plastic tubing, with an internal diameter of 10mm, was attached at the top of each sample tube, allowing the concentration samples to be siphoned into separate 80 litre collection bins.

Following completion of each experiment, the water volume within each bin was measured and carefully pumped out, leaving the small quantity of sediment undisturbed at the bottom. These samples were dried overnight before being collected for weighing and sieve analysis. The total and fractional sediment concentrations (C and C_i) were determined from the ratio of the total and fractional sample weights to the measured volume of water collected in the bin.

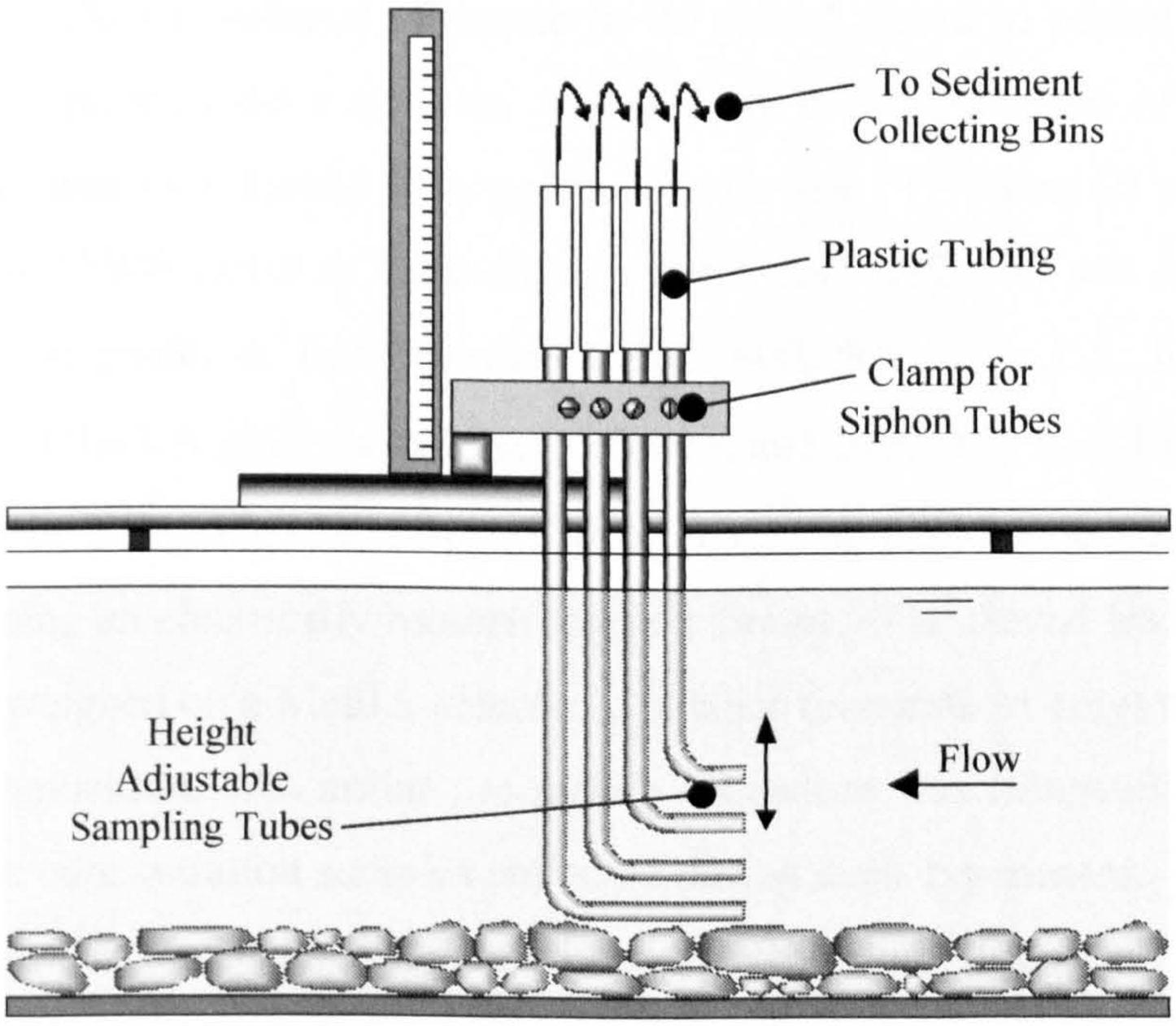

Figure 3.24 - Schematic diagram of sediment concentration sampling equipment

3.5.3.3 ADV Probe Measurements

The three-dimensional vertically orientated Acoustic Doppler Velocimeter (ADV) probe was used to obtain detailed measurements of the mean and fluctuating (turbulent) flow velocities for the range of flow conditions used in the study at the approximate locations at which the sediment concentrations were sampled. The operating principles of the ADV probe, along with its advantages and limitations have been previously detailed in §3.4.3.4, pp.76, and in Appendix 3.1.

As before, the ADV measurements were generally taken at vertical incremental distances of between 1mm and 5mm from the bed boundary upward (highest resolution in near-bed flow region). Velocity profiles were also measured at various *y/B* locations across the channel width to assess lateral variation in mean flow and turbulent characteristics.

3.5.3.4 Post Experiment Apparatus and Procedure

Following the completion of each experiment, the centreline traps containing the deposited fine sediment were removed from the flume bed, drained and placed in a series of ovens, where they were dried at ~100°C. Each dried sample was then weighed on an electric balance (accurate to 0.1g) and stored in sealed and labelled polythene bags prior to sieve analysis. A carefully divided fraction of each sample (up to ~100g) was then sieved in accordance with BS 1377 (Part 2) using 200mm diameter BS410/1986 sieves of different aperture sizes. Different sets of sieves were used for the two grades of fine sediment tested: 600, 500, 425, 355, 300, 250, 212, 150, 125μm for the LA grade sand (D_{50} = 250μm) and 212, 150, 125, 106, 90, 63, 53, 45, 38μm for the DB grade sand (D_{50} = 97μm). Each sample was sieved for about 10-15 minutes using an electrically motored sieve vibrator. The sieved fractions of each sample were weighed on a Mettler electronic balance (accurate to 1mg) to obtain their fractional composition. A similar processing procedure was followed for the sieve analysis of the concentration samples collected during each experiment.

A summary of the full experimental procedure followed during each experiment in Series 2, including the flume set-up, feed rate calibration, flow velocity and concentration measurements, and the post-experiment analysis is given in Appendix 3.3.

3.6 Summary of Experimental Studies

Two distinct series of experiments investigating the transport and depositional processes of fine sediment in turbulent open channel flow conditions over rough, porous bed layers were conducted in two different laboratory flume facilities.

Series 1 comprised of three separate sets of visualisation experiments carried out in the glass walled Armfield S5-10 flume, in which the fine sediment behaviour was observed and analysed directly from recorded images of particle motion in the

XZ flow domain and within the bed surface layers. An array of visualisation equipment including a fixed-position high speed MotionCorder (recording at up to 600 fps) and a digital video camera (25 fps) mounted on a mobile trolley system recorded both stationary and moving images of particle trajectories within the flow. Analysis of the particle trajectories was carried out with image analysis software, applying particle-tracking techniques. The camera mounted on the mobile trolley system was also employed to observe the typical large-scale structure of the open channel flow, while a vertically orientated three-dimensional ADV probe was used to obtain detailed statistical information of the mean and turbulent flow characteristics. The results obtained from the Series 1 experiments are presented in Chapters 4 - 5 and the associated appendices.

A total of twelve experiments were conducted in Series 2. These were carried out in a larger flume facility and employed non-visual techniques to study the transport and deposition of two grades of fine sediment within a turbulent open channel flow over porous layers of bed gravel. This study relied on the analysis of the fractional composition of deposited samples collected in a series of traps underlying the bed layer and concentration samples taken within the flow. Measurements of mean and turbulent flow characteristics were again taken with the 3-D ADV probe for the range of flow conditions used in the study. The results from the Series 2 experiments are presented in Chapter 6 and the associated appendices.

3.7 Programme of Experimental Work

The time scale and order in which the experimental studies were developed and carried out and the period of time taken for analysis of the results is presented schematically as a bar charts for the two experimental series in Appendix 3.4.

CHAPTER 4

Experimental Results (Series 1A and 1B)

4.1 Introduction

The intention of this chapter is to report experimental results for the observed behaviour of LA sand in turbulent open channel flow conditions set up in the Armfield S5-10 flume. These experiments are in three parts,

- Calibration experiments to ascertain the fall velocity of sieved LA grade size fractions in still water conditions.
- Preliminary visualisation experiments of sediment particle motion in the near-bed flow and within the surface bed layers (Series 1A).
- Particle tracking experiments to obtain quantitative data on sediment particle motion within open channel shear flow conditions (Series 1B).

Measurement of particle fall velocity in still water conditions is a clear prerequisite for examining the influence of turbulence on the vertical motion and depositional characteristics of the LA sand fractions within open channel flow conditions (§4.2). It is also important to compare these measured still water fall velocities with semi-theoretical and empirical expressions developed from previous investigations in order to assess whether the settling behaviour of LA sand is consistent with such studies.

§4.3 of this chapter reports on the mainly qualitative observations obtained during the preliminary series of visualisation experiments (Series 1A) conducted in the Armfield S5-10 Flume. These initial experiments also provided limited quantitative data on the near-bed motion of LA sand particles and their deposition through the surface layers of a rhombically-packed bed of uniform 15mm spheres.

More detailed quantitative data on the motion of LA sand particles in turbulent open channel flow conditions was obtained during the particle tracking experiments (Series 1B), reported in §4.4. Results from these experiments provide the first true body of evidence suggesting that flow turbulence may significantly affect the fall velocity of the LA grade sand fractions in open channel flow compared to the calibration values obtained under still water conditions.

Further visualisation experiments (Series 1C) were performed in the Armfield S5-10 flume in order to observe the large-scale turbulent structure of the open channel flow and assess how the transported particles interact with the structures. The mainly qualitative findings from these experiments are presented in Chapter 5.

Limitations with the visualisation techniques employed in Series 1 and with the flume facility in which the experiments were performed (§3.5, pp.79) deemed it necessary to carry out a further series of experiments (Series 2) to provide independent verification of the main findings from Series 1. The results from Series 2 are reported separately in Chapter 6.

4.2 Still Water Fall Velocity of LA Grade Sand Fractions

4.2.1 Introduction

An initial experiment was conducted to measure the still water fall velocity of each of the six main size classes of Loch Aline sand sieved from its natural grading. The main purpose of this test was to act as a benchmark with which to compare the fall velocity of the sediment measured within turbulent open channel flow conditions. Additionally, the experiment also allowed the measured still water fall velocities of the LA grade sand fractions to be calibrated against corresponding values obtained from a number of equations derived from previous studies of fall velocity in quiescent conditions.

4.2.2 Experimental Technique and Results

The experimental measurements of still water fall velocity for the LA sand were conducted in quiescent fluid conditions in a 1.0m deep by 0.15m wide transparent-walled tank. A quantity of the sediment was sieved into the six size fractions, and one hundred individual grains from each fraction were released, in turn, at the surface to settle through the fluid. Each grain was manually timed as it settled in the region between 0.5 m and 0.75 m below the water surface. This ensured that the particles reach their terminal velocity w_s within the initial 0.5 m of fluid before their fall velocities were measured.

The histograms and related statistics in Figures 4.1(a) to (f) overleaf, show the distribution of measured fall velocities for each sediment fraction. The coarsest 500-425μm fraction is shown to have the greatest spread of measured w_s values, and a general trend of decreasing standard deviation in w_s with decreasing particle size d_i is observed. The explanation for this may be provided by the microscopic examination of each individual size fraction. The finer sediment fractions were found to be relatively uniform in shape, being well rounded and often almost spherical, while the coarser fractions tended to be far more irregular and angular in shape. This influence of particle shape would result in a more uniform drag coefficient (C_D) for the finer fractions than for the coarser fractions, in turn, resulting in a lower standard deviation in the measured still water fall velocities of individual particles.

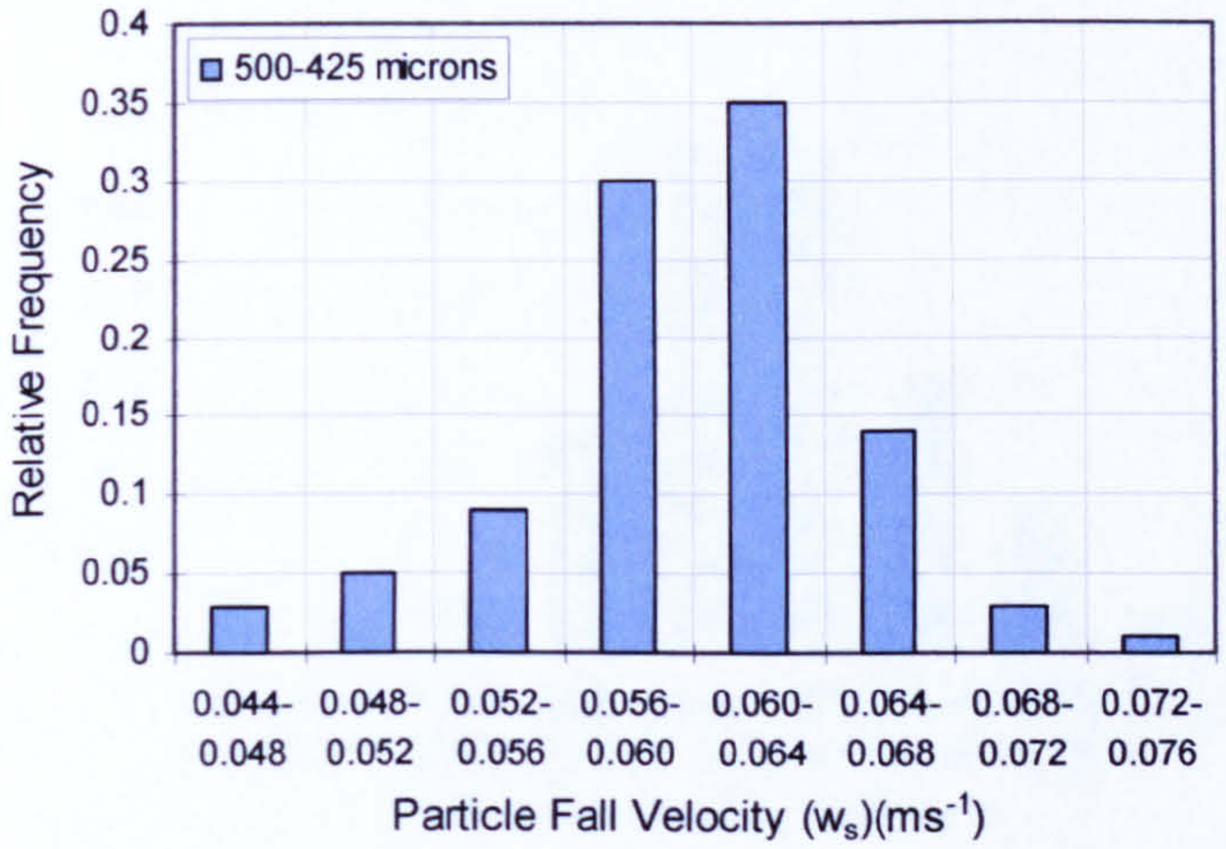

500-425 micron Particles	
Mean	0.0600
Standard Error	0.0005
Median	0.0603
Mode	0.0610
Standard Deviation	0.0051
Sample Variance	2.59E-05
Range	0.0279
Minimum	0.0443
Maximum	0.0723
Confidence Level (95.0%)	0.0010

(a)

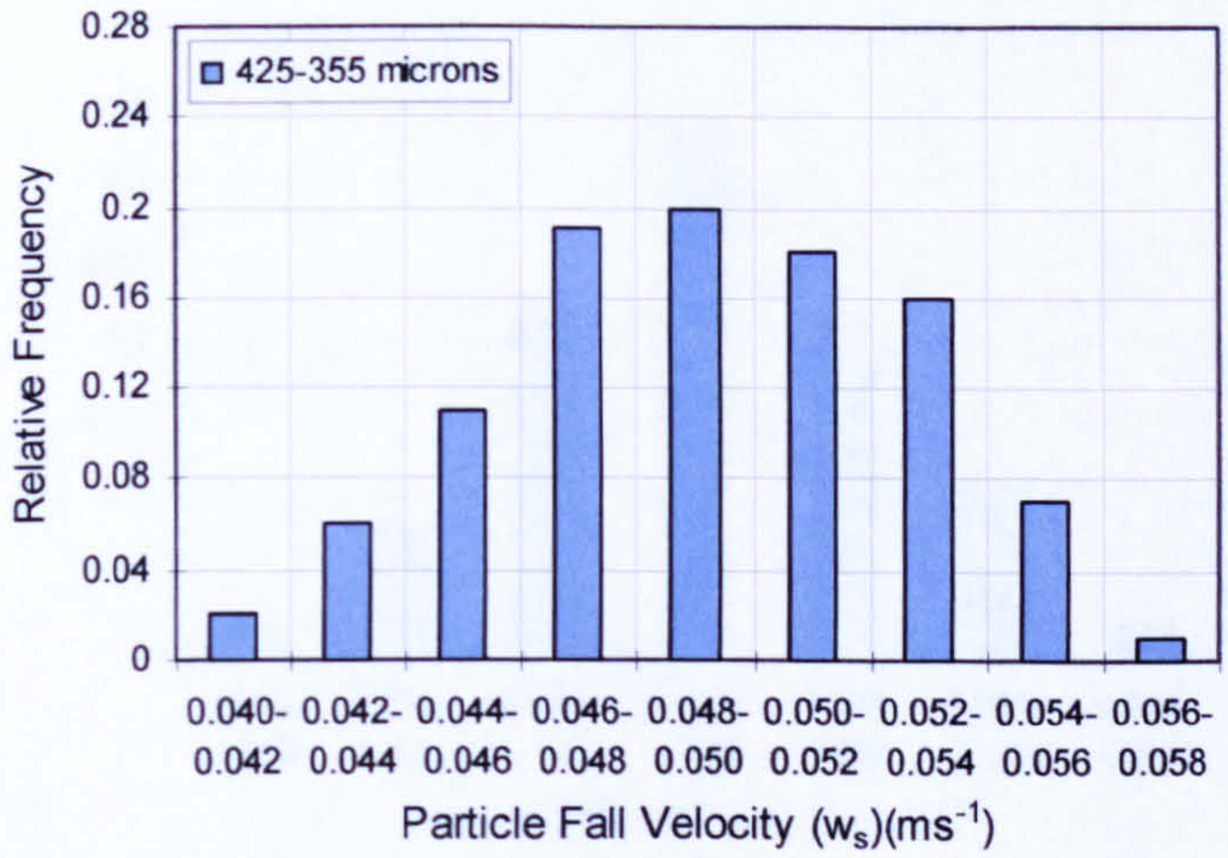

425-355 micron Particles	
Mean	0.0491
Standard Error	0.0003
Median	0.0490
Mode	0.0526
Standard Deviation	0.0034
Sample Variance	1.19E-05
Range	0.0159
Minimum	0.0407
Maximum	0.0566
Confidence Level (95.0%)	0.0007

(b)

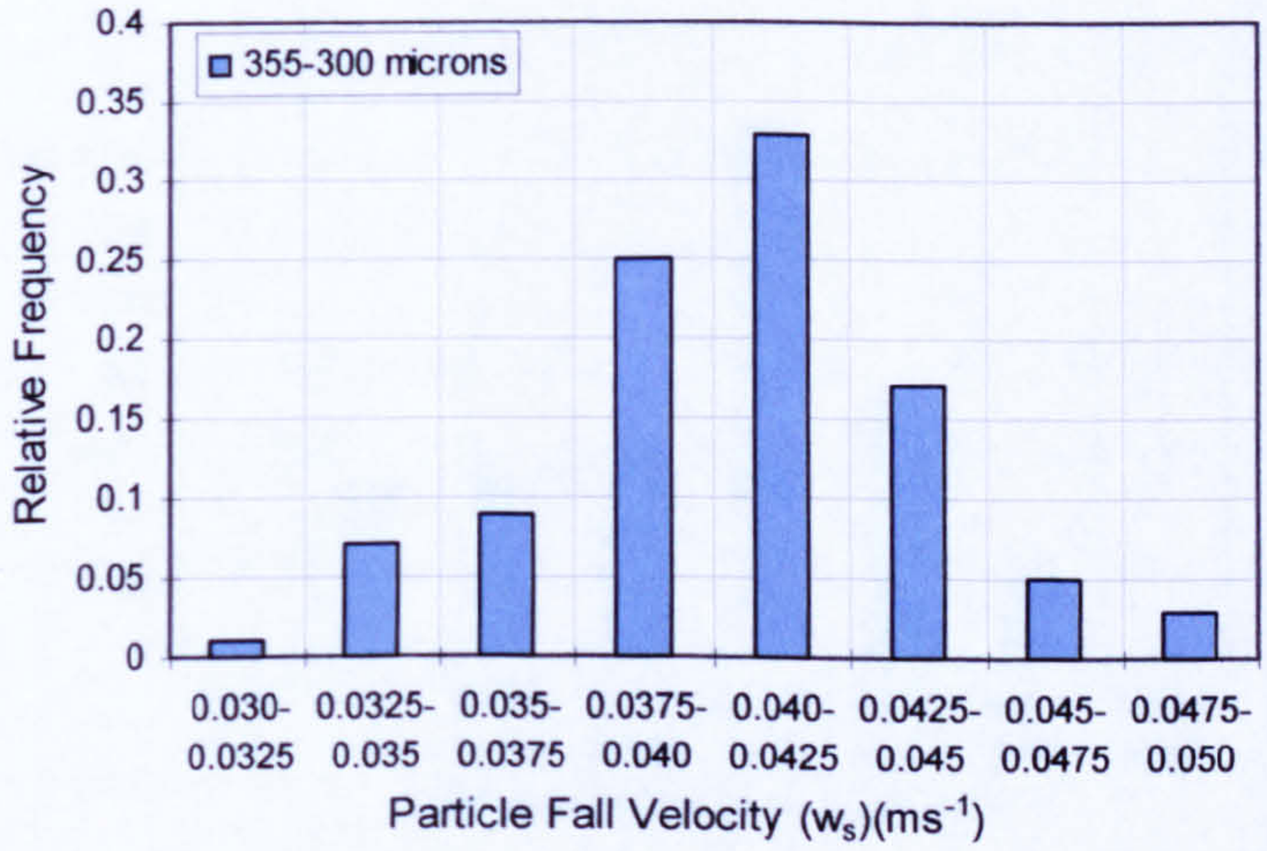

355-300 micron Particles	
Mean	0.0405
Standard Error	0.0003
Median	0.0409
Mode	0.0410
Standard Deviation	0.0033
Sample Variance	1.11E-05
Range	0.0187
Minimum	0.0307
Maximum	0.0494
Confidence Level (95.0%)	0.0007

(c)

Figure 4.1a-c - Frequency histograms of measured particle fall velocity (w_s) in quiescent fluid conditions and corresponding statistical data: (a) 500-425 microns; (b) 425-355 microns; (c) 355-300 microns.

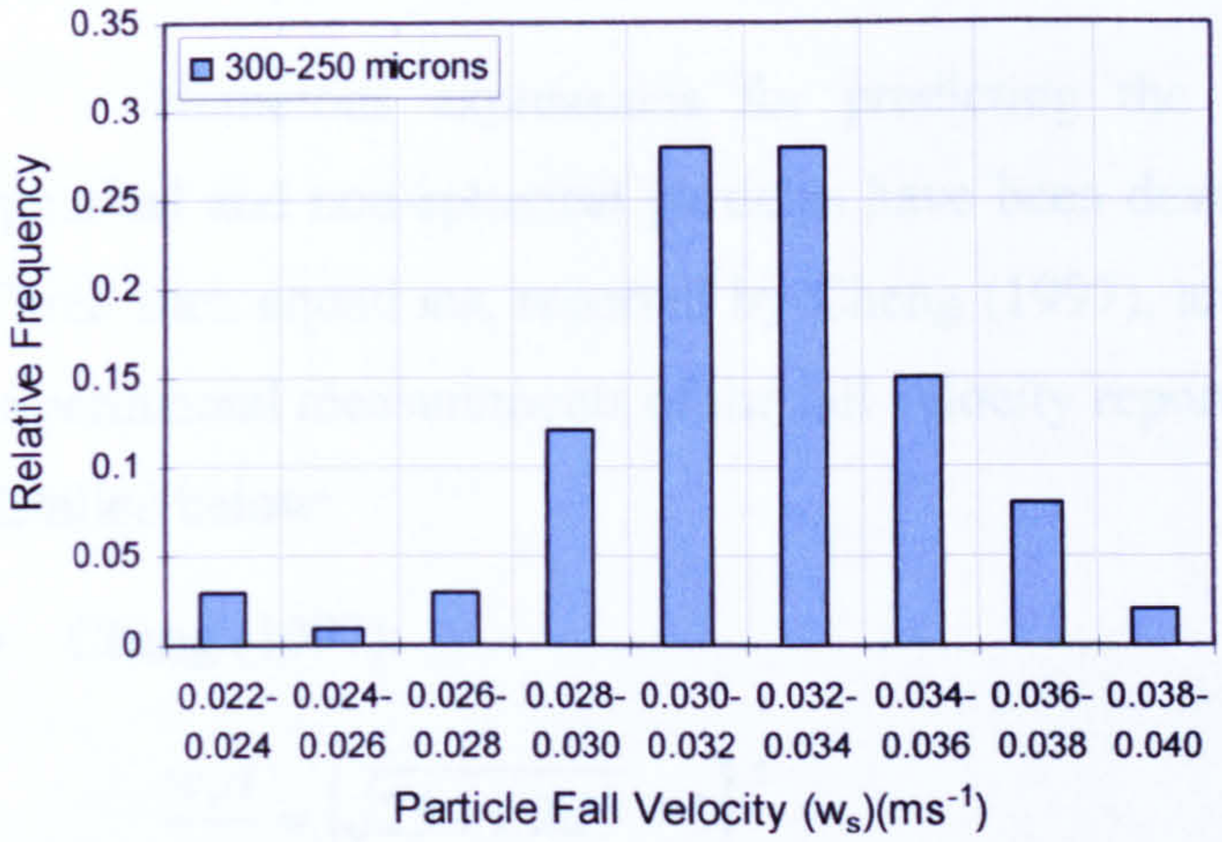

300-250 micron Particles	
Mean	0.0322
Standard Error	0.0003
Median	0.0323
Mode	0.0312
Standard Deviation	0.0031
Sample Variance	9.69E-06
Range	0.0154
Minimum	0.0229
Maximum	0.0383
Confidence Level (95.0%)	0.0006

(d)

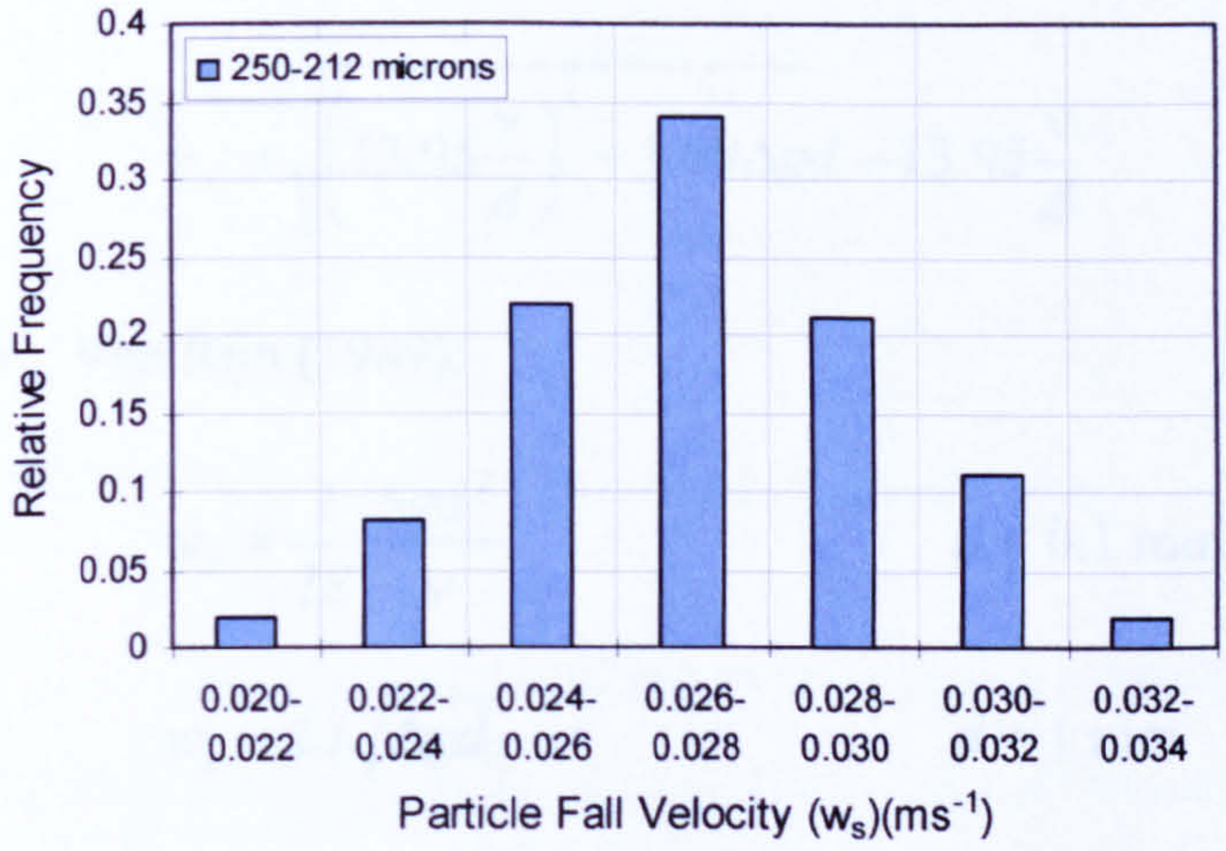

250-212 micron Particles	
Mean	0.0270
Standard Error	0.0002
Median	0.0268
Mode	0.0291
Standard Deviation	0.0023
Sample Variance	5.42E-06
Range	0.0114
Minimum	0.0210
Maximum	0.0324
Confidence Level (95.0%)	0.0005

(e)

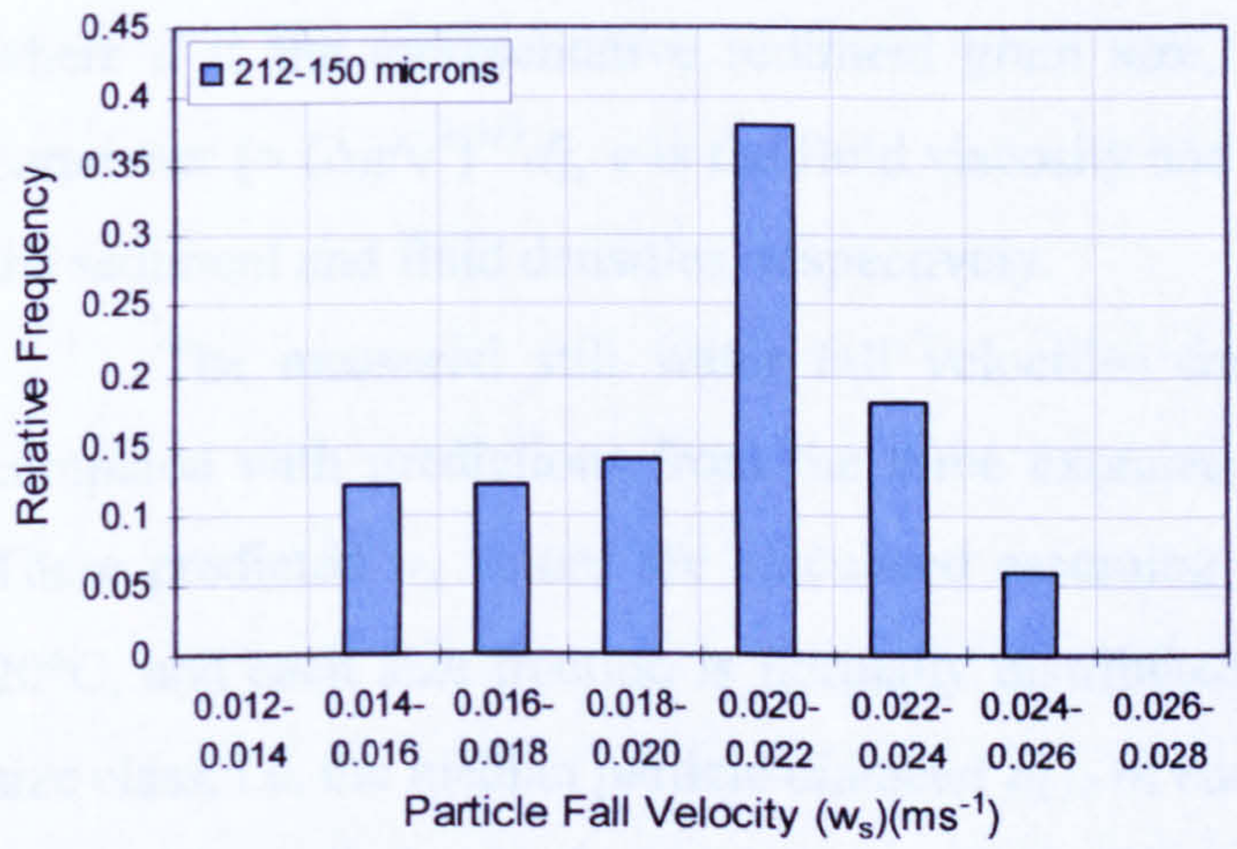

212-150 micron Particles	
Mean	0.0201
Standard Error	0.0004
Median	0.0208
Mode	0.0212
Standard Deviation	0.0027
Sample Variance	7.31E-06
Range	0.0110
Minimum	0.0141
Maximum	0.0251
Confidence Level (95.0%)	0.0008

(f)

Figure 4.1d-f - Frequency histograms of measured particle fall velocity w_s in quiescent fluid conditions and corresponding statistical data: (d) 300-250 microns; (e) 250-212 microns; (f) 212-150 microns.

4.2.3 Comparison with Semi-Theoretical and Empirical Expressions for w_s

Numerous expressions for predicting the still water fall velocity w_s of spherical and non-spherical particles have been developed by different investigators. Three such equations, reported by Cheng (1997), are used as a comparison with the experimental measurements of the fall velocity reported above. These expressions are detailed below:

- Cheng (1997):

$$\frac{w_s d}{\nu} = \left(\sqrt{25 + 1.2 d_*^2} - 5\right)^{1.5} \qquad \text{....(4.1)}$$

- Zhang (1989):

$$w_s = \sqrt{\left(13.95\frac{\nu}{d}\right)^2 + 1.09\Delta g d} - 13.95\frac{\nu}{d} \qquad \text{....(4.2)}$$

- Van Rijn (1989):

$$w_s = \frac{1}{18}\frac{\Delta g d^2}{\nu} \qquad d < 0.1 \text{ mm} \qquad \text{....(4.3a)}$$

$$w_s = 1.1\sqrt{\Delta g d} \qquad d > 1 \text{ mm} \qquad \text{....(4.3b)}$$

$$w_s = 10\frac{\nu}{d}\left(\sqrt{1 + 0.01 d_*^3} - 1\right) \qquad d = 0.1 \sim 1 \text{ mm} \qquad \text{....(4.3c)}$$

where d is the representative sediment grain size, d_* is the dimensionless particle parameter [$= (\Delta g/\nu^2)^{1/3} d$], ν is the fluid viscosity and $\Delta = (\rho_s - \rho)/\rho$, where ρ_s and ρ are the sediment and fluid densities, respectively.

The measured still water fall velocities for the six LA size fractions are compared with predictions from the three expressions detailed above in Table 4.1. These predicted w_s values are calculated assuming a standard water temperature of 20°C, and each size fraction is normally distributed around the central value in the size class, i.e. the median particle diameter $d_{i,50}$ of each size fraction i.

The variation in the measured and calculated w_s values with the dimensionless particle diameter d_* are illustrated in Figure 4.2. The error bars shown on the measured data represent ± one standard deviation from the calculated mean values of w_s for each size fraction.

It is clearly seen that the measured fall velocities are in quantitative agreement with the predicted values of w_s obtained from the empirical and semi-theoretical expressions. A calculation of the relative error assesses the accuracy of each of these three expressions in predicting the fall velocity of the LA grade sand, where

$$Relative\ Error = \frac{(calculated\ w_s - measured\ w_s)}{measured\ w_s} \times 100 \qquad ....(4.4)$$

Sediment Size Fraction (μm)	Median Diameter (d) (μm)	Measured Fall Velocity (w_s) (ms^{-1})	Calculated Fall Velocities (ms^{-1}) and Relative Errors (%)					
			Cheng (1997) Eq. 4.1	Relative Error (Cheng)	Zhang (1989) Eq. 4.2	Relative Error (Zhang)	van Rijn (1989) Eq. 4.3	Relative Error (van Rijn)
500-425	462.5	0.0600	0.0560	-6.7	0.0651	+8.5	0.0676	+12.7
425-355	390.0	0.0491	0.0465	-5.3	0.0546	+11.2	0.0578	+17.7
355-300	327.5	0.0405	0.0379	-6.4	0.0445	+12.3	0.0484	+19.5
300-250	275.0	0.0322	0.0303	-5.9	0.0354	+9.9	0.0396	+23.0
250-212	231.0	0.0270	0.0239	-11.5	0.0275	+1.9	0.0316	+17.0
212-150	181.0	0.0201	0.0166	-17.4	0.0185	-8.0	0.0221	+10.0
	Average	**0.0382**		**-8.9**		**+6.0**		**+16.7**

Table 4.1 Comparison of Measured and Predicted Values of w_s

The calculated relative errors of each expression in predicting w_s for each size fraction are given in Table 4.1, along with an average error value. It is clear that the predictions of Cheng (1997) and Zhang (1989) demonstrate a good degree of accuracy against the experimental data, with average relative errors of –8.9% (under-prediction) and +6.0% (over-prediction), respectively. The predictive accuracy of van Rijn's (1989) formulae, however, is considerably worse, with an average over-prediction of +16.6% in the values of w_s. Cheng (1997), when comparing the three relationships against U.S. Inter-Agency Committee data (1957), reported similar findings. The calculated absolute relative errors for equations 4.1, 4.2 and 4.3 were 6.1%, 8.7% and 21.7%, respectively.

In summary, this initial experiment has served as a calibration or benchmark with which to compare the vertical motion of LA sand particles in the turbulent open-channel flow conditions. The experimental data reported shows good quantitative agreement with a number of expressions developed from previous investigations, and in particular, Cheng (1997) and Zhang (1989).

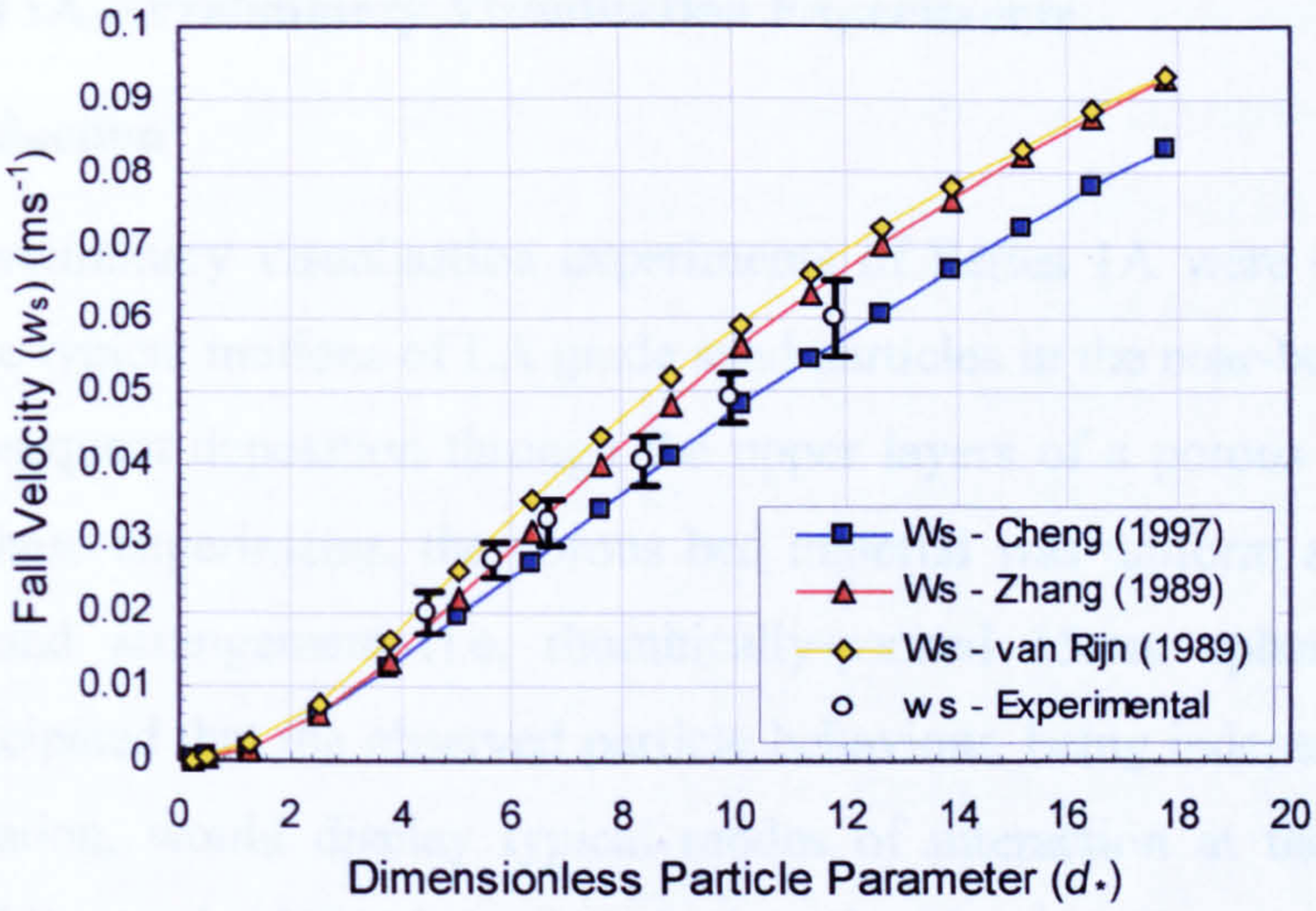

Figure 4.2 - Variation of sediment fall velocity w_s in quiescent fluid with the dimensionless particle parameter d_*. Comparison between measured w_s for LA grade sand fractions and predicted values of w_s from Cheng (1997), Zhang (1989) and van Rijn (1984). Experimental values are mean values ± the standard deviation.

4.3 Series 1A – Preliminary Visualisation Experiments

4.3.1 Introduction

The preliminary visualisation experiments of Series 1A were carried out to investigate the typical motions of LA grade sand particles in the near-bed flow region and their subsequent deposition through the upper layers of a porous bed. For the majority of these experiments, the porous bed material was uniform and regular in size, shape and arrangement (i.e. rhombically-packed 15mm spheres). It was therefore anticipated that the observed particle behaviour, being independent of local bed configuration, would display typical modes of interaction at the bed surface interface. While much of this behaviour is described in a qualitative manner, some preliminary quantitative measurements of streamwise and vertical particle velocities in the near-bed flow region (u_s and w'_s) and deposition velocities within the surface layers of the bed (w_d) were also made directly from the video recordings.

Detailed information on the set-up of the visualisation equipment employed in this series of experiments and the procedures followed in obtaining both the qualitative and quantitative data are given in §3.4.3.1, pp.67.

4.3.2 Experimental Conditions

The experiments were carried out under steady, uniform flow conditions. Individual LA grade sediment fractions were fed into the flow at the free surface; a sufficient distance upstream to ensure the particles entered the view field of the VHS video camera. The extent of this view field generally covered the lower 20-30mm of flow (i.e. near-bed region $z/H \leq 0.2$), as well as including at least two surface layers of uniform spheres, which allowed the deposition motion of sediment particles to be recorded adjacent to the flume wall (Figures 3.8 and 3.9, pp.68). It was generally observed that deposited sediment particles were rarely re-suspended from below this level by turbulent fluctuations.

A total of five separate visualisation experiments were carried out in Series 1A. Each of these experiments was subdivided into five individual runs to consider the behaviour of each size fraction of LA sand (d_i = 427.5, 327.5, 275, 231 and 181μm). For each experiment, the bed slope s_0 was set constant at 0.004 (1:250) using the method described in §3.4.3.4, pp.79. Experiments S1A_EX1 to EX3 were

each conducted with the uniform bed configuration, with the flow conditions being altered by varying the flow depth H alone. Quantitative measurements of particle motion were made from analysis of individual particle trajectories during these experiments. By contrast, experiments S1A_EX4 and EX5 were carried out for solely qualitative observation purposes. These considered the influence of bed configuration on particle motion, replacing the 15mm uniform spheres initially with larger 25mm spheres, and then with natural gravel (D_{50} = 17.3mm; σ_g = 1.31). A summary of the main experimental variables for the five experiments is given in Table 4.2.

Longitudinal flow velocities profiles were measured with a mini-propeller at five locations across the width of the flume (y/B = 0.17, 0.33, 0.50, 0.67 and 0.83). These were integrated to provide the section-averaged longitudinal velocity U. The shear velocity u_* was calculated from the equation,

$$u_* = \sqrt{gRS_f} \qquad \text{....(4.5)}$$

where R is the hydraulic radius and S_f is the slope of the energy line ($\sim S_0$ for steady, uniform flow conditions).

Experiment No.	S1A_EX1	S1A_EX2	S1A_EX3	S1A_EX4	S1A_EX5
Hydraulic Parameters					
Bed Slope (S_o)	0.0038	0.0038	0.0038	0.0038	0.0038
Flow Depth (H) (m)	0.118	0.143	0.093	0.143	0.143
Average Flow Velocity (U) (ms^{-1})	0.624	0.673	0.575	-	-
Flow Rate (Q) (ls^{-1})	22.1	28.9	16.0	-	-
Flow Reynolds No. (R_e)	2.95 E+05	3.85 E+05	2.14 E+05	-	-
Froude Number (F_r)	0.580	0.568	0.602	-	-
Bed Shear Velocity (u_*) (ms^{-1})	0.049	0.052	0.046	-	-
Bed Material Properties					
Type	Spheres	Spheres	Spheres	Spheres	Gravel
Bed Material D_{50} (m)	0.015	0.015	0.015	0.025	0.0173
Bed Material D_{84} (m)	-	-	-	-	0.0216
Standard Deviation (σ_g)	-	-	-	-	1.31
Bed Roughness (k_s) (m)	0.0248	0.0309	0.0177	-	-
Bed Porosity (λ)	0.26	0.26	0.26	0.26	0.42
Fine Sediment Properties					
Fine Sediment Type	LA Sand	LA Sand	LA Sand	LA Sand	LA Sand
Size Range (μm)	150-500	150-500	150-500	150-500	150-500
Particle Reynolds No. ($R_{*p} = u_*d/\nu$)	~ 8-33	~ 8-33	~ 8-33	~ 8-33	~ 8-33
Feed Rate from Hopper I_R (gs^{-1})	1.35	1.35	1.35	1.35	1.35
Initial Concentration (C_0) (mg/l)	61.1	46.7	84.4	-	-

Table 4.2 - Main experimental parameters for Series 1A. [Note: kinematic viscosity of water ν is assumed to be 1.0 10^{-6} m^2s^{-1} (i.e. at 20°C)].

4.3.3 Observed Behaviour of Sediment Particles

4.3.3.1 Particle Trajectories in Near-bed Flow Region

A selection of the recorded particle trajectories in the near-bed region of the flow are shown in Figure 4.3(a), (b) and (c) for the size fractions d_i = 427.5μm, 275μm and 181μm, respectively. Whilst these plotted trajectories were obtained under the experimental conditions for S1A_EX1, it was noted that similar particle trajectory characteristics were also observed for experiments S1A_EX2 and EX3.

The coarser grades of LA sand (i.e. d_i = 427.5 and 327.5μm) generally had steeper trajectories towards the bed than the finer grades. The average angle of trajectory for the 427.5μm particles ranged from about 8 to 12° to the mean flow direction, and between 7-10° for the 327.5μm particles. These angles of trajectory were generally found to reduce as the flow Reynolds number R_e increased. Very few particles from coarser size fractions were observed to have upward trajectories (i.e. away from the bed surface) suggesting that gravitational forces dominate the vertical motion of the larger particles. Steeper than average downward particle trajectories (up to ~30°) were also observed, especially in the vicinity of the bed surface, where magnitude of the longitudinal flow velocity is reduced.

For intermediate size fractions (i.e. d_i = 275μm and 231μm), the average angle of settling trajectory ranged from about 6 to 8°. Many particles were again observed to have steep than average trajectories (up to ~20°) in the vicinity of the bed surface. A larger number of particles were also observed to have trajectories approximately parallel to the mean flow direction or even upward away from the bed, suggesting that intermediate sized particles may be influenced to a greater extent by the turbulent fluctuations within the flow than coarser fractions.

The average particle trajectories of the finest LA sand size fraction (d_i = 181μm) generally ranged from about 4 to 7° to the normal flow direction, but again showed considerable variations between individual particle trajectories. A number of particles with initially downward trajectories were shown to gain upward trajectories prior to coming into contact with the bed surface, while others again had relatively steep downward trajectories (up to ~20°) towards the bed surface. This variation again suggests that flow turbulence significantly influences the near-bed particle trajectories for the finest LA sand fraction.

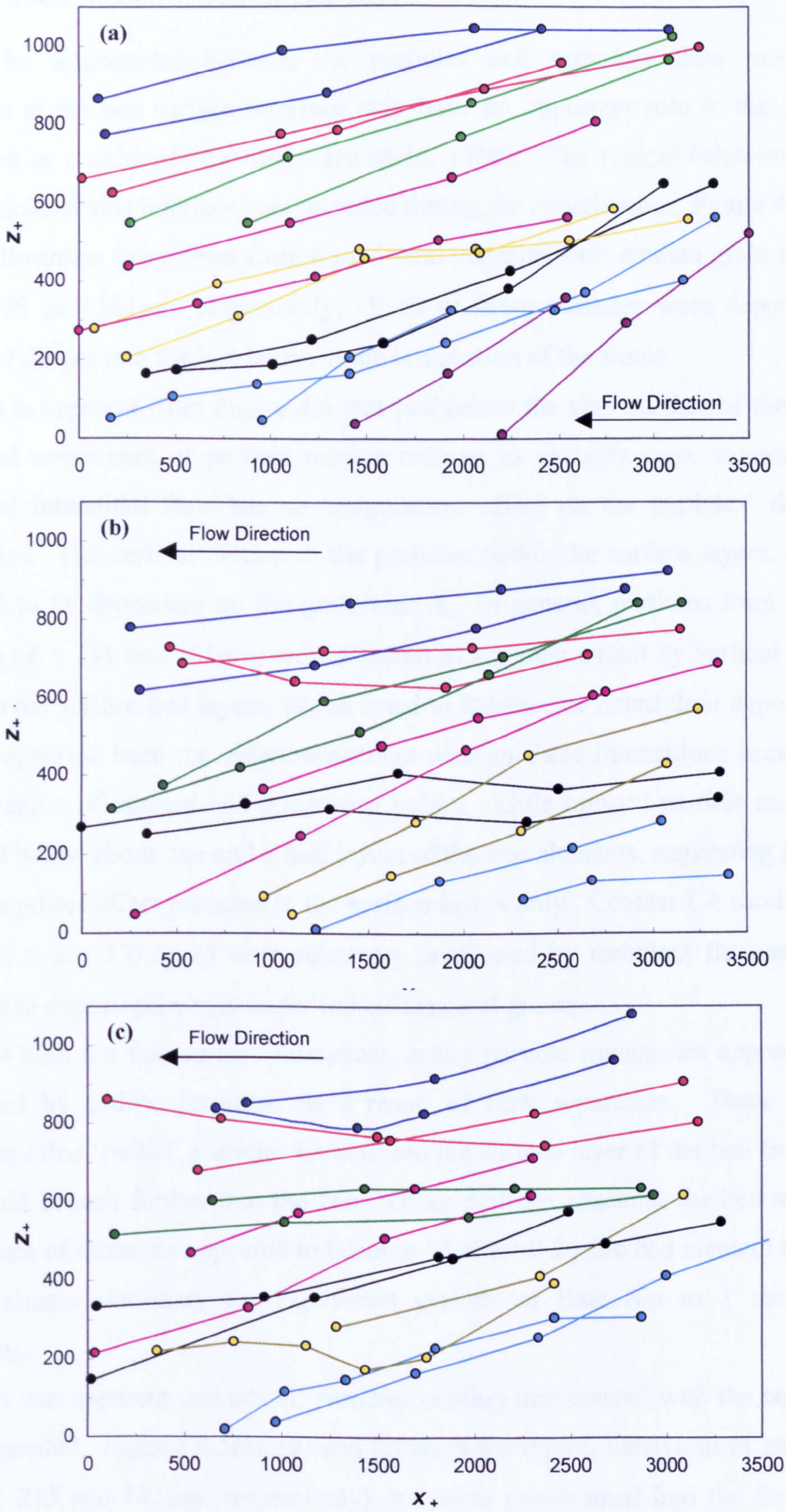

Figure 4.3 - Typical trajectories of LA sand particles in the near bed region of flow, S1A_EX1: (a) d_i = 427.5μm, (b) d_i = 275μm and (c) d_i = 181μm.

4.3.3.2 Particle Motion in Surface Bed Layers

The interactions between the particles and turbulent flow mechanisms generated at the bed surface interface may have an important role in the particles' deposition or continued suspension (Einstein, 1968). The typical behaviour of LA sand particles at this interface was recorded during the experiments. Figure 4.4(a), (b) and (c) illustrates trajectories from 6 or 7 sand particles with median grain sizes d_i = 427.5, 275 and 181μm, respectively. Each of these particles were deposited and infiltrated deeper into the bed layers in the test section of the flume.

It is apparent from Figure 4.4 that just below the very surface of the bed, the horizontal component of particle motion reduces to virtually zero, suggesting that horizontal interstitial flow has an insignificant effect on the particles' deposition trajectories. The vertical motion of the particles within the surface layers, however, appeared to be dependent on the grain size d_i. In general, particles from finer LA fractions (d_i = 231 and 181μm) were affected to a greater extent by vertical turbulent pulses in the surface bed layers, which acted to enhance or retard their deposition. It was not apparent from the video recordings whether these fluctuations occurred in a cyclic manner of upward and downward pulses. Little upward particle motion was observed below about one and a half layers of the bed elements, suggesting that these turbulent pulses affect particles in the surface layers only. Coarser LA sand fractions (d_i = 427.5 and 327.5μm) were relatively unaffected by turbulent fluctuations and appeared to deposit primarily under the influence of gravity.

Within the bed surface interstices, many particle trajectories appeared to be influenced by eddies generated as a result of flow separation. These turbulent structures often 'pulled' particles around into the surface layer of the bed from where they could deposit further into the bed. Other particles reaching the bed surface on the lee side of elements appeared to become 'sheltered' by the bed element and could remain almost stationary for significant periods of time (up to 1 sec.) before depositing.

It was apparent that not all particles coming into contact with the bed surface were deposited. Figures 4.5(a), (b) and (c) show the typical behaviour of particles (d_i = 427.5, 275 and 181μm, respectively) that were re-entrained into the flow having come into contact with the bed. In general, the video recordings indicated that fewer coarser grained particles were re-entrained than finer particles

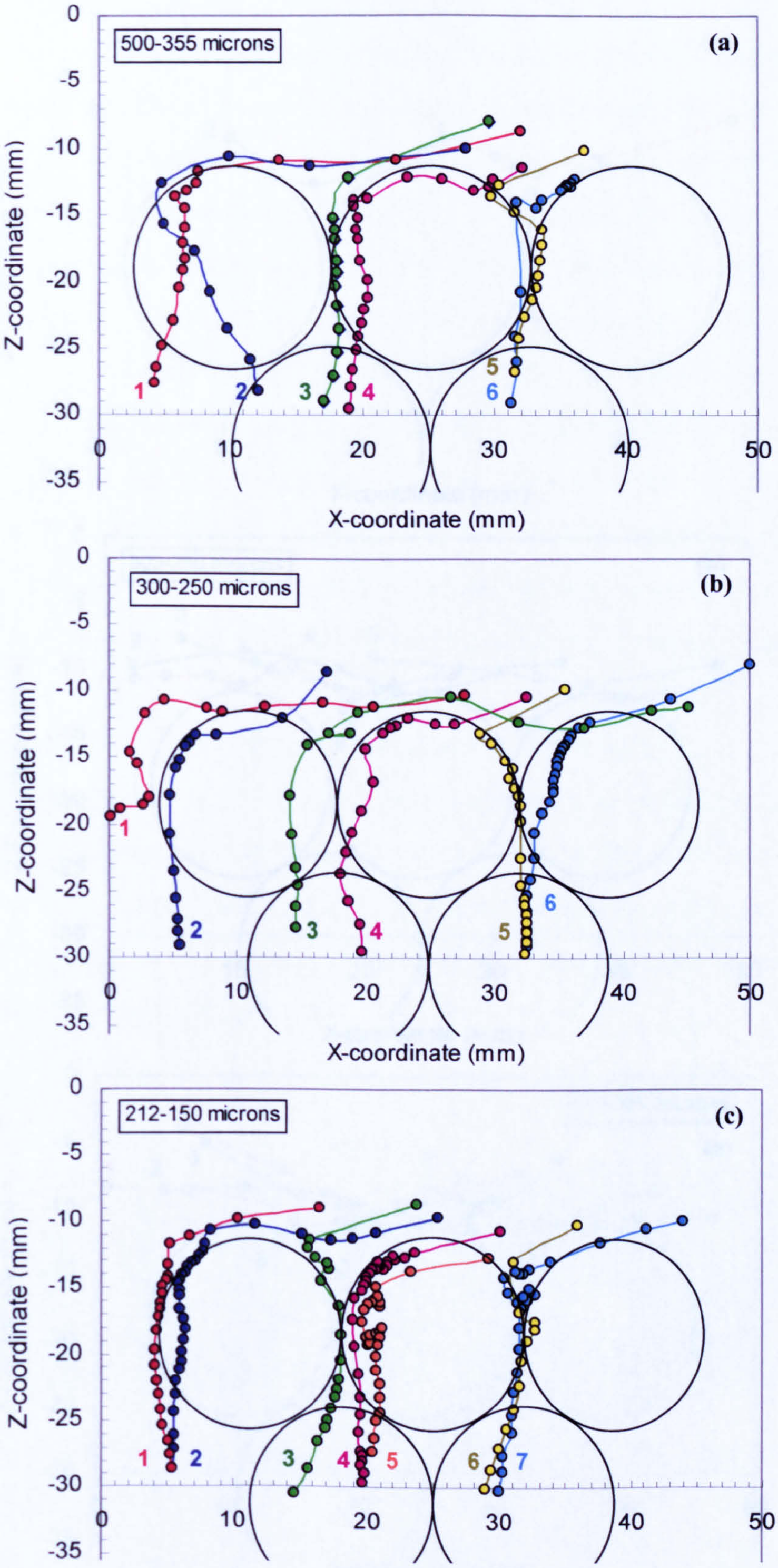

Figure 4.4 - Typical trajectories of depositing LA sand particles - S1A_EX1: (a) d_i = 427.5μm, (b) d_i = 275μm and (c) d_i = 181μm. (Note – Bed elements shown for illustrative purposes only.)

Figure 4.5 - Typical trajectories of re-suspended LA sand particles - S1A_EX1: (a) d_i = 427.5μm, (b) d_i = 275μm and (c) d_i = 181μm.(Note:- Bed elements shown for illustrative purposes only)

All particle classes appeared to exhibit similar modes of behaviour that resulted in their re-suspension back into the flow (Figure 4.5). A number of particles were observed to interact with the flow separation eddies generated in the bed surface interstices. This interaction, on occasion, resulted in the particle following an orbital path within the interstice before being ejected back into the flow. Other particles were also observed to collide with and deflect off the upstream faces of bed elements. As was previously stated, some particles appeared to be deflected from a downward trajectory into an upward trajectory without coming into contact with the bed. It is hypothesised that this apparent particle deflection may result from the expansion and release of flow separation eddies from the bed surface interstices into the main flow body, analogous to the ejection mechanism proposed by Kirkbride (1993). Finally, upward vertical turbulent pulses within the bed were observed, on occasion, to re-entrain finer particles sizes from within the surface layer of the bed back into the flow.

Influence of Bed Configuration on Deposition Characteristics

Experiments S1A_EX4 and 5 were carried out to determine the influence of bed configuration on particle behaviour at the bed surface interface and within the surface layers. Figure 4.6(a) and (b) schematically illustrates the observed modes of particle behaviour at the surface of the bed of 25mm uniform spheres and natural gravel (D_{50} = 17.3mm), respectively.

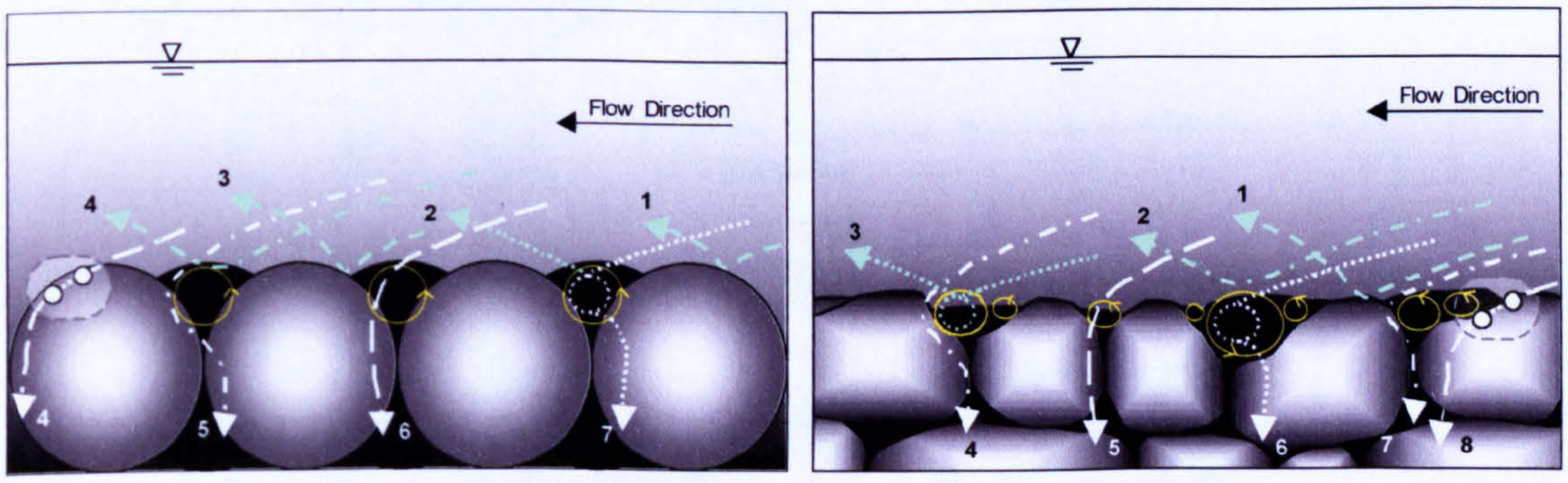

Figure 4.6 – Typical modes of particle behaviour at the bed surface of (a) 25mm uniform spheres and (b) natural gravel (D_{50} = 17.3mm).

These typical modes of particle behaviour were generally similar to those described at the bed of 15mm uniform spheres. In summary, three main modes of re-entrainment were observed: (i) ricochet with the upstream face of a bed element; (ii) entrapment and ejection from flow separation eddy forming in surface interstice; and

(iii) apparent deflection off expanding eddy. Similarly, consistent modes of particle deposition were also observed: (i) deposition path partially influenced by flow separation eddy; (ii) depositing particle sheltered in lee of bed element before depositing under gravity; (iii) entrapment and release from surface eddy; and (iv) deposition under gravity with little or no bed surface interaction (coarser particles). Particle behaviour at the surface of the gravel bed was shown to be dependent on local configuration of bed elements; with larger flow separation eddies forming in the lee of protruding bed elements.

4.3.3.3 Assessment of Deposition Probability

An approximation of the probability of deposition p was made for individual LA sand fractions from the video recordings of experiments S1A_EX1 to EX3. The trajectories of all particles approaching the bed surface within the view field of the camera were observed over a period of time (generally 30-60secs.) and their fate (deposited or re-entrained) noted. The estimate of the deposition probability p was then obtained from the ratio of deposited particles to the total number of particles observed.

Figure 4.7 below plots the deposition probability p against representative grain size for each fraction d_i. The three data sets show a consistent trend of increasing values of p with increasing grain size d_i, although values appear to stabilise for the coarser fractions (d_i = 427.5 and 327.5μm).

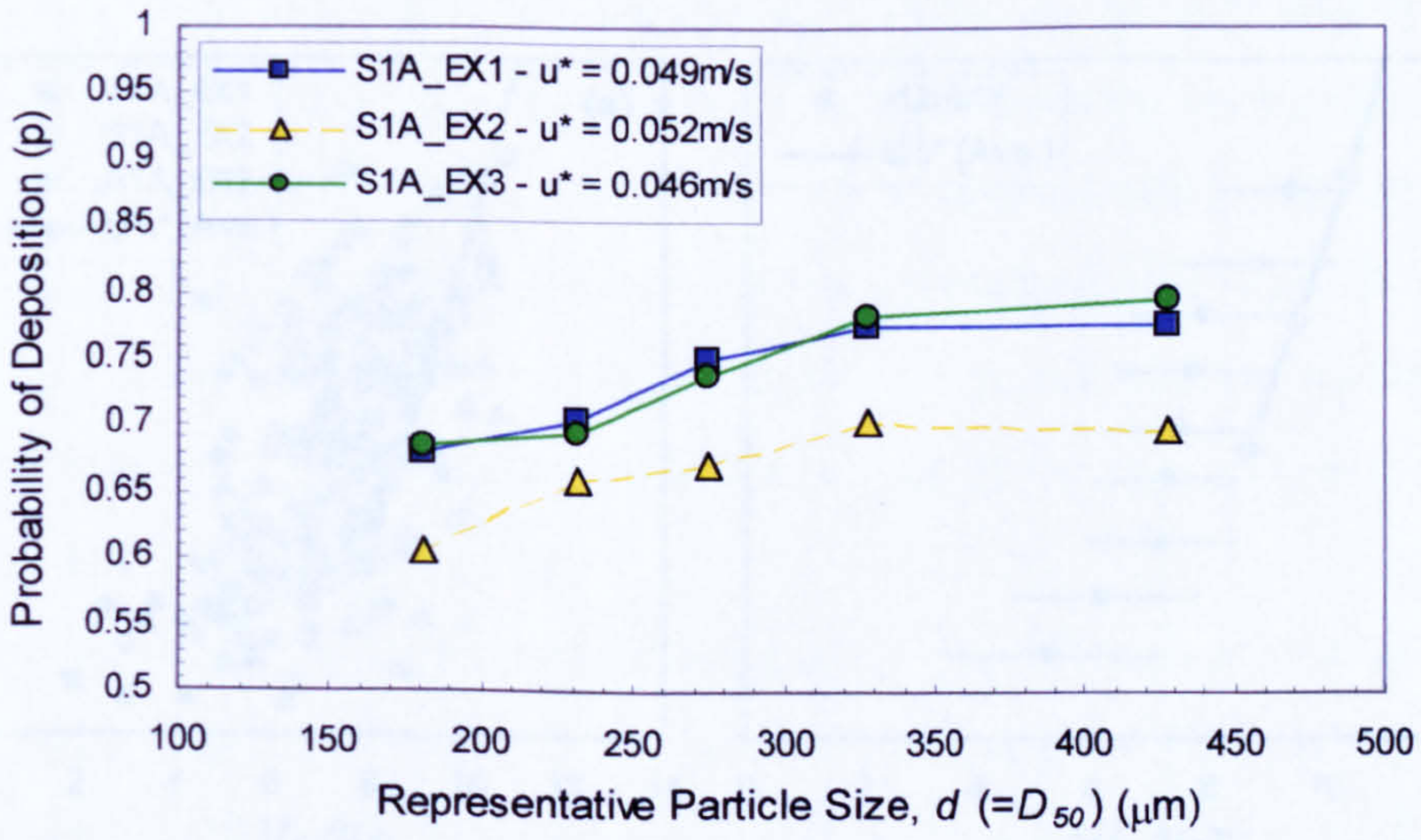

Figure 4.7 - Variation of estimated probability of deposition p for LA sand fractions plotted against representative grain size d_i for experiments S1A_EX1-3.

For the limited experimental conditions considered, p varied from 0.6-0.68 for the finest size fraction (d_i = 181μm) up to 0.7-0.8 for the coarsest fraction (d_i = 427.5μm). This generally agrees with qualitative observations that fewer coarse grained particles are re-entrained after initial contact with the bed surface than finer particles. No definitive trends are observed with regards to the influence of the hydraulic conditions, but the lowest p values were consistently obtained for the experiment with highest u_*, H and U values (i.e. S1A_EX2).

4.3.4 Measurement of Particle Velocities

4.3.4.1 Streamwise Component of Near-bed Particle Velocity

Non-dimensional streamwise components of particle velocity (u_s/u_*) were calculated from the recorded trajectories of individual sediment particles in the near-bed flow region. The values obtained for three LA fractions (d_i = 427.5, 275 and 181μm) are plotted in Figure 4.8(a) against elevation from the bed surface, expressed in terms of wall units z_+ (= u_*H/ν). The average vertical position of each recorded particle trajectory was calculated from the equation (Sumer and Deigaard, 1981),

$$\bar{z}_+ = \frac{1}{2}\left(z_{+,or} + z_{+,t}\right) \qquad \text{....(4.6)}$$

where $z_{+,or}$ and $z_{+,t}$ are the vertical positions of the particle at the origin and termination of the observed trajectory. The experiment-averaged flow velocity profile (U/u_*), obtained by a mini-propeller, is also shown for comparison.

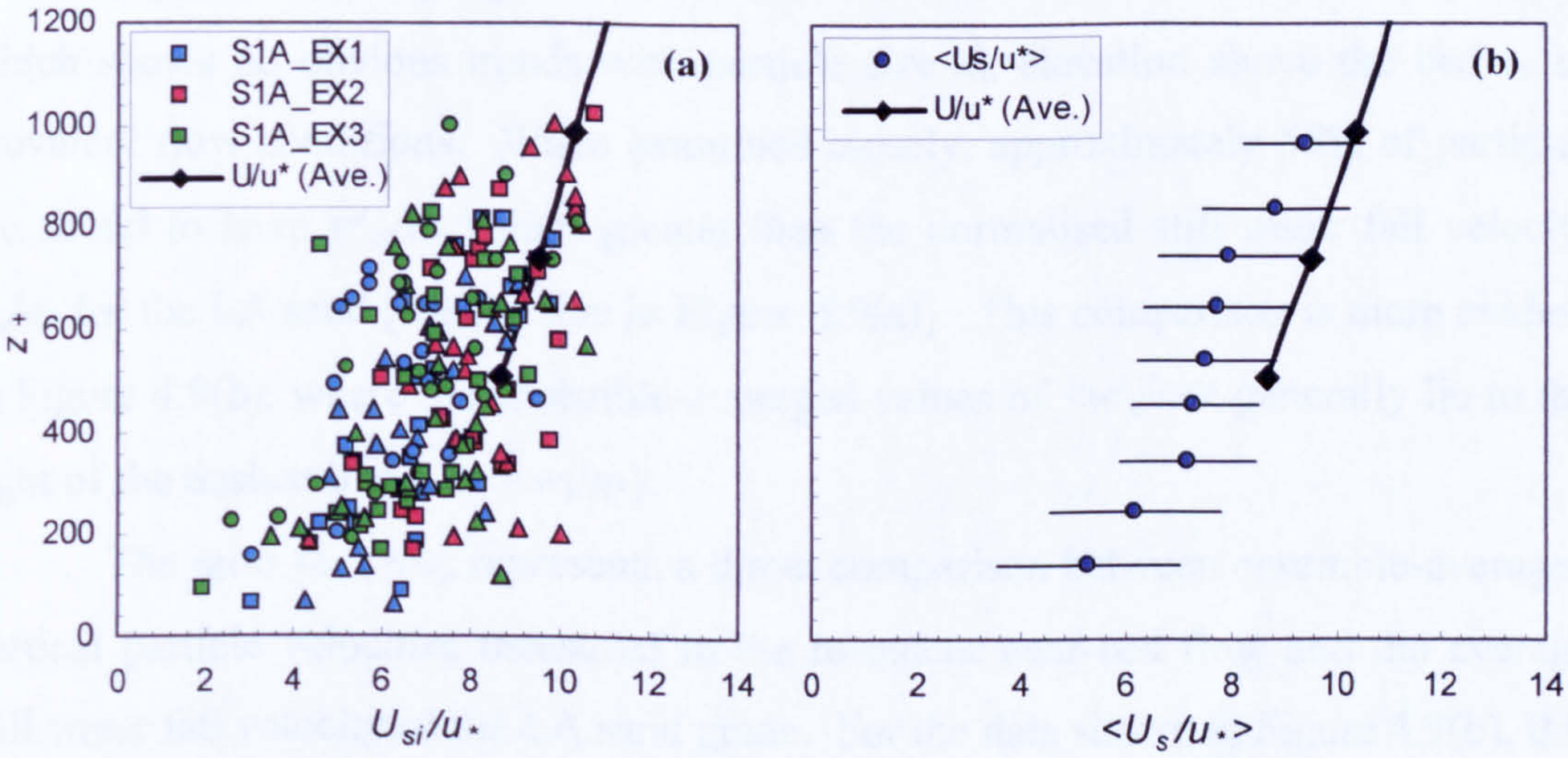

Figure 4.8 - Non-dimensional streamwise particle velocities u_s/u_* plotted against z_+ for: (a) individual size fractions [□ d_i = 427.5μm Δ d_i = 275μm O d_i = 181μm] (b) ensemble-averaged values (error bars represent ± 1 standard deviation for each data point).

The streamwise particle velocity data is shown in Figure 4.8(a) to be well scattered with no clear trend existing between the magnitude of u_{si}/u_* and particle size d_i. The plot does suggest that particle velocities tend to be lower than the measured flow velocity in the surrounding fluid (i.e. $u_{si}/u_* < U/u_*$), although this comparison is limited to the flow region above $z_+ \sim 500$ due to the mini-propeller configuration.

The experiment- and fraction-averaged streamwise particle velocities $<u_s/u_*>$ and corresponding standard deviations were computed from the individual particle data shown in Figure 4.8(a). To facilitate this, the near-bed flow was divided into a series of intervals of height $\Delta z_+ = 100$. An average $<u_s/u_*>$ value was obtained for the particles contained within each interval, in a similar manner to previous studies (e.g. Sumer and Oğuz 1971; Nino and Garcia 1996), and plotted against z_+ in Figure 4.8(b). In the flow region in which comparison could be made ($z_+ > 500$), $<u_s/u_*>$ values were on average 14% lower than surrounding fluid velocities, probably resulting from a combination of particle inertia effects and measurement errors.

4.3.4.2 Vertical Component of Near-bed Particle Velocity

The non-dimensional vertical particle velocity w'_s/u_* is plotted against z_+ in Figure 4.9 for: (a) individual LA sand fractions ($d_i = 427.5$, 275 and 181μm); and (b) the experiment- and fraction-averaged values $<w'_s/u_*>$. It is noted that while particles with upward trajectories (i.e. $w'_s/u_* < 0$) are not shown in Figure 4.9(a), they are included in the ensemble-average computations for Figure 4.9(b).

Figure 4.9(a) highlights the considerable scatter in the raw data for w'_{si}/u_*, which shows no obvious trends with particle size d_i, elevation above the bed z_+ or prevalent flow conditions. When examined closely, approximately 65% of particles are found to have w'_{si}/u_* values greater than the normalised still water fall velocity w_s/u_* for the LA sand [dashed line in Figure 4.9(a)]. This comparison is more evident in Figure 4.9(b), where the ensemble-averaged values of $<w'_s/u_*>$ generally lie to the right of the dashed line (i.e. $> w_s/u_*$).

The ratio $<w'_s>/w_s$ represents a direct comparison between ensemble-averaged vertical particle velocities measured in the turbulent near-bed flow and the average still water fall velocity of the LA sand grade. For the data shown in Figure 4.9(b), this ratio can be calculated to range from 0.89 to 1.67 in the flow region considered.

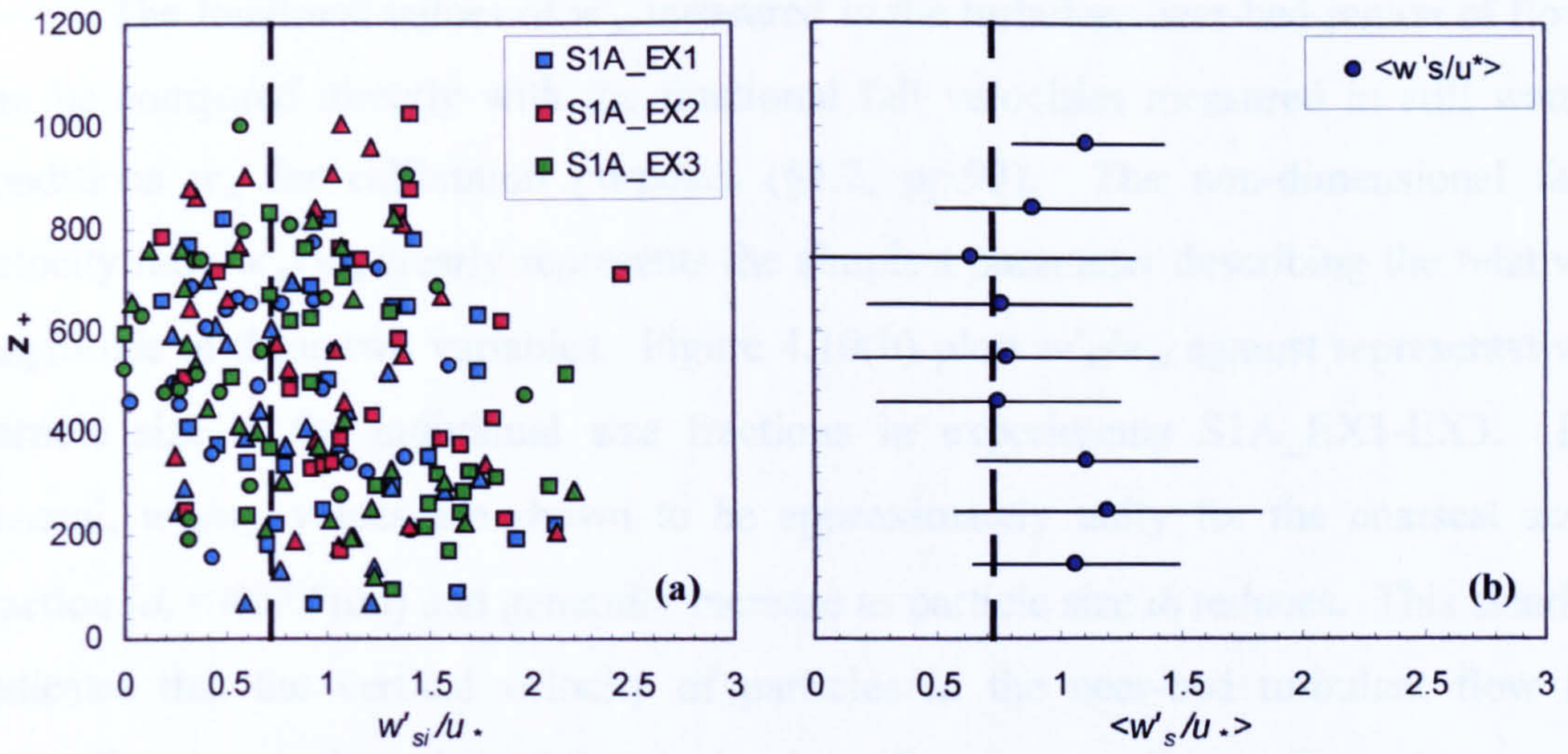

Figure 4.9 - Non-dimensional vertical particle velocities w'_s/u_* plotted against z_+ for: (a) individual LA fractions [□ d_i = 427.5μm Δ d_i = 275μm O 181μm] and (b) ensemble-averaged values (error bars shown represent ± 1 standard deviation). Note: dashed lines represent the normalised average still water fall velocity w_s/u_* for LA sand.

Variations in measured vertical particle velocities w'_{si} between the individual LA size fractions are assessed in greater detail. Average values of w'_{si} are shown in Figure 4.10(a) to increase consistently with increases in the particle Reynolds number R_{e*p} (= $u_*.d_i/\nu$). A power equation trendline of the form $y = ax^b$ is fitted to this data and is shown to have reasonable correlation ($R^2 = 0.77$).

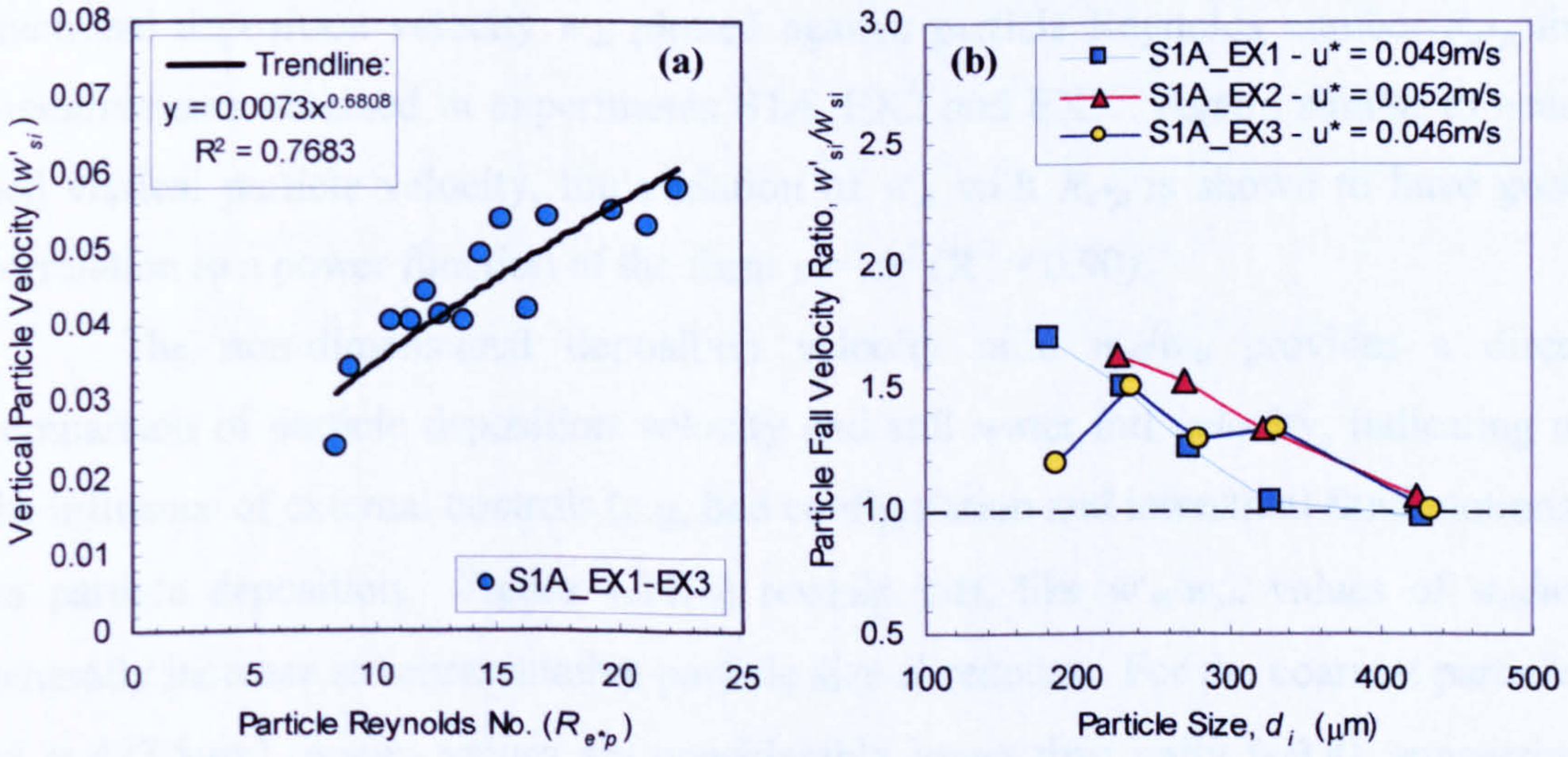

Figure 4.10 - (a) Vertical particle velocity w'_{si} plotted against particle Reynolds number R_{e*p} for individual LA grade fractions in experiments S1A_EX1-EX3. (b) Variation of non-dimensional fall velocity ratio w'_{si}/w_{si} with representative particle size d_i.

The fractional values of w'_{si} measured in the turbulent near-bed region of flow can be compared directly with the fractional fall velocities measured in still water conditions w_{si} for calibration purposes (§4.2, pp.93). The non-dimensional fall velocity ratio w'_{si}/w_{si} clearly represents the simplest parameter describing the relative magnitude of these two variables. Figure 4.10(b) plots w'_{si}/w_{si} against representative particle size d_i for individual size fractions in experiments S1A_EX1-EX3. In general, w'_{si}/w_{si} values are shown to be approximately unity for the coarsest size fraction (d_i = 427.5μm) and generally increase as particle size d_i reduces. This clearly indicates that the vertical velocity of particles in the near-bed turbulent flow is generally greater than their fall velocity in still water conditions (i.e. $w'_{si} > w_{si}$). Values of w'_{si}/w_{si} can approach 1.7 for finer fractions (d_i = 231 and 181μm), indicating that w'_{si} values were up to 70% higher than still water fall velocities for the experimental conditions considered.

4.3.4.3 Deposition Velocity of Particles within Bed Surface Layers

Deposition velocities w_{di} were calculated for each individual particle trajectory observed to deposit from the bed surface interface, down through the recorded surface bed layers and out of the camera view field. Typical trajectory paths for these particles were previously shown in Figure 4.4 (pp.104). Figure 4.11(a) shows the fractional deposition velocity w_{di} plotted against particle Reynolds number R_{e*p} for measurements obtained in experiments S1A_EX2 and EX3. Again, similar to near-bed vertical particle velocity, the variation of w_{di} with R_{e*p} is shown to have good correlation to a power function of the form $y = ax^b$ ($R^2 = 0.90$).

The non-dimensional deposition velocity ratio w_{di}/w_{si} provides a direct comparison of particle deposition velocity and still water fall velocity, indicating of the influence of external controls (e.g. bed configuration and interstitial fluid motions) on particle deposition. Figure 4.11(b) reveals that, like w'_{si}/w_{si}, values of w_{di}/w_{si} generally increase as representative particle size d_i reduces. For the coarsest particles (d_i = 427.5μm), w_{di}/w_{si} values are considerably lower than unity (~0.8), suggesting that their deposition is hindered in comparison to their fall velocity in still water. By contrast, w_{di}/w_{si} values for the finest particles (d_i = 181μm) are greater than unity (~1.2), indicating enhanced deposition in comparison to the still water fall velocity.

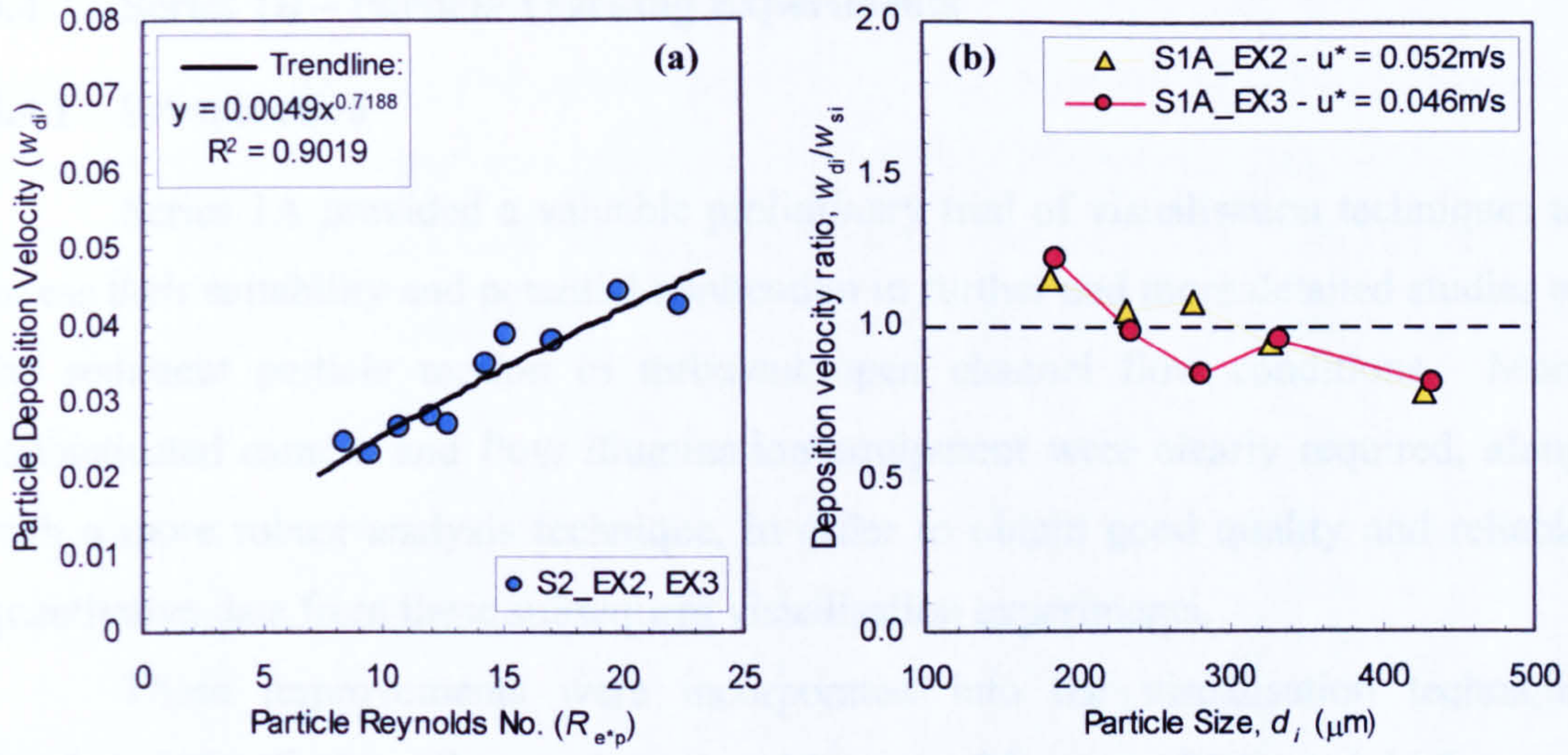

Figure 4.11 - (a) Deposition velocity w_{di} plotted against particle Reynolds number R_{e*p} for LA sand fractions and experiments S1A_EX2 and 3. (b) Variation of non-dimensional deposition velocity ratio w_{di}/w_{si} with representative particle size d_i.

4.3.5 Summary

The preliminary visualisation experiments conducted in Series 1A have served to highlight the typical motion of LA sand particles within the near-bed flow region; their interactions at the bed surface interface; and their eventual deposition through the surface bed layers. Initial quantitative measurements in the turbulent near-bed flow have revealed that streamwise velocity of particles (u_s) may be lower than that of the surrounding fluid (U), while vertical particle velocities (w'_{si}) can show significant departure from their measured fall velocity in still water conditions (w_s). Deposition velocities (w_d) within the surface bed layers also reveal a particle-size-dependent deviation from still water fall velocities (w_s). Many of these aspects are considered in greater detail in the following section (§4.4) and within subsequent chapters.

4.4 Series 1B – Particle Tracking Experiments

4.4.1 Introduction

Series 1A provided a valuable preliminary trial of visualisation techniques to assess their suitability and potential application in further and more detailed studies of the sediment particle motion in turbulent open channel flow conditions. More sophisticated camera and flow illumination equipment were clearly required, along with a more robust analysis technique, in order to obtain good quality and reliable quantitative data from these subsequent visualisation experiments.

These improvements were incorporated into the visualisation technique developed for Series 1B experiments. Most notably, a sophisticated high-speed camera, the Kodak™ MotionCorder Analyser, was used to acquire images of particle motions at a frame rate of 240fps within an illuminated sheet of flow at the centreline of the Armfield S5-10 flume (i.e. y/B =0.5). These acquired images were transferred to a PC and analysed using image analysis software and particle tracking techniques. A detailed description of the visualisation equipment and techniques employed in Series 1B is given in §3.4.3.2 (pp.69), while a schematic diagram of the experimental set-up is given in Figure 3.11 (pp.71).

4.4.2 Experimental Conditions and Procedures

All Series1B experiments were conducted under steady, uniform flow conditions set up using the procedure detailed in Appendix 3.2. As for Series 1A, the experiments tested Loch Aline (LA) sand, which was sieved into six individual size fractions (d_i = 462.5, 390, 327.5, 275, 231 and 181μm). Note: coarsest size fraction tested in Series 1A (d_i = 427.5μm) was split into two separate fractions for Series 1B.

The bed slope of the Armfield flume bed was set constant at 0.004 (1:250) using the method outlined in §3.4.3.4 (pp.79). The flume bed and trap configuration at the test section was the same as in Series 1A (§3.4.1.2, pp.60).

A total of five separate particle-tracking experiments (i.e. S1B_EX1–EX5) were carried out in Series 1B. Two flow depths were used (H = 0.143m and 0.093m); and two bed configurations were tested, initially rhombically-packed uniform spheres (D = 15mm), then replaced in the final two experiments by natural gravel (D_{50} = 17.3mm, σ_g = 1.31). The experimental conditions used in Series 1B resulted in sub-critical Froude numbers F_R ranging from 0.36 to 0.60, while corresponding flow

Reynolds numbers R_e ranged from about $1.37\ 10^5$ to $4.22\ 10^5$. The input rate of the each sediment fraction remained constant for the duration of each experiment, although slight variations were observed between the different size classes (I_R = 1.32-2.07g/s). The initial sediment concentrations within the flow were relatively low ($C_0 = I_R/Q$, generally less than 200mg.ℓ^{-1}). The main experimental parameters for Series 1B are summarised in Table 4.3 below.

Experiment Number	S1B_EX1	S1B_EX2	S1B_EX3	S1B_EX4	S1B_EX5
Hydraulic Parameters					
Bed Slope, S_0	0.004	0.004	0.004	0.004	0.004
Discharge, Q (m^3s^{-1})	0.029	0.016	0.029	0.022	0.010
Depth, H (m)	0.143	0.093	0.143	0.143	0.093
Shear Velocity, u_* (ms^{-1})	0.047	0.038	0.047	0.050	0.040
Ave. Velocity, U (ms^{-1})	0.68	0.57	0.68	0.50	0.34
Froude Number, F_r	0.576	0.598	0.576	0.425	0.357
Kinematic Viscosity, ν	9.22E-07	9.22E-07	9.22E-07	9.22E-07	9.22E-07
Reynolds Number, R_e	4.21E+05	2.30E+05	4.21E+05	3.10E+05	1.37E+05
Bed Material Properties					
Type	Spheres	Spheres	Spheres	Gravel	Gravel
D_{50} (mm)	15.0	15.0	15.0	17.3	17.3
D_{84} (mm)	-	-	-	21.6	21.6
Standard Deviation, σ_g	-	-	-	1.31	1.31
Bed Surface Porosity, λ	0.26	0.26	0.26	0.42	0.42
Fine Sediment Properties					
Type	LA Sand	LA Sand	LA Sand	LA Sand	LA Sand
Size Range (μm)	500-150	500-150	500-150	500-150	500-150
Particle Reynolds No, R_{e_p}	~ 8-25	~ 6-21	~ 8-25	~ 8-27	~ 7-22
Input Rate, I_R (gs^{-1})	1.32-2.07	1.32-2.07	1.32-2.07	1.32-2.07	1.32-2.07
Initial Concentration, C_0 (mg.l^{-1})	45-71	83-130	45-71	60-94	132-207

Shear velocity, u_*, calculated from mean velocity distribution (Clauser 1956) (§4.3.4.2), average flow velocity, U, obtained from integration of measured velocity profiles (or at z/H = 0.396). Froude number, $F_r = U/(gH)^{0.5}$, Reynolds number, $R_e = 4UH/\nu$, kinematic viscosity of fluid, ν, calculated for average measured flow temperature of 24°C, particle Reynolds number, $R_{e_p} = u_* d_i/\nu$, where d_i is the representative size of each size fraction of fine sediments ($d_i = d_{i,50}$).

Table 4.3 - Main experimental parameters for Series 1B.

Experiments were sub-divided to consider the behaviour of individual LA size fractions, which were fed into the open channel flow, in turn, at the free surface from the calibrated sediment hopper (§3.4.3.4, pp.78). Images of particle motion were acquired by the high-speed camera at various z/H elevations within the illuminated flow region, as detailed in Table 4.4 overleaf.

The majority of the recorded images of particle motion were acquired within the open channel flow directly above the test section of the flume incorporating the sediment trap. In order to assess whether the porous bed configuration at this location has a specific influence on the motion of particles, especially within the near-bed flow, images acquired during S1B_EX3 were obtained 1m downstream of test section,

where the bed comprised of a single layer of bed material supported on an impermeable polystyrene layer.

	z/H - POS. 1	*z/H* - POS. 2	*z/H* - POS. 3
S1B_EX1	0.0 – 0.17	0.14 – 0.46	0.42 – 0.79
S1B_EX2	0.0 – 0.50	0.43 – 0.94	n/a
S1B_EX3	0.0 – 0.30	0.27 – 0.63	0.57 – 0.92
S1B_EX4	0.0 – 0.25	0.20 – 0.45	0.45 – 0.72
S1B_EX5	0.0 – 0.43	0.37 – 0.81	n/a

Table 4.4 - Relative vertical positions (*z/H* range) of high-speed camera view field for recording particle motion in flow.

4.4.3 Measurement of Flow Velocity and Turbulence Characteristics

The Sontek™ 3-D vertically orientated ADV probe (§3.4.3.4, pp.76) was used to measure mean and fluctuating flow characteristics at five lateral positions within the test section (y/B = 0.17, 0.33, 0.50, 0.67 and 0.83). Measurements were generally taken for each flow condition prior to the release of sediments and acquisition of images. Figure 4.12 below shows the ADV probe operating in the near-wall flow region of the Armfield flume.

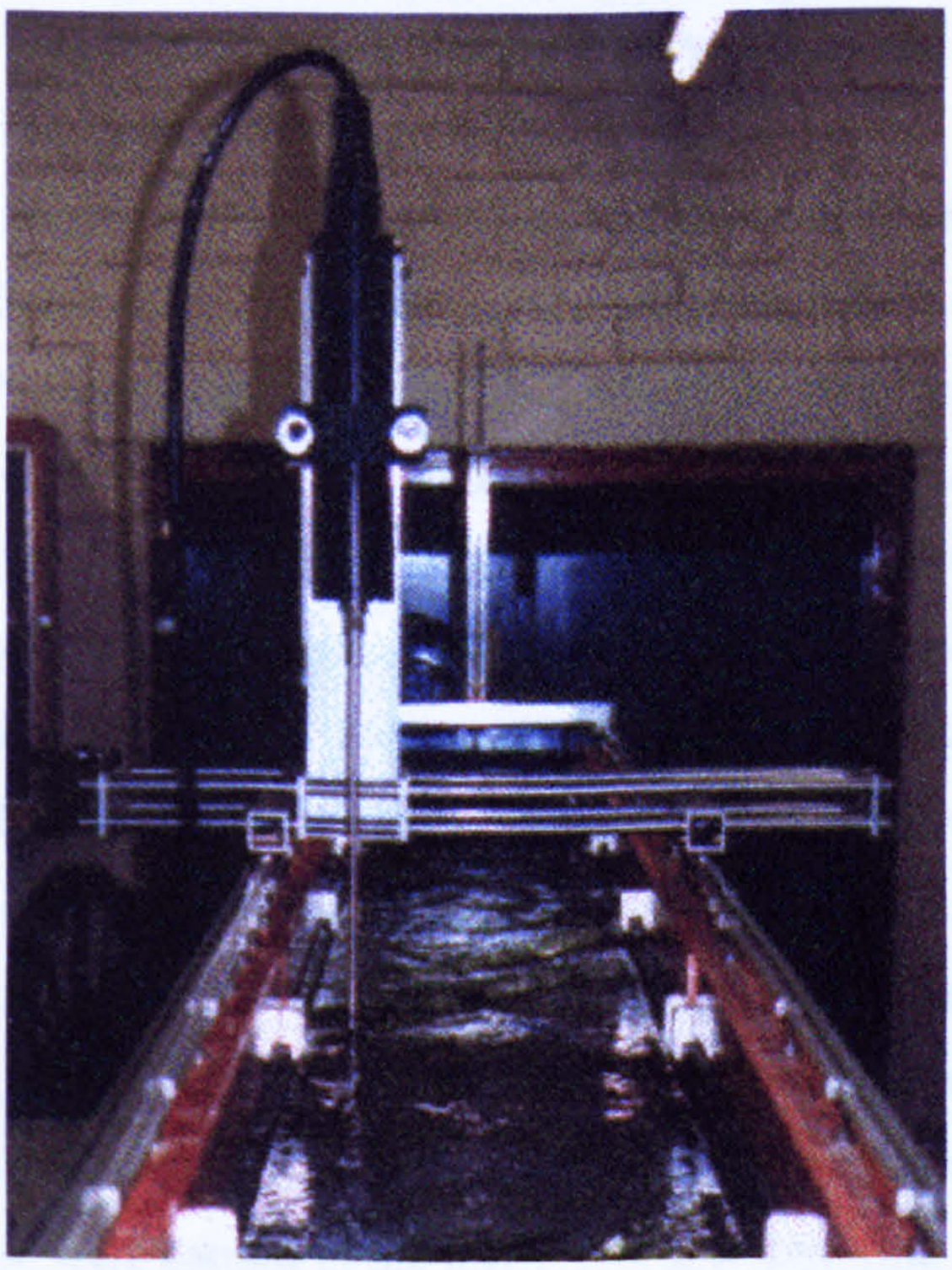

Figure 4.12 - ADV probe measurements being taken in Armfield S5-10 flume

The configuration of the vertically orientated ADV probe, limited the vertical extent in which velocity measurements could be obtained to the flow region $z/H \leq 0.55$ for experiments S1B_EX1, 3 and 4 ($H = 143$mm) and $z/H = 0.35$ for experiments S1B_EX2 and 4 ($H = 93$mm). In some experiments, additional measurements were taken with a calibrated mini-propeller to provide longitudinal flow velocity profiles over a greater depth range. In flow regions where comparison was possible, the agreement between the ADV and mini-propeller measurements was good, especially at the centreline of the flume ($y/B = 0.5$). The relative difference between the two methods was estimated at a number of vertical positions within each profile, resulting in an average variation of only 3.9 % for S1B_EX1 and 6.3 % for S1B_EX2 (Appendix 4.1).

The raw data obtained by the ADV probe was processed by the supporting software package WinADV. This package also automatically calculated statistical turbulence parameters such as longitudinal and vertical turbulent intensities (i.e. u'_{rms} and w'_{rms}) and the covariance between longitudinal and vertical velocity fluctuations ($\overline{u'w'}$). Additional adjustments were made to the ADV measurements obtained over the gravel bed (i.e. S1B_EX4 and EX5) to account for local variations in the bed surface elevation. This method and the longitudinal velocity profiles for experiments S1B_EX4 and EX5 are presented in Appendix 4.2.

Figure 4.13 shows example plots of longitudinal velocity profiles measured by the ADV and mini-propeller. The near-surface mini-propeller measurements reveal the presence of a 'velocity dip' characteristic, where the maximum velocity occurs some distance below the free surface. This phenomenon is common in rectangular channels with low flow aspect ratios [i.e. $\alpha < 5$, Nezu and Rodi (1985)] and results from the influence of the flume walls. In Series 1B, the flow aspect ratios α were 2.1 and 3.2 for the flow depths H of 143mm and 93mm, respectively. Mini-propeller profiles taken at different lateral positions across the flow suggest that the 'velocity dip' tends to increase as the flume walls are approached (Appendix 4.1).

In order to assess what influence the flume walls have on the three-dimensional nature of these low aspect ratio flows, detailed ADV measurements were taken across the flume width ($y/B = 0.15 - 0.85$) at lateral intervals of about 10mm. These measurements were carried in the lower half of a flow with depth 143mm ($\alpha = 2.1$), over a bed of rhombically packed uniform spheres. The resulting time-averaged

flow velocity field in the YZ plane is shown in Figure 4.14. This reveals the presence of secondary fluid motions, most notably a vortex cell in the left-hand side of the flow field. Analysis of individual lateral and vertical flow velocities (v and w) revealed their average magnitudes are ~2.0 and ~1.6% of the streamwise flow velocity U, respectively. In relation to the section-averaged streamwise flow velocity $\overline{U}$ (= 0.68ms^{-1}), the averaged lateral and vertical velocities ($\overline{v}$ and $\overline{w}$) are 0.014 and 0.011ms^{-1}, respectively.

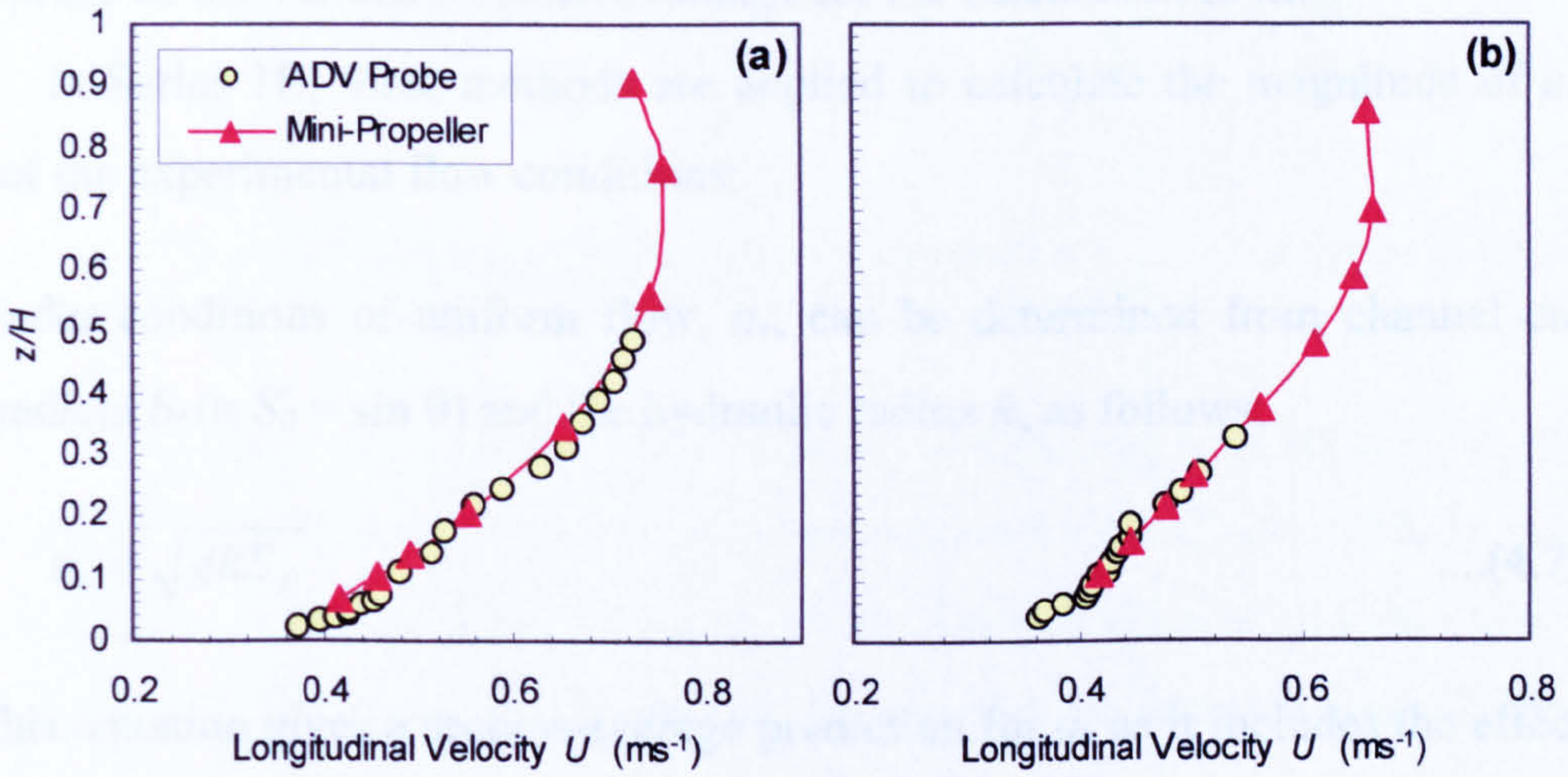

Figure 4.13 - Plots of U against z/H, obtained from ADV and mini-propeller measurements at $y/B = 0.5$ (i.e. centreline) for experiments: (a) S1B_EX1 and; (b) S1B_EX2.

In the illuminated flow region where particle motions were recorded (y/B = 0.5), the vertical fluid velocities shown in Figure 4.14 generally appear to be relatively small and positive (upward) in direction. It would therefore be anticipated that their influence on vertical particle motion would be to inhibit their fall velocity in the turbulent flow, although the extent of this influence may be negligible.

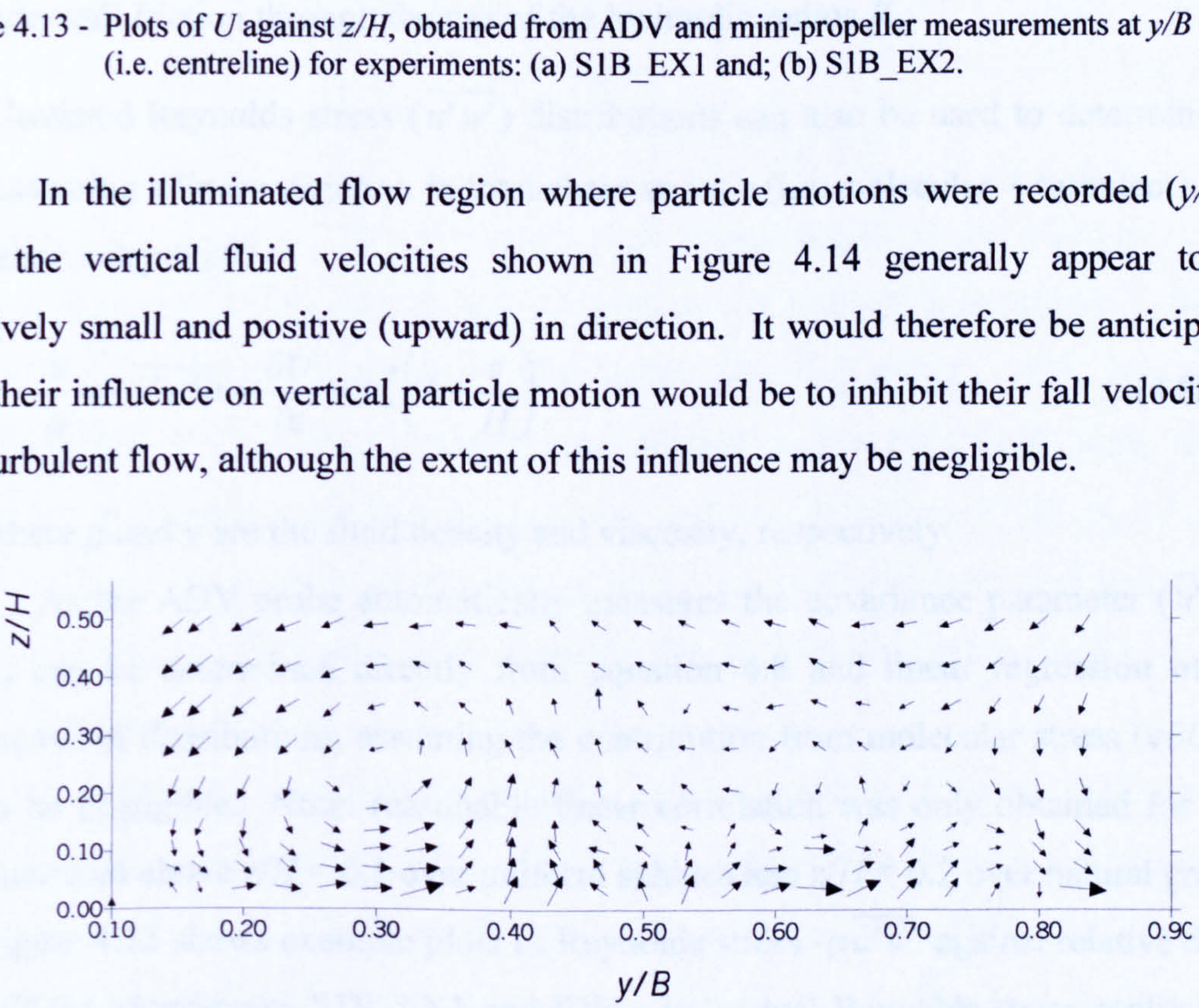

Figure 4.14 - Flow velocity field in the YZ plane produced from detailed ADV measurements, illustrating three-dimensionality of flow in Armfield S5-10 flume.

4.4.3.1 Calculation of Bed Shear Velocity

The accurate prediction of the bed shear (or friction) velocity (u_*) is important in the study of turbulence in open-channel flow as it is the most fundamental velocity scale used to normalise mean velocities and turbulence parameters (Nezu and Nakagawa 1993). Muste and Patel (1997) stated that u_* is the parameter most likely to be subjected to errors from both experimental methods and data analysis when used in the analysis of velocity profiles. It is therefore important to consider the most appropriate of the various methods available for the calculation of u_*.

In Series 1B, three methods are applied to calculate the magnitude of u_* for each of the experimental flow conditions:

1. Under conditions of uniform flow, u_*, can be determined from channel energy gradient $S_f (\cong S_0 = \sin\theta)$ and the hydraulic radius R, as follows:

$$u_* = \sqrt{gRS_f} \qquad \text{....(4.7)}$$

This equation gives a section-average prediction for u_* as it includes the effects of side-wall friction through the use of the hydraulic radius R.

2. Measured Reynolds stress ($\overline{u'w'}$) distributions can also be used to determine u_*. Assuming a linear variation in total shear stress τ (i.e. molecular + turbulent) with relative depth z/H,

$$\frac{\tau}{\rho} = -\overline{u'w'} + \nu\frac{\partial U}{\partial z} = u_*^2\left(1 - \frac{z}{H}\right) \qquad \text{....(4.8)}$$

where ρ and ν are the fluid density and viscosity, respectively.

As the ADV probe automatically measures the covariance parameter ($\overline{u'w'}$), u_* can be determined directly from equation 4.8 and linear regression of the measured distributions, assuming the contribution from molecular stress ($\nu\partial U/\partial z$) to be negligible. Note: reasonable linear correlation was only obtained for data measured above $z/H = 0.1$ over uniform spheres and $z/H = 0.2$ over natural gravel. Figure 4.15 shows example plots of Reynolds stress $-\rho\overline{u'w'}$ against relative depth z/H for experiments S1B_EX1 and EX4. Individual Reynolds stress profiles for each of the Series 1B experiments are presented in Appendix 4.3.

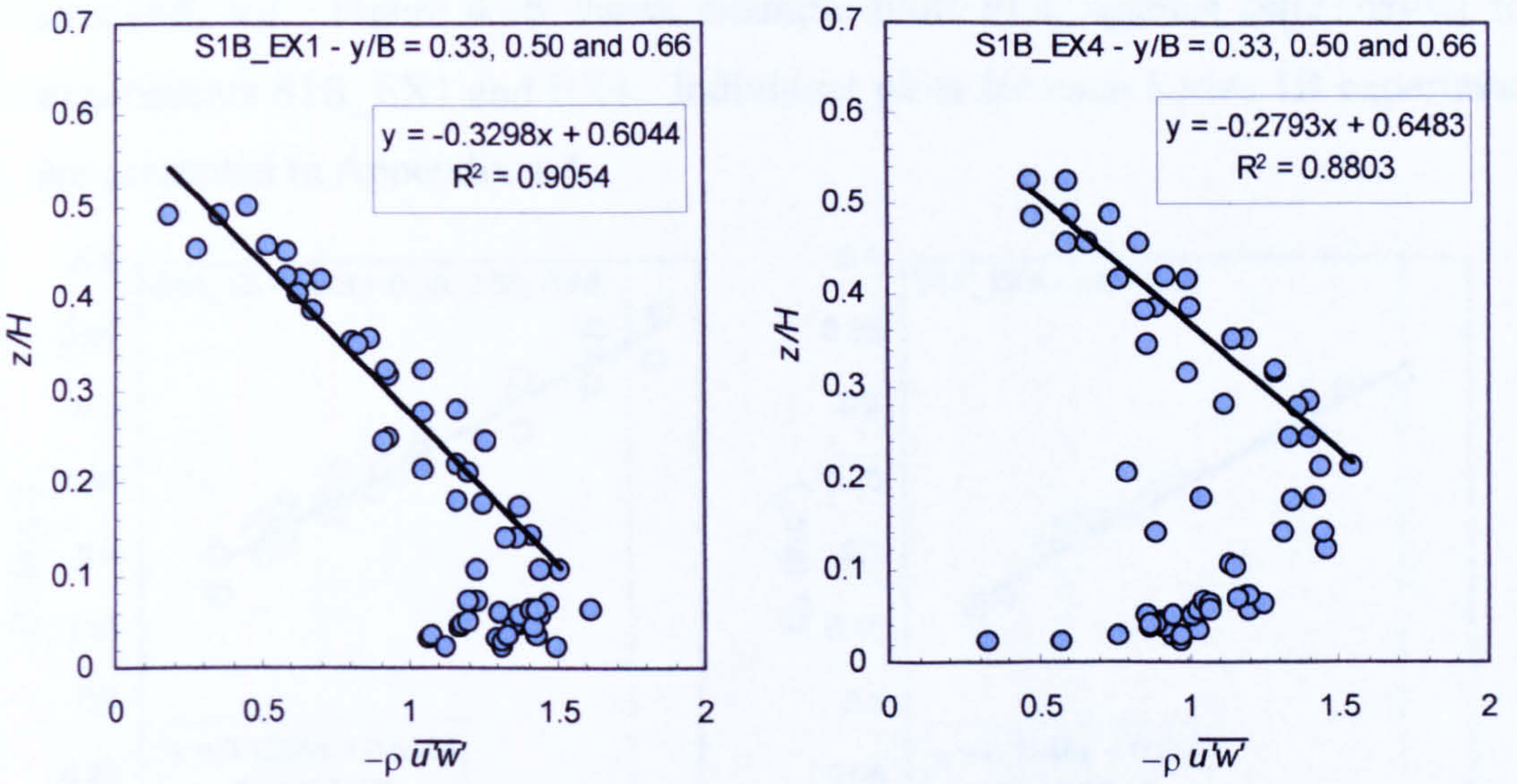

Figure 4.15 - Plots of Reynolds stress variation with relative depth *z/H*. Note reciprocal of gradient of best-fit straight line = 1/m = $-\rho u_*^2$, therefore $u_* = [-1/(m\rho)]^{0.5}$.

3. A further method for predicting u_* uses mean longitudinal velocity data, measured in the near-bed flow region. This method, known as the Clauser (1956) method, applies least squares fitting to the data in the form of a logarithmic law (i.e. law-of-the-wall). For rough bed boundaries, this law has the form (Song et al. 1994),

$$\frac{U}{u_*} = \frac{1}{\kappa} ln\left(\frac{z+\delta z}{k_s}\right) + B_r \qquad (z/H < 0.2) \qquad \text{....(4.9)}$$

where k_s is the Nikuradse equivalent sand roughness, δz is the reference (zero-velocity) level and B_r is an integration constant. No universal accord exists on the location of the reference level (δz) within the bed (Hinze 1975, Nezu and Nakagawa 1993). Experimental data relating to the ratio $\delta z/k_s$ have shown variation in previous studies, ranging from $\delta z/k_s = 0.18$ (Grass, 1971) up to $\delta z/k_s = 0.25$ (Song et al. 1994). In the present study, the reference level was assumed to be $\delta z/k_s = 0.25$, as the prevalent hydraulic and bed conditions are similar to those of Song et al. (1994).

The prediction of u_* is obtained by plotting measured near-bed velocities U ($z/H \leq 0.2$) against $ln[(z+\delta z)/k_s]$. The gradient of the linear regression trendline is therefore equal to u_*/κ. The value of the von Kármán constant κ is generally assumed to be 0.40 in open channel flow. The constant of integration (B_r) can also be determined from the intercept of the extrapolated best-fit line with the U

axis ($=B_r\ u_*$). Figure 4.16 shows example plots of U against $ln[(z+\delta z)/k_s]$ for experiments S1B_EX1 and EX4. Individual plots for each Series 1B experiment are presented in Appendix 4.4.

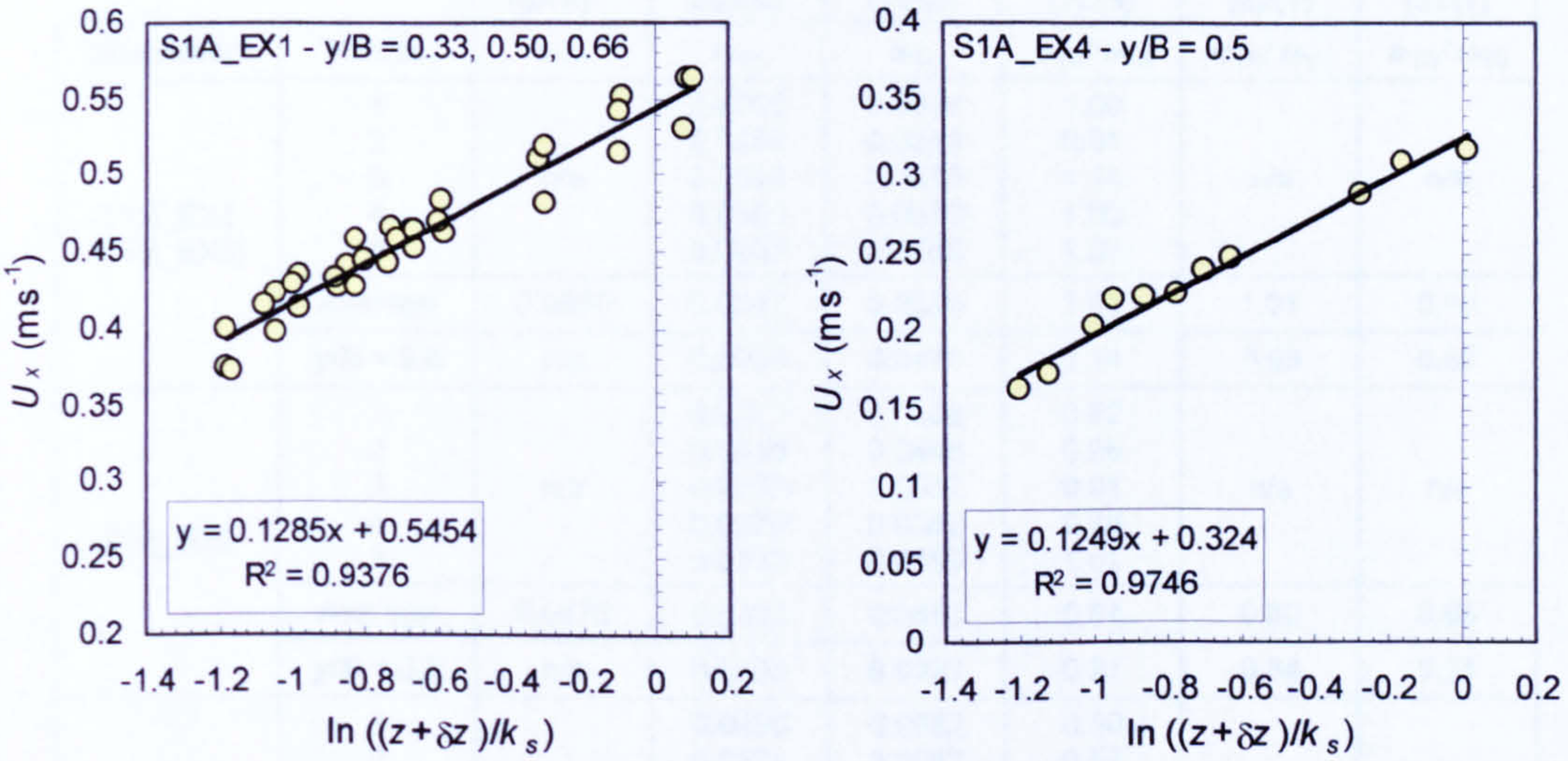

Figure 4.16 - Plots of U against ln $((z+\delta z)/k_s)$ in near-bed flow region for experiments S1B_EX1 and EX4. Note: gradient of best-fit line = m = u_*/κ, therefore u_* = mκ.

Table 4.5 overleaf summarises the computed values of u_* using each of the above methods. Method (1) is clearly the simplest to apply. It should, however, be considered to provide an overall or "global" value of u_* rather than a local value for steady, uniform open channel flows (Nezu and Nakagawa 1993).

The near-bed scatter in the Reynolds stresses (Figure 4.15) is thought to be related to the large-scale roughness of the bed surface (D/H = 0.10-0.19). The porous nature of the bed may also have resulted in discrepant values of $\overline{u'w'}$ being recorded by the ADV probe in measurements taken close to the bed surface. This is known to be a problem when the sample volume of the probe is positioned within a surface void in the bed material. Outwith the near-bed region, good linear correlation was obtained for profiles measured in the higher flow depth condition (H = 143mm), with average correlation values (R^2) of 0.94 and 0.96 for S1B_EX1 and EX4 respectively, compared to R^2 = 0.61 for S1B_EX2 (H = 93mm). Reynolds stress profiles measured during S1B_EX5 (H = 93mm) did not provide satisfactory data to compute a reliable shear stress value.

Velocity data used to compute u_* using the Clauser (1956) method generally revealed excellent correlation in the near-bed flow region ($z/H < 0.2$), with average values of R^2 equal to 0.98 and 0.96 for experiments S1B_EX1 and EX2, respectively.

Corresponding average R^2 values for experiments S1B_EX4 and EX5 were 0.97 and 0.87, respectively.

		$u_{*(1)} = (gRS)^{0.5}$	Reynolds Stress	Clauser (1956)	Methods (2)/(3)	Methods (2)/(1)	Methods (3)/(1)
Experiment	**Profile**	$u_{*(1)}$	$u_{*(2)}$	$u_{*(3)}$	$u_{*(2)}/u_{*(3)}$	$u_{*(2)}/u_{*(1)}$	$u_{*(3)}/u_{*(1)}$
S1B_EX1 (S1B_EX3)	1	n/a	0.0559	0.0558	1.00	n/a	n/a
	2		0.0462	0.0510	0.91		
	3		0.0534	0.0470	1.14		
	4		0.0560	0.0559	1.00		
	5		0.0601	0.0582	1.03		
	Average	0.0539	0.0543	0.0536	1.01	1.01	0.99
	$y/B = 0.5$	n/a	0.0534	**0.0470**	1.14	0.99	0.87
S1B_EX2	1	n/a	0.0377	0.0608	0.62	n/a	n/a
	2		0.0435	0.0446	0.98		
	3		0.0305	0.0337	0.91		
	4		0.0279	0.0368	0.76		
	5		0.0503	0.0499	1.01		
	Average	0.0475	0.0380	0.0451	0.84	0.80	0.95
	$y/B = 0.5$	n/a	0.0305	**0.0337**	0.91	0.64	0.71
S1B_EX4	1	n/a	0.0490	0.0982	0.50	n/a	n/a
	2		0.0521	0.0917	0.57		
	3		0.0546	0.0500	1.09		
	4		0.0570	0.0500	1.14		
	5		0.0511	0.0544	0.94		
	Average	0.0539	0.0528	0.0689	0.77	0.98	1.28
	$y/B = 0.5$	n/a	0.0546	**0.0500**	1.09	1.01	0.93
S1B_EX5	1	n/a	-	0.0771	-	n/a	n/a
	2		0.0365	0.0788	0.46		
	3		-	0.0408	-		
	Average	0.0475	-	0.0656	-	-	1.42
	$y/B = 0.5$	n/a	-	**0.0408**	-	-	0.88

Table 4.5 - Calculation of shear velocity u_* by three methods: (1) "Global" value, $u_* = (gRS_f)^{0.5}$; (2) Reynolds stress profiles; (3) Clauser (1956) using mean longitudinal velocity profiles.

Compared with the shear velocity predictions obtained from the Clauser (1956) method ($u_{*(3)}$), the values of $u_{*(2)}$ obtained from the Reynolds stress profiles were on average about 15% lower. When the values of $u_{*(2)}$ (Reynolds stress) and $u_{*(3)}$ (Clauser) are averaged over the five profiles obtained for each experiment, reasonable agreement is generally observed between the predictions of u_* calculated from each of the three methods, with an average relative difference of only 11%.

The problems associated in obtaining predictions of u_* from the Reynolds stress profiles in the near-bed flow region ($z/H < 0.2$) meant that the Clauser (1956) method was adopted for the calculation of shear velocity. The values of u_* used in the subsequent analysis of the experimental data were obtained from the near-bed velocity profiles measured at the centre of the flume ($y/B = 0.5$), where the influence of the flume walls would be minimum.

4.4.3.2 Calculation of Nikuradse Equivalent Bed Roughness

The Nikuradse equivalent sand roughness k_s is often used to describe bed surface roughness. Its influence on the flow conditions can be classified in terms of the non-dimensional roughness Reynolds number ($k_s^+ = k_s.u*/\nu$) in three categories (Yalin 1992; Nezu and Nakagawa 1993):

- $k_s^+ > 70$ – rough turbulent regime (completely rough bed) ....(4.10a)
- $70 \geq k_s^+ \geq 5$ – intermediate regime (incompletely rough bed) ....(4.10b)
- $k_s^+ < 5$ – smooth regime (hydraulically smooth bed) ....(4.10c)

Two expressions were used to calculate the equivalent bed roughness k_s: the modified Colebrooke-White and Keulegan (1938) friction factor equations (4.11 and 4.12, respectively),

$$\frac{1}{\sqrt{f_b}} = -2\log\left(\frac{k_s}{14.8R_b} + \frac{0.6275}{R_{eb}\sqrt{f_b}}\right) \quad ....(4.11)$$

$$\frac{1}{\sqrt{f_b}} = 2.03\log\left(\frac{12.27R_b}{k_s}\right) \quad ....(4.12)$$

where subscript b refers to parameters relating to the bed, f_b is the Darcy-Weisbach friction factor, R_b is the hydraulic radius and R_{eb} is the flow Reynolds number.

An Excel spreadsheet was set up to calculate the hydraulic parameters relating to the bed using the Vanoni and Brooks (1957) method for composite channel roughness. An example calculation of k_s from the spreadsheet is shown in Appendix 4.5. The calculated values of k_s using equations 4.11 and 4.12 are detailed for each experiment in Table 4.6 below.

Experiment Number *Bed Material Type*	**S1B_EX1 (EX3)** *Uniform Spheres*	**S1B_EX2** *Uniform Spheres*	**S1B_EX4** *Natural Gravel*	**S1B_EX5** *Natural Gravel*
D_{50} (mm)	15.0	15.0	17.3	17.3
D_{84} (mm)	-	-	21.6	21.6
$k_{s(1)}$ (Colebrooke-White) (mm)	27.2	17.2	90.2	101.0
$k_{s(2)}$ (Keulegan) (mm)	24.0	15.2	78.2	87.0
$k_s^+{}_{(1)}$; $k_s^+{}_{(2)}$	1387 ; 1223	709 ; 626	4892 ; 4241	4382 ; 3774
$k_{s(1)}/H$; $k_{s(2)}/H$	0.190 ; 0.168	0.185 ; 0.163	0.631 ; 0.547	1.086 ; 0.935
$k_{s(1)}/D_{50}$; $k_{s(2)}/D_{50}$	1.81 ; 1.60	1.15 ; 1.01	5.21 ; 4.52	5.84 ; 5.03
$k_{s(1)}/D_{84}$; $k_{s(2)}/D_{84}$	-	-	4.18 ; 3.62	4.67 ; 4.03

Table 4.6 - Nikuradse equivalent sand roughness k_s for bed conditions in Series 1B

The predicted roughness Reynolds numbers (k_s^+) show flow conditions to be rough turbulent ($k_s^+ > 70$), with both bed configurations having large-scale relative roughness [i.e. k_s/H = 0.16-0.19 (uniform spheres) and 0.55-1.1 (natural gravel)]. Values of k_s obtained from Keulegan (1938) are generally 12-14% lower than predicted from the Colebrooke-White equation. Values of k_s/D_{50} for the uniform spheres were in reasonable agreement with Meland and Norrman (1969), who found k_s/D_{50} = 1.1 in open-channel flow over a similar bed configuration. For the natural gravel bed, k_s values obtained from Keulegan (1938) showed reasonable agreement with $k_s = 3.5D_{84}$ from Hey (1979) and $k_s = 3D_{90}$ from van Rijn (1982). The k_s values obtained from the Keulegan (1938) have been adopted for this study.

4.4.3.3 Turbulent Characteristics of Open Channel Flow

The root-mean-square values of longitudinal and vertical flow velocity fluctuations (u'_{rms} and w'_{rms}) were calculated by the support software package WinADV from the raw ADV probe measurements using

$$u'_{rms} = \left[\frac{1}{n}\sum_{i=1}^{n}(u_i - \overline{u})^2\right]^{0.5} \quad ; \quad w'_{rms} = \left[\frac{1}{n}\sum_{i=1}^{n}(w_i - \overline{w})^2\right]^{0.5} \qquad \text{....(4.13)}$$

where u' represents the instantaneous fluctuation in longitudinal velocity ($=u_i - \overline{u}$), and w' is the corresponding vertical velocity fluctuation ($=w_i - \overline{w}$). The longitudinal and vertical turbulence intensities were obtained by dividing these root-mean-square velocity fluctuations by the shear velocity u_*.

Figure 4.17 shows the turbulence intensity distributions plotted with relative depth z/H for Series 1B experiments. Longitudinal turbulence intensities u'_{rms}/u_* are lower in magnitude than the universal exponential law proposed by Nezu and Rodi (1986) (eqn. 2.11, pp.22). Measurements taken over a bed of uniform spheres show some agreement with a similar relationship proposed by Kironoto and Graf (1994), who measured turbulence intensity in open channel flow over quasi-uniform gravel. By contrast, vertical turbulence intensities w'_{rms}/u_* are considerably lower than both forms of the universal exponential law. Possible reasons for this difference include: (i) the high relative roughness of the two bed conditions (k_s/H = 0.16 – 1.1), which may significantly alter the near-bed turbulent flow structure; (ii) the low aspect ratio of the flow ($2.1 \leq \alpha \leq 3.2$), resulting in 3-D flow conditions and interference from the side-walls of the flume; (iii) the short working section of the flume preventing full

development of the turbulent boundary layer; or (iv) possible measurement errors from the ADV probe.

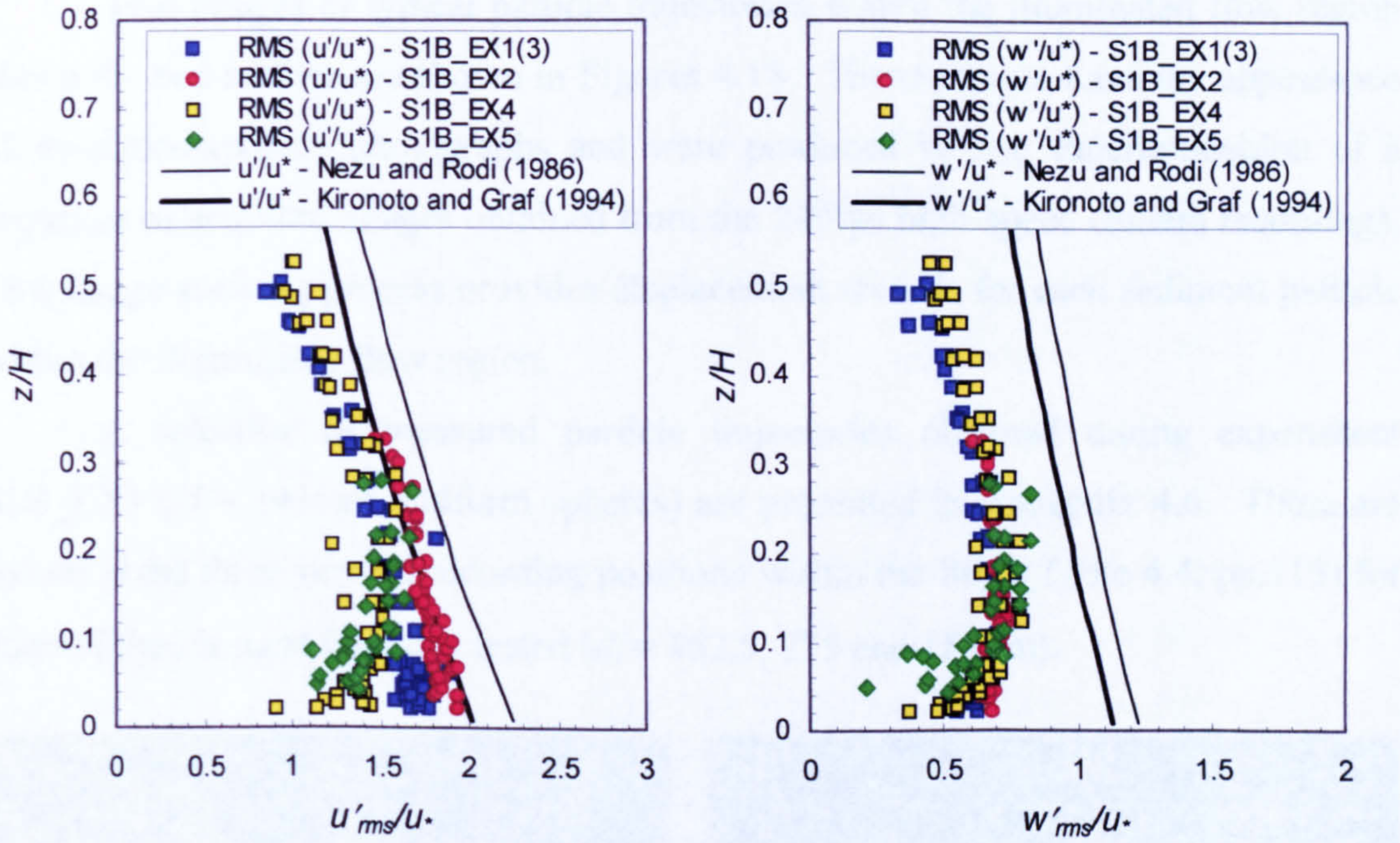

Figure 4.17 - Variation of longitudinal and vertical turbulence intensities (u'_{rms}/u_* and w'_{rms}/u_*) with relative depth z/H for Series 1B experiments. Universal distributions proposed by Nezu and Rodi (1986) and Kironoto and Graf (1994) shown for comparison.

Figure 4.17 also reveals a reduction in the magnitude of the turbulence intensities in the near-bed flow region ($z/H \leq 0.2$). This characteristic is particularly evident in all the w'_{rms}/u_* distributions and the u'_{rms}/u_* distributions measured over the natural gravel bed. In each case, the maximum turbulence intensities occur at z/H = 0.2-0.3. Previous experimental investigations in open channel flows over rough bed conditions have also highlighted similar near-bed reductions in turbulence intensity (e.g. McQuivey and Richardson 1969; Grass 1971; Song et al. 1994). Bayazit (1976) found that the values of u'_{rms}/u_* decreased considerably as the relative roughness size of the bed (k_s/H) increased. The results presented in Figure 4.17 would appear to be consistent with this finding, with larger reductions in near-bed u'_{rms}/u_* values occurring over the gravel bed (k_s/H = 0.54 – 1.1) compared to over the uniform spheres (k_s/H = 0.16 – 0.19). Nowell and Church (1979) also found that the degree of reduction to the u'_{rms}/u_* values in the near-bed flow region increased as the roughness density of the bed elements (defined as the ratio of the plan area of bed elements to the total plan area of the flume bed) increased.

4.4.4 Experimental Results

4.4.4.1 Characteristics of Observed Sediment Particle Motion

Two images of typical particle trajectories within the illuminated flow region above the bed surface are shown in Figures 4.18. These images have the appearance of multiple-exposure photographs and were produced by the superimposition of a sequence of acquired images obtained from the 240fps high-speed camera recordings. This image stacking process provides displacement records for each sediment particle within the illuminated flow region.

A selection of measured particle trajectories obtained during experiment S1B_EX1 (H = 143mm, uniform spheres) are presented in Appendix 4.6. These are shown at the three vertical recording positions within the flow (Table 4.4, pp.115) for three of the six sand fractions tested (d_i = 462.5, 275 and 181μm).

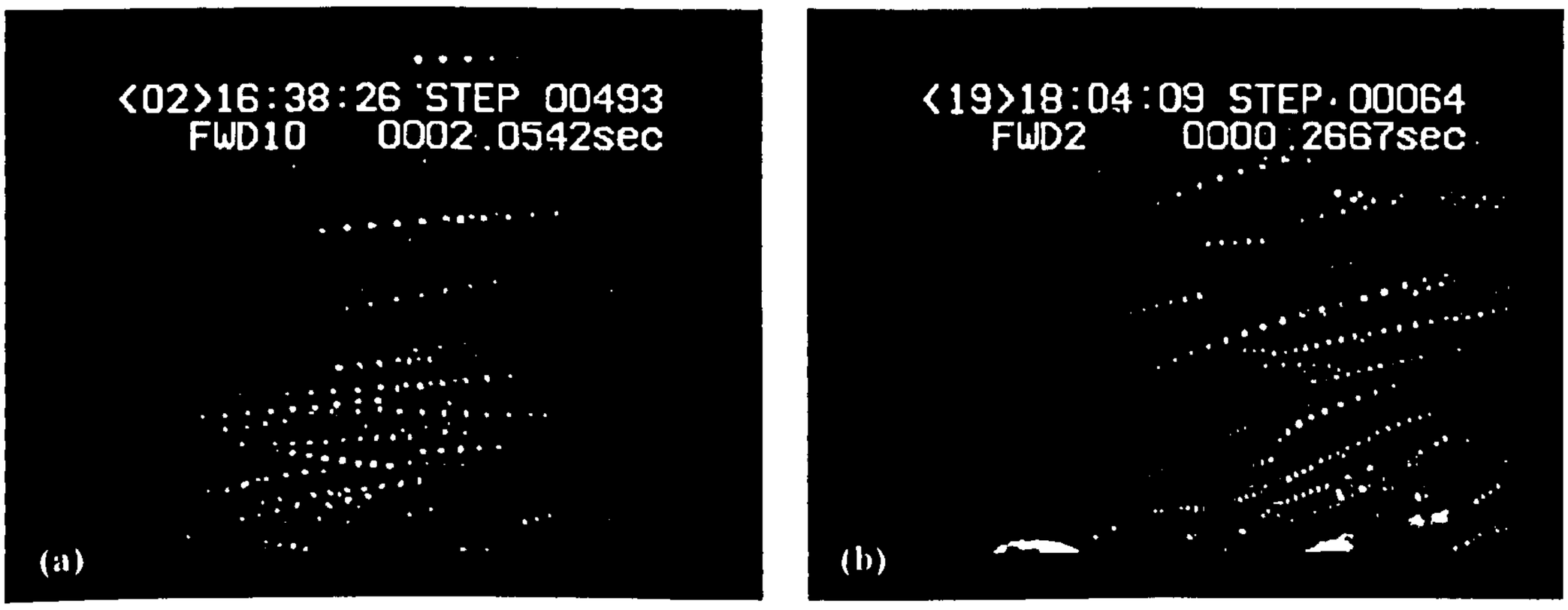

Figure 4.18 - Examples of stacked images recorded using the high-speed camera (240 fps) showing typical trajectories of 500-425μm particles: (a) S1B_EX2 (uniform spheres) – z/H = 0.0–0.47; (b) S1B_EX5 (natural gravel) – z/H = 0.0–0.50.

Overall, the typical characteristics of particle motion illustrated by the measured particle trajectories appear to be influenced by the sediment size d_i and the vertical position within the flow. In the outermost region of recorded flow ($z/H >$ ~0.4), the motion of particles from the three sand fractions appeared to be relatively uniform (Figures A4.6a, A4.7a and A4.8a, Appendix 4.6). The average angles of particle trajectories in this flow region were estimated to be 3.6°, 2.9° and 2.6° for d_i = 462.5, 275 and 181μm, respectively. In the two recorded flow regions nearer to the bed surface ($z/H \leq 0.2$ and $0.2 < z/H \leq 0.4$), greater variation was generally observed in sediment particle motions (Figures A4.6-A4.8 b and c, Appendix 4.6). The average

particle trajectory angles in the flow region $0.2 < z/H \leq 0.4$ were 6.0°, 5.3° and 5.1° for $d_i = 462.5$, 275 and 181μm, respectively, whilst for the near-bed flow ($z/H \leq 0.2$), corresponding values increased to 11.4°, 10.2° and 7.5°. These near-bed particle trajectories are in quantitative agreement with the values reported in Series 1A. Similar near-bed particle trajectory plots for experiment S1B_EX4 (H = 143mm, natural gravel bed) are presented in Figure A4.9 (Appendix 4.6) for comparison purposes. Average particle trajectories angles in this flow region ($z/H \leq 0.2$) above the natural gravel bed were 15.5°, 8.5° and 7.0° for particle sizes $d_i = 462.5$, 275 and 181μm, respectively.

Over both bed configurations, variations in particle trajectories were characterised by an increasing number of particles observed with upward trajectories as both relative depth z/H and particle size d_i reduced. In terms of the influence of bed configuration, greater variation was observed in near-bed trajectories for d_i = 181μm particles over the natural gravel bed [-30° to 50°] than over the rhombically-packed bed of uniform spheres [-20° to 30°] (Figures A4.8c and A4.9c, Appendix 4.6). This is most probably an effect of the irregular bed surface and higher relative roughness of the natural gravel bed.

4.4.4.2 Particle Velocity Measurements

(a) Fraction-Averaged Particle Velocities

Local instantaneous values of streamwise and vertical particle velocities were obtained from analysis of the individual particle trajectories. Fraction-averaged particle velocities and corresponding standard deviations were computed for individual Series 1B experiments using the data obtained from each of the six LA sand fractions tested. Similar to the averaging procedure employed in Series 1A, the flow field in which particle tracks were recorded was divided into a series of intervals, generally of height $\Delta z = 0.05H$, with the average velocity calculated from all the individual particle velocities measured within each interval. When considering the near-bed flow region only, intervals were expressed in wall units z_+ (= $z.u_*/\nu$), generally of height $\Delta z_+ = 100$.

The results from this averaging procedure are presented in Figures 4.19(a) and (b) for streamwise particle velocities measured in experiments S1B_EX1 and EX4, respectively, with mean flow velocity profiles obtained from ADV and mini-propeller

measurements also shown for comparison purposes. Both flow and particle velocities are made non-dimensional by the shear velocity u_*. Similar plots are presented in Appendix 4.7 for other Series 1B experiments.

Fraction-averaged streamwise particle velocities u_s/u_* are generally shown to be close to the mean velocity of the surrounding fluid U/u_* in the flow regions where comparisons could be made. The vast majority of experimental data points lie within the region defined by the $(U \pm u'_{rms})/u_*$ profiles (dotted lines, Figure 4.19). The standard deviations for fraction-averaged particle velocities (shown as ± error bars in Figure 4.19) are clearly of the same order as the $\pm\, u'_{rms}/u_*$ values and generally decrease as z/H increases. This dependence on z/H is expected since the trajectory plots (Appendix 4.6) revealed that particle motions in the flow region $z/H > 0.4$ were relatively more uniform than those nearer to the bed surface. It may have been expected that standard deviations of streamwise particle velocities would be generally smaller than the u'_{rms}/u_* values due to inertial effects affecting the particles' response to high frequency fluid motions (Niño and Garcia 1996), especially in regions of high turbulence intensity. However, this increased scatter may result from differences in streamwise particle velocities that exist between individual size fractions of LA sand.

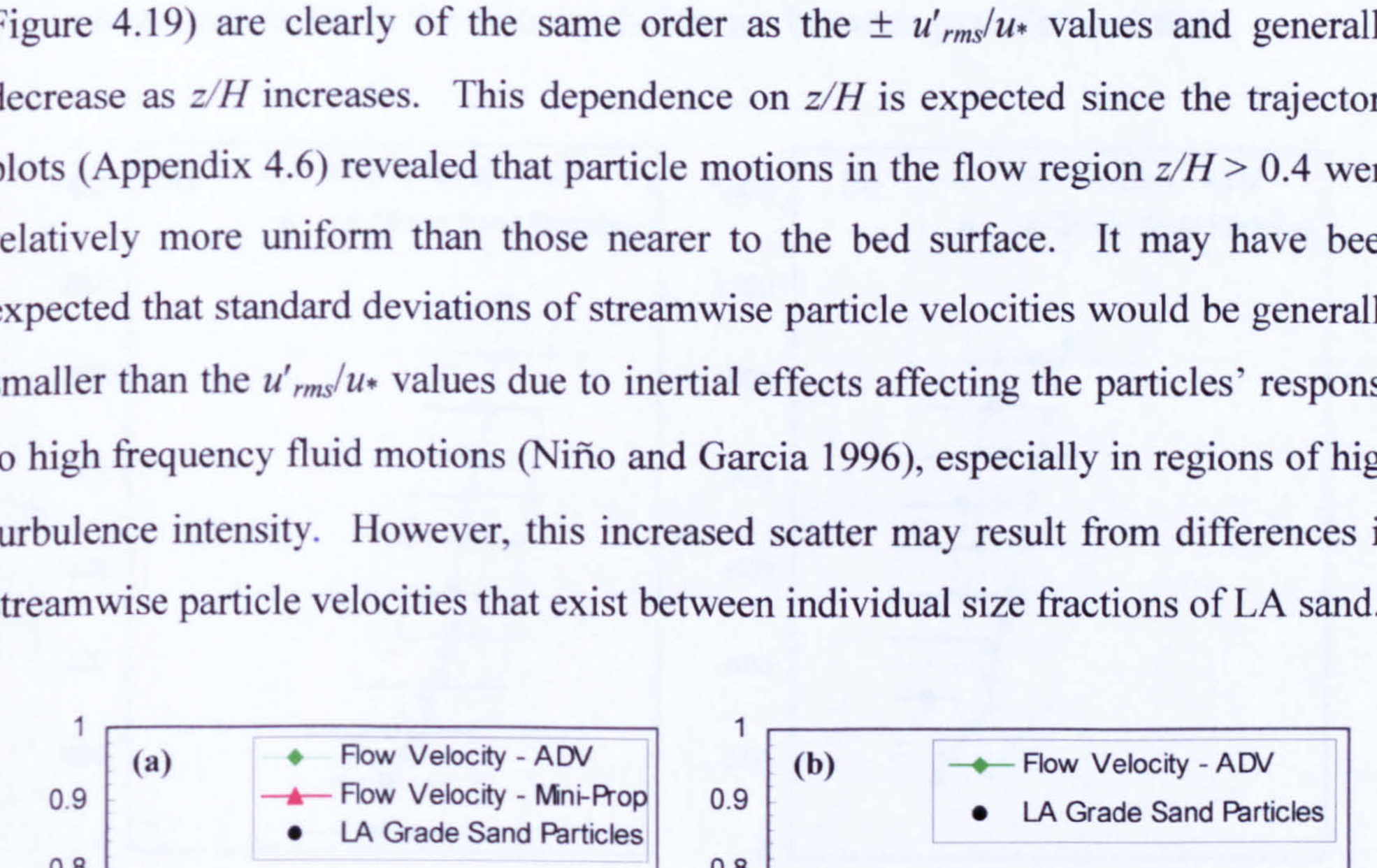

Figure 4.19 - Fraction-averaged non-dimensional streamwise particle velocities plotted against z/H for experiment: (a) S1B_EX1 – H = 143mm, uniform spheres; (b) S1B_EX4 – H = 143mm, natural gravel. Error bars on data points represent ± one standard deviation. Dashed lines represent $(U \pm u'_{rms})/u_*$, obtained from the ADV measurements.

In consideration of the near-bed region of flow ($z_+ \leq 1200$) alone, Figures 4.20(a) and (b) show that u_s/u_* values measured in S1B_EX1 and EX4 are generally less than or equal to the local mean flow velocity, lying between the U/u_* and $(U-u'_{rms})/u_*$ profiles. Similar findings are also shown for other Series 1B experiments presented in Appendix 4.7 and are in agreement with observations by Kaftori et al. (1995) and Niño and Garcia (1996). In general, particle velocities appear to be closer to the surrounding mean fluid velocity (i.e. $u_s \sim U$) in the near-bed flow over uniform spheres than over natural gravel, suggesting that the relative bed roughness k_s/H may be an important factor in the velocity difference between particles and fluid.

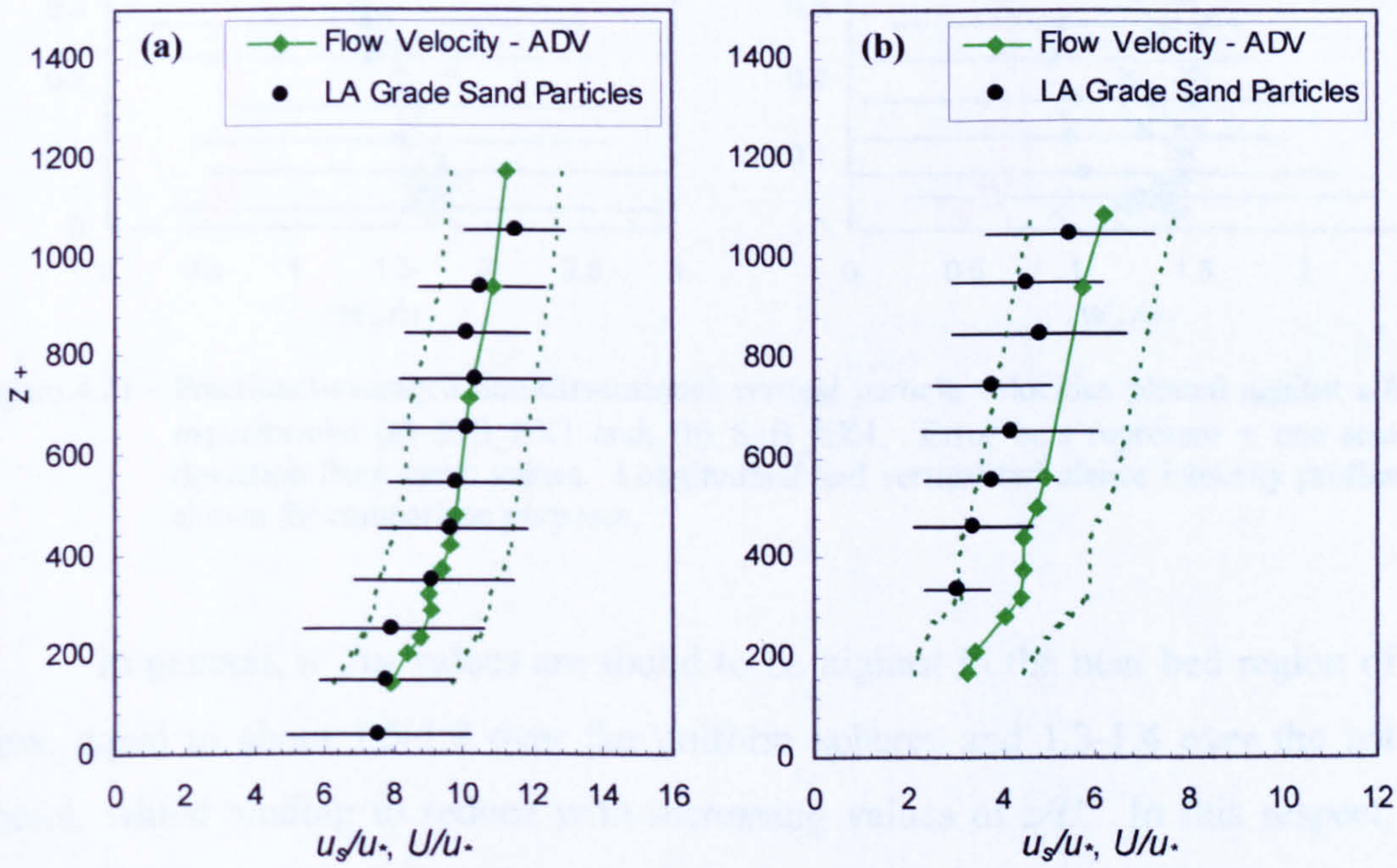

Figure 4.20 - Fractional-averaged non-dimensional streamwise particle velocities plotted against z_+ for measurements in near-bed flow region ($z_+ \leq 1200$): (a) S1B_EX1; (b) S1B_EX4. Error bars and dashed lines as defined above (Figure 4.19)

Similar distributions of the fractional-averaged vertical particle velocities can be plotted in the non-dimensional form w'_s/u_* against relative depth z/H. Figures 4.21(a) and (b) present this data for experiments S1B_EX1 and EX4, respectively, while similar plots for other Series 1B experiments are presented in Appendix 4.7. Profiles of longitudinal and vertical turbulence intensities (i.e. u'_{rms}/u_* and w'_{rms}/u_*) obtained from ADV probe measurements are shown for comparison.

Individual particles with observed upward trajectories (i.e. negative fall velocities, $w'_s < 0$) were included in the calculation of fractional-averaged values of w'_s/u_*. However, the averaging procedure applied to obtain w'_s/u_* values generally

resulted in downward vertical particle velocities (i.e. $w'_s > 0$) due to the dominance of gravitational forces on the particles' vertical motion.

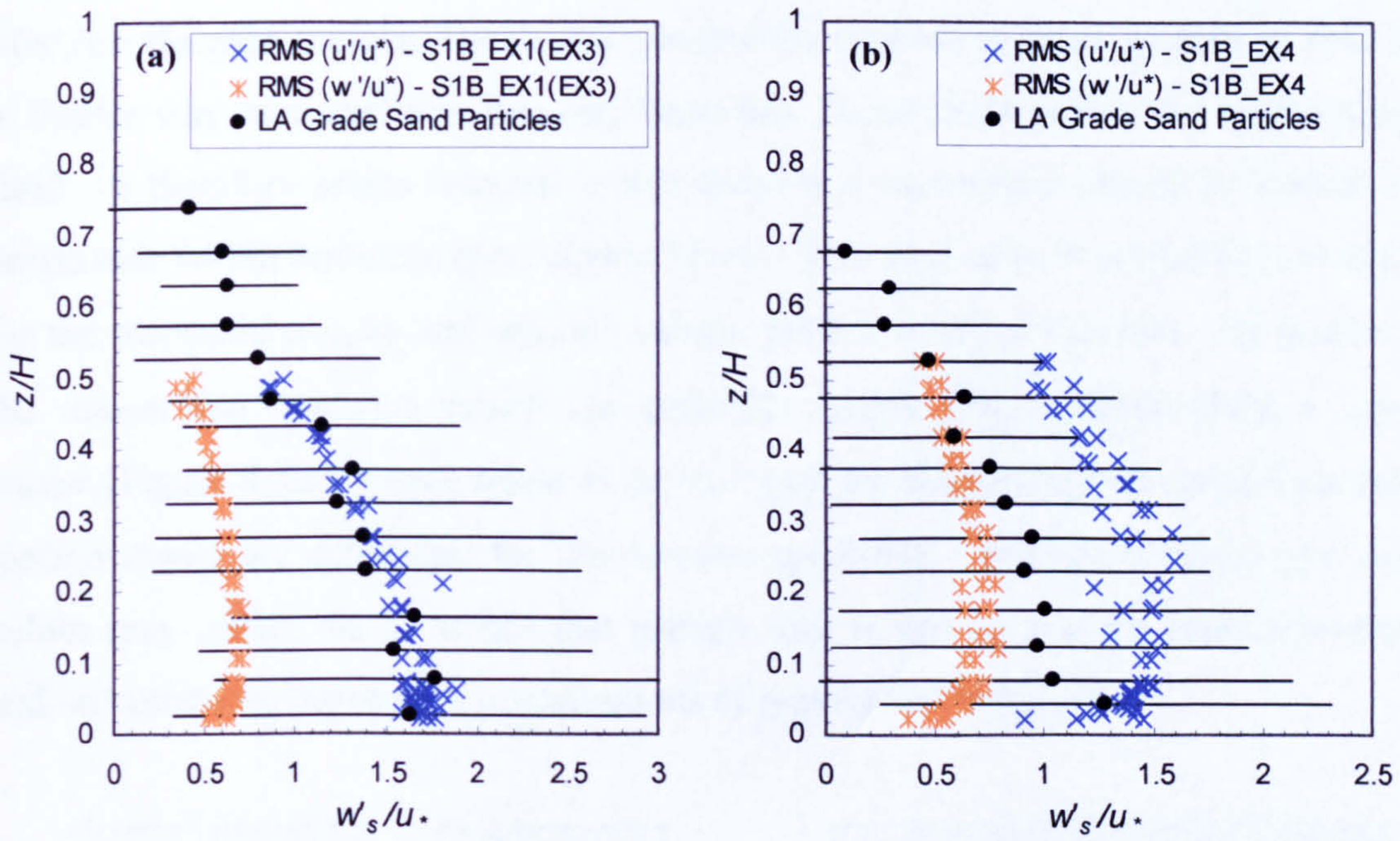

Figure 4.21 - Fractional-averaged non-dimensional vertical particle velocities plotted against *z/H* for experiments: (a) S1B_EX1 and; (b) S1B_EX4. Error bars represent ± one standard deviation from mean values. Longitudinal and vertical turbulence intensity profiles are shown for comparison purposes.

In general, w'_s/u_* values are found to be highest in the near bed region of the flow, equal to about 1.5-1.8 over the uniform spheres and 1.3-1.4 over the natural gravel, whilst tending to reduce with increasing values of *z/H*. In this respect, the w'_s/u_* distributions have distinct similarities with the measured longitudinal and vertical turbulence intensities. The w'_s/u_* values are also often significantly higher than measured vertical turbulence intensities w'_{rms}/u_*, especially in the near-bed region ($z/H \leq 0.2$) where no significant reduction in average w'_s/u_* values was observed, except for experiment S1B_EX3 [Figure A4.13(b), Appendix 4.7]. However, with increasing *z/H*, the w'_s/u_* values appear to approach w'_{rms}/u_* values, although generally remaining higher. The notable exception to this is S1B_EX4 (Figure 4.21b) where these w'_s/u_* and w'_{rms}/u_* values coincide at $z/H = \sim 0.5$.

Calculated standard deviations for the fraction-averaged w'_s/u_* values were also shown to generally reduce with increasing *z/H*, from about 1.0-1.3 in the near-bed flow region to about 0.5-0.7 in the outer flow. This again indicates greater variation in particle motions closer to the bed compared with in the outer flow region.

The distributions of these standard deviations with relative depth z/H are shown in Figure 4.22 for experiments S1B_EX1 and EX4, along with the corresponding turbulence intensities (u'_{rms}/u_* and w'_{rms}/u_*). It can be argued that $\sigma(u_s/u_*)$ and $\sigma(w'_s/u_*)$ describe the streamwise and vertical fluctuations in mean particle motion in a similar way as turbulence intensity describes fluctuations within the surrounding fluid. It therefore seems reasonable that these two parameters should be similar in magnitude within turbulent open channel flow. This similarity is particularly evident for the measured u'_{rms}/u_* and $\sigma(u_s/u_*)$ values, plotted in Figure 4.22(a). By contrast, the reason that $\sigma(w'_s/u_*)$ values are generally higher than corresponding w'_{rms}/u_* values [Figure 4.22(b)] may relate to the fact that the fluctuations in vertical particle motion shown are calculated for fraction-averaged data. Therefore, larger $\sigma(w'_s/u_*)$ values may reflect the influence that particle size d_i has on vertical particle motion and, in particular, the relative contributions of gravity and turbulence.

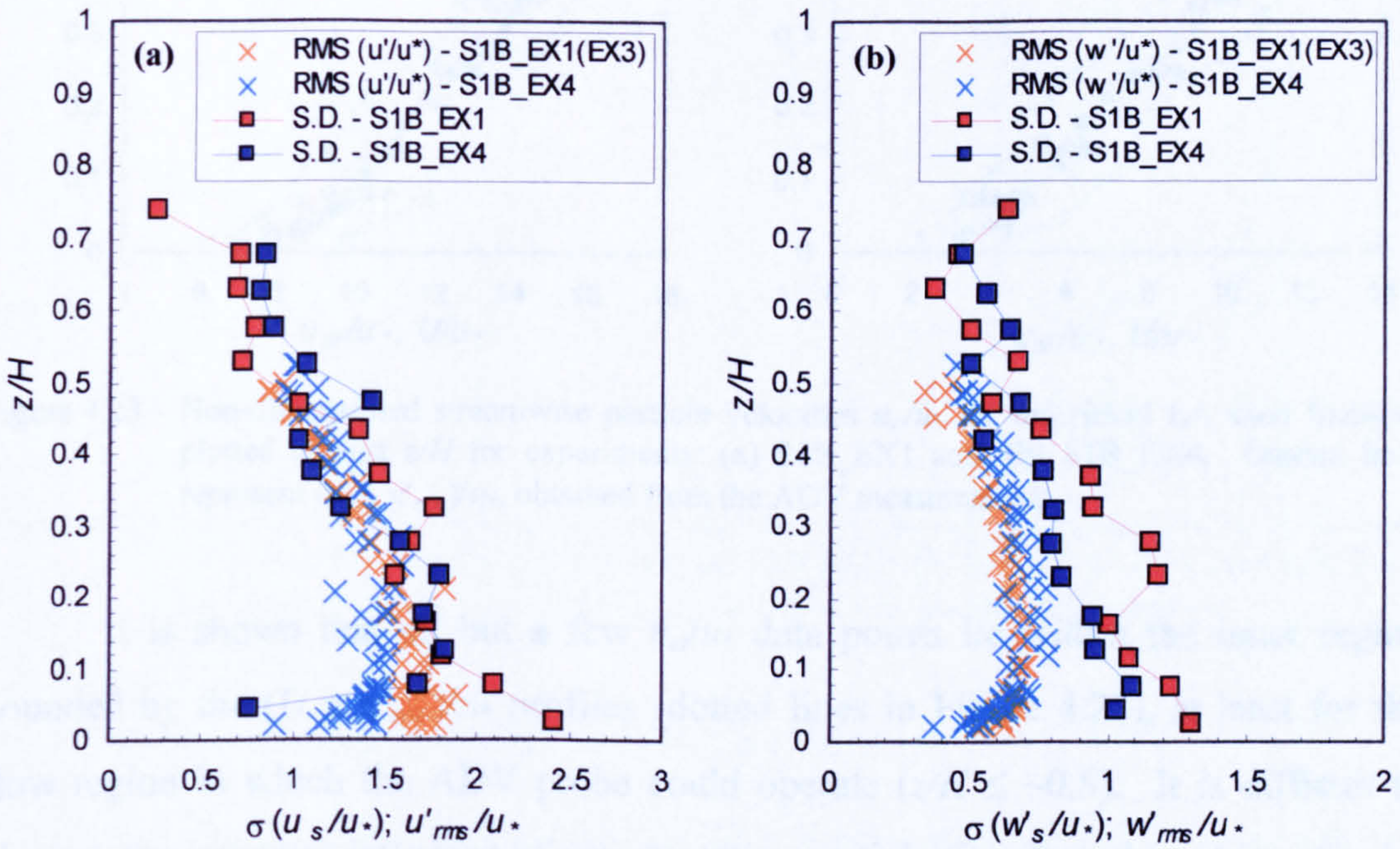

Figure 4.22 - Comparison between distributions of turbulence intensities u'_{rms}/u_* and w'_{rms}/u_* and standard deviations in observed particle motions $\sigma(u_s/u_*)$ and $\sigma(w'_s/u_*)$ for experiments S1B_EX1 and EX4.

(b) Particle Velocities for Individual Size Fractions

Streamwise and vertical particle velocities for individual LA size fractions (u_{si} and w'_{si}) can be plotted to highlight the influence of representative particle size d_i on observed particle motions. These velocity components are again made non-dimensional by dividing by the shear velocity u_*. Vertical distributions of u_{si}/u_* and

w'_{si}/u_* were obtained by discretising the flow depth into z/H intervals in the same way as was carried out for previous fraction-averaged particle velocity plots.

The profiles of fractional streamwise particle velocity u_{si}/u_* are plotted against z/H in Figure 4.23 for experiments S1B_EX1 and EX4, and in Appendix 4.8 for the remaining experiments in Series 1B. Mean flow velocity profiles obtained from the ADV and mini-propeller measurements are also shown, as well as the ADV profiles defined by $(U \pm u'_{rms})/u_*$ as before.

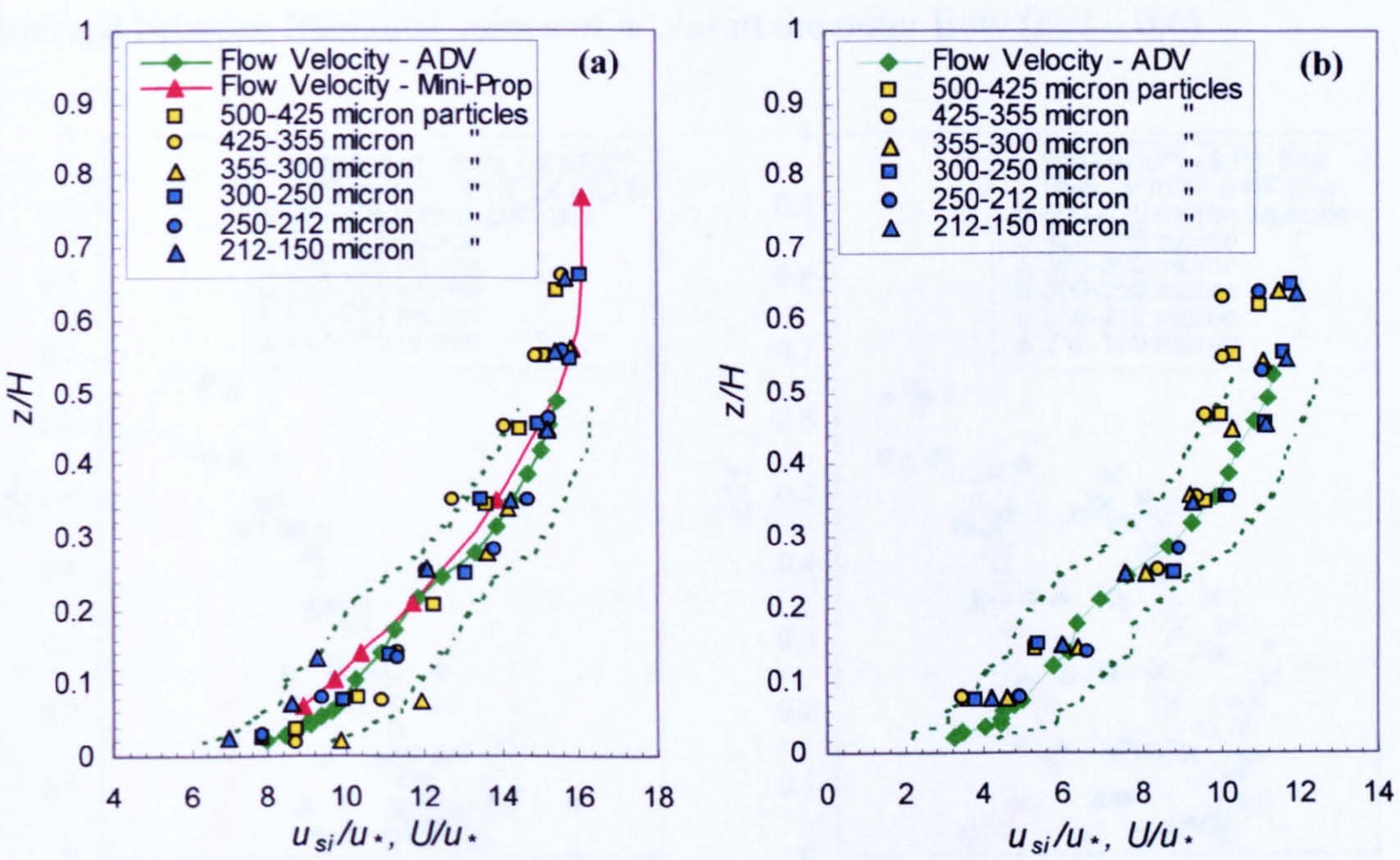

Figure 4.23 - Non-dimensional streamwise particle velocities u_{si}/u_* for individual LA sand fractions plotted against z/H for experiments: (a) S1B_EX1 and; (b) S1B_EX4. Dashed lines represent $(u_x \pm u'_{rms})/u_*$, obtained from the ADV measurements.

It is shown that all but a few u_{si}/u_* data points lie within the inner region bounded by the $(U \pm u'_{rms})/u_*$ profiles (dotted lines in Figure 4.23), at least for the flow region in which the ADV probe could operate ($z/H \leq \sim 0.5$). It is difficult to observe any apparent influence of representative particle size d_i on the values of u_{si}/u_* as considerable scatter is observed within distributions for each size fraction. In summary, these observations suggest that LA sand particles are generally transported in the streamwise direction at rates close to the mean velocity of the surrounding fluid (i.e. within ± 1 standard deviation), independent of particle size d_i.

Distributions of non-dimensional vertical particle velocity for individual size fractions w'_{si}/u_* are plotted against relative depth z/H in Figures 4.24 for experiments S1B_EX1 and EX4 and Appendix 4.8 for the remaining Series 1B experiments.

Measured longitudinal and vertical turbulence intensity profiles (u'_{rms}/u_* and w'_{rms}/u_*) are also shown for comparison. Although these plots show considerable scatter in the data sets, the largest w'_{si}/u_* values tend to occur in the near bed flow ($z/H \leq 0.2$), and generally decrease as z/H increases. The influence of particle size d_i also appears to be greatest within the near-bed flow, with larger size fractions (d_i = 462.5, 390 and 327.5μm) typically having the largest w'_{si}/u_* values. By contrast, the influence of d_i appears to diminish further away from the bed surface, with little distinction often observed between fractional values of w'_{si}/u_* in the outer flow ($z/H \sim 0.6$).

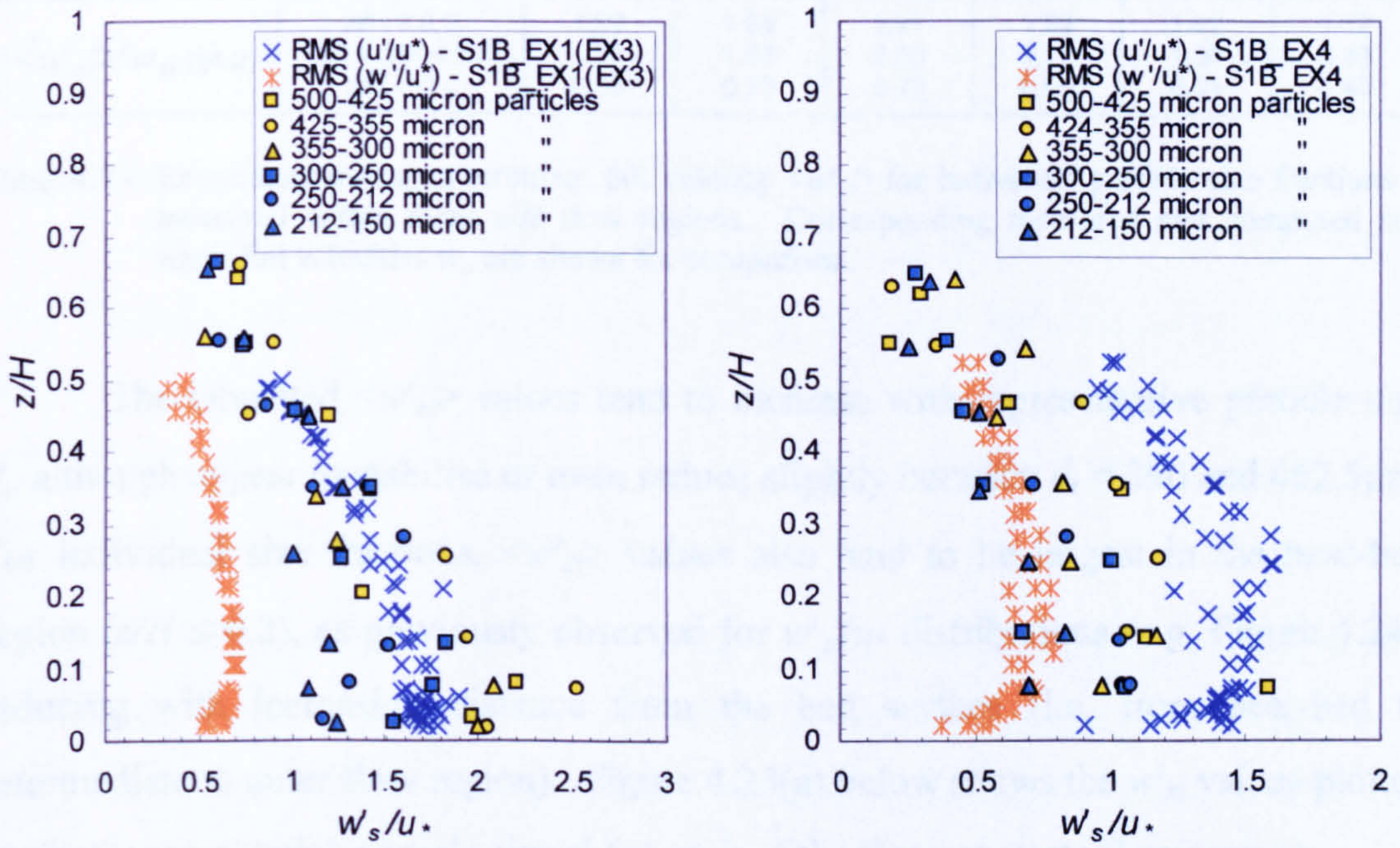

Figure 4.24 - Non-dimensional vertical particle velocities w'_{si}/u_* for individual LA sand fractions plotted against z/H for experiments: (a) S1B_EX1; (b) S1B_EX4. Measured turbulence intensity profiles (u'_{rms}/u_* and w'_{rms}/u_*) are shown for comparison purposes.

4.4.4.3 Settling Characteristics for Particle Size Fractions

The fractional w'_{si}/u_* distributions do not adequately reveal how the vertical particle motion differs between individual LA size fractions or how particle fall velocities w'_{si}, in different z/H regions of the turbulent open channel flow, vary from their measured fall velocity in still water conditions w_{si}.

For the combined experimental data obtained in Series 1B, the average fractional values of $\langle w'_{si} \rangle$ were calculated in three distinct flow regions: (i) $z/H \leq 0.2$ (near-bed region); (ii) $0.2 < z/H \leq 0.5$ (intermediate region); and (iii) $z/H > 0.5$ (outer region). These experiment-averaged $\langle w'_{si} \rangle$ values are presented in Table 4.7 along

with corresponding w_{si} values obtained from the initial fall velocity calibration measurements (§4.2, pp.93) and from the predictive equation proposed by Cheng (1997) (equation 4.1, pp.96).

Size Class (μm)		212-150	250-212	300-250	355-300	425-355	500-425
Representative Particle Size d_i (μm)		181μm	231μm	275μm	327.5μm	390μm	462.5μm
$\langle w'_{si} \rangle$ (ms^{-1})	*Flow Region:-*						
	z/H < 0.2	0.0387	0.0511	0.0549	0.0655	0.0698	0.0672
	0.2 < z/H < 0.5	0.0349	0.0425	0.0418	0.0472	0.0510	0.0499
	z/H > 0.5	0.0192	0.0196	0.0254	0.0279	0.0300	0.0243
w_{si} (§4.2) (ms^{-1})		0.0201	0.0270	0.0322	0.0405	0.0491	0.0600
w_{si} (Cheng) (ms^{-1})		0.0178	0.0254	0.0321	0.0398	0.0485	0.0581
$\langle w'_{si} \rangle / w_{si}$ (§4.2)	*z/H < 0.2*	1.92	1.89	1.71	1.62	1.42	1.12
	0.2 < z/H < 0.5	1.73	1.57	1.30	1.16	1.04	0.83
	z/H > 0.5	0.95	0.73	0.79	0.69	0.61	0.40

Table 4.7 - Experiment-averaged turbulent fall velocity $\langle w'_{si} \rangle$ for individual particle size fractions d_i measured within three z/H flow regions. Corresponding measured and computed still water fall velocities w_{si} are shown for comparison.

The tabulated $\langle w'_{si} \rangle$ values tend to increase with representative particle size d_i, although appear to stabilise or even reduce slightly between d_i = 390 and 462.5μm. For individual size fractions, $\langle w'_{si} \rangle$ values also tend to be largest in the near-bed region ($z/H \leq 0.2$), as previously observed for w'_{si}/u_* distributions (e.g. Figure 4.24), reducing with increasing distance from the bed surface (i.e. from near-bed to intermediate to outer flow region). Figure 4.25(a) below shows the w'_{si} values plotted against representative particle size d_i for each of the three separate flow regions.

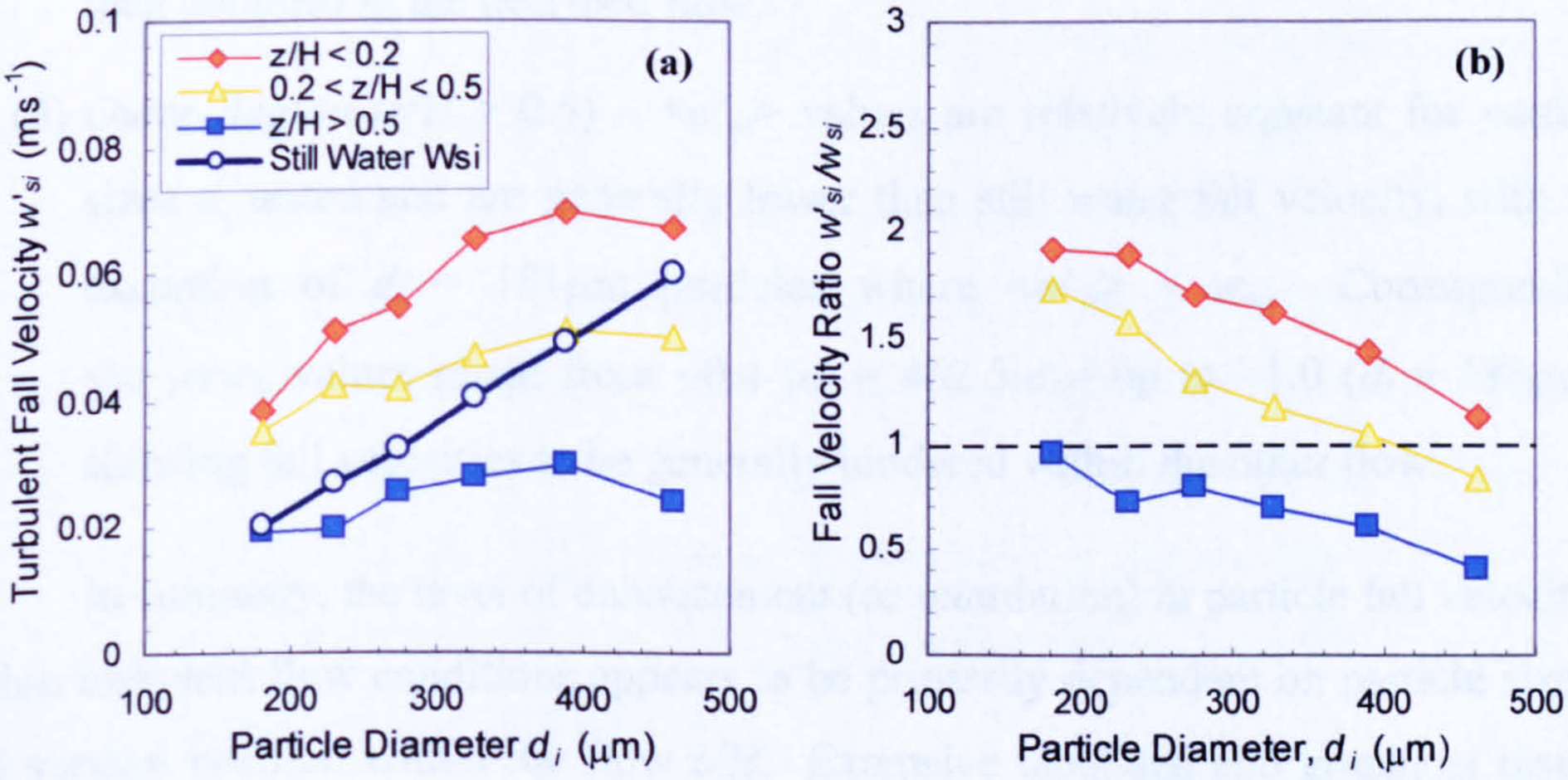

Figure 4.25 – (a) Experiment-averaged turbulent fall velocities $\langle w'_{si} \rangle$ and (b) non-dimensional fall velocity ratio $\langle w'_{si} \rangle / w_{si}$ plotted against particle size d_i for each of the three predefined z/H regions. Measured still water fall velocities w_{si} are shown in (a) for comparison.

The non-dimensional fall velocity ratio w'_{si}/w_{si} provides a direct comparison between the fractional particle fall velocities within turbulent open channel flow and their corresponding fall velocities in still water conditions. Values of this non-dimensional fall velocity ratio clearly describe the relative degree of enhancement/ retardation of vertical particle motion with respect to still water fall velocity. Figure 4.25(b) plots the variation of $\langle w'_{si}\rangle/w_{si}$ with representative particle size d_i for the three flow regions considered, revealing a consistent trend of decreasing $\langle w'_{si}\rangle/w_{si}$ values as particle size d_i increases.

From the results presented in Table 4.7 and Figure 4.25, a number of trends indicated by the experiment-averaged $\langle w'_{si}\rangle$ values for LA sand are detailed below:

(1) *Near Bed Region* ($z/H < 0.2$) – $\langle w'_{si}\rangle$ values are higher than still water fall velocities w_{si} for all size fractions, but appear to converge for the coarsest fraction ($d_i = 462.5\mu m$). Corresponding values of $\langle w'_{si}\rangle/w_{si}$ range from ~1.1 for $d_i = 462.5\mu m$ up to ~1.9 for $d_i = 181\mu m$. This suggests that fall velocities in the near-bed turbulent flow are on average 10-90% higher than still water fall velocities (i.e. enhanced).

(2) *Intermediate Region* ($0.2 < z/H < 0.5$) – $\langle w'_{si}\rangle$ values are generally larger than still water fall velocities w_{si}, although this difference diminishes as d_i increases, with $\langle w'_{si}\rangle \sim w_{si}$ for $d_i \sim 390\mu m$. Corresponding $\langle w'_{si}\rangle/w_{si}$ values, ranging from ~0.8 ($d_i = 462.5\mu m$) up to ~1.7 ($d_i = 181\mu m$), are clearly lower than obtained in the near-bed flow.

(3) *Outer Region* ($z/H > 0.5$) – $\langle w'_{si}\rangle$ values are relatively constant for particle sizes d_i tested and are generally lower than still water fall velocity, with the exception of $d_i = 181\mu m$ particles where $\langle w'_{si}\rangle \sim w_{si}$. Corresponding $\langle w'_{si}\rangle/w_{si}$ values range from ~0.4 ($d_i = 462.5\mu m$) up to ~1.0 ($d_i = 181\mu m$), showing fall velocities to be generally hindered within the outer flow.

In summary, the level of enhancement (or retardation) in particle fall velocities within turbulent flow conditions appears to be primarily dependent on particle size d_i and vertical position within the flow z/H. Extensive tabulated and graphical results presenting measured turbulent fall velocities w'_{si} and corresponding values of the non-dimensional fall velocity ratio w'_{si}/w_{si} are provided in Appendix 4.9 for individual

Series 1B experiments. These results generally show similar trends to those observed for the experiment-averaged data (Table 4.7, Figure 4.25). A summary of the range of w'_{si}/w_{si} values obtained from the individual Series 1B experiments is presented in Table 4.8 below.

Experiment Number	z/H < 0.2	0.2 ≤ z/H < 0.5	z/H ≥ 0.5
S1B_EX1	2.74 – 1.61	2.65 – 1.10	1.48 – 0.58
S1B_EX2	1.52 – 1.08	1.68 – 0.69	0.85 – 0.46
S1B_EX3	2.19 – 1.08	1.44 – 0.98	0.57 – 0.33
S1B_EX4	1.97 – 1.06	1.44 – 0.80	0.78 – 0.18
S1B_EX5	1.64 – 0.76	1.45 – 0.59	0.98 – 0.47

Table 4.8 - Non-dimensional fall velocity ratios w'_{si}/w_{si} for LA sand fractions tested in Series 1B.

The influence of shear velocity u_* and bed configuration on w'_{si}/w_{si} within the three z/H regions is investigated in Figures 4.26 overleaf. Initial consideration of the data presented appears to reveal no clear definitive trends in the data. However, considering experiments S1B_EX1 and EX2 in isolation (i.e. uniform spheres), it is shown that higher w'_{si}/w_{si} values are obtained within each z/H region under the higher shear velocity condition (i.e. S1B_EX1, $u_* = 0.047 m.s^{-1}$). The difference between w'_{si}/w_{si} values for *'high'* and *'low'* shear velocities is largest for the finest $d_i = 181\mu m$ particles and generally decreases as d_i increases. In the outer flow region [$z/H \geq 0.5$, Figure 4.26(c)], only small differences are noted for the three coarsest fractions (d_i = 462.5, 390 and 327.5μm).

For experiments S1B_EX4 and EX5 (i.e. natural gravel bed), the influence of u_* is less apparent. Within the near-bed and intermediate flow regions, differences between w'_{si}/w_{si} values for '*high*' and '*low*' shear velocities [$u_* = 0.05 m.s^{-1}$ (S1B_EX4) and $0.04 m.s^{-1}$ (S1B_EX5), respectively] are generally smaller than observed over the bed of uniform spheres, and these differences vary inconsistently for different particle sizes d_i and z/H position. A general trend is revealed within the outer flow region, where w'_{si}/w_{si} values are typically lower for the higher value of u_* (i.e. S1B_EX4), but this trend appears to be in contradiction with the overall trend suggested by the S1B_EX1 and EX2 data.

The influence of bed material type on w'_{si}/w_{si} values, assessed through comparison of data sets in Figure 4.26 with similar hydraulic conditions [i.e.

S1B_EX1 and EX4 (H = 143mm; u_* = 0.047-0.05ms^{-1}) and S1B_EX2 and EX5 ((H = 93mm; u_* = 0.038-0.041m.s^{-1})], is also shown to be inconclusive.

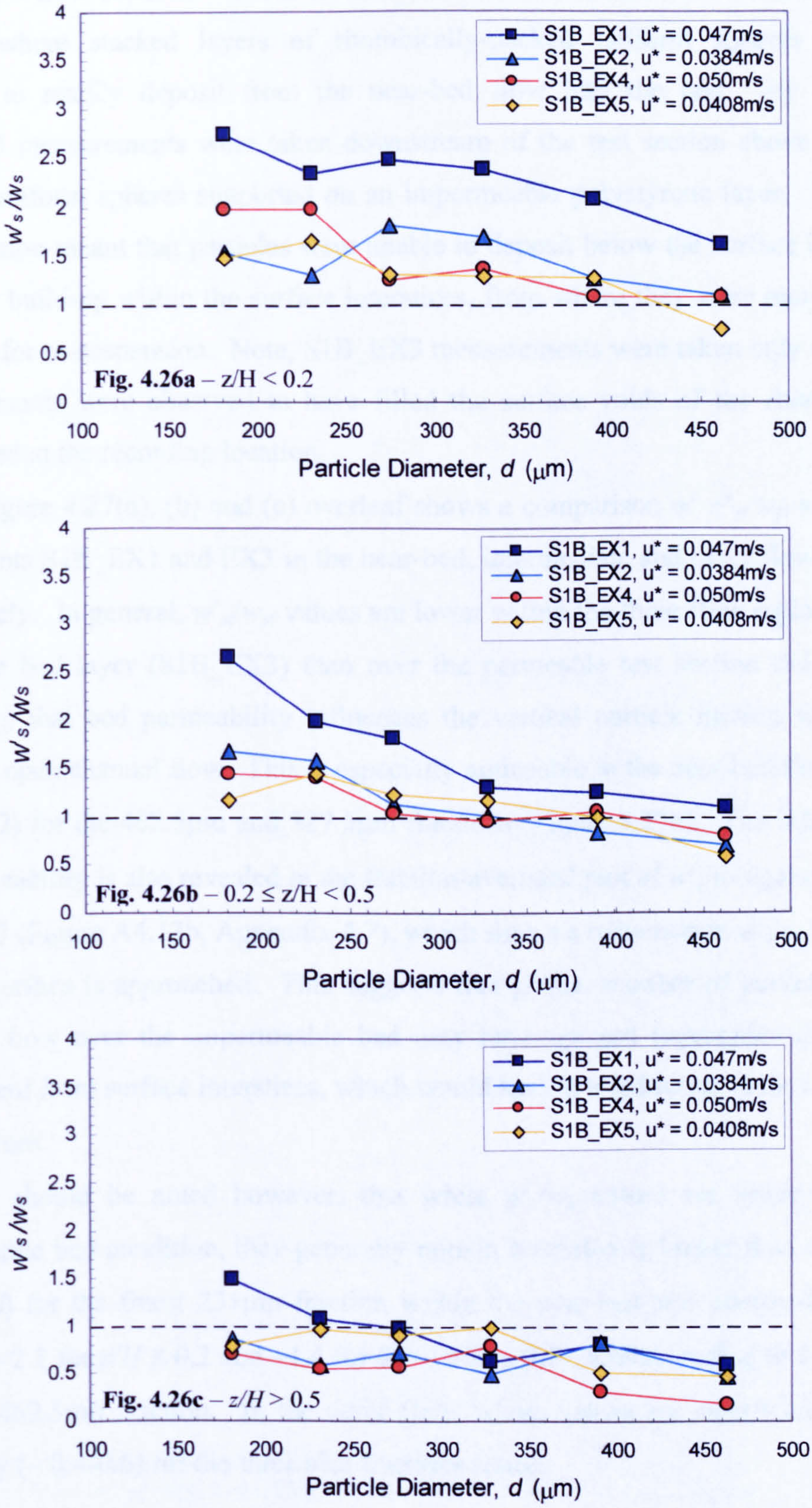

Figure 4.26 - Non-dimensional fall velocity ratio w'_{si}/w_{si} plotted against representative particle size d_i for different shear velocities u_* and bed material types.

The influence of bed permeability was assessed by comparing data from experiments S1B_EX1 and S1B_EX3, both of which were carried out over uniform spheres at a flow depth H = 143mm. S1B_EX1 measurements were taken at the test section, where stacked layers of rhombically-packed uniform spheres allowed particles to readily deposit from the near-bed flow into the bed. By contrast, S1B_EX3 measurements were taken downstream of the test section above a single layer of uniform spheres supported on an impermeable polystyrene layer. This bed configuration meant that particles were unable to deposit below the surface layer and tended to build-up within the surface interstices, from where they were more readily available for re-suspension. Note, S1B_EX3 measurements were taken only when the fine sediments were observed to have filled the surface voids of the rhombically-packed bed at the recording location.

Figure 4.27(a), (b) and (c) overleaf shows a comparison of w'_{si}/w_{si} values for experiments S1B_EX1 and EX3 in the near-bed, intermediate and outer flow regions, respectively. In general, w'_{si}/w_{si} values are lower within the three flow regions above the single bed layer (S1B_EX3) than over the permeable test section (S1B_EX1), suggesting that bed permeability influences the vertical particle motion within the turbulent open channel flow. This is especially noticeable in the near-bed flow region ($z/H \leq 0.2$) for the 462.5μm and 327.5μm fractions (Figure 4.27a). The influence of bed permeability is also revealed in the fraction-averaged plot of w'_s/u_* against z/H for S1B_EX3 (Figure A4.13b, Appendix 4.7), which shows a reduction in w'_s/u_* values as the bed surface is approached. This suggests that greater number of particles in the near-bed flow over the impermeable bed may have upward trajectories due to re-entrainment from surface interstices, which would lead to a reduction in the computed w'_s/u_* values.

It should be noted however, that while w'_s/w_s values are lower over the impermeable bed condition, they generally remain consistently higher than unity (i.e. *enhanced*) for the finest 231μm fraction within the near-bed and intermediate flow regions (~2.2 for $z/H \leq 0.2$ and ~1.4 for $0.2 < z/H \leq 0.5$), whilst tending to 1.0 for the coarsest 462.5μm fraction. In the outer flow, w'_s/w_s values are significantly lower than unity (~ 0.4-0.6) for the three size fractions tested.

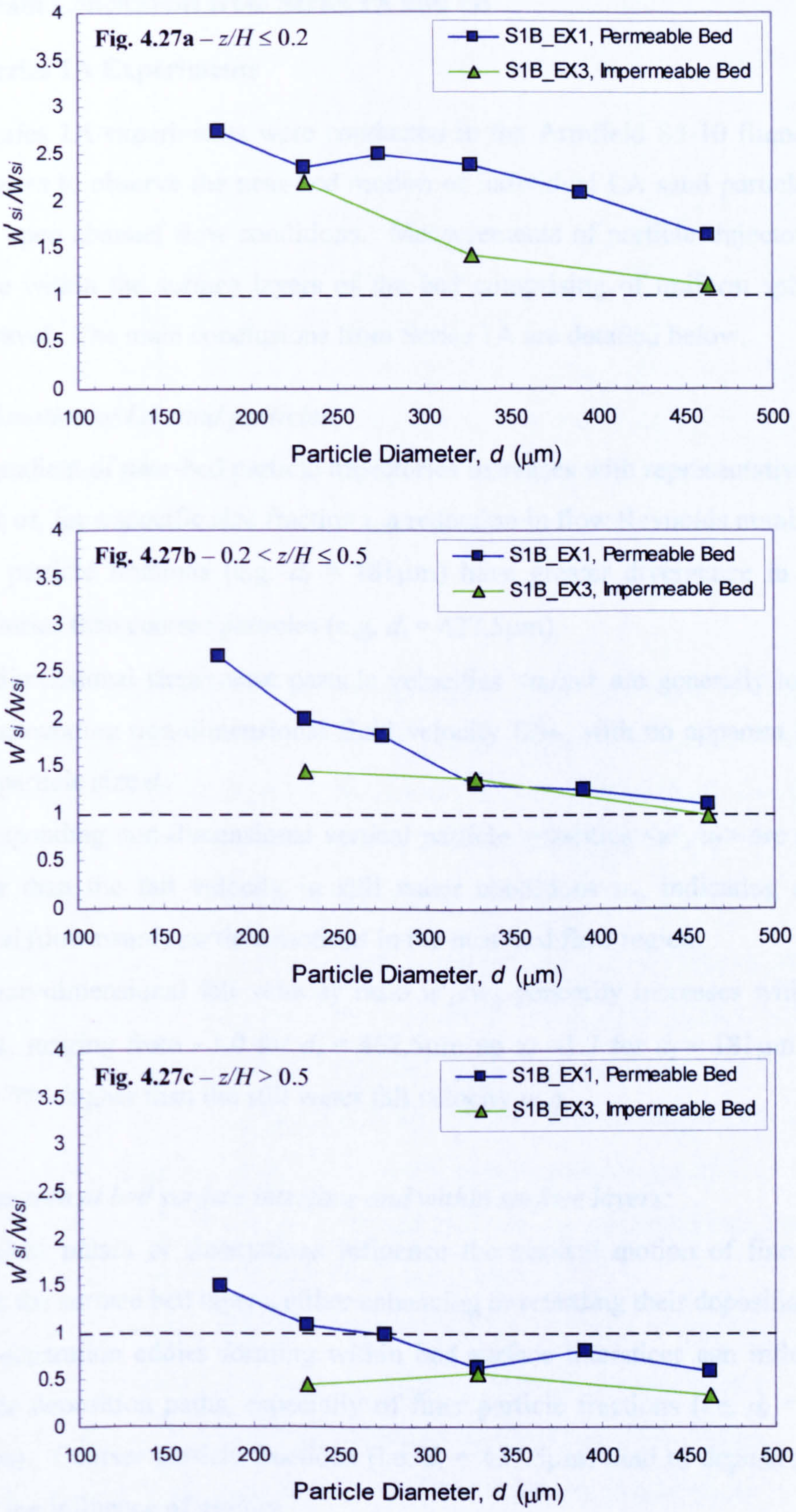

Figure 4.27 - Non-dimensional fall velocity ratio w'_{si}/w_{si} plotted against particle size d_i, illustrating the influence of bed permeability on the vertical motion of LA sand fractions within the three z/H flow regions.

4.5 Main Conclusions from Series 1A and 1B

4.5.1 Series 1A Experiments

Series 1A experiments were conducted in the Armfield S5-10 flume using a video camera to observe the near-bed motion of individual LA sand particles within turbulent open channel flow conditions. Measurements of particle trajectories were also made within the surface layers of the bed comprising of uniform spheres and natural gravel. The main conclusions from Series 1A are detailed below.

Near-bed motion of LA sand particles:

- The gradient of near-bed particle trajectories increases with representative particle size d_i or, for a specific size fraction i, a reduction in flow Reynolds number R_e.
- Finer particle fractions (e.g. d_i = 181μm) have greater divergence in near-bed trajectories than coarser particles (e.g. d_i = 427.5μm).
- Non-dimensional streamwise particle velocities $<u_s/u_*>$ are generally lower than the surrounding non-dimensional fluid velocity U/u_*, with no apparent influence from particle size d_i.
- Corresponding non-dimensional vertical particle velocities $<w'_s/u_*>$ are generally higher than the fall velocity in still water conditions w_s, indicating *enhanced* vertical (downward) particle motions in the near-bed flow region.
- The non-dimensional fall velocity ratio w'_{si}/w_{si} generally increases with particle size d_i, ranging from ~1.0 for d_i = 462.5μm up to ~1.7 for d_i = 181μm particles (i.e. ~70% higher than the still water fall velocity w_{si}).

Particle motion at bed surface interface and within surface layers:

- Turbulent pulses or fluctuations influence the vertical motion of fine particles within the surface bed layers, either enhancing or retarding their deposition.
- Flow-separation eddies forming within bed surface interstices can influence the particle deposition paths, especially of finer particle fractions (i.e. d_i = 181 and 231μm). Coarser particle fractions (i.e. d_i = 427.5μm) tend to deposit primarily under the influence of gravity.
- Some depositing particles are observed to 'shelter' in the lee side of bed elements, remaining virtually stationary for an extended period (~1 sec.) before depositing further into the bed.

- Three principal modes of re-entrainment are generally observed for particles at the bed surface interface: (i) entrapment and ejection from flow-separation eddies formed in surface interstices; (ii) deflection off an expanding flow-separation eddy; and (iii) ricochet off the upstream face of a bed element.
- The probability of deposition p increases with particle size d_i, ranging from ~0.6-0.7 for d_i = 181μm particles up to ~0.7-0.8 for d_i = 427.5μm particles, with the lower values corresponding to higher shear velocity u_*.
- The non-dimensional deposition velocity ratio w_{di}/w_{si} varies between ~0.8 for 427.5μm particles, increasing with reducing particle size d_i up to ~1.25 for 181μm particles. This indicates enhanced depositional characteristics for finer particles and hindered deposition for the coarser particles.

4.5.2 Series 1B Experiments

Series 1B experiments were also conducted in the S5-10 flume using a high-speed camera and particle tracking technique to record and measure the typical streamwise and vertical motions of the individual LA sand fractions turbulent open channel shear flows over beds of uniform spheres and natural gravel. The main findings from Series 1B are summarised below.

- Streamwise particle velocities u_{si}/u_* are often close to the surrounding streamwise fluid velocity (U/u_*) and generally lie within $(U \pm u'_{rms})/u_*$, with no clear trend shown between different particle sizes d_i.
- Within the near-bed flow region ($z/H \leq 0.2$), fractional-averaged u_s/u_* values are typically lower than U/u_* values, especially over the natural gravel bed.
- Fractional-averaged vertical particle velocities w'_s/u_* are highest adjacent to the bed surface and generally reduce with increasing z/H.
- Distributions of w'_s/u_* with z/H have similar characteristics to the fluid turbulence intensity distributions (u'_{rms}/u_* and w'_{rms}/u_*), although the near-bed reductions in u'_{rms}/u_* and w'_{rms}/u_* values are not generally replicated in w'_s/u_* values.
- Standard deviations $\sigma(u_s/u_*)$ and $\sigma(w'_s/u_*)$ are similar in magnitude to local values of fluid turbulence intensity (u'_{rms}/u_* and w'_{rms}/u_*), both of which generally decrease with increasing z/H.

- In the near-bed flow, fractional values of vertical particle velocity w'_{si}/u_* are generally highest for the larger particle sizes (i.e. d_i = 462.5 and 390μm), whereas in the outer flow, less distinction is observed between w'_{si}/u_* values.
- Overall, for individual LA sand fractions, turbulent fall velocities w'_{si} generally increase with grain size up to d_i = 390μm before stabilising or even slightly reducing for the coarsest 462.5μm size fraction.
- In the near-bed flow ($z/H \leq 0.2$), the non-dimensional fall velocity ratio $\langle w'_{si} \rangle / w_{si}$ is significantly greater than 1 for the finest 181μm particles, reducing with particle size d_i to around unity for the coarsest 462.5μm particles. This suggests that finer particle settling in the near-bed turbulent flow is generally enhanced over settling in still water conditions whereas coarser particles tend to settle under gravity.
- In the intermediate flow ($0.2 < z/H \leq 0.5$), $\langle w'_{si} \rangle / w_{si}$ values again reduce with increasing d_i, with $\langle w'_{si} \rangle / w_{si} > 1$ (i.e. enhanced fall velocities) for particle sizes below d_i = 390μm and $\langle w'_{si} \rangle / w_{si} < 1$ for the coarsest d_i = 462.5μm particles (i.e. hindered fall velocities).
- In the outer flow region ($z/H > 0.5$), $w'_{si} / w_{si} \leq 1$, typically, decreasing with d_i from around unity for d_i = 181μm particles to values significantly lower than 1 for the coarser particle fractions (i.e. increasingly hindered fall velocities).
- The influence of the shear velocity u_* and the bed material type on w'_{si} / w_{si} values remain inconclusive. However, w'_{si} / w_{si} values were found to reduce, for near-bed particle trajectory measurements in particular, over a single layer of uniform spheres supported on an impermeable polystyrene layer (i.e. S1B_EX3) in comparison measurements over the porous test section (i.e. S1B_EX1). This suggests that bed configuration and the ability for particles to deposit into the bed influences near-bed particle trajectories.

CHAPTER 5

Flow Visualisation Experiments (Series 1C)

5.1 Introduction

Series 1A and 1B experiments have indicated that the vertical motion of individual LA grade sand fractions can exhibit enhanced fall velocities in turbulent open channel shear flows over porous bed configurations compared to their fall velocity in still water conditions. The main findings from Series 1B suggest that the degree of enhancement is greatest in the near-bed flow ($z/H \leq 0.2$) for the finer size fractions (i.e. $d_i = 181$ and $231\mu m$) and generally decreases with increasing grain size d_i and relative depth z/H above the bed surface.

This chapter details additional visualisation experiments conducted to observe the flow structure over a porous bed of coarse, well-sorted gravel, as well as their influence on the motion of LA sand particles within the open channel shear flow. The objectives of these experiments are as follows,

- To highlight the existence and determine typical characteristics of coherent turbulent structures present within the open channel shear flow.
- To study typical interactions that exist between individual LA sand fractions and these coherent structures with the aim of highlighting possible mechanisms responsible for the enhanced fall velocities previously noted.

For this purpose, a camera system was developed whereby the seeded flow and sediment particles were recorded in an illuminated section of the open channel flow by a digital video camera mounted on a mobile frame, allowing the camera to move in the streamwise flow direction. This allowed Lagrangian characteristics of the coherent flow structures and their interaction with the sand particles to be monitored.

5.2 Experimental Set-up and Conditions

These additional flow visualisation experiments (Series 1C) were again carried out in the Armfield S5-10 flume under steady, uniform flow conditions. The flume bed was covered by a layer of natural gravel (D_{50} = 17.3mm; σ_g = 1.31) on average about 40mm thick. The experiments were conducted at a bed slope of 0.004 and at flow depths of 93mm and 143mm as in Series 1B. The flume was extended to 6.2m in length (§3.4.1.2, pp.60) to provide more stable flow conditions at the upstream end and a greater working section length in which measurements could be made.

The flow visualisation technique used a 1m-long halogen (500W) light rig to illuminate a thin 5mm wide vertical slice of the open-channel flow as shown in Figure 3.13 (pp.75). The lateral position of this illuminated slice could be varied and recordings were generally made at y/B = 0.1, 0.2, 0.33 and 0.5 from the near side flume wall. As the longitudinal position of the lighting rig could also be varied along the working length of the flume, video recordings were made in each of the four perspex windows between supports (Figure 3.1, pp.53).

A total of four visualisation experiments were carried out in Series 1C (S1C_EX1 – EX4). Initially, recordings were made in the absence of LA sand particles with the flow seeded with Dantec neutrally buoyant 50μm polyamid particles to highlight coherent turbulent structures present within the illuminated flow (S1_EX1 and EX2). Then, under the same hydraulic conditions, the six individual LA sand fractions were released into the flow at a free surface location upstream of the illuminated flow region. This allowed the interaction between the different sized sand particles and coherent flow structures to be observed (S1_EX3 and EX4). Table 5.1 below provides a summary of the main experimental parameters used in Series 1C.

Experimental Parameters	S1C_EX1	S1C_EX2	S1C_EX3	S1C_EX4
Flow Depth, H (m)	0.093	0.143	0.093	0.143
Bed Slope, S_o	0.004	0.004	0.004	0.004
Discharge, Q ($\ell.s^{-1}$)	0.010	0.022	0.010	0.022
Average Velocity, $\bar{U}$ (ms^{-1})	0.36	0.51	0.36	0.51
Froude Number, F_r	0.38	0.43	0.38	0.43
Fine Material Type	50μm Seeding only	50μm Seeding only	50μm Seeding + LA fractions	50μm Seeding + LA fractions

Table 5.1 – Main experimental parameters for Series 1C experiments.

Recordings were made with a JVC GR-DVL9000 digital video camera operating at 25 fps, a shutter speed of 0.02 sec., and a maximum resolution of 320×240 pixels. The camera was mounted in a frame attached to a trolley system, which allowed it to be moved along the 1m length of illuminated flow at a constant speed approximately equal to the average flow velocity (Figure 3.13, pp. 75). In general, up to 20 individual recordings of the illuminated, seeded flow were made at each location within the working section of the flume and, for experiments with LA sand, every individual size fraction d_i tested at each of these locations.

The images stored on the digital video camera were transferred to a PC through an image capture software package called Asymetrix Video Capture. This enabled sequenced groups of images to be linked in 'stacks' and analysed using the Scion Image software package. An image processing software package, Paint Shop Pro V4.0, was also used to enhance many of the individual images presented herein.

5.3 Experiments with Neutrally Buoyant Particles

With steady, uniform flow conditions set up within the flume, a quantity of seeding material was added at the downstream sump tank and allowed to re-circulate until evenly distributed throughout the flow. The vertical extent of the camera view field was generally set to record the lower region of seeded flow extending from the bed surface to an elevation equivalent to $3D_{84}$ (z = 60-65mm), although images of the full flow depth were also recorded.

Recordings of the illuminated flow field at the various longitudinal and lateral positions within the working section revealed the presence of large-scale coherent structures within the flow, the typical characteristics of which are described in some detail in the subsequent section. Individual snapshot images of these structures along with schematic representations of the flow streamlines around and in the vicinity of these structures are presented. These schematic representations were developed from the analysis of grouped 'stacks' of up to 25 sequenced images (i.e. up to ~1 sec. real-time) using the Scion Image package.

5.3.1 Observed Coherent Flow Structures

Snapshot images of coherent flow structures obtained from the moving camera system are presented in Figures 5.1 and 5.2 for recordings made during experiments

S1C_EX1 and EX2, respectively. These images clearly reveal that the turbulent structure of the seeded flow is characterised by the presence of large-scale coherent vortices. These vortices were often observed to occur in pairs or groups, each with the same rotational sense (anti-clockwise) for the mean flow direction moving from right to left within each frame. Analysis of image 'stacks' suggests that the vortices originate in the near-bed region, possibly resulting from flow separation within the surface interstices of the coarse gravel bed.

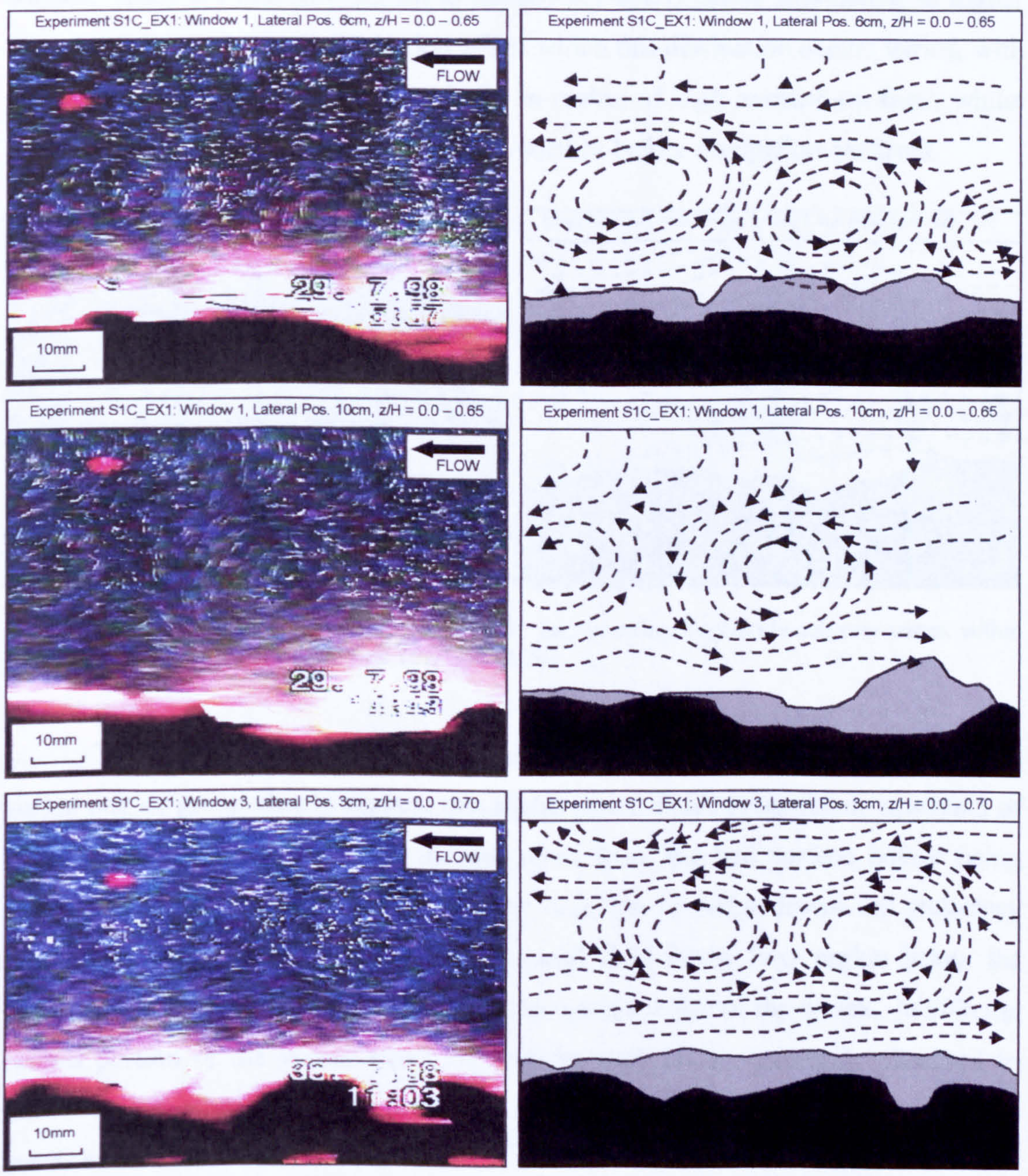

Figure 5.1 – Snapshot images from experiment S1C_EX1 showing large-scale coherent vortices within the illuminated flow field ($z/H \leq 0.65$-0.70). Schematic representations of the flow field obtained from analysis of image stacks are also shown.

Previous observations from Series 1A revealed the presence of flow-separation eddies within bed surface interstices. These eddies had the same rotational sense as the large-scale coherent vortices shown in Figure 5.1 and 5.2 and were found to exert an influence on the motion of depositing particles and could result in finer particles being re-entrained.

Recordings in Series 1C also suggest that the vortices expand in size within the near-bed flow region as they move away from the bed in the direction of the free surface. They are typically shown to occupy 0.1-0.4H, before dissipating in higher momentum outer flow. The elevation z/H at which this dissipation occurs varied, with some vortices being destroyed quickly by in-rushes of high momentum fluid, whilst others were found to rise almost to the free-surface before dissipation occurred.

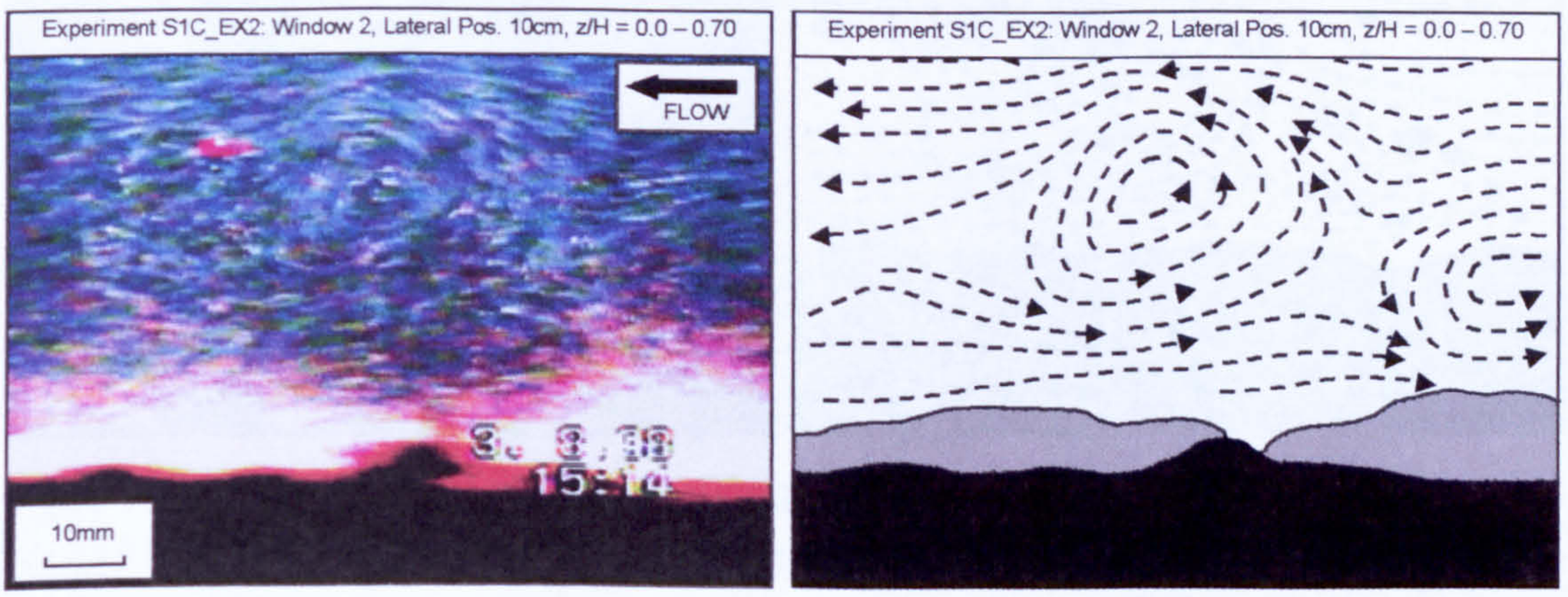

Figure 5.2 – Example image from experiment S1C_EX2 showing large-scale coherent vortex within the illuminated flow field (z/H up to 0.70).

The schematic representations of the flow field surrounding an isolated vortex, vortex pair or group clearly suggest that higher speed fluid, immediately upstream of the vortex is generally deflected upward away from the bed surface before being pulled around the perimeter of the vortex core into a steep downward trajectory towards the bed. At the same time, low-speed fluid in the flow region below the vortex is drawn away from the bed around the upstream side of the vortex. Within the central portion of the vortex structure, seeding particles are generally observed to follow closed orbits, with only a few particles appearing to be trapped at the very centre of the vortex core.

These observations would clearly suggest that the development and rise of a vortex away from the bed surface may be inherently related to the interaction of the faster moving outer flow fluid and slower moving near-bed flow.

A further snapshot image of a typical interaction between the high and low momentum flows is shown in Figure 5.3 below. This appears to show a sequence of small vortices form along an interface (inclined at ~20° to the bed) between high momentum outer fluid and low momentum near-bed fluid. These vortex structures seem to develop from the outward expansion of the low momentum fluid, in turn causing the high momentum outer fluid to deflect upward away from the bed. As the low momentum flow continues to rise, the vortex structures generally appear to expand and dissipate, occasionally followed by an in-rush of the released high momentum fluid towards the bed surface.

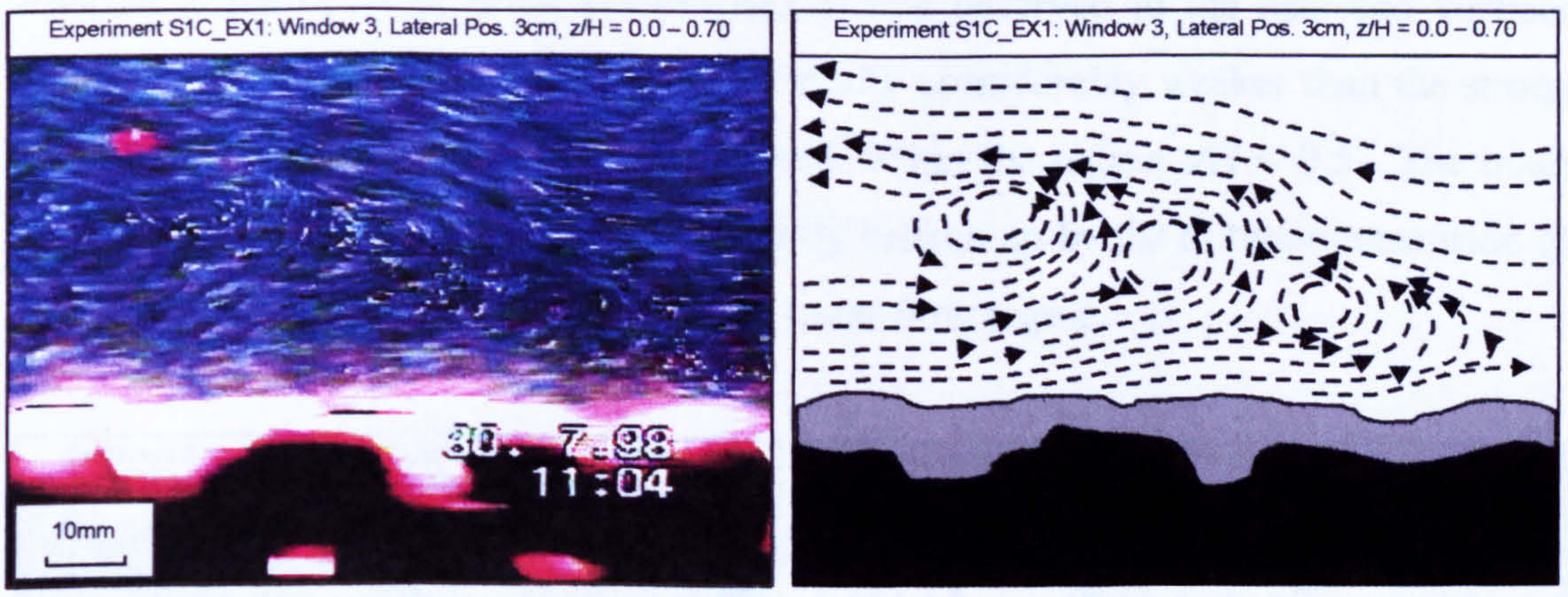

Figure 5.3 – Example image showing the interation of low momentum fluid in the near-bed flow region and higher momentum fluid in the outer flow.

Whilst it is acknowledged that the characteristics of the observed vortex structures are continually changing with time, typical measurements of their longitudinal and vertical diameters (ϕ_x and ϕ_z) and estimations of their rotational velocity (Ω_0) were made from calibrated images using the Scion Image software package. It was generally found that the vortices are elliptical rather than spherical in shape with the major axis lying on or slightly inclined to the horizontal plane. Typical dimensions of these visualised structures ranged from ϕ_x = 25-50mm and ϕ_z = 15-30mm, although smaller vortices (ϕ ~ 10mm) such as those shown in Figure 5.3 were also noted. The ratio of horizontal to vertical dimension ϕ_x/ϕ_z generally ranged between 1.25-1.70, with an average value of about 1.45.

The rotational frequency Ω was estimated for a small number of the observed vortices from the measurement of streak lengths, divided by the camera shutter speed (0.02sec.) and the distance to the estimated centre of the vortex. It should be noted

that these measurements assume the vortex core rotates as a rigid spherical body with constant rotational frequency Ω and that the instantaneous tangential velocity U_r is directly proportional to the distance from the centre of the vortex r (i.e. a *forced* vortex). This is clearly not the case as firstly, the vortices are elliptical in shape, and secondly, their size and strength are constantly changing with time. The resulting values of Ω, which should therefore be regarded as purely indicative, ranged from about 2.8-7.3 sec^{-1}, with an average value of about 5.6 sec^{-1}.

The dominant flow structure of the near-surface flow was less apparent. The images 'stacks' recorded over the full flow depth appear to show an overall fluid rotation in the opposite sense (clockwise) to that observed in the near-bed vortices (Figure 5.4). These fluid rotations are generally considerably weaker than the strong vorticity of the large-scale vortices observed within the region $z/H < 0.5$. The outer flow rotations also appear to be intermittently broken up by the outward expansion of the near-bed low momentum flow into the outer flow region.

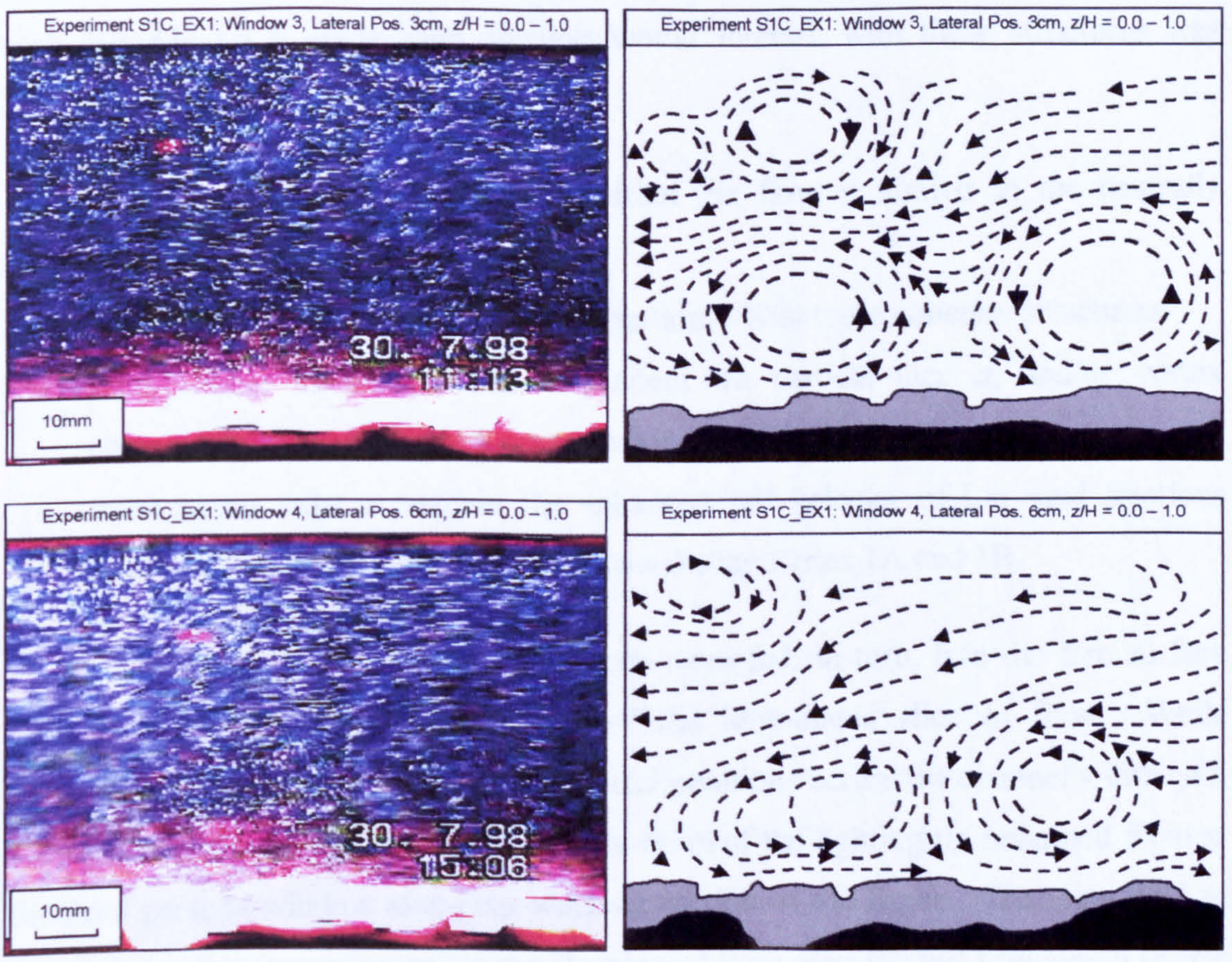

Figure 5.4 – Images showing examples of typical flow fields for full flow depth (S1C_EX1)

It is thought that the development of these weaker fluid rotations in the near-surface flow may originate from the low aspect ratio ($\alpha = y/B$ = 2.1-3.2) of the flow and the corresponding reduction in the streamwise flow velocity at the free surface (i.e. velocity-dip phenomenon).

Overall, the characteristics of the coherent structures observed within the flow were found to be similar for the two experimental conditions used (H = 93mm and 143mm). The longitudinal and lateral position of the illuminated flow region within the working section of the flume also appeared to have little influence on the form and nature of these coherent vortices. A number of individual images of the visualised flow are contained within Appendix 5.1 for experiments S1C_EX1 and EX2. A more detailed discussion of the visualised flow structures is given in Chapter 7.

5.4 Experiments with LA Grade Sand Fractions

Having identified the presence of large-scale coherent vortices within the illuminated, seeded open channel flow over a coarse gravel bed, understanding how each individual LA grade sand fraction would interact with these structures was sought by studying whether,

- the motion of LA sand particles within the flow is similar to the neutrally buoyant seeding material.
- LA sand particles have a 'preferred' motion within these coherent structures.
- fluid-particle interactions are dependent on particle size d_i and/or vortex characteristics such as size $\phi_{x,z}$ or rotation velocity Ω.
- mechanisms exist to explain the enhanced fall velocity of LA sand fractions observed in turbulent open channel flow during Series 1A and 1B.

The six individual LA sand fractions were fed, in turn, into the free surface flow at a calibrated position upstream of the illuminated slice of flow. While recordings were again made at the four lateral positions across the channel width (y/B = 0.1, 0.2, 0.33 and 0.5), the longitudinal position of the lighting rig remained fixed at the third perspex window along the working section of the flume. The view field of the digital video camera recorded the illuminated flow over the full flow depth (z/H = 0.0 - 1.0) for experiment S1C_EX3 (H = 93mm) and over the flow region defined by $z/H \leq 0.75$ for experiment S1C_ EX4 (H = 143mm).

As with the seeded flow experiments, image 'stacks' of up to 25 frames (~1 sec. real time) were obtained from the video recordings and analysed using Scion Image. Selected individual snapshot images showing typical particle-vortex interactions are presented as figures herein.

5.4.1 Observed Particle-Vortex Interactions

The recorded images reveal that each of the six fractions of LA grade sand interact to a lesser or greater extent with coherent vortex structures whilst in the process of settling towards the bed surface. The degree of interaction appears to be dependent on particle size d_i and vortex characteristics $\phi_{x,z}$ and Ω. In general, less frequent interactions occur for coarser particle fractions (i.e. d_i = 462.5 and 390μm), which are most often observed to settle primarily under the influence of gravity. The influence of vortices on the motion of sand particles appears to increase with reducing particle size d_i and with increasing vortex strength Ω.

Individual images obtained from the moving camera system are presented in Figures 5.5 and 5.6 for experiments S1C_EX3 and S1C_EX4, respectively. These figures reveal typical characteristics of the particle-vortex interactions observed. Further snapshot images obtained from the video recordings are presented in Appendix 5.2.

Figures 5.5 and 5.6 reveal that similar particle-vortex interactions are observed for virtually all size fractions, with only the trajectories of the coarsest d_i = 462.5μm particles remaining relatively unaffected.

In general, groups of particles appear to be transported in high momentum fluid within the outer flow region, from which they typically approach a slower-moving vortex structure on the upstream side and from above. The resulting particle-vortex interaction commonly results in particles being gathered into similar trajectory paths or orbits around the top periphery of the vortex core. In interactions where the vortex is observed to be rising within the flow and/or expanding in size, particles approaching the vortex structure from the upstream side are often deflected upward prior to being pulled into orbit around the top of the vortex. A similar characteristic was also observed in the seeded flow experiments, where high momentum fluid upstream of the expanding vortex was deflected upward around the top of the coherent structure.

In following their orbital paths around the top periphery of the vortex core, the particle groups are pulled around into a steep downward trajectory on the downstream (downward flow) side of the vortex. This observed motion appeared to transfer the particles rapidly from the high-momentum fluid above the vortex to low-momentum fluid in the flow region below the vortex structure.

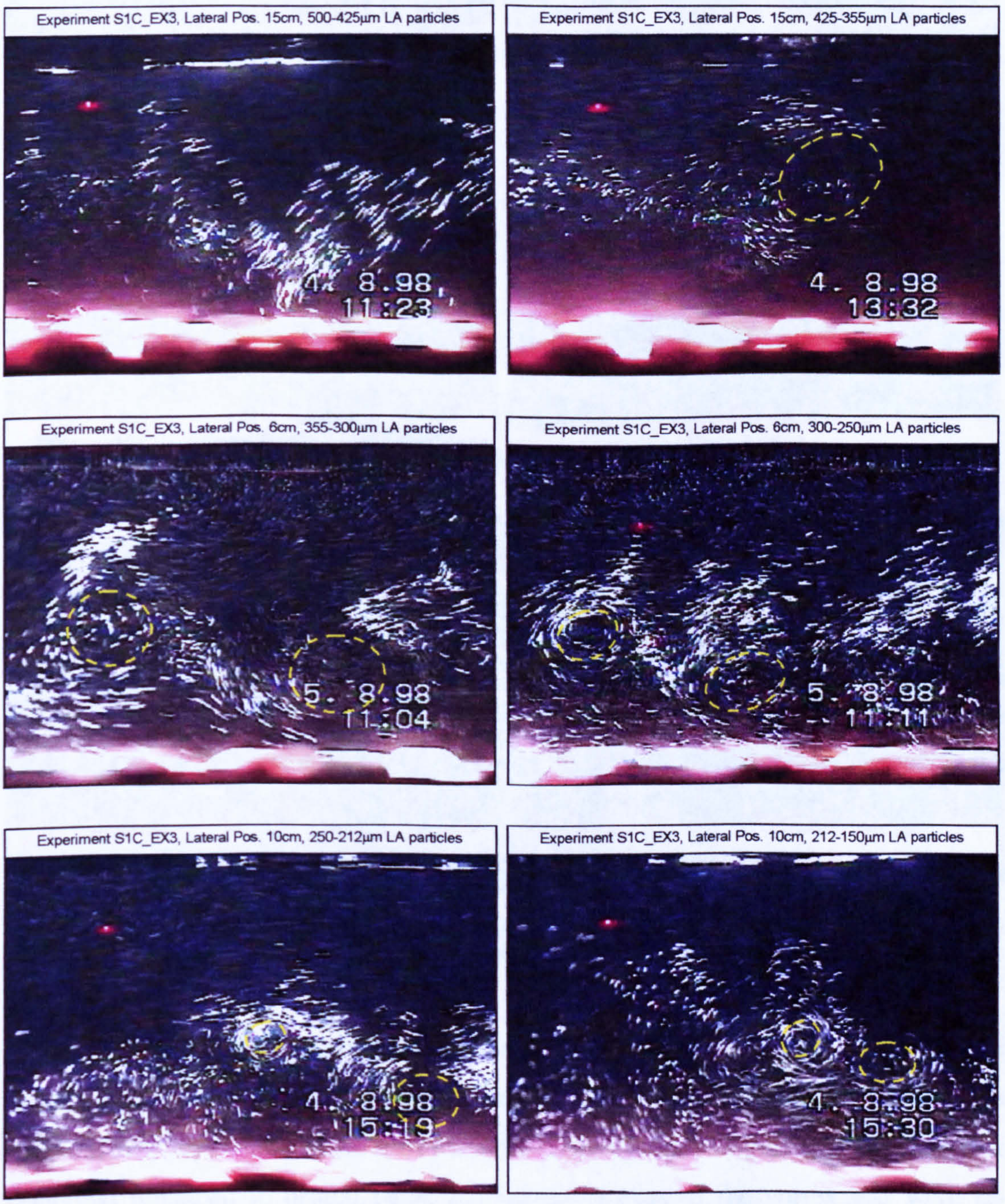

Figure 5.5 – Images from experiment S1C_EX3 (H = 93mm) showing interactions between individual LA grade size fractions and large-scale vortex structures.

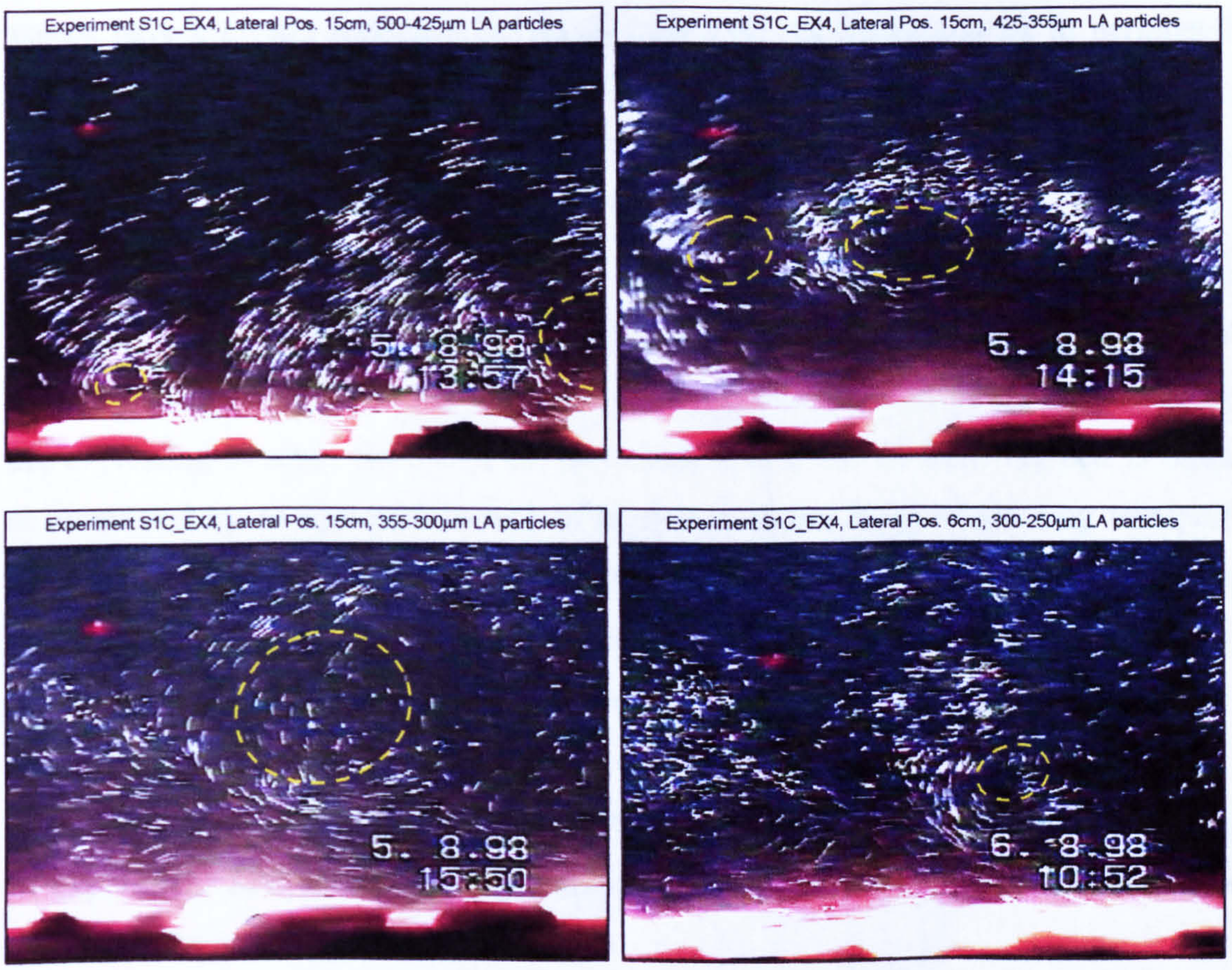

Figure 5.6 – Images from experiment S1C_EX4 (H = 143mm) showing interactions between individual LA grade size fractions and large-scale vortex structures.

The bulk of the particles transported on the down-flow side of the vortex appear to be shed from their orbital paths in the low-momentum flow beneath the eddy. However, a small number of particles (although more significant for finer size fractions) remained in orbital paths around the bottom of the vortex and were re-entrained on the upstream (upward flow) side, thus keeping them in suspension for an extended period. The number re-entrained also appears to increase with the rotation velocity Ω. It is also apparent that particles in orbital paths closest to the centre of the

vortex have a greater tendency to remain in suspension than particles in peripheral orbits. Particles shed from beneath the vortex core are often observed to interact with the down-flow side of neighbouring upstream structures, although others appear to deposit directly into the gravel bed.

The expansion, rise and dissipation of a vortex structure from the near-bed flow may also have an important role in fluid-particle interactions. Firstly, particle shedding from vortex structures appears to increase on occasions where the structures are expanding in size. Secondly, the detachment of a vortex from the bed is often accompanied by an upstream in-rush of high-momentum fluid, which may transport particles in a steep trajectory towards the bed surface. Thirdly, detached vortices generally dissipate relatively quickly in the outer flow and often as a result of being 'drowned-out' by an in-rush of high momentum fluid. This will result in the release of any particles trapped within the vortex core.

Figure 5.7 below shows a snapshot image obtained from the video recordings of experiment S1C_EX3, detailing some of the important fluid-particle interactions discussed above.

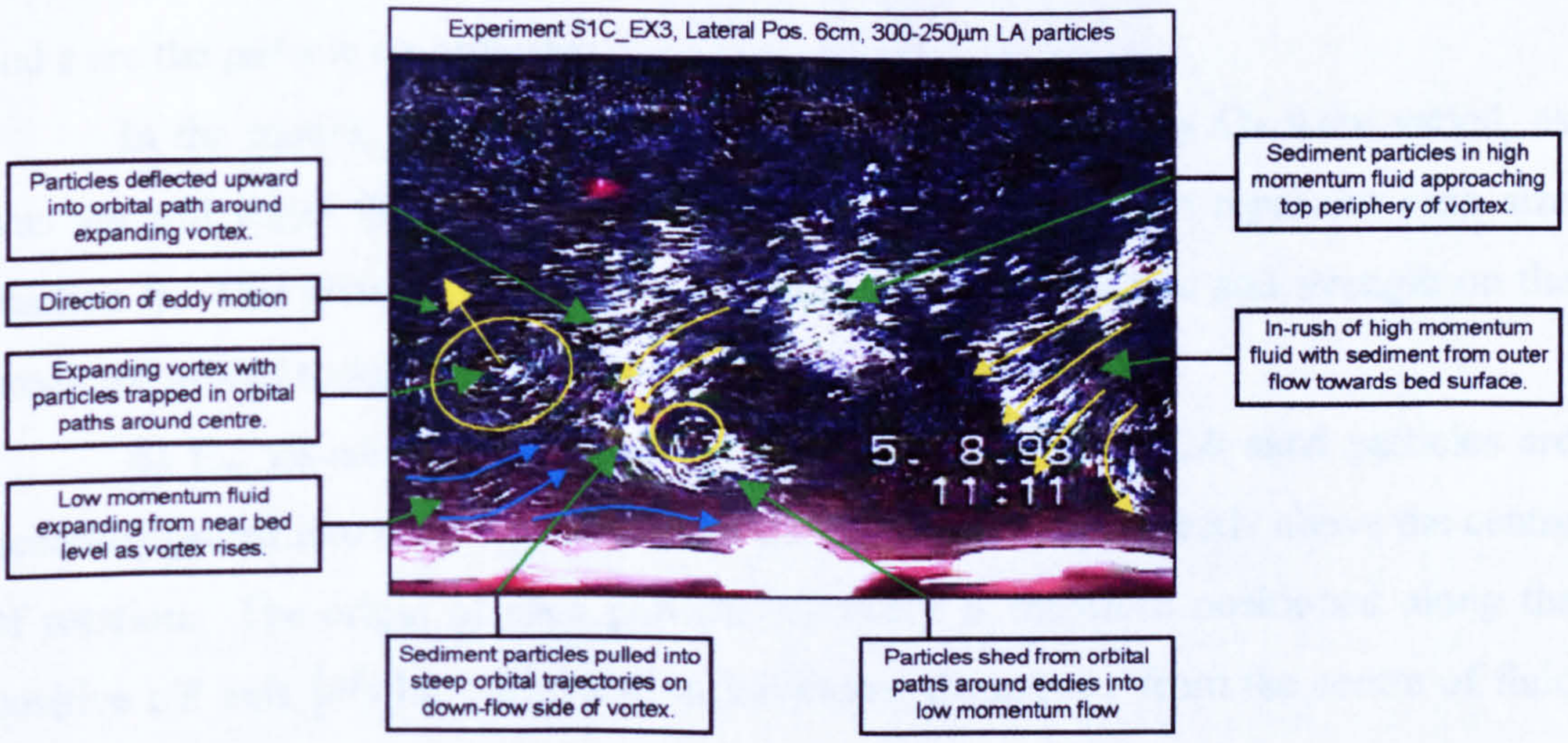

Figure 5.7 – Image describing typical interactions between the large-scale coherent vortices and d_i = 275µm LA sand particles.

5.4.2 Rankine Vortex Model

A simple model was developed in Excel to demonstrate the predicted orbital trajectories of settling sand particles interacting with a vortex structure. This model is based on a zero-order approach in which the fluid accelerations are neglected and the relative velocity between the particles and the fluid is equal to the still water fall

velocity w_s. Based on these assumptions, the motion of a sediment particle in the XZ fluid domain can be described by the equation (Nielsen 1984),

$$\vec{u}_s(x,z) = \vec{u}(x,z) + w_s(0,z) \qquad \text{....(5.1)}$$

where $\vec{u}_s(x,z)$ is the particle velocity components in the XZ plane, $\vec{u}(x,z)$ is the fluid velocity components and $w_s(0,z)$ is the still water fall velocity of the particles.

A reasonable representation of the flow field of a natural vortex is given by the theoretical Rankine vortex (Nielsen 1984). The characteristics of this model are that the inner vortex core rotates as a rigid body, with the instantaneous fluid velocity proportional to the distance from the centre. Further away from the centre, the flow velocity becomes inversely proportional to this distance. The equation defining the velocity field of the Rankine vortex is as follows,

$$\vec{u}(x,z) = \frac{-\Omega_0 R}{1 + (x/R)^2 + (z/R)^2} \begin{pmatrix} -z/R \\ x/R \end{pmatrix} \qquad \text{....(5.2)}$$

where Ω_0 is the rotation frequency, R is the characteristic radius of the vortex and x and z are the particle co-ordinates.

In the model, the vortex radius R and rotation frequency Ω_0 were varied, as was the still water fall velocity of the sand particles w_s (i.e. to represent each size fraction i). This allowed the relative influence of the vortex size and strength on the predicted orbital trajectories of each size fraction to be assessed.

As the visualised particle-vortex interactions revealed, LA sand particles are generally pulled into orbital paths around the top of the eddy, directly above the centre of rotation. The origin of each particle trajectory is therefore positioned along the positive z/R axis $[\vec{u}(x) \leq 0, \vec{u}(z) = 0]$ at increasing distances r from the centre of fluid rotation (0,0).

Figure 5.8 illustrates the predicted trajectories of d_i = 181, 275 and 462.5μm particles in the Rankine vortex flow field with characteristic radius R = 12.5mm and rotation frequency $\Omega_0 = 5.6\text{sec}^{-1}$. These characteristics were assumed to represent the average values of size and strength for vortices observed in the visualised flow. The typical shape of the velocity distribution for the Rankine flow field (equation 5.2) is also shown. Clearly, the degree of interaction exhibited between the particles and the

vortex is dependent on particle size d_i. The predicted settling trajectories of the 462.5μm particles appear to have little interaction with the rotating velocity field of the Rankine vortex, showing only a very limited tendency to form orbital paths on the down-flow size of the vortex before settling out. This limited degree of particle-vortex interaction for the coarsest LA sand particles is also indicated in experimental observations.

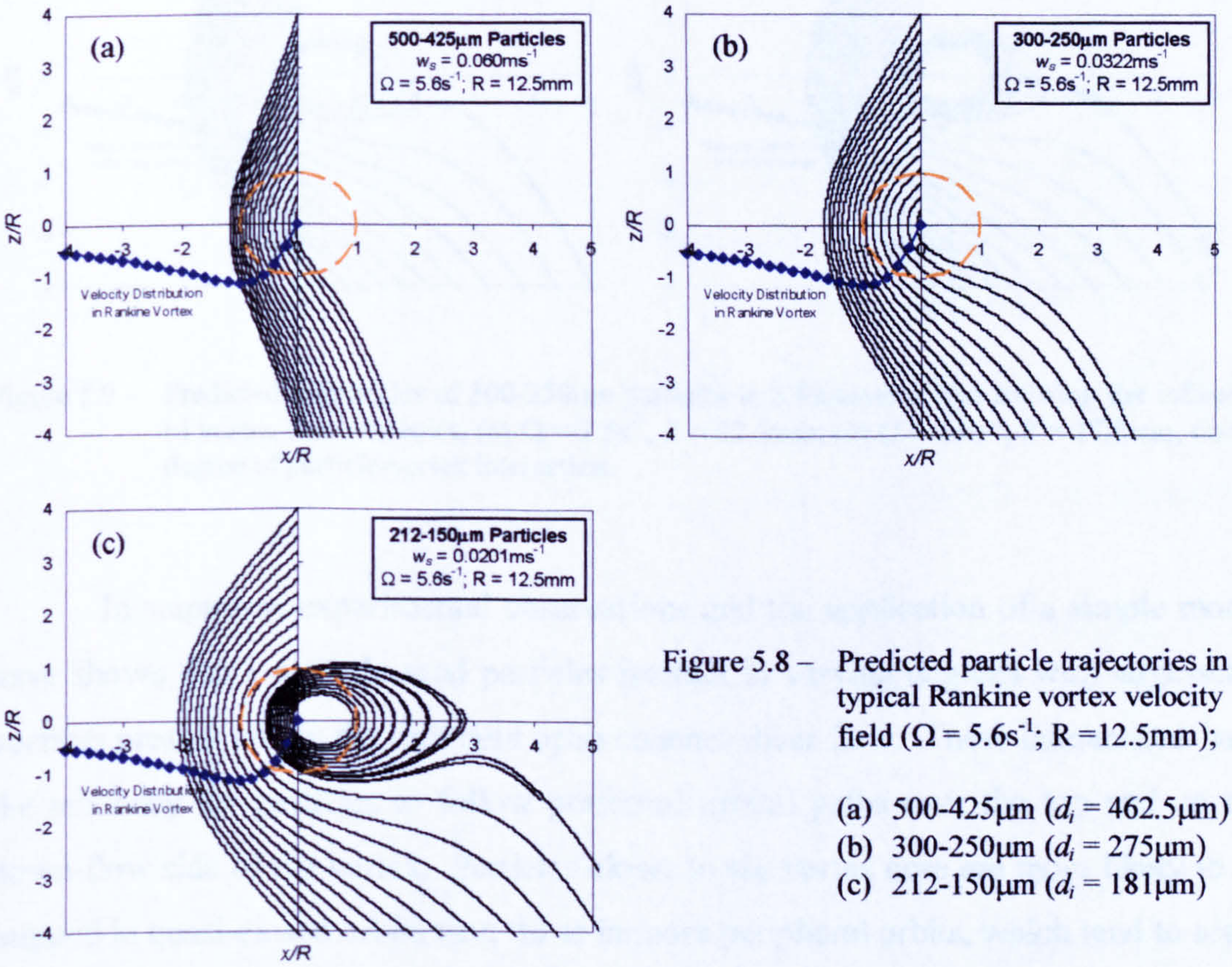

Figure 5.8 – Predicted particle trajectories in a typical Rankine vortex velocity field (Ω = 5.6s^{-1}; R =12.5mm);

(a) 500-425μm (d_i = 462.5μm)
(b) 300-250μm (d_i = 275μm)
(c) 212-150μm (d_i = 181μm)

The 275μm and 181μm particles show increasing interaction with the rotational velocity field, forming curved trajectory paths on the down-flow side of the vortex. Particle-vortex interactions appear to be strongest for the particle paths closest to the centre of rotation (0,0) and are sufficient to trap individual 181μm particles in quasi-closed orbits around the vortex core. These closed trajectories appear to expand in size with each orbit, eventually leading to particle shedding at the bottom of the orbital path.

The influence of the vortex characteristics (R and Ω_0) are shown in Figure 5.9(a) and (b) for 275μm particles. Comparing particle trajectories with those shown in Figure 5.8(b), it is clear that an increase in vortex size R or rotation frequency Ω_0

will result in more significant particle-vortex interactions. Increasing Ω_0 and/or R will also increase the tendency for particles within inner orbits to become trapped in quasi-closed paths around the vortex.

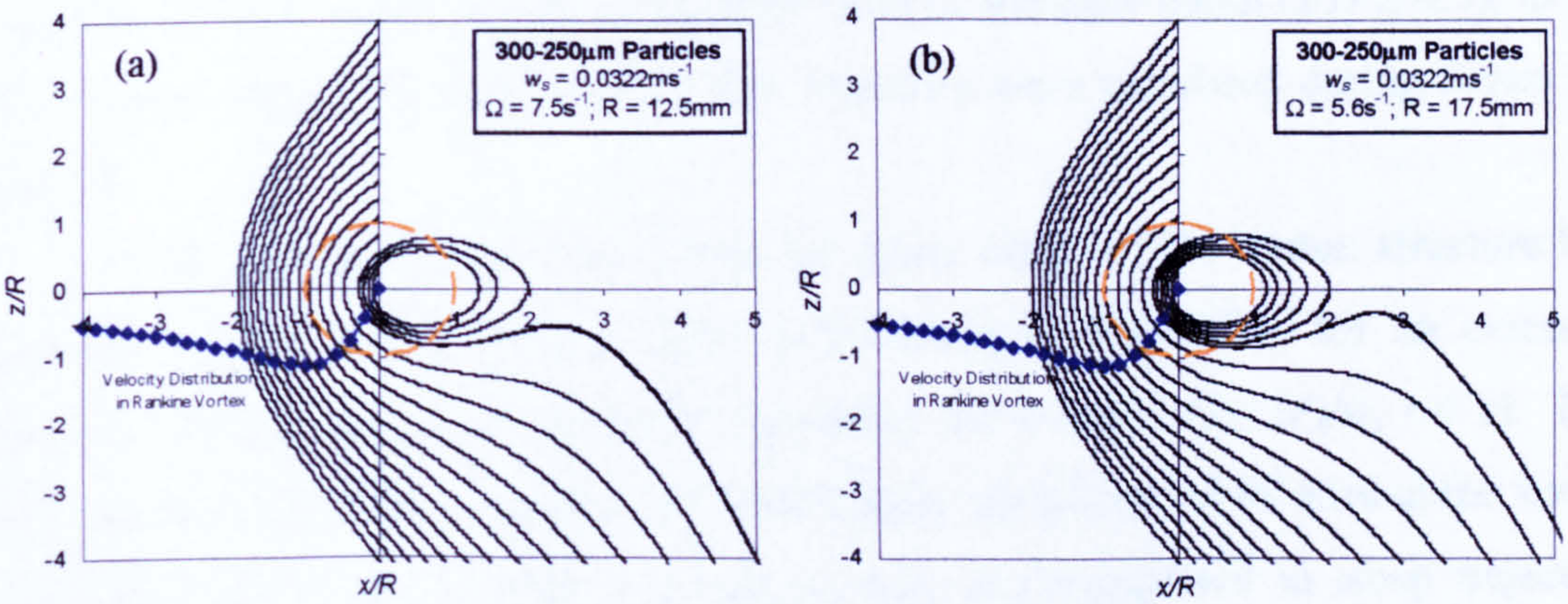

Figure 5.9 – Predicted trajectories of 300-250µm particles in a Rankine vortex showing the influence of vortex characteristics, (a) $\Omega = 7.5s^{-1}$, $R = 12.5$mm; (b) $\Omega = 5.6s^{-1}$, $R = 17.5$mm, on the degree of particle-vortex interaction.

In summary, experimental observations and the application of a simple model have shown that LA grade sand particles interact in varying degrees with large-scale vortices present within the turbulent open channel shear flow. These interactions have the tendency for particles to follow preferred orbital paths over the top and on the down-flow side of the vortex. Particles closer to the vortex core are more likely to be trapped in quasi-closed orbits than those in more peripheral orbits, which tend to settle out beneath the vortex. Decreasing particle size d_i or increasing either vortex size R or rotation frequency Ω_0 increases the likelihood of inner particles being trapped in these quasi-closed paths.

It is apparent that particle trapping can only occur in cases where the maximum vertical component of fluid velocity $\vec{u}(z)$ exceeds the still water fall velocity of the sediment w_s (i.e. when an upward particle motion occurs). For the Rankine vortex model, the maximum value of $\vec{u}(z)$ occurs on the positive x/R axis at $x/R = 1$ (i.e. $z/R = 0$). Substituting these values into equation 5.2 yields a maximum value of $\vec{u}(z) = \Omega_0 R/2$, and hence particle trapping occurs only when $w_s < \Omega_0 R/2$.

5.4.3 Influence on Fall Velocity of LA Grade Sand

So far it has not been considered to what extent the fall velocity of the LA sand particles is affected by their interaction with large-scale coherent vortices. It has been noted from the recordings made with the moving camera system that the vast majority of these vortices exist in the lower half of the flow depth ($z/H \leq 0.5$), in the flow region where enhanced particle fall velocities were measured during Series 1A and 1B.

It is evident that particles within the inner orbits of the vortex structure that become trapped in quasi-closed paths will remain in suspension for an extended period and therefore have significantly hindered fall velocity (i.e. $w'_s/w_s << 1$). It is hypothesised, however, that particles travelling in peripheral orbits around the vortex can experience enhanced fall velocities as they are transported in steep trajectory paths on the down-flow side of the vortex. This would result from the downward vertical component of fluid velocity $\vec{u}(z)$ acting in conjunction with the particles' gravitational settling tendency described by the fall velocity in still water conditions, i.e. $\vec{u}_s(z) = w'_s = w_s + \vec{u}(z)$.

This hypothesis is shown to be correct when the settling characteristics of 462.5, 275 and 181μm particles are considered in the Rankine vortex flow field (Ω = 5.6s^{-1}, R = 12.5mm) shown in Figure 5.8. The average fall velocity of each particle w'_{si} was calculated from the origin of the particle trajectory to the location where they cross the lower boundary of the plots (i.e. at z/R = -4). These were then compared with measured still water fall velocities w_{si} and the non-dimensional fall velocity ratio w'_{si}/w_{si} was calculated.

For the 462.5μm particles, average particle fall velocities in peripheral paths on the down-flow side of the vortex are about 18% higher than the still water fall velocity (i.e. $w'_s/w_s = 1.18$). This suggests that the interaction between these particles and the rotational flow field results in an enhancement of particle fall velocities away from the vortex core. This enhancement gradually diminishes as the orbit radius of the particle path reduces, with particles in trajectory paths closest to the vortex core shown to have hindered fall velocities (i.e. $w'_s/w_s = 0.86$).

The divergence between enhanced fall velocities for particles in periphery paths (i.e. $w'_s/w_s > 1.0$) and hindered fall velocities for particle paths closest to vortex core (i.e. $w'_s/w_s < 1.0$) tends to increase as the particle size d_i reduces. The 275μm

particles in peripheral orbits are enhanced by up to 36% (i.e. w'_s/w_s = 1.36), while particles near the centre of the vortex have increasingly hindered fall velocities with w'_s/w_s = 0.52. For the 181μm particles in peripheral orbits, w'_s/w_s values increases up to 1.58, suggesting a significant enhancement of fall velocity over that measured in still water. By contrast, values of w'_s/w_s in the quasi-closed particle trajectories near the vortex core will clearly tend to zero.

The experimental observations of particle-vortex interactions suggest that the vast majority of particles travel on steep downward trajectory paths on the periphery of the down-flow side of vortices, some distance away from the vortex core. It is therefore suggested that the particle-vortex mechanisms described above may account, at least in part, for the enhanced fall velocities of LA grade sand fractions measured in Series 1A and 1B.

CHAPTER 6

Experimental Results (Series 2)

6.1 Introduction

The particle tracking experiments reported in Chapter 4 and the flow visualisation studies of Chapter 5 have highlighted interesting results regarding the vertical motion of LA grade sand in turbulent open channel flow. The main findings from these experiments were: (a) the turbulent fall velocity of the sediment is often *enhanced* over that observed in still water conditions (i.e. $w'_{si}/w_{si} > 1.0$); (b) this *enhancement* generally increases with reducing grain size d_i; and (c) the non-dimensional fall velocity ratio w'_{si}/w_{si} decreases with increasing z/H, becoming hindered in the outer flow (i.e. $w'_s/w_s < 1.0$). In addition, the flow visualisation experiments revealed distinct interactions between particles and large-scale coherent vortices, which may, at least in part, account for these *enhanced* fall velocities. However, two main limitations within these experiments were identified as meriting further investigation:

(1) The low aspect ratios of uniform flows set up in the Armfield S5-10 flume ($B/H < 3.2$) were shown to result in the formation of secondary currents in the YZ plane, and no central region was identified in which predominantly two-dimensional flow could be considered to occur.

(2) The particle tracking technique employed required low sediment input rates in order to track individual particles. This meant that the influence of sediment concentration on characteristics of particle motion could not be assessed.

A further series of experiments was designed to address these limitations and provide an independent data set with which to compare the main findings from Series

1. These experiments were conducted in a larger flume facility (8m-long by 0.76m-wide) and employed non-visual techniques based on the measurement of deposition fluxes and concentration profiles to assess the settling and depositional characteristics of the fine sediments.

A summary of the experimental procedure and conditions for Series 2 is provided in the subsequent sections. Full details of the flume facility specifications and other instrumentation employed are given in §3.5 of Chapter 3, 'Experimental Studies - Apparatus and Procedures'

6.2 Experimental Procedure

The experiments were carried out under steady, uniform flow conditions. Fine sand was introduced at the surface of the flow from an electrically driven sediment hopper (§3.5.3.1, pp.87) at the upstream end of the gravel-bedded flume. Flow conditions were carefully controlled to ensure the gravel bed remained predominantly static throughout the duration of each experiment.

A matrix of 36 traps underlying the 25-35mm thick porous gravel bed layer collected the sediment as it deposited along the length of the flume. The set-up and arrangement of the bed traps is described in some detail in §3.5.1.2 (pp.81). Following the completion of each experiment, the gravel layer was carefully washed in-situ to ensure all deposited material trapped in the gravel interstices was transferred into the underlying traps so as to be included in the subsequent analysis. After the gravel and mesh layers were removed, the sediment deposits were carefully collected from the underlying traps for drying and sieve analysis.

The overall and fractional deposition rates (Δ_b and Δ_{bi}) for each individual trap were calculated by dividing the sediment mass collected by the bed surface area overlying the trap and by the duration of the sediment feed.

Sediment concentration profiles were collected by sampling tubes (§3.5.3.2, pp.87) positioned at five predetermined locations along the length of the flume. Each profile was defined by four individual samples collected at different depths within the flow, including a near-bed concentration sample generally siphoned off at 5mm above the bed surface (i.e. 0.5 x diameter of copper sample tube). The lateral positions of the sampling tubes were offset by about 50mm either side of the centreline to limit the influence of upstream measurements on subsequent downstream concentration

profiles. During each experiment, concentration samples were siphoned from the flow concurrently over a period of approximately 15 minutes, each sample being collected in separate 80-litre bins. In the post-experiment analysis, the overall and fractional sediment concentrations (C and C_i) were obtained for individual samples by dividing the recovered and dried sediment mass by the measured volume of water collected in the 80-litre bin.

The Sontek™ vertically orientated ADV probe was used to measure the 3-D mean and fluctuating components of flow velocity. In general, flow measurements were made prior to the release of the fine sediment, with velocity profiles measured along the centreline (i.e. $y/B = 0.5$) at downstream locations corresponding to the locations at which sediment concentration samples were to be taken. Selected profiles were also taken at lateral positions across the width of the flume in order to assess the region of two-dimensional flow.

A full description of the experimental procedure followed during each experiment is given in Appendix 3.3.

6.3 Experimental Conditions

The experimental parameters for the twelve Series 2 experiments are summarised in Table 6.1 overleaf.

Two types of gravel were used as bed material to assess the influence of the relative roughness k_s/H on the deposition rates: (i) S2_grv1 (D_{50} = 17.3mm; σ_g = 1.31) and; (ii) S2_grv2 (D_{50} = 6.98mm; σ_g = 1.24). The grading curves and properties of these gravel grades are given in §3.5.2.1 (pp.84). In later experiments (SC_EX9 and 10), the finer S2_grv2 grade gravel was also used as fill for the sediment traps to assess the influence of substrate material on the deposition rate and composition of the deposited sediments (Figure 6.1).

The fine sediment tested was predominantly the LA sand (d_{50} = 250μm). However, two experiments were also conducted with the finer DB sand (d_{50} = 97μm). In all experiments, the fine sediment was introduced into the flow at a constant rate in its natural grade rather than as a series of individually sieved size fractions. The fine sediment input rate I_R was varied between experiments, ranging from ~5 to 30 g.s^{-1}. With the flow rate also varying between experiments (Q ~ 36 to 55 ℓ.s^{-1}), the initial sediment concentration C_0 (= $I_R.10^3/Q$) ranged between 110 and 590 mg.ℓ$^{-1}$.

(1) Run	Hydraulic Conditions									Fine Sediment					Bed Material		
	(2) H (m)	(3) S_0	(4) Q (m^3s^{-1})	(5) $\bar{U}$ (ms^{-1})	(6) u_* (ms^{-1})	(7) F_r	(8) ν (m^2s^{-1})	(9) R_e	(10) k_s (mm)	(11) Grade	(12) d_{50} (μm)	(13) I_R (gs^{-1})	(14) C_0 (mgl^{-1})	(15) T_R (min)	(16) Grade	(17) D_{50} (mm)	(18) σ_g
EXT1	0.117	0.004	0.0548	0.590	0.063	0.55	1.12e-06	2.47e+05	32.8	LA	250	30.8	562	14	Grv1	17.3	1.21
EX1	0.109	0.004	0.0548	0.609	0.061	0.59	1.09e-06	2.37e+05	21.0	LA	250	21.1	385	17.25	Grv1	17.3	1.21
EX2	0.111	0.004	0.0547	0.603	0.061	0.58	1.21e-06	2.44e+05	23.3	LA	250	6.0	110	25.5	Grv1	17.3	1.21
EX3	0.110	0.004	0.0547	0.608	0.063	0.59	1.13e-06	2.37e+05	21.7	LA	250	10.9	199	34	Grv1	17.3	1.21
EX4	0.080	0.004	0.0361	0.520	0.048	0.59	1.21e-06	1.38e+05	14.0	LA	250	7.4	205	30	Grv1	17.3	1.21
EX5	0.077	0.004	0.0362	0.562	0.046	0.65	1.18e-06	1.47e+05	9.6	LA	250	7.3	202	30	Grv2	7.0	1.24
EX6	0.100	0.004	0.0548	0.606	0.048	0.61	1.13e-06	2.15e+05	11.9	LA	250	20.8	380	23	Grv2	7.0	1.24
EX7	0.077	0.004	0.0359	0.560	0.045	0.64	1.12e-06	1.54e+05	10.0	DB	97	5.1	142	25	Grv2	7.0	1.24
EX8	0.079	0.010	0.0518	0.730	0.066	0.83	1.18e-06	1.95e+05	19.9	LA	250	6.7	129	40	Grv1	17.3	1.21
EX9	0.080	0.010	0.0518	0.737	0.068	0.83	1.12e-06	2.11e+05	21.1	LA	250	7.5	145	46	Grv1*	17.3	1.21
EX10	0.079	0.010	0.0519	0.723	0.065	0.82	1.12e-06	2.04e+05	20.1	LA	250	30.6	590	30	Grv1*	17.3	1.21
EX11	0.109	0.001	0.0357	0.399	0.035	0.39	1.15e-06	1.51e+05	5.0	DB	97	9.4	263	30	Grv2	7.0	1.24

H – flow depth, S_0 – bed slope, Q – flow rate, $\bar{U}$– mean flow velocity, u_* - shear velocity, F_r – Froude number, ν - fluid kinematic viscosity, z_0 – roughness length, k_s – Nikuradse equivalent sand roughness, d_{50} – median size of fine sediment, I_R – fine sediment input rate, C_0 – initial sediment concentration, T_R – time of sediment input, D_{50} – median size of bed material, σ_g – standard deviation in bed material size (sorting index).

* S2_grv2 gravel used to fill ½ trap width along length of flume beneath coarser surface layer of S2_grv1 gravel.

Table 6.1 - Main experimental parameters for twelve Series S2 Experiments

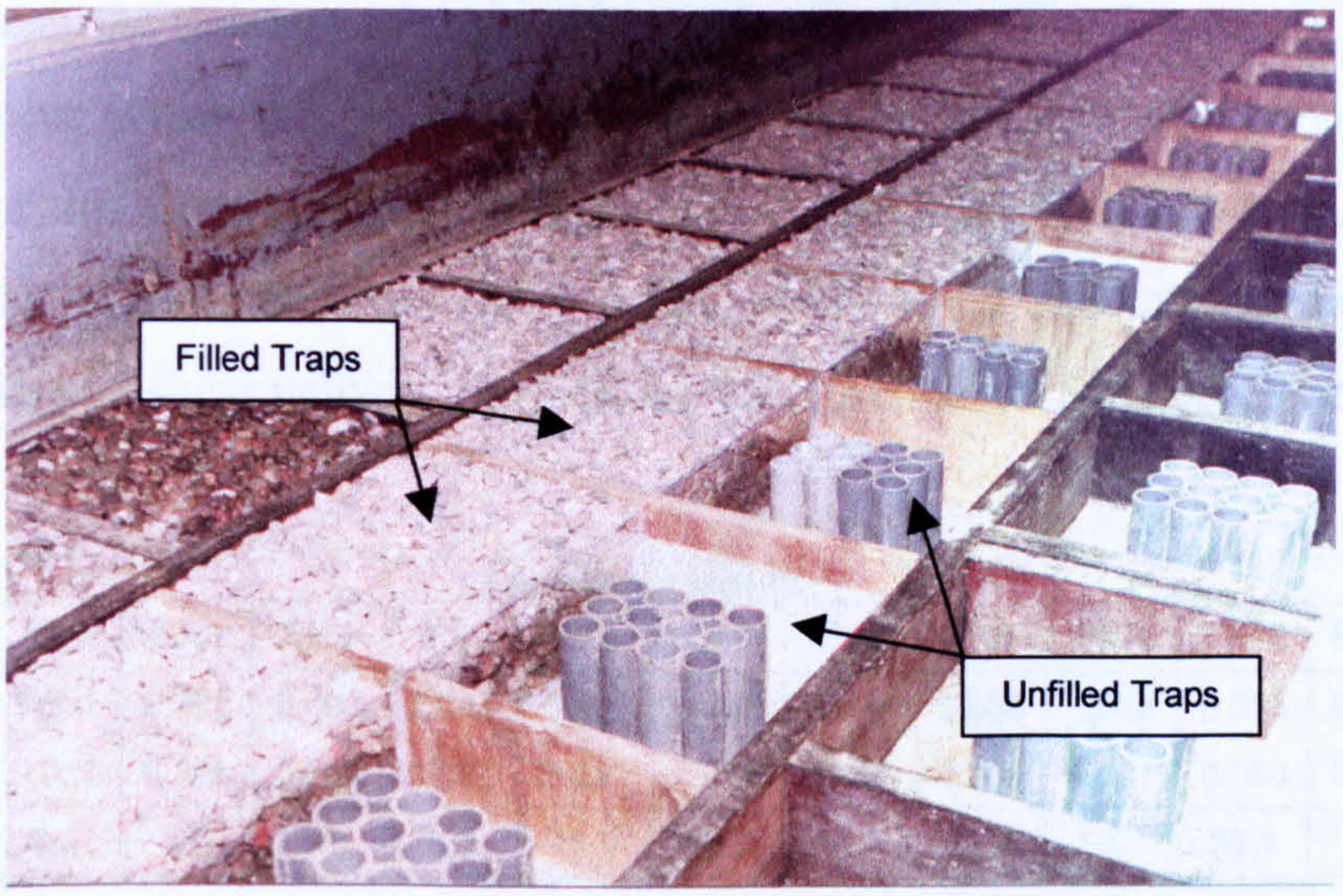

Figure 6.1 – Centreline trap arrangement for experiments S2_EX9 and S2_EX10 (i.e. half filled with S2_grv2 gravel.

Initially, the fine sediment was released into the flow at the upstream end of the flume. However, from experiment S2_EX3 onwards, the sediment hopper was repositioned to release at a location about 0.8m from the upstream end of the flume, where more uniform flow conditions were considered to occur.

Three bed slopes were used in the experiments, namely: 0.004, 0.010 and 0.001. The average flow depth H, calculated as the mean difference between the measured bed surface and water surface elevations, varied between 77 and 117 mm. The mean flow velocity $\overline{U}$, estimated from the measured ADV profiles taken for each flow condition at an elevation $z = 0.396H$, ranged from ~0.40 to 0.73 $m.s^{-1}$. This resulted in a range of Froude numbers F_r between 0.39 and 0.83 (i.e. subcritical flow conditions). The flow conditions also correspond to values of flow Reynolds number R_e in the range from about $1.4\ 10^5$ to $2.5\ 10^5$.

6.3.1 Shear Velocity Calculation

The shear velocity was estimated by the Clauser (1956) method using equation 4.9 (pp.119), with the near-bed ADV velocity profiles used in its estimation presented in Appendix 6.1. The predicted values obtained from Clauser ($u_{*(1)}$) are compared with values obtained from the universal expression for shear velocity (eqn. 4.7, pp.118) in Table 6.2 below. In general, reasonable agreement is observed between the two methods, with the average relative difference of ~13%. The largest differences are noted to occur under the steepest bed slope condition ($S_0 = 0.01$). Near-bed velocity data for this flow condition (Figure A6.6, Appendix 6.1), however, reveals the largest scatter in measurements ($R^2 = 0.82$), which could account for the higher relative differences in shear velocity predictions for experiments S2_EX8, 9 and 10.

	Experiment Number											
	EXT1	EX1	EX2	EX3	EX4	EX5	EX6	EX7	EX8	EX9	EX10	EX11
$u_{*(1)}$ (ms^{-1})	0.063	0.061	0.061	0.063	0.048	0.046	0.048	0.045	0.066	0.068	0.065	0.035
$u_{*(2)}$ (ms^{-1})	0.059	0.057	0.058	0.059	0.052	0.051	0.056	0.050	0.080	0.081	0.080	0.029
E_r (%)	6.3	6.6	4.9	6.3	8.3	10.9	16.7	11.1	21.2	19.1	23.1	17.1

Table 6.2 - Comparison of Clauser (1956) and universal predictions of u_*

The shear velocity calculated by the Clauser method is shown to vary from 0.035 to 0.068 $m.s^{-1}$ for the experimental conditions considered. Generally, lower values of u_* are predicted for experiments with lower flow depths, reduced bed slope or where the finer gravel grade (S2_grv2) is used as the bed material.

6.3.2 Calculation of Nikuradse Equivalent Sand Roughness

Values of the equivalent sand roughness k_s were obtained from the Colebrooke-White and Keulegan (1938) equations using the developed Excel spreadsheet (Appendix 4.5). The experiment-averaged values of k_s obtained from both methods are detailed in Table 6.3 for the two grades of bed gravel.

Bed Material	S2_grv1	S2_grv2
D_{50} (mm)	17.3	7.0
D_{84} (mm)	21.6	8.6
$k_{s(1)}$ (Keulegan) (mm)	21.7	9.1
$k_{s(2)}$ (Colebrooke-White) (mm)	24.7	10.2
$k_{s(1)}/D_{50}$	1.25	1.30
$k_{s(1)}/D_{84}$	1.00	1.06
$k_{s(2)}/D_{50}$	1.43	1.46
$k_{s(2)}/D_{84}$	1.14	1.19

Table 6.3 – Experiment-averaged values of Nikuradse equivalent sand roughness k_s and dimensionless ratios k_s/D_{50} and k_s/D_{84} for two grades of bed gravel used in Series 2.

The values of k_s obtained from both methods are shown to have consistent relationships with the representative bed material sizes D_{50} and D_{84} for both gravel types, with $k_s \sim 1.3D_{50}$ and $k_s \sim 1.0D_{84}$ for Keulegan (1938) and $k_s \sim 1.45D_{50}$ and $k_s \sim 1.15D_{84}$ for Colebrooke-White. For consistency with Series 1B, the k_s values obtained from Keulegan (1938) were adopted for this study, and are shown for each individual experiment in Table 6.1 (column 10).

The relative roughness of the bed material k_s/H varied between ~0.1 and 0.3 for experiment-averaged values of k_s. The corresponding range of roughness Reynolds numbers k_s^+ [$= k_s u_*/\nu$ (Nezu and Nakagawa, 1993)] varied between about 300 and 1500, categorising the flow conditions in the hydraulically rough regime (i.e. $k_s^+ > 70$).

6.4 Experimental Results

This section details the results and observations from the twelve experiments conducted in Series 2. Within these experiments, the fine sediment transport and depositional characteristics are determined from concentration profiles measured at predetermined locations within the flow and deposition samples collected in traps beneath the experimental bed. The main findings from these experiments are reported

herein, whilst a more comprehensive discussion of their implications is given in Chapter 7.

6.4.1 Experimental Flow Conditions

It was desirable that the experiments were conducted under two-dimensional steady, uniform flow conditions. This required that the channel flow aspect ratio (α) be above a critical value α_c (= 5.0) to allow two-dimensional flow conditions to develop within a central flow region. Steady, uniform flow conditions were carefully set up during each experiment using the standard method outlined in Appendix 3.2.

6.4.1.1 Mean Longitudinal Flow Velocity Profiles

Longitudinal flow velocity profiles are presented in Appendix 6.2 for each range of experimental flow conditions used in Series 2. In general, they show good consistency at each centreline location where profiles were measured, suggesting relatively uniform flow conditions exist along the length of the flume working section. Logarithmic 'best-fit' profiles of the form given in equation 6.1 (Song et al.1994) are obtained through least-squares regression to each set of velocity measurements.

$$\frac{u}{u_*} = \frac{1}{\kappa} ln\left(\frac{z+\delta z}{k_s}\right) + B_r \qquad ....(6.1)$$

where z is the elevation, δz is the reference bed level ($\delta z = 0.2k_s$) and B_r is the constant of integration. The main characteristics for these fitted logarithmic profiles are given in Table 6.4 overleaf.

The constant of integration B_r for the fitted logarithmic profiles was found to vary between about 6 and 9.5, but did not show any clear correlation with the relative roughness of the experimental bed conditions (k_s/H). The average value of 8.54 does however provide good agreement with the typical value of 8.5 reported by Schlichting (1968) for a completely rough wall condition

Experiment	u_* (ms^{-1})	δz (m)	k_s (m)	B_r
S2_EXT1	0.063	0.0066	0.0328	8.42
S2_EX1-3	0.061	0.0044	0.0220	8.10
S2_EX4	0.048	0.0028	0.0140	8.64
S2_EX5, 7	0.046	0.0020	0.0098	9.53
S2_EX6	0.048	0.0024	0.0119	9.35
S2_EX8-10	0.066	0.0041	0.0204	9.69
S2_EX11	0.035	0.0010	0.0050	6.09
B_r – integration constant.			**Average**	**8.54**

Table 6.4 - Main characteristics of measured longitudinal velocity profiles at $y/B = 0.5$

6.4.1.2 Two Dimensional Flow Conditions

For the prevalent hydraulic conditions, the flow aspect ratio α (= B/H) ranged from ~6.5 to 9.9, which is higher than the critical value $\alpha_c = 5.0$ (Nezu ad Rodi 1985). In order to assess the central width in which two-dimensional flow conditions prevail, ADV measurements were made at seven lateral positions across the channel width. Three experimental flow conditions were considered: (i) H = 0.11m; α = 6.95; S2_grv1 bed material (10-25mm), (ii) H = 0.08m; α = 9.55; S2_grv1 bed material (10-25mm), and (iii) H = 0.08m; α = 9.55; S2_grv2 bed material (5-10mm). These correspond to experiments S2_EX1-3, S2_EX4 and S2_EX5, respectively.

The time-averaged secondary fluid motions in the YZ plane obtained for flow condition (ii) are plotted in vector form in Figure 6.2. Similar plots for flow conditions (i) and (iii) are given in Appendix 6.3. These show that the measured lateral and vertical components of flow velocity are small in a central flow region extending from $y/B \sim 0.32$ to 0.68 compared with that measured outwith this region. In relation to the longitudinal flow velocities, the average magnitude of the secondary fluid motions range from 0.9-1.4% inside and 2.0-3.7% outside of this central flow region, thus indicating that predominantly two-dimensional flow conditions exist within the central third of the flume width.

The width of the centreline traps in which the deposition samples were collected are 0.305m wide, corresponding to central flow region extending from y/B = 0.3 to 0.7. It therefore seems reasonable to assume that fine sediments are deposited in the centreline traps under essentially two-dimensional flow conditions.

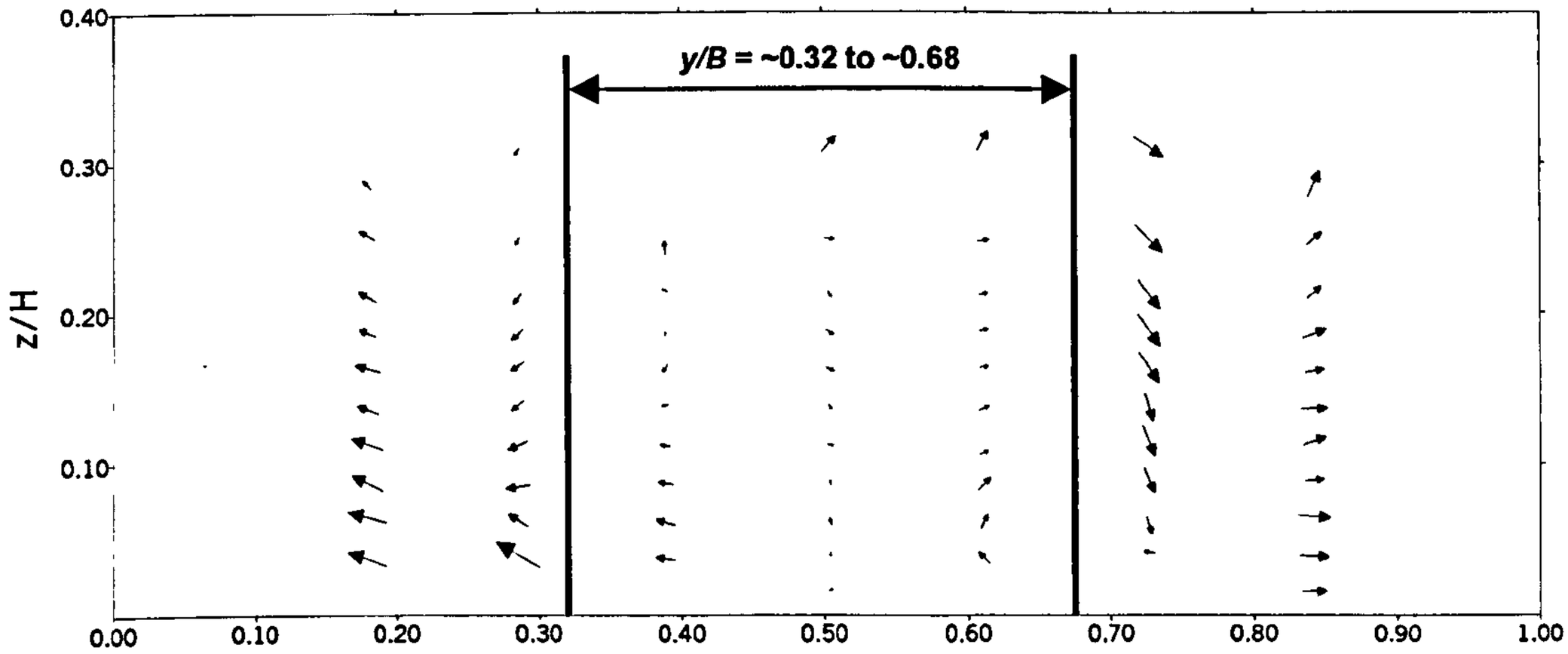

Figure 6.2 - Measured secondary flow velocities – S2_EX4 flow conditions

6.4.2 Fine Sediment Settling and Depositional Characteristics

6.4.2.1 Calculation Techniques and Methods

Unlike the techniques employed in Series 1, where the vertical motion of the fine sediment fractions within the flow and surface bed layers was determined from individual particle trajectories, no explicit measurement of the turbulent fall velocity w'_{si} or the deposition velocity w_{di} can be made using non-visual techniques. Calculation of these parameters requires back-calculation from the longitudinal variation in sediment deposition flux and the measured sediment concentration profiles downstream of the source.

(i) Turbulent Fall Velocity of Sediment Fractions (w'_{si})

The longitudinal distribution of deposition within the centreline traps is used to estimate the mean and median settling lengths for the fine sediment ($\overline{L}_i$ and $\widetilde{L}_i$). Knowledge of the mean flow conditions, described by depth H and average flow velocity $\overline{U}$, allows the calculation of a depth-averaged turbulent fall velocity for the overall sediment grades ($\overline{w}'_s$ and $\widetilde{w}'_s$) and for individual sand fractions ($\overline{w}'_{si}$ and $\widetilde{w}'_{si}$), i.e.

$$\overline{w}'_s\left(or\ \widetilde{w}'_s\right)=\frac{\overline{U}.H}{\overline{L}\left(or\ \widetilde{L}\right)};\qquad \overline{w}'_{si}\left(or\ \widetilde{w}'_{si}\right)=\frac{\overline{U}.H}{\overline{L}_i\left(or\ \widetilde{L}_i\right)} \qquad ....(6.2)$$

where $\overline{w}'_{si}$ refers to the to the mean depth-averaged turbulent fall velocity of sediment size fraction i and $\widetilde{w}'_{si}$ refers to the corresponding median value. There are

two main assumptions associated with equation 6.2: (a) the depth-averaged streamwise component of particle velocity is equal to the depth-averaged flow velocity; (b) the sediment particles deposit upon first contact with the bed surface.

The first assumption would appear reasonable from Series 1B results, where the ensemble-averaged streamwise particle velocities were generally close to the streamwise velocity of the surrounding fluid. In terms of the second assumption, measurements from Series 1A indicated that between 60-80% of the near-bed sediment particles observed deposited on reaching the bed surface. Assuming similar values of deposition probability would apply here, the depth-averaged turbulent fall velocities computed from equation 6.2 will be lower as a result of subsequent longitudinal motions of the 20-40% of sediment particles that are not immediately deposited. Consequently, $\overline{w}'_{si}$ and $\widetilde{w}'_{si}$ values can be considered as a lower bound for the particle fall velocities in turbulent flow conditions.

A second, more-involved method was employed to calculate the turbulent fall velocity from measured concentration and flow velocity profiles. This method was based on the solution of the dimensionless, integrated form of the two-dimensional advection-diffusion equation for suspended sediment, proposed by Jobson and Sayre (1970),

$$\frac{\partial}{\partial X}\int_{Z_1}^{1}\frac{U}{u_*}c_i\,dZ = \left.\frac{\varepsilon_{szi}}{H.u_*}\right|_{Z_1}\left.\frac{\partial c_i}{\partial Z}\right|_{Z_1} - \left.\frac{w'_{si}}{u_*}\right|_{Z_1} c_i\big|_{Z_1} \qquad \text{....(6.3)}$$

where $X = x/H$, $Z = z/H$, c_i is the non-dimensional fractional sediment concentration (= C_i/C_{0i}), ε_{szi} is the fractional sediment diffusion coefficient and w'_{si} is the fractional fall velocity in turbulent flow conditions. The derivation of equation 6.3 from the standard two-dimensional advection-diffusion equation for suspended sediment, as well as the curve-fitting and numerical techniques employed in its solution are detailed in Appendix 6.4.

Solution of equation 6.3 provides vertical distributions of the two unknown variables, w'_{si}/u_* and ε_{szi}/Hu_*. One of the main drawbacks of this method, however, is that it is extremely arduous to perform, even with NAG Fortran Library routines employed to carry out the cubic spline curve fitting to the sediment concentration data. It was therefore only used for three Series 2 experiments in order to provide

vertical profiles of w'_{si}/u_* to compare directly with similar distributions obtained during Series 1B experiments.

(ii) Fractional Sediment Deposition Rate (Δ_{bi}) and Deposition Velocity (w_{di})

Following the completion of each experiment, the overall deposition rates (Δ_b) were measured in each centreline trap by dividing the collected sediment mass by the bed surface area overlying each trap and by the duration of the sediment feed. Fractional deposition rates (Δ_{bi}) were obtained from sieve analysis of each deposited sample. The measured near-bed concentration samples (C_b) obtained during the experiments at five pre-determined locations along the flume length were also sieved to provide details of their fractional composition (C_{bi}). Overall and fractional near-bed concentrations (C_b *and* C_{bi}) were related to corresponding local deposition rates (Δ_b and Δ_{bi}) through the expressions (Peloutier, 1998),

$$w_d = \frac{\Delta_b}{C_b} \quad \text{and} \quad w_{di} = \frac{\Delta_{bi}}{C_{bi}} \qquad \text{....(6.4)}$$

where w_d and w_{di} have the units of velocity ($m.s^{-1}$) and are referred to as the overall and fractional deposition velocities, respectively. These define the average transfer velocity of sediment particles from the near-bed flow, through the bed layer and into the underlying traps.

6.4.2.2 Longitudinal Distribution of Deposited Fine Sediments

(1) Overall Distribution of Sediment Deposition

A typical plot showing the longitudinal distribution of sediment deposition (by weight) is presented in Figure 6.3 for LA sand and experiment S2_EX1. The release of sediment at the free surface results in relatively low amounts of sediment deposited in traps 1A and 1B as the sediment requires an initial settling length before coming into contact with the gravel bed. The amount of sediment deposited in the sequential traps downstream rapidly increases to a maximum, before tailing off with a concave profile and approaching zero deposition in the downstream traps 11 and 12. This longitudinal pattern of deposition is similar to that observed by Jobson and Sayre (1970) for both coarse and fine sediments in a non-porous roughened bed.

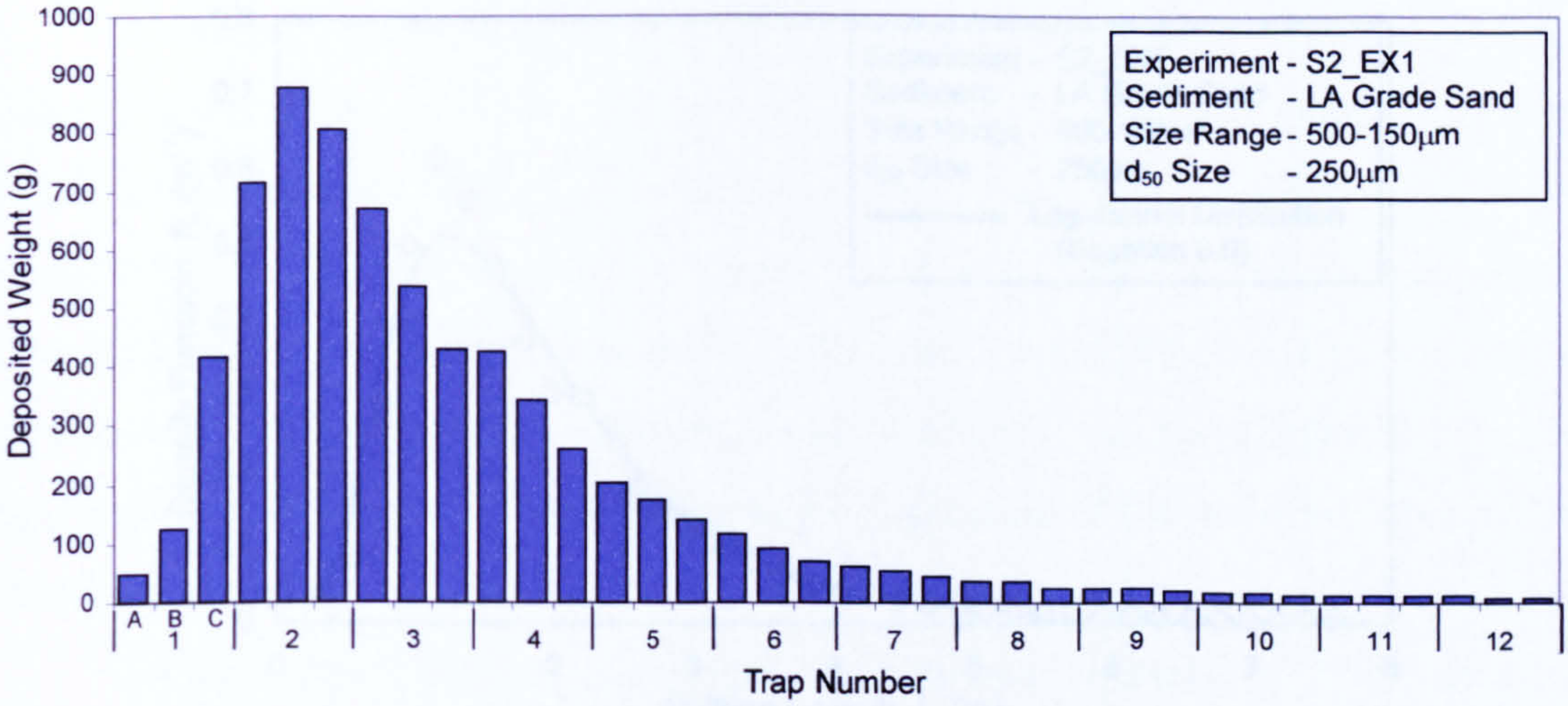

Figure 6.3 - Longitudinal distribution of LA sand deposited in centreline traps for S2_EX1 conditions

The ordinates of a probability density function (p.d.f) for longitudinal deposition length were calculated by dividing the mass of each deposit by the overall mass of material deposited in the centreline traps along the flume and then dividing by the length of the trap in the streamwise (x) direction, i.e.

$$f_{L,j} = \left[\frac{Mass\ deposited\ in\ trap\ j}{\sum Total\ mass\ deposited}\right] \times Trap\ Length_j^{-1} \qquad ....(6.5)$$

where $f_{L,j}$ is the p.d.f ordinate for trap j. The resulting probability density function for deposition length L and experiment S2_EX1 is plotted in Figure 6.4, with similar plots presented in Appendix 6.5 for the other experiments. These p.d.f. distributions for the LA grade sand are well represented by a log-normal distribution of the form proposed by Li and Shen (1975),

$$f_L(x) = \frac{1}{\sqrt{2\pi}\beta_3 x} exp\left[-\frac{1}{2}\left(\frac{ln\,x - \alpha_3}{\beta_3}\right)^2\right] I_{(0,\infty)}(x) \qquad ....(6.6)$$

$$\alpha_3 = \sum\left[ln(x_j) f_j\right]; \quad \beta_3 = \sqrt{\sum\left((ln\,x_j - \alpha_3)^2 . f_j\right)} \qquad ....(6.7)$$

where α_3 and β_3 represent the mean and standard deviation of the log-normal distribution, respectively; x_j is the distance from the source to the centre of trap j; and f_j is the fraction of the total deposited material deposited in trap j.

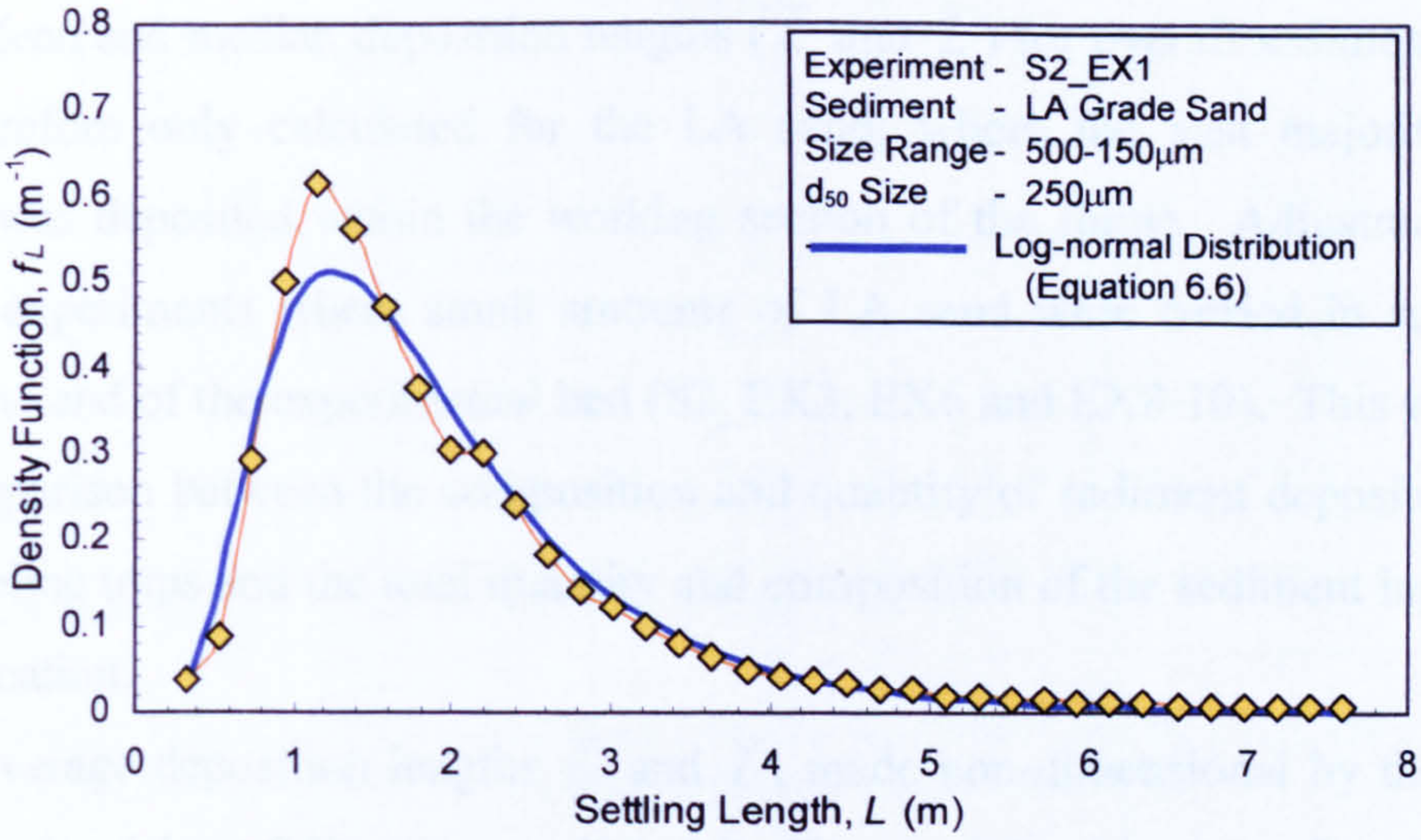

Figure 6.4 - Probability density function of longitudinal deposition length L for LA sand and experiment S2_EX1.

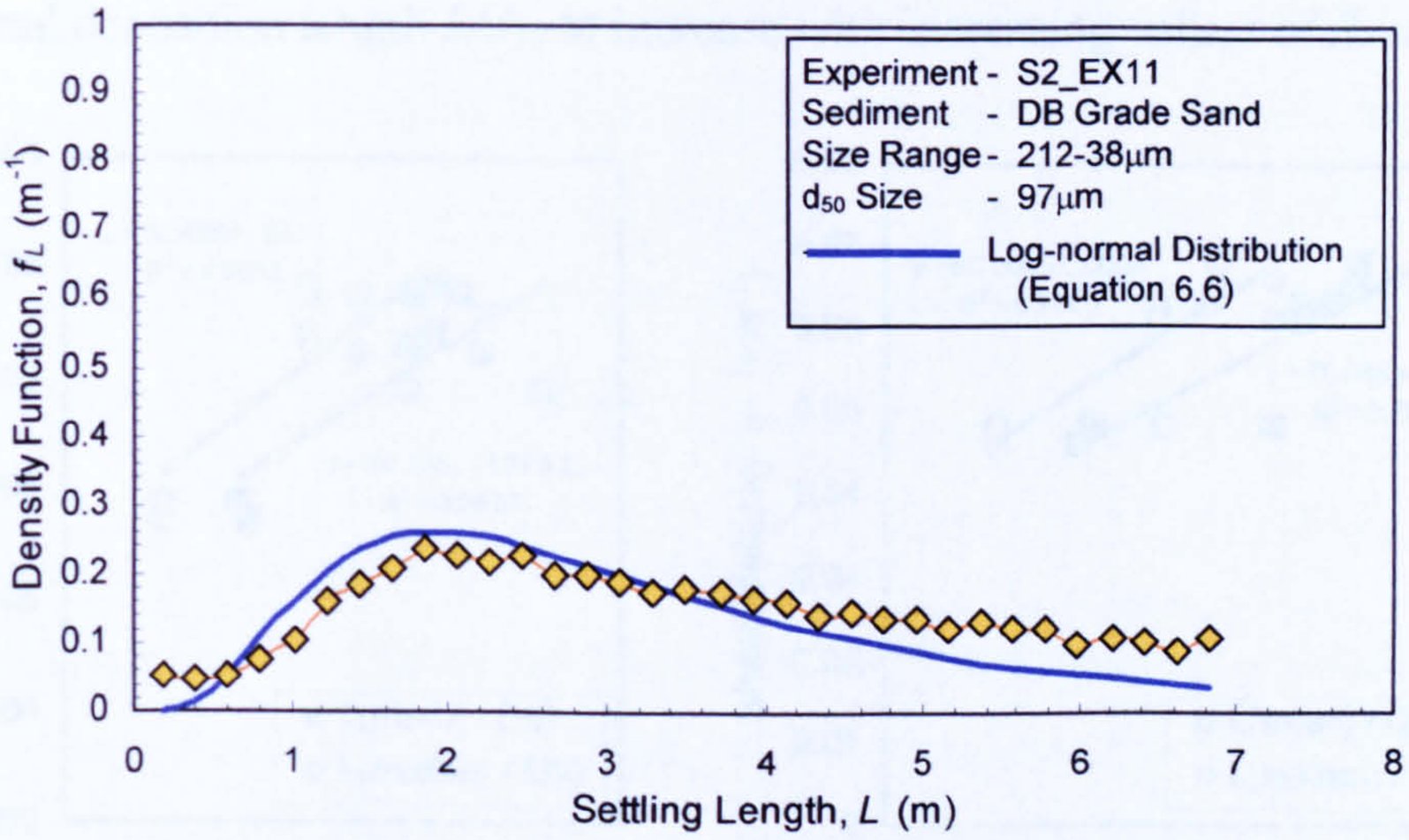

Figure 6.5 - Probability density function of longitudinal deposition length L for DB sand and experiment S2_EX11.

The p.d.f distributions for the two experiments using the finer DB grade sand [Figure 6.5 and A6.25 (Appendix 6.5)] do not show as good a correlation with the semi-theoretical log-normal distribution defined by equation 6.6. This is thought to result from the significant amounts of DB grade sand that remained in suspension and were transported over the tailgate at the downstream end of the flume. Significant quantities of DB sand were also deposited in traps underlying the upstream end of the experimental gravel bed, even in traps upstream of the sediment input location (i.e. traps 1A and 1B). This clearly suggests that a quantity of DB sand was re-circulated through the pump and delivery pipe and into the upstream entry flow from which it was available for deposition.

Mean and median deposition lengths ($\overline{L}$ and $\widetilde{L}$) for overall sediment grading were therefore only calculated for the LA sand, where the vast majority of the material was deposited within the working section of the flume. Adjustments were made in experiments where small amounts of LA sand were carried in suspension beyond the end of the experimental bed (S2_EX3, EX6 and EX8-10). This was based on a comparison between the composition and quantity of sediment deposited within the centreline traps and the total quantity and composition of the sediment input at the source location.

Average deposition lengths $\overline{L}$ and $\widetilde{L}$, made non-dimensional by the median LA grain size (d_{50} = 250μm), are plotted in Figures 6.6 against the flow Reynolds number R_e and shear velocity u_*. These indicate a general tendency for the non-dimensional deposition length L/d_{50} to increase with increasing values of R_e and u_*.

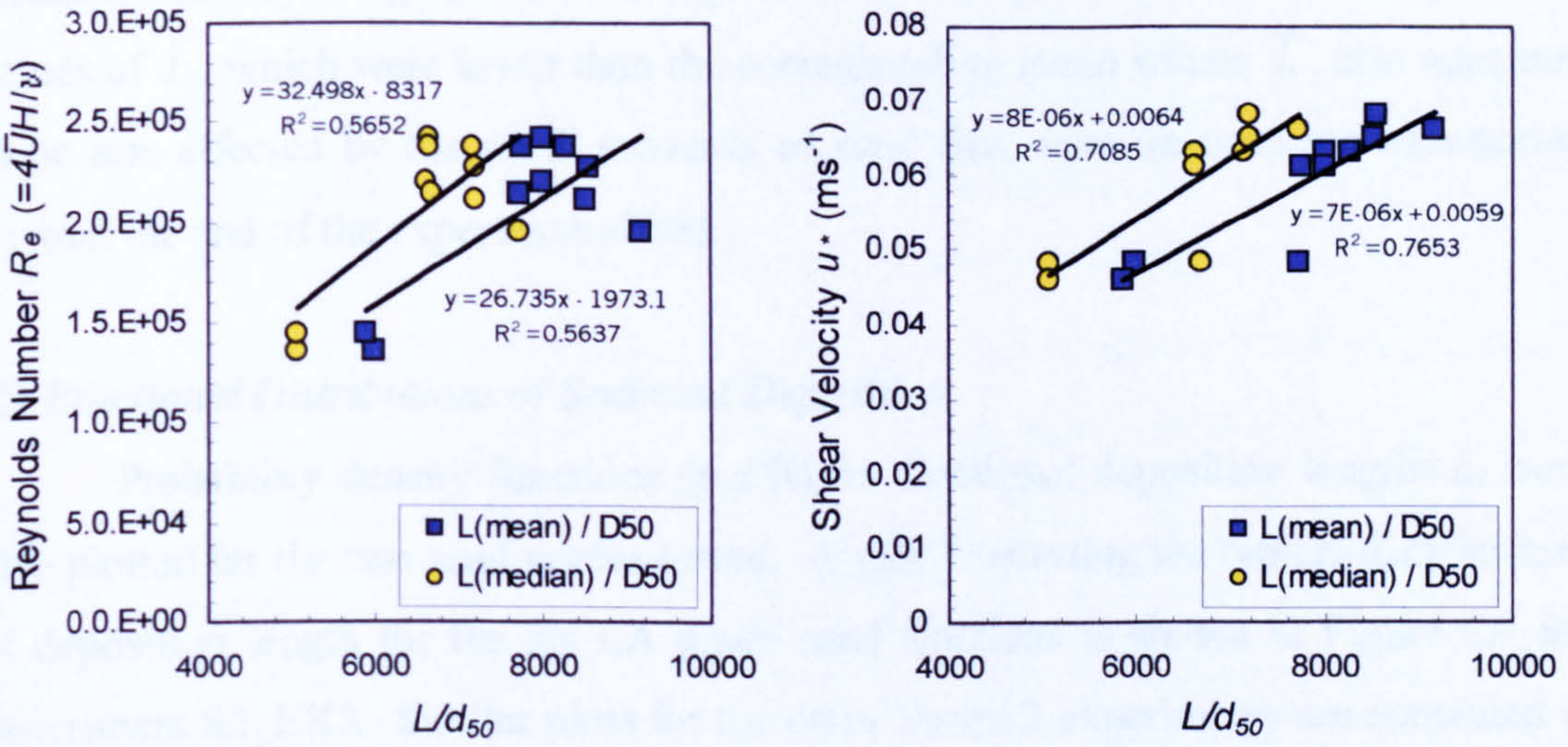

Figure 6.6 - Variation in non-dimensional ratio of average deposition length and median particle size L/d_{50} with (a) flow Reynolds number R_e and (b) shear velocity u_*. Data points shown for all experiments with LA grade sediment.

A summary of depth-averaged turbulent fall velocities ($\overline{w}'_s$ and $\widetilde{w}'_s$) is given in Table 6.5. The turbulent fall velocities calculated from median settling lengths $\widetilde{w}'_s$ varied from 0.030ms^{-1} to 0.042ms^{-1} and were shown to be somewhat larger than corresponding mean values $\overline{w}'_s$, which varied from 0.024 ms^{-1} to 0.035 ms^{-1}. As the average measured still water fall velocity w_s of LA sand is about 0.0296ms^{-1} (§4.2, pp.93), the values of $\widetilde{w}'_s$ are clearly enhanced over this value (by about 21% on average). By contrast, $\overline{w}'_s$ values are on average about equal to the still water fall velocity w_s.

	Experiment Number											
	T1*	1*	2*	3	4	5	6	8	9(i)	9(ii)†	10(i)	10(ii)†
$\bar{L}$ (m)	2.00	1.94	2.00	2.07	1.50	1.47	1.93	2.29	2.14	2.19	2.13	2.43
$\tilde{L}$ (m)	1.66	1.66	1.66	1.79	1.27	1.27	1.67	1.93	1.80	1.87	1.80	1.87
U (ms^{-1})	0.590	0.609	0.603	0.608	0.520	0.562	0.606	0.730	0.737	0.737	0.723	0.723
H (m)	0.117	0.109	0.111	0.110	0.080	0.077	0.10	0.079	0.080	0.080	0.079	0.079
$\bar{w}'_s$ (ms^{-1})	0.035	0.034	0.033	0.032	0.028	0.029	0.031	0.025	0.028	0.027	0.027	0.024
$\tilde{w}'_s$ (ms^{-1})	0.042	0.040	0.040	0.037	0.033	0.034	0.036	0.030	0.033	0.032	0.032	0.031

* Source at 0.1m from u/s end of flume, experiments S2_EX3 onwards, source moved to 0.8m d/s.
† Centreline traps split in two, one half filled with S2_grv2 gravel (5-10mm)

Table 6.5 - Summary of overall mean and median settling lengths and corresponding values of depth-averaged turbulent fall velocity for experiments with LA sand.

Overall, it is generally thought that the median settling lengths ($\tilde{L}$) are the more representative average values as they define the location where 50% of the released sand (by weight) has been deposited in the upstream centreline traps. The values of $\tilde{L}$, which were lower than the corresponding mean values $\bar{L}$, also appeared to be less affected by the small amounts of sand that were on occasion transported beyond the end of the experimental bed.

(2) Fractional Distributions of Sediment Deposition

Probability density functions (p.d.fs) for fractional deposition lengths L_i were also plotted for the two sand grades tested. A plot illustrating the typical distributions of deposition length for the six LA grade sand fractions is shown in Figure 6.7 for experiment S2_EX3. Similar plots for the other Series 2 experiments are contained in Appendix 6.6. Additional data points were often added to the downstream distributions of the d_i = 231 and 181μm particles to account for the small amount of fine sand transported beyond the end of the centreline traps (Figure 6.7). These adjustments were found to have only marginal effects on the predicted median deposition lengths for these finer size fractions.

For LA grade sand, the p.d.f. distributions for the deposition of individual sand fractions generally reveal similar log-normal characteristics to those observed for the full sand grade. Coarser fractions tend to deposit near the upstream end of the flume with a low degree of dispersion in deposition lengths (i.e. low values of coefficients α_3 and β_3, eqn. 6.7). Conversely, the finer fractions deposit with a greater degree of dispersion along the flume (i.e. higher β_3 value). Overall, the median values of

fractional deposition length ($\widetilde{L}_i$) tend to increase with decreasing grain size d_i (i.e. α_3 increase as d_i reduces).

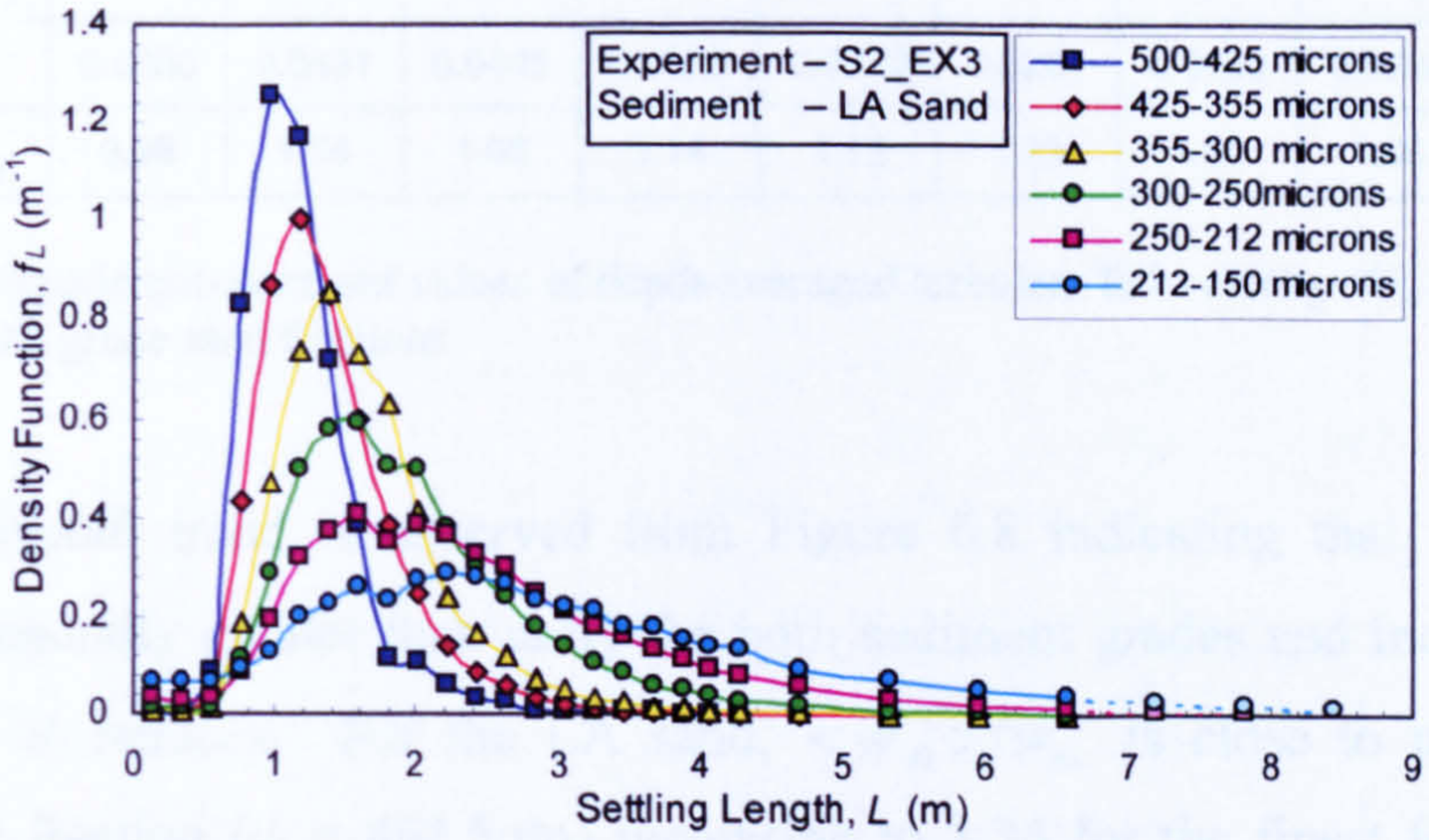

Figure 6.7 - Probability density function of settling length for individual fractions of LA sand measured during S2_EX3.

Corresponding p.d.f. distributions of deposition length for DB grade sediment show considerable scatter (Appendix 6.7), especially for the finer size fractions (d_i < ~90μm). Estimations of $\widetilde{L}_i$ were obtained from experiment S2_EX11 for size fractions with representative particle sizes d_i = 181, 137.5, 115.5 and 98μm size only. These $\widetilde{L}_i$ values were adjusted to account for the quantity of sediment transported beyond the downstream end of the flume. Upstream traps 1 and 2 were not included in the estimations as their deposits were thought to be mainly composed of re-circulated sediment, confirmed later through a sieve analysis of their composition.

Measured values of $\widetilde{L}_i$ and corresponding values of depth-averaged turbulent fall velocity ($\widetilde{w}'_{si}$) are tabulated in Appendices 6.6 and 6.7 for individual experiments with LA and DB sand, respectively. Experiment-averaged $<\widetilde{w}'_{si}>$ values are presented in Table 6.6 for both LA and DB sand. These $<\widetilde{w}'_{si}>$ values clearly show a decreasing tendency as the representative grain size d_i reduces.

A direct comparison between the depth-averaged turbulent fall velocities $<\widetilde{w}'_{si}>$ and still water fall velocities w_{si} is obtained by plotting the non-dimensional fall velocity ratio $<\widetilde{w}'_{si}>/w_{si}$ against representative grain size d_i (Figure 6.8). Note that w_{si} values for DB sand fractions were computed directly from Cheng (1997) (eqn. 4.1, pp.96) as no formal measurements of still water fall velocity were undertaken.

	LA Grade Sediment (μm)						DB Grade Sediment (μm)			
	500-425	**425-355**	**355-300**	**300-250**	**250-212**	**212-150**	**212-150**	**150-125**	**125-106**	**106-90**
d_i (μm)	462.5	390	327.5	275	231	181	181	137.5	115.5	98
$<\tilde{w}'_{si}>$ (m/s)	0.0587	0.0512	0.0436	0.0367	0.0303	0.0248	0.0195	0.0158	0.0109	0.0084
w_{si} (m/s)	0.0600	0.0491	0.0405	0.0322	0.0270	0.0201	0.0150	0.0095	0.0070	0.0052
$<\tilde{w}'_{si}>/w_{si}$	**0.98**	**1.04**	**1.08**	**1.14**	**1.12**	**1.23**	**1.30**	**1.66**	**1.56**	**1.62**

Table 6.6 - Experiment-averaged values of depth-averaged turbulent fall velocity $<\tilde{w}_{si}>$ for LA and DB grade sand fractions

An overall trend is observed from Figure 6.8 indicating that $<\tilde{w}'_{si}>/w_{si}$ values are generally greater than unity for both sediment grades and increase as the particle size d_i reduces. For the LA sand, $<\tilde{w}'_{si}>/w_{si}$ is close to unity for the coarsest size fraction (d_i = 462.5μm) increasing to 1.24 for the finest fraction (d_i = 181μm), representing a 24% enhancement in turbulent fall velocity. For the DB sand, $<\tilde{w}'_{si}>/w_{si}$ values range from about 1.30 to 1.65, representing a 30-65% enhancement of turbulent fall velocity. A degree of uncertainty must be attached to the predicted $<\tilde{w}'_{si}>/w_{si}$ values for the DB sand as they are based on the results from just one experiment (S2_EX11) and require adjustment to the calculated median settling lengths L_i to account for material deposited outwith the flume and re-circulation effects.

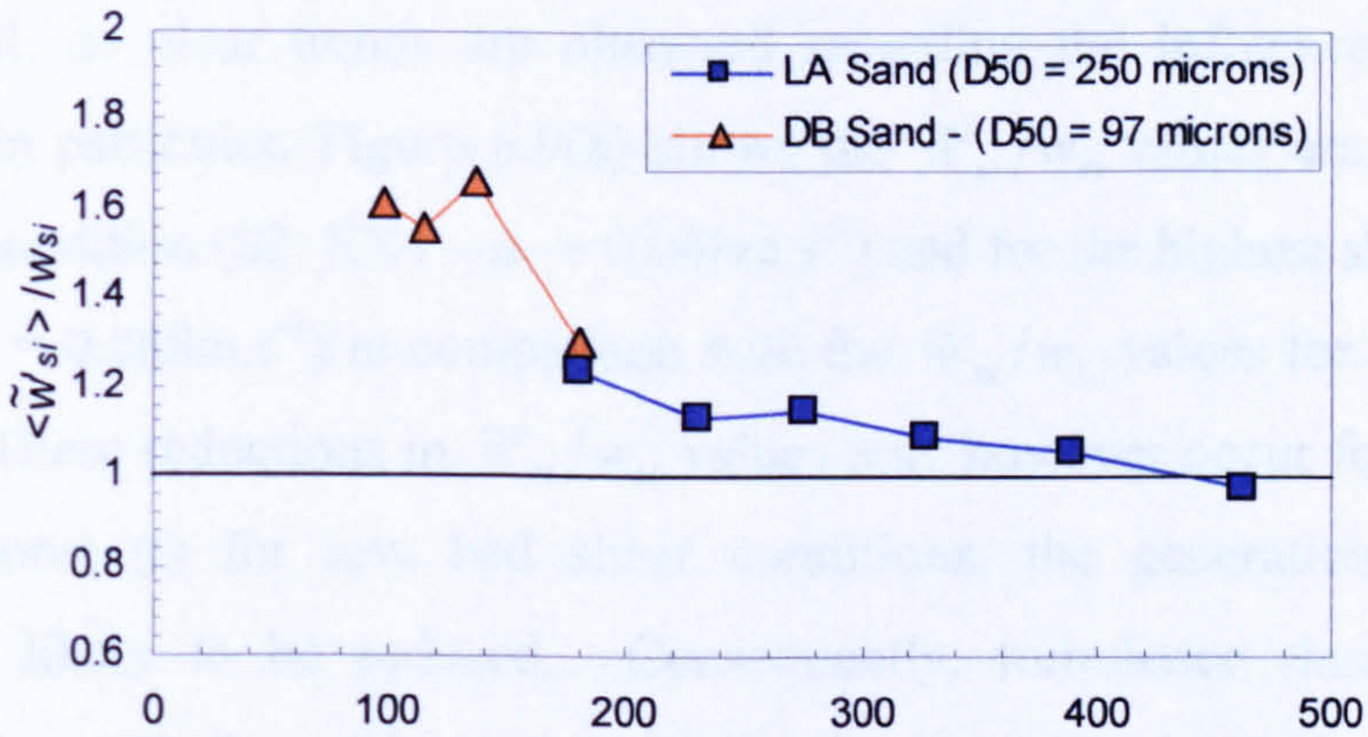

Figure 6.8 - Variation of experiment-averaged non-dimensional fall velocity ratio $<\tilde{w}'_{si}>/w_{si}$ with grain size d_i for individual LA and DB sand fractions.

Figure 6.9 presents two plots for LA sand showing the depth-averaged non-dimensional fall velocity ratio $\tilde{w}'_{si}/w_{si}$ against particle size d_i for experiments with different bed materials and varying shear velocity conditions u_*.

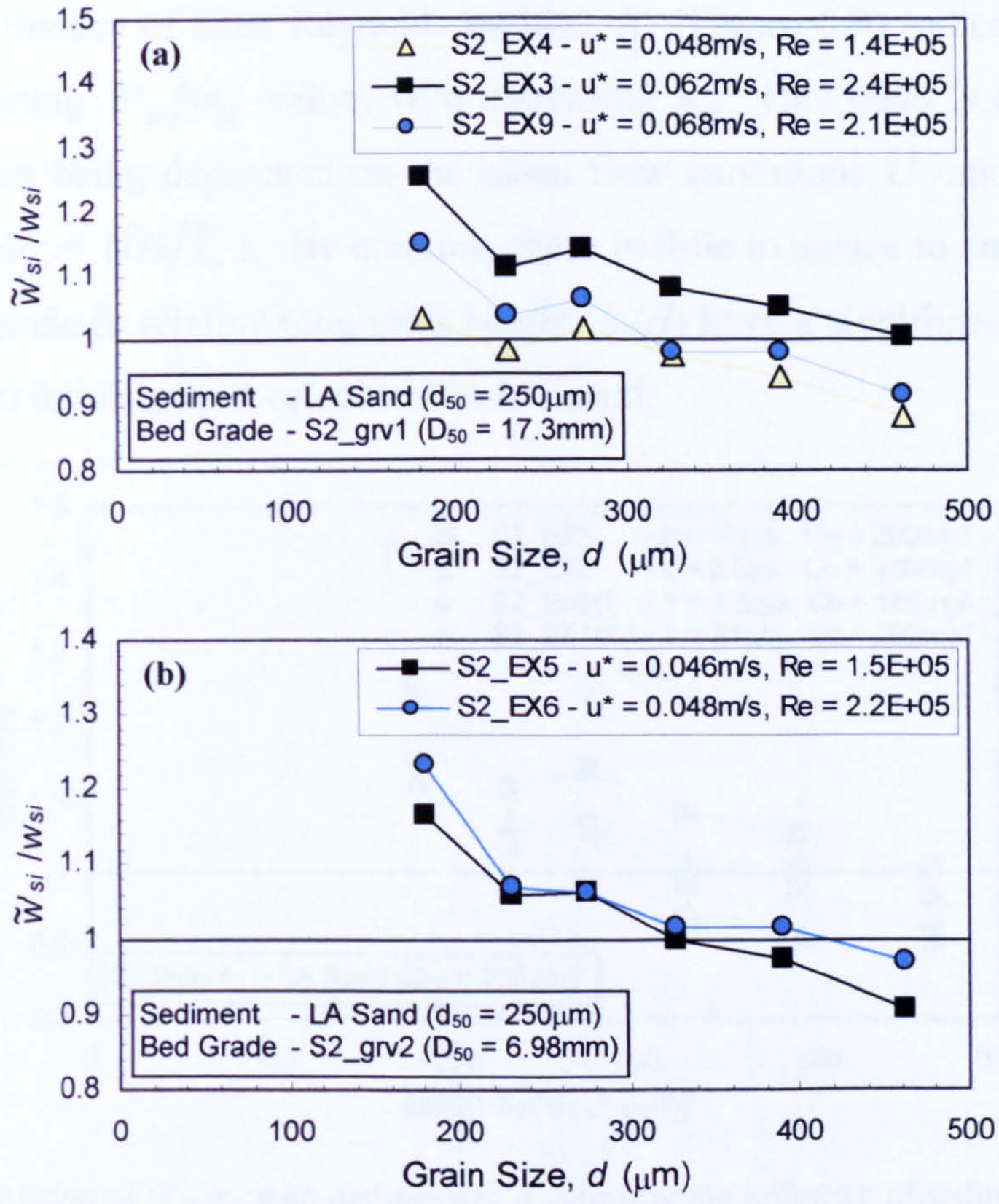

Figure 6.9 - Variation of $\tilde{w}'_{si}/w_{si}$ with particle size d_i, showing the influence of bed gravel grade, shear velocity u_* and flow Reynolds number R_e.

Overall, no clear trends are observed regarding the influence of the shear velocity u_*. In particular, Figure 6.9(a) shows the $\tilde{w}'_{si}/w_{si}$ values are lower for the lowest shear condition (S2_EX4 – $u_* = 0.048\text{m.s}^{-1}$) and for the highest shear condition (S2_EX9 – $u_* = 0.068\text{m.s}^{-1}$) in comparison with the $\tilde{w}'_{si}/w_{si}$ values for S2_EX3 ($u_* = 0.062\text{m.s}^{-1}$). These reductions in $\tilde{w}'_{si}/w_{si}$ values may however occur for two entirely different reasons: (i) for low bed shear conditions, the generation of near-bed turbulence is likely to be reduced. Consequently, turbulence should have less influence on the vertical particle motion and the depth-averaged turbulent fall velocity should approach that in still water conditions (i.e. $\tilde{w}'_{si} \approx w_{si}$); (ii) for high bed shear conditions, the probability of particle deposition on initial contact with the bed surface may be reduced, as suggested in Series 1A (Figure 4.8, pp.107). Subsequent particle motions will therefore increase the median deposition length $\tilde{L}_i$ and, hence, reduce in the depth-averaged turbulent fall velocity.

The influence of flow Reynolds number R_e (Figure 6.9) indicates a general trend of increasing $\widetilde{w}'_{si}/w_{si}$ values with increasing R_e. This trend is expected with both parameters being dependent on the mean flow conditions $\overline{U}$ and H (i.e. $R_e = 4\overline{U}H/\nu$ and $\widetilde{w}'_{si} = \overline{U}H/\widetilde{L}_i$). By contrast, there is little evidence to suggest that the bed material grade or relative roughness height (k_s/H) have a significant effect on the depth-averaged turublent fall velocities for LA sand.

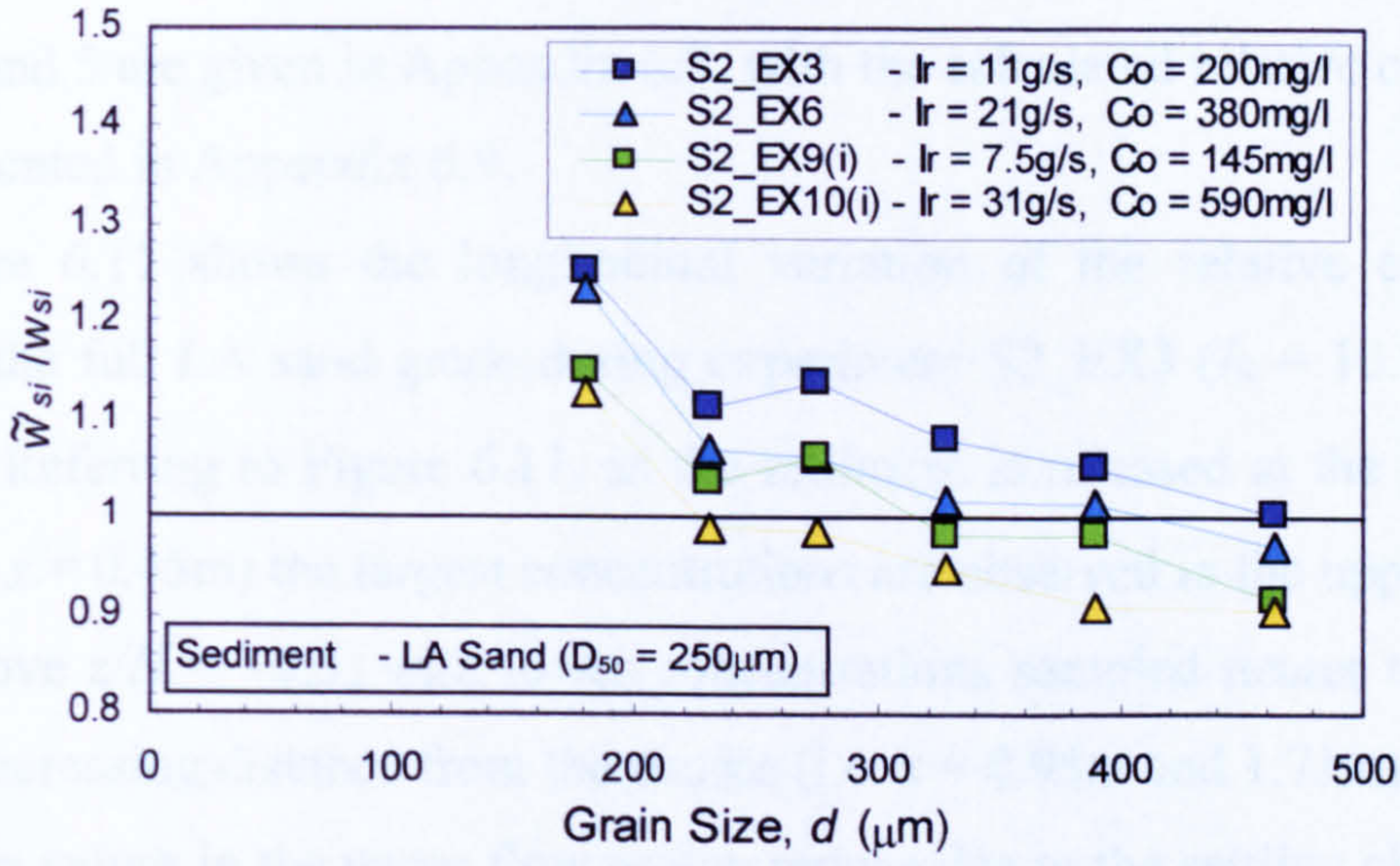

Figure 6.10 - Variation of $\widetilde{w}'_{si}/w_{si}$ with particle size d_i, showing the influence of sediment input rate I_R and initial sediment concentration C_0.

Figure 6.10 above presents the results for $\widetilde{w}'_{si}/w_{si}$ from four experiments split into two pairs with similar mean hydraulic conditions to consider the influence of sediment input rate I_R and initial concentration C_0. The results for experiments S2_EX3 and EX6 (H = 0.1-0.11m, U = ~0.6m.s^{-1}) were obtained with sediment input rates of 11g.s^{-1} and 21g.s^{-1} (C_0 = 200 and 380mg.ℓ^{-1}), respectively, while S2_EX9(i) and EX10(i) (H = 0.08m, U = ~0.73m.s^{-1}) were run at input rates of 7.5 and 31 g.s^{-1} (C_0 = 145 and 590mg.ℓ^{-1}), respectively. Figure 6.10 shows that the $\widetilde{w}'_{si}/w_{si}$ values are generally larger for the experiments with lower input rates I_R and initial concentration C_0, although the differences appear to diminish at the extremities of the LA particle size distribution (i.e. d_i = 462.5 and 181μm). It is possible that the influence of fractional input rate and concentration (I_{Ri} and C_{0i}) diminishes for LA sand fractions at the extremities of the LA size distribution as they constitute only a small percentage of the overall LA grade.

6.4.2.3 Measured Sediment Concentration Profiles

Suspended sediment concentration profiles were measured at five locations along the length of the flume, each profile consisting of four samples taken at different elevations within the flow. Once collected, each concentration sample was sieved to obtain its fractional composition and divided by the initial fractional concentrations at the source (C_{0i}) to obtain the non-dimensional relative concentration C_i/C_{0i}. Detailed sediment concentration data sets measured during experiments S2_EX3, 4 and 5 are given in Appendix 6.8, with the calculated relative concentration profiles presented in Appendix 6.9.

Figure 6.11 shows the longitudinal variation of the relative concentration profiles for the full LA sand grade during experiment S2_EX3 (I_R = 10.9 g.s^{-1}; C_0 = 200 mg.ℓ). Referring to Figure 6.11, as the sediment is released at the free surface, initially (i.e. x = 0.45m) the largest concentrations are observed in the upper section of the flow above z/H = ~0.5, with lower concentrations sampled nearer to the gravel bed. With increasing distance from the source (i.e. x = 0.95m and 1.71m), the relative concentration values in the upper flow region reduce due to the settling characteristics of the sand. This coincides with initially increased relative concentration measurements at the near-bed sampling locations. However, increasing deposition of near-bed material through the bed layer reduces the sediment concentration remaining within the near-bed flow at sample locations further downstream (i.e. x = 2.71m and 3.71m).

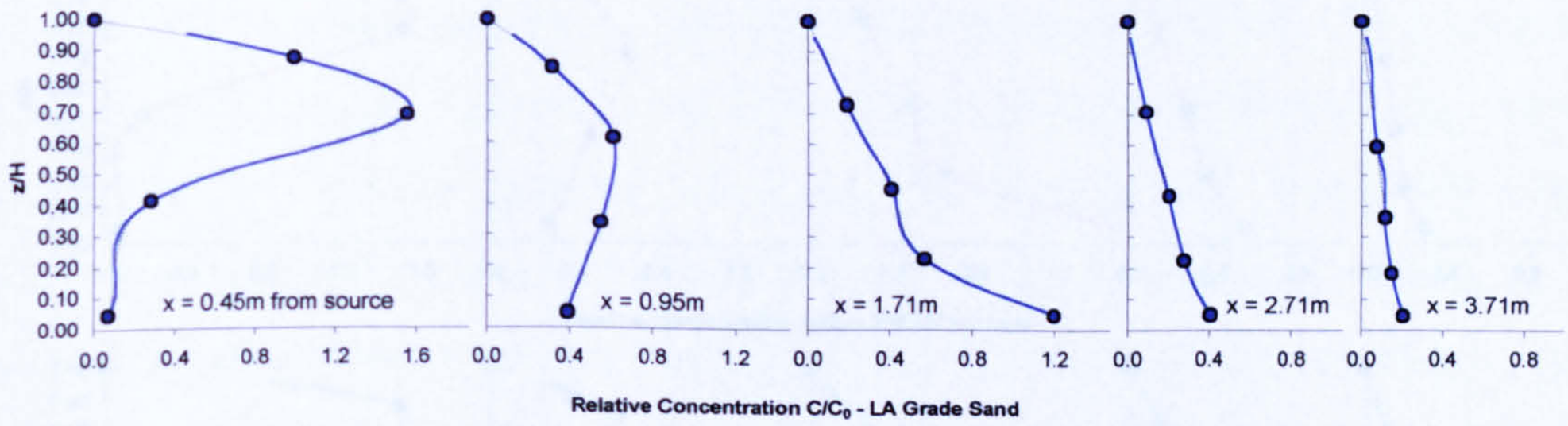

Figure 6.11 - Relative concentration profiles for LA sand and experiment S2_EX3 at 1.25m, 1.75m, 2.5m, 3.5m and 4.5m from upstream end of flume. (Note: sediment source @ 0.795m downstream).

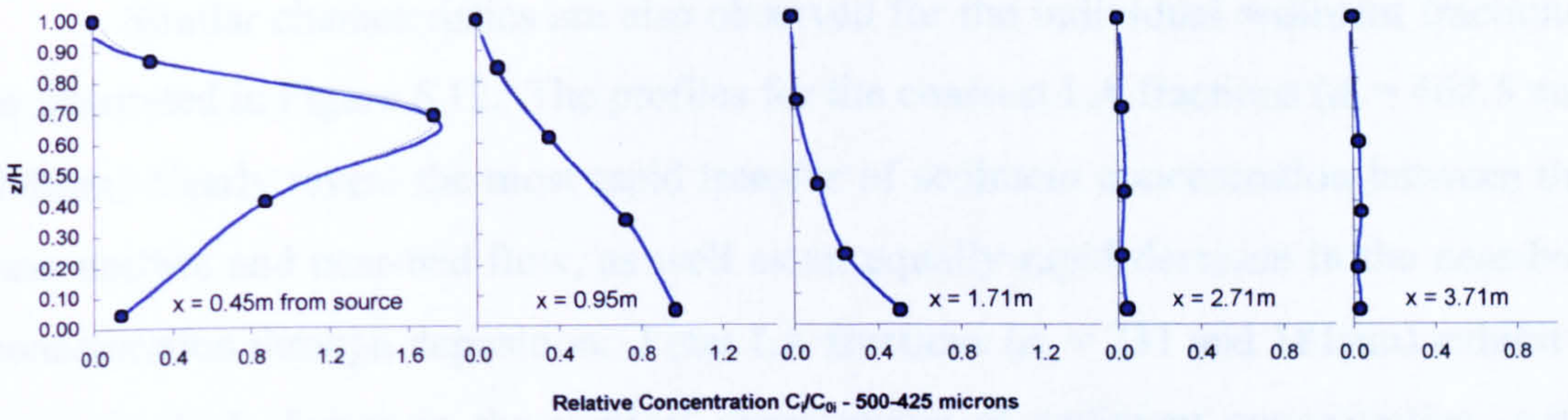

Figure 6.12 - Relative concentration profiles for individual LA sand fractions (S2_EX3).

Similar characteristics are also observed for the individual sediment fractions, as illustrated in Figure 6.12. The profiles for the coarsest LA fractions (d_i = 462.5 and 390μm) clearly reveal the most rapid transfer of sediment concentration between the near surface and near-bed flow, as well as an equally rapid decrease in the near-bed concentration through deposition. Finer LA fractions (d_i = 231 and 181μm) exhibit a more gradual change in the vertical distributions of sediment concentration, with larger near-bed concentrations remaining at the downstream sample locations.

The main purpose in measuring the longitudinal and vertical variations in sediment concentration was to determine the non-dimensional turbulent fall velocity w'_{si}/u_* and vertical turbulent transfer coefficient $\varepsilon_{szi}/H.u_*$ of the LA sand from solution of the non-dimensional, integrated transfer equation (eqn. 6.3, pp.168). Note: the cubic spline approximations to the measured sediment concentration data, computed from two NAG Fortran Library routines, are shown as the solid coloured curves in Figures 6.11 and 6.12. The method by which unknowns w'_{si}/u_* and $\varepsilon_{szi}/H.u_*$ were calculated is detailed in Appendix 6.4.

(1) Overall and Fractional Sediment Settling Characteristics

Figure 6.13 presents three computed distributions of w'_s/u_* with relative depth z/H for the full LA sand grade and experiments S2_EX3, 4 and 5. The two data sets represented in each plot are obtained from (i) solving equation 6.3 using concentration profiles generated from the unsieved samples; and (ii) averaging the w'_{si}/u_* distributions obtained from individual fractional concentration profiles. Figure 6.13 reveals similar characteristics to the fractional-averaged plots of w'_s/u_* obtained during Series 1B (e.g. Figure 4.21, pp.129). Values of w'_s/u_* are highest at a relative depth of z/H = ~0.2 and decrease with increasing values of z/H. Below z/H = 0.2, w'_s/u_* values appear to remain relatively constant or slightly reduce in magnitude. It should be noted however that the vertical extent of the near-bed concentration sample tubes (i.e. diameter = 10mm; z/H range = 0.0-0.125) and disturbances caused by its position relative to the local bed arrangement may influence the predicted w'_s/u_* values in the proximity of the bed. Figures 6.13(b) and (c) show the largest standard deviations in w'_s/u_* values (shown as error bars) occur in the near-bed region and generally reduce with increasing z/H. This trend was also observed in Series 1B.

The maximum values of w'_s/u_*, ranging from about 0.9 to 1.5, are generally lower than similar values obtained in Series 1B, which ranged from 1.3 to 1.8. This difference might again be due to the sampling methods employed in both cases [i.e. the non-intrusive particle tracking technique (Series 1B) against the intrusive concentration sampling equipment (Series 2)].

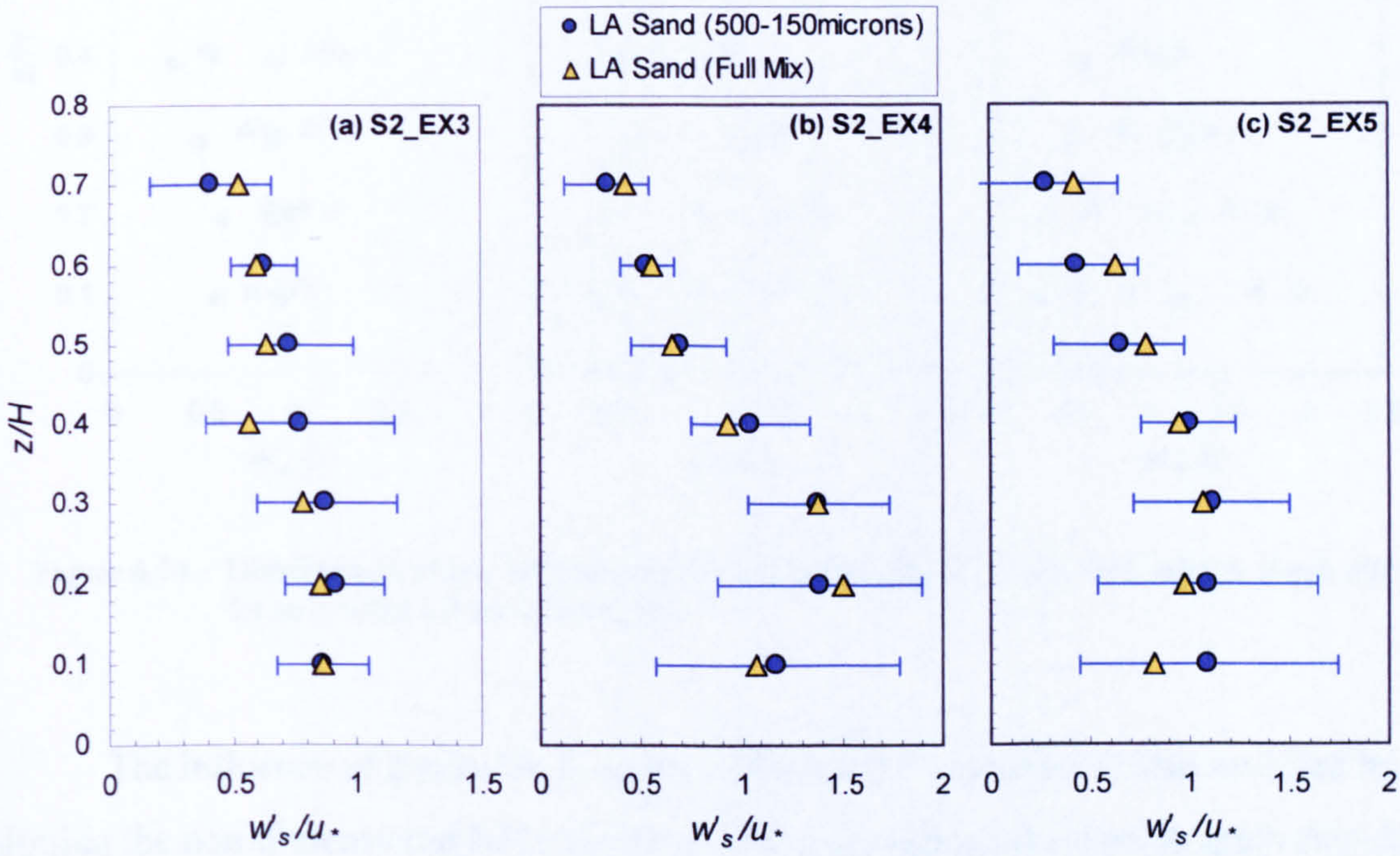

Figure 6.13 - Distributions of non-dimensional turbulent fall velocity w'_s/u_* with relative depth z/H for LA sand tested in experiments S2_EX3, 4 and 5. Error bars on "LA sand (500-150microns)" data sets represent ± one standard deviation in the average value obtained from individual size fractions.

Figure 6.14 presents fractional plots of w'_{si}/u_* against z/H for the LA grade sand. Comparison with equivalent plots obtained during Series 1B (e.g. Figure 4.24, pp.132) again reveals common trends: (i) the values of fractional settling parameter w'_{si}/u_* generally increases with grain size d_i; (ii) the measured data becomes more scattered with increasing proximity to the bed surface (except for S2_EX3); and (iii) less distinction is observed between w'_{si}/u_* values for different fractions in the outer flow region.

The maximum values of w'_{si}/u_* are shown to approach 2.0 for the coarsest fraction (d_i = 462.5μm) at z/H = 0.1, which is comparable with the maximum values obtained from the particle tracking experiments (i.e. w'_{si}/u_* = 1.5-2.5 at a similar location).

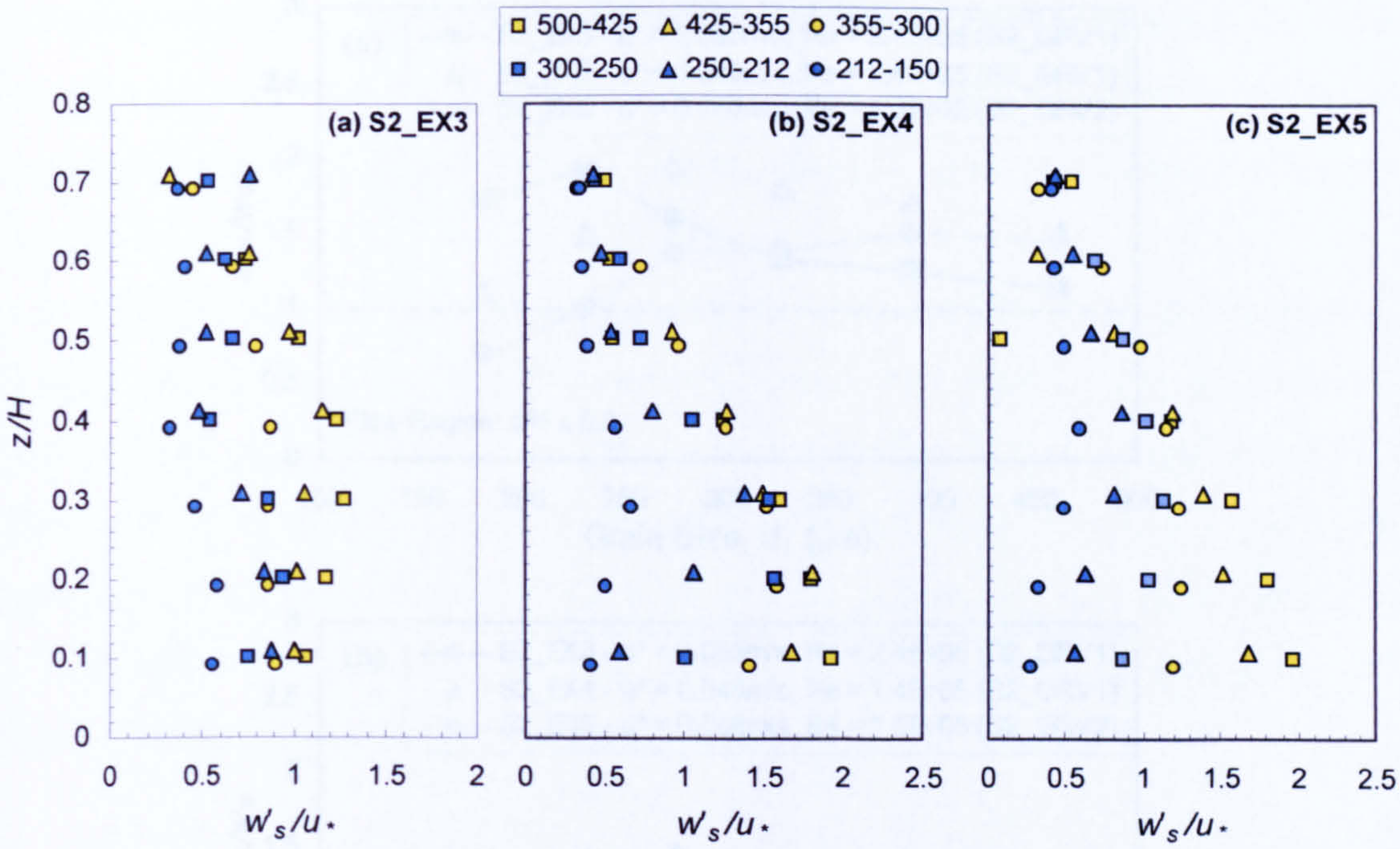

Figure 6.14 - Distributions of non-dimensional turbulent fall velocity w'_{si}/u_* with relative depth z/H for individual LA sand fractions.

The influence of grain size d_i on the turbulent fall velocities is also revealed by plotting the non-dimensional fall velocity ratio w'_{si}/w_{si} against the median grain size d_i for individual LA sand size fractions. The results from experiments S2_EX3, 4 and 5 are presented separately in Figure 6.15 within two flow regions defined as: (i) $z/H \leq 0.2$ (near-bed); (ii) $0.2 < z/H \leq 0.6$ (intermediate). In the outer flow region ($z/H \geq 0.6$), insufficient concentration and velocity data was available with which to compute w'_{si}/w_{si} values with any degree of certainty.

. Figure 6.15 reveals some similar characteristics to equivalent plots obtained in Series 1B (Figure 4.26, pp.136). The ratio w'_{si}/w_{si} is generally greater than unity, suggesting that turbulent fall velocities are often enhanced over still water fall velocities in the flow region considered (i.e. $z/H \leq 0.6$). This *enhancement* is greatest in the near-bed region of flow ($z/H \leq 0.2$) with w'_{si}/w_{si} reaching about 2.0, similar to that obtained in the Series 1B experiments over a natural gravel bed [i.e. $w'_{si}/w_{si\,max} = 1.97$, (S1B_EX4)]. Contrary to the Series 1B results, however, there is no clear trend of increasing w'_{si}/w_{si} values as particle size d_i reduces. In fact, the opposite is shown to occur for S2_EX5 data.

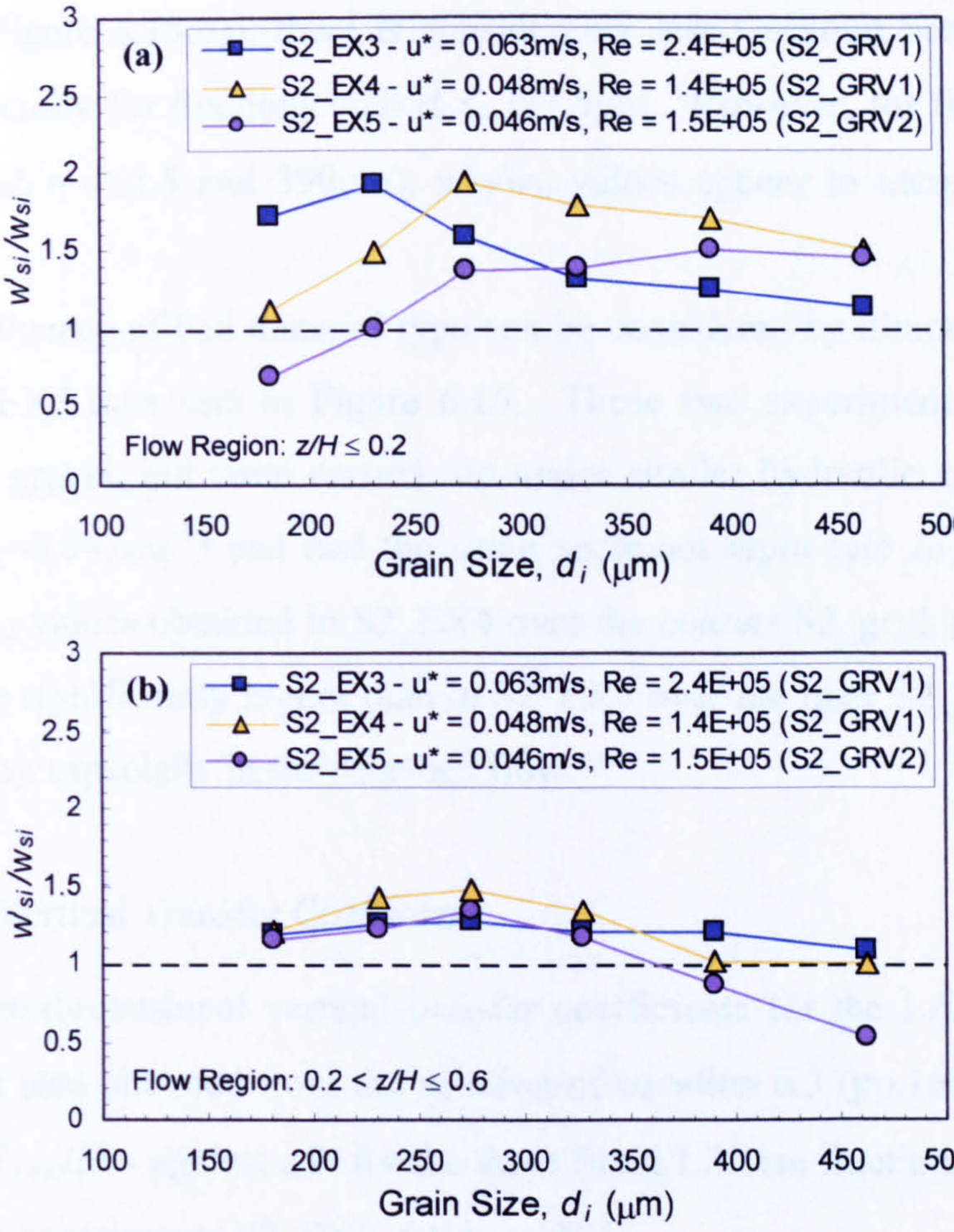

Figure 6.15 - Non-dimensional fall velocity ratio w'_{si}/w_{si} against grain size d_i for individual LA sand fractions: (a) near-bed flow (z/H ≤ 0.2); (b) intermediate flow ($0.2 < z/H \leq 0.6$).

In the intermediate flow region [Figure 6.15(b)], the w'_{si}/w_{si} values are also generally greater than unity, with a maximum value approaching 1.5. In general, the levels of enhancement observed were comparable with those obtained in Series 1B (e.g. Figure 4.26, pp.136). For the coarsest LA fraction (d_i = 462.5μm) in the experiment S2_EX5 data series, $w'_{si}/w_{si} \sim 0.5$, suggesting considerably hindered turbulent fall velocity. This characteristic is also observed in some of the Series 1B results obtained for the d_i = 462.5μm fraction.

The influence of shear velocity u_* on the non-dimensional fall velocity ratio (w'_{si}/w_{si}) again fails to reveal any conclusive trends in either flow region. Comparing the S2_EX1 data set (u_* = 0.063m.s^{-1}) with S2_EX4 and EX5 data sets (u_* = 0.048 and 0.046m.s^{-1}, respectively) in Figure 6.15(a), the w'_{si}/w_{si} values are highest for finer d_i = 181 and 231μm fractions under high shear conditions (i.e. S2_EX1). However, w'_{si}/w_{si} values for coarser fractions (i.e. $d_i \geq$ 327.5μm) are also shown to be generally

higher for the lower shear conditions (i.e. S2_EX3 and EX4). Within the intermediate flow region [Figure 6.15(b)], there is considerably less variation between the three data sets, especially for fractions with $d_i \leq 327.5\mu m$. However, for the two coarsest fractions (i.e. d_i = 462.5 and 390μm), w'_{si}/w_{si} values appear to increase with shear velocity u_*.

The influence of bed material type can be considered by direct comparison of S2_EX4 and EX5 data sets in Figure 6.15. These two experiments had different grades of bed gravel, but were carried out under similar hydraulic conditions (H = ~80mm, u_* = ~0.047ms^{-1}) and had the same sediment input rate I_R (~7.3g.s^{-1}). In general, w'_{si}/w_{si} values obtained in S2_EX4 over the coarser S2_grv1 gravel bed (D_{50} = 17.3mm) are significantly higher than in S2_EX5 over the finer S2_grv2 grade bed (D_{50} = 6.98mm), especially in the near-bed flow.

(2) Measured Vertical Transfer Coefficient

The non-dimensional vertical transfer coefficients for the LA sand fractions (ε_{szi}/Hu_*) were also obtained from the solution of equation 6.3 (pp.168). Figure 6.16 shows plots of ε_{szi}/Hu_* against z/H for the three finest LA size fractions (d_i = 275, 231 and 181μm) in experiments S2_EX3, EX4 and EX5.

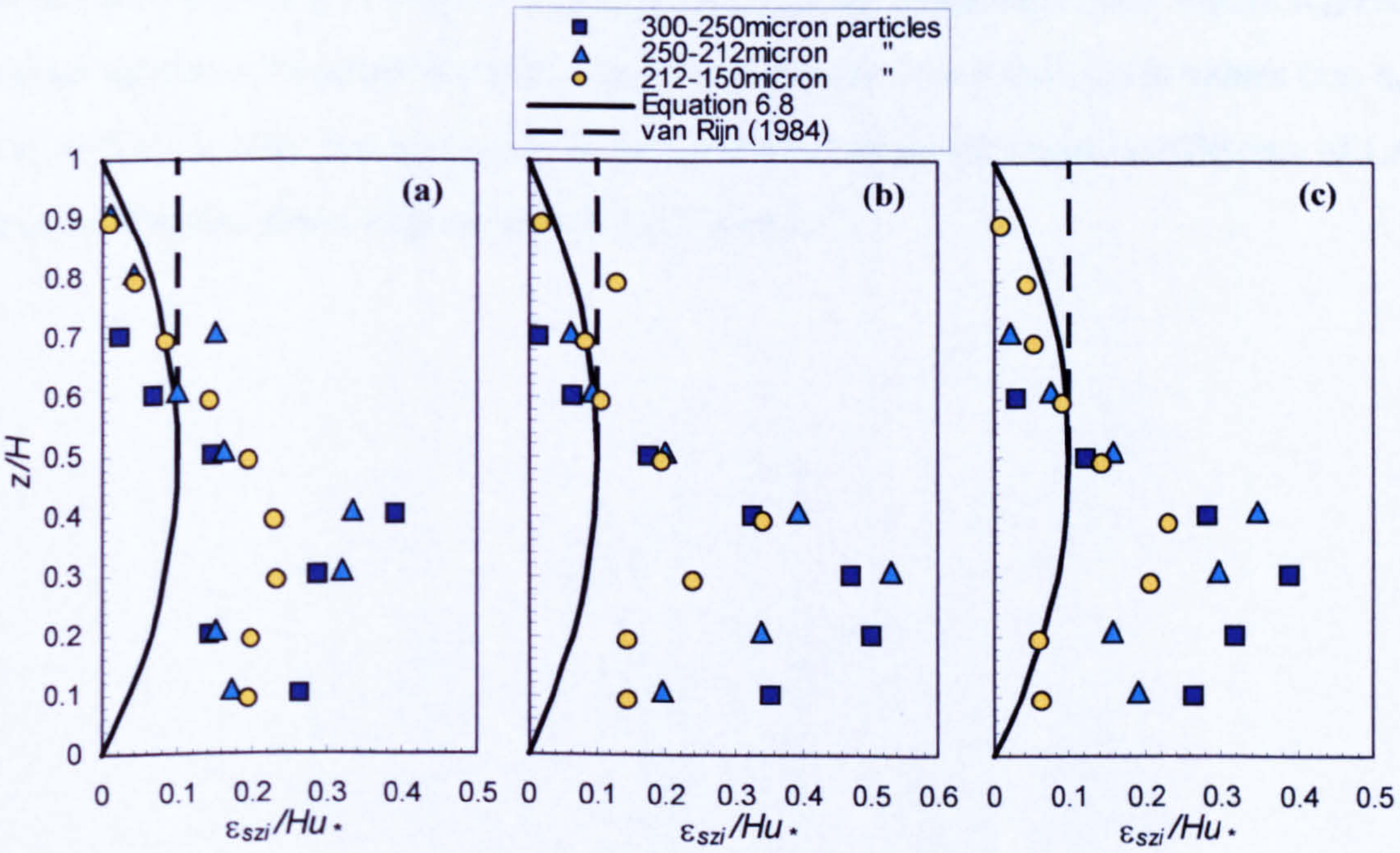

Figure 6.16 - Variation of non-dimensional vertical sediment transfer coefficient ε_{szi}/Hu_* with z/H for experiments: (a) S2_EX3 (H = 0.11m, u_* = 0.063ms^{-1}); (b) S2_EX4 (H = 0.08m, u_* = 0.048ms^{-1}) and; (c) S2_EX5 (H = 0.077m, u_* = 0.046ms^{-1}).

The significant levels of scatter suggest that no clear or consistent trends exist relating the vertical sediment transfer coefficient ε_{szi} to the hydraulic conditions ($H.u_*$) or to the grain size d_i.

The maximum values of ε_{szi}/Hu_* (up to ~0.5) arise in the region defined by $0.2 \leq z/H \leq 0.4$, which also corresponds to the flow region with the largest spread in data. In the flow region $z/H > 0.4$, the values of ε_{szi}/Hu_* tend to reduce with increasing z/H, whilst in the near-bed flow region ($z/H \leq 0.2$) a reduction in ε_{szi}/Hu_* is observed as the bed surface is approached. It is useful to compare the measured vertical transfer coefficients of the LA sand with the vertical transfer coefficients for fluid momentum (ε_f). The latter quantity is often assumed to have a parabolic distribution of the form,

$$\varepsilon_f = \kappa u_* z\left(1-\frac{z}{H}\right) \quad \text{or} \quad \frac{\varepsilon_f}{Hu_*} = \kappa\frac{z}{H}\left(1-\frac{z}{H}\right) \qquad \ldots.(6.8)$$

where ε_f is the transfer coefficient of fluid momentum and κ is the Von Karman constant (= 0.4, assumed). The parabolic distribution for ε_f/Hu_* is symmetric about $z/H = 0.5$, whereas the corresponding profiles of ε_{szi}/Hu_* are clearly skewed downwards towards the lower half of the flow ($z/H \leq 0.5$). Consequently, the ε_{szi}/Hu_* values are significantly higher than the corresponding ε_f/Hu_* values in the lower half of the flow ($z/H \leq 0.5$) (i.e. $\varepsilon_{sz} > \varepsilon_f$ or $\beta > 1$). In the outer flow ($z/H > 0.6$), ε_{szi}/Hu_* values appear to be approximately equal to or slightly lower than ε_f/Hu values (i.e. $\varepsilon_{sz} \leq \varepsilon_f$ or $\beta \leq 1$). The characteristics of the measured vertical transfer coefficients of LA sand will be discussed in greater detail in Chapter 7.

6.4.2.4 Deposition Rates, Initial and Near-bed Concentrations

Average overall and fractional deposition rates (Δ_0 and Δ_{0i}) within the centreline traps were calculated for each experiment from the total weight of material deposited in the traps divided by the overall trap surface area and the duration of the sediment release from the source point. Calculated values of Δ_0 for the LA and DB grade sands are tabulated in Table 6.7 along with corresponding values of the initial sediment concentration (C_0).

Run No.	EXT1	EX1	EX2	EX3	EX4	EX5	EX6
Sand Grade	LA	LA	LA	LA	LA	LA	LA
C_0 (mg.ℓ^{-1})	561.1	385.0	109.1	199.1	205.6	201.9	378.9
Δ_0 (g.s^{-1}.m^{-2})	5.84	3.31	0.96	1.87	1.23	1.27	3.83
Δ_0 (g.min^{-1}.m^{-2})	350.4	198.6	57.5	112.1	73.6	76.0	230.1
Run No.	**EX7**	**EX8**	**EX9(i)**	**EX9(ii)**	**EX10(i)**	**EX10(ii)**	**EX11**
Sand Grade	DB	LA	LA	LA	LA	LA	DB
C_0 (mg.ℓ^{-1})	140.7	129.2	144.0	129.2	589.2	589.2	264.5
Δ_0 (g.s^{-1}.m^{-2})	0.73	1.24	1.27	1.46	5.77	5.33	1.30
Δ_0 (g.min^{-1}.m^{-2})	43.9	74.5	76.3	87.5	346.0	319.8	77.9

Table 6.7 - Tabulated values of the average overall deposition rate Δ_0 within the centreline traps and corresponding values of initial sediment concentration C_0

In accordance with Carling (1984), the overall deposition rate Δ_0 is shown in Figure 6.17 to increase linearly with initial sediment concentration C_0 for both grades of sand and good correlation is obtained with the experimental data in both cases (R^2 = 0.96 – LA sand; R^2 = 0.99 – DB sand).

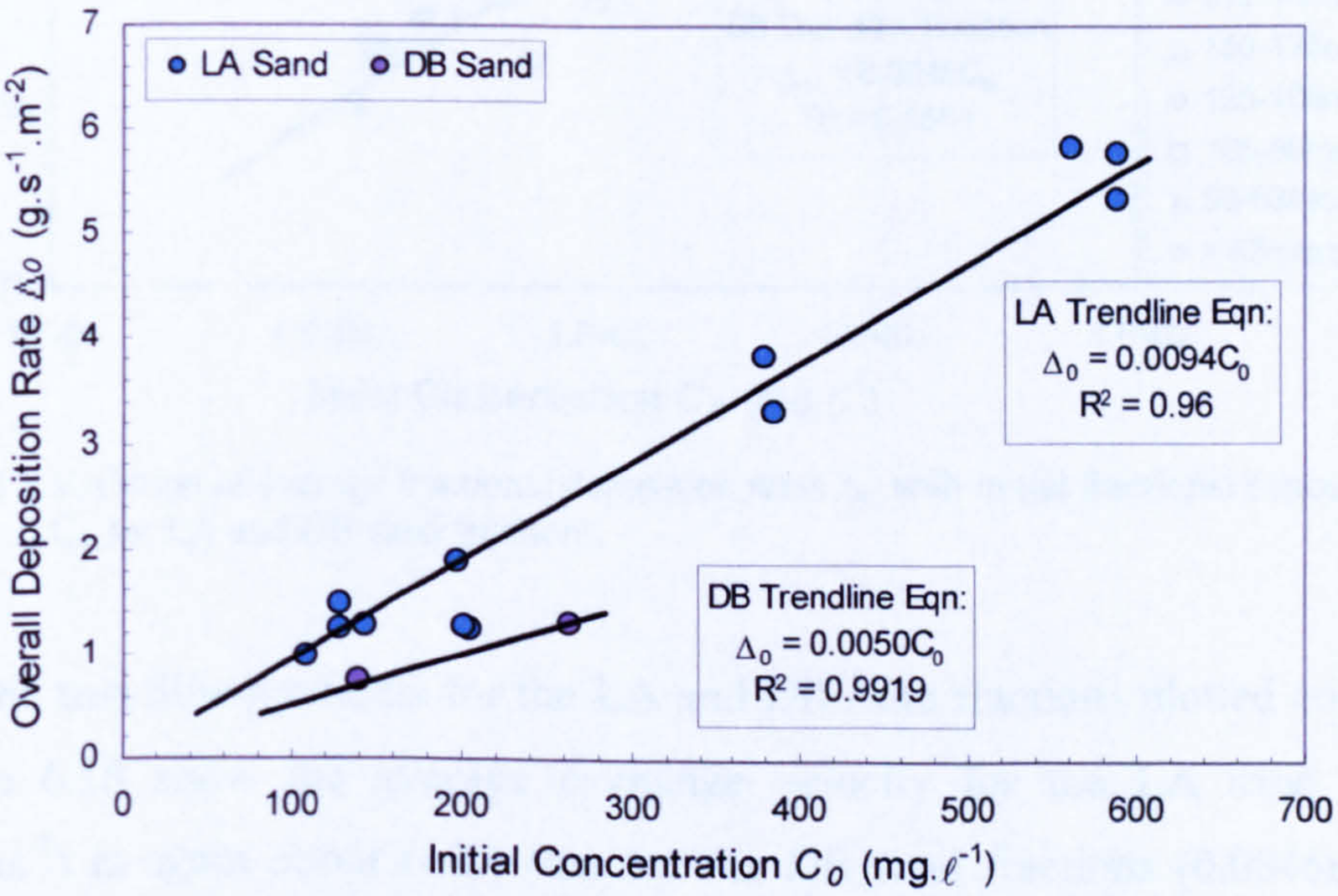

Figure 6.17 - Variation of average overall deposition rate Δ_0 with the initial sediment concentration C_0 for LA and DB sand

The linear trendlines, shown in Figure 6.17, intercept with the plot axes at the origin (i.e. $\Delta_0 = 0$ when $C_0 = 0$). Their gradients have the dimensions of velocity (m/s) and represent the average exchange velocity between the flow and the gravel bed (Carling 1984). The value of this exchange velocity for the LA grade sand is shown to be approximately twice that observed for the finer DB grade sand. However, this difference results from the significant quantity of DB sand that is transported beyond the downstream end of the flume. Clearly, a longer working section allowing both sediment grades to fully deposit within the flume bed would make the average exchange velocity independent of particle size d_i.

This is demonstrated in Figure 6.18, in which the average deposition rates and the initial sediment concentrations for individual LA sand size fractions reveal good linear correlation with each other ($R^2 = 0.96$). By comparison, more scatter is generally observed between fractional DB sand data ($R^2 = 0.86$) again resulting from the quantity of finer sand fractions, in particular, that are deposited outwith the working section of the flume.

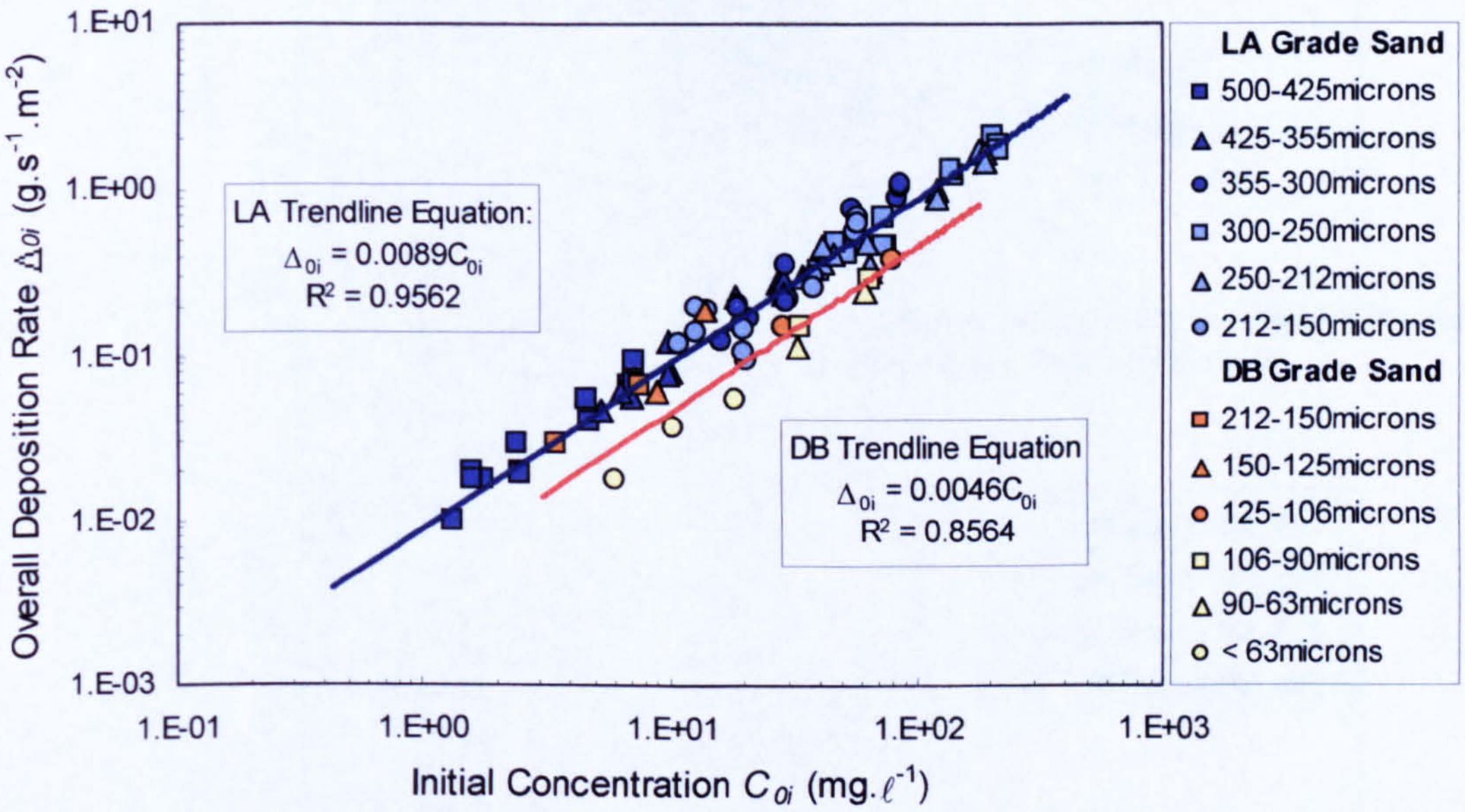

Figure 6.18 – Variation of average fractional deposition rates Δ_{0i} with initial fractional concentration C_{0i} for LA and DB sand fractions.

The trendline gradients for the LA and DB sand fractions plotted collectively in Figure 6.18 show the average exchange velocity for the LA sand fractions ($0.0089 ms^{-1}$) is again about twice that for the DB sand fractions ($0.0046 ms^{-1}$) and similar to the values shown in Figure 6.17 for the overall grading of the two sands.

(1) Longitudinal Variation in Deposition Rate (Δ_b) and Near-bed Concentration (C_b)

Comprehensive data on the quantity and composition of the deposited sediment samples collected along the centreline traps is tabulated in Appendix 6.10 for each Series 2 experiment. The longitudinal variation in sediment deposition (by weight) has previously been used in calculating the probability density functions (p.d.fs) for the overall and fractional deposition lengths of the LA and DB grade sands. It would therefore seem obvious that the longitudinal distributions of deposition rate (Δ_b and Δ_{bi}) will have similar lognormal characteristics, as confirmed by Figure 6.19 for experiments S2_EX3, 4, 8 and 11.

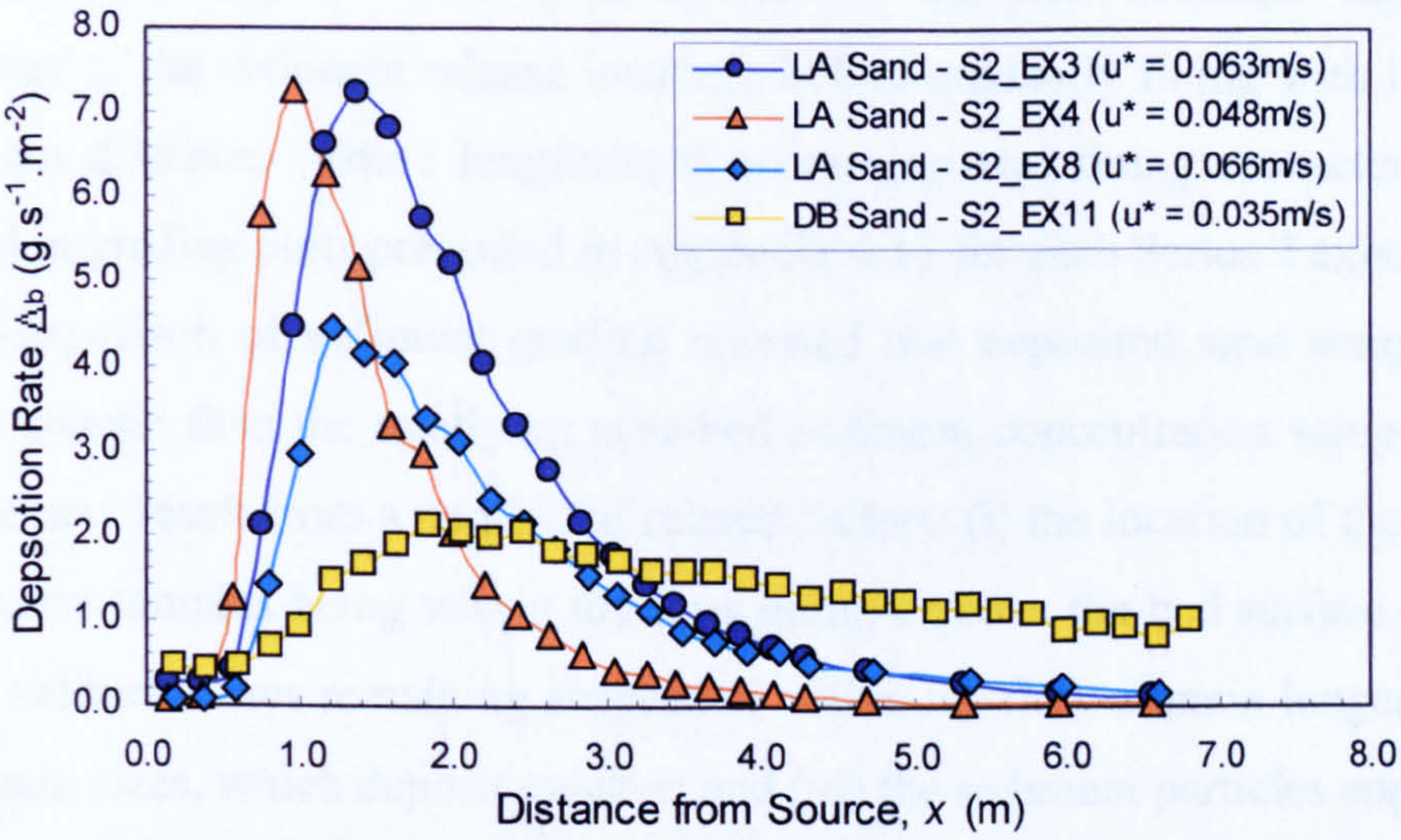

Figure 6.19 - Variation in deposition rate Δ_b with increasing distance from the sediment input location x for experiments S2_EX3, 4 and 8 (LA sand) and S2_EX11 (DB sand).

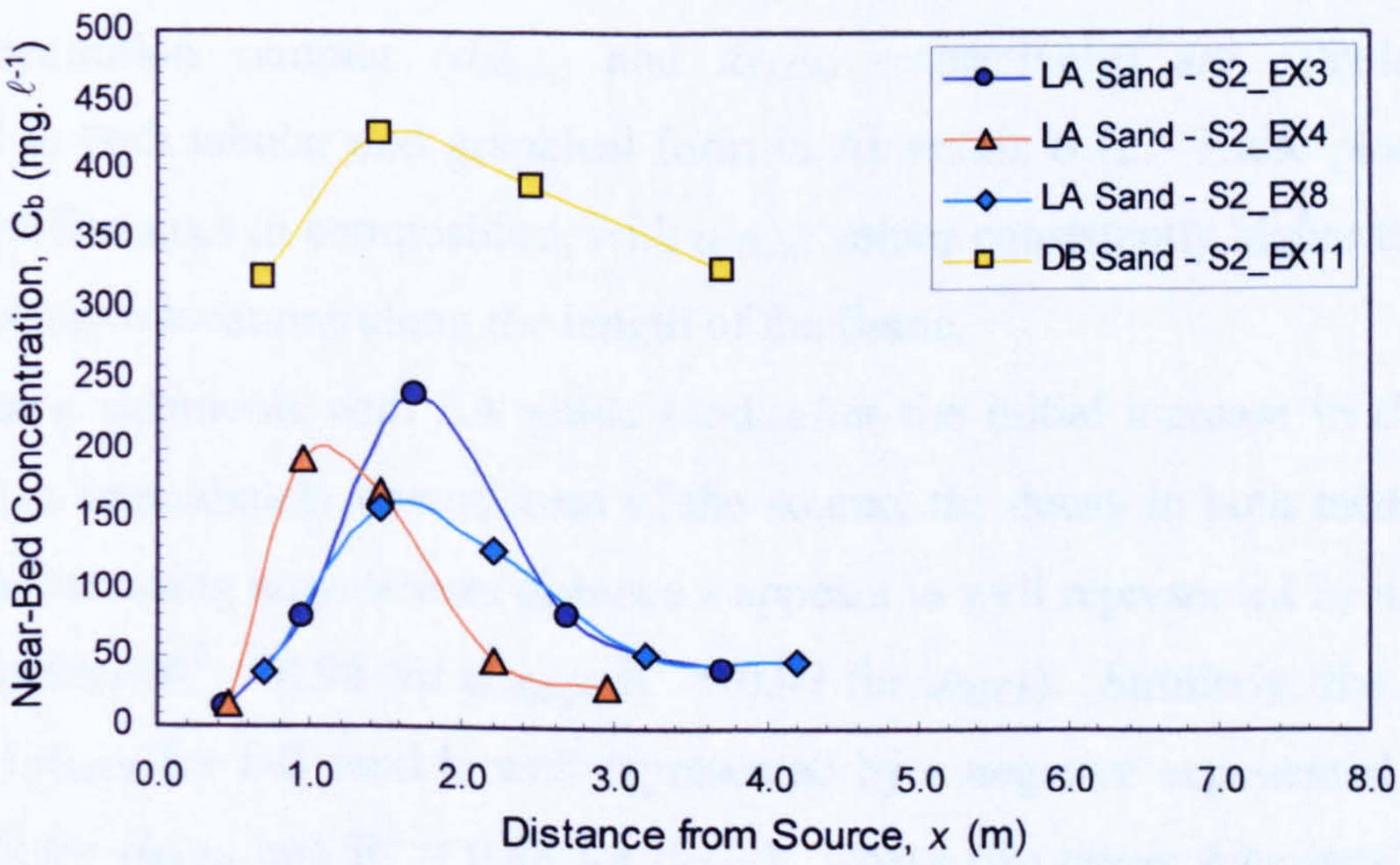

Figure 6.20 - Variation in near-bed concentration C_b with increasing distance from the sediment input location x for experiments S2_EX3, 4 and 8 (LA sand) and S2_EX11 (DB sand).

Corresponding distributions of near-bed concentration (C_b) for these four experiments (Figure 6.20) also show a similar log-normal type variation with increasing distance from the sediment source, although these distributions are not as well defined as for the deposition rate Δ_b. This is primarily due to the limited sampling locations along the flume length (5 max.), but may also be sensitive to the location of the sample tubes in relation to the local bed configuration.

(2) Composition of Near-bed and Deposited Sediment

Sieve analysis of the deposition and near-bed concentration samples revealed an initial coarsening in their composition for samples obtained immediately downstream of the sediment release location, before gradually fining with increasing downstream distance. These longitudinal coarsening and fining characteristics are illustrated in grading plots presented in Appendix 6.11 for each Series 2 experiment.

Comparison of sediment grading revealed that deposited sand samples were generally coarser than the overlying near-bed sediment concentration samples. This difference may result from a number of related factors: (i) the location of the near-bed concentration samples being within the flow domain above the bed surface interface; (ii) finer sediment sizes remaining suspended within the flow domain longer than the coarser grain sizes, which deposit quicker; and (iii) the sediment particles approaching the bed may not necessarily deposit on first contact with the bed (i.e. probability of deposition $p < 1$ – as shown in §4.3.4.3, pp.107).

The longitudinal variation of median grain size for both deposited and near-bed concentration samples ($d_{50,dep}$ and $d_{50,Cb}$, respectively) are calculated and presented in both tabular and graphical form in Appendix 6.12. These plots further highlight differences in composition, with $d_{50,dep}$ values consistently higher than $d_{50,Cb}$ values at sample locations along the length of the flume.

For experiments with LA grade sand, after the initial increase in $d_{50,dep}$ and $d_{50,Cb}$ values immediately downstream of the source, the decay in both median grain sizes with increasing downstream distance x appears to well represented by a negative power function ($R^2 = 0.98$ for $d_{50,dep}$; $R^2 = 0.97$ for $d_{50,Cb}$). Similarly, the decay of $d_{50,dep}$ and $d_{50,Cb}$ for DB sand is well represented by a negative exponential function ($R^2 = 0.99$ for $d_{50,dep}$ and $R^2 = 0.85$ for $d_{50,Cb}$). These two decay functions have the general form,

$$D_{50,(Cb,dep)} = a.x^{-b} \qquad \text{(LA grade sand)} \qquad \text{....(6.9a)}$$

$$D_{50,(Cb,dep)} = a.e^{-bx} \qquad \text{(DB grade sand)} \qquad \text{....(6.9b)}$$

where coefficients a and b are dependent on the experimental conditions and sediment properties. The concave profiles produced by these two decay functions are similar in form to natural downstream fining processes caused by size-selective transport and abrasion of bed materials that occur almost universally in gravel bed river channels (e.g. Parker 1991; Hoey and Ferguson 1994).

Figure A6.70 of Appendix 6.12 compares the downstream decay of $d_{50,dep}$ in experiments S2_EX9 and 10 for both filled and unfilled centreline traps, allowing the influence of a substrate layer (S2_grv2 gravel) to be assessed. For the low sediment input rate used in S2_EX9 (I_R = 7.5 g/s), no apparent difference in the $d_{50,dep}$ values was observed along the flume length. However, for the high sediment input rate used in S2_EX10 (I_R = 30.6 g/s), the $d_{50,dep}$ values for material deposited within the filled half of each trap were generally larger than corresponding $d_{50,dep}$ values in the unfilled half. It was noted that under this high input rate, complete intrusion (or siltation) occurred within some of the substrate filled traps, resulting in a build up of fines within the overlying gravel bed layer (Figure 6.21 below).

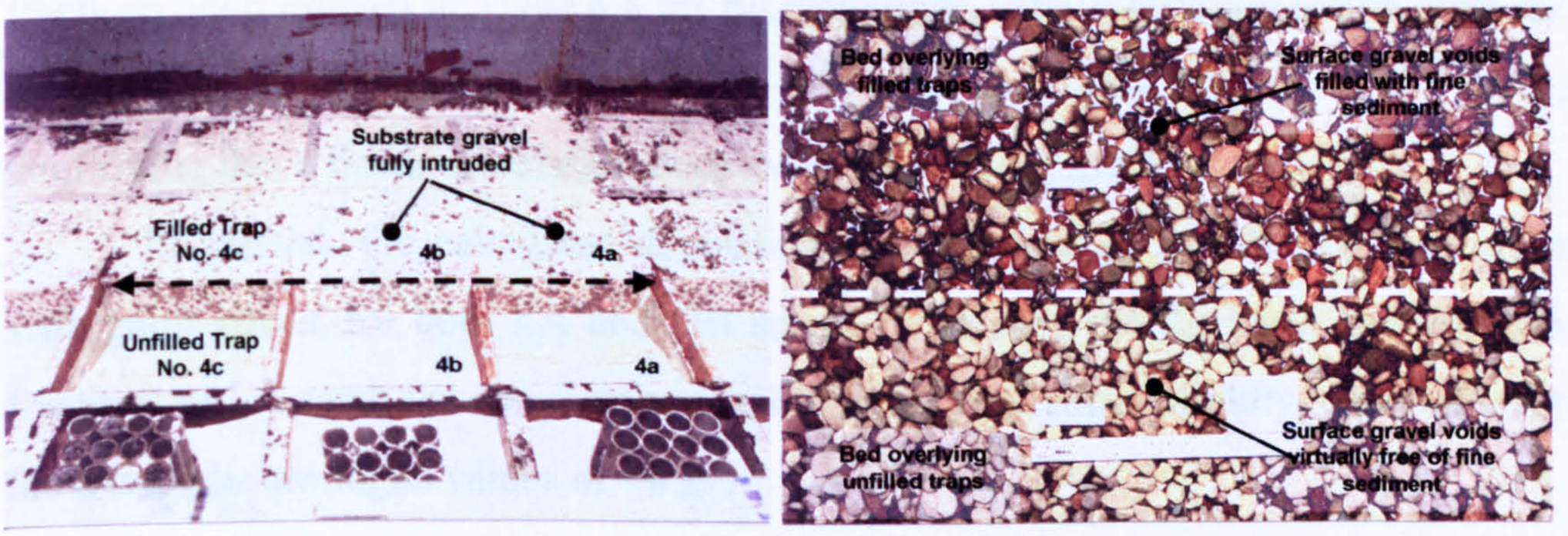

Figure 6.21 - (a) Photograph showing fine sediment intrusion into the filled and unfilled sections of the centreline traps, experiment S2_EX10; (b) Photograph looking down on bed surface, showing fines trapped in surface interstices of bed layer overlying filled traps.

The presence of fine sediments within the surface layer resulting from of complete intrusion of the underlying substrate material will clearly reduce the probability of deposition p, with fine sediments more susceptible to re-entrainment at these specific locations. Consequently, sediments that reach the fully silted bed surface are likely to be transported further downstream to a location where intrusion

below the gravel surface layer is possible, thus increasing $d_{50,dep}$ values at locations immediately downstream of the fully silted bed.

6.4.2.5 Prediction of Deposition Velocity

The linear relationship between the average deposition rate (Δ_0) and the initial sediment concentration (C_0) is well established for both full LA and DB sand grading and individual size fractions *i*. Similar linear correlations have been found to exist between the near-bed sediment concentrations (C_b and C_{bi}) and local sediment deposition rates (Δ_b and Δ_{bi}) in underlying traps (e.g. Peloutier, 1998). From equation 6.4 (pp.169), the ratios Δ_b/C_b and Δ_{bi}/C_{bi} represent the overall and fractional deposition velocities (w_d and w_{di}), previously defined by Peloutier (1998) as the vertical transfer velocity through the experimental bed layer.

A comprehensive set of experimental results containing all measured values of Δ_b, C_b and w_d (Δ_{bi}, C_{bi} and w_{di}) is presented in Appendix 6.13 for each Series 2 experiment. Average values of w_{di} for each size fraction of LA and DB sand in individual experiments were obtained by two methods: (i) the arithmetic mean of the individual Δ_{bi}/C_{bi} values; (ii) the gradient of the 'best-fit' trendline through the Δ_{bi}/C_{bi} data. Experiment-averaged deposition velocities $\langle w_{di} \rangle$ for both LA and DB sand fractions are presented in Table 6.8 for both methods. The correlation coefficients for method (ii) are shown to be reasonable high for each size fraction ($R^2 > 0.70$), confirming that a linear correlation does exist between Δ_{bi} and C_{bi}.

In general, the calculated deposition velocities $\langle w_{di} \rangle$ are shown to increase with grain size d_i for both LA and DB sands. However, for the three coarsest size fractions of LA sand, the $\langle w_{di} \rangle$ values stabilise or even reduce slightly, especially for the arithmetic-averaged values of $\langle w_{di} \rangle$.

The non-dimensional ratio w_{di}/w_{si} provides a direct comparison between predicted deposition velocities w_{di} and corresponding fall velocities in still water conditions w_{si} for individual size fractions of LA and DB sands. Detailed results for w_{di}/w_{si} values obtained from both the arithmetic mean and trendline gradient values of w_{di} are again presented in Appendix 6.13, while experimental-averaged $\langle w_{di} \rangle/w_{si}$ values are shown in Tables 6.8.

LA Grade Sand			Gradient of Linear Correlation			Arithmetic Mean	
Size Class	d_i (μm)	w_{si} (ms^{-1}) *	$<w_{di}>$ (ms^{-1})	R^2	$<w_{di}>/w_{si}$ *	$<w_{di}>$ (ms^{-1})	$<w_{di}>/w_{si}$ *
500-425μm	462.5	0.0600	0.0588	0.89	0.98	0.0458	0.76
425-355μm	390	0.0491	0.0614	0.91	1.25	0.0489	1.00
355-300μm	327.5	0.0405	0.0557	0.92	1.38	0.0493	1.22
300-250μm	275	0.0322	0.0369	0.94	1.14	0.0379	1.18
250-212μm	231	0.0270	0.0210	0.88	0.78	0.0254	0.94
212-150μm	181	0.0201	0.0134	0.70	0.67	0.0160	0.80
Full Mix	250	0.0296	0.0309	0.91	1.04	0.0306	1.03
DB Grade Sand			**Gradient of Linear Correlation**			**Arithmetic Mean**	
Size Class	d_i (μm)	w_{si} (ms^{-1}) †	$<w_{di}>$ (ms^{-1})	R^2	$<w_{di}>/w_{si}$ †	$<w_{di}>$ (ms^{-1})	$<w_{di}>/w_{si}$ †
212-150μm	181	0.0166	0.0196	0.80	1.18	0.0217	1.31
150-125μm	137.5	0.0106	0.0144	0.97	1.36	0.0111	1.05
125-106μm	115.5	0.0079	0.0073	0.94	0.93	0.0071	0.90
106-90μm	98	0.0059	0.0053	0.91	0.91	0.0053	0.91
90-63μm	76.5	0.0037	0.0031	0.96	0.84	0.0031	0.84
63-53μm	58	0.0022	0.0018	-	0.83	0.0018	0.83
53-45μm	49	0.0016	0.0014	-	0.89	0.0015	0.95
45-38μm	41.5	0.0011	0.0012	-	1.06	0.0013	1.14
Full Mix	97	0.0057	0.0049	0.69	0.85	0.0054	0.94

Table 6.8 - Experiment-averaged values of deposition velocity $<w_{di}>$ for LA and DB sand fractions. † w_{si} calculated from Cheng (1997) * w_{si} obtained from measurements (§4.2).

The variation of $<w_{di}>/w_{si}$ with grain size d_i is plotted graphically in Figure 6.22. In general, it is shown that the arithmetic mean and trendline gradient $<w_{di}>/w_{si}$ values show common trends for similar fine sediment types.

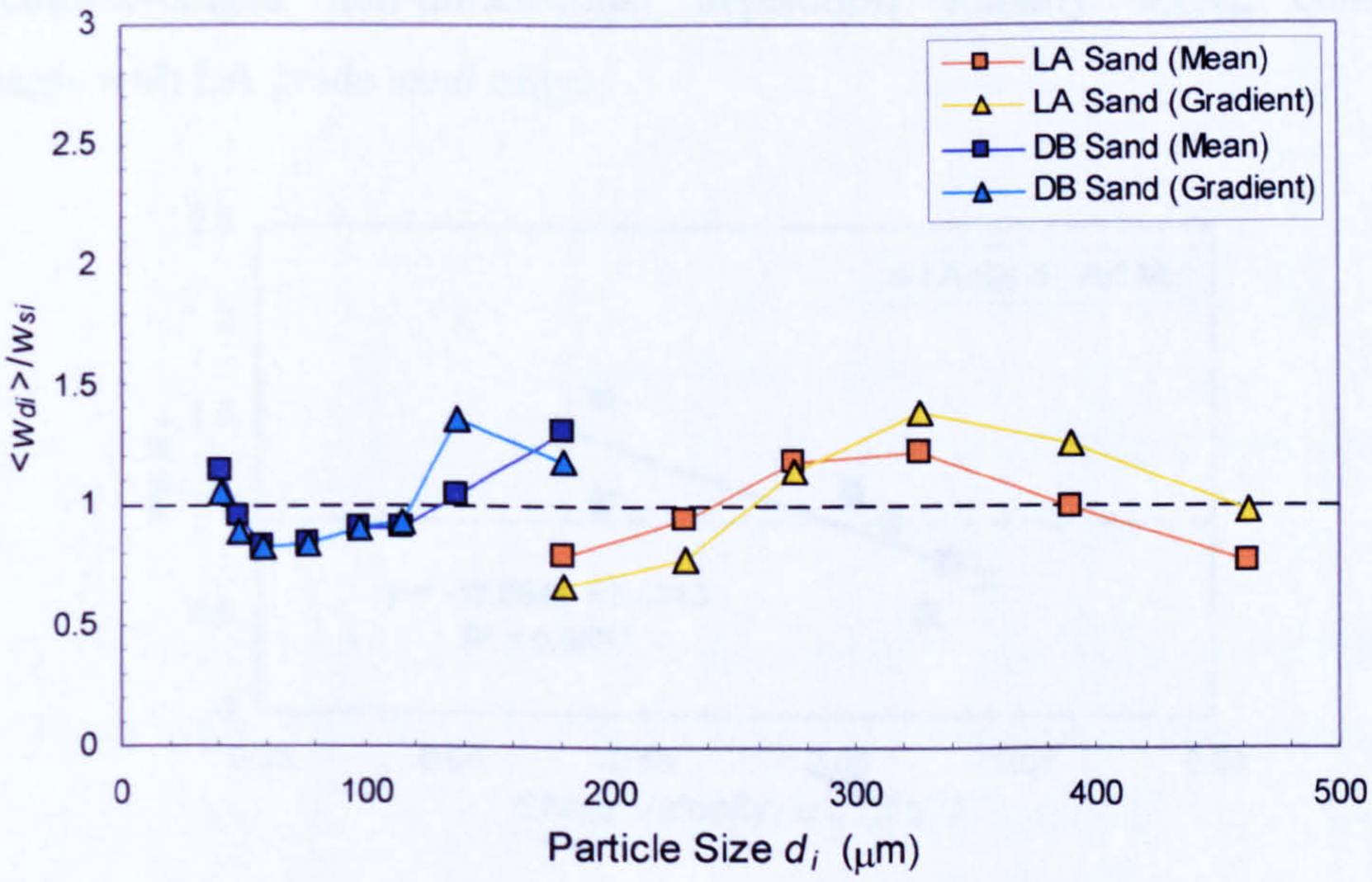

Figure 6.22 - Variation of $<w_{di}>/w_{si}$ with particle size d_i for the LA and DB sands.

For the LA sand, $\langle w_{di}\rangle/w_{si}$ values, close to or lower than unity for the coarsest size fraction (d_i = 462.5 μm), are shown to increase with reducing grain size d_i, reaching maximum values of between 1.2 and 1.4 (i.e. enhanced deposition) at $d_i \sim$ 327.5μm. For the three finest size fractions $\langle w_{di}\rangle/w_{si}$ values reduce with d_i, becoming retarded (i.e. $\langle w_{di}\rangle/w_{si} < 1.0$) for the finest LA sand fractions (d_i = 231 and 181 μm). By contrast, the opposite trend is observed for DB sand (Figure 6.22). Generally, $\langle w_{di}\rangle/w_{si}$ values are enhanced (i.e. $\langle w_{di}\rangle/w_{si} > 1.0$) at the extremities of the size distribution (d_i = 181, 137.5 and 41.5 μm), whilst being lower than unity (i.e. retarded) for intermediate size fractions.

The clear discrepancy between the LA and DB data sets plotted in Figure 6.22 may arise from the limited experimental data available from which the DB grade values of $\langle w_{di}\rangle$ were predicted (experiments S2_EX7 and 11 only). In particular, the average shear velocity conditions under which the limited DB sand experiments were conducted ($\overline{u}_* = 0.040\text{ms}^{-1}$) was considerably lower than for the remaining LA sand experiments ($\overline{u}_* = 0.058\text{ms}^{-1}$). Furthermore, $\langle w_{di}\rangle$ values for the DB fractions are on average about an order of magnitude lower than $\langle w_{di}\rangle$ values for LA fractions. Therefore any uncertainties associated with the prediction of w_{si} from Cheng (1997) will have a magnified effect on the predicted values of $\langle w_{di}\rangle/w_{si}$, especially for the finer DB fractions.

The influence of the shear velocity u_* is illustrated in Figure 6.23 below for the fraction-averaged non-dimensional deposition velocity w_d/w_s, considering experiments with LA grade sand only.

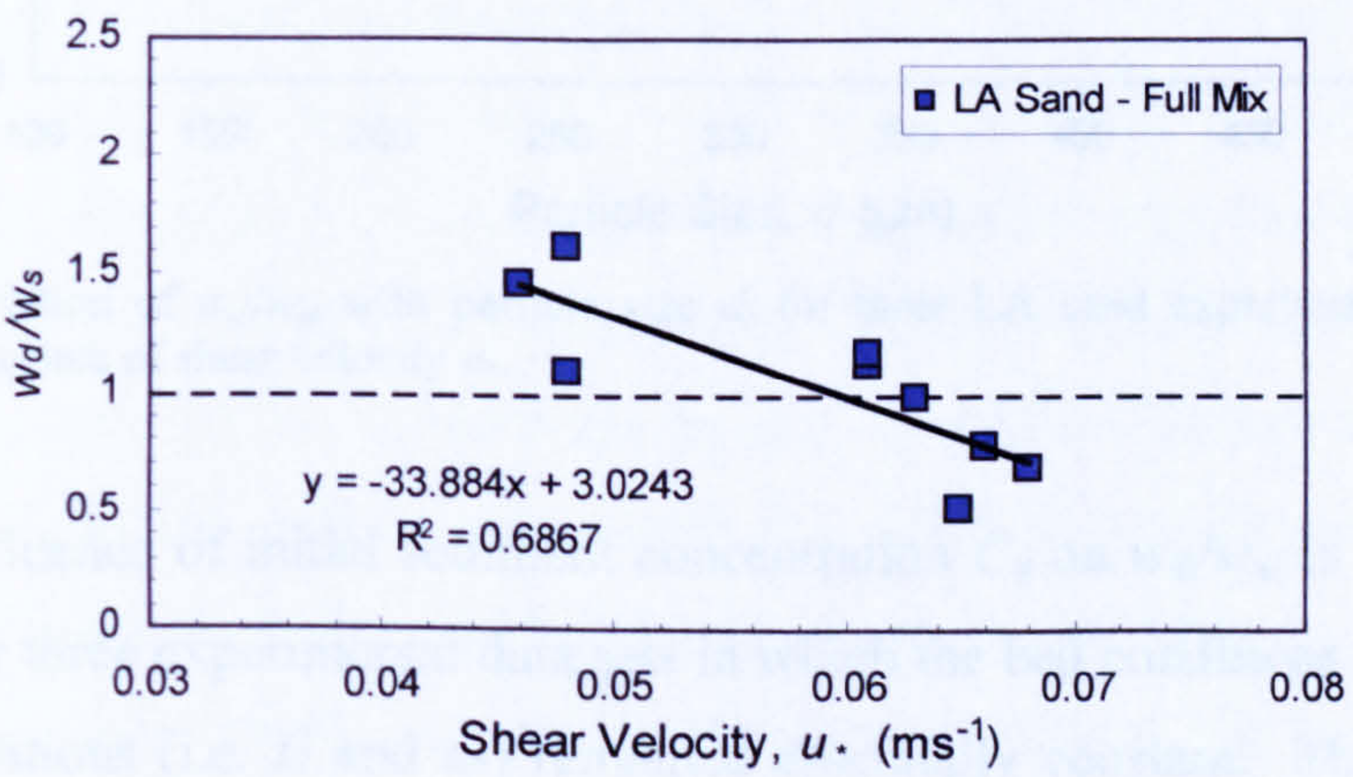

Figure 6.23 – Variation of fraction-averaged w_d/w_s with shear velocity u_* for experiments with LA sand.

This plot reveals a general trend of increasing w_d/w_s values as the shear velocity u_* reduces. The linear trendline plotted through the data shows some degree of correlation ($R^2 = 0.69$) with this trend, and suggests that $w_d/w_s > 1.0$ (i.e. enhanced) when $u_* \leq \sim 0.06 ms^{-1}$.

In terms of the influence of shear velocity u_* on grain size d_i dependent values of w_{di}/w_{si}, Figure 6.24 presents results for three experiments with similar bed conditions (S2_grv1 gravel). This plot suggests a trend of higher w_{di}/w_{si} values occurring under lower shear velocity conditions and vice versa. This trend is most evident when comparing the data sets for experiments S2_EX4 and S2_EX8, which had similar flow depths ($H \sim 80mm$) but different bed slopes ($S_0 = 0.004$ and 0.01, respectively). It is noted that the w_{di}/w_{si} values are very similar for the four finest fractions ($d_i = 181$, 231, 275 and 327.5μm), but remain consistently higher for the lower shear conditions prevalent in S2_EX4. Above $d_i = 327.5\mu m$, the two data sets diverge, with w_{di}/w_{si} remaining above unity for $d_i = 390\mu m$ and 462.5μm in S2_EX4, while reducing to less than 1.0 for the same d_i values in S2_EX8.

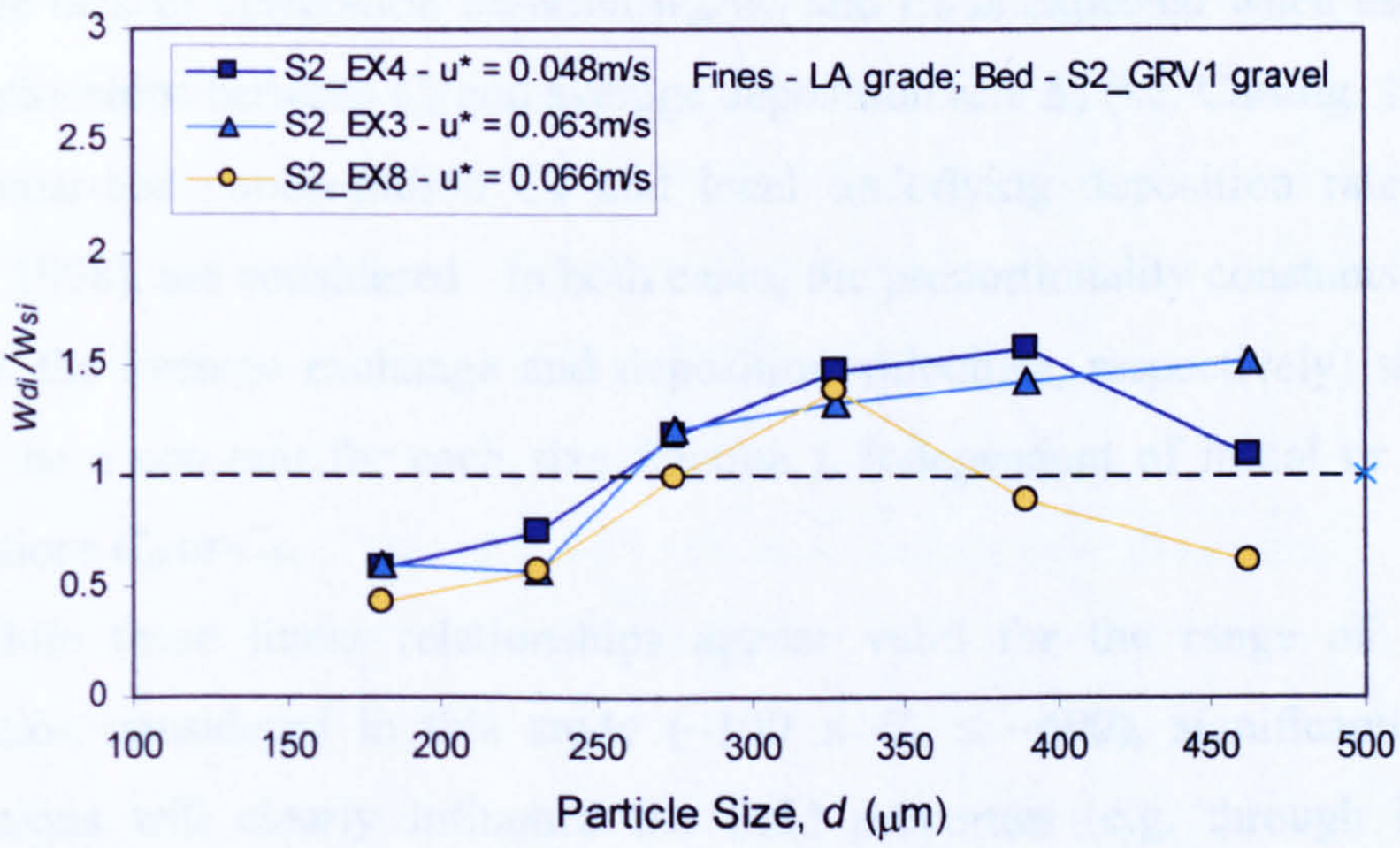

Figure 6.24 - Variation of w_{di}/w_{si} with particle size d_i for three LA sand experiments showing the influence of shear velocity u_*.

The influence of initial sediment concentration C_0 on w_{di}/w_{si} is considered in Figure 6.25 for three experimental data sets in which the bed conditions and prevalent hydraulic conditions (i.e. H and u_*) remained essentially constant. This plot shows that no definitive trends exist for initial concentrations of 110, 200 and 390 mg.ℓ^{-1} and that w_{di}/w_{si} values are similar (~1.2 to1.4) for intermediate values of d_i (i.e. 275, 327.5

and 390μm). Greater divergence in w_{di}/w_{si} values is observed for the coarsest (d_i = 462.5μm) and two finest fractions of LA sand (d_i = 181 and 231μm), again however without any clear dependency on C_0.

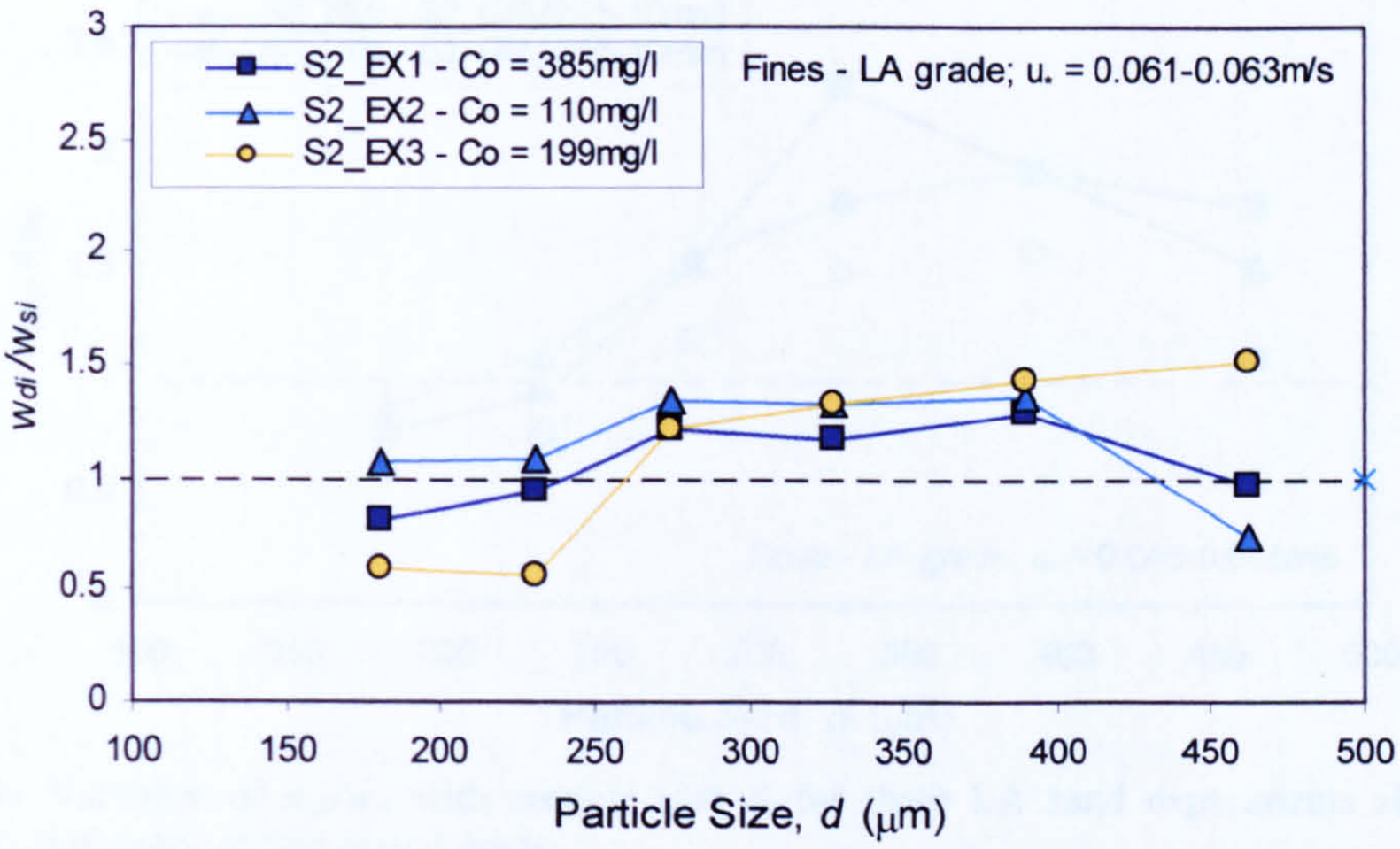

Figure 6.25 - Variation of w_{di}/w_{si} with particle size d_i for three LA sand experiments showing the influence of initial sediment concentration C_0.

The lack of correlation between w_{di}/w_{si} and C_0 is expected when established linear relationships between C_0 and average deposition rate Δ_0 (i.e. Carling, 1984) and between near-bed concentration C_b and local underlying deposition rate Δ_b (i.e. Peloutier, 1998), are considered. In both cases, the proportionality constants Δ_0/C_0 or Δ_b/C_b (i.e. the average exchange and deposition velocities, respectively) should by definition be a constant for each size fraction i, independent of initial or near-bed concentrations C_0 or C_b.

While these linear relationships appear valid for the range of sediment concentration considered in this study (~100 ≤ C_0 ≤ ~600), significantly higher concentrations will clearly influence the fluid properties (e.g. through increased viscosity) and the prevalent flow conditions (e.g. through the damping of turbulence). These changes may alter the physical mechanisms by which sediment is deposited at the bed surface, which may in turn affect the universal validity of these linear relationships between deposition rates and sediment concentrations.

For three experiments with similar hydraulic conditions, the influence of bed material type on w_{di}/w_{si} values is assessed in Figure 6.26 for the two gravel grades used in Series 2. While the three data sets are shown to have similar variations with

d_i, the w_{di}/w_{si} values in experiments with the finer S2_grv2 gravel (D_{50} = 6.98mm) are consistently higher than in the coarser S2_grv1 gravel bed (D_{50} = 17.3mm).

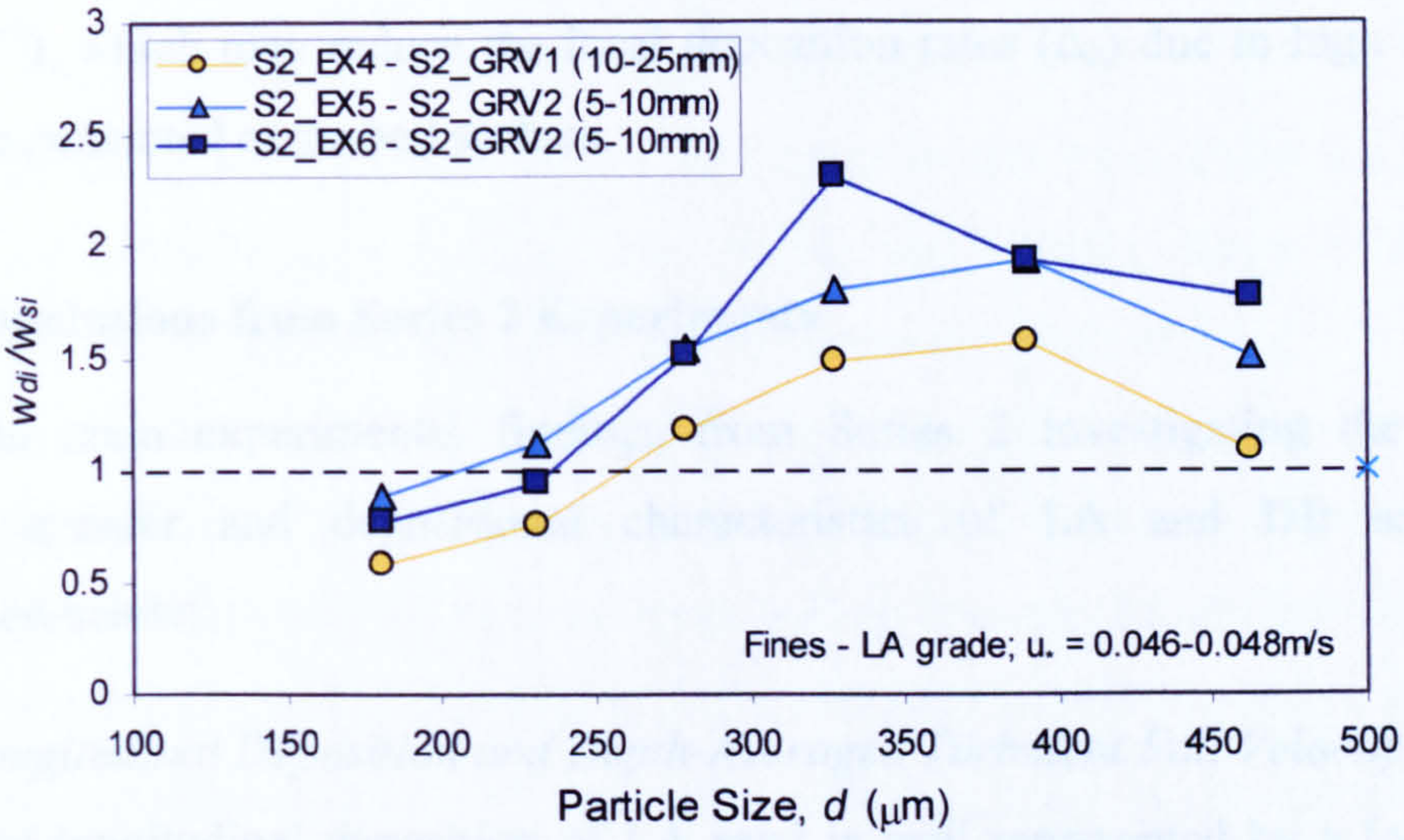

Figure 6.26 - Variation of w_{di}/w_{si} with particle size d_i for three LA sand experiments showing the influence of bed gravel grade.

Finally, the influence of a substrate material layer present within the centreline traps is shown in Figure 6.27. Clearly, the w_{di}/w_{si} values obtained when the traps were unfilled (i.e. S2_EX8) are generally greater than when the underlying traps were filled with S2_grv2 gravel. This would suggest that the presence of a finer substrate layer below a coarser surface layer acts to hinder the deposition of the LA sand, compared to when the underlying traps are left empty.

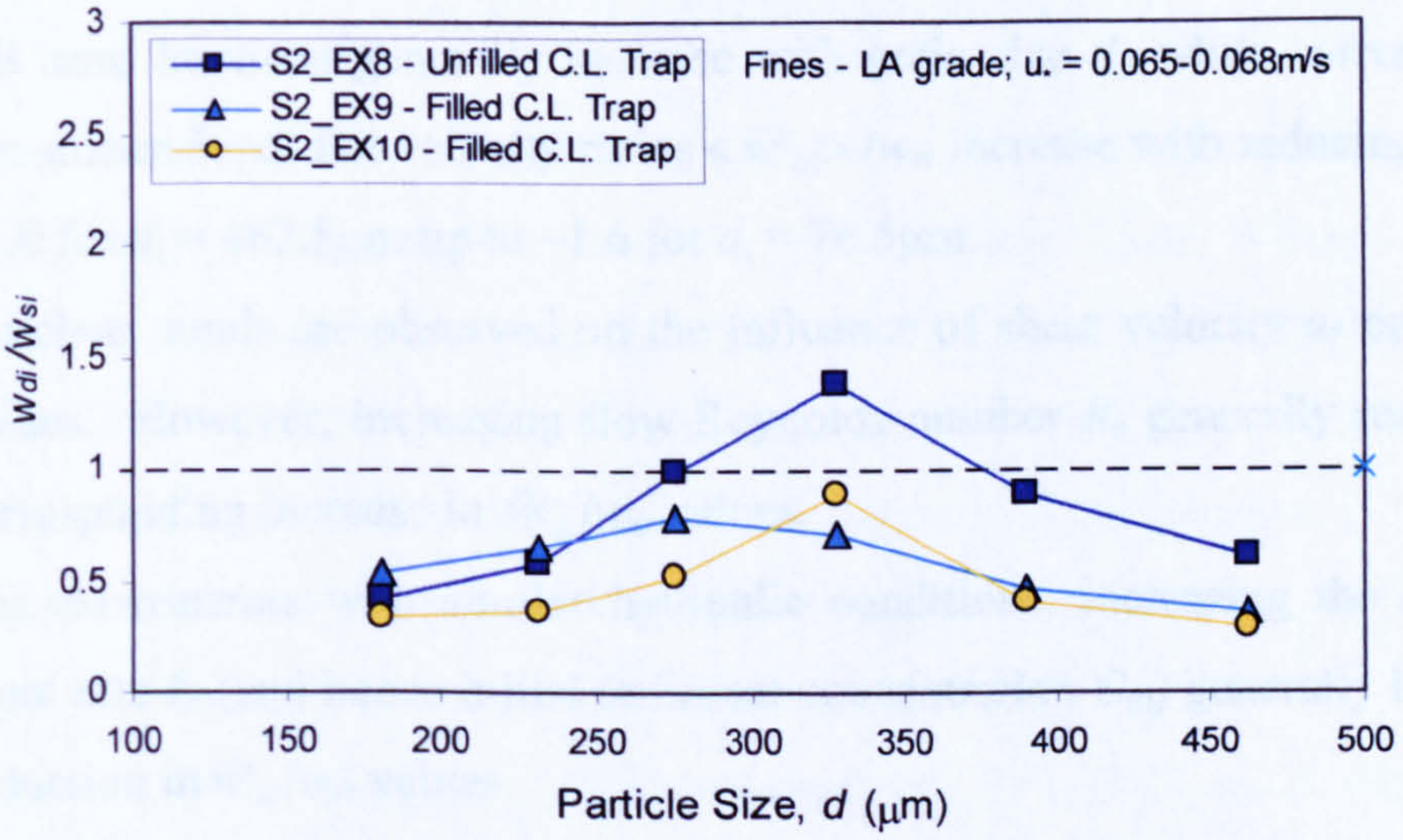

Figure 6.27 - Variation of w_{di}/w_{si} with particle size d_i for LA sand experiments showing the influence of substrate material within the underlying traps.

It is interesting to note that the majority of w_{di}/w_{si} data presented in Figure 6.27 is less than unity (i.e. retarded). This would appear to highlight the influence of the prevalent flow conditions in the three experiments (H = ~0.08m; S_0 = 0.01; u_* = ~0.067ms^{-1}), which may reduce the local deposition rates (Δ_b) due to high levels of turbulence generated at the bed surface.

6.5 Conclusions from Series 2 Experiments

The main experimental findings from Series 2 investigating the vertical turbulent transfer and depositional characteristics of LA and DB sands are summarised below:

(1) Longitudinal Deposition and Depth-Averaged Turbulent Fall Velocity

- The longitudinal deposition of LA sand is well represented by a log-normal distribution, while the finer DB sand is more uniformly distributed along the flume length, due mainly to the re-circulation of sediment transported beyond the downstream end of the flume.
- Depth-averaged turbulent fall velocities $\tilde{w}'_s$ for LA sand are on average 21% higher than the average still water fall velocity w_s.
- The longitudinal deposition of individual LA and DB sand fractions also reveal log-normal characteristics, with the median and standard deviation ($\tilde{L}_i$ and β_3) increasing as grain size d_i reduces.
- Experiment- and depth-averaged turbulent fall velocities $<\tilde{w}'_{si}>$ for LA and DB sand fractions generally increase with grain size d_i, while corresponding non-dimensional fall velocity ratios $<\tilde{w}'_{si}>/w_{si}$ increase with reducing d_i from ~1.0 for d_i = 462.5μm up to ~1.6 for d_i = 76.5μm.
- No clear trends are observed on the influence of shear velocity u_* on $\tilde{w}'_{si}/w_{si}$ values. However, increasing flow Reynolds number R_e generally results in a corresponding increase in $\tilde{w}'_{si}/w_{si}$ values.
- For experiments with similar hydraulic conditions, increasing the sediment input rate I_R (and hence initial sediment concentration C_{0i}) generally leads to a reduction in $\tilde{w}'_{si}/w_{si}$ values.

(2) Turbulent Fall Velocity and Transfer Coefficient for LA Sand

- Distributions of overall and fractional non-dimensional turbulent fall velocity (w'_s/u_* and w'_{si}/u_*) with relative depth z/H have common characteristics with similar distributions obtained in Series 1B (§4.3).
- Maximum values of w'_s/u_* tend to occur at a relative depth $z/H \approx 0.2$, reducing consistently with increasing z/H. Within the near-bed flow, w'_s/u_* values reduce or remain constant as the bed surface is approached.
- Standard deviations in w'_s/u_* values are generally largest in the near-bed region ($z/H \leq 0.2$), resulting from the considerable scatter in fractional w'_{si}/u_* values. This scatter tends to decrease with increasing z/H and little distinction is observed between fractional w'_{si}/u_* values in the outer flow ($z/H > 0.6$).
- The non-dimensional fall velocity ratios w'_{si}/w_{si} again reveal similar characteristics to Series 1B results, with generally enhanced fall velocities ($w'_{si}/w_{si} > 1.0$) observed within the near-bed and intermediate flow regions.
- Under similar hydraulic conditions, experiments over the coarser S2_grv1 gravel bed have w'_{si}/w_{si} values are significantly higher than over the finer S2_grv2 gravel.
- The dimensionless vertical transfer coefficients ε_{szi}/Hu_* for $d_i \leq 275\mu m$ show considerable variation with z/H. Vertical profiles of ε_{szi}/Hu_* are generally skewed towards the lower half of the flow depth and deviate significantly from the commonly adopted parabolic or parabolic-constant distributions based on the vertical transfer coefficient for fluid momentum ε_{fz}.

(3) Deposition Rates and Composition, Initial and Near-bed Concentrations

- In agreement with previous studies (e.g. Carling 1984, Peloutier 1998), average and local deposition rates (Δ_0 and Δ_b) are directly proportional to initial and near-bed sediment concentrations (C_0 *and* C_b), respectively, for both overall LA and DB sand grades and individual size fractions.
- The composition of deposited sediment samples is significantly coarser than the overlying near-bed concentration samples.
- After an initial coarsening, downstream fining in median grain sizes ($d_{50,dep}$ and $d_{50,Cb}$) is well represented by a negative power decay function for the LA sand and an exponential decay function for the DB sand.

- Experimental-averaged fractional deposition velocities $<w_{di}>$ generally increase with grain size d_i over both LA and DB sand grades, although stabilising for coarser LA sand fractions.
- For LA sand, the non-dimensional deposition velocity ratio $<w_{di}>/w_{si}$ is greater than unity (up to 1.4) for intermediate size fractions d_i = 390, 327.5 and 275μm (i.e. enhanced deposition) but lower than unity for the coarsest and two finest fractions d_i = 462.5, 231 and 181μm (i.e. retarded deposition).
- Limited experimental data for DB sand, suggests $w_{di}/w_{si} > 1.0$ at the extremities of the size distribution, while $w_{di}/w_{si} < 1.0$ for intermediate size fractions.
- The influence of shear velocity u_* on the deposition of the overall LA sand grade reveals a reasonable linear trend of increasing w_d/w_s values for reducing u_* values. The results also suggests that enhanced deposition (i.e. $w_{di}/w_{si} > 1.0$) occurs when $u_* \leq \sim 0.06 ms^{-1}$.
- Sediment input rate I_R (and hence initial sediment concentration C_{0i}) appears to have no direct influence on w_{di}/w_{si} values over the experimental range considered.
- The influence of bed material appears to yield higher w_{di}/w_{si} values for LA sand particles depositing through the finer S2_grv2 gravel than through the coarser S2_grv1 gravel.
- The presence of substrate material within traps underlying the bed surface layer appears to hinder the deposition of LA sand ($w_{di}/w_{si} < 1.0$) in comparison to experiments where the underlying traps are left empty.

CHAPTER 7

Discussion and Analysis

7.1 Introduction

It is known that flow turbulence has a crucial role in the suspension and transportation of sediments (Tooby et al. 1977). Although extensive research has been conducted on the complex relationships between sediment transport mechanics and turbulent processes, they are not yet completely understood (Kaftori et al. 1995a, Nino and Garcia 1996). In view of these complexities, traditional modelling approaches have assumed an analogy exists between the motion of the suspended sediment particles and the fluid diffusion-dispersion processes (Jobson and Sayre 1970, Cao et al. 1996). While this assumption has been successfully adopted in many instances, its fundamental limitation is that quasi-ordered or coherent structures present within the turbulent flow and their influence on particle motion cannot be considered. Recent studies have unequivocally revealed that near-bed coherent structures, and the *bursting* process in particular, play a crucial role in sediment entrainment from the near-wall flow (e.g. Sumer and Oğuz 1978; Sumer and Deigaard 1981; Kaftori et al. 1995; Garcia et al. 1996; Nino and Garcia 1996). Other studies have revealed the importance of coherent vortices in the suspension of fine sediments (e.g. Tooby et al. 1977, Nielsen 1984).

In this context, it is therefore imperative that continued progress in understanding of the physical mechanisms governing suspended sediment transport and associated processes such as deposition and entrainment requires improvements in the knowledge of turbulent structure in open-channel flows. Experimental investigations of these processes also require greater emphasis on studying the nature of the interactions that exist between sediment particles and coherent fluid motions.

The outline aims of this chapter are twofold: (i) to summarise and discuss the main findings from the experimental results presented in Chapters 4, 5 and 6 and their relation to previous investigations; (ii) to develop an analytical interpretation of the main experimental findings relating the observed motion of the sediment particles to the mean and turbulent characteristics of the flow.

7.2 Particle Fall Velocity in Turbulent Open Channel Flow

Various methods have been employed to investigate the influence of turbulence, generated in open channel flow over rough porous bed conditions, on the vertical transfer of fine- to medium-sized sand particles. In the visualisation studies (Series 1A and 1B, Chapter 4), the turbulent fall velocity w'_{si} of LA grade sand (d = 500-150μm, d_{50} = 250μm) was obtained from the measurement of individual particle trajectories. Series 1B employed a high-speed camera (operating at 240 fps) and a particle tracking technique to measure the trajectories of around 7,600 sand particles spread over six size fractions. These measurements were made in three distinct flow regions, corresponding approximately to the wall ($z/H \leq 0.2$); intermediate ($0.2 < z/H \leq 0.5$) and outer regions ($z/H > 0.5$) (Nezu and Nakagawa, 1993).

Series 2 consisted of twelve separate experiments employing non-visual techniques to measure w'_{si} for two grades of sediment, LA sand and DB sand (d = 212-38μm, d_{50} = 97μm) (Chapter 6). Depth-averaged turbulent fall velocities $\tilde{w}'_{si}$ were estimated from longitudinal distributions of sediment deposition in a series of centreline traps running the full length of the flume. Vertical distributions of turbulent fall velocity w'_{si} were also computed by solving a non-dimensional, integrated form of the two-dimensional sediment transfer equation using measured concentration and flow velocity profiles.

Comparison of the results obtained from each of these methods revealed many common attributes, particularly with respect to the influence of particle size d_i and relative depth z/H on the measured turbulent fall velocities w'_{si}. The main experimental findings from the visual and non-visual experiments reported in Chapters 4 and 6, respectively, are reiterated overleaf:

(1) In relation to the LA grade sediment (d_{50} = 250μm), the turbulent fall velocity w'_{si} is often significantly higher than the fall velocity measured in still water conditions w_{si}, suggesting that the vertical motion of sediment particles can be enhanced in turbulent flow conditions.

(2) This enhancement is particularly evident in the near-bed region ($z/H \leq 0.2$), where the non-dimensional fall velocity ratio w'_{si}/w_{si} can exceed values of 2.0. In the intermediate flow region ($0.2 < z/H \leq 0.6$), values of w'_{si}/w_{si} are generally lower, but remain enhanced (i.e. $w'_{si}/w_{si} > 1.0$) for all fractions except the coarsest (d_i = 462.5μm).

(3) By contrast, turbulent fall velocities are generally lower than still water fall velocities (i.e. $w'_{si} < w_{si}$) within the outer flow region ($z/H > 0.6$), indicating hindered vertical sediment transfer in the near-surface flow.

(4) Distributions of the non-dimensional turbulent fall velocity w'_{si}/u_* reveal similar characteristics to vertical turbulence intensity w'_{rms}/u_* profiles, with maximum values often occurring at $z/H \sim 0.2$, and generally reducing with increasing values of z/H.

(5) For the finer DB grade sediment (d_{50} = 97μm), the depth-averaged turbulent fall velocities $\tilde{w}'_{si}$ were also enhanced, with $\tilde{w}'_{si}/w_{si}$ ranging from about 1.3 (d_i = 181μm) to 1.6 (d_i = 98μm). Corresponding values of $\tilde{w}'_{si}/w_{si}$ for the LA grade sand ranged from about 1.0 (d_i = 462.5μm) to 1.2 (d_i = 181μm).

(6) Overall, the influence of particle size d_i on the turbulent fall velocity w'_{si} is largely independent of position within the flow z/H. Whilst, local and depth-averaged turbulent fall velocities (w'_{si} and $\tilde{w}'_{si}$, respectively) for both LA and DB grade sands generally increase with particle size d_i, the corresponding values of w'_{si}/w_{si} typically reduce with increasing d_i.

The notion of turbulence-enhanced fall velocity is clearly in conflict with the perceived 'conventional logic' that suggests flow turbulence should impede the sediment particles from reaching the bed surface by keeping them in suspension (e.g. Bagnold, 1966). Similarly, the vortex-trapping arguments proposed by Tooby et al. (1977); Nielsen (1984) and Sene, Hunt and Thomas (1994) suggest that under certain conditions particles can become trapped within the core of coherent vortices (or

eddies) and be transported significant distances downstream in suspension. Either way, the net effect would result in turbulent fall velocities that are lower than in still water conditions (i.e. hindered settling characteristics). Alternatively, if turbulent flow is considered as a stochastic random process, the average settling rate of heavy particles should be unaffected by the normally-distributed random turbulent motions, with the turbulent fall velocity equal to the terminal fall velocity in still water (e.g. Reeks, 1977).

Experimental evidence supporting this notion of turbulence-enhanced fall velocity is sparse, with only Jobson and Sayre's (1970) study of the vertical transfer of sediment in turbulent open channel flow supporting the findings of current study. Their results revealed that measured turbulent fall velocities for fine spherical glass beads (d_{50} = 123μm) were generally enhanced (w'_s/w_s up to ~2.0), while coarser sand particles (d_{50} = 390μm) settled at a rate close to the still water fall velocity (w'_s/w_s ~ 1.0). The author's results indicated that gravity was the dominant vertical transfer mechanism for the coarse sand particles, whereas turbulent diffusion dominated the vertical transfer of the finer glass beads.

7.2.1 Influence of Particle Size

Hoyal et al. (1995) defined a parameter w_* (= $w_s H/2\varepsilon_s \approx w_s/u_*$) to quantify the competing effects of gravity and turbulence in the vertical transfer of sediment particles. Below a critical value of w_* = 0.1 (light particles), the authors found the vertical transfer of sediment to be dominated by turbulence, resulting in turbulence-enhanced fall velocities (i.e. $w'_s/w_s > 1.0$). For $w_* > 1.0$ (heavy particles), vertical transfer was found to be completely dominated by gravity, with turbulence having negligible effect on the fall velocity (i.e. $w'_s/w_s \sim 1.0$).

In the Series 1B and Series 2 experiments, the values of w_* ranged from ~0.4 to ~1.6 and ~0.3 to ~1.3, respectively, for the LA grade sand (d = 150-500μm). Similarly, for the four DB grade sand fractions measured in Series 2 (d = 90-212μm), the w_* values range between ~0.1 and ~0.4. Many of these values correspond to an intermediate region ($0.1 \leq w_* \leq 1$) where vertical sediment transport is controlled both by gravity and turbulence effects. Hoyal et al. (1995) found that the non-dimensional fall velocity ratio w'_s/w_s in this region increased non-linearly from about 1.0 to 3.0 as w_* decreased from 1.0 to 0.1.

Based on this criteria, LA grade sand particles larger than ~360μm in Series 1B (i.e. $w_s \approx u_* = 0.0445\text{ms}^{-1}$) and ~455μm in Series 2 ($w_s \approx u_* = 0.0589\text{ms}^{-1}$) should be unaffected by turbulence and settle primarily under the influence of gravity with $w'_{si}/w_{si} \sim 1.0$. By contrast, DB grade particles smaller than ~84μm ($w_s \approx 0.1u_* = 0.004\text{ms}^{-1}$) should be completely dominated by turbulence and should have significantly enhanced values of w'_s, according to Hoyal et al. (1995).

The experiment-averaged values of $<\tilde{w}'_{si}>/w_{si}$, calculated independently from the Series 1B and 2 experiments for the LA and DB grade sediments, are plotted against w_* in Figure 7.1 below. This data demonstrates reasonable overall accord with the criteria proposed by Hoyal et al. (1995) over the range of particle sizes tested and experimental conditions considered in the current study. In specific agreement with Hoyal et al., the non-dimensional fall velocity ratios $<w'_{si}>/w_{si}$ are generally greater than 1.0 and decrease with increasing values of w_*, approaching unity as $w_* \rightarrow$ 1.0. Divergence from the criteria is observed for data points with lower w_* values [including Jobson and Sayre's (1970) data], suggesting the overall levels of enhancement for finer particles are lower than predicted by Hoyal et al. Considerable doubt must however be cast over the validity of Hoyal's criteria for fine-grained particles ($w_* << 0.1$), where w'_s/w_s values can reach values in excess of 10^1 or 10^2.

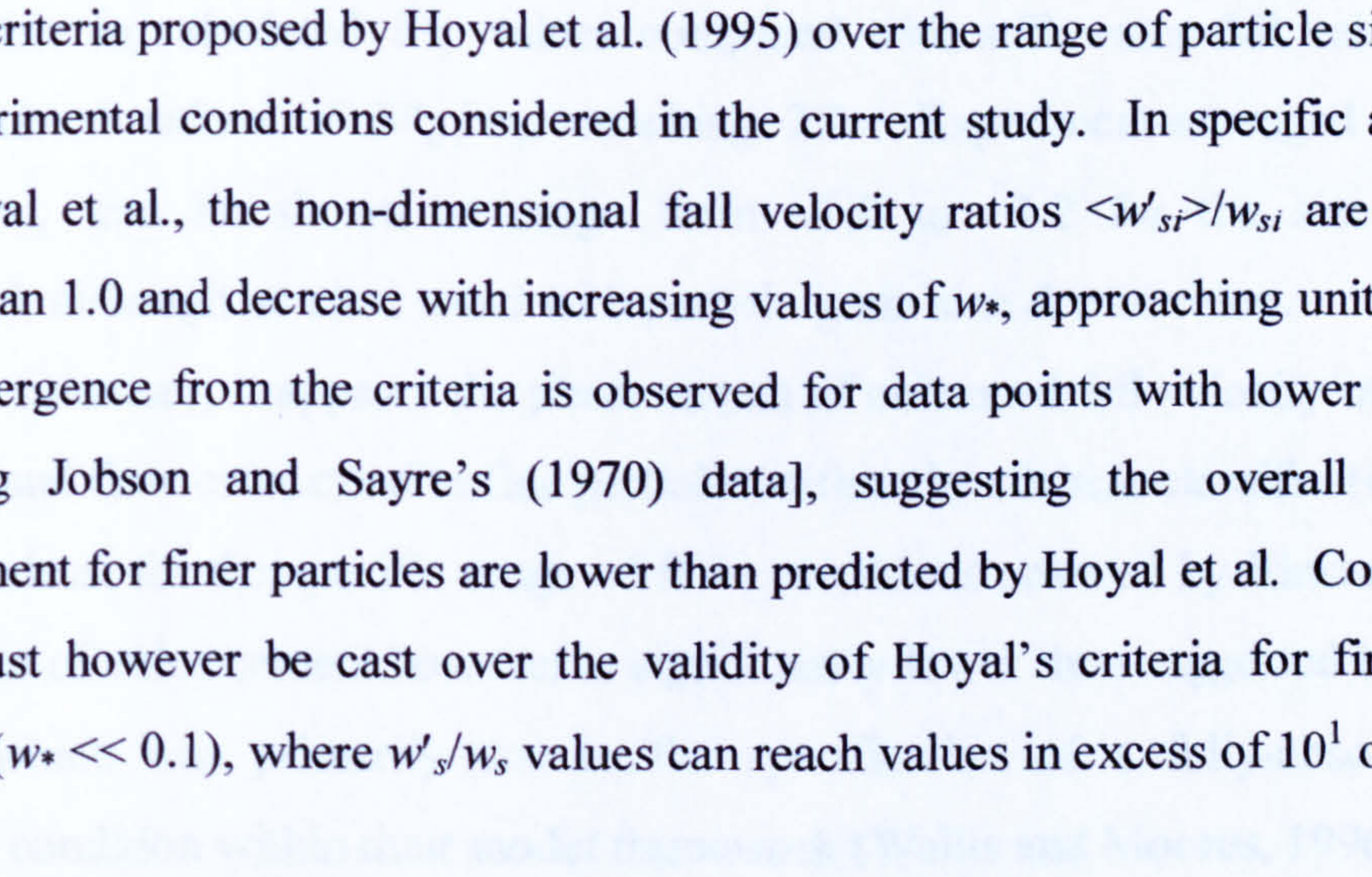

Figure 7.1 - Non-dimensional fall velocity ratio $<w'_{si}>/w_{si}$ plotted against w_* for experiment- and depth-averaged data obtained from Series 1B and 2 experiments. Jobson and Sayre (1970) data for fine and coarse sediments also shown for comparison purposes.

Re-examination of the flume data provided by Einstein (1968) on the deposition of silica flour particles (d = 3.5-30μm) into a stable gravel bed offers an invaluable extension to the range of grain sizes tested in the current study. Einstein (1968) calculated the depth-averaged turbulent fall velocity $\overline{w}'_s$ from the estimated half-life T of a known quantity of fine sediment released in a re-circulating open channel flume (eqn. 2.19, pp.41). This half-life parameter T is clearly equivalent to the ratio of median deposition length $\widetilde{L}$ and the depth-averaged flow velocity $\overline{U}$, used in the calculation of the depth-averaged turbulent fall velocity $\widetilde{w}'_s$ in Series 2 (eqn. 6.2, pp.167). Solution of equation 2.19 using Einstein's data indicates similar enhancement in calculated $\overline{w}'_s$ values compared with still water fall velocities w_s, with fractional values of $\overline{w}'_{si}/w_{si}$ reaching 2.3. Experiment-averaged values of $<\overline{w}'_{si}>/w_{si}$ can be shown to range from ~1.0 to ~1.2 for the size fractions considered, although no clear trend with particle grain size d_i was noted.

In summary, it appears the phenomenon of enhanced fall velocity in turbulent open channel flow can extend to fine particles within the silt size classification (d ~ 3-30μm), at least for the specific range of flow conditions covered by Einstein (1968). The degree of enhancement however is significantly lower than suggested by Hoyal's criteria, which was primarily due to the specification of a fully-absorbing bed boundary condition within their model framework (Wallis and Moores, 1996).

7.2.2 Influence of Elevation above Bed Surface

It was expected that the turbulent fall velocity w'_s associated with the vertical motion of sediment particles in the turbulent flow conditions would vary in the depthwise direction z/H. This may be primarily due to the non-uniformity of the turbulent structure through depth and the resulting interactions with the suspended sediment particles, but other factors such as sediment injection method and bed conditions may also play an important role.

Experiment-averaged distributions of the non-dimensional turbulent fall velocity $<w'_s/u_*>$ and fall velocity ratio $<w'_s>/w_s$ with relative depth z/H are shown in Figure 7.2 for the LA grade sand results obtained in Series 1B and Series 2. The plots reveal excellent agreement between the results obtained from the two independent experimental series, and highlight common attributes in their distributions with z/H.

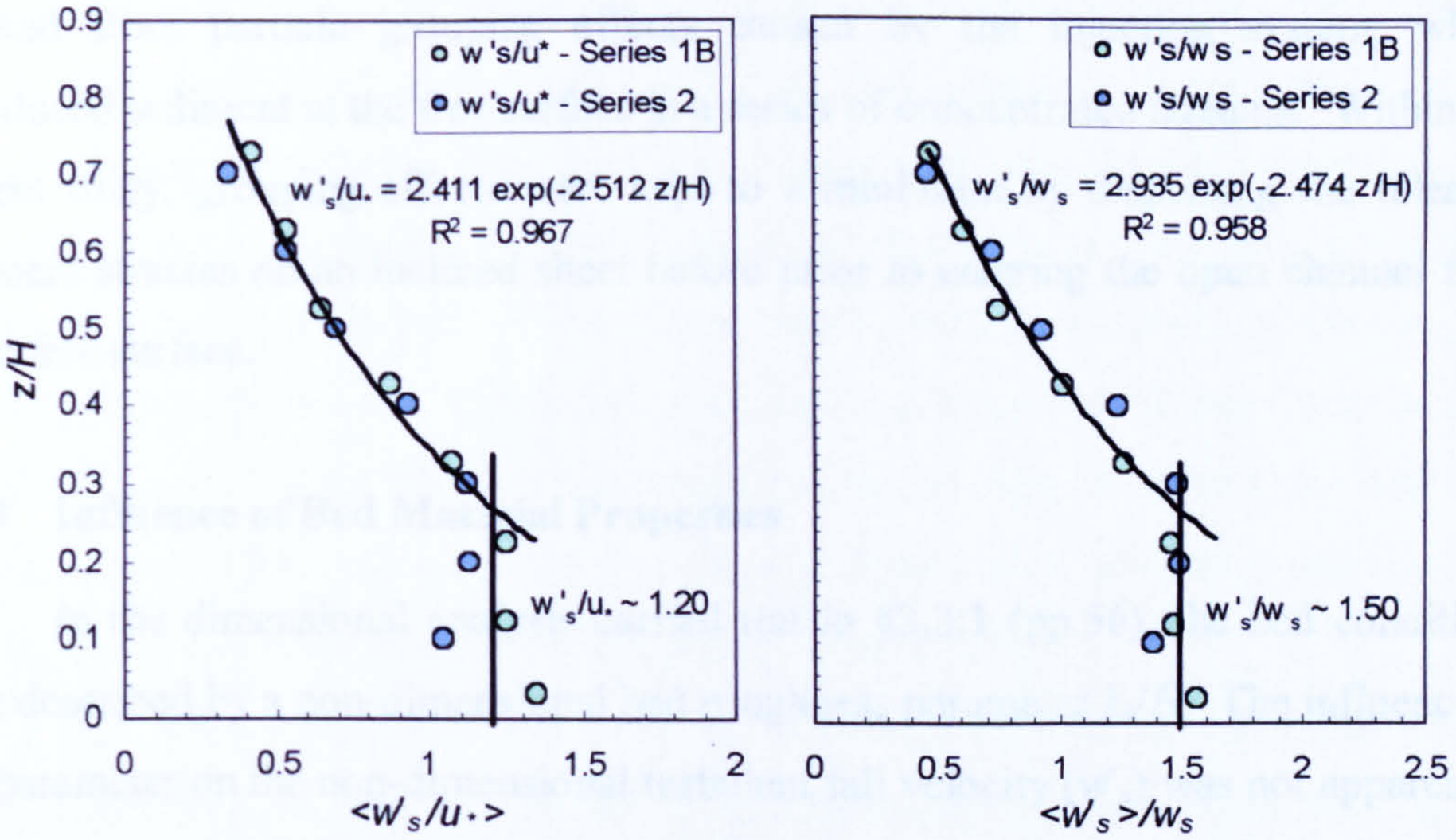

Figure 7.2 - Experiment-averaged distributions of $\langle w'_s/u_* \rangle$ and $\langle w'_s \rangle/w_s$ with relative depth z/H for LA sand and Series 1B and 2 experiments.

Trendlines fitted to both plots in Figure 7.2 reveal that the experimental data appears to reduce exponentially with increasing z/H in the region defined by z/H ≥ ~0.27. These functions clearly have a similar form to the exponential law proposed for turbulence intensity w'_{rms}/u_* by Nezu and Rodi (1986) (eqn. 2.11, pp.22). In the flow region defined by $z/H < \sim 0.27$, greater scatter in the $\langle w'_s/u_* \rangle$ data makes it more difficult to define an appropriate trendline. However, as the $\langle w'_s \rangle/w_s$ data appears to have a relatively constant value around 1.5, it is assumed that $\langle w'_s/u_* \rangle$ will have an average value around 1.2 within this region.

Solution of the exponential function relating $\langle w'_s \rangle/w_s$ to z/H suggests that turbulent fall velocities are only enhanced (i.e. $\langle w'_s \rangle/w_s > 1.0$) in the flow region defined by $z/H < 0.44$, while being hindered (i.e. $\langle w'_s \rangle/w_s < 1.0$) outwith this region. The occurrence of increasingly hindered fall velocities in the outer flow may suggest that, after release at the free surface, the sediment particles require an certain adjustment time to accelerate under the combined influence of gravity and turbulence. This adjustment will be especially important under release conditions where the entry velocity of the sediment particles at the free surface is kept to a minimum.

In this respect, the distributions of $\langle w'_s/u_* \rangle$ and $\langle w'_s/w_s \rangle$ plotted in Figure 7.2 are clearly different from the results obtained by Jobson and Sayre (1970) (Figure 2.4, pp.17). Here, the authors found generally higher fall velocities in the near-surface flow than at lower elevations within the flow. They concluded that this largely

resulted from particle grouping effects caused by the injection system, which introduced sediment at the free surface in a series of concentrated streams. Within the current study, grouping effects were kept to a minimum by dispersing the released sediment streams on an inclined sheet before prior to entering the open channel flow at the free surface.

7.2.3 Influence of Bed Material Properties

In the dimensional analysis carried out in §3.3.1 (pp.56), the bed conditions were described by a non-dimensional bed roughness parameter k_s/H. The influence of this parameter on the non-dimensional turbulent fall velocity (w'_s) was not apparent in the particle tracking experiments (Series 1B), where both uniform spheres and natural gravel bed configurations were used. However, Series 2 experiments with LA grade sand show a linear reduction ($R^2 = 0.90$) in the depth-averaged values of $\tilde{w}'_s/u_*$ for increasing k_s/H values (Figure 7.3), suggesting lower settling rates occur over rougher bed conditions. This linear trend appears to be valid for the two natural gravel grades (S2_grv1 and S2_grv2) used in Series 2.

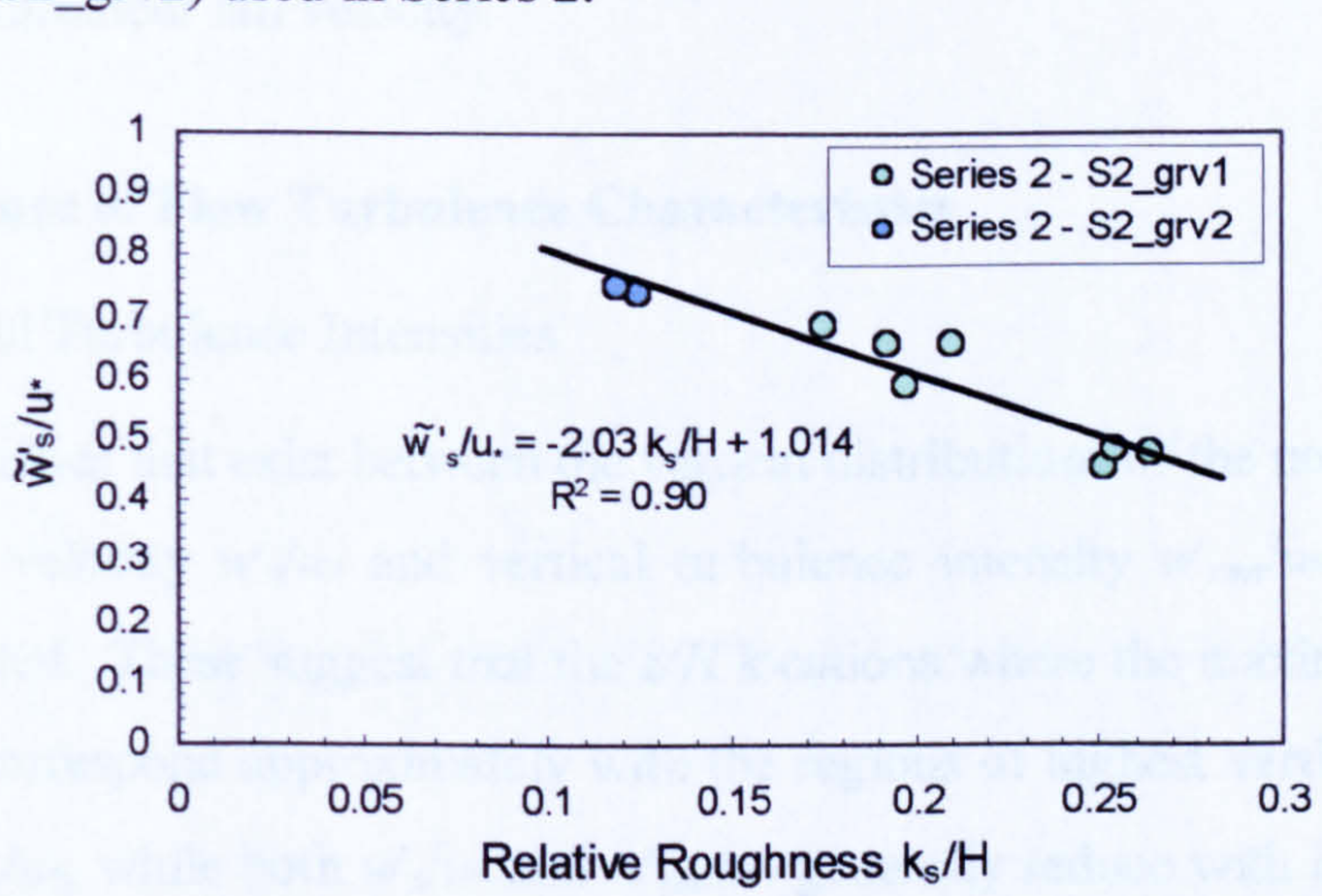

Figure 7.3 - Variation of depth-averaged non-dimensional turbulent fall velocity $\tilde{w}'_s/u_*$ with relative roughness k_s/H for Series 2 experiments with LA sand

It should be noted that the experimental bed conditions considered in the current studies lay consistently within the hydraulically rough regime ($k_s^+ = k_s u_*/\nu > 70$). Additionally, the relative grain size between the bed material and fine sediment was generally large ($D_{50}/d_{50} \geq 28$), allowing fine sediments to be readily deposited to the porous bed, which was initially clean of fine sediments. These factors may clearly

have an important role in the enhanced fall velocities observed in both Series 1 and 2. Hoyal et al. (1995) determined fully-absorbing bed boundary conditions to be the primary factor resulting in enhanced fine sediment deposition and suggested that filtration processes within the upper regions of porous beds may produce similar effects in laboratory studies. These filtration processes are known to be complex phenomena involving many mechanisms for the deposition of particles from the fluid to the collectors (Tien, 1989). These mechanisms are dependent on grain and pore sizes (fines and filter material), density of fine sediment, fluid properties and the fluid and sediment velocities through the bed pores (Tien, 1989).

The specific bed conditions used in the current experiments were assumed to be representative of naturally flushed or mechanically cleansed open-work gravel beds in shallow upland reaches (Carling, 1984). Clearly, a useful extension to the scope of the current study would be to consider gravel beds that are initially clogged with fine sediments to assess the influence of bed filtration processes. Experiments over smooth ($k_s^+ < 5$) and intermediate-rough ($5 \leq k_s^+ \leq 70$) bed conditions would also serve to highlight how changes in turbulent characteristics and structure may influence the turbulent fall velocity.

7.2.4 Influence of Flow Turbulence Characteristics

7.2.4.1 Vertical Turbulence Intensities

Similarities that exist between the vertical distributions of the non-dimensional turbulent fall velocity w'_s/u_* and vertical turbulence intensity w'_{rms}/u_* have already been highlighted. These suggest that the z/H locations where the maximum values of w'_s/u_* occur correspond approximately with the regions of highest vertical turbulence intensity w'_{rms}/u_*, while both w'_s/u_* and w'_{rms}/u_* generally reduce with increasing z/H. Bennett et al. (1998) found similar depthwise associations between instantaneous upward and downward fluid velocities and the corresponding vertical sediment particle velocities in experiments conducted over upper stage plane beds.

7.2.4.2 Asymmetry of Turbulence

Bagnold (1966) stated that the maintenance of suspended sediment within turbulent flow conditions requires the vertical turbulence to be anisotropic, with a net

upward (positive) stress balancing the submerged weight of the sediment grains. This condition requires that the root-mean-square value of upward turbulent fluctuations $w'_{+,rms}$ exceeds the rms value of the downward fluctuations $w'_{-,rms}$. From this, Bagnold (1966) defined the coefficient of anisotropy *an* as follows,

$$an = \frac{w'_{+,rms} - w'_{-,rms}}{2\left(w'_{+,rms} + w'_{-,rms}\right)} \qquad \ldots.(7.1)$$

Values of *an* were calculated at six *z/H* elevations from the time-series of instantaneous vertical velocities obtained by the ADV probe during experiments S1B_EX1 and S1B_EX4 (Table 7.1). Corresponding values of the *skewness* coefficient for the vertical velocity distribution, also shown in Table 7.1, were obtained from the equation,

$$Sk_{w'} = \frac{n}{(n-1)(n-2)} \sum_{i=1}^{n} \left(\frac{w_i - \overline{w}}{\sigma_{w_i}} \right)^3 \qquad \ldots.(7.2)$$

where w_i is the instantaneous vertical component of flow velocity, $\overline{w}$ is the mean value and σ is the standard deviation.

	z/H Value	0.05	0.15	0.25	0.35	0.45	0.52
S1B_EX1	*an*	0.004	0.031	0.027	0.052	0.072	0.073
	$Sk_{w'}$	0.01	0.31	0.22	0.50	0.63	0.64
S1B_EX4	*an*	-0.016	0.002	0.026	0.031	0.056	0.045
	$Sk_{w'}$	-0.09	0.03	0.20	0.31	0.53	0.40

Table 7.1 - Skewness and anisotropy coefficients ($Sk_{w'}$ and *an*) for w' distributions obtained in experiments S1B_EX1 and EX4 at different *z/H* elevations above bed

In general, both the $Sk_{w'}$ and *an* values are positive, suggesting a net upward momentum flux exists within the flow region considered, as predicted by Bagnold (1966). The asymmetry of vertical turbulent fluctuations (*an*) is shown to increase with relative depth (*z/H*), suggesting that upward turbulent fluctuations ($w'_{+,rms}$) become increasingly dominant higher in the flow compared with downward turbulent fluctuations ($w'_{-,rms}$). Good linear correlation is also observed between the *an* and $Sk_{w'}$ values in both experiments. Overall, these finding are consistent with previous studies over rough bed conditions (e.g. Grass 1971, Bennett et al. 1998).

7.2.4.3 Suspension Criterion for Sediment

Bagnold's (1966) suspension criterion was based on the assumption that the sediment particle can only remain in suspension if the upward vertical fluid velocity fluctuation was greater than the fall velocity of the sediment particle, i.e. $w'_{+,rms} > w_s$. Bridge and Bennett (1992) applied the following assumptions: (a) $w'_{+,rms} = 1.55w'_{rms}$ ($an = 0.207$) and; (b) $w'_{rms} \approx 0.8\ u_*$ (averaged over flow depth H), to define Bagnold's suspension criterion in the form,

$$w_s \leq w'_{+,rms} = (1.55)0.8u_* = 1.25u_* \qquad ....(7.3)$$

Bridge and Bennett (1992) suggested that this criterion was incomplete, as it does not consider the influence of the negative (downward) vertical velocity fluctuations $w'_{-,rms}$ on the suspended sediment. They proposed that sediment particles would remain suspended only if the average upward turbulent fluctuations exceeded the sum of the downward turbulent fluctuations and the settling velocity, i.e.

$$w_s \leq w'_{+,rms} - w'_{-,rms} = 0.91w'_{rms} \qquad ....(7.4)$$

where $w'_{-,rms} = 0.643w'_{rms}$, averaged over depth (Bagnold, 1966). However, analysis of instantaneous vertical velocities measured during experiments S1B_EX1 and EX4 yields $w'_{+,rms} \sim 1.07w'_{rms}$ and $w'_{-,rms} \sim 0.93w'_{rms}$, averaged over the z/H locations detailed in Table 7.1. Hence, the validity of equation 7.4 must be questioned as clearly for weakly anisotropic turbulence ($an \rightarrow 0$), the term ($w'_{+,rms} - w'_{-,rms}$) will clearly tend to zero.

Bagnold's (1966) original criterion can be written in the general form: $w_s \leq w'_{+,rms} = b.u_*$, where b is an experiment dependent variable. The critical particle size for suspension can therefore be determined by considering the flow conditions prevalent in the current study. Assuming $w'_{+,rms} \approx w'_{rms} \approx 0.8\ u_*$, the suspension criterion would read: $w_s \leq 0.8\ u_*$ (i.e. $b = 0.8$), which is the same as that suggested by Engelund and Fredsøe (1982). In the Series 1B experiments, the average shear velocity $\overline{u}_* = 0.0444$ m.s^{-1}, hence $w_s \leq 0.8(0.0444) \leq 0.0355$ m.s^{-1}, equivalent to a threshold particle size d_i in suspension of ~300μm. Assuming this criterion can also be applied to the Series 2 experiments, where $\overline{u}_* = 0.0589$ m.s^{-1}, the threshold particle size d_i in suspension would be ~380μm.

The criteria proposed by Hoyal et al. (1995) to determine the relative effect of gravity and turbulence on sediment deposition (§7.2.1) is clearly analogous to Bagnold's suspension criterion, except that $b = 1.0$, i.e. particles are unaffected by turbulence and settle out of suspension under gravity when $w_* = w_s/u_* = 1.0$.

The main limitation of these suspension criteria lies in the fact they are time- and depth-averaged. Clearly, their applicability cannot extend to the influence of individual coherent turbulent cycles (i.e. burst-sweep events) on the vertical motion of suspended sediment particles.

7.2.4.4 Statistical Analysis of Flow Turbulence – Quadrant Analysis

Previous investigations into the turbulent structure of boundary layer flows have revealed the existence coherent fluid motions that exhibited a quasi-cyclical temporal structure (i.e. Kline et al. 1967, Corino and Brodkey 1969, Grass 1971). These coherent structures are generally accepted to comprise of ejections (or 'bursts') of low momentum fluid from the near-wall region into the outer flow and return inrushes (or 'sweeps') towards the bed (§2.3.3, pp.25) and appear to occur irrespective of the bed surface roughness conditions (i.e. Grass, 1971).

Quadrant analysis techniques have been employed to distinguish between the different types of turbulent events and provide detailed information on their relative contribution to the overall turbulence production at a particular location within the flow (e.g. Willmarth and Lu, 1972; Wallace et al, 1972; Raupach, 1981).

Quadrant analysis requires each instantaneous pair of u' and w' fluctuations to be split into four quadrants defined as follows,

(1) $u' > 0$, $w' > 0$ (outward interaction) (2) $u' < 0$, $w' > 0$ (ejection event)

(3) $u' < 0$, $w' < 0$ (inward interaction) (4) $u' > 0$, $w' < 0$ (inrush event)

The product of each u', w' pair (i.e. $u'w'$), defining the instantaneous Reynolds stress, is compared to a multiple of the product of u'_{rms} and w'_{rms} by the equation,

$$H_L = \frac{|u'w'|}{[(u'_{rms})(w'_{rms})]} \qquad \text{....(7.5)}$$

where H_L is the threshold value defining the size of the hyperbolic hole region for detection of specific ejection or inrush events. Varying H_L permits the investigation of the fractional contributions to the total Reynolds stress for different magnitude events in each quadrant ($\overline{u'w'}_Q$) using the expressions (Bennett et al. 1998),

$$\left.\begin{aligned} \overline{u'w'}_Q &= \frac{1}{n}\sum_{i=1}^{n} X_Q(u'_i w'_i) \\ \overline{u'w'} &= \sum_{i=1}^{Q} \overline{u'w'}_Q \end{aligned}\right\} \qquad \text{....(7.6)}$$

where the indicator function X_Q obeys the following conditions (Raupach, 1981),

$$X_Q = \begin{cases} 1, \text{ if } (u',w') \text{ is in quadrant } Q \text{ and } |u'w'| \geq H_L|\overline{u'w'}| \\ 0, \text{ otherwise} \end{cases} \qquad \text{....(7.7)}$$

Individual pairs of u' and w' fluctuations were determined from ADV probe measurements taken during experiment S1B_EX4 at four heights above the bed surface (z/H = 0.05, 0.15, 0.25 and 0.45). These u', w' fluctuations are plotted in their appropriate quadrants in Figure 7.4(a) for each z/H elevation, with the hyperbolic hole region defined for a threshold value H_L = 1.0 in each quadrant. The data points outlying this hyperbolic region indicate that the majority of the higher magnitude events lie within quadrants 2 and 4, suggesting that turbulence production is dominated by ejection and inrush events (i.e. burst-sweep cycle).

This is confirmed by considering the fractional contributions from each quadrant to the total Reynolds stress (Figure 7.4(b)) for increasing threshold values H_L ranging between 0 and 7. These plots indicate that quadrant 2 (ejection events) and quadrant 4 (inrush events) are the dominant contributors to total Reynolds stress, as shown in previous studies by Wallace et al. (1972), Willmarth and Lu (1972), Raupach (1981) and Bennett et al. (1998). Immediately above the bed surface (z/H = 0.05), inrushes events (quadrant 4) appear to have a higher contribution than the ejection events (quadrant 2), explaining why the asymmetry of the vertical turbulent fluctuations is downward at this elevation (i.e. negative Sk_w and *an* values – Table 7.1). The contribution from inrushes, however, diminishes in comparison to that from ejection events higher up in the flow, explaining why vertical turbulence asymmetry (*an* values) generally becomes increasingly positive at higher z/H elevations.

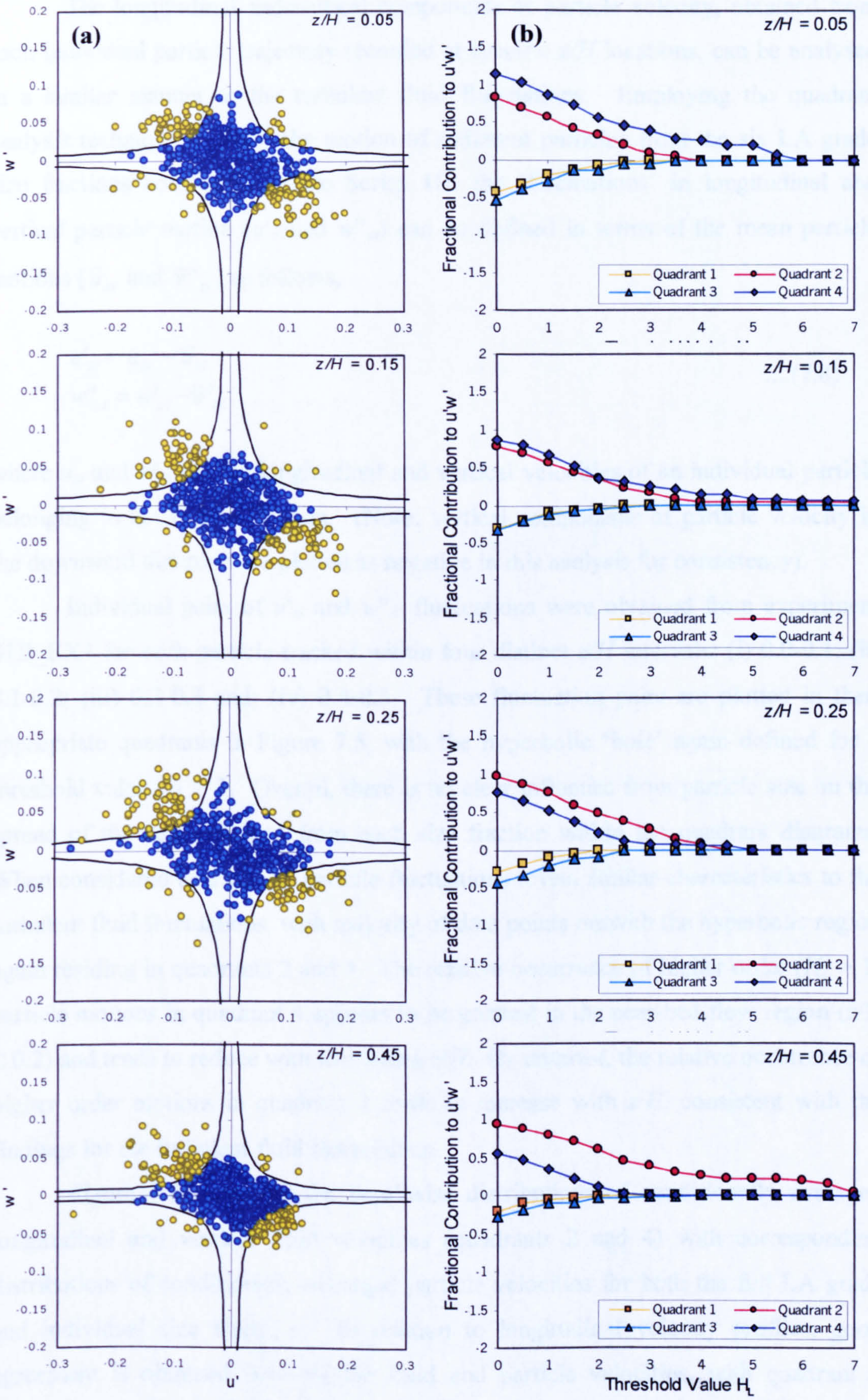

Figure 7.4 - (a) Individual u', w' pairs plotted in quadrant form with hyperbolic hole region ($H_L = 1$) defined and; (b) fractional contributions to the total Reynolds stress for varying threshold H_L values, both obtained from ADV measurements for S1B_EX4 at four z/H locations.

The longitudinal and vertical components of particle velocity, obtained from each individual particle trajectory recorded at specific *z/H* locations, can be analysed in a similar manner to the turbulent fluid fluctuations. Employing the quadrant analysis technique to study the motion of sediment particles from the six LA grade size fractions considered in the Series 1B, the 'fluctuations' in longitudinal and vertical particle motion (u'_{si} and w''_{si}) can be defined in terms of the mean particle motions ($\overline{u}_{si}$ and $\overline{w}'_{si}$) as follows,

$$u'_{si} = u_{si} - \overline{u}_{si}$$
$$w''_{si} = w'_{si} - \overline{w}'_{si} \qquad \text{....(7.8)}$$

where u_{si} and w'_{si} are the longitudinal and vertical velocities of an individual particle belonging to the i^{th} size fraction. (Note: vertical components of particle velocity in the downward direction are plotted as negative in this analysis for consistency).

Individual pairs of u'_{si} and w''_{si} fluctuations were obtained from experiment S1B_EX4 for each particle tracked within four distinct *z/H* intervals: (i) 0.0-0.1; (ii) 0.1-0.2; (iii) 0.2-0.3 and; (iv) 0.4-0.5. These fluctuation pairs are plotted in their appropriate quadrants in Figure 7.5, with the hyperbolic 'hole' again defined for a threshold value $H_L = 1$. Overall, there is no clear influence from particle size on the spread of the data obtained from each size fraction within the quadrant diagrams. When considered as a whole, particle fluctuations reveal similar characteristics to the turbulent fluid fluctuations, with majority of data points outwith the hyperbolic region again residing in quadrants 2 and 4. The relative occurrence of higher order ($H_L > 1$) particle motions in quadrant 4 appears to be greatest in the near-bed flow region ($z/H \leq 0.2$) and tends to reduce with increasing *z/H*. By contrast, the relative occurrence of higher order motions in quadrant 2 tends to increase with *z/H*, consistent with the findings for the turbulent fluid fluctuations.

Figure 7.6 compares the depthwise distributions of conditionally averaged longitudinal and vertical fluid velocities (quadrants 2 and 4) with corresponding distributions of conditionally averaged particle velocities for both the full LA grade and individual size fractions. In relation to longitudinal velocity profiles, good agreement is obtained between the fluid and particle velocities, with quadrant 2 (ejection) profiles clearly lower in magnitude than quadrant 4 (inrush) profiles for the range of *z/H* considered.

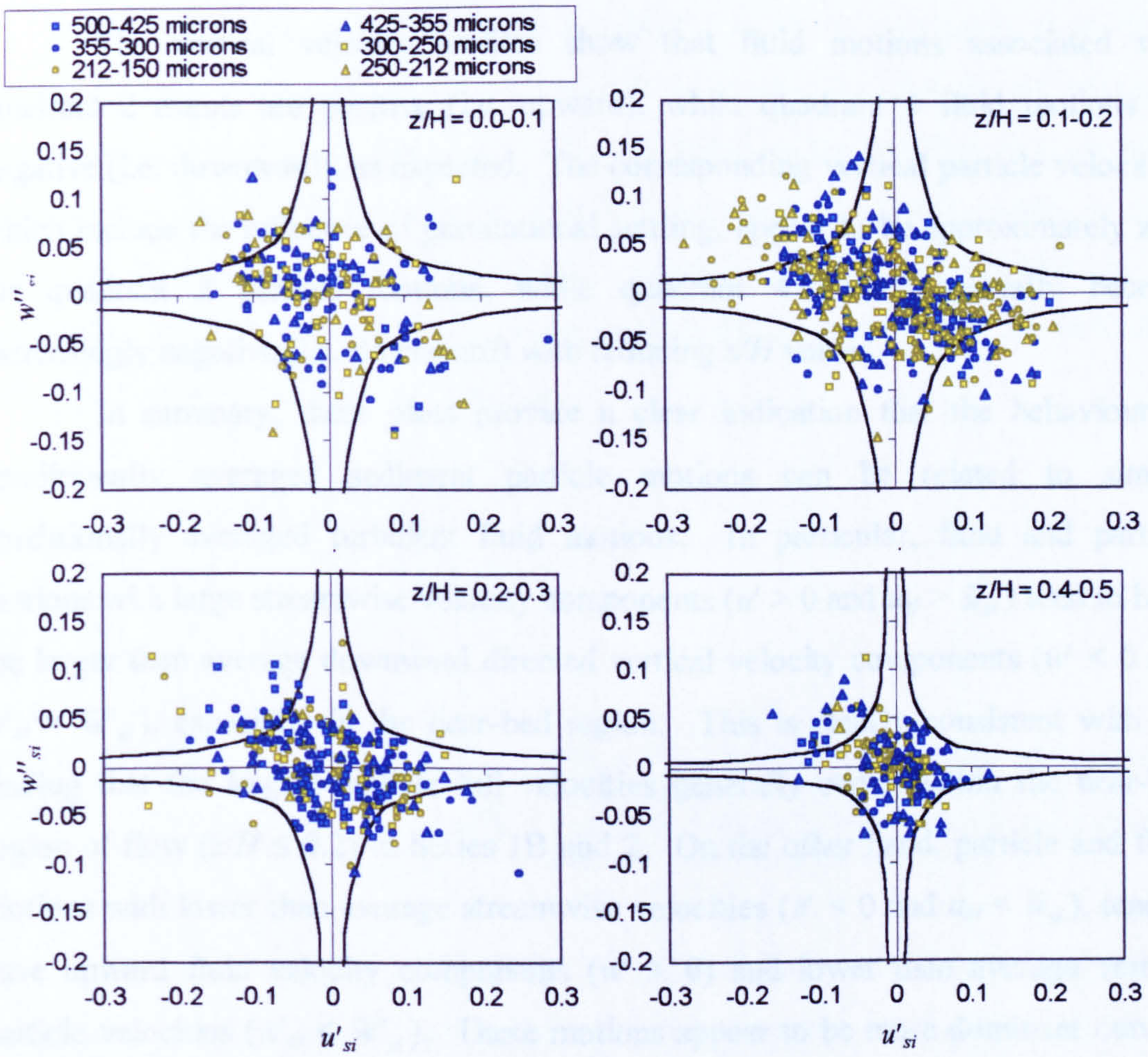

Figure 7.5 - Quadrant analysis of individual particle velocities obtained from S1B_EX4 recordings at four z/H locations. Hyperbolic hole region defined for threshold value $H_L = 1$.

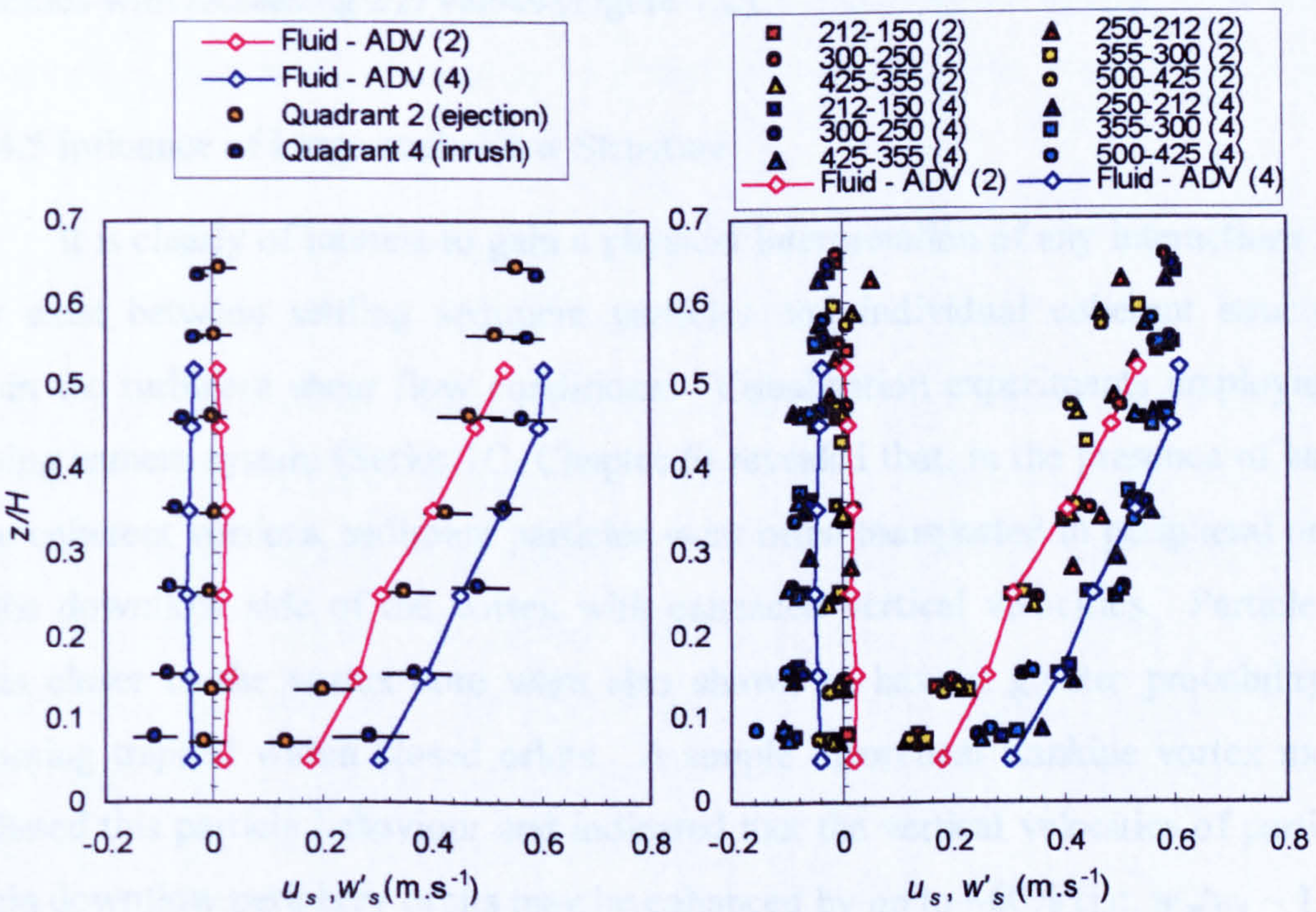

Figure 7.6 - Vertical distributions of (a) ensemble-averaged and (b) fractional-averaged longitudinal and vertical fluid and particle velocities for all quadrant 2 and 4 events. Error bars show ± one standard deviation. Note: downward particle fall velocities plotted as negative.

The vertical velocity profiles show that fluid motions associated with quadrant 2 events are positive (i.e. upward), while quadrant 4 fluid motions are negative (i.e. downward), as expected. The corresponding vertical particle velocities, which include the influence of gravitational settling, appear to be approximately zero for quadrant 2 particle motions, while quadrant 4 events generally become increasingly negative (i.e. downward) with reducing z/H values.

In summary, these plots provide a clear indication that the behaviour of conditionally averaged sediment particle motions can be related to similar conditionally averaged turbulent fluid motions. In particular, fluid and particle motions with large streamwise velocity components ($u' > 0$ and $u_{si} > \overline{u}_{si}$) tend to have the larger than average downward directed vertical velocity components ($w' < 0$ and $w'_{si} > \overline{w}'_{si}$), especially in the near-bed region. This is clearly consistent with the finding that the largest particle fall velocities generally occur within the near-bed region of flow ($z/H \leq 0.2$) in Series 1B and 2. On the other hand, particle and fluid motions with lower than average streamwise velocities ($u' < 0$ and $u_{si} < \overline{u}_{si}$), tend to have upward fluid velocity components ($w' > 0$) and lower than average vertical particle velocities ($w'_{si} < \overline{w}'_{si}$). These motions appear to be more dominant outwith the near-bed flow and are consistent with the observed reduction in particle fall velocities with increasing z/H values (Figure 7.2).

7.2.4.5 Influence of Large-scale Flow Structure

It is clearly of interest to gain a physical interpretation of any interactions that may exist between settling sediment particles and individual coherent structures within the turbulent shear flow conditions. Visualisation experiments employing a moving camera system (Series 1C, Chapter 5) revealed that, in the presence of large-scale coherent vortices, sediment particles were often transported in peripheral orbits on the downflow side of the vortex with enhanced vertical velocities. Particles in orbits closer to the vortex core were also shown to have a greater probability of becoming trapped within closed orbits. A simple theoretical Rankine vortex model predicted this particle behaviour and indicated that the vertical velocities of particles within downflow periphery orbits may be enhanced by up to ~60% (i.e. $w'_s/w_s \sim 1.60$) under the experimental conditions considered.

Wang and Maxey (1993) predicted similar levels of enhancement in direct numerical simulations (DNS) of the motion of heavy particles in an isotropic, homogeneous turbulent velocity field. They established the mechanism responsible for this enhancement resulted from two physical processes were also similar to those observed in Series 1C: (a) inertial bias causing particle accumulation in the peripheries of local vortices; (b) *preferential sweeping* of particles on the downflow side of local vortices (Figure 7.7 below).

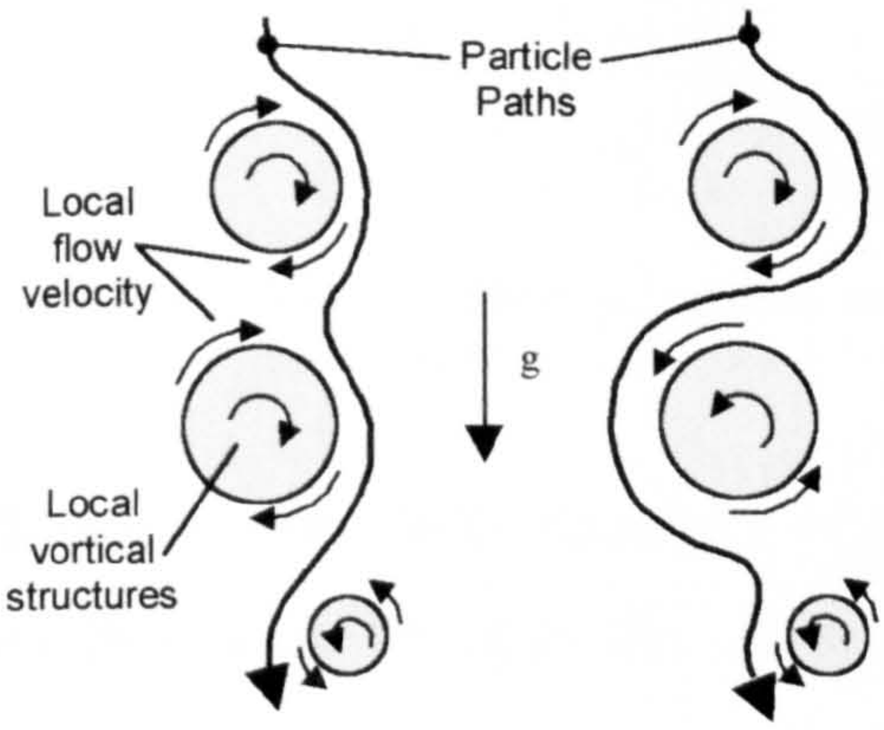

Figure 7.7 - Sketch showing preferential sweeping mechanism for a heavy particle interacting with local flow vortical structures under its inertia and body force (modified from Wang and Maxey, 1993).

This second process was thought to result from a combination of the local velocity field, particle inertia, and the initial approach angle of the particles relative to the vortex (i.e. from above). Raju and Meiburg (1995) suggested that the motion of small, heavy particles in a temporally evolving two-dimensional mixing layer can be characterised by two dimensionless parameters: the Stokes and Froude numbers (S_t and F_r),

$$S_t = \frac{\rho'_s \, d_s^{\,2}}{18\mu} \cdot \frac{\Delta u}{\delta}, \quad F_r = \frac{\Delta u}{\sqrt{g\delta}} \qquad \text{....(7.9)}$$

where ρ'_s and d_s are the submerged particle density (ρ_s-ρ) and particle diameter, respectively, μ is the fluid viscosity, Δu is the velocity difference across the mixing layer and δ is the mixing layer thickness. The Stokes number was interpreted to define the ratio between the particle response time due to inertia t_a and the characteristic flow time t_f. A third time scale t_s was also introduced to account for gravity, defining the time taken for a particle to fall with its terminal velocity over a distance equivalent to the mixing layer thickness δ, i.e.

$$t_a = \frac{\rho'_s \, d_s^2}{18\mu}, \quad t_f = \frac{\delta}{\Delta u}, \quad t_s = \frac{18\mu\delta}{\rho'_s \, d_s^2 g} \qquad \text{....(7.10)}$$

Considering a solid body vortex, with core radius R (i.e. $\delta = 2R$) and vorticity Ω_0, moving with an average streamwise velocity $\overline{U}$, the velocity difference Δu can be defined as $\Delta u = u_1 - u_2 = 2\Omega_0.R$ (Figure 7.8). Hence the Stokes number S_t and the Froude number F_r can be redefined as follows,

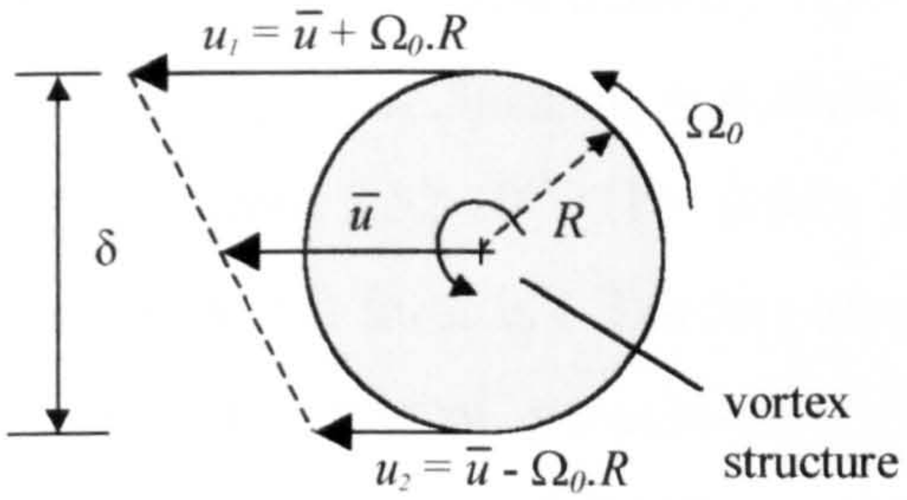

$$\left.\begin{aligned} S_t &= \frac{\rho'_s\, d_s^2}{18\mu}\cdot\Omega_0 \\ F_r^2 &= \frac{2\Omega_0^2 R}{g} \end{aligned}\right\} \qquad \text{....(7.11)}$$

Figure 7.8 - Velocity difference across a solid body vortex.

With kinematic fluid viscosity $\nu = \mu/\rho$ and the specific density $\Delta = \rho'_s/\rho$, the ratio of the Stokes number S_t to the square of the Froude number F_r can be written in the form,

$$\frac{S_t}{F_r^2} = \frac{1}{18}\frac{\Delta g d_s^2}{\nu}\cdot\frac{1}{2\Omega_0 R} = \frac{w_s}{2\Omega_0 R} \qquad \text{....(7.12)}$$

where w_s is the terminal fall velocity in still fluid. This ratio clearly defines the relative influence of gravity and fluid vorticity on the particle motion and is equivalent to the reciprocal of the bubble '*trapping*' parameter Γ proposed by Sene, Hunt and Thomas (1994) (§2.5.2, pp.38). This parameter was one of two key dimensionless groups deduced by Sene et al. (1994) to determine whether isolated or shear layer vortices can trap bubbles, the other being the '*relaxation*' parameter Π, defined for an isolated vortex as follows,

$$\Pi = \frac{\Delta u^2}{g\delta} \equiv \frac{2\Omega_0^2 R}{g} = F_r^2, \qquad \Gamma = \frac{\Delta u}{V_T} \equiv \frac{2\Omega_0 R}{w_s} = \frac{F_r^2}{S_t} \qquad \text{....(7.13)}$$

where V_T is the terminal rise speed of the bubble in still water (which can be considered equivalent to the terminal fall velocity of heavy particles w_s).

For the typical characteristics of the large-scale vortices observed in Series 1C, indicative values of the relaxation parameter Π are shown to range from about $1.50\ 10^{-2}$ (for $R = 0.01$m; $\Omega_0 = 2.7$ H_z) to about $2.72\ 10^{-1}$ (for $R = 0.025$m; $\Omega_0 = 7.3$ H_z).

These values suggest that the inertial force is approximately 1-2 orders of magnitude lower than the gravitational force for the typical vortex dimensions quoted.

Corresponding values of the trapping parameter Γ for LA grade sand particles range from 2.7 (Π = 0.015) to 18.2 (Π = 0.272) for the finest size fraction (d_i = 181μm; $w_s = 0.02 ms^{-1}$) and from 0.9 (Π = 0.015) to 6.1 (Π = 0.272) for the coarsest size fraction (d_i = 462.5μm; $w_s = 0.06 ms^{-1}$). Finally, the corresponding Π/Γ values, which range from $5.52\ 10^{-3}$ (Π = 0.015; Γ = 2.7) to $1.66\ 10^{-1}$ (Π = 0.015; Γ = 0.9), suggest that the lift force is 1-3 orders of magnitude lower than the drag force.

Thus for typical particle-vortex interactions observed in Series 1C, the assumption that inertia and lift forces are weak in comparison to gravitational and drag forces appears reasonable in the majority of cases and the problem can be approximated by a zero-order solution (i.e. inertial and lift forces are neglected). At this point it should be re-emphasised that this analysis has implicitly assumed the vortex rotates as a solid circular body with constant radius *R*. Clearly, this is a significant assumption as observed vortices in Series 1C are generally elliptical in shape and constantly changing with time.

The equation of balance for the remaining gravitational and drag forces acting on a particle can be written in the following form,

$$(\rho_s - \rho)g \cdot \frac{\pi d_s^3}{6} = \frac{1}{2} C_D \cdot \frac{\pi d_s^2}{4} \cdot \rho(\vec{u}_s - \vec{u})|\vec{u}_s - \vec{u}| \qquad ....(7.14)$$

where C_D is the fluid drag coefficient on the particle and $(\vec{u}_s - \vec{u})$ is the relative velocity between the particle and the fluid. Rearranging equation 7.14 we obtain,

$$(\vec{u}_s - \vec{u})|\vec{u}_s - \vec{u}| = \frac{8(\rho_s - \rho)g \cdot \pi d_s^3}{6 C_D \cdot \rho \cdot \pi d_s^2} = \frac{4}{3}\frac{\Delta g d_s}{C_D} = w_s^2 \qquad ....(7.15)$$

$$\text{or} \qquad \vec{w}_s = \vec{u}_s - \vec{u} \qquad ....(7.16)$$

Hence, the relative velocity between the fluid and the particle is equal to the terminal fall velocity in still water conditions, as was demonstrated previously in the simple theoretical Rankine vortex model used to predict particle trajectories (§5.4.2, pp.153). The Rankine model is a fair reflection of many natural vortices, having a core that rotates as a rigid body, with the velocity proportional to the distance from the centre, whilst becoming inversely proportional further away (Nielsen, 1984).

Assuming the Rankine vortex has a velocity field given by equation 5.2 (pp.154), equation 7.16 can be re-arranged and re-written in vector form,

$$\vec{u}_s(x,z) = \frac{d\chi(x,z)}{dt} = w_s\begin{pmatrix}0\\-1\end{pmatrix} + \frac{\Omega_0 R}{1+(x/R)^2+(z/R)^2}\begin{pmatrix}-z/R\\x/R\end{pmatrix} \qquad \text{....(7.17)}$$

or, $$\chi_t(x,z) = \Delta t\left[w_s\begin{pmatrix}0\\-1\end{pmatrix} + \frac{\Omega_0 R}{1+(x/R)^2+(z/R)^2}\begin{pmatrix}-z/R\\x/R\end{pmatrix}\right] + \chi_{t-1}(x,z) \qquad \text{....(7.18)}$$

where $\chi(x,z)$ is the displacement vector of the particle relative to the centre of vorticity (0,0) and Δt is the time step.

A feature of the zero-order solution is that particle trapping is only possible if the maximum vertical flow velocity exceeds the settling velocity of the sediment particles, that is $\Omega_0 R/2 > w_s$. The resulting ratio $\Omega_0 R/2w_s > 1$ clearly represents the critical value of the trapping parameter $\Gamma > 1$ (Sene et al. 1994), modified for the Rankine vortex velocity field. Under these conditions, it can be shown that particles will only become trapped if their orbits or trajectories lie within a certain trapping width, which increases with Γ (i.e. vorticity/radius increases or fall velocity reduces) (Figure 7.10 overleaf). Particles released within the central blue ovoid areas shown in each plot are trapped in closed orbits. Clearly when $\Gamma < 1$ (Figure 7.10f), no ovoid region exists in which the particles can become trapped.

The relationship between the relative trapping width X/R and the trapping parameter Γ is shown in Figure 7.9 below.

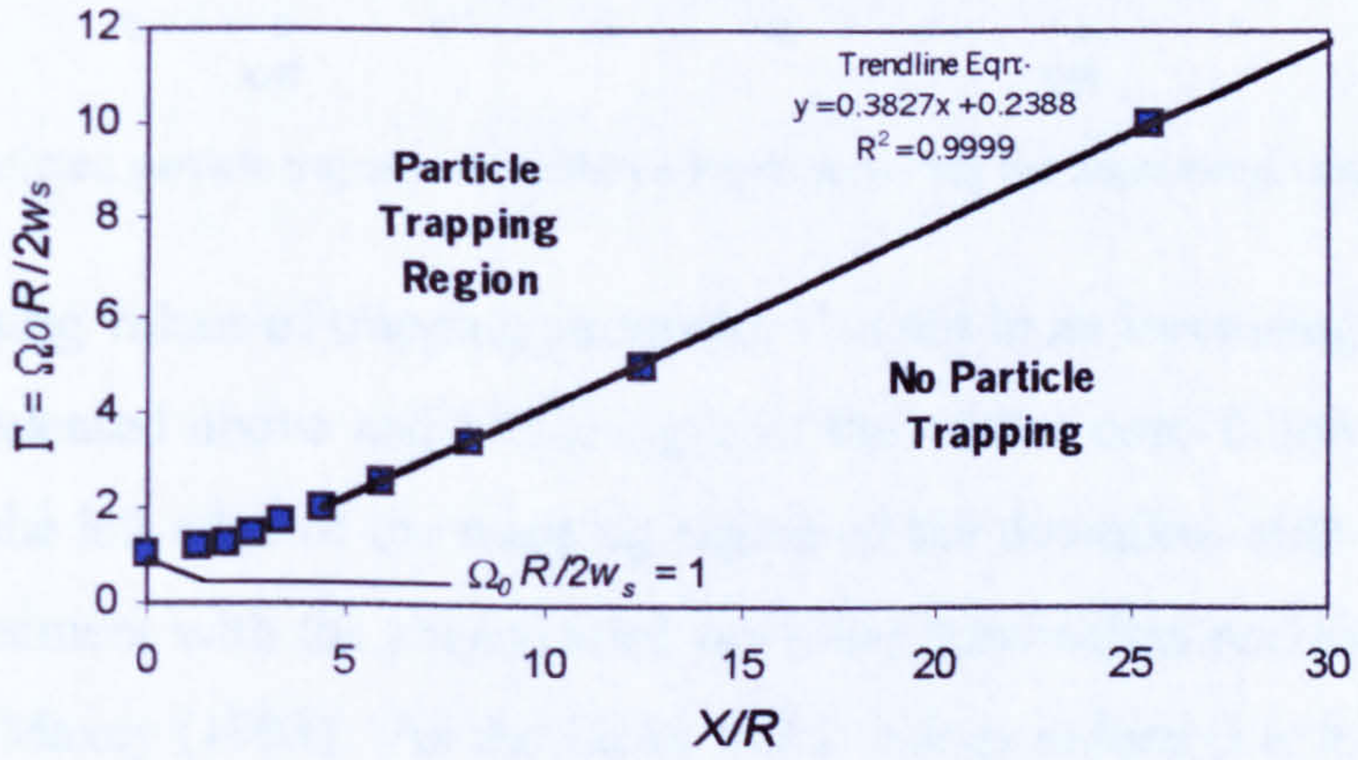

Figure 7.9 - Relationship between relative trapping width X/R and the particle trapping parameter Γ ($= \Omega_0 R/2w_s$). Note, trapping width $X/R = 0$ when $\Gamma = 1.0$.

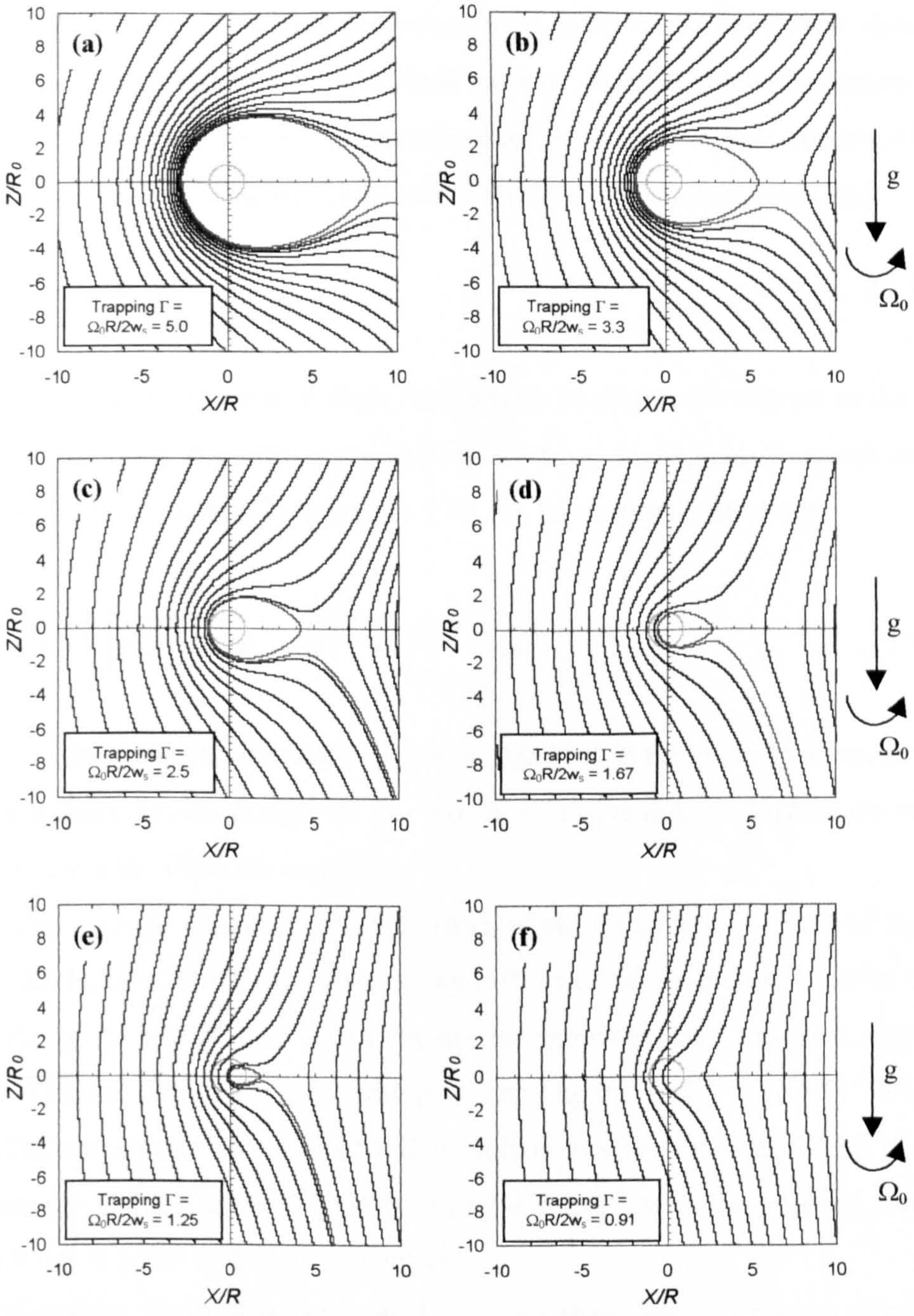

Figure 7.10 - Predicted particle trajectories within a Rankine vortex for decreasing values of Γ.

Increasing values of trapping parameter Γ result in an increasing proportion of the particles released above and to the right of the vortex core following trajectory paths around the left edge of the trapping region of the downflow side of the vortex. This is in agreement with the *preferential sweeping* mechanism previously observed by Wang and Maxey (1993). As the Ω_0/w_s and Γ values reduce (i.e. low vorticity or high fall velocity), the vortex has a reducing influence on the particle trajectories, with the relative trapping width $X/R \rightarrow 0$. Above $\Gamma \sim 2$, the relative trapping width X/R is shown to increase linearly with the trapping parameter Γ (Figure 7.9).

Particle trajectories on the downflow side of a vortex have their downward motion due to gravity enhanced by the fluid motion. For the zero-order solution (i.e. $\vec{u}_s = \vec{u} + \vec{w}_s$), this enhancement will be highest as the particle crosses the negative x/R axis (i.e. downflow side - Figure 7.10), where $u_s(x) = 0$ and $u_s(z)$ is given by,

$$u_s(z) = -w_s + \frac{\Omega_0 x}{1 + (x/R)^2} \qquad \text{....(7.19)}$$

Substituting $x = \alpha_r.R$, where α_r defines the particle position with respect to the vortex radius, and assuming the still water fall velocity w_s is adequately represented by Cheng (1997) (eqn. 4.1, pp.12), equation 7.19 can be written in the form,

$$w'_s = \frac{\nu}{d_s}\left[\sqrt{25 + 1.2d_{s*}^2} - 5\right]^{1.5} + \left|\frac{\alpha_r}{1 + \alpha_r^2}\right|\Delta u \qquad \text{....(7.20)}$$

where w'_s is the turbulent fall velocity [i.e. $\equiv u_s(z)$], d_s is the particle diameter, d_{s*} is the dimensionless particle parameter [$d_{s*} = d_s(\Delta g/\nu^2)^{1/3}$] and Δu ($= \Omega_0 R$) is the velocity difference across the Rankine vortex.

Using average indicative characteristics of vortex structures observed in Series 1C ($\Omega_0 = 5.6$ H_z, $R = 0.0125$ m), the velocity difference across a typical vortex may be in the order of $\Delta u = 0.07$ m.s^{-1}. For illustrative purposes, four sediment sizes, d_s = 500, 250, 125 and 63μm, are used with $\rho_s = 2650$ kg.m^{-3} and $\nu = 1.0\times10^{-6}$ m^{2}s^{-1} (i.e. 20°C). The corresponding terminal fall velocities in still water according to Cheng (1997) are w_s = 0.0607, 0.0267, 0.0090 and 0.0026 m.s^{-1}, with the trapping parameter Γ values = 0.6, 1.3, 3.9 and 13.5, respectively.

Clearly for the 500μm particles, $\Gamma < 1$ and therefore no trapping width exists for the vortex characteristics considered. The relative trapping width for the other particle sizes can be estimated from Figure 7.9, while the location relative to the centre of the vortex can be derived from the solution of equation 7.19 for $w_s = u(z)$, which defines the upflow boundary of the trapping region outwith the vortex core. Using this method, it can be demonstrated that 250μm particles are trapped in the region defined by $-0.1 \leq \alpha_r \leq 2.1$, fine 125μm particles are trapped between $-1.9 \leq \alpha_r \leq 7.7$ and very fine 63μm particles are trapped between $-7.7 \leq \alpha_r \leq 27.0$.

The maximum vertical particle velocities on the downflow side of the vortex are calculated for the four selected particle sizes from equation 7.20 with α_r values

ranging between -1 and -10, detailed in Table 7.2. Note shaded cells refer to particle trajectories lying within predicted trapping regions.

d_s (μm)	w_s (ms^{-1})	Max. vertical velocities on downflow side of vortex w'_s (equation 7.20) (ms^{-1})									
	(Cheng)	α_r = -1	α_r = -2	α_r = -3	α_r = -4	α_r = -5	α_r = -6	α_r = -7	α_r = -8	α_r = -9	α_r = -10
63	0.0026	0.0376	0.0306	0.0236	0.0191	0.0161	0.0139	0.0124	0.0112	0.0103	0.0095
125	0.0090	0.0440	0.0370	0.0300	0.0255	0.0225	0.0205	0.0188	0.0176	0.0167	0.0159
250	0.0267	0.0617	0.0547	0.0477	0.0432	0.0402	0.0381	0.0365	0.0353	0.0344	0.0336
500	0.0607	0.0957	0.0887	0.0817	0.0772	0.0742	0.0721	0.0705	0.0693	0.0684	0.0676

Table 7.2 - Predicted maximum values of enhanced settling velocity w'_s at various α_r locations on the downflow side of a Rankine vortex (Ω_0 = 5.6 Hz., R = 12.5mm) for four sediment sizes.

The corresponding w'_s/w_s values indicate the maximum levels of enhancement in the vertical particle velocities occur whilst being transported in the downflow side of the vortex. For the 500μm and 250μm particles, w'_s/w_s values calculated from Table 7.2 values are shown to range from 1.58-1.11 and 2.31-1.26, respectively, for α_r values increasing from -1 to -10. For the fine 125μm sand grade, particles at α_r = -1 are within the trapping region and will therefore follow closed orbits, with $w'_s \rightarrow 0$. Outwith the particle trapping region, w'_s/w_s values vary from 4.11 at α_r = -2 to 1.76 at α_r = -10. Finally, for the very fine 63μm sand, while particle trapping clearly occurs at the majority of α_r values shown, w'_s/w_s values vary from 4.31 at α_r = -8 to 3.65 at α_r = -10.

In summary, it has been demonstrated that observed interactions between coherent vortices and sediment particles, and specific phenomenon such as trapping, can be reasonably described by considering the relative strengths of vorticity and the gravitational settling tendencies of the particles. It has also been shown that the enhancement of vertical particle velocities on the downflow side of vortices [or *preferential sweeping*, Wang and Maxey (1993)], represents a mechanism which may at least, in part, be responsible for the enhanced turbulent fall velocities observed during Series 1B and 2 experiments.

7.3 Vertical Turbulent Transfer Coefficient

The balance between the downward settling flux ($w_s.C$) and the upward turbulent diffusion flux ($\varepsilon_{sz} \partial C/\partial z$) is commonly used to describe the vertical transfer of suspended sediment particles in turbulent open channel shear flow. From the

experimental findings and the subsequent discussion in §7.2 above, the validity of the widely applied assumption that sediment particle fall velocities are unaffected by turbulent fluctuations within the surrounding fluid has been examined in detail. Significant doubt also remains on the general validity of the use of the Fickian diffusion concept to describe suspended sediment particle motion. This traditionally assumes the existence of a simple analogy between the turbulent diffusion of sediment particles ε_s and the transfer of fluid momentum ε_f (or eddy viscosity ν_t) through an empirical constant β, i.e. $\varepsilon_s = \beta.\varepsilon_f$.

Vertical distributions of the non-dimensional transfer coefficient for LA sand particles (ε_{sz}/Hu_*) were calculated from solution of the integrated two-dimensional sediment transfer equation (eqn. 6.3, pp.168) using concentration and velocity profiles measured during three experiments in Series 2 (i.e. S2_EX3 - EX5). Distributions obtained for the three finest LA sand fractions (d_i = 275, 231 and 181μm) showed considerable deviation from the parabolic distribution, commonly assumed in suspended sediment modelling (Figure 6.16, pp.184). In general, the ε_{szi}/Hu_* profiles appeared to be skewed towards the lower half of the flow ($z/H < 0.5$), where $\varepsilon_{sz} > \varepsilon_f$. In this region, maximum values of ε_{szi}/Hu_* occurred between $0.2 \leq z/H \leq 0.4$. Values of ε_{szi}/Hu_* generally reduced with increasing z/H and, in the outer flow ($z/H > 0.6$), $\varepsilon_{sz} \leq \varepsilon_f$ typically. ε_{szi}/Hu_* values also reduced as the bed surface was approached.

These characteristics are consistent with ε_{sz}/Hu_* profiles obtained by Jobson and Sayre (1970) for coarse-grained sand (d_i = 390μm), while corresponding ε_{sz}/Hu_* profiles for finer glass beads (d_i = 123μm) revealed closer association with the parabolic distribution of fluid momentum transfer ε_f.

7.3.1 Model for Sediment Transfer Coefficient

The above considerations suggest that the validity of the assumed analogy between the turbulent diffusion of sediment ε_s and the momentum transfer of fluid ε_f may depend on particle grain size d_i. Clearly, for very fine sediments such as clays and silts, particle motions will be dominated by turbulent motions within the fluid, resulting in the particles tending to follow the fluid elements closely (i.e. $w_s = \vec{u}_s - \vec{u} \rightarrow 0$), in turn, suggesting that the assumed analogy may be reasonable in this case. At the other extreme, the motion of coarse sand particles will clearly be dominated by

gravity, resulting in large relative velocities between the particles and surrounding fluid (= w_s), and significant departure from the analogy.

The nature of interactions between sediment particles and turbulence is known to be related to the Stokes number S_t, which defines the ratio between particle response time t_a and the local turbulent fluctuating time scale of the fluid t_f. This parameter, previously defined in equation 7.9 for a temporally evolving two-dimensional mixing layer (Raju and Meiburg, 1995), can be used to relate ε_s to ε_f through,

$$\varepsilon_s = \frac{\varepsilon_f}{(1+S_t)} = \frac{\varepsilon_f}{(1+t_a/t_f)} \qquad \ldots.(7.21)$$

Cao et al. (1996) assumed that the vertical components of both ε_s and ε_f could be written in terms of Lagrangian integral time scales (T_{LF} and T_{LS}) and corresponding rms values of vertical fluid and particle velocity fluctuations [i.e. w'_{rms} and $\sigma(w'_s)$], resulting in the algebraic formulation of Hinze (1959),

$$\varepsilon_{sz} = T_{LS}[\sigma(w'_s)]^2 = \frac{T_{LF}(w'_{rms})^2}{(1+t_a/t_f)} \qquad \ldots.(7.22)$$

Vertical distributions of w'_{rms}/u_* and $\sigma(w'_s/u_*)$ for Series 1B experiments (Figure 4.22(b), pp.130) gave some indication of an association between these two parameters, with $\sigma(w'_s/u_*) > w'_{rms}/u_*$, generally. Experimental results from Series 1B also suggested that a similar association exists between non-dimensional turbulent particle fall velocity w'_s/u_* and vertical turbulence intensity w'_{rms}/u_*. Experimental-averaged distributions of w'_s/u_*, $\sigma(w'_s/u_*)$ and w'_{rms}/u_* with z/H are shown in Figure 7.11(a). A more direct comparison of w'_s/u_* and $\sigma(w'_s/u_*)$ values with corresponding w'_{rms}/u_* values obtained at similar z/H locations is plotted in Figure 7.11(b), revealing linear relationships between these parameters ($R^2 = 0.94$ and 0.97, respectively). It is acknowledged that these linear relationships are only valid for LA sand under the limited experimental conditions considered and over a specific z/H range in which measurements could be compared ($0.1 \leq z/H \leq \sim 0.5$). Clearly, for the lower limit of flow conditions where $w'_{rms} \rightarrow 0$ (i.e. laminar flow, still water), it would be expected that $w'_s \rightarrow w_s$ (i.e. still water fall velocity) and $\sigma(w'_s) \rightarrow 0$, assuming no vertical

component of fluid velocity exists. These conditions would represent a significant departure from the linear relationships plotted in Figure 7.11(b).

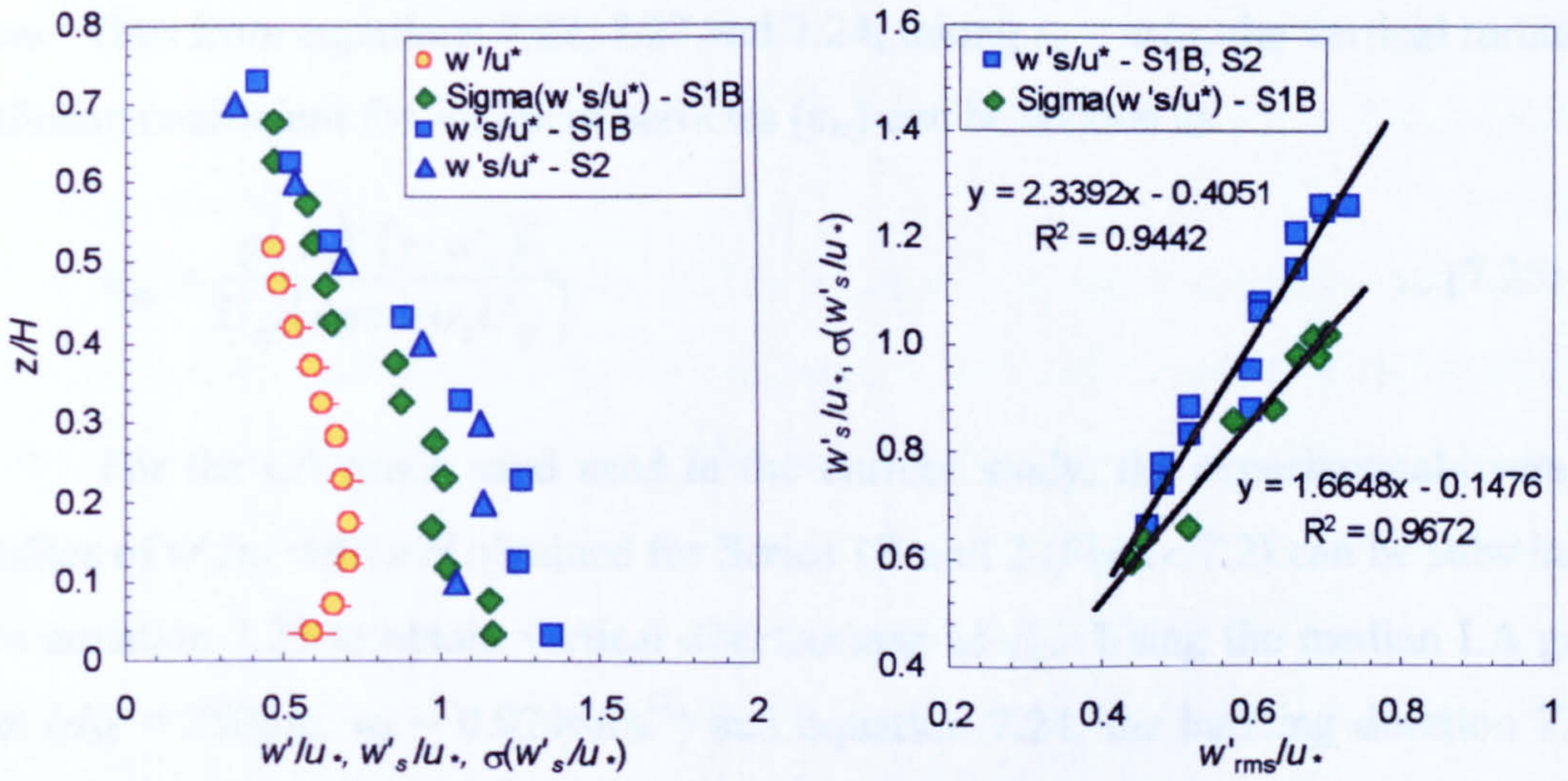

Figure 7.11 - (a) Experimental-averaged distributions of w'_s/u_*, $\sigma(w'_s/u_*)$ and w'_{rms}/u_* with relative depth z/H. (b) Linear relationship of experiment-averaged values of w'_s/u_* and $\sigma(w'_s/u_*)$ with the w'_{rms}/u_* values at corresponding z/H elevations (outwith $z/H \leq 0.1$).

Returning to the turbulent diffusion coefficient ε_{sz}, the relationship between w'_s/u_* and w'_{rms}/u_* suggests that it may be reasonable to rewrite equation 7.22 as follows,

$$\varepsilon_{sz} = \frac{T_{LF}\left(\gamma \cdot w'_s\right)^2}{\left(1 + t_a/t_f\right)} \qquad \ldots.(7.23)$$

where γ is an experimentally-determined coefficient relating turbulence intensity w'_{rms} to the turbulent particle fall velocity w'_s at any given location z/H.

At this point, the main problem lies in defining appropriate values for the various time scales in equation 7.23, as well as the experimental coefficient γ. Cao et al. (1996) stated that as the turbulent bursting process controls the suspension of particles, the two fluid time scales t_f and T_{LF} should be set equal to the mean duration of turbulent bursts T_D, defined as

$$T_D = A \cdot z/U_{sf} \qquad \ldots.(7.24)$$

where A is a grain size dependent model parameter calibrated from previous experimental data [$= 4.2 + 11.4\left(w_s/\kappa u_*\right)$], z is the elevation and U_{sf} is the free-surface flow velocity. This expression assumes the mean burst duration increases linearly

with distance from the bed surface z, recognising that more energetic and longer duration bursts will be capable of suspending particles to higher elevations within the flow. Thus from equations 7.22, 7.23 and 7.24, taking $t_a \sim w_s/g$, the vertical turbulent diffusion coefficient for sediment particles (ε_{sz}) can be written as

$$\varepsilon_{sz} = \frac{g(Az)^2(\gamma \cdot w'_s)^2}{U_{sf}\left(Agz + w_s U_{sf}\right)} \qquad \text{....(7.25)}$$

For the LA grade sand used in the current study, the experimental-averaged profiles of w'_s/u_* with z/H obtained for Series 1B and 2 (Figure 7.2) can be substituted into equation 7.25 to obtain vertical distributions of ε_{sz}. Using the median LA grain size (d_{50} = 250μm, $w_s \sim 0.0296 ms^{-1}$) and equation 7.24, the bursting duration T_D is estimated to increase linearly from 0.0 ~ 2.7s as z/H increases from 0 to 1. The particle inertial response time t_a can be estimated as ~0.003s from the ratio w_s/g and hence is generally negligible in comparison to T_D.

Figure 7.12 below compares the measured ε_{sz} distributions from experiments S2_EX3 - EX5 with corresponding computed ε_{sz} profiles from equation 7.25, both of which are normalised by the product of H and u_*. The experiment coefficient γ (= w'/w'_s) is taken as 0.7, which would appear to be reasonable given that γ values vary from 0.55-0.72 for the w'_s/u_* and w'_{rms}/u_* data plotted in Figure 7.11(b).

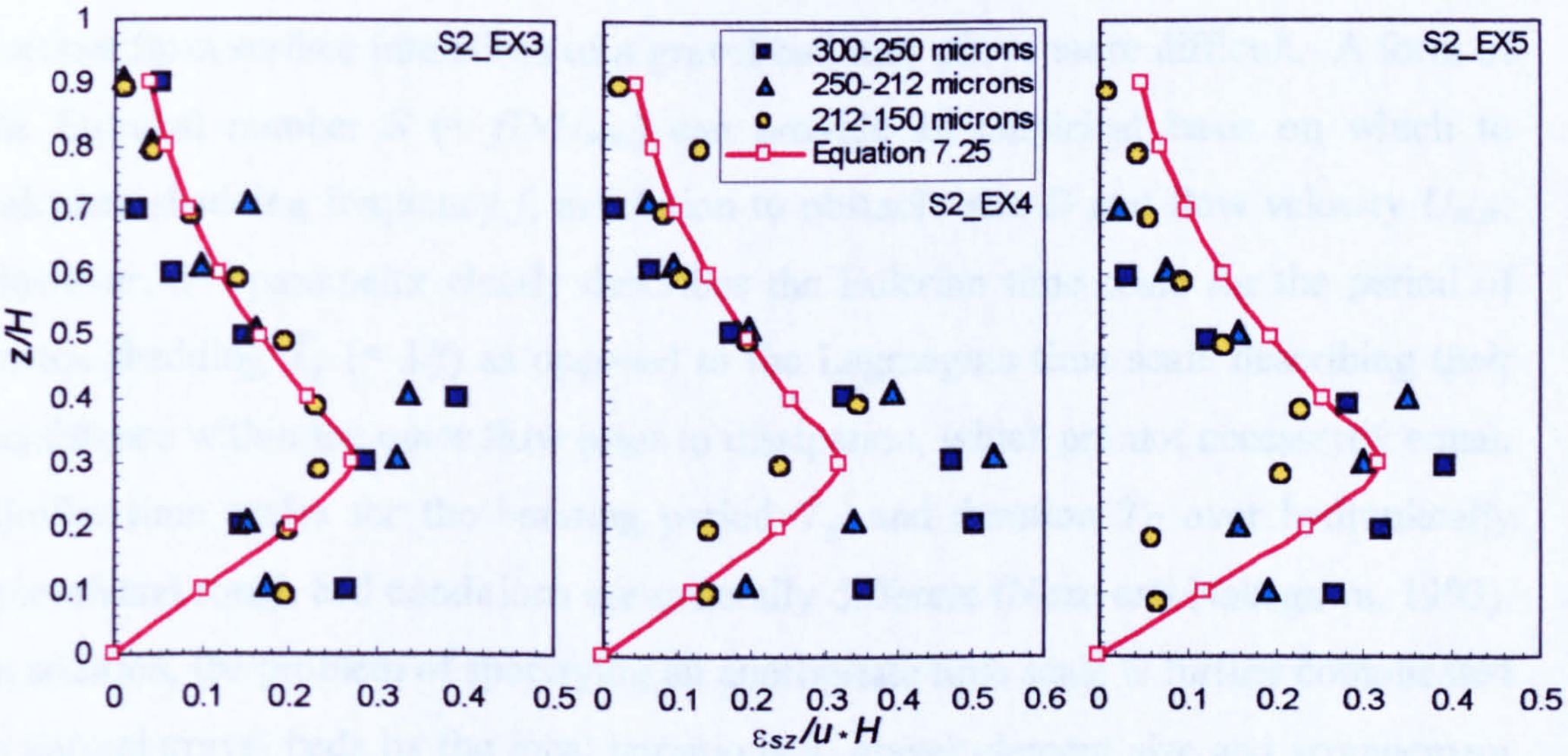

Figure 7.12 - Comparison of measured and computed distributions of ε_{sz}/Hu_* with z/H for the three experiments S2_EX3, EX4 and EX5 in Series 2.

Although there is considerable scatter within the experimental data, the computed profiles in general show reasonably good agreement with the measured distributions, particularly with respect to their shape. Notably, they produce a similar skew towards the lower half of the flow ($z/H < 0.5$), with maximum values of ε_{sz}/Hu_* occurring at $z/H = 0.3$.

One problem with equation 7.25 is the prediction of a non-zero value of ε_{sz} at the free surface. This is due to the assumption that the exponential distribution of w'_s/u_* shown in Figure 7.2 extends to the near surface flow, outwith the extent of the measurements. Clearly, if it were assumed that the particles are released at the free surface with no initial downward velocity w'_s then $\varepsilon_{sz} = 0$ at $z/H = 1.0$.

Overall, the predictive model for ε_{sz} (eqn. 7.25) clearly provides better agreement with experimental data than a parabolic distribution derived from the assumed analogy between ε_s and ε_f [i.e. $\varepsilon_s = \beta.\varepsilon_f = \beta.\kappa.u_*.z(1-z/H)$]. However, the applicability of the assumed fluid and particle Lagrangian time scales related to turbulent bursting requires to be investigated for hydraulically rough, porous bed conditions (i.e. gravel beds), where little knowledge is currently available.

Flow visualisations from Series 1C suggested that large-scale vortex structures rise and expand outward from the bed region into the outer flow before dissipating, similar to observations of vortex shedding by Kirkbride (1993) (§2.3.3.1, pp.28). The selection of an appropriate time scale to represent this quasi-cyclical shedding of vortices from surface interstices of a gravel bed may prove more difficult. A form of the Strouhal number S (= fD/U_{max}) can provide an empirical basis on which to calculate shedding frequency f, in relation to obstacle size D and flow velocity U_{max}. However, this parameter clearly describes the Eulerian time scale for the period of vortex shedding $\overline{T}_s$ (= $1/f$) as opposed to the Lagrangian time scale describing their persistence within the outer flow prior to dissipation, which are not necessarily equal. Similar time scales for the bursting period T_B and duration T_D over hydraulically smooth and rough bed conditions are generally different (Nezu and Nakagawa, 1993). In addition, the problem of specifying an appropriate time scale is further complicated in natural gravel beds by the local variations in gravel element size and arrangement (e.g. protruding elements) at the bed surface. These variations will clearly generate an array of different-sized vortices with various shedding frequencies, each of which are capable of suspending sediment particles of different sizes.

7.4 Sediment Deposition Characteristics

The net exchange of fine sediment between the near-bed flow and the surface layers of a gravel bed is governed by the relative magnitudes of two distinct processes: *entrainment* and *deposition.* Whilst not being primarily considered in this study, the entrainment of fine sediments from bed surface interstices is known to be controlled by turbulent fluid motions within the near-bed flow and the turbulent bursting process in particular (e.g. Sutherland 1967; Grass 1974; Sumer and Oğuz 1978; Sumer and Deigaard 1981; Niño and Garcia 1996). By contrast, sediment deposition is generally assumed to occur under the primary influence of gravity and is often represented by the product of near-bed concentration C_b and the fall velocity w_s of the sediment.

Previous investigations have indicated that a linear relationship does indeed exist between the sediment deposition flux and the local near-bed sediment concentration (i.e. Carling 1984, Peloutier 1998). This is also suggested by the concentration and deposition measurements obtained during the Series 2 experiments (§6.4.2.5, pp.191). The proportionality constant in this linear relationship, having the dimensions of velocity, describes the vertical transfer velocity of sediment particles across the bed surface interface, i.e. from the near-bed flow region into the surface bed layers. The common assumption that this transfer or deposition velocity w_d can be approximated by the fall velocity in still water w_s implies that near-bed turbulence has negligible influence on particle deposition.

The validity of this assumption must be questioned as, firstly, particle-turbulence interactions clearly had an unequivocal influence on vertical particle motion within the main body of flow above the bed surface (e.g. preferential sweeping around vortices). Secondly, the turbulent structures that actuate many of these interactions (i.e. large-scale vortices) appear to be generated within the bed surface interstices. It would therefore seem obvious that these turbulent structures should also have some degree of influence on deposition of particles across the bed surface interface, and particularly on the deposition velocity w_d.

The main experimental findings from Series 2 appear to confirm this. Experimental-averaged results for LA sand revealed that the deposition velocities of the coarsest and finest particles (d_i >400μm and <200μm, respectively) are lower than

their fall velocities in still water (i.e. hindered deposition), while intermediate grain sizes are deposited at higher velocities (i.e. enhanced deposition).

These findings are compared directly with similar results obtained by Peloutier (1998) in Figure 7.13. The author reported that particles below ~200μm tended to undergo enhanced deposition ($<w_{di}>/w_{si} > 1$), while particles above ~350μm were deposited at lower velocities than their still water fall velocity ($<w_{di}>/w_{si} < 1$). This latter finding is consistent with the results from Series 2, while examination of Peloutier's data reveals that the significant divergence in $<w_{di}>/w_{si}$ values observed for finer particle sizes [Figure 7.13(b)] results primarily from differences in the specification of still water fall velocity w_{si}. Peloutier used Cheng's (1997) equation to provide predictions of w_{si}, which were on average 9% less than measured values for the LA sand fractions and up to 17% lower for the finest particles (§4.2.3, pp.96). When Peloutier's $<w_{di}>$ values are normalised by measured w_{si} values [yellow data set, Figure 7.13(b)], the deposition characteristics become hindered for the finest particles ($<w_{di}>/w_{si} < 1$), in agreement with Series 2 data. This clearly highlights the importance of conducting accurate calibration measurements of particle fall velocity in still water conditions, as opposed to relying on predictions from established formulations for w_s.

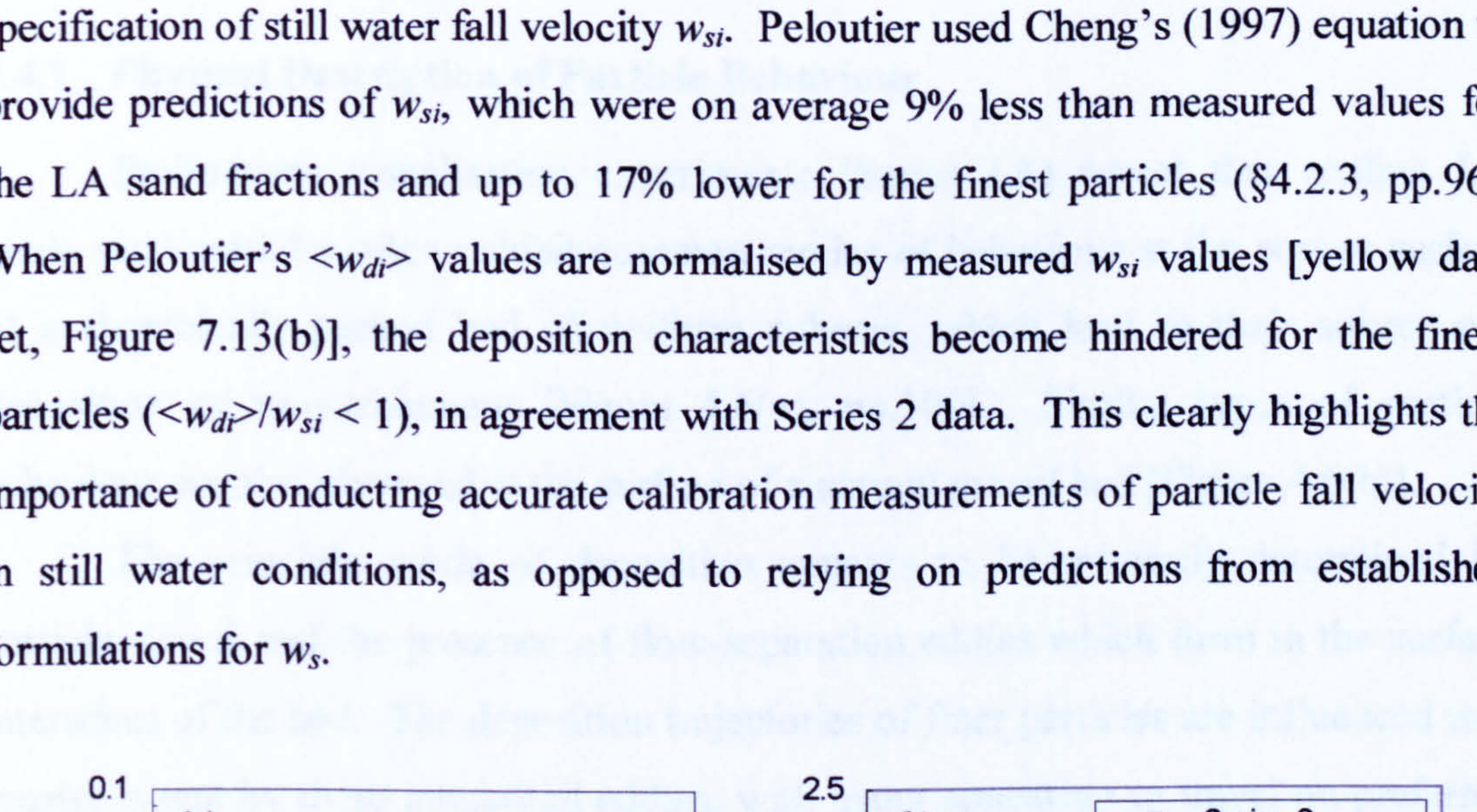

Figure 7.13 - Comparison of experiment-averaged values of: (a) deposition velocity $<w_{di}>$; and (b) non-dimensional deposition velocity $<w_{di}>/w_{si}$ for Series 2 experiments and data obtained from Peloutier (1998).

The other main experimental finding from Series 2 suggests that near-bed turbulence influences particle deposition in that larger shear velocities u_* appear in general to result in lower fraction-averaged deposition velocities w_d. This finding is also consistent with experimental results from Peloutier (1998), and implies that higher turbulence intensity in the near-bed flow tends to reduce the sediment deposition flux Δ_b at the bed surface. This can be envisaged as higher bed shear velocities forming a 'barrier' against deposition, which results in greater quantities of particles being re-suspended within the near-bed flow by the higher intensity turbulence generated within bed surface interstices.

7.4.1 Physical Description of Particle Behaviour

Preliminary visualisation experiments (Series 1A) reveal that settling LA grade sand particles often exhibit common modes of behaviour at the porous surface of a rhombically-packed bed of uniform spheres, which lead to their subsequent deposition or re-entrainment [Figure 4.6(a), pp.106]. Similar types of particle behaviour are also observed at the surface of a natural gravel bed [Figure 4.6(b)].

The principle mode of deposition appears to be primarily determined by particle size d_i and the presence of flow-separation eddies which form in the surface interstices of the bed. The deposition trajectories of finer particles are influenced to a greater extent by these interstitial eddies, with many appearing to travel on preferred paths on the downflow side of the eddy before being released to deposit deeper into the bed. Coarser particles, by contrast, tend to be less influenced by interstitial turbulence and appear to deposit primarily under the influence of gravity.

The fact that not all particles are immediately deposited on first contact with the bed surface is also apparent from Series 1A observations. As well as transporting fine particles on preferred downflow paths, interstitial eddies can also trap particles in a quasi-closed orbits before either releasing them for deposition or ejecting them back into the near-bed flow region. This eddy trapping mechanism appears to be important for the re-entrainment of depositing finer particles in particular.

The bed elements themselves provide a physical barrier to deposition, with both fine and coarse particles observed to ricochet off exposed upstream faces of individual bed elements. This generally results in the particles either being re-

suspended back into the near-bed flow or performing a 'saltation-type' motion before coming into contact with the bed surface further downstream (Figure 4.5, pp.105).

The re-entrainment of particles following an initial contact with bed elements or interaction with interstitial eddies will clearly result in imbalances between measured near-bed sediment concentrations C_b and local deposition rates Δ_b, reflected in the prediction of reduced deposition velocities w_d. Initial estimations of the deposition probability p for individual LA sand fractions suggest that p generally reduces as particle size d_i decreases and shear velocity u_* increases. Therefore, the higher percentage of re-entrained particles occurring under high shear conditions result in reduced local deposition rates Δ_b and correspondingly lower w_d values, in agreement with subsequent Series 2 results.

In many respects, the observed particle-fluid interactions occurring at the bed surface appear to mirror the interactions observed between particles and large-scale vortices present within the open channel shear flow above the bed surface (Series 1C). In particular, the apparent preference of particles to travel on the downflow side of the interstitial eddy is clearly analogous to the *preferential sweeping* mechanism, discussed previously (§7.2.4.5, pp.217). Therefore, it may be valuable to consider these interstitial particle-fluid interactions in a similar manner.

As an initial approximation, if a typical interstitial eddy is considered to be circular in shape with radius R and rotate as a rigid body with vorticity Ω_0, then clearly its ability to trap particles can be defined, as before, by the *trapping* parameter Γ ($= \Delta U/w_s = 2\Omega_0 R/w_s$). It can also be assumed that the corresponding *relaxation* parameter Π ($=2\Omega_0^2 R/g$) = 0, as inertial effects are often not significant for sand grain motions (Nielsen, 1984).

Typical rotation frequencies for the large-scale vortices observed in Series 1C range between about 3 and 7sec^{-1}, with an average value about 5.7sec^{-1}. Series 1A particle trajectories forming quasi-closed orbits within surface interstices (Figure 4.5, pp.105) yield similar Ω_0 values between about 5 and 6.3sec^{-1}. The characteristic size of interstitial eddies will clearly be related to the size of the surface voids in which they form. For rhombically-packed uniform spheres (D = 15mm), this can be determined from geometrical considerations to be in the order of $D/3$, i.e. $R \sim D/6$ = 2.5mm, while for the natural gravel bed, the size of the interstitial eddies will vary significantly depending on local bed grading and configuration. However on average,

these are likely to be larger than in the rhombically-packed uniform spheres as both the median gravel size (D_{50} = 17.3mm) and bed porosity ($\lambda \sim 0.4$) are larger in the gravel bed.

Nielsen (1984) stated that particles can only become trapped in closed orbits when the maximum vortex flow speed $\Omega_0 R$ exceeds the terminal particle fall velocity w_s, i.e. $\Omega_0 R > w_s$, equivalent to $\Gamma > 2$ (Sene et al. 1994). Therefore, for an interstitial eddy with characteristic vorticity $\Omega_0 = 6\text{sec}^{-1}$, the eddy radius R required to trap the finest 181μm LA sand particles ($w_s = 0.0201\text{ms}^{-1}$) must be at least 3.4mm, which is larger than the estimated eddy size for the rhombically-packed spheres. This critical value of R will also clearly increase as particle size d_i (through w_{si}) increases.

The requirement that $\Gamma > 2$ for particles trapping is also useful for determining the maximum particle size d_i which can be trapped by any given interstitial eddy. As an example, consider an eddy with characteristic radius R = 5mm and vorticity $\Omega_0 = 7\text{sec}^{-1}$. The corresponding trapping parameters Γ for d_i = 462.5, 390, 327.5, 275, 231 and 181μm LA particles are 1.17, 1.43, 1.73, 2.17, 2.59 and 3.48, respectively. This suggests that depositing particles with $d_i \leq 300\mu$m will be significantly influenced by the presence of the eddy and can become trapped in quasi-closed orbits, whereas particles with $d_i > 300\mu$m will be relatively less affected by the eddy.

It should be noted that the critical parameter $\Gamma = 2$ represents the minimum value of Γ required for depositing particles to become trapped within interstitial eddies. Clearly, the proportion of depositing particles that become trapped will increase as Γ increases. In this respect, Shibiyama and Horikawa (1980) found that trapping of sand grains in vortices induced by sand-ripples required a minimum value of $\Gamma = 8$, while all grains were observed to be trapped when $\Gamma \approx 13$. Their results also highlight a significant increase in the minimum Γ value required for flow-separation vortices to entrain and trap sand particles when they are initially at rest on the bed surface. This feature is discussed further in §7.5 below.

7.5 Implications for Entrainment in Graded Sediment

Experiments in the current study were predominantly conducted under static bed conditions in which the surface bed pores essentially remained clean from depositing fine sediments. This was partly due to the large size ratio between the

framework and matrix-sized sediments (i.e. D_{50}/d_{50} ~ 28-70 for LA sand) allowing depositing particles to infiltrate below the surface bed layers to a position where they were protected from re-entrainment. These experimental bed conditions were assumed to represent open-work gravel beds with a low matrix content.

Situations can arise where a gravel bed becomes completely clogged with matrix-sized sediments [e.g. extended periods of low flow conditions: (i) summer flows; (ii) regulated river reaches]. This provides the opportunity for fine sediments trapped within surface interstices to be re-entrained and re-suspended by turbulence generated at the bed surface interface.

Research into graded sediment transport has often considered the mobility of different grain sizes in terms of empirical hiding functions (e.g. Einstein 1950, Parker 1990 and Sutherland 1991), which recognise that finer matrix particles within the bed can be 'sheltered' from entrainment in the lee of larger framework particles. By contrast, the larger protruding framework elements within the bed surface can be relatively easier to entrain into the flow. However, none of these hiding functions have as yet adequately addressed the complex physical mechanisms governing the interactions between graded particles and near-bed turbulent structure, which occur at the bed surface.

One area that has been neglected is the role played by channel bed pressure fluctuations in the entrainment of graded particles. These pressure fluctuations at a specific location within the bed will result from the passage of small and large-scale turbulent flow structures. These turbulence structures range from Kolmogorov microturbulent fluctuations, which scale with the viscous length $l = \nu/u_*$, up to macroturbulent asymmetric structures, which scale with the flow depth H (Figure 2.16 and 2.17, pp.30 and 31). Clearly included within this wide range of turbulence scales are the coherent vortices observed in Series 1C, which typically occupy 10-40% of the flow depth H and the smaller, related interstitial eddies observed in Series 1A.

Within the context of the current study, it would be profitable to determine which of these turbulent scales is most likely to be dominant in the entrainment of fine sediments sheltering in the surface interstices of a non-uniform gravel bed.

Consider the passage of a typical vortex-pair over a bed surface interstice in which fine particles are sheltered from the mean flow (Figure 7.14 overleaf). The passage of each vortex will induce pressure fluctuations at the bed surface, with the

vertical pressure difference resulting from the circulation velocity U_r within each vortex. From consideration of Bernoulli's equation, the maximum head difference resulting from this vertical pressure variation must be $\overline{U}_r^2/2g$, corresponding to a maximum dynamic pressure of $\rho\overline{U}_r^2/2$, where $\overline{U}_r$ is the mean vortex circulation velocity. If intergranular friction effects are ignored for the meantime, the vertical forces acting on the sheltered particles (forces due to dynamic pressure and submerged particle weight) should be in balance at the point of entrainment, i.e.

$$\frac{1}{2}\rho\overline{U}_r^2\frac{\pi}{4}d^2 = (\rho_s - \rho)g\frac{\pi}{6}d^3 \qquad \text{....(7.26)}$$

or $$\overline{U}_r = 1.15\sqrt{(S_s - 1)gd} \qquad \text{....(7.27)}$$

where $S_s = \rho_s/\rho$. Using equation 7.27, the mean vortex circulation velocities $\overline{U}_r$ required for the entrainment of LA sand particles range from 0.062ms^{-1} for the finest 181μm particles up to 0.10ms^{-1} for the coarsest 462.5μm particles. From Series 1C observations, the average vortex characteristics (R = 12.5mm, Ω_0 = 5.6 sec^{-1}) yield a mean vortex circulation velocity $\overline{U}_r$ ($=\Omega_0 R/2$) of 0.035ms^{-1}, which is markedly lower than the $\overline{U}_r$ values required for the entrainment of LA sand particles.

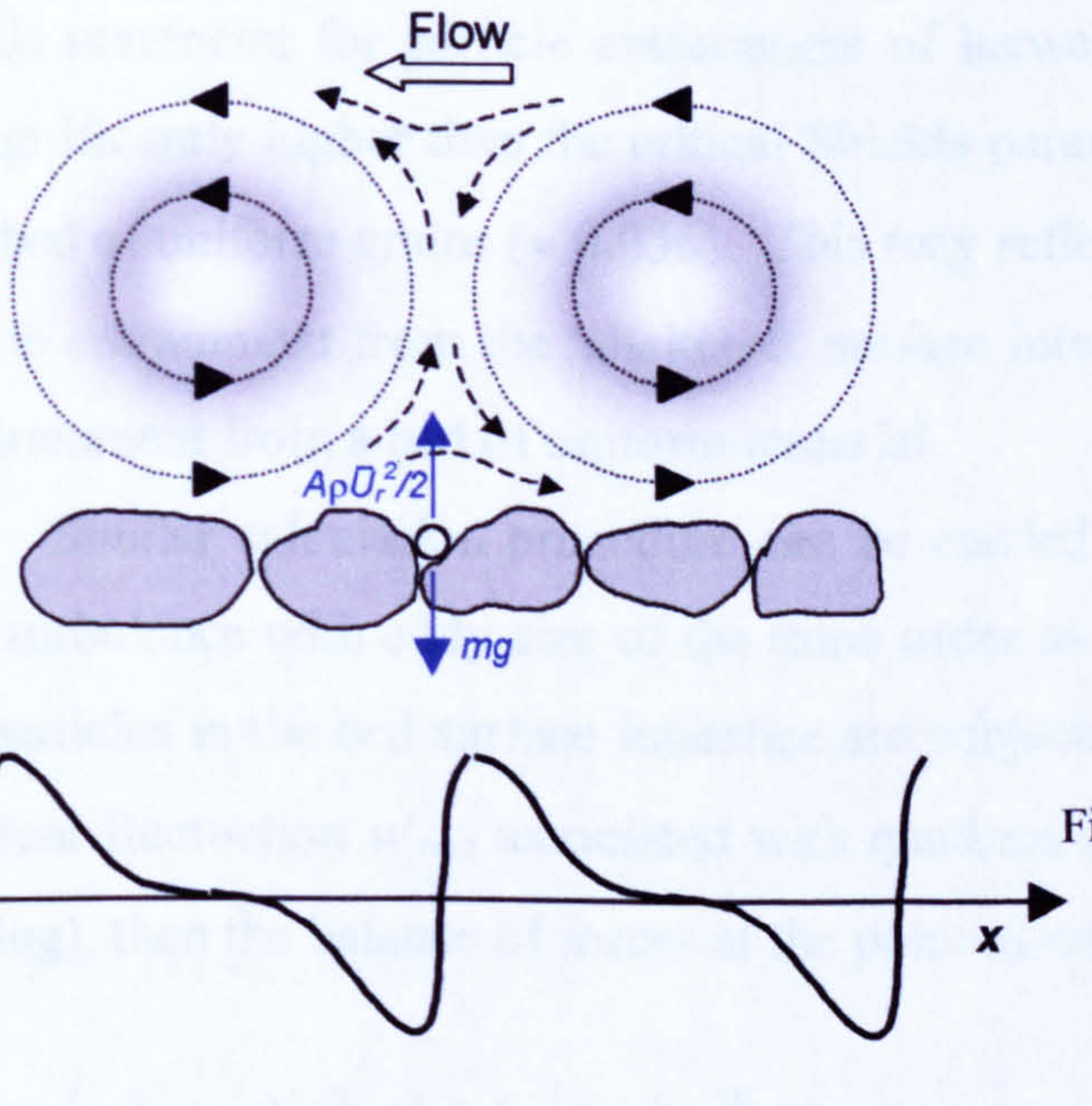

Figure 7.14 - Schematic representation of vortex pair passing over surface interstice containing fine sediment particles. Variation of associated pressure distribution also shown.

In order satisfy the threshold conditions for all size fractions to be entrained from the bed surface, $\overline{U}_r \geq 0.1$ms^{-1}, which corresponds to vortices with trapping parameters Γ ($= 4\overline{U}_r/w_s$) ranging from 19.9 for 181μm particles down to 6.7 for

462.5μm particles. These values are significantly higher that the critical Γ value of 2 required to trap depositing particles, in agreement with Shibiyama and Horikawa (1980), and illustrate that stronger vortices (i.e. larger $\Omega_0 R$) are required to entrain sediment particles from bed surface interstices than to trap depositing particles

In relation to the mean flow velocity $\overline{U}$, the mean vortex circulation velocity for the entrainment of LA sand particles varies between $\overline{U}_r = \overline{U}/5 \rightarrow \overline{U}/3$, hence

$$\overline{U} = 3.45\sqrt{(S_s - 1)gd} \rightarrow 5.75\sqrt{(S_s - 1)gd} \qquad \text{....(7.28)}$$

or expressed in terms of the shear velocity $u_* = \overline{U}\sqrt{f_b/8}$, where f_b is the Darcy-Weisbach bed friction factor, as

$$\frac{u_*}{\sqrt{(S_s - 1)gd}} = 3.45\sqrt{\frac{f_b}{8}} \rightarrow 5.75\sqrt{\frac{f_b}{8}} \qquad \text{....(7.29)}$$

or
$$\frac{u_*^2}{(S_s - 1)gd} = 1.49 f_b \rightarrow 4.13 f_b \qquad \text{....(7.30)}$$

The term on the left side of equation 7.30 is the Shields parameter. For the flow conditions in which the large scale vortices were observed (Series 1C), the Darcy-Weisbach friction factor for the bed f_b varied between 0.15 and 0.21, giving a critical Shields parameter for particle entrainment of between 0.22 and 0.87. These values are significantly higher than the critical Shields parameter for the initiation of motion for a bed of uniform grains (≈ 0.056). This may reflect the increased difficulty of fine particle entrainment from the 'sheltered' surface interstices of a gravel bed compared to entrainment from a bed of uniform material.

Similar calculation procedure can be carried out for higher frequency small-scale turbulence with eddy size of the same order as the fine particle diameter. If the fine particles in the bed surface interstice are subjected to a root-mean-square vertical turbulent fluctuation w'_{rms} associated with quadrant 2 'ejection' events (i.e. turbulent bursting), then the balance of forces at the point of entrainment is

$$\frac{1}{2}\rho(w'_{rms})^2 \frac{\pi}{4} d^2 = (\rho_s - \rho) g \frac{\pi}{6} d^3 \qquad \text{....(7.31)}$$

or
$$\frac{w'_{rms}}{\sqrt{(S_s - 1)gd}} = 1.15 \qquad \text{....(7.32)}$$

The value of w'_{rms} near the bed surface ($z/H = 0.05$) for ejection events was shown in Figure 7.6 (pp.215) was estimated to be 0.04ms^{-1}. In terms of shear velocity, $w' \sim 0.8u_*$, which incidentally is equivalent to the sediment suspension criterion proposed by Engelund and Fredsøe (1982) (§7.2.4.3, pp.210). Substituting this criterion into equation 7.32 yields,

$$\frac{u_*^2}{(S_s - 1)gd} = 2.07 \qquad \text{....(7.33)}$$

This value of 2.07 is significantly in excess of the critical Shields parameter for the initiation of particle motion on a uniform bed (~0.056) and is clearly higher than the range of Shields parameters estimated for the 'rolling vortex' mechanism (0.22-0.87). This suggests that particle entrainment from the bed surface interstices is more likely to result from the passing of large-scale vortices than through small-scale turbulence.

Finally, a third possible mechanism for particle entrainment for bed surface interstices is considered. Several authors (e.g. Klaven and Kopaliani 1973; Shvidchenko and Pender 2001) have identified the existence of large asymmetric flow structures that typically occupy the full flow depth H and extend between 4-5H on average in the streamwise direction of an open channel flow (Figure 2.17, pp.31). These structures have an associated upwelling mechanism on the upstream side (equivalent to a fluid ejection) and downwelling mechanism on the downstream side (equivalent to a fluid inrush). Shvidchenko (1999) revealed from quadrant analysis that the passage of structures, which had an average period of 0.4sec, is most likely to be responsible for the initiation of particle motion within a bed of graded sediment. While no observations of these large-scale asymmetric flow structures were made during the current study, it seems reasonable to assume that the rolling mechanism associated with their streamwise motion will have a similar influence on particle entrainment as the smaller coherent vortices observed in Series 1C.

It therefore appears that the passage of large flow structures and their associated pressure fluctuations is the most likely mechanism to result in the entrainment of fine sediment particles from the surface interstices of a gravel bed. The magnitude of these pressure fluctuations is shown to scale with the mean circulation velocity within the passing vortices, while their period ($1/f$) can be expected to scale with the Strouhal number S for vortex shedding and with outer flow variables H and U_{max}, in the form $H/(SU_{max})$.

7.6 Critical Reflection

The transport of fine to medium grade sands in turbulent open channel shear flow and their subsequent deposition into hydraulically rough, porous beds have been investigated experimentally using both visualisation techniques and concentration/ deposition measurements. Many common attributes were revealed relating the quantitative results obtained by each of these two distinct experimental methods. In particular, the magnitude of particle fall velocities in turbulent flow conditions (w'_s) were found to be primarily influenced by the grain size d_i and relative depth z/H. Both series of experiments also revealed the importance of parameter w_* (= w_s/u_*), which defines the relative influence of gravity and turbulence on vertical particle motion (Hoyal et al. 1995).

For the majority of experimental conditions and particle sizes d_i tested, w_* values were found to lie within a transitional region ($0.1 \leq w_* \leq 1$) between gravity-dominated and turbulence-dominated transport. Within this region, depth-averaged values of the non-dimensional fall velocity ratio $\langle w'_s \rangle / w_s$ were shown to be typically enhanced (i.e. $\langle w'_s \rangle / w_s > 1$) and increased with reducing values of w_*. Coarser LA particles (> ~400μm, $w_* \rightarrow 1$) were relatively unaffected by turbulence and appeared to settle primarily under the influence of gravity, with $\langle w'_s \rangle / w_s \sim 1$. Both findings were in general agreement with the numerical study of sediment deposition conducted by Hoyal et al. (1995) and by experimental data provided by Jobson and Sayre (1970).

However, a discrepancy appears to exist between numerical and experimental results for small, light particles with $w_* < 0.1$ (i.e. Stokes range), where particle transport is completely dominated by turbulence. In specifying a fully absorbent bed boundary condition, Hoyal et al. (1995) suggested that w'_s/w_s values would reach 10^1 or 10^2 (i.e. highly enhanced) as $w_* << 0.1$. However, while experimental results clearly show the existence of turbulence-enhanced fall velocities under specific experimental conditions, a genuine physical mechanism that would result in w'_s/w_s values approaching 10^2 is not apparent.

Considering the bed boundary in isolation, Series 1A observations suggested that not all particles were immediately deposited on reaching the bed surface, with the bed elements themselves and turbulence generated within bed surface interstices often acting as a physical barrier to particle deposition. The resulting probability of

deposition p was found to be lower than unity for all LA sand fractions ($p_{max} \sim 0.8$), reducing further with decreasing particle size d_i or increasing shear velocity u_* conditions. If it is considered that a grain of size d_i can equally be represented by its still water fall velocity w_{si}, then clearly the probability of deposition p will decrease as w_{si}/u_* (i.e. w_*) decreases. Furthermore, as a lower limit to particle deposition characteristics, neutrally buoyant particles (i.e. $w_s = w_* = 0$) by definition should have no tendency to deposit (i.e. $p = 0$), irrespective of the bed boundary condition. This suggests that the specification of fully absorbing boundary conditions (i.e. $p = 1$) within numerical studies of sediment deposition may be highly unrealistic, especially for small w_* values.

It is acknowledged that the porous 'open-work' bed conditions used in the current study and the large relative size of bed materials compared to fine sands (D/d) still provide an ideal environment in which the majority of particles can readily deposit into subsurface bed layers where they become protected from re-entrainment. Under static bed conditions, the absence of sediment deposits within the bed surface interstices therefore suppresses the amount of fine sediment that can be re-entrained back into the flow [i.e. through surface winnowing processes (e.g. Diplas and Parker, 1992)]. The resulting imbalance between deposition and entrainment should therefore result in a greater number of particles with downward motions as opposed to upward motions, especially within the near-bed flow and at the bed surface interface. This effect will have clear implications for the observed vertical particle motion and would appear to be, at least in part, responsible for the enhanced fall velocities observed in the near-bed flow (i.e. $w'_s/w_s > 1$). This is consistent with results obtained from an experiment conducted over a single layer of bed elements supported on an impermeable layer (S1B_EX3). Here, the near-bed values of w'_s/w_s were generally reduced (but remained enhanced) compared to similar w'_s/w_s values obtained over fully porous bed conditions. Clearly, further experiments conducted over different bed conditions would be required in order to assess the full extent of this influence.

The unequivocal influence that turbulence has on particle fall velocity w'_s was further reinforced by the evident similarities between distributions of non-dimensional fall velocity $\langle w'_s/u_* \rangle$ and vertical turbulence intensity w'_{rms}/u_* with relative depth z/H. In particular, the largest values of $\langle w'_s/u_* \rangle$ (about 1.2-1.4) and w'_{rms}/u_* (~ 0.7) were found to approximately coincide in the near-bed flow region ($z/H \leq 0.2$), while

generally decreasing with increasing *z/H*. However, suspension criteria based on the balance between still water fall velocity w_s and the root-mean-square of turbulent fluctuations w'_{rms} (e.g. Bagnold 1966) suggest that particles should remain in suspension while $w_s < w'_{rms} \approx 0.8u_*$ (Engelund and Fredsøe, 1982). An apparent contradiction therefore arises between these suspension criteria and the fact that particle fall velocities are often significantly enhanced in regions of highest turbulence intensity. This would apparently imply that the vast majority of particles must therefore be transported in downward fluid motions towards the bed surface, and again, may be partly attributed to the imbalance between deposition and entrainment resulting from the porous bed conditions.

A quadrant analysis technique was applied to individual pairs of velocity fluctuations (u' and w') obtained by the ADV probe at four elevations (z/H = 0.05, 0.15, 0.25 and 0.45). This analysis revealed that *inrush* events towards the bed (i.e. quadrant 4: $u' > 0$; $w' < 0$) had a higher contribution to Reynolds stress in the near-bed flow region, while *ejection* events away from the be surface (quadrant 2: $u' < 0$; $w' > 0$) became more dominant outwith the near-bed flow with increasing *z/H*. This finding implies that the larger particle fall velocities occurring in the near-bed flow region may also be associated with dominant fluid inrushes towards the bed, while the progressive reduction in particle fall velocities with increasing *z/H* may be associated with the increasing dominance of outward fluid ejections away from the bed surface. Applying a similar quadrant technique to analyse individual pairs of particle fluctuations (u'_{si} and w''_{si}) indeed revealed that larger streamwise particle velocities ($u'_{si} > 0$) were generally associated with larger particle fall velocities ($w''_{si} > 0$), especially within the near-bed flow. Particle ejection events ($u'_{si} < 0$, $w''_{si} < 0$) were again shown to be more dominant in the outer flow. Profiles of conditionally averaged particle velocities also revealed that $w'_s \sim 0$ for particle ejection events, consistent with a suspension or trapping mechanism within the turbulent flow, while $w'_s > w_s$ for particle inrush events suggested that vertical particle motion is enhanced through a *sweeping* mechanism.

The suspension of sediment particles by fluid ejection events associated with the quasi-cyclic turbulent bursting process formed the basis on which Cao et al. (1996) developed a heuristic diffusion model for suspended sediments. This model was based on the assumption that vertical transfer coefficients of fluid and sediment

particles (ε_f and ε_{sz}) could be described by their Lagrangian time scales (T_{LS} and T_{LF}) and *rms* values of vertical fluid and particle fluctuations [w'_{rms} and $\sigma(w'_s/u_*)$]. A modified version of this model, incorporating the observed association between w'_s/u_* and $\sigma(w'_s/u_*)$ profiles, allowed ε_{sz} to be expressed in terms of particle fall velocity w'_s and the turbulent bursting duration T_D. The model was shown to replicate the downward skew shown in the distributions of non-dimensional transfer coefficient ε_{sz}/Hu_* obtained for finer LA sand fractions (Series 2), with maximum values of ε_{sz}/Hu_* occurring at z/H = 0.3. However, it was acknowledged that improved knowledge of time scales associated with the large-scale turbulent structures generated over hydraulically rough, porous bed conditions is clearly required.

The development of the moving camera system employed in Series 1C proved extremely fruitful in providing good qualitative evidence of large-scale vortex structures generated within the open channel shear flow above the porous gravel bed conditions. Additionally, the typical interactions observed between LA sand particles and these structures provided a basis on which to develop a kinematic description of particle motion within the open-channel flow. In particular, the limited interaction observed between large-scale vortices and coarser LA particles is clearly consistent with the vertical particle motions being dominated by gravity (i.e. $w'_s/w_s \sim 1$), as was previously indicated by experimental results. By contrast, the tendency for finer LA particles to be transported on preferred paths around the top periphery and into steep trajectories on the downflow side of the vortex structures suggested that large-scale turbulent structure has a more significant role in the vertical motion of finer particles.

Development and application of a simple Rankine vortex model revealed that vertical particle velocities on preferred paths were enhanced by up to 60% [i.e. $w'_s/w_s \sim 1.60$] for the finest 181μm particles using the average vortex characteristics (Ω_0 and R) observed in Series 1C. This level of enhancement shows reasonable quantitative agreement with (i) near-bed values of w'_s/w_s obtained during the current experimental studies, (ii) experimental data from Jobson and Sayre (1970) and (iii) direct numerical simulations conducted by Wang and Maxey (1993).

Further application of the Rankine vortex model revealed that the tendency for sediment particles to be transported in enhanced downflow trajectories was dependent on a trapping parameter Γ and the associated relative trapping width X/R. The trapping parameter Γ was based on the assumption that particle trapping within a

vortex is only possible if the maximum vertical flow velocity within the vortex ($\Omega_0 R/2$) exceeds the terminal particle fall velocity w_s, the value of Γ being determined by the ratio of the two quantities. For $\Gamma < 1$, it was demonstrated that particles cannot become trapped within vortices and their vertical motion will becoming increasingly dominated by gravity as $\Gamma \rightarrow 0$ (i.e. heavy particles or weak vortices). However, for $\Gamma > 1$, the relative width of the trapping region X/R was shown to increase (linearly with Γ when $\Gamma > \sim 2$) and increasing numbers of particles were predicted to accumulate in peripheral orbits outwith the trapping region on the downflow side of the vortex. An analytical equation was developed to predict the maximum downward velocity $w'_{s,max}$ of these particles (i.e. on crossing the negative x/R axis). This equation was obtained by modifying Cheng's (1997) equation for the still water fall velocity w_s to account for the vortex characteristics (Ω_0 and R) and the particle position relative to the centre of rotation ($\alpha_r = x/R$). The equation predicted that the largest enhancements in vertical particle velocity w'_s/w_s occur for finer particles accumulated in peripheral orbits immediately outwith the trapping region, while reducing with increasing distance from the centre of rotation α_r and particle size d_i, although remaining enhanced throughout ($w'_s/w_s > 1$). Overall, the analytical consideration of typical particle-vortex interactions observed during Series 1C suggests that a mechanism similar to *preferential sweeping* (Wang and Maxey, 1993), whereby the majority of particles are transported in downward flow, will result in particle fall velocities which exceed those in still water conditions.

It was apparent from Series 1A observations that similar particle-fluid interactions also occur at the bed surface between depositing fine LA sand particles and eddies generated within surface interstices as a result of flow separation. An analytical interpretation of these interactions using the trapping parameter Γ provided an indication of the interstitial eddy characteristics (Ω_0 and R) required to trap depositing LA particles. The critical value of Γ for trapping depositing particles was also shown to be significantly lower than the minimum trapping parameter Γ required to entrain particles that are initially at rest on a rippled sand bed (i.e. Shibiyama and Horikawa, 1980). This indicated that significantly stronger interstitial vorticity (i.e. larger Γ values) would be required in order to entrain LA particles that were trapped within surface interstices.

The implications for fine sediment entrainment from surface interstices of a static gravel bed were considered in terms of the dynamic pressure fluctuation exerted on the bed surface resulting from the passage of large-scale vortices. Analytical consideration of the main force-balance at the point of entrainment indicated that this 'rolling vortex' mechanism is more likely to be responsible for particle entrainment than forces exerted on the particles by small-scale microturbulent fluctuations. Both mechanisms were noted to predict ranges of critical Shields parameters that were well in excess of that required the initiation of particle motion on a flat bed of uniform material (~ 0.056), indicating the increased levels of turbulence required to entrain 'sheltered' fine particles from the interstices of larger framework bed particles.

CHAPTER 8

Conclusions

8.1 Summary of Main Experimental Findings

The influx of natural or anthropogenic-derived fine sediments into a gravel bed river can have significant detrimental consequences for the river environment and aquatic species therein. Improved understanding of the processes controlling the transport and eventual fate of these fine sediments within the turbulent flow environment, provided by a gravel bed river, is therefore essential in assessing their ecological impact on the river.

Interactions between fluid turbulence and fine sediment particles are generally acknowledged to feature predominantly in all sedimentation processes occurring either within the main body of flow or at the bed surface interface of a gravel bed river. However, the physical mechanisms underpinning these interactions are known to be complex and remain poorly researched and understood. Consequently, various assumptions, often based on empiricism, have been adopted in the past to describe the transport and subsequent deposition of fine sediments mathematically.

Two distinct series of experiments (Series 1 and 2) were conducted in separate flume facilities to investigate the motion of fine to medium sand particles within turbulent shear flows generated over hydraulically rough, porous bed conditions and study their subsequent deposition characteristics within the surface layers of the bed. Series 1A was conducted as a set of preliminary visualisation experiments aimed at recording and analysing LA sand particle trajectories in the near-bed flow region ($z/H < 0.2$) and their typical interactions at the bed surface interface. The main findings from these experiments are re-iterated overleaf:

- Streamwise particle velocities in the near-bed flow are generally lower than that of the surrounding fluid. Corresponding particle fall velocities are generally higher than the fall velocity measured in still water (i.e. *enhanced*) and increase with particle Reynolds number R_{e*p}.

- The non-dimensional fall velocity ratio w'_{si}/w_{si} increases with reducing particle size d_i, with the enhancement in near-bed turbulent fall velocities highest for the finer particle fractions (up to ~70%) and negligible for the coarsest particles (i.e. $w'_{si}/w_{si} \sim 1$).

- Settling particles are observed to exhibit typical modes of behaviour on reaching the surface layer of the porous bed, which results in their subsequent deposition or re-entrainment back into the near-bed flow:

  (a) Particle ricochet off exposed upstream faces of individual bed element leading to re-entrainment.
  (b) Particle interaction with eddies forming within the surface interstices of the bed leading to deposition or trapping and re-entrainment.
  (c) Particle sheltering in the lee of bed elements prior to deposition
  (d) Turbulent pulses/fluctuations enhancing or inhibiting particle deposition.

- The probability of deposition p, estimated from observed particle behaviour at the bed surface, is shown to increase with increasing particle size d_i and for lower shear velocity u_* conditions.

- Deposition velocities w_{di}, estimated from depositing particle trajectories, were enhanced (i.e. w_{di}/w_{si} up to 1.25) for finer LA particles (<300μm), while coarser particles (>300μm) were generally hindered (i.e. w_{di}/w_{si} down to 0.8).

Series 1B experiments were developed in order to obtain reliable quantitative measurements of LA sand particle motions within the turbulent shear flow conditions generated above the porous bed, using a sophisticated high-speed camera and a particle tracking technique to record and analyse particle trajectories. The main experimental conclusions are detailed overleaf:

- Non-dimensional streamwise particle velocities u_s/u_* typically lie within ± one standard deviation of the local mean streamwise flow velocity [i.e. $(U \pm u'_{rms})/u_*$].
- Turbulent fall velocities w'_{si} generally increase with particle size d_i before stabilising for the coarser particle sizes (i.e. above ~390μm).
- Vertical distributions of non-dimensional particle fall velocity w'_s/u_* and its standard deviation $\sigma(w'_s/u_*)$ display similar characteristics to distributions of turbulence intensity (u'_{rms}/u_* and w'_{rms}/u_*), with maximum values often occurring in the near-bed flow and generally decreasing with increasing z/H.
- The non-dimensional fall velocity ratio w'_{si}/w_{si} is also highest in the near-bed flow ($z/H < 0.2$), where experiment-averaged $\langle w'_{si} \rangle / w_{si}$ values approach ~2.0 for the finest particles (i.e. *enhanced*), reducing with increasing particle size d_i to ~1.0 for the coarsest particles.
- Within the intermediate flow ($0.2 < z/H < 0.5$) and outer flow ($z/H > 0.5$) regions, $\langle w'_{si} \rangle / w_{si}$ values have a similar dependence on particle size d_i, but reduce with increasing z/H, becoming generally hindered within the outer flow (i.e. $\langle w'_{si} \rangle / w_{si} < 1$).
- The influence of both shear velocity u_* and bed material type are inconclusive. However, measurements taken over a single layer of bed elements supported on an impermeable layer suggest that w'_{si}/w_{si} values reduce in the near-bed flow over this configuration, while generally remaining enhanced.

Series 1C experiments were principally designed to provide a mainly qualitative description of (a) the turbulent flow structure generated within the open channel shear flow over a porous bed of well-sorted gravel and (b) the fluid-particle interactions existing between the large-scale flow structure and the transported LA sand particles. The main observations from Series 1C are re-emphasised below:

- Large-scale coherent vortices occurring individually or in pairs with the same rotational sense are identified to exist, primarily within the lower flow region ($z/H < 0.5$), typically occupying between $0.1H$ - $0.4H$. These appear to rise

and expand outward from the bed surface before being dissipated in higher momentum outer flow.

- Smaller vortices are also observed to develop along a shear layer inclined at ~20° to the bed surface, which form as a result of the interaction between low-momentum fluid expanding away from the near-bed region and deflected higher-momentum outer flow.
- The structure of near-surface flow is less apparent, but appears to indicate weaker fluid rotations in the opposite sense to the large-scale vortices closer to the bed. These weaker motions appear to be intermittently broken up by expansions of low-momentum fluid into the outer flow.
- Interactions between transported LA sand particles and large-scale vortex structures appear to be determined by the vortex characteristics (Ω_0 and R) and the particle size d_i. In general, coarser LA particles have fewer interactions with vortices, settling primarily under the influence of gravity.
- Finer LA particles, approaching a vortex on the upstream side and from above, are generally transported in peripheral orbits around the top and on the downflow side of the vortex. Particles in orbits closer to the vortex core have a greater tendency to become trapped in quasi-closed orbits, while the majority of particles are shed beneath the vortex core from more peripheral orbits.
- A simple numerical model developed to predict particle trajectories within a Rankine vortex indicates good agreement with the above experimental observations of particle-vortex interactions. It also demonstrates that particles in peripheral orbits can experience enhanced fall velocities (i.e. $w'_s/w_s > 1$), while particles close to the vortex core can have hindered fall velocities (i.e. $w'_s/w_s < 1$) as a result of vortex trapping.

A further series of experiments (Series 2) was conducted in a larger flume facility employing non-visual measurement techniques to investigate the transport of fine to medium sands (DB and LA grades) in turbulent open channel flow and their deposition into porous gravel beds. One of the aims of these experiments was to provide independent validation of the main findings obtained through the visualisation techniques employed Series 1. The main results from Series 2 indicated that:

- The longitudinal deposition of LA sand is well-represented by a log-normal distribution, while DB sand appears to be more uniformly deposited along the flume due to the re-circulation of finer size fractions.

- Experiment- and depth-averaged turbulent fall velocities $< \tilde{w}'_{si} >$, calculated from mean flow characteristics and median deposition lengths $\tilde{L}$, generally increase with particle size d_i for both sand grades. Corresponding non-dimensional fall velocity ratios $< \tilde{w}'_{si} > / w_{si}$ increase with reducing d_i from around unity for 462.5μm LA sand particles up to about 1.6 for 98μm DB sand particles.

- No consistent trend is observed regarding the influence of shear velocity u_* on $\tilde{w}'_{si}/w_{si}$ values. However, larger flow Reynolds numbers R_e and lower sediment input rates I_R appear to increase $\tilde{w}'_{si}/w_{si}$ values for all LA sand fractions.

- Vertical distributions of non-dimensional particle fall velocities w'_s/u_*, calculated from the solution of a normalised and integrated sediment transfer equation, display similar characteristics to the w'_s/u_* profiles measured during Series 1B (described above).

- Corresponding w'_{si}/w_{si} values also reveal similarities with Series 1B results; with generally enhanced fall velocities (i.e. $w'_{si}/w_{si} > 1.0$) again observed in the near-bed and intermediate flow regions ($z/H \leq 0.5$). However, the influence of particle size d_i is less apparent in Series 2, especially within the near-bed flow, where one data set suggests w'_{si}/w_{si} values decrease as d_i decreases, in contradiction to the findings in Series 1B.

- Profiles of the non-dimensional sediment transfer coefficient ε_{szi}/Hu_* with z/H, also obtained from the normalised, integrated sediment transfer equation, reveal distributions for finer LA sand particles to be skewed towards the lower half of the flow ($z/H < 0.5$). This represents a significant departure from the commonly applied parabolic or parabolic-constant models for ε_{sz}.

- In agreement with previous studies (e.g. Carling 1984, Peloutier 1998), overall and local deposition rates (Δ_0 and Δ_b) are noted to be linearly dependent on initial and near-bed sediment concentrations (C_0 and C_b), respectively.

- Experimental-averaged deposition velocities $\langle w_{di} \rangle$ generally increase with grain size d_i for DB sand fractions and fine to intermediate LA sand fractions (i.e. <350μm). However, for coarser LA sand fractions, $\langle w_{di} \rangle$ values are predicted to stabilise or even slightly reduce.

- For experiments with LA sand, the non-dimensional deposition velocity ratio $\langle w_{di} \rangle / w_{si}$ is enhanced (by up to 40%) for intermediate fractions (250μm ≤ d_i ≤ 390μm) and hindered for the coarsest and finest fractions. For the finer DB grade sand, $\langle w_{di} \rangle / w_{si}$ values are generally hindered.

- Fraction-averaged w_d/w_s values generally increase with decreasing shear velocity u_* and appear to be enhanced when $u_* < \sim 0.06 ms^{-1}$. The influence of u_* on w_{di}/w_{si} values for individual LA sand fractions is less defined, with little difference observed in values for $d_i < \sim 330 \mu m$ (for $u_* = 0.048–0.066 ms^{-1}$).

- The sediment input rate I_R appears to have no direct influence on w_{di}/w_{si} values over the experimental range considered.

- Finer bed gravel generally yields higher w_{di}/w_{si} values for LA sand particles, while the presence of substrate material tends to hinder the deposition of LA sand in comparison to experiments where the underlying traps were empty.

Discussion, analysis and critical reflection raised a number of important observations and issues pertaining to the experimental results, some of which remain as yet unresolved:

- Calculated values of w_* (= w_s/u_*) reveal that most particle sizes d_i tested reside within a transitional region ($0.1 \leq w_* \leq 1.0$) where particle motion is expected to be influenced by both gravity and turbulence. In agreement with Hoyal et al. (1995), coarser particles with $w_* \rightarrow 1$ tend to settle primarily under gravity, while finer particles with $w_* \rightarrow 0.1$ are enhanced by the turbulence. However, it is acknowledged that much of the enhanced deposition predicted by Hoyal et al. (1995) is accredited to the authors' use of fully absorbent bed boundary conditions (Wallis and Moores, 1996), which are shown to be unrealistic for small w_* values. This hypothesis of enhanced settling/deposition clearly

requires to be tested for a wider range of particle sizes d_i (i.e. silt – coarse sand) and hydraulic conditions (i.e. increased shear velocity u_* range).

- The porous nature of the bed conditions considered in this study provides a suitable environment for the deposition and infiltration of fine sediments, whilst suppressing particle entrainment from the bed. In this net deposition situation, the vertical transfer of particles will clearly be skewed by the dominance of downward motions towards the bed (i.e. deposition). This may account at least in part for the enhanced fall velocities observed during the experiments and requires further investigation for different bed conditions (e.g. silted gravel beds).

- Equivalence between turbulent fluid and particle motions is demonstrated through quadrant analysis. In the near-bed flow, the greater number of inrush events observed is consistent with particles being transported towards the bed in enhanced fluid 'sweeping' motions (i.e. resulting in higher fall velocities). At greater elevations within the flow, the increasing dominance of ejection events is also consistent with the suspension or trapping of particles within ejected fluid (i.e. resulting in lower fall velocities).

- The particle motions described above can clearly be associated with the observed interactions between sand particles and large-scale coherent vortices, recorded by the moving camera system. Particles accumulated and transported in peripheral paths on the downflow side of the vortex have enhanced vertical velocities towards the bed, while particles remaining in orbit around the vortex core are trapped and transported downstream in suspension (i.e. $w'_s \rightarrow 0$). In general a greater number of particles are observed to travel on the downflow side as a result of '*preferential sweeping*'. This mechanism therefore appears to be responsible to some degree for the enhanced particle fall velocities observed in the flow region $z/H < 0.5$, where large-scale vortices are most prominent. More detailed quantitative analysis of the large-scale turbulent flow structure and the resulting particle-fluid interactions should provide improved knowledge of this *'preferential sweeping'* mechanism and the range of experimental conditions under which it occurs.

- Application of a simple Rankine vortex model reveals that the tendency for particle to be transported in enhanced downflow trajectories is dependent on the magnitude of the trapping parameter Γ and associated relative trapping width X/R, both of which are dependent on particle size d_i (through w_{si}) and vortex characteristics (Ω_0 and R).

- Particle trapping is also shown to be an important mechanism at the bed surface, where interactions between depositing particles and flow-separation eddies forming within surface interstices can result in particles being trapped and re-entrained back into the flow. In this situation, the trapping parameter Γ may be modified to assess proportion of particles likely to be re-suspended by specific vortex characteristics occurring at the bed surface.

- Analytical consideration of mechanisms responsible for the entrainment of fine sediments 'sheltered' within bed surface interstices suggest that dynamic pressure fluctuations exerted by the passage of the large-scale vortices are more likely to result in particle entrainment than forces exerted by small-scale microturbulence.

In summary, the particle-turbulence interactions resulting in '*preferential sweeping*' on the downflow size of large-scale vortices, coupled with the porous open-work bed conditions appear to be the dominant mechanisms responsible for enhanced particle fall velocities observed within turbulent open channel shear flows. Particle-vortex interactions are also shown to have important implications for the deposition and entrainment of fine sediment within surface interstices of a porous bed.

8.2 Limitations and Potential Areas of Future Study

The current investigation has provided a basis on which further, more extensive experimental studies of particle motion within turbulent open channel flow can be conducted. A larger range of flow conditions (H and u_*) and fine sediment sizes d_i should be tested in order to improve knowledge of the range of experimental conditions under which turbulence-enhanced particle fall velocities are obtained. A wider range of sediment concentrations C is also required to assess how higher concentrations, in particular, affect the turbulent flow structure (i.e. turbulence

damping) and the resulting characteristics of particle-fluid interactions. Further experiments should also consider the influence of the bed boundary condition (e.g. roughness, porosity, matrix content, bedforms, etc.) to assess their relative contribution to enhanced settling/deposition processes.

It may also be desirable to conduct further experiments in a larger test facility. The limitations provided by the 5-6m working length within the Armfield S5-10 flume restricted the range of hydraulic conditions and particle sizes that would ensure particle deposition occurred within the working section of the flume. Additionally, a longer working section (say >10m) would also provide sufficient length in which fully developed flow conditions could be assured, while an increased channel width would also permit larger flow aspect ratios, ensuring two-dimensional flow conditions were formed at the centre of the channel.

The visualisation techniques employed within Series 1 were successful in obtaining both good quality quantitative data and qualitative descriptions of particle motion in relation to the surrounding fluid. However, time constraints on the use of camera equipment, coupled with the lack of a reliable algorithm to perform automated particle tracking analysis of the data, again limited the range of experimental conditions and particle sizes tested using these techniques.

The application of more sophisticated visualisation techniques such as *particle tracking velocimetry* (PTV) or *particle image velocimetry* (PIV), which are extensively employed in the field of experimental fluid mechanics, could represent an improved approach for studying fine sediment motions within turbulent flows. The PTV and PIV techniques would themselves also provide greater resolution on the mean and turbulent characteristics within the recorded flow field, which could be used to generate instantaneous vector plots or contour maps of flow velocity and vorticity. These could feasibly be compared with the observed distributions of sediment particles within the recorded flow field, allowing quantitative aspects of particle-vortex interactions, and the '*preferential sweeping*' mechanism in particular, to be investigated in greater detail.

References

Alonso, C.V. 1981, 'Stochastic Models of Suspended Sediment Dispersion', *Journal of the Hydraulics Division*, ASCE, Vol. 107, No. HY6, pp. 733-756.

Ashworth, P.J. and Ferguson, R.I. 1989, 'Size Selective Entrainment of Bed Load in Gravel Bed Streams', *Water Resources Research*, Vol. 25, No. 4, pp. 627-634.

Bagnold, R.A. 1966, 'An Approach to the Sediment Transport Problem for General Physics', *Geological Survey Paper 422-I*, Washington, D.C.]

Bayazit, M. 1976, 'Free surface flow in a channel of large relative roughness', *Journal of Hydraulic Research,* IAHR, Vol. 14, pp. 115-126.

Bechteler, W. and Färber, K. 1985, 'Stochastic Model of Suspended Solid Dispersion', *Journal of Hydraulic Engineering*, ASCE, Vol. 111, No. 1, pp. 64-78.

Bennett, S.J., Bridge, J.S. and Best, J.L. 1998, 'Fluid and sediment dynamics of upper stage plane beds', *Journal of Geophysical Research*, Vol. 103, No. C1, pp.1239-1274.

Beschta, R.L. and Jackson, W.L. 1979, 'The Intrusion of Fine Sediments into a Stable Gravel Bed', *Journal of the Fisheries Research Board*, Vol. 36, pp. 204-210.

Bridge, J.S. and Bennett, S.J. 1992, 'A Model for the Entrainment and Transport of Sediment Grains of Mixed Sizes, Shapes and Densities', *Water Resources Research*, Vol. 28, No. 2, pp. 337-363.

Camp, T.R. 1943, 'The effect of turbulence on retarded settling', *Proceedings of the 2nd Hydraulics Conference*, University of Iowa, Studies in Engineering, Bulletin 27, pp. 307-317.

Cantwell, B.J. 1981, 'Organized Motion in Turbulent Flow', *Annual Review of Fluid Mechanics*, Annual Reviews Inc., Vol. 13, pp. 457-515

Cao, Z., Zhang, X. and Xi, H. 1996, 'Turbulent bursting-based diffusion model for suspended sediment in open channel flows', *Journal of Hydraulic Research*, IAHR, Vol. 34, No. 4, pp. 457-472.

Cao, Z. 1997, 'Turbulent Bursting-Based Sediment Entrainment Function', *Journal of Hydraulic Engineering*, ASCE, Vol. 123, No. 3, pp. 233-236.

Carling, P.A. 1984, 'Deposition of Fine and Coarse Sand in an Open-Work Gravel Bed', *Canadian Journal of Fisheries and Aquatic Sciences*, Vol. 41, No. 2, pp. 263-270.

Carling, P.A. 1988, 'Channel Change and Sediment Transport in Regulated U.K. Rivers', *Regulated Rivers: Research and Management*, Vol. 2, pp. 369-387.

Celik, I. And Rodi, W.R. 1988, 'Modelling Suspended Sediment Transport in Nonequilibrium Situations', *Journal of Hydraulic Engineering*, ASCE, Vol. 114, No. 10, pp.1157-1191.

Cheng, N-S. 1997a, 'Simplified Settling Velocity Formula for Sediment Particle', *Journal of Hydraulic Engineering*, ASCE, Vol. 123, No. 2, pp. 149-152.

Cheng, N-S. 1997b, 'Effect of Concentration on Settling Velocity of Sediment Particles', *Journal of Hydraulic Engineering*, ASCE, Vol. 123, No. 8, pp. 728-731.

Clauser, F.H. 1956, 'The turbulent boundary layer', *Adv. Appl. Mech.*, 4, pp. 1-31.

Clifford, N.J. and French, J.R. 1993, ' Monitoring and Modelling Turbulent Flow: Historical and Contemporary Perspectives', in *Turbulence: Perspectives on Flow and Sediment Transport*, Clifford, N.J., French, J.R. and Hardisty, J. (eds.), John Wiley and Sons Ltd.

Coleman, N.L. 1970, 'Flume Studies of Sediment Transfer Coefficient', *Water Resources Research*, Vol. 6, No. 3.

Corino, E.R. and Brodkey, R.S. 1969, 'A visual investigation of the wall region in turbulent flow', *Journal of Fluid Mechanics*, Vol. 37, pp.1-30.

Defina, A. 1996, 'Transverse Spacing of Low-speed Streaks in a Channel Flow over a Rough Bed', in *Coherent Flow Structures in Open Channels*, Ashworth, P.J., Bennett, S.J., Best, J.L. and McLelland, S.J. (eds.), John Wiley and Sons Ltd, pp. 87-99.

Diplas, P. and Parker, G. 1992, 'Deposition and Removal of Fines in Gravel-Bed Streams', in *Dynamics of Gravel-Bed Rivers*, Billi, P., Hey, R.D., Thorne C.R. and Tacconi, P. (eds.), John Wiley & Sons Ltd., pp. 313-329.

Einstein, H.A. 1950, 'Bed-load function for sediment transport in open channels', *Technical Bulletin 1026*, US Department of Agriculture.

Einstein, H.A. 1968, 'Deposition of Suspended Particles in a Gravel Bed', *Journal of the Hydraulics Division*, ASCE, Vol. 94, No. HY5, pp. 1197-1205.

Engelund, F. and Hansen, E. 1967, 'A Monograph on Sediment Transport to Alluvial Streams', *Copenhagen: Teknik Vorlag.*

Engelund, F. and Fredsøe, J. 1982, 'Hydraulic theory of alluvial rivers', *Advances in Hydroscience*, Vol. 13, pp.187-215.

Frostick, L.E., Lucas, P.M. and Reid, I. 1984, 'The infiltration of fine matrices into coarse-grained alluvial sediments and its implications for stratigraphical interpretation', *Journal of the Geological Society of London*, Vol. 141, pp. 955-965.

Garcia, M. and Parker, G. 1991, 'Entrainment of Bed Sediment into Suspension', *Journal of Hydraulic Engineering,* ASCE, Vol. 117, No. 4, pp. 414-435.

Garcia, M., Niño, Y. and Lopez, F. 1996, 'Laboratory Observations of Particle Entrainment into Suspension by Turbulent Bursting', in *Coherent Flow Structures in Open Channels*, Ashworth, P.J., Bennett, S.J., Best, J.L. and McLelland, S.J. (eds.), John Wiley and Sons.

Garde, R.J. and Ranga Raju, K.G. 1977, 'Mechanics of Sediment Transportation and Alluvial Stream Problems', Wiley Eastern Ltd., New Delhi.

Gibbons, D.R. and Salo, E.O. 1973, 'An annotated bibliography of the effects of logging on fish of the western United States and Canada', *U.S. Department of Agriculture and Forestry*, General Technical Report PNW-10, 145pp.

Goldstein, S. 1929, 'The steady flow of viscous fluid past a fixed spherical obstacle at small Reynolds number', *Proceedings of the Royal Society of London*, Vol. 123A, pp. 225-235.

Grass, A.J. 1971, 'Structural features of turbulent flow over smooth and rough boundaries', *Journal of Fluid Mechanics*, Vol. 50, Part 2, pp. 233-255.

Grass, A.J. 1974, 'Transport of fine sand on a flat bed: turbulence and suspension mechanics', in *Euromech*, 48, pp. 33-34. Inst. Hydrodynamic and Hydraulic Engng. Tech. Univ. Denmark.

Grass, A.J. and Mansour-Tehrani, M. 1996, 'Generalised Scaling of Coherent Bursting Structures in the Near-wall Region of Turbulent Flow over Smooth and Rough Boundaries' in *Coherent Flow Structures in Open Channels*, Ashworth, P.J., Bennett, S.J., Best, J.L. and McLelland, S.J. (eds.), John Wiley and Sons Ltd, pp. 41-61.

Grass, A.J., Stuart, R.J. and Mansour-Tehrani, M. 1991, 'Vortical structures and coherent motion in turbulent flow over smooth and rough boundaries', *Philosophical Transactions of the Royal Society of London*, Vol. 336, pp. 35-65.

Gulliver, J.S. and Halverson, M.J. 1987, 'Measurements of large streamwise vortices in an open-channel flow', *Water Resources Research*, Vol. 23, No. 1, pp. 115.

Hey, R.D. 1979, 'Flow Resistance in Gravel-Bed Rivers', *Journal of the Hydraulics Division*, ASCE, No. HY4.

Hinze, J.O. 1959, 'Turbulence', McGraw-Hill.

Hinze, J.O. 1975, 'Turbulence (2nd Edition)', McGraw-Hill.

Ho, H-W. 1964, 'Fall Velocity of a Sphere in a Field of Oscillating Fluid', Ph.D. Thesis presented to the State University of Iowa, Iowa City.

Hoey, T.B. and Ferguson, R. 1994, 'Numerical simulation of downstream fining by selective transport in gravel bed rivers: Model development and illustration', *Water Resources Research*, Vol. 30, No. 7, pp. 2251-2260.

Hoyal, D.C.J.D., DePinto, J.V., Atkinson, J.F. and Taylor, S.W. 1995, 'The effect of turbulence on sediment deposition', *Journal of Hydraulic Research*, IAHR, Vol. 33, No. 3, pp. 349-360.

Iwamoto, R.N., Salo, E.O., Madej, M.A., McComas, R.L. and Rulifson, R.L. 1978, 'Sediment and Water Quality: a review of the literature including a suggested approach for water quality criteria with summary of workshop and conclusions and recommendations', U.S. Environmental Protection Agency, 910, 151pp.

Jobson, H.E. and Sayre, W.W. 1970a, 'Vertical Transfer in Open Channel Flow', *Journal of the Hydraulics Division*, ASCE, Vol. 96, No. HY3, pp. 703-724.

Jobson, H.E. and Sayre, W.W. 1970b, 'Predicting Concentration Profiles in Open Channels', *Journal of the Hydraulics Division,* ASCE, Vol. 96, No. HY10, pp. 1983-1996.

Julien, P.Y. 1995, 'Erosion and Sedimentation', Cambridge University Press.

Kaftori, D., Hetsroni, G. and Banerjee, S. 1995a, 'Particle behaviour in the turbulent boundary layer. I. Motion, deposition and entrainment', *Physics of Fluids*, Vol. 7, No. 5, pp. 1095-1106.

Kaftori, D., Hetsroni, G. and Banerjee, S. 1995b, 'Particle behaviour in the turbulent boundary layer. II. Velocity and distribution profiles', *Physics of Fluids*, Vol. 7, No. 5, pp. 1107-1121.

Kandala, A.S. 1966, 'Fall Velocity of Spheres in Open Channel Flow', Ph.D. Thesis presented to Colorado State University, Fort Collins.

Keulegan, G.H. 1938, 'Laws of Turbulent Flow in Open Channels', *J. Res.*, Nat. Bureau Stand., US Department of Commerce, 21, pp.707-741.

Kim, H.T., Kline, S.J. and Reynolds, W.C. 1971, 'The production of turbulence near a smooth wall in a turbulent boundary layer', *Journal of Fluid Mechanics*, Vol. 50, Part 1, pp. 133-160.

Kirkbride, A. 1993, 'Observations of the Influence of Bed Roughness on Turbulence Structure in Depth Limited Flows over Gravel Beds', in *Turbulence: Perspectives on Flow and Sediment Transport,* Clifford, N.J., French, J.R. and Hardisty, J. (eds.), John Wiley and Sons Ltd.

Kironoto, B.A. and Graf, W.H. 1994, 'Turbulence characteristics in rough uniform open-channel flow', *Proceedings of the Institution of Civil Engineers*, Water Maritime and Energy, Vol. 106 (12), pp. 333-344.

Klaven, A.B. and Kopaliani, Z.D. 1973, 'Laboratory study of kinematic structure of turbulent flow over rough beds', Trans. State Hyd. Inst., 209, pp. 67-90, Leningrad, USSR, (in Russian).

Kline, S.J., Reynolds, W.C., Schraub, F.A. and Runstadler, P.W. 1967, 'The structure of turbulent boundary layers', *Journal of Fluid Mechanics*, Vol. 3, Part 4, pp.741 - 773.

Krone, R.B. 1962, 'Flume Studies of the Transport of Sediment in Estuarial Shoaling Processes', *Final Report*, Hydraulic Engineering Laboratory, University of California, Berkeley.

Kuhnle, R.A. 1993, 'Incipient Motion of Sand-Gravel Sediment Mixtures', *Journal of Hydraulic Engineering*, Vol. 119, No. 12, pp. 1400-1415.

Laufer, J. 1954, 'The Structure of Turbulence in Fully Developed Pipe Flow', *NACA Technical Report 1174.*

Leopold, L.B., Wolman, M.G. and Miller, J.P. 1964, 'Fluvial Processes in Geomorphology', Freeman, San Francisco.

Lewis, W.K., Gilliland, E.R. and Bauer, W.C. 1949, 'Characteristics of Fluidized Particles', *Industrial Engineering Chem.*, Vol. 41, pp.1104-1114.

Li, R.M. and Shen, H.W. 1975, 'Solid Particle Settlement in Open Channel Flow', *Journal of the Hydraulics Division*, ASCE, Vol. 101, No. HY7, pp. 917-931.

Lisle, T.E. 1989, 'Sediment Transport and Resulting Deposition in Spawning Gravels, North Coastal California', *Water Resources Research*, Vol. 35, No. 6, pp. 1303-1319.

McCave, I.N. and Swift, S.A. 1976, ' A Physical Model for the Rate of Deposition of Fine-grained Sediments in the Deep Sea', *Geological Society of America* Bulletin 87, pp. 541-546.

McNown, J.S. and Lin, P.N. 1952, 'Sediment Concentration and Fall Velocity', *Proceedings, 2nd Midwest. Conf. Fluid Mech.*, pp. 401-411.

McQuivey, R.S. and Richardson, E.V. 1969, 'Some Turbulence Measurements in Open-Channel Flow', *Journal of the Hydraulics Division*, ASCE, Vol. 95, No. HY1, pp. 209-223.

Meland, N. and Norrman, J.O. 1969, 'Transport velocities of individual size fractions in heterogeneous bed load', *Geogr. Am. Ser.*, A51, pp. 127-144.

Milhous, R.T. 1973, 'Sediment Transport in a Gravel-Bottomed Stream', Ph.D. Thesis presented to Oregon State University, 232pp.

Muste, M. and Patel, V.C. 1997, 'Velocity profiles for particles and liquid in open-channel flow with suspended sediment', *Journal of Hydraulic Engineering*, ASCE, Vol. 123, No. 9, pp. 742-751.

Nielsen, P. 1984, 'On the Motion of Suspended Sand Particles', *Journal of Geophysical Research*, Vol. 89, No. C1, pp. 616-626.

Nezu, I. And Nakagawa, H. 1993, 'Turbulence in Open-Channel Flow', *International Association of Hydraulic Research (IAHR)*, Monograph Series, A.A. Balkema, Netherlands.

Nezu, I. and Rodi, W. 1985, 'Experimental study on secondary currents in open channel flow', *Proc. of 21st IAHR Congress*, Melbourne, Vol. 2, pp. 115-119.

Nezu, I. and Rodi, W. 1986, 'Open-channel Flow Measurements with a Laser Doppler Anemometer', *Journal of Hydraulic Engineering,* ASCE, Vol. 112, No. 5, pp. 335-355.

Niño, Y. and Garcia, M.H. 1996, 'Experiments on particle-turbulence interactions in the near-wall region of an open channel flow: implications for sediment transport', *Journal of Fluid Mechanics*, Vol. 326, pp. 285-319.

Novak, P. and Cabelka, J. 1981, 'Models in Hydraulic Engineering: Physical Principles and Design Applications', Pitman Advanced Publishing Program, London.

Nowell, A.R. and Church, M. 1979, 'Turbulent Flow in a Depth-Limited Boundary Layer', *Journal of Geophysical Research*, Vol. 84, No. C8, pp. 4816-4824.

Nychas, S.G., Hershey, H.C. and Brodkey, R.S. 1973, 'A visual study of turbulent shear flow', *Journal of Fluid Mechanics*, Vol. 61, pp. 513-540.

O'Brien, J.S. 1987, 'A Case Study of Minimum Streamflow for Fishery Habitat in the Yampa River', in *Sediment Transport in Gravel-bed Rivers*, Thorne, C.R., Bathurst, J.C. and Hey, R.D. (eds.), John Wiley & Sons Ltd, pp. 921-946.

Offen, G.R. and Kline, S.J. 1974, 'Combined dye-streak and hydrogen-bubble visualisation observations of a turbulent boundary layer', *Journal of Fluid Mechanics*, Vol. 62, Part 2, pp. 223-239.

Offen, G.R. and Kline, S.J. 1975, 'A proposed model of the bursting process in turbulent boundary layers', *Journal of Fluid Mechanics*, Vol. 70, Part 2, pp. 209-228.

Oseen, C.W. 1927, 'Neuere methoden und ergebnisse in der hydrodynamik', Akademische Verlagsgesellschaft, Leipzig, Germany.

Owen, M.W. 1969, 'Discussion of: Deposition of suspended particles in a gravel bed', *Journal of the Hydraulics Division*, ASCE, Vol. 95, No. HY3, pp.1085-1087.

Parker, G., Klingeman, P.C., McLean, D.G. 1982, 'Bedload and Size Distribution in Paved Gravel-Bed Streams', *Journal of the Hydraulics Division*, ASCE, Vol. 108, No. HY4, pp. 544-571.

Parker, G. 1990, 'Surface based bedload transport relation for gravel rivers', *Journal of Hydraulic Research*, IAHR, Vol. 28, No. 4, pp.417-436.

Parker, G. 1991, 'Selective Sorting and Abrasion of River Gravel. I: Theory', *Journal of Hydraulic Engineering*, ASCE, Vol. 117, No. 2, pp. 131-149.

Peloutier, V. 1998, 'Flume study of the deposition of fine sediment into river gravel', Ph.D. Thesis presented to the Department of Civil Engineering, University of Glasgow.

Petts, G.E. 1984, 'Sedimentation within a Regulated River', *Earth, Surface Processes and Landforms*, Vol. 9, pp. 125-134.

Praturi, A.K. and Brodkey, R.S. 1978, 'A stereoscopic visual study of coherent structures in turbulent shear flow', *Journal of Fluid Mechanics*, Vol. 89, pp. 251-272.

Raju, N. and Meilburg, E. 1995, 'The accumulation and dispersion of heavy particles in forced two-dimensional mixing layers. Part 2: The effect of gravity', *Physics of Fluids*, Vol. 7(6), pp. 1241-1264.

Rashidi, M. and Banerjee, S. 1988, 'Turbulence structure in free-surface channel flows', *Physics of Fluids,* Vol. 31, No. 9, pp. 2491-2503.

Raudkivi, A.J. 1990, 'Loose Boundary Hydraulics', 3rd Edition, Pergamon Press plc, Oxford.

Raupach, M.R. 1981, 'Conditional statistics of Reynolds stress in rough-wall and smooth-wall turbulent boundary layers', *Journal of Fluid Mechanics*, Vol. 108, pp. 363-382.

Reeks, M.W. 1977, 'On the dispersion of small particles suspended in an isotropic turbulent fluid', Journal of Fluid Mechanics, Vol. 83, pp.529-546.

Reiser, D.W. 1998, 'Sediment in Gravel Bed Rivers: Ecological and Biological Considerations', from *Gravel Bed Rivers in the Environment*, Klingeman, P.C., Beschta, R.L., Komar, P.D., Bradley, J.B. (eds.), Water Resources Publications, Colorado, pp. 199-228.

Reynolds, C.S., White, M.L., Clarke, R.T. and Marker, A.F. 1990, 'Suspension and settlement of particles in flowing water: comparison of the effects of varying depth and velocity in circulating channels', *Freshwater Biology*, Vol. 24, pp. 23-34.

Richardson, J.F. and Zaki, W.N. 1954, 'Sedimentation and Fluidisation: Part 1', *Transactions of the Institute of Chemical Engineers*, Vol. 32(1), pp. 35-53.

Robinson, S.K. 1991, 'Coherent Motions in the Turbulent Boundary Layer', *Annual Review of Fluid Mechanics*, Vol. 23, pp. 601-639.

Sakthivadivel, R. and Einstein, H.A. 1970, 'Clogging of Porous Column of Spheres by Sediment', *Journal of the Hydraulics Division*, ASCE, Vol.96, No. HY2, pp. 461-472.

Schlichting, H. 1968, 'Boundary-Layer Theory', *6th Edn,* McGraw Hill Book Company, New York.

Sear, D.A. 1992, 'Impact of Hydroelectric Power Releases on Sediment Transport Processes in Pool-Riffle Sequences', from *Dynamics of Gravel-Bed Rivers*, Billi, P., Hey, R.D., Thorne, C.R. and Tacconi, P. (eds.), John Wiley and Sons Ltd, pp. 629-650.

Sear, D.A. 1993, 'Fine Sediment Infiltration into Gravel Spawning Beds within a Regulated River Experiencing Floods: Ecological Implications for Salmonoids', *Regulated Rivers: Research & Management*, Vol. 8, pp. 373-390.

Sene, K.J., Hunt, J.C.R. and Thomas, N.H. 1994, 'The Role of Coherent Structures in Bubble Transport by Turbulent Shear Flows', *Journal of Fluid Mechanics*, Vol. 259, pp. 219-240.

Shibiyama, T. and Horikawa, K. 1980, 'Laboratory study of sediment transport mechanism due to wave action', *Proceedings of the Japanese Society of Mechanical Engineers*, Vol. 296, pp.131.

Shvidchenko, A.B. 1999, 'Modelling graded sediment behaviour in rivers', Internal Report, University of Glasgow.

Shvidchenko, A.B. and Pender, G. 2001, 'Discussion: Large flow structures in a turbulent open channel flow', *Journal of Hydraulic Research*, IAHR, Vol. 39, No. 1, pp. 109-111.

Smith, C.R. 1996, 'Coherent Flow Structures in Smooth-wall Turbulent Boundary Layers: Facts, Mechanisms and Speculation', in *Coherent Flow Structures in Open Channels*, Ashworth, P.J., Bennett, S.J., Best, J.L. and McLelland, S.J. (eds.), John Wiley and Sons Ltd.

Song, T., Graf, W.H., Lemmin, U. 1994, 'Uniform flow in open channels with moveable bed', *Journal of Hydraulic Research*, IAHR, Vol. 32, No. 6, pp. 861-876.

Stokes, G.G. 1851, 'On the Effect of Internal Friction of Fluids on the Motion of Pendulums', *Transactions*, Cambridge Philosophical Society, 9(2), pp. 8-106.

Sumer, B.M. and Oğuz, B. 1978, 'Particle motions near the bottom in turbulent flow in an open channel', *Journal of Fluid Mechanics*, Vol. 86, Part 1, pp. 109-127.

Sumer, B.M. and Deigaard, R. 1981, 'Particle motions near the bottom in turbulent flow in an open channel. Part 2', *Journal of Fluid Mechanics*, Vol. 109, pp. 311-337.

Sutherland, A.J. 1967, 'Proposed mechanism for sediment entrainment by turbulent flows', *Journal of Geophysical Research*, Vol. 72, pp. 191-198.

Sutherland, A.J. 1991, 'Hiding function to predict self-armouring', Research Report, University of Canterbury, New Zealand.

Tamburrino, A. and Gulliver, J.S. 1999, 'Large flow structures in a turbulent open channel flow', *Journal of Hydraulic Research*, IAHR, Vol. 37, No. 3, pp. 363-380.

Theodorsen, T. 1955, 'The Structure of Turbulence', in *50 Jahre Grenzschichtforsung*, Gortier, H. and Tollmein, W. (eds.), Braunschweig, Veiweg & Sohn, pp. 55.

Thomas, A.S.W. and Bull, M.K. 1983, 'On the role of wall-pressure fluctuations in deterministic motions in the turbulent boundary layer', *Journal of Fluid Mechanics*, Vol. 128, pp. 283-322.

Tien, C. 1989, 'Granular filtration of Hydrosols and Aerosols', Butterworths Series on Chemical Engineering, London, 365pp.

Tooby, P.F., Wick, G.L. and Isaacs, J.D. 1977, 'The Motion of a Small Sphere in a Rotating Velocity Field: A Possible Mechanism for Suspending Particles in Turbulence', *Journal of Geophysical Research*, Vol. 82, No. 15, pp.2096-2100.

Toso, J.W. 1986, 'The magnitude and extent of extreme pressure fluctuations in the hydraulic jump', Ph.D Thesis presented to University of Minnesota, August 1986.

U.S. Inter-Agency Committee 1957, 'Some fundamentals of particle size analysis. A study of methods used in the measurement and analysis of sediment loads in streams', *Report No. 12*, Sub-committee on Sedimentation, U.S. Inter-Agency on Water Resources, Minneapolis.

Vanoni, V.A. and Brooks, N.H. 1957, 'Laboratory Studies of the Roughness and Suspended Load of Alluvial Streams', Sedimentation Laboratory, California Inst. Tech., Report E-68.

van Rijn, L.C. 1982, 'Equivalent Roughness of Alluvial Bed', *Journal of the Hydraulics Division*, ASCE, No. HY10.

van Rijn, L.C. 1984, 'Sediment Transport, Part II: Suspended Load Transport', *Journal of Hydraulic Engineering*, ACSE, Vol. 110, No.11, pp.1613-1641.

van Rijn, L.C. 1986, 'Mathematical Modelling of Suspended Sediment in Nonuniform Flows', *Journal of Hydraulic Engineering*, ASCE, Vol. 112, No. 6, pp. 433-455.

van Rijn, L.C. 1989, 'Handbook: sediment transport by currents and waves', *Report H461*, Delft Hydraulics, Delft, Netherlands.

Wallace, J.M., Eckelmann, H. and Brodkey, R.S. 1972, 'The wall region in turbulent shear flow', *Journal of Fluid Mechanics*, Vol. 54, Part 1, pp. 39-48.

Walling, D.E. and Webb, B.W. 1987, 'Sediment Load in Gravel-Bed Rivers: UK Experience', in *Sediment Transport in Gravel-bed Rivers*, Thorne, C.R., Bathurst, J.C. and Hey, R.D. (eds.), John Wiley & Sons Ltd, pp. 691-732.

Wallis, S.G. and Moores, A. 1996, 'Discussion: The effect of turbulence on sediment deposition', *Journal of Hydraulic Research*, IAHR, Vol. 34, No. 4, pp. 562-566.

Wang, L.P. and Maxey, M.R. 1993, 'Settling velocity and concentration distribution of heavy particles in homogeneous isotropic turbulence', *Journal of Fluid Mechanics*, Vol. 256, pp.27-68.

Wilcock, P.R., Kondolf, G.M., Matthews, W.G. and Barta, A.F. 1996, 'Specification of sediment maintenance flows for a large gravel-bed river', *Water Resources Research*, Vol. 32, No. 9, pp. 2911-2921.

Willmarth, W.W. and Lu, S.S. 1972, 'Structure of Reynolds stress near the wall', *Journal of Fluid Mechanics*, Vol. 55, Part 1, pp. 65-92.

Yalin, M.S. 1977, 'Mechanics of Sediment Transport', Pergamon Press Ltd., Oxford.

Yalin, M.S. 1992, 'River Mechanics', Pergamon Press Ltd., Oxford.

Zhang, R.J. 1989, 'Sediment dynamics in rivers', Water Resources Press (in Chinese).

Appendices

Appendix 3.1 3-D Acoustic Doppler Velocimeter (ADV)

A3.1.1 Principles of ADV Operation

The basic principle on which the ADV operates is known as the Doppler effect. Figure A3.1 shows a target, with velocity v_t, moving towards a fixed source emitting sound waves at a frequency f_0 (= C/λ_0), where C is the speed of sound and λ_0 is the wavelength. This results in the frequency of the sound received by the moving target being higher than if the target is stationary. This is due to the additional waves ($v_t T/\lambda_0$) experienced by the target during a time T. Conversely, when the target is moving away from the source, the frequency of sound received by the target is lower. Thus the frequency of sound f received by the target is

$$f = f_0\left(\frac{C \pm v_t}{C}\right) \qquad \ldots.(A3.1)$$

In the situation where the source is moving towards a stationary target (Figure A3.2) with velocity v_s, the wavelength of the sound received by the target is shortened

$$\lambda' = \left(\frac{C - v_s}{f_0}\right) \qquad \ldots.(A3.2)$$

Thus the frequency of the sound received by the target is

$$f = \frac{C}{\lambda'} = f_0\left(\frac{C}{C \pm v_s}\right) \qquad \ldots.(A3.3)$$

depending on whether the source is moving towards or away from the target.

The ADV probe uses both these scenarios to calculate the flow velocity. The acoustic sensor at the end of the probe consists of one central transmit transducer and three receive transducers orientated at 120° to each other (Figure A3.3a). The transmit transducer (*fixed source*) generates short acoustic pulses at a known frequency, which propagate vertically downward. As these pulses pass through a sample volume approximately 55mm below the probe tip, the acoustic pulses are reflected by particles (sediment, air bubbles, small organisms, etc.) in the fluid medium (*moving target*). A proportion of these reflections (*moving source*) travel along the axis of the receive transducers, where they are sampled by the ADV (*fixed target*) and the change in frequency is measured. This change in frequency ($F_{doppler}$) is known as the Doppler shift and is related to the original frequency of the acoustic pulses (F_{source}) by the equation,

$$F_{doppler} = -F_{source}\left(v_r / C\right) \quad \text{....(A3.4)}$$

where v_r is the relative velocity between the particles and the receiver.

The Doppler shift is proportional to the velocity of the particles along an axis known as the bistatic axis, located halfway between the axis of the transmit transducer and the receive transducer (Figure A3.3b). The bistatic velocities measured at each of the receivers are converted by the ADV into Cartesian (XYZ) velocities using the probe geometry. This, therefore, provides the three-dimensional flow velocities and turbulence characteristics relative to the orientation of the probe.

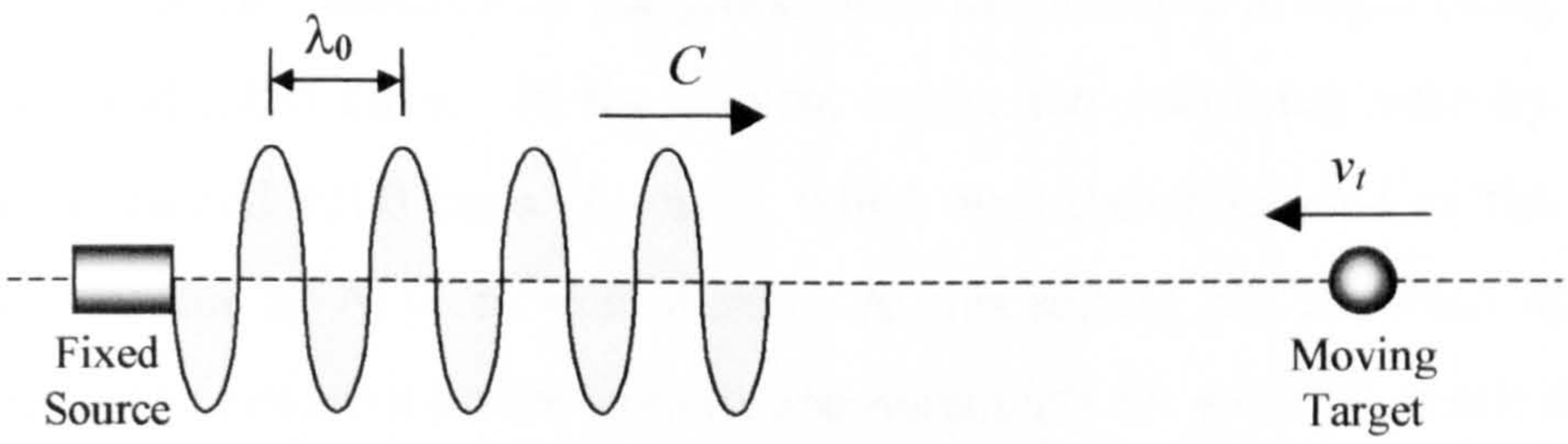

Figure A3.1 - Target moving towards stationary source emitting acoustic waves at a known frequency

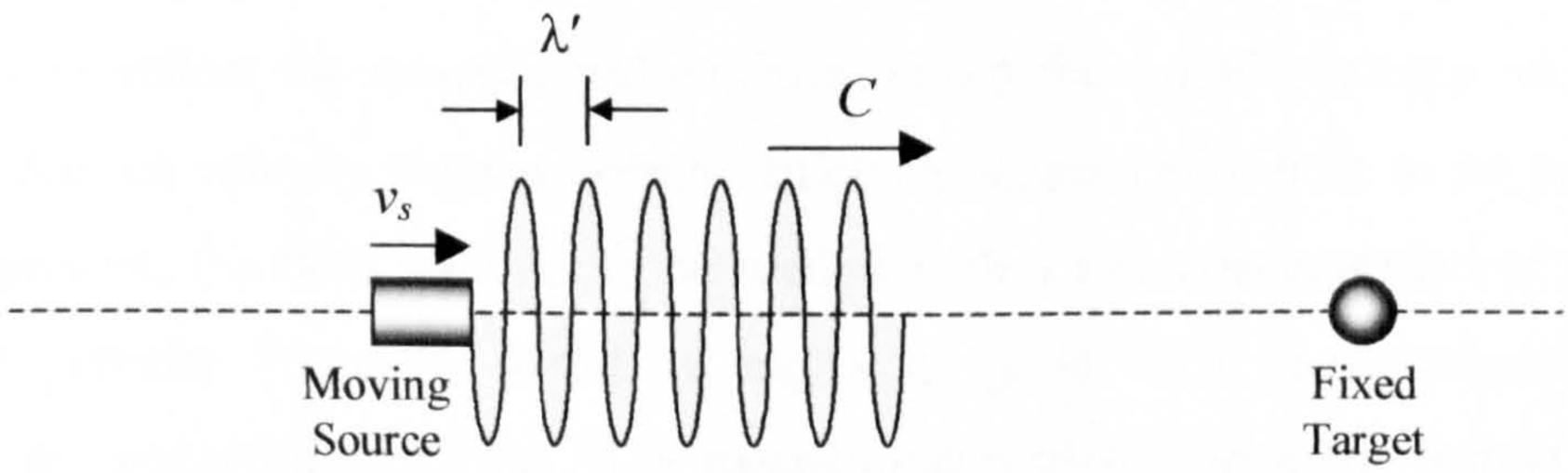

Figure A3.2 - Moving source emitting acoustic waves approaching a fixed target

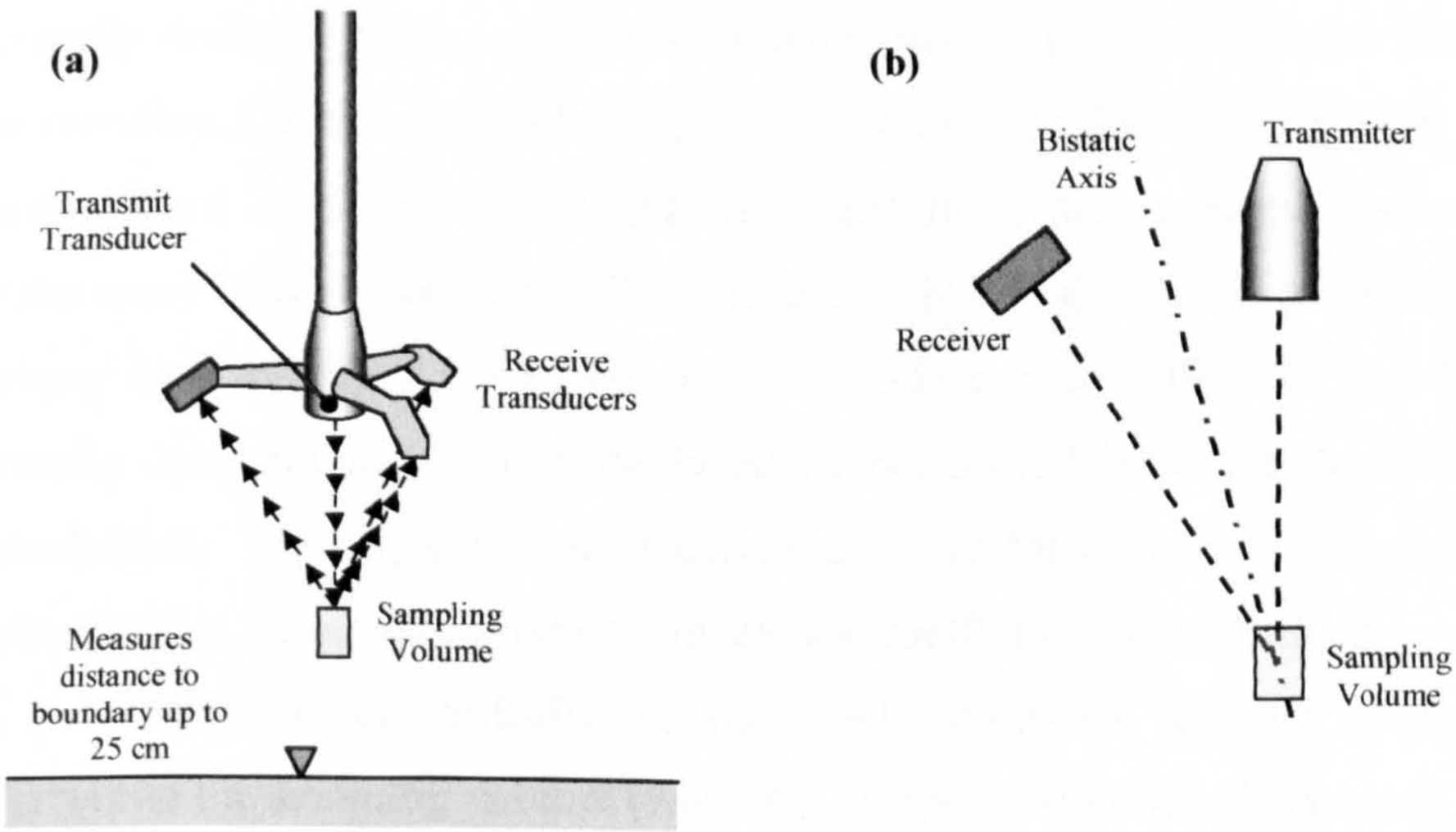

Figure A3.3 - (a) Basic operation of ADV probe; (b) definition of bistatic axis

A3.1.2 ADV User-Defined Specifications and Set-up

Velocity measurements are collected by the ADV probe at a user-specified frequency, known as the sampling rate, which can vary within the range 0.1 Hz to 25 Hz. As the probe has an internal pinging rate of between 200-250 Hz (a 'ping' is defined as a single estimate of the three-dimensional velocity), each set of velocity measurements are obtained from the average of the 'pings' to meet the user defined sampling rate. A sample rate of 25 Hz was generally adopted in the current study.

A user-specified maximum velocity range setting defines the magnitude of velocity that can be measured by the probe, with the standard settings being ±3, ±10, ±30, ±100 and ±250 cm/s. In the current study, the maximum velocity was not expected to exceed ±100 cm/s (±1 m/s), which was therefore used as the standard velocity range for all ADV measurements. At this setting, the expected noise level introduces a ±1 cm/s error on the velocity measurements for a sampling rate of 25 Hz.

The signal strength is a measure of the intensity of the reflected acoustic signal. It signifies whether there are a sufficient number of particles scattered within the flow to reflect the acoustic pulses from within the sample volume, in order to obtain accurate velocity measurements. In circumstances with little or no particulate matter present, the flow requires to be seeded with a low concentration of neutrally buoyant particles (typically about 10 mg/l) for good ADV measurements. This seeding was not required for the ADV measurements taken during the current study.

The ADV correlation coefficient is a data quality parameter, with a perfect correlation of 100% indicating reliable, low-noise velocity measurements. It is generally desirable to be operating with the correlation between 70 and 100%. When the correlation is less than 70% it may indicate: (i) the ADV is operating in difficult measurement conditions (i.e. highly turbulent flow, highly aerated water); (ii) the probe is not fully submerged; (iii) the sound-to-noise ratio (SNR) is too low; or (iv) a general fault with the ADV probe. Low correlation values affect the variability in the velocity data, due to the increase in noise, but do not influence the mean velocity calculations. Consequently, an accurate study of turbulence characteristics within open-channel flow requires a high correlation coefficient to be obtained.

The ADV automatically measures and records the distance to any boundary adjacent to the sampling volume (when the sampling volume is between 2 and 25 cm away from the boundary). With the vertically orientated probe configuration, it is

possible to place the leading edge of the sample volume very close to the boundary (within about 0.5mm), allowing measurements to be taken within a few mm of the boundary. Care is required to ensure that the lower portion of the sampling volume is not impinging into the boundary, as this would reduce the magnitude of the velocity measurements from their true values. For this reason, ADV measurements were taken at elevations no less than 3mm above the bed boundary throughout this study.

Appendix 3.2 Set-up Procedure for Steady, Uniform Flow

Each series of experiments within the current study were conducted under steady, uniform flow conditions. Unfortunately, the high relative roughness (k_s/H) of the bed conditions employed in the study meant that there were local variations in both the measured bed surface elevations and water levels. In order to achieve uniform flow conditions, the bed surface elevations were first measured on the top of bed elements at 0.5m intervals along the three parallel lengths of the flume, one along the centreline and two adjacent to the flume walls. Adjustments to the gravel bed layer were made in order to obtain the required bed slope along each of the parallel lengths, with the average bed slope calculated from the three sets of measurements. Water surface elevations were then measured with pointer gauges along the three parallel lengths and uniform flow conditions were achieved when the average water surface slope was equal to the average bed slope.

A graphical technique was employed to establish the downstream tailgate settling required to give uniform flow conditions for a known discharge:-

- Set discharge in flume to required magnitude.
- Record initial tailgate elevation (Figure A3.5).
- Measure the water surface elevations along the length of the flume and calculate the best-fit average water surface slope.
- Adjust the tailgate elevation (up or down) depending on the backwater profile (Figure A3.5) and recalculate water surface slope.

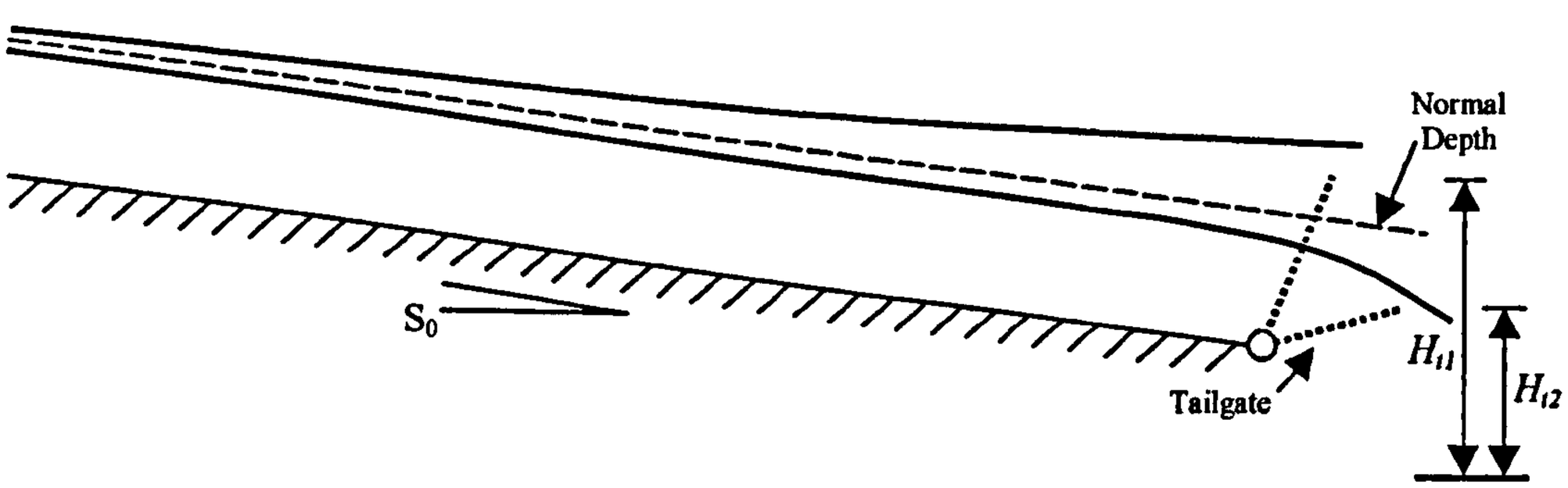

Figure A3.5 - Tailgate settings producing backwater profiles with different water surface slopes.

- Once four or five water surface slopes have been calculated for corresponding tailgate positions, plot water surface slope (S_f) against tailgate height (H_t) (Figure A3.6).
- The required tailgate height for uniform flow conditions at the specified discharge rate can be obtained from interpolation of the data plotted in Figure A3.6, i.e. the height at which $S_f = S_0$.
- Finally, set tailgate height to interpolated value and check whether uniform flow conditions exist.

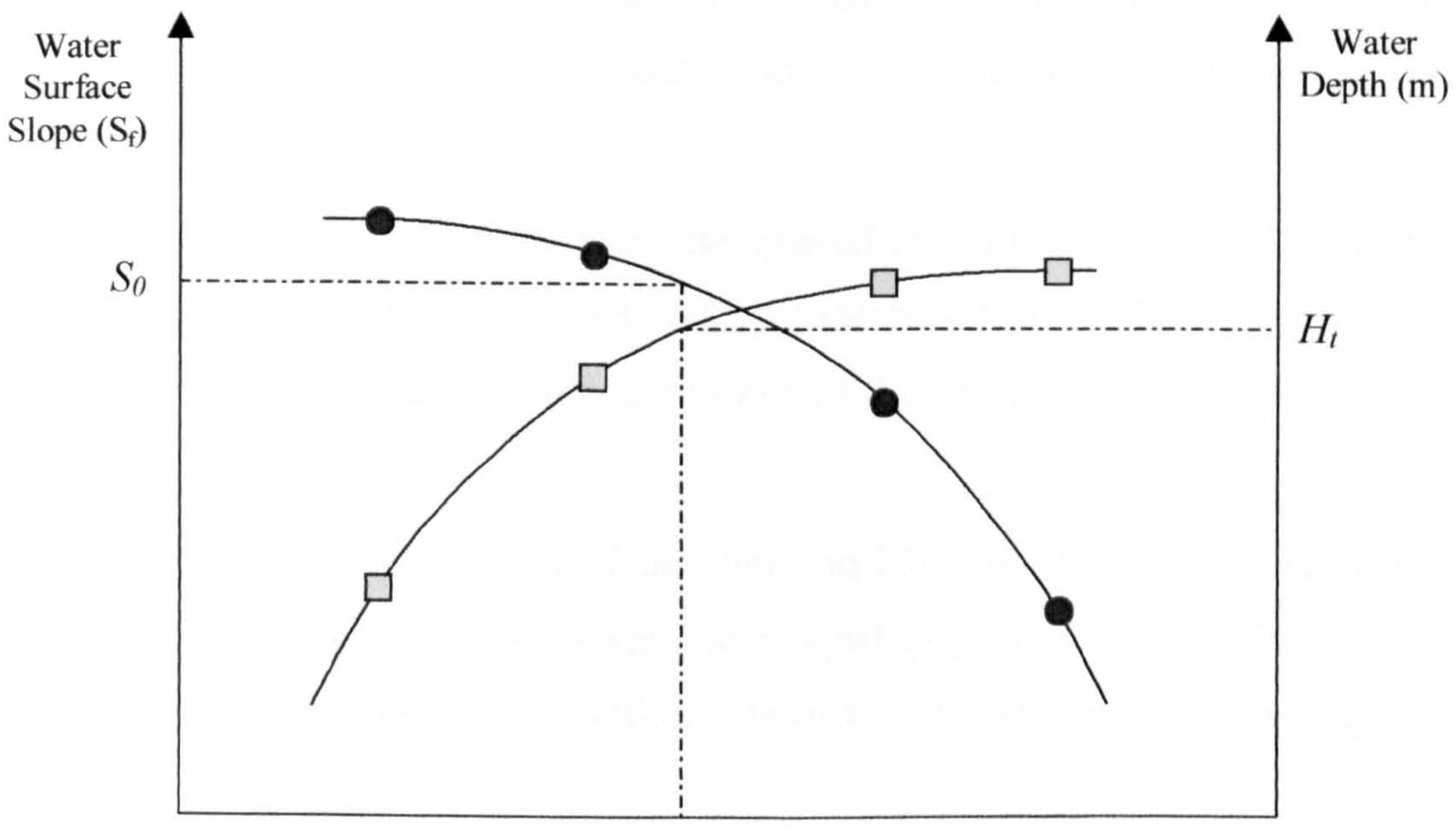

Figure A3.6 - Graphical method for settling tailgate position for uniform flow conditions

Appendix 3.3 Experimental Procedure for Series 2 Experiments

This Appendix provides a summary of the typical procedure followed during the completion of each experiment, from the set-up of the flume through to the post-experiment analyses. This outline procedure, developed over the first three experiments (SC_EXT1, 1 and 2) was followed for the subsequent nine experiments (SC_EX4, 5, 6, 7, 8, 9, 10 and 11).

(1) Flume Set-up

- The bed of the flume facility was set to the required slope by raising and lowering the series of bolts supporting the flume along its length on both sides. An optical level was used to ensure the bed slope was uniform along the length of the flume.
- The cleaned sediment traps were then placed in bed of flume, along with the groups of vertical tubes used to support mesh and gravel layers. Each 1m section of coarse mesh (3mm aperture) was then placed and secured over the traps.
- The washed gravel was placed in a uniform 25-35mm thick layer over mesh and underlying traps. This layer was tamped to provide a relatively flat bed surface, with approximately uniform porosity and no clearly protruding bed elements.
- The bed slope of the gravel surface was measured using the optical level. Adjustments to the local gravel bed layer thickness were made, where required, to achieve the desired bed slope.
- Using a pointer gauge, the mean bed surface elevation was then measured at 0.5m intervals along the length of the flume.

(2) Setting the Sediment Feed Rate

- The dial on the control panel controlling the rate of release of the sediment was previously calibrated by measuring the sediment mass collected on the tray over a specified time period at various settings.
- Before each experiment, a clean tray was placed under the seven nozzles of the electrically driven hopper from which sediment is fed into the flume.

- With the dial set to the appropriate position for the required feed rate, the hopper was switched on and sediment was collected on the tray over specific time period (30-60 seconds).
- The mass of sediment collected was weighed on the Mettler B4C1000 electronic balance and divided by the feed time to obtain sediment feed rate I_R (gs^{-1}).
- The dial on the sediment hopper was adjusted, if required, and the procedure repeated until the sediment feed was at the desired rate.
- This measurement procedure was repeated at the end of the experiment to ensure the feed rate remained consistent throughout the duration of the experiment.

*(3) Setting Up Uniform Flow Conditions (See **Appendix 3.2**)*

(4) Flow Velocity Measurements

- Once uniform flow conditions were established, mean and fluctuating velocity measurements were taken using the ADV probe at predctermined locations both along the centreline and laterally across the width of the flume.

(5) Sediment Feed and Concentration Measurements

- The concentration sample tubes were positioned at their locations in the XZ flow domain prior to the start of the sediment feed.
- The electrically driven sediment hopper and a stopwatch were started simultaneously to allow the time of sediment feed to be monitored.
- After a predetermined time, the concentration samples were started. The water and sediment mixture was extracted for about 15 minutes, or until the 80-litre storage bins were approaching full.
- This abstraction of water from the flume meant that a compensation flow had to be input into the two downstream storage tanks of the flume to maintain the volume of water in the facility.
- Once the concentration samples had been taken, the sediment feed was left to run for a set length of time (generally 15-45 minutes from start of feed).

- The sediment hopper was stopped and the overall sediment feed time noted. The uniform flow conditions within the flume were generally left to run without feed for a further 15-20 minutes to allow fine sediments to settle through the gravel bed layer and into the traps.
- Gradually the flow rate in the flume was reduced by slowly shutting the flow regulation valve and the pump was switched off. The weir at the downstream end of the flume was wound down horizontal to allow the remaining water to drain from working section of the flume.

(6) Other Experimental Measurements

- The water temperature was monitored throughout the duration of the experiment.

(7) Post-Experiment Procedure

Deposited Samples:

- Once the flume had drained fully, the gravel surface layer was carefully washed to ensure all deposited material passed through the mesh into the traps. The cleaned gravel and coarse mesh sections were then removed and stored.
- Each of the centre traps was slowly drained, in turn, leaving the deposited sediment undisturbed.
- The deposited sediment samples were then slowly oven-dried within the traps at a temperature of about 100°C. Once dry, the deposited samples from each individual trap section (i.e. A, B and C) were retrieved and weighed on the Mettler B4C1000 electronic scales (accurate to nearest milligram) before being stored in sealed and labelled polythene bags for future sieve analysis.

Concentration Samples:

- The volume of water collected in each of the storage bins was measured for the individual concentration samples.
- This water was then carefully pumped out in order to retrieve the sediment samples for drying, weighing and sieve analysis (as for deposition samples).

Sieve Analysis of Concentration and Deposited Samples:

- Sieve analysis of deposition and concentration samples was carried out in accordance with BS 1377 (Part 2) using 200mm BS410/1986 sieves of different apertures.
- Two sets of sieves were used for the different grades of fine sediment used – 625, 500, 425, 355, 300, 250, 212, 150, 125μm aperture sieves for the LA grade sand and 212, 150, 125, 106, 90, 75, 63, 53, 45, 38μm aperture sieves for the DB grade sand.

Appendix 3.4 Work Schedule for Experimental Studies

PROGRAMME OF EXPERIMENTAL STUDIES - SERIES 1

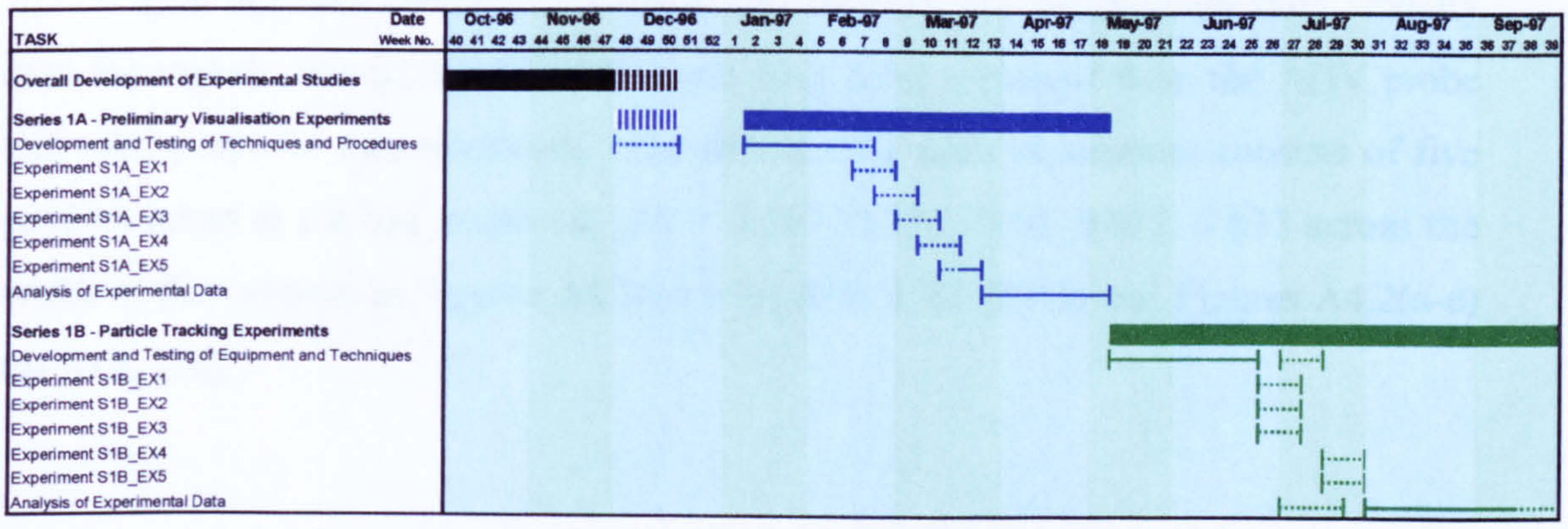

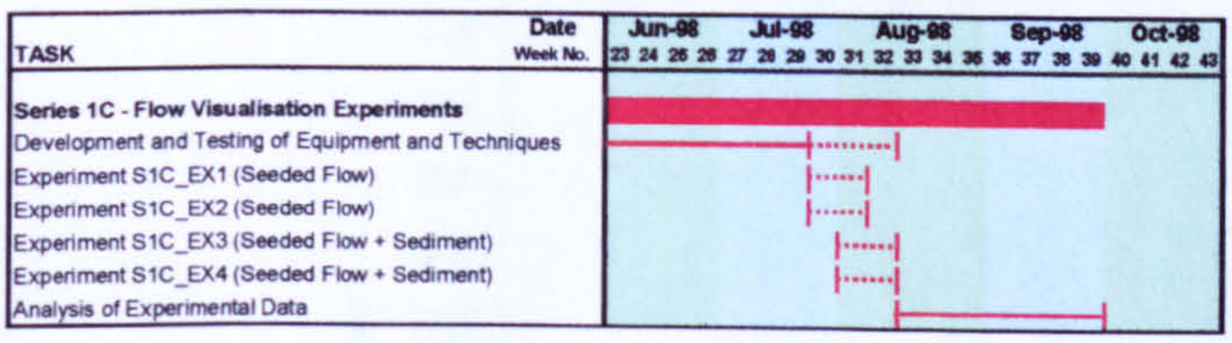

NOTES:

(1) The development and testing of the equipment and techniques employed in Series 1 included: (a) an initial conception stage for visualisation techniques; (b) checks on the availability of required equipment and apparatus; (c) completion of modifications to Armfield flume and assembly of other equipment (where required); (d) preparation of sediments used in studies (bed material and fine sediment); (e) development of procedure for conducting experiments and post-experiment analysis of data; (f) calibrating camera/illumination equipment for best quality images; etc....

(2) The completion of each experiment included: (a) initial set-up of flume, bed layer, equipment etc.; (b) initial measurements of flow rate, temperature, etc. (c) set-up of uniform flow conditions; (d) recordings with camera equipment and transfer of images to PC for analysis; (e) ADV/mini-prop measurements of mean/turbulent flow conditions; (e) cleaning flume/equipment following completion of experiment.

(3) Analysis of experimental data included: (a) analysis of recorded images (e.g. particle tracking); (b) processing ADV/mini-prop data for mean/turbulent flow conditions

PROGRAMME OF EXPERIMENTAL STUDIES - SERIES 2

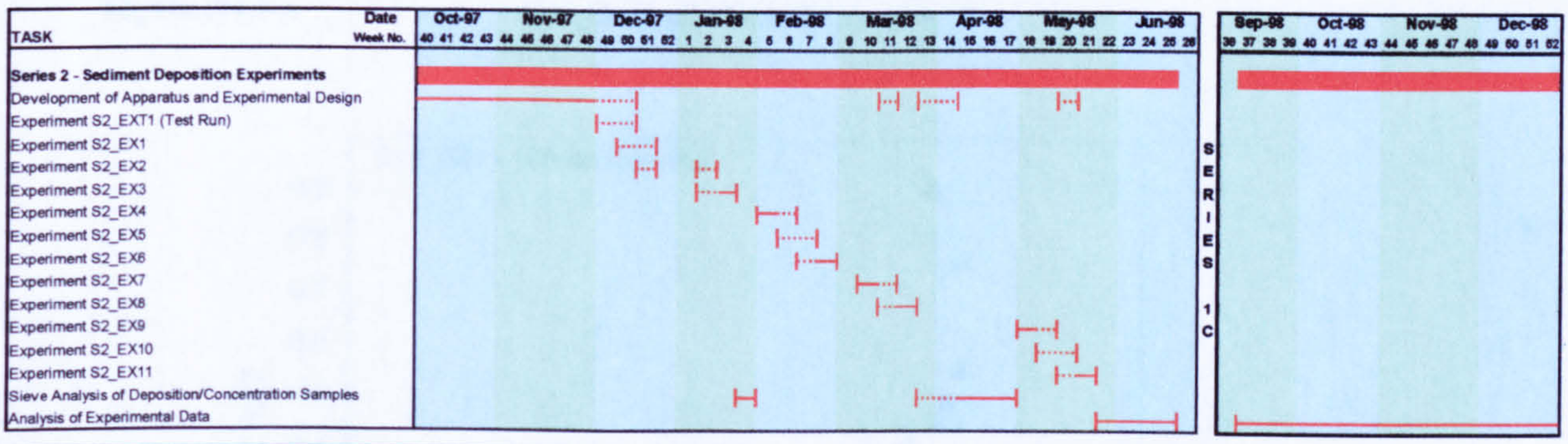

NOTES:

(1) Development of apparatus and experimental design included: (a) initial conception stage for Series 2; (b) design and construction of traps and bed arrangement; (c) assembly of sediment concentration sampling equipment; (d) preparation of bed gravel and fine sediment grades used; (e) setting bed slope to required level (0.004; 0.0; 0.001); etc...

(2) The completion of each individual experiment included: (a) emptying, cleaning and re-filling of sump/reservoir tanks; (b) set-up of bed/trap arrangement within flume; (c) calibration of feed rate to required level; (d) set-up of uniform flow conditions; (e) measurement of mean and turbulent flow conditions with ADV probe; (f) timed release of fine sediment from calibrated hopper; (g) measurement of sediment concentration samples; (h) removal and cleaning of bed layer; (i) removal and oven drying of centreline traps containing deposited samples.

(3) The sieve analysis of the deposition and concentration samples, along with the processed ADV data for longitudinal velocity profiles, provided the required information for the analysis of the experimental data

Appendix 4.1 Comparison of ADV and Mini-Propeller Velocity Profiles (Experiments S1B_EX1 – EX3, Series 1B)

This Appendix presents a comparison between the longitudinal flow velocity data for experiments S1B_EX1 (EX3) and S1B_EX2, obtained from the ADV probe and mini-propeller measurements. The data set for each experiment consists of five profiles taken at the test section at y/B = 0.167, 0.333, 0.50, 0.667, 0.833 across the width of flow shown in Figures A4.1(a-e) for S1B_EX1 (EX3) and Figures A4.2(a-e) for S1B_EX2.

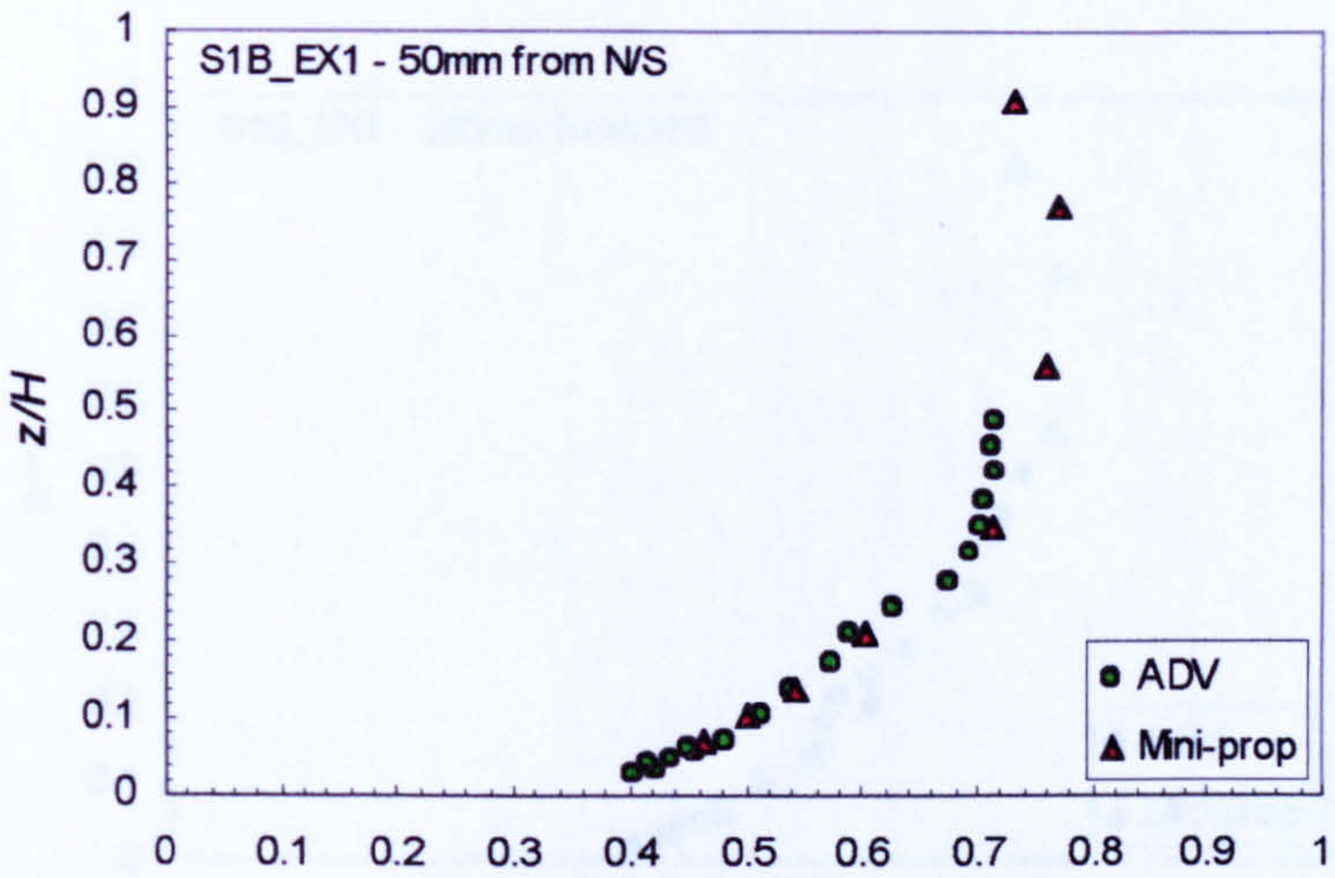

Figure A4.1 a

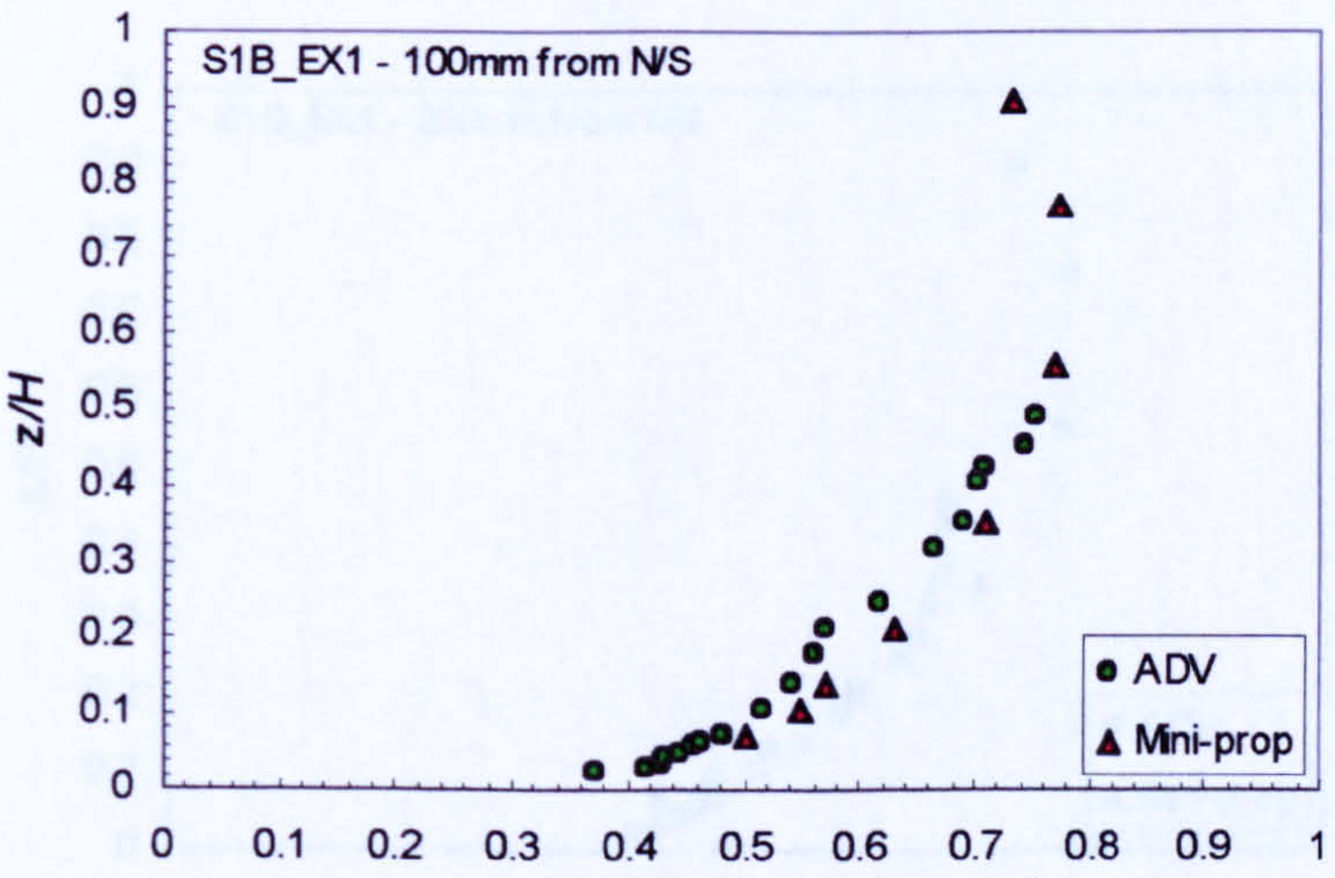

Figure A4.1 b

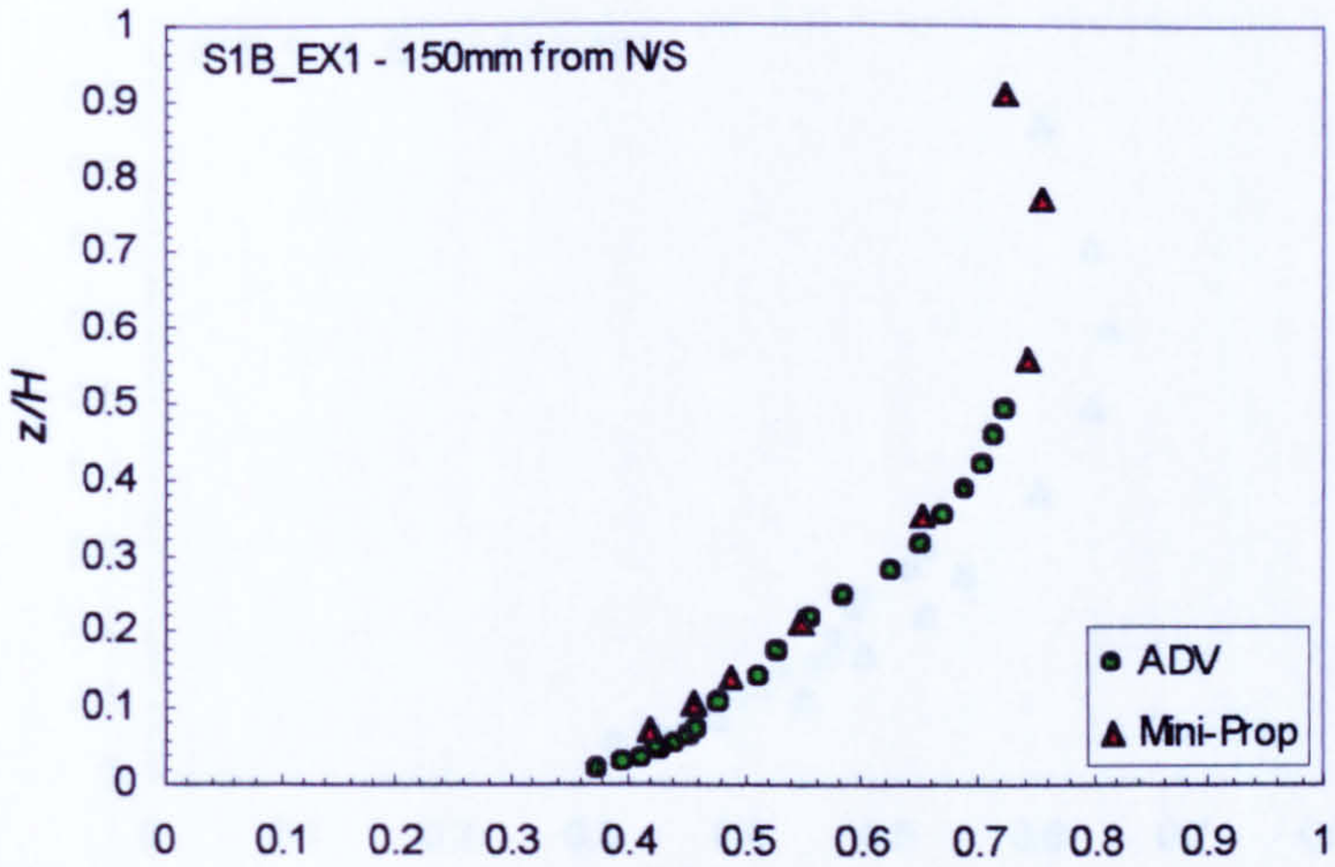

Figure A4.1 c

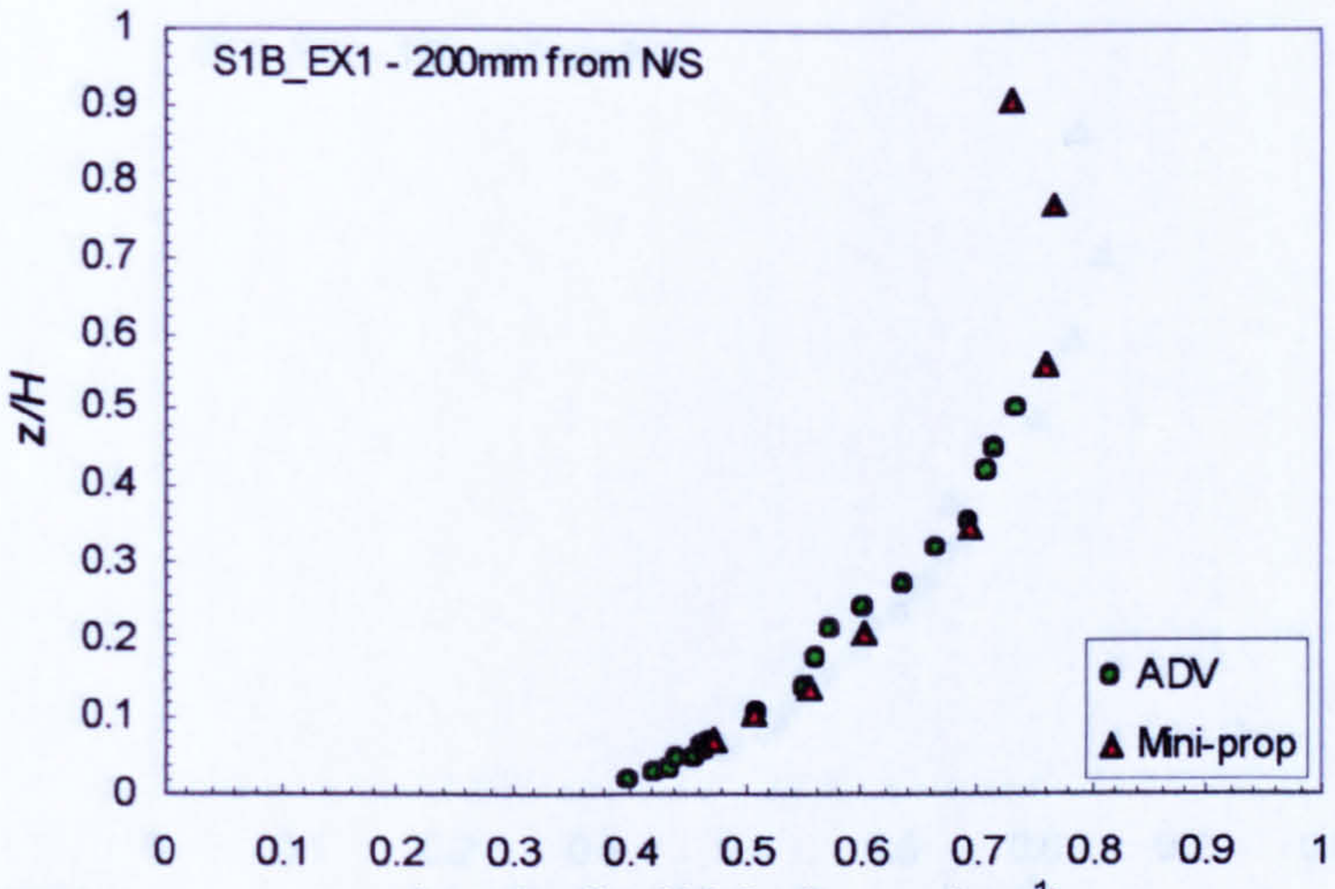

Figure A4.1 d

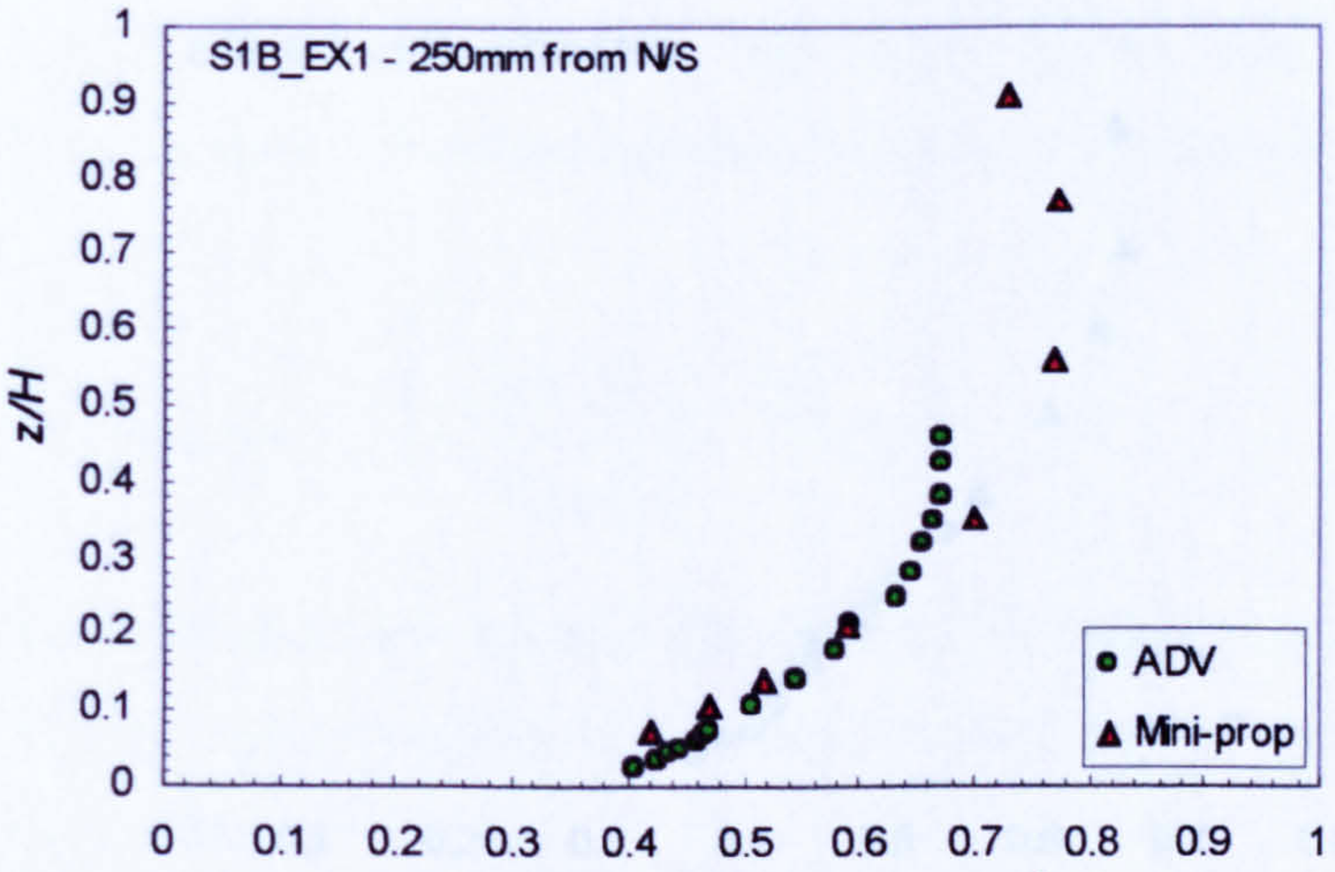

Figure A4.1 e

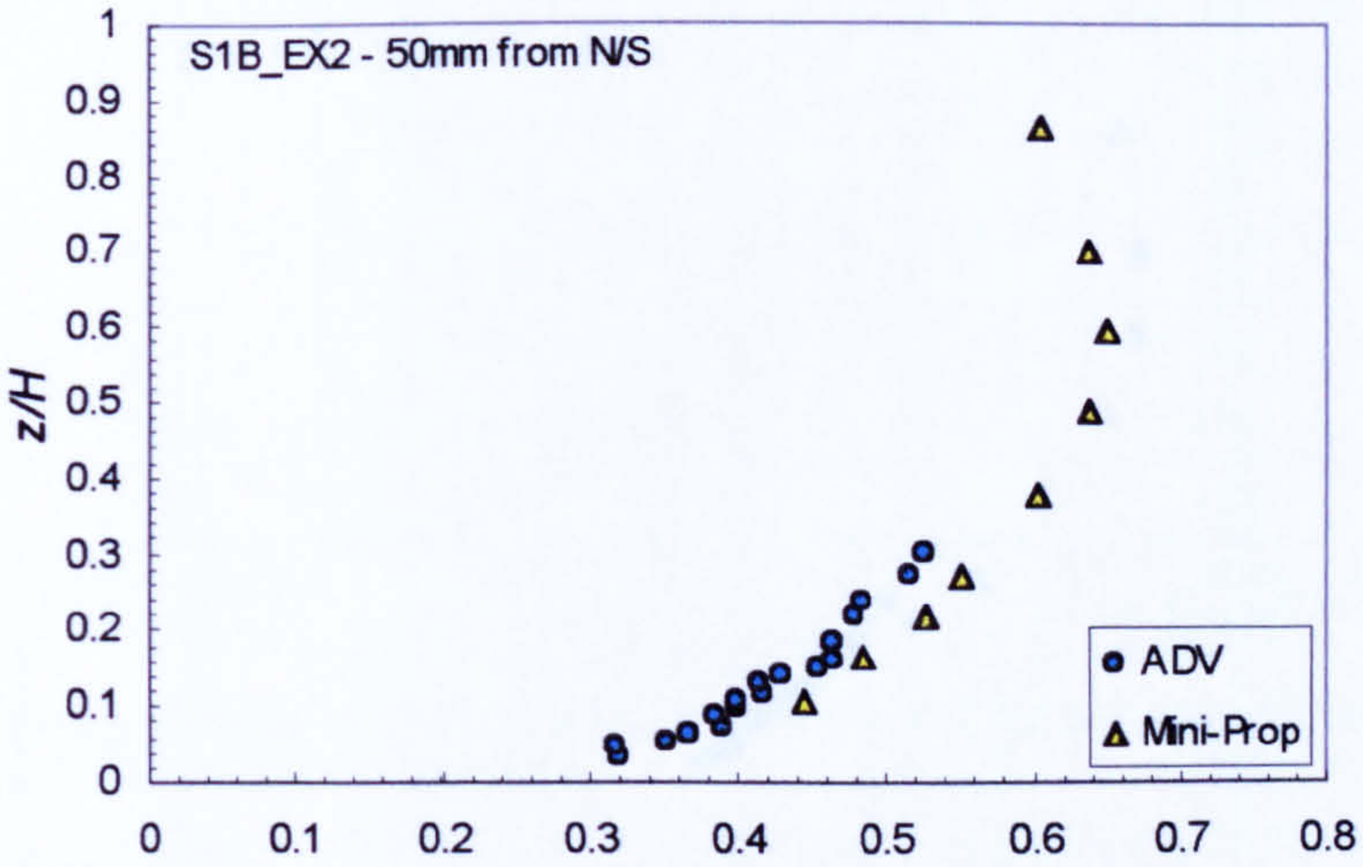

Figure A4.2 a

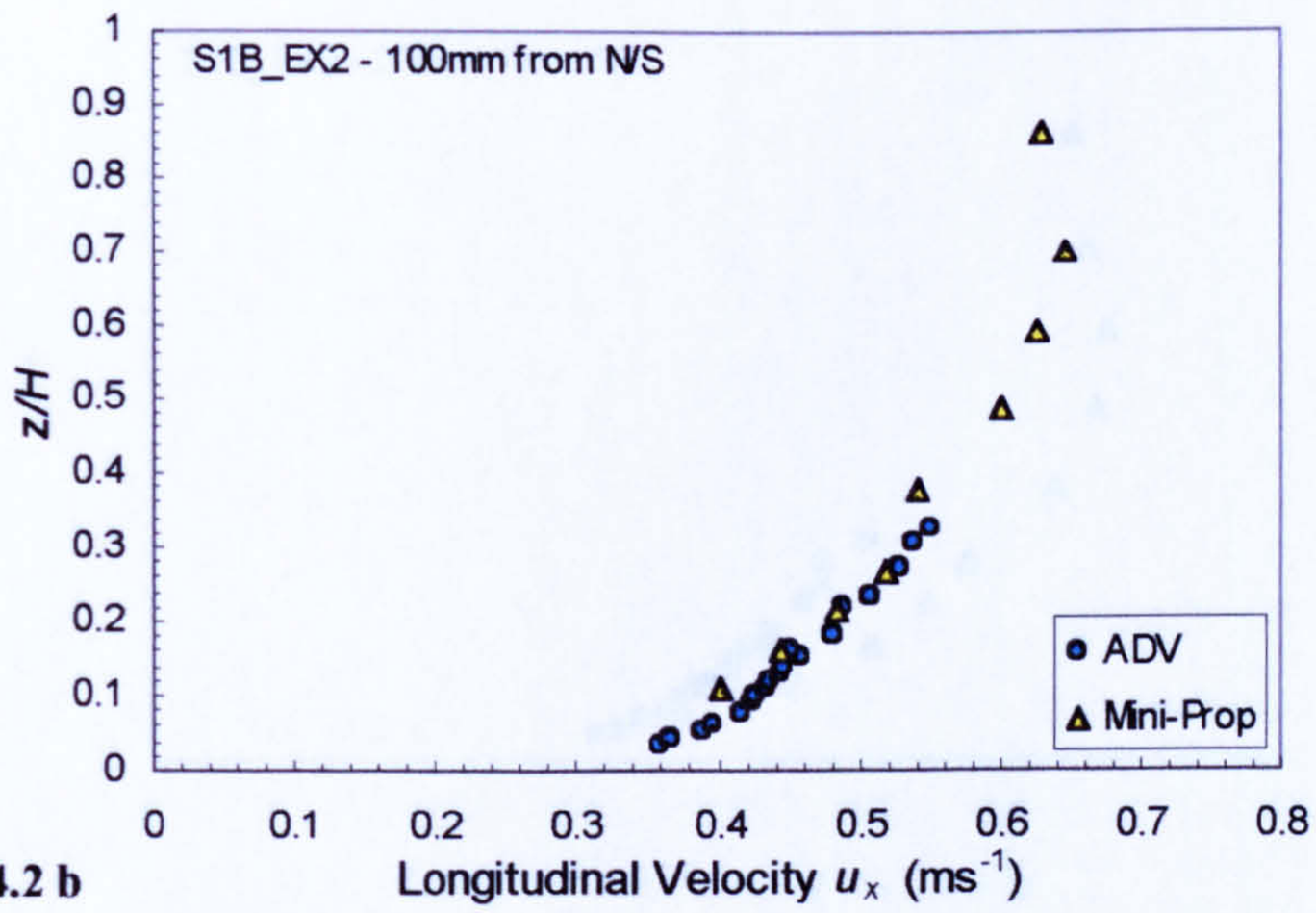

Figure A4.2 b

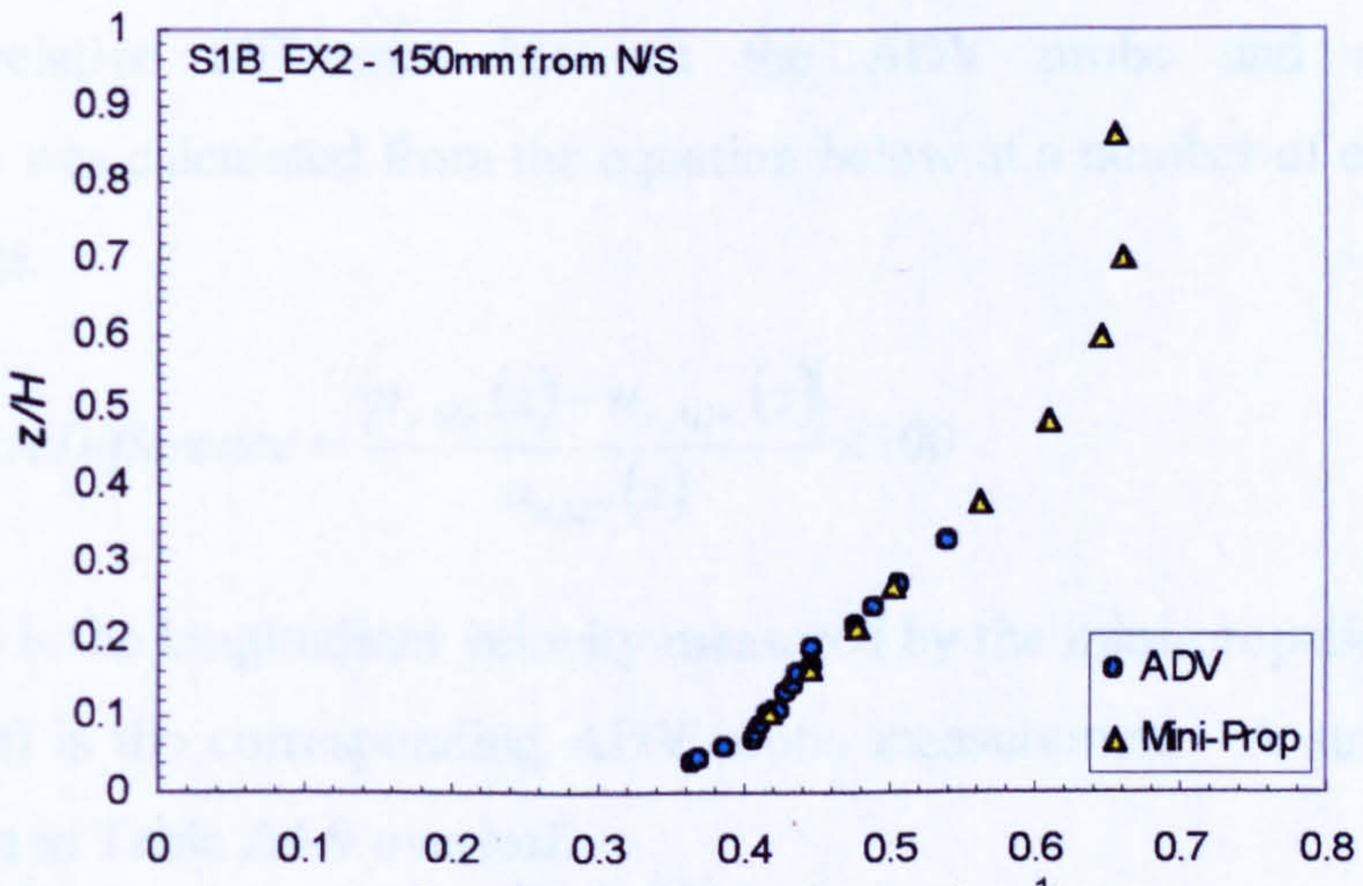

Figure A4.2 c

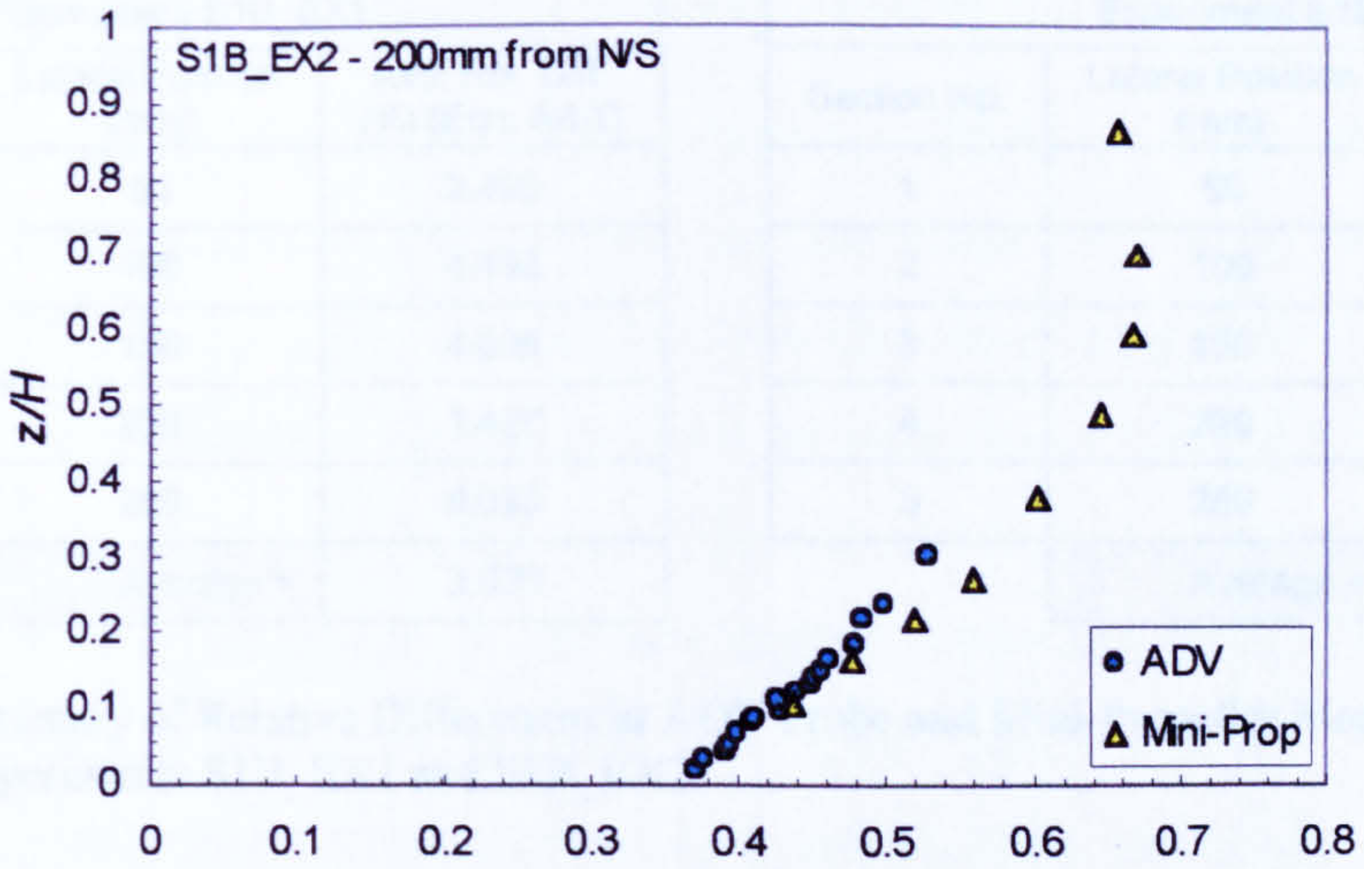

Figure A4.2 d

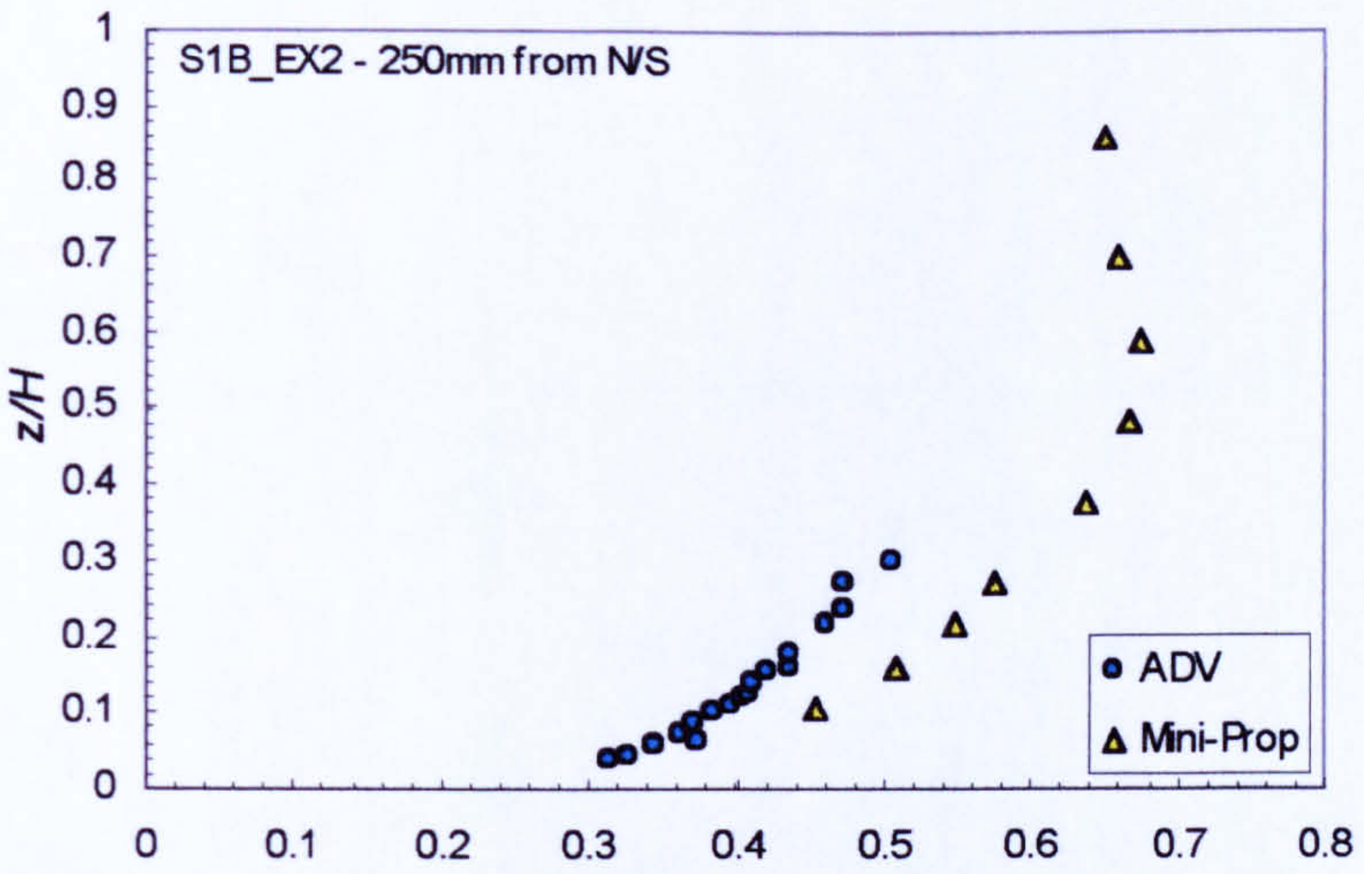

Figure A4.2 e

The relative difference between the ADV probe and mini-propeller measurements was calculated from the equation below at a number of elevations, and for each profile.

$$Relative Difference = \frac{\left|u_{x,MP}(z) - u_{x,ADV}(z)\right|}{u_{x,MP}(z)} \times 100 \qquad \text{....(A4.1)}$$

where $u_{x,MP}(z)$ is the longitudinal velocity measured by the mini-propeller at elevation z, and $u_{x,ADV}(z)$ is the corresponding ADV probe measurement. A summary of the results is given in Table A4.9 overleaf.

Experiment S1B_EX1		
Section No.	Lateral Position (mm)	Ave. Rel. Diff (%) (Eqn. A4.1)
1	50	2.496
2	100	4.492
3	150	4.538
4	200	1.427
5	250	6.693
	Average =	3.929

Experiment S1B_EX2		
Section No.	Lateral Position (mm)	Ave. Rel. Diff (%) (Eqn. A4.1)
1	50	7.502
2	100	3.048
3	150	0.786
4	200	5.008
5	250	15.029
	Average =	6.274

Table A4.9 - Summary of Relative Differences in ADV Probe and Mini-Propeller Measurements for Experiments S1B_EX1 and S1B_EX2.

Appendix 4.2 Mean Longitudinal Velocity Profiles for S1B_EX4 and EX5

This Appendix presents mean longitudinal velocity profiles measured by the ADV probe at five locations across width of the flume (y/B = 0.167, 0.333, 0.50, 0.667 and 0.833). The profiles for the flow conditions of experiment S1B_EX4 are shown in Figures A4.4 (a-e). Similar profiles for experiment S1B_EX5 are presented in Figures A4.5 (a-e). Each profile was adjusted according to the relative height to account for the local variations in the bed surface elevation from which the ADV measurements were taken, as shown in Figure A4.3 below. Where ADV measurements were taken above a protruding bed element, the height of the sample volume was adjusted according to the lowest measured bed elevation, i.e.

$$z_2 = z_{2,ADV} + \left(z_{2,POINT} - z_{1,POINT}\right) = z_1 \qquad \text{....(A4.2)}$$

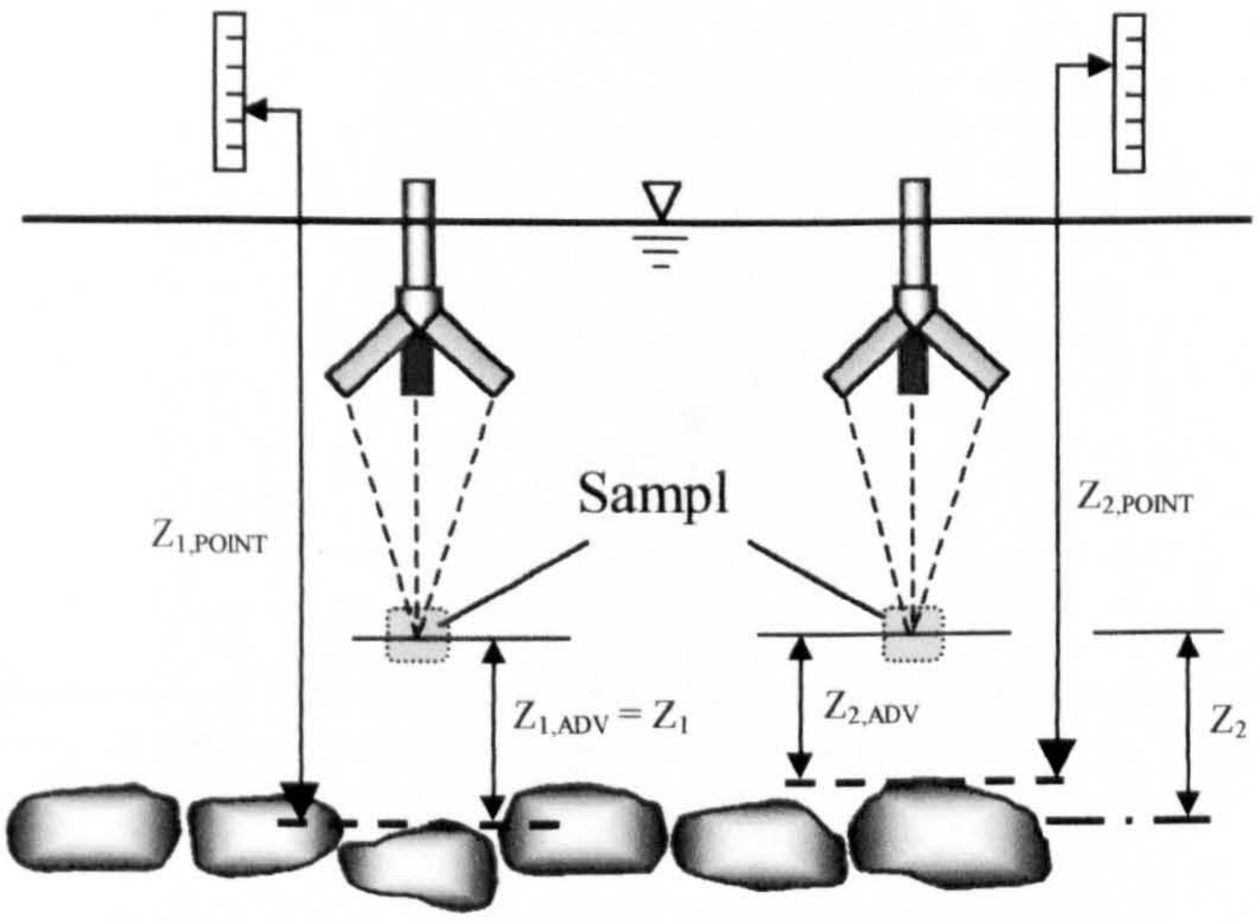

Figure A4.3 – Elevation adjustment of ADV measurements to account for localised variations in bed surface elevation

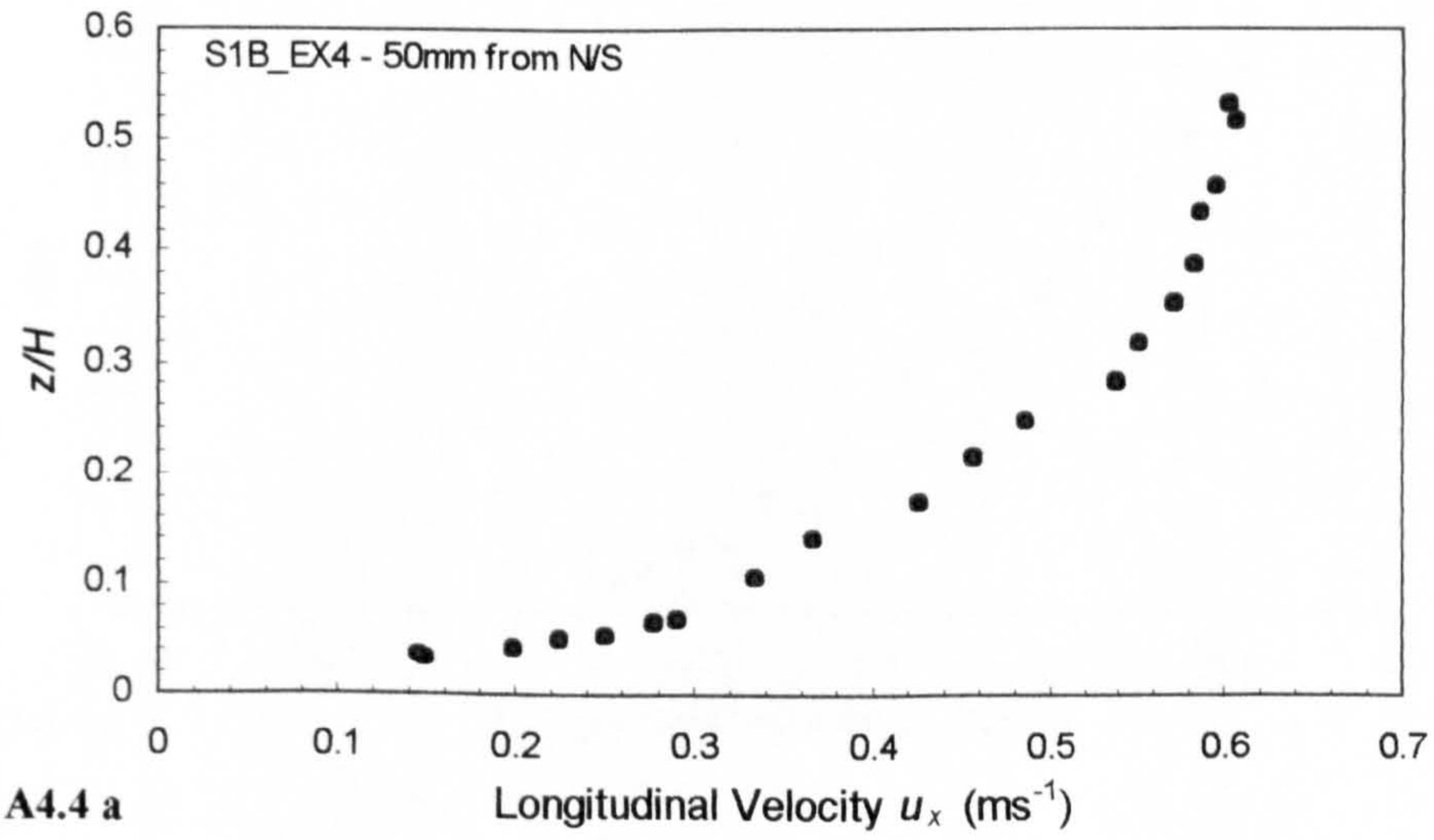

Figure A4.4 a

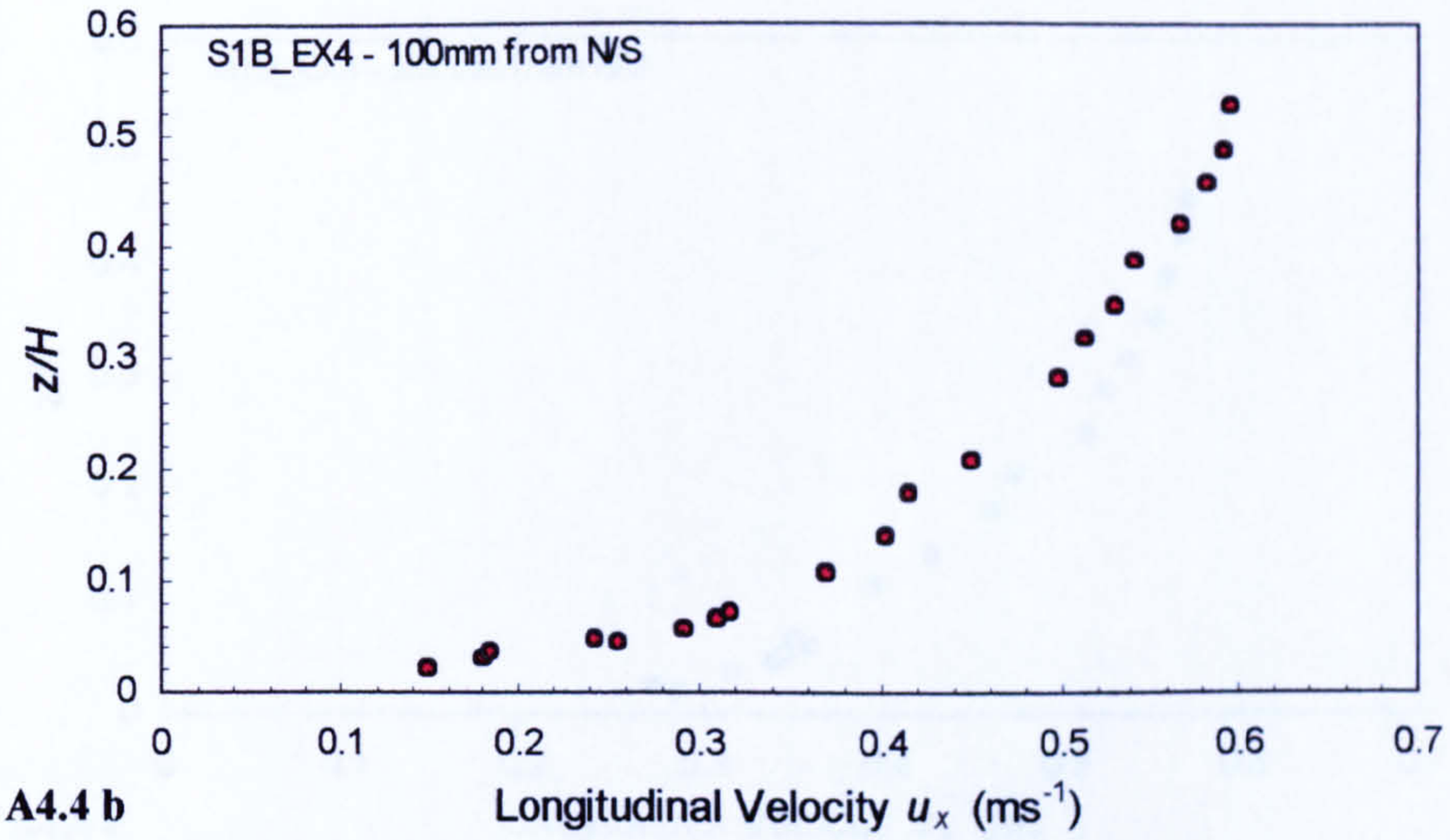

Figure A4.4 b

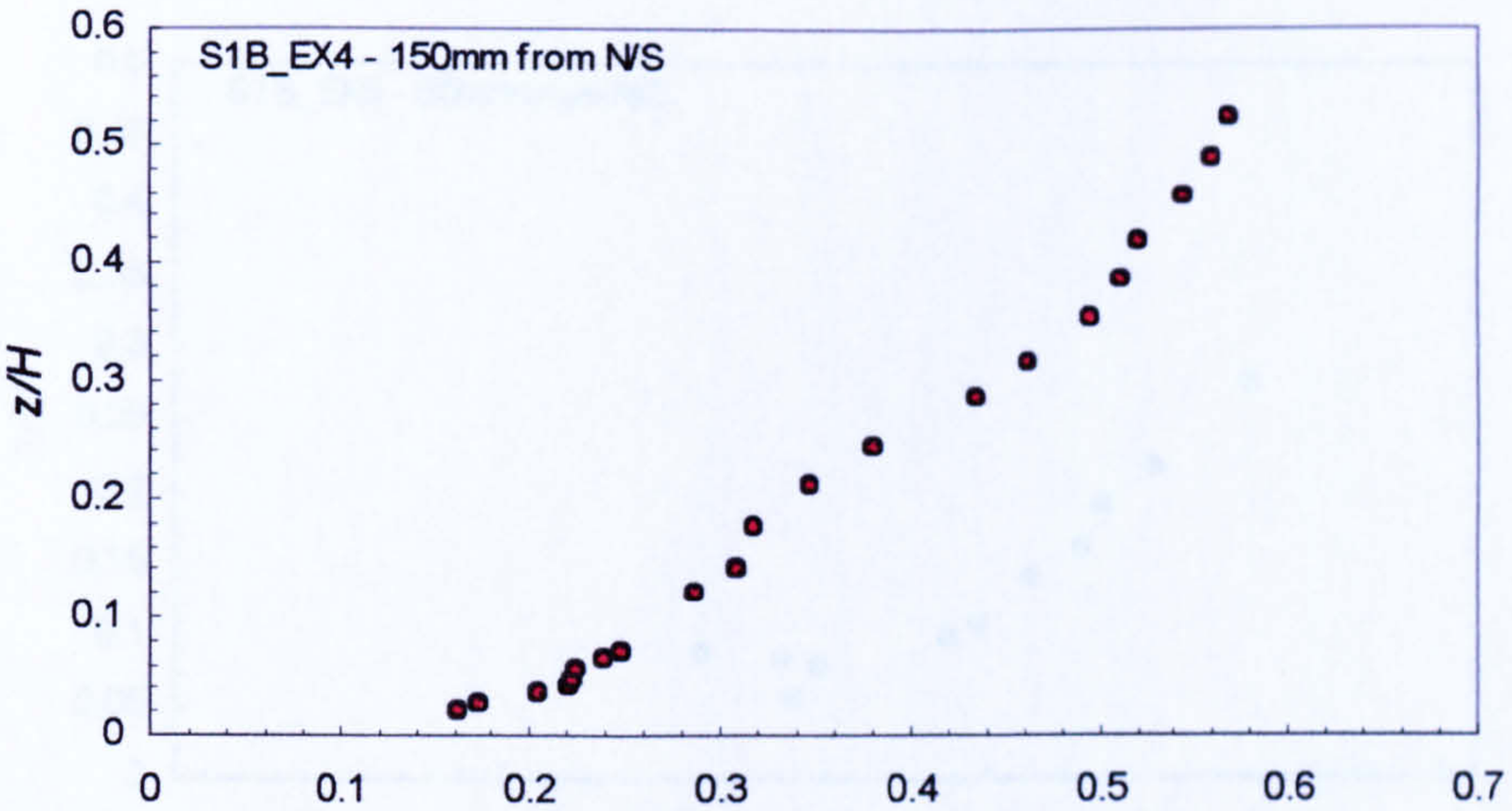

Figure A4.4 c

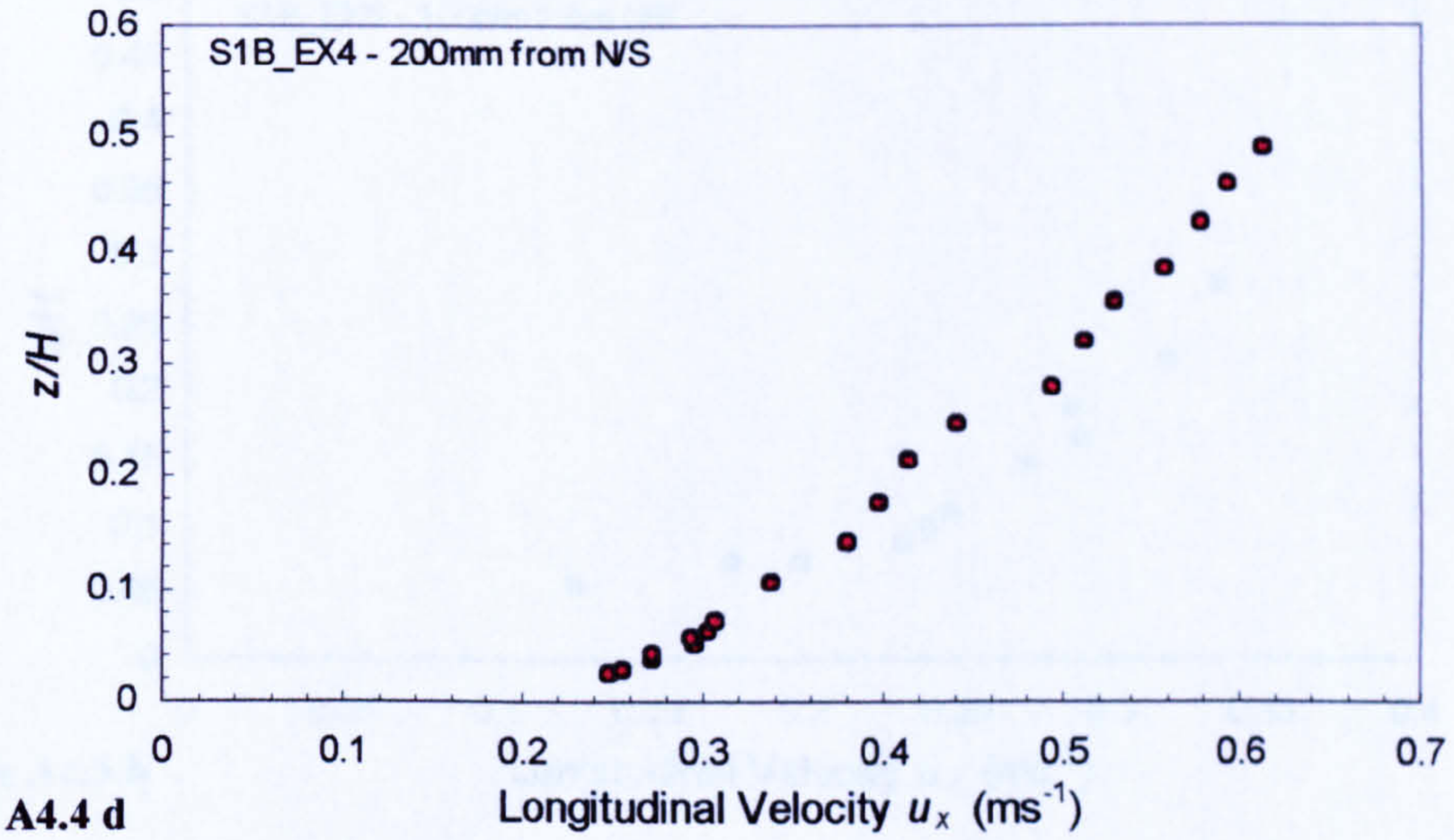

Figure A4.4 d

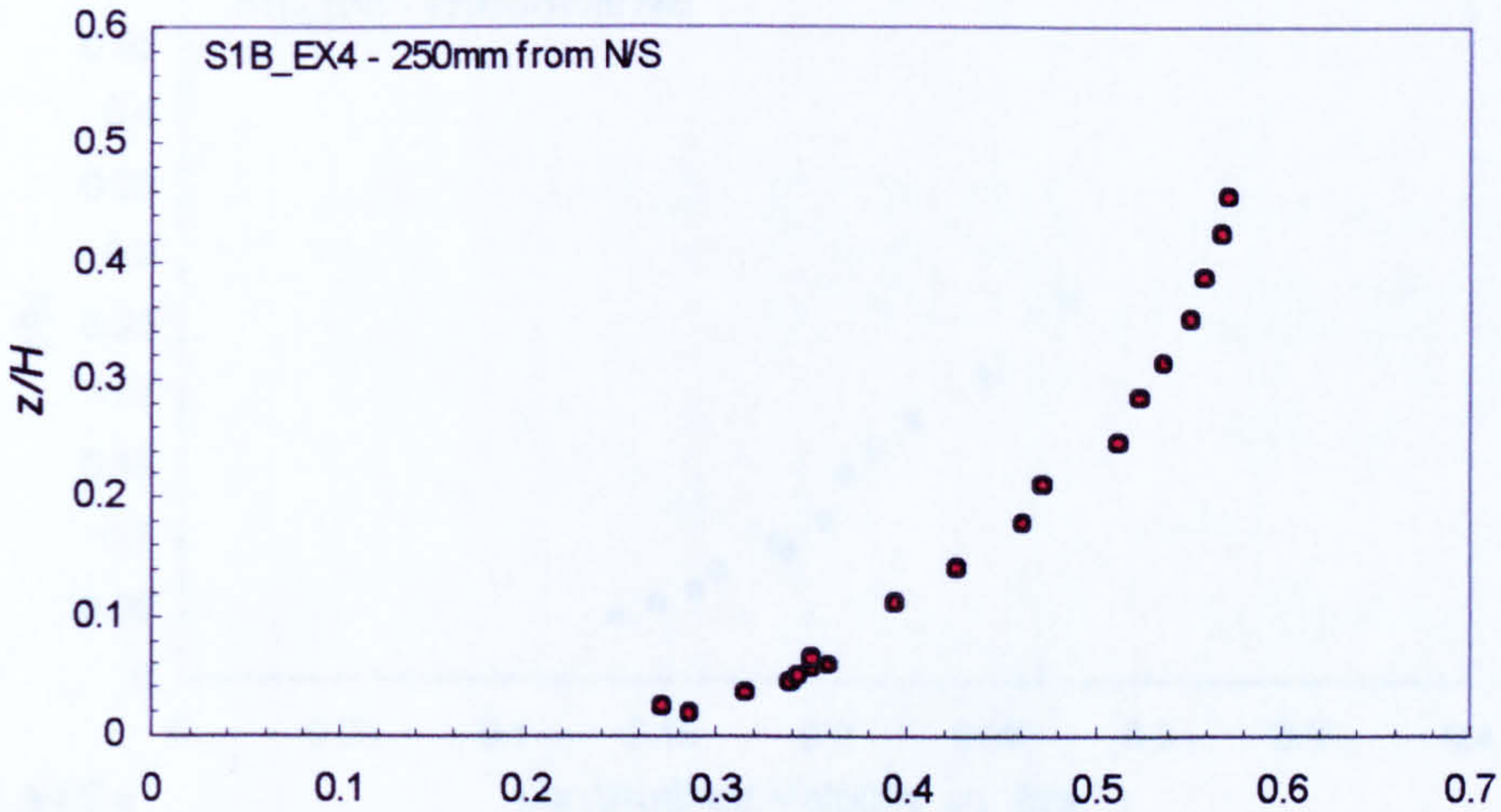

Figure A4.4 e

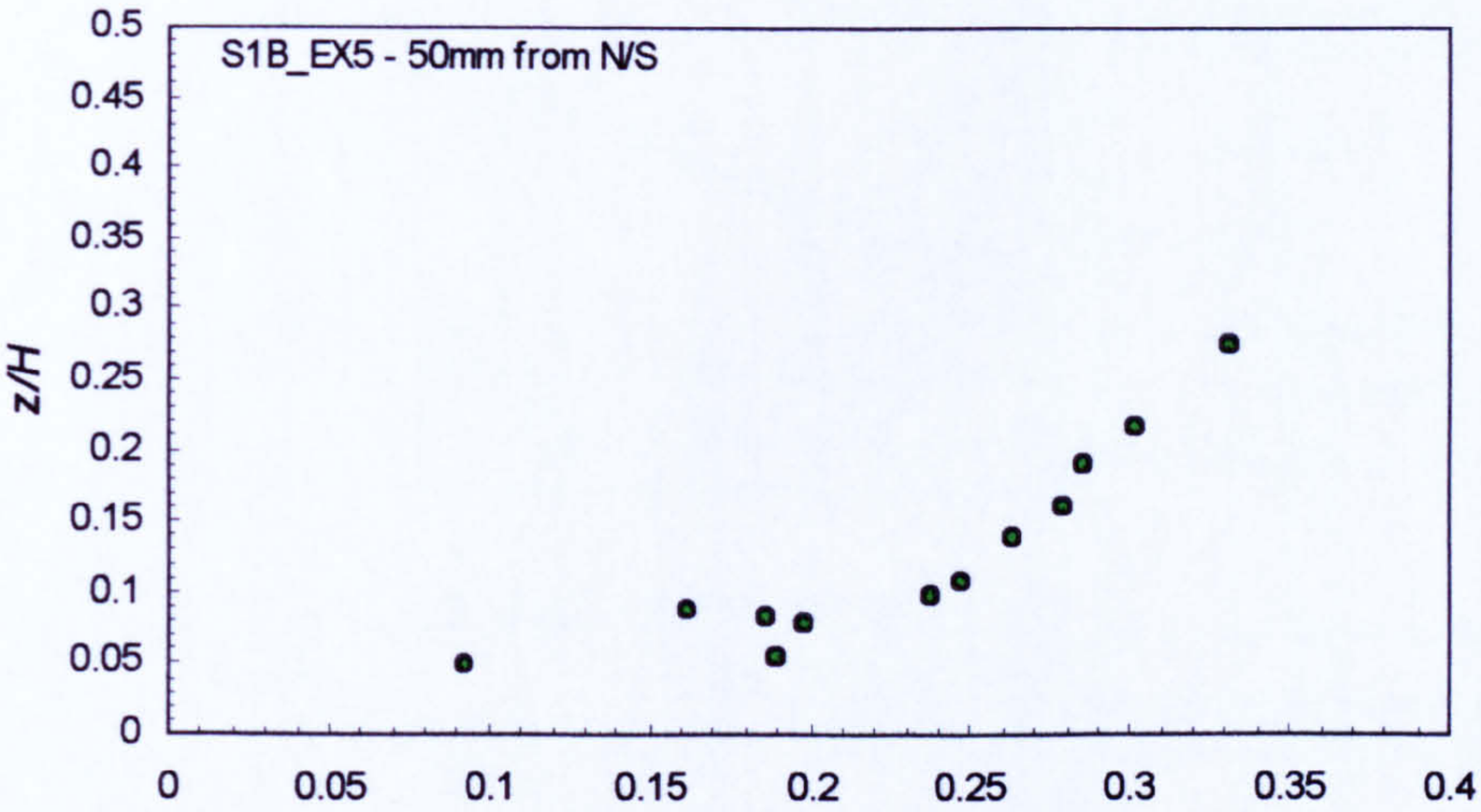

Figure A4.5 a

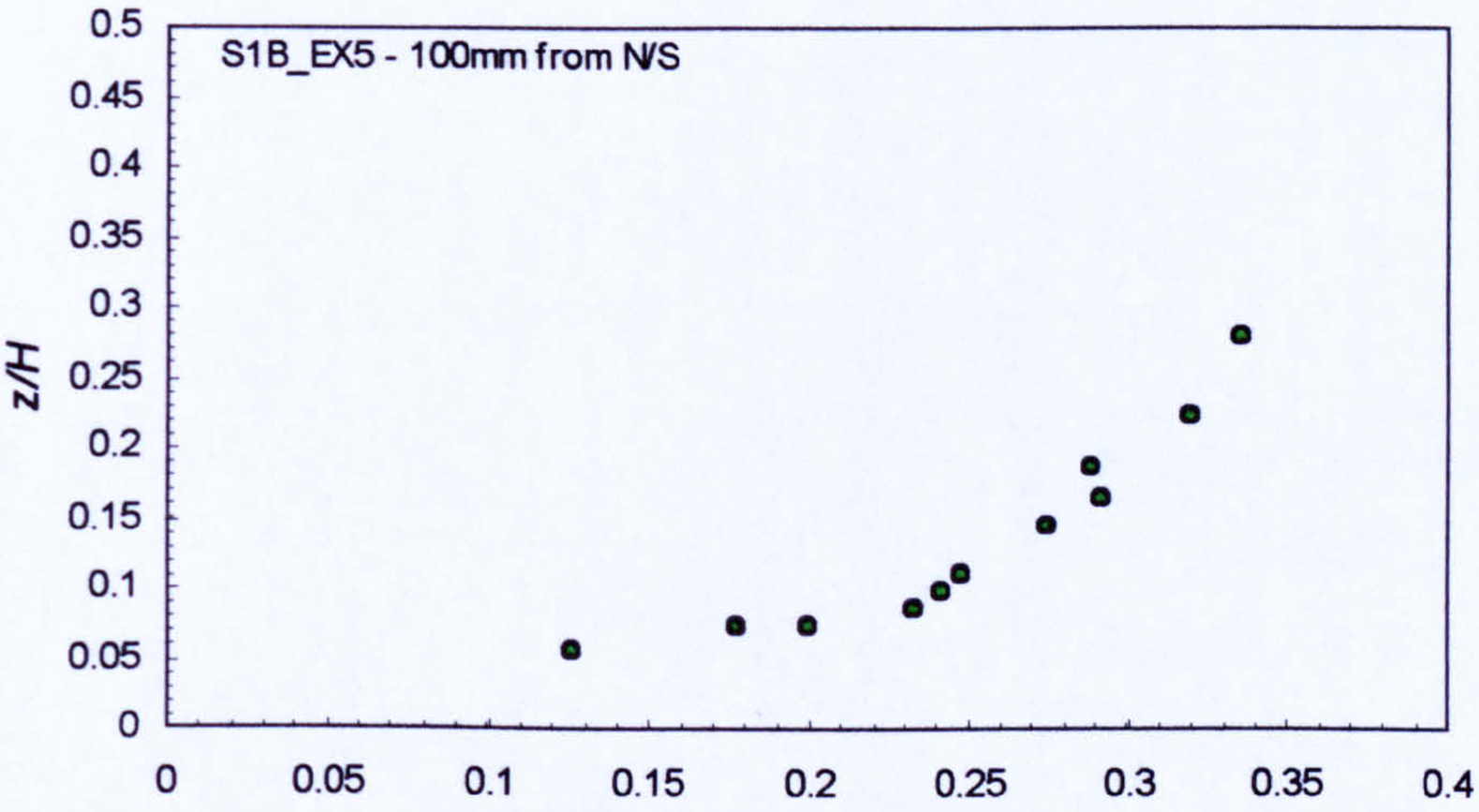

Figure A4.5 b

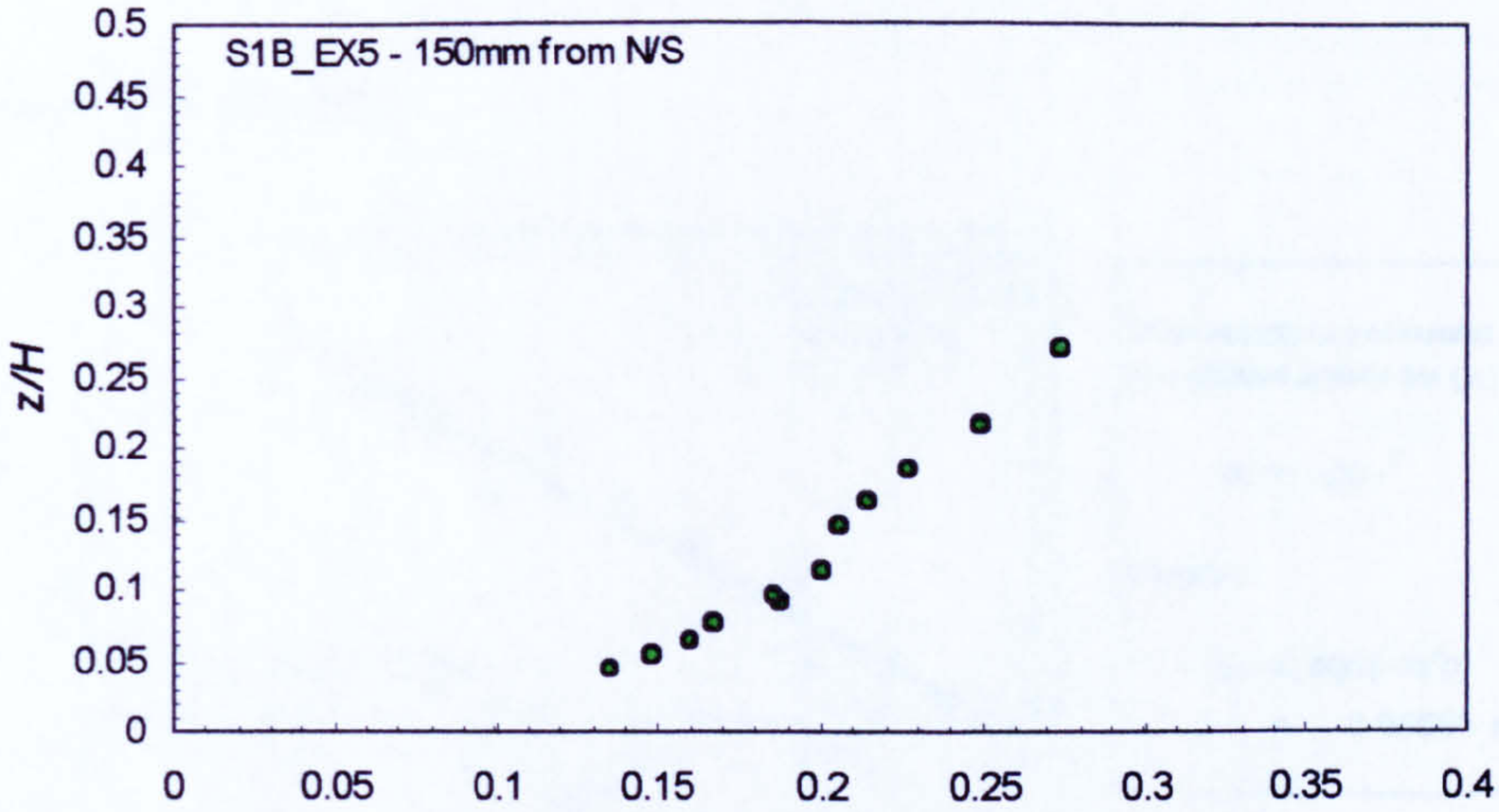
S1B_EX5 - 150mm from N/S
z/H
0.5
0.45
0.4
0.35
0.3
0.25
0.2
0.15
0.1
0.05
0
0
0.05
0.1
0.15
0.2
0.25
0.3
0.35
0.4
Longitudinal Velocity u_x (ms^{-1})

Figure A4.5 c

Appendix 4.3 Shear Velocity Calculation from Reynolds Stress Profiles

(i) Experiment S1B_EX1

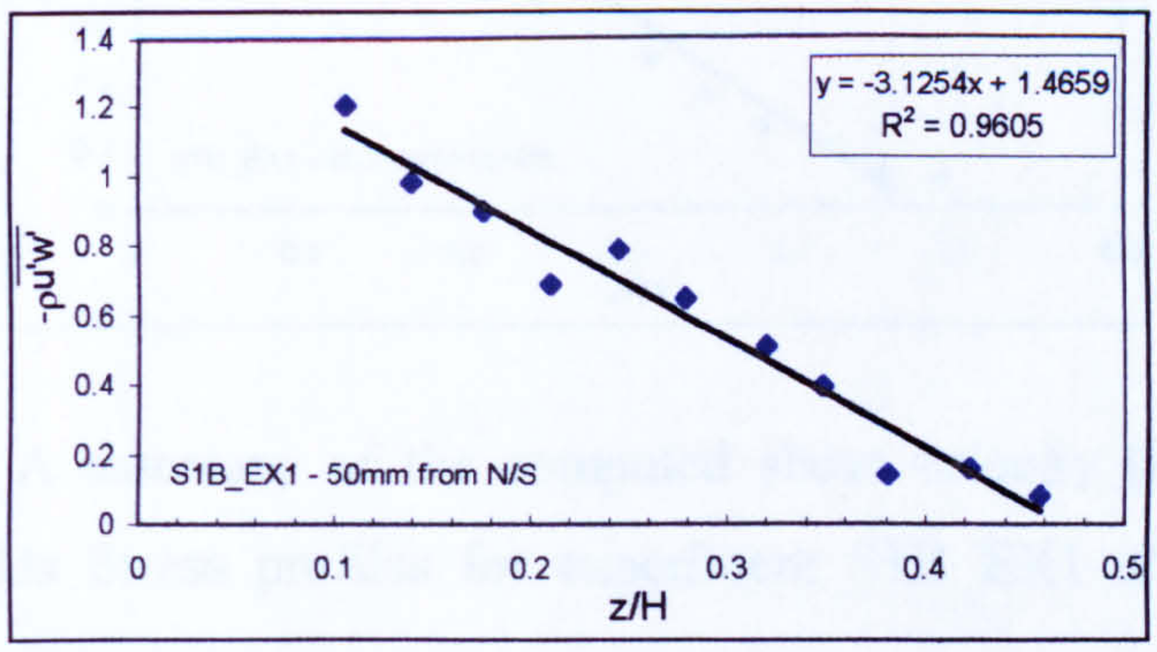

Shear Velocity (u_*) calculated from gradient of trend line (m)

$$m = -\rho u_*^2$$

Therefore:-

$$u_* = sqrt(-m/\rho)$$

$$= \mathbf{0.05591\ ms^{-1}}$$

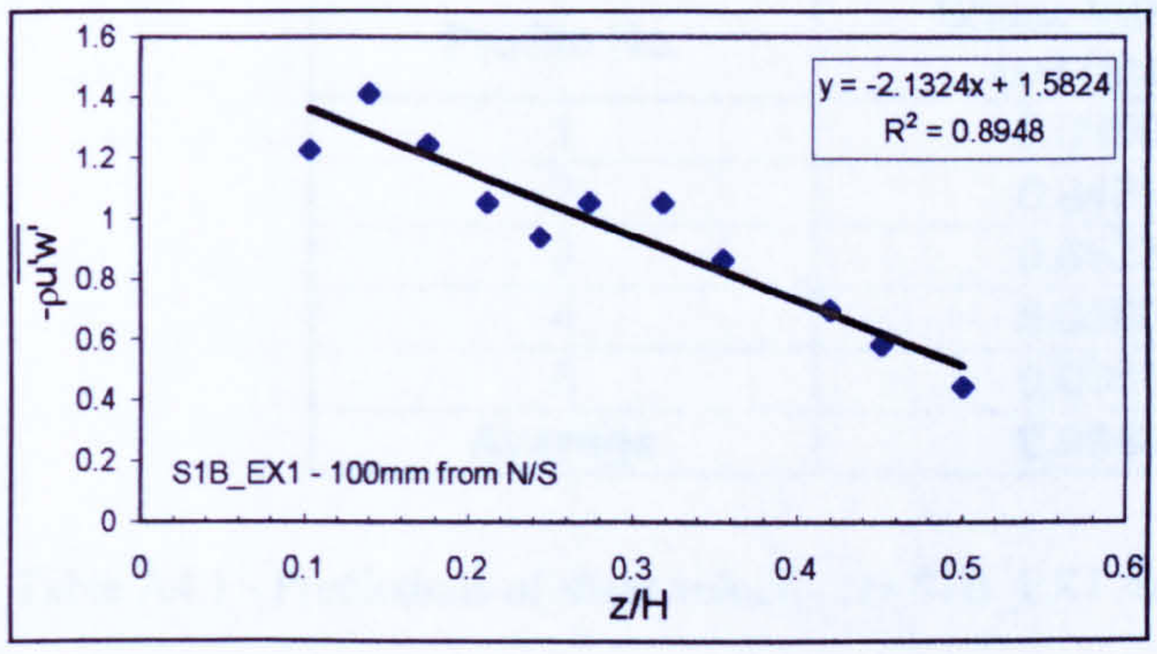

Shear Velocity (u_*) calculated from gradient of trend line (m)

$$m = -\rho u_*^2$$

Therefore:-

$$u_* = sqrt(-m/\rho)$$

$$= \mathbf{0.04618\ ms^{-1}}$$

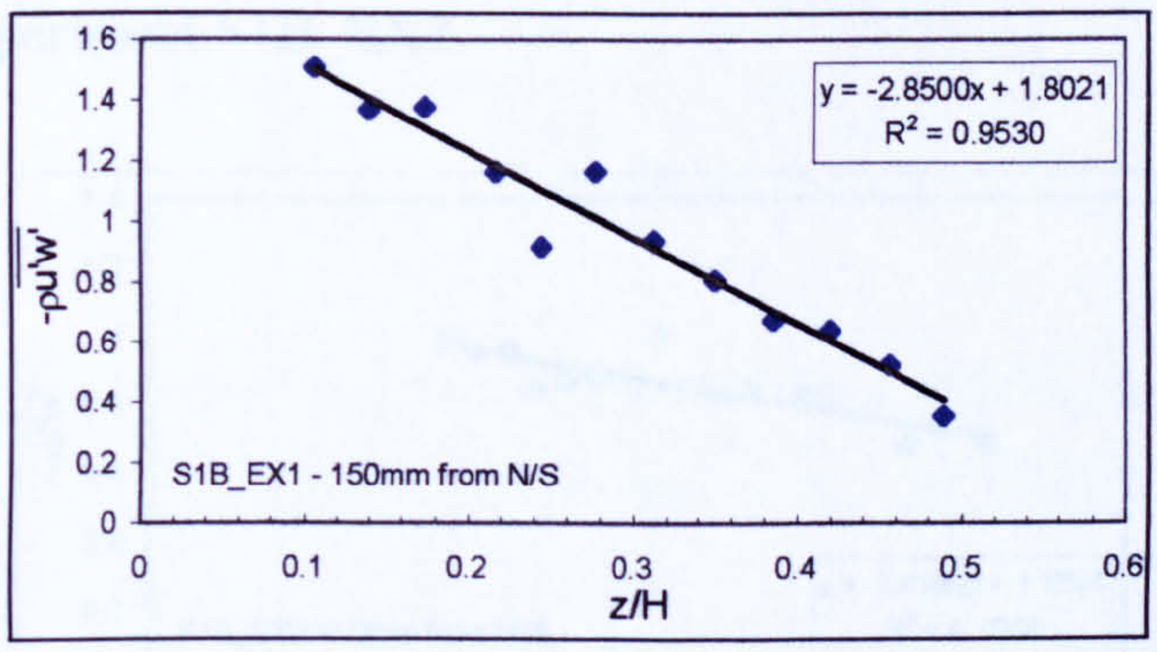

Shear Velocity (u_*) calculated from gradient of trend line (m)

$$m = -\rho u_*^2$$

Therefore:-

$$u_* = sqrt(-m/\rho)$$

$$= \mathbf{0.05339\ ms^{-1}}$$

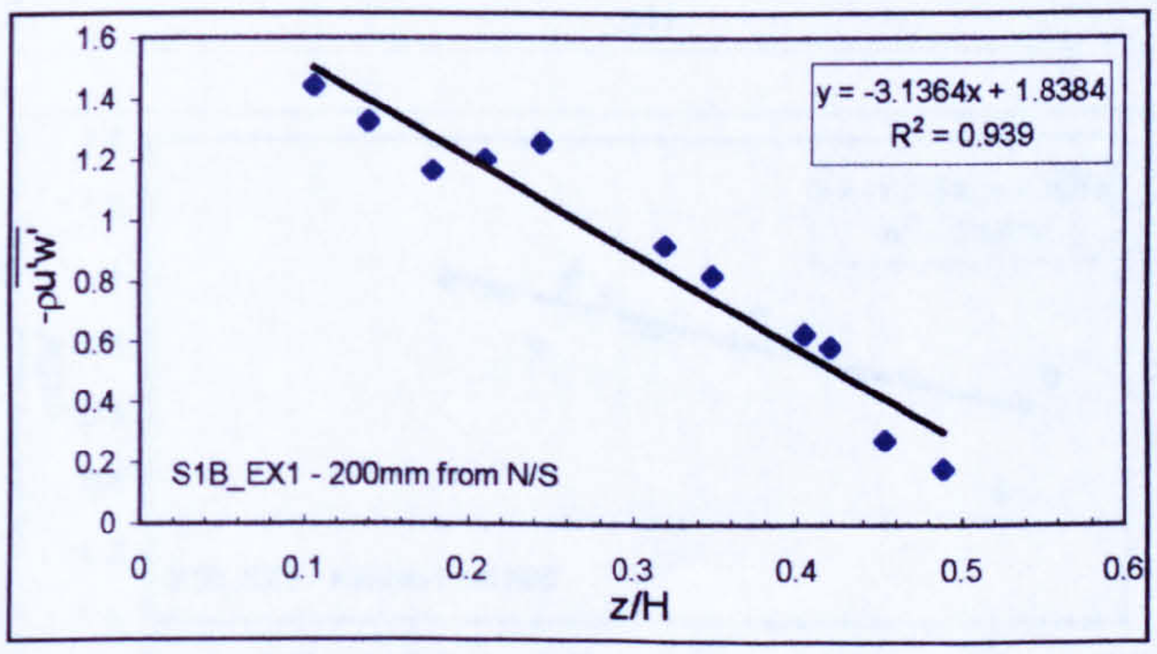

Shear Velocity (u_*) calculated from gradient of trend line (m)

$$m = -\rho u_*^2$$

Therefore:-

$$u_* = sqrt(-m/\rho)$$

$$= \mathbf{0.056\ ms^{-1}}$$

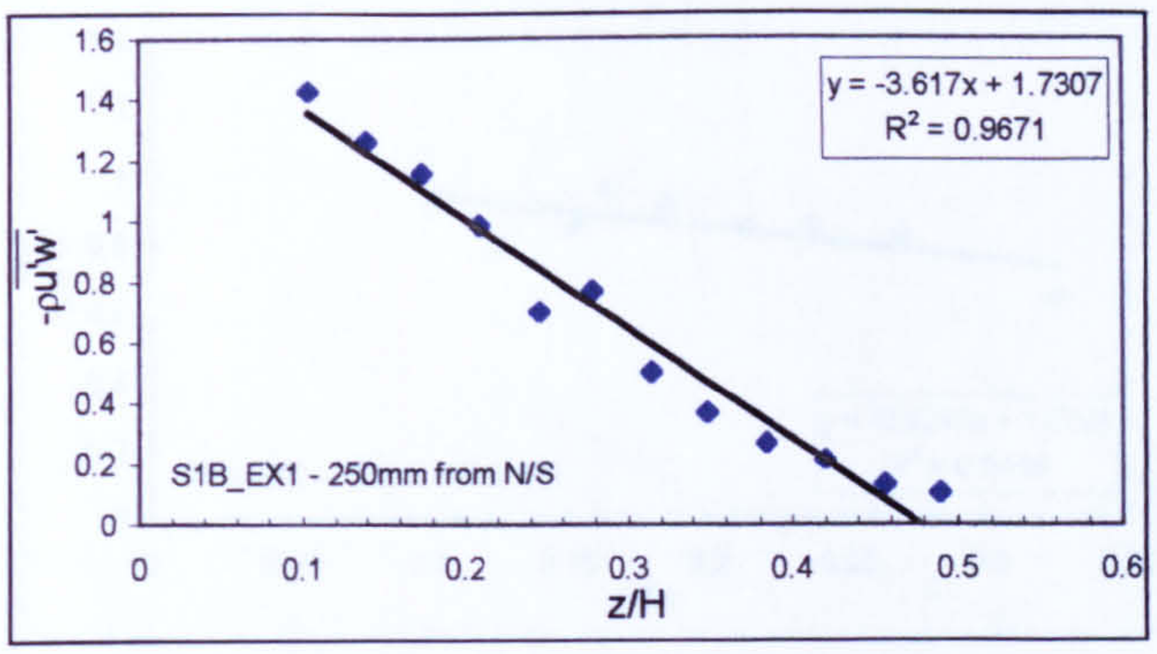

Shear Velocity (u_*) calculated from gradient of trend line (m)

$$m = -\rho u_*^2$$

Therefore:-

$$u_* = sqrt(-m/\rho)$$

$$= \mathbf{0.06014\ ms^{-1}}$$

A summary of the computed shear velocity (u_*) from the ADV measured Reynolds Stress profiles for experiment S1B_EX1 above is given in Table A4.1 below.

Profile No.	Shear Velocity (u_*) (ms^{-1})
1	0.05591
2	0.04618
3	0.05339
4	0.05600
5	0.06014
Average	**0.05432**

Table A4.1 - Predictions of shear velocity for S1B_EX1 from Reynolds stress profiles

(ii) Experiment S1B_EX2

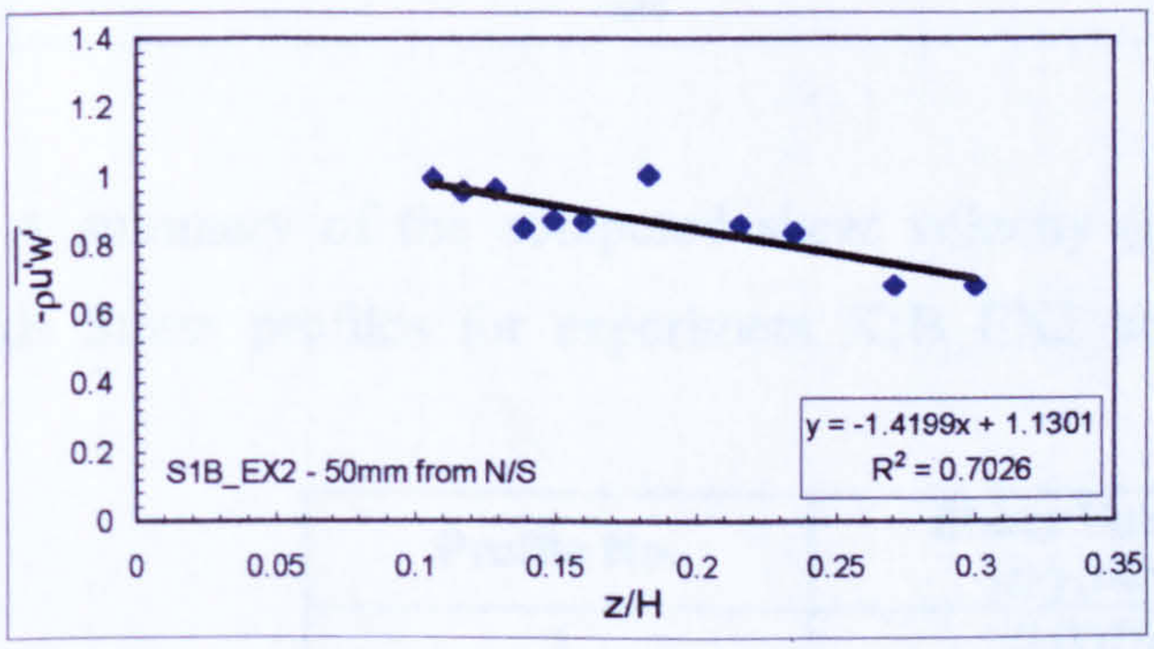

Shear Velocity (u_*) calculated from gradient of trend line (m)

$$m = -\rho u_*^2$$

Therefore:-

$$u_* = sqrt(-m/\rho)$$

$$= \mathbf{0.03768\ ms^{-1}}$$

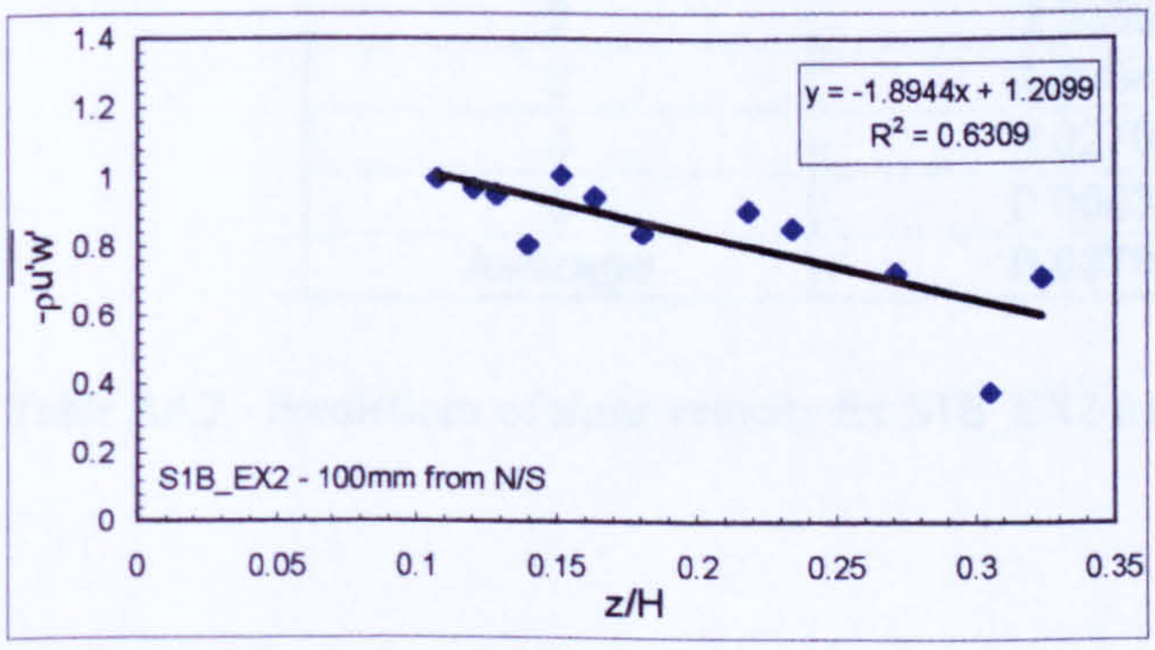

Shear Velocity (u_*) calculated from gradient of trend line (m)

$$m = -\rho u_*^2$$

Therefore:-

$$u_* = sqrt(-m/\rho)$$

$$= \mathbf{0.04352\ ms^{-1}}$$

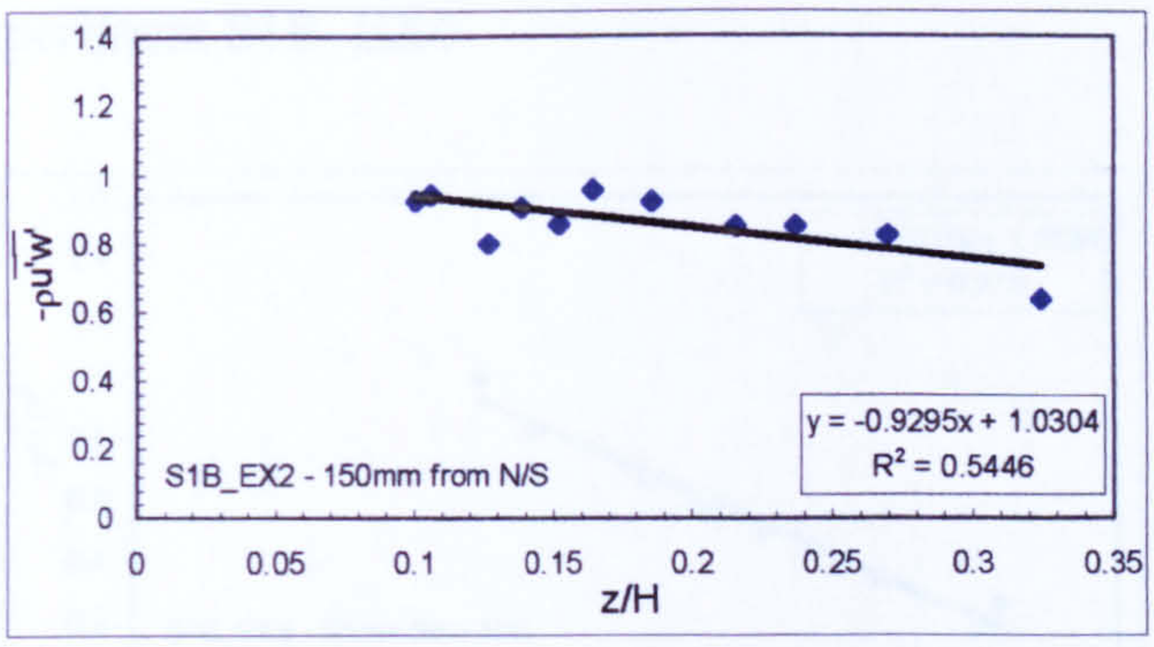

Shear Velocity (u_*) calculated from gradient of trend line (m)

$m = -\rho u_*^2$

Therefore:-

$u_* = sqrt(-m/\rho)$

$= 0.03049\ ms^{-1}$

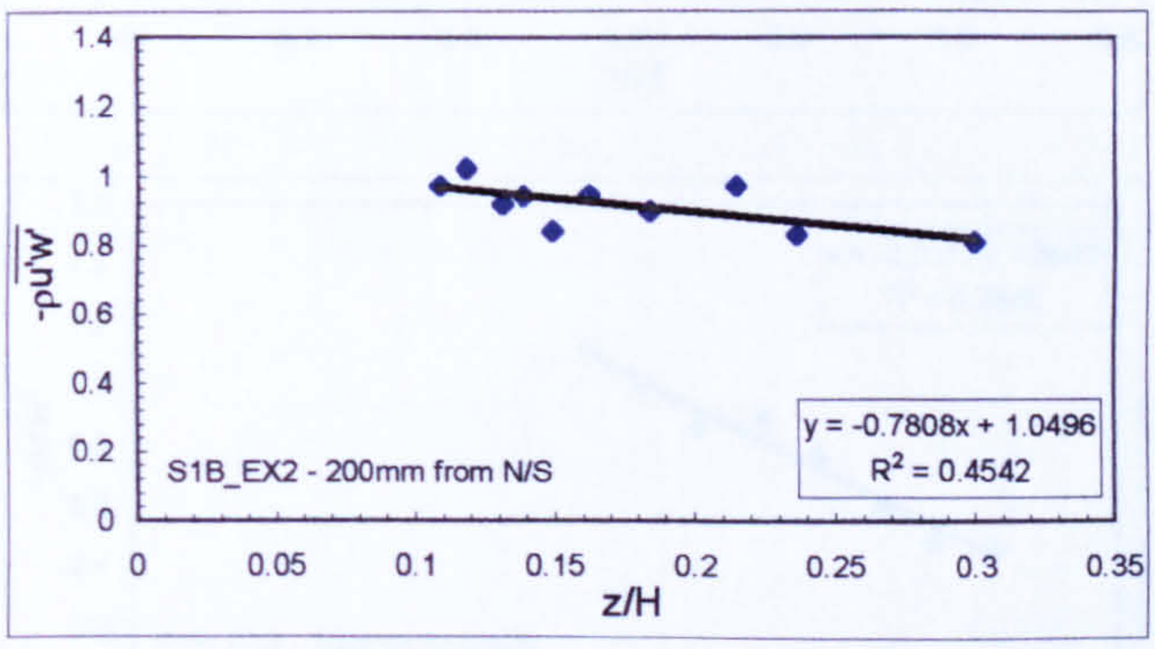

Shear Velocity (u_*) calculated from gradient of trend line (m)

$m = -\rho u_*^2$

Therefore:-

$u_* = sqrt(-m/\rho)$

$= 0.02794\ ms^{-1}$

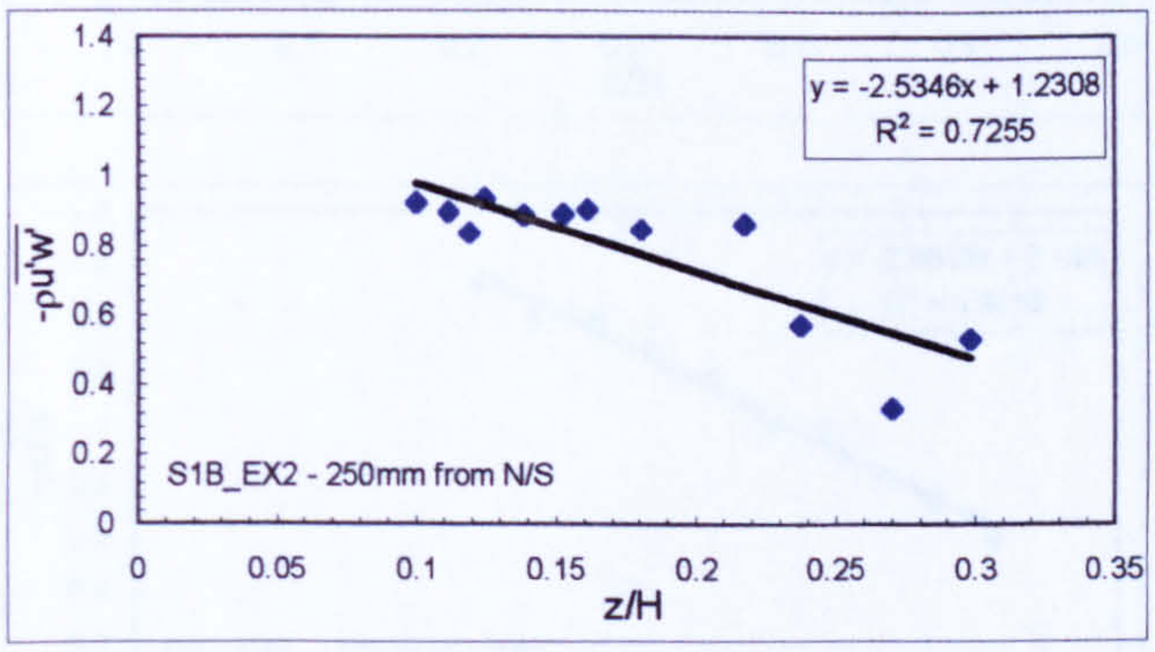

Shear Velocity (u_*) calculated from gradient of trend line (m)

$m = -\rho u_*^2$

Therefore:-

$u_* = sqrt(-m/\rho)$

$= 0.05034\ ms^{-1}$

A summary of the computed shear velocity (u_*) from the ADV measured Reynolds Stress profiles for experiment S1B_EX2 above is given in Table A4.2 below.

Profile No.	Shear Velocity (u_*) (ms^{-1})
1	0.03768
2	0.04352
3	0.03049
4	0.02794
5	0.05034
Average	**0.03799**

Table A4.2 - Predictions of shear velocity for S1B_EX2 from Reynolds stress profiles

(iii) Experiment S1B_EX4

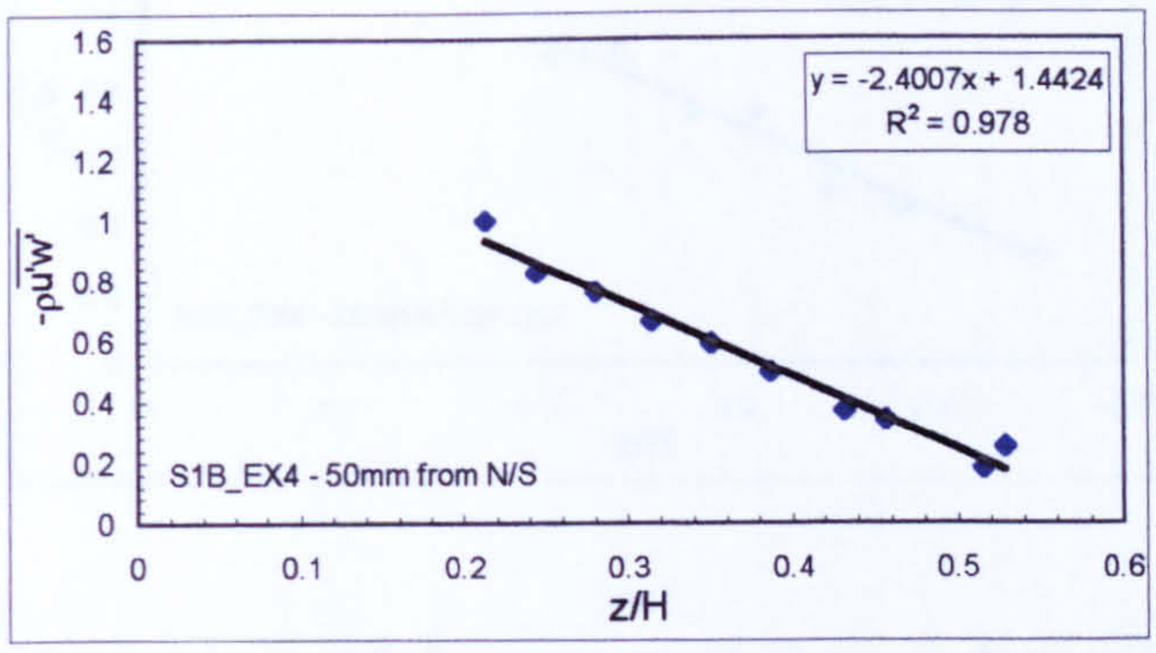

Shear Velocity (u_*) calculated from gradient of trend line (m)

$m = -\rho u_*^2$

Therefore:-

$u_* = sqrt(-m/\rho)$

$= \quad \mathbf{0.049\ ms^{-1}}$

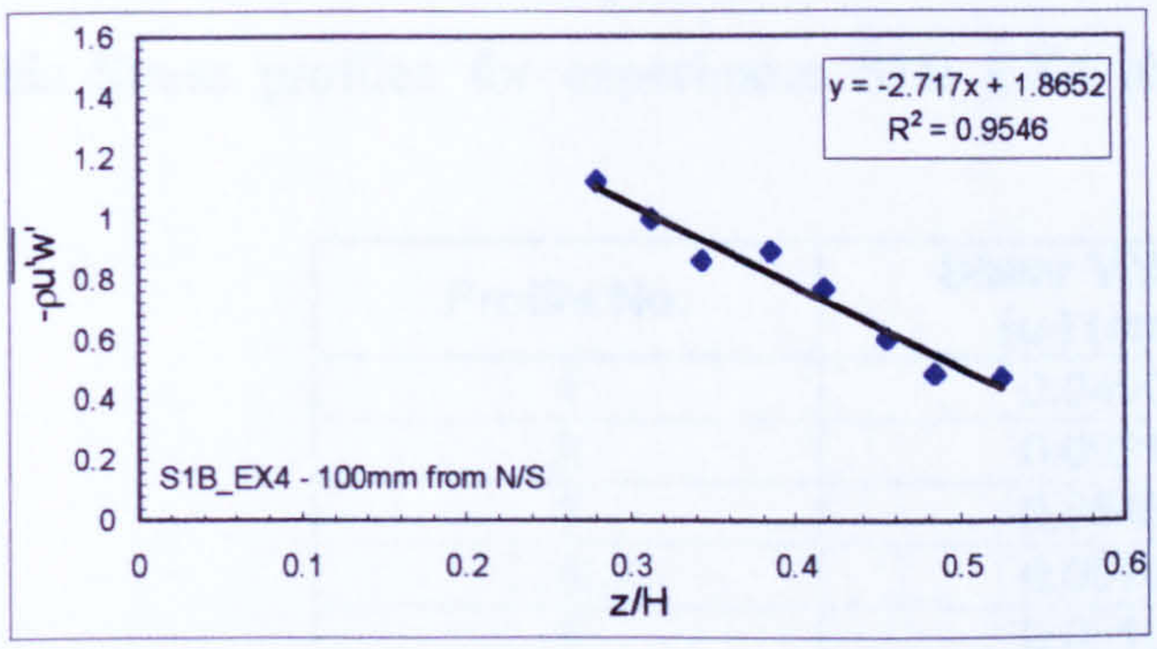

Shear Velocity (u_*) calculated from gradient of trend line (m)

$m = -\rho u_*^2$

Therefore:-

$u_* = sqrt(-m/\rho)$

$= \quad \mathbf{0.05212\ ms^{-1}}$

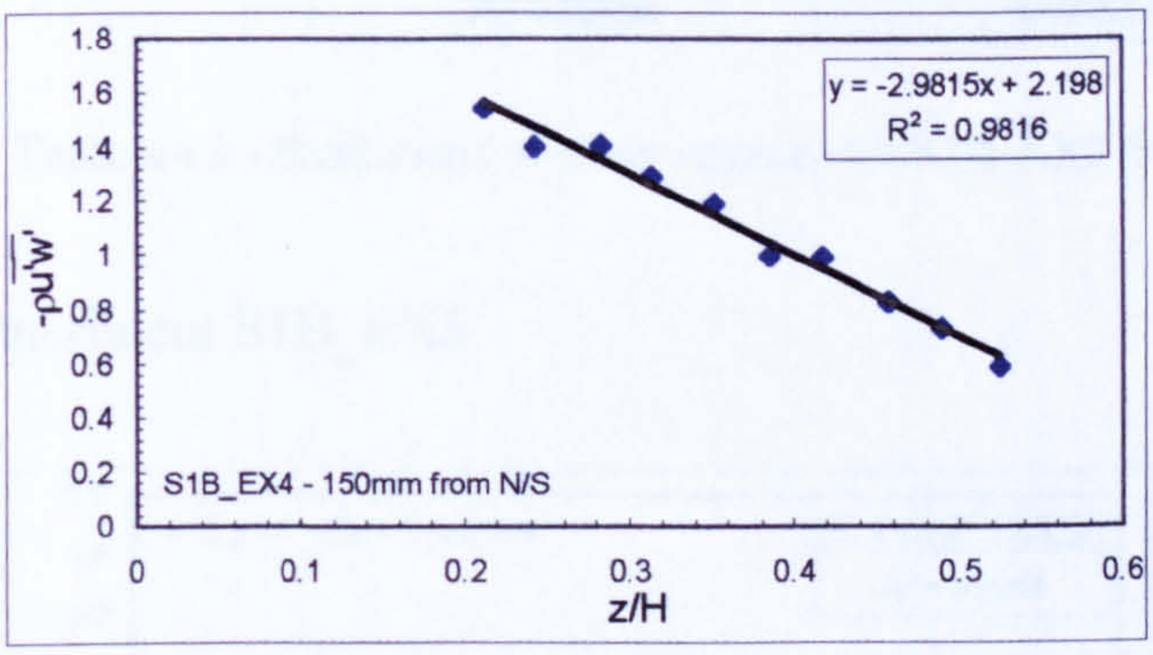

Shear Velocity (u_*) calculated from gradient of trend line (m)

$m = -\rho u_*^2$

Therefore:-

$u_* = sqrt(-m/\rho)$

$= \quad \mathbf{0.0546\ ms^{-1}}$

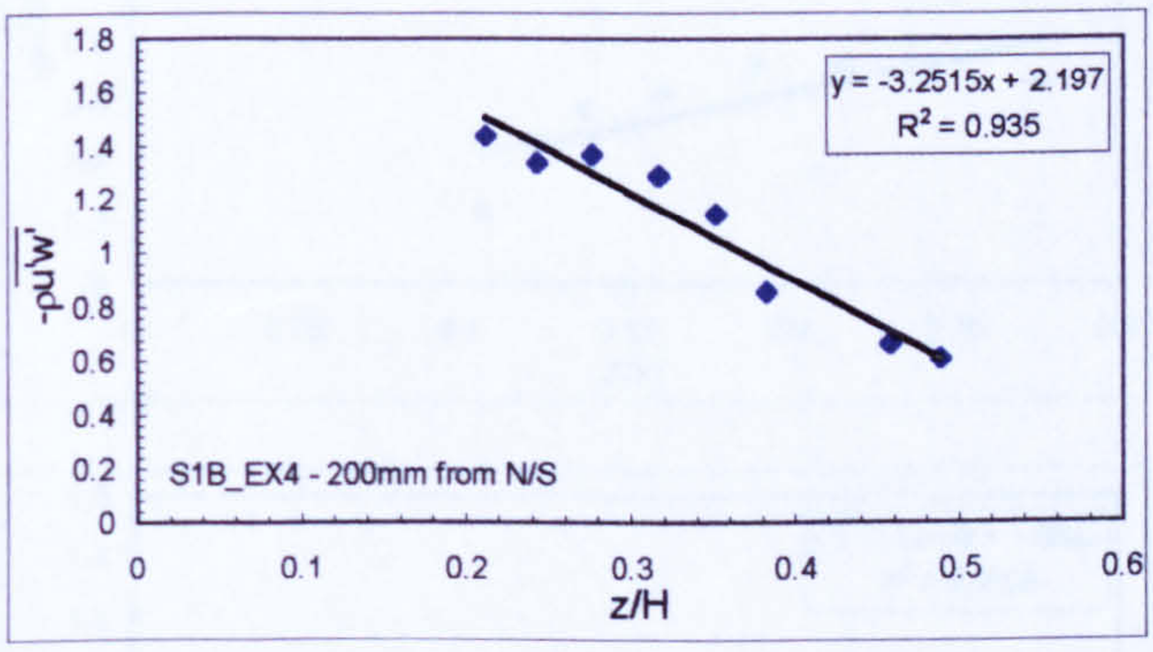

Shear Velocity (u_*) calculated from gradient of trend line (m)

$m = -\rho u_*^2$

Therefore:-

$u_* = sqrt(-m/\rho)$

$= \quad \mathbf{0.05702\ ms^{-1}}$

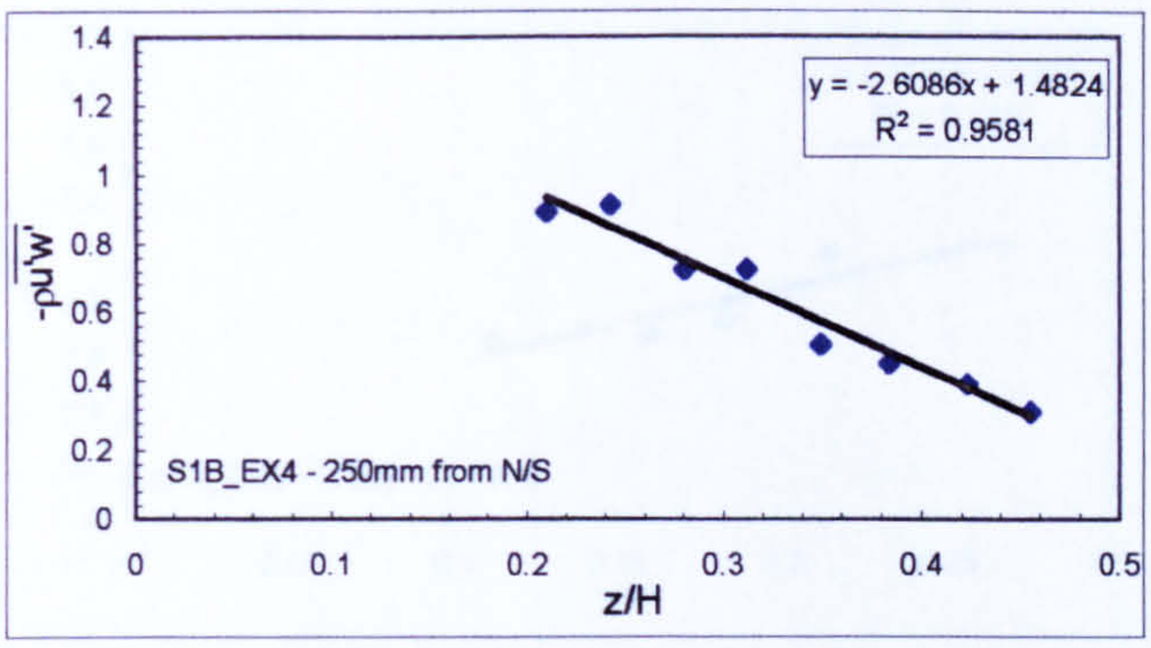

Shear Velocity (u_*) calculated from gradient of trend line (m)

$$m = -\rho u_*^2$$

Therefore:-

$$u_* = sqrt(-m/\rho)$$

$$= \mathbf{0.05107\ ms^{-1}}$$

A summary of the computed shear velocity (u_*) from the ADV measured Reynolds Stress profiles for experiment S1B_EX4 above is given in Table A4.3 below.

Profile No.	Shear Velocity (u_*) (ms^{-1})
1	0.04900
2	0.05212
3	0.05460
4	0.05702
5	0.05107
Average	**0.05276**

Table A4.3 - Predictions of shear velocity for S1B_EX2 from Reynolds stress profiles

(iv) Experiment S1B_EX5

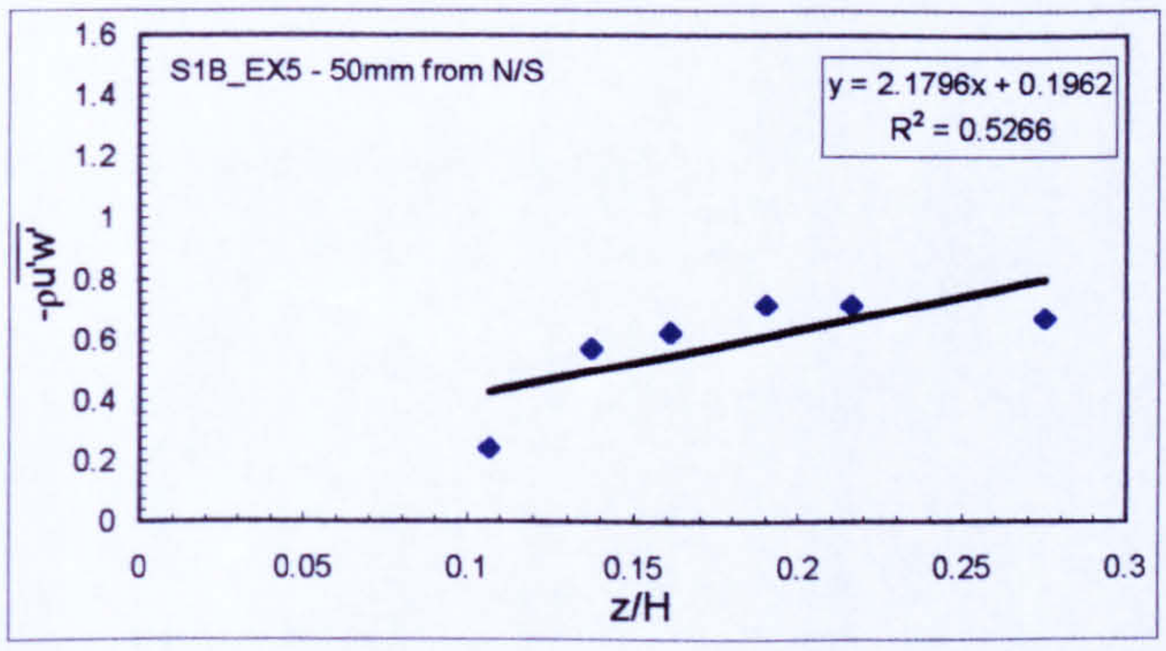

Shear Velocity (u_*) calculated from gradient of trend line (m)

$$m = -\rho u_*^2$$

Therefore:-

$$u_* = sqrt(-m/\rho)$$

$$= \mathbf{\#NUM!\ ms^{-1}}$$

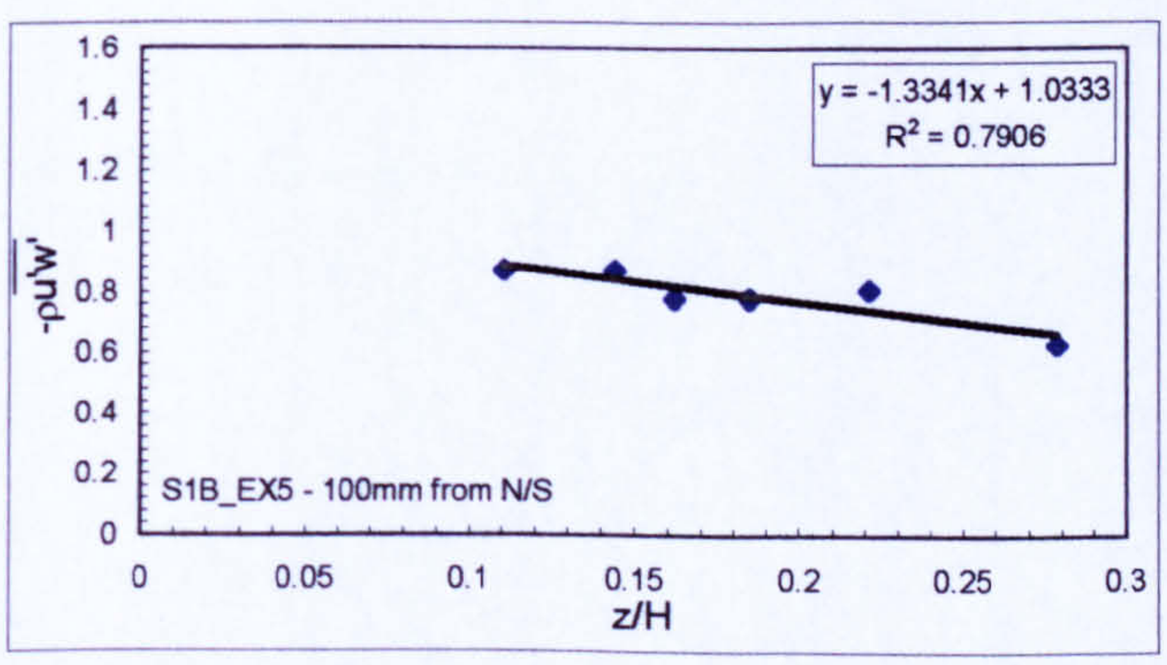

Shear Velocity (u_*) calculated from gradient of trend line (m)

$$m = -\rho u_*^2$$

Therefore:-

$$u_* = sqrt(-m/\rho)$$

$$= \mathbf{0.0365\ ms^{-1}}$$

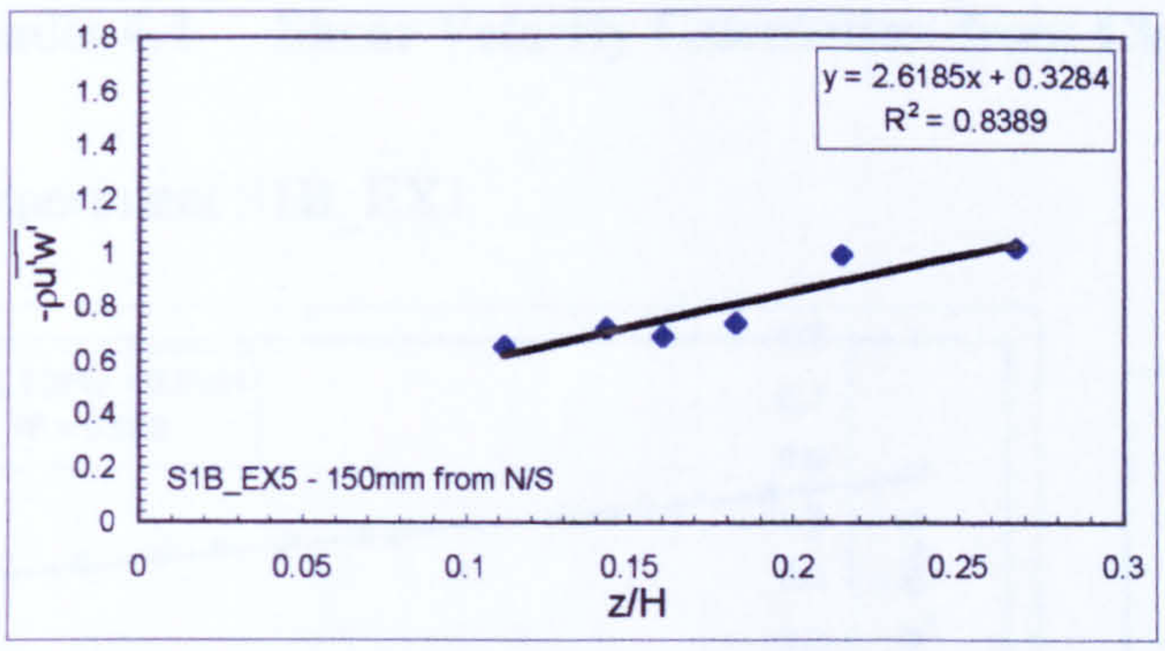

Shear Velocity (u_*) calculated from gradient of trend line (m)

$$m = -\rho u_*^2$$

Therefore:-

$$u_* = sqrt(-m/\rho)$$

$$= \text{\#NUM!} \quad ms^{-1}$$

A summary of the computed shear velocity (u_*) from the ADV measured Reynolds Stress profiles for experiment S1B_EX5 above is given in Table A4.4 below.

Profile No.	Shear Velocity (u_*) (ms^{-1})
1	-
2	0.0365
3	-
Average	**-**

Table A4.4 - Predictions of shear velocity for S1B_EX5 from Reynolds stress profiles

Appendix 4.4 Shear Velocity Calculation from Clauser (1956) Method

(i) Experiment S1B_EX1

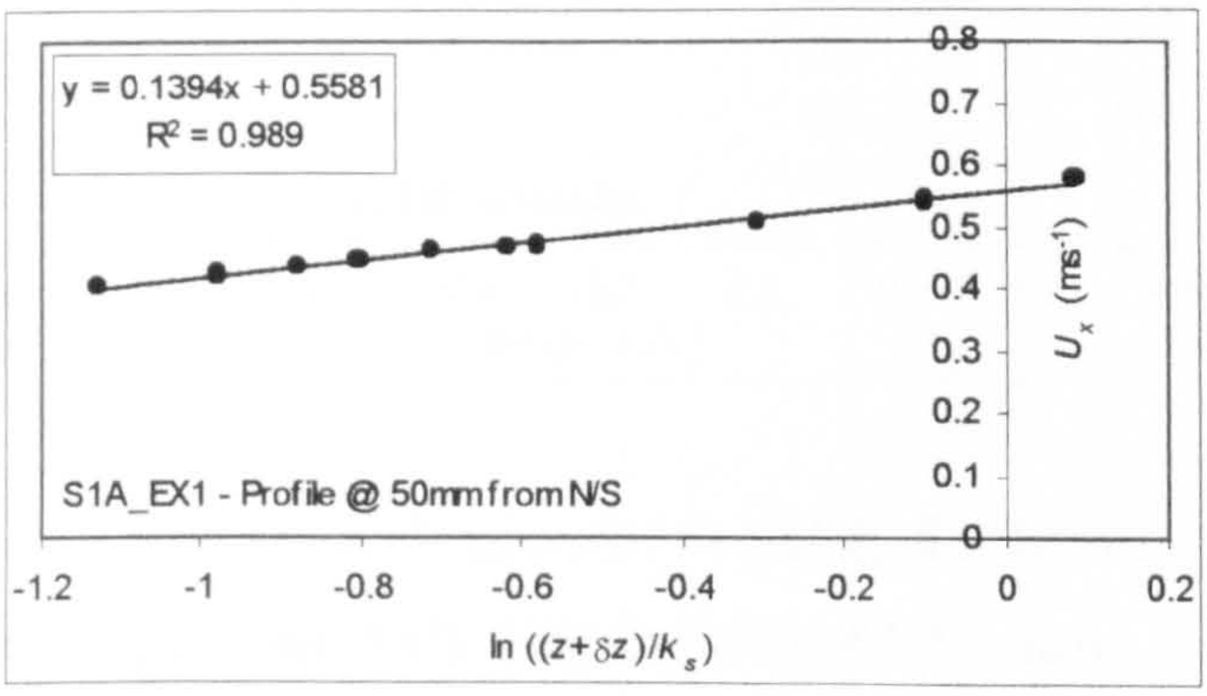

Shear velocity (u_*) and constant of integration (B_r) from gradient (m) and constant (C):-

$m = u_*/\kappa$ (where $\kappa = 0.4$).
$C = u_* B_r$

Therefore:-

$\boldsymbol{u_* = m\kappa = 0.05576\ ms^{-1}}$
$\boldsymbol{B_r = C/u_* = 10.009}$

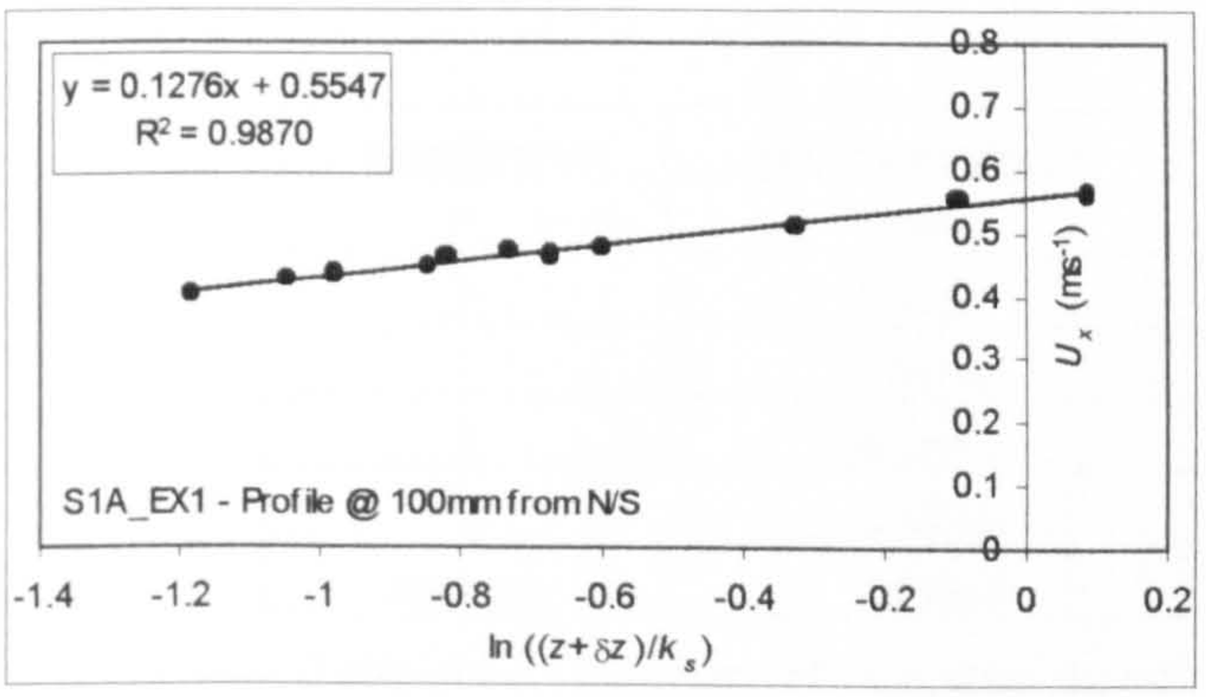

Shear velocity (u_*) and constant of integration (B_r) from gradient (m) and constant (C):-

$m = u_*/\kappa$ (where $\kappa = 0.4$).
$C = u_* B_r$

Therefore:-

$\boldsymbol{u_* = m\kappa = 0.05104\ ms^{-1}}$
$\boldsymbol{B_r = C/u_* = 10.868}$

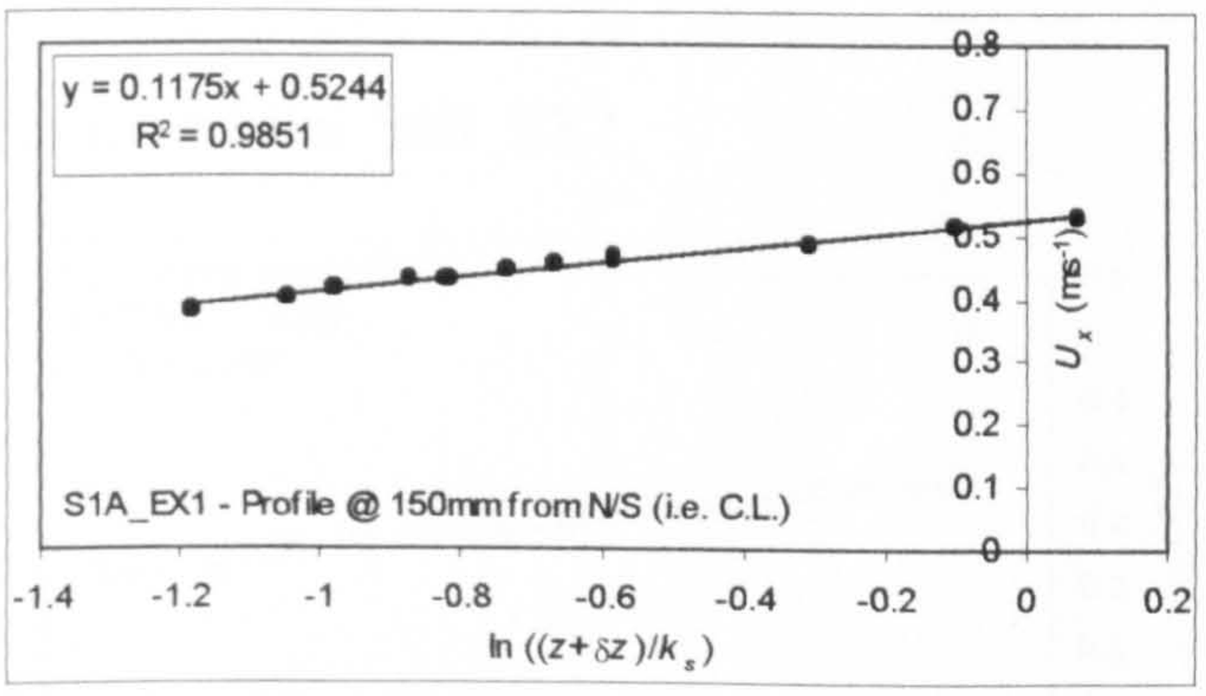

Shear velocity (u_*) and constant of integration (B_r) from gradient (m) and constant (C):-

$m = u_*/\kappa$ (where $\kappa = 0.4$).
$C = u_* B_r$

Therefore:-

$\boldsymbol{u_* = m\kappa = 0.0470\ ms^{-1}}$
$\boldsymbol{B_r = C/u_* = 11.157}$

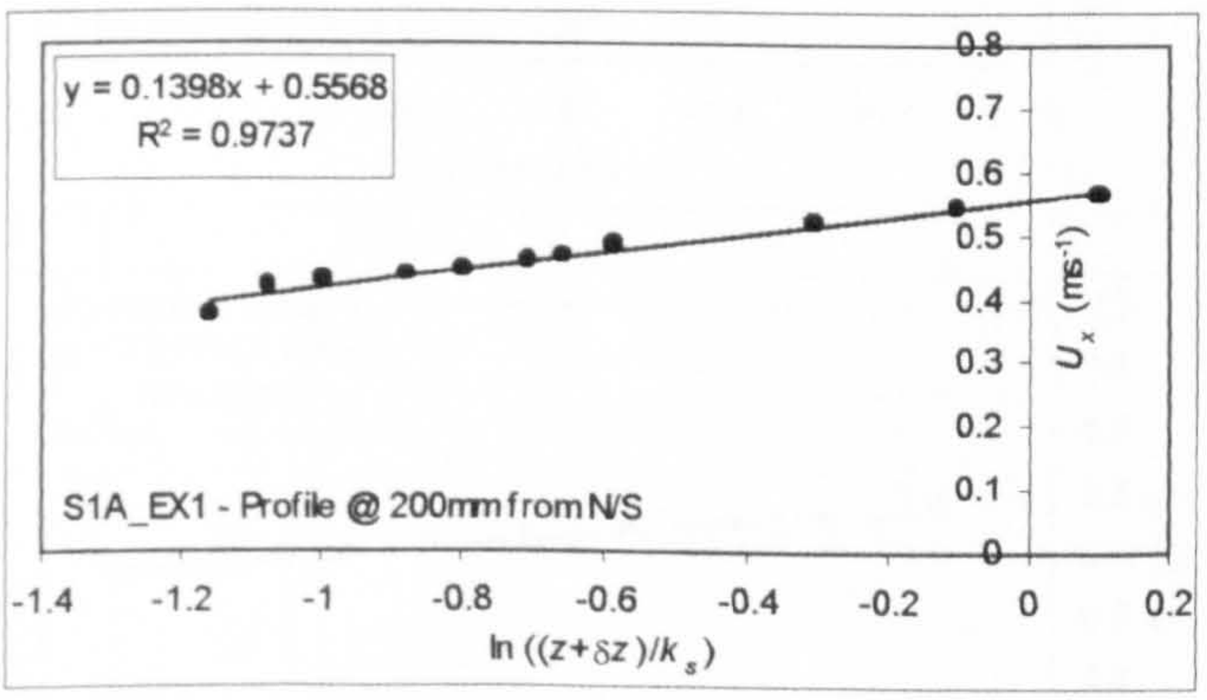

Shear velocity (u_*) and constant of integration (B_r) from gradient (m) and constant (C):-

$m = u_*/\kappa$ (where $\kappa = 0.4$).
$C = u_* B_r$

Therefore:-

$\boldsymbol{u_* = m\kappa = 0.05592\ ms^{-1}}$
$\boldsymbol{B_r = C/u_* = 9.957}$

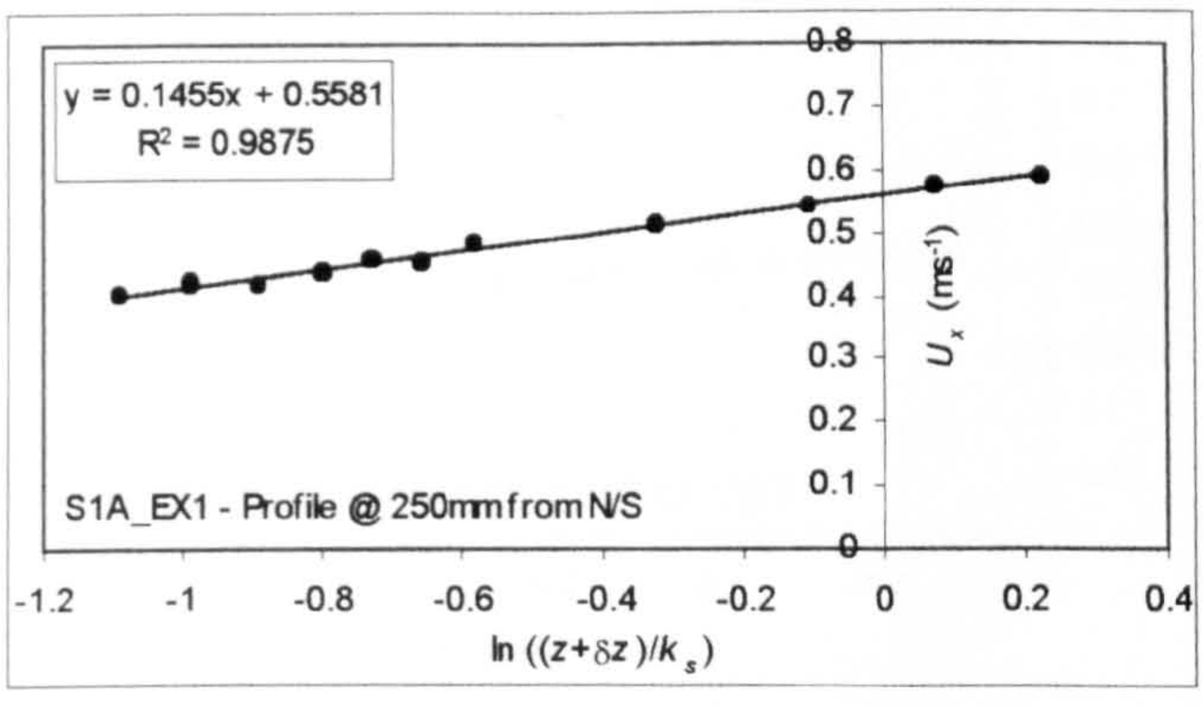

Shear velocity (u_*) and constant of integration (B_r) from gradient (m) and constant (C):-

$m = u_*/\kappa$ (where $\kappa = 0.4$).
$C = u_* B_r$

Therefore:-

$\boldsymbol{u_* = m\kappa = 0.0582\ ms^{-1}}$
$\boldsymbol{B_r = C/u_* = 9.589}$

Calculated values of u_* and B_r for the measured ADV profiles are summaried for experiment S1B_EX1 in Table A4.5 below.

Profile Number	Shear Velocity (u_*)	Integration Const. (B_r)
1	0.05576	10.009
2	0.05104	10.868
3	0.04700	11.157
4	0.05592	9.957
5	0.05820	9.589
Average	**0.05358**	**10.316**

Table A4.5 - Summary of calculated u_* and B_r for experiment S1B_EX1

(ii) Experiment S1B_EX2

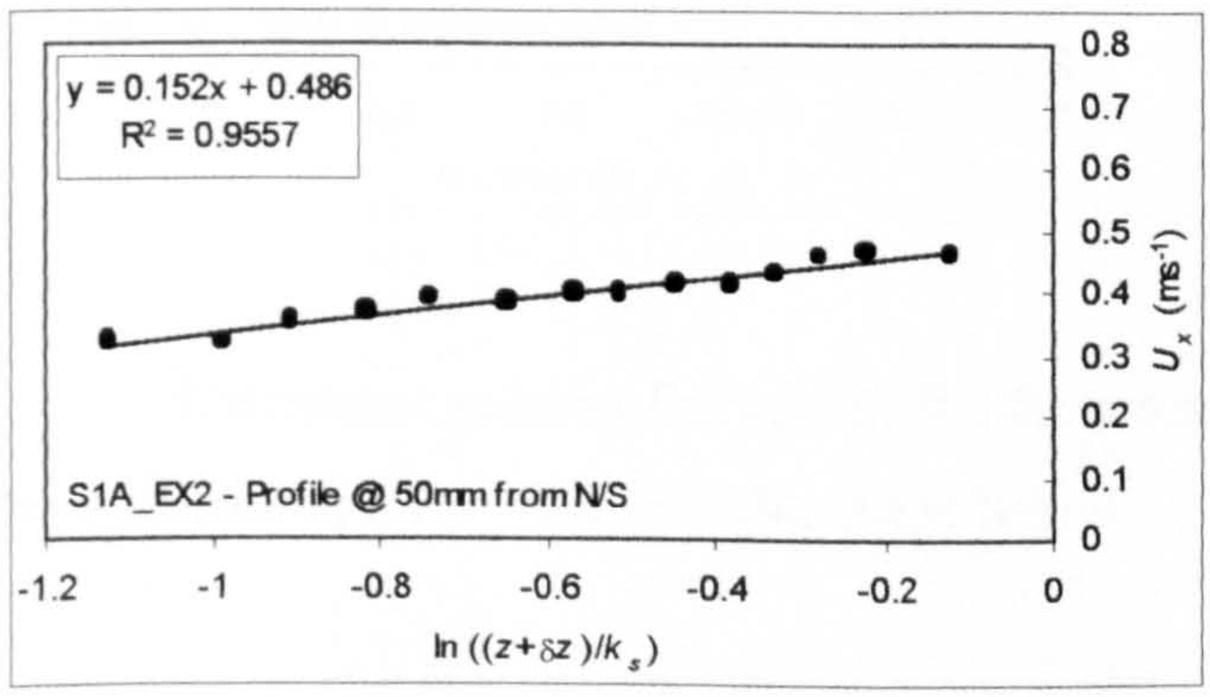

Shear velocity (u_*) and constant of integration (B_r) from gradient (m) and constant (C):-

$m = u_*/\kappa$ (where $\kappa = 0.4$).
$C = u_* B_r$

Therefore:-

$\boldsymbol{u_* = m\kappa = 0.0608\ ms^{-1}}$
$\boldsymbol{B_r = C/u_* = 7.993}$

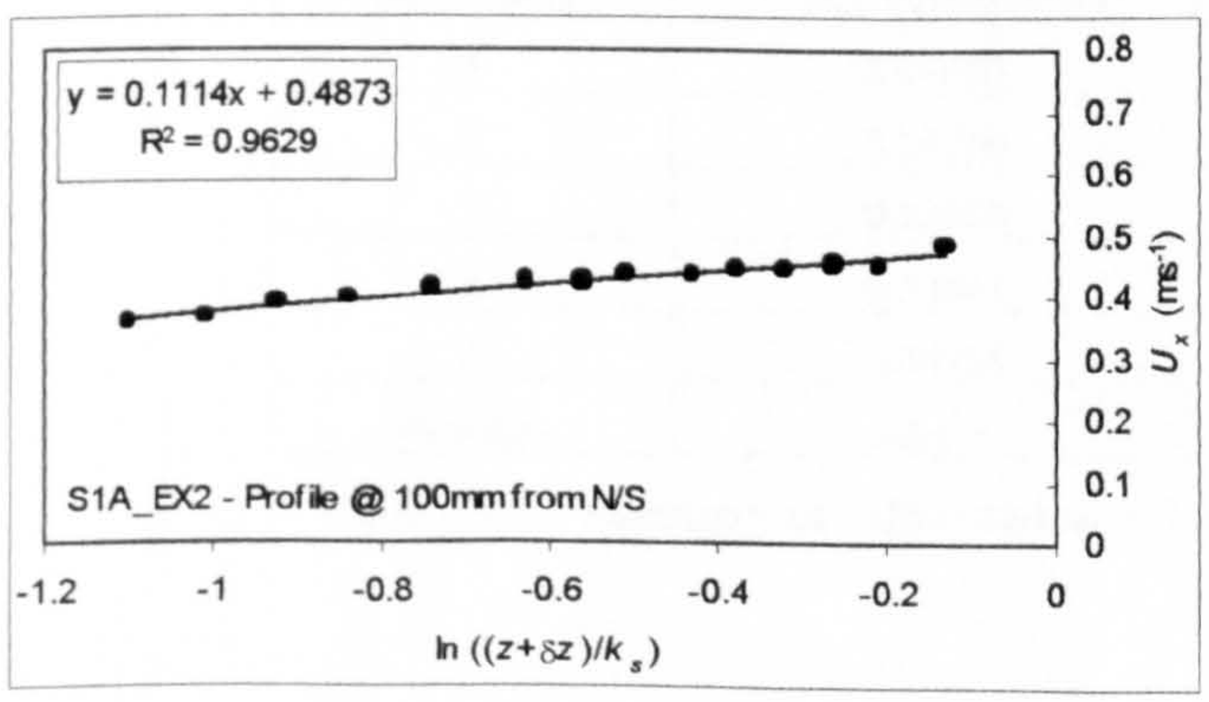

Shear velocity (u_*) and constant of integration (B_r) from gradient (m) and constant (C):-

$m = u_*/\kappa$ (where $\kappa = 0.4$).
$C = u_* B_r$

Therefore:-

$\boldsymbol{u_* = m\kappa = 0.04456\ ms^{-1}}$
$\boldsymbol{B_r = C/u_* = 10.936}$

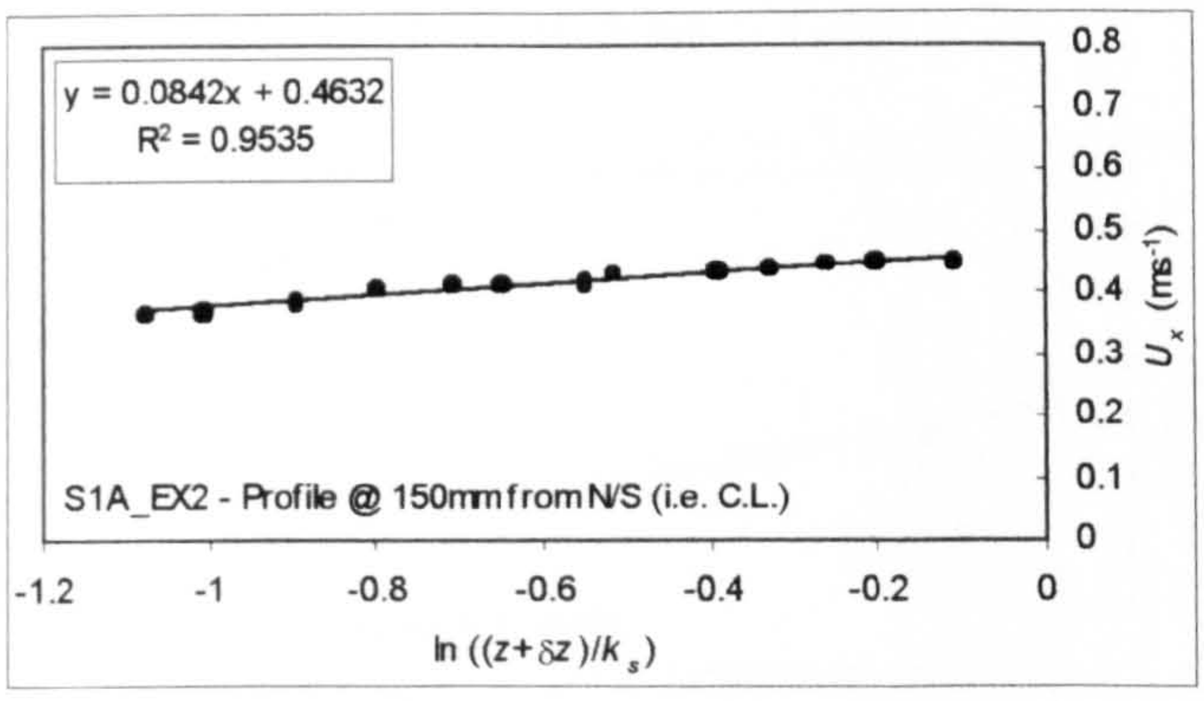

Shear velocity (u_*) and constant of integration (B_r) from gradient (m) and constant (C):-

$m = u_*/\kappa$ (where $\kappa = 0.4$).
$C = u_* B_r$

Therefore:-

$\boldsymbol{u_* = m\kappa = 0.03368\ ms^{-1}}$
$\boldsymbol{B_r = C/u_* = 13.753}$

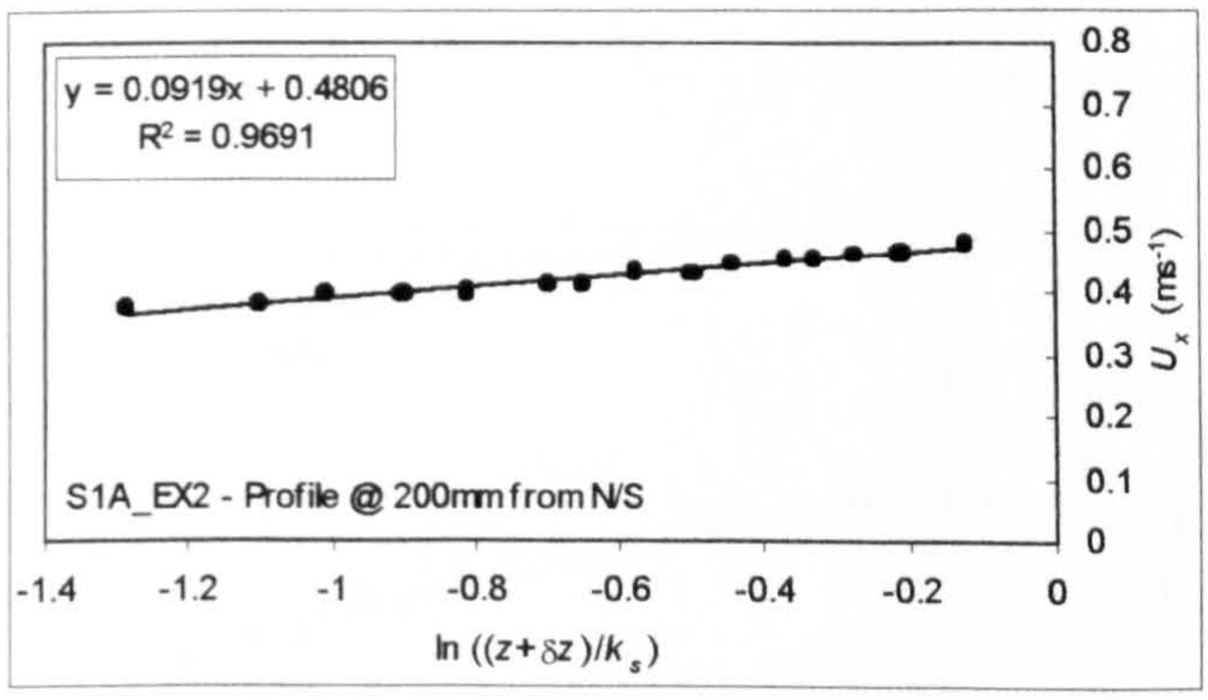

Shear velocity (u_*) and constant of integration (B_r) from gradient (m) and constant (C):-

$m = u_*/\kappa$ (where $\kappa = 0.4$).
$C = u_* B_r$

Therefore:-

$\boldsymbol{u_* = m\kappa = 0.03676\ ms^{-1}}$
$\boldsymbol{B_r = C/u_* = 13.074}$

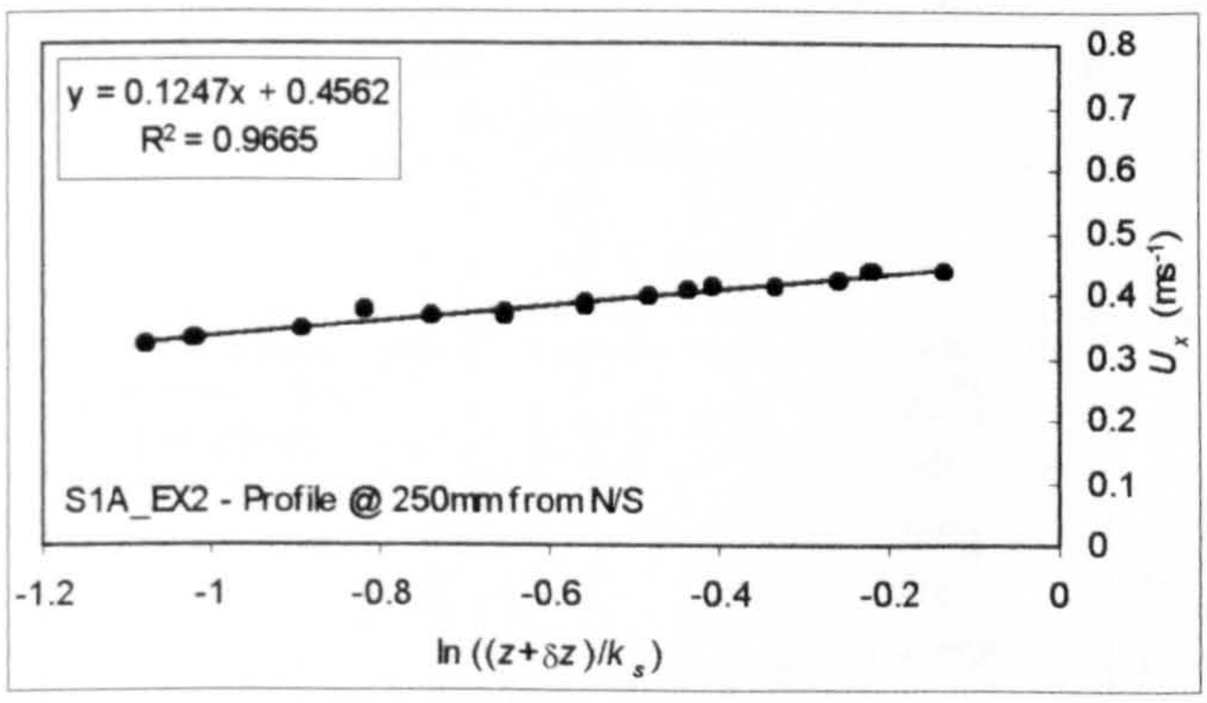

Shear velocity (u_*) and constant of integration (B_r) from gradient (m) and constant (C):-

$m = u_*/\kappa$ (where $\kappa = 0.4$).
$C = u_* B_r$

Therefore:-

$\boldsymbol{u_* = m\kappa = 0.04988\ ms^{-1}}$
$\boldsymbol{B_r = C/u_* = 9.146}$

Calculated values of u_* and B_r for the measured ADV profiles are summaried for experiment S1B_EX2 in Table A4.6 below.

Profile Number	Shear Velocity (u_*)	Integration Const. (B_r)
1	0.06080	7.993
2	0.04456	10.936
3	0.03368	13.753
4	0.03676	13.074
5	0.04988	9.146
Average	**0.0451**	**10.980**

Table A4.6 - Summary of calculated u_* and B_r for experiment S1B_EX2

(iii) Experiment S1B_EX4

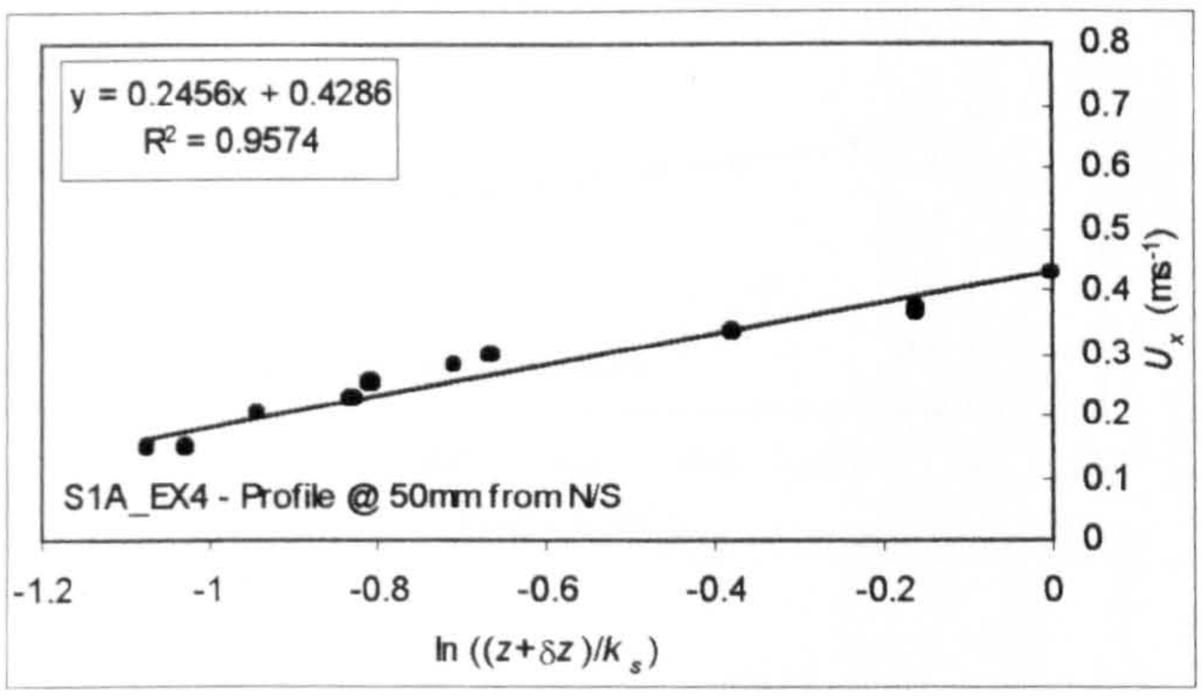

Shear velocity (u_*) and constant of integration (B_r) from gradient (m) and constant (C):-

$m = u_*/\kappa$ (where $\kappa = 0.4$).
$C = u_* B_r$

Therefore:-

$\boldsymbol{u_* = m\kappa = 0.09824\ ms^{-1}}$
$\boldsymbol{B_r = C/u_* = 4.363}$

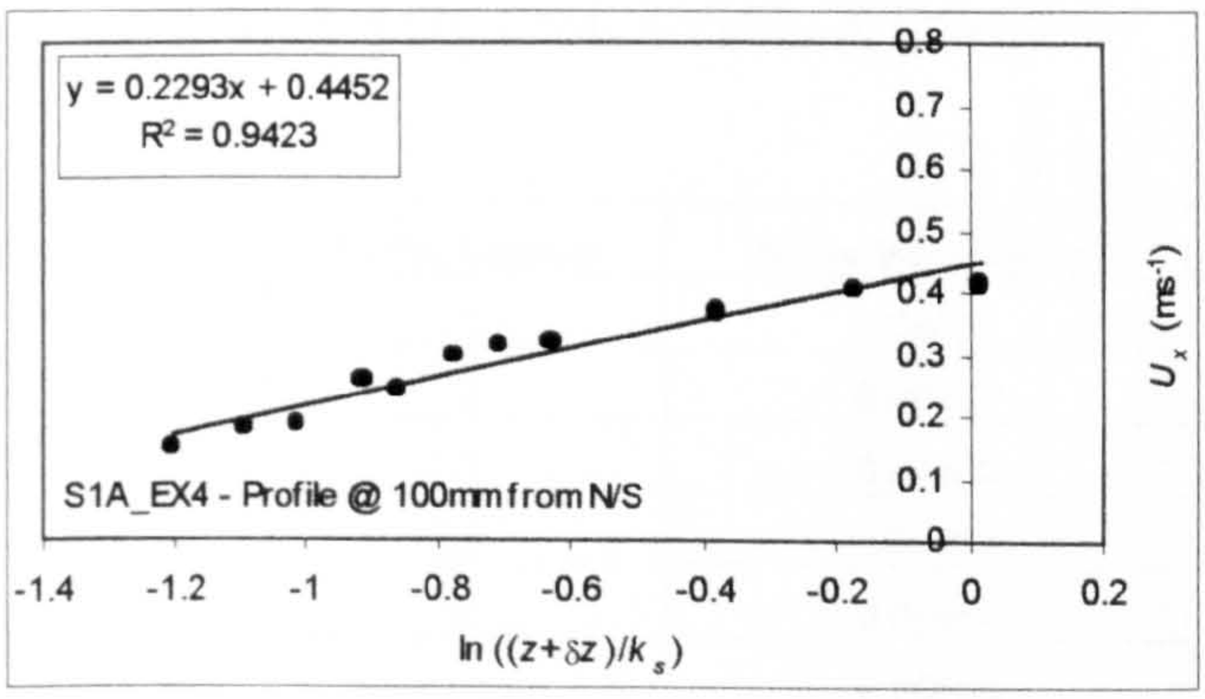

Shear velocity (u_*) and constant of integration (B_r) from gradient (m) and constant (C):-

$m = u_*/\kappa$ (where $\kappa = 0.4$).
$C = u_* B_r$

Therefore:-

$\boldsymbol{u_* = m\kappa = 0.09172\ ms^{-1}}$
$\boldsymbol{B_r = C/u_* = 4.854}$

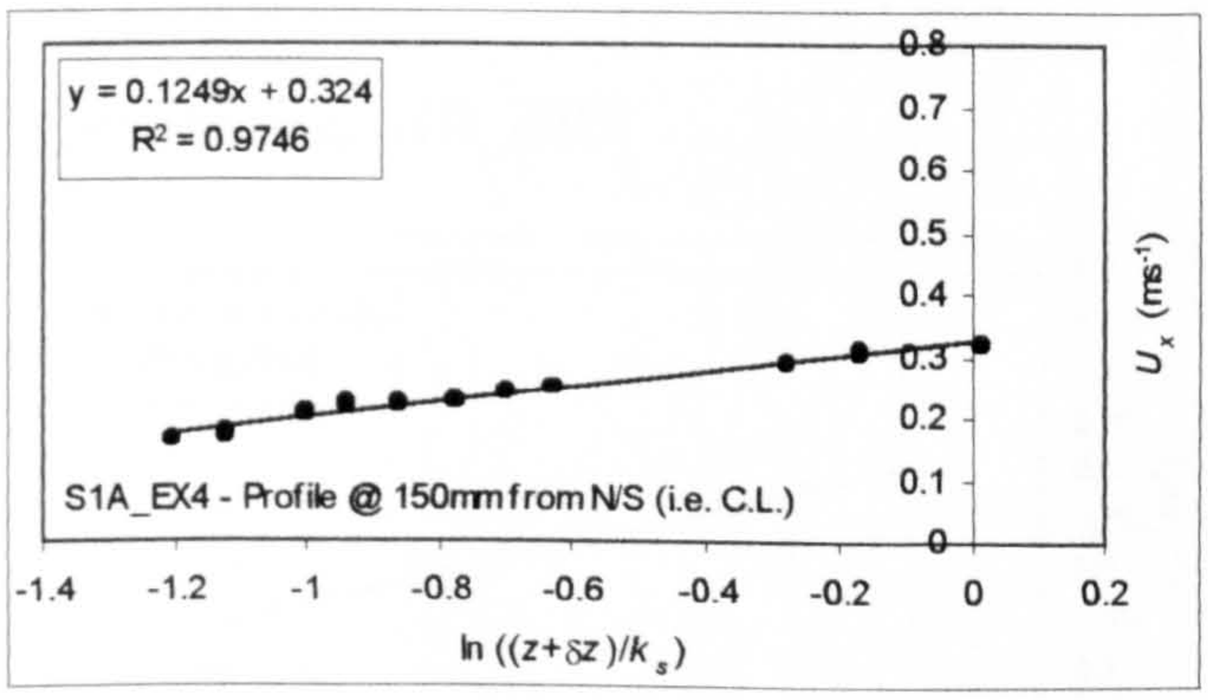

Shear velocity (u_*) and constant of integration (B_r) from gradient (m) and constant (C):-

$m = u_*/\kappa$ (where $\kappa = 0.4$).
$C = u_* B_r$

Therefore:-

$\boldsymbol{u_* = m\kappa = 0.04996\ ms^{-1}}$
$\boldsymbol{B_r = C/u_* = 6.485}$

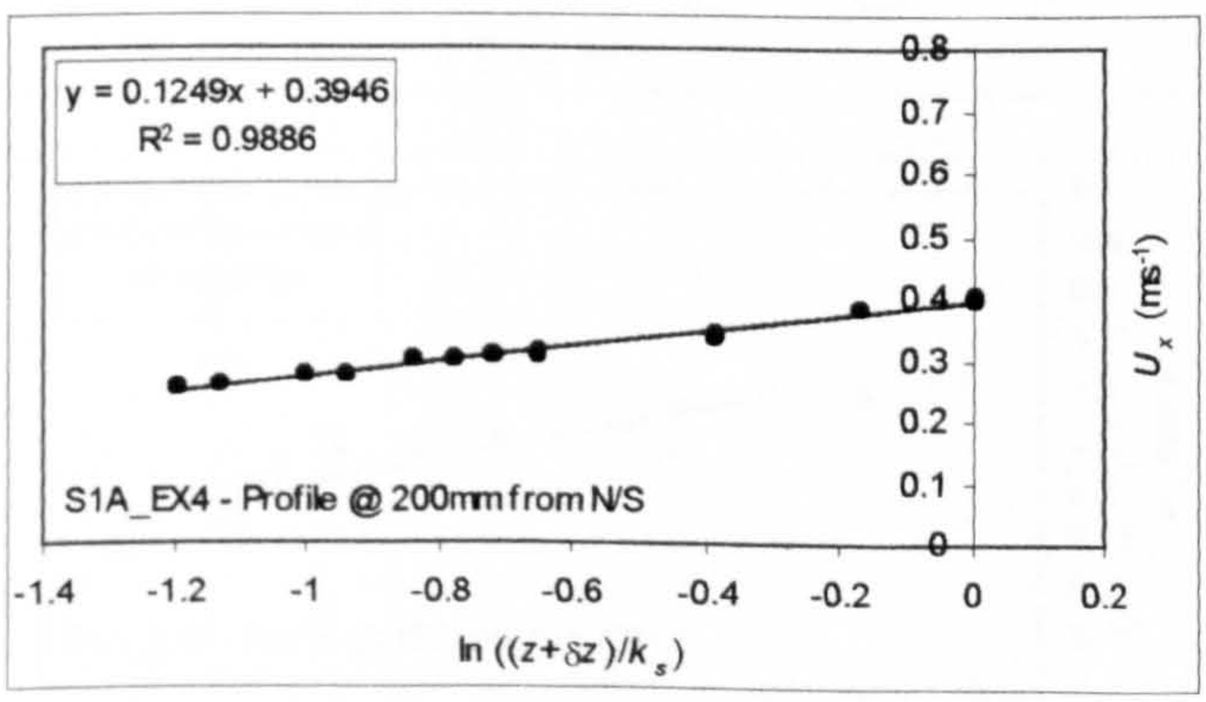

Shear velocity (u_*) and constant of integration (B_r) from gradient (m) and constant (C):-

$m = u_*/\kappa$ (where $\kappa = 0.4$).
$C = u_* B_r$

Therefore:-

$\boldsymbol{u_* = m\kappa = 0.04996\ ms^{-1}}$
$\boldsymbol{B_r = C/u_* = 7.898}$

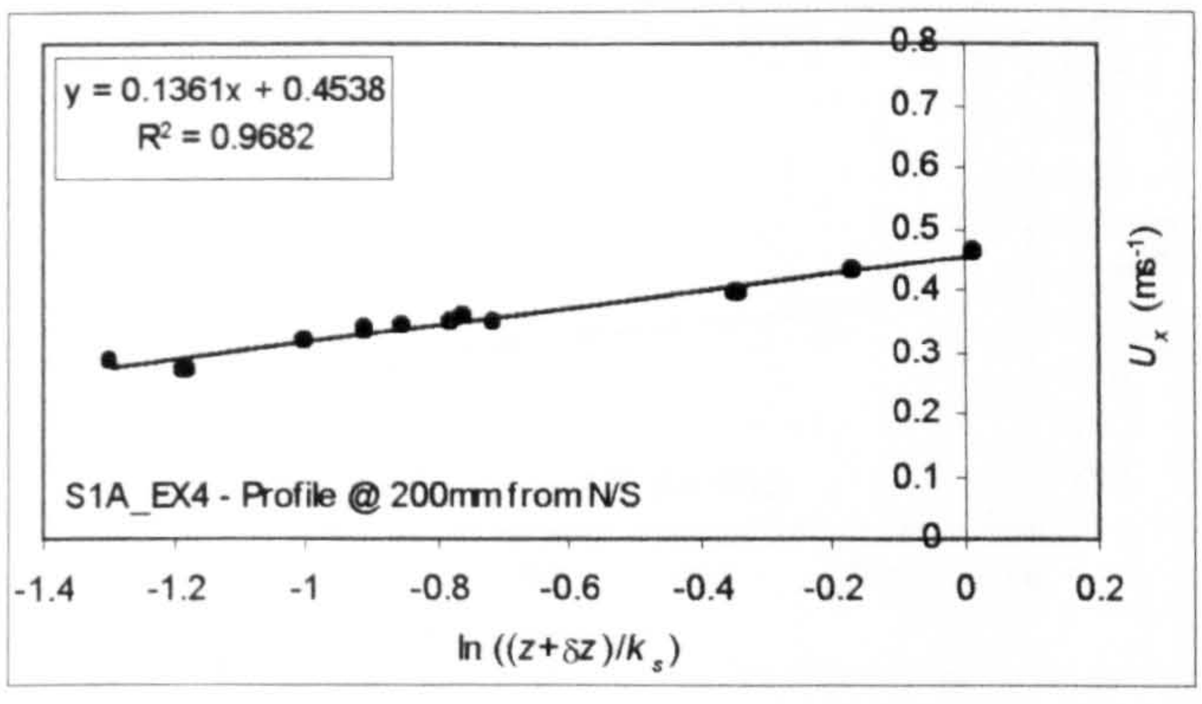

Shear velocity (u_*) and constant of integration (B_r) from gradient (m) and constant (C):-

$m = u_*/\kappa$ (where $\kappa = 0.4$).
$C = u_* B_r$

Therefore:-

$\boldsymbol{u_* = m\kappa = 0.05444\ ms^{-1}}$
$\boldsymbol{B_r = C/u_* = 8.336}$

Calculated values of u_* and B_r for the measured ADV profiles are summaried for experiment S1B_EX4 in Table A4.7 below.

Profile Number	Shear Velocity (u_*)	Integration Const. (B_r)
1	0.09824	4.363
2	0.09172	4.854
3	0.04996	6.485
4	0.04996	7.898
5	0.05444	8.336
Average	**0.06886**	**6.387**

Table A4.7 - Summary of calculated u_* and B_r for experiment S1B_EX4

(iv) Experiment S1B_EX5

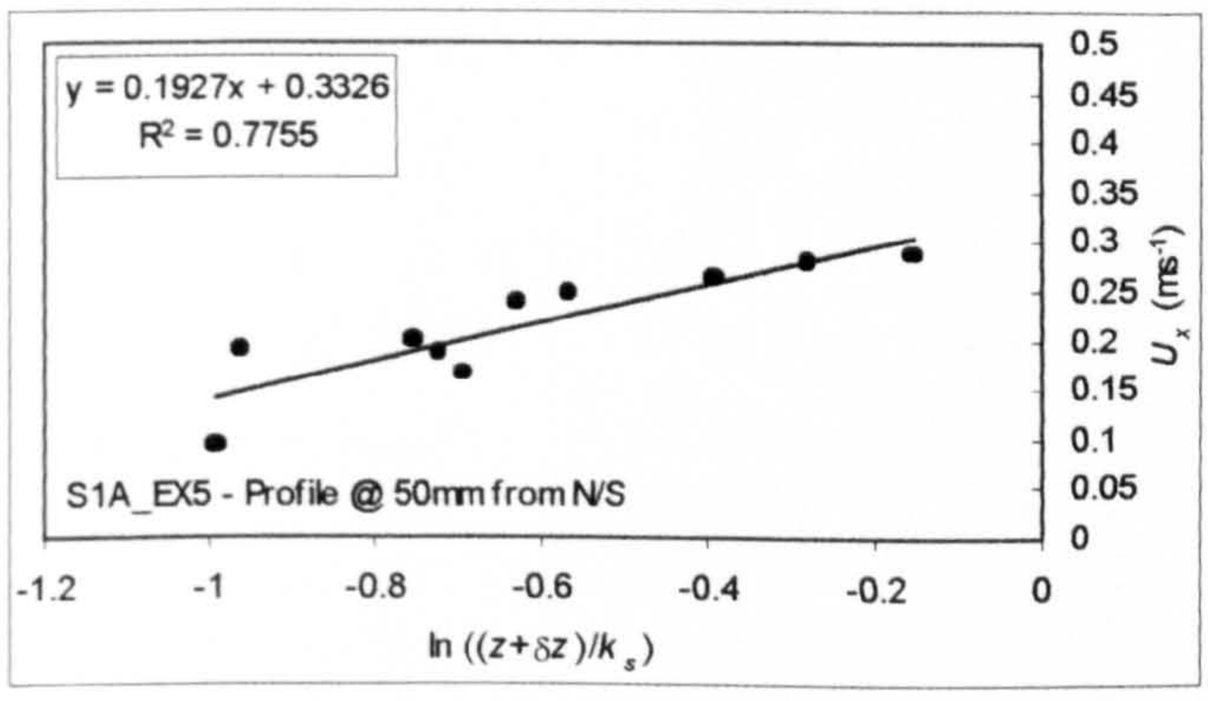

Shear velocity (u_*) and constant of integration (B_r) from gradient (m) and constant (C):-

$m = u_*/\kappa$ (where $\kappa = 0.4$).
$C = u_* B_r$

Therefore:-

$\boldsymbol{u_* = m\kappa = 0.07708\ ms^{-1}}$
$\boldsymbol{B_r = C/u_* = 4.315}$

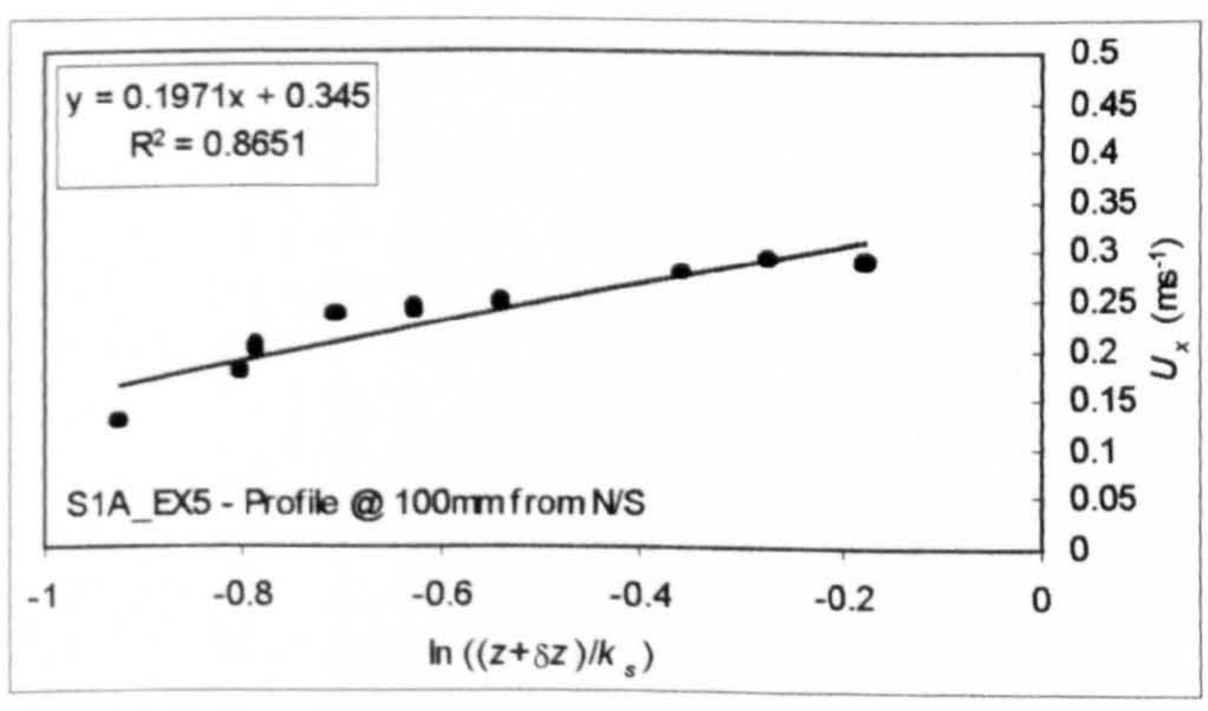

Shear velocity (u_*) and constant of integration (B_r) from gradient (m) and constant (C):-

$m = u_*/\kappa$ (where $\kappa = 0.4$).
$C = u_* B_r$

Therefore:-

$\boldsymbol{u_* = m\kappa = 0.07884\ ms^{-1}}$
$\boldsymbol{B_r = C/u_* = 4.376}$

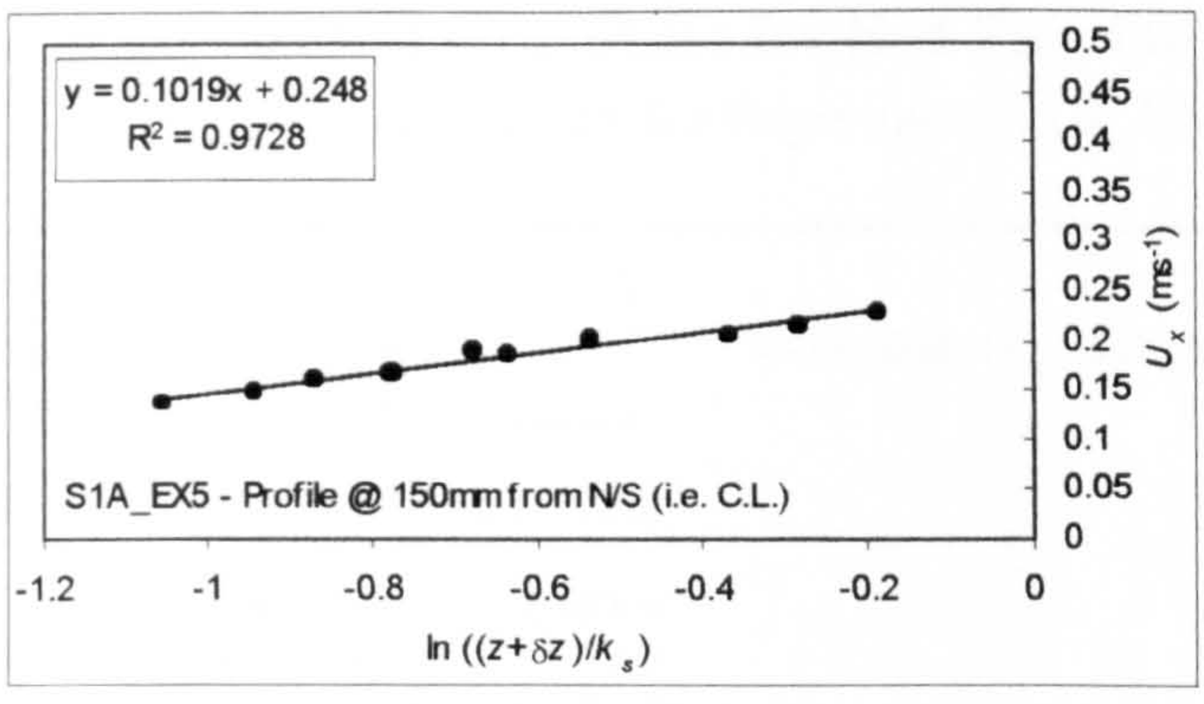

Shear velocity (u_*) and constant of integration (B_r) from gradient (m) and constant (C):-

$m = u_*/\kappa$ (where $\kappa = 0.4$).
$C = u_* B_r$

Therefore:-

$\boldsymbol{u_* = m\kappa = 0.04076\ ms^{-1}}$
$\boldsymbol{B_r = C/u_* = 6.084}$

Calculated values of u_* and B_r for the measured ADV profiles are summaried for experiment S1B_EX5 in Table A4.8.

Profile Number	Shear Velocity (u_*)	Integration Const. (B_r)
1	0.07708	4.315
2	0.07884	4.376
3	0.04076	6.084
Average	**0.06556**	**4.925**

Table A4.8 - Summary of calculated u_* and B_r for experiment S1B_EX5

Appendix 4.5 - Calculation Sheet for Bed Friction Factors

(Example shown for Experiment S1B_EX5)

Key -
Blue no.s Requires Input
Red no.s - Formulae

EXPERIMENT: **S1B_EX5**

(1) MAIN HYDRAULIC PARAMETERS

Flow Depth (H) =	**0.093**	m
Flow Width (B) =	**0.3**	m
Cross-Sectional Area (A) =	0.0279	m^2
Section Averaged Velocity (U) =	0.358423	m/s
Wetted Perimeter (P) =	0.486	m
Slope of Bed (S_o) =	**0.004**	
Flow Rate (Q) =	**0.01**	m^3/s
Hydraulic Radius (R) =	0.057407	m
Viscosity (n) =	**9.22E-07**	24 degrees C

(2) CALCULATION OF EQUIVALENT MANNING'S n_e FOR COMPOSITE SECTION

From Manning-Strickler Equation:- $$n = \frac{1}{Q} A R^{2/3} \sqrt{S_0}$$ *Equation (1)*

n_e = 0.026259

(3) CALCULATION OF MANNING'S 'n' FOR BED ONLY

Manning's 'n' for Perspex Walls (n_w) = **0.009**

(i) Horton (1933) and Einstein & Banks (1950)

$U_{av} = U_{av1} = U_{av2} = \ldots = U_{avN}$ **$F_T = F_1 + F_2 + F_3 + \ldots + F_N$** **$Q_T = Q_1 + Q_2 + Q_3 + \ldots + Q_N$**

$$n_e = \left[\frac{\sum_{i=1}^{N} \left(P_i n_i^{3/2} \right)}{P} \right]^{2/3}$$ *Equation (2)*

$$n_e = \left[\frac{\sum_{i=1}^{N} \left(P_i n_i^{2} \right)}{P} \right]^{1/2}$$ *Equation (3)*

$$n_e = \frac{P R^{5/3}}{\sum_{i=1}^{N} \frac{P_i R_i^{5/3}}{n_i}}$$ *Equation (4)*

Eqn. 2	Eqn. 3	Eqn. 4
From Eqn. 1, n_e = 0.026259	From Eqn. 1, n_e = 0.026259	From Eqn. 1, n_e = 0.0262591
Guess n_b = **0.0343**	**Guess n_b =** **0.0327**	**Guess n_b =** **0.0345**
n_e (eqn. 1) = 0.02623	n_e (eqn. 2) = 0.026288	n_e (eqn. 3) = 0.026357
Tolerance = 0.00003	Tolerance = 0.00003	Tolerance = 0.00010

(ii) Vanoni and Brooks (1957)

Darcy-Weisbach Friction coefficient (f) = 0.14028 (For whole section)
Reynolds No. for Channel (Re) = 8.93E+04

Check on f:-
0.14028

$R_w/f_w = R/f$ = 6.36E+05

From Geometric Considerations **$A = A_b + A_w$;**

From 'Graph' :- f_w = **0.025** (from R_w/f_w against f_w plot)
Therefore f_b = 0.211753
R_b = 0.086657
U^*_b = 0.058313

X Sectional Area (A) = 0.0279 m^2
Area (Bed) (A_b) = 0.025997 m^2
Area (Walls) (A_w) = 0.001903 m^2

Hydraulic Radius (Bed) (R_b) = 0.086657 m
Hydraulic Radius (Walls) (R_w) = 0.010231 m

Manning's 'n' for Bed (n_b) = **0.034554**

(4) SUMMARY OF FRICTION FACTORS CALCULATED

(a) MANNING'S 'n' FRICTION FACTORS

Manning's 'n' for Channel (n_e) =	0.0263
Manning's 'n' for Walls (n_w) =	*0.0090*
Horton (1933) - Equation (1) (n_b) =	0.0343
Horton (1933) - Equation (2) (n_b) =	0.0327
Horton (1933) - Equation (3) (n_b) =	0.0345
Vanoni & Brooks (1957) (n_b) =	0.0346

Average Manning's 'n' for bed (n_b) = 0.0340

(b) DARCY-WEISBACH FRICTION FACTORS

Darcy-Weis 'f' for Channel (f_e) =	0.14028
Darcy-W 'f' for Walls (f_w) =	*0.016479*
Horton (1933) - Equation (1) (f_b) =	0.208647
Horton (1933) - Equation (2) (f_b) =	0.189636
Horton (1933) - Equation (3) (f_b) =	0.211088
Vanoni & Brooks (1957) (f_b) =	0.211753

Average Darcy-W 'f' for bed (f_b) = 0.205281

(5) CALCULATION OF BED ROUGHNESS COEFFICIENT (k_s)

(a) Colebrook-White Equation :-

$$\frac{1}{\sqrt{f_b}} = -2\log\left(\frac{k_s}{14.8R_b} + \frac{0.6275}{R_{eb}\sqrt{f_b}}\right)$$

Colebrooke-White Equation

Re_b =	134749.7	134749.7
LHS =	2.207118	
Guess k_s =	**0.101**	**101** mm
RHS =	2.207373	
Tolerance =	0.000	

(b) Keulegan-Type Equation (Zagni and Smith 1976):-

$$\frac{1}{\sqrt{f_b}} = 2.03\log\left(\frac{12.27R_b}{k_s}\right)$$

Keulegan Type Equation

LHS =	2.207118	
Guess k_s =	**0.087**	**87** mm
RHS =	2.20687	
Tolerance =	0.000	

(c) Summary of k_s values calulcated

Colebrooke-White Bed Roughness k_s = 0.101 m = 101 mm

Keulegan Bed Roughness k_s = 0.087 m = 87 mm

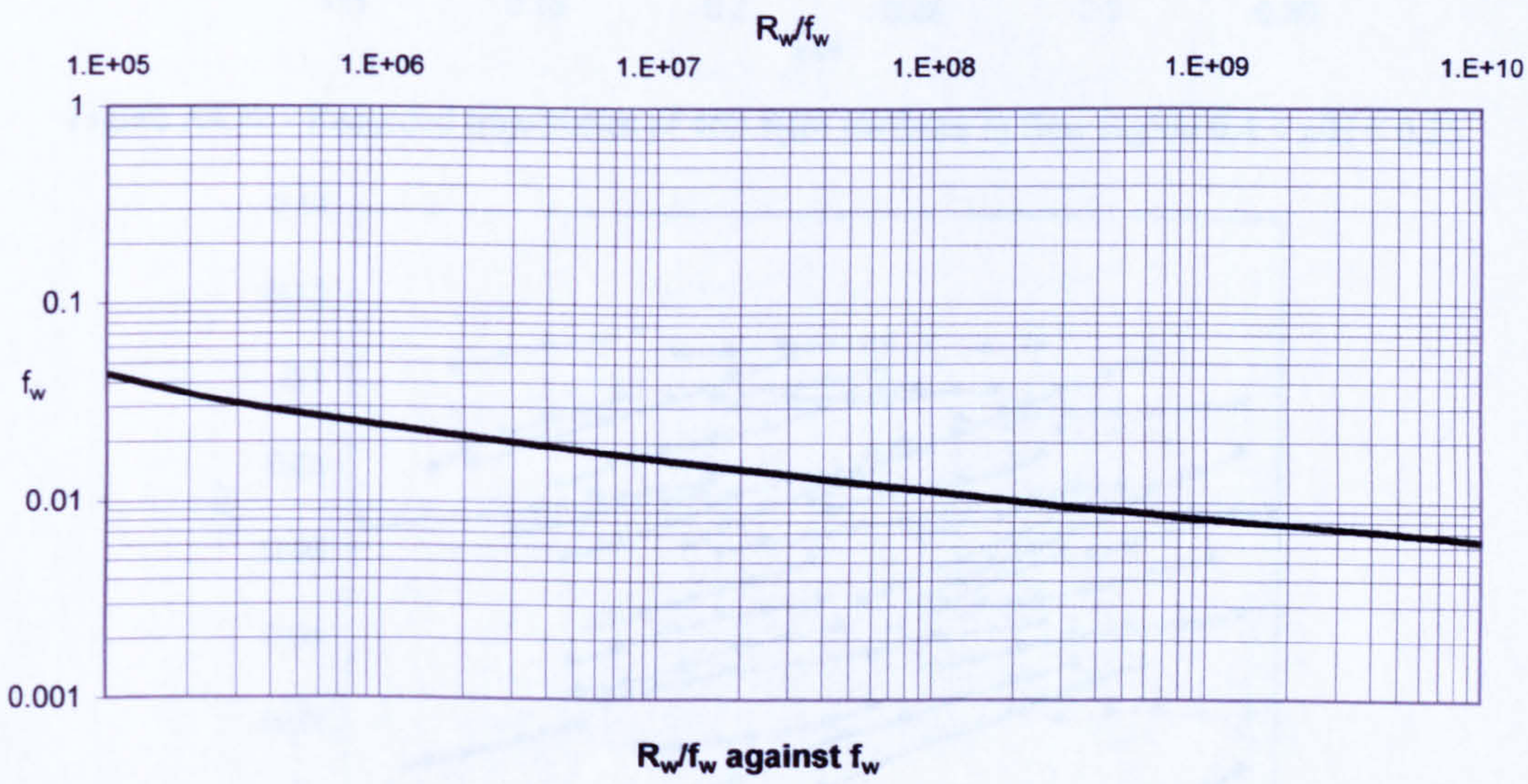

R_w/f_w against f_w

Appendix 4.6 Measured Particle Trajectories

Experiment S1B_EX1:

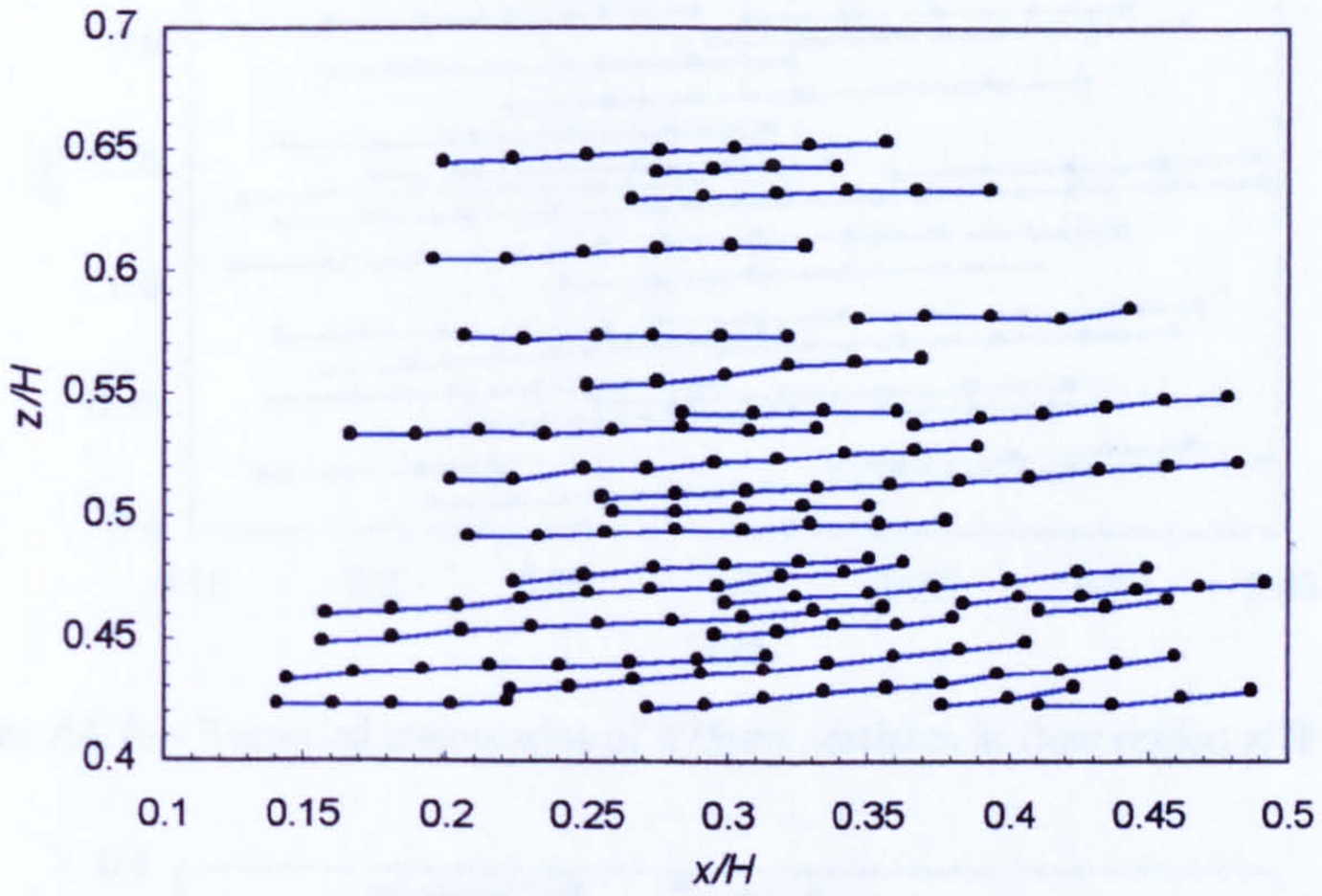

Figure A4.6a - Recorded trajectories of 462.5μm particles in flow region $z/H > 0.4$

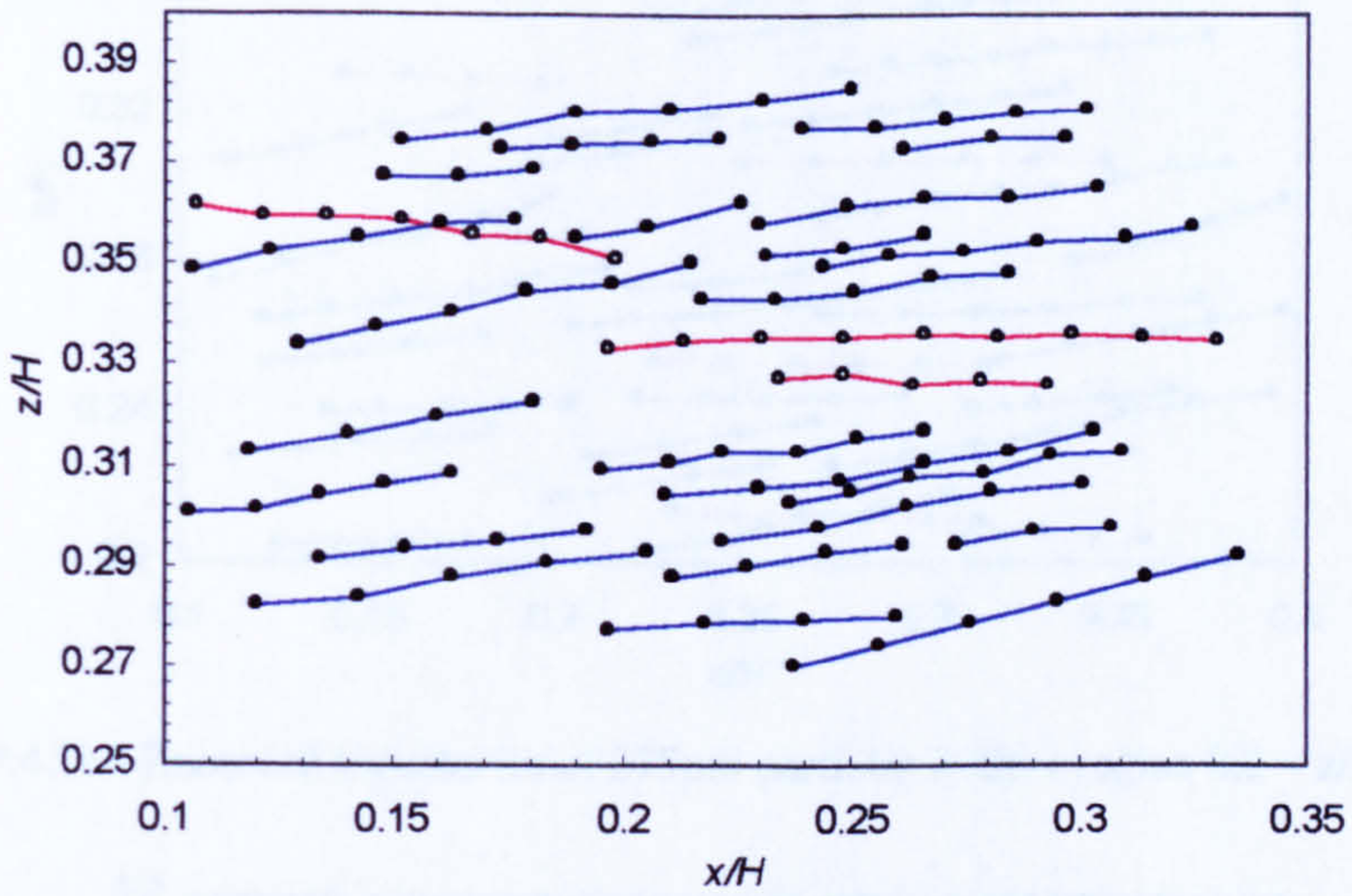

Figure A4.6b - Recorded trajectories of 462.5μm particles in flow region $0.4 < z/H < 0.25$

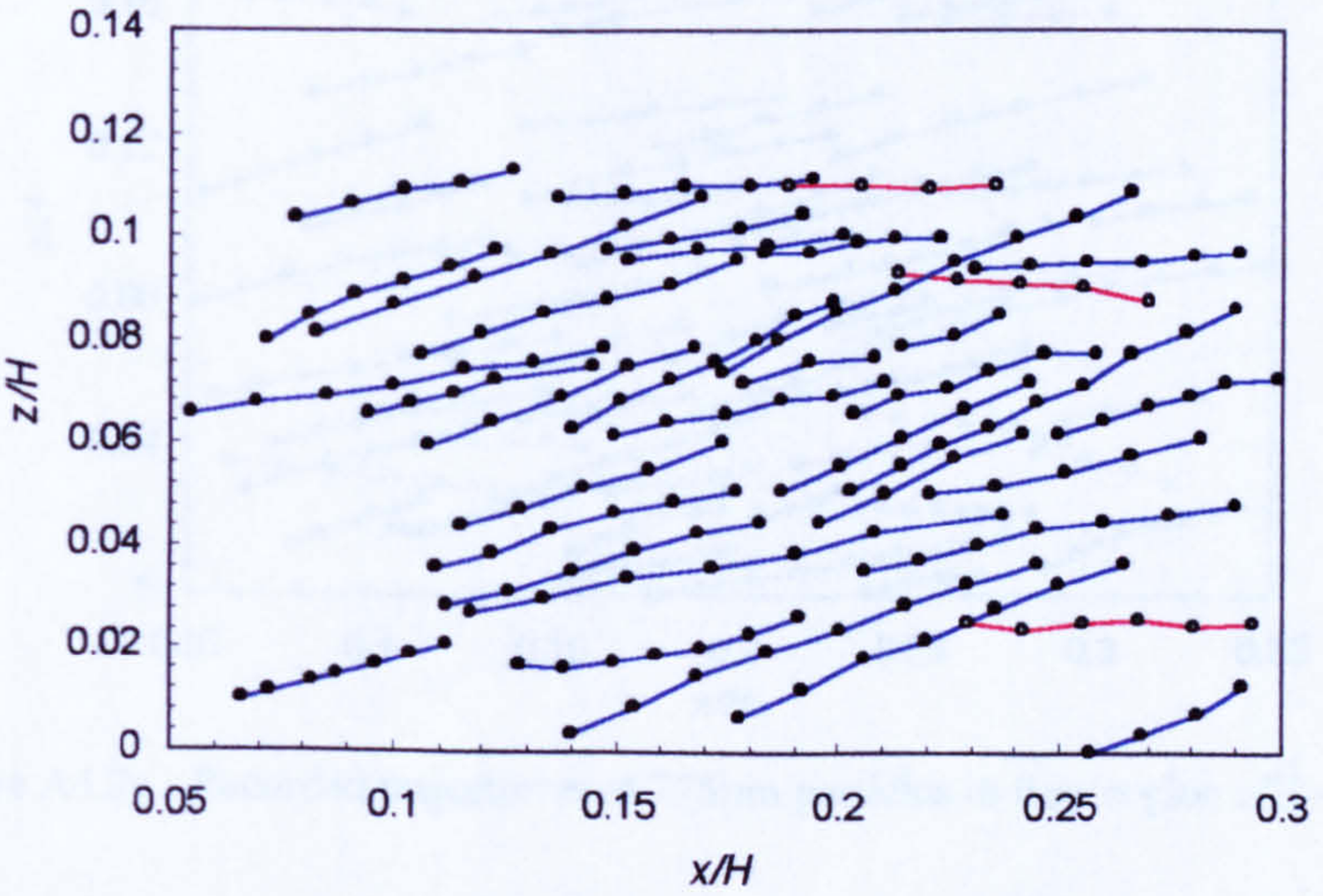

Figure A4.6c - Recorded trajectories of 462.5μm particles in flow region $z/H < 0.14$

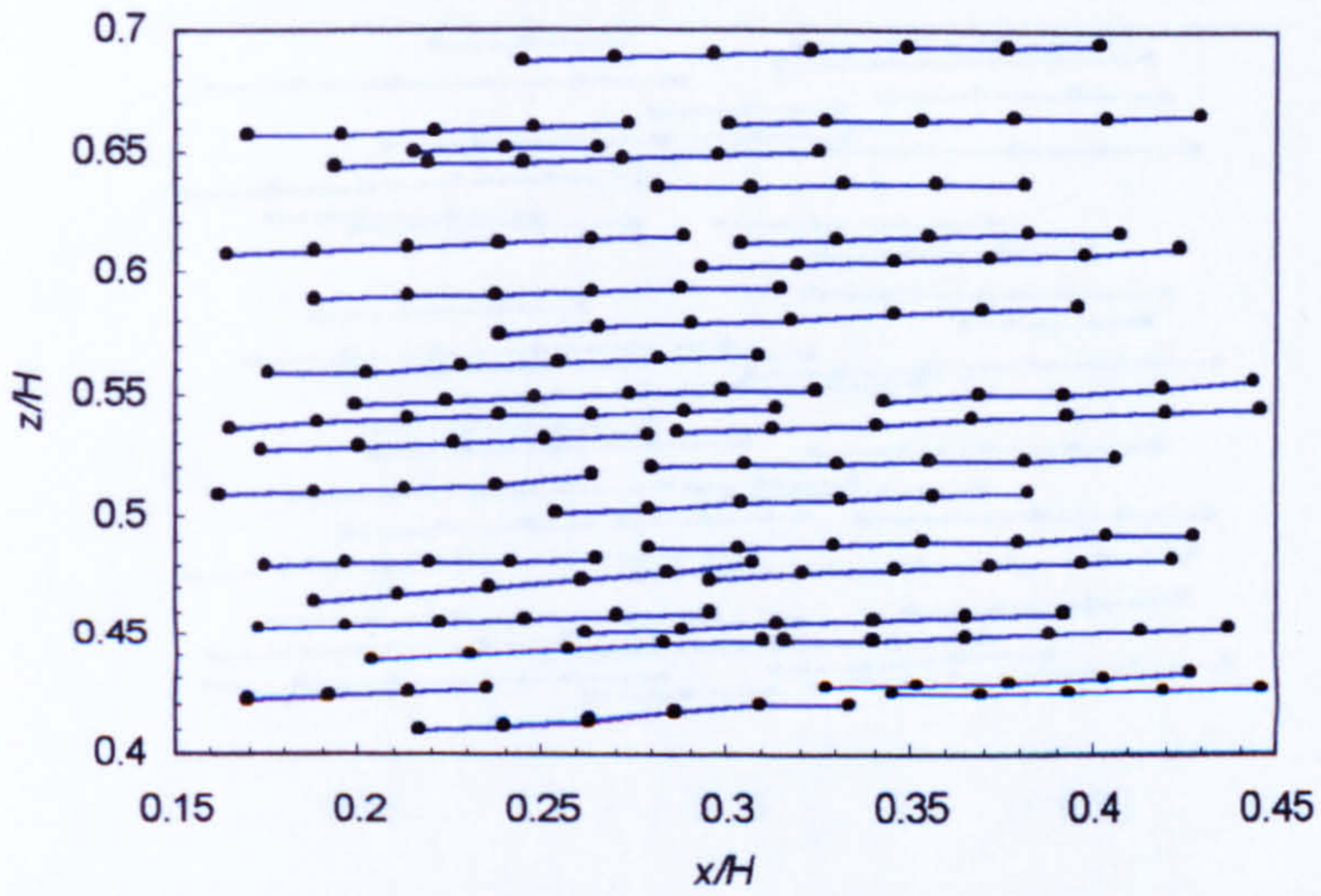

Figure A4.7a - Recorded trajectories of 275μm particles in flow region z/H > 0.4

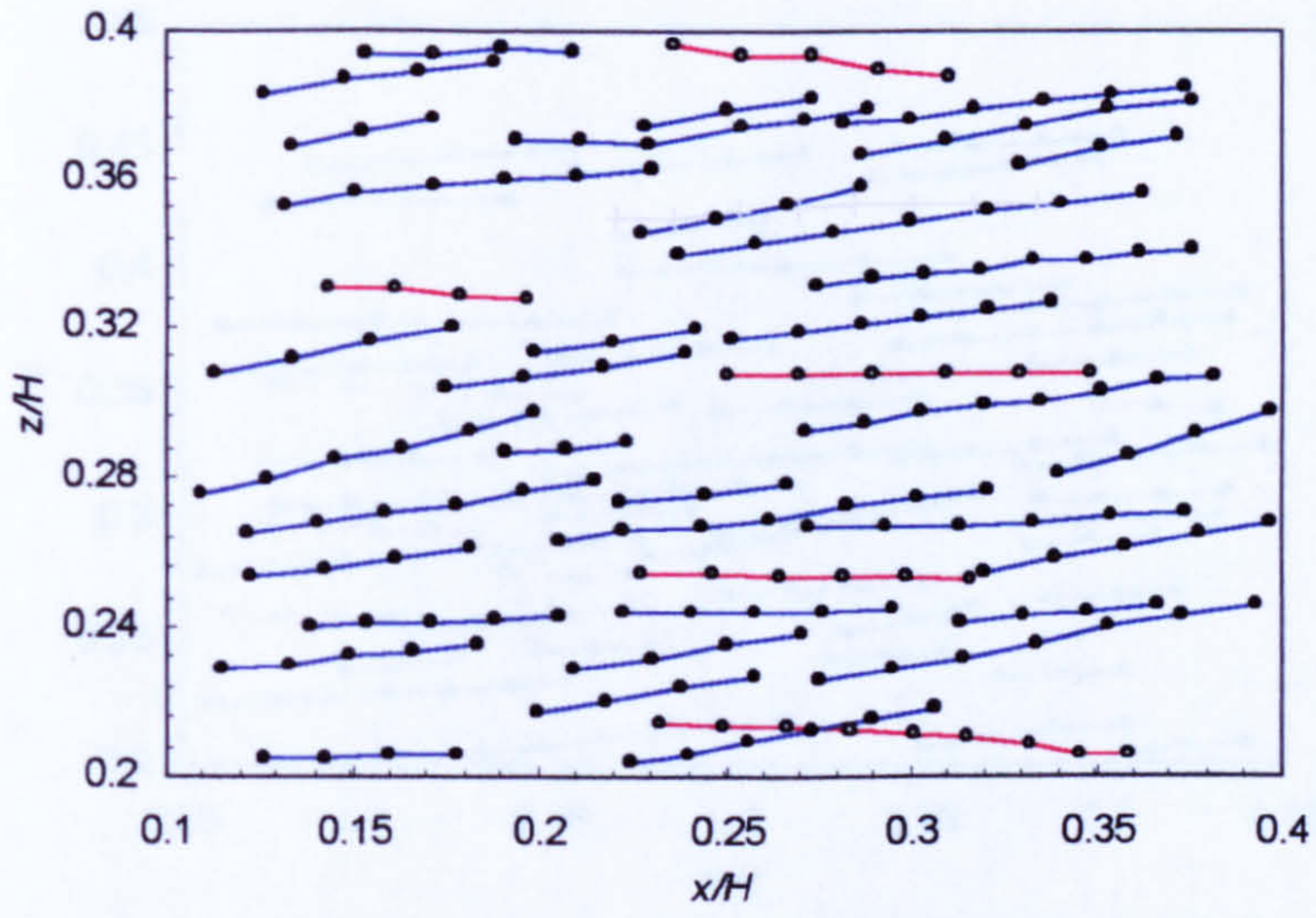

Figure A4.7b - Recorded trajectories of 275μm particles in flow region 0.2 < z/H < 0.4

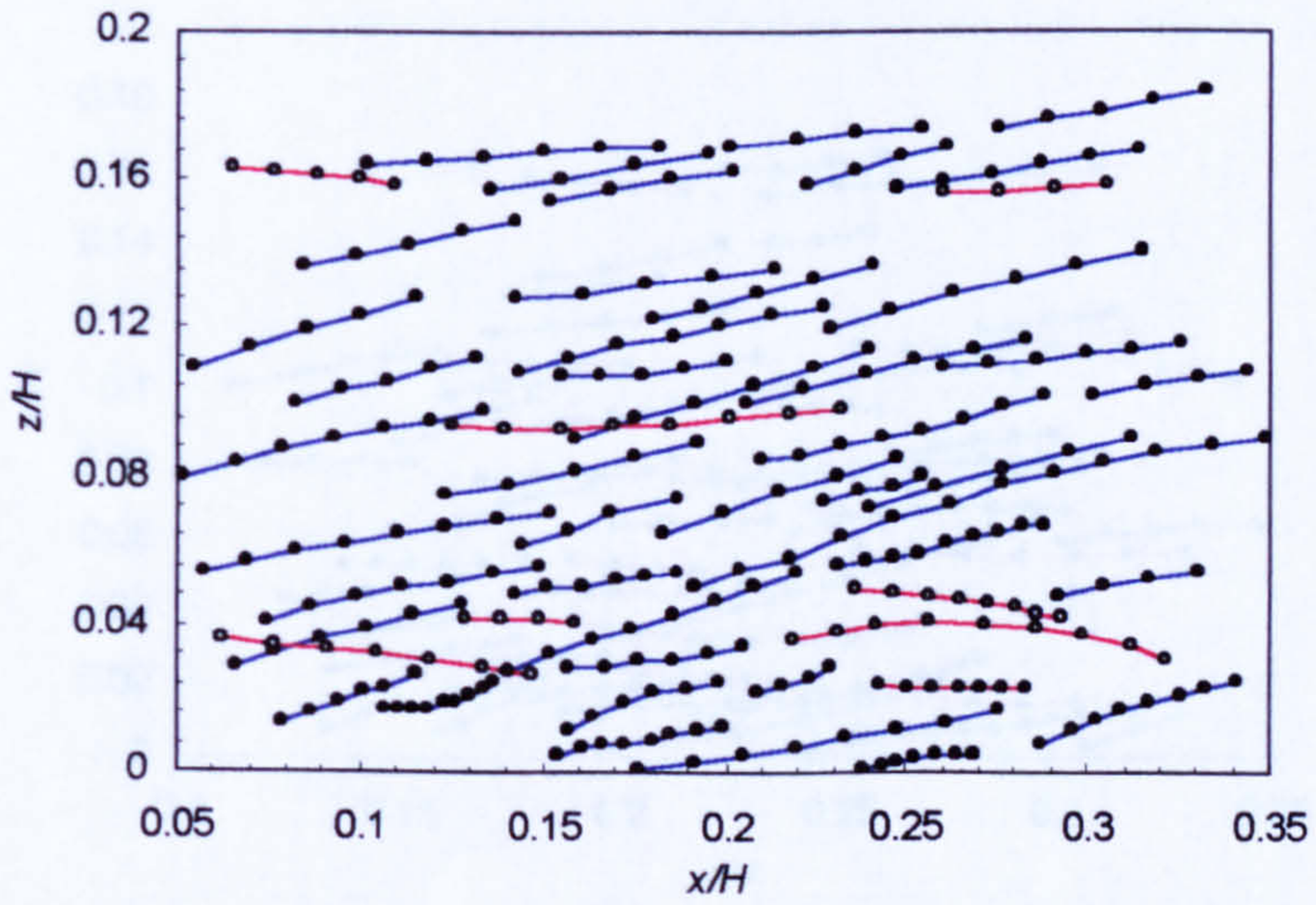

Figure A4.7c - Recorded trajectories of 275μm particles in flow region z/H < 0.2

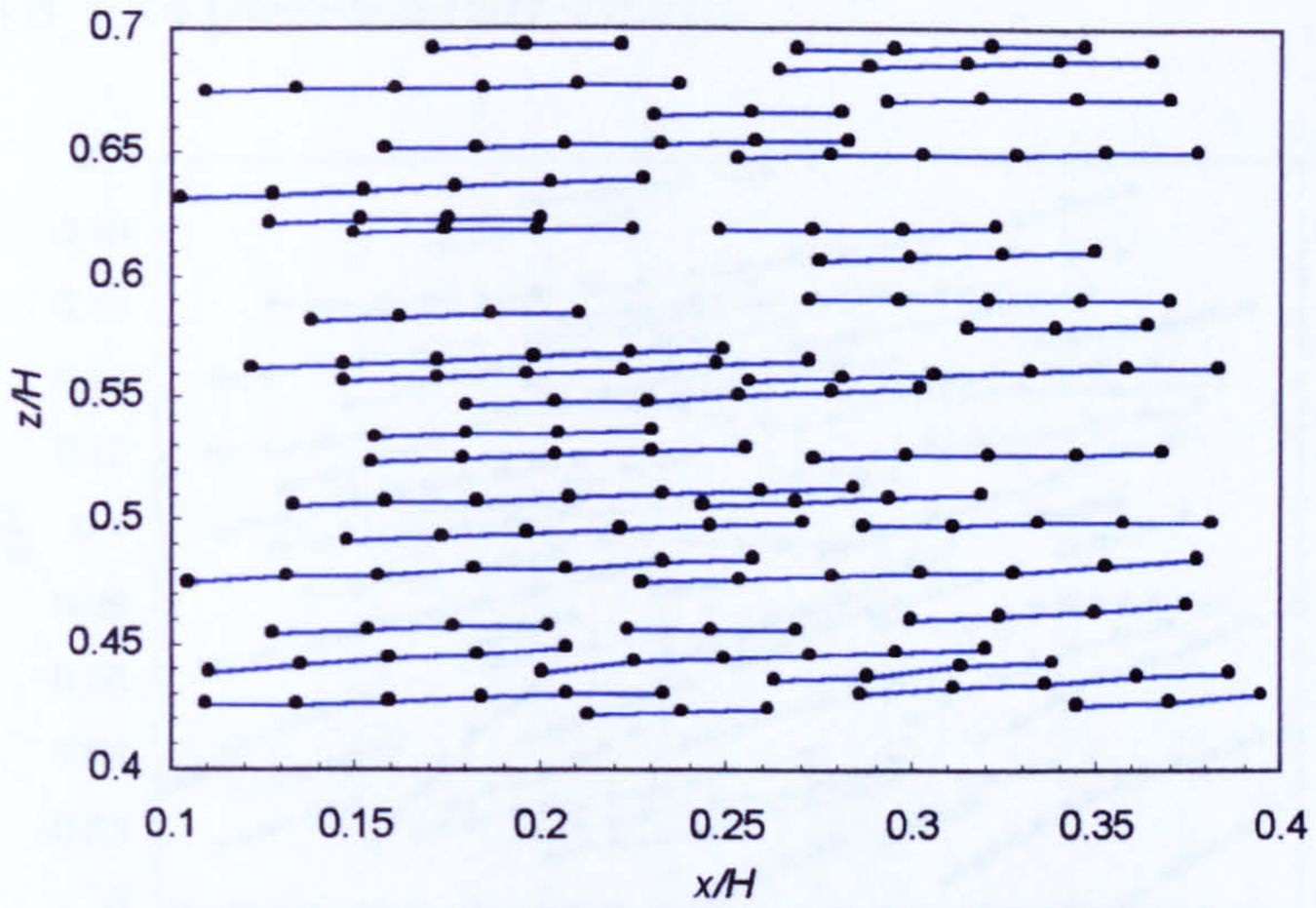

Figure A4.8a - Recorded trajectories of 181μm particles in flow region $z/H > 0.4$

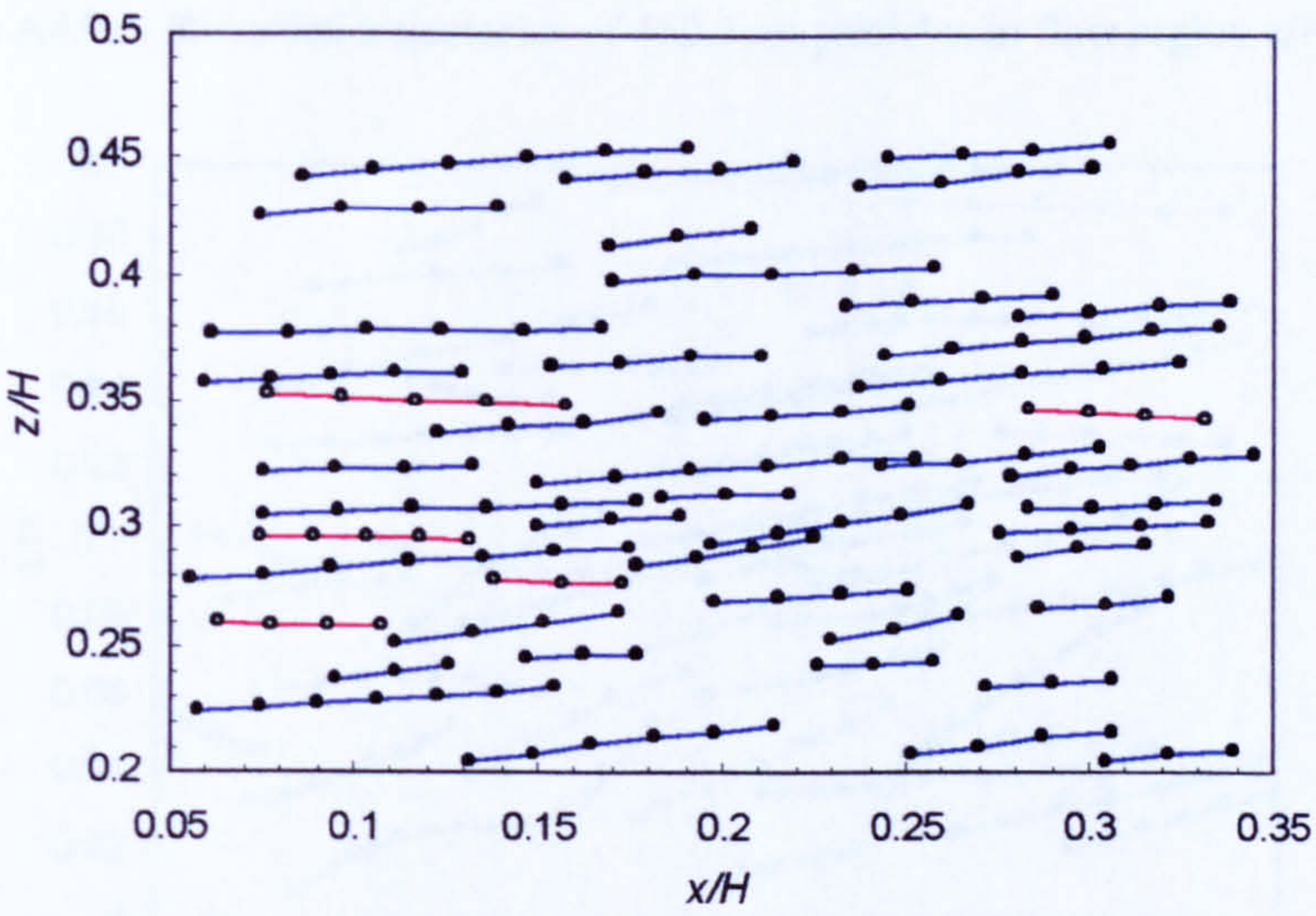

Figure A4.8b - Recorded trajectories of 181μm particles in flow region $0.2 < z/H < 0.45$

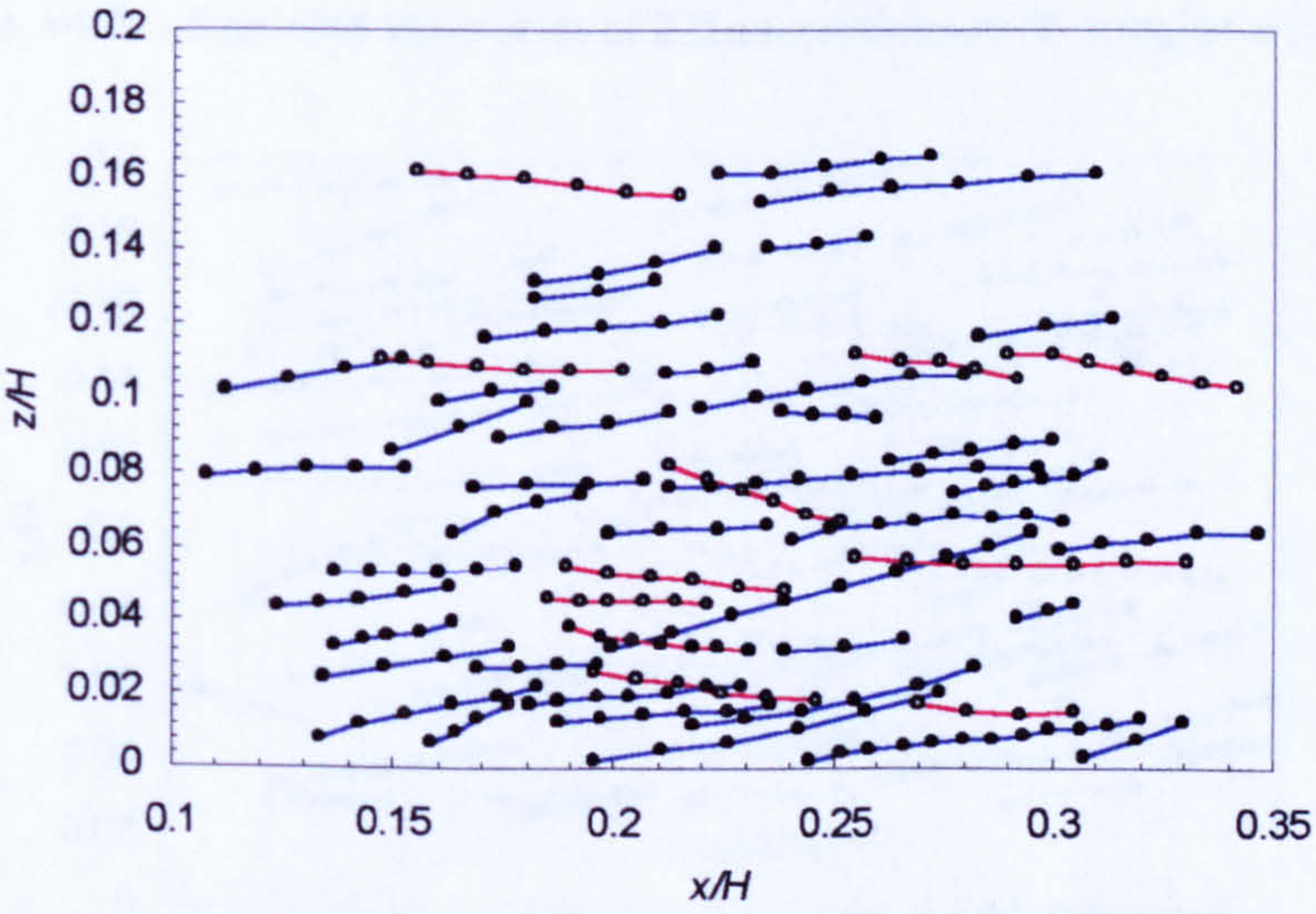

Figure A4.8c - Recorded trajectories of 181μm particles in flow region $z/H < 0.2$

Experiment S1B_EX4 [Near-bed ($z/H < 0.2$)]:

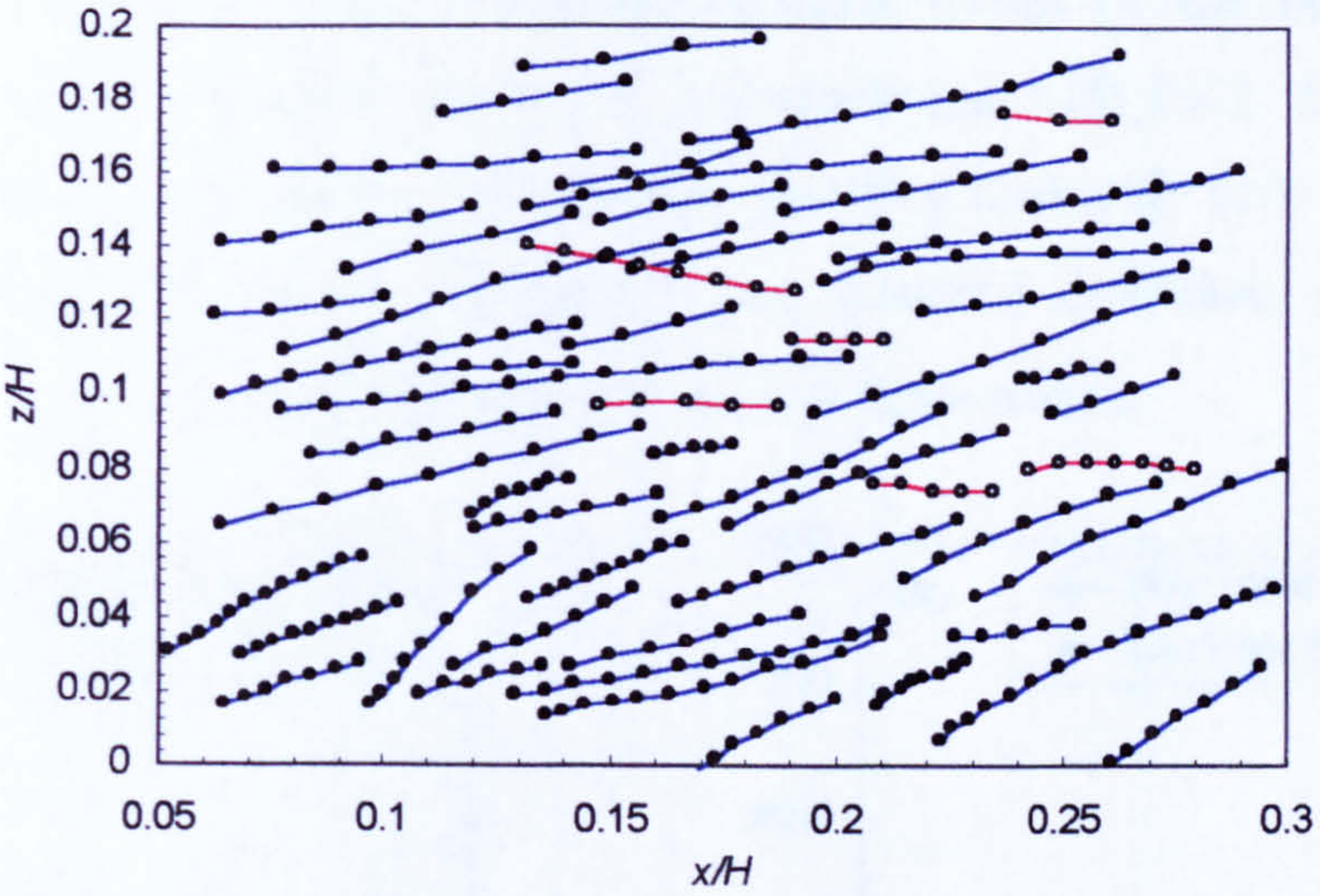

Figure A4.9a - Recorded trajectories of 462.5μm particles in flow region z/H < 0.2

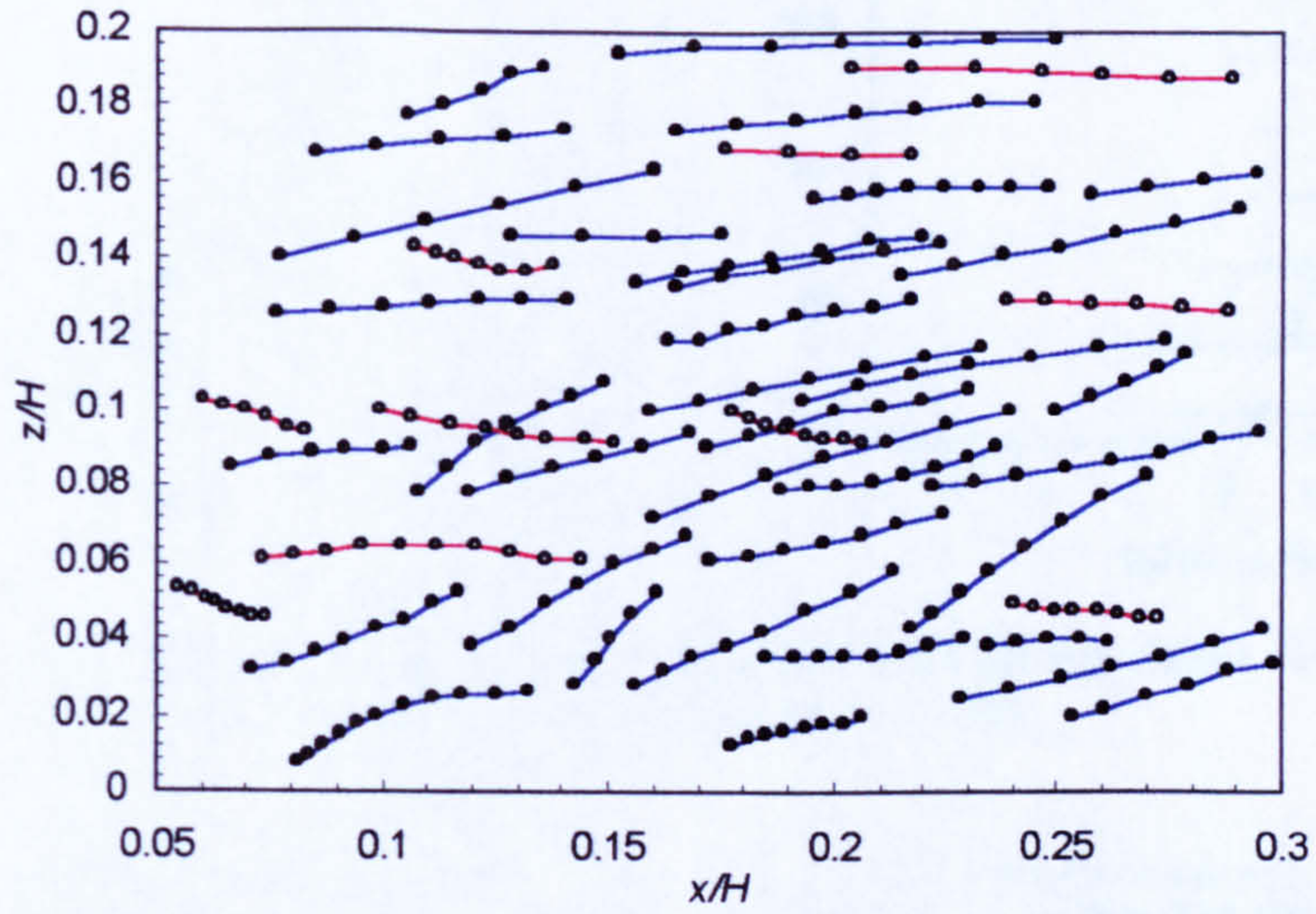

Figure A4.9b - Recorded trajectories of 275μm particles in flow region z/H < 0.2

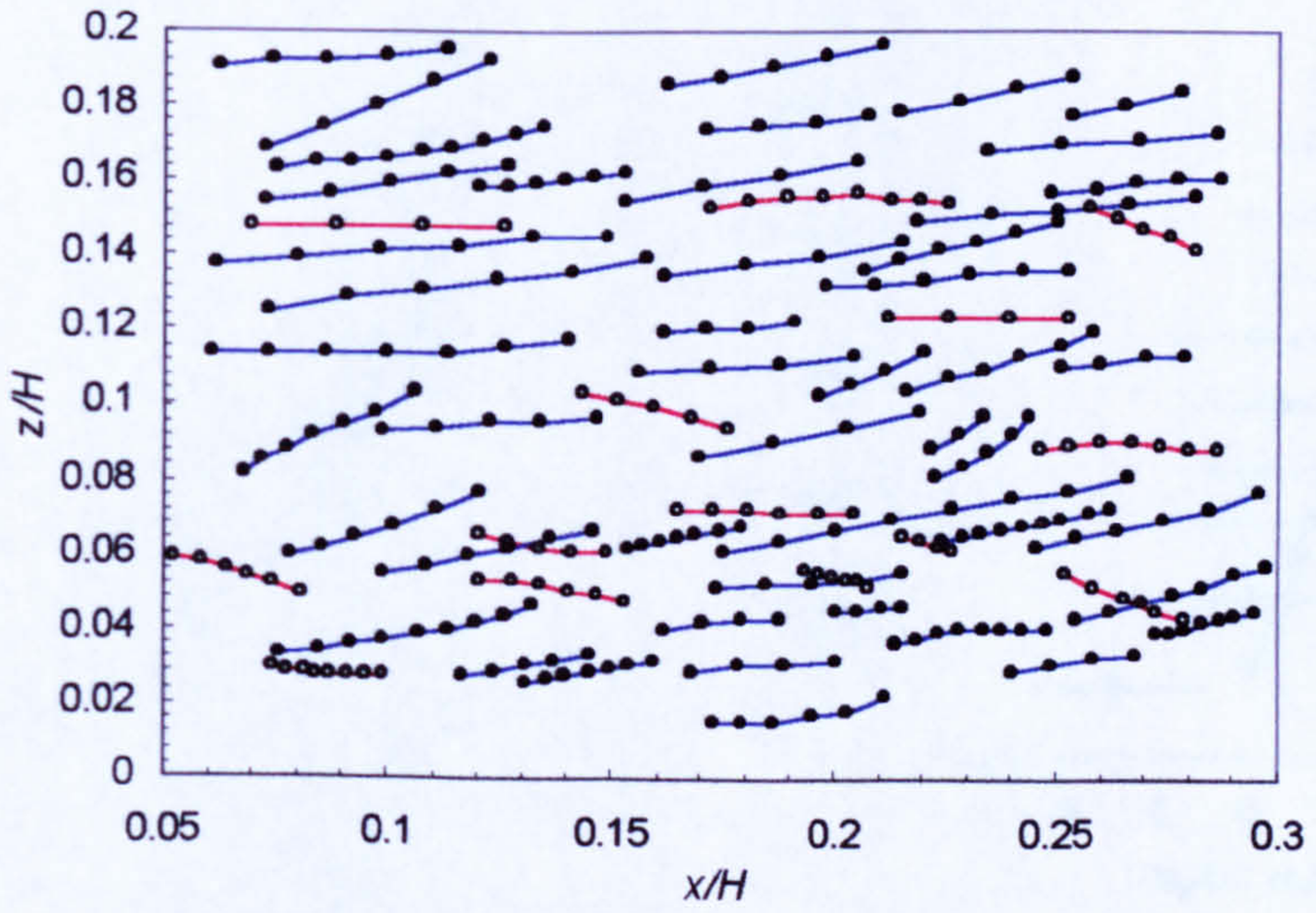

Figure A4.9c - Recorded trajectories of 181μm particles in flow region z/H < 0.2

Appendix 4.7 Fraction-Averaged Particle Velocities

The plots below show fractional-averaged values of the non-dimensional streamwise particle velocities measured in experiment S1B_EX2, EX3 and EX5, plotted for the full flow depth (z/H) and the near-bed flow only (z_+). Error bars on particle velocity data points represent ± one standard deviation. Dashed lines represent $(u_x \pm u'_{rms})/u_*$, obtained from the ADV measurements.

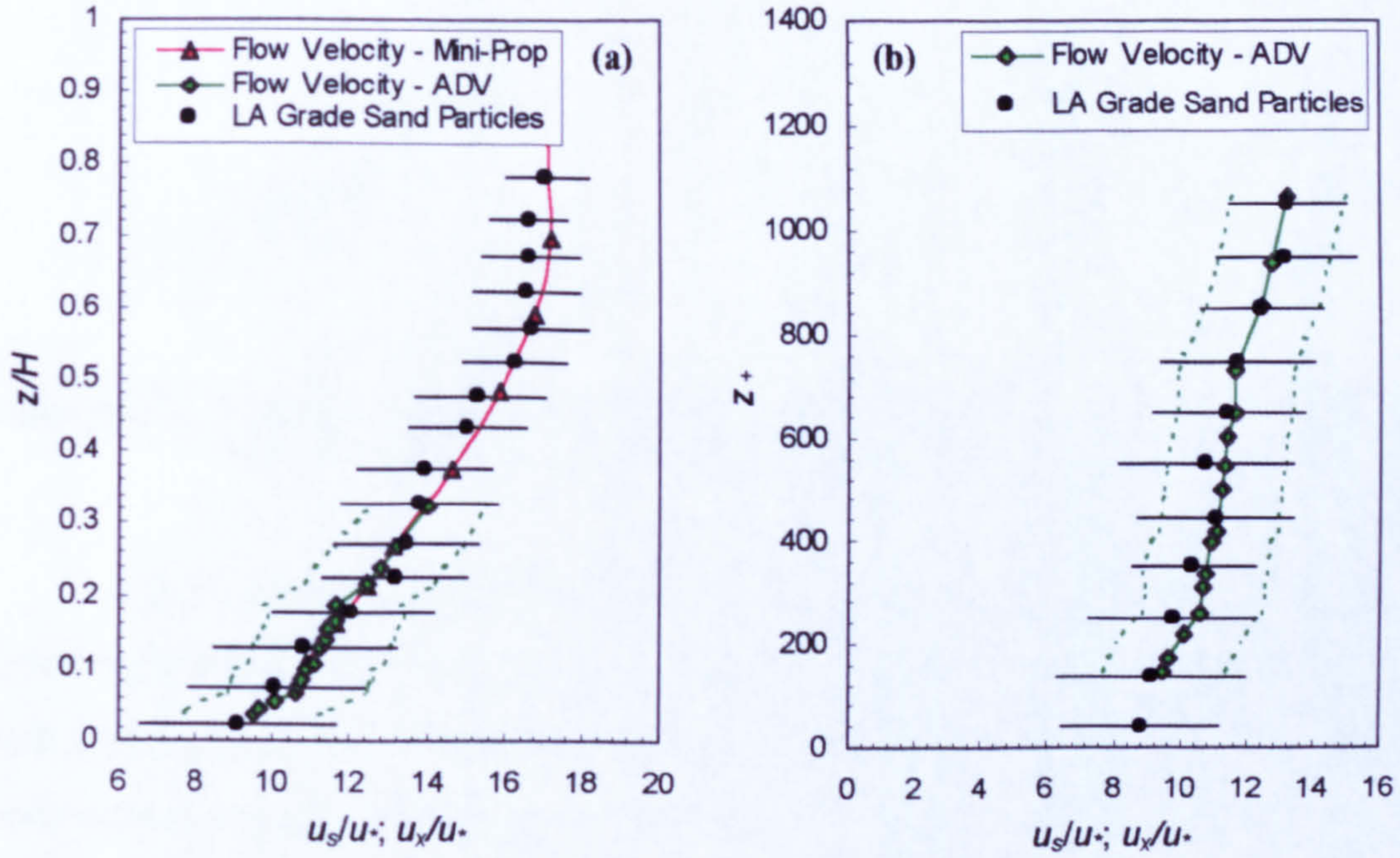

Figure A4.10 - Ensemble-averaged streamwise particle velocities for experiment S1B_EX2 obtained in the flow regions: (a) z/H = 0.0-0.8; and (b) $z_+ < 1100$.

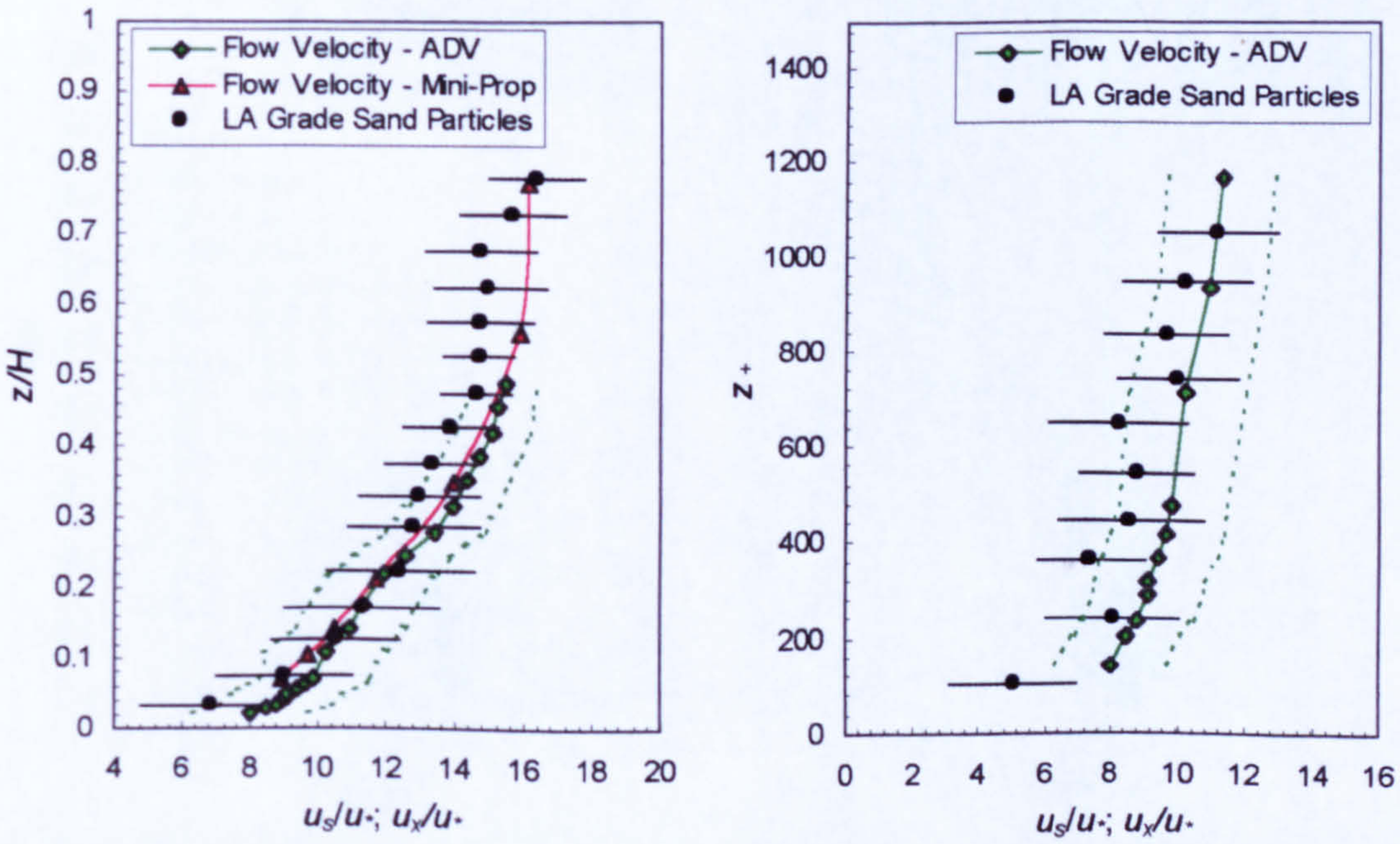

Figure A4.11 - Ensemble-averaged streamwise particle velocities for experiment S1B_EX3 obtained in the flow regions: (a) z/H = 0.0-0.8; and (b) $z_+ < 1200$.

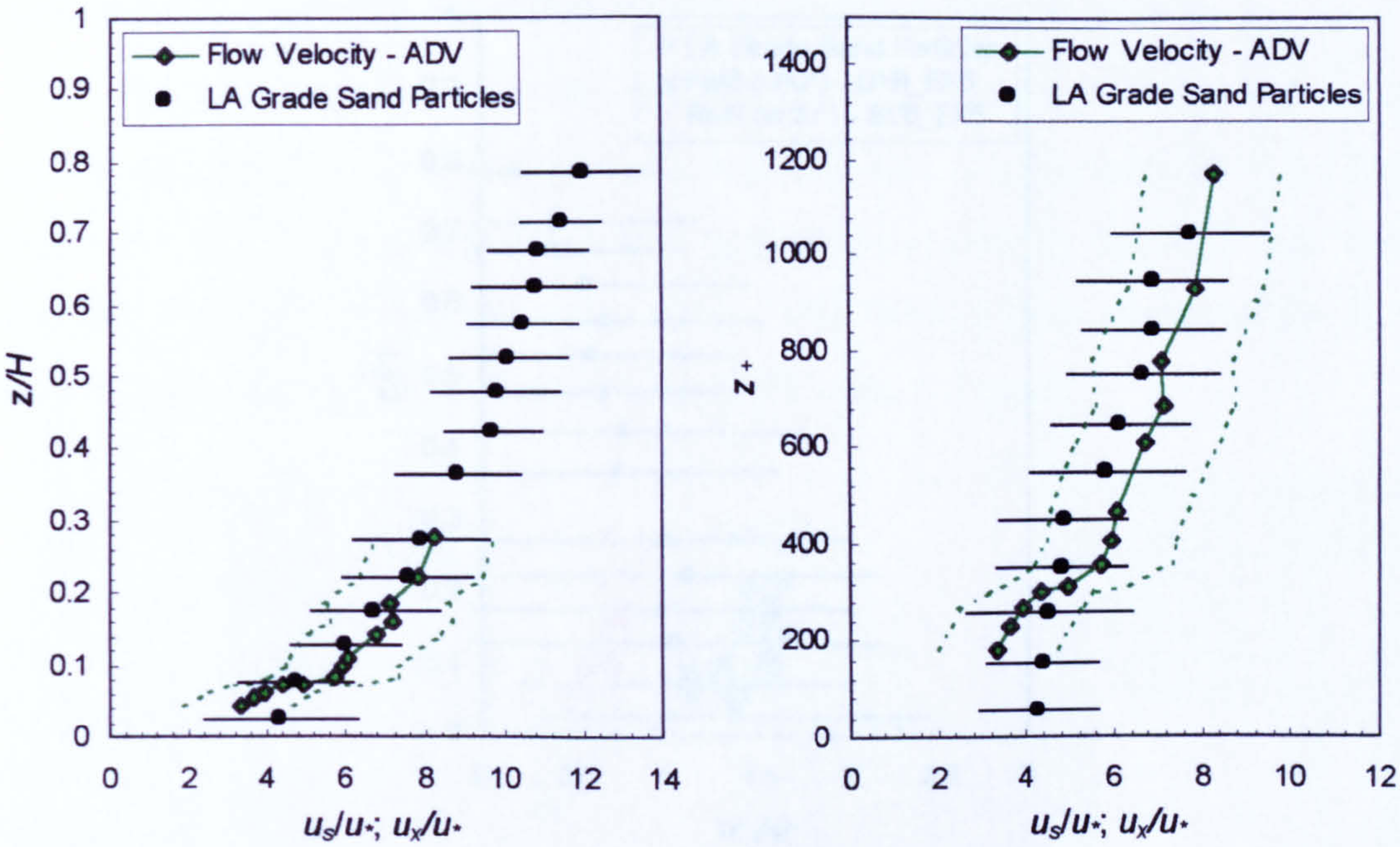

Figure A4.12 - Ensemble-averaged streamwise particle velocities for experiment S1B_EX5 obtained in the flow regions: (a) z/H = 0.0-0.8; and (b) $z_+ < 1100$.

Fraction-averaged non-dimensional vertical particle fall velocities obtained from experiment S1B_EX2, EX3 and EX5 measurements are plotted against *z/H* below in Figure A4.13. Error bars represent ± one standard deviation. Longitudinal and vertical turbulence intensity profiles obtained by the ADV probe measurements are shown for comparison purposes.

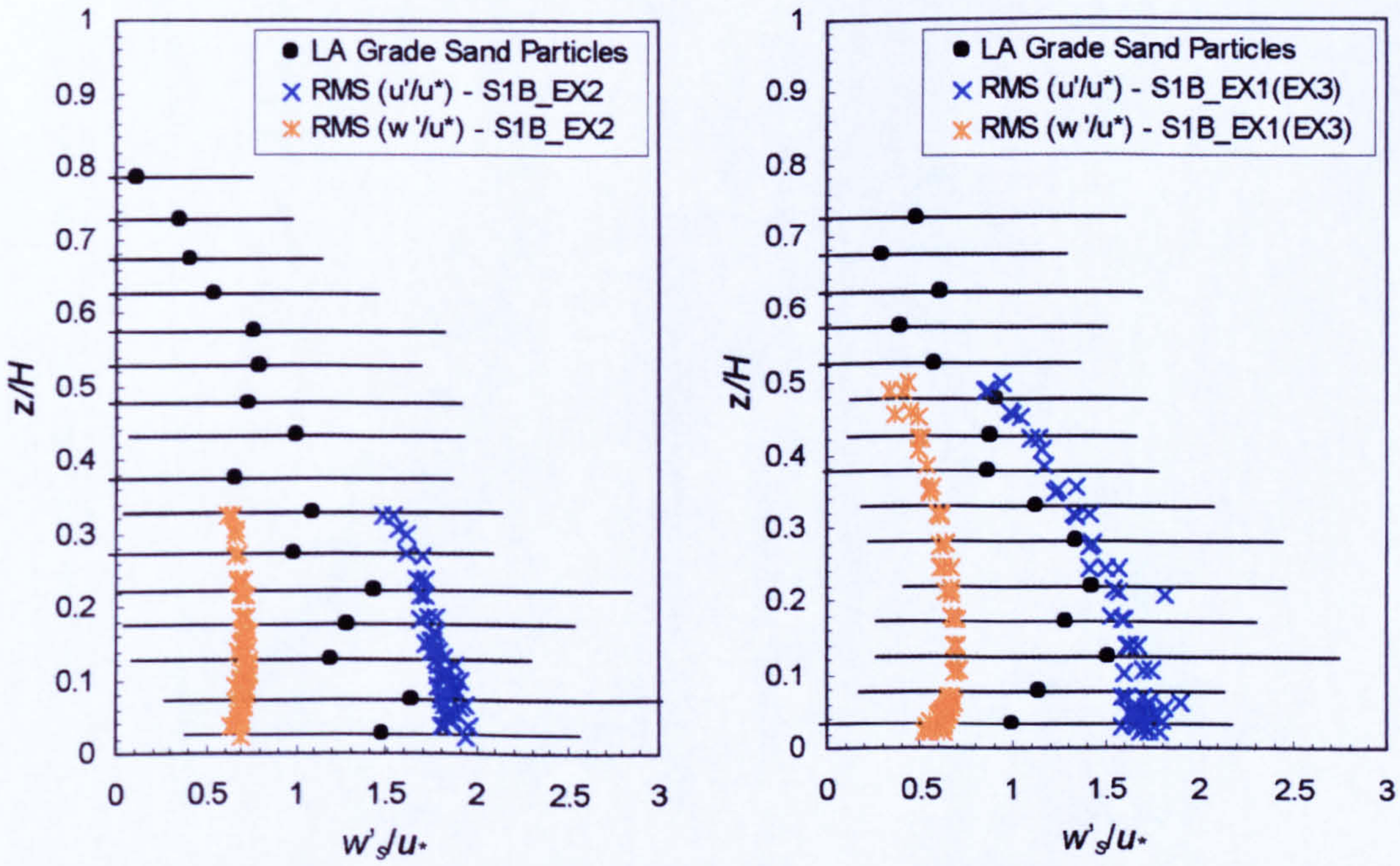

Figure A4.13 - Ensemble-averaged vertical particle velocities for experiments: (a) S1B_EX2; and (b) S1B_EX3, plotted against *z/H*. Longitudinal and vertical turbulence intensity profiles plotted for comparison purposes.

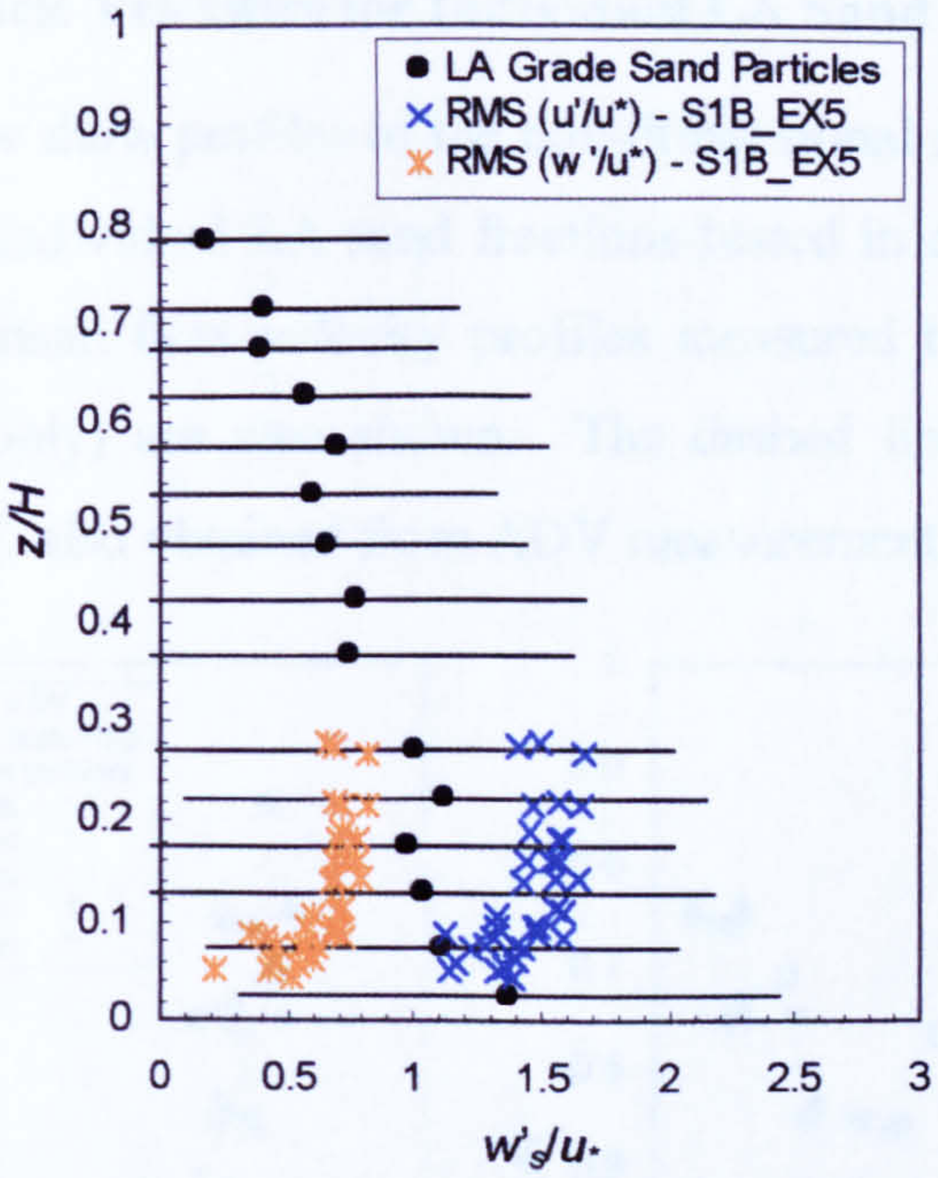

Figure A4.13(c) - Ensemble-averaged vertical particle velocities for experiment S1B_EX5 plotted against z/H. Corresponding longitudinal and vertical turbulence intensity profiles plotted for comparison purposes.

Appendix 4.8 Particle Velocities for Individual LA Sand Fractions

The plots below show profiles of the non-dimensional streamwise and vertical particle velocities for individual LA sand fractions tested in experiments S1B_EX2, EX3 and EX5. The mean flow velocity profiles measured by the ADV and mini-propeller (S1B_EX2 only) are also shown. The dashed lines represent the ADV profiles $[(u_x \pm u'_{rms})/u_*]$, also obtained from ADV measurements.

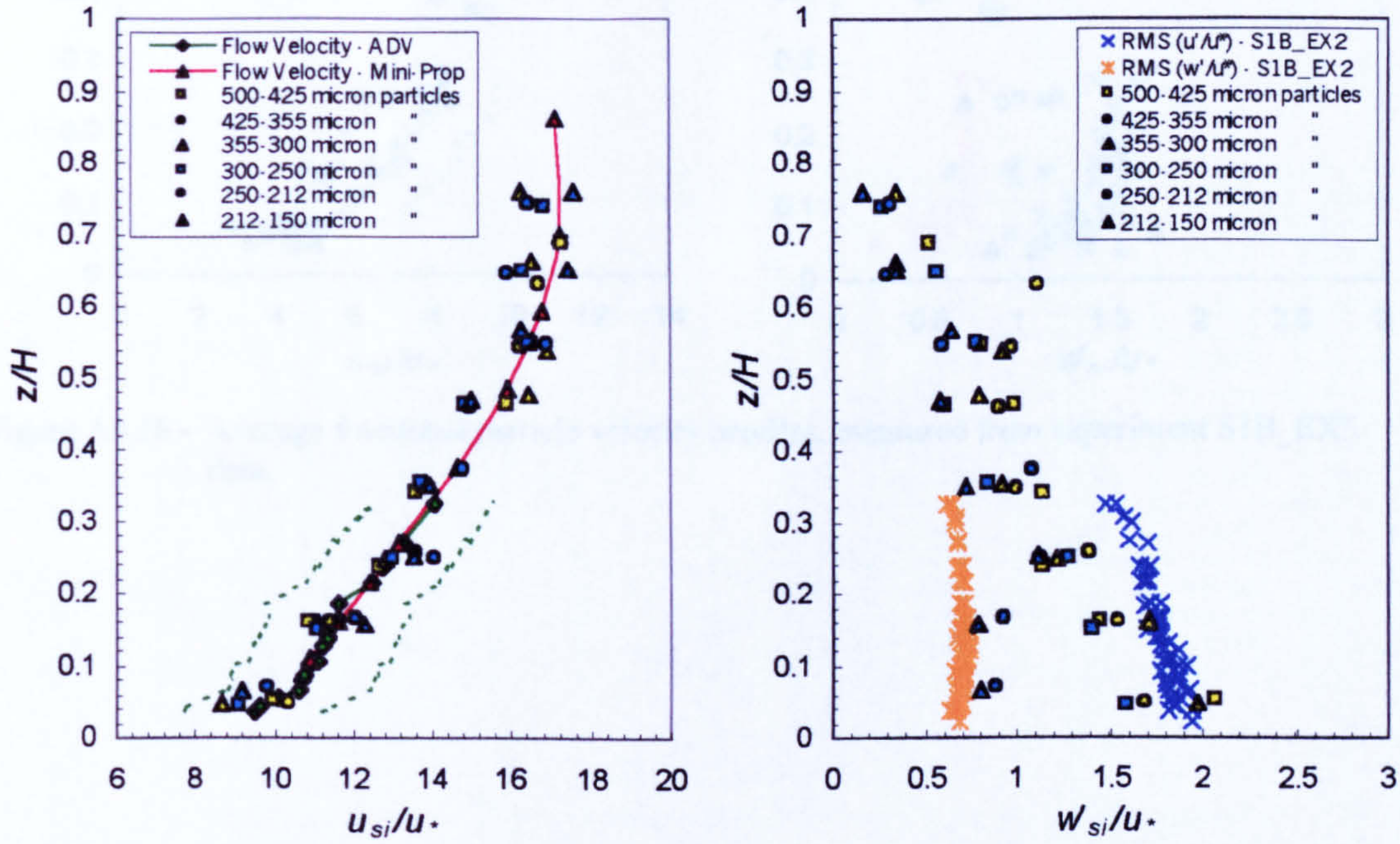

Figure A4.14 - Average fractional particle velocity profiles, measured from experiment S1B_EX2 data.

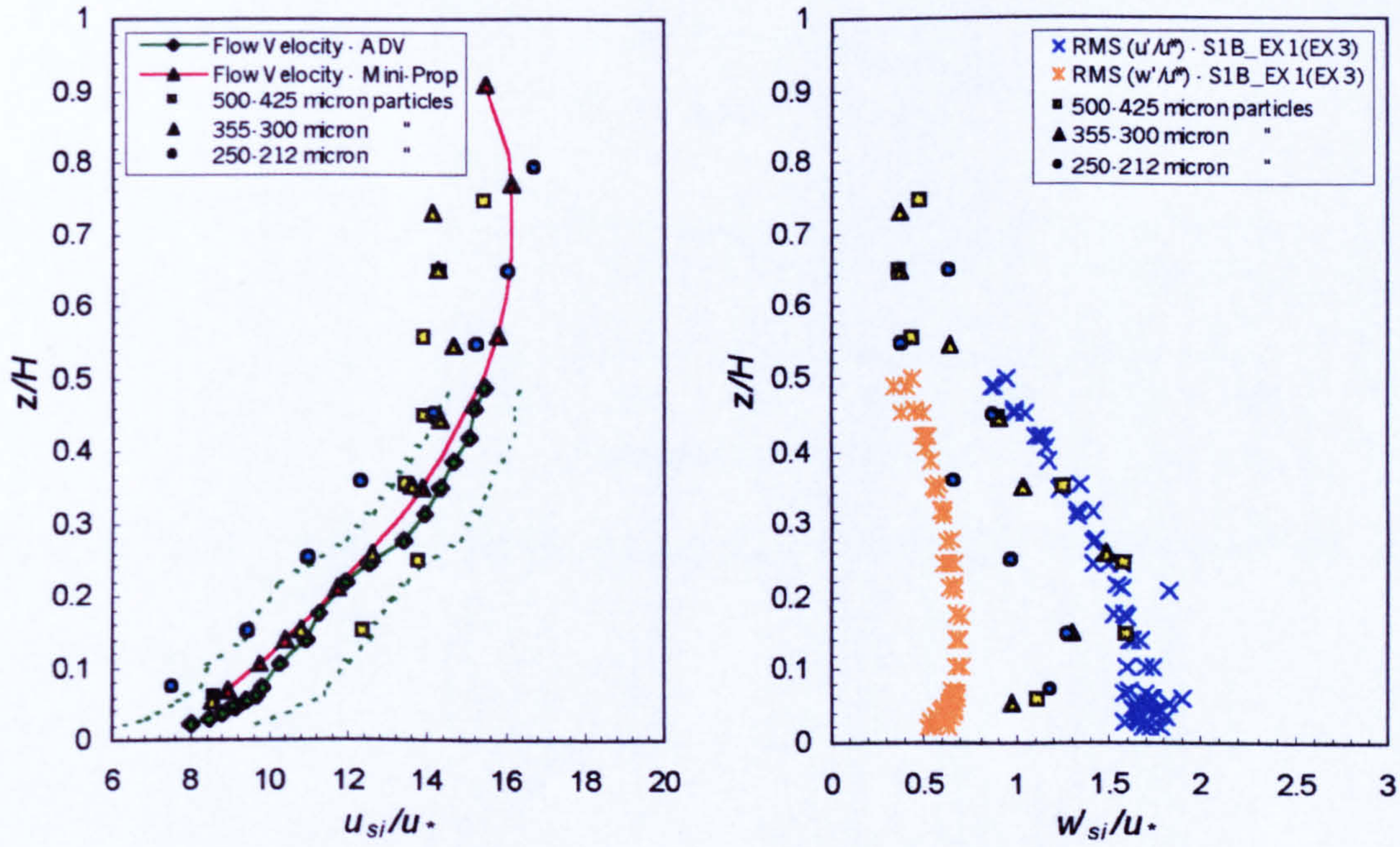

Figure A4.15 - Average fractional particle velocity profiles, measured from experiment S1B_EX3 data.

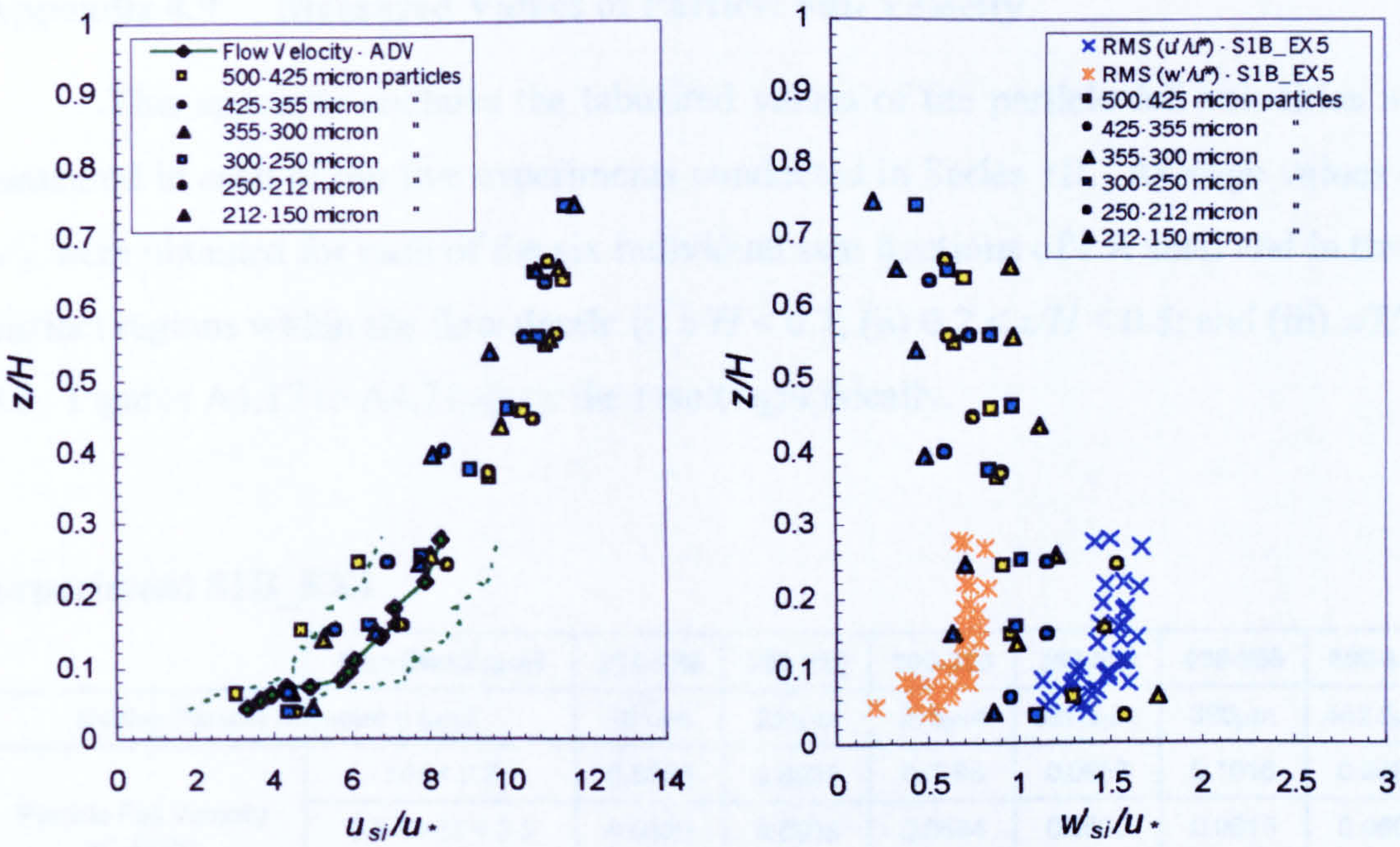

Figure A4.16 - Average fractional particle velocity profiles, measured from experiment S1B_EX5 data.

Appendix 4.9 Measured Values of Particle Fall Velocity

This appendix contains the tabulated values of the particle fall velocities w'_{si} measured in each of the five experiments conducted in Series 1B. Average values of w'_{si} were obtained for each of the six individual size fractions of LA sand and in three distinct regions within the flow depth: (i) $z/H < 0.2$; (ii) $0.2 < z/H < 0.5$; and (iii) $z/H > 0.5$. Figures A4.17 to A4.21 show the results graphically.

Experiment S1B_EX1

Size Class (μm)		212-150	250-212	300-250	355-300	425-355	500-425
Median Particle Diameter d (μm)		181μm	231μm	275μm	327.5μm	390μm	462.5μm
Particle Fall Velocity w'_{si} (m/s)	$z/H < 0.2$	0.0550	0.0631	0.0796	0.0958	0.1016	0.0968
	$0.2 < z/H < 0.5$	0.0533	0.0538	0.0584	0.0530	0.0615	0.0659
	$z/H > 0.5$	0.0297	0.0292	0.0317	0.0251	0.0394	0.0349
w_{si} (measured) (m/s)		0.0201	0.0270	0.0322	0.0405	0.0491	0.0600
Non-dimensional Fall Velocity Ratio w'_{si}/w_{si}	$z/H < 0.2$	2.74	2.34	2.47	2.36	2.07	1.61
	$0.2 < z/H < 0.5$	2.65	1.99	1.81	1.31	1.25	1.10
	$z/H > 0.5$	1.48	1.08	0.99	0.62	0.80	0.58

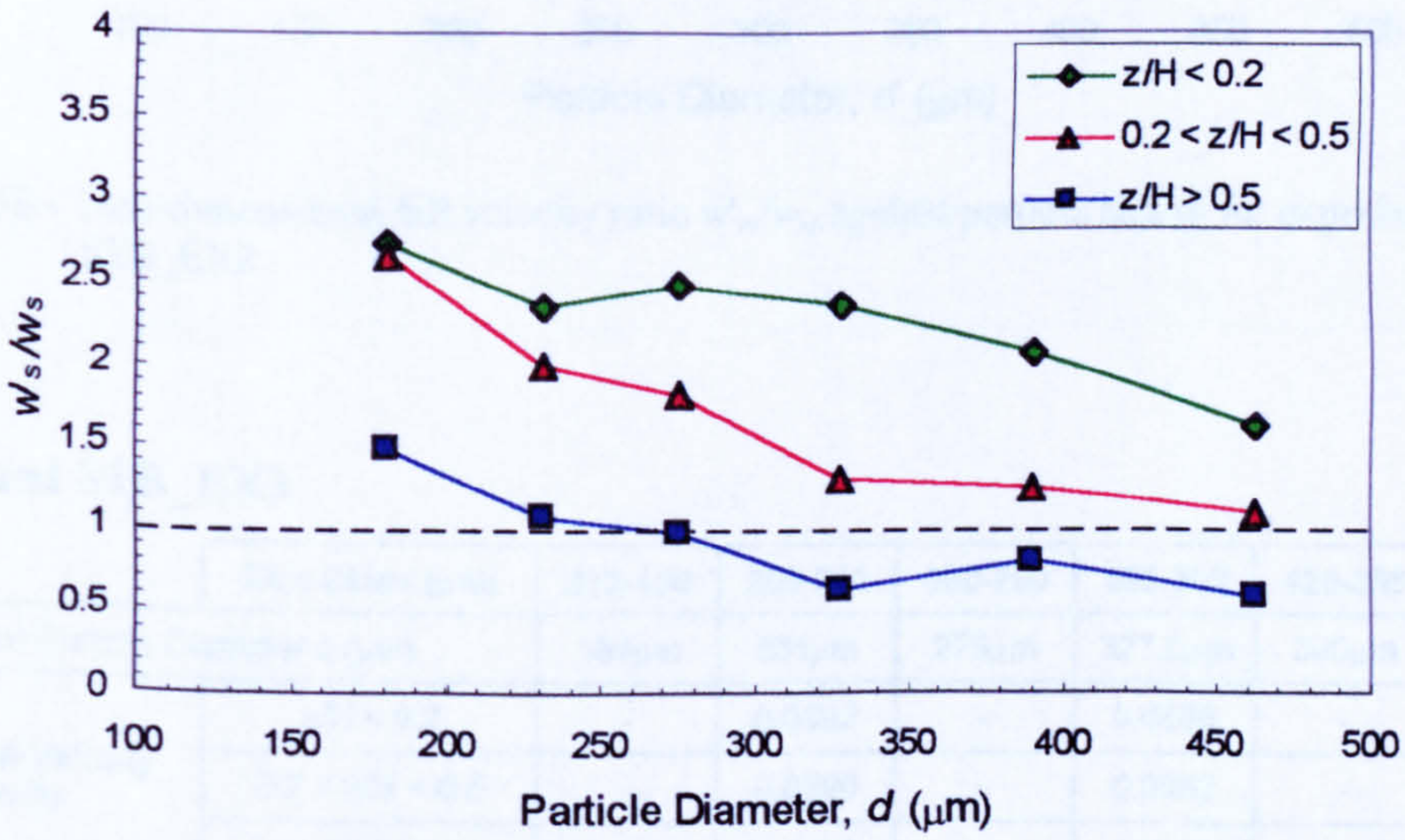

Figure A4.17 - Non-dimensional fall velocity ratio w'_{si}/w_{si} against particle size d_i for experiment S1B_EX1.

Experiment S1B_EX2

	Size Class (μm)	212-150	250-212	300-250	355-300	425-355	500-425
Median Particle Diameter d (μm)		181μm	231μm	275μm	327.5μm	390μm	462.5μm
Particle Fall Velocity w'_{si} (m/s)	*z/H < 0.2*	0.0306	0.0354	0.0578	0.0684	0.0625	0.0650
	0.2 < z/H < 0.5	0.0337	0.0425	0.0364	0.0408	0.0409	0.0417
	z/H > 0.5	0.0171	0.0159	0.0233	0.0201	0.0400	0.0278
w_{si} (measured) (m/s)		0.0201	0.0270	0.0322	0.0405	0.0491	0.0600
Non-dimensional Fall Velocity Ratio w'_{si}/w_{si}	*z/H < 0.2*	1.52	1.31	1.80	1.69	1.27	1.08
	0.2 < z/H < 0.5	1.68	1.57	1.13	1.01	0.83	0.69
	z/H > 0.5	0.85	0.59	0.72	0.50	0.82	0.46

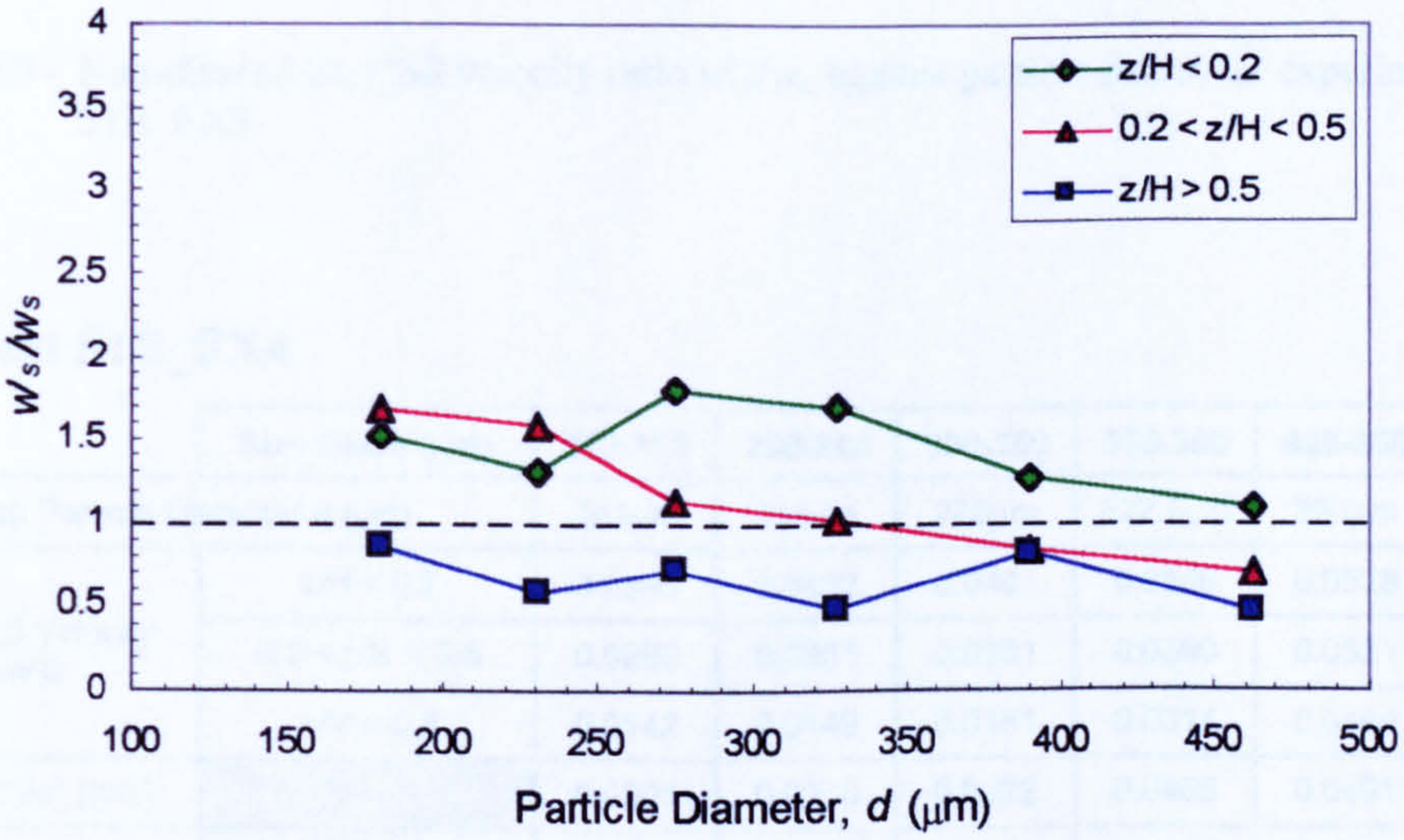

Figure A4.18 - Non-dimensional fall velocity ratio w'_{si}/w_{si} against particle size d_i for experiment S1B_EX2.

Experiment S1B_EX3

	Size Class (μm)	212-150	250-212	300-250	355-300	425-355	500-425
Median Particle Diameter d (μm)		181μm	231μm	275μm	327.5μm	390μm	462.5μm
Particle Fall Velocity w'_{si} (m/s)	*z/H < 0.2*	-	0.0592	-	0.0568	-	0.0650
	0.2 < z/H < 0.5	-	0.0390	-	0.0552	-	0.0590
	z/H > 0.5	-	0.0122	-	0.0232	-	0.0198
w_{si} (measured) (m/s)		0.0201	0.0270	0.0322	0.0405	0.0491	0.0600
Non-dimensional Fall Velocity Ratio w'_{si}/w_{si}	*z/H < 0.2*	-	2.19	-	1.40	-	1.08
	0.2 < z/H < 0.5	-	1.44	-	1.36	-	0.98
	z/H > 0.5	-	0.45	-	0.57	-	0.33

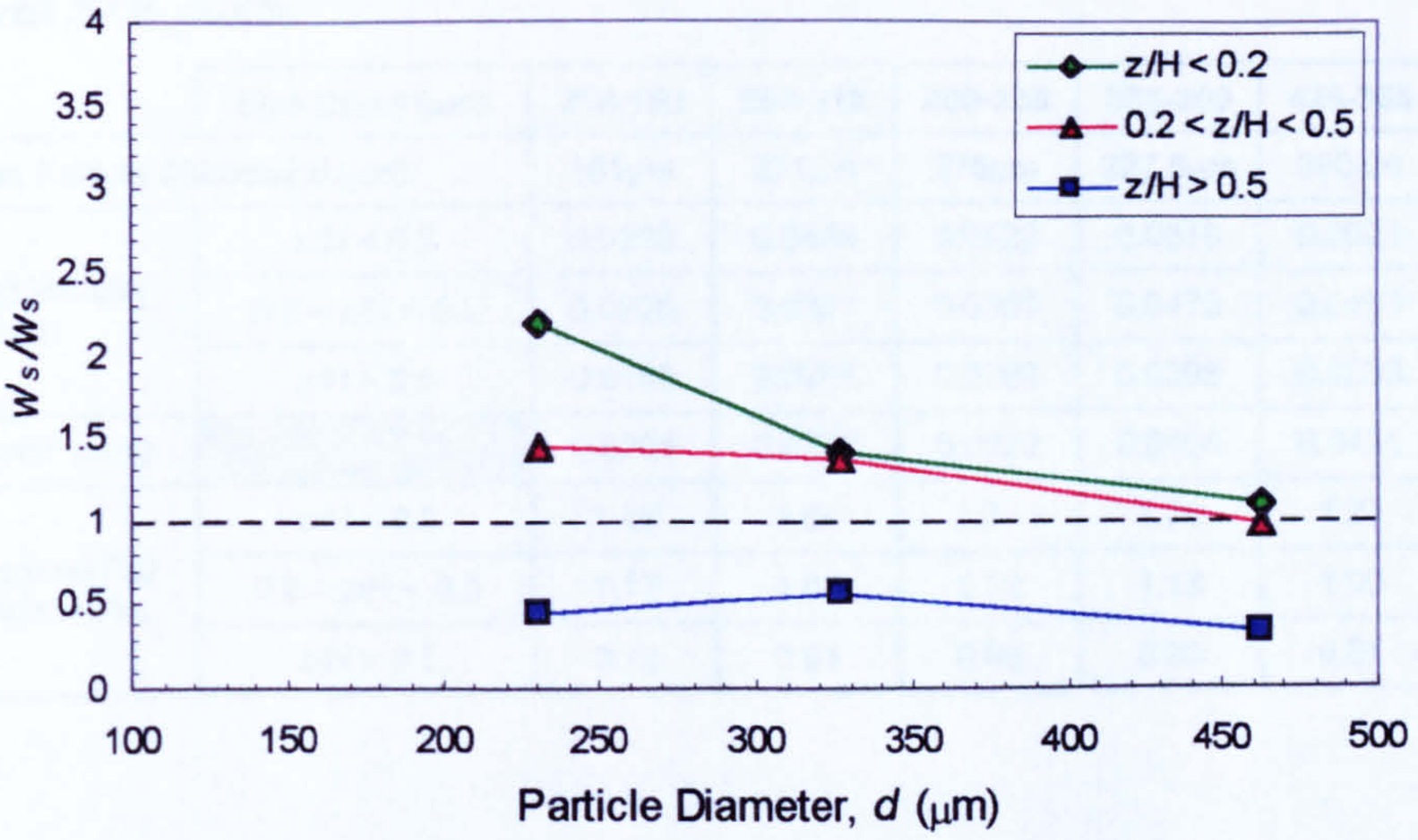

Figure A4.19 - Non-dimensional fall velocity ratio w'_{si}/w_{si} against particle size d_i for experiment S1B_EX3.

Experiment S1B_EX4

Size Class (μm)		212-150	250-212	300-250	355-300	425-355	500-425
Median Particle Diameter d (μm)		181μm	231μm	275μm	327.5μm	390μm	462.5μm
Particle Fall Velocity w'_{si} (m/s)	*z/H < 0.2*	0.0396	0.0532	0.0401	0.0548	0.0528	0.0639
	0.2 < z/H < 0.5	0.0290	0.0381	0.0331	0.0390	0.0521	0.0478
	z/H > 0.5	0.0142	0.0149	0.0181	0.0314	0.0154	0.0108
w_{si} (measured) (m/s)		0.0201	0.0270	0.0322	0.0405	0.0491	0.0600
Non-dimensional Fall Velocity Ratio w'_{si}/w_{si}	*z/H < 0.2*	1.97	1.97	1.24	1.35	1.08	1.06
	0.2 < z/h < 0.5	1.44	1.41	1.03	0.96	1.06	0.80
	z/H > 0.5	0.71	0.55	0.56	0.78	0.31	0.18

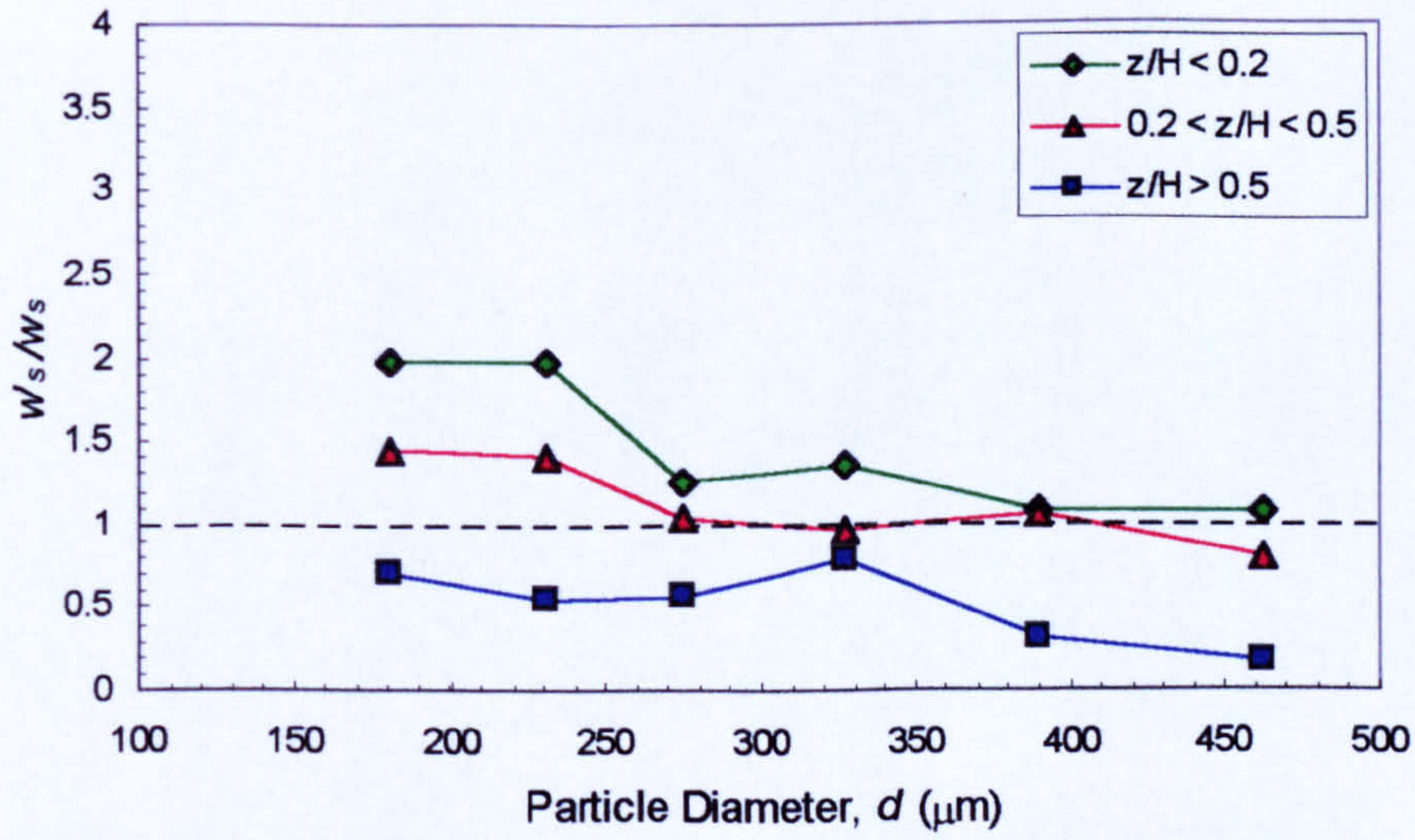

Figure A4.20 - Non-dimensional fall velocity ratio w'_{si}/w_{si} against particle size d_i for experiment S1B_EX4.

Experiment S1B_EX5

	Size Class (μm)	212-150	250-212	300-250	355-300	425-355	500-425
Median Particle Diameter d (μm)		181μm	231μm	275μm	327.5μm	390μm	462.5μm
Particle Fall Velocity w'_{si} (m/s)	*z/H < 0.2*	0.0295	0.0444	0.0422	0.0518	0.0621	0.0453
	0.2 < z/H < 0.5	0.0235	0.0391	0.0393	0.0478	0.0493	0.0353
	z/H > 0.5	0.0158	0.0257	0.0286	0.0395	0.0253	0.0280
w_{si} (measured) (m/s)		0.0201	0.0270	0.0322	0.0405	0.0491	0.0600
Non-dimensional Fall Velocity Ratio w'_{si}/w_{si}	*z/H < 0.2*	1.47	1.64	1.31	1.28	1.27	0.76
	0.2 < z/H < 0.5	1.17	1.45	1.22	1.18	1.00	0.59
	z/H > 0.5	0.79	0.95	0.89	0.98	0.51	0.47

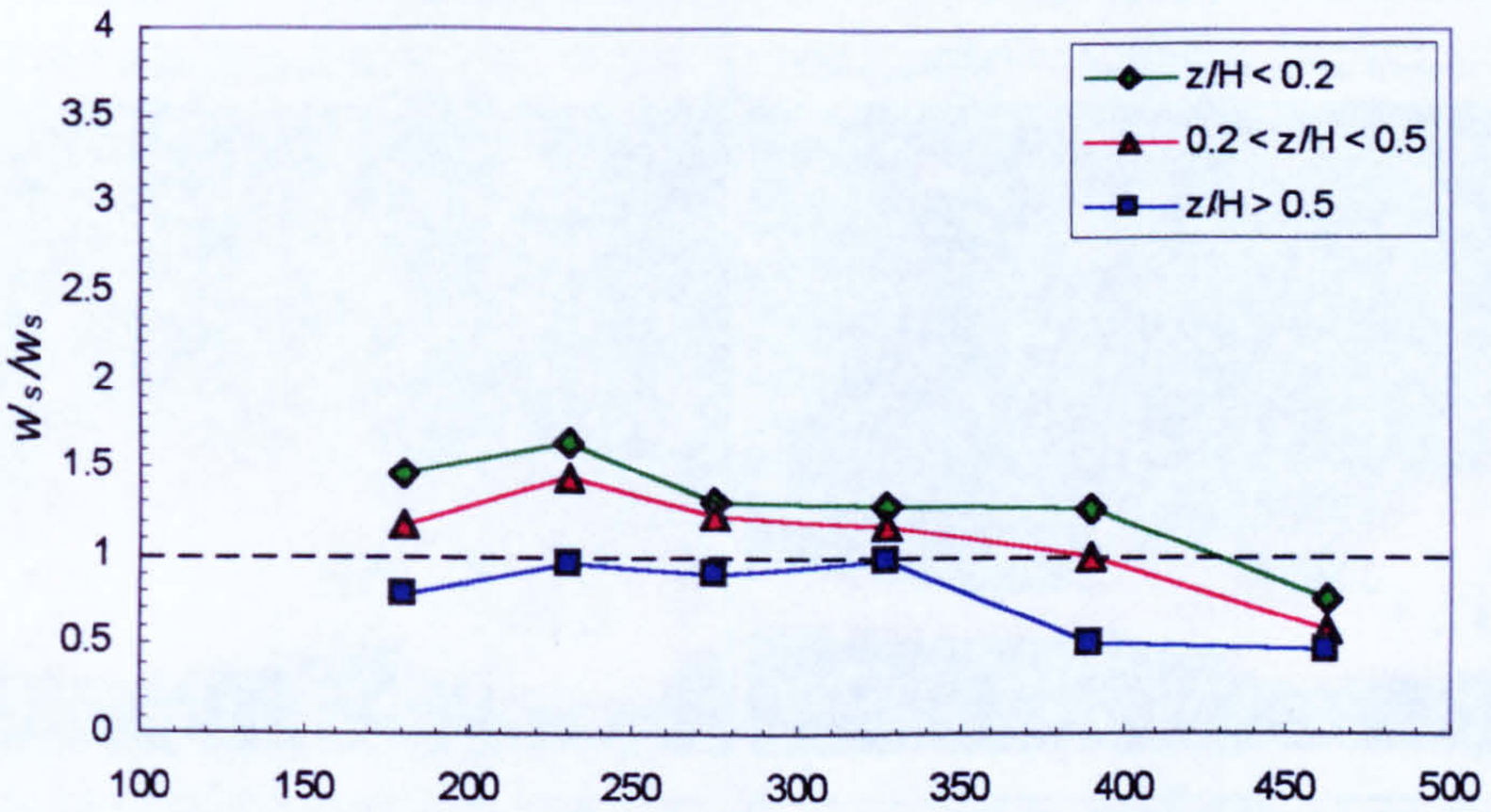

Figure A4.21 - Non-dimensional fall velocity ratio w'_{si}/w_{si} against particle size d_i for experiment S1B_EX5.

Appendix 5.1 Flow Visualisation Images from Series 1C

(1) Experiment S1C_EX1 Images ($z/H = 0.0 - 0.70$)

Experiment S1C_EX1: Window 1, Lateral Pos. 6cm, z/H = 0.0 – 0.65

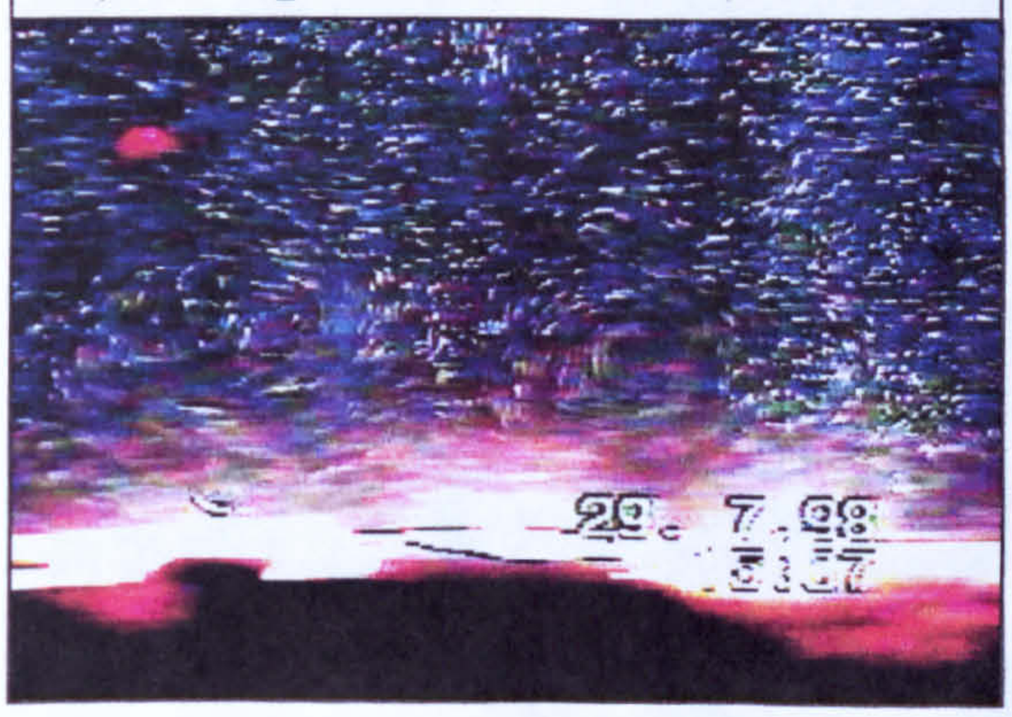

Experiment S1C_EX1: Window 1, Lateral Pos. 6cm, z/H = 0.0 – 0.65

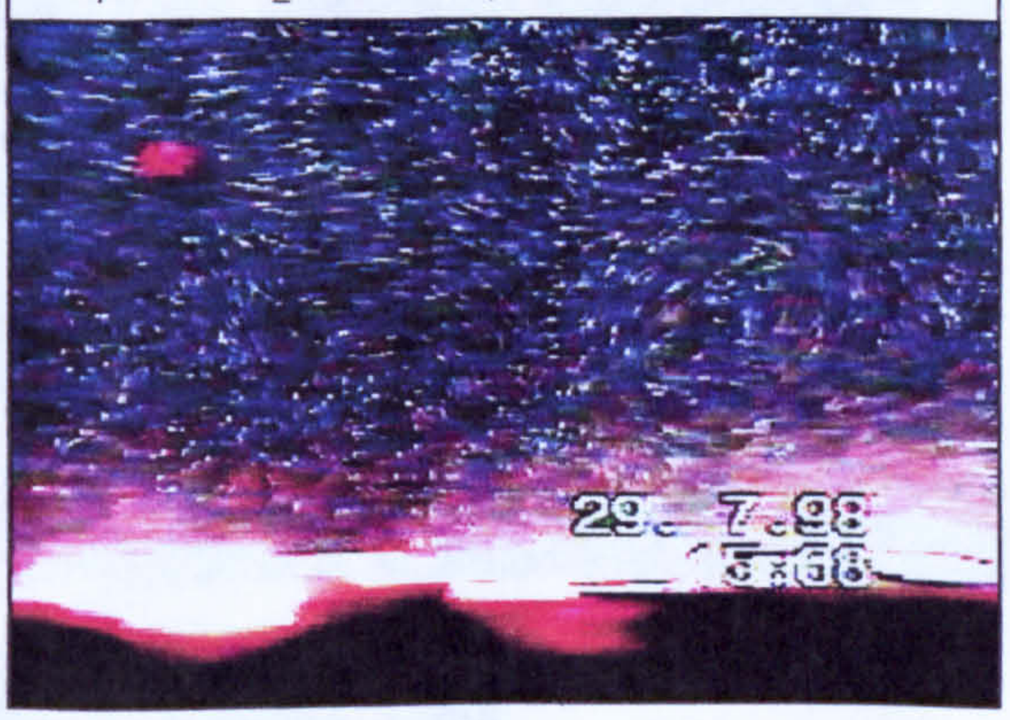

Experiment S1C_EX1: Window 1, Lateral Pos. 10cm, z/H = 0.0 – 0.65

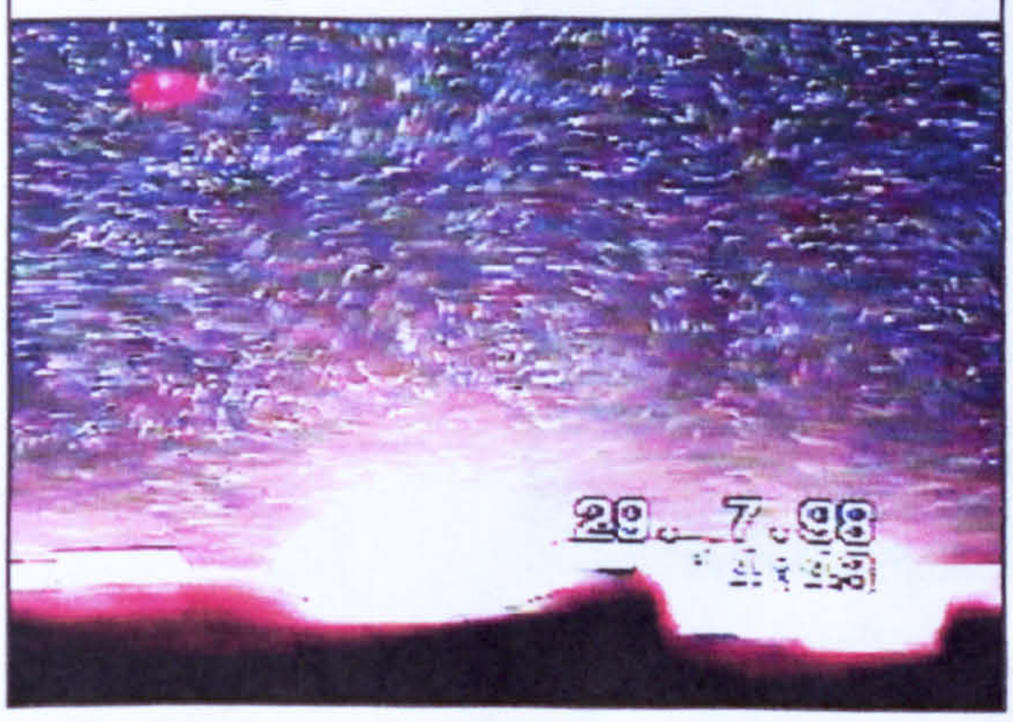

Experiment S1C_EX1: Window 1, Lateral Pos. 10cm, z/H = 0.0 – 0.65

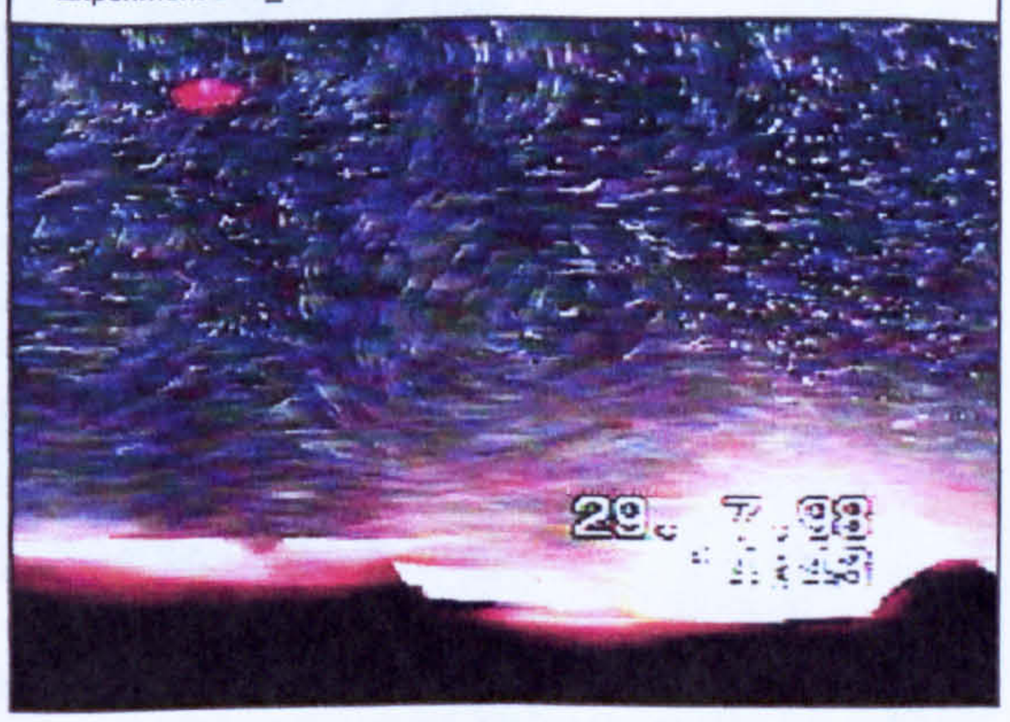

Experiment S1C_EX1: Window 2, Lateral Pos. 3cm, z/H = 0.0 – 0.70

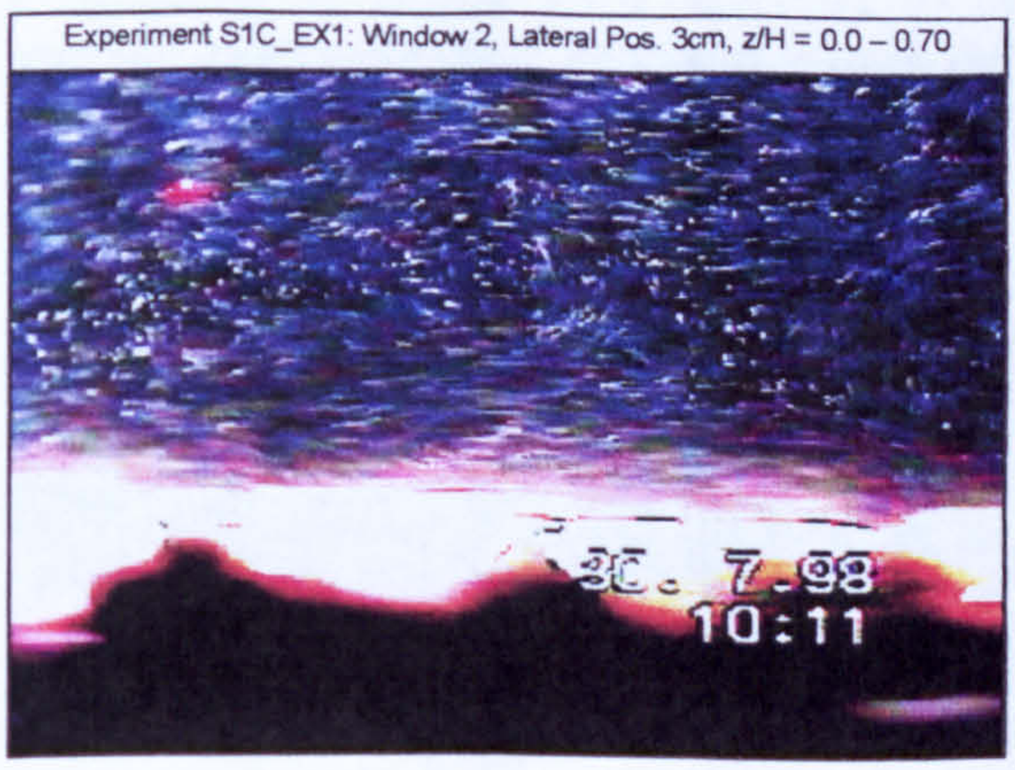

Experiment S1C_EX1: Window 2, Lateral Pos. 6cm, z/H = 0.0 – 0.70

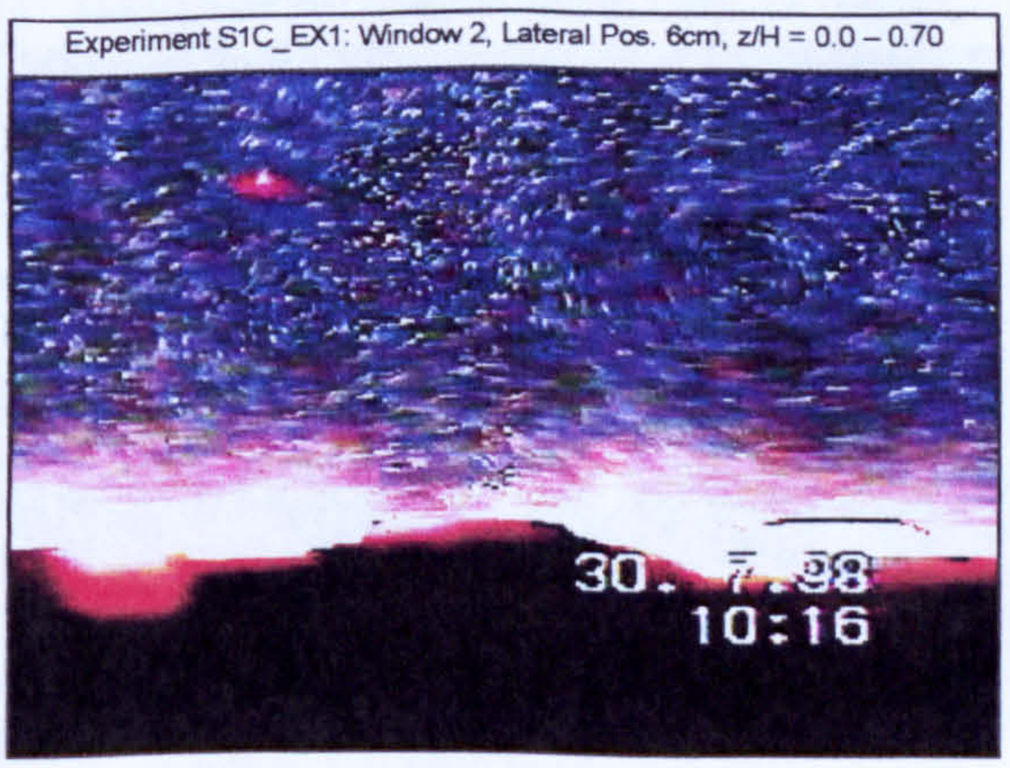

Experiment S1C_EX1: Window 2, Lateral Pos. 6cm, z/H = 0.0 – 0.70

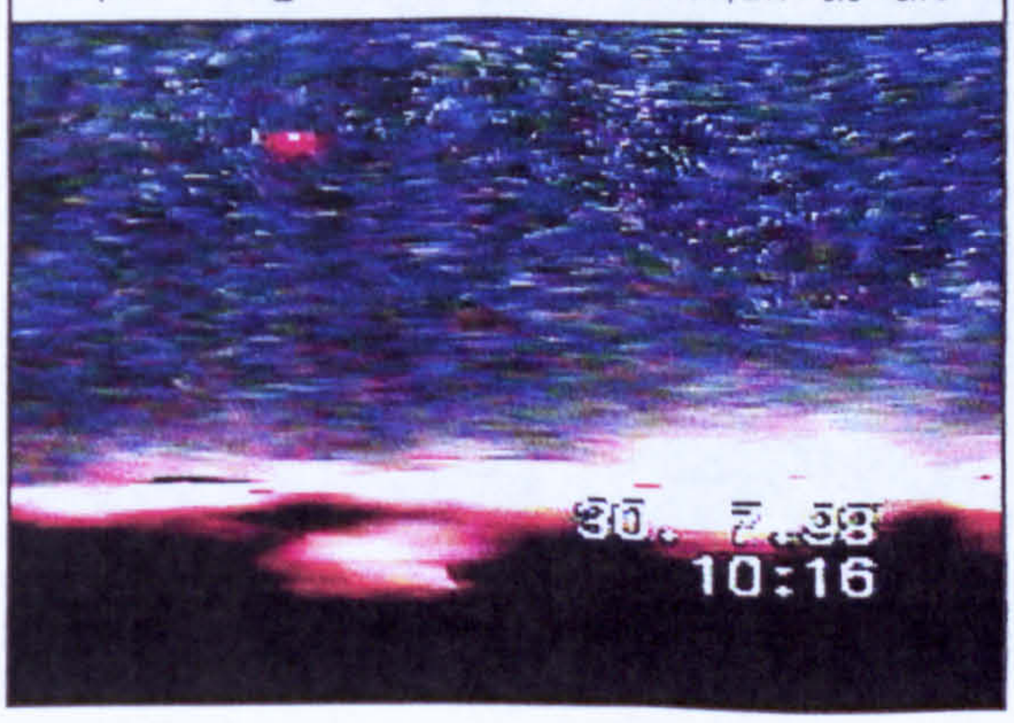

Experiment S1C_EX1: Window 3, Lateral Pos. 3cm, z/H = 0.0 – 0.70

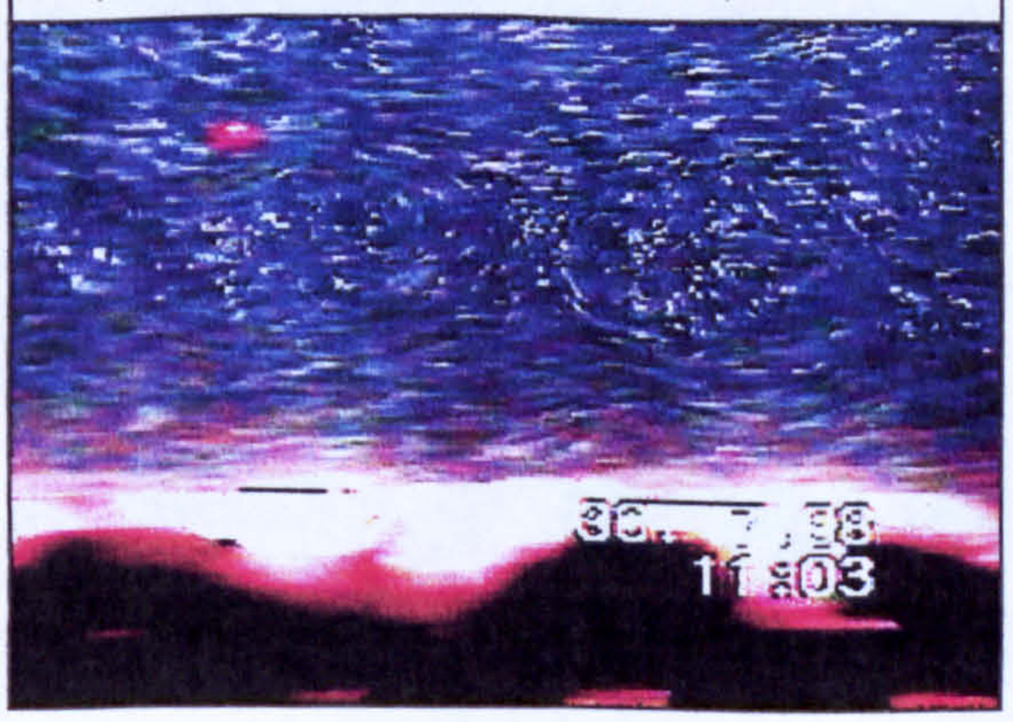

(1) Experiment S1C_EX1 Images ($z/H = 0.0 - 0.70$) cont/d.

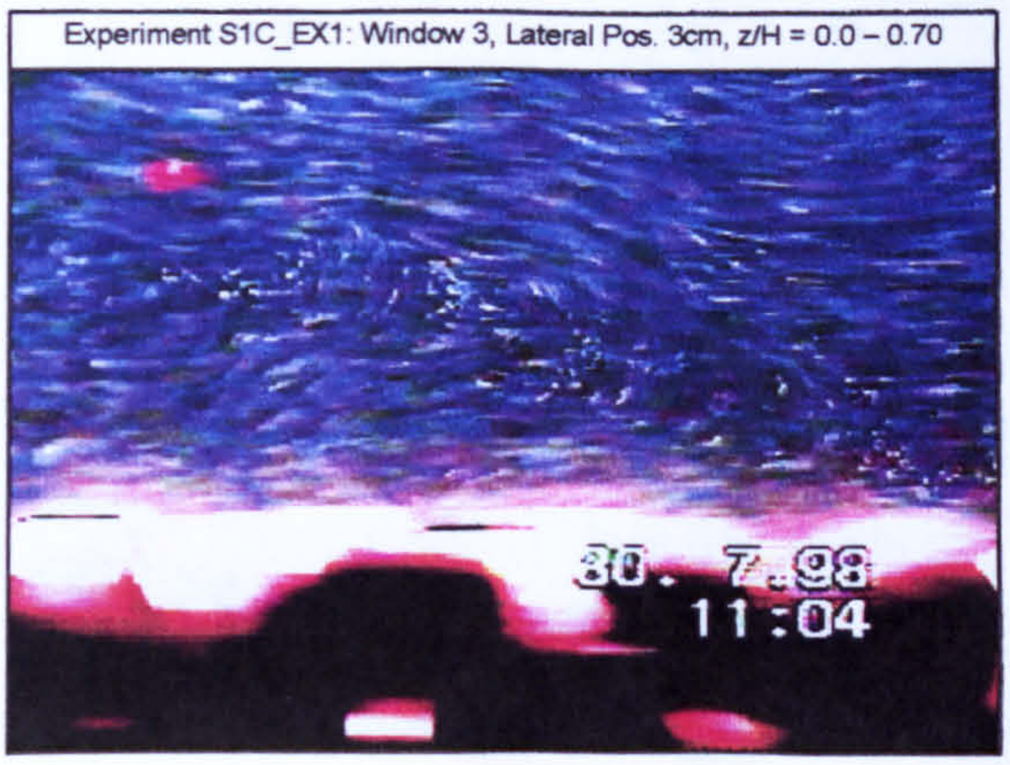

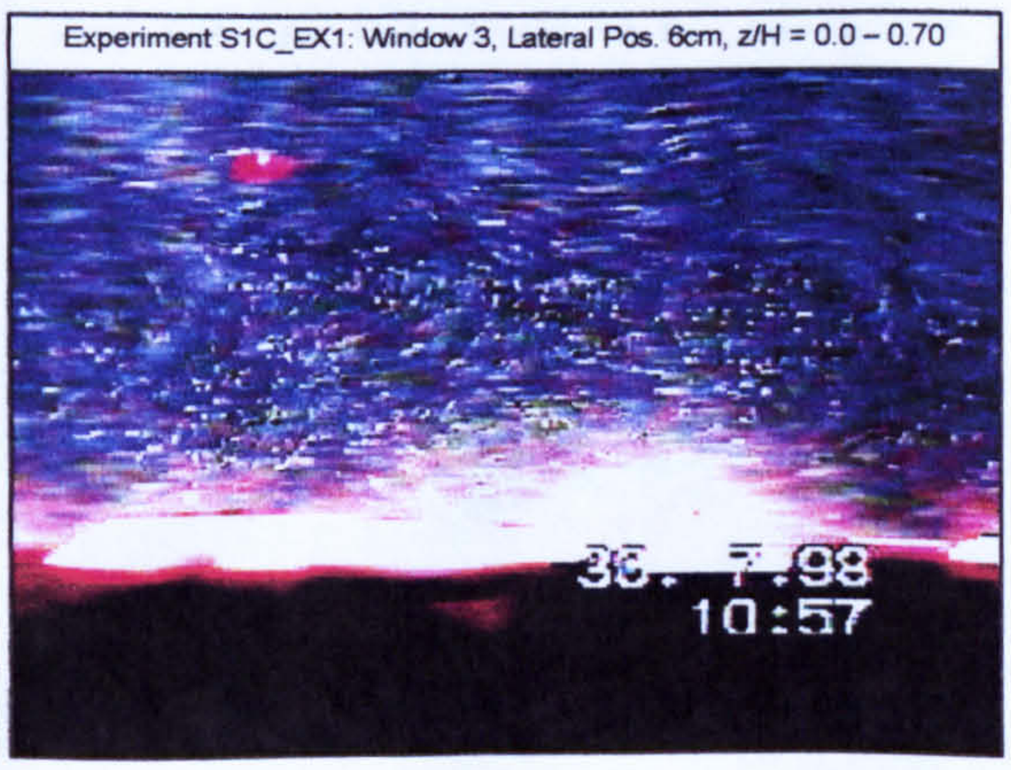

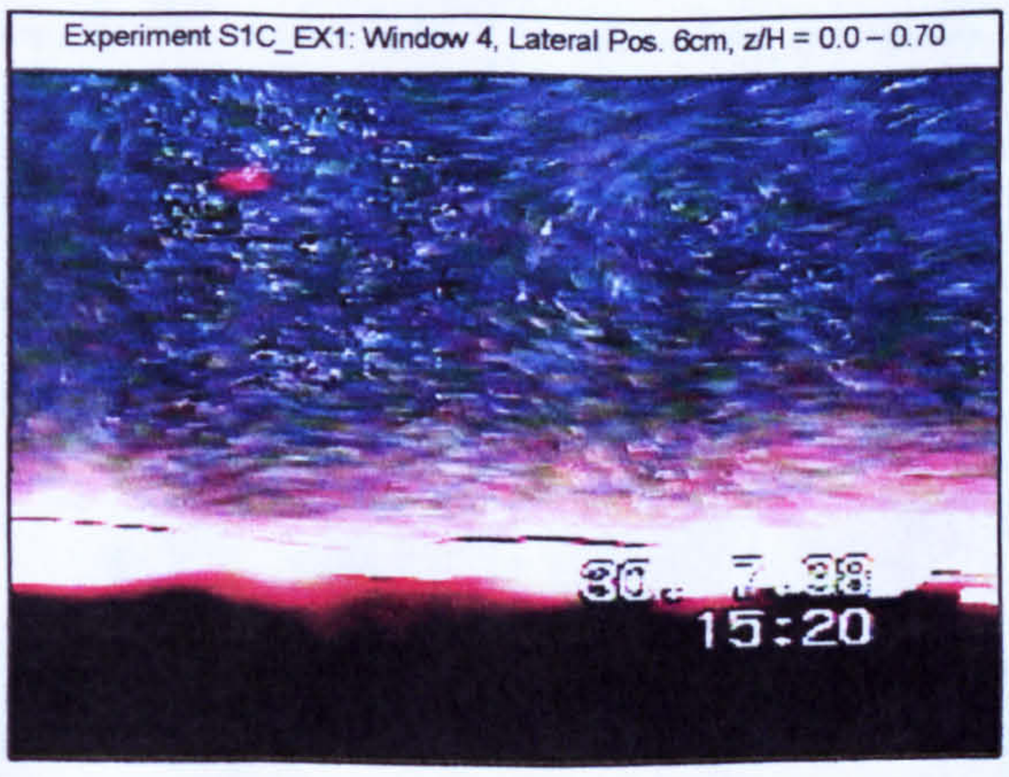

(2) Experiment S1C_EX1 Images ($z/H = 0.0 - 1.0$)

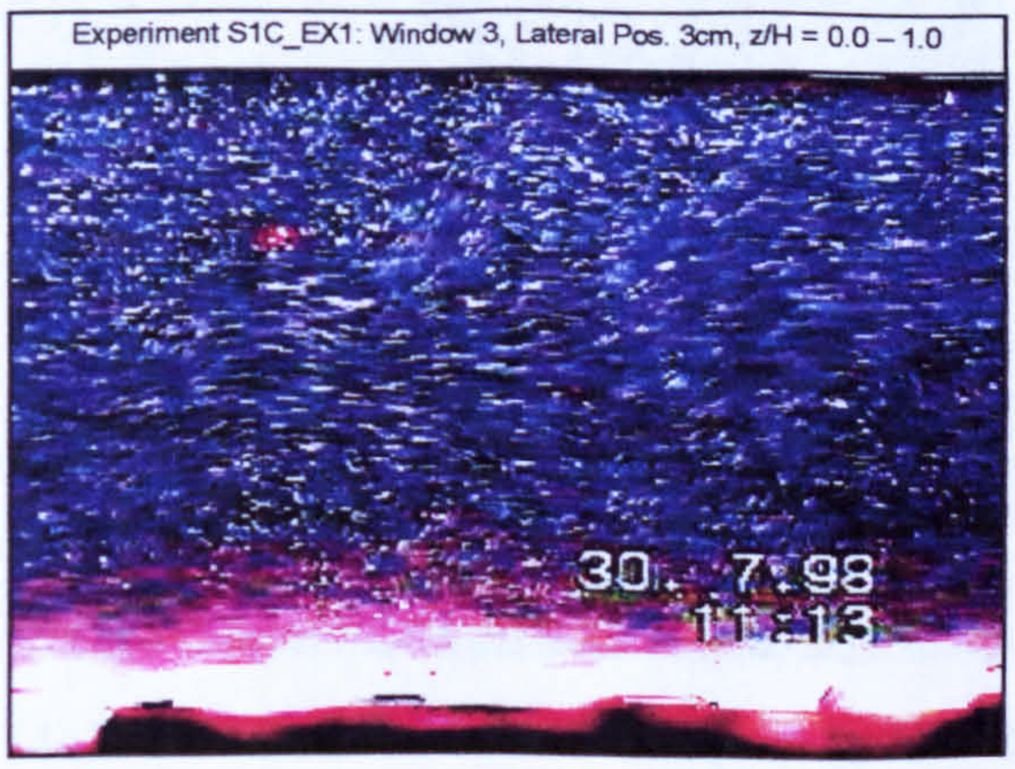

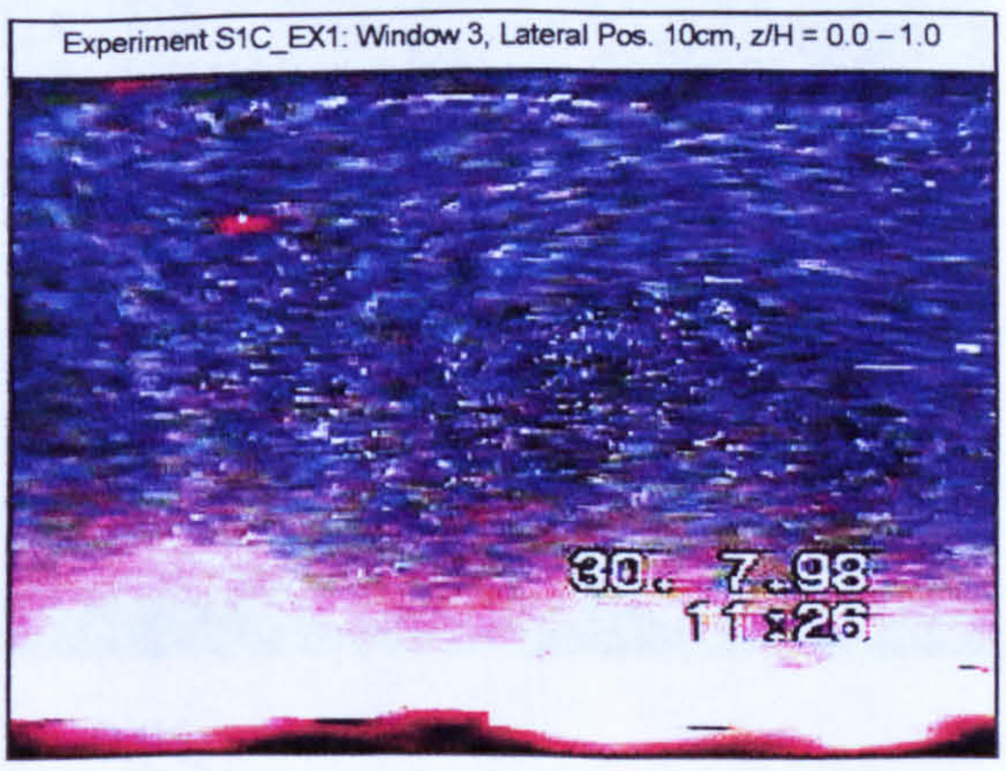

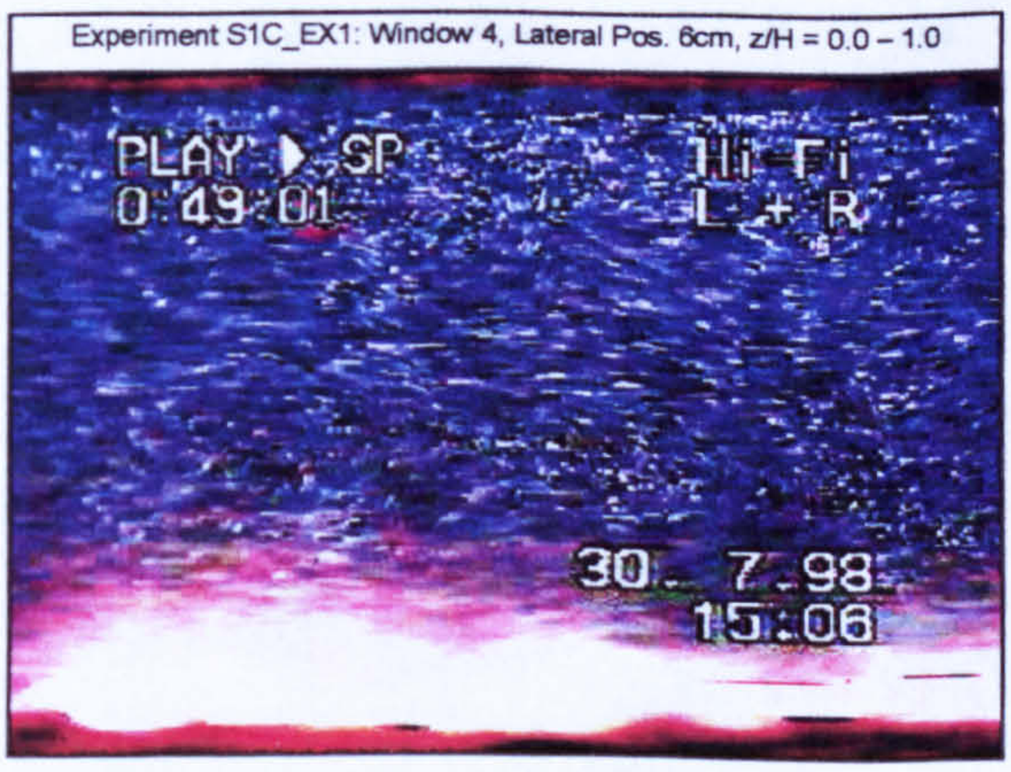

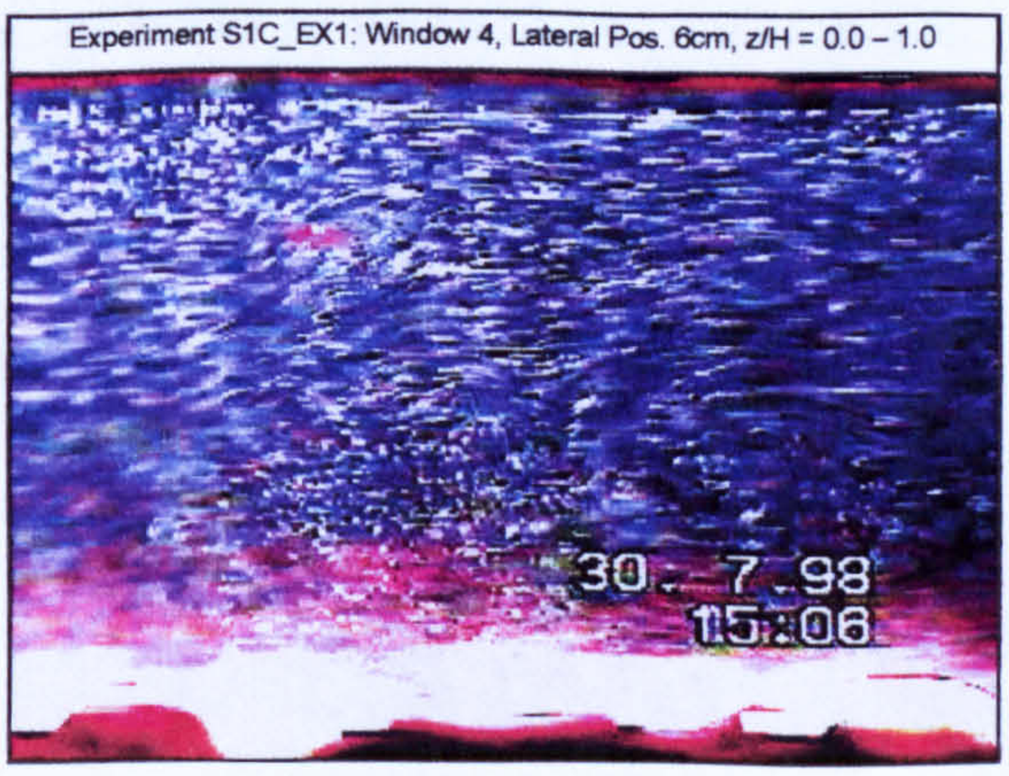

(3) Experiment S1C_EX2 Images ($z/H = 0.0 - 0.70$)

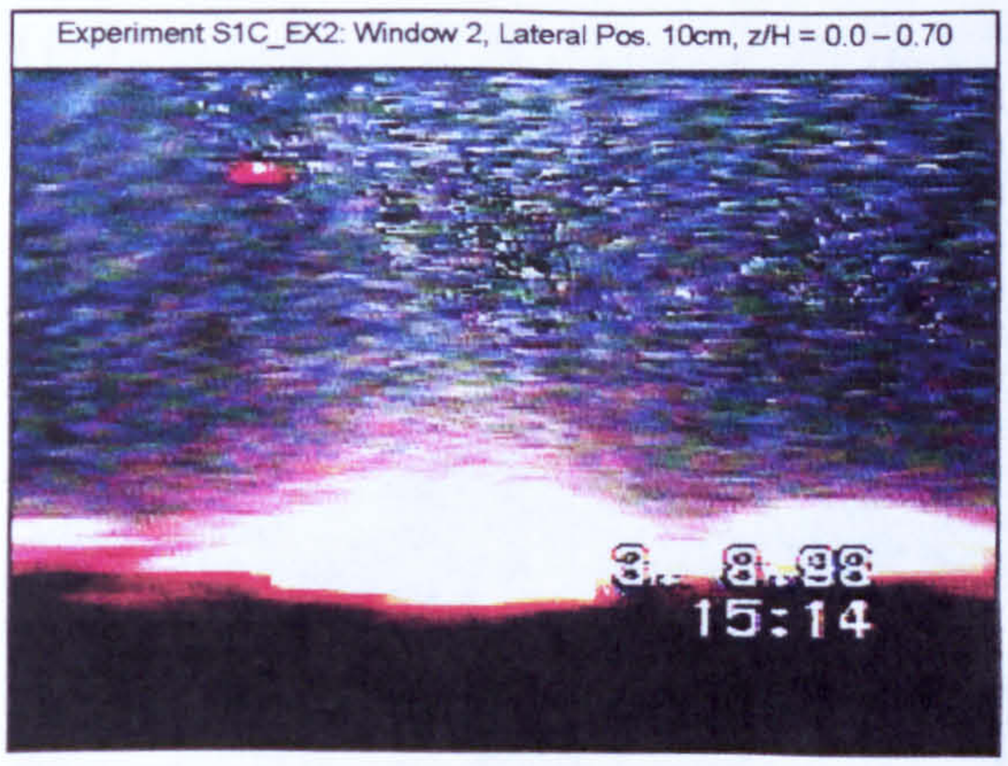

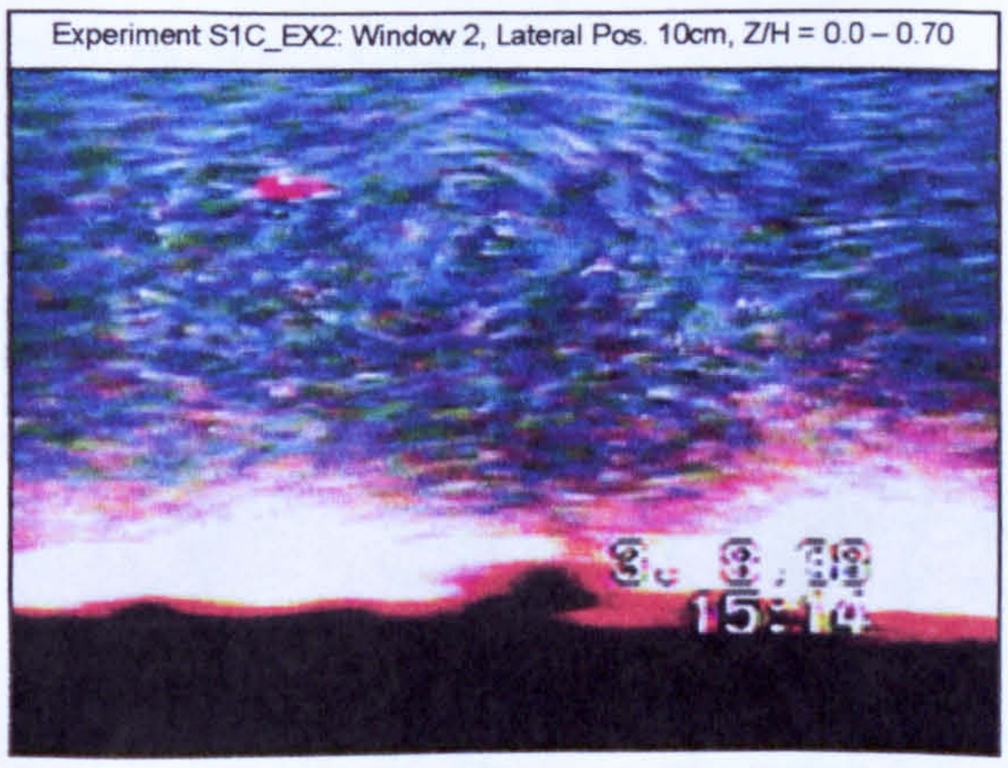

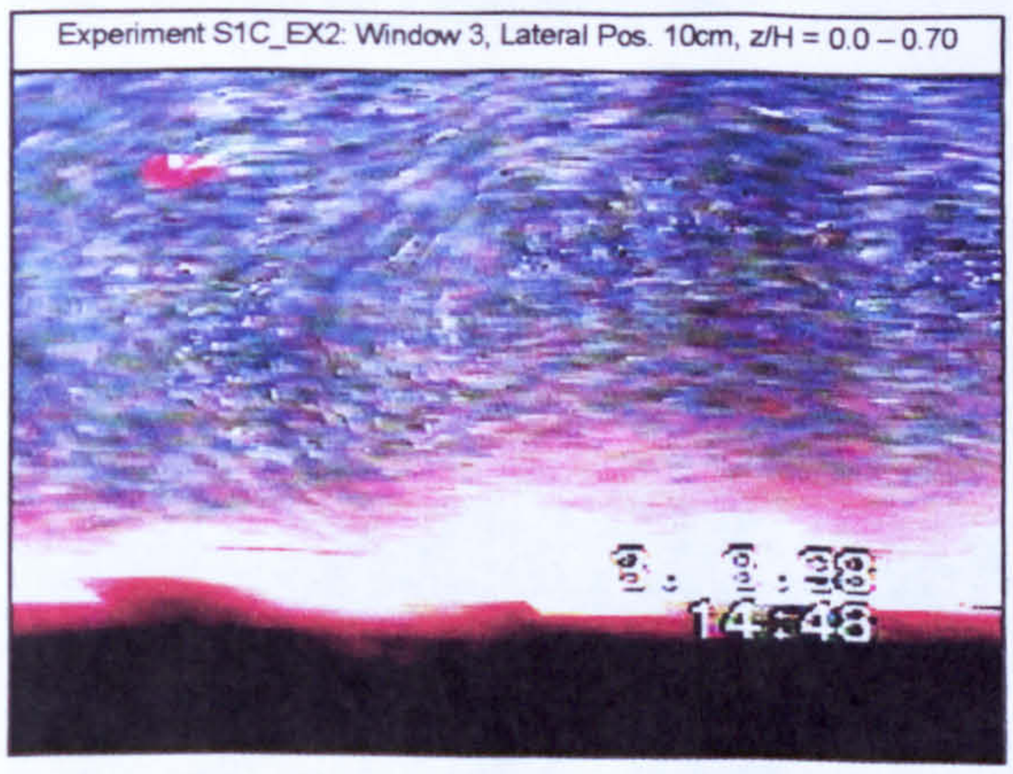

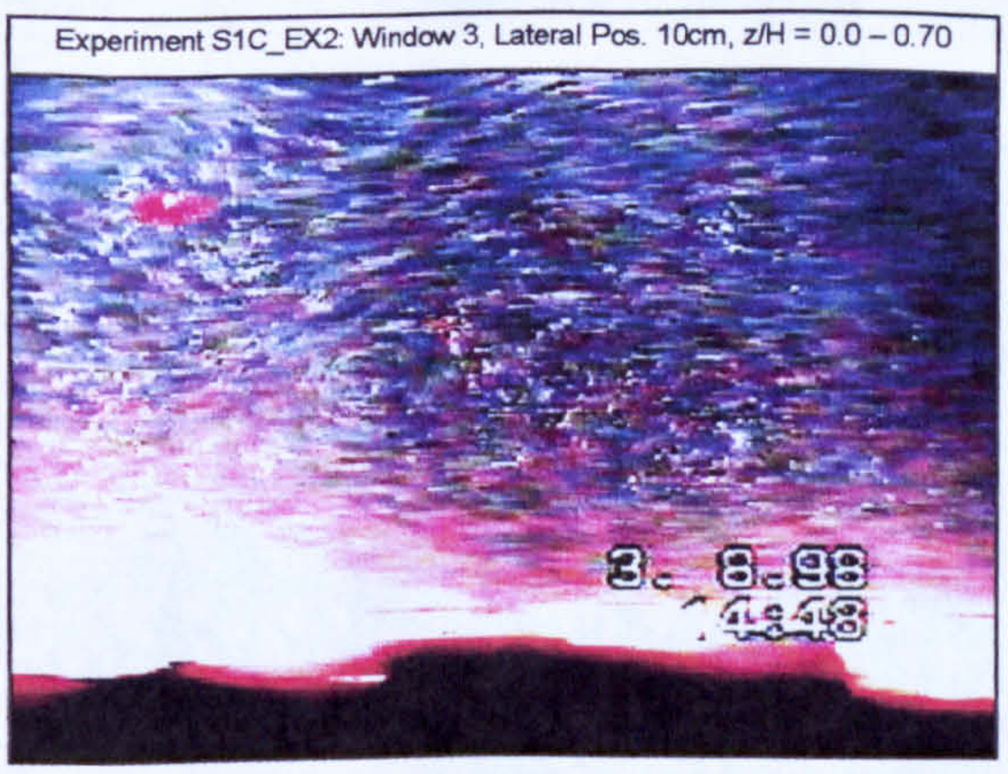

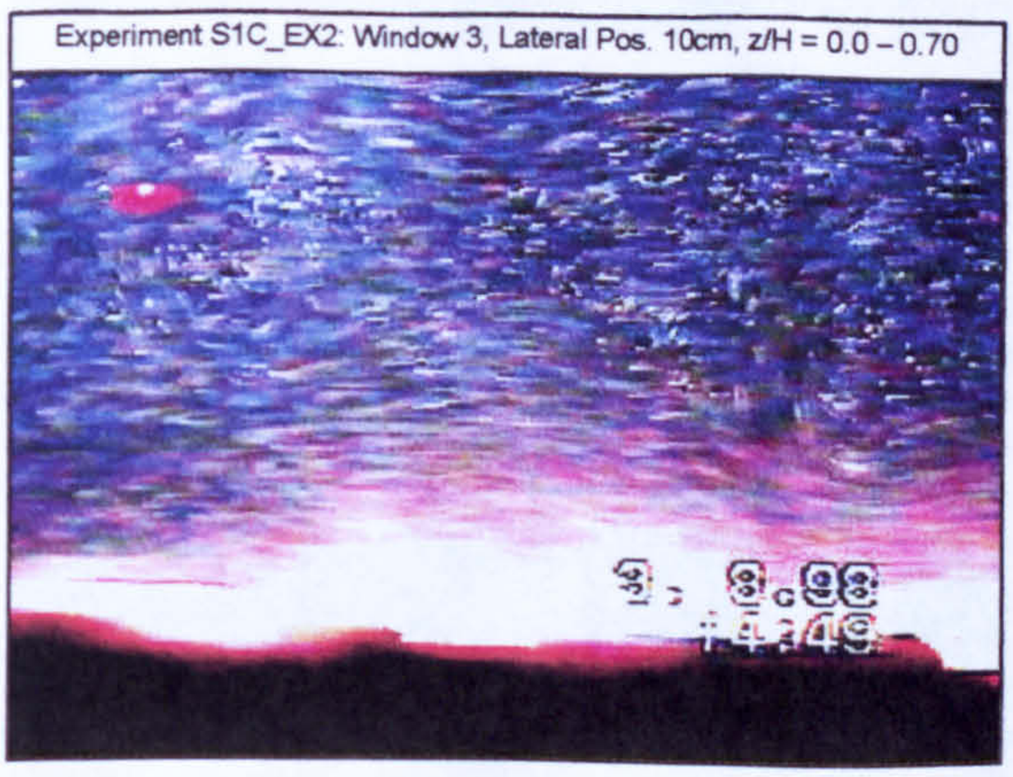

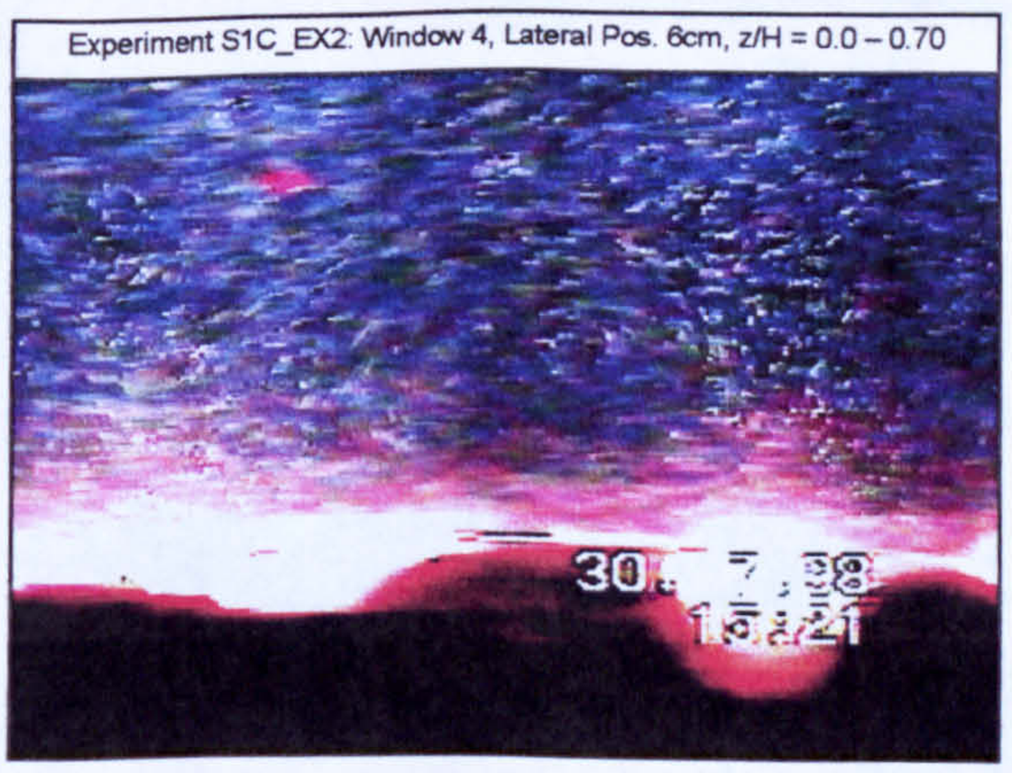

(4) Experiment S1C_EX2 Images ($z/H = 0.0 - 0.95$)

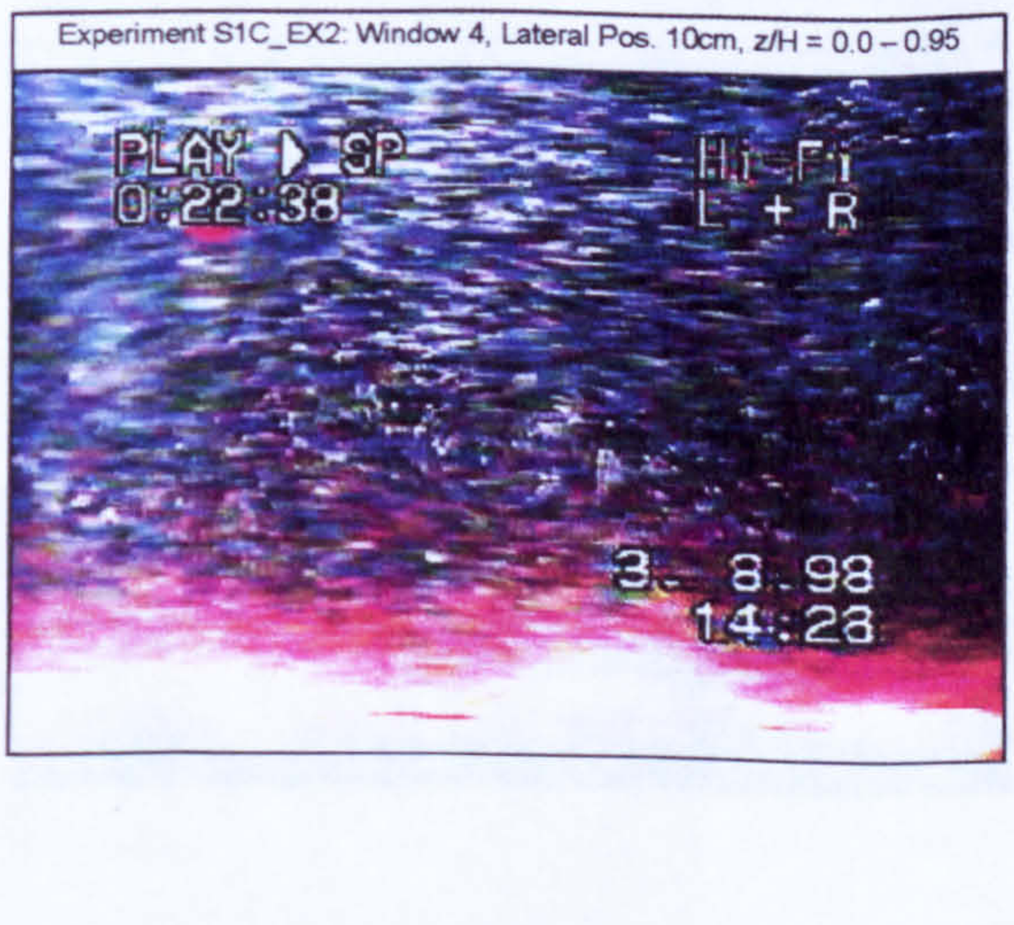

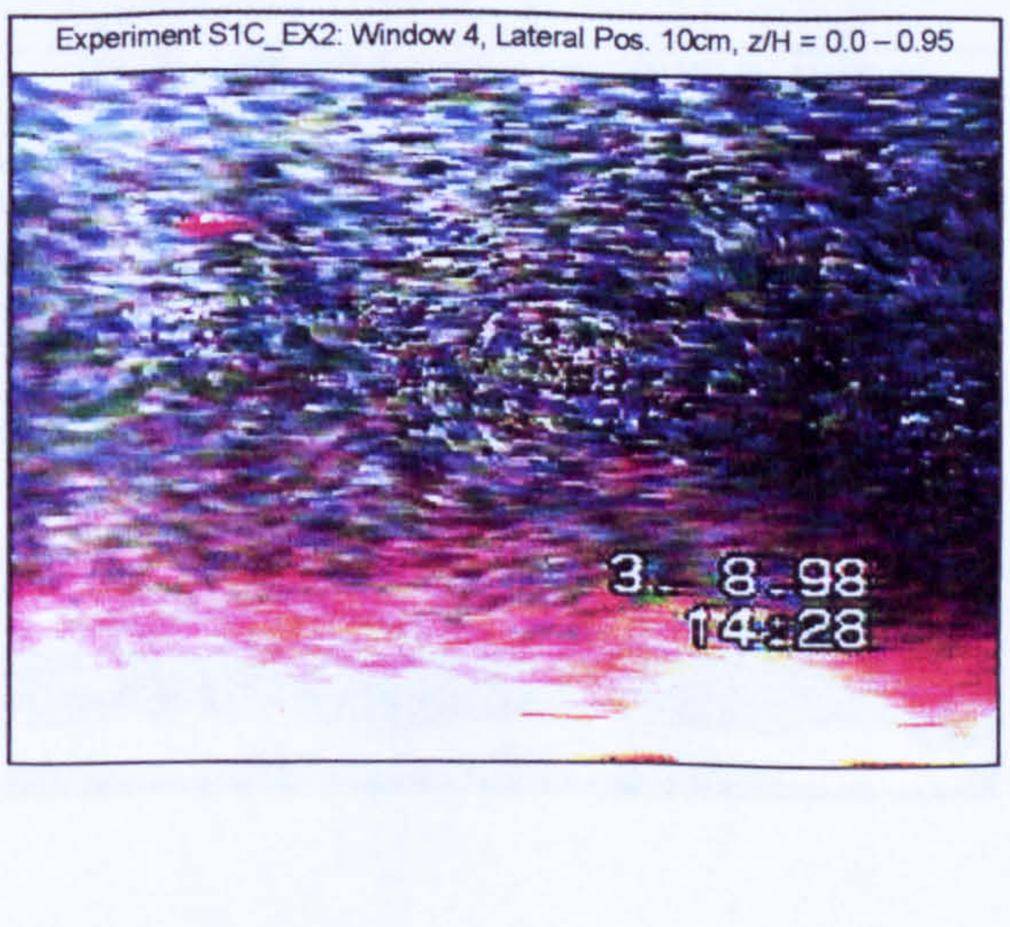

Appendix 5.2 Images of Particle-Flow Interactions

(1) Images for Individual LA Grade Size Fractions (S1C_EX3)

Experiment S1C_EX3, Lateral Pos. 6cm, 500-425μm LA particles

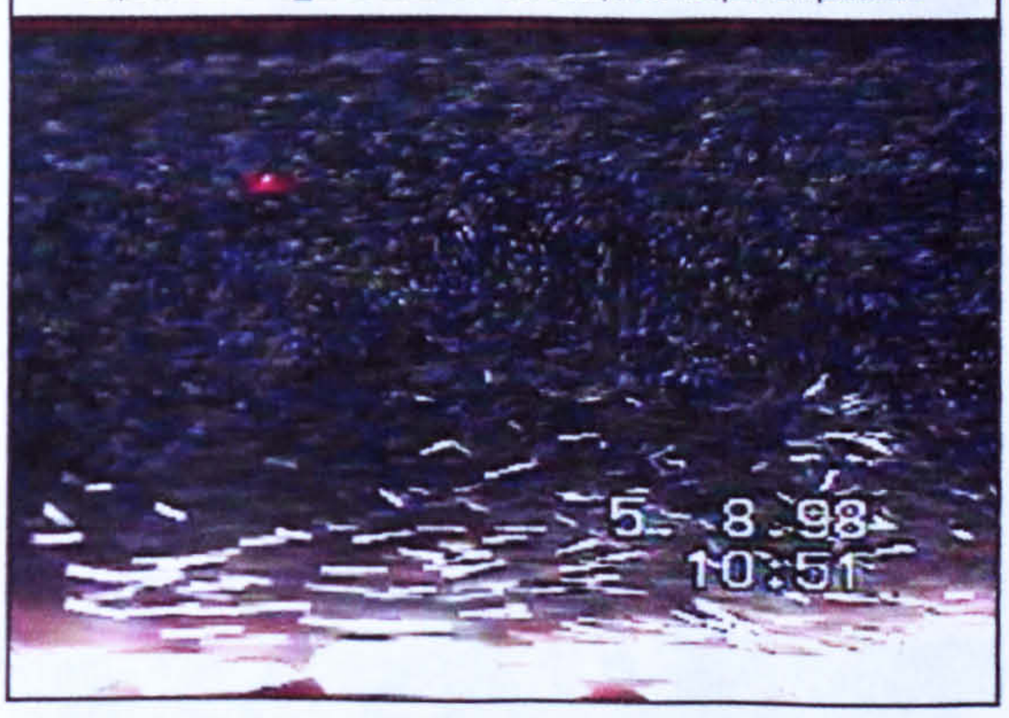

Experiment S1C_EX3, Lateral Pos. 6cm, 500-425μm LA particles

Experiment S1C_EX3, Lateral Pos. 10cm, 500-425μm LA particles

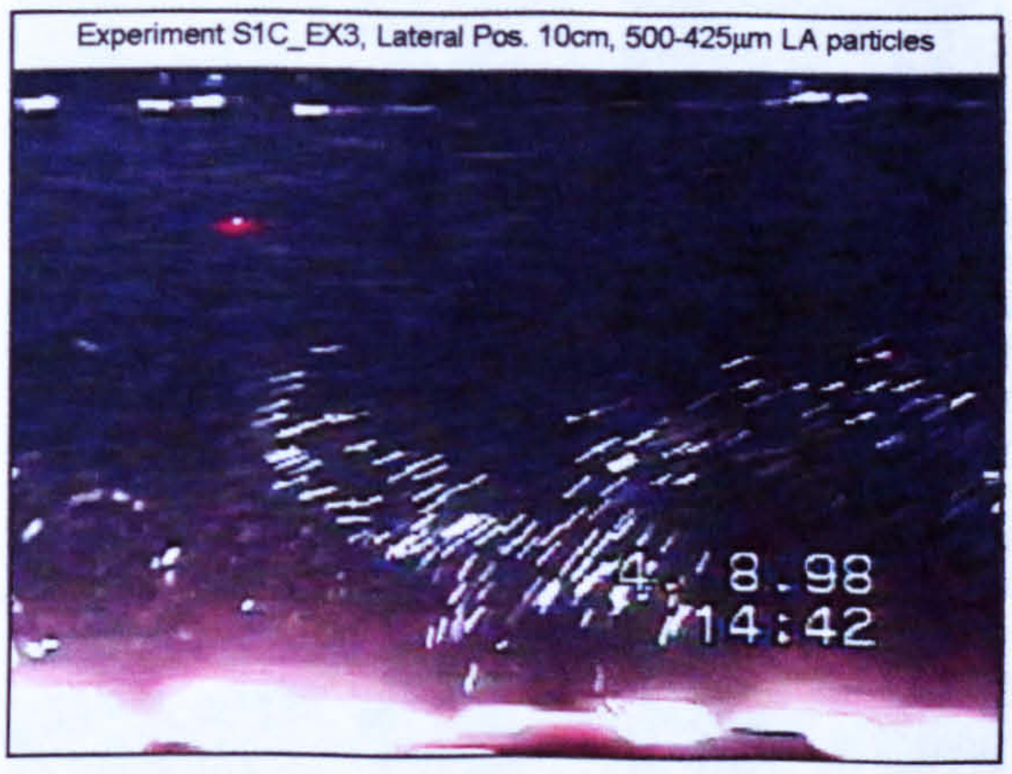

Experiment S1C_EX3, Lateral Pos. 10cm, 500-425μm LA particles

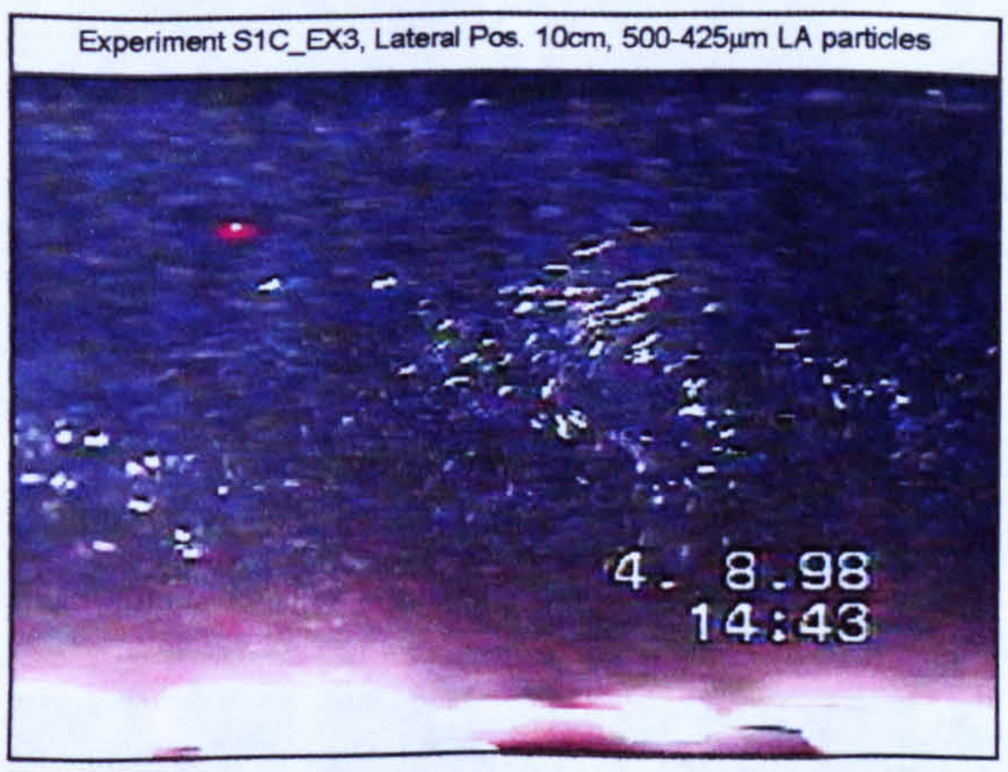

Experiment S1C_EX3, Lateral Pos. 15cm, 500-425μm LA particles

Experiment S1C_EX3, Lateral Pos. 10cm, 425-355μm LA particles

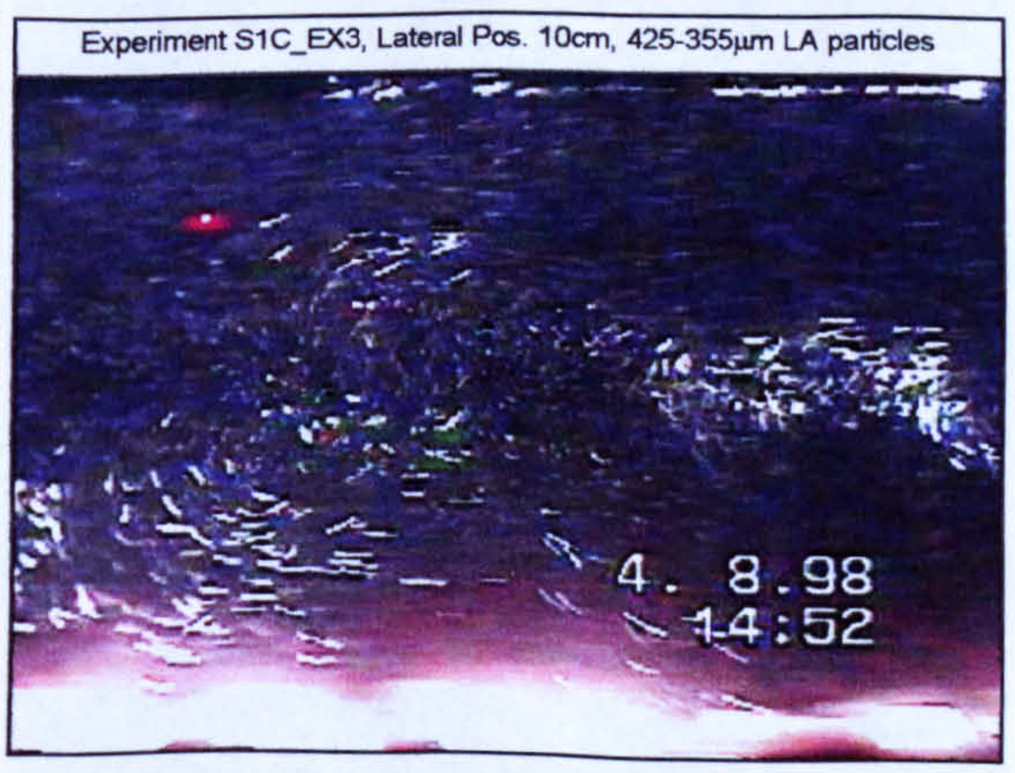

Experiment S1C_EX3, Lateral Pos. 15cm, 425-355μm LA particles

Experiment S1C_EX3, Lateral Pos. 6cm, 355-300μm LA particles

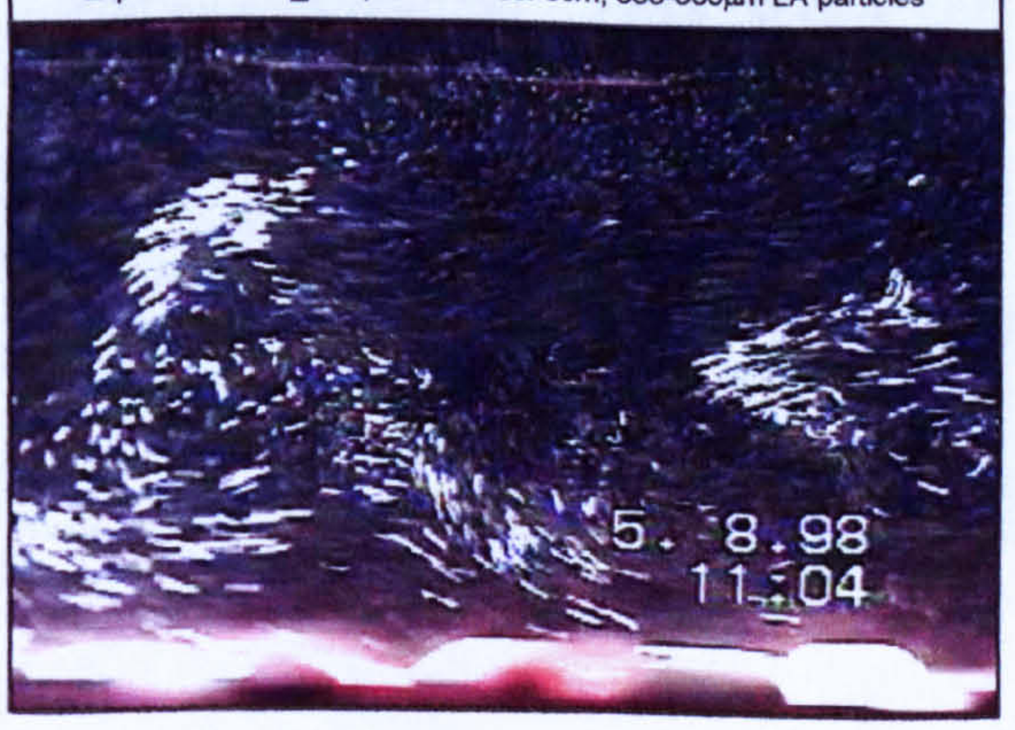

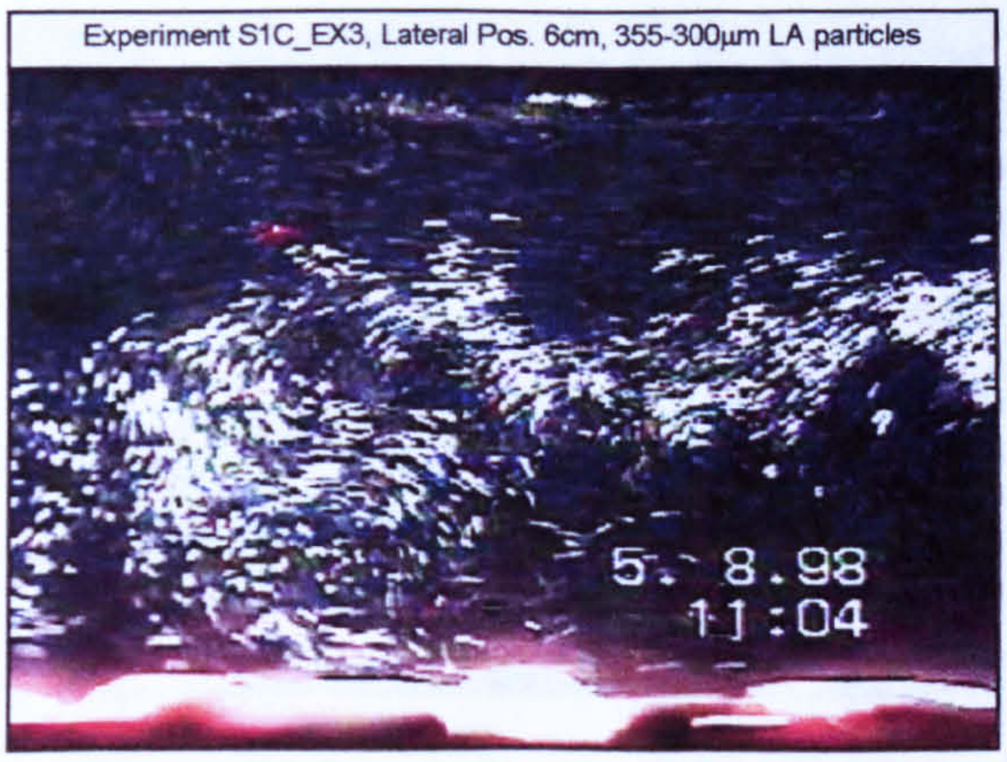
Experiment S1C_EX3, Lateral Pos. 6cm, 355-300µm LA particles
5. 8.98
11:04

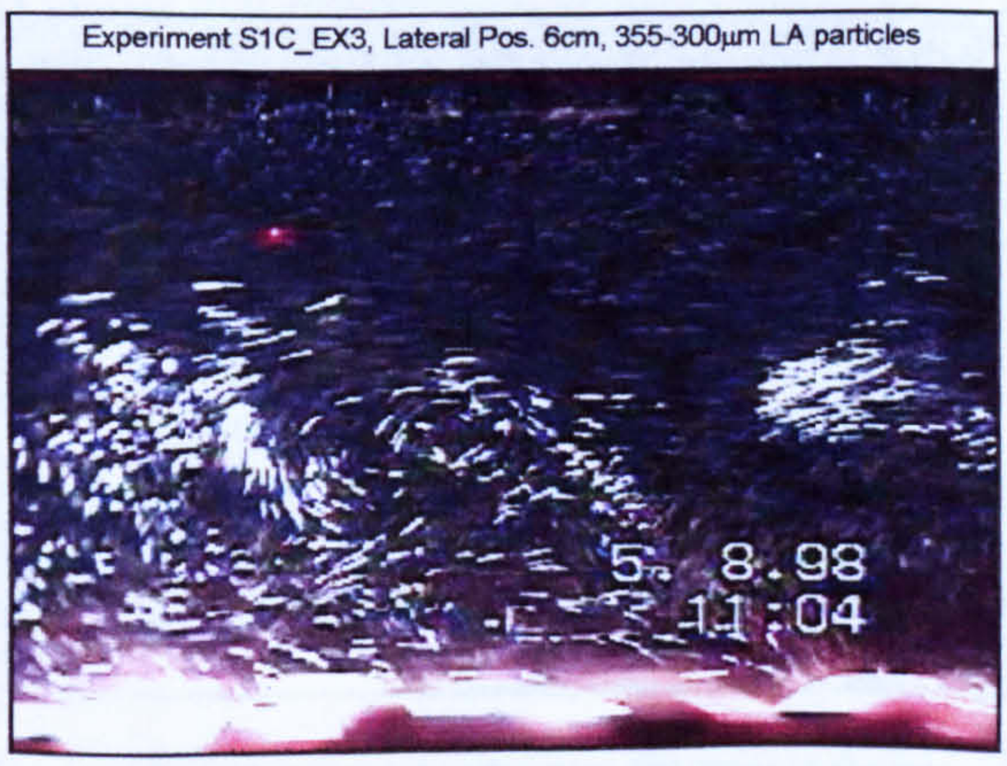
Experiment S1C_EX3, Lateral Pos. 6cm, 355-300µm LA particles
5. 8.98
11:04

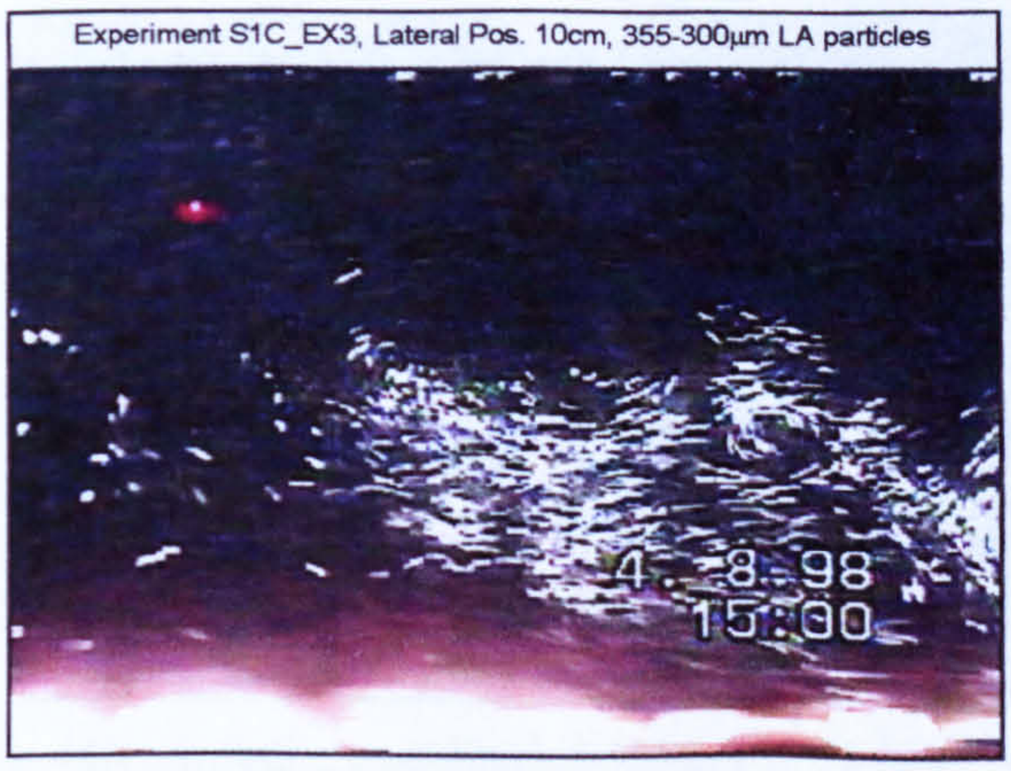
Experiment S1C_EX3, Lateral Pos. 10cm, 355-300µm LA particles
4. 8.98
15:00

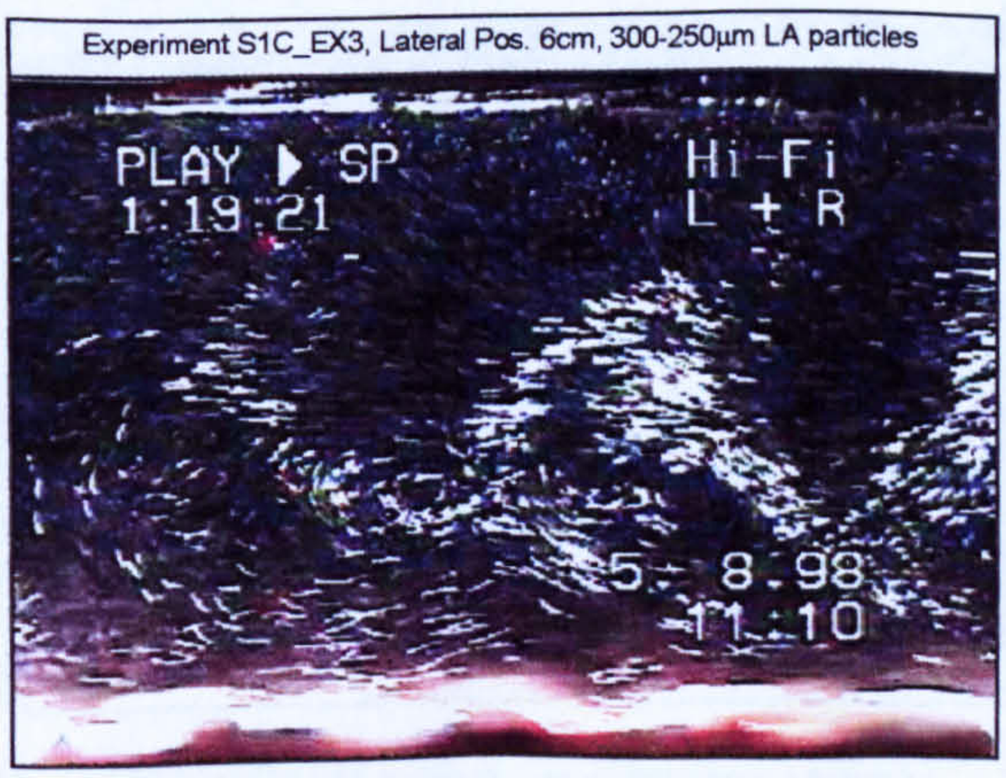
Experiment S1C_EX3, Lateral Pos. 6cm, 300-250µm LA particles
PLAY ▶ SP
1:19:21
Hi-Fi
L + R
5. 8.98
11:10

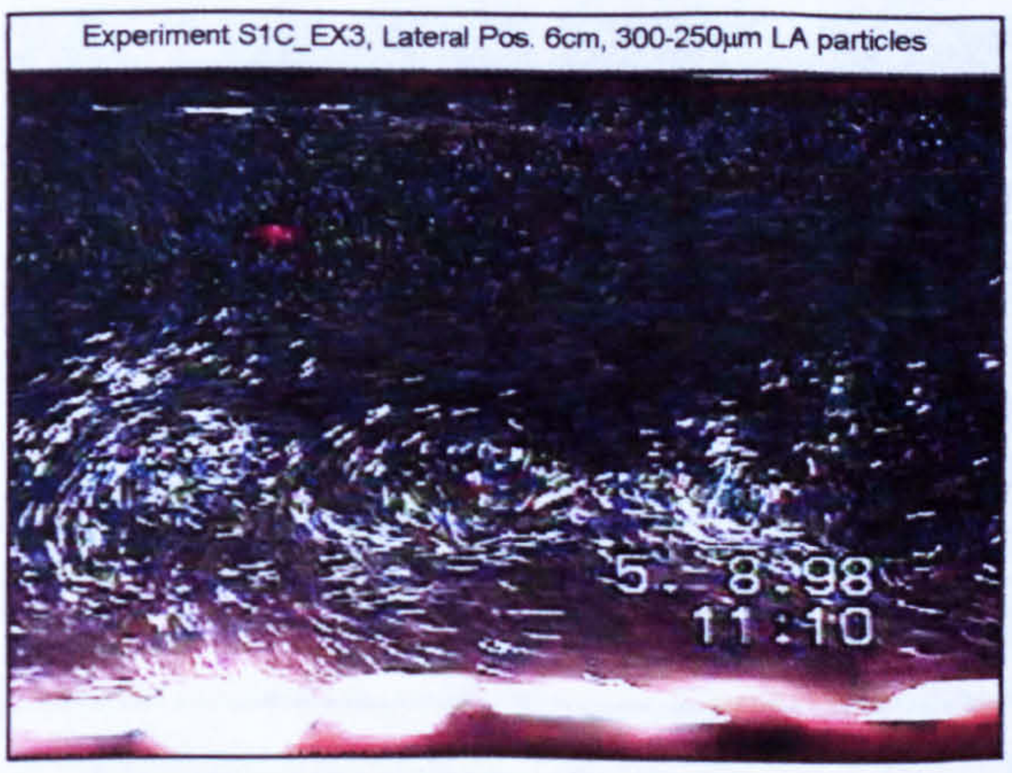
Experiment S1C_EX3, Lateral Pos. 6cm, 300-250µm LA particles
5. 8.98
11:10

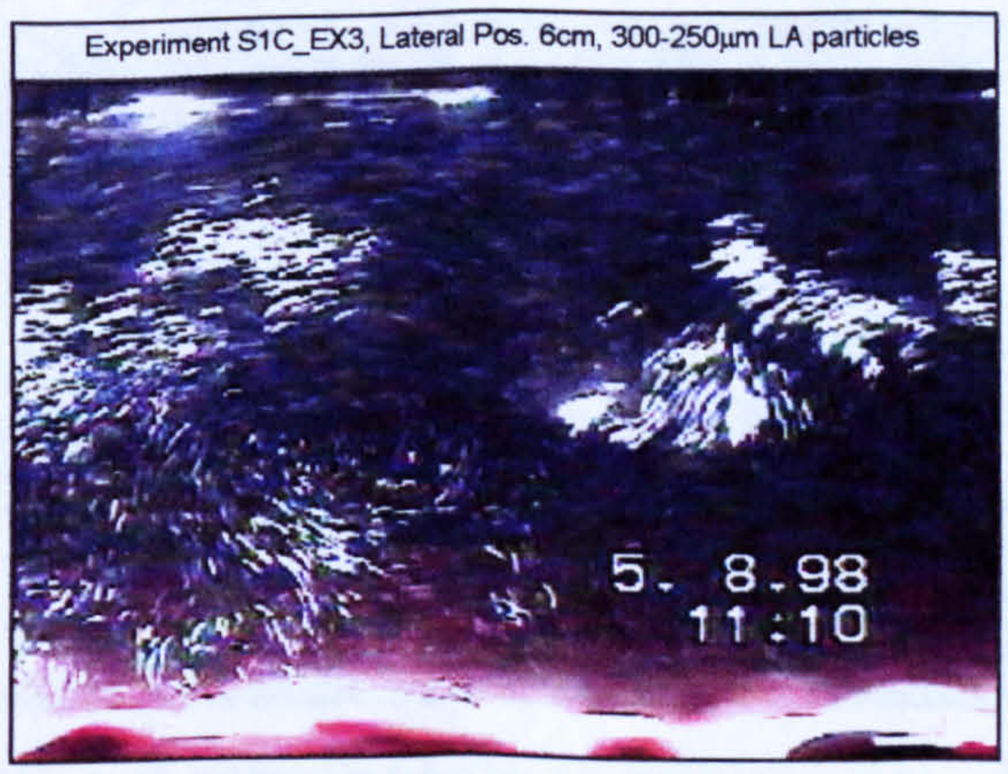
Experiment S1C_EX3, Lateral Pos. 6cm, 300-250µm LA particles
5. 8.98
11:10

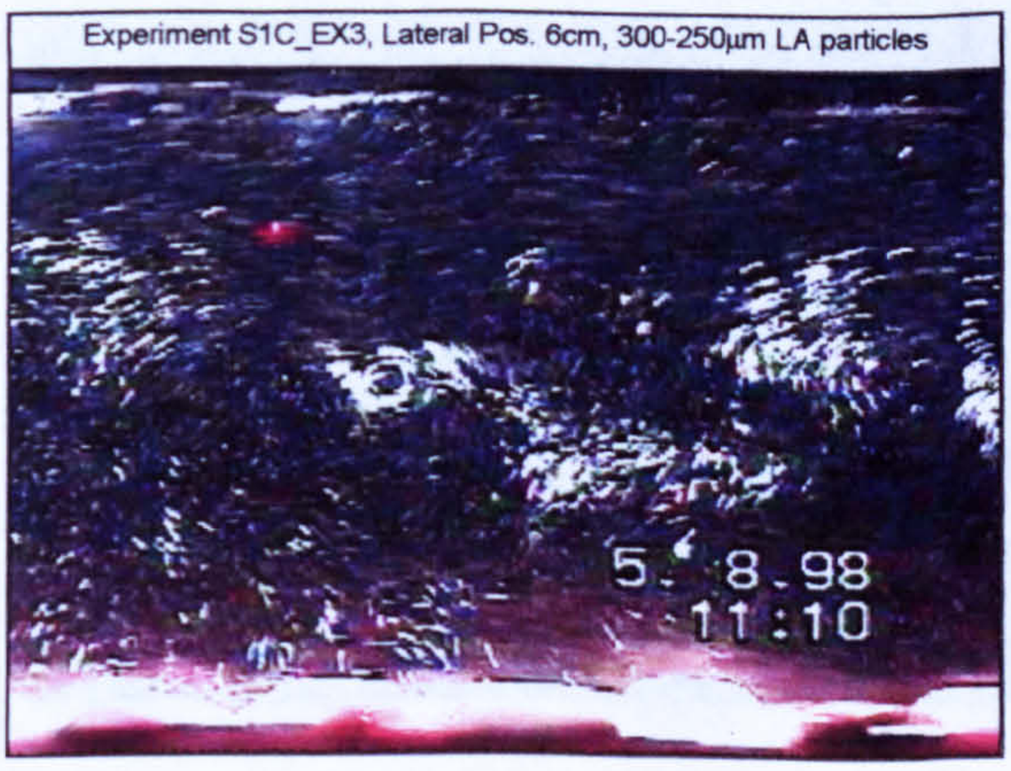
Experiment S1C_EX3, Lateral Pos. 6cm, 300-250µm LA particles
5. 8.98
11:10

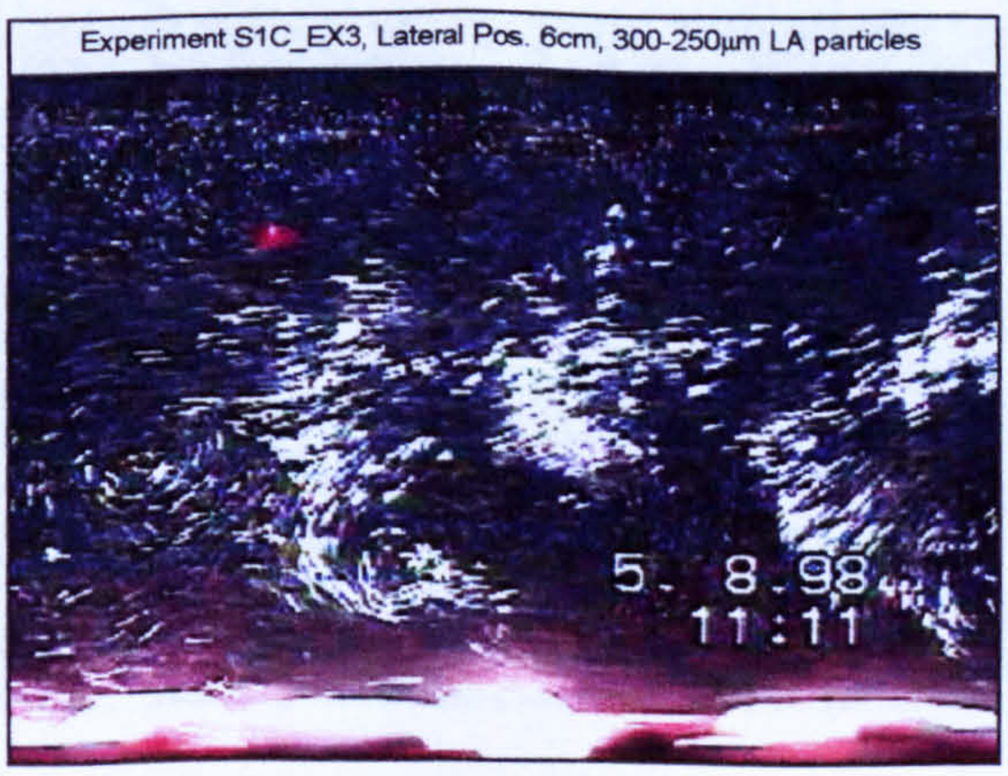
Experiment S1C_EX3, Lateral Pos. 6cm, 300-250µm LA particles
5. 8.98
11:11

Experiment S1C_EX3, Lateral Pos. 6cm, 300-250μm LA particles

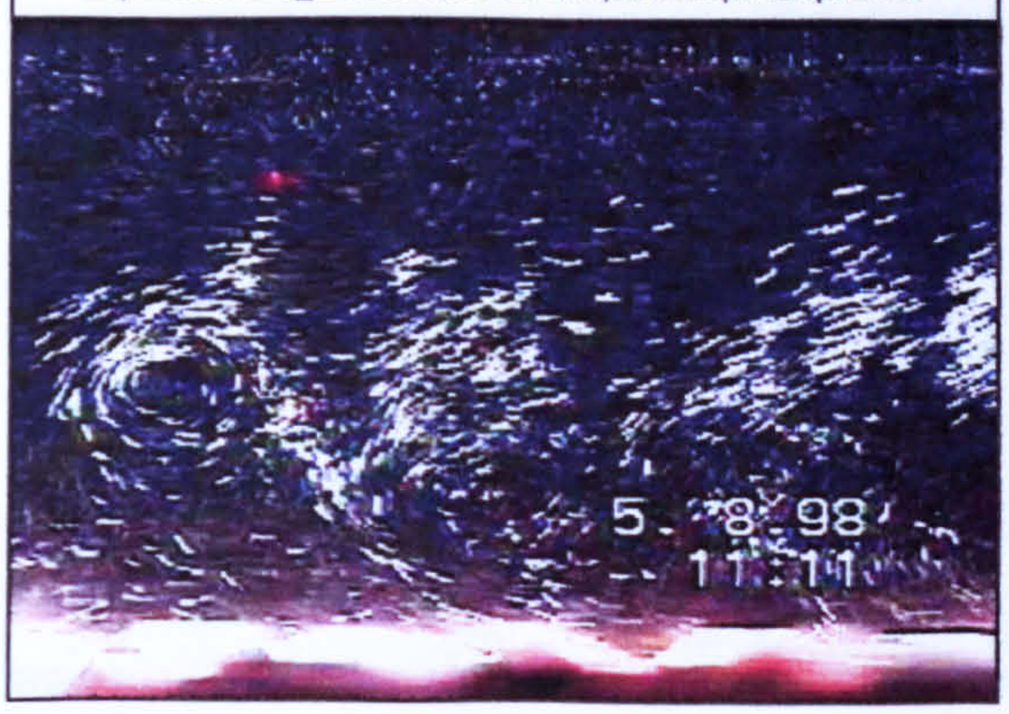

Experiment S1C_EX3, Lateral Pos. 10cm, 300-250μm LA particles

Experiment S1C_EX3, Lateral Pos. 10cm, 300-250μm LA particles

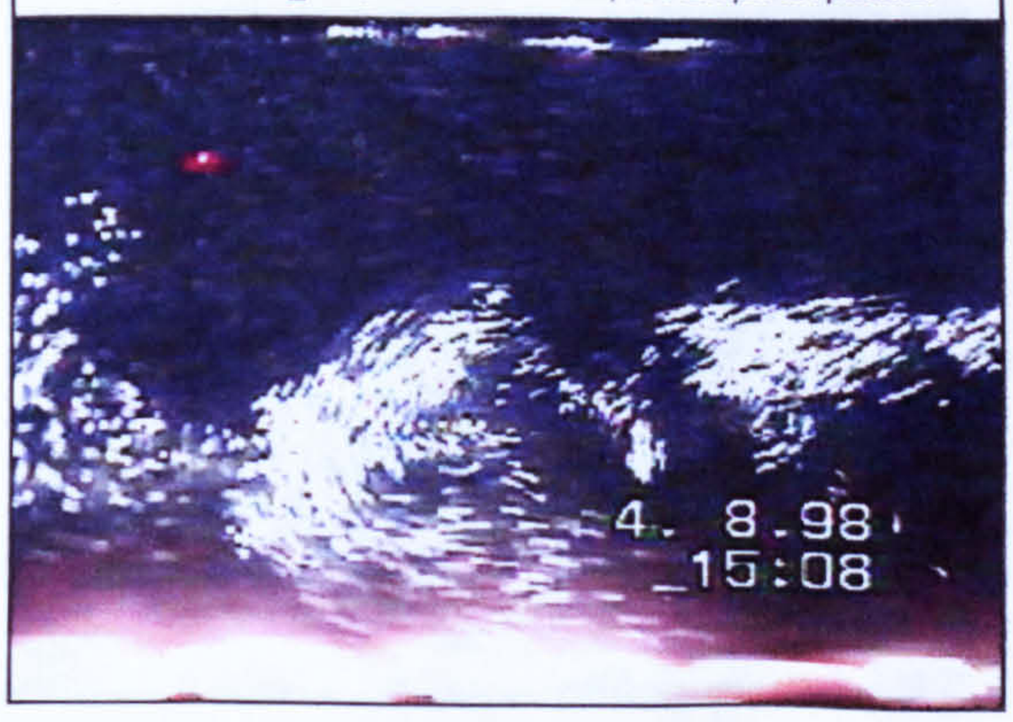

Experiment S1C_EX3, Lateral Pos. 10cm, 300-250μm LA particles

Experiment S1C_EX3, Lateral Pos. 10cm, 300-250μm LA particles

Experiment S1C_EX3, Lateral Pos. 15cm, 300-250μm LA particles

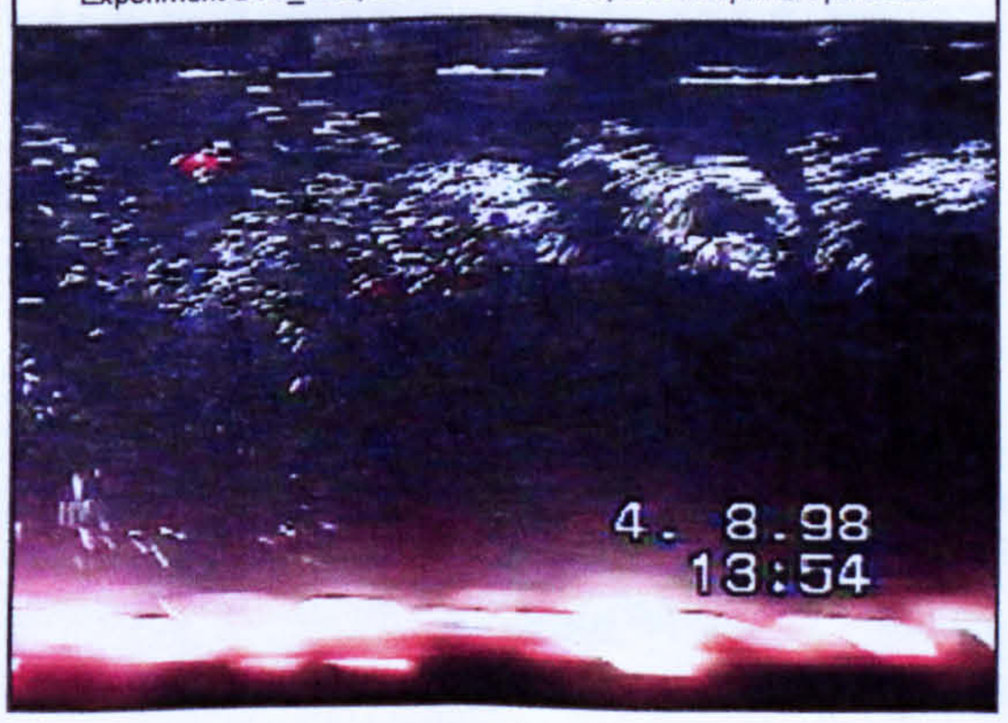

Experiment S1C_EX3, Lateral Pos. 15cm, 300-250μm LA particles

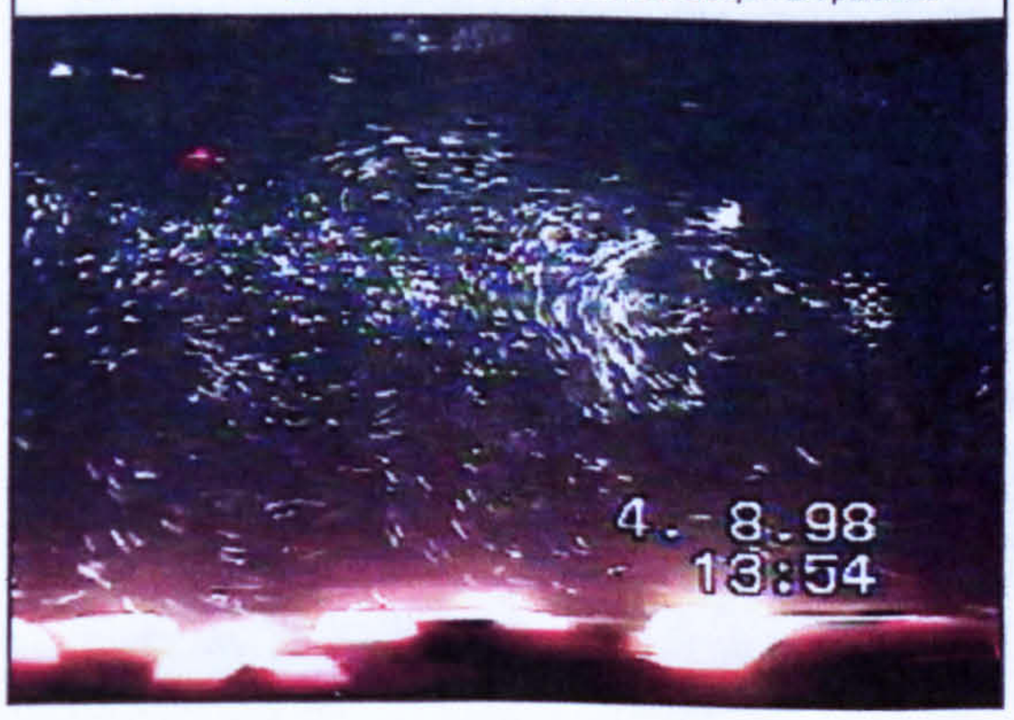

Experiment S1C_EX3, Lateral Pos. 6cm, 250-212μm LA particles

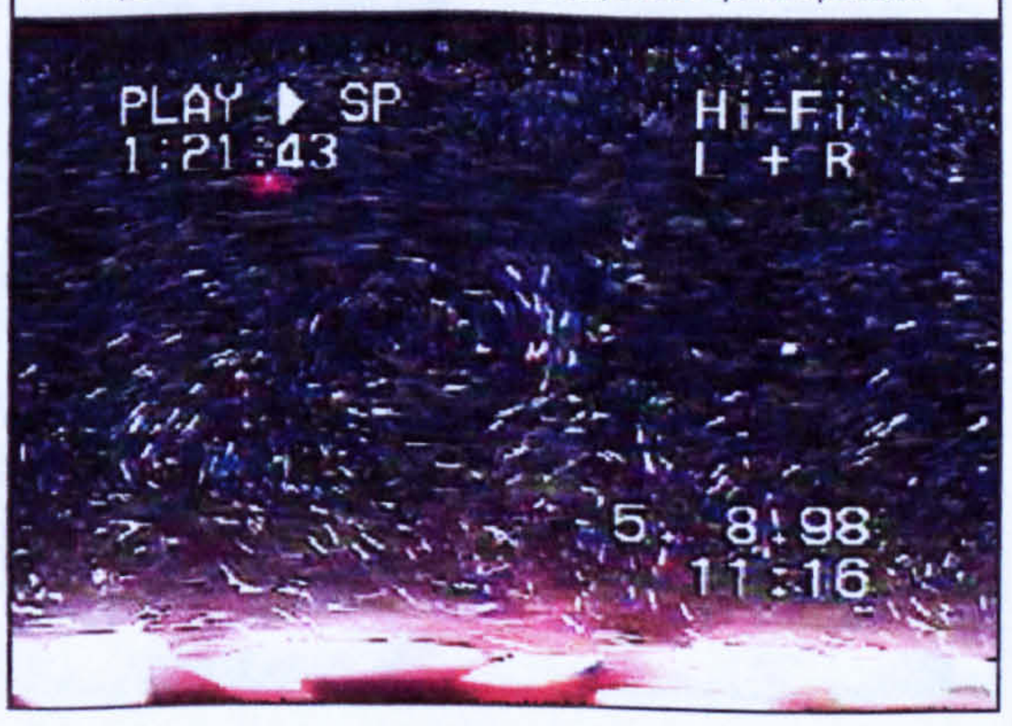

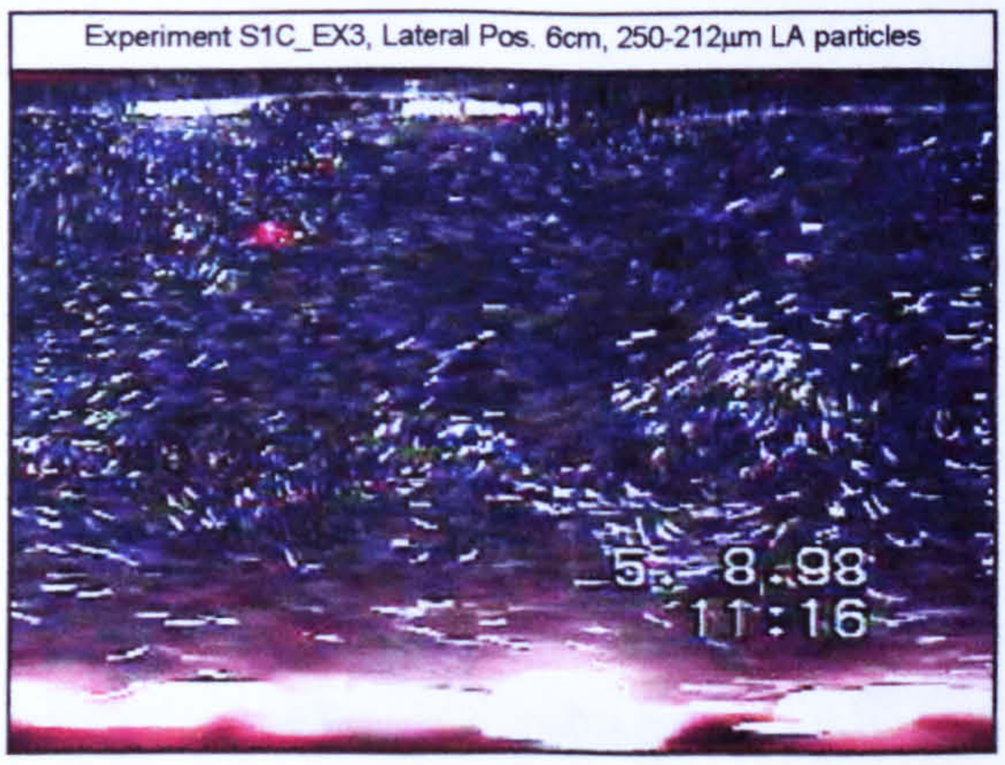
Experiment S1C_EX3, Lateral Pos. 6cm, 250-212µm LA particles
5. 8.98
11:16

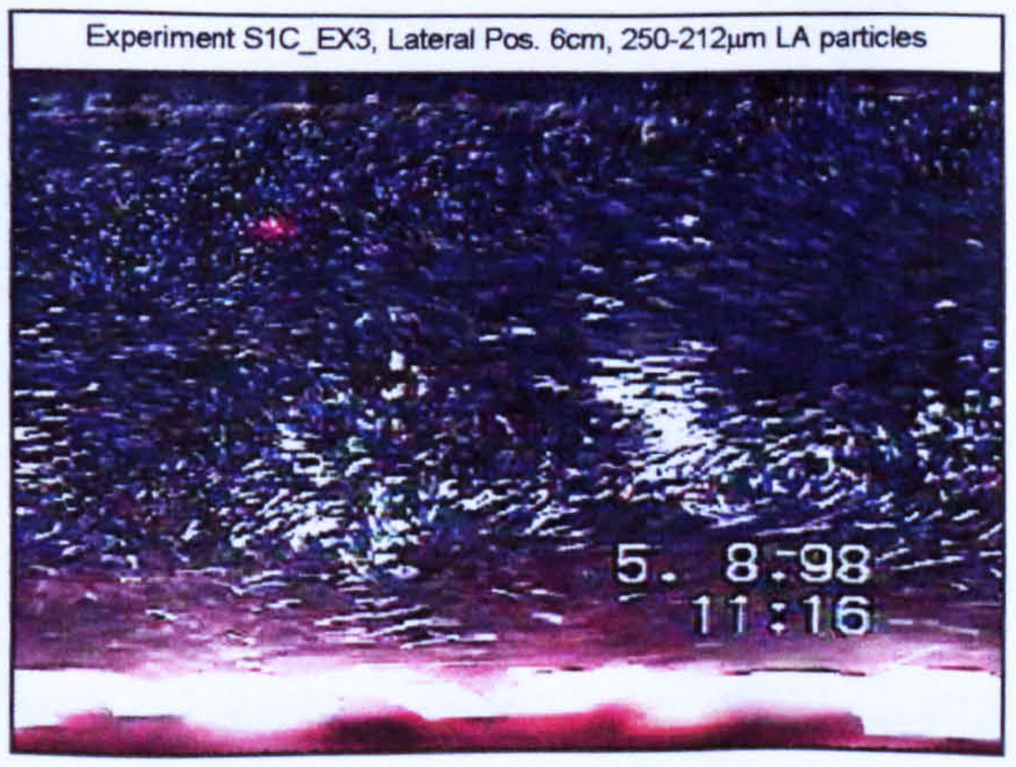
Experiment S1C_EX3, Lateral Pos. 6cm, 250-212µm LA particles
5. 8.98
11:16

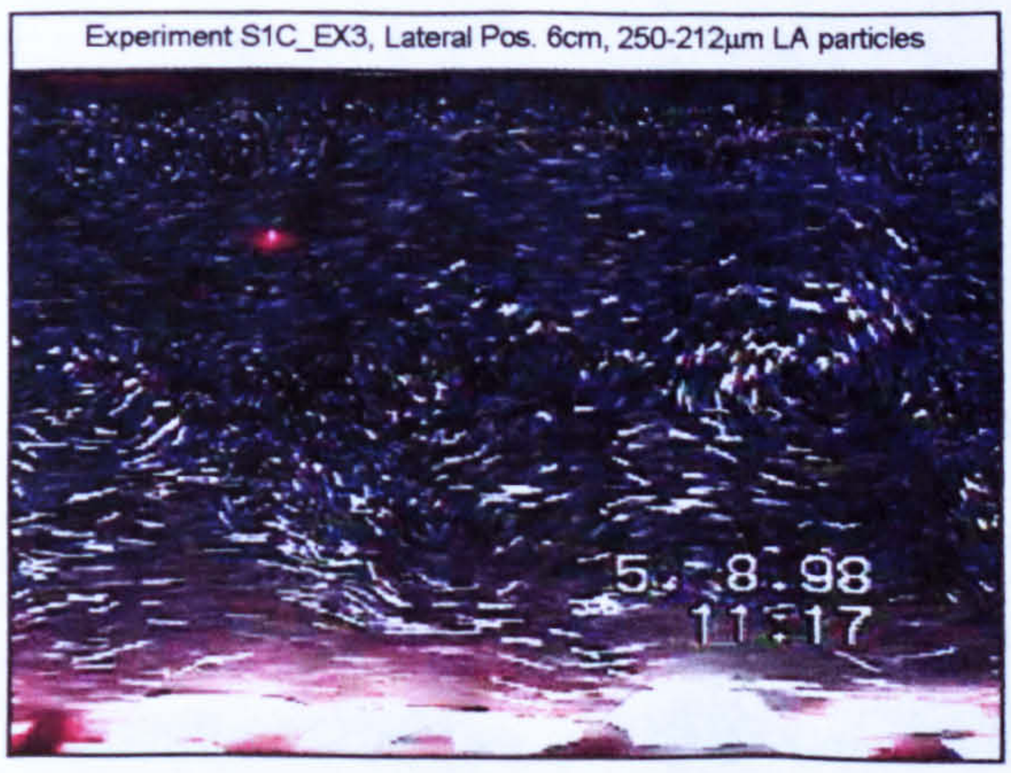
Experiment S1C_EX3, Lateral Pos. 6cm, 250-212µm LA particles
5. 8.98
11:17

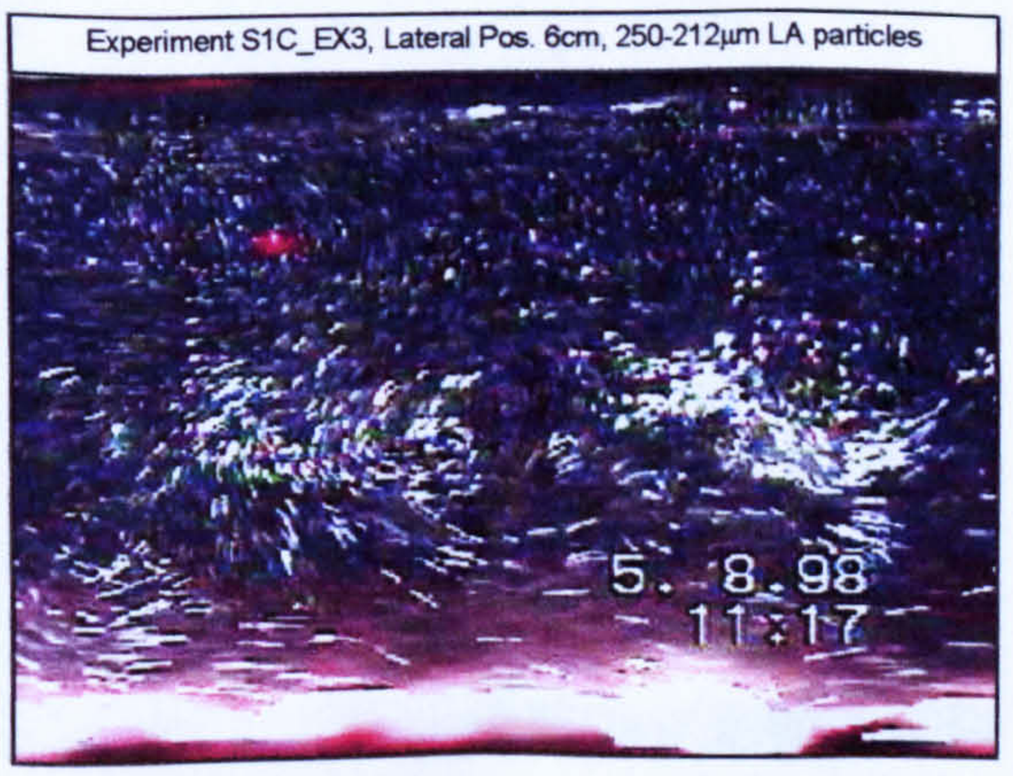
Experiment S1C_EX3, Lateral Pos. 6cm, 250-212µm LA particles
5. 8.98
11:17

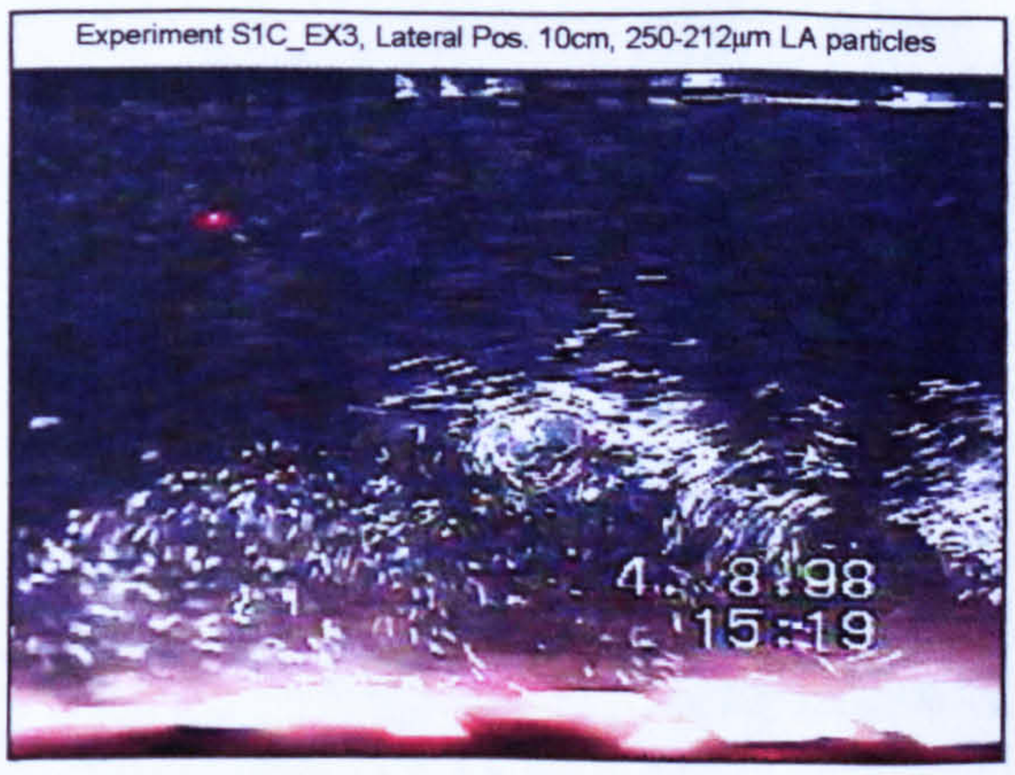
Experiment S1C_EX3, Lateral Pos. 10cm, 250-212µm LA particles
4. 8.98
15:19


Experiment S1C_EX3, Lateral Pos. 10cm, 250-212µm LA particles
4. 8.98
15:21

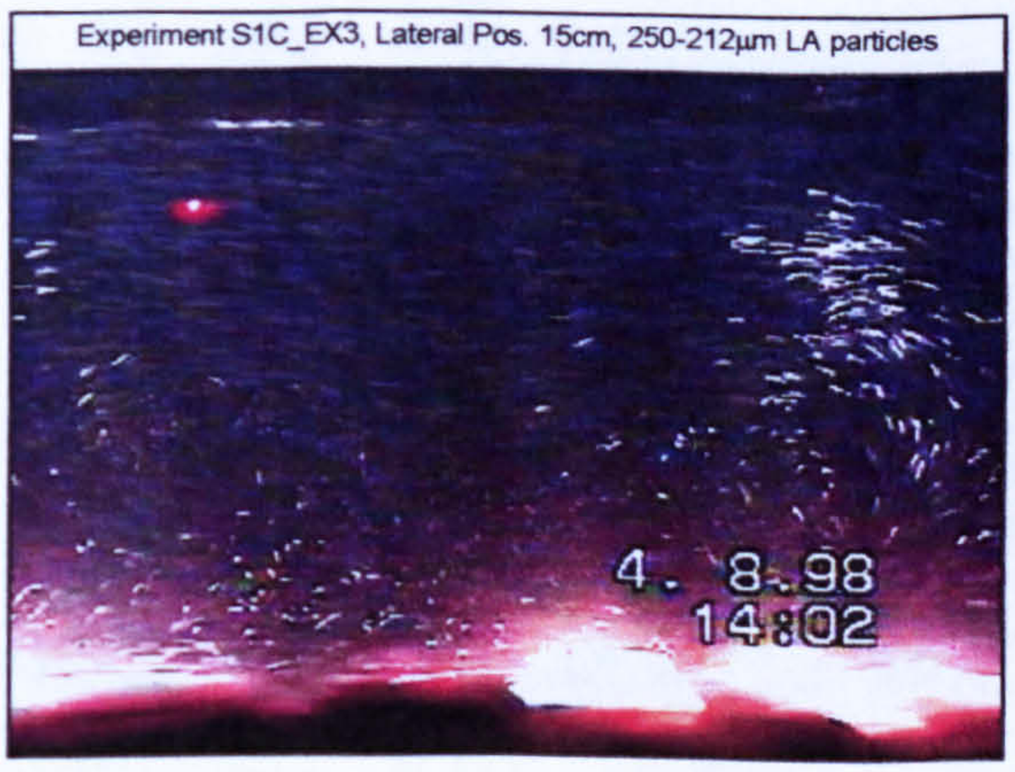
Experiment S1C_EX3, Lateral Pos. 15cm, 250-212µm LA particles
4. 8.98
14:02

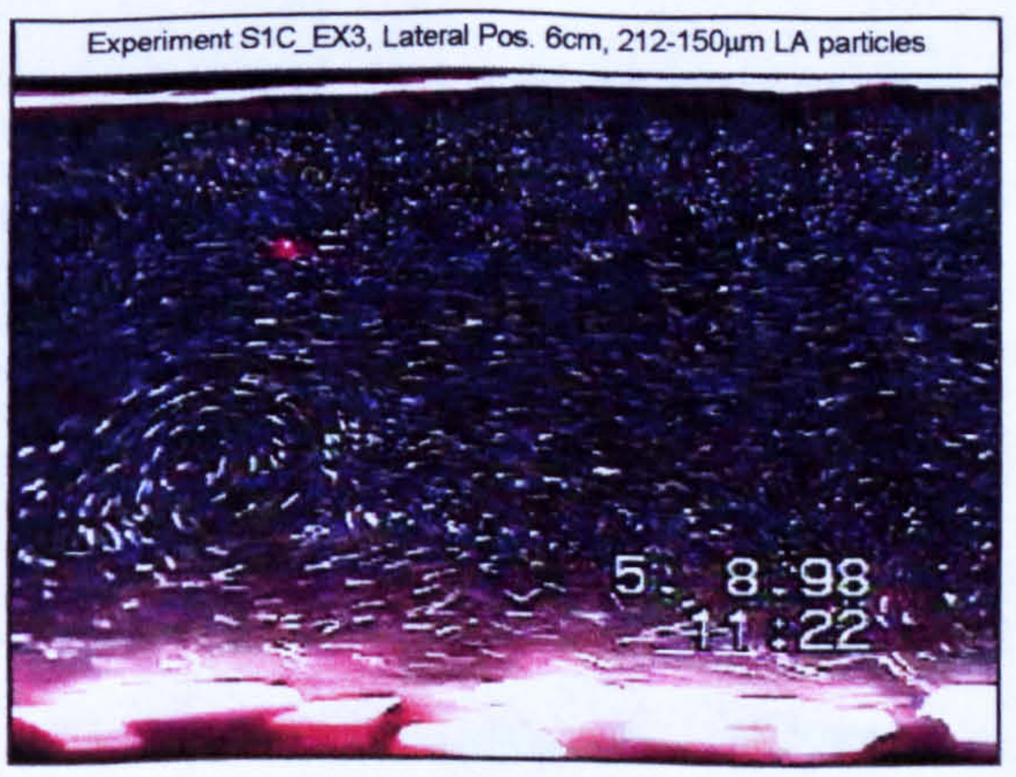
Experiment S1C_EX3, Lateral Pos. 6cm, 212-150µm LA particles
5. 8.98
11:22


Experiment S1C_EX3, Lateral Pos. 6cm, 212-150µm LA particles
5. 8.98
11:22

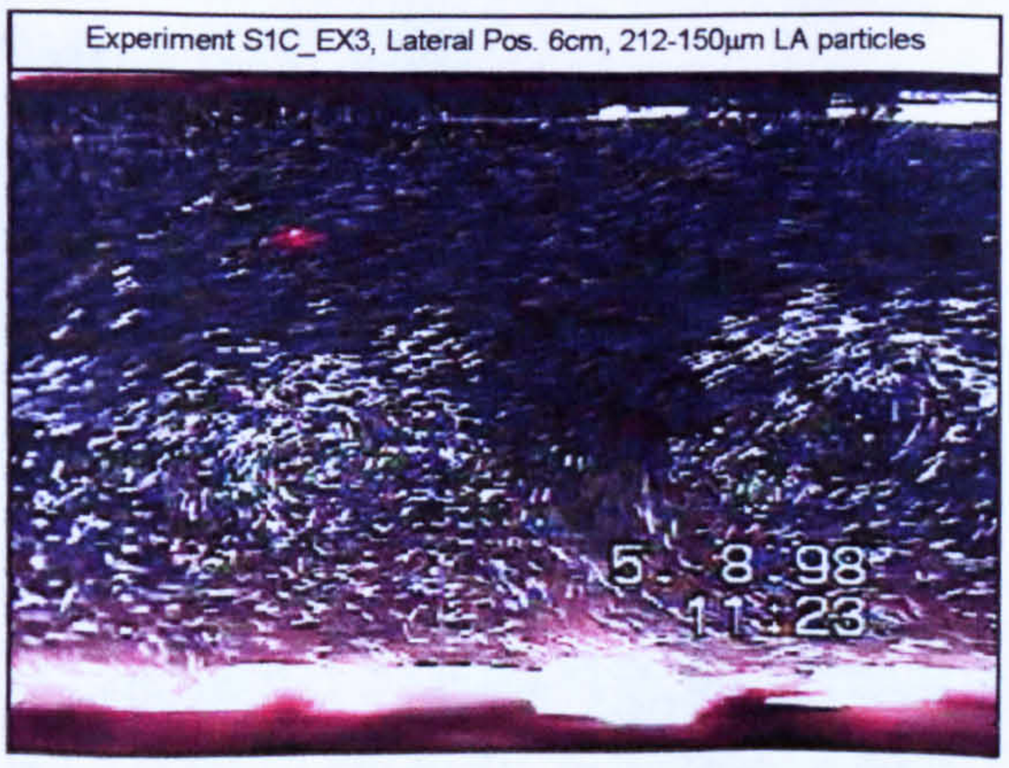
Experiment S1C_EX3, Lateral Pos. 6cm, 212-150µm LA particles
5. 8.98
11:23


Experiment S1C_EX3, Lateral Pos. 6cm, 212-150µm LA particles
5. 8.98
11:23

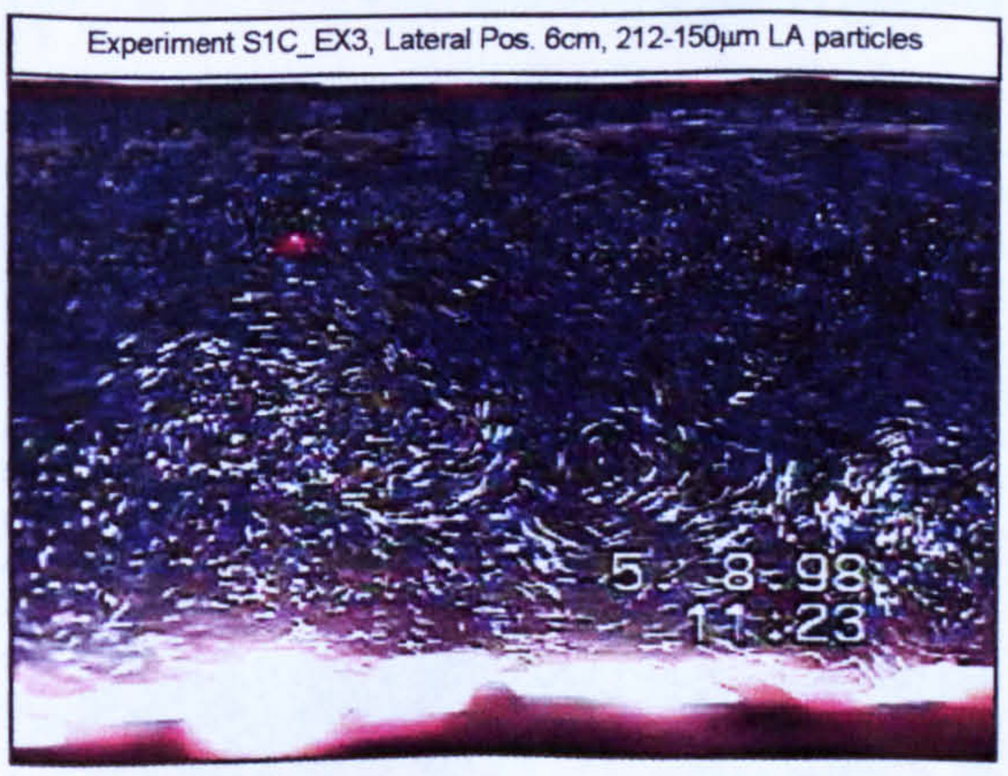
Experiment S1C_EX3, Lateral Pos. 6cm, 212-150µm LA particles
5. 8.98
11:23

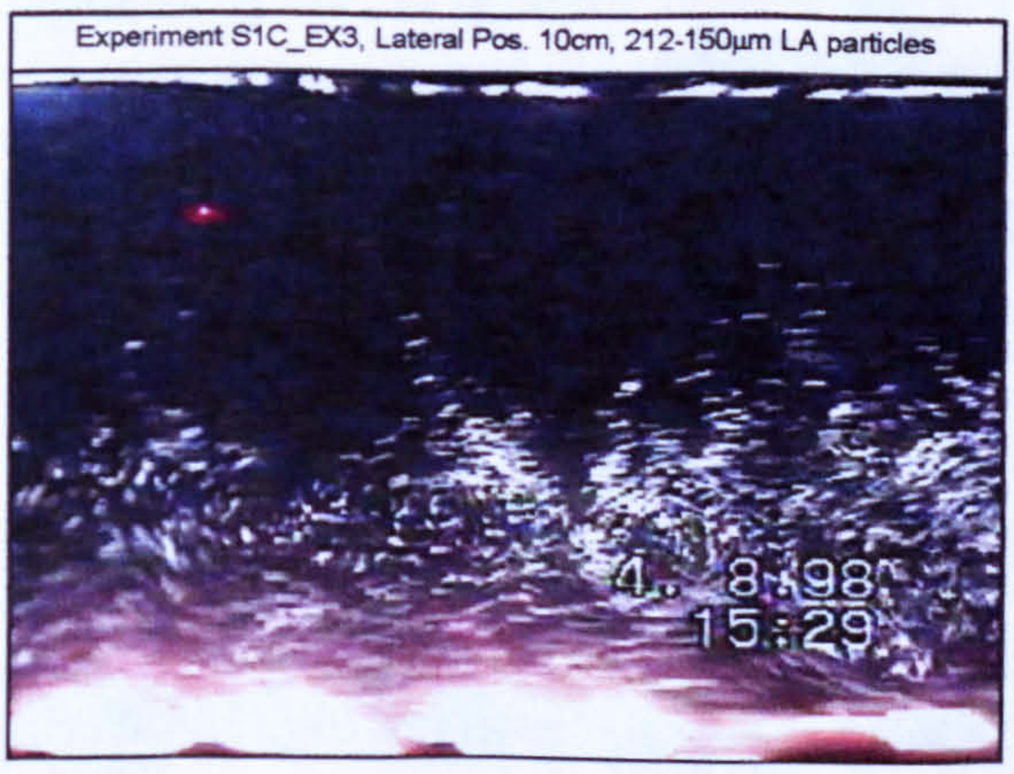
Experiment S1C_EX3, Lateral Pos. 10cm, 212-150µm LA particles
4. 8.98
15:29

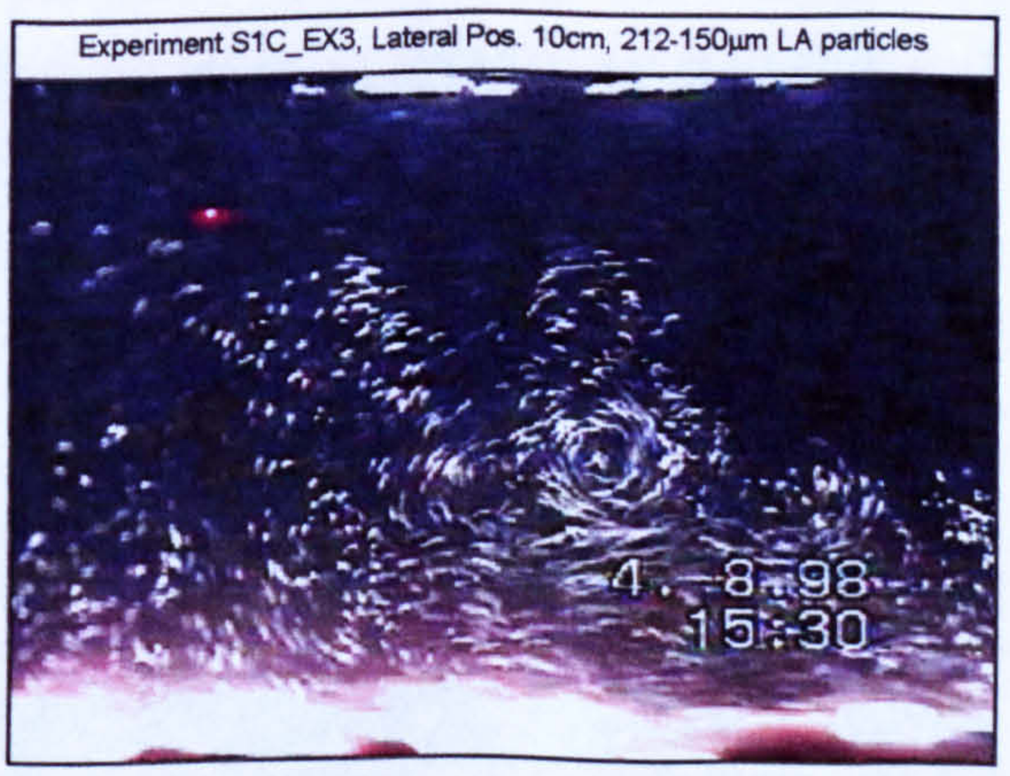
Experiment S1C_EX3, Lateral Pos. 10cm, 212-150µm LA particles
4. 8.98
15:30


Experiment S1C_EX3, Lateral Pos. 10cm, 212-150µm LA particles
4. 8.98
15:30

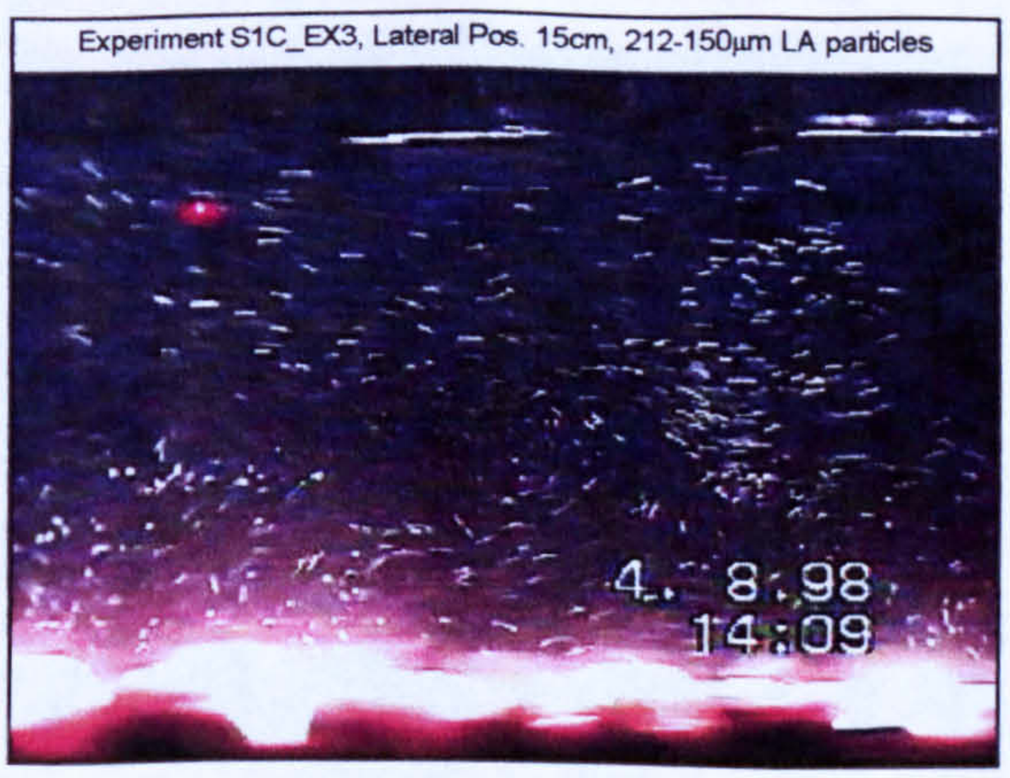
Experiment S1C_EX3, Lateral Pos. 15cm, 212-150µm LA particles
4. 8.98
14:09

(2) Images for Individual LA Grade Size Fractions (S1C_EX4)

Experiment S1C_EX4, Lateral Pos. 6cm, 500-425µm LA particles

Experiment S1C_EX4, Lateral Pos. 10cm, 500-425µm LA particles

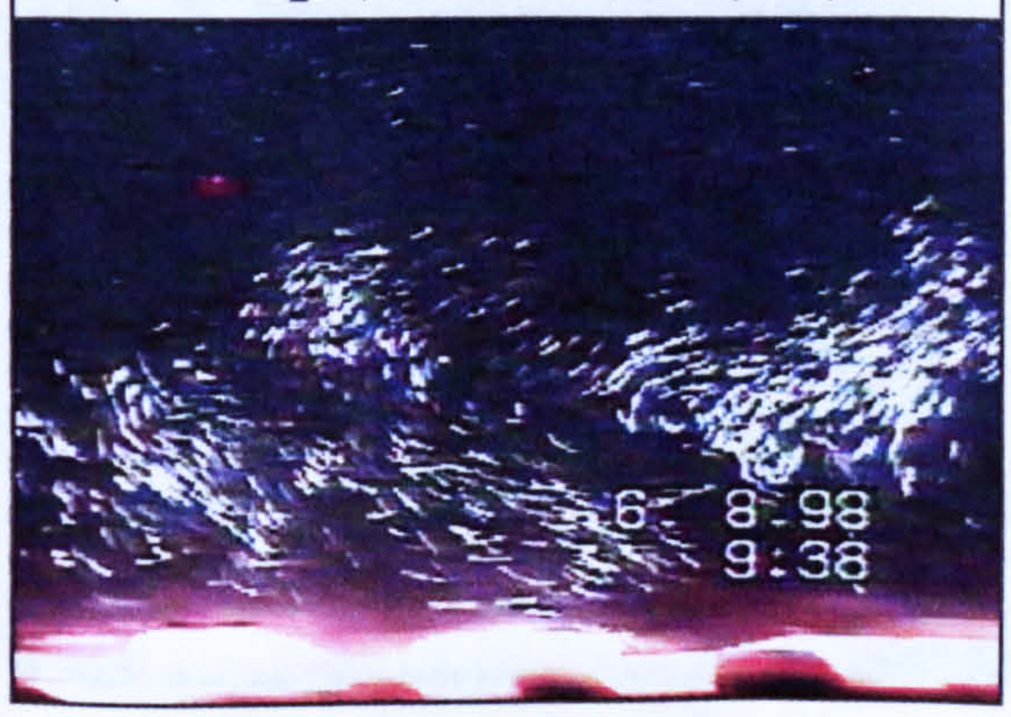

Experiment S1C_EX4, Lateral Pos. 15cm, 500-425µm LA particles

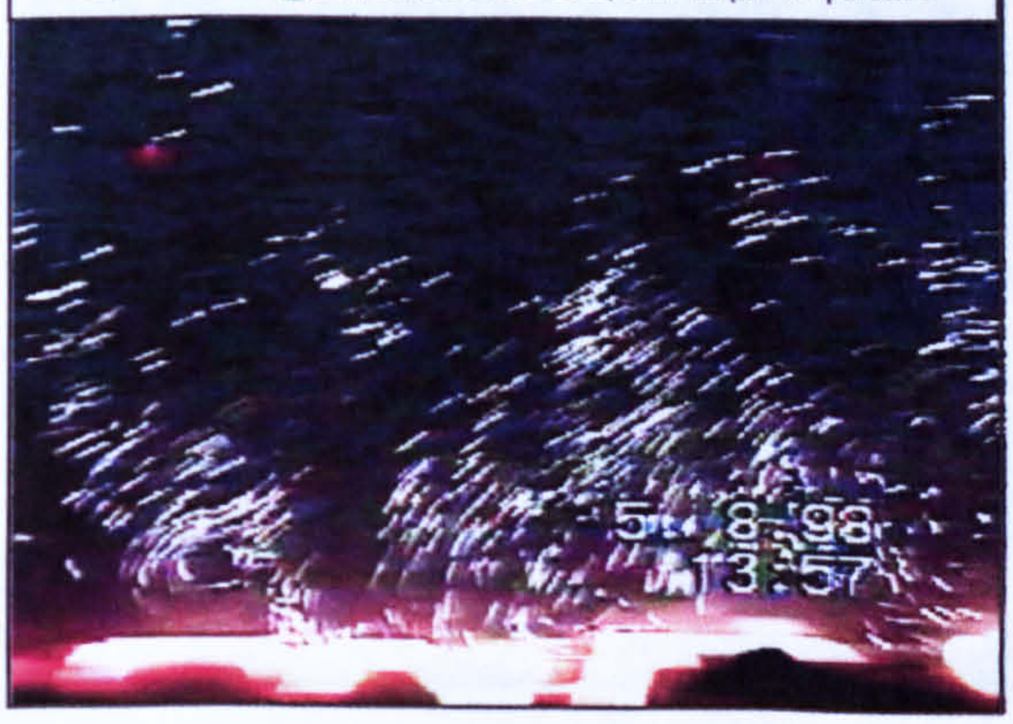

Experiment S1C_EX4, Lateral Pos. 6cm, 425-355µm LA particles

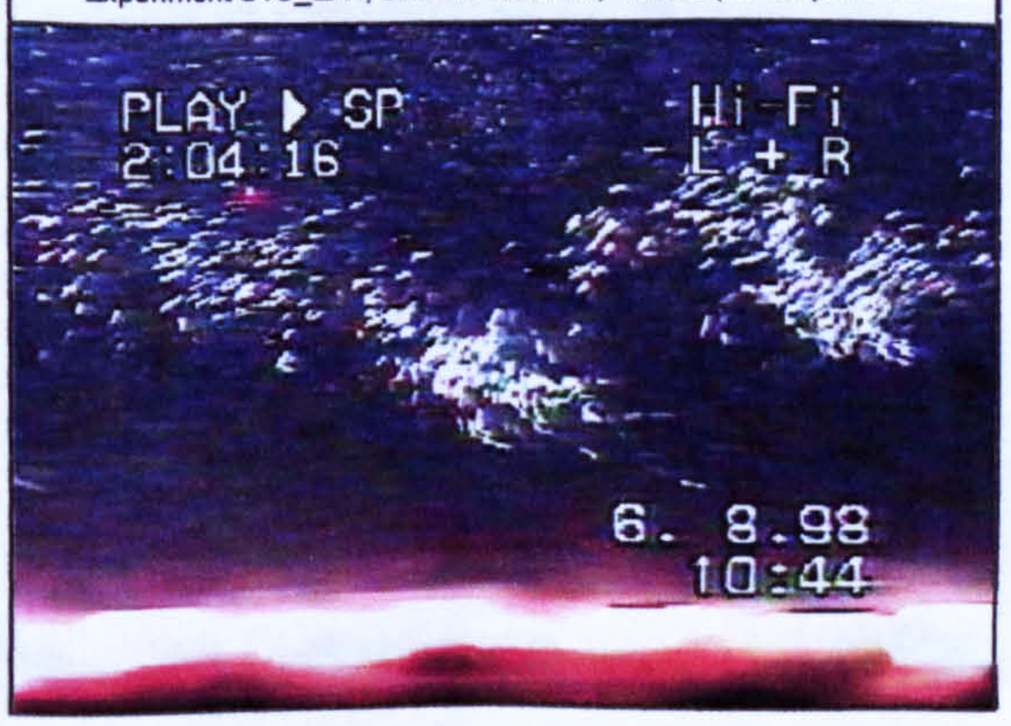

Experiment S1C_EX4, Lateral Pos. 6cm, 425-355µm LA particles

Experiment S1C_EX4, Lateral Pos. 10cm, 425-355µm LA particles

Experiment S1C_EX4, Lateral Pos. 15cm, 425-355µm LA particles

Experiment S1C_EX4, Lateral Pos. 15cm, 425-355µm LA particles

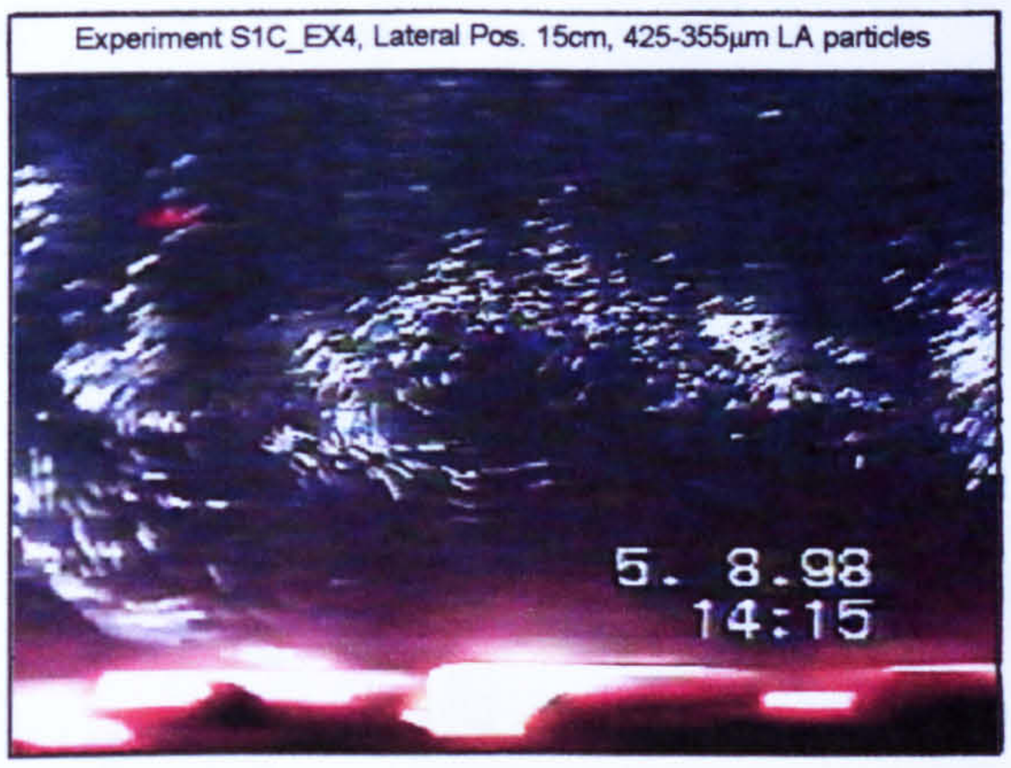
Experiment S1C_EX4, Lateral Pos. 15cm, 425-355µm LA particles
5. 8.98
14:15

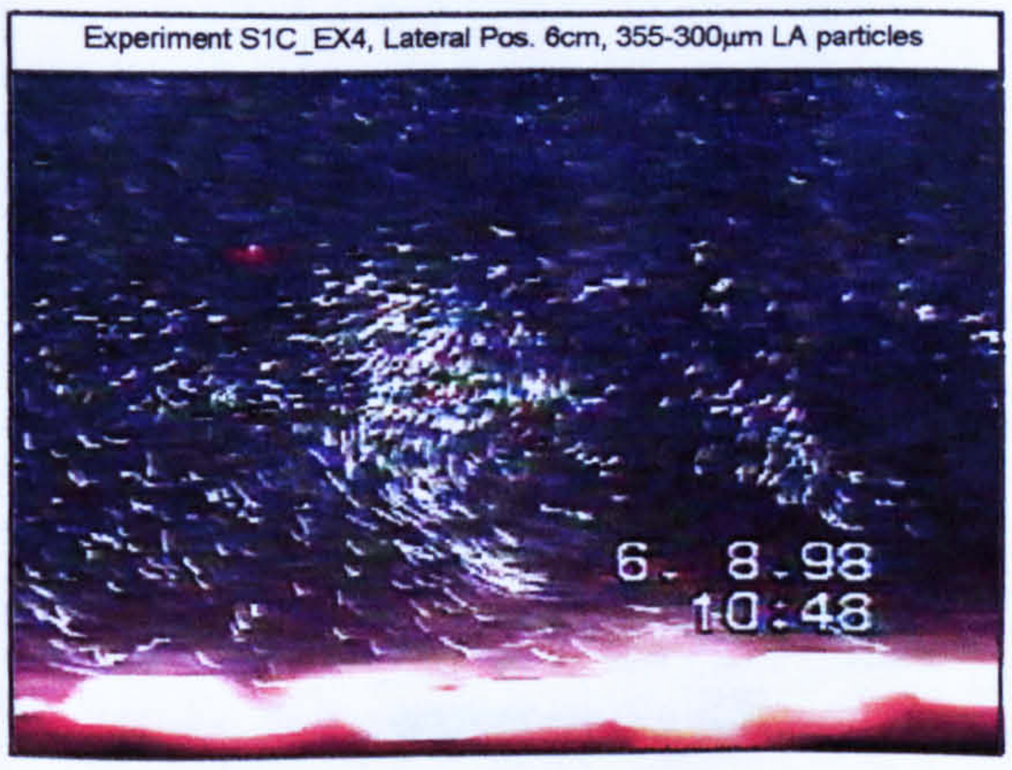
Experiment S1C_EX4, Lateral Pos. 6cm, 355-300µm LA particles
6. 8.98
10:48

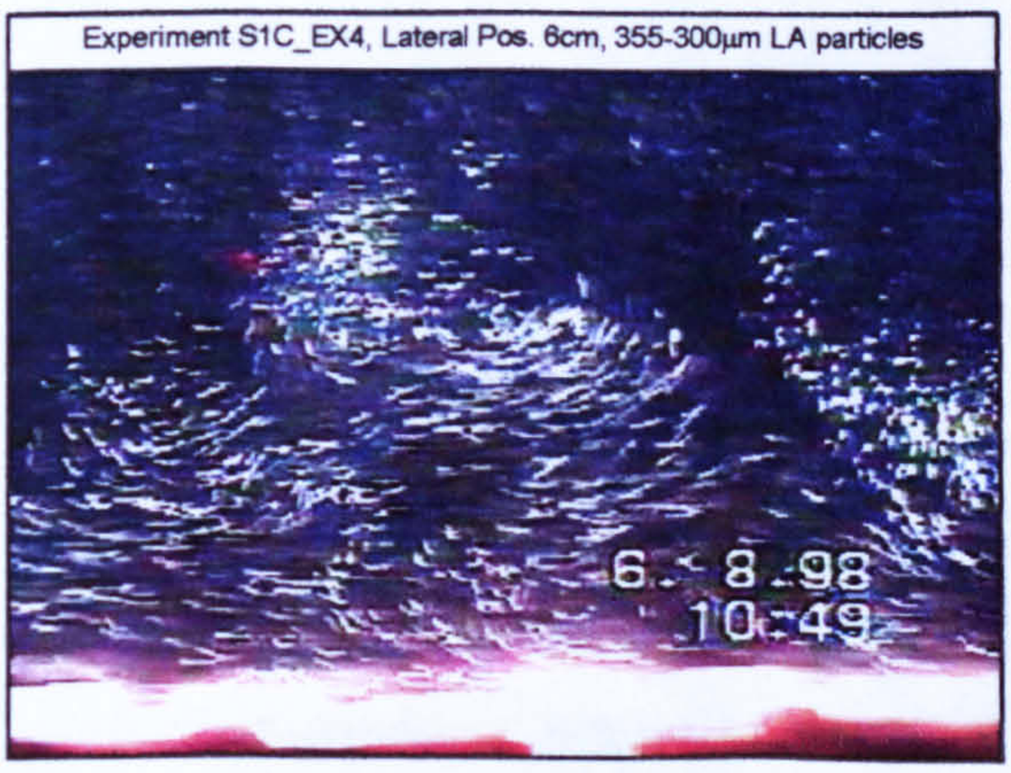
Experiment S1C_EX4, Lateral Pos. 6cm, 355-300µm LA particles
6. 8.98
10:49

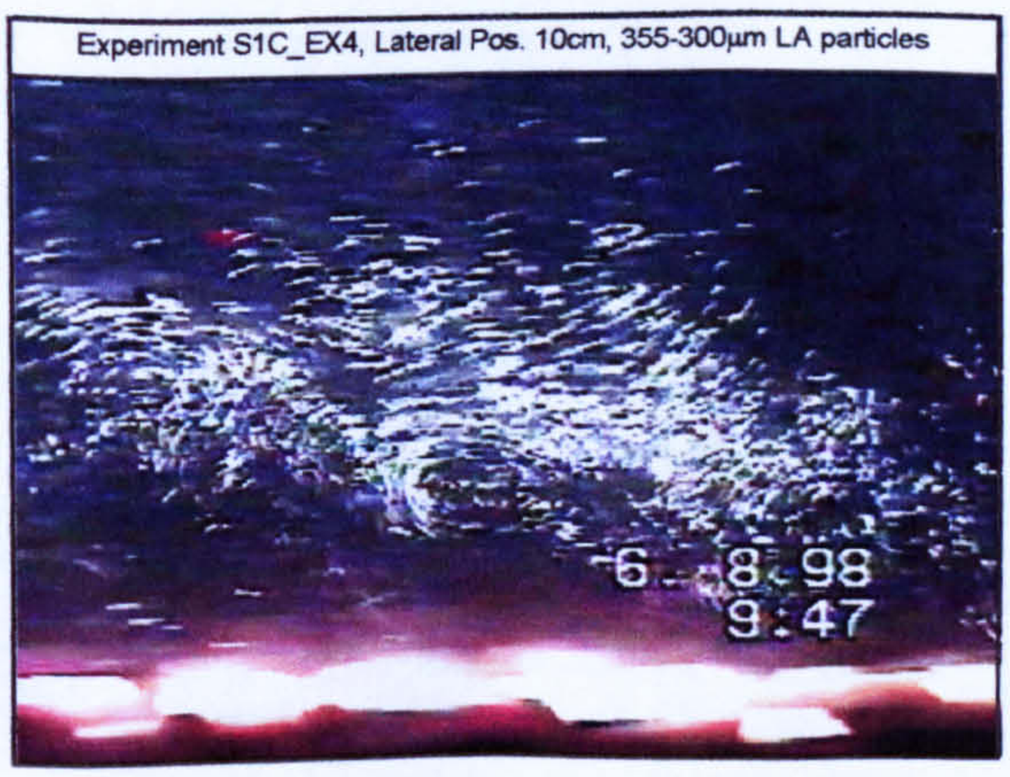
Experiment S1C_EX4, Lateral Pos. 10cm, 355-300µm LA particles
6. 8.98
9:47

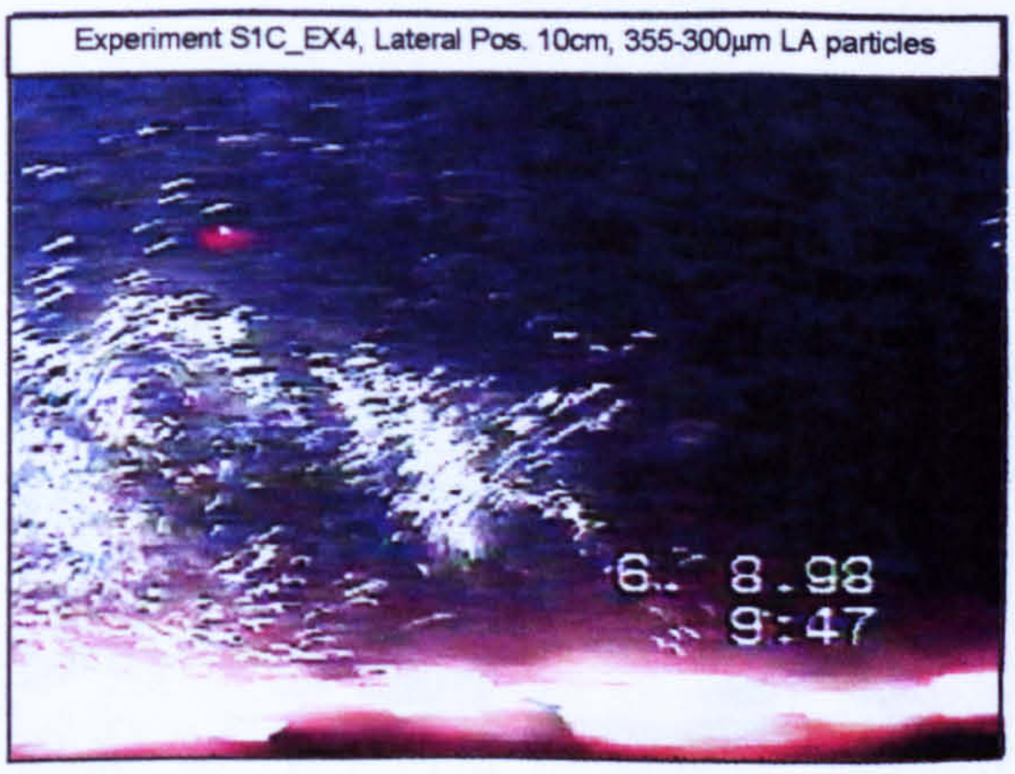
Experiment S1C_EX4, Lateral Pos. 10cm, 355-300µm LA particles
6. 8.98
9:47

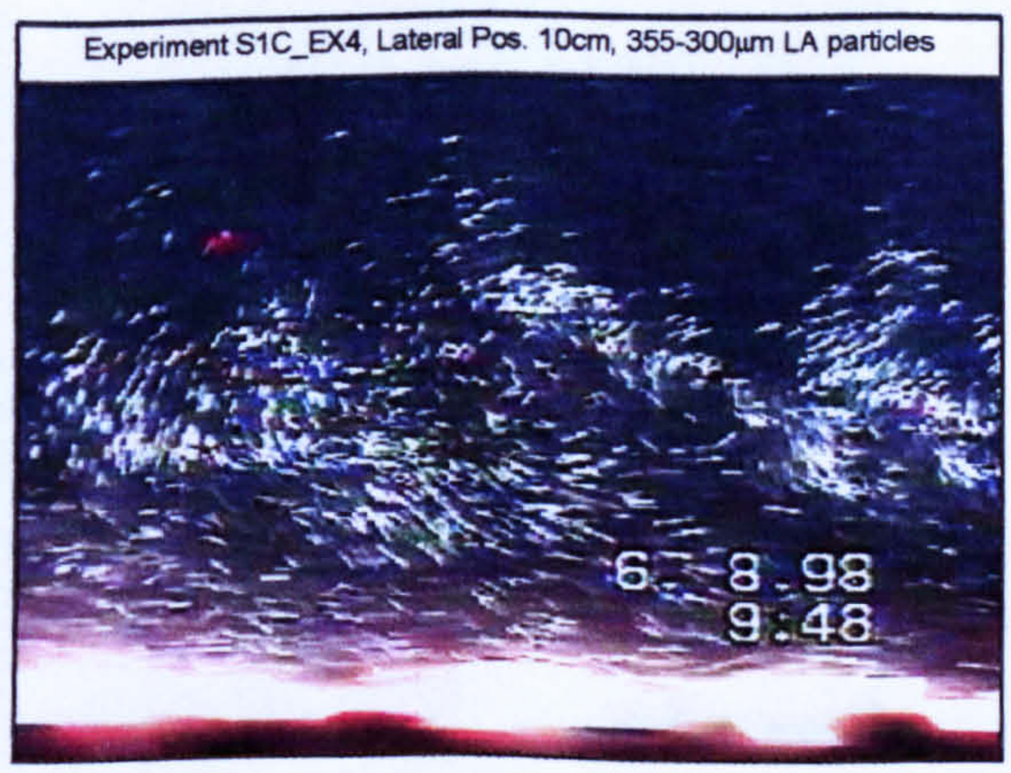
Experiment S1C_EX4, Lateral Pos. 10cm, 355-300µm LA particles
6. 8.98
9:48

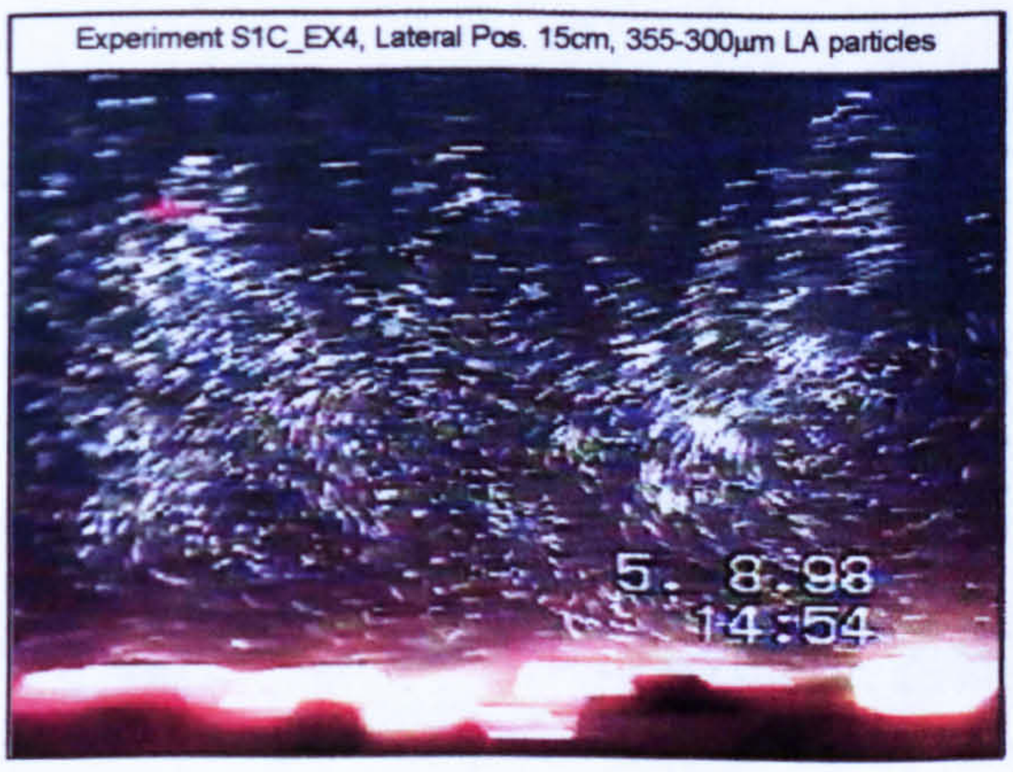
Experiment S1C_EX4, Lateral Pos. 15cm, 355-300µm LA particles
5. 8.98
14:54

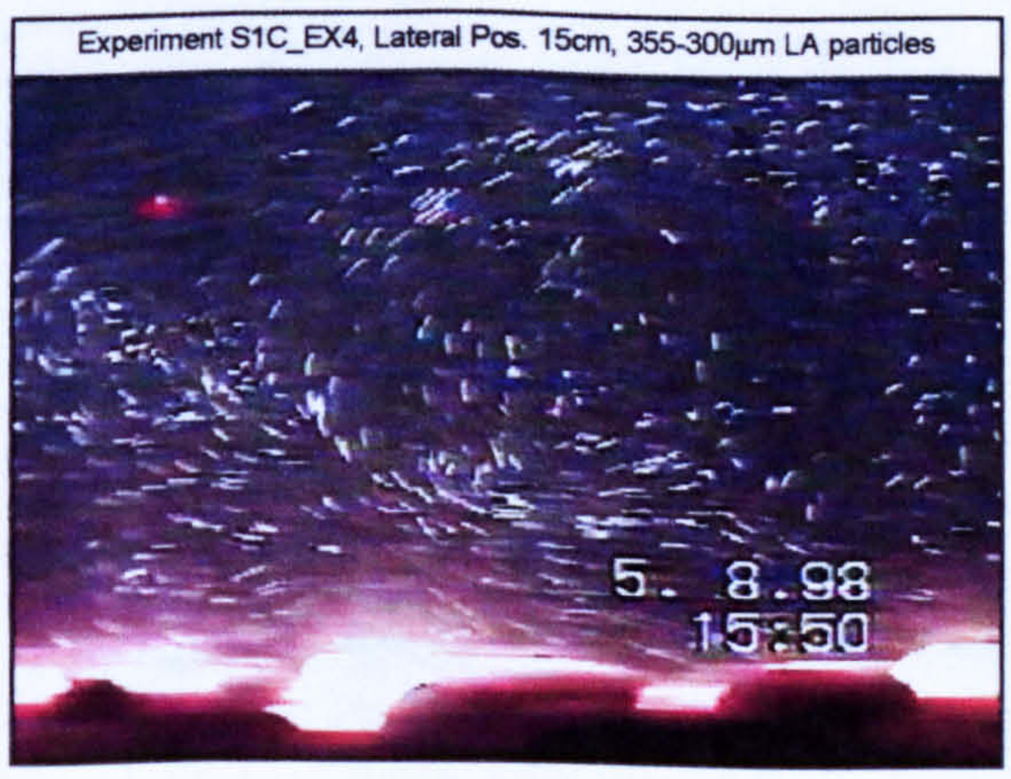
Experiment S1C_EX4, Lateral Pos. 15cm, 355-300µm LA particles
5. 8.98
15:50

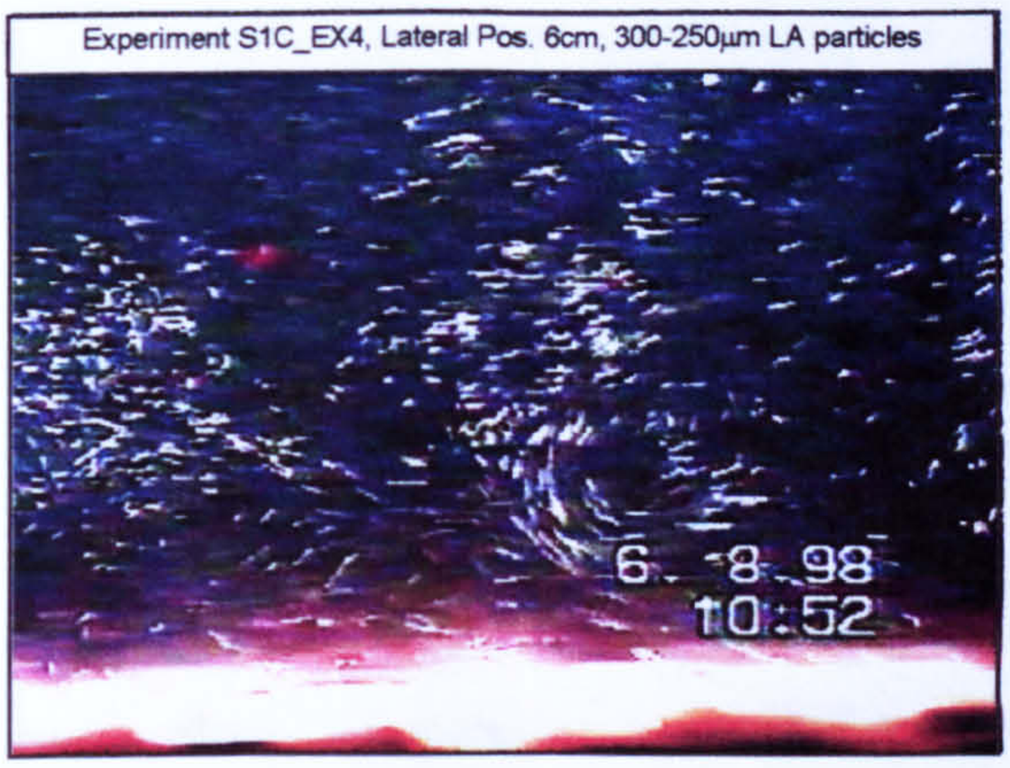
Experiment S1C_EX4, Lateral Pos. 6cm, 300-250µm LA particles
6. 8.98
10:52

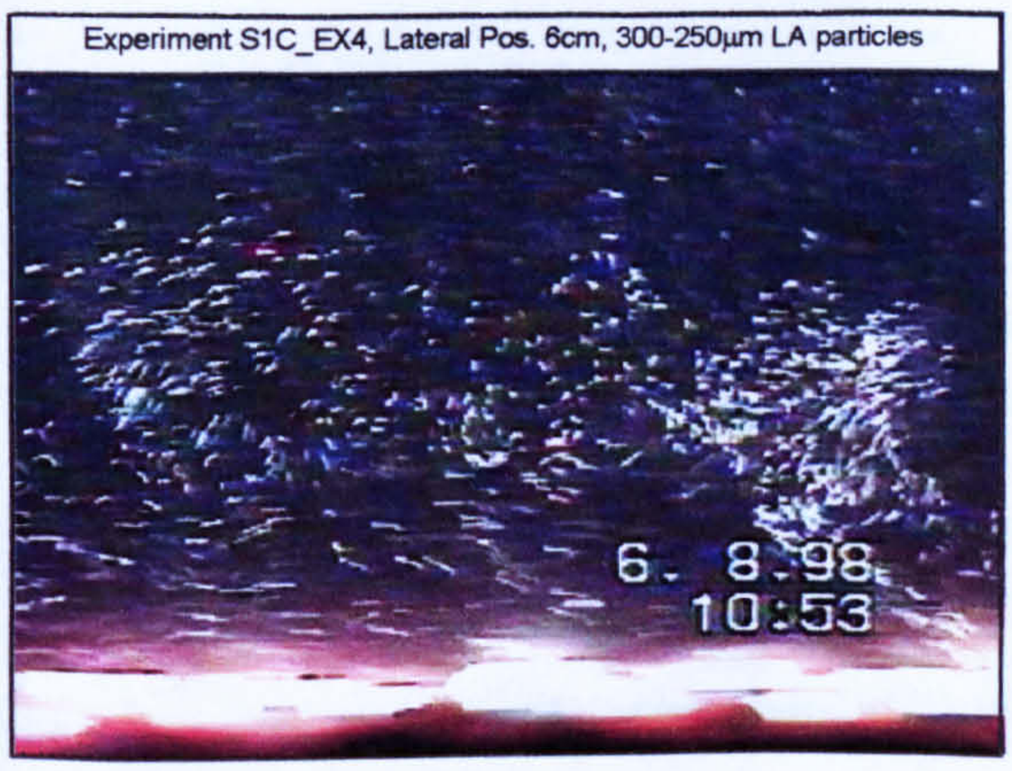
Experiment S1C_EX4, Lateral Pos. 6cm, 300-250µm LA particles
6. 8.98
10:53

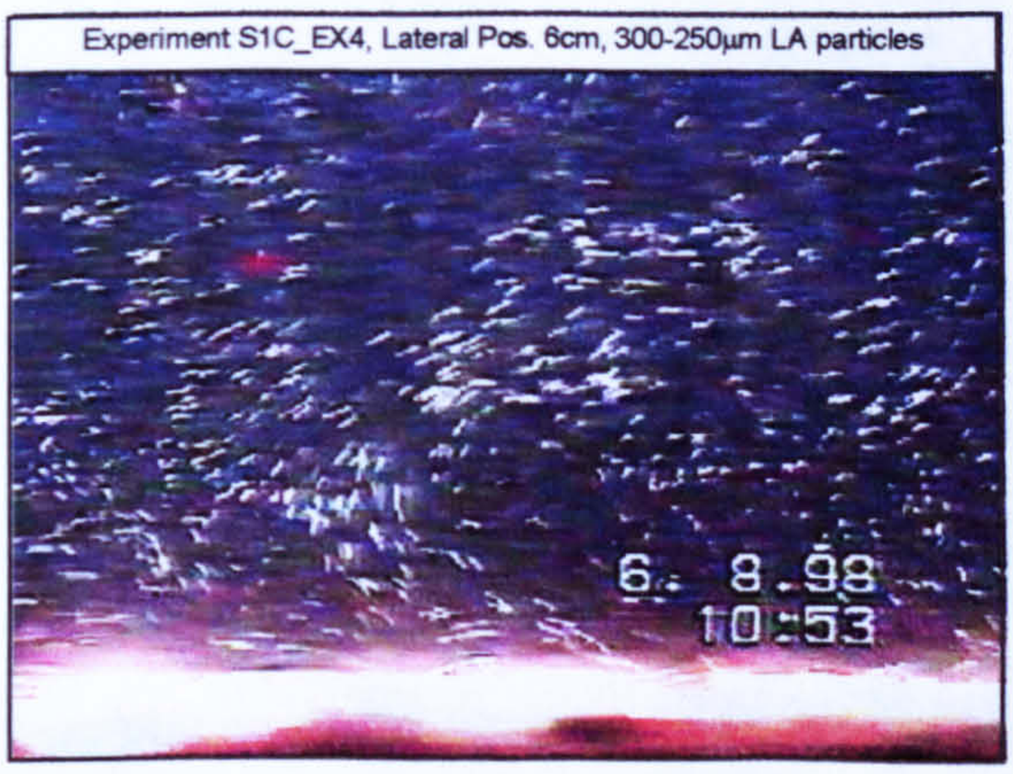
Experiment S1C_EX4, Lateral Pos. 6cm, 300-250µm LA particles
6. 8.98
10:53

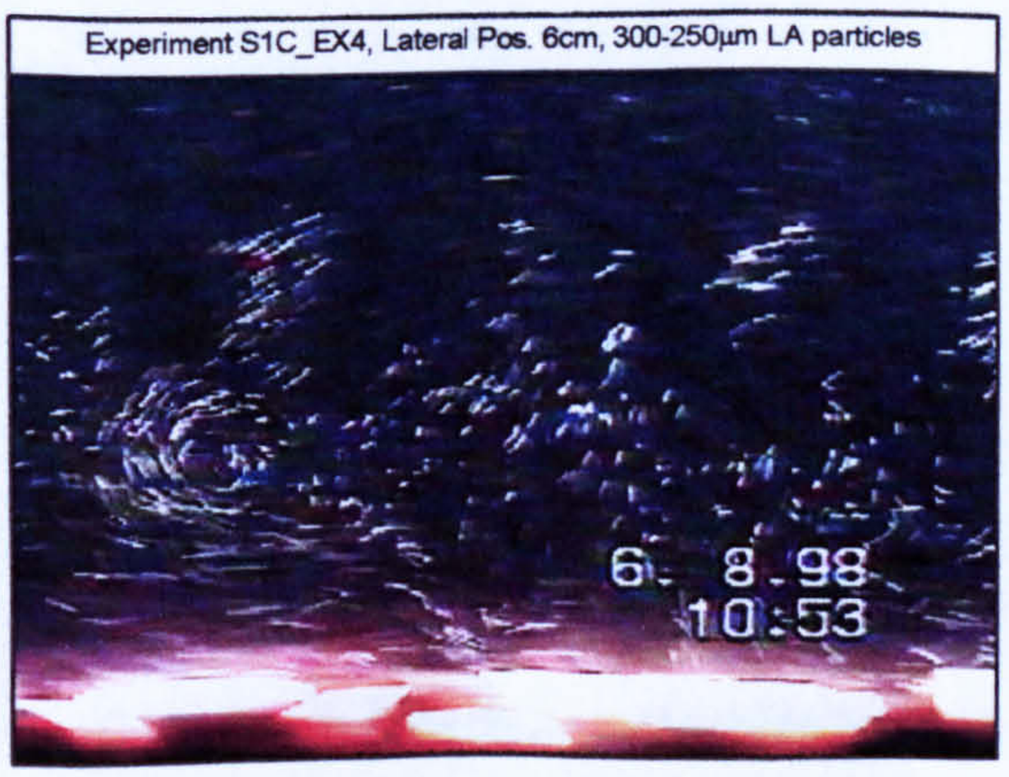
Experiment S1C_EX4, Lateral Pos. 6cm, 300-250µm LA particles
6. 8.98
10:53

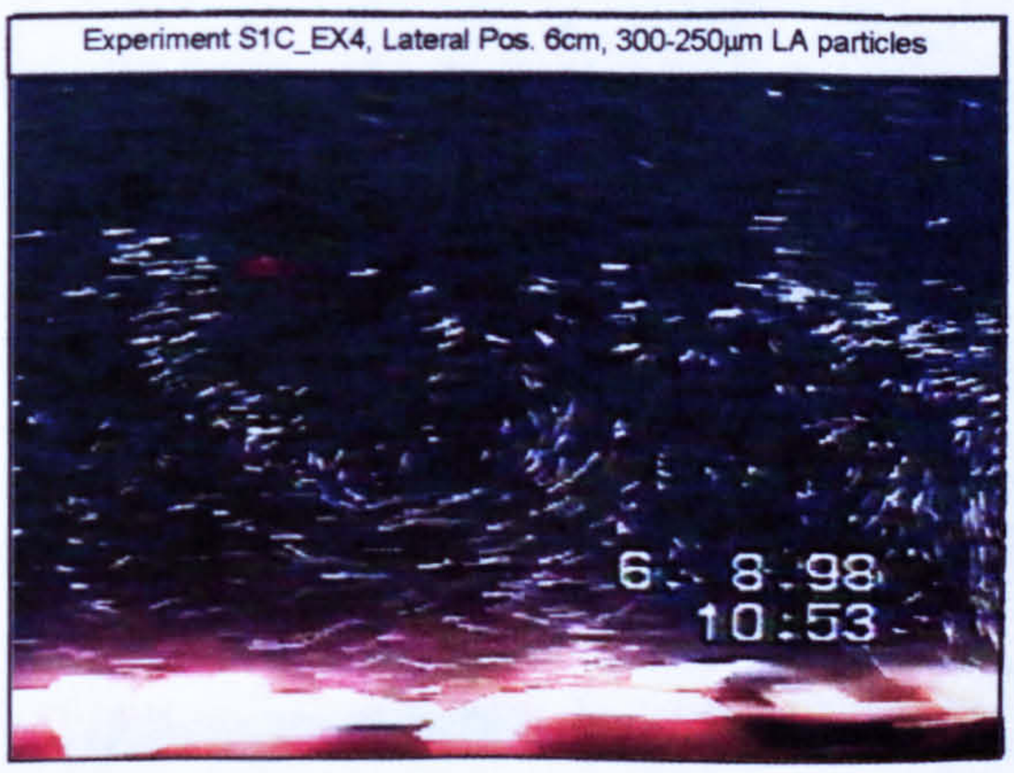
Experiment S1C_EX4, Lateral Pos. 6cm, 300-250µm LA particles
6. 8.98
10:53


Experiment S1C_EX4, Lateral Pos. 10cm, 300-250µm LA particles
6. 8.98
9:52

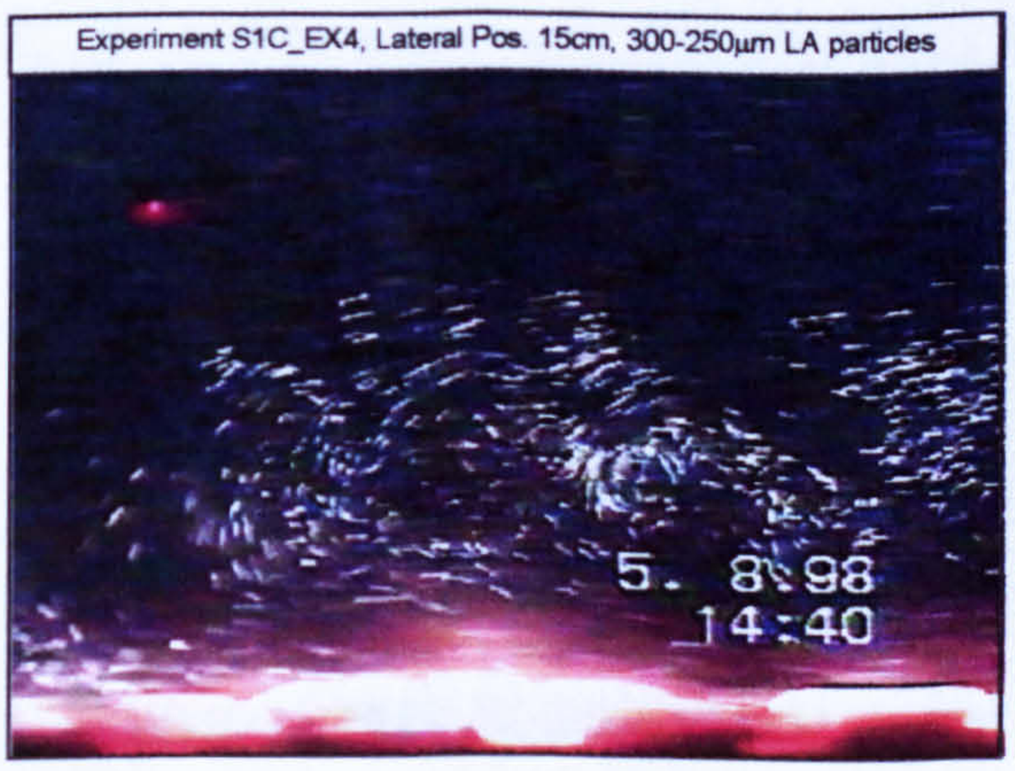
Experiment S1C_EX4, Lateral Pos. 15cm, 300-250µm LA particles
5. 8.98
14:40

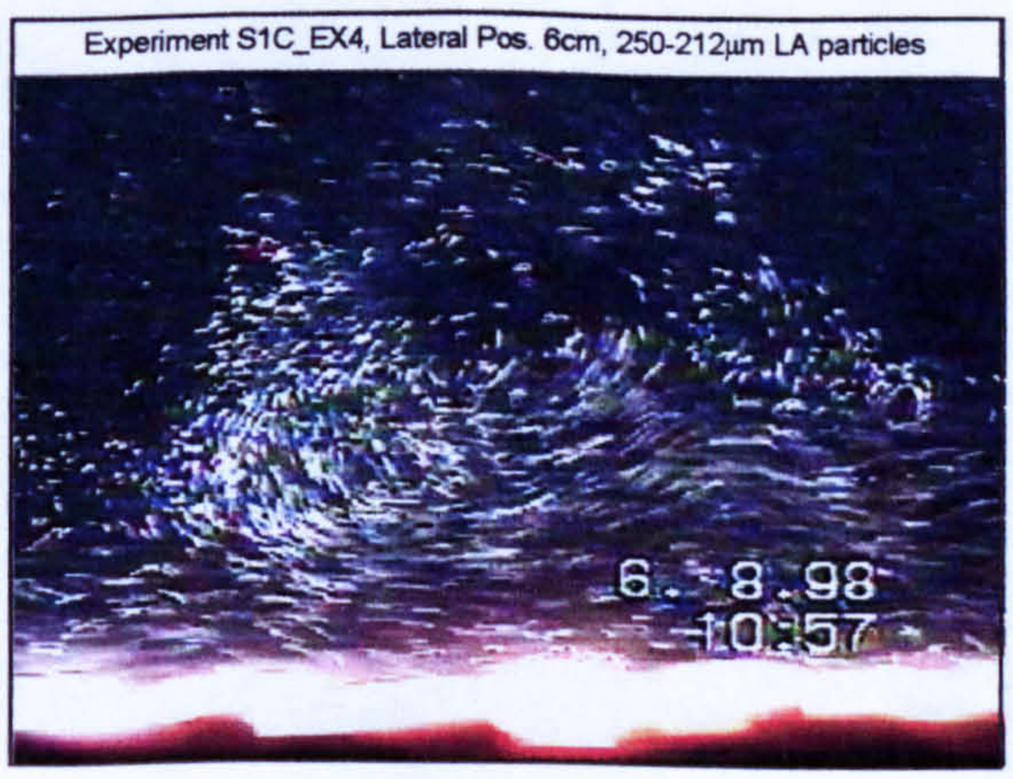
Experiment S1C_EX4, Lateral Pos. 6cm, 250-212µm LA particles
6. 8.98
10:57

Experiment S1C_EX4, Lateral Pos. 6cm, 250-212μm LA particles

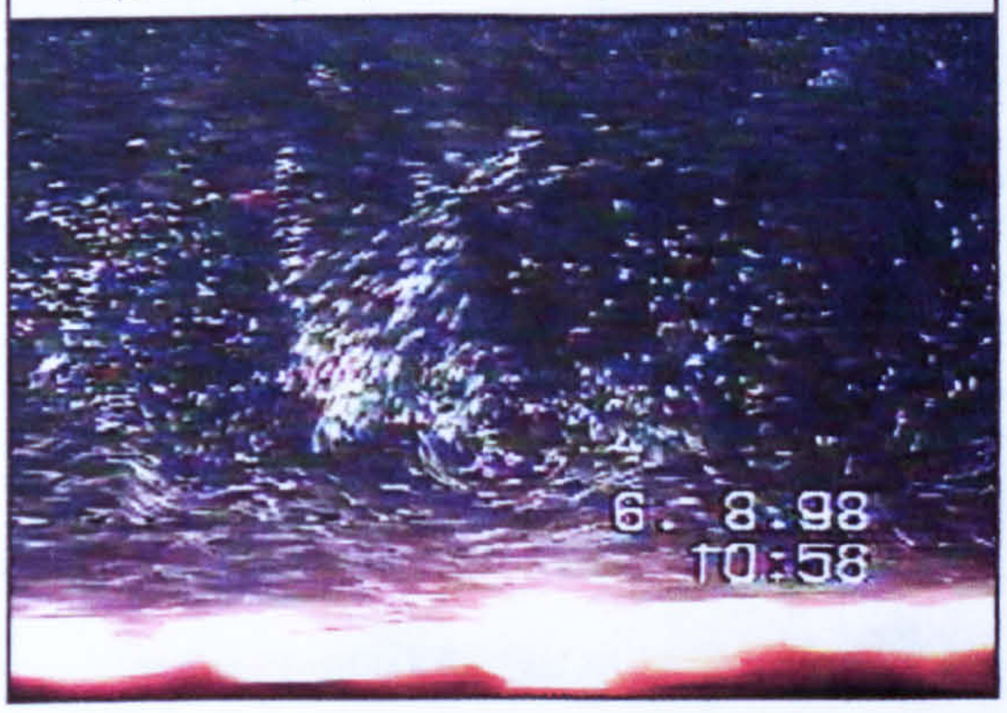

Experiment S1C_EX4, Lateral Pos. 10cm, 250-212μm LA particles

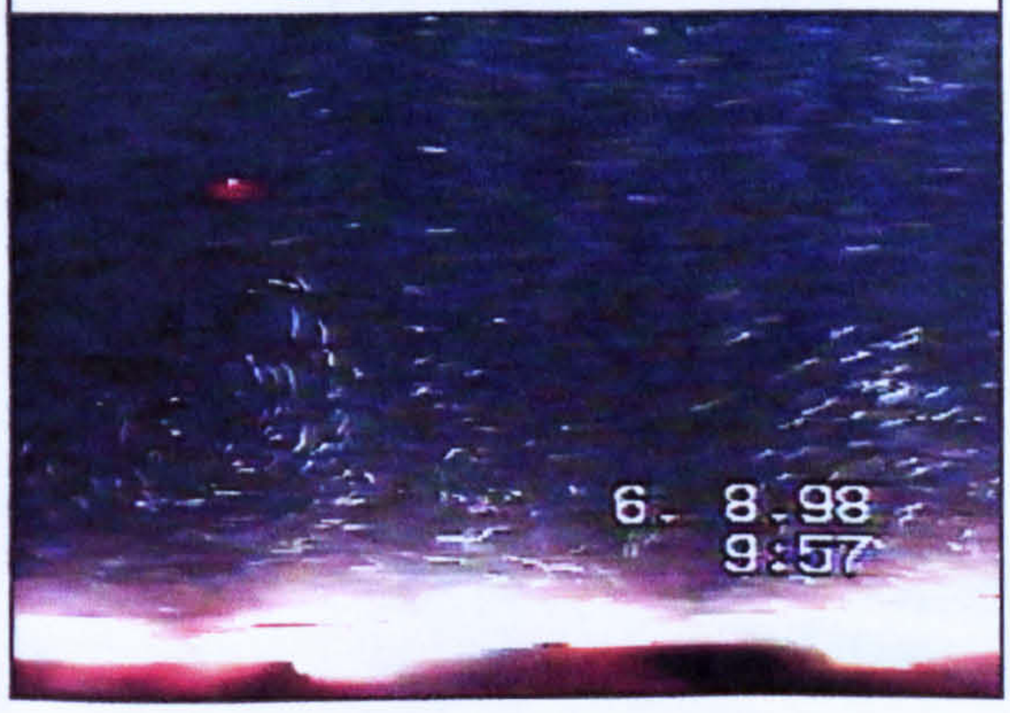

Experiment S1C_EX4, Lateral Pos. 10cm, 250-212μm LA particles

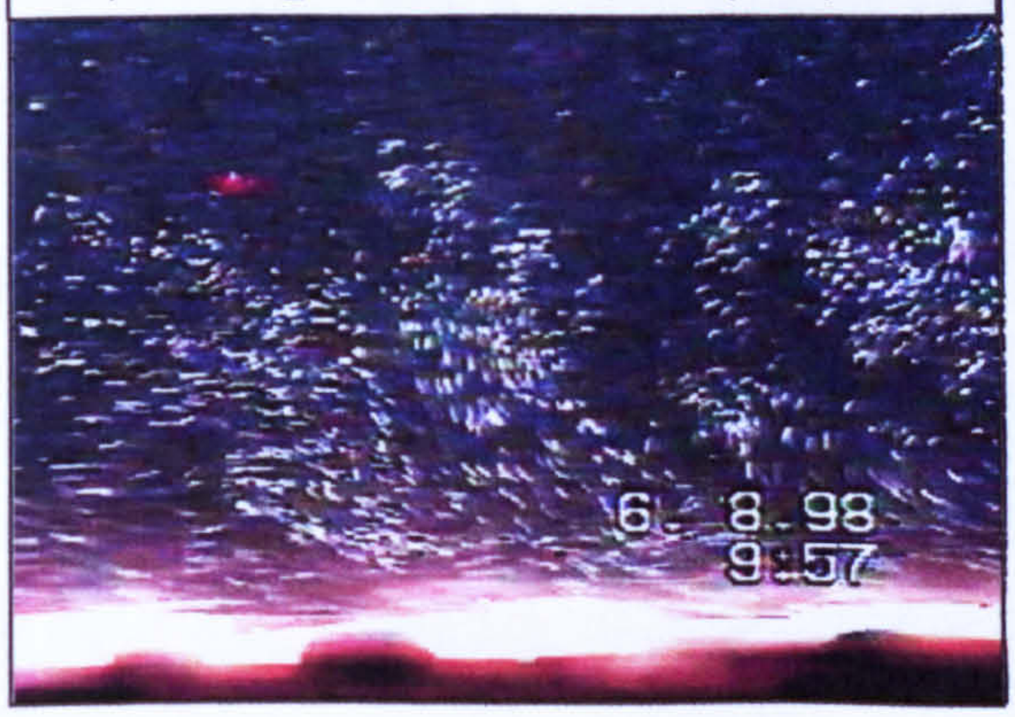

Experiment S1C_EX4, Lateral Pos. 15cm, 250-212μm LA particles

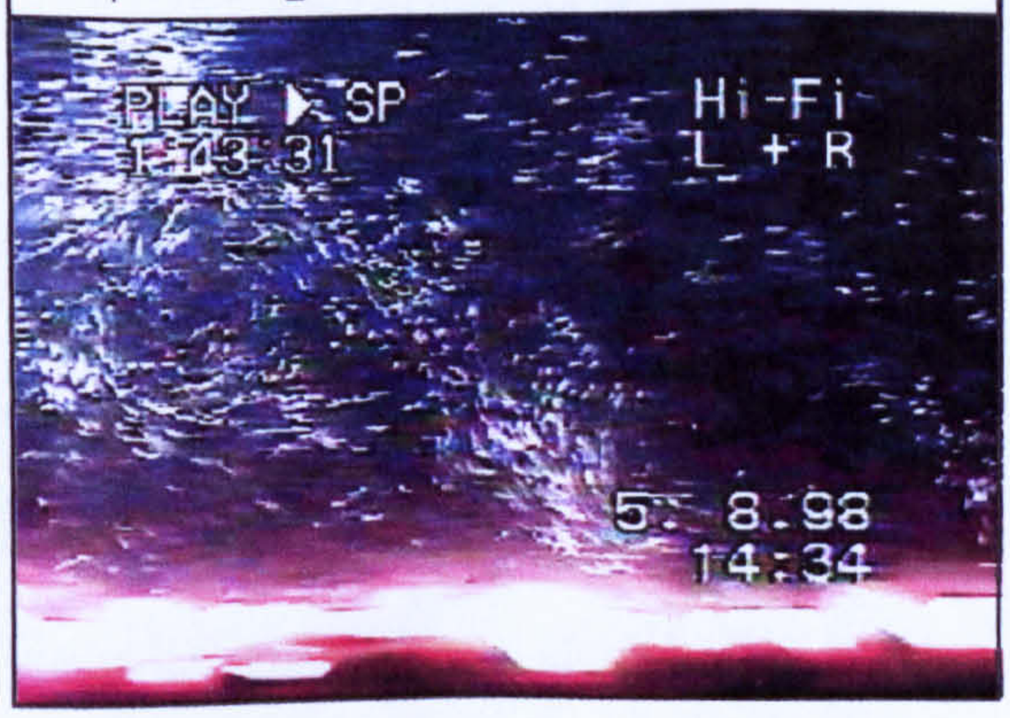

Experiment S1C_EX4, Lateral Pos. 15cm, 250-212μm LA particles

Experiment S1C_EX4, Lateral Pos. 6cm, 212-150μm LA particles

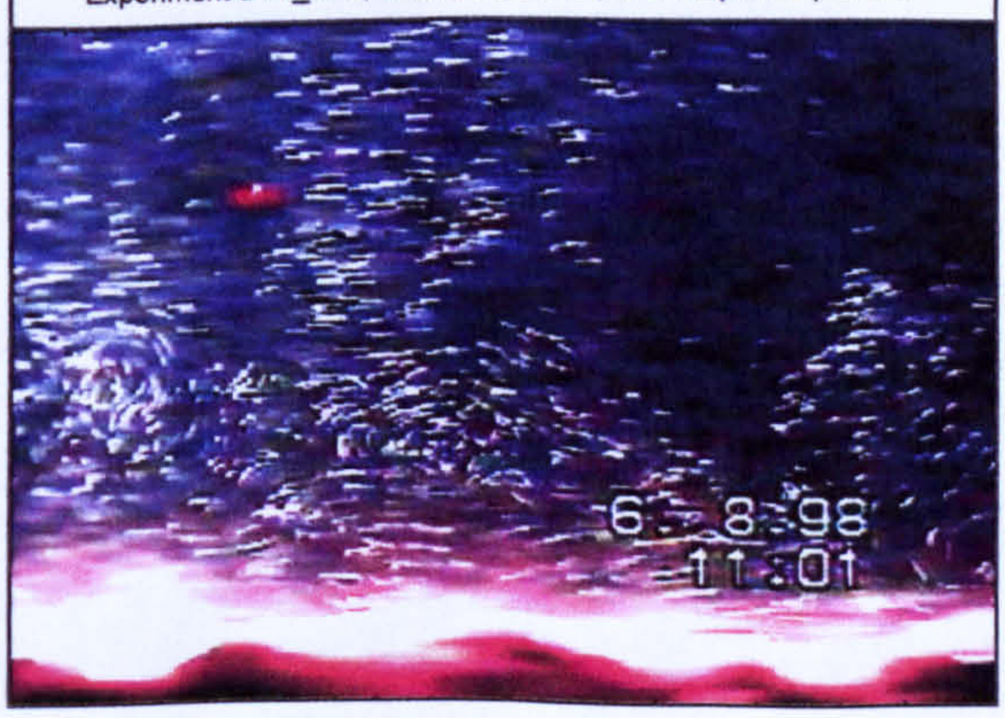

Experiment S1C_EX4, Lateral Pos. 6cm, 212-150μm LA particles

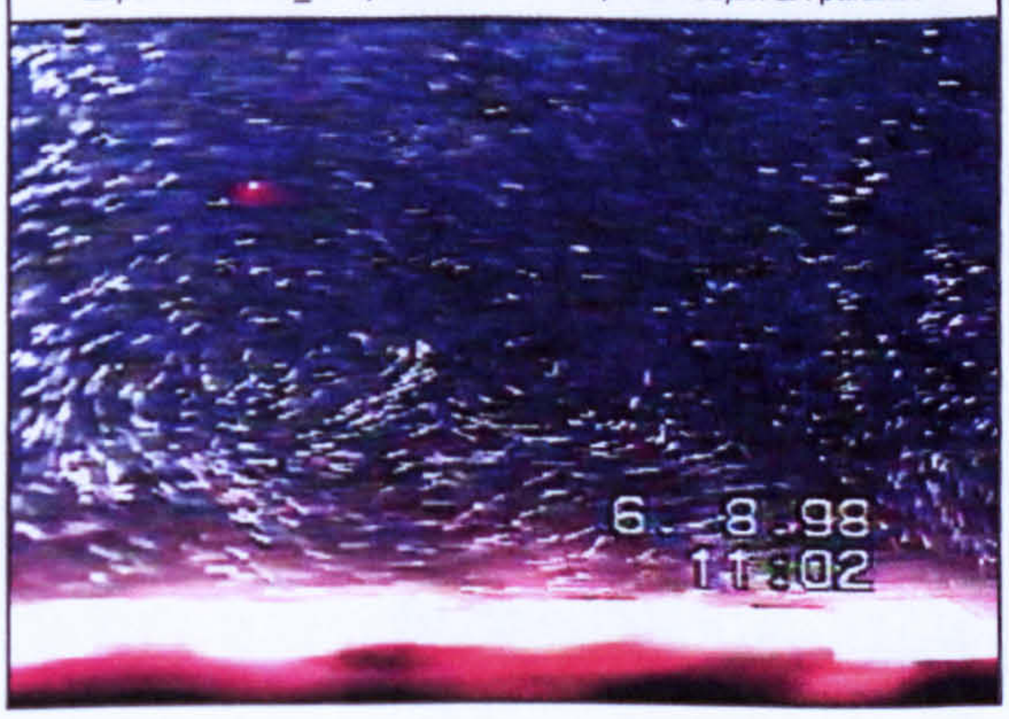

Experiment S1C_EX4, Lateral Pos. 10cm, 212-150μm LA particles

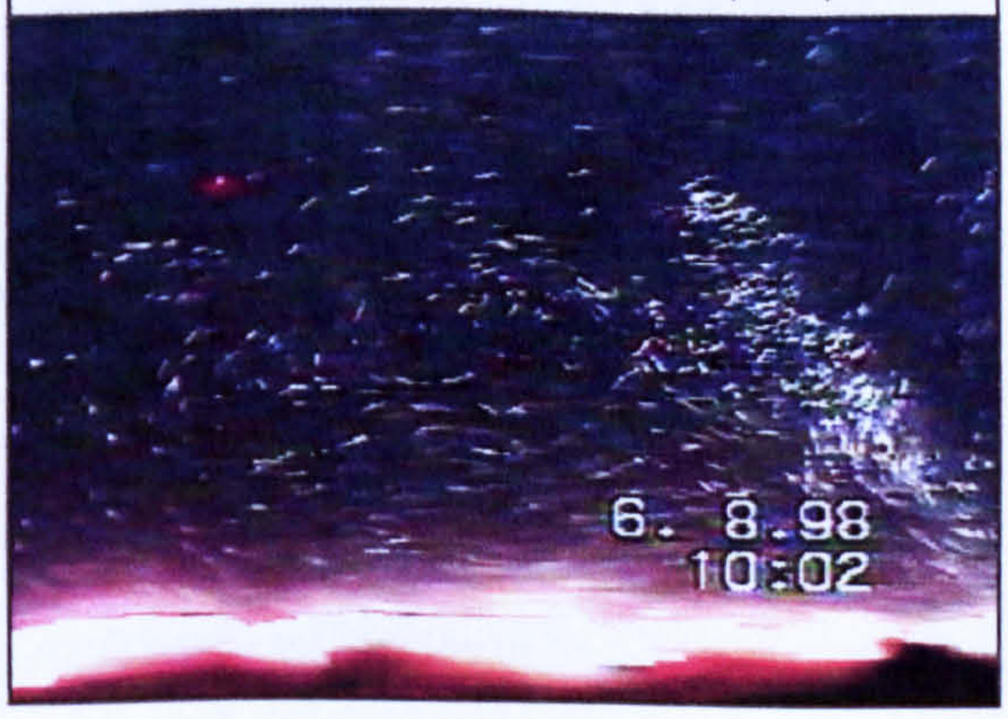

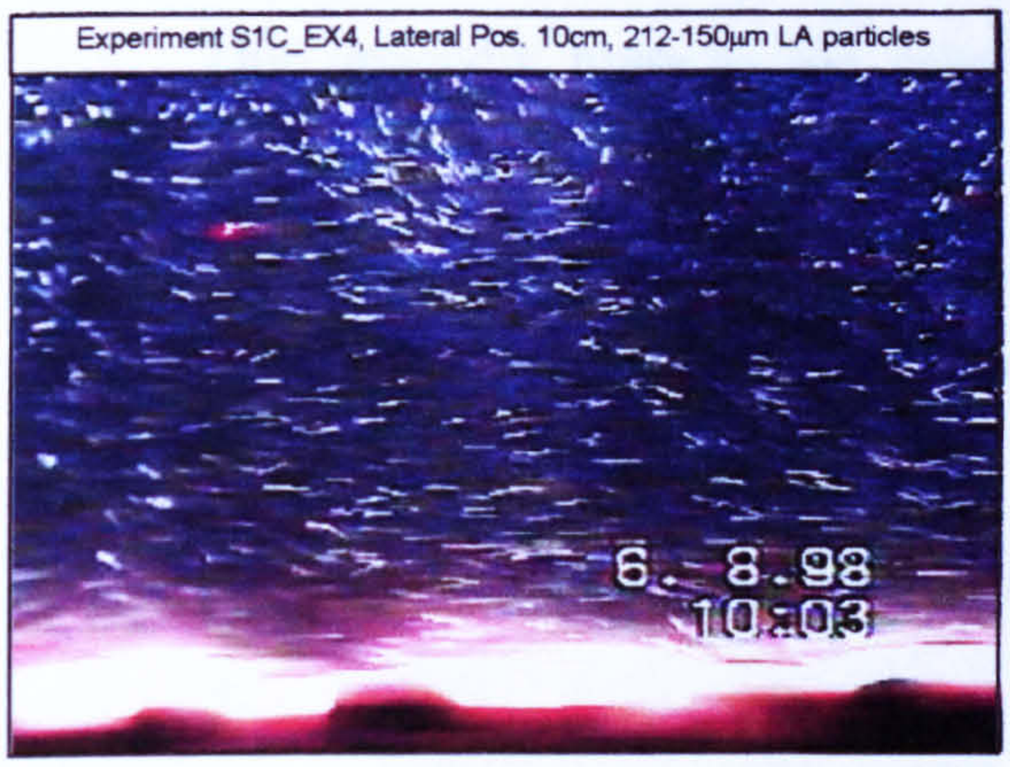
Experiment S1C_EX4, Lateral Pos. 10cm, 212-150µm LA particles
6. 8.98
10:03

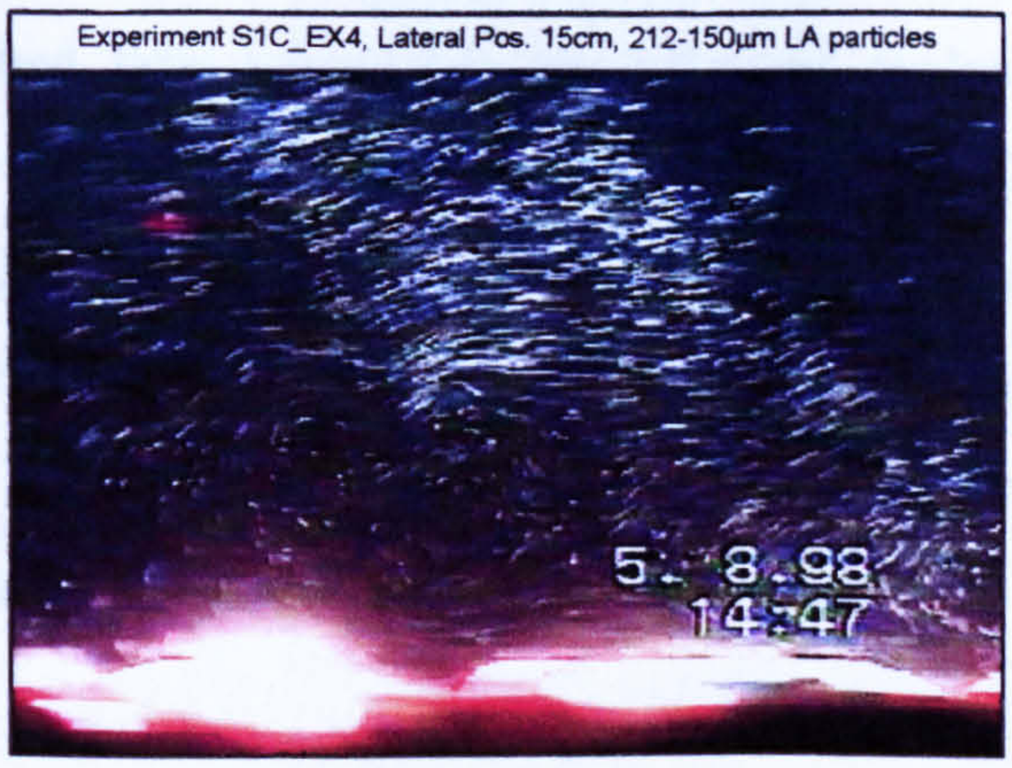
Experiment S1C_EX4, Lateral Pos. 15cm, 212-150µm LA particles
5. 8.98
14:47

Appendix 6.1 Shear Velocity Calculation using Clauser (1956) Method

This appendix presents the near-bed flow velocity profiles plotted against $\ln[(z+\delta z)/k_s]$ for each flow condition set-up in the 0.764m-wide flume for Series 2 experiments. From each condition, the shear velocity u_* was calculated by fitting the least-squares best-fit straight line to the data set, the gradient of which is equal to u_*/κ (where κ is generally taken to be 0.4). The constant of integration (B_r) for each profile was also calculated from the constant in the equation of best-fit line ($=B_r/u_*$).

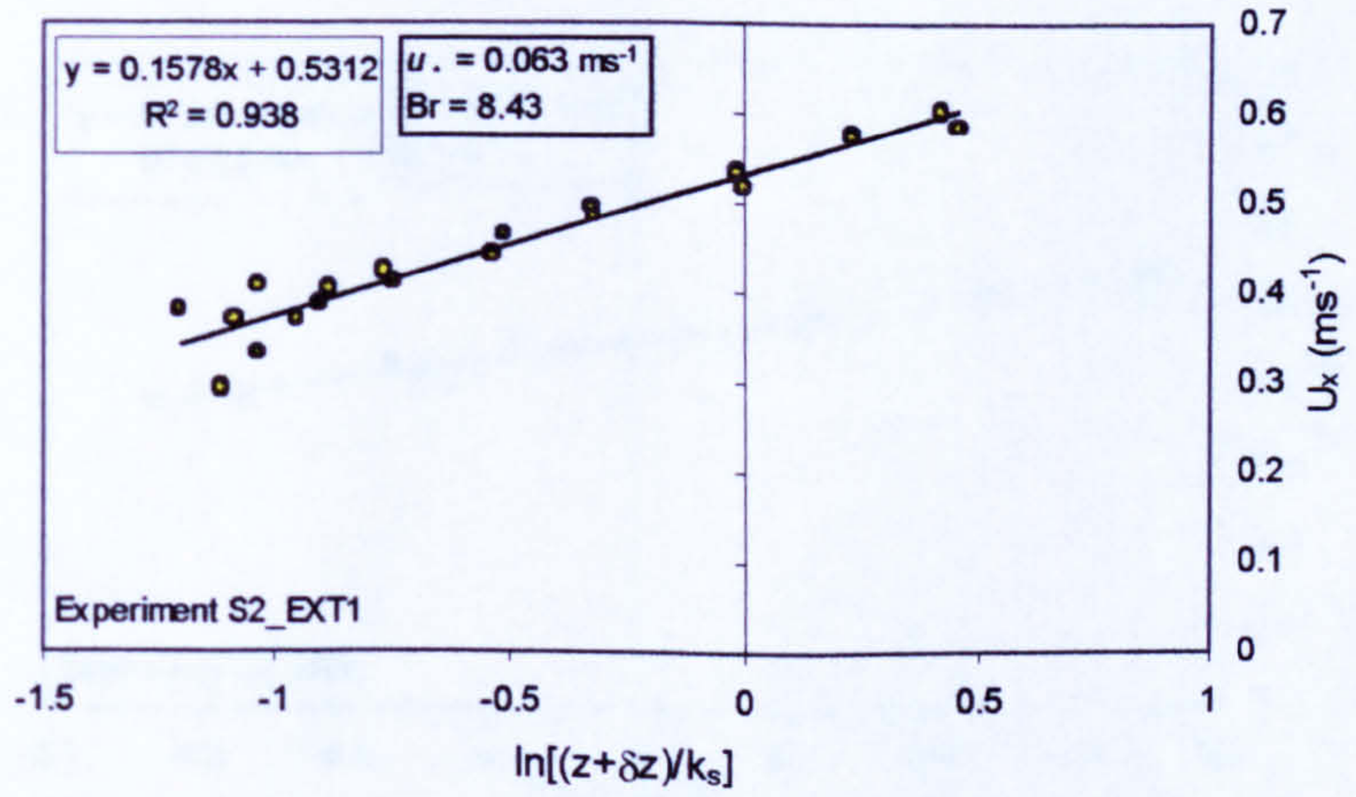

Figure A6.1

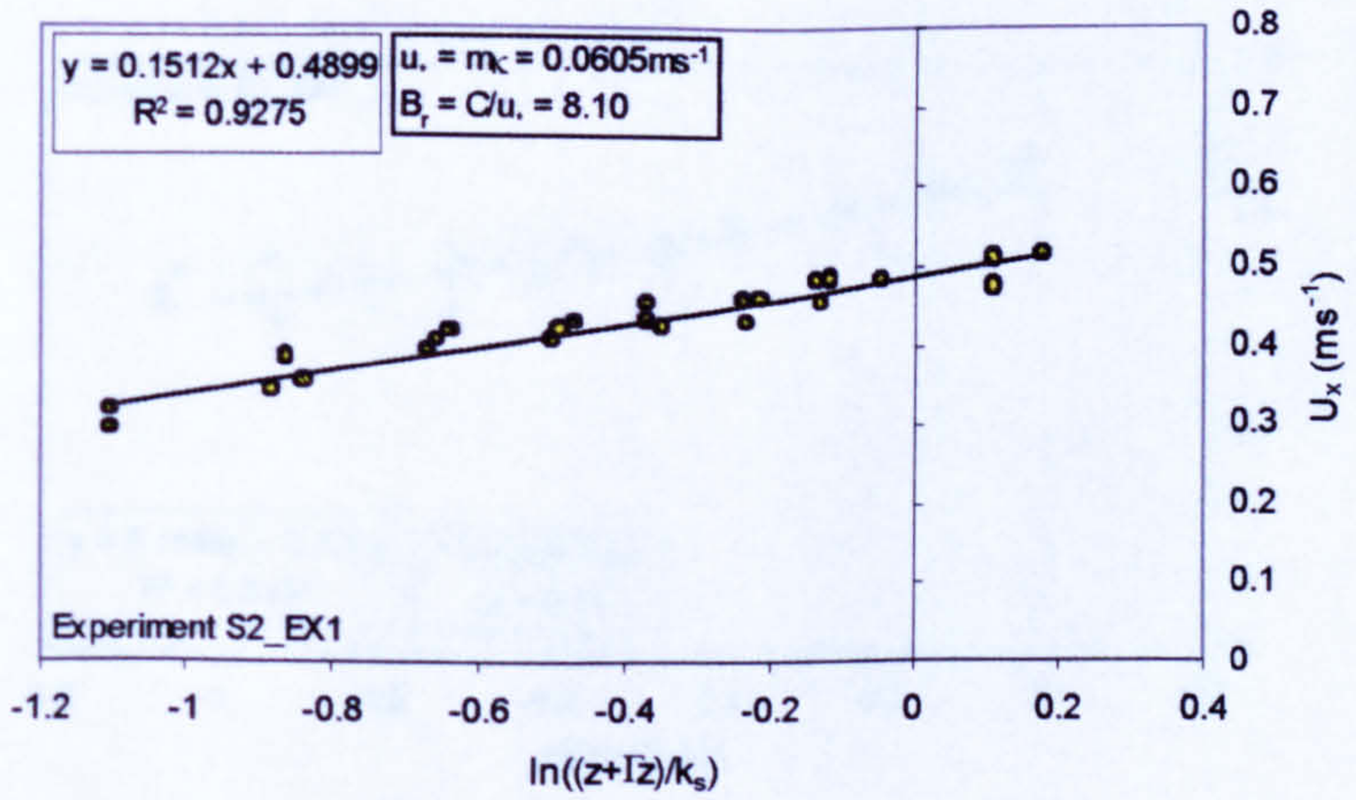

Figure A6.2

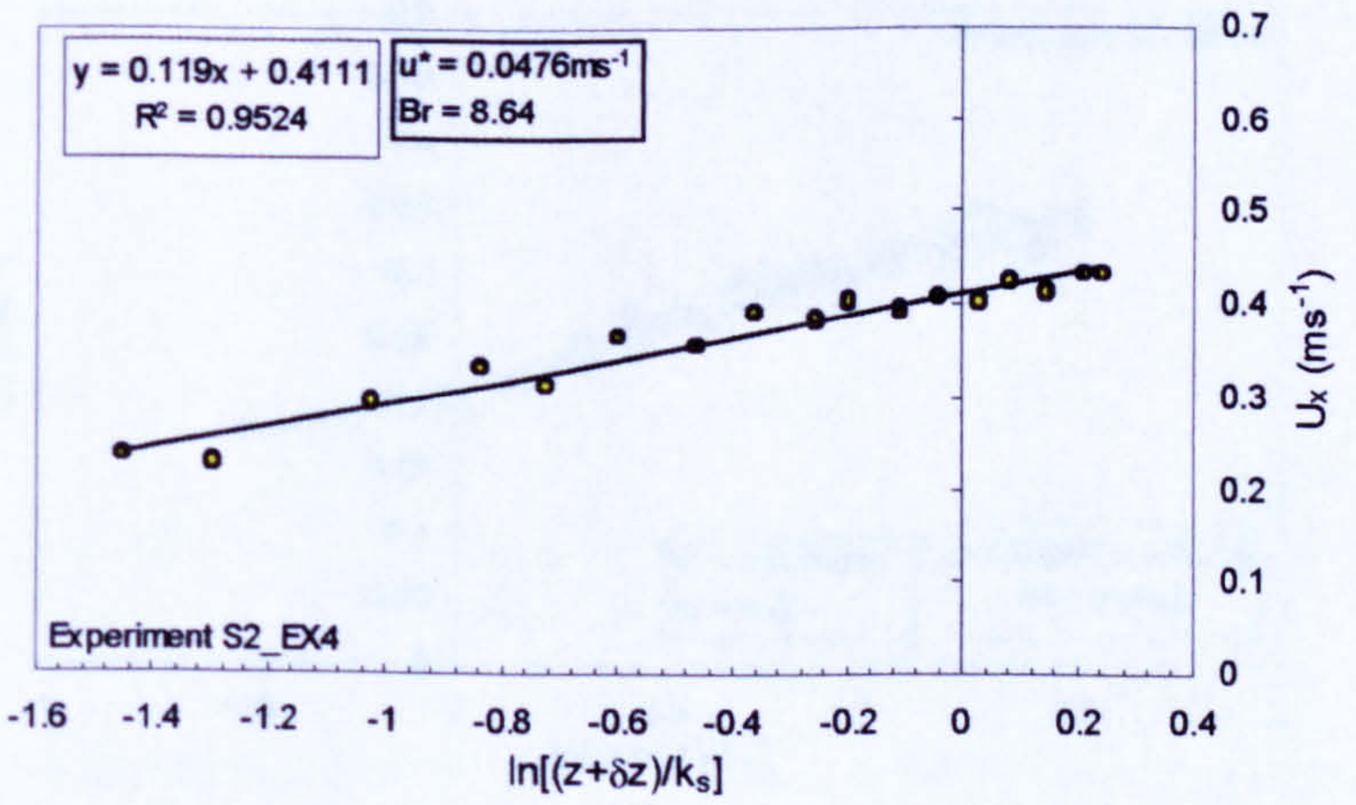

Figure A6.3

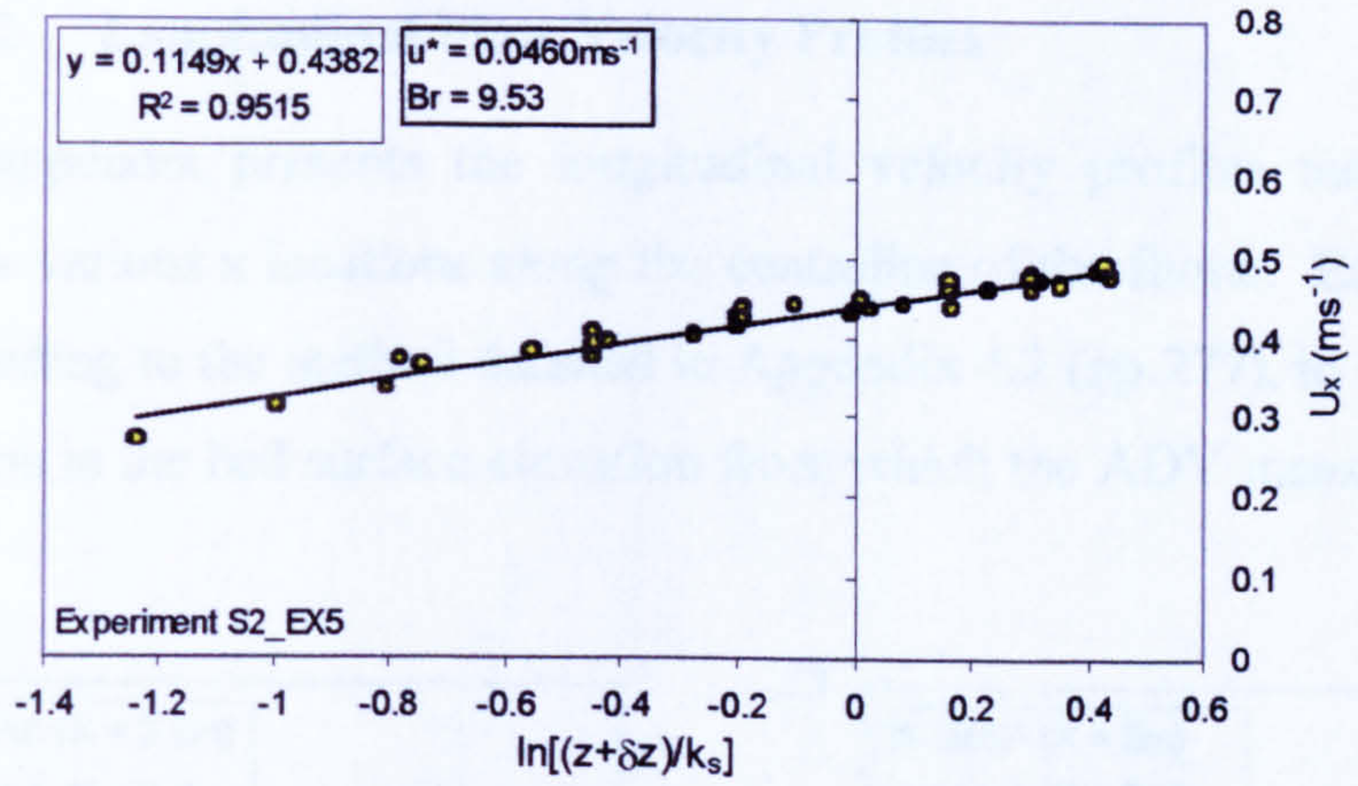

Figure A6.4

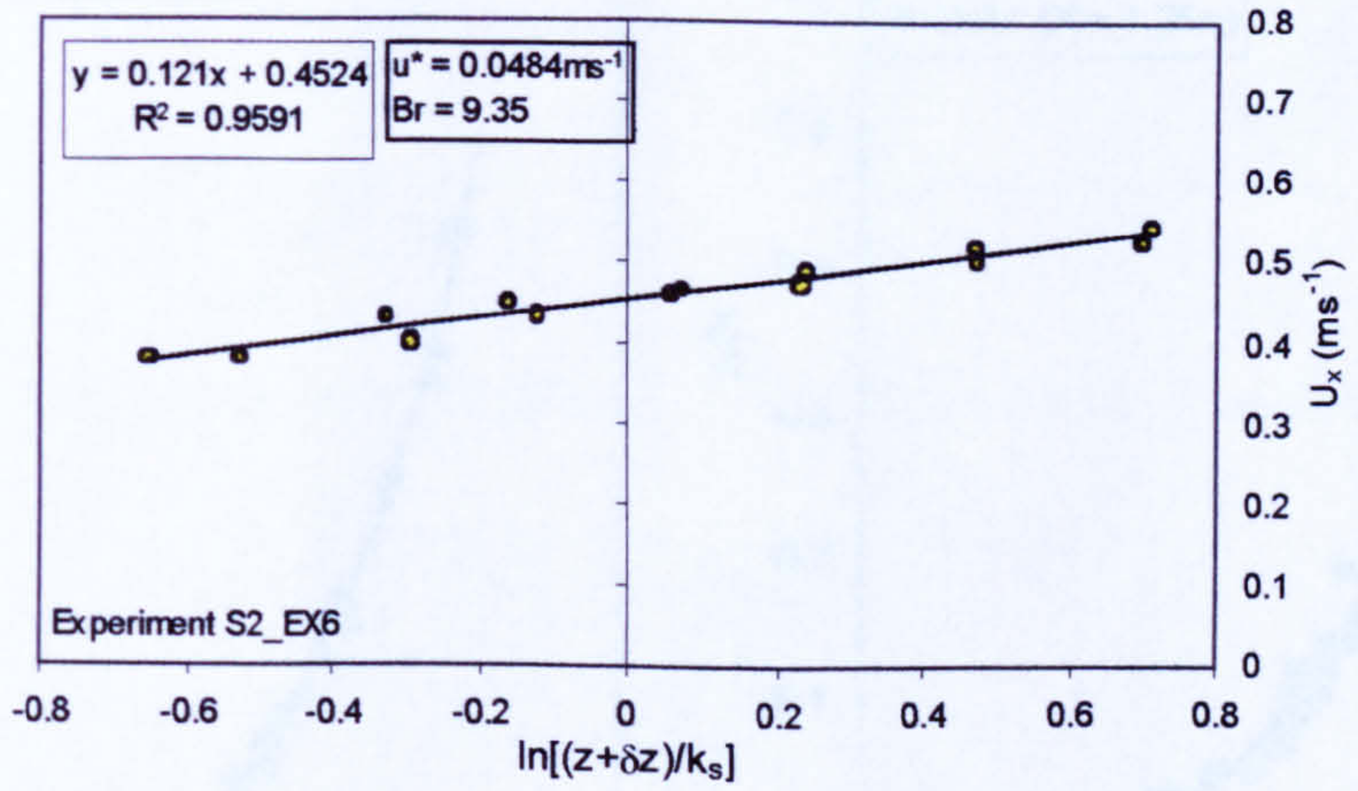

Figure A6.5

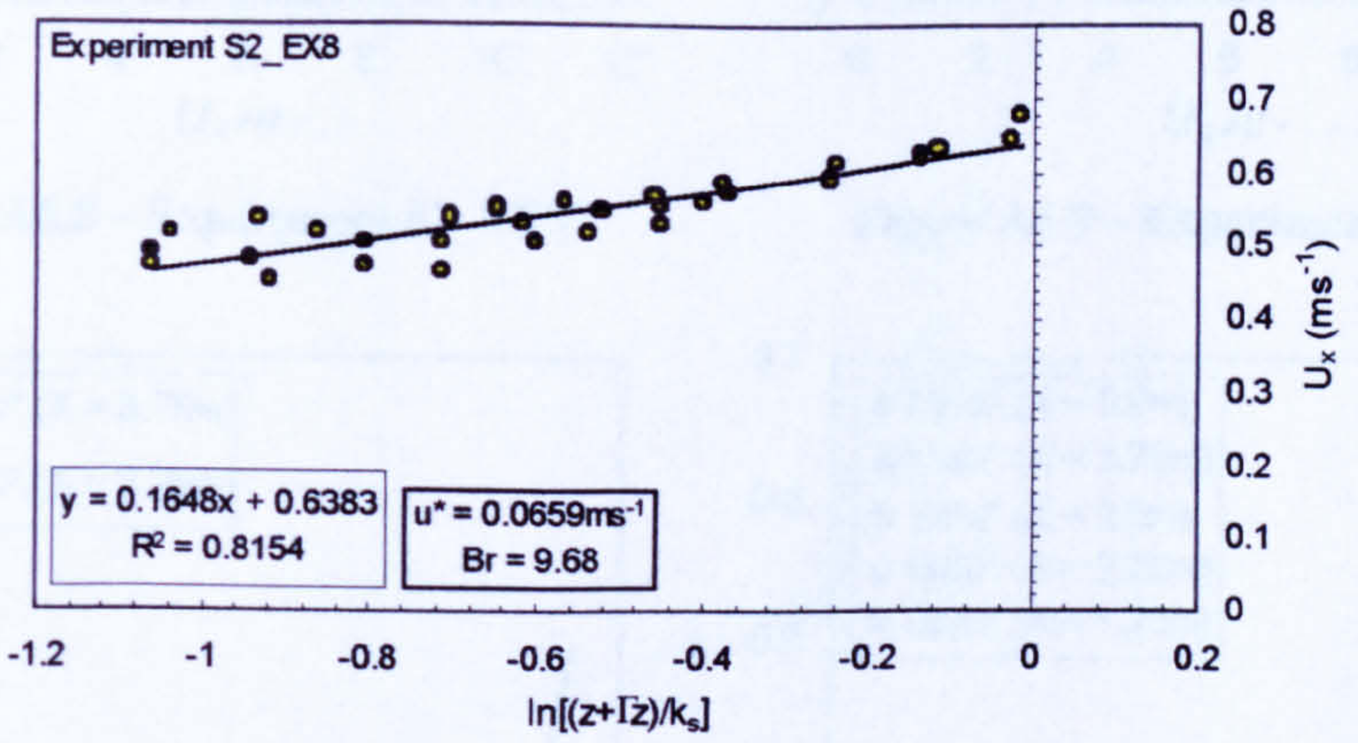

Figure A6.6

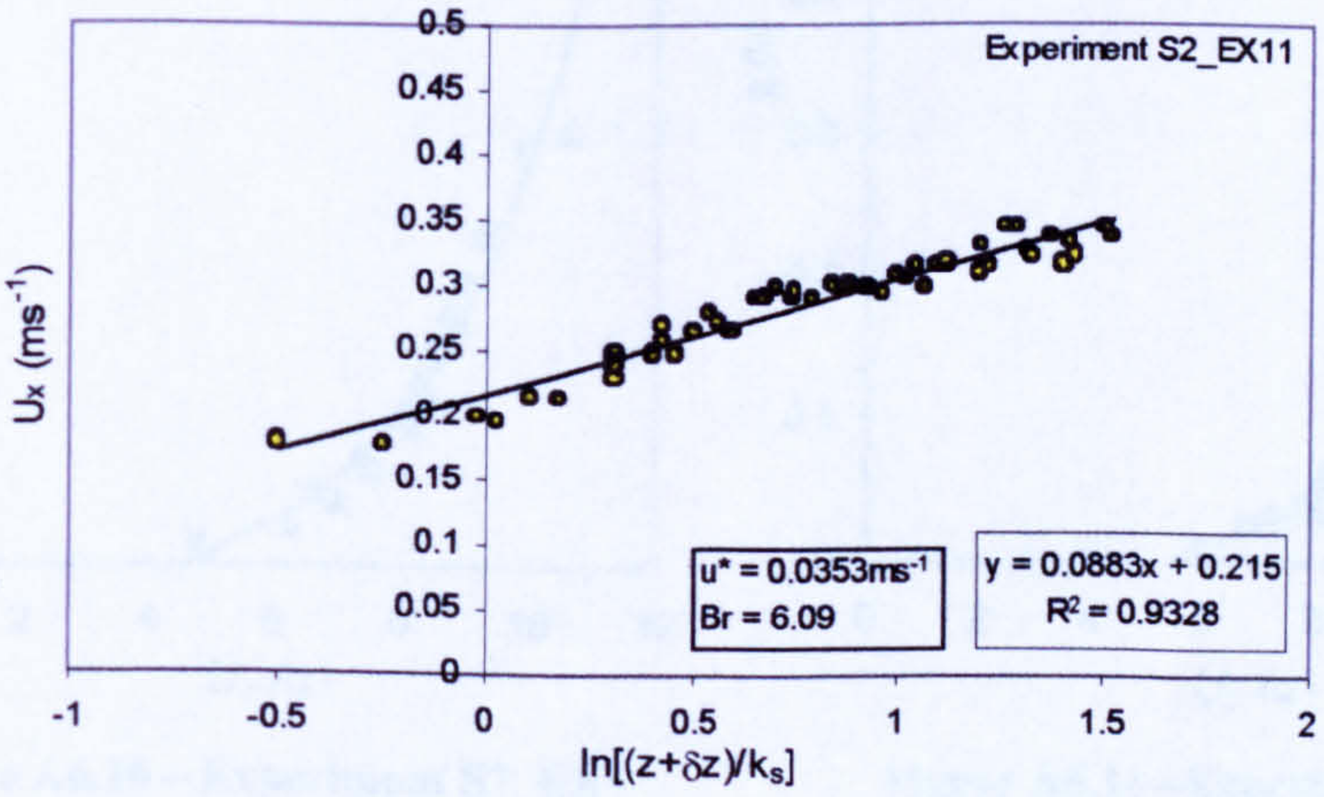

Figure A6.7

Appendix 6.2 Longitudinal Flow Velocity Profiles

This appendix presents the longitudinal velocity profiles measured by the ADV probe at various x locations along the centreline of the flume. Each profile was adjusted according to the method detailed in Appendix 4.2 (pp.277), to account for the local variations in the bed surface elevation from which the ADV measurements were taken.

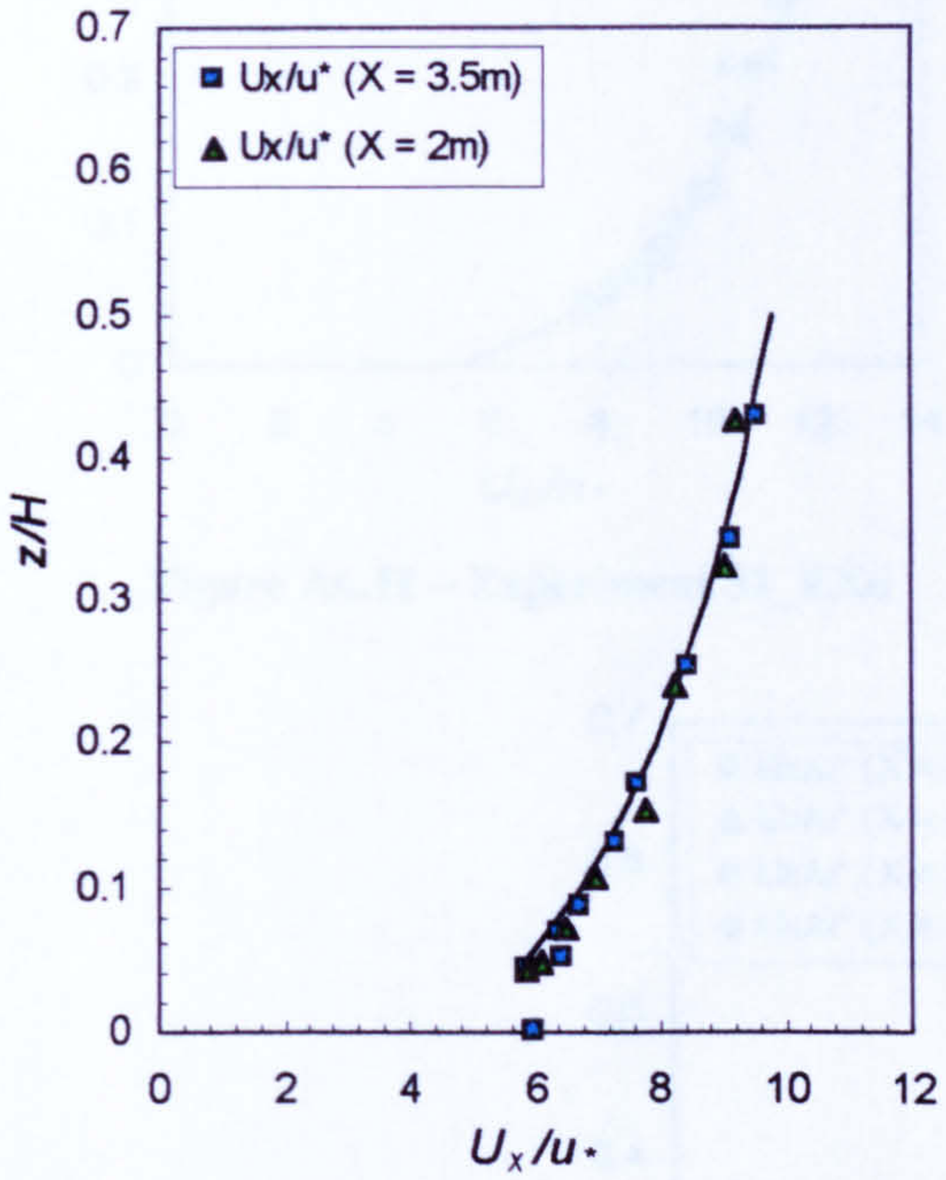

Figure A6.8 – Experiment S2_EXT1

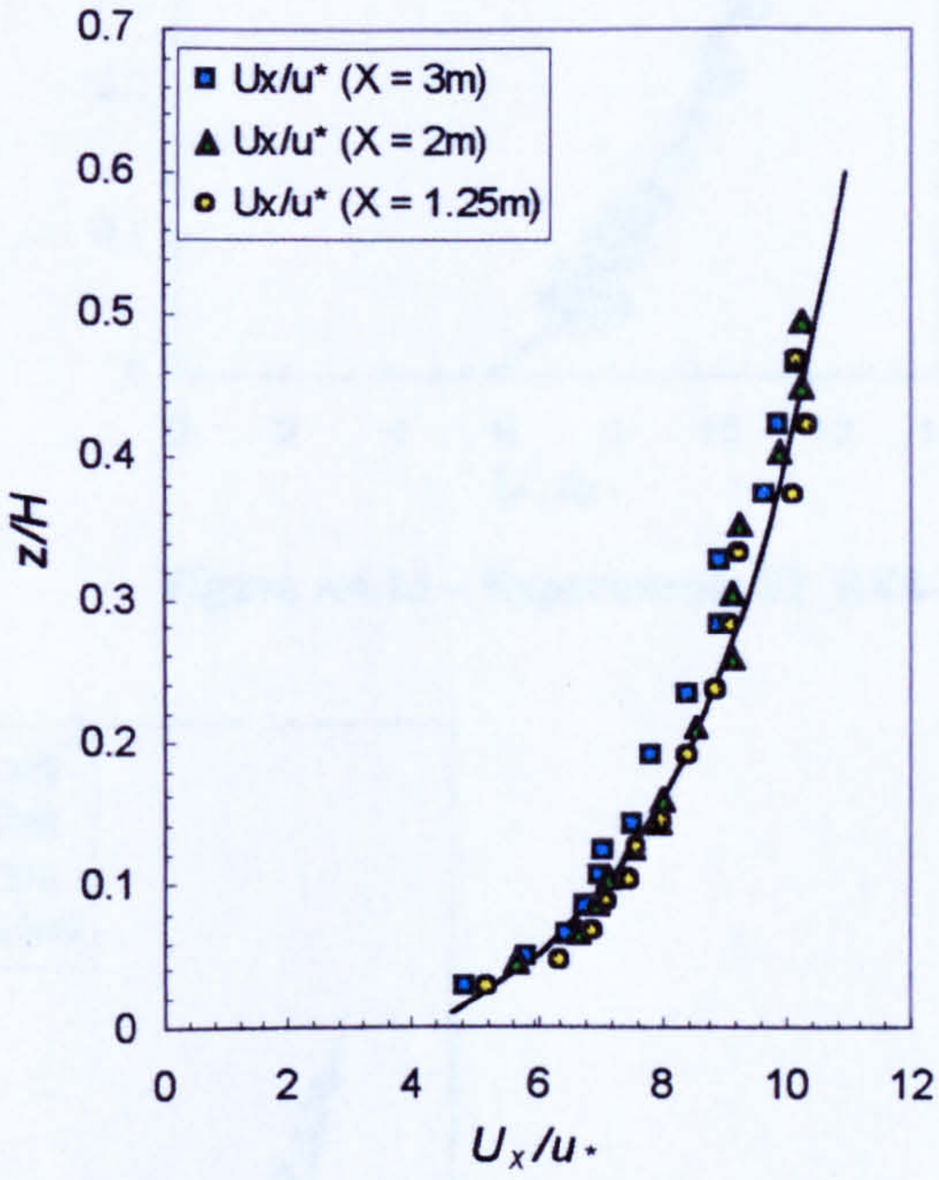

Figure A6.9 – Experiments S2_EX1-3

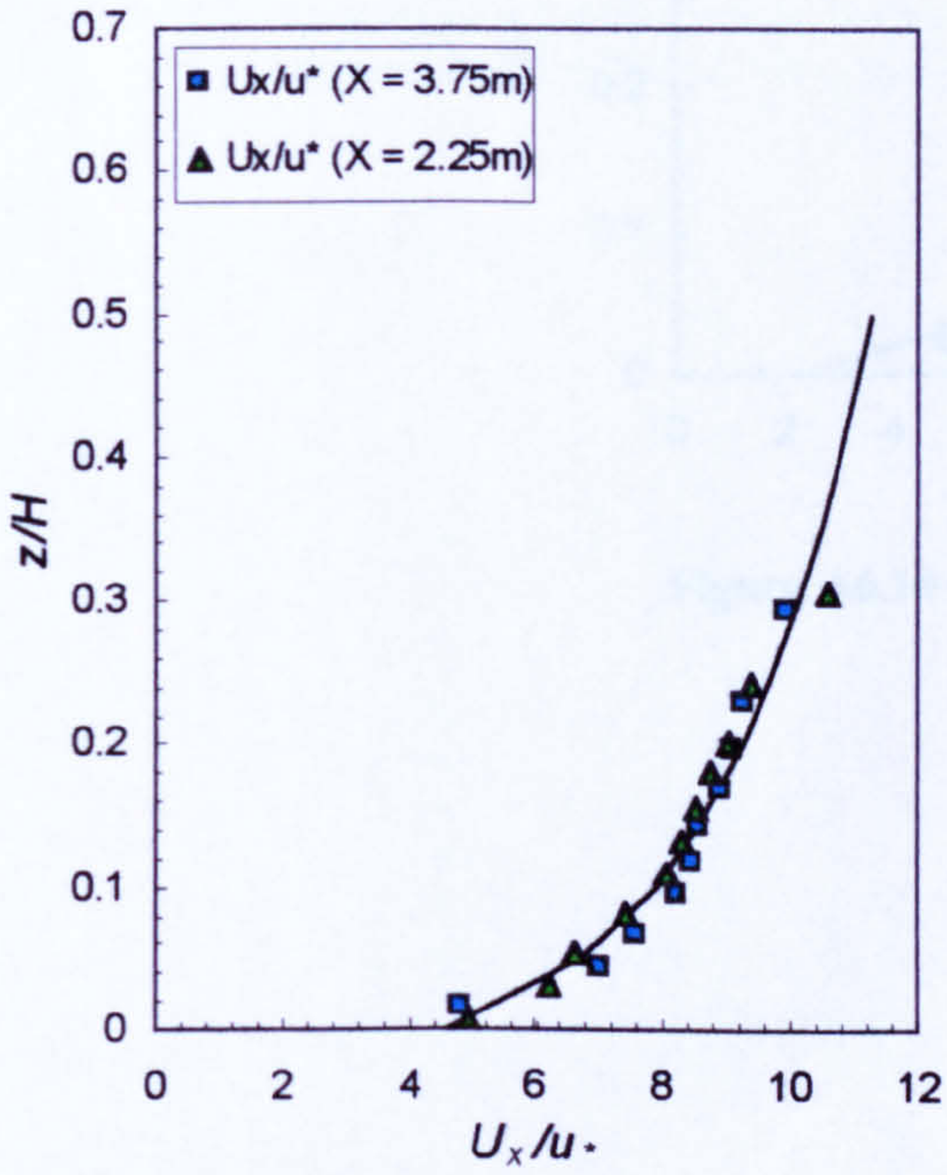

Figure A6.10 – Experiment S2_EX4

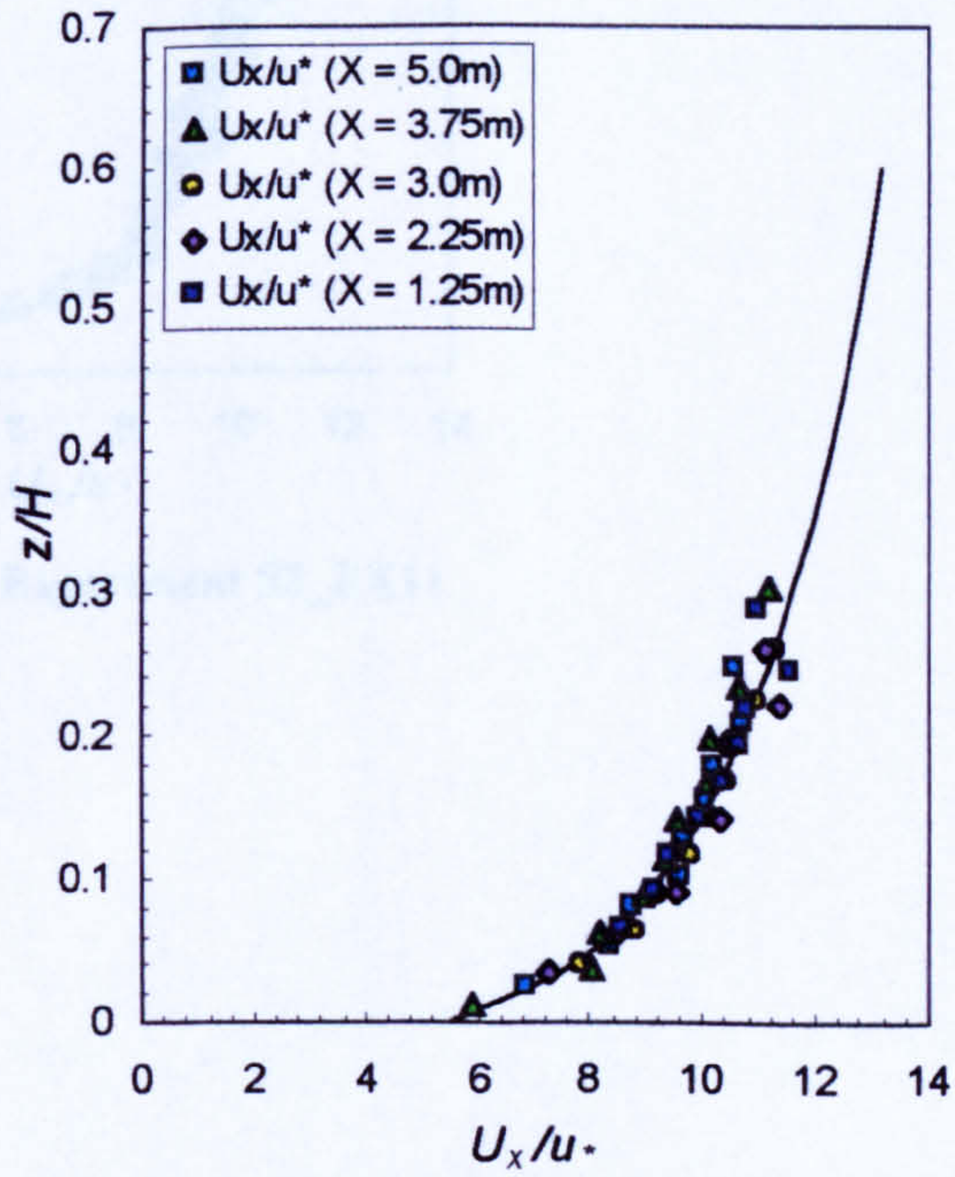

Figure A6.11 –Experiments S2_EX5, 7

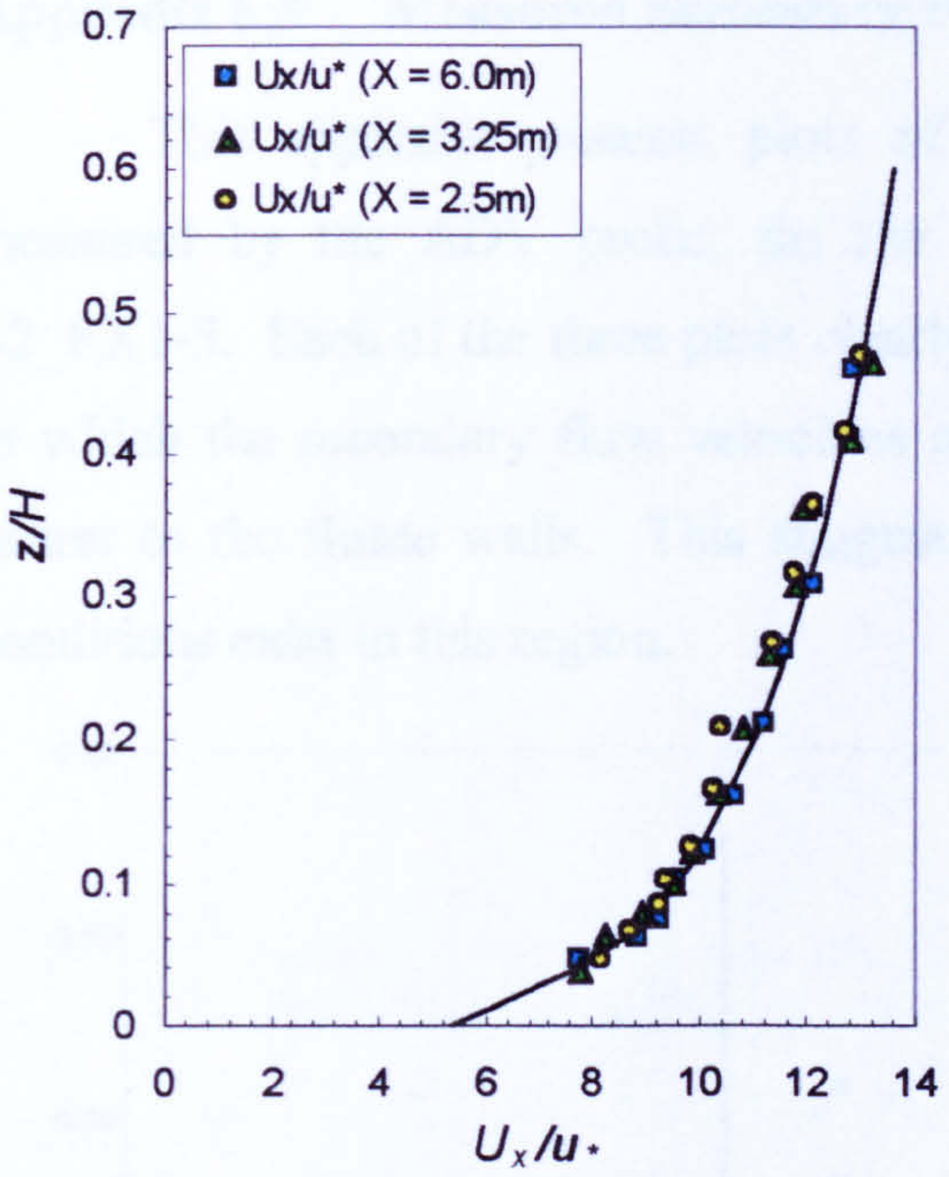

Figure A6.12 – Experiment S2_EX6

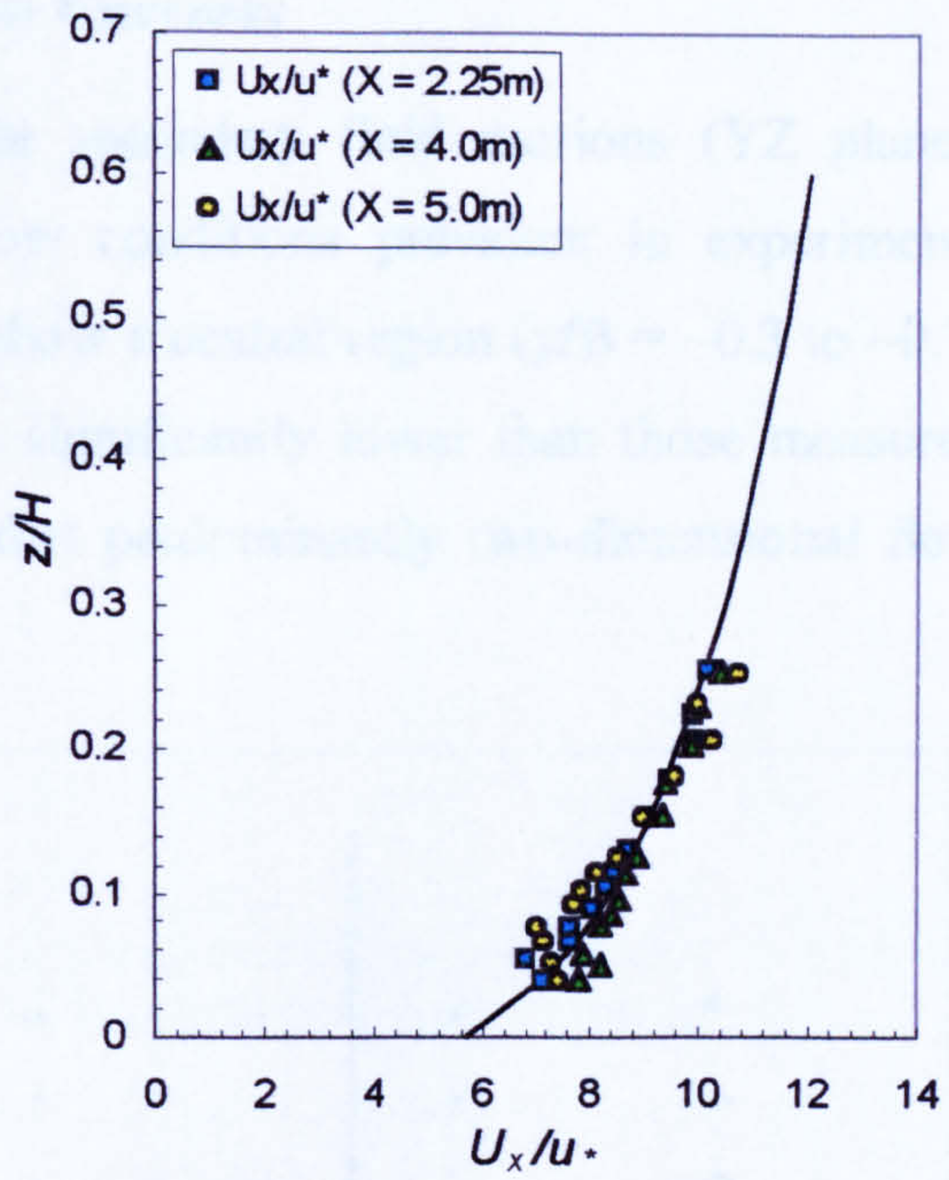

Figure A6.13 – Experiments S2_EX8-10

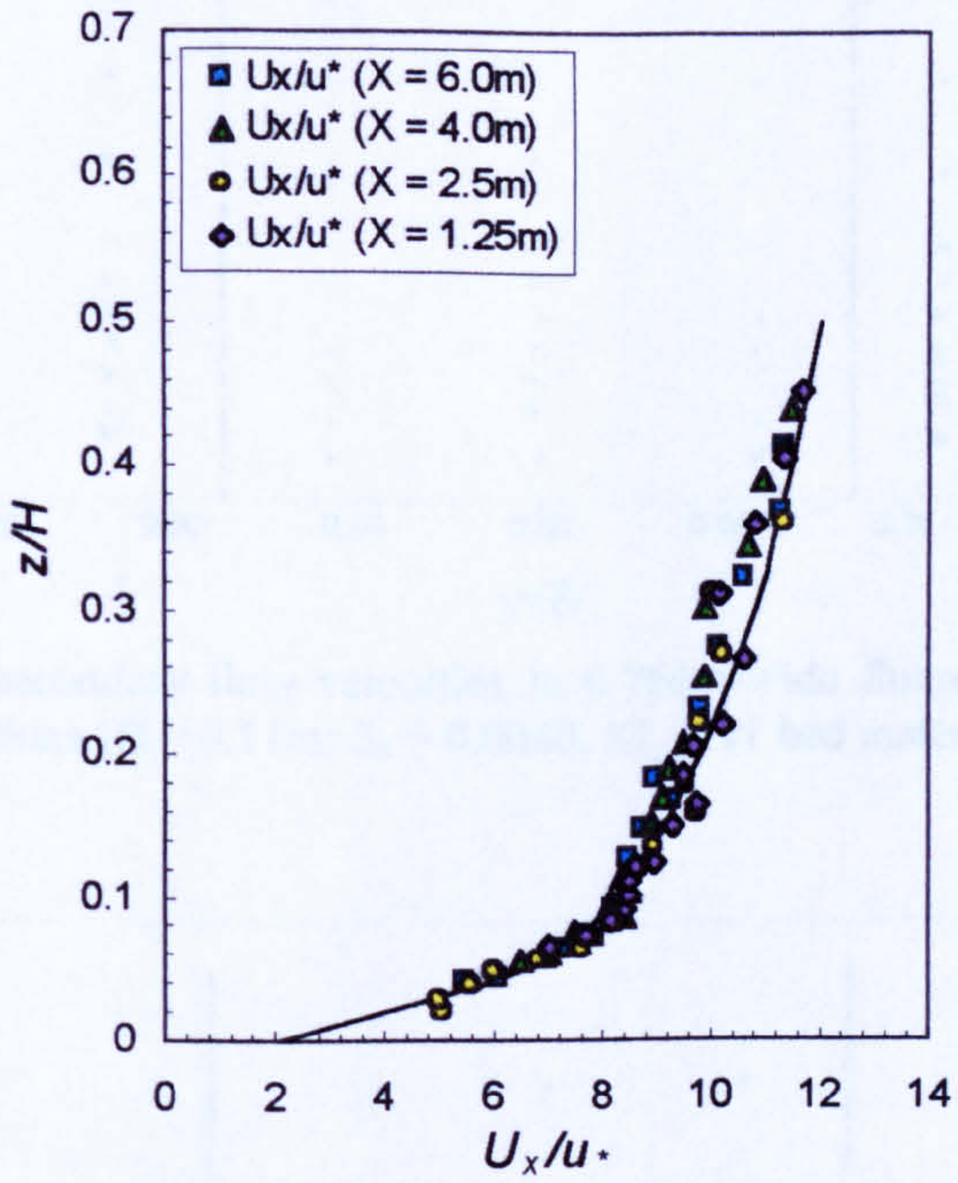

Figure A6.14 – Experiment S2_EX11

Appendix 6.3 Measured Secondary Flow Currents

This appendix presents plots of the secondary fluid motions (YZ plane), measured by the ADV probe, for the flow conditions prevalent in experiments S2_EX1-5. Each of the three plots clearly show a central region (y/B = ~0.3 to ~0.7) in which the secondary flow velocities are significantly lower than those measured nearer to the flume walls. This suggests that predominantly two-dimensional flow conditions exist in this region.

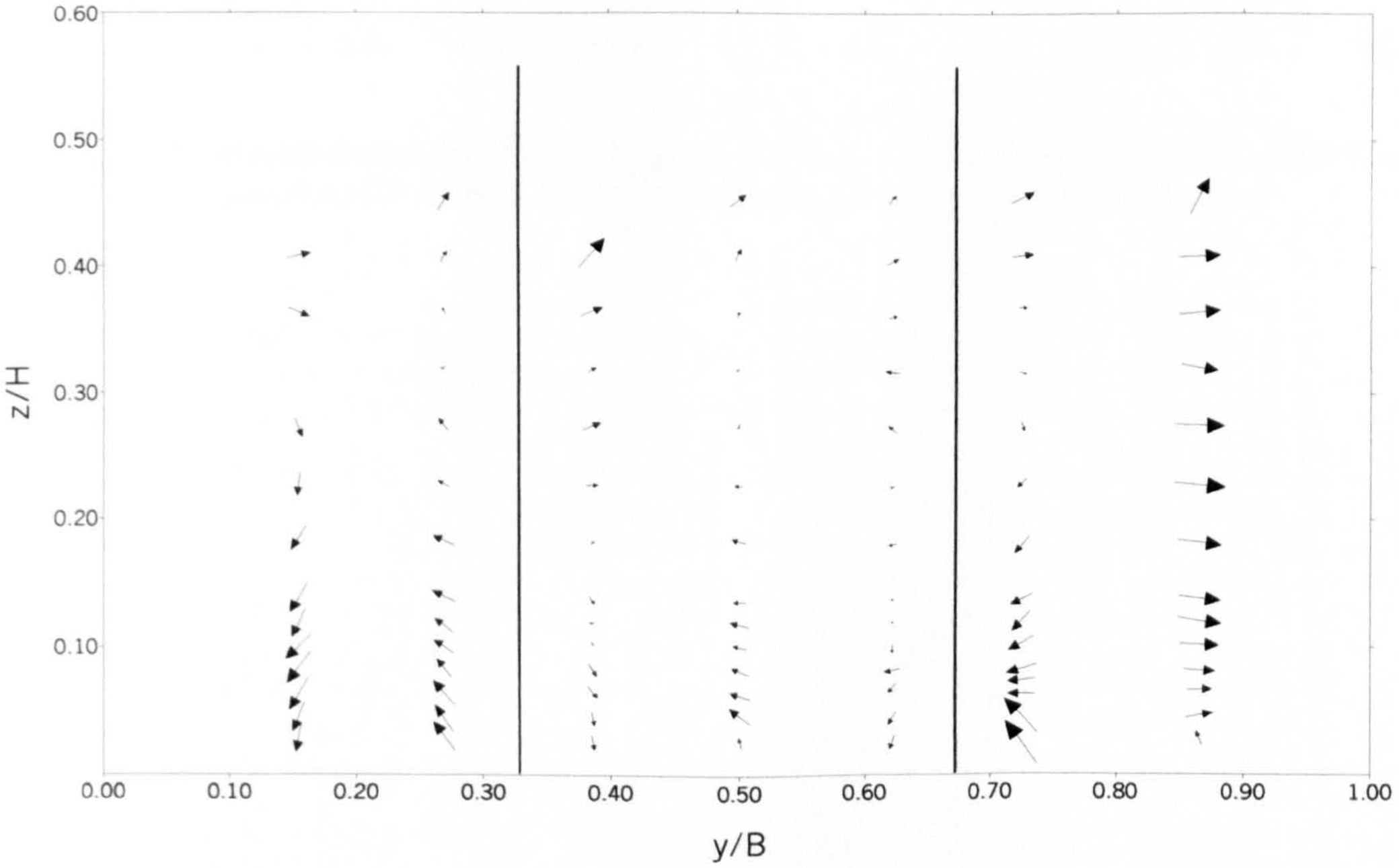

Figure A6.15 - Measured secondary flow velocities in 0.764m-wide flume – Experiment S2_EX1-3 flow conditions [H = 0.11m; S_0 = 0.0040, S2_grv1 bed material (coarse 10-25mm)]

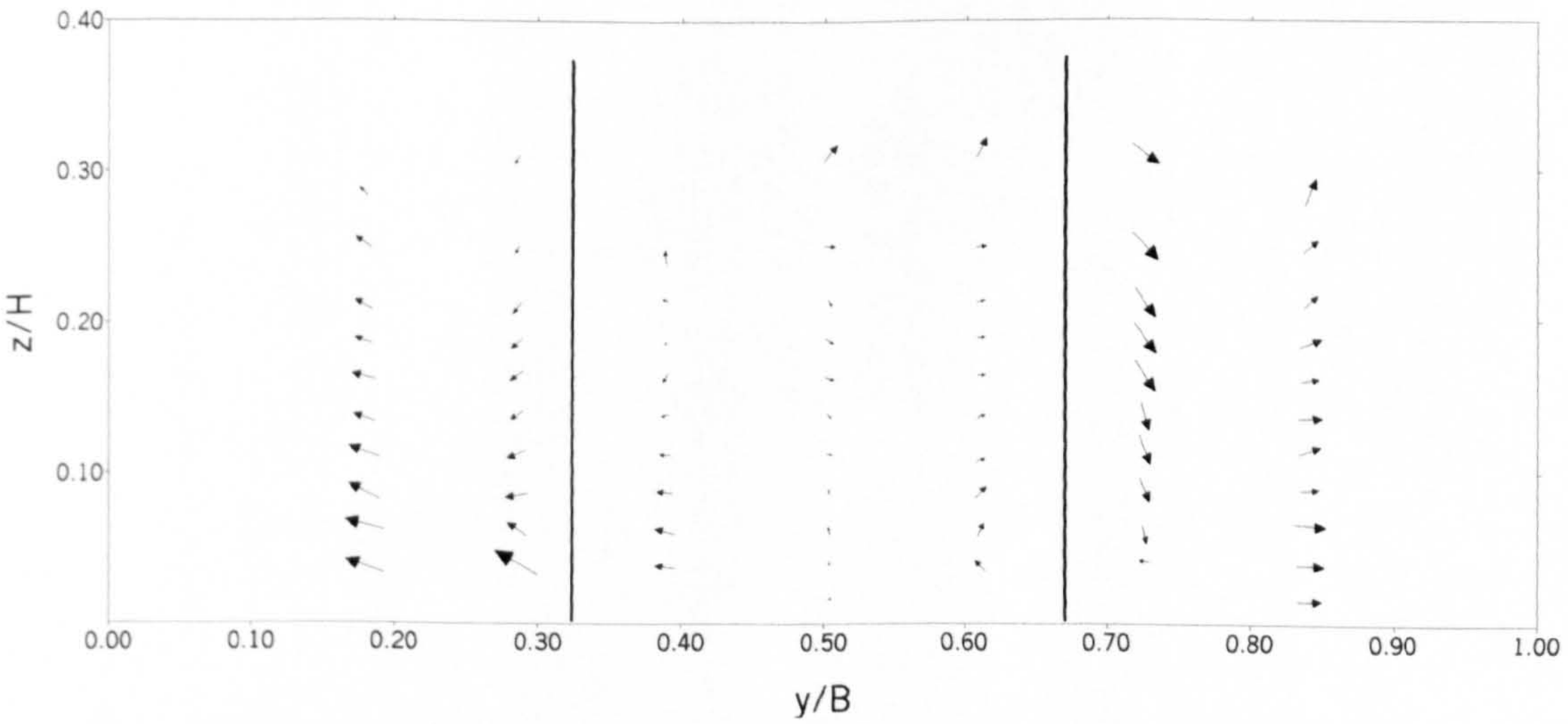

Figure A6.16 - Measured secondary flow velocities in 0.764m-wide flume – Experiment S2_EX4 flow conditions [H = 0.08m; S_0 = 0.0040; S2_grv1 bed material (coarse 10-25mm)]

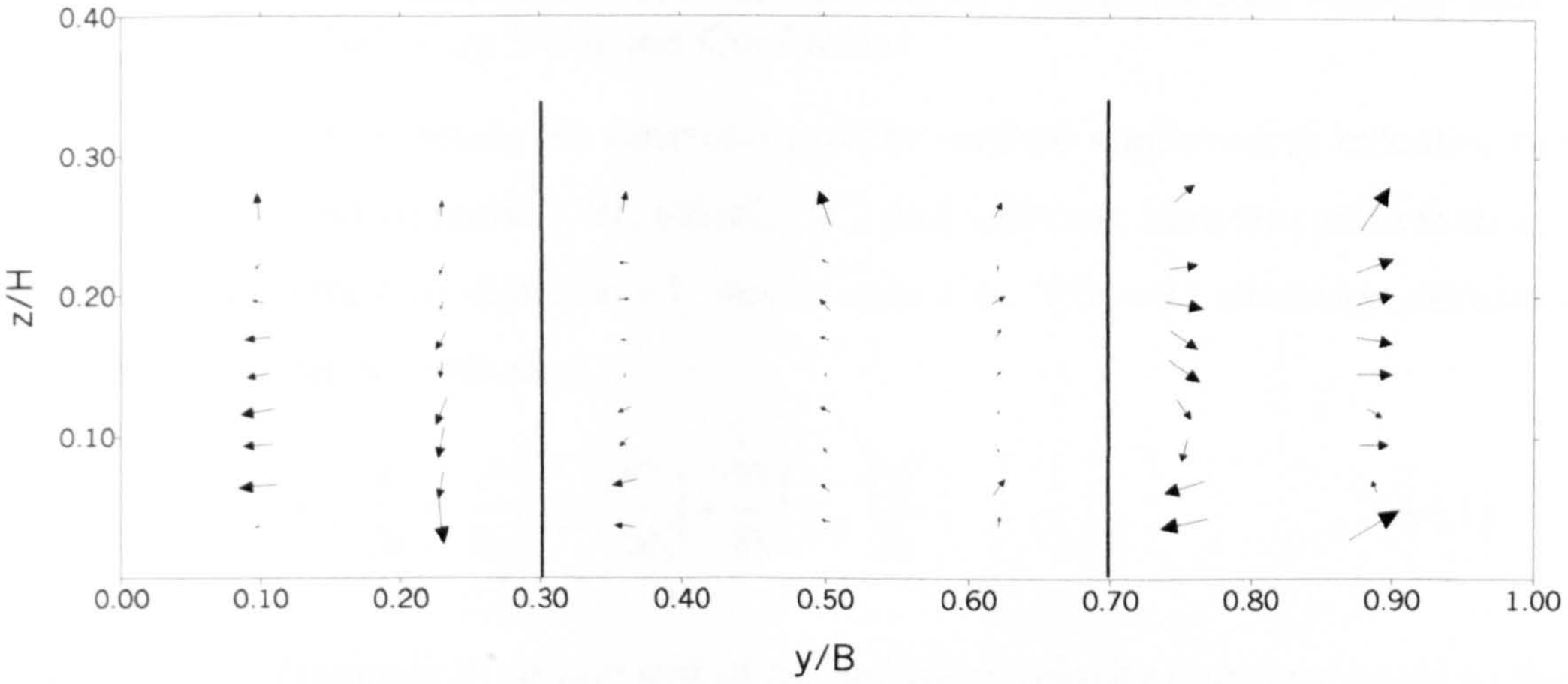

Figure A6.17 - Measured secondary flow velocities in 0.764m-wide flume – Experiment S2_EX5 flow conditions [H = 0.08m; S_0 = 0.0040; S2_grv2 bed material (fine 5-10mm)]

Appendix 6.4 Calculation Method for Fractional Turbulent Fall Velocity and Sediment Diffusion Coefficient

This appendix details the derivation of the method employed to calculate the vertical distributions of particle fall velocity w'_{si} and sediment transfer coefficients ε_{szi} from solution of the two-dimensional, steady state (i.e. $\partial/\partial t = 0$) advection-diffusion equation for suspended sediment,

$$u_s \frac{\partial C}{\partial x} - w'_s \frac{\partial C}{\partial z} = \frac{\partial}{\partial x}\left(\varepsilon_{sx} \frac{\partial C}{\partial x}\right) + \frac{\partial}{\partial z}\left(\varepsilon_{sz} \frac{\partial C}{\partial z}\right) \qquad \text{....(A6.1)}$$

where u_s is the longitudinal component of the sediment velocity (assumed equal to the local flow velocity, u_x), w'_s is the turbulent fall velocity of the sediment, and ε_{sx} and ε_{sz} are the longitudinal and vertical turbulent mixing coefficients for the sediment. Writing equation A6.1 in terms of each individual sediment size fraction and neglecting the longitudinal diffusive transport term, which is usually an order of magnitude smaller than the other terms in the equation (Jobson 1968, van Rijn 1986), we obtain,

$$u_x \frac{\partial C_i}{\partial x} = \frac{\partial}{\partial z}\left(\varepsilon_{szi} \frac{\partial C_i}{\partial z} + w'_{si} C_i\right) \qquad \text{....(A6.2)}$$

where the subscript i refers to the individual sediment size fractions. Equation A6.2 is made non-dimensional by introducing scaling factors for each variables. The length variables x and z are normalised by the flow depth H, whilst the shear velocity u_* is used as a scaling factor for the velocity variables u_x and w'_{si}. The fractional concentration term C_i is made dimensionless by dividing by the initial fractional concentration (C_{0i}) at the source, which is obtained from the fractional feed rate (I_{Ri}) and the flow rate (Q). This results in an expression of the form,

$$\frac{u_x}{u_*}\frac{\partial c_i}{\partial X} = \frac{\partial}{\partial Z}\left(\frac{\varepsilon_{szi}}{H.u_*}\frac{\partial c_i}{\partial Z} + \frac{w'_{si}}{u_*} c_i\right) \qquad \text{....(A6.3)}$$

where $X = x/H$, $Z = z/H$ and $c_i = C_i/C_{0i}$. In order to solve equation 5.3 for the two unknowns ε_{szi} and w'_{si}, the expression is integrated between some arbitrary depth Z_1 and the water surface, i.e.

$$\frac{\partial}{\partial X}\int_{Z_1}^{1}\frac{u_x}{u_*}c_i dZ = \int_{Z_1}^{1}\frac{\partial}{\partial Z}\left(\frac{\varepsilon_{szi}}{H.u_*}\frac{\partial c_i}{\partial Z}+\frac{w'_{si}}{u_*}c_i\right)dZ \qquad \text{....(A6.4)}$$

or
$$\frac{\partial}{\partial X}\int_{Z_1}^{1}\frac{u_x}{u_*}c_i dZ = -\frac{\varepsilon_{szi}}{H.u_*}\bigg|_{Z_1}\frac{\partial c_i}{\partial Z}\bigg|_{Z_1} - \frac{w'_{si}}{u_*}\bigg|_{Z_1} c_i\big|_{Z_1} \qquad \text{....(A6.5)}$$

The solution of equation A6.5 requires smooth curves to be fitted to the non-dimensional concentration profiles for the individual sediment fractions (C_i/C_{0i}) and non-dimensional longitudinal velocity profiles (u_x/u_*). During each experiment, the sediment concentration was monitored in the vertical at five predetermined locations downstream of the source, with the collected samples being analysed to provide fractional concentration profiles for each individual size class. Curve fitting to the concentration profiles was performed computationally by an existing numerical routine (E02BAF – NAG Fortran Workstation Library), which computed the weighted least-squares approximation to the concentration data set by a cubic spline. Program E02BCF was then used to evaluate the cubic spline and the first three derivatives for incremental values of Z (= z/H) ranging from 0.1 to 0.9. For the longitudinal velocity profiles, a logarithmic relationship was fitted to the measured data using least-squares regression. This relation was of the form proposed by Song et al. (1994) for flow over hydraulically rough beds, shown in equation 4.9 (pp.119).

Three of the terms in equation A6.5 are shown to vary with X, and can be defined as follows,

$$\left.\begin{aligned}\Sigma_i &= \frac{\partial C_i}{\partial \eta}\bigg|_{\eta_1}\\ \Psi_i &= C_i\big|_{\eta_1}\\ \Omega_i &= \frac{\partial}{\partial X}\int_{\eta_1}^{1}\frac{U_x}{u_*}C_i d\eta\end{aligned}\right\} \qquad \text{....(A6.6)}$$

Using this notation, equation A6.6 can be re-written in the form,

$$\Omega_i + \frac{\varepsilon_{szi}}{Hu_*}\Sigma_i + \frac{w'_{si}}{u_*}\Psi_i = E_r \qquad \text{....(A6.7)}$$

where E_r represents the error term which is equal to zero when the equation balances.

In the solution method to equation A6.7, values of Ω_i, Σ_i and Ψ_i were determined from the concentration and velocity profiles and plotted as functions of X (= x/H) for each increment of Z (= z/H). Cubic splines were again fitted to the resulting data sets using NAG routines E02BAF and E02BCF, with Ω_i, Σ_i and Ψ_i being calculated for 30 values of X. The coefficients $\varepsilon_{szi}/H.u_*$ and w'_{si}/u_* were obtained by squaring and summing equation A6.7 over all the X values, i.e.

$$\left(\Omega_i + \frac{\varepsilon_{szi}}{Hu_*}\Sigma_i + \frac{w'_{si}}{u_*}\Psi_i\right)^2 = E_r^2 \qquad \text{....(A6.8)}$$

$$\Omega_i^2 + \left(\frac{\varepsilon_{szi}}{Hu_*}\right)^2 \Sigma_i^2 + \left(\frac{w'_{si}}{u_*}\right)^2 \Psi_i^2 + 2\Omega_i\Sigma_i\left(\frac{\varepsilon_{szi}}{Hu_*}\right) + 2\Omega_i\Psi_i\left(\frac{w'_{si}}{u_*}\right) +$$

$$2\Sigma_i\Psi_i\left(\frac{\varepsilon_{szi}}{Hu_*}\right)\left(\frac{w'_{si}}{u_*}\right) = E_r^2 \qquad \text{....(A6.9)}$$

The sum of the error term E_r^2 is minimised by taking derivatives with respect to ε_{szi} and w'_{si} and setting them equal to zero (i.e. $E_r^2 = 0$). This results in two equations, given below (A6.10), which can be solved simultaneously for ε_{szi}/Hu_* and w'_{si}/u_*, providing estimates of the fractional turbulent fall velocity (w'_{si}) and the vertical turbulent transfer coefficient (ε_{szi}) for Z values (= z/H) = 0.1-0.9,

$$\left.\begin{aligned} \frac{2\Sigma_i^2}{Hu_*}\left(\frac{\varepsilon_{szi}}{Hu_*}\right) + \frac{2\Sigma_i\Psi_i}{Hu_*}\left(\frac{w'_{si}}{u_*}\right) + \frac{2\Omega_i\Sigma_i}{Hu_*} &= \frac{dE_r^2}{d\varepsilon_{szi}} = 0 \\ \frac{2\Sigma_i\Psi_i}{u_*}\left(\frac{\varepsilon_{szi}}{Hu_*}\right) + \frac{2\Psi_i^2}{u_*}\left(\frac{w'_{si}}{u_*}\right) + \frac{2\Omega_i\Psi_i}{u_*} &= \frac{dE_r^2}{dw'_{si}} = 0 \end{aligned}\right\} \qquad \text{....(A6.10)}$$

Appendix 6.5 - Longitudinal Distribution of Sediment Deposition

This Appendix presents the probability density functions for the distributions of longitudinal deposition length for the LA and DB grade sediments. Log-normal distributions, of the form given in equation 6.6 (pp.170), are shown for comparison purposes. A summary of the calculated depth-averaged turulent fall velocities calculated for mean and median deposition lengths is given in Table A6.1.

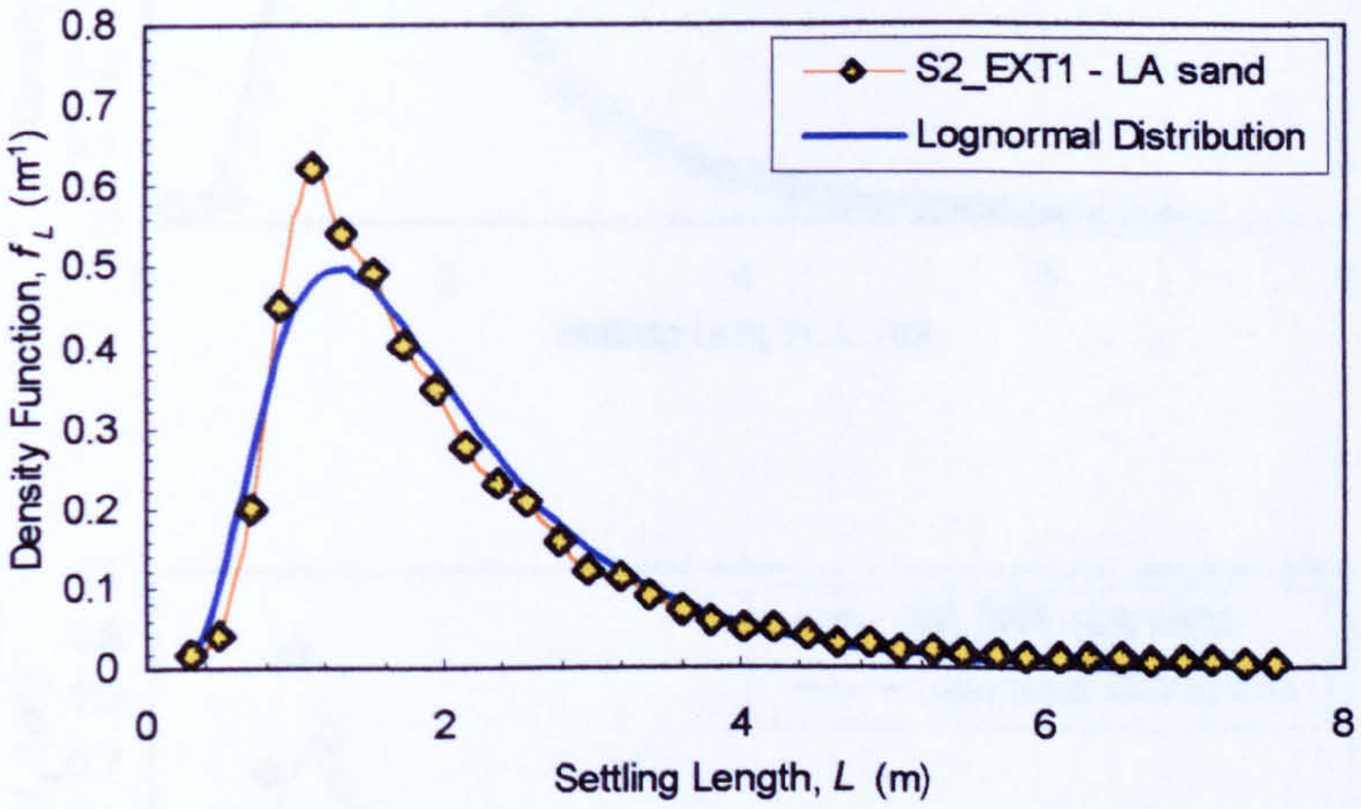

Figure A6.18- S2_EXT1

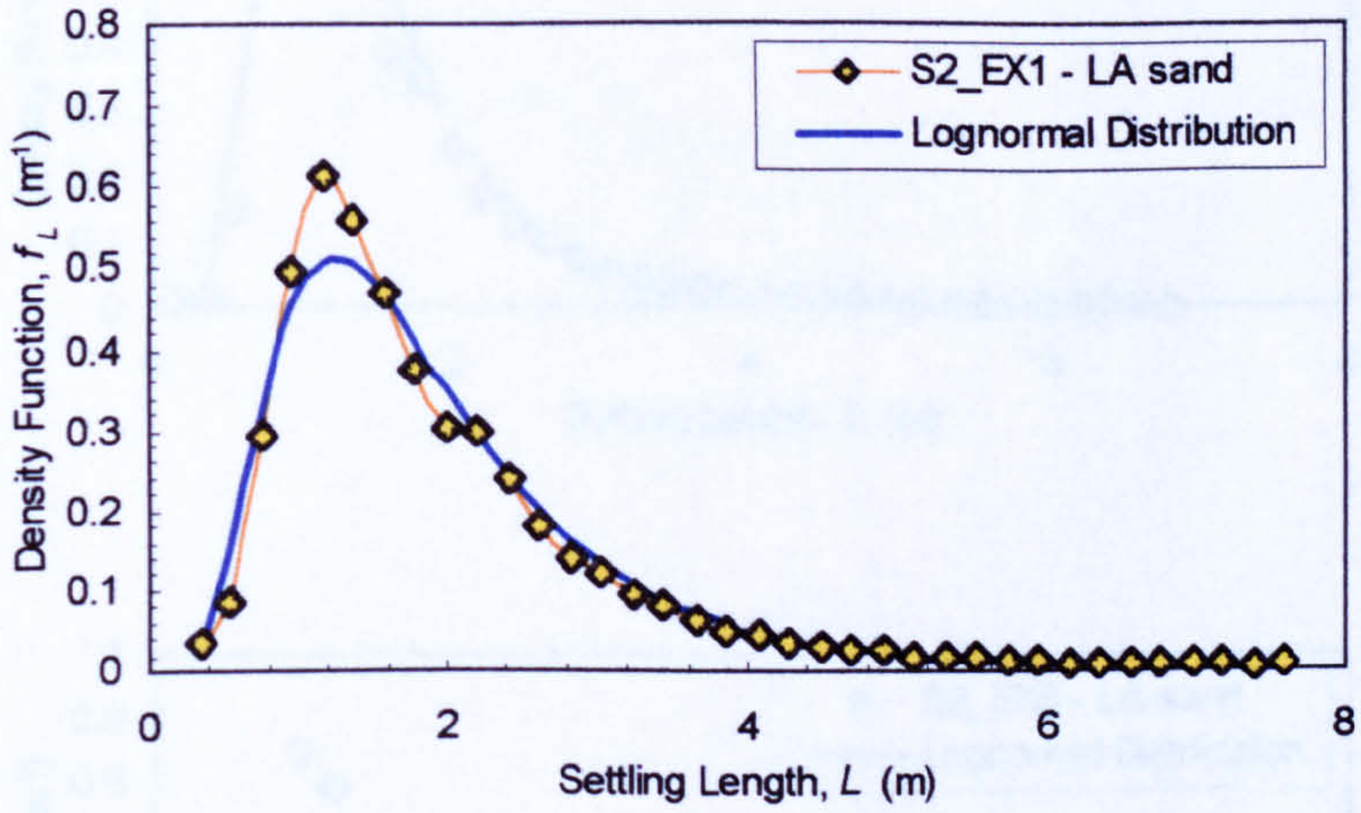

Figure A6.19 - S2_EX1

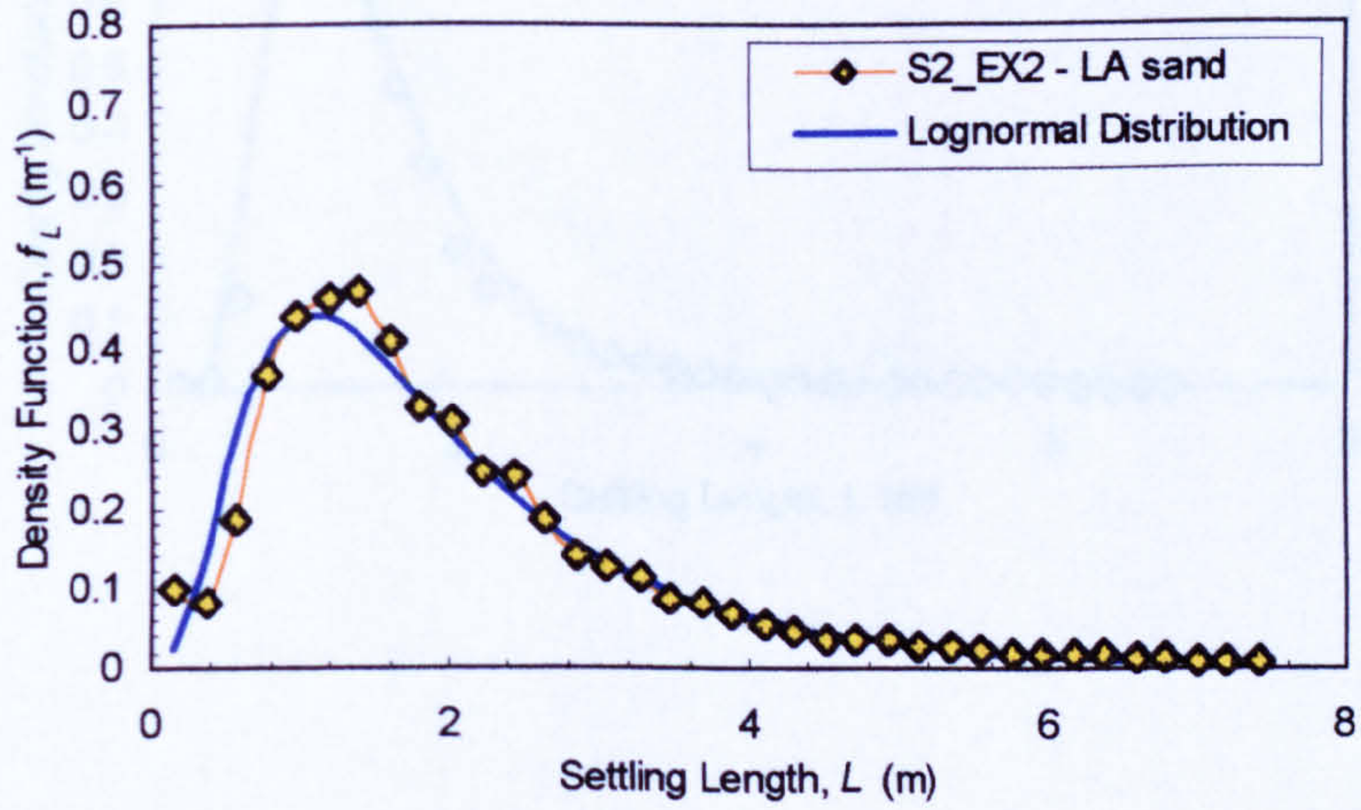

Figure A6.20 - S2_EX2

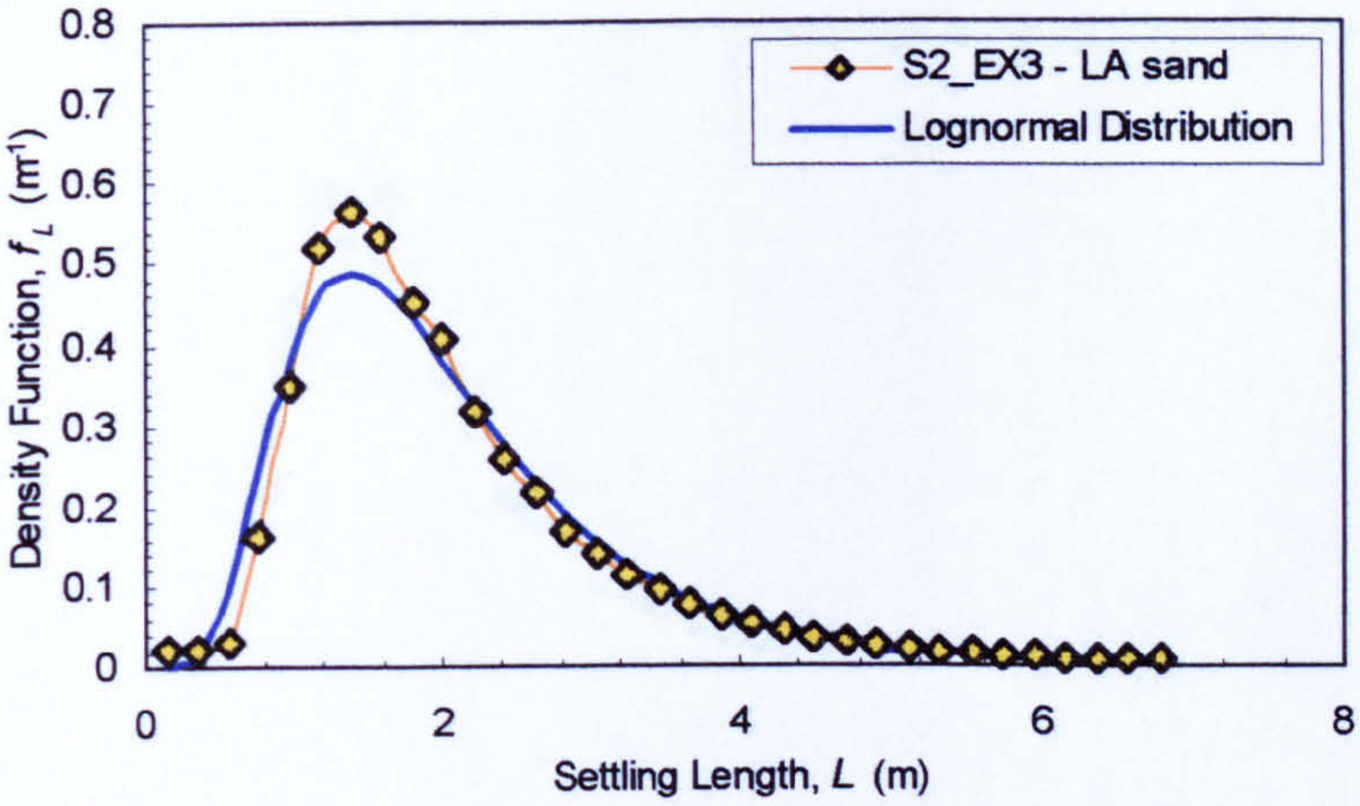

Figure A6.21 - S2_EX3

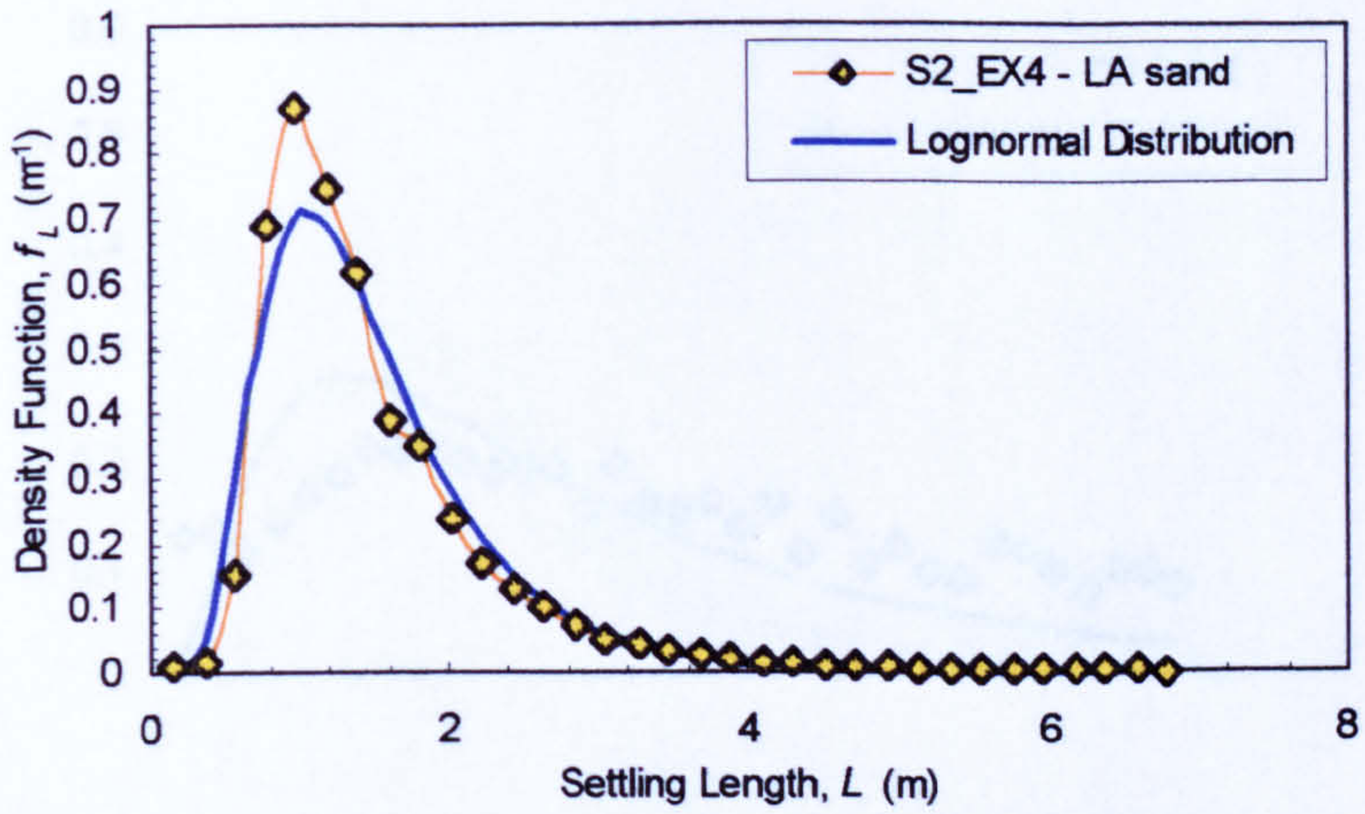

Figure A6.22 - S2_EX4

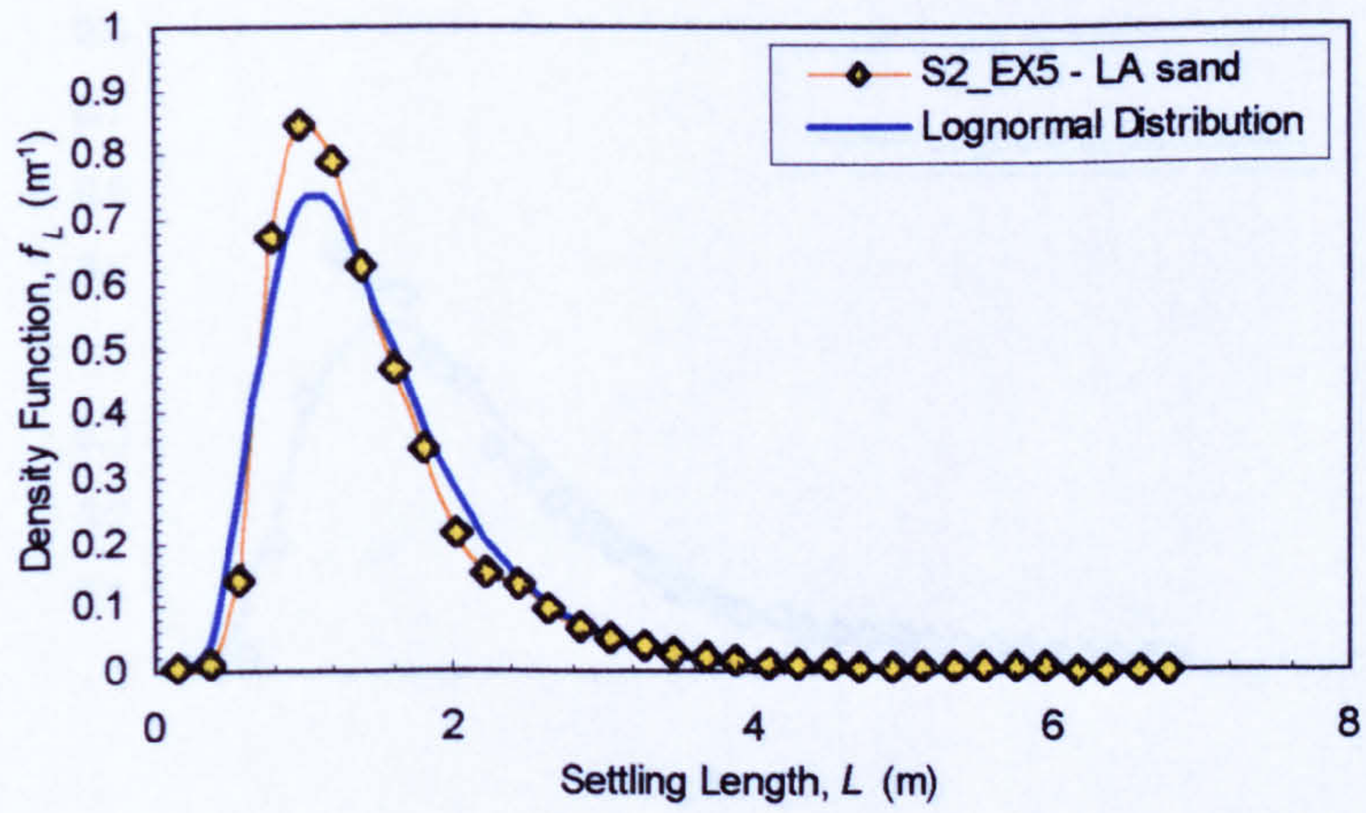

Figure A6.23 - S2_EX5

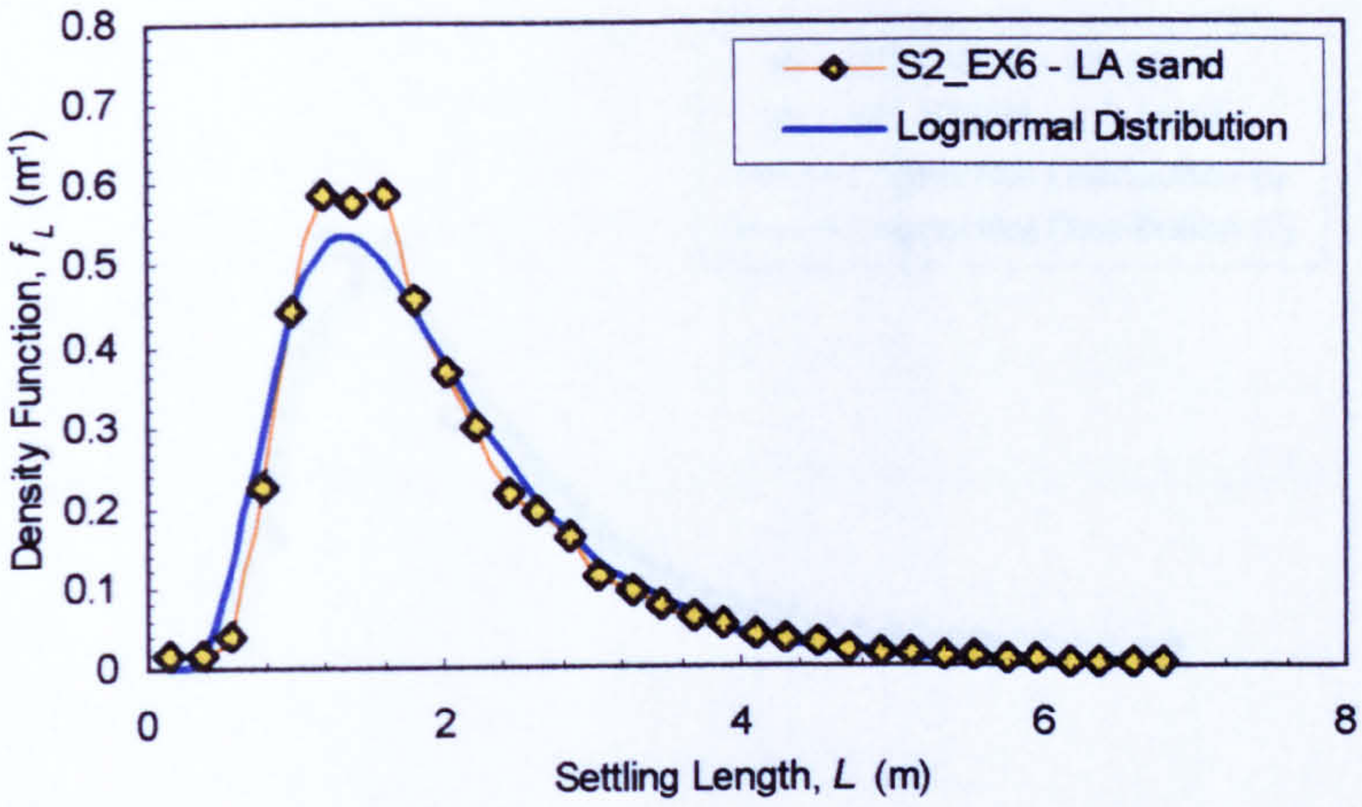

Figure A6.24 - S2_EX6

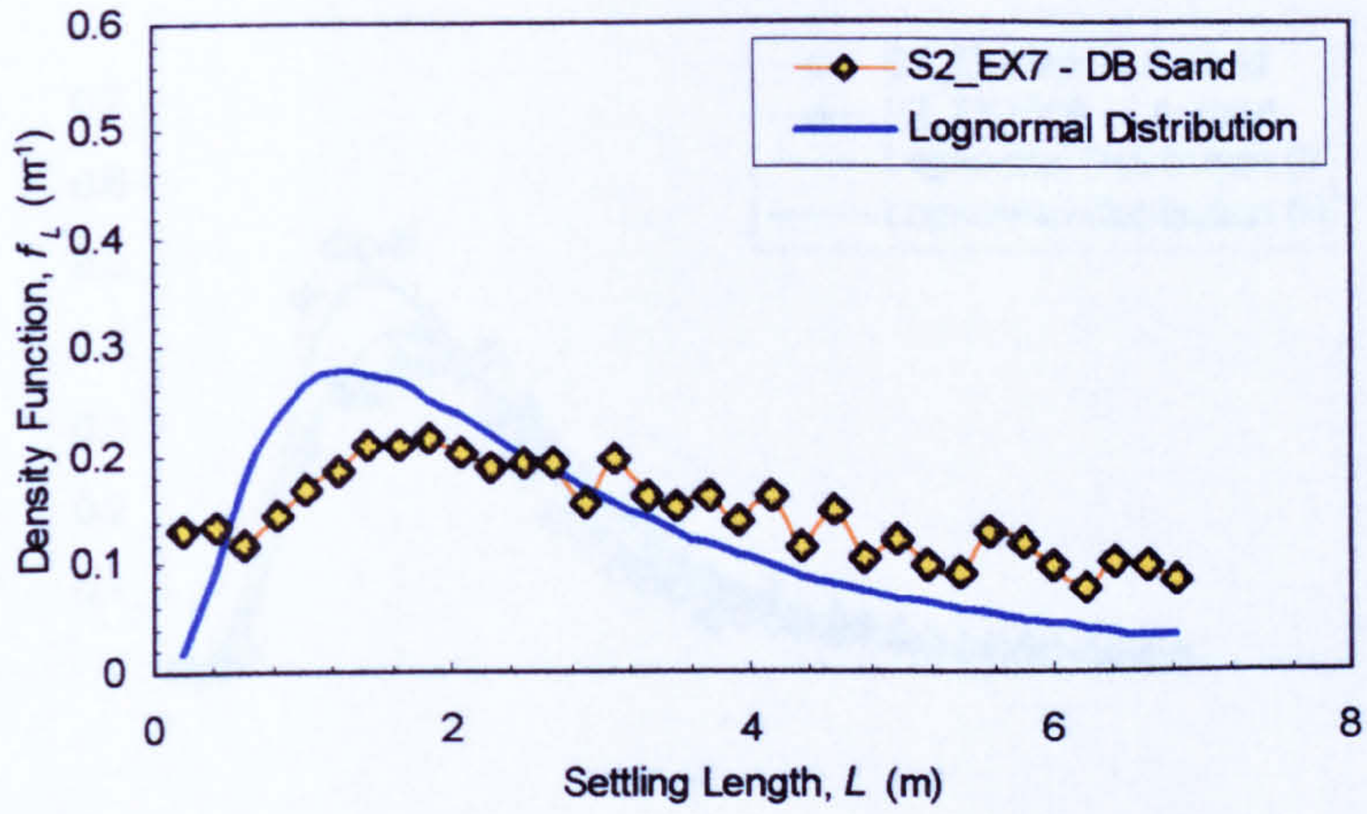

Figure A6.25 - S2_EX7

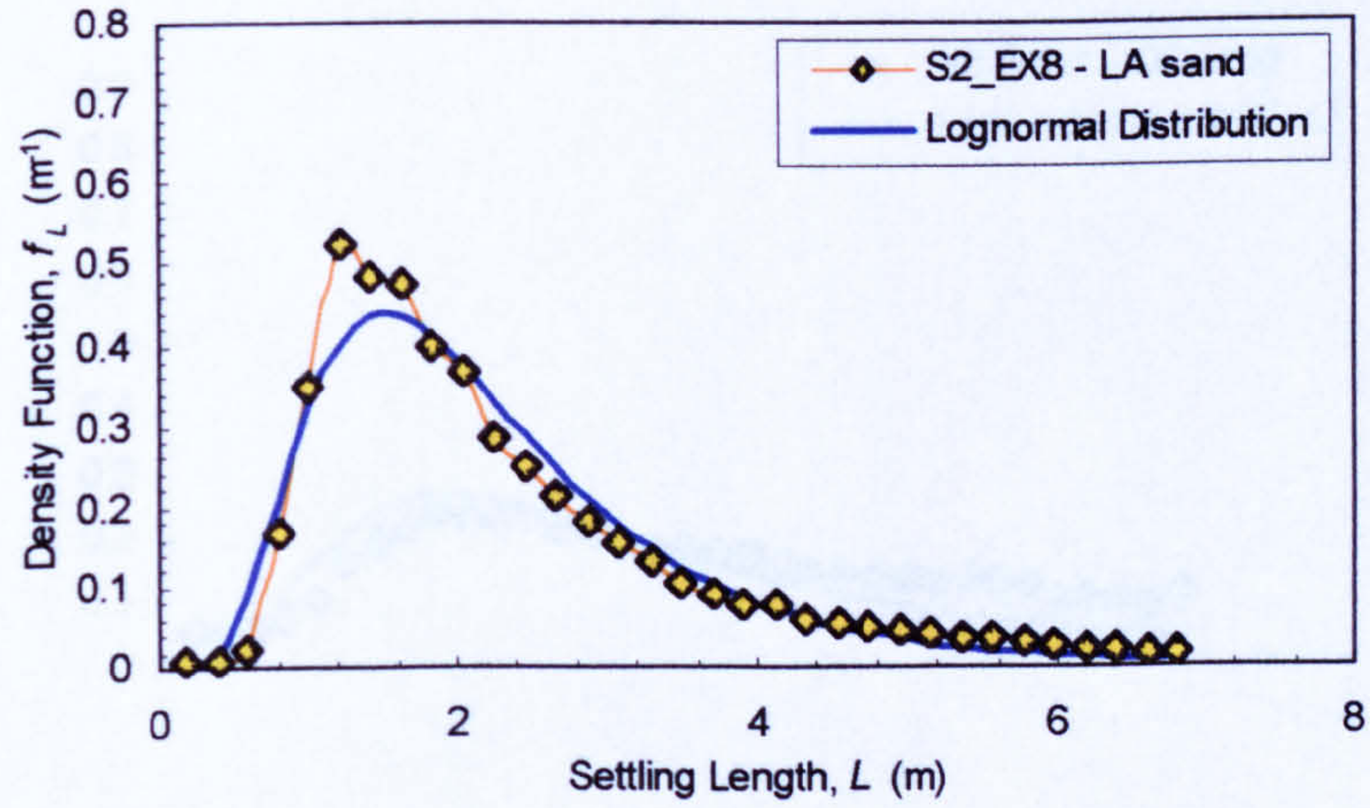

Figure A6.26 - S2_EX8

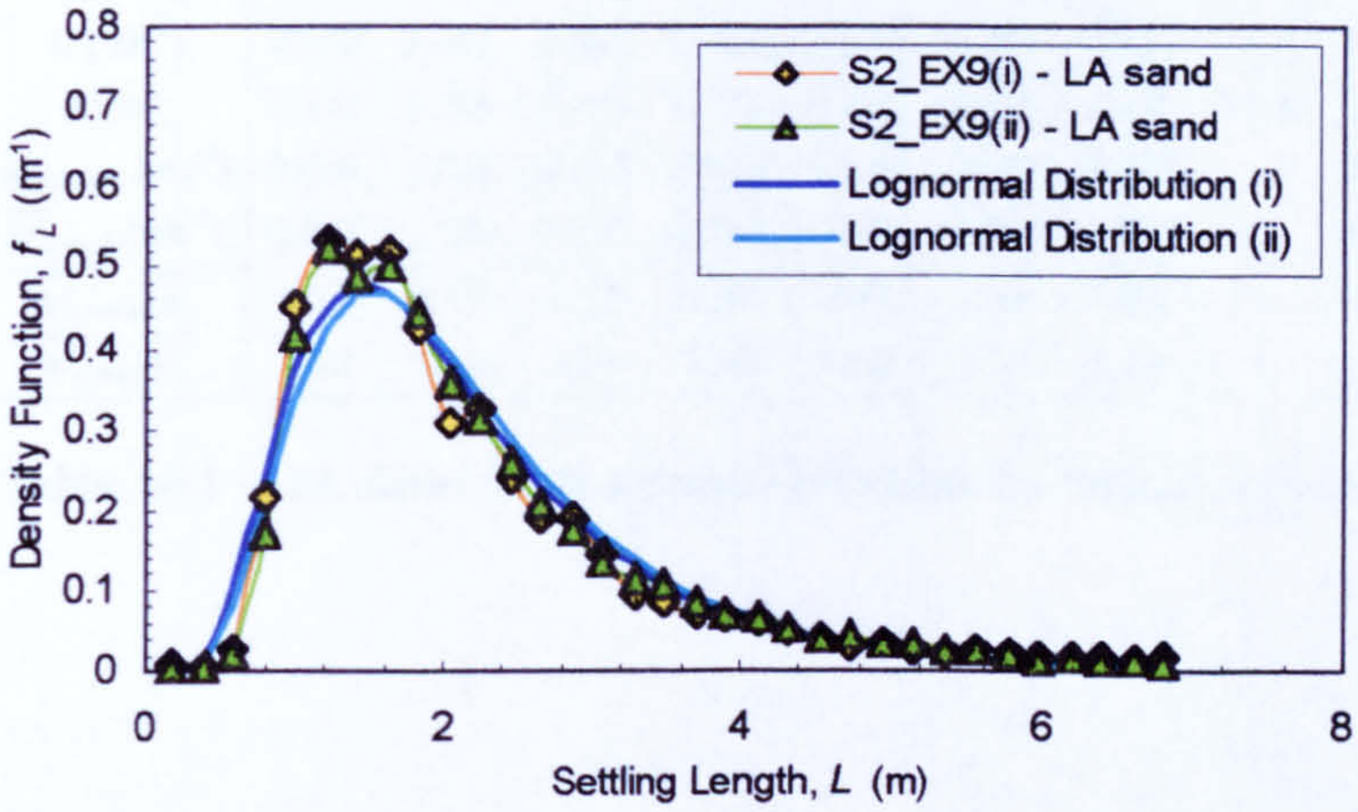

Figure A6.27 - S2_EX9

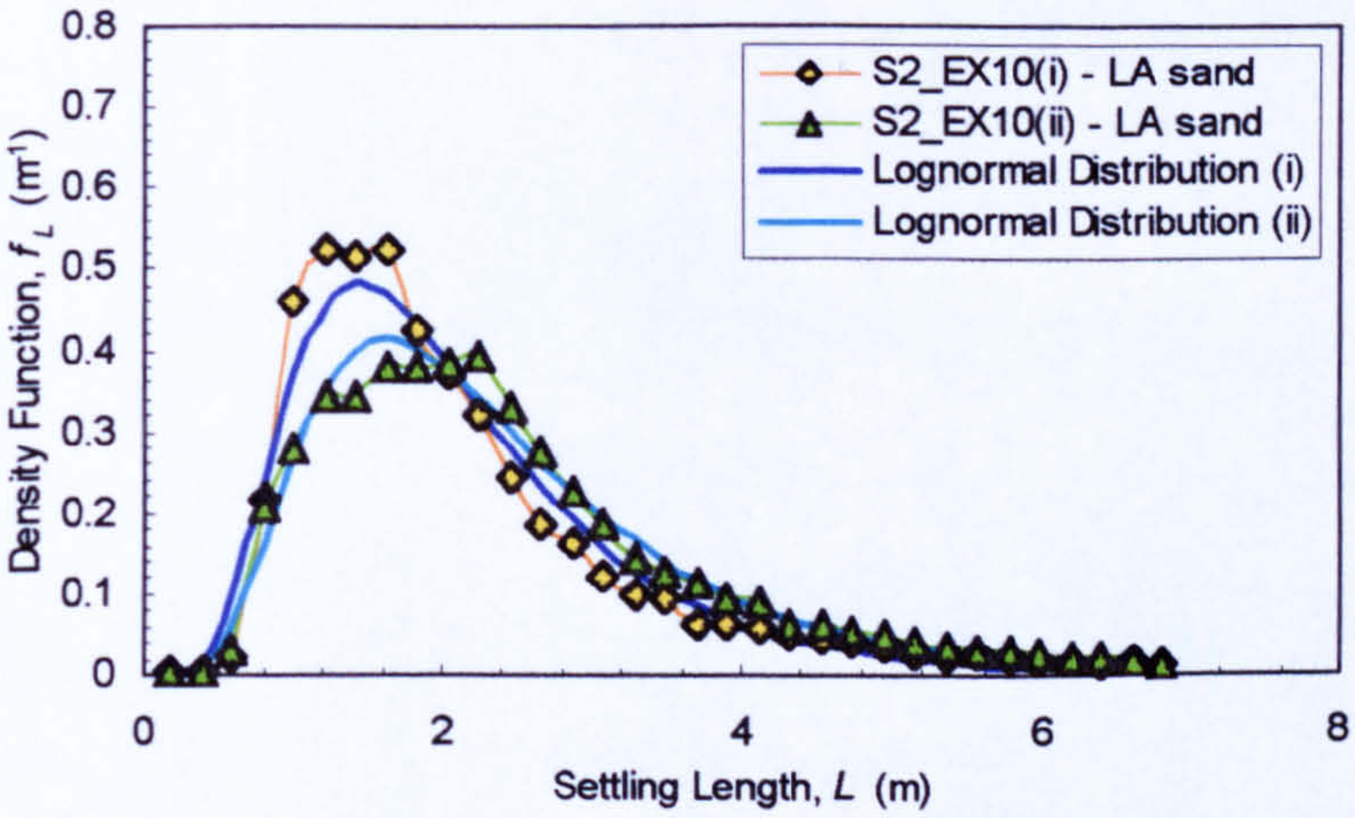

Figure A6.28 - S2_EX10

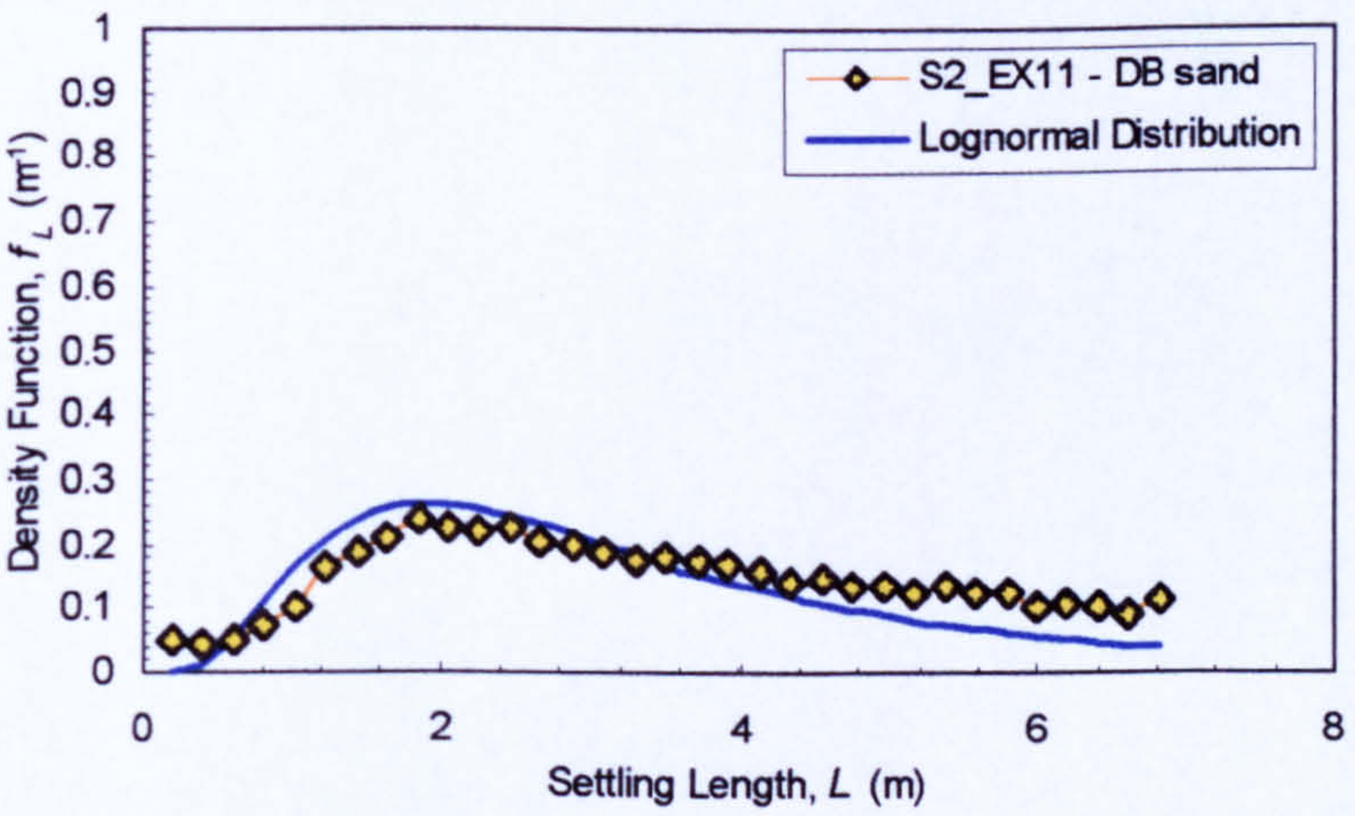

Figure A6.29 - S2_EX11

	Experiment Number													
	T1	**1**	**2**	**3**	**4**	**5**	**6**	**7**	**8**	**9(i)**	**9(ii)**	**10(i)**	**10(ii)**	**11**
L_{mean} (m)	2.00	1.94	2.12	2.07	1.50	1.47	1.93	-	2.29	2.14	2.19	2.13	2.43	-
L_{med} (m)	1.66	1.66	1.78	1.79	1.27	1.27	1.67	-	1.93	1.80	1.87	1.80	1.87	-
U (ms^{-1})	0.580	0.595	0.599	0.608	0.510	0.555	0.603	0.553	0.726	0.737	0.737	0.723	0.723	0.399
H (m)	0.117	0.109	0.111	0.110	0.080	0.077	0.10	0.077	0.079	0.080	0.080	0.079	0.079	0.109
$\overline{w'_{s,mean}}$ (ms^{-1})	0.034	0.033	0.031	0.032	0.027	0.029	0.031	-	0.025	0.028	0.027	0.027	0.024	-
$\overline{w'_{s,med}}$ (ms^{-1})	0.041	0.039	0.037	0.037	0.032	0.034	0.036	-	0.030	0.033	0.032	0.032	0.031	-
$\overline{w'_{s,mean}}/\overline{w_s}$	1.15	1.11	1.05	1.08	0.91	0.98	1.05	-	0.84	0.95	0.91	0.91	0.81	-
$\overline{w'_{s,med}}/\overline{w_s}$	1.39	1.32	1.25	1.25	1.08	1.15	1.22	-	1.01	1.11	1.08	1.08	1.05	-

Table A6.1 - Calculated depth-averaged turbulent fall velocities for mean and median settling lengths

Appendix 6.6 - Longitudinal Distribution of Fractional Sediment Deposition (LA Sand)

This Appendix presents the probability density function plots (p.d.fs) for measured distributions of fractional sediment deposition length for Series 2 experiments with LA grade sand. Values of the depth-averaged turbulent fall velocities $\tilde{w}'_{si}$ are calculated for each size fraction from knowledge of the mean flow conditions (H and U) and the median deposition lengths $\tilde{L}_i$ estimated from the distributions.

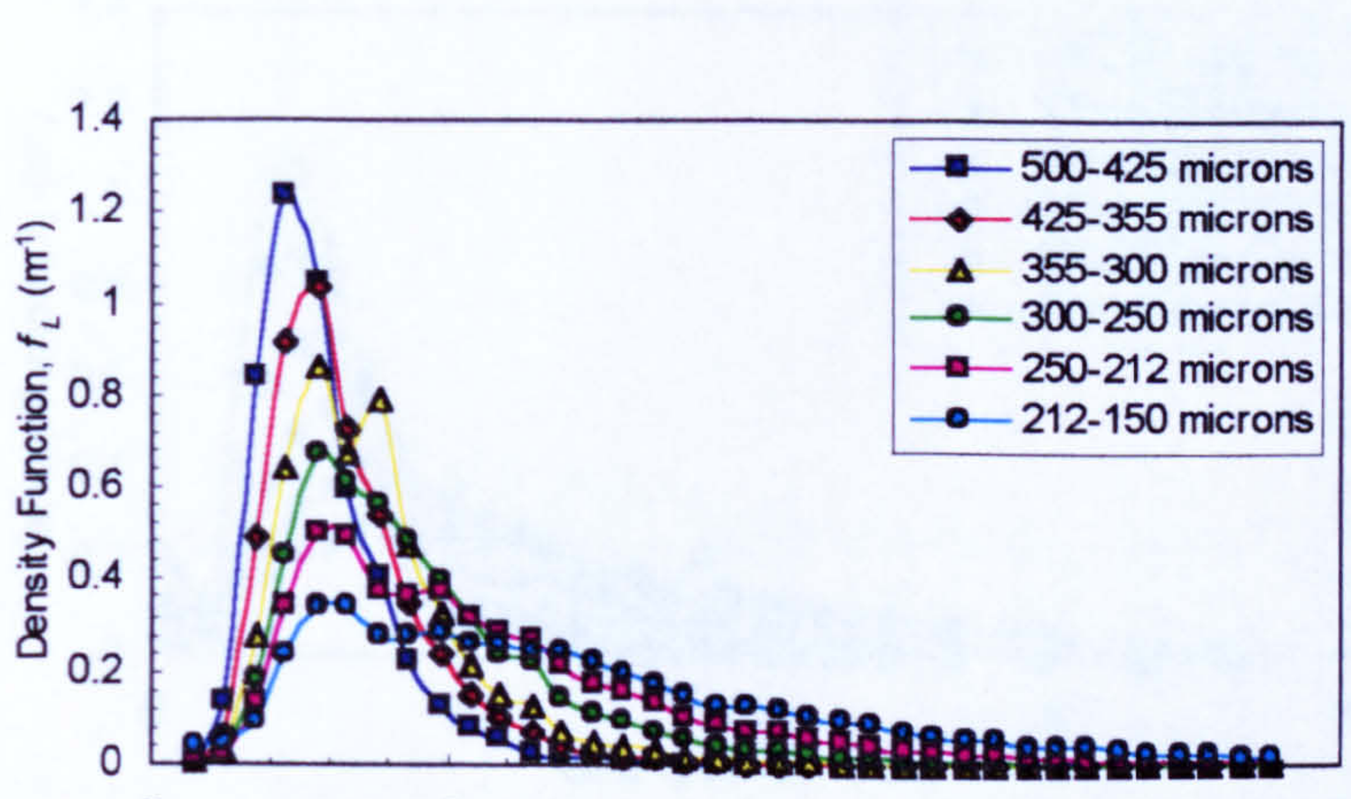

Figure A6.30 - S2_EXT1

S2_EXT1	Q = 0.0548 m^{3}s^{-1}; U = 0.59 ms^{-1}; H = 0.117m; Bed Grade = S2_grv1 (10-25 mm)					
	LA Grade Sand – Fraction Size (microns)					
	500-425	**425-355**	**355-300**	**300-250**	**250-212**	**212-150**
d_i (μm)	462.5	390	327.5	275	231	181
$L_{i,med}$ (m)	1.05	1.20	1.41	1.60	1.94	2.43
$w'_{si,med}$ (ms^{-1})	0.0656	0.0576	0.0491	0.0431	0.0356	0.0285
w_{si} (ms^{-1})	0.0600	0.0491	0.0409	0.0322	0.0270	0.0201
$w'_{si,med}/w_{si}$	**1.093**	**1.172**	**1.201**	**1.339**	**1.319**	**1.416**

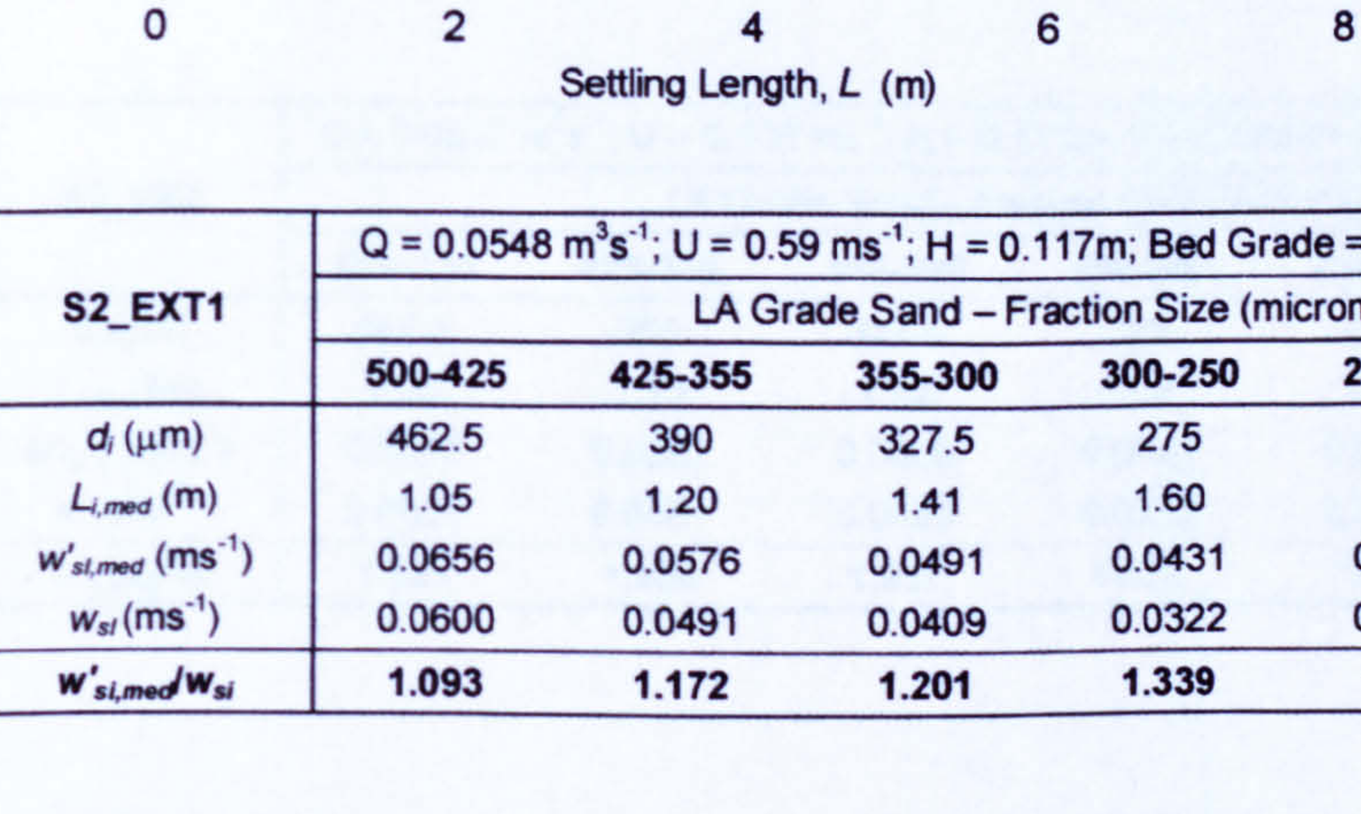

Figure A6.31 - S2_EX1

S2_EX1	Q = 0.0548 m^3s^{-1}; U = 0.609 ms^{-1}; H = 0.109m; Bed Grade = S2_grv1 (10-25 mm)					
	LA Grade Sand - Fraction Size (microns)					
	500-425	**425-355**	**355-300**	**300-250**	**250-212**	**212-150**
d_i (μm)	462.5	390	327.5	275	231	181
$L_{i,med}$ (m)	1.04	1.16	1.32	1.57	1.88	2.33
$w'_{s,med}$ (ms^{-1})	0.0641	0.0572	0.0501	0.0423	0.0353	0.0285
w_s (ms^{-1})	0.0600	0.0491	0.0409	0.0322	0.0270	0.0201
$w'_{s,med}/w_s$	**1.068**	**1.164**	**1.225**	**1.313**	**1.306**	**1.417**

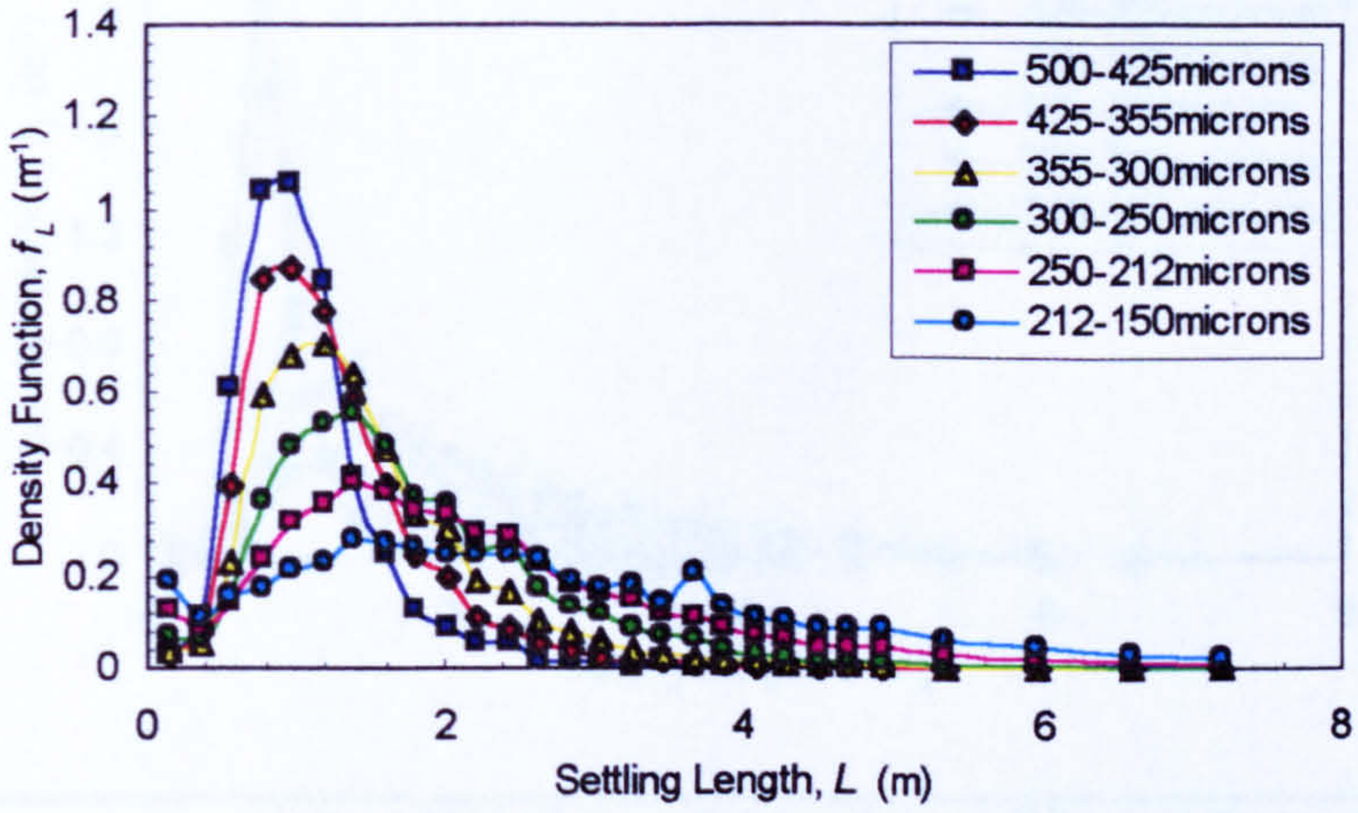

Figure A6.32 - S2_EX2

S2_EX2	Q = 0.0547 m^3s^{-1}; U = 0.603 ms^{-1}; H = 0.111m; Bed Grade = S2_grv1 (10-25 mm)					
	LA Grade Sand - Fraction Size (microns)					
	500-425	**425-355**	**355-300**	**300-250**	**250-212**	**212-150**
d_i (μm)	462.5	390	327.5	275	231	181
$L_{i,med}$ (m)	1.00	1.13	1.32	1.57	1.93	2.37
$w'_{s,med}$ (ms^{-1})	0.0673	0.0592	0.0506	0.0425	0.0347	0.0282
w_s (ms^{-1})	0.0600	0.0491	0.0409	0.0322	0.0270	0.0201
$w'_{s,med}/w_s$	**1.121**	**1.206**	**1.237**	**1.320**	**1.285**	**1.405**

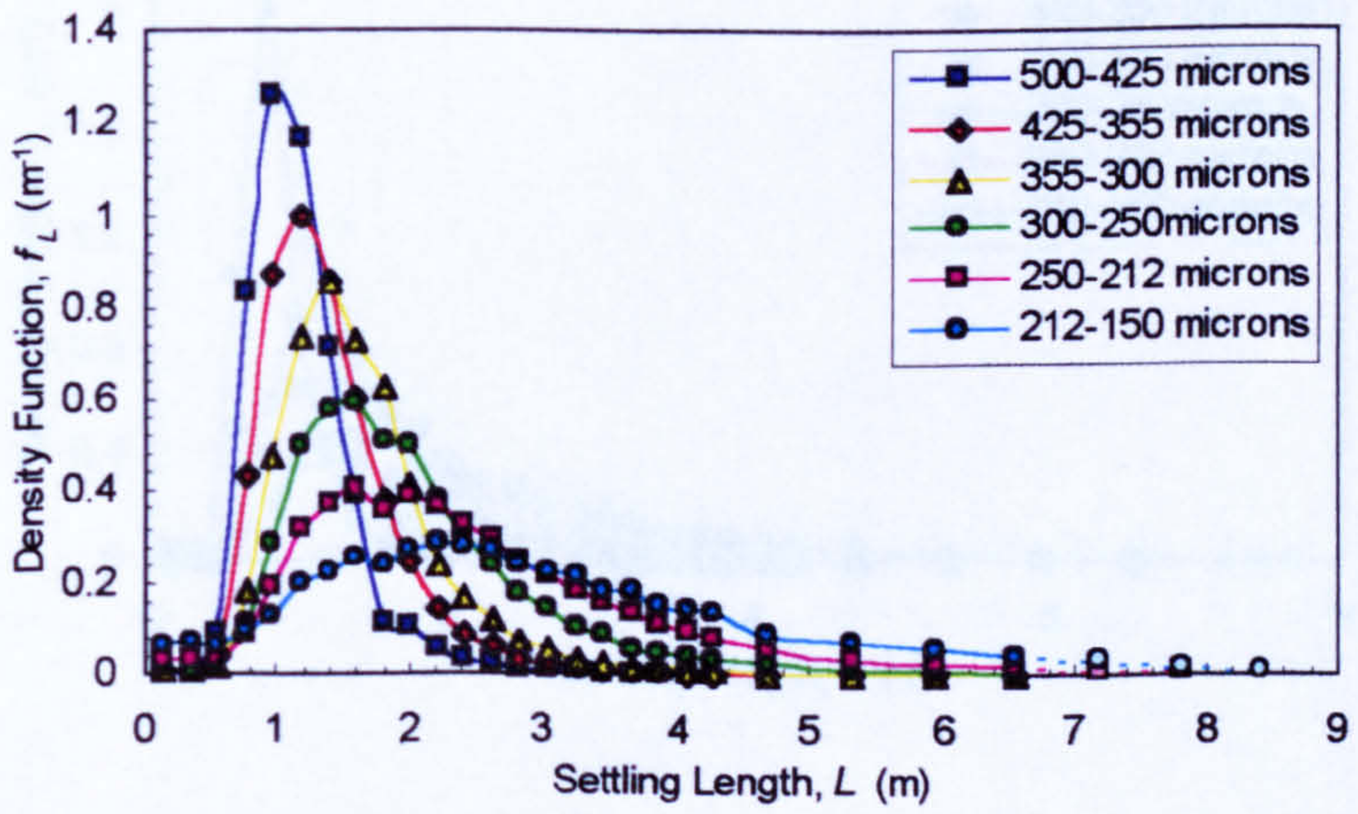

Figure A6.33 - S2_EX3

S2_EX3	Q = 0.0547 m^3s^{-1}; U = 0.608 ms^{-1}; H = 0.110m; Bed Grade = S2_grv1 (10-25 mm)					
	LA Grade Sand - Fraction Size (microns)					
	500-425	**425-355**	**355-300**	**300-250**	**250-212**	**212-150**
d_i (μm)	462.5	390	327.5	275	231	181
$L_{i,med}$ (m)	1.11	1.30	1.53	1.82	2.22	2.65
$w'_{s,med}$ (ms^{-1})	0.0603	0.0516	0.0437	0.0367	0.0301	0.0252
w_s (ms^{-1})	0.0600	0.0491	0.0409	0.0322	0.0270	0.0201
$w'_{s,med}/w_s$	**1.004**	**1.050**	**1.069**	**1.139**	**1.116**	**1.256**

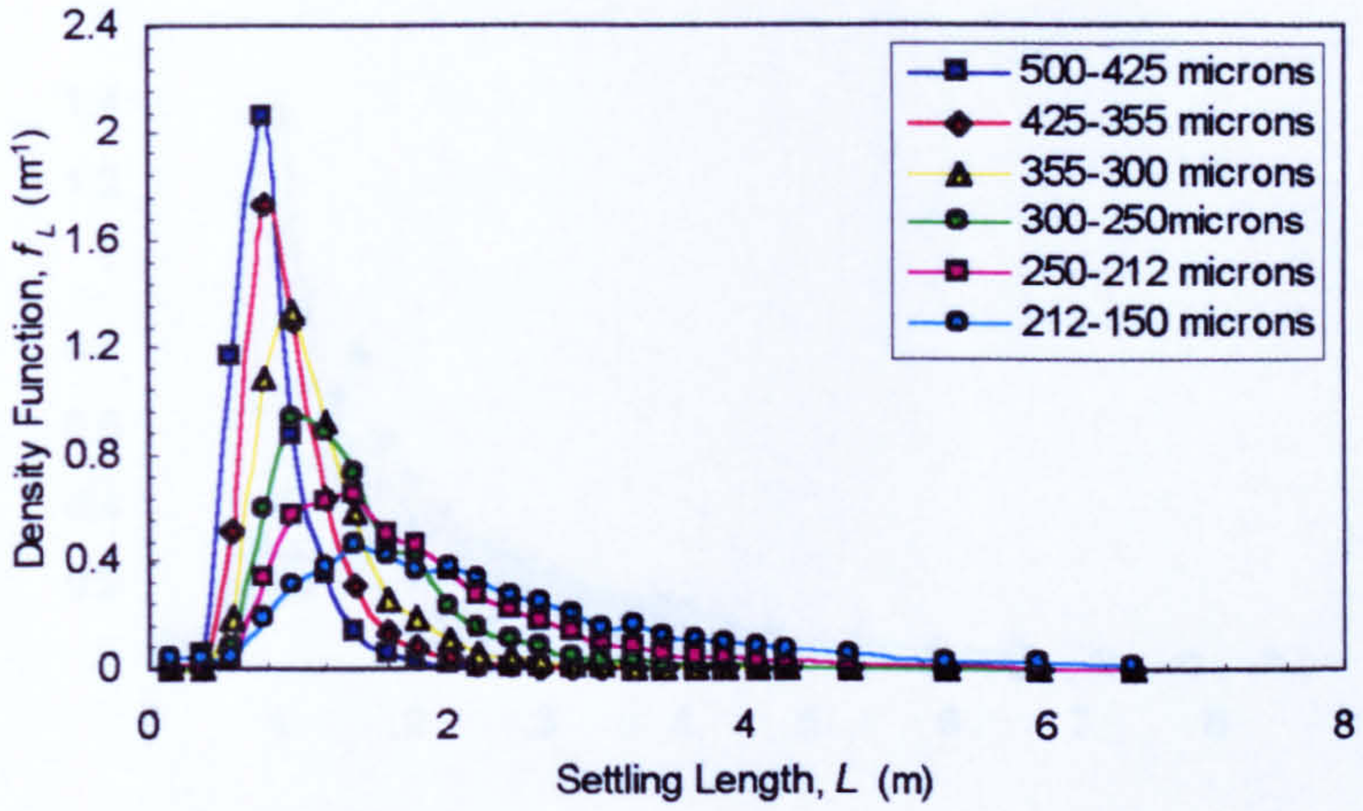

Figure A6.34 - S2_EX4

S2_EX4	Q = 0.0361 m^3s^{-1}; U = 0.510 ms^{-1}; H = 0.080m; Bed Grade = S2_grv1 (10-25 mm)					
	LA Grade Sand - Fraction Size (microns)					
	500-425	**425-355**	**355-300**	**300-250**	**250-212**	**212-150**
d_i (μm)	462.5	390	327.5	275	231	181
$L_{i,med}$ (m)	0.79	0.90	1.05	1.27	1.56	2.00
$w'_{s,med}$ (ms^{-1})	0.0529	0.0464	0.0396	0.0328	0.0266	0.0208
w_s (ms^{-1})	0.0600	0.0491	0.0409	0.0322	0.0270	0.0201
$w'_{s,med}/w_s$	**0.882**	**0.944**	**0.968**	**1.018**	**0.985**	**1.036**

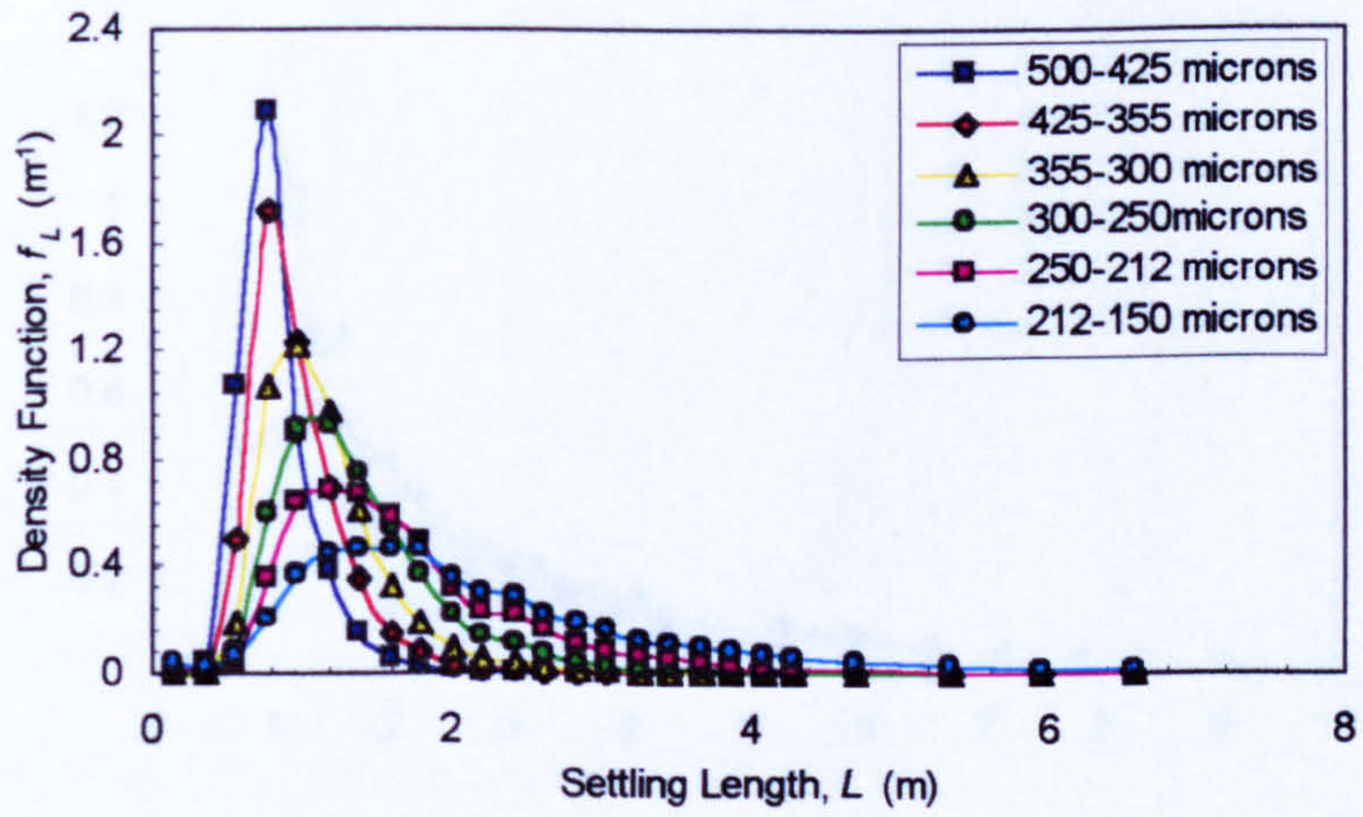

Figure A6.35 - S2_EX5

Appendix 6.6 Longitudinal Distribution of Fractional Sediment Deposition (LA Sand)

S2_EX5	Q = 0.0362 m^3s^{-1}; U = 0.555 ms^{-1}; H = 0.077m; Bed Grade = S2_grv2 (5-10 mm)					
	LA Grade Sand - Fraction Size (microns)					
	500-425	**425-355**	**355-300**	**300-250**	**250-212**	**212-150**
d_i (μm)	462.5	390	327.5	275	231	181
$L_{i,med}$ (m)	0.80	0.91	1.07	1.26	1.51	1.85
$w'_{s,med}$ (ms^{-1})	0.0543	0.0478	0.0405	0.0342	0.0286	0.0234
w_s (ms^{-1})	0.0600	0.0491	0.0409	0.0322	0.0270	0.0201
$w'_{s,med}/w_s$	**0.905**	**0.973**	**0.991**	**1.063**	**1.061**	**1.162**

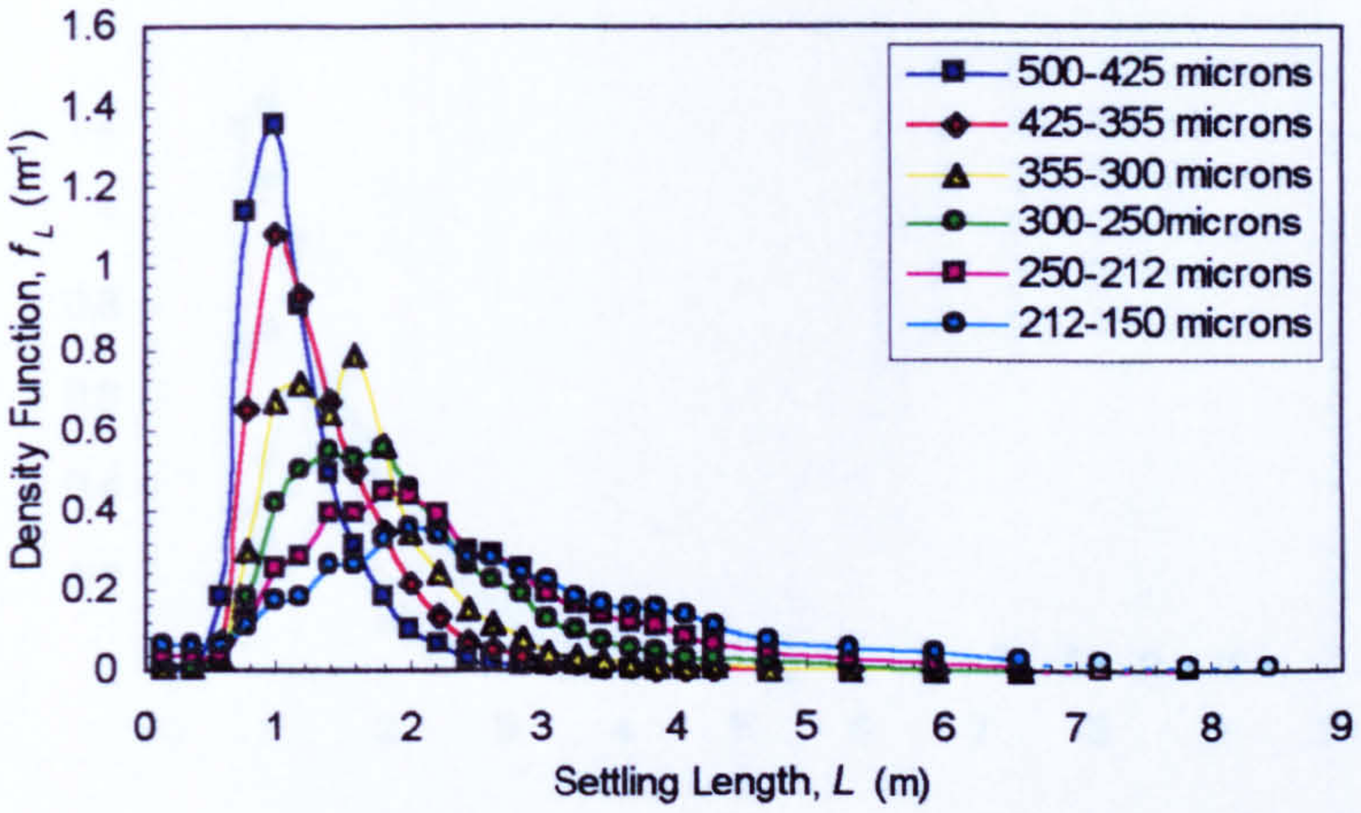

Figure A6.36 - S2_EX6

S2_EX6	Q = 0.0548 m^3s^{-1}; U = 0.603 ms^{-1}; H = 0.100m; Bed Grade = S2_grv2 (5-10 mm)					
	LA Grade Sand - Fraction Size (microns)					
	500-425	**425-355**	**355-300**	**300-250**	**250-212**	**212-150**
d_i (μm)	462.5	390	327.5	275	231	181
$L_{i,med}$ (m)	1.04	1.21	1.47	1.77	2.10	2.44
$w'_{s,med}$ (ms^{-1})	0.0582	0.0499	0.0412	0.0342	0.0289	0.0248
w_s (ms^{-1})	0.0600	0.0491	0.0409	0.0322	0.0270	0.0201
$w'_{s,med}/w_s$	**0.970**	**1.016**	**1.008**	**1.063**	**1.069**	**1.236**

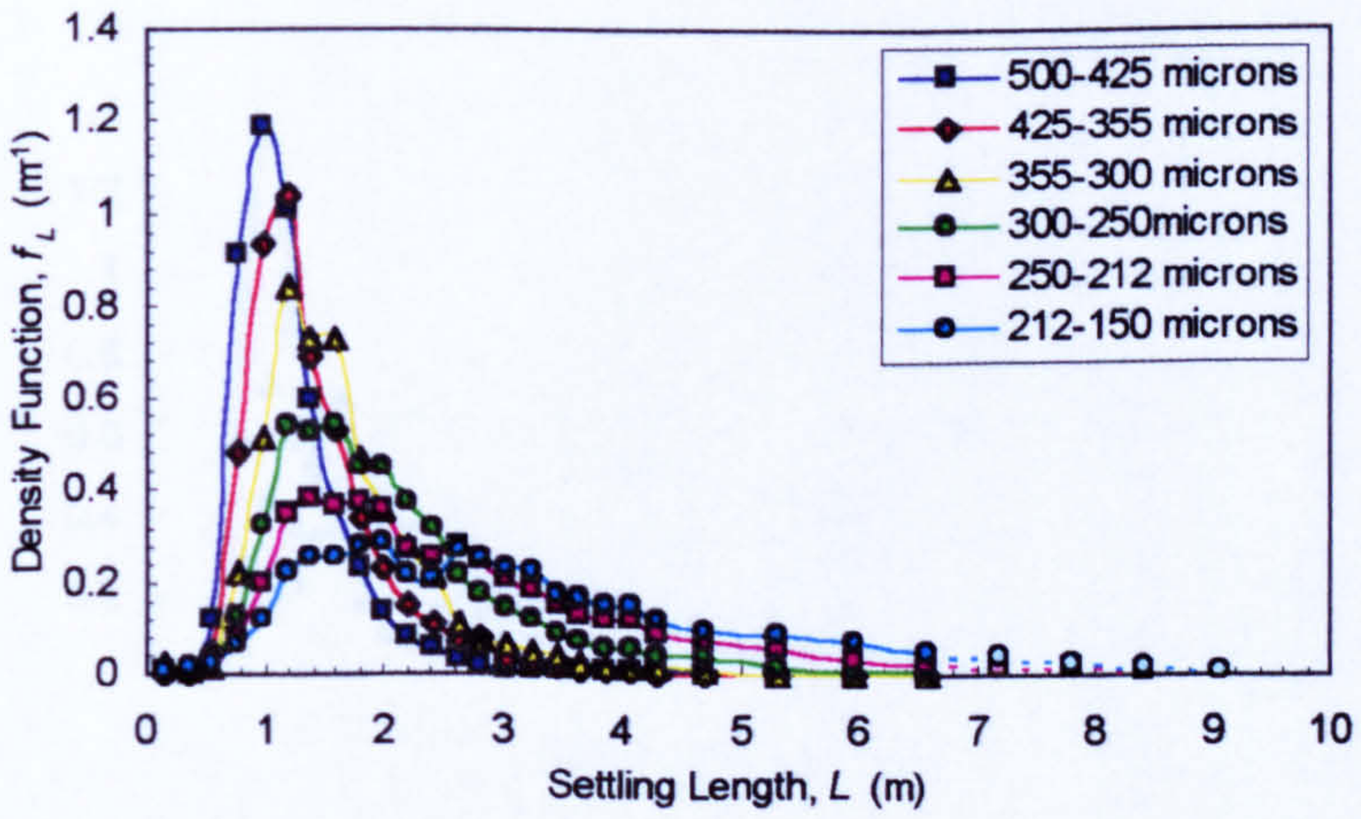

Figure A6.37 - S2_EX8

S2_EX8	Q = 0.0518 m^3s^{-1}; U = 0.726 ms^{-1}; H = 0.079m; Bed Grade = S2_grv1 (10-25 mm)					
	LA Grade Sand - Fraction Size (microns)					
	500-425	**425-355**	**355-300**	**300-250**	**250-212**	**212-150**
d_i (μm)	462.5	390	327.5	275	231	181
$L_{i,med}$ (m)	1.12	1.27	1.52	1.86	2.33	2.83
$w'_{s,mean}$ (ms^{-1})	0.0515	0.0454	0.0380	0.0309	0.0248	0.0204
w_s (ms^{-1})	0.0600	0.0491	0.0409	0.0322	0.0270	0.0201
$w'_{s,med}/w_s$	**0.858**	**0.925**	**0.929**	**0.961**	**0.917**	**1.014**

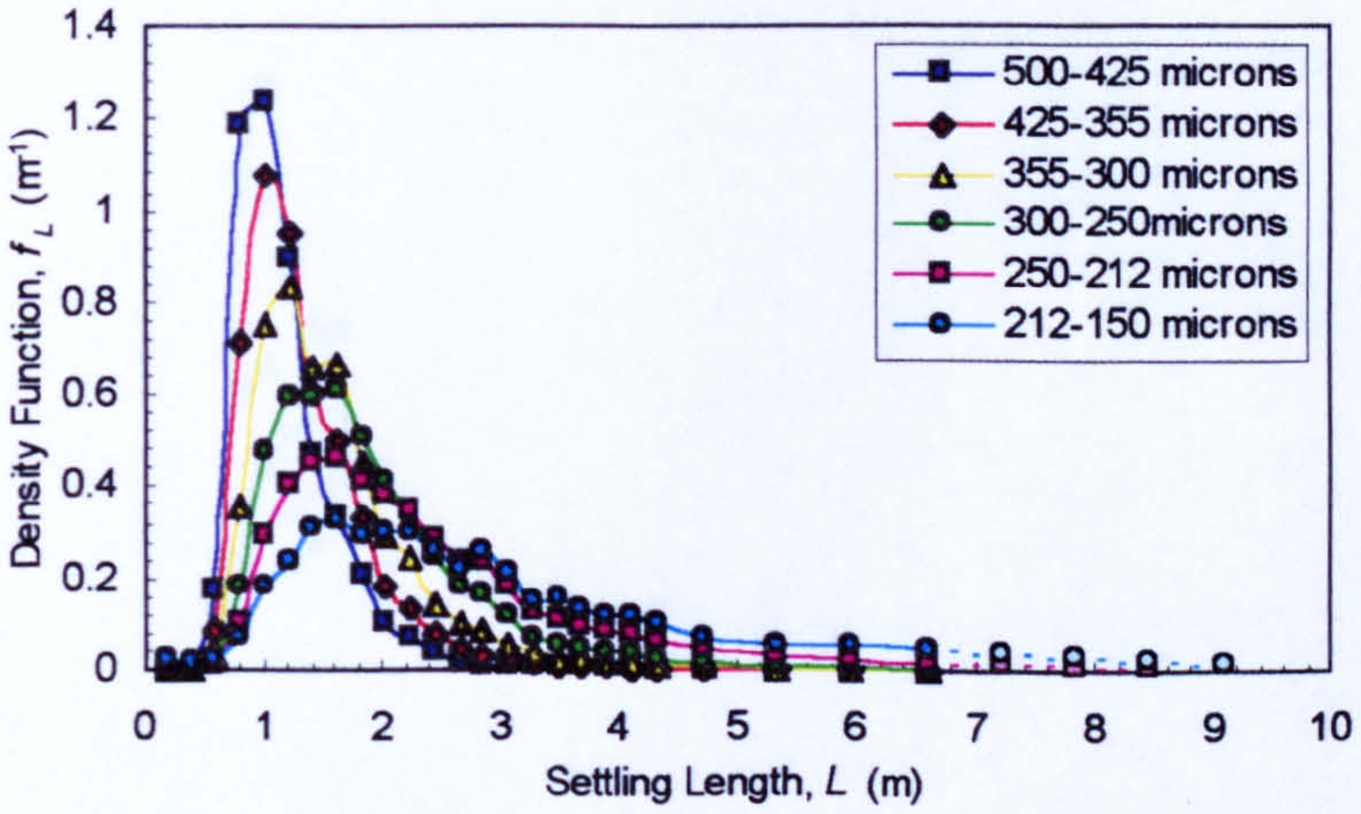

Figure A6.38 - S2_EX9(i)

S2_EX9(i)	Q = 0.0518 m^3s^{-1}; U = 0.737 ms^{-1}; H = 0.080m; Bed Grade = S2_grv1 (10-25 mm)					
	LA Grade Sand - Fraction Size (microns)					
	500-425	**425-355**	**355-300**	**300-250**	**250-212**	**212-150**
d_i (μm)	462.5	390	327.5	275	231	181
$L_{i,med}$ (m)	1.05	1.20	1.43	1.69	2.06	2.50
$w'_{s,med}$ (ms^{-1})	0.0562	0.0492	0.0412	0.0350	0.0286	0.0236
w_s (ms^{-1})	0.0600	0.0491	0.0409	0.0322	0.0270	0.0201
$w'_{s,med}/w_s$	**0.936**	**1.002**	**1.008**	**1.087**	**1.060**	**1.173**

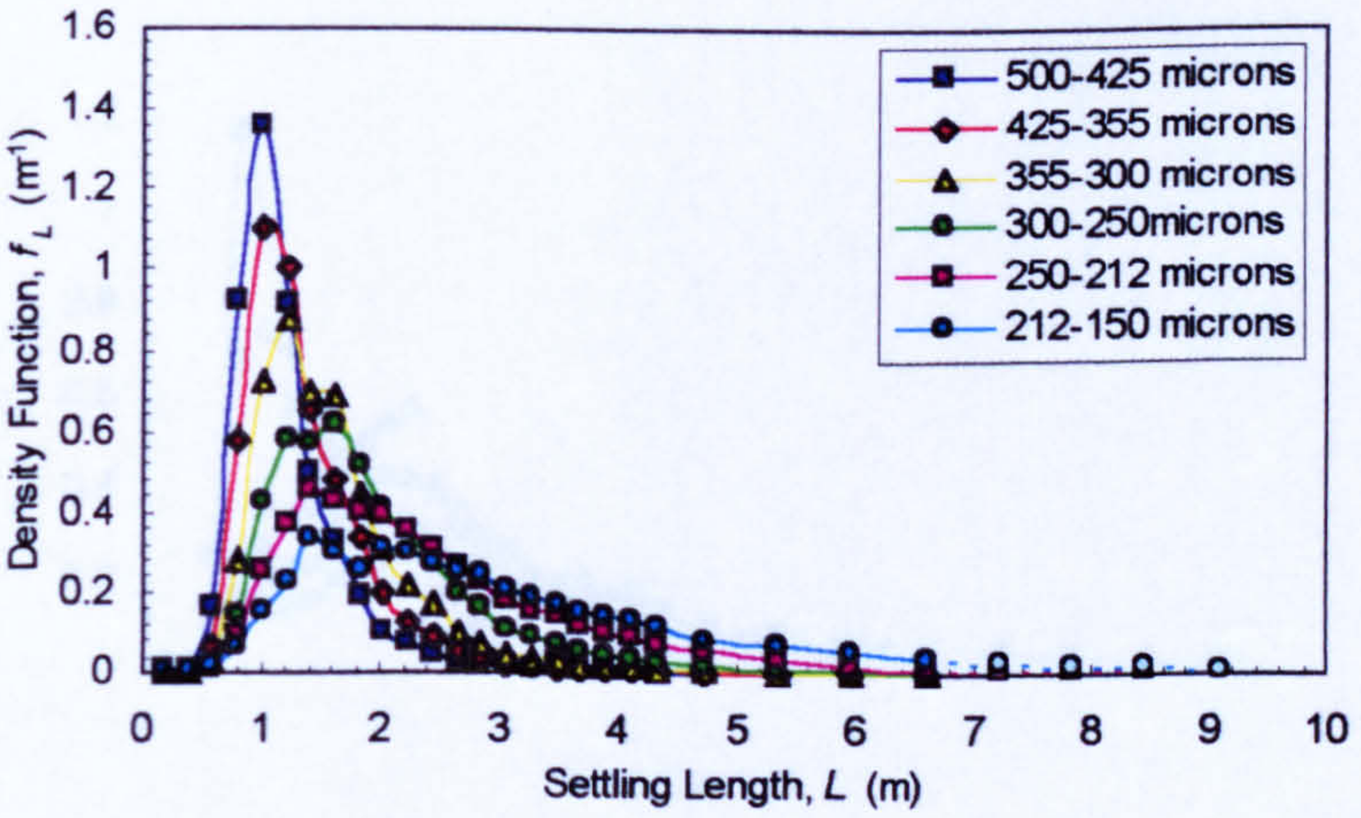

Figure A6.39 - S2_EX9(ii)

S2_EX9(ii)	Q = 0.0518 m^3s^{-1}; U = 0.737 ms^{-1}; H = 0.080m; Bed Grade = S2_grv1 (10-25 mm)					
	LA Grade Sand - Fraction Size (microns)					
	500-425	**425-355**	**355-300**	**300-250**	**250-212**	**212-150**
d_i (μm)	462.5	390	327.5	275	231	181
$L_{i,med}$ (m)	1.10	1.25	1.54	1.77	2.15	2.61
$w'_{s,med}$ (ms^{-1})	0.0536	0.0472	0.0383	0.0333	0.0274	0.0226
w_s (ms^{-1})	0.0600	0.0491	0.0409	0.0322	0.0270	0.0201
$w'_{s,med}/w_s$	**0.893**	**0.962**	**0.936**	**1.034**	**1.016**	**1.124**

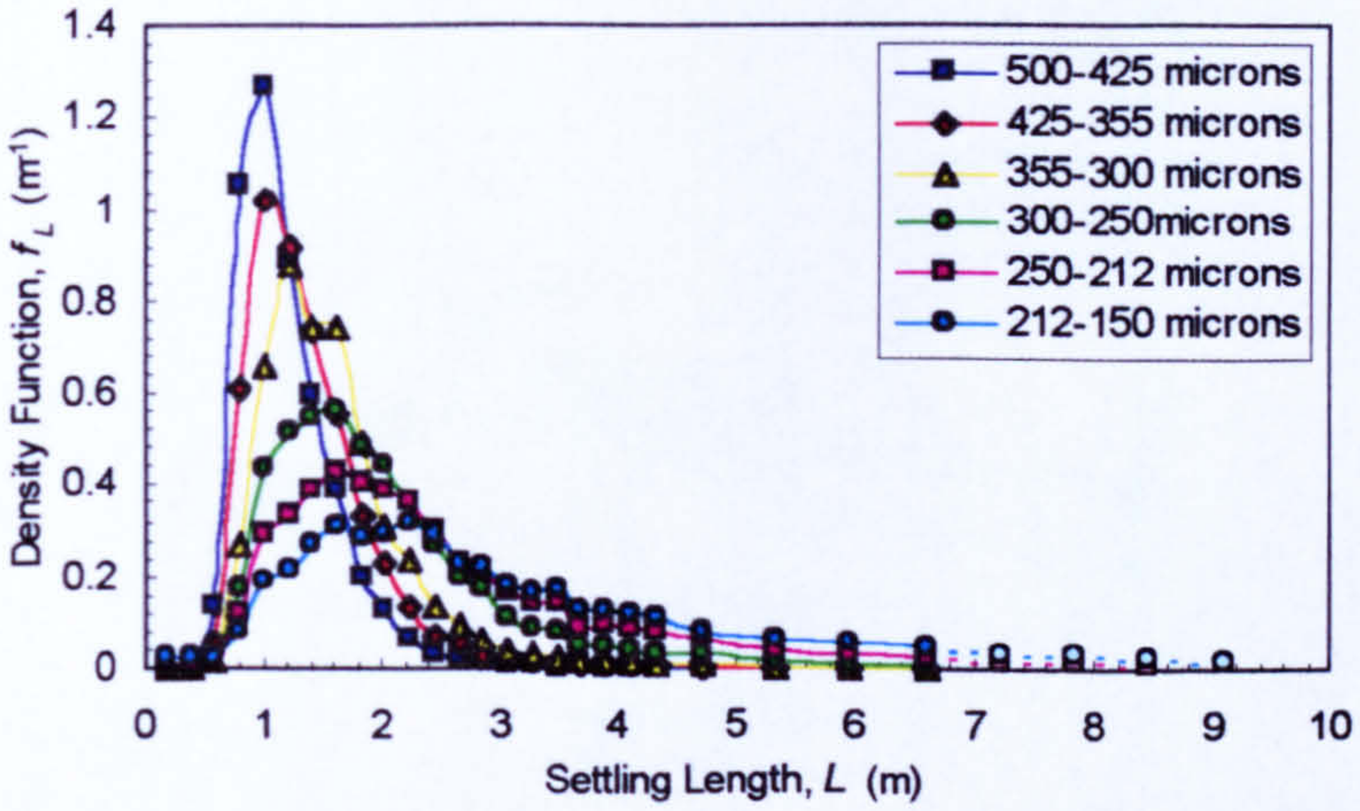

Figure A6.40 - S2_EX10(i)

S2_EX10(i)	Q = 0.0519 m^3s^{-1}; U = 0.723 ms^{-1}; H = 0.079m; Bed Grade = S2_grv1 (10-25 mm)					
	LA Grade Sand - Fraction Size (microns)					
	500-425	**425-355**	**355-300**	**300-250**	**250-212**	**212-150**
d_i (μm)	462.5	390	327.5	275	231	181
$L_{i,med}$ (m)	1.05	1.28	1.48	1.80	2.14	2.52
$w'_{s,med}$ (ms^{-1})	0.0544	0.0447	0.0385	0.0317	0.0267	0.0227
w_s (ms^{-1})	0.0600	0.0491	0.0409	0.0322	0.0270	0.0201
$w'_{s,med}/w_s$	**0.907**	**0.911**	**0.941**	**0.984**	**0.989**	**1.128**

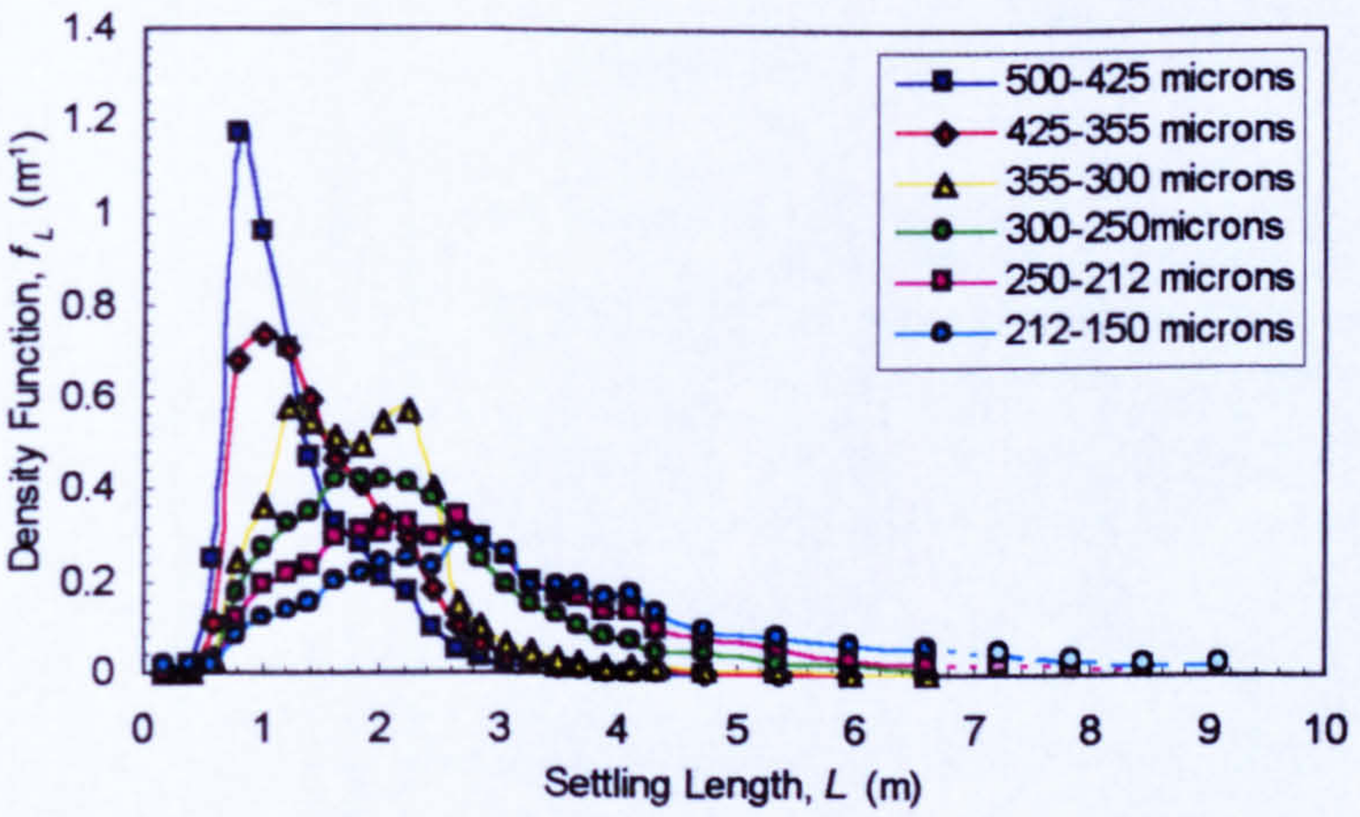

Figure A6.41 - S2_EX10(ii)

S2_EX10(ii)	Q = 0.0519 m^3s^{-1}; U = 0.723 ms^{-1}; H = 0.079m; Bed Grade = S2_grv1 (10-25 mm)					
	LA Grade Sand - Fraction Size (microns)					
	500-425	**425-355**	**355-300**	**300-250**	**250-212**	**212-150**
d_i (μm)	462.5	390	327.5	275	231	181
$L_{i,med}$ (m)	1.12	1.38	1.79	2.16	2.58	3.13
$w'_{s,med}$ (ms^{-1})	0.0511	0.0413	0.0319	0.0265	0.0221	0.0182
w_s (ms^{-1})	0.0600	0.0491	0.0409	0.0322	0.0270	0.0201
$\boldsymbol{w'_{s,med}/w_s}$	**0.851**	**0.841**	**0.780**	**0.822**	**0.820**	**0.908**

Appendix 6.7 – Longitudinal Distribution of Fractional Sediment Deposition (DB Sand)

This appendix presents the p.d.f.s for the measured distributions of fractional deposition length for the two experiments with DB grade sand (d_{50} = 97 μm).

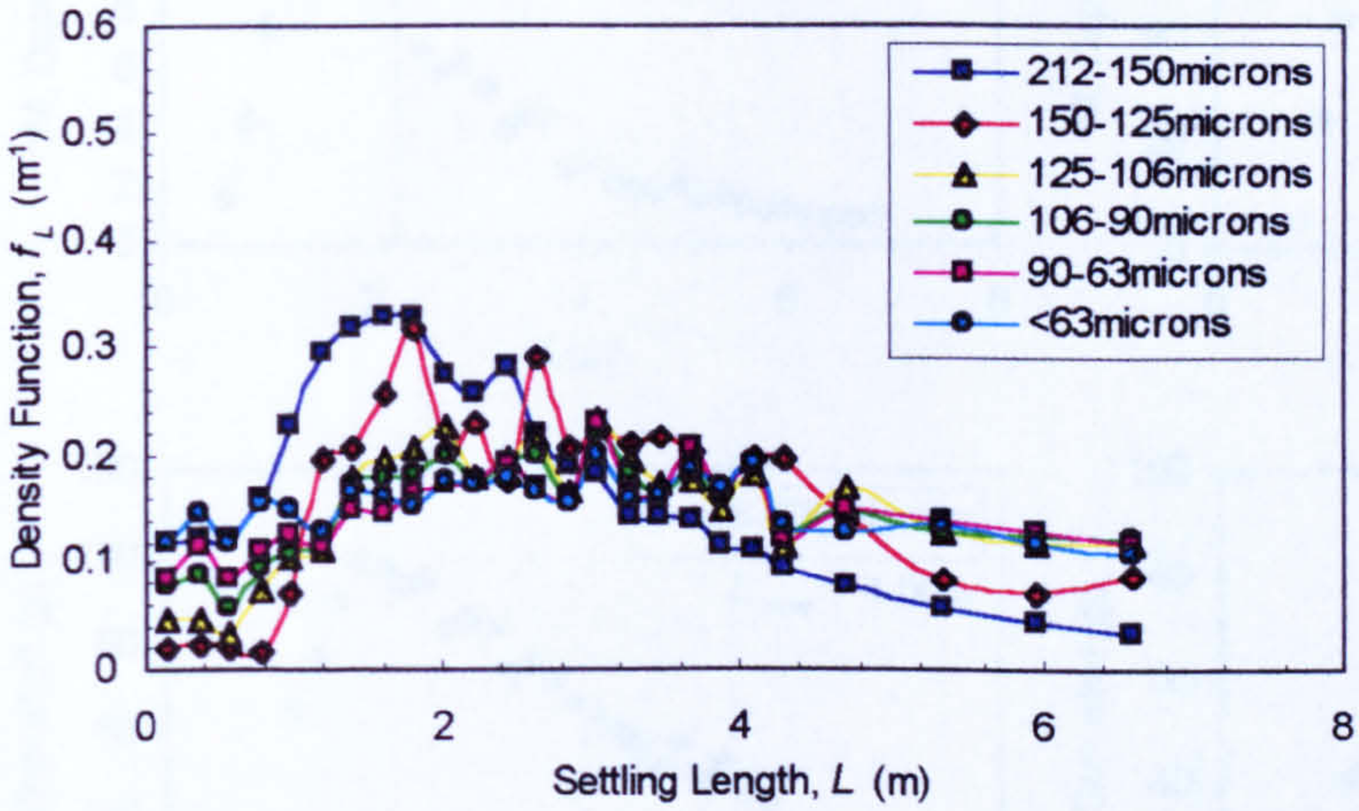

Figure A5.42 - S2_EX7

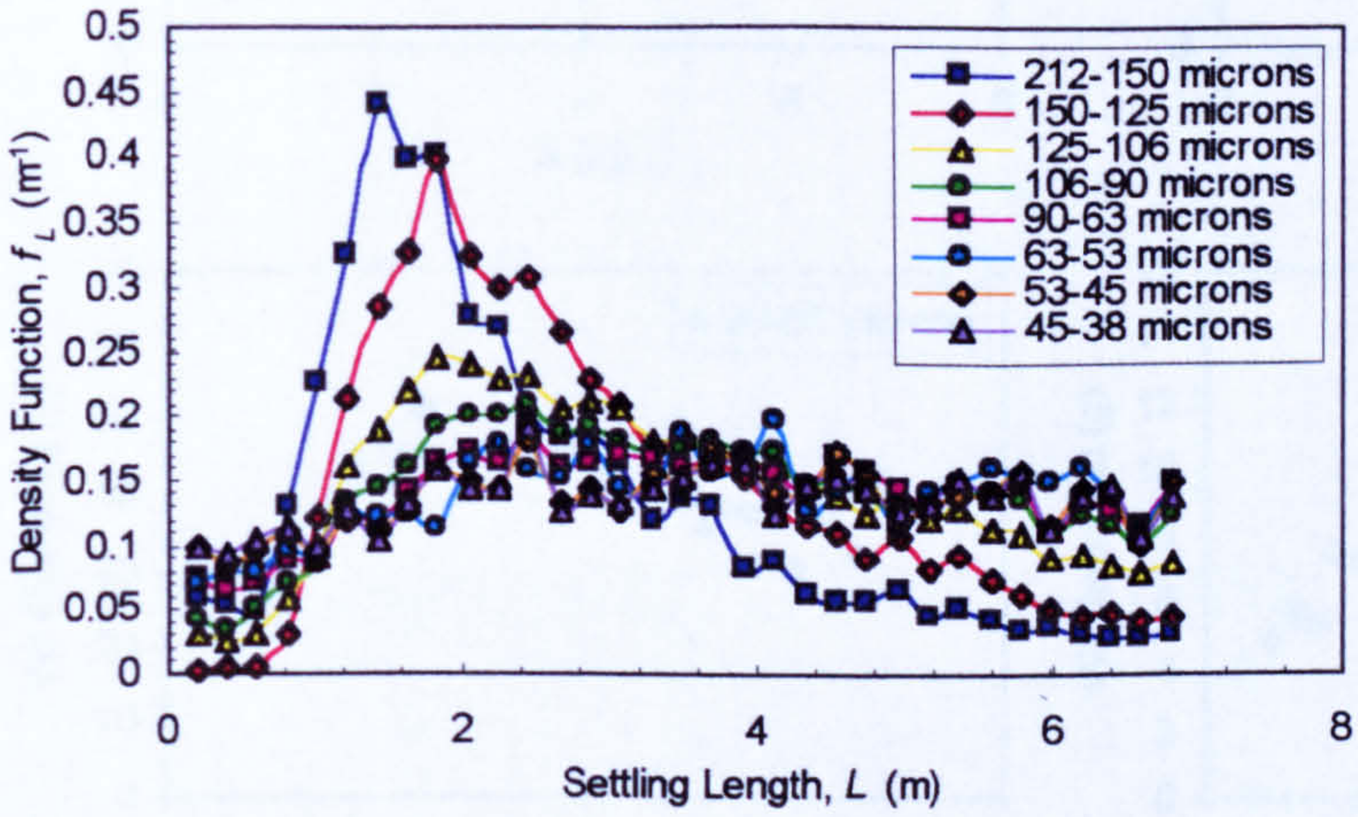

Figure A5.43 - S2_EX11

S2_EX11	Q = 0.0357m^{3}s^{-1}; H = 0.109m; S2_grv2 (5-10mm)			
	Sediment Size Fraction – DB Grade Sand (μm)			
	212-150	**150-125**	**125-106**	**106-90**
$\widetilde{L}_i$ (m)	2.228	2.753	4.000	5.206
$\widetilde{w}'_{si}$ (ms^{-1})	0.0195	0.0158	0.0109	0.0084
w_{si} (ms^{-1})	0.0150	0.0095	0.0070	0.0052
$\widetilde{w}'_{si} / w_{si}$	1.30	1.66	1.56	1.62

w_{si} calculated for DB sand from Cheng (1997) (Equation 2.6, pp 12)

The individual p.d.f. distributions for each DB sand fraction measured in S2_EX11 are shown in Figure A6.44 below, with values of $\tilde{L}_i$ shown for d_i = 181, 137.5, 115.5 and 98μm fractions.

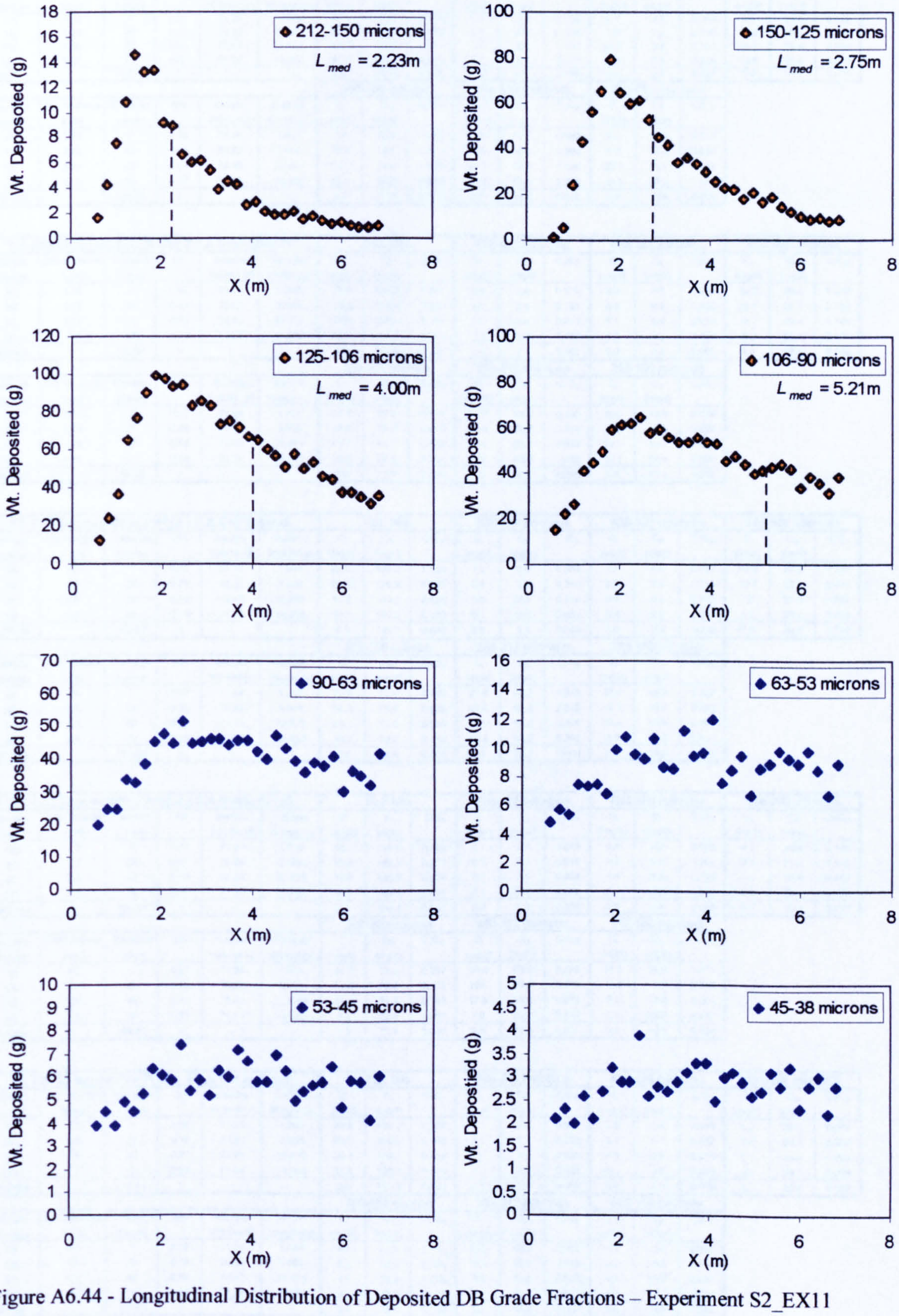

Figure A6.44 - Longitudinal Distribution of Deposited DB Grade Fractions – Experiment S2_EX11

Appendix 6.8 - Measured Sediment Concentration Data

(a) Experiment S2_EX3

S2 EX3 Concentration Profile 1 (LA Grade Sand)						Full Mix			500-425 microns			425-355 microns			355-300 microns		
Sample Number	D/S Distance x (m)	Elevation z (mm)	z/H	Sample Volume (ℓ)	Sample Weight (g)	C (mg/ℓ)	C_0 (mg/ℓ)	C/C_0	C_i (mg/ℓ)	C_{0i} (mg/ℓ)	C_i/C_{0i}	C_i (mg/ℓ)	C_{0i} (mg/ℓ)	C_i/C_{0i}	C_i (mg/ℓ)	C_{0i} (mg/ℓ)	C_i/C_{0i}
1A	1.25	7	0.07	71.24	1.004	14.1	199.2	0.071	0.3	2.4	0.139	0.7	9.8	0.069	0.9	29.4	0.032
1B	1.25	45	0.41	70.22	3.908	55.7	199.2	0.279	2.1	2.4	0.874	7.0	9.8	0.719	10.6	29.4	0.359
1C	1.25	75	0.68	73.43	22.679	308.9	199.2	1.551	4.2	2.4	1.733	21.0	9.8	2.150	50.1	29.4	1.705
1D	1.25	95	0.87	71.24	14.062	197.4	199.2	0.991	0.7	2.4	0.289	5.2	9.8	0.530	19.5	29.4	0.663
Surface		109.53	1	-	-	0.0	199.2	0.000	0.0	2.4	0.000	0.0	9.8	0.000	0.0	29.4	0.000
						300-250 micron			250-212 microns			212-150 microns					
Sample Number	D/S Distance x (m)	Elevation z (mm)	z/H	Sample Volume (ℓ)	Sample Weight (g)	C_i (mg/ℓ)	C_{0i} (mg/ℓ)	C_i/C_{0i}	C_i (mg/ℓ)	C_{0i} (mg/ℓ)	C_i/C_{0i}	C_i (mg/ℓ)	C_{0i} (mg/ℓ)	C_i/C_{0i}			
1A	1.25	7	0.05	71.24	1.004	2.6	72.9	0.036	4.4	63.2	0.069	4.2	19.9	0.210			
1B	1.25	45	0.41	70.22	3.908	16.8	72.9	0.231	12.0	63.2	0.190	4.2	19.9	0.210			
1C	1.25	75	0.68	73.43	22.679	112.1	72.9	1.539	95.1	63.2	1.504	23.3	19.9	1.168			
1D	1.25	95	0.87	71.24	14.062	64.8	72.9	0.889	76.2	63.2	1.205	29.6	19.9	1.488			
Surface		109.53	1	-	-	0.0	72.9	0.000	0.0	63.2	0.000	0.0	19.9	0.000			

S2 EX3 Concentration Profile 2 (LA Grade Sand)						Full Mix			500-425 microns			425-355 microns			355-300 microns		
Sample Number	D/S Distance x (m)	Elevation z (mm)	z/H	Sample Volume (ℓ)	Sample Weight (g)	C (mg/ℓ)	C_0 (mg/ℓ)	C/C_0	C_i (mg/ℓ)	C_{0i} (mg/ℓ)	C_i/C_{0i}	C_i (mg/ℓ)	C_{0i} (mg/ℓ)	C_i/C_{0i}	C_i (mg/ℓ)	C_{0i} (mg/ℓ)	C_i/C_{0i}
2A	1.75	7	0.07	71.24	1.004	78.0	199.2	0.391	2.4	2.4	0.970	8.3	9.8	0.852	15.2	29.4	0.516
2B	1.75	38	0.34	70.22	3.908	109.6	199.2	0.550	1.8	2.4	0.725	8.8	9.8	0.898	20.7	29.4	0.703
2C	1.75	68	0.62	73.43	22.679	120.8	199.2	0.607	0.9	2.4	0.353	5.1	9.8	0.525	16.7	29.4	0.566
2D	1.75	93	0.84	71.24	14.062	63.2	199.2	0.317	0.3	2.4	0.105	1.3	9.8	0.132	5.0	29.4	0.171
Surface		109.53	1	-	-	0.0	199.2	0.000	0.0	2.4	0.000	0.0	9.8	0.000	0.0	29.4	0.000
						300-250 micron			250-212 microns			212-150 microns					
Sample Number	D/S Distance x (m)	Elevation z (mm)	z/H	Sample Volume (ℓ)	Sample Weight (g)	C_i (mg/ℓ)	C_{0i} (mg/ℓ)	C_i/C_{0i}	C_i (mg/ℓ)	C_{0i} (mg/ℓ)	C_i/C_{0i}	C_i (mg/ℓ)	C_{0i} (mg/ℓ)	C_i/C_{0i}			
2A	1.75	7	0.07	71.24	1.004	24.9	72.9	0.341	18.3	63.2	0.289	6.6	19.9	0.329			
2B	1.75	38	0.34	70.22	3.908	37.5	72.9	0.515	30.6	63.2	0.484	8.4	19.9	0.422			
2C	1.75	68	0.62	73.43	22.679	41.7	72.9	0.573	42.5	63.2	0.672	13.1	19.9	0.656			
2D	1.75	93	0.84	71.24	14.062	18.5	72.9	0.254	24.8	63.2	0.392	12.1	19.9	0.609			
Surface		109.53	1	-	-	0.0	72.9	0.000	0.0	63.2	0.000	0.0	19.9	0.000			

S2 EX3 Concentration Profile 3 (LA Grade Sand)						Full Mix			500-425 microns			425-355 microns			355-300 microns		
Sample Number	D/S Distance x (m)	Elevation z (mm)	z/H	Sample Volume (ℓ)	Sample Weight (g)	C (mg/ℓ)	C_0 (mg/ℓ)	C/C_0	C_i (mg/ℓ)	C_{0i} (mg/ℓ)	C_i/C_{0i}	C_i (mg/ℓ)	C_{0i} (mg/ℓ)	C_i/C_{0i}	C_i (mg/ℓ)	C_{0i} (mg/ℓ)	C_i/C_{0i}
3A	2.5	7	0.07	71.24	1.004	238.1	199.2	1.196	1.2	2.4	0.509	7.7	9.8	0.787	33.3	29.4	1.131
3B	2.5	25	0.23	70.22	3.908	112.5	199.2	0.565	0.6	2.4	0.245	3.3	9.8	0.340	12.7	29.4	0.433
3C	2.5	50	0.46	73.43	22.679	81.2	199.2	0.408	0.3	2.4	0.119	1.7	9.8	0.176	7.7	29.4	0.263
3D	2.5	80	0.73	71.24	14.062	37.6	199.2	0.189	0.1	2.4	0.023	0.4	9.8	0.044	2.2	29.4	0.073
Surface		109.53	1	-	-	0.0	199.2	0.000	0.0	2.4	0.000	0.0	9.8	0.000	0.0	29.4	0.000
						300-250 micron			250-212 microns			212-150 microns					
Sample Number	D/S Distance x (m)	Elevation z (mm)	z/H	Sample Volume (ℓ)	Sample Weight (g)	C_i (mg/ℓ)	C_{0i} (mg/ℓ)	C_i/C_{0i}	C_i (mg/ℓ)	C_{0i} (mg/ℓ)	C_i/C_{0i}	C_i (mg/ℓ)	C_{0i} (mg/ℓ)	C_i/C_{0i}			
3A	2.5	7	0.07	71.24	1.004	70.6	72.9	0.969	97.6	63.2	1.543	26.4	19.9	1.327			
3B	2.5	25	0.23	70.22	3.908	38.3	72.9	0.525	41.0	63.2	0.649	15.2	19.9	0.766			
3C	2.5	50	0.46	73.43	22.679	26.1	72.9	0.358	31.2	63.2	0.494	13.2	19.9	0.665			
3D	2.5	80	0.73	71.24	14.062	10.2	72.9	0.140	15.5	63.2	0.245	8.3	19.9	0.416			
Surface		109.53	1	-	-	0.0	72.9	0.000	0.0	63.2	0.000	0.0	19.9	0.000			

S2 EX3 Concentration Profile 4 (LA Grade Sand)						Full Mix			500-425 microns			425-355 microns			355-300 microns		
Sample Number	D/S Distance x (m)	Elevation z (mm)	z/H	Sample Volume (ℓ)	Sample Weight (g)	C (mg/ℓ)	C_0 (mg/ℓ)	C/C_0	C_i (mg/ℓ)	C_{0i} (mg/ℓ)	C_i/C_{0i}	C_i (mg/ℓ)	C_{0i} (mg/ℓ)	C_i/C_{0i}	C_i (mg/ℓ)	C_{0i} (mg/ℓ)	C_i/C_{0i}
4A	3.5	7	0.07	71.24	1.004	80.1	199.2	0.402	0.1	2.4	0.043	0.6	9.8	0.066	4.3	29.4	0.145
4B	3.5	25	0.22	70.22	3.908	55.2	199.2	0.277	0.0	2.4	0.019	0.5	9.8	0.051	2.8	29.4	0.096
4C	3.5	48	0.43	73.43	22.679	40.6	199.2	0.204	0.1	2.4	0.032	0.4	9.8	0.038	1.9	29.4	0.065
4D	3.5	78	0.71	71.24	14.062	18.2	199.2	0.091	0.1	2.4	0.023	0.1	9.8	0.011	0.6	29.4	0.022
Surface		109.53	1	-	-	0.0	199.2	0.000	0.0	2.4	0.000	0.0	9.8	0.000	0.0	29.4	0.000
						300-250 micron			250-212 microns			212-150 microns					
Sample Number	D/S Distance x (m)	Elevation z (mm)	z/H	Sample Volume (ℓ)	Sample Weight (g)	C_i (mg/ℓ)	C_{0i} (mg/ℓ)	C_i/C_{0i}	C_i (mg/ℓ)	C_{0i} (mg/ℓ)	C_i/C_{0i}	C_i (mg/ℓ)	C_{0i} (mg/ℓ)	C_i/C_{0i}			
4A	3.5	7	0.07	71.24	1.004	21.7	72.9	0.297	35.3	63.2	0.559	16.8	19.9	0.841			
4B	3.5	25	0.22	70.22	3.908	14.4	72.9	0.198	23.4	63.2	0.370	13.0	19.9	0.652			
4C	3.5	48	0.43	73.43	22.679	10.4	72.9	0.142	17.6	63.2	0.278	9.2	19.9	0.464			
4D	3.5	78	0.71	71.24	14.062	3.9	72.9	0.053	7.9	63.2	0.124	5.0	19.9	0.252			
Surface		109.53	1	-	-	0.0	72.9	0.000	0.0	63.2	0.000	0.0	19.9	0.000			

S2 EX3 Concentration Profile 5 (LA Grade Sand)						Full Mix			500-425 microns			425-355 microns			355-300 microns		
Sample Number	D/S Distance x (m)	Elevation z (mm)	z/H	Sample Volume (ℓ)	Sample Weight (g)	C (mg/ℓ)	C_0 (mg/ℓ)	C/C_0	C_i (mg/ℓ)	C_{0i} (mg/ℓ)	C_i/C_{0i}	C_i (mg/ℓ)	C_{0i} (mg/ℓ)	C_i/C_{0i}	C_i (mg/ℓ)	C_{0i} (mg/ℓ)	C_i/C_{0i}
5A	4.5	7	0.07	71.24	1.004	40.8	199.2	0.205	0.1	2.4	0.030	0.2	9.8	0.019	1.2	29.4	0.041
5B	4.5	20	0.18	70.22	3.908	29.0	199.2	0.146	0.1	2.4	0.023	0.1	9.8	0.012	0.8	29.4	0.026
5C	4.5	40	0.37	73.43	22.679	22.8	199.2	0.114	0.1	2.4	0.038	0.2	9.8	0.016	0.7	29.4	0.024
5D	4.5	65	0.59	71.24	14.062	15.1	199.2	0.076	0.1	2.4	0.029	0.1	9.8	0.009	0.4	29.4	0.013
Surface		109.53	1	-	-	0.0	199.2	0.000	0.0	2.4	0.000	0.0	9.8	0.000	0.0	29.4	0.000
						300-250 micron			250-212 microns			212-150 microns					
Sample Number	D/S Distance x (m)	Elevation z (mm)	z/H	Sample Volume (ℓ)	Sample Weight (g)	C_i (mg/ℓ)	C_{0i} (mg/ℓ)	C_i/C_{0i}	C_i (mg/ℓ)	C_{0i} (mg/ℓ)	C_i/C_{0i}	C_i (mg/ℓ)	C_{0i} (mg/ℓ)	C_i/C_{0i}			
5A	4.5	7	0.07	71.24	1.004	8.2	72.9	0.112	18.2	63.2	0.289	11.7	19.9	0.587			
5B	4.5	20	0.18	70.22	3.908	5.5	72.9	0.076	12.4	63.2	0.195	8.9	19.9	0.445			
5C	4.5	40	0.37	73.43	22.679	4.5	72.9	0.061	9.8	63.2	0.155	6.6	19.9	0.332			
5D	4.5	65	0.59	71.24	14.062	2.3	72.9	0.032	5.9	63.2	0.093	5.3	19.9	0.265			
Surface		109.53	1	-	-	0.0	72.9	0.000	0.0	63.2	0.000	0.0	19.9	0.000			

(b) Experiment S2_EX4

S2 EX4 Concentration Profile 1 (LA Grade Sand)						Full Mix			500-425 microns			425-355 microns			355-300 microns		
Sample Number	D/S Distance x (m)	Elevation z (mm)	z/H	Sample Volume (ℓ)	Sample Weight (g)	C (mg/ℓ)	C_0 (mg/ℓ)	C/C_0	C_i (mg/ℓ)	C_{0i} (mg/ℓ)	C_i/C_{0i}	C_i (mg/ℓ)	C_{0i} (mg/ℓ)	C_i/C_{0i}	C_i (mg/ℓ)	C_{0i} (mg/ℓ)	C/C_{0i}
1A	1.25	7	0.09	74.61	1.248	16.7	205.6	0.081	1.6	2.5	0.658	2.6	10.1	0.262	3.2	30.4	0.105
1B	1.25	37	0.46	72.42	10.091	139.3	205.6	0.678	5.0	2.5	1.978	15.8	10.1	1.568	31.4	30.4	1.034
1C	1.25	57	0.71	75.79	23.607	311.5	205.6	1.515	2.5	2.5	0.995	13.4	10.1	1.332	49.7	30.4	1.637
1D	1.25	72	0.90	74.61	8.062	108.1	205.6	0.526	0.2	2.5	0.080	1.6	10.1	0.160	7.5	30.4	0.248
Surface		80.13	1	-	-	0.0	205.6	0.000	0.0	2.5	0.000	0.0	10.1	0.000	0.0	30.4	0.000
						300-250 micron			250-212 microns			212-150 microns					
Sample Number	D/S Distance x (m)	Elevation z (mm)	z/H	Sample Volume (ℓ)	Sample Weight (g)	C_i (mg/ℓ)	C_{0i} (mg/ℓ)	C_i/C_{0i}	C_i (mg/ℓ)	C_{0i} (mg/ℓ)	C_i/C_{0i}	C_i (mg/ℓ)	C_{0i} (mg/ℓ)	C_i/C_{0i}			
1A	1.25	7	0.09	74.61	1.248	3.6	75.2	0.048	2.1	65.3	0.031	1.3	20.6	0.062			
1B	1.25	37	0.46	72.42	10.091	47.2	75.2	0.628	30.0	65.3	0.460	7.4	20.6	0.360			
1C	1.25	57	0.71	75.79	23.607	113.3	75.2	1.507	101.4	65.3	1.554	30.1	20.6	1.464			
1D	1.25	72	0.90	74.61	8.062	32.6	75.2	0.433	44.0	65.3	0.674	21.6	20.6	1.051			
Surface		80.13	1	-	-	0.0	75.2	0.000	0.0	65.3	0.000	0.0	20.6	0.000			

S2 EX4 Concentration Profile 2 (LA Grade Sand)						Full Mix			500-425 microns			425-355 microns			355-300 microns		
Sample Number	D/S Distance x (m)	Elevation z (mm)	z/H	Sample Volume (ℓ)	Sample Weight (g)	C (mg/ℓ)	C_0 (mg/ℓ)	C/C_0	C_i (mg/ℓ)	C_{0i} (mg/ℓ)	C_i/C_{0i}	C_i (mg/ℓ)	C_{0i} (mg/ℓ)	C_i/C_{0i}	C_i (mg/ℓ)	C_{0i} (mg/ℓ)	C/C_{0i}
1A	1.75	7	0.09	72.92	14.089	193.2	205.6	0.940	1.6	2.5	0.646	9.2	10.1	0.913	33.0	30.4	1.087
1B	1.75	27.5	0.34	72.92	8.47	116.1	205.6	0.565	0.5	2.5	0.181	3.2	10.1	0.316	13.9	30.4	0.459
1C	1.75	47.5	0.59	74.10	5.896	79.6	205.6	0.387	0.2	2.5	0.092	1.3	10.1	0.127	6.8	30.4	0.224
1D	1.75	67.5	0.84	71.24	1.904	26.7	205.6	0.130	0.04	2.5	0.017	0.2	10.1	0.017	1.1	30.4	0.037
Surface	1.75	80.13	1	-	-	0.0	205.6	0.000	0.0	2.5	0.000	0.0	10.1	0.000	0.0	30.4	0.000
						300-250 micron			250-212 microns			212-150 microns					
Sample Number	D/S Distance x (m)	Elevation z (mm)	z/H	Sample Volume (ℓ)	Sample Weight (g)	C_i (mg/ℓ)	C_{0i} (mg/ℓ)	C_i/C_{0i}	C_i (mg/ℓ)	C_{0i} (mg/ℓ)	C_i/C_{0i}	C_i (mg/ℓ)	C_{0i} (mg/ℓ)	C_i/C_{0i}			
1A	1.75	7	0.09	72.92	14.089	73.5	75.2	0.977	59.9	65.3	0.917	15.3	20.6	0.745			
1B	1.75	27.5	0.34	72.92	8.47	41.8	75.2	0.556	42.4	65.3	0.650	13.9	20.6	0.676			
1C	1.75	47.5	0.59	74.10	5.896	26.1	75.2	0.347	32.2	65.3	0.493	12.7	20.6	0.616			
1D	1.75	67.5	0.84	71.24	1.904	5.8	75.2	0.077	11.1	65.3	0.171	8.1	20.6	0.393			
Surface		80.13	1	-	-	0.0	75.2	0.000	0.0	65.3	0.000	0.0	20.6	0.000			

S2 EX4 Concentration Profile 3 (LA Grade Sand)						Full Mix			500-425 microns			425-355 microns			355-300 microns		
Sample Number	D/S Distance x (m)	Elevation z (mm)	z/H	Sample Volume (ℓ)	Sample Weight (g)	C (mg/ℓ)	C_0 (mg/ℓ)	C/C_0	C_i (mg/ℓ)	C_{0i} (mg/ℓ)	C_i/C_{0i}	C_i (mg/ℓ)	C_{0i} (mg/ℓ)	C_i/C_{0i}	C_i (mg/ℓ)	C_{0i} (mg/ℓ)	C/C_{0i}
1A	2.25	7	0.09	74.44	12.53	168.3	205.6	0.819	0.3	2.5	0.107	2.4	10.1	0.235	12.9	30.4	0.426
1B	2.25	25	0.31	71.40	6.781	95.0	205.6	0.462	0.2	2.5	0.084	1.5	10.1	0.153	8.3	30.4	0.274
1C	2.25	45	0.56	67.52	4.21	62.4	205.6	0.303	0.1	2.5	0.030	0.8	10.1	0.082	4.7	30.4	0.154
1D	2.25	70	0.87	73.60	1.702	23.1	205.6	0.112	0.04	2.5	0.016	0.1	10.1	0.015	1.2	30.4	0.040
Surface	2.25	80.13	1	-	-	0.0	205.6	0.000	0.0	2.5	0.000	0.0	10.1	0.000	0.0	30.4	0.000
						300-250 micron			250-212 microns			212-150 microns					
Sample Number	D/S Distance x (m)	Elevation z (mm)	z/H	Sample Volume (ℓ)	Sample Weight (g)	C_i (mg/ℓ)	C_{0i} (mg/ℓ)	C_i/C_{0i}	C_i (mg/ℓ)	C_{0i} (mg/ℓ)	C_i/C_{0i}	C_i (mg/ℓ)	C_{0i} (mg/ℓ)	C_i/C_{0i}			
1A	2.25	7	0.09	74.44	12.53	54.1	75.2	0.719	70.3	65.3	1.076	27.8	20.6	1.355			
1B	2.25	25	0.31	71.40	6.781	31.7	75.2	0.421	37.9	65.3	0.581	14.9	20.6	0.726			
1C	2.25	45	0.56	67.52	4.21	19.4	75.2	0.259	26.0	65.3	0.398	11.0	20.6	0.536			
1D	2.25	70	0.87	73.60	1.702	5.9	75.2	0.078	10.1	65.3	0.155	5.4	20.6	0.265			
Surface	2.25	80.13	1	-	-	0.0	75.2	0.000	0.0	65.3	0.000	0.0	20.6	0.000			

S2 EX4 Concentration Profile 4 (LA Grade Sand)						Full Mix			500-425 microns			425-355 microns			355-300 microns		
Sample Number	D/S Distance x (m)	Elevation z (mm)	z/H	Sample Volume (ℓ)	Sample Weight (g)	C (mg/ℓ)	C_0 (mg/ℓ)	C/C_0	C_i (mg/ℓ)	C_{0i} (mg/ℓ)	C_i/C_{0i}	C_i (mg/ℓ)	C_{0i} (mg/ℓ)	C_i/C_{0i}	C_i (mg/ℓ)	C_{0i} (mg/ℓ)	C/C_{0i}
1A	3.0	7	0.09	67.35	3.325	49.4	205.6	0.240	0.06	2.5	0.024	0.19	10.1	0.019	1.71	30.4	0.056
1B	3.0	25	0.31	67.35	2.477	36.8	205.6	0.179	0.03	2.5	0.012	0.13	10.1	0.013	1.47	30.4	0.048
1C	3.0	40	0.50	64.82	1.788	27.6	205.6	0.134	0.03	2.5	0.012	0.12	10.1	0.012	1.02	30.4	0.034
1D	3.0	65	0.81	69.72	0.859	12.3	205.6	0.060	0.00	2.5	0.000	0.06	10.1	0.006	0.37	30.4	0.012
Surface	3.0	80.13	1	-	-	0.0	205.6	0.000	0.00	2.5	0.000	0.00	10.1	0.000	0.00	30.4	0.000
						300-250 micron			250-212 microns			212-150 microns					
Sample Number	D/S Distance x (m)	Elevation z (mm)	z/H	Sample Volume (ℓ)	Sample Weight (g)	C_i (mg/ℓ)	C_{0i} (mg/ℓ)	C_i/C_{0i}	C_i (mg/ℓ)	C_{0i} (mg/ℓ)	C_i/C_{0i}	C_i (mg/ℓ)	C_{0i} (mg/ℓ)	C_i/C_{0i}			
1A	3.0	7	0.09	67.35	3.325	11.8	75.2	0.157	22.0	65.3	0.337	13.2	20.6	0.640			
1B	3.0	25	0.31	67.35	2.477	8.3	75.2	0.111	16.5	65.3	0.253	9.9	20.6	0.480			
1C	3.0	40	0.50	64.82	1.788	6.0	75.2	0.080	12.5	65.3	0.191	7.6	20.6	0.369			
1D	3.0	65	0.81	69.72	0.859	2.2	75.2	0.030	5.4	65.3	0.082	4.1	20.6	0.198			
Surface	3.0	80.13	1	-	-	0.0	75.2	0.000	0.0	65.3	0.000	0.0	20.6	0.000			

S2 EX4 Concentration Profile 5 (LA Grade Sand)						Full Mix			500-425 microns			425-355 microns			355-300 microns		
Sample Number	D/S Distance x (m)	Elevation z (mm)	z/H	Sample Volume (ℓ)	Sample Weight (g)	C (mg/ℓ)	C_0 (mg/ℓ)	C/C_0	C_i (mg/ℓ)	C_{0i} (mg/ℓ)	C_i/C_{0i}	C_i (mg/ℓ)	C_{0i} (mg/ℓ)	C_i/C_{0i}	C_i (mg/ℓ)	C_{0i} (mg/ℓ)	C/C_{0i}
1A	3.75	7	0.09	69.21	2.155	31.1	205.6	0.151	0.01	2.5	0.006	0.09	10.1	0.009	0.6	30.4	0.019
1B	3.75	22	0.27	71.57	1.161	16.2	205.6	0.079	0.04	2.5	0.017	0.03	10.1	0.003	0.3	30.4	0.009
1C	3.75	37	0.46	66.17	0.81	12.2	205.6	0.060	0.00	2.5	0.000	0.08	10.1	0.008	0.3	30.4	0.009
1D	3.75	62	0.77	70.39	0.461	6.5	205.6	0.032	0.03	2.5	0.011	0.01	10.1	0.001	0.1	30.4	0.004
Surface	3.75	80.13	1	-	-	0.0	205.6	0.000	0.00	2.5	0.000	0.00	10.1	0.000	0.0	30.4	0.000
						300-250 micron			250-212 microns			212-150 microns					
Sample Number	D/S Distance x (m)	Elevation z (mm)	z/H	Sample Volume (ℓ)	Sample Weight (g)	C_i (mg/ℓ)	C_{0i} (mg/ℓ)	C_i/C_{0i}	C_i (mg/ℓ)	C_{0i} (mg/ℓ)	C_i/C_{0i}	C_i (mg/ℓ)	C_{0i} (mg/ℓ)	C_i/C_{0i}			
1A	3.75	7	0.09	69.21	2.155	5.2	75.2	0.069	13.7	65.3	0.209	11.1	20.6	0.538			
1B	3.75	22	0.27	71.57	1.161	2.5	75.2	0.033	6.7	65.3	0.102	6.4	20.6	0.311			
1C	3.75	37	0.46	66.17	0.81	2.0	75.2	0.026	5.2	65.3	0.079	4.4	20.6	0.215			
1D	3.75	62	0.77	70.39	0.461	0.9	75.2	0.012	2.6	65.3	0.040	2.7	20.6	0.131			
Surface	3.75	80.13	1	-	-	0.0	75.2	0.000	0.0	65.3	0.000	0.0	20.6	0.000			

(c) Experiment S2_EX5

S2 EX5 Concentration Profile 1 (LA Grade Sand)						Full Mix			500-425 microns			425-355 microns			355-300 microns		
Sample Number	D/S Distance x (m)	Elevation z (mm)	z/H	Sample Volume (ℓ)	Sample Weight (g)	C (mg/ℓ)	C_0 (mg/ℓ)	C/C_0	C_i (mg/ℓ)	C_{0i} (mg/ℓ)	C_i/C_{0i}	C_i (mg/ℓ)	C_{0i} (mg/ℓ)	C_i/C_{0i}	C_i (mg/ℓ)	C_{0i} (mg/ℓ)	C_i/C_{0i}
1A	1.25	7	0.09	70.90	0.741	10.5	201.9	0.052	1.0	2.5	0.413	1.6	9.9	0.158	1.9	29.8	0.063
1B	1.25	35	0.45	69.97	9.01	128.8	201.9	0.638	4.3	2.5	1.742	15.3	9.9	1.544	29.4	29.8	0.985
1C	1.25	55	0.71	72.50	22.488	310.2	201.9	1.536	2.0	2.5	0.801	11.5	9.9	1.164	41.3	29.8	1.387
1D	1.25	70	0.90	61.95	5.217	84.2	201.9	0.417	0.2	2.5	0.092	1.3	9.9	0.131	5.2	29.8	0.175
Surface	1.25	77.38	1	-	-	0.0	201.9	0.000	0.0	2.5	0.000	0.0	9.9	0.000	0.0	29.8	0.000
						300-250 micron			250-212 microns			212-150 microns					
Sample Number	D/S Distance x (m)	Elevation z (mm)	z/H	Sample Volume (ℓ)	Sample Weight (g)	C_i (mg/ℓ)	C_{0i} (mg/ℓ)	C_i/C_{0i}	C_i (mg/ℓ)	C_{0i} (mg/ℓ)	C_i/C_{0i}	C_i (mg/ℓ)	C_{0i} (mg/ℓ)	C_i/C_{0i}			
1A	1.25	7	0.09	70.90	0.741	1.9	73.9	0.026	1.6	64.1	0.025	1.0	20.2	0.051			
1B	1.25	35	0.45	69.97	9.01	43.5	73.9	0.589	27.2	64.1	0.424	6.5	20.2	0.324			
1C	1.25	55	0.71	72.50	22.488	111.3	73.9	1.507	107.1	64.1	1.671	27.8	20.2	1.377			
1D	1.25	70	0.90	61.95	5.217	23.4	73.9	0.316	34.7	64.1	0.541	18.7	20.2	0.928			
Surface	1.25	77.38	1	-	-	0.0	73.9	0.000	0.0	64.1	0.000	0.0	20.2	0.000			

S2 EX5 Concentration Profile 2 (LA Grade Sand)						Full Mix			500-425 microns			425-355 microns			355-300 microns		
Sample Number	D/S Distance x (m)	Elevation z (mm)	z/H	Sample Volume (ℓ)	Sample Weight (g)	C (mg/ℓ)	C_0 (mg/ℓ)	C/C_0	C_i (mg/ℓ)	C_{0i} (mg/ℓ)	C_i/C_{0i}	C_i (mg/ℓ)	C_{0i} (mg/ℓ)	C_i/C_{0i}	C_i (mg/ℓ)	C_{0i} (mg/ℓ)	C_i/C_{0i}
1A	1.75	7	0.09	69.97	10.698	152.9	201.9	0.757	1.2	2.5	0.494	6.9	9.9	0.697	23.7	29.8	0.796
1B	1.75	30	0.39	70.05	8.447	120.6	201.9	0.597	0.6	2.5	0.244	3.7	9.9	0.374	14.8	29.8	0.496
1C	1.75	50	0.65	72.00	5.491	76.3	201.9	0.378	0.2	2.5	0.090	1.3	9.9	0.131	6.4	29.8	0.214
1D	1.75	70	0.90	68.53	1.149	16.8	201.9	0.083	0.1	2.5	0.041	0.3	9.9	0.027	0.8	29.8	0.026
Surface	1.75	77.38	1	-	-	0.0	201.9	0.000	0.0	2.5	0.000	0.0	9.9	0.000	0.0	29.8	0.000
						300-250 micron			250-212 microns			212-150 microns					
Sample Number	D/S Distance x (m)	Elevation z (mm)	z/H	Sample Volume (ℓ)	Sample Weight (g)	C_i (mg/ℓ)	C_{0i} (mg/ℓ)	C_i/C_{0i}	C_i (mg/ℓ)	C_{0i} (mg/ℓ)	C_i/C_{0i}	C_i (mg/ℓ)	C_{0i} (mg/ℓ)	C_i/C_{0i}			
1A	1.75	7	0.09	69.97	10.698	57.0	73.9	0.772	49.0	64.1	0.764	14.3	20.2	0.710			
1B	1.75	30	0.39	70.05	8.447	42.5	73.9	0.575	44.2	64.1	0.690	14.4	20.2	0.714			
1C	1.75	50	0.65	72.00	5.491	24.0	73.9	0.324	30.7	64.1	0.479	13.4	20.2	0.664			
1D	1.75	70	0.90	68.53	1.149	3.5	73.9	0.047	6.7	64.1	0.104	4.5	20.2	0.223			
Surface	1.75	77.38	1	-	-	0.0	73.9	0.000	0.0	64.1	0.000	0.0	20.2	0.000			

S2 EX5 Concentration Profile 3 (LA Grade Sand)						Full Mix			500-425 microns			425-355 microns			355-300 microns		
Sample Number	D/S Distance x (m)	Elevation z (mm)	z/H	Sample Volume (ℓ)	Sample Weight (g)	C (mg/ℓ)	C_0 (mg/ℓ)	C/C_0	C_i (mg/ℓ)	C_{0i} (mg/ℓ)	C_i/C_{0i}	C_i (mg/ℓ)	C_{0i} (mg/ℓ)	C_i/C_{0i}	C_i (mg/ℓ)	C_{0i} (mg/ℓ)	C_i/C_{0i}
1A	2.25	7	0.09	69.89	8.355	119.6	201.9	0.592	0.31	2.5	0.128	2.1	9.9	0.214	11.8	29.8	0.395
1B	2.25	25	0.32	66.85	5.464	81.7	201.9	0.405	0.13	2.5	0.055	1.2	9.9	0.117	6.0	29.8	0.202
1C	2.25	40	0.52	65.92	3.657	55.5	201.9	0.275	0.09	2.5	0.037	0.8	9.9	0.078	4.3	29.8	0.144
1D	2.25	60	0.78	69.13	1.307	18.9	201.9	0.094	0.03	2.5	0.012	0.2	9.9	0.019	1.0	29.8	0.035
Surface	2.25	77.38	1	-	-	0.0	201.9	0.000	0.00	2.5	0.000	0.0	9.9	0.000	0.0	29.8	0.000
						300-250 micron			250-212 microns			212-150 microns					
Sample Number	D/S Distance x (m)	Elevation z (mm)	z/H	Sample Volume (ℓ)	Sample Weight (g)	C_i (mg/ℓ)	C_{0i} (mg/ℓ)	C_i/C_{0i}	C_i (mg/ℓ)	C_{0i} (mg/ℓ)	C_i/C_{0i}	C_i (mg/ℓ)	C_{0i} (mg/ℓ)	C_i/C_{0i}			
1A	2.25	7	0.09	69.89	8.355	40.5	73.9	0.549	47.5	64.1	0.741	16.9	20.2	0.836			
1B	2.25	25	0.32	66.85	5.464	25.2	73.9	0.341	33.8	64.1	0.527	15.1	20.2	0.746			
1C	2.25	40	0.52	65.92	3.657	17.0	73.9	0.230	23.4	64.1	0.364	9.7	20.2	0.479			
1D	2.25	60	0.78	69.13	1.307	4.7	73.9	0.063	8.0	64.1	0.125	4.7	20.2	0.234			
Surface	2.25	77.38	1	-	-	0.0	73.9	0.000	0.0	64.1	0.000	0.0	20.2	0.000			

S2 EX5 Concentration Profile 4 (LA Grade Sand)						Full Mix			500-425 microns			425-355 microns			355-300 microns		
Sample Number	D/S Distance x (m)	Elevation z (mm)	z/H	Sample Volume (ℓ)	Sample Weight (g)	C (mg/ℓ)	C_0 (mg/ℓ)	C/C_0	C_i (mg/ℓ)	C_{0i} (mg/ℓ)	C_i/C_{0i}	C_i (mg/ℓ)	C_{0i} (mg/ℓ)	C_i/C_{0i}	C_i (mg/ℓ)	C_{0i} (mg/ℓ)	C_i/C_{0i}
1A	3.0	7	0.09	58.16	3.375	58.0	201.9	0.287	0.07	2.5	0.028	0.36	9.9	0.037	2.7	29.8	0.092
1B	3.0	25	0.32	68.37	2.234	32.7	201.9	0.162	0.06	2.5	0.024	0.20	9.9	0.021	1.4	29.8	0.046
1C	3.0	40	0.52	73.01	1.857	25.4	201.9	0.126	0.05	2.5	0.022	0.12	9.9	0.012	1.0	29.8	0.033
1D	3.0	60	0.78	39.49	0.598	15.1	201.9	0.075	0.10	2.5	0.041	0.23	9.9	0.023	0.6	29.8	0.020
Surface	3.0	77.38	1	-	-	0.0	201.9	0.000	0.00	2.5	0.000	0.00	9.9	0.000	0.0	29.8	0.000
						300-250 micron			250-212 microns			212-150 microns					
Sample Number	D/S Distance x (m)	Elevation z (mm)	z/H	Sample Volume (ℓ)	Sample Weight (g)	C_i (mg/ℓ)	C_{0i} (mg/ℓ)	C_i/C_{0i}	C_i (mg/ℓ)	C_{0i} (mg/ℓ)	C_i/C_{0i}	C_i (mg/ℓ)	C_{0i} (mg/ℓ)	C_i/C_{0i}			
1A	3.0	7	0.09	58.16	3.375	14.9	73.9	0.202	25.9	64.1	0.404	13.6	20.2	0.673			
1B	3.0	25	0.32	68.37	2.234	7.6	73.9	0.103	14.3	64.1	0.222	8.9	20.2	0.440			
1C	3.0	40	0.52	73.01	1.857	5.8	73.9	0.078	11.3	64.1	0.176	6.8	20.2	0.339			
1D	3.0	60	0.78	39.49	0.598	3.1	73.9	0.042	6.4	64.1	0.100	4.3	20.2	0.212			
Surface	3.0	77.38	1	-	-	0.0	73.9	0.000	0.0	64.1	0.000	0.0	20.2	0.000			

S2 EX5 Concentration Profile 5 (LA Grade Sand)						Full Mix			500-425 microns			425-355 microns			355-300 microns		
Sample Number	D/S Distance x (m)	Elevation z (mm)	z/H	Sample Volume (ℓ)	Sample Weight (g)	C (mg/ℓ)	C_0 (mg/ℓ)	C/C_0	C_i (mg/ℓ)	C_{0i} (mg/ℓ)	C_i/C_{0i}	C_i (mg/ℓ)	C_{0i} (mg/ℓ)	C_i/C_{0i}	C_i (mg/ℓ)	C_{0i} (mg/ℓ)	C_i/C_{0i}
1A	3.75	7	0.09	69.63	1.762	25.3	201.9	0.125	0.04	2.5	0.018	0.11	9.9	0.012	0.59	29.8	0.020
1B	3.75	25	0.32	72.25	0.982	13.6	201.9	0.067	0.04	2.5	0.017	0.04	9.9	0.004	0.36	29.8	0.012
1C	3.75	40	0.52	66.85	0.781	11.7	201.9	0.058	0.04	2.5	0.018	0.09	9.9	0.009	0.34	29.8	0.012
1D	3.75	60	0.78	68.70	0.471	6.9	201.9	0.034	0.06	2.5	0.024	0.06	9.9	0.006	0.15	29.8	0.005
Surface	3.75	77.38	1	-	-	0.0	201.9	0.000	0.00	2.5	0.000	0.00	9.9	0.000	0.00	29.8	0.000
						300-250 micron			250-212 microns			212-150 microns					
Sample Number	D/S Distance x (m)	Elevation z (mm)	z/H	Sample Volume (ℓ)	Sample Weight (g)	C_i (mg/ℓ)	C_{0i} (mg/ℓ)	C_i/C_{0i}	C_i (mg/ℓ)	C_{0i} (mg/ℓ)	C_i/C_{0i}	C_i (mg/ℓ)	C_{0i} (mg/ℓ)	C_i/C_{0i}			
1A	3.75	7	0.09	69.63	1.762	4.5	73.9	0.061	11.1	64.1	0.174	8.5	20.2	0.422			
1B	3.75	25	0.32	72.25	0.982	2.3	73.9	0.031	5.8	64.1	0.091	4.8	20.2	0.237			
1C	3.75	40	0.52	66.85	0.781	2.0	73.9	0.028	4.9	64.1	0.076	4.0	20.2	0.200			
1D	3.75	60	0.78	68.70	0.471	1.0	73.9	0.013	2.8	64.1	0.044	2.6	20.2	0.131			
Surface	3.75	77.38	1	-	-	0.0	73.9	0.000	0.0	64.1	0.000	0.0	20.2	0.000			

Appendix 6.9 Non-Dimensional Concentration Profiles for LA Sand

This appendix presents the relative concentration profiles for the LA grade sand, measured during three Series 2 experiments for (i) the overall sand grade and, (ii) for the six individual size fractions obtained from sieve analysis of concentration samples. The circular data points (joined by the dashed line) refer to the actual concentration measurements, while the solid coloured lines show the cubic spline approximation to the measured data, obtained for subsequent analysis.

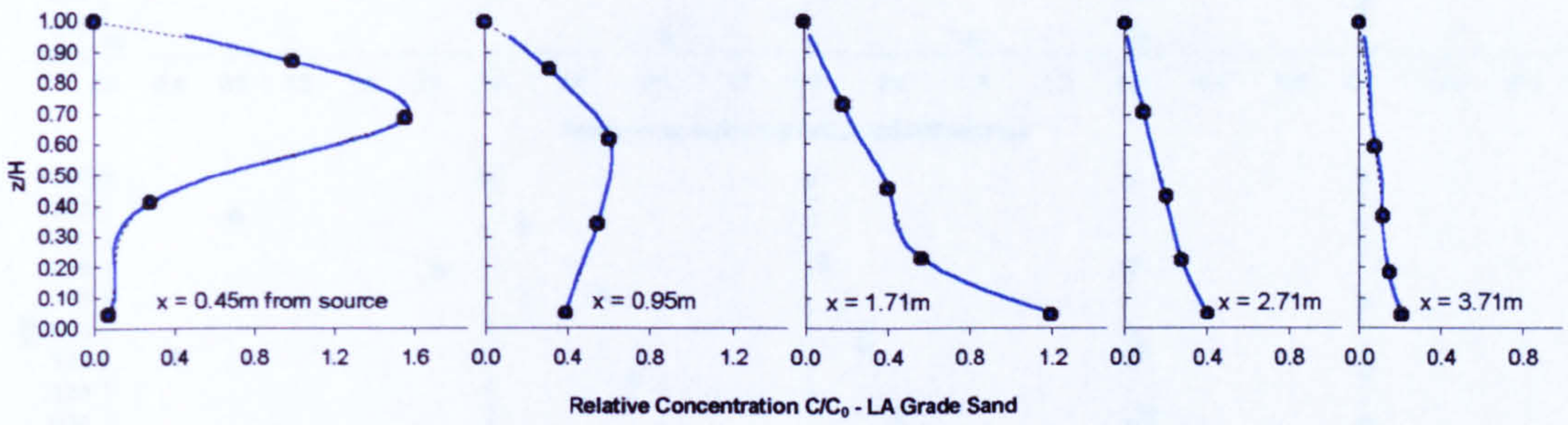

Figure A6.45 - Overall relative concentration profiles - Experiment S2_EX3

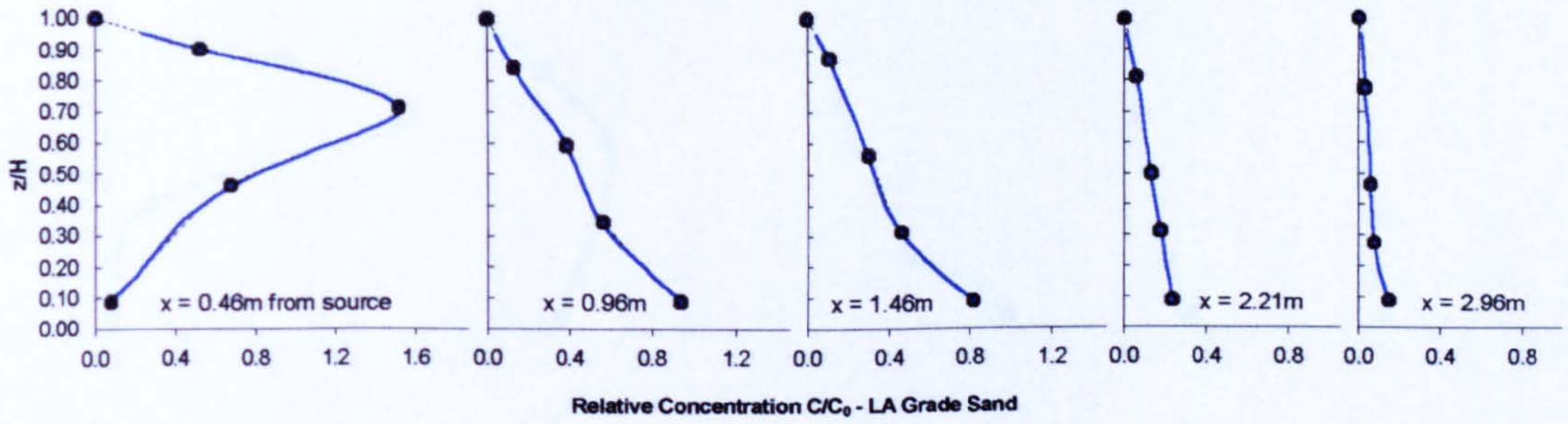

Figure A6.46 - Overall relative concentration profiles - Experiment S2_EX4

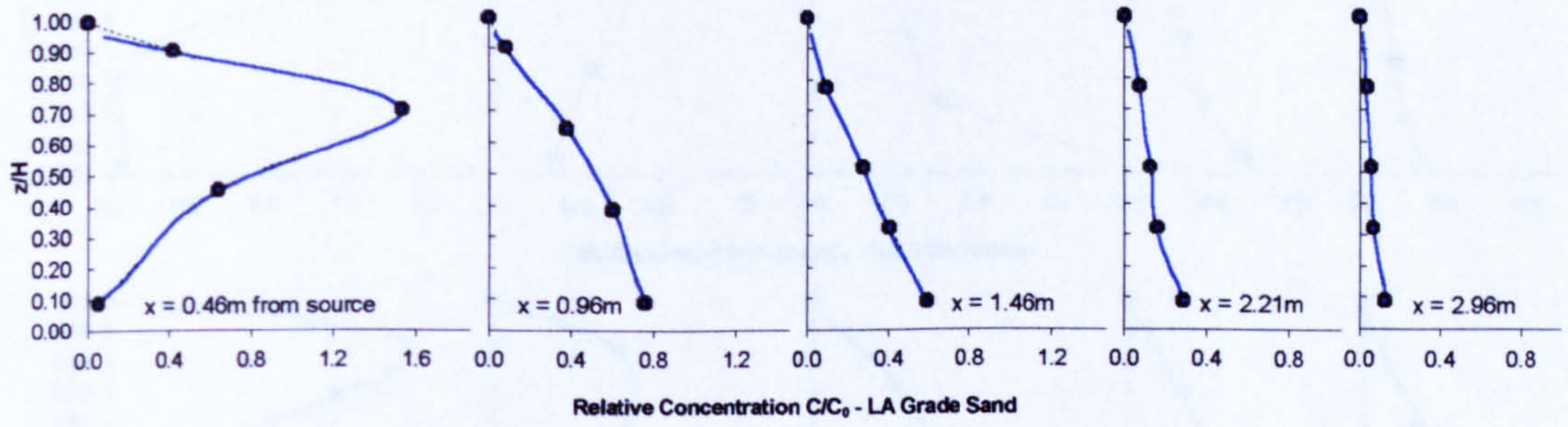

Figure A6.47 - Overall relative concentration profiles - Experiment S2_EX5

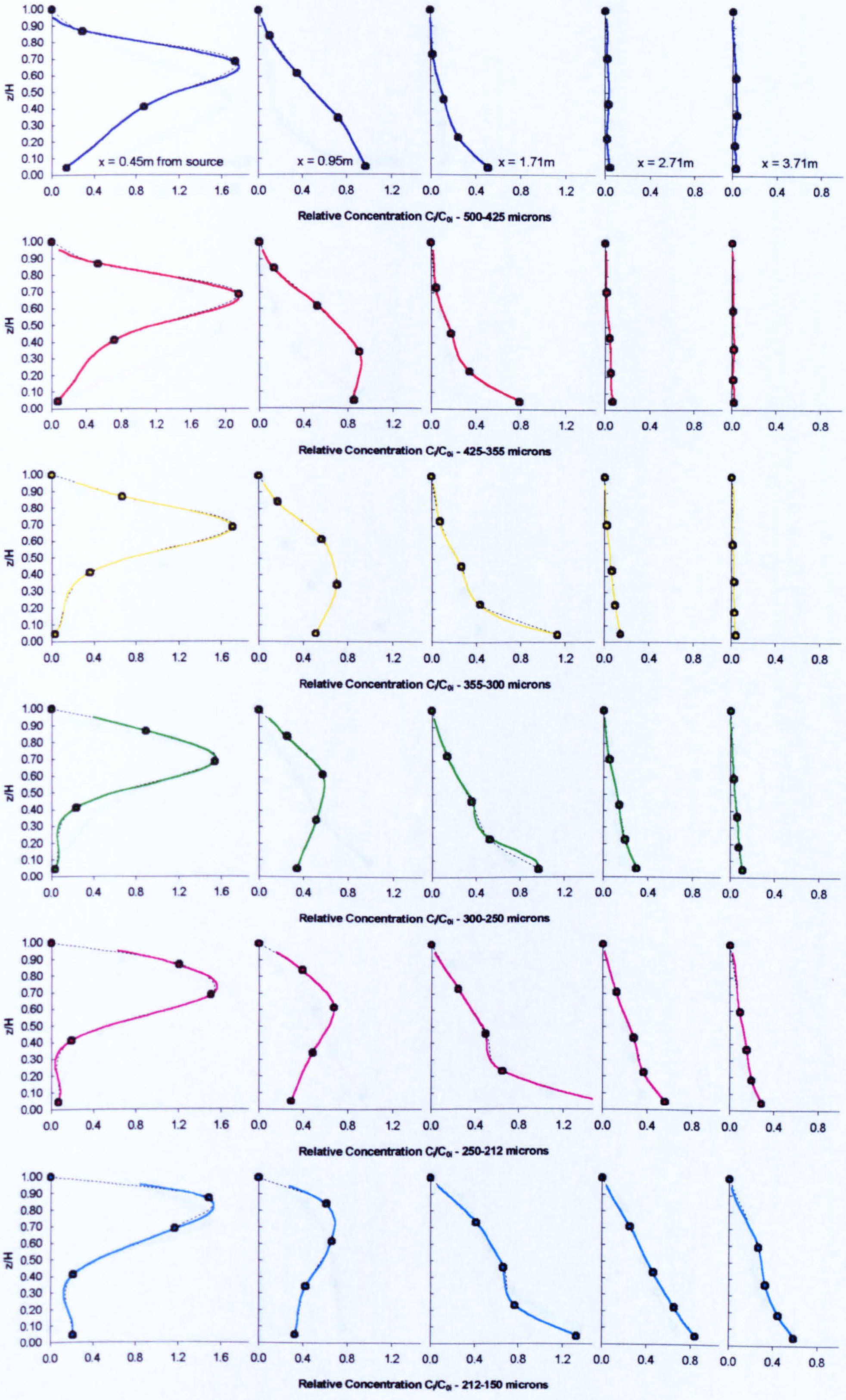

Figure A6.48 - Fractional relative concentration profiles - Experiment S2_EX3

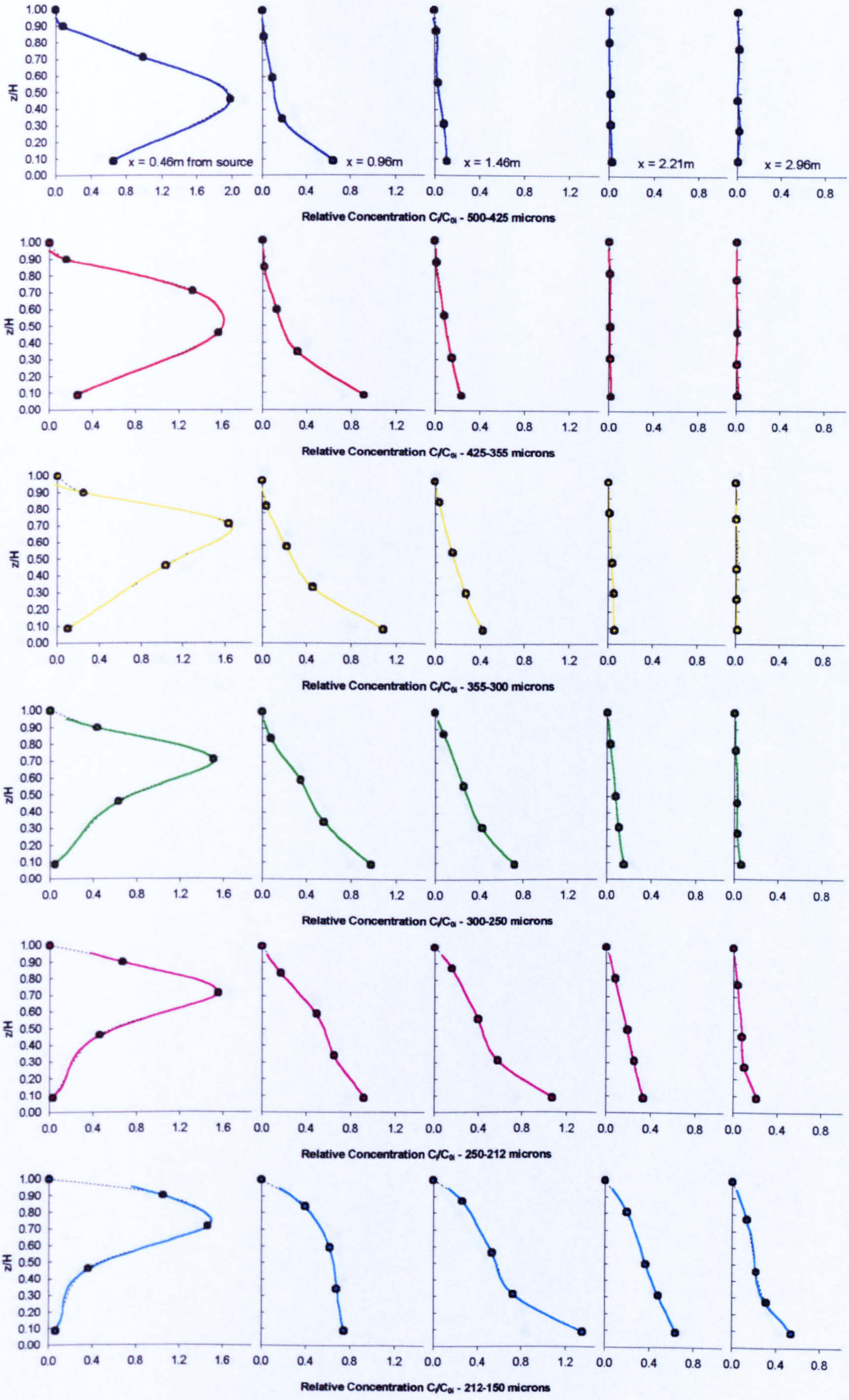

Figure A6.49 - Fractional relative concentration profiles - Experiment S2_EX4

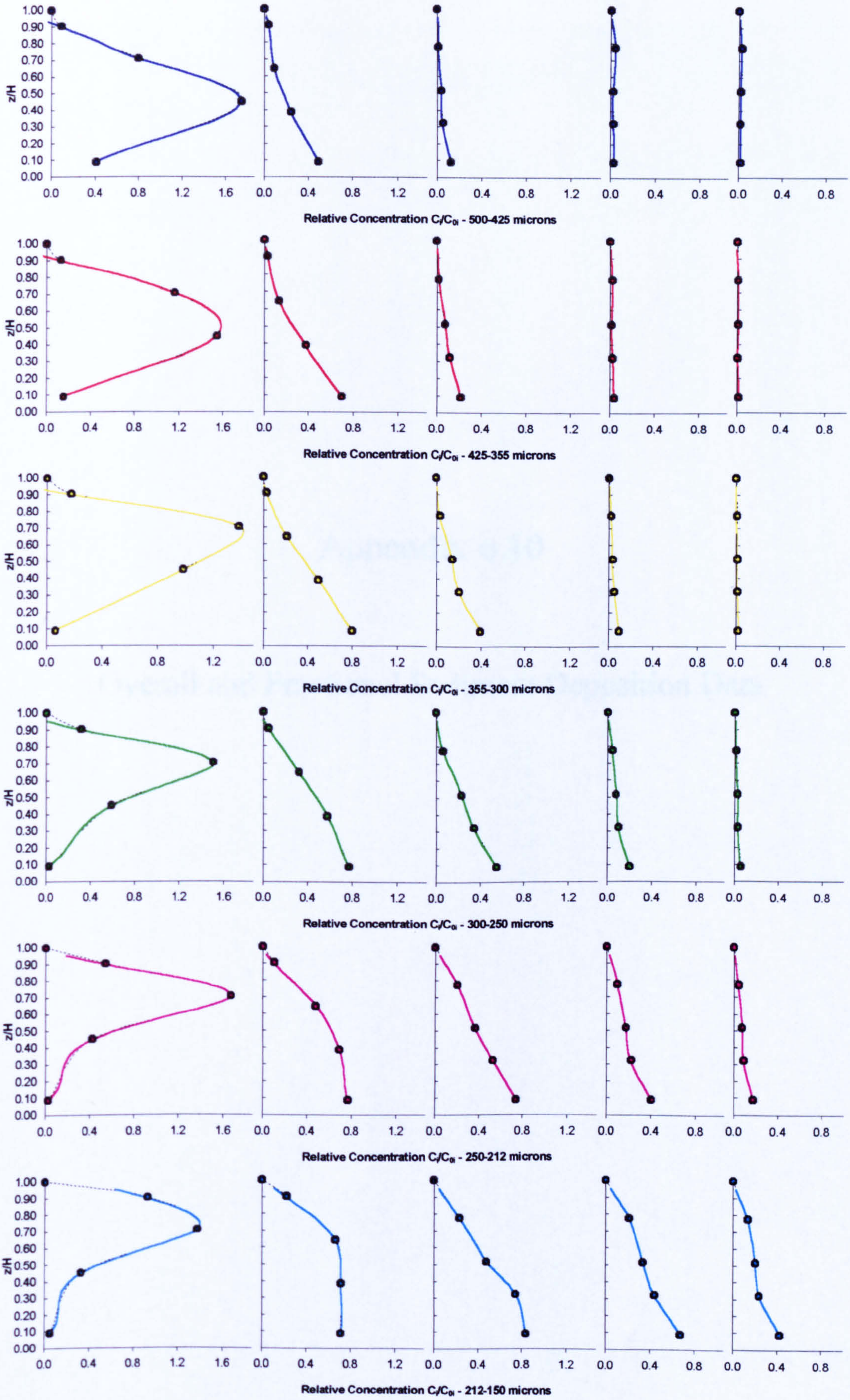

Figure A6.50 - Fractional relative concentration profiles - Experiment S2_EX5

Appendix 6.10

Overall and Fractional Sediment Deposition Data

S2_EXT1		Q = 0.0548 m^3s^{-1}			Bed Grade - S2_grv1 (10-25mm)			
		H = 0.117 m			Fines Grade - LA Grade Sand			
		Sediment Input Rates (I_R & I_{Ri}) and Initial Sediment Concentrations (C_0 & C_{0i})						
		Full Mix	500-425 μm	425-355 μm	355-300 μm	300-250 μm	250-212 μm	212-150 μm	6 500-150(μm)
Size Class Fraction		1.00	0.0122	0.0490	0.1476	0.3658	0.3175	0.1000	0.99
I_R ($g.s^{-1}$)		30.75	0.38	1.51	4.54	11.25	9.76	3.07	30.51
C_0 ($mg.\ell^{-1}$)		561.13	6.84	27.47	82.84	205.28	178.17	56.10	556.71
		Overall and Fractional Deposition Rates (D & D_i)							
Trap No.	$X_{AVE.}$ (m)	Full Mix Δ ($kg.s^{-1}.m^{-2}$)	500-425 μm Δ_i ($kg.s^{-1}.m^{-2}$)	425-355 μm Δ_i ($kg.s^{-1}.m^{-2}$)	355-300 μm Δ_i ($kg.s^{-1}.m^{-2}$)	300-250 μm Δ_i ($kg.s^{-1}.m^{-2}$)	250-212 μm Δ_i ($kg.s^{-1}.m^{-2}$)	212-150 μm Δ_i ($kg.s^{-1}.m^{-2}$)	6 500-150(μm) Δ ($kg.s^{-1}.m^{-2}$)
1A	0.291	0.00075	4.79E-06	0.00002	0.00003	0.00011	0.00020	0.00017	0.00053
1B	0.495	0.00168	0.00007	0.00014	0.00021	0.00039	0.00035	0.00019	0.00135
1C	0.702	0.00874	0.00041	0.00102	0.00184	0.00281	0.00169	0.00041	0.00817
2A	0.910	0.01972	0.00061	0.00192	0.00427	0.00700	0.00439	0.00099	0.01919
2B	1.117	0.02726	0.00051	0.00217	0.00579	0.01047	0.00647	0.00141	0.02682
2C	1.324	0.02373	0.00029	0.00152	0.00448	0.00941	0.00629	0.00143	0.02341
3A	1.531	0.02144	0.00020	0.00112	0.00528	0.00866	0.00476	0.00115	0.02115
3B	1.739	0.01758	0.00011	0.00073	0.00317	0.00745	0.00473	0.00116	0.01734
3C	1.946	0.01508	0.00006	0.00050	0.00216	0.00614	0.00476	0.00121	0.01483
4A	2.153	0.01207	0.00004	0.00032	0.00143	0.00487	0.00405	0.00110	0.01182
4B	2.361	0.00996	0.00003	0.00022	0.00101	0.00369	0.00362	0.00111	0.00967
4C	2.568	0.00908	0.00001	0.00015	0.00084	0.00340	0.00343	0.00102	0.00886
5A	2.775	0.00681	6.20E-06	0.00009	0.00049	0.00223	0.00277	0.00102	0.00661
5B	2.983	0.00538	0.00001	0.00005	0.00033	0.00166	0.00221	0.00091	0.00517
5C	3.190	0.00485	3.10E-06	0.00004	0.00026	0.00148	0.00205	0.00083	0.00466
6A	3.397	0.00403	4.65E-06	0.00003	0.00019	0.00114	0.00172	0.00075	0.00383
6B	3.604	0.00313	0	0.00002	0.00013	0.00083	0.00136	0.00062	0.00295
6C	3.812	0.00265	1.55E-06	0.00001	0.00010	0.00065	0.00114	0.00053	0.00244
7A	4.019	0.00222	0	0.00001	0.00006	0.00050	0.00096	0.00052	0.00205
7B	4.226	0.00213	1.55E-06	0.00001	0.00005	0.00046	0.00093	0.00050	0.00195
7C	4.434	0.00174	1.55E-06	4.65E-06	0.00004	0.00034	0.00075	0.00043	0.00156
8A	4.641	0.00146	0	3.10E-06	0.00002	0.00024	0.00060	0.00040	0.00127
8B	4.848	0.00133	0	3.10E-06	0.00002	0.00021	0.00053	0.00036	0.00113
8C	5.056	0.00107	0	1.55E-06	0.00001	0.00015	0.00042	0.00029	0.00087
9A	5.263	0.00096	1.55E-06	1.55E-06	0.00001	0.00013	0.00038	0.00026	0.00078
9B	5.470	0.00078	0	4.65E-06	0.00001	0.00009	0.00029	0.00022	0.00062
9C	5.677	0.00073	0	1.55E-06	6.20E-06	0.00008	0.00026	0.00022	0.00057
10A	5.885	0.00060	0	0	4.65E-06	0.00006	0.00021	0.00017	0.00045
10B	6.092	0.00057	1.55E-06	0	4.65E-06	0.00004	0.00018	0.00017	0.00040
10C	6.299	0.00058	3.10E-06	3.10E-06	6.20E-06	0.00004	0.00015	0.00015	0.00036
11A	6.507	0.00050	1.55E-06	1.55E-06	4.65E-06	0.00003	0.00013	0.00013	0.00031
11B	6.714	0.00038	0	1.55E-06	1.55E-06	0.00002	0.00009	0.00011	0.00022
11C	6.921	0.00035	0	1.55E-06	1.55E-06	0.00002	0.00008	0.00009	0.00020
12A	7.129	0.00035	0	0	1.55E-06	0.00002	0.00008	0.00009	0.00019
12B	7.336	0.00028	0	1.55E-06	1.55E-06	0.00002	0.00006	0.00006	0.00014
12C	7.543	0.00029	1.55E-06	0	1.55E-06	0.00001	0.00006	0.00007	0.00015
Average $\Im_{0i}$ ($kg.s^{-1}.m^{-2}$)		**0.00584**	**0.00007**	**0.00028**	**0.00090**	**0.00208**	**0.00173**	**0.00056**	**0.00561**
Average $\Im_{0i}$ ($g.s^{-1}.m^{-2}$)		**5.840**	**0.066**	**0.280**	**0.896**	**2.080**	**1.726**	**0.563**	**5.611**

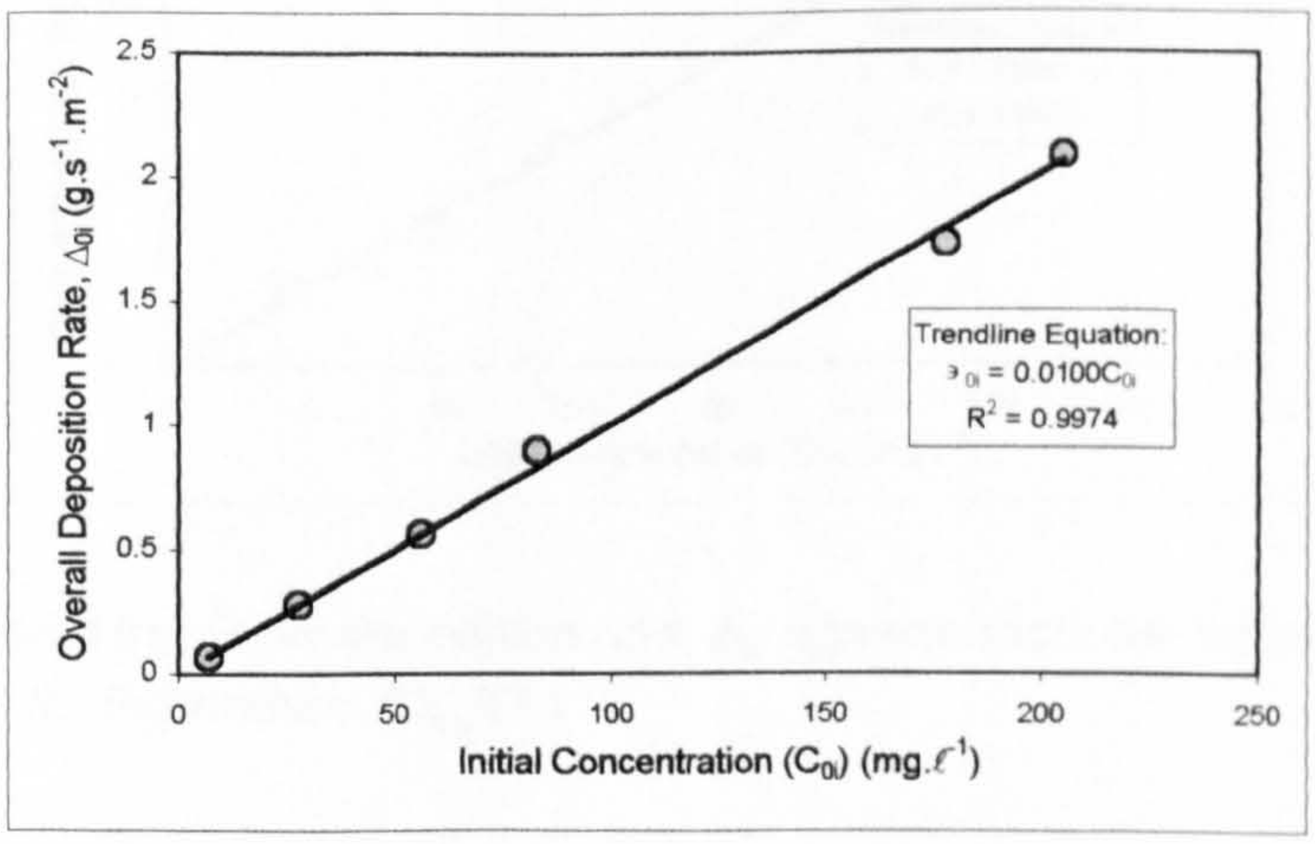

Figure A6.51 - Overall fractional deposition rate, Δ_{0i} against fractional initial concentration, C_{0i} for Experiment S2_EXT1

S2_EX1		Q = 0.0548 m^3s^{-1}			Bed Grade - S2_grv1 (10-25mm)			
		H = 0.109 m			Fines Grade - LA Grade Sand			
		Sediment Input Rates (I_R & I_{Ri}) and Initial Sediment Concentrations (C_0 & C_{0i})						
		Full Mix	500-425 μm	425-355 μm	355-300 μm	300-250 μm	250-212 μm	212-150 μm	6 500-150μm)
Size Class Fraction		1.00	0.0122	0.0490	0.1476	0.3658	0.3175	0.1000	0.99
I_R ($g.s^{-1}$)		21.10	0.26	1.03	3.12	7.72	6.70	2.11	20.93
C_0 ($mg.\ell^{-1}$)		385.04	4.69	18.85	56.85	140.86	122.26	38.49	382.00
		Overall and Fractional Deposition Rates (Δ & Δ_i)						
Trap No.	$X_{AVE.}$ (m)	Full Mix **Δ ($kg.s^{-1}.m^{-2}$)**	500-425 μm **Δ_i ($kg.s^{-1}.m^{-2}$)**	425-355 μm **Δ_i ($kg.s^{-1}.m^{-2}$)**	355-300 μm **Δ_i ($kg.s^{-1}.m^{-2}$)**	300-250 μm **Δ_i ($kg.s^{-1}.m^{-2}$)**	250-212 μm **Δ_i ($kg.s^{-1}.m^{-2}$)**	212-150 μm **Δ_i ($kg.s^{-1}.m^{-2}$)**	6 500-150μm) **Δ ($kg.s^{-1}.m^{-2}$)**
1A	0.336	0.00087	7.12E-06	0.00002	0.00006	0.00021	0.00030	0.00018	0.00077
1B	0.540	0.00212	0.00009	0.00023	0.00036	0.00061	0.00046	0.00017	0.00192
1C	0.747	0.00725	0.00031	0.00092	0.00159	0.00244	0.00134	0.00031	0.00692
2A	0.955	0.01234	0.00034	0.00126	0.00270	0.00459	0.00261	0.00056	0.01206
2B	1.162	0.01514	0.00029	0.00124	0.00336	0.00584	0.00348	0.00071	0.01492
2C	1.369	0.01390	0.00016	0.00088	0.00274	0.00574	0.00349	0.00073	0.01374
3A	1.576	0.01158	0.00009	0.00056	0.00198	0.00480	0.00328	0.00075	0.01145
3B	1.784	0.00932	0.00005	0.00034	0.00135	0.00376	0.00296	0.00075	0.00921
3C	1.991	0.00746	0.00003	0.00021	0.00095	0.00302	0.00249	0.00064	0.00734
4A	2.198	0.00736	0.00002	0.00017	0.00087	0.00312	0.00250	0.00060	0.00727
4B	2.406	0.00594	0.00001	0.00010	0.00056	0.00231	0.00223	0.00063	0.00584
4C	2.613	0.00451	0.00001	0.00006	0.00035	0.00164	0.00178	0.00058	0.00441
5A	2.820	0.00347	3.46E-06	0.00003	0.00021	0.00113	0.00146	0.00055	0.00338
5B	3.028	0.00297	1.73E-06	0.00002	0.00017	0.00097	0.00124	0.00046	0.00287
5C	3.235	0.00240	1.73E-06	0.00002	0.00012	0.00073	0.00103	0.00040	0.00230
6A	3.442	0.00200	0	0.00001	0.00009	0.00057	0.00087	0.00036	0.00191
6B	3.649	0.00160	1.73E-06	0.00001	0.00006	0.00042	0.00071	0.00031	0.00151
6C	3.857	0.00124	1.68E-06	0.00000	0.00004	0.00030	0.00054	0.00026	0.00115
7A	4.064	0.00107	1.73E-06	0.00000	0.00003	0.00024	0.00047	0.00024	0.00098
7B	4.271	0.00091	1.73E-06	0.00000	0.00002	0.00019	0.00040	0.00022	0.00083
7C	4.479	0.00082	0	1.73E-06	0.00002	0.00016	0.00035	0.00020	0.00073
8A	4.686	0.00063	1.73E-06	1.73E-06	0.00001	0.00011	0.00026	0.00017	0.00054
8B	4.893	0.00064	0	1.73E-06	0.00001	0.00009	0.00026	0.00018	0.00054
8C	5.101	0.00046	0	1.73E-06	0.00001	0.00006	0.00017	0.00013	0.00038
9A,B,C	5.515	0.00040	1.15E-06	1.15E-06	0.00001	0.00005	0.00015	0.00011	0.00032
10A,B,C	6.137	0.00027	5.76E-07	1.15E-06	2.30E-06	0.00002	0.00008	0.00008	0.00019
11A,B,C	6.759	0.00022	5.76E-07	1.15E-06	2.88E-06	0.00002	0.00006	0.00006	0.00014
12A,B,C	7.381	0.00017	1.15E-06	5.76E-07	1.73E-06	0.00001	0.00004	0.00004	0.00010
Average Δ_{0i} ($kg.s^{-1}.m^{-2}$)		0.00331	0.00004	0.00017	0.00049	0.00120	0.00099	0.00030	0.00320
Average Δ_{0i} ($g.s^{-1}.m^{-2}$)		**3.310**	**0.040**	**0.170**	**0.492**	**1.204**	**0.991**	**0.304**	**3.201**

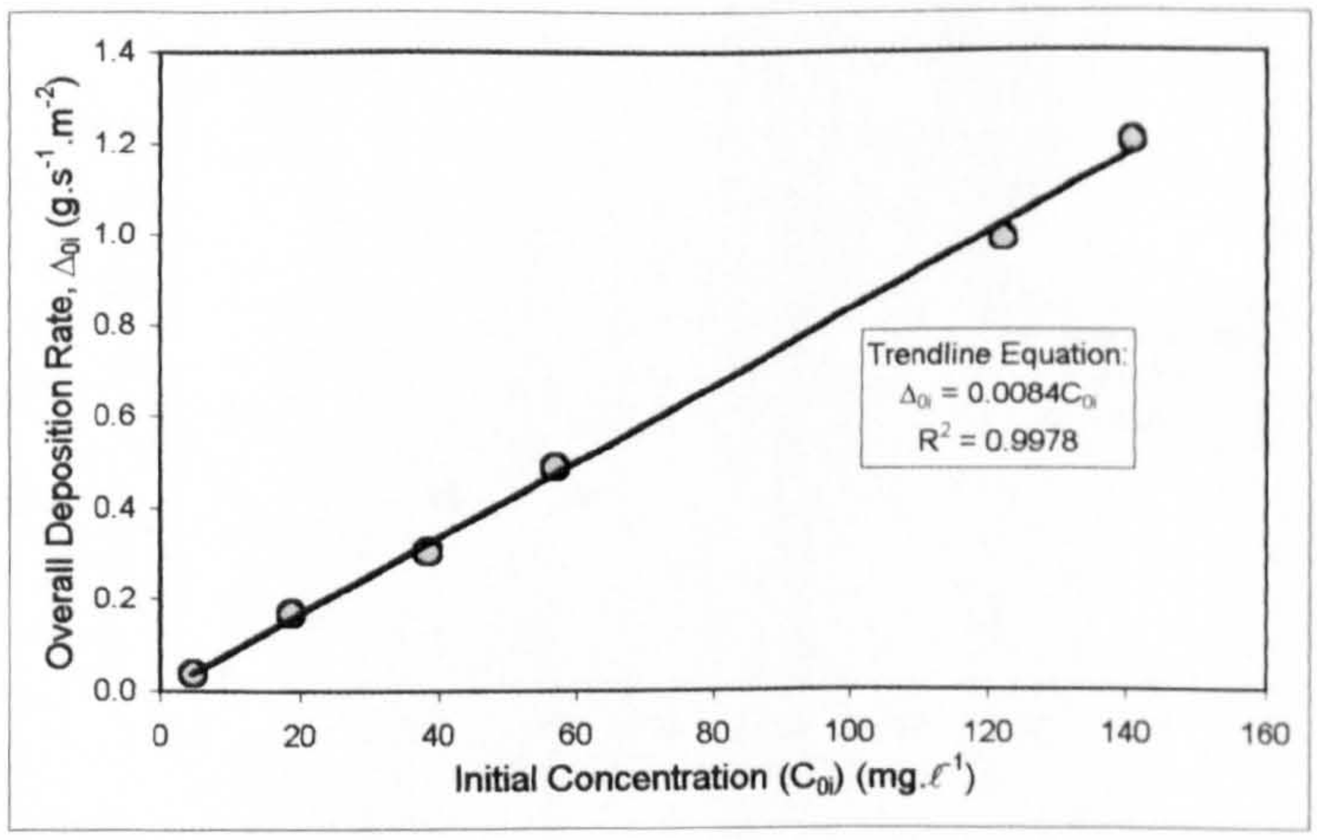

Figure A6.52 - Overall fractional deposition rate, Δ_{0i} against fractional initial concentration, C_{0i} for Experiment S2_EX1

S2_EX2	Q = 0.0547 m^3s^{-1}			Bed Grade - S2_grv1 (10-25mm)			
	H = 0.111 m			Fines Grade - LA Grade Sand			
	Sediment Input Rates (I_R & I_{Ri}) and Initial Sediment Concentrations (C_0 & C_{0i})						
	Full Mix	500-425 Πm	425-355 Πm	355-300 Πm	300-250 Πm	250-212 Πm	212-150 Πm	6 500-150Πm)
Size Class Fraction, fi	1.00	0.0122	0.0490	0.1476	0.3658	0.3175	0.1000	0.99
I_R ($g.s^{-1}$)	5.97	0.07	0.29	0.88	2.19	1.90	0.60	5.93
C_0 ($mg.\ell^{-1}$)	109.21	1.33	5.35	16.12	39.95	34.68	10.92	108.35
	Overall and Fractional Deposition Rates (Δ & Δ_i)						
Trap No. $X_{AVE.}$ (m)	Total **Δ ($kg.s^{-1}.m^{-2}$)**	500-425 Πm **Δ_i ($kg.s^{-1}.m^{-2}$)**	425-355 Πm **Δ_i ($kg.s^{-1}.m^{-2}$)**	355-300 Πm **Δ_i ($kg.s^{-1}.m^{-2}$)**	300-250 Πm **Δ_i ($kg.s^{-1}.m^{-2}$)**	250-212 Πm **Δ_i ($kg.s^{-1}.m^{-2}$)**	212-150 Πm **Δ_i ($kg.s^{-1}.m^{-2}$)**	6 500-150Πm) **Δ ($kg.s^{-1}.m^{-2}$)**
1A 0.151	0.00069	2.13E-06	0.00001	0.00004	0.00017	0.00029	0.00017	0.00067
1B 0.355	0.00057	0.00001	0.00003	0.00005	0.00015	0.00019	0.00010	0.00053
1C 0.562	0.00132	0.00004	0.00014	0.00021	0.00039	0.00032	0.00014	0.00124
2A 0.770	0.00261	0.00010	0.00029	0.00054	0.00088	0.00055	0.00015	0.00251
2B 0.977	0.00312	0.00007	0.00030	0.00062	0.00117	0.00072	0.00019	0.00306
2C 1.184	0.00329	0.00005	0.00027	0.00064	0.00128	0.00080	0.00020	0.00324
3A 1.391	0.00336	0.00003	0.00020	0.00059	0.00133	0.00092	0.00024	0.00331
3B 1.599	0.00290	0.00002	0.00014	0.00043	0.00116	0.00087	0.00024	0.00285
3C 1.806	0.00233	0.00001	0.00008	0.00030	0.00090	0.00077	0.00023	0.00229
4A 2.013	0.00220	0.00001	0.00007	0.00027	0.00086	0.00075	0.00022	0.00217
4B 2.221	0.00176	4.13E-06	0.00004	0.00017	0.00062	0.00067	0.00021	0.00172
4C 2.428	0.00171	4.13E-06	0.00003	0.00015	0.00062	0.00065	0.00021	0.00167
5A 2.635	0.00131	1.03E-06	0.00002	0.00010	0.00043	0.00052	0.00021	0.00127
5B 2.843	0.00101	1.03E-06	0.00001	0.00007	0.00032	0.00041	0.00016	0.00098
5C 3.050	0.00091	1.03E-06	0.00001	0.00006	0.00028	0.00038	0.00015	0.00088
6A 3.257	0.00080	0	0.00001	0.00004	0.00022	0.00034	0.00016	0.00076
6B 3.464	0.00063	1.03E-06	4.13E-06	0.00003	0.00017	0.00027	0.00012	0.00060
6C 3.672	0.00058	0	3.10E-06	0.00002	0.00015	0.00025	0.00018	0.00060
7A 3.879	0.00047	0	2.07E-06	0.00001	0.00010	0.00020	0.00012	0.00044
7B 4.086	0.00038	1.03E-06	1.03E-06	0.00001	0.00008	0.00016	0.00010	0.00035
7C 4.294	0.00033	0	2.07E-06	0.00001	0.00006	0.00014	0.00009	0.00030
8A 4.501	0.00027	1.03E-06	1.03E-06	0.00001	0.00005	0.00011	0.00008	0.00024
8B 4.708	0.00026	0	2.07E-06	4.13E-06	0.00004	0.00010	0.00008	0.00023
8C 4.916	0.00025	1.03E-06	0	4.13E-06	0.00004	0.00010	0.00008	0.00023
9A,B,C 5.330	0.00018	3.45E-07	3.45E-07	2.76E-06	0.00002	0.00007	0.00005	0.00015
10A,B,C 5.952	0.00013	3.45E-07	6.89E-07	2.41E-06	0.00002	0.00005	0.00004	0.00011
11A,B,C 6.574	0.00010	3.45E-07	6.89E-07	1.38E-06	0.00001	0.00003	0.00003	0.00007
12A,B,C 7.196	0.00007	3.45E-07	3.45E-07	1.03E-06	0.00001	0.00002	0.00002	0.00005
Average $\Im_{0i}$ ($kg.s^{-1}.m^{-2}$)	0.00096	0.00001	0.00005	0.00012	0.00032	0.00030	0.00012	0.00092
Average $\Im_{0i}$ ($g.s^{-1}.m^{-2}$)	**0.96**	**0.01**	**0.05**	**0.12**	**0.32**	**0.30**	**0.12**	**0.92**

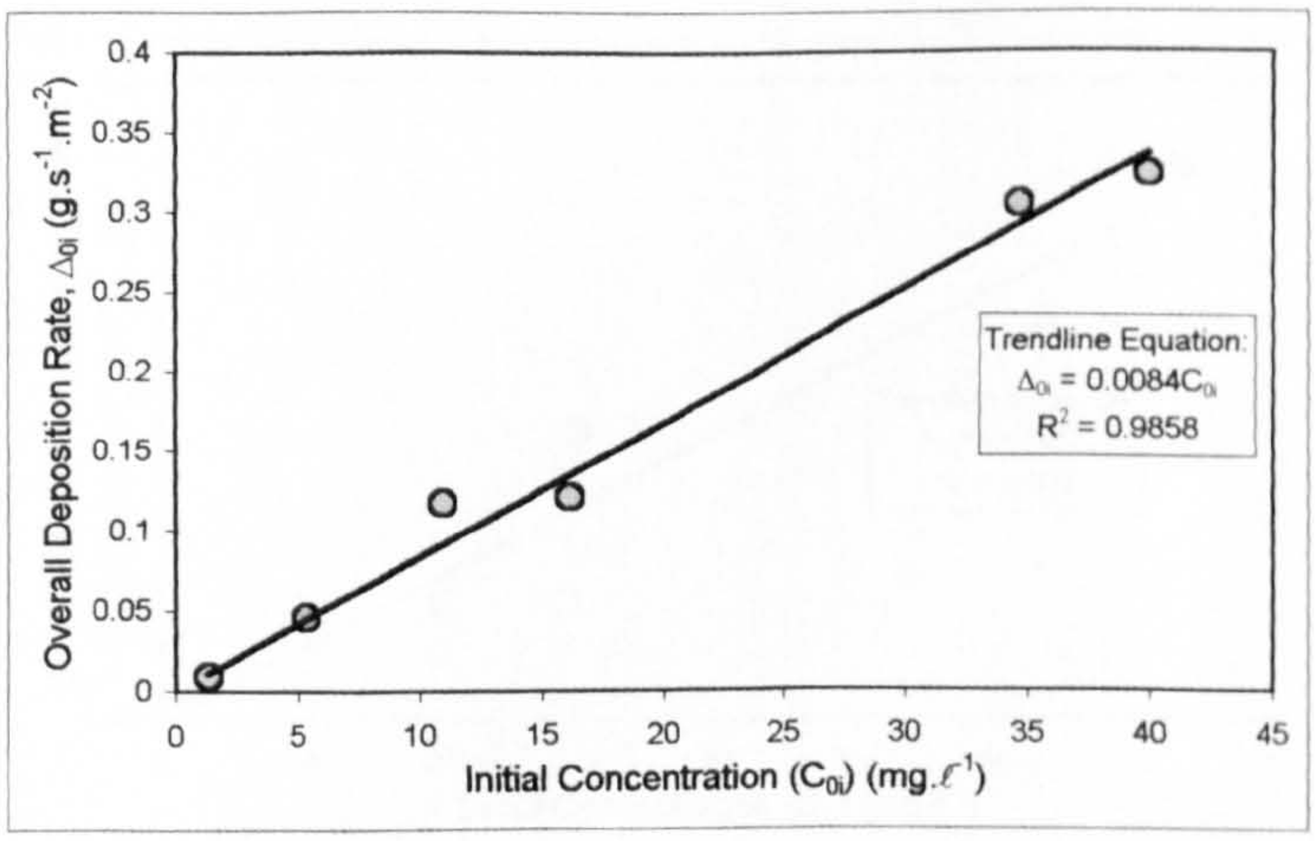

Figure A6.53 - Overall fractional deposition rate, Δ_{0i} against fractional initial concentration, C_{0i} for Experiment S2_EX2

S2_EX3		Q = 0.0547 m^3s^{-1}			Bed Grade - S2_grv1 (10-25mm)			
		H = 0.11 m			Fines Grade - LA Grade Sand			
		Sediment Input Rates (I_R & I_{Ri}) and Initial Sediment Concentrations (C_0 & C_{0i})						
		Full Mix	500-425 μm	425-355 μm	355-300 μm	300-250 μm	250-212 μm	212-150 μm	δ 500-150(μm)
I_R ($g.s^{-1}$)		10.89	0.13	0.53	1.61	3.98	3.46	1.09	10.80
C_0 ($mg.\ell^{-1}$)		199.04	2.43	9.75	29.39	72.81	63.20	19.90	197.47
		Overall and Fractional Deposition Rates (Δ & Δ_i)							
Trap No.	X_{AVE} (m)	Total Δ ($kg.s^{-1}.m^{-2}$)	500-425 μm Δ_i ($kg.s^{-1}.m^{-2}$)	425-355 μm Δ_i ($kg.s^{-1}.m^{-2}$)	355-300 μm Δ_i ($kg.s^{-1}.m^{-2}$)	300-250 μm Δ_i ($kg.s^{-1}.m^{-2}$)	250-212 μm Δ_i ($kg.s^{-1}.m^{-2}$)	212-150 μm Δ_i ($kg.s^{-1}.m^{-2}$)	δ 500-150(μm) Δ ($kg.s^{-1}.m^{-2}$)
1A									
1B									
1C									
2A	0.145	0.00028	7.75E-07	4.65E-06	0.00001	0.00006	0.00011	0.00007	0.00026
2B	0.352	0.00026	1.55E-06	4.65E-06	0.00001	0.00005	0.00010	0.00007	0.00024
2C	0.559	0.00042	0.00002	0.00003	0.00004	0.00007	0.00010	0.00007	0.00033
3A	0.766	0.00210	0.00017	0.00037	0.00046	0.00052	0.00028	0.00010	0.00189
3B	0.974	0.00443	0.00026	0.00073	0.00116	0.00135	0.00064	0.00012	0.00427
3C	1.181	0.00662	0.00024	0.00084	0.00182	0.00234	0.00107	0.00020	0.00651
4A	1.388	0.00725	0.00015	0.00072	0.00210	0.00274	0.00125	0.00023	0.00719
4B	1.596	0.00683	0.00008	0.00051	0.00179	0.00280	0.00135	0.00026	0.00679
4C	1.803	0.00575	0.00002	0.00032	0.00155	0.00239	0.00118	0.00024	0.00570
5A	2.010	0.00520	0.00002	0.00021	0.00101	0.00236	0.00130	0.00028	0.00518
5B	2.218	0.00402	0.00001	0.00012	0.00059	0.00177	0.00122	0.00029	0.00400
5C	2.425	0.00330	0.00001	0.00007	0.00042	0.00141	0.00110	0.00028	0.00328
6A	2.632	0.00277	0.00001	0.00005	0.00029	0.00113	0.00099	0.00027	0.00274
6B	2.839	0.00213	1.55E-06	0.00003	0.00018	0.00083	0.00083	0.00024	0.00210
6C	3.047	0.00177	1.55E-06	0.00002	0.00013	0.00067	0.00071	0.00022	0.00175
7A	3.254	0.00143	1.55E-06	0.00001	0.00008	0.00050	0.00060	0.00021	0.00141
7B	3.461	0.00120	7.75E-07	0.00001	0.00007	0.00040	0.00053	0.00018	0.00118
7C	3.669	0.00097	7.75E-07	4.65E-06	0.00004	0.00028	0.00044	0.00018	0.00095
8A	3.876	0.00083	0	4.65E-06	0.00003	0.00024	0.00038	0.00016	0.00081
8B	4.083	0.00068	0	2.33E-06	0.00002	0.00018	0.00032	0.00014	0.00066
8C	4.291	0.00058	7.75E-07	1.55E-06	0.00002	0.00014	0.00026	0.00013	0.00056
9A,B,C	4.705	0.00041	2.58E-07	1.03E-06	0.00001	0.00010	0.00020	0.00009	0.00039
10A,B,C	5.327	0.00025	2.58E-07	7.75E-07	4.39E-06	0.00005	0.00011	0.00007	0.00024
11A,B,C	5.949	0.00016	0	5.17E-07	2.33E-06	0.00002	0.00007	0.00005	0.00015
12A,B,C	6.571	0.00012	2.58E-07	5.17E-07	1.29E-06	0.00001	0.00005	0.00004	0.00010
Average Δ_{0i} ($kg.s^{-1}.m^{-2}$)		0.00187	0.00003	0.00012	0.00036	0.00069	0.00049	0.00014	0.00183
Average Δ_{0i} ($g.s^{-1}.m^{-2}$)		**1.87**	**0.03**	**0.12**	**0.36**	**0.69**	**0.49**	**0.14**	**1.83**

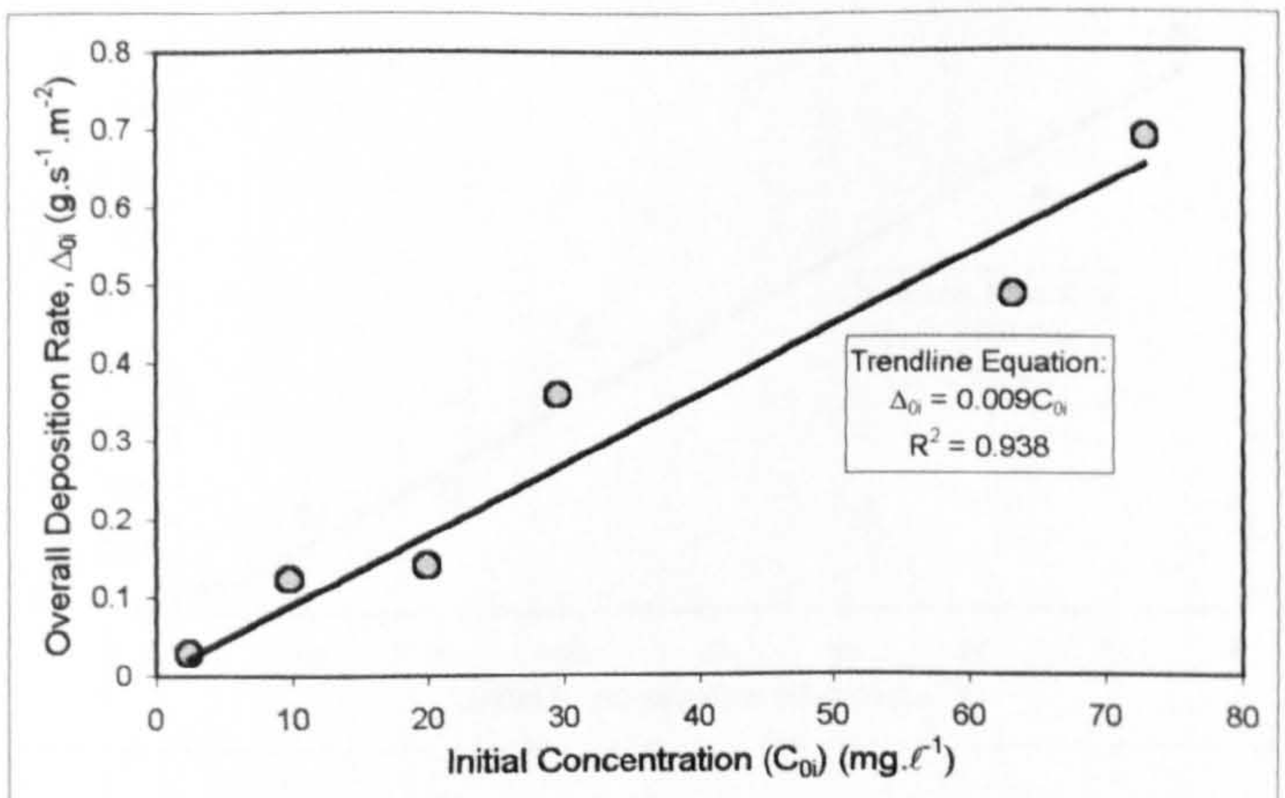

Figure A6.54 - Overall fractional deposition rate, Δ_{0i} against fractional initial concentration, C_{0i} for Experiment S2_EX3

S2_EX4		Q = 0.0361 $m^3.s^{-1}$			Bed Grade - S2_grv1 (10-25mm)			
		H = 0.08 m			Fines Grade - LA Grade Sand			
		Sediment Input Rates (I_R & I_{Ri}) and Initial Sediment Concentrations (C_0 & C_{0i})						
		Full Mix	500-425 μm	425-355 μm	355-300 μm	300-250 μm	250-212 μm	212-150 μm	6 500-150(μm)
I_R ($g.s^{-1}$)		7.41	0.09	0.36	1.09	2.71	2.35	0.74	7.35
C_0 ($mg.\ell^{-1}$)		205.32	2.50	10.05	30.31	75.11	65.19	20.53	203.70
		Overall and Fractional Deposition Rates (Δ & Δ_i)							
Trap No.	X_{AVE} (m)	Total Δ ($kg.s^{-1}.m^{-2}$)	500-425 μm Δ_i ($kg.s^{-1}.m^{-2}$)	425-355 μm Δ_i ($kg.s^{-1}.m^{-2}$)	355-300 μm Δ_i ($kg.s^{-1}.m^{-2}$)	300-250 μm Δ_i ($kg.s^{-1}.m^{-2}$)	250-212 μm Δ_i ($kg.s^{-1}.m^{-2}$)	212-150 μm Δ_i ($kg.s^{-1}.m^{-2}$)	6 500-150(μm) Δ ($kg.s^{-1}.m^{-2}$)
1A									
1B									
1C									
2A	0.150	0.00008	8.79E-07	2.64E-06	4.39E-06	0.00001	0.00002	0.00002	0.00006
2B	0.357	0.00012	0.00001	0.00001	0.00001	0.00001	0.00002	0.00002	0.00008
2C	0.564	0.00127	0.00016	0.00028	0.00029	0.00025	0.00010	0.00003	0.00111
3A	0.771	0.00578	0.00028	0.00095	0.00167	0.00189	0.00075	0.00012	0.00566
3B	0.979	0.00729	0.00012	0.00071	0.00202	0.00292	0.00127	0.00021	0.00724
3C	1.186	0.00626	0.00005	0.00035	0.00141	0.00277	0.00141	0.00025	0.00624
4A	1.393	0.00516	0.00002	0.00017	0.00088	0.00231	0.00146	0.00030	0.00515
4B	1.601	0.00330	0.00001	0.00007	0.00040	0.00139	0.00113	0.00027	0.00328
4C	1.808	0.00295	4.39E-06	0.00004	0.00030	0.00131	0.00103	0.00024	0.00293
5A	2.015	0.00202	1.76E-06	0.00002	0.00016	0.00074	0.00083	0.00024	0.00200
5B	2.223	0.00140	8.79E-07	0.00001	0.00008	0.00046	0.00062	0.00022	0.00138
5C	2.430	0.00108	8.79E-07	0.00001	0.00006	0.00034	0.00049	0.00018	0.00106
6A	2.637	0.00086	8.79E-07	3.51E-06	0.00004	0.00024	0.00041	0.00016	0.00084
6B	2.844	0.00060	8.79E-07	1.76E-06	0.00002	0.00014	0.00029	0.00014	0.00059
6C	3.052	0.00042	0	1.76E-06	0.00001	0.00010	0.00020	0.00010	0.00041
7A	3.259	0.00038	8.79E-07	8.79E-07	0.00001	0.00007	0.00018	0.00010	0.00036
7B	3.466	0.00028	8.79E-07	8.79E-07	0.00001	0.00005	0.00013	0.00008	0.00027
7C	3.674	0.00022	0	8.79E-07	3.51E-06	0.00004	0.00010	0.00007	0.00021
8A	3.881	0.00019	8.79E-07	8.79E-07	2.64E-06	0.00002	0.00008	0.00006	0.00017
8B	4.088	0.00014	0	8.79E-07	1.76E-06	0.00002	0.00005	0.00005	0.00012
8C	4.296	0.00013	8.79E-07	0	1.76E-06	0.00001	0.00005	0.00005	0.00011
9A,B,C	4.710	0.00009	2.93E-07	5.86E-07	8.79E-07	0.00001	0.00003	0.00003	0.00008
10A,B,C	5.332	0.00005	2.93E-07	2.93E-07	5.86E-07	3.81E-06	0.00002	0.00002	0.00004
11A,B,C	5.954	0.00003	2.93E-07	2.93E-07	2.93E-07	1.76E-06	0.00001	0.00001	0.00002
12A,B,C	6.576	0.00003	2.93E-07	2.93E-07	2.93E-07	1.17E-06	4.69E-06	0.00001	0.00002
Average Δ_{0i} ($kg.s^{-1}.m^{-2}$)		0.00123	0.00002	0.00008	0.00022	0.00046	0.00033	0.00009	0.00120
Average Δ_{0i} ($g.s^{-1}.m^{-2}$)		**1.23**	**0.02**	**0.08**	**0.22**	**0.46**	**0.33**	**0.09**	**1.20**

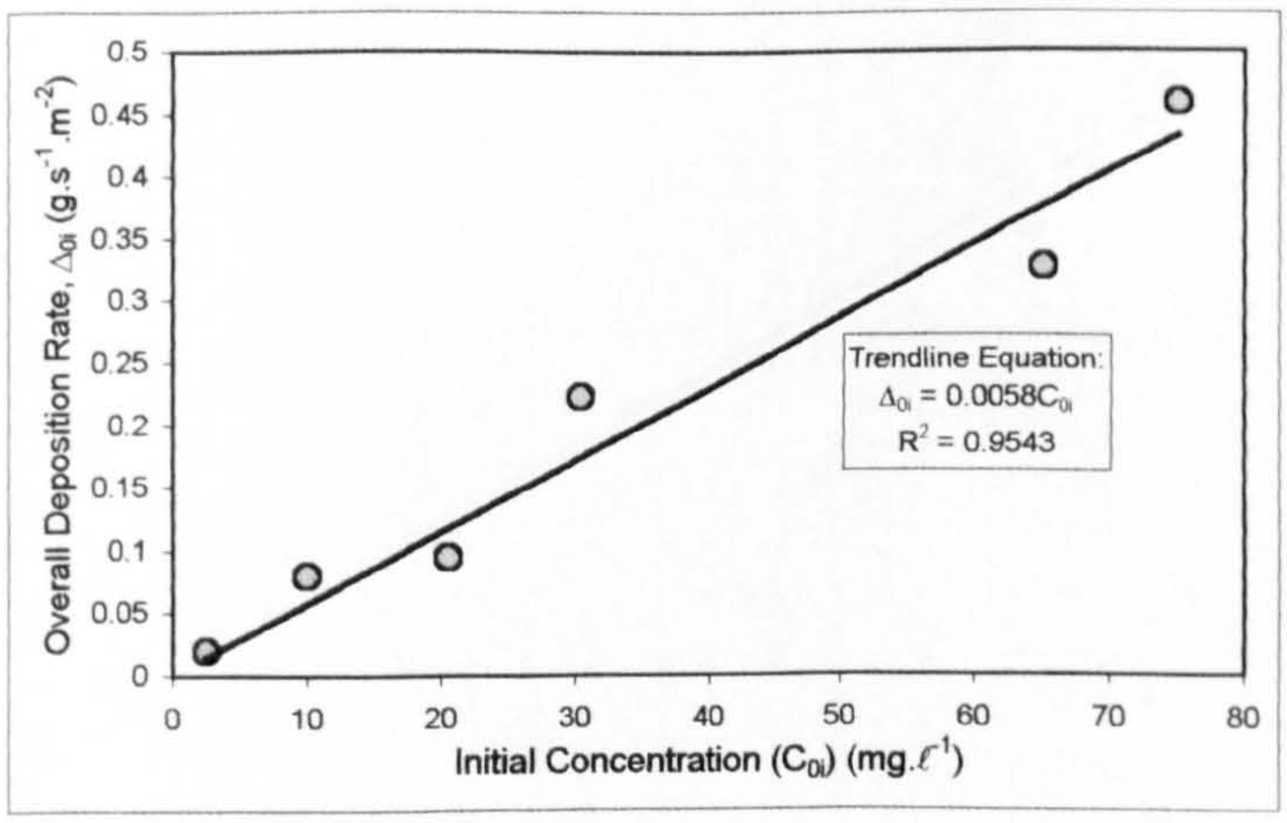

Figure A6.55 - Overall fractional deposition rate, Δ_{0i} against fractional initial concentration, C_{0i} for Experiment S2_EX4

S2_EX5	Q = 0.0362 $m^3.s^{-1}$			Bed Grade - S2_grv2 (5-10mm)			
	H = 0.077 m			Fines Grade - LA Grade Sand			
	Sediment Input Rates (I_R & I_{Ri}) and Initial Sediment Concentrations (C_0 & C_{0i})						
	Full Mix	500-425 μm	425-355 μm	355-300 μm	300-250 μm	250-212 μm	212-150 μm	6 (500-150 μm)
I_R ($g.s^{-1}$)	7.31	0.09	0.36	1.08	2.67	2.32	0.73	7.25
C_0 ($mg.\ell^{-1}$)	201.81	2.46	9.88	29.80	73.83	64.08	20.17	200.22
	Overall and Fractional Deposition Rates (Δ & Δ_i)							
Trap No. / X_{AVE} (m)	Total Δ ($kg.s^{-1}.m^{-2}$)	500-425 μm Δ_i ($kg.s^{-1}.m^{-2}$)	425-355 μm Δ_i ($kg.s^{-1}.m^{-2}$)	355-300 μm Δ_i ($kg.s^{-1}.m^{-2}$)	300-250 μm Δ_i ($kg.s^{-1}.m^{-2}$)	250-212 μm Δ_i ($kg.s^{-1}.m^{-2}$)	212-150 μm Δ_i ($kg.s^{-1}.m^{-2}$)	6 (500-150 μm) Δ ($kg.s^{-1}.m^{-2}$)
1A								
1B								
1C								
2A 0.150	0.00007	8.79E-07	1.76E-06	3.51E-06	0.00001	0.00002	0.00003	0.00006
2B 0.357	0.00010	0.00001	0.00001	0.00001	0.00001	0.00002	0.00002	0.00007
2C 0.564	0.00124	0.00014	0.00026	0.00029	0.00026	0.00010	0.00005	0.00110
3A 0.771	0.00581	0.00027	0.00090	0.00159	0.00192	0.00085	0.00014	0.00569
3B 0.979	0.00735	0.00012	0.00065	0.00181	0.00291	0.00155	0.00027	0.00730
3C 1.186	0.00685	0.00005	0.00036	0.00145	0.00296	0.00167	0.00033	0.00682
4A 1.393	0.00544	0.00002	0.00018	0.00090	0.00236	0.00162	0.00033	0.00541
4B 1.601	0.00408	0.00001	0.00008	0.00049	0.00174	0.00142	0.00034	0.00407
4C 1.808	0.00300	3.51E-06	0.00004	0.00027	0.00115	0.00119	0.00033	0.00299
5A 2.015	0.00188	1.76E-06	0.00002	0.00013	0.00068	0.00078	0.00025	0.00187
5B 2.223	0.00132	8.79E-07	0.00001	0.00007	0.00042	0.00058	0.00022	0.00131
5C 2.430	0.00116	8.79E-07	0.00001	0.00005	0.00036	0.00052	0.00021	0.00115
6A 2.637	0.00082	8.79E-07	2.64E-06	0.00003	0.00021	0.00039	0.00016	0.00081
6B 2.844	0.00058	0	8.79E-07	0.00002	0.00013	0.00028	0.00014	0.00057
6C 3.052	0.00043	0	1.76E-06	0.00001	0.00009	0.00020	0.00011	0.00042
7A 3.259	0.00033	8.79E-07	8.79E-07	0.00001	0.00006	0.00016	0.00009	0.00032
7B 3.466	0.00025	0	1.76E-06	4.39E-06	0.00004	0.00012	0.00008	0.00024
7C 3.674	0.00021	0	8.79E-07	2.64E-06	0.00003	0.00009	0.00007	0.00020
8A 3.881	0.00016	8.79E-07	8.79E-07	1.76E-06	0.00002	0.00007	0.00006	0.00014
8B 4.088	0.00012	8.79E-07	8.79E-07	8.79E-07	0.00001	0.00005	0.00005	0.00011
8C 4.296	0.00010	0	0	1.76E-06	0.00001	0.00004	0.00004	0.00009
9A,B,C 4.710	0.00007	1.76E-06	2.93E-07	1.17E-06	0.00001	0.00003	0.00003	0.00006
10A,B,C 5.332	0.00004	2.93E-07	5.86E-07	2.93E-07	2.05E-06	0.00001	0.00002	0.00003
11A,B,C 5.954	0.00003	2.93E-07	2.93E-07	2.93E-07	8.79E-07	4.98E-06	0.00001	0.00002
12A,B,C 6.576	0.00002	0	2.93E-07	2.93E-07	2.93E-07	2.34E-06	0.00001	0.00001
Average Δ_{0i} ($kg.s^{-1}.m^{-2}$)	0.00127	0.00002	0.00008	0.00022	0.00047	0.00036	0.00011	0.00125
Average Δ_{0i} ($g.s^{-1}.m^{-2}$)	**1.27**	**0.02**	**0.08**	**0.22**	**0.47**	**0.36**	**0.11**	**1.25**

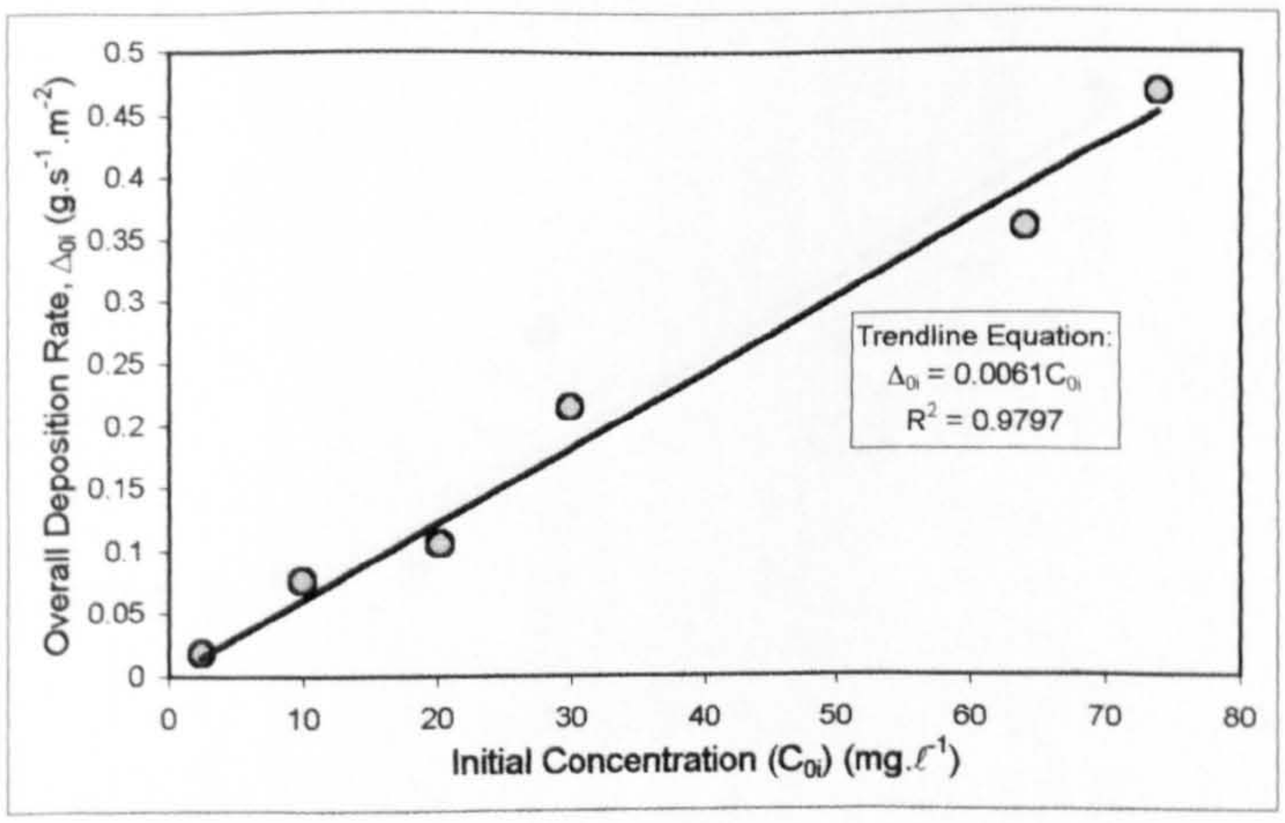

Figure A6.56 - Overall fractional deposition rate, Δ_{0i} against fractional initial concentration, C_{0i} for Experiment S2_EX5

S2_EX6	Q = 0.0548 m^3s^{-1}			Bed Grade - S2_grv2 (5-10mm)			
	H = 0.1 m			Fines Grade - LA Grade Sand			
	Sediment Input Rates (I_R & I_{Ri}) and Initial Sediment Concentrations (C_0 & C_{0i})						
	Full Mix	500-425 μm	425-355 μm	355-300 μm	300-250 μm	250-212 μm	212-150 μm	6 500-150μm)
I_R (g.s^{-1})	20.77	0.25	1.02	3.07	7.60	6.59	2.08	20.60
C_0 (mg.ℓ$^{-1}$)	378.96	4.62	18.55	55.95	138.63	120.33	37.88	375.97
	Overall and Fractional Deposition Rates (Δ & Δ_i)						
Trap No. / $X_{AVE.}$ (m)	Total **Δ (kg.s^{-1}.m^{-2})**	500-425 μm **Δ_i (kg.s^{-1}.m^{-2})**	425-355 μm **Δ_i (kg.s^{-1}.m^{-2})**	355-300 μm **Δ_i (kg.s^{-1}.m^{-2})**	300-250 μm **Δ_i (kg.s^{-1}.m^{-2})**	250-212 μm **Δ_i (kg.s^{-1}.m^{-2})**	212-150 μm **Δ_i (kg.s^{-1}.m^{-2})**	6 500-150μm) **Δ (kg.s^{-1}.m^{-2})**
1A								
1B								
1C								
2A 0.150	0.00052	2.29E-06	0.00001	0.00003	0.00012	0.00021	0.00012	0.00050
2B 0.357	0.00050	2.29E-06	0.00001	0.00003	0.00011	0.00020	0.00012	0.00047
2C 0.564	0.00101	0.00007	0.00012	0.00015	0.00022	0.00021	0.00012	0.00089
3A 0.771	0.00592	0.00043	0.00101	0.00156	0.00162	0.00078	0.00020	0.00560
3B 0.979	0.01164	0.00051	0.00169	0.00356	0.00370	0.00160	0.00032	0.01137
3C 1.186	0.01541	0.00034	0.00146	0.00380	0.00445	0.00176	0.00033	0.01213
4A 1.393	0.01516	0.00018	0.00104	0.00343	0.00480	0.00239	0.00048	0.01233
4B 1.601	0.01542	0.00012	0.00077	0.00420	0.00469	0.00244	0.00048	0.01269
4C 1.808	0.01195	0.00007	0.00054	0.00298	0.00494	0.00278	0.00060	0.01190
5A 2.015	0.00965	0.00004	0.00033	0.00184	0.00405	0.00271	0.00063	0.00961
5B 2.223	0.00780	0.00002	0.00021	0.00129	0.00324	0.00239	0.00061	0.00776
5C 2.430	0.00566	0.00001	0.00012	0.00080	0.00232	0.00186	0.00052	0.00563
6A 2.637	0.00506	0.00001	0.00008	0.00063	0.00204	0.00177	0.00050	0.00502
6B 2.844	0.00424	4.58E-06	0.00005	0.00041	0.00171	0.00159	0.00044	0.00421
6C 3.052	0.00300	2.29E-06	0.00003	0.00024	0.00109	0.00120	0.00041	0.00297
7A 3.259	0.00250	2.29E-06	0.00002	0.00020	0.00092	0.00101	0.00033	0.00248
7B 3.466	0.00201	1.15E-06	0.00001	0.00014	0.00068	0.00085	0.00030	0.00199
7C 3.674	0.00165	1.15E-06	0.00001	0.00009	0.00051	0.00074	0.00028	0.00162
8A 3.881	0.00143	0	0.00001	0.00006	0.00041	0.00066	0.00028	0.00141
8B 4.088	0.00110	1.15E-06	3.44E-06	0.00005	0.00028	0.00051	0.00024	0.00108
8C 4.296	0.00091	1.15E-06	3.44E-06	0.00004	0.00022	0.00042	0.00020	0.00089
9A,B,C 4.710	0.00064	3.82E-07	1.53E-06	0.00002	0.00016	0.00030	0.00014	0.00062
10A,B,C 5.332	0.00036	3.82E-07	7.64E-07	0.00001	0.00006	0.00017	0.00010	0.00034
11A,B,C 5.954	0.00022	3.82E-07	3.82E-07	3.06E-06	0.00003	0.00009	0.00008	0.00020
12A,B,C 6.576	0.00012	3.82E-07	3.82E-07	1.15E-06	0.00001	0.00005	0.00005	0.00011
Average Δ_{0i} (kg.s^{-1}.m^{-2})	0.00383	0.00005	0.00023	0.00078	0.00130	0.00091	0.00026	0.00353
Average Δ_{0i} (g.s^{-1}.m^{-2})	**3.83**	**0.05**	**0.23**	**0.78**	**1.30**	**0.91**	**0.26**	**3.53**

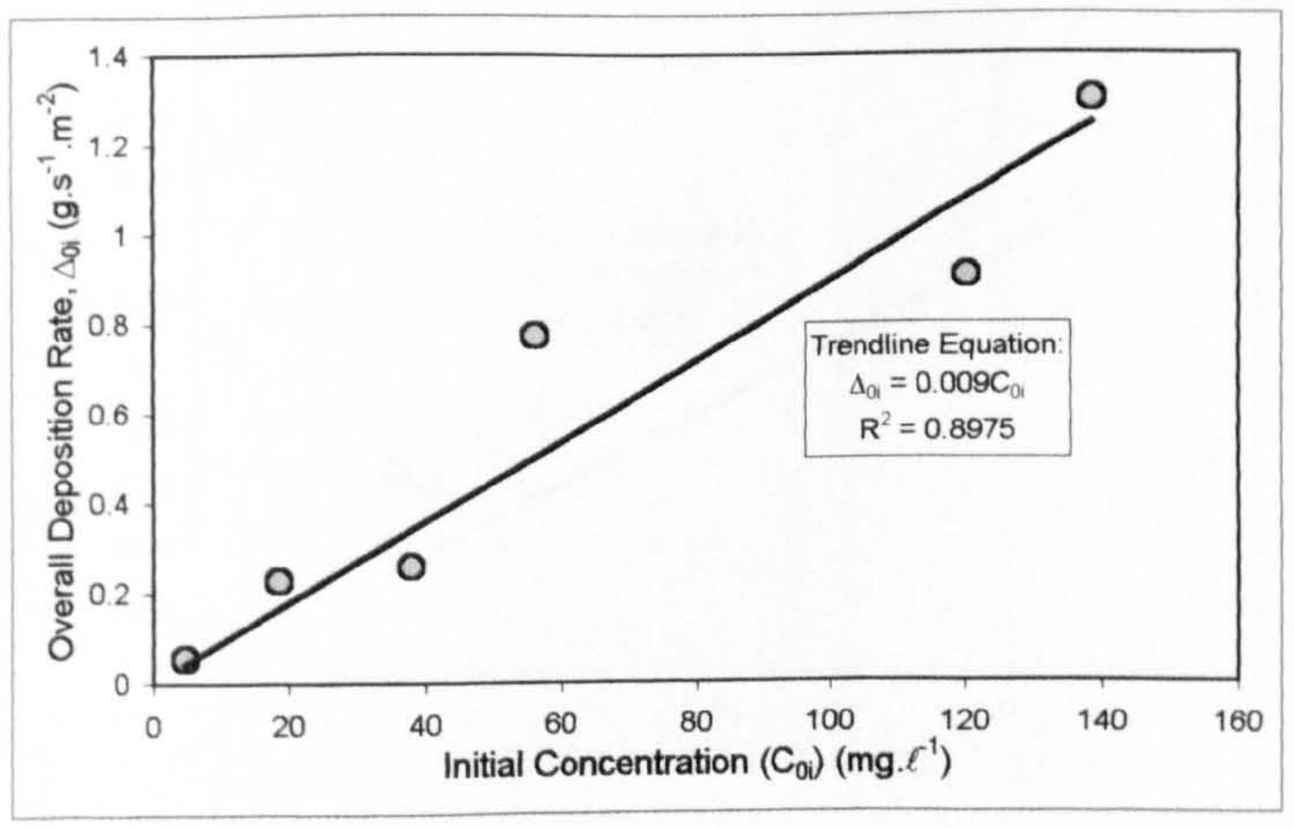

Figure A6.57 - Overall fractional deposition rate, Δ_{0i} against fractional initial concentration, C_{0i} for Experiment S2_EX6

S2_EX7	Q = 0.0359 m^3s^{-1}							
	H = 0.077 m							
	Bed Grade - S2_grv2 (5-10mm)							
	Fines Grade - DB Grade Sand (Fine)							
	Sediment Input Rates (I_R & I_{Ri}) and Initial Sediment Concentrations (C_0 & C_{0i})							
	Full Mix	212-150 μm	150-125 μm	125-106 μm	106-90 μm	90-63 μm		6 500-150μm)
I_R (g.s^{-1})	5.05	0.27	0.32	1.05	1.20	1.17		4.01
C_0 (mg.ℓ$^{-1}$)	140.67	7.51	8.86	29.12	33.41	32.68		111.58
	Overall and Fractional Deposition Rates (Δ & Δ_i)							
Trap No. X_{AVE} (m)	Total Δ (kg.s^{-1}.m^{-2})	212-150 μm Δ_i (kg.s^{-1}.m^{-2})	150-125 μm Δ_i (kg.s^{-1}.m^{-2})	125-106 μm Δ_i (kg.s^{-1}.m^{-2})	106-90 μm Δ_i (kg.s^{-1}.m^{-2})	90-63 μm Δ_i (kg.s^{-1}.m^{-2})		6 500-150μm) Δ (kg.s^{-1}.m^{-2})
1A								
1B								
1C								
2A 0.150	0.00066	0.00005	0.00001	0.00005	0.00008	0.00007		0.00026
2B 0.357	0.00068	0.00005	0.00001	0.00005	0.00009	0.00009		0.00029
2C 0.564	0.00059	0.00005	0.00001	0.00003	0.00006	0.00007		0.00022
3A 0.771	0.00073	0.00007	0.00001	0.00007	0.00010	0.00009		0.00034
3B 0.979	0.00085	0.00010	0.00003	0.00011	0.00011	0.00010		0.00045
3C 1.186	0.00092	0.00013	0.00008	0.00011	0.00012	0.00009		0.00054
4A 1.393	0.00106	0.00014	0.00009	0.00018	0.00018	0.00011		0.00070
4B 1.601	0.00106	0.00015	0.00011	0.00020	0.00019	0.00011		0.00075
4C 1.808	0.00108	0.00015	0.00013	0.00021	0.00019	0.00013		0.00081
5A 2.015	0.00102	0.00012	0.00008	0.00023	0.00021	0.00013		0.00078
5B 2.223	0.00094	0.00012	0.00010	0.00018	0.00018	0.00014		0.00071
5C 2.430	0.00097	0.00013	0.00007	0.00020	0.00020	0.00015		0.00075
6A 2.637	0.00096	0.00010	0.00012	0.00022	0.00021	0.00013		0.00078
6B 2.844	0.00079	0.00008	0.00009	0.00017	0.00017	0.00012		0.00063
6C 3.052	0.00099	0.00008	0.00009	0.00024	0.00023	0.00018		0.00082
7A 3.259	0.00081	0.00006	0.00009	0.00020	0.00019	0.00013		0.00067
7B 3.466	0.00076	0.00006	0.00009	0.00017	0.00017	0.00012		0.00062
7C 3.674	0.00082	0.00006	0.00008	0.00018	0.00019	0.00016		0.00067
8A 3.881	0.00069	0.00005	0.00007	0.00015	0.00017	0.00013		0.00056
8B 4.088	0.00082	0.00005	0.00008	0.00019	0.00020	0.00015		0.00067
8C 4.296	0.00058	0.00004	0.00008	0.00012	0.00013	0.00009		0.00047
9A,B,C 4.710	0.00063	0.00003	0.00006	0.00017	0.00015	0.00011		0.00053
10A,B,C 5.332	0.00053	0.00003	0.00004	0.00013	0.00014	0.00011		0.00043
11A,B,C 5.954	0.00049	0.00002	0.00003	0.00012	0.00013	0.00010		0.00040
12A,B,C 6.576	0.00047	0.00002	0.00004	0.00012	0.00013	0.00009		0.00039
Average Δ_{0i} (kg.s^{-1}.m^{-2})	0.00073	0.00007	0.00006	0.00015	0.00015	0.00011		0.00054
Average Δ_{0i} (g.s^{-1}.m^{-2})	**0.73**	**0.07**	**0.06**	**0.15**	**0.15**	**0.11**		**0.54**

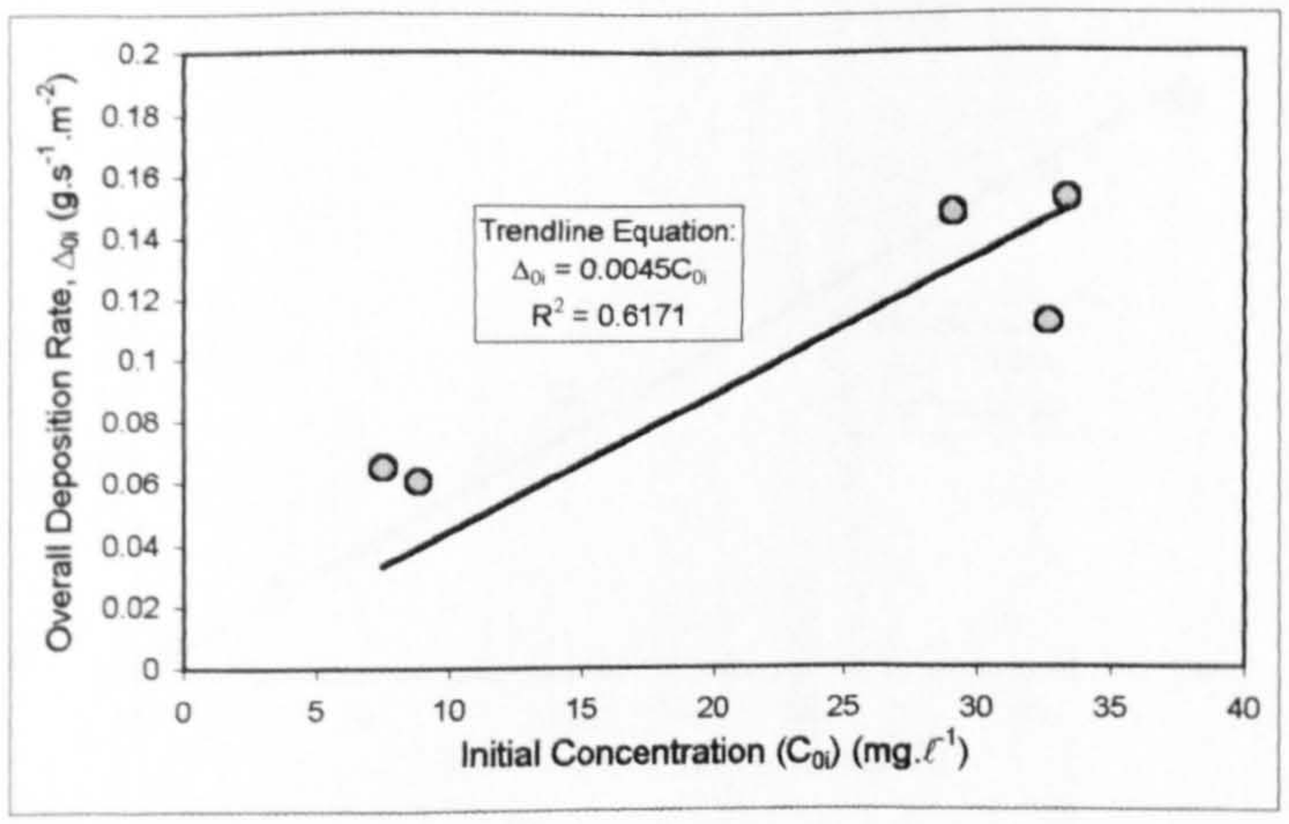

Figure A6.58 - Overall fractional deposition rate, Δ_{0i} against fractional initial concentration, C_{0i} for Experiment S2_EX7

S2_EX8		Q = 0.0518 m^3s^{-1}			Bed Grade - S2_grv1 (10-25mm)			
		H = 0.079 m			Fines Grade - LA Grade Sand			
		Sediment Input Rates (I_R & I_{Ri}) and Initial Sediment Concentrations (C_0 & C_{0i})						
		Full Mix	500-425 μm	425-355 μm	355-300 μm	300-250 μm	250-212 μm	212-150 μm	6 500-150μm)
I_R (g.s^{-1})		6.69	0.08	0.33	0.99	2.45	2.12	0.67	6.64
C_0 (mg.ℓ$^{-1}$)		129.15	1.57	6.32	19.07	47.25	41.01	12.91	128.13
		Overall and Fractional Deposition Rates (Δ & Δ_i)						
Trap No.	X_{AVE} (m)	Total Δ (kg.s^{-1}.m^{-2})	500-425 μm Δ_i (kg.s^{-1}.m^{-2})	425-355 μm Δ_i (kg.s^{-1}.m^{-2})	355-300 μm Δ_i (kg.s^{-1}.m^{-2})	300-250 μm Δ_i (kg.s^{-1}.m^{-2})	250-212 μm Δ_i (kg.s^{-1}.m^{-2})	212-150 μm Δ_i (kg.s^{-1}.m^{-2})	6 500-150μm) Δ (kg.s^{-1}.m^{-2})
1A									
1B									
1C									
2A	0.180	0.00008	6.59E-07	1.32E-06	0.00003	0.00002	0.00001	0.00001	0.00007
2B	0.387	0.00008	1.32E-06	6.59E-07	0.00001	0.00002	0.00002	0.00001	0.00006
2C	0.594	0.00020	0.00002	0.00002	0.00002	0.00003	0.00002	0.00002	0.00013
3A	0.801	0.00141	0.00012	0.00020	0.00031	0.00035	0.00021	0.00007	0.00126
3B	1.009	0.00294	0.00016	0.00039	0.00071	0.00092	0.00050	0.00012	0.00281
3C	1.216	0.00446	0.00014	0.00043	0.00117	0.00152	0.00089	0.00022	0.00436
4A	1.423	0.00413	0.00008	0.00029	0.00102	0.00146	0.00096	0.00025	0.00406
4B	1.631	0.00402	0.00005	0.00022	0.00102	0.00151	0.00092	0.00025	0.00397
4C	1.838	0.00337	0.00003	0.00014	0.00065	0.00128	0.00095	0.00028	0.00333
5A	2.045	0.00311	0.00002	0.00009	0.00050	0.00128	0.00090	0.00029	0.00307
5B	2.253	0.00243	0.00001	0.00006	0.00039	0.00104	0.00068	0.00021	0.00239
5C	2.460	0.00213	0.00001	0.00005	0.00030	0.00089	0.00064	0.00020	0.00209
6A	2.667	0.00182	4.61E-06	0.00003	0.00016	0.00061	0.00071	0.00027	0.00178
6B	2.874	0.00154	2.64E-06	0.00003	0.00010	0.00050	0.00062	0.00025	0.00150
6C	3.082	0.00130	1.32E-06	0.00001	0.00009	0.00040	0.00053	0.00023	0.00126
7A	3.289	0.00112	1.32E-06	0.00001	0.00006	0.00032	0.00047	0.00022	0.00109
7B	3.496	0.00089	1.32E-06	0.00001	0.00005	0.00025	0.00037	0.00017	0.00086
7C	3.704	0.00077	6.59E-07	4.61E-06	0.00004	0.00021	0.00033	0.00017	0.00074
8A	3.911	0.00067	6.59E-07	3.30E-06	0.00003	0.00016	0.00029	0.00015	0.00064
8B	4.118	0.00067	6.59E-07	2.64E-06	0.00002	0.00016	0.00030	0.00015	0.00064
8C	4.326	0.00049	6.59E-07	1.32E-06	0.00002	0.00010	0.00022	0.00012	0.00046
9A,B,C	4.740	0.00043	2.20E-07	1.10E-06	0.00001	0.00010	0.00019	0.00010	0.00040
10A,B,C	5.362	0.00031	2.20E-07	6.59E-07	0.00001	0.00005	0.00014	0.00009	0.00028
11A,B,C	5.984	0.00022	2.20E-07	6.59E-07	2.86E-06	0.00003	0.00009	0.00007	0.00019
12A,B,C	6.606	0.00015	2.20E-07	2.20E-07	1.54E-06	0.00001	0.00007	0.00005	0.00013
Average Δ_{0i} (kg.s^{-1}.m^{-2})		0.00124	0.00002	0.00006	0.00020	0.00041	0.00036	0.00014	0.00120
Average Δ_{0i} (g.s^{-1}.m^{-2})		**1.24**	**0.02**	**0.06**	**0.20**	**0.41**	**0.36**	**0.14**	**1.20**

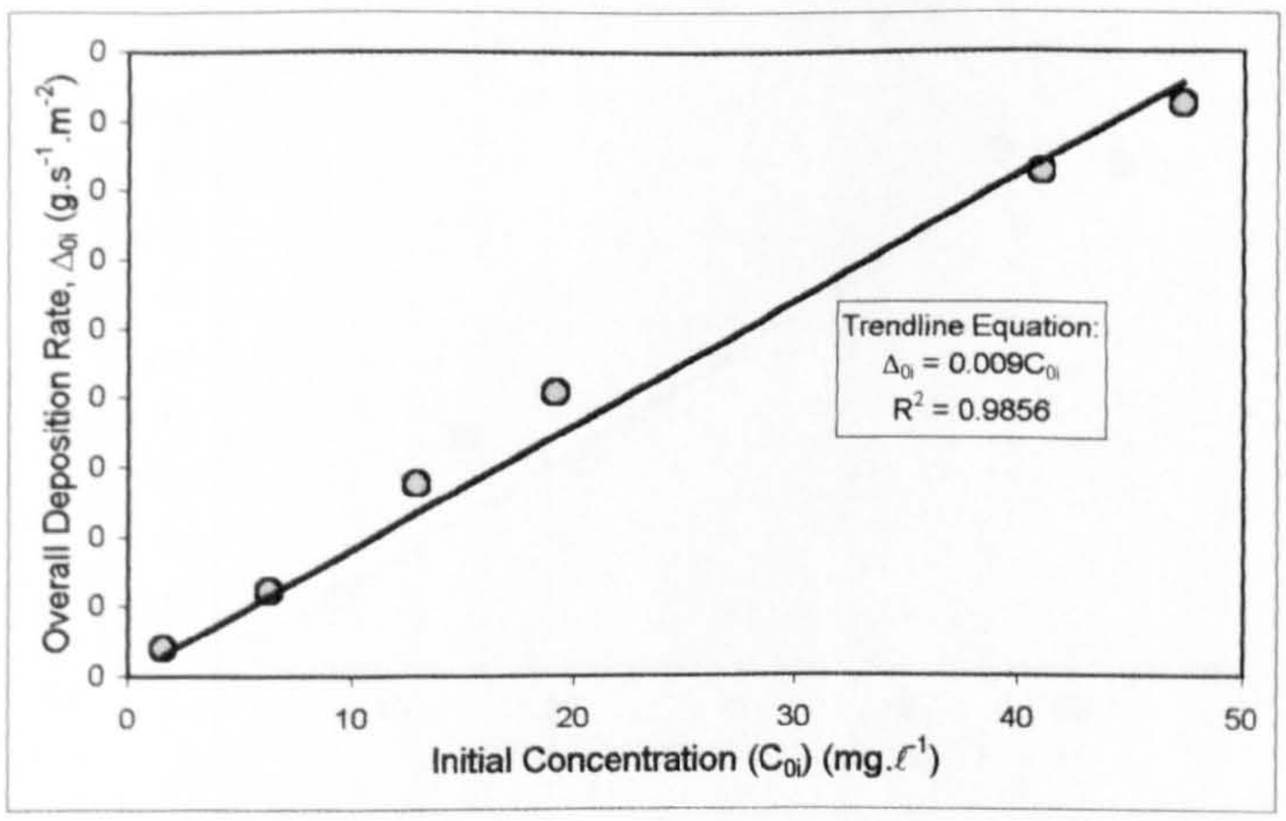

Figure A6.59 - Overall fractional deposition rate, Δ_{0i} against fractional initial concentration, C_{0i} for Experiment S2_EX8

S2_EX9(i)	Q = 0.0518 m^3s^{-1}			Bed Grade - S2_grv1 (10-25mm)				
	H = 0.079 m			Fines Grade - LA Grade Sand				
	Sediment Input Rates (I_R & I_{Ri}) and Initial Sediment Concentrations (C_0 & C_{0i})							
	Full Mix	500-425 μm	425-355 μm	355-300 μm	300-250 μm	250-212 μm	212-150 μm	Σ 500-150(μm)
I_R ($g.s^{-1}$)	7.46	0.09	0.37	1.10	2.73	2.37	0.75	7.40
C_0 ($mg.\ell^{-1}$)	144.00	1.76	7.05	21.26	52.68	45.72	14.40	142.86
	Overall and Fractional Deposition Rates (Δ & Δ_i)							
Trap No. / X_{AVE} (m)	Total Δ ($kg.s^{-1}.m^{-2}$)	500-425 μm Δ_i ($kg.s^{-1}.m^{-2}$)	425-355 μm Δ_i ($kg.s^{-1}.m^{-2}$)	355-300 μm Δ_i ($kg.s^{-1}.m^{-2}$)	300-250 μm Δ_i ($kg.s^{-1}.m^{-2}$)	250-212 μm Δ_i ($kg.s^{-1}.m^{-2}$)	212-150 μm Δ_i ($kg.s^{-1}.m^{-2}$)	Σ 500-150(μm) Δ ($kg.s^{-1}.m^{-2}$)
1A								
1B								
1C								
2A 0.180	0.00007	0	1.15E-06	1.15E-06	4.58E-06	0.00002	0.00003	0.00006
2B 0.387	0.00005	1.15E-06	1.15E-06	1.15E-06	3.44E-06	0.00001	0.00002	0.00004
2C 0.594	0.00024	0.00002	0.00003	0.00004	0.00004	0.00003	0.00003	0.00019
3A 0.801	0.00187	0.00015	0.00028	0.00040	0.00051	0.00030	0.00010	0.00174
3B 1.009	0.00392	0.00015	0.00042	0.00085	0.00131	0.00084	0.00025	0.00382
3C 1.216	0.00464	0.00011	0.00037	0.00094	0.00165	0.00118	0.00032	0.00458
4A 1.423	0.00447	0.00006	0.00024	0.00074	0.00166	0.00131	0.00042	0.00442
4B 1.631	0.00451	0.00004	0.00019	0.00075	0.00169	0.00135	0.00044	0.00447
4C 1.838	0.00371	0.00003	0.00013	0.00051	0.00140	0.00121	0.00040	0.00368
5A 2.045	0.00269	0.00001	0.00007	0.00033	0.00113	0.00112	0.00041	0.00307
5B 2.253	0.00282	0.00001	0.00005	0.00028	0.00095	0.00102	0.00041	0.00272
5C 2.460	0.00209	4.58E-06	0.00003	0.00016	0.00067	0.00084	0.00036	0.00207
6A 2.667	0.00167	2.29E-06	0.00002	0.00012	0.00051	0.00069	0.00030	0.00165
6B 2.874	0.00164	1.15E-06	0.00001	0.00010	0.00045	0.00069	0.00036	0.00162
6C 3.082	0.00125	1.15E-06	0.00001	0.00006	0.00033	0.00054	0.00029	0.00123
7A 3.289	0.00084	1.15E-06	0.00001	0.00004	0.00021	0.00036	0.00021	0.00083
7B 3.496	0.00077	1.15E-06	4.58E-06	0.00003	0.00016	0.00033	0.00021	0.00074
7C 3.704	0.00062	1.15E-06	2.29E-06	0.00002	0.00013	0.00027	0.00018	0.00061
8A 3.911	0.00058	1.15E-06	2.29E-06	0.00002	0.00012	0.00025	0.00017	0.00056
8B 4.118	0.00054	1.15E-06	1.15E-06	0.00001	0.00010	0.00024	0.00017	0.00053
8C 4.326	0.00043	0	1.15E-06	0.00001	0.00007	0.00018	0.00015	0.00041
9A,B,C 4.740	0.00031	3.82E-07	7.64E-07	0.00001	0.00005	0.00013	0.00010	0.00029
10A,B,C 5.362	0.00023	3.82E-07	3.82E-07	3.44E-06	0.00003	0.00010	0.00008	0.00021
11A,B,C 5.984	0.00017	0	3.82E-07	1.53E-06	0.00001	0.00006	0.00007	0.00015
12A,B,C 6.606	0.00015	3.82E-07	7.64E-07	1.53E-06	0.00001	0.00005	0.00007	0.00013
Average Δ_{0i} ($kg.s^{-1}.m^{-2}$)	0.00127	0.00002	0.00006	0.00017	0.00041	0.00042	0.00019	0.00125
Average Δ_{0i} ($g.s^{-1}.m^{-2}$)	**1.27**	**0.02**	**0.06**	**0.17**	**0.41**	**0.42**	**0.19**	**1.25**

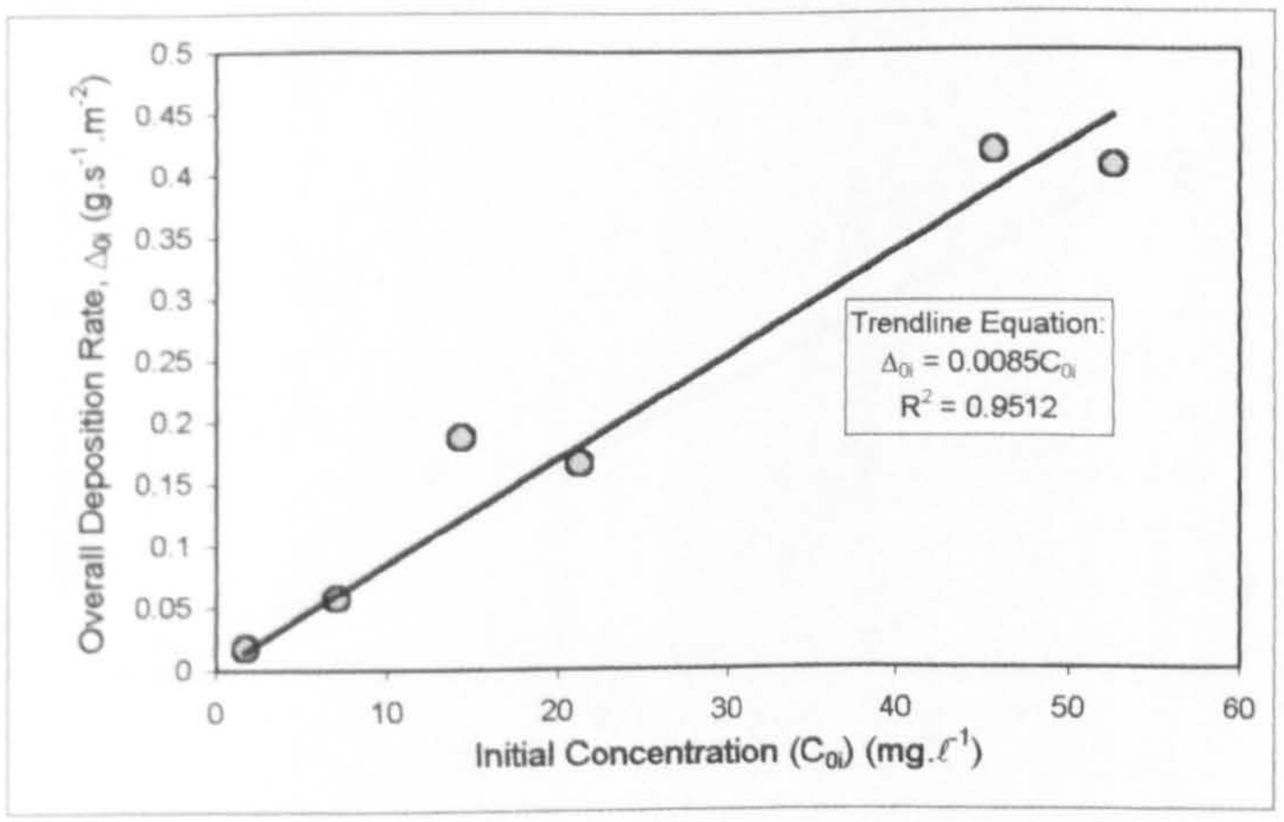

Figure A6.60 - Overall fractional deposition rate, Δ_{0i} against fractional initial concentration, C_{0i} for Experiment S2_EX9(i) - Unfilled Traps

S2_EX9(ii)		Q = 0.0518 m^3s^{-1}				Bed Grade - S2_grv1 (10-25mm)			
		H = 0.079 m				Fines Grade - LA Grade Sand			
		Sediment Input Rates (I_R & I_{Ri}) and Initial Sediment Concentrations (C_0 & C_{0i})							
		Full Mix	500-425 μm	425-355 μm	355-300 μm	300-250 μm	250-212 μm	212-150 μm	Σ 500-150(μm)
I_R (g.s^{-1})		6.69	0.08	0.33	0.99	2.45	2.12	0.67	6.64
C_0 (mg.ℓ$^{-1}$)		129.15	1.57	6.32	19.07	47.25	41.01	12.91	128.13
		Overall and Fractional Deposition Rates (Δ & Δ_i)							
Trap No.	$X_{AVE.}$ (m)	Total Δ (kg.s^{-1}.m^{-2})	500-425 μm Δ_i (kg.s^{-1}.m^{-2})	425-355 μm Δ_i (kg.s^{-1}.m^{-2})	355-300 μm Δ_i (kg.s^{-1}.m^{-2})	300-250 μm Δ_i (kg.s^{-1}.m^{-2})	250-212 μm Δ_i (kg.s^{-1}.m^{-2})	212-150 μm Δ_i (kg.s^{-1}.m^{-2})	Σ 500-150(μm) Δ (kg.s^{-1}.m^{-2})
1A									
1B									
1C									
2A	0.180	0.00005	1.15E-06	1.15E-06	1.15E-06	4.58E-06	0.00001	0.00002	0.00004
2B	0.387	0.00005	1.15E-06	1.15E-06	2.29E-06	0.00001	0.00001	0.00002	0.00004
2C	0.594	0.00022	0.00002	0.00003	0.00003	0.00003	0.00003	0.00002	0.00017
3A	0.801	0.00172	0.00011	0.00025	0.00038	0.00047	0.00029	0.00009	0.00159
3B	1.009	0.00414	0.00017	0.00047	0.00097	0.00138	0.00080	0.00021	0.00401
3C	1.216	0.00521	0.00011	0.00043	0.00119	0.00189	0.00116	0.00033	0.00512
4A	1.423	0.00440	0.00002	0.00014	0.00060	0.00169	0.00142	0.00047	0.00435
4B	1.631	0.00500	0.00004	0.00021	0.00093	0.00199	0.00136	0.00043	0.00495
4C	1.838	0.00487	0.00006	0.00028	0.00094	0.00186	0.00127	0.00036	0.00477
5A	2.045	0.00356	0.00001	0.00008	0.00042	0.00133	0.00123	0.00044	0.00350
5B	2.253	0.00312	0.00001	0.00005	0.00029	0.00116	0.00113	0.00042	0.00306
5C	2.460	0.00258	0.00001	0.00004	0.00023	0.00089	0.00098	0.00039	0.00253
6A	2.667	0.00208	3.44E-06	0.00002	0.00014	0.00065	0.00083	0.00036	0.00201
6B	2.874	0.00177	2.29E-06	0.00001	0.00010	0.00053	0.00072	0.00034	0.00171
6C	3.082	0.00135	2.29E-06	0.00001	0.00006	0.00035	0.00056	0.00030	0.00129
7A	3.289	0.00114	1.15E-06	0.00001	0.00005	0.00028	0.00048	0.00027	0.00108
7B	3.496	0.00106	3.44E-06	0.00001	0.00004	0.00025	0.00044	0.00025	0.00100
7C	3.704	0.00086	2.29E-06	4.58E-06	0.00003	0.00019	0.00036	0.00022	0.00081
8A	3.911	0.00073	1.15E-06	3.44E-06	0.00002	0.00014	0.00031	0.00020	0.00068
8B	4.118	0.00070	2.29E-06	2.29E-06	0.00002	0.00013	0.00029	0.00020	0.00064
8C	4.326	0.00053	0	2.29E-06	0.00001	0.00009	0.00023	0.00017	0.00050
9A,B,C	4.740	0.00039	7.64E-07	1.15E-06	0.00001	0.00006	0.00017	0.00012	0.00036
10A,B,C	5.362	0.00030	1.15E-06	1.15E-06	4.97E-06	0.00004	0.00012	0.00010	0.00027
11A,B,C	5.984	0.00018	3.82E-07	3.82E-07	1.53E-06	0.00002	0.00007	0.00007	0.00016
12A,B,C	6.606	0.00012	3.82E-07	0	7.64E-07	0.00001	0.00004	0.00006	0.00011
Average Δ_{0i} (kg.s^{-1}.m^{-2})		0.00146	0.00002	0.00006	0.00020	0.00048	0.00046	0.00020	0.00141
Average Δ_{0i} (g.s^{-1}.m^{-2})		**1.46**	**0.02**	**0.06**	**0.20**	**0.48**	**0.46**	**0.20**	**1.41**

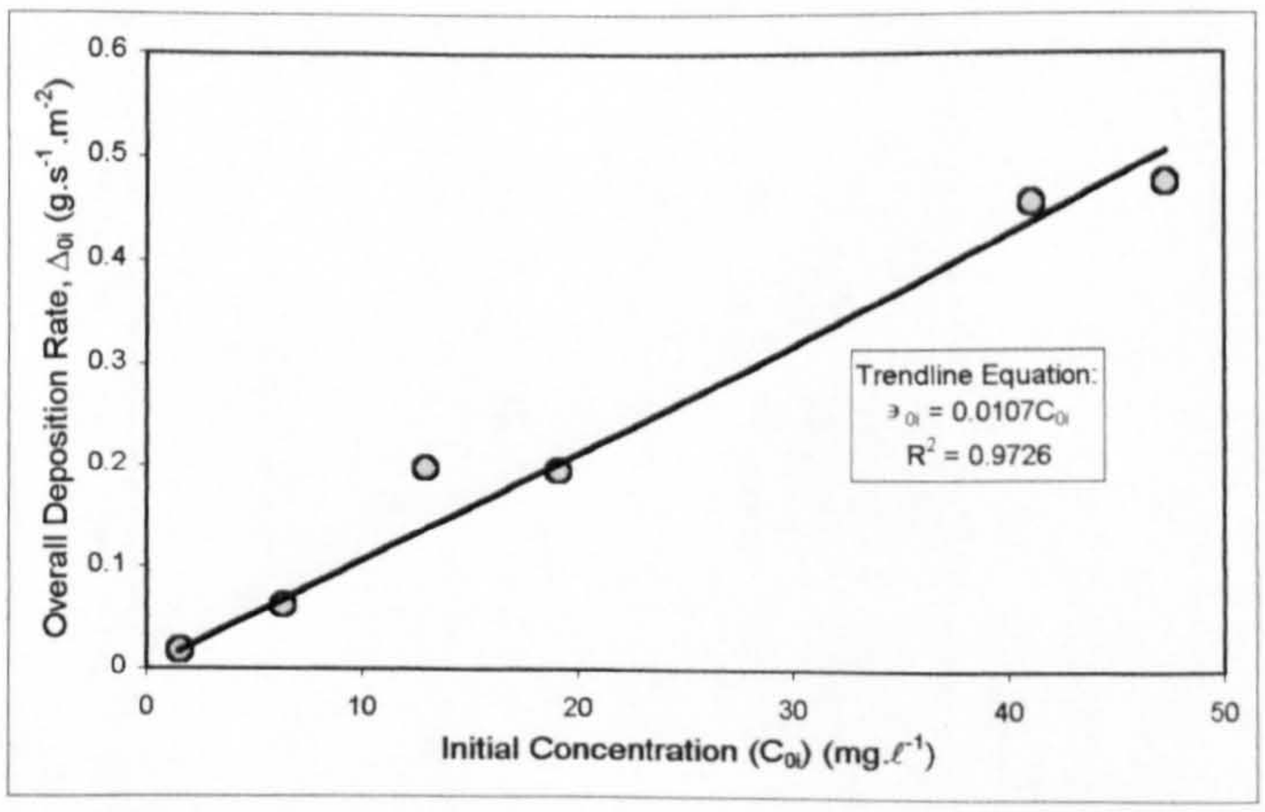

Figure A6.61 - Overall fractional deposition rate, Δ_{0i} against fractional initial concentration, C_{0i} for Experiment S2_EX9(ii) - Filled Traps

S2_EX10(i)	Q = 0.0519 $m^3.s^{-1}$			Bed Grade - S2_grv1 (10-25mm)				
	H = 0.079 m			Fines Grade - LA Grade Sand				
	Sediment Input Rates (I_R & I_{Ri}) and Initial Sediment Concentrations (C_0 & C_{0i})							
	Full Mix	500-425 μm	425-355 μm	355-300 μm	300-250 μm	250-212 μm	212-150 μm	6 500-150(μm)
I_R ($g.s^{-1}$)	30.58	0.37	1.50	4.51	11.19	9.71	3.06	30.34
C_0 ($mg.\ell^{-1}$)	589.21	7.18	28.85	86.99	215.55	187.09	58.90	584.56
	Overall and Fractional Deposition Rates (Δ & Δ_i)							
Trap No. / X_{AVE} (m)	Total Δ ($kg.s^{-1}.m^{-2}$)	500-425 μm Δ_i ($kg.s^{-1}.m^{-2}$)	425-355 μm Δ_i ($kg.s^{-1}.m^{-2}$)	355-300 μm Δ_i ($kg.s^{-1}.m^{-2}$)	300-250 μm Δ_i ($kg.s^{-1}.m^{-2}$)	250-212 μm Δ_i ($kg.s^{-1}.m^{-2}$)	212-150 μm Δ_i ($kg.s^{-1}.m^{-2}$)	6 500-150(μm) Δ ($kg.s^{-1}.m^{-2}$)
1A								
1B								
1C								
2A 0.180	0.00021	0	1.76E-06	3.51E-06	0.00001	0.00005	0.00011	0.00018
2B 0.387	0.00024	3.51E-06	3.51E-06	3.51E-06	0.00001	0.00006	0.00012	0.00021
2C 0.594	0.00085	0.00009	0.00011	0.00013	0.00013	0.00010	0.00010	0.00066
3A 0.801	0.00850	0.00068	0.00124	0.00197	0.00228	0.00134	0.00040	0.00791
3B 1.009	0.01814	0.00082	0.00207	0.00479	0.00565	0.00339	0.00095	0.01767
3C 1.216	0.02065	0.00057	0.00185	0.00640	0.00666	0.00381	0.00106	0.02036
4A 1.423	0.02030	0.00038	0.00150	0.00540	0.00708	0.00443	0.00132	0.02011
4B 1.631	0.02067	0.00025	0.00112	0.00542	0.00730	0.00489	0.00154	0.02051
4C 1.838	0.01678	0.00013	0.00067	0.00358	0.00628	0.00460	0.00141	0.01667
5A 2.045	0.01456	0.00008	0.00047	0.00227	0.00569	0.00450	0.00146	0.01446
5B 2.253	0.01258	0.00004	0.00027	0.00174	0.00469	0.00420	0.00156	0.01249
5C 2.460	0.00959	0.00002	0.00014	0.00095	0.00353	0.00342	0.00143	0.00949
6A 2.667	0.00723	0.00002	0.00011	0.00067	0.00255	0.00268	0.00113	0.00716
6B 2.874	0.00640	0.00001	0.00006	0.00044	0.00227	0.00245	0.00109	0.00632
6C 3.082	0.00475	0.00001	0.00005	0.00031	0.00148	0.00193	0.00091	0.00469
7A 3.289	0.00391	0.00001	0.00003	0.00024	0.00116	0.00161	0.00081	0.00385
7B 3.496	0.00377	1.76E-06	0.00002	0.00018	0.00105	0.00161	0.00084	0.00371
7C 3.704	0.00245	3.51E-06	0.00001	0.00011	0.00063	0.00104	0.00061	0.00241
8A 3.911	0.00247	1.76E-06	0.00001	0.00009	0.00063	0.00105	0.00063	0.00242
8B 4.118	0.00228	0	0.00001	0.00009	0.00055	0.00098	0.00060	0.00223
8C 4.326	0.00201	0	0.00001	0.00007	0.00046	0.00087	0.00056	0.00196
9A,B,C 4.740	0.00161	5.86E-07	4.10E-06	0.00005	0.00040	0.00070	0.00041	0.00156
10A,B,C 5.362	0.00105	5.86E-07	1.17E-06	0.00002	0.00020	0.00046	0.00033	0.00101
11A,B,C 5.984	0.00075	0	1.17E-06	0.00001	0.00011	0.00033	0.00027	0.00072
12A,B,C 6.606	0.00057	0	5.86E-07	0.00001	0.00006	0.00024	0.00023	0.00054
Average Δ_{0i} ($kg.s^{-1}.m^{-2}$)	0.00577	0.00009	0.00030	0.00106	0.00189	0.00164	0.00068	0.00567
Average Δ_{0i} ($g.s^{-1}.m^{-2}$)	**5.77**	**0.09**	**0.30**	**1.06**	**1.89**	**1.64**	**0.68**	**5.67**

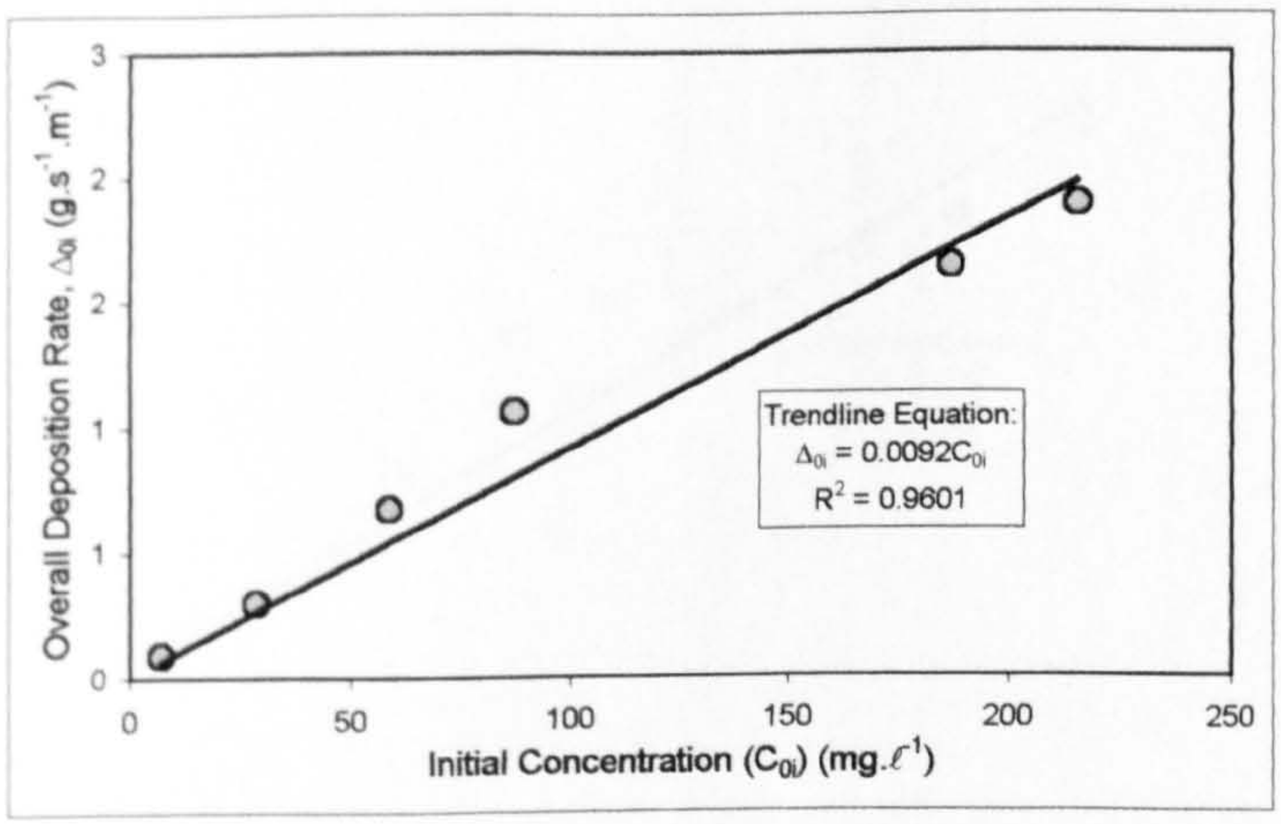

Figure A6.62 - Overall fractional deposition rate, Δ_{0i} against fractional initial concentration, C_{0i} for Experiment S2_EX10(i) - Unfilled Traps

S2_EX10(ii)	Q = 0.0518 m^3s^{-1}			Bed Grade - S2_grv1 (10-25mm)				
	H = 0.079 m			Fines Grade - LA Grade Sand				
	Sediment Input Rates (I_R & I_{Ri}) and Initial Sediment Concentrations (C_0 & C_{0i})							
	Full Mix	500-425 µm	425-355 µm	355-300 µm	300-250 µm	250-212 µm	212-150 µm	6 500-150(µm)
I_R ($g.s^{-1}$)	30.58	0.37	1.50	4.51	11.19	9.71	3.06	30.34
C_0 ($mg.\ell^{-1}$)	590.35	7.20	28.90	87.16	215.97	187.45	59.02	585.69
	Overall and Fractional Deposition Rates (Δ & Δ_i)							
Trap No. / $X_{AVE.}$ (m)	Total Δ ($kg.s^{-1}.m^{-2}$)	500-425 µm Δ_i ($kg.s^{-1}.m^{-2}$)	425-355 µm Δ_i ($kg.s^{-1}.m^{-2}$)	355-300 µm Δ_i ($kg.s^{-1}.m^{-2}$)	300-250 µm Δ_i ($kg.s^{-1}.m^{-2}$)	250-212 µm Δ_i ($kg.s^{-1}.m^{-2}$)	212-150 µm Δ_i ($kg.s^{-1}.m^{-2}$)	6 500-150(µm) Δ ($kg.s^{-1}.m^{-2}$)
1A								
1B								
1C								
2A 0.180	0.00020	3.51E-06	3.51E-06	0.00001	0.00001	0.00003	0.00008	0.00014
2B 0.387	0.00024	0.00001	0.00001	0.00001	0.00002	0.00004	0.00008	0.00018
2C 0.594	0.00120	0.00012	0.00017	0.00022	0.00024	0.00015	0.00009	0.00098
3A 0.801	0.00765	0.00056	0.00110	0.00182	0.00211	0.00120	0.00037	0.00717
3B 1.009	0.01029	0.00046	0.00118	0.00265	0.00319	0.00196	0.00056	0.01000
3C 1.216	0.01259	0.00034	0.00114	0.00424	0.00384	0.00219	0.00065	0.01240
4A 1.423	0.01261	0.00022	0.00095	0.00402	0.00418	0.00237	0.00072	0.01247
4B 1.631	0.01378	0.00016	0.00076	0.00376	0.00502	0.00301	0.00094	0.01365
4C 1.838	0.01383	0.00014	0.00066	0.00366	0.00502	0.00323	0.00100	0.01371
5A 2.045	0.01400	0.00010	0.00055	0.00402	0.00497	0.00314	0.00111	0.01388
5B 2.253	0.01440	0.00008	0.00047	0.00420	0.00496	0.00339	0.00117	0.01427
5C 2.460	0.01205	0.00005	0.00029	0.00297	0.00450	0.00305	0.00107	0.01192
6A 2.667	0.01011	0.00002	0.00016	0.00113	0.00377	0.00352	0.00139	0.01000
6B 2.874	0.00828	0.00002	0.00011	0.00073	0.00294	0.00306	0.00133	0.00818
6C 3.082	0.00683	0.00001	0.00006	0.00049	0.00230	0.00265	0.00121	0.00671
7A 3.289	0.00524	0.00001	0.00004	0.00034	0.00183	0.00204	0.00090	0.00516
7B 3.496	0.00456	3.51E-06	0.00003	0.00024	0.00151	0.00179	0.00090	0.00447
7C 3.704	0.00409	3.51E-06	0.00002	0.00020	0.00120	0.00170	0.00089	0.00401
8A 3.911	0.00340	1.76E-06	0.00002	0.00014	0.00094	0.00143	0.00079	0.00332
8B 4.118	0.00325	1.76E-06	0.00001	0.00010	0.00083	0.00139	0.00082	0.00316
8C 4.326	0.00237	1.76E-06	0.00001	0.00009	0.00055	0.00102	0.00063	0.00230
9A,B,C 4.740	0.00201	1.76E-06	0.00001	0.00007	0.00059	0.00082	0.00045	0.00194
10A,B,C 5.362	0.00133	1.76E-06	3.51E-06	0.00003	0.00029	0.00057	0.00038	0.00127
11A,B,C 5.984	0.00097	1.17E-06	1.76E-06	0.00001	0.00029	0.00031	0.00029	0.00089
12A,B,C 6.606	0.00067	1.17E-06	1.76E-06	0.00001	0.00008	0.00027	0.00026	0.00062
Average Δ_{0i} ($kg.s^{-1}.m^{-2}$)	0.00533	0.00007	0.00024	0.00107	0.00175	0.00146	0.00063	0.00522
Average Δ_{0i} ($g.s^{-1}.m^{-2}$)	**5.33**	**0.07**	**0.24**	**1.07**	**1.75**	**1.46**	**0.63**	**5.22**

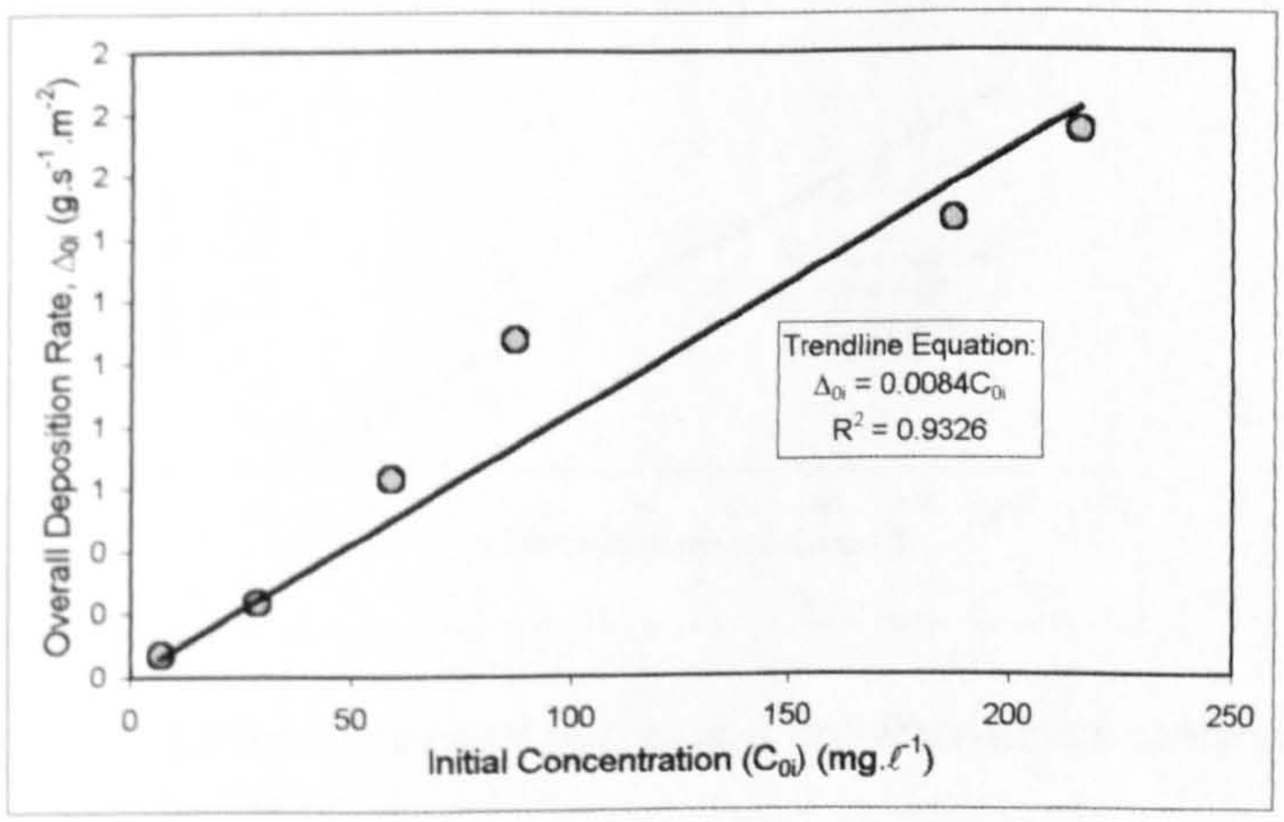

Figure A6.63 - Overall fractional deposition rate, Δ_{0i} against fractional initial concentration, C_{0i} for Experiment S2_EX10(ii) - Filled Traps

S2 EX11		Q = 0.0357 m^3s^{-1}			Bed Grade - S2_grv2 (5-10mm)						
		H = 0.109 m			Fines Grade - DB Grade Sand (Fine)						
		Sediment Input Rates (I_R & I_{Ri}) and Initial Sediment Concentrations (C_0 & C_{0i})									
		Full Mix	212-150 μm	150-125 μm	125-106 μm	106-90 μm	90-63 μm	63-53 μm	53-45 μm	45-38 μm	Σ (212-38μm)
	I_R (g.s^{-1})	9.44	0.13	0.49	2.81	2.32	2.19	0.66	0.37	0.21	9.19
	C_0 (mg.ℓ$^{-1}$)	264.29	3.52	13.80	78.63	65.12	61.37	18.53	10.41	6.00	257.36
		Overall and Fractional Deposition Rates (Δ & Δ_i)									
Trap No.	X_{mid} (m)	Full Mix Δ (kg/m^2/s)	212-150 μm Δ_i (kg/m^2/s)	150-125 μm Δ_i (kg/m^2/s)	125-106 μm Δ_i (kg/m^2/s)	106-90 μm Δ_i (kg/m^2/s)	90-63 μm Δ_i (kg/m^2/s)	63-53 μm Δ_i (kg/m^2/s)	53-45 μm Δ_i (kg/m^2/s)	45-38 μm Δ_i (kg/m^2/s)	Σ (212-38μm) Δ (kg/m^2/s)
1A											
1B											
1C											
2A	0.190	0.00044	0.00001	3.95E-06	0.00009	0.00009	0.00013	0.00003	0.00003	0.00001	0.00039
2B	0.397	0.00040	0.00001	0.00001	0.00007	0.00007	0.00012	0.00003	0.00002	0.00001	0.00035
2C	0.604	0.00045	0.00001	0.00001	0.00009	0.00010	0.00013	0.00003	0.00003	0.00001	0.00041
3A	0.811	0.00067	0.00003	0.00004	0.00016	0.00014	0.00016	0.00004	0.00003	0.00002	0.00062
3B	1.019	0.00093	0.00005	0.00016	0.00024	0.00017	0.00016	0.00004	0.00003	0.00001	0.00086
3C	1.226	0.00145	0.00007	0.00028	0.00043	0.00027	0.00022	0.00005	0.00003	0.00002	0.00138
4A	1.433	0.00164	0.00010	0.00037	0.00051	0.00029	0.00021	0.00005	0.00003	0.00001	0.00157
4B	1.641	0.00187	0.00009	0.00043	0.00059	0.00033	0.00026	0.00005	0.00003	0.00002	0.00179
4C	1.848	0.00211	0.00009	0.00052	0.00065	0.00039	0.00030	0.00004	0.00004	0.00002	0.00206
5A	2.055	0.00203	0.00006	0.00042	0.00064	0.00040	0.00032	0.00007	0.00004	0.00002	0.00197
5B	2.263	0.00194	0.00006	0.00039	0.00061	0.00041	0.00030	0.00007	0.00004	0.00002	0.00190
5C	2.470	0.00202	0.00004	0.00040	0.00062	0.00043	0.00034	0.00006	0.00005	0.00003	0.00197
6A	2.677	0.00178	0.00004	0.00035	0.00055	0.00038	0.00029	0.00006	0.00004	0.00002	0.00173
6B	2.884	0.00178	0.00004	0.00030	0.00057	0.00039	0.00030	0.00007	0.00004	0.00002	0.00172
6C	3.092	0.00168	0.00004	0.00027	0.00055	0.00037	0.00031	0.00006	0.00003	0.00002	0.00164
7A	3.299	0.00155	0.00003	0.00022	0.00048	0.00035	0.00031	0.00006	0.00004	0.00002	0.00151
7B	3.506	0.00159	0.00003	0.00024	0.00049	0.00035	0.00029	0.00007	0.00004	0.00002	0.00154
7C	3.714	0.00157	0.00003	0.00022	0.00047	0.00037	0.00030	0.00006	0.00005	0.00002	0.00152
8A	3.921	0.00148	0.00002	0.00020	0.00044	0.00035	0.00030	0.00006	0.00004	0.00002	0.00144
8B	4.128	0.00143	0.00002	0.00017	0.00043	0.00035	0.00028	0.00008	0.00004	0.00002	0.00138
8C	4.336	0.00126	0.00001	0.00015	0.00039	0.00030	0.00026	0.00005	0.00004	0.00002	0.00123
9A	4.543	0.00132	0.00001	0.00015	0.00037	0.00031	0.00031	0.00006	0.00005	0.00002	0.00127
9B	4.750	0.00122	0.00001	0.00012	0.00033	0.00029	0.00029	0.00006	0.00004	0.00002	0.00116
9C	4.957	0.00121	0.00001	0.00014	0.00038	0.00026	0.00026	0.00004	0.00003	0.00002	0.00114
10A	5.165	0.00110	0.00001	0.00011	0.00033	0.00027	0.00024	0.00006	0.00004	0.00002	0.00106
10B	5.372	0.00118	0.00001	0.00012	0.00035	0.00028	0.00026	0.00006	0.00004	0.00002	0.00114
10C	5.579	0.00110	0.00001	0.00010	0.00030	0.00029	0.00025	0.00006	0.00004	0.00002	0.00106
11A	5.787	0.00109	0.00001	0.00008	0.00029	0.00028	0.00027	0.00006	0.00004	0.00002	0.00105
11B	5.994	0.00088	0.00001	0.00007	0.00024	0.00022	0.00020	0.00006	0.00003	0.00002	0.00085
11C	6.201	0.00096	0.00001	0.00006	0.00025	0.00025	0.00024	0.00006	0.00004	0.00002	0.00093
12A	6.409	0.00091	0.00001	0.00006	0.00023	0.00023	0.00023	0.00006	0.00004	0.00002	0.00087
12B	6.616	0.00081	0.00001	0.00006	0.00021	0.00021	0.00021	0.00004	0.00003	0.00001	0.00078
12C	6.823	0.00098	0.00001	0.00006	0.00023	0.00025	0.00028	0.00006	0.00004	0.00002	0.00095
Average Λ_{qs} (kg.s^{-1}.m^{-2})		0.00130	0.00003	0.00019	0.00038	0.00029	0.00025	0.00005	0.00004	0.00002	0.00125
Average Λ_{qs} (g.s^{-1}.m^{-2})		**1.30**	**0.03**	**0.19**	**0.38**	**0.29**	**0.25**	**0.05**	**0.04**	**0.02**	**1.25**

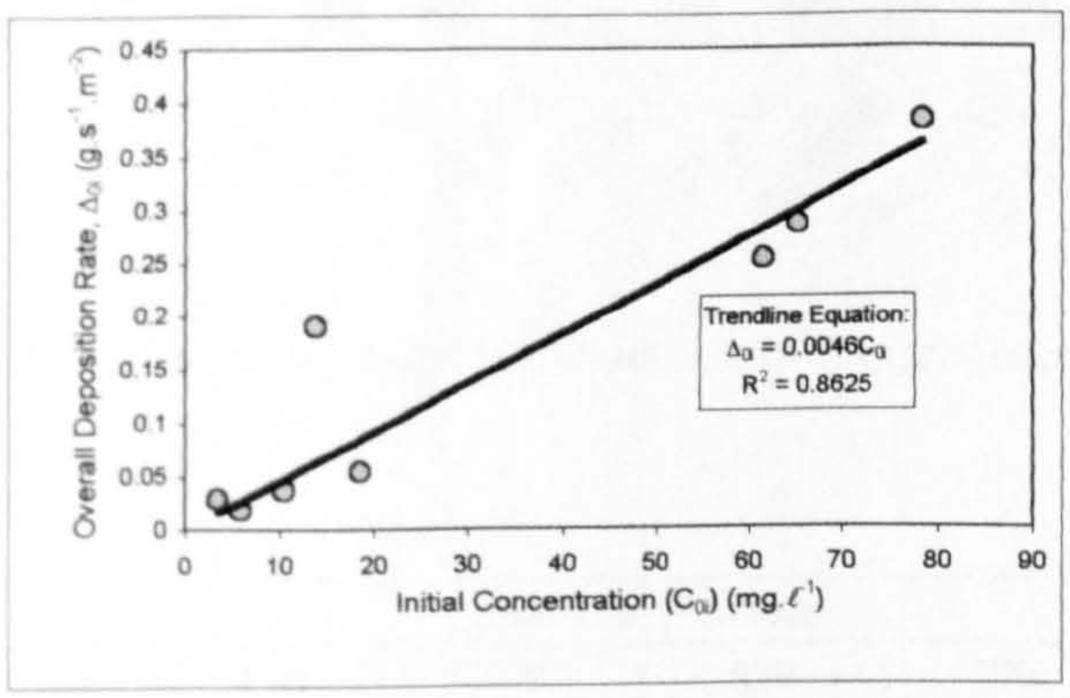

Figure A6.64 - Overall fractional deposition rate, Δ_{0i} against fractional initial concentration, C_{0i} for Experiment S2_EX11

Appendix 6.11 Fractional Composition of Deposited Sediments

This Appendix presents the data relating to the fractional composition of the deposited material recovered from the centreline traps along the length of the flume. Figure 6.65 illustrates the comparison between the natural grading of the LA grade sand and the overall composition of the deposited sediment recovered from the twelve traps during experiments S2_EX1-6 and 8-10. The remaining figures and tables show the longitudinal variation in composition of the deposited sediment for each experiment. The data presented in the tables show the variation in the median grain size, D_{50}, along the length of the flume.

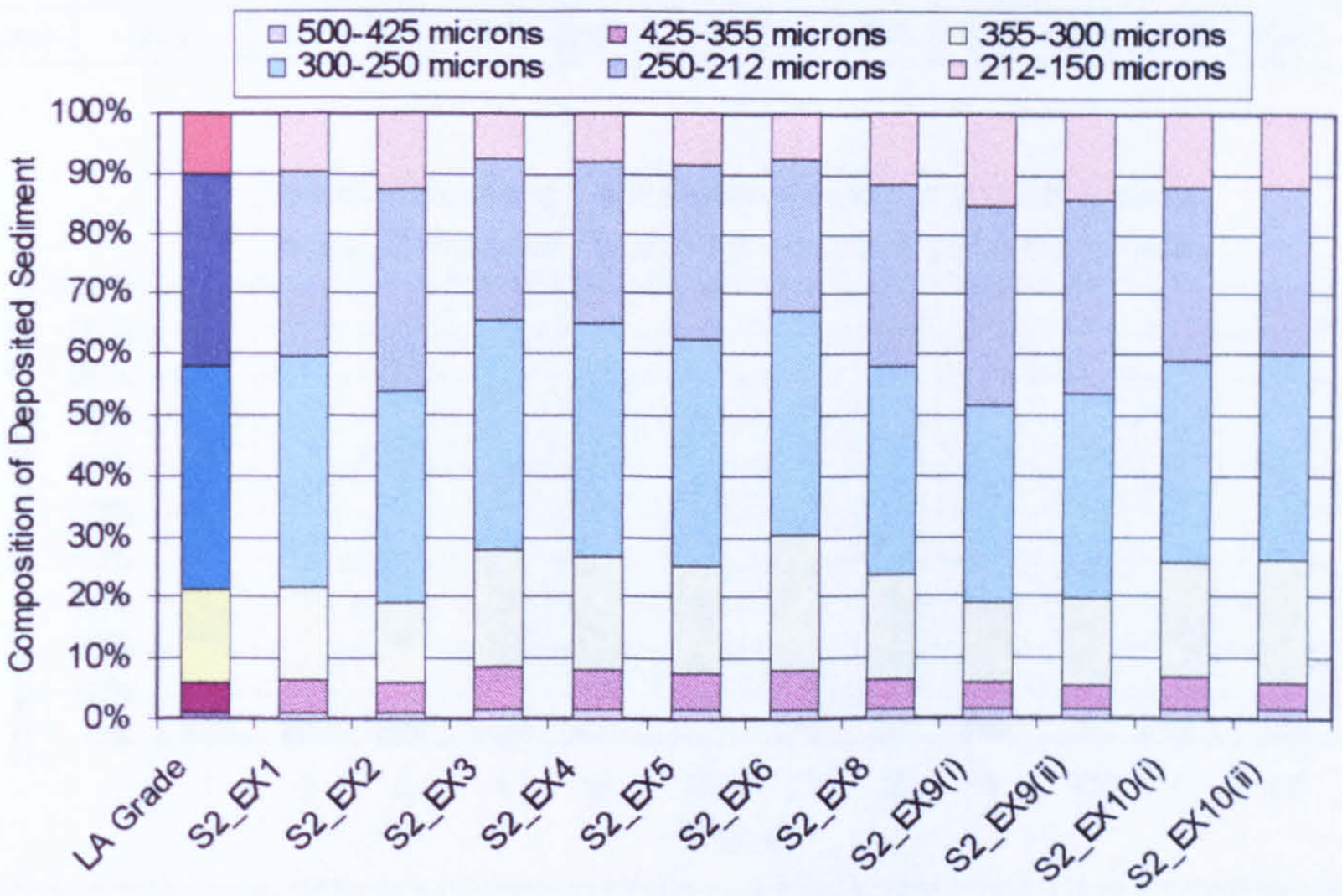

Figure A6.65 - Overall composition of deposited LA Grade sand – Experiments S2_EX1-6, 8-10

	Experiment Number					
	LA Grade	**EX1**	**EX2**	**EX3**	**EX4**	**EX5**
D_{16} (μm)	209	220	216	224	223	222
D_{50} (μm)	250	263	256	271	270	267
D_{84} (μm)	306	321	314	334	332	329
	Experiment Number					
	EX6	**EX8**	**EX9(i)**	**EX9(ii)**	**EX10(i)**	**EX10(ii)**
D_{16} (μm)	225	218	213	214	217	217
D_{50} (μm)	273	262	253	255	264	265
D_{84} (μm)	335	325	313	315	328	328

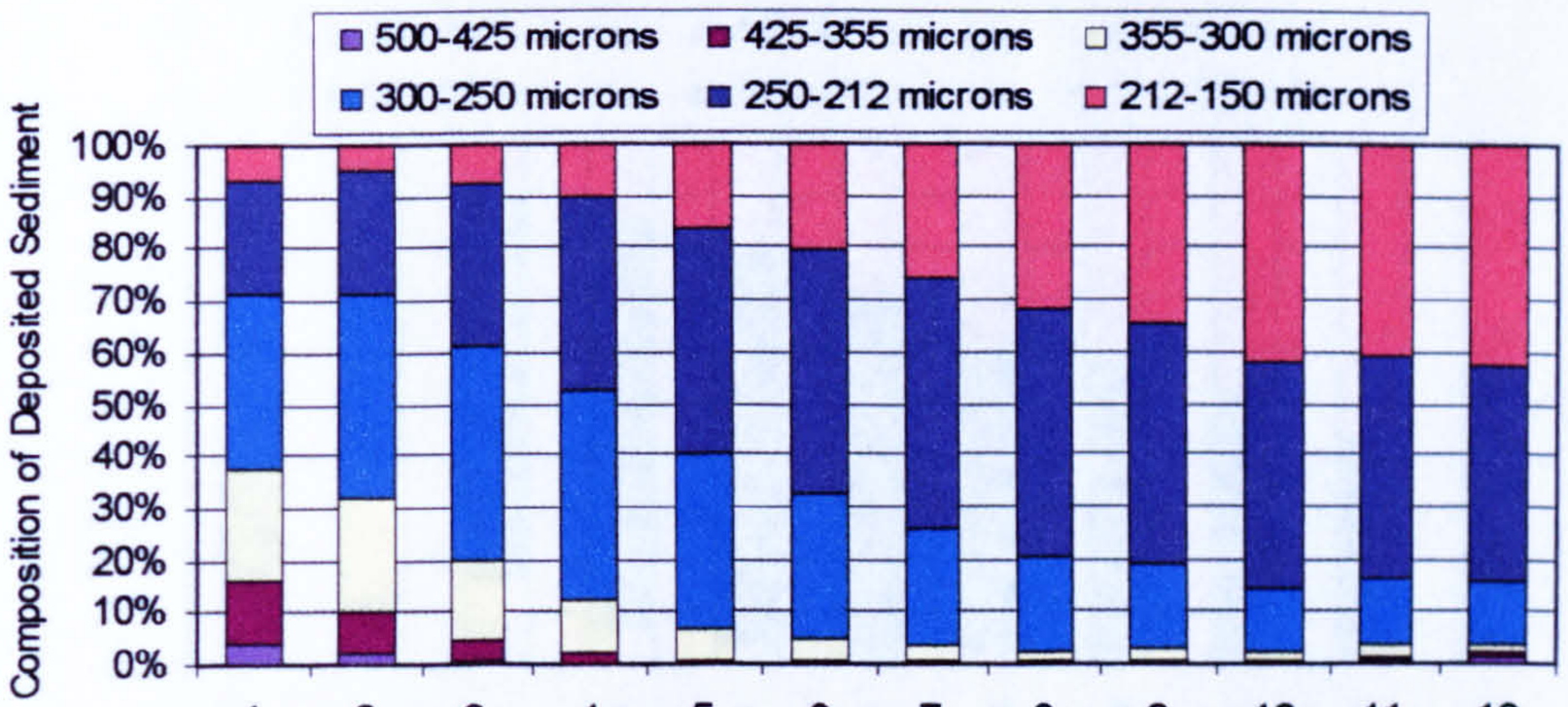

S2_EX1	LA Grade	Trap Number											
		1	2	3	4	5	6	7	8	9	10	11	12
D_{50} (μm)	250	281	277	264	253	241	236	231	226	225	219	220	218

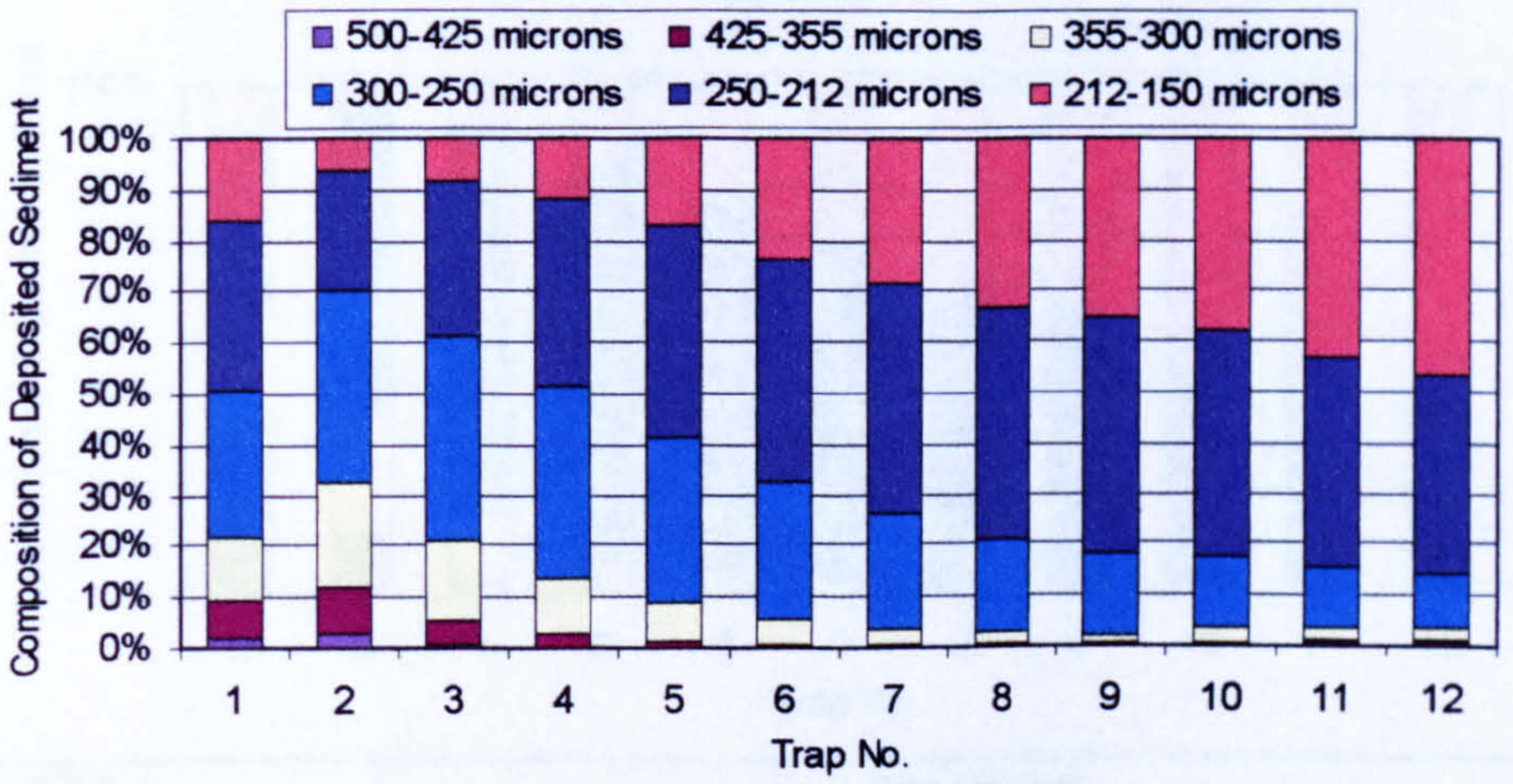

S2_EX2	LA Grade	Trap Number											
		1	2	3	4	5	6	7	8	9	10	11	12
D_{50} (μm)	250	251	277	264	252	242	235	230	226	224	222	218	215

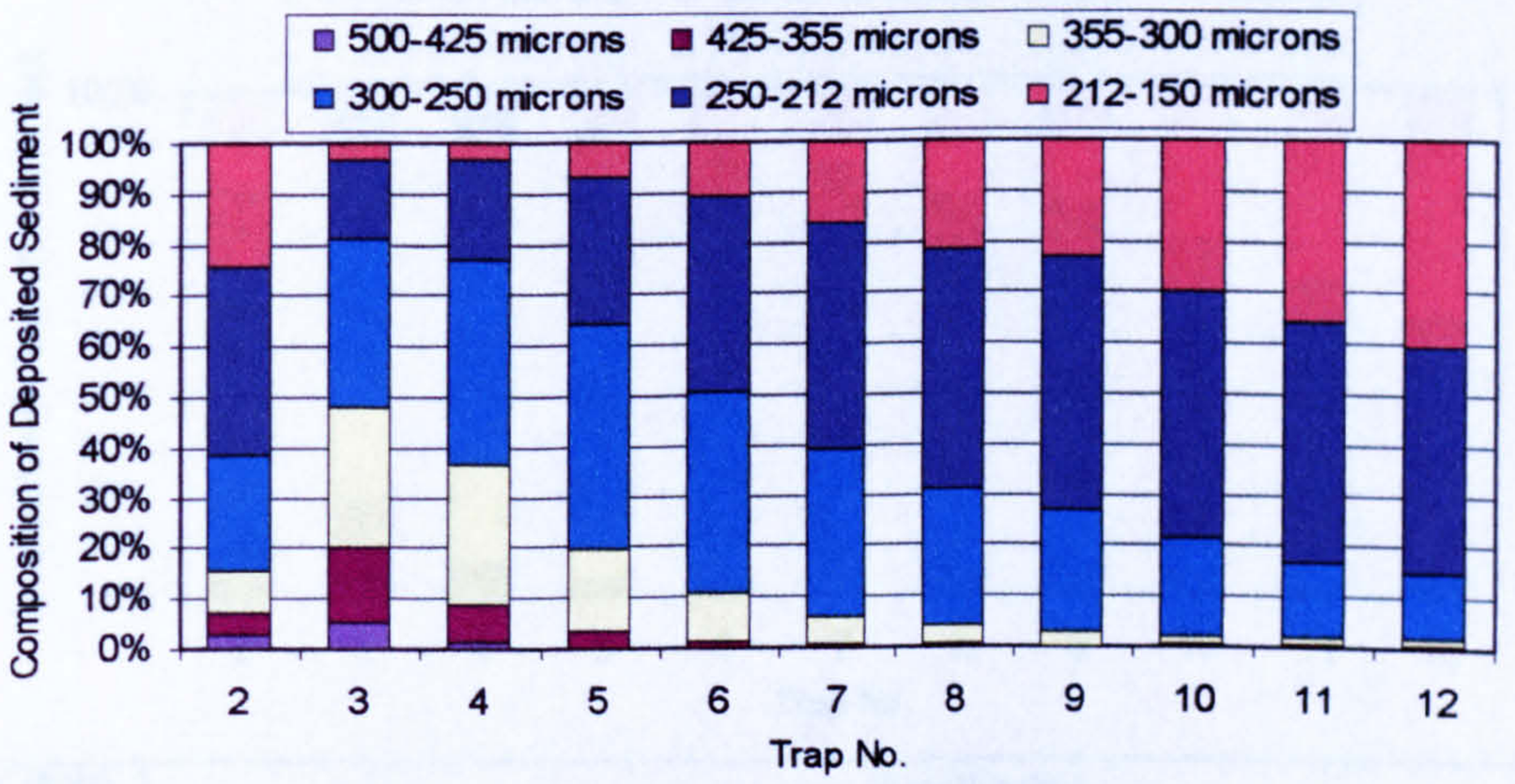

S2_EX3	LA Grade	Trap Number										
		2	3	4	5	6	7	8	9	10	11	12
D_{50} (μm)	250	238	297	284	266	251	241	235	233	228	223	220

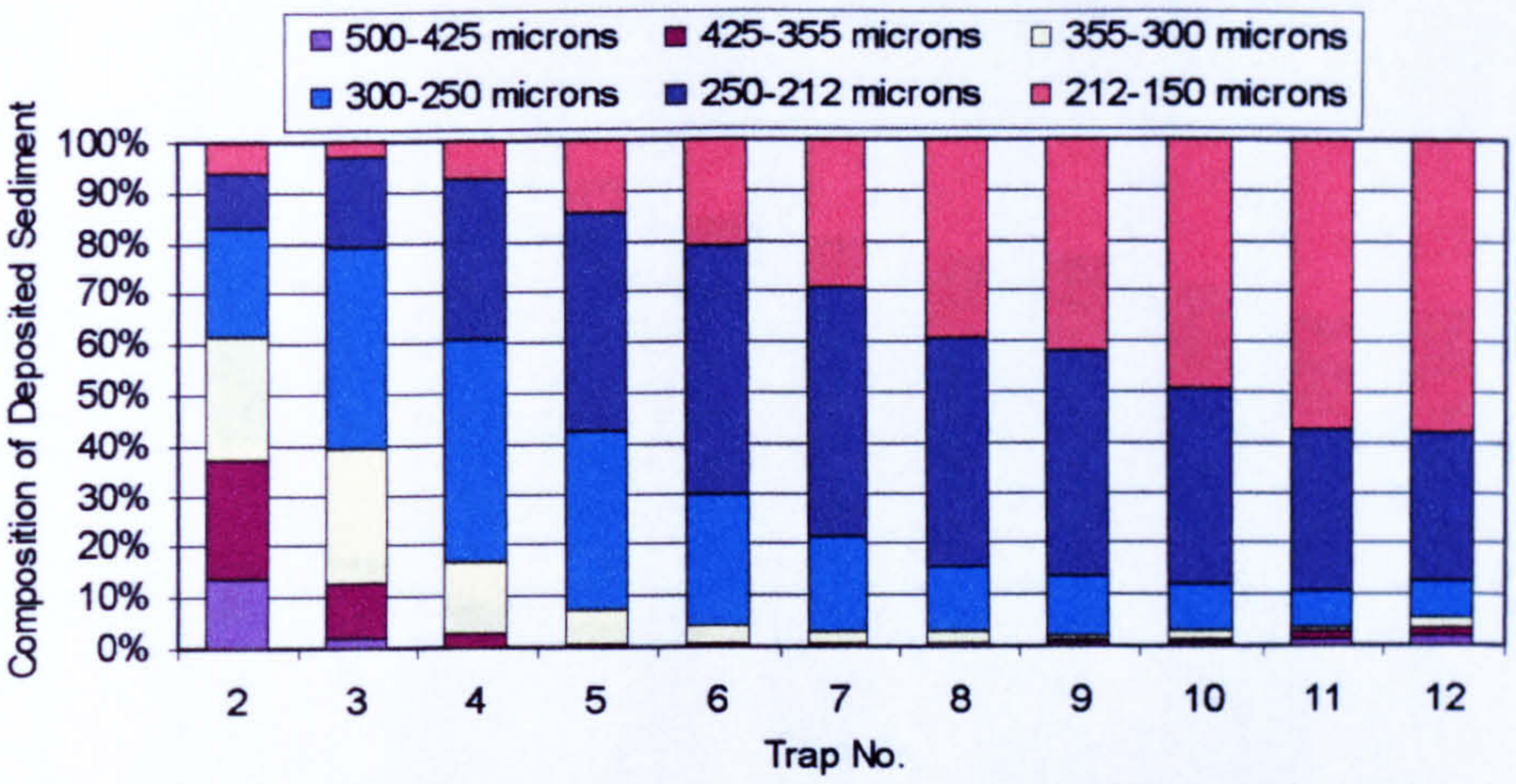

S2_EX4	LA Grade	Trap Number										
		2	3	4	5	6	7	8	9	10	11	12
D_{50} (μm)	250	325	287	262	243	234	228	221	219	212	204	203

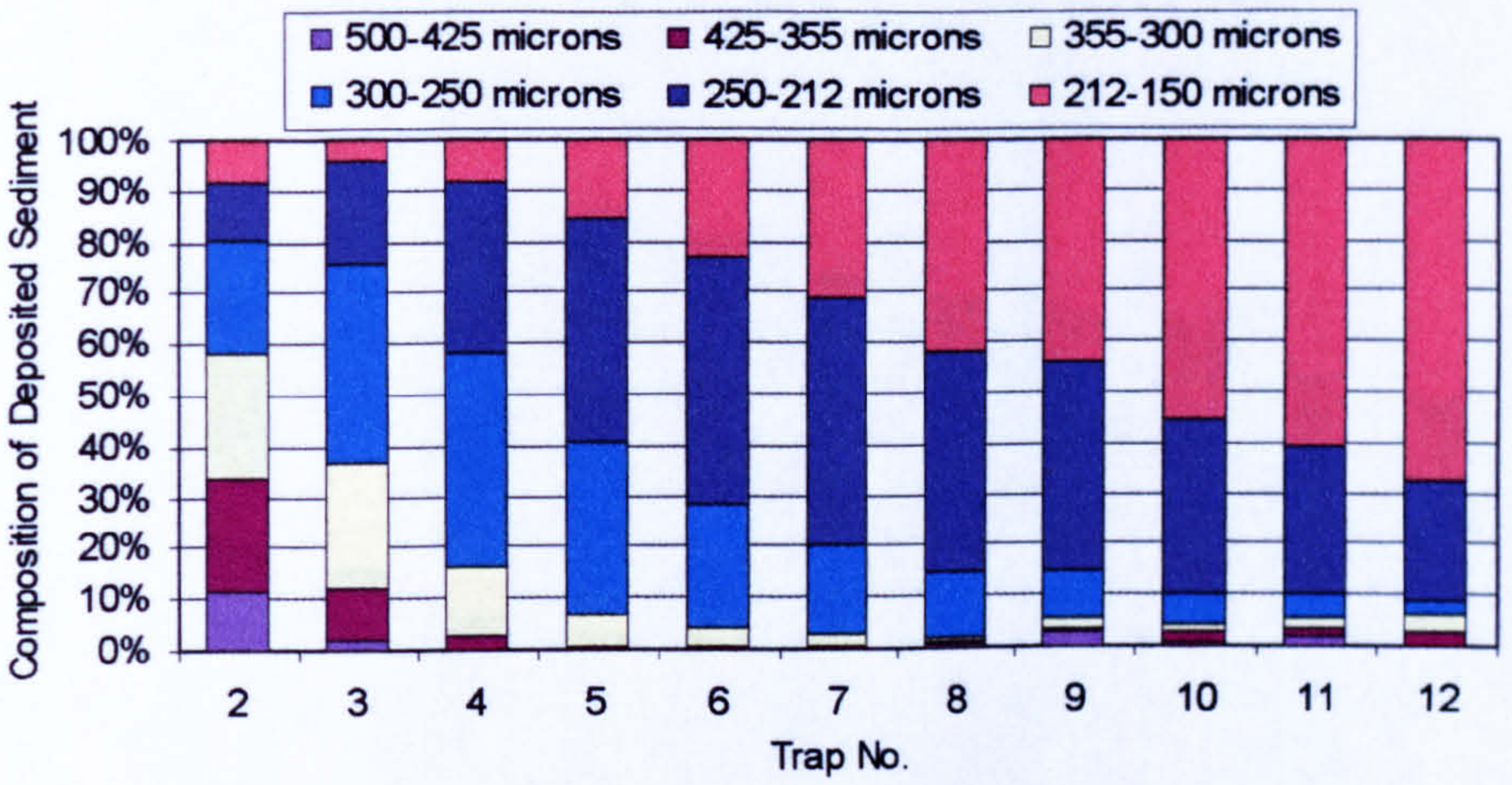

S2_EX5	LA Grade	Trap Number										
		2	3	4	5	6	7	8	9	10	11	12
D_{50} (μm)	250	318	283	260	242	233	227	219	217	206	201	196

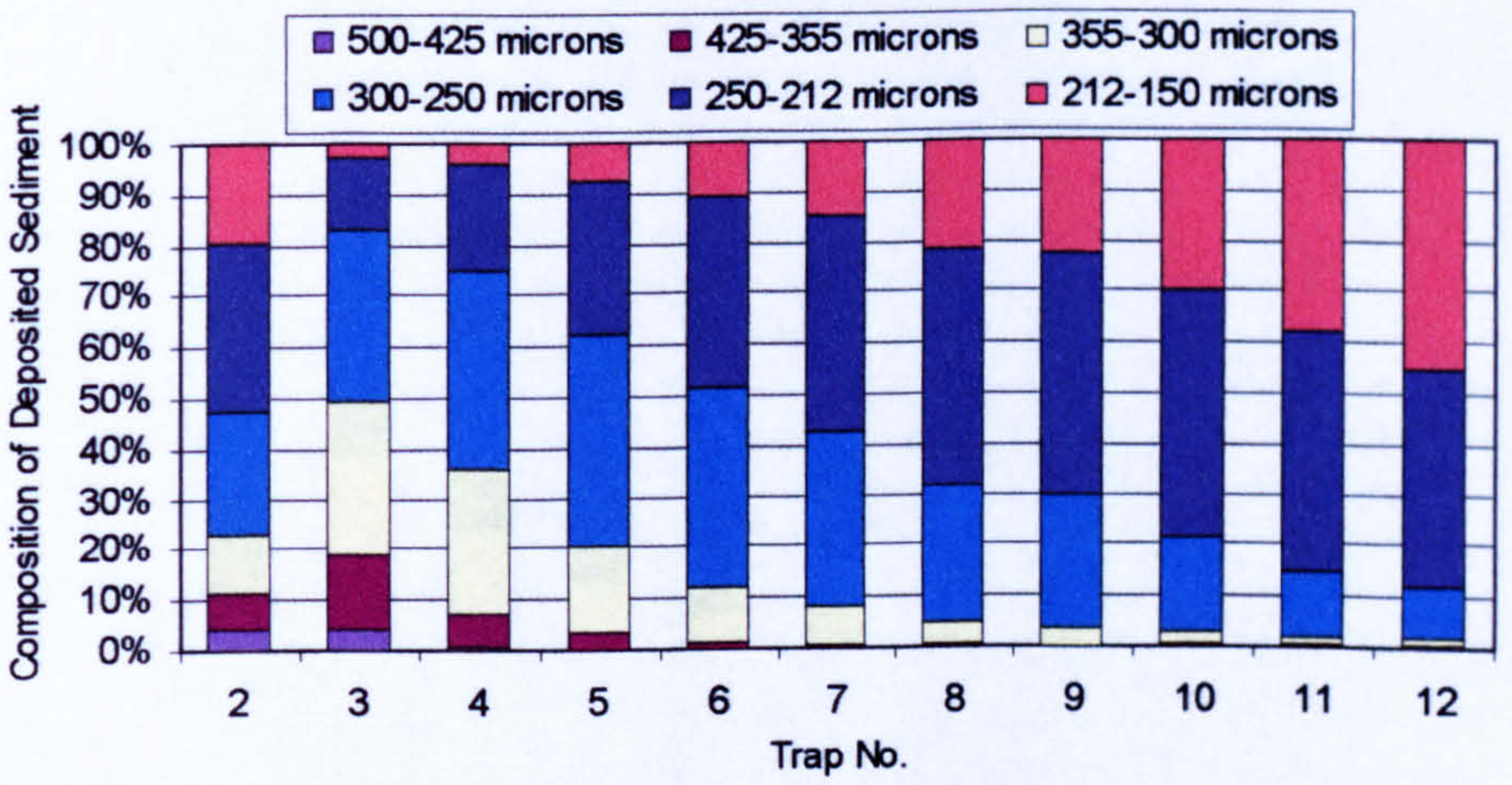

S2_EX6	LA Grade	Trap Number										
		2	3	4	5	6	7	8	9	10	11	12
D_{50} (μm)	250	244	299	282	264	252	243	235	234	228	222	216

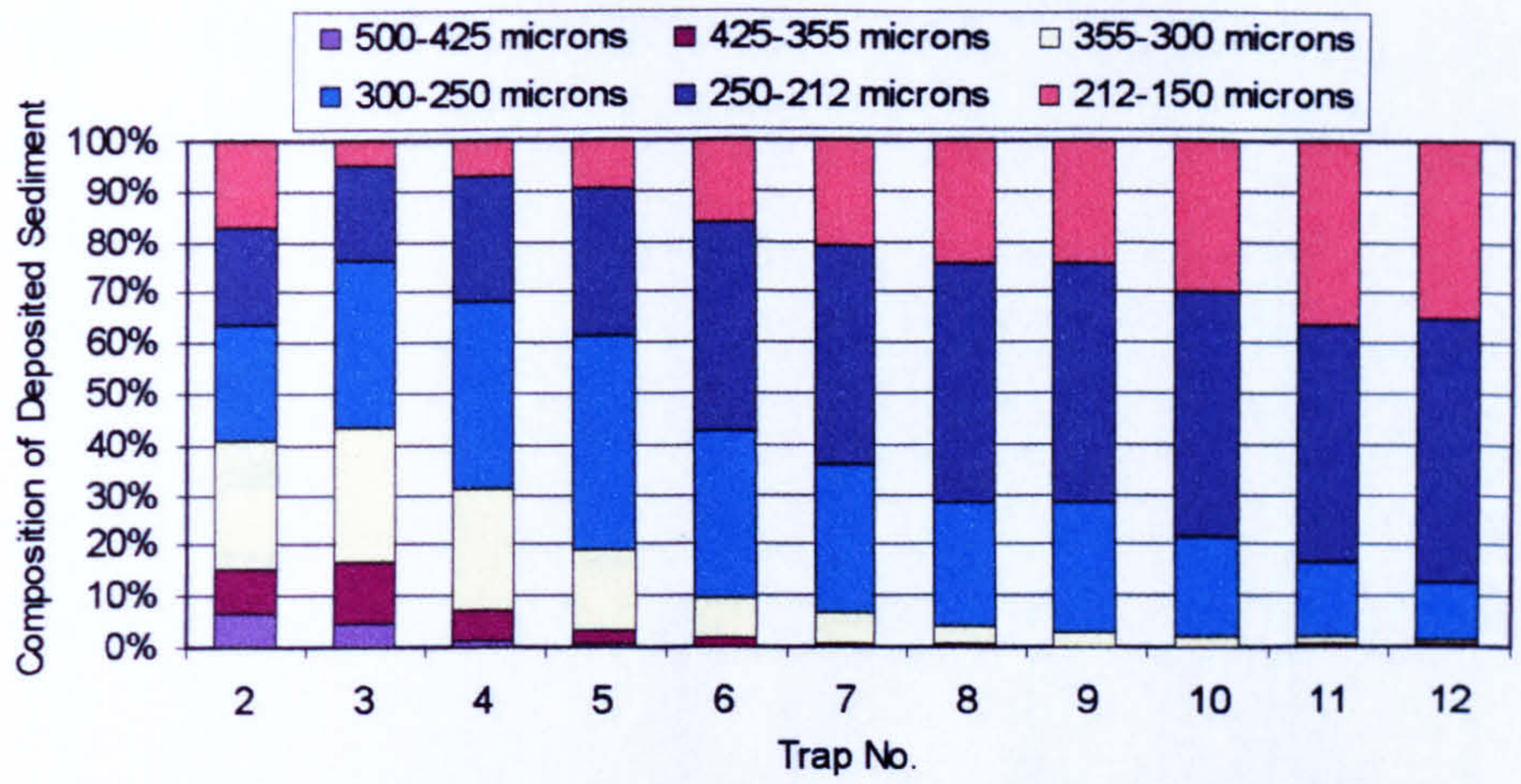

S2_EX8	LA Grade	Trap Number										
		2	3	4	5	6	7	8	9	10	11	12
D_{50} (μm)	250	279	290	274	263	243	237	233	233	228	223	223

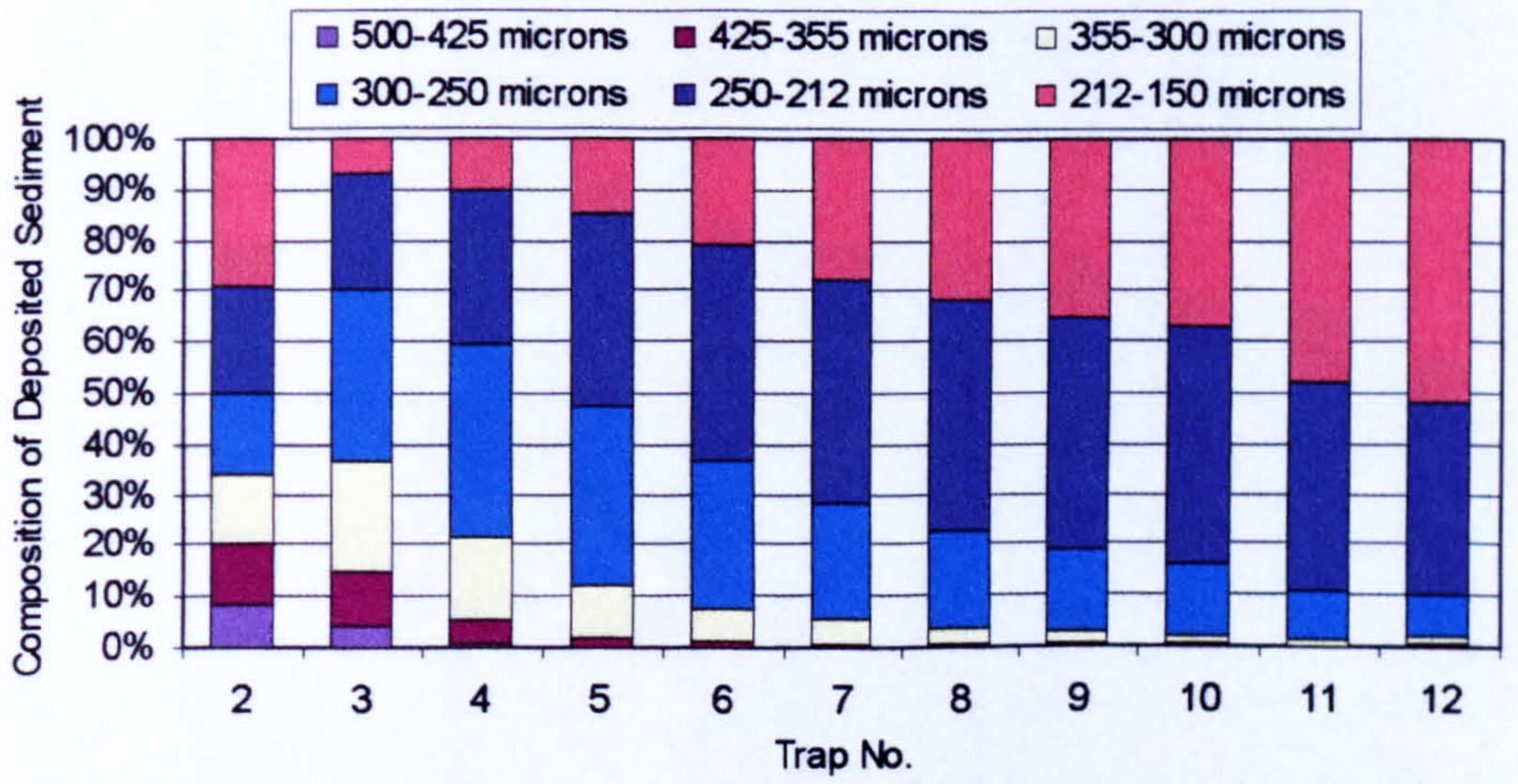

S2_EX9(i)	LA Grade	Trap Number										
		2	3	4	5	6	7	8	9	10	11	12
D_{50} (μm)	250	251	280	262	247	238	231	227	224	222	214	209

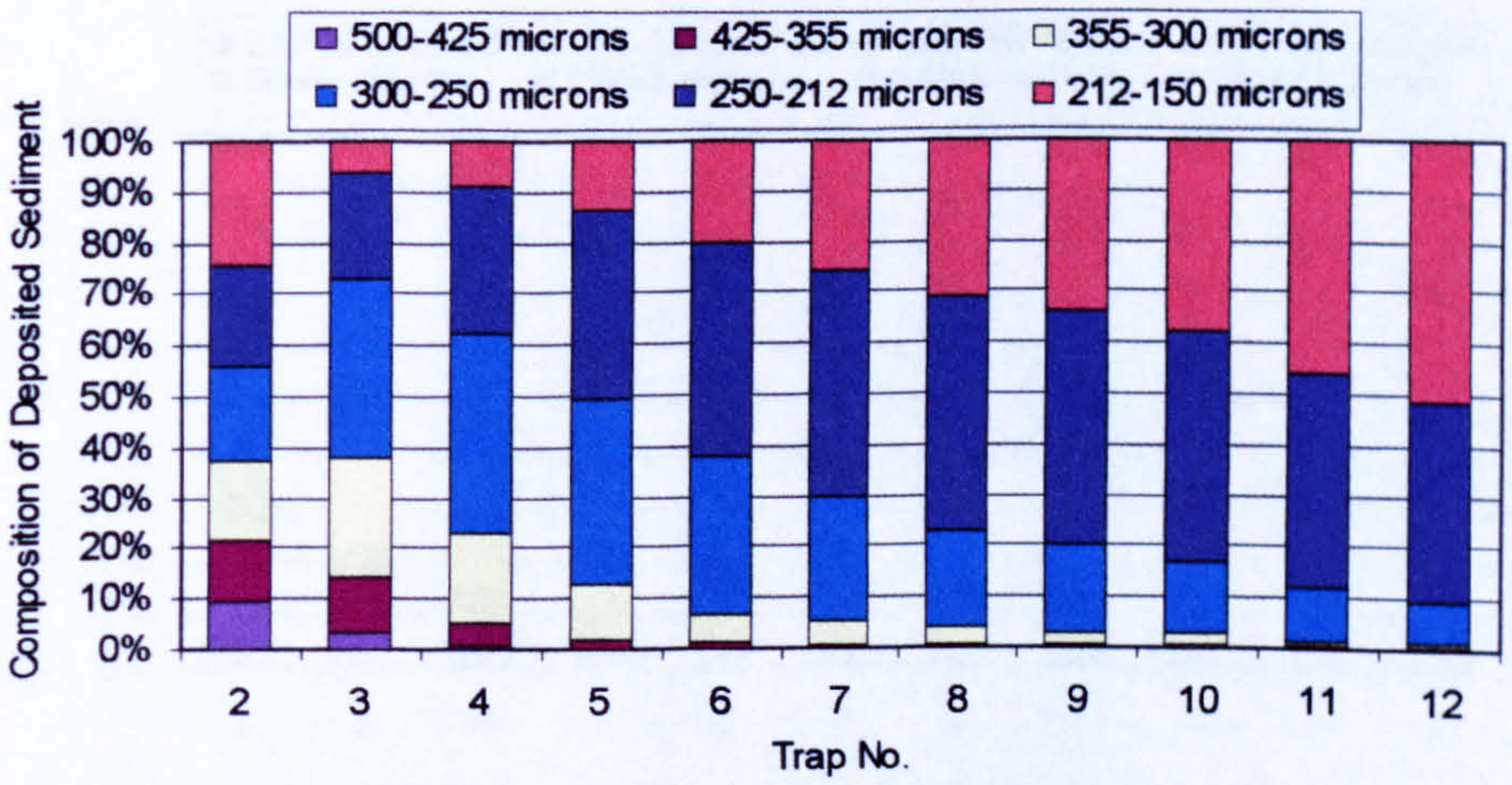

S2_EX9(ii)	LA Grade	Trap Number										
		2	3	4	5	6	7	8	9	10	11	12
D_{50} (μm)	250	266	283	266	250	239	233	228	225	222	216	210

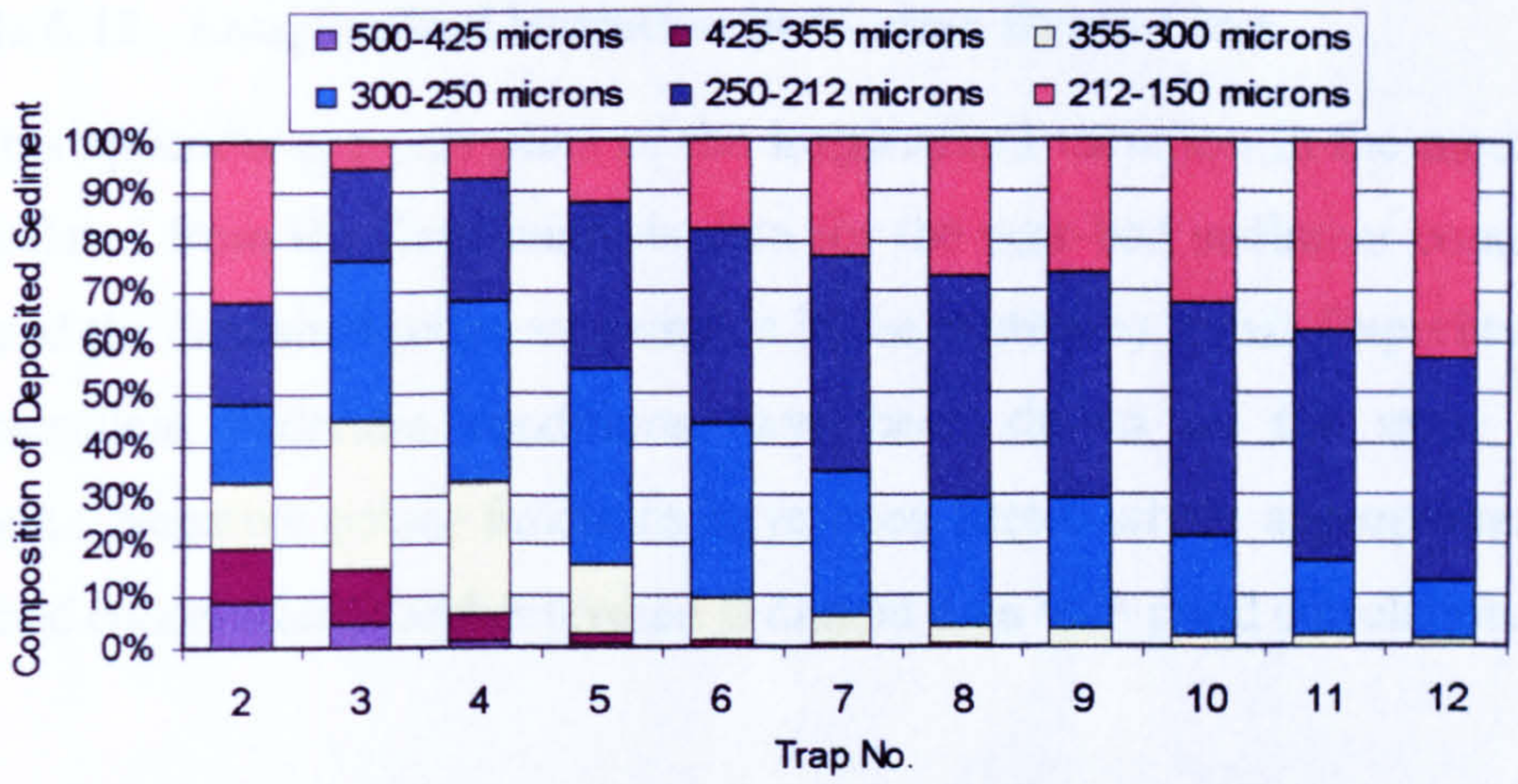

S2_EX10(i)	LA Grade	Trap Number										
		2	3	4	5	6	7	8	9	10	11	12
D_{50} (μm)	250	246	291	275	256	244	236	232	232	227	222	218

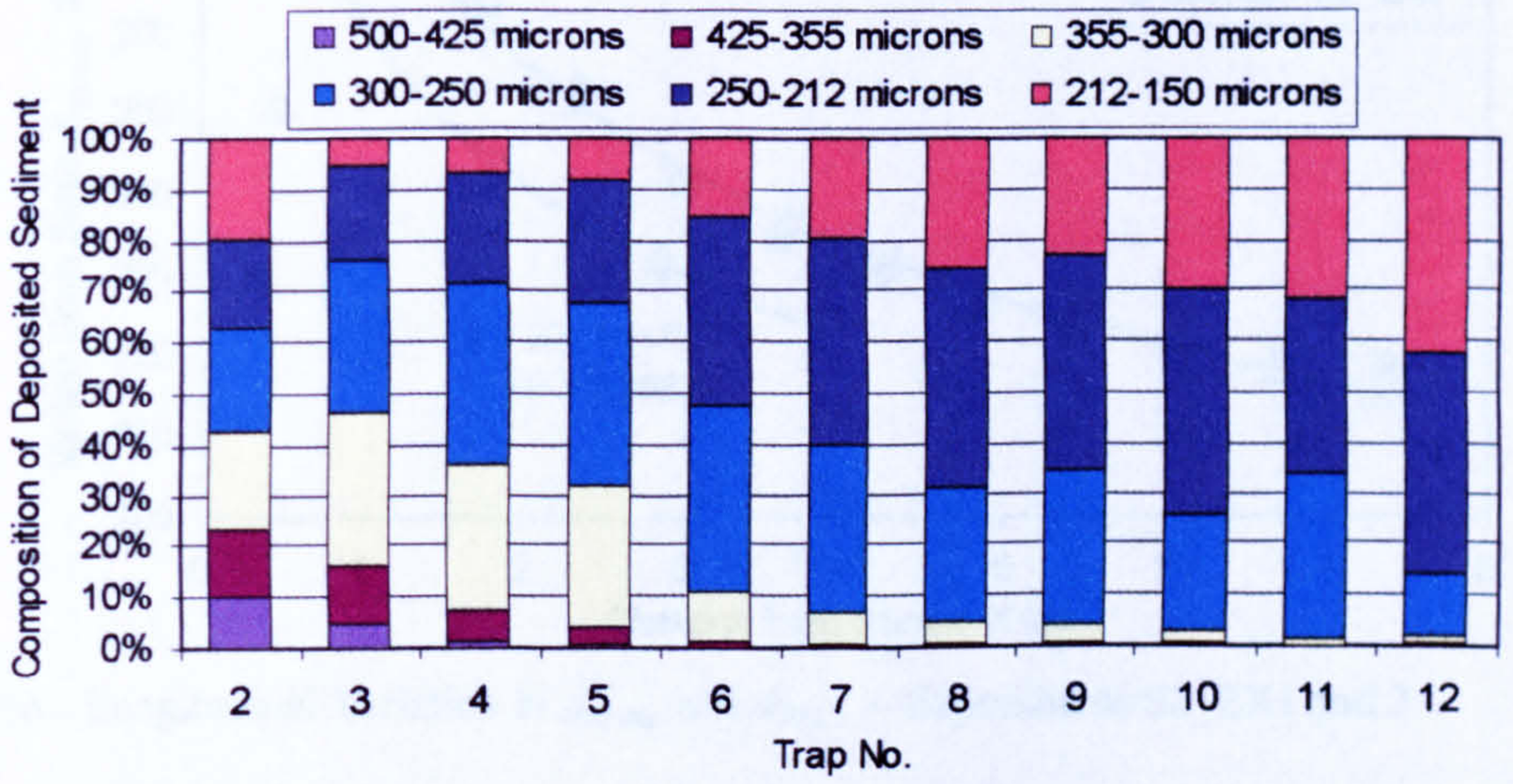

S2_EX10(ii)	LA Grade	Trap Number										
		2	3	4	5	6	7	8	9	10	11	12
D_{50} (μm)	250	282	293	280	275	247	240	233	236	229	232	219

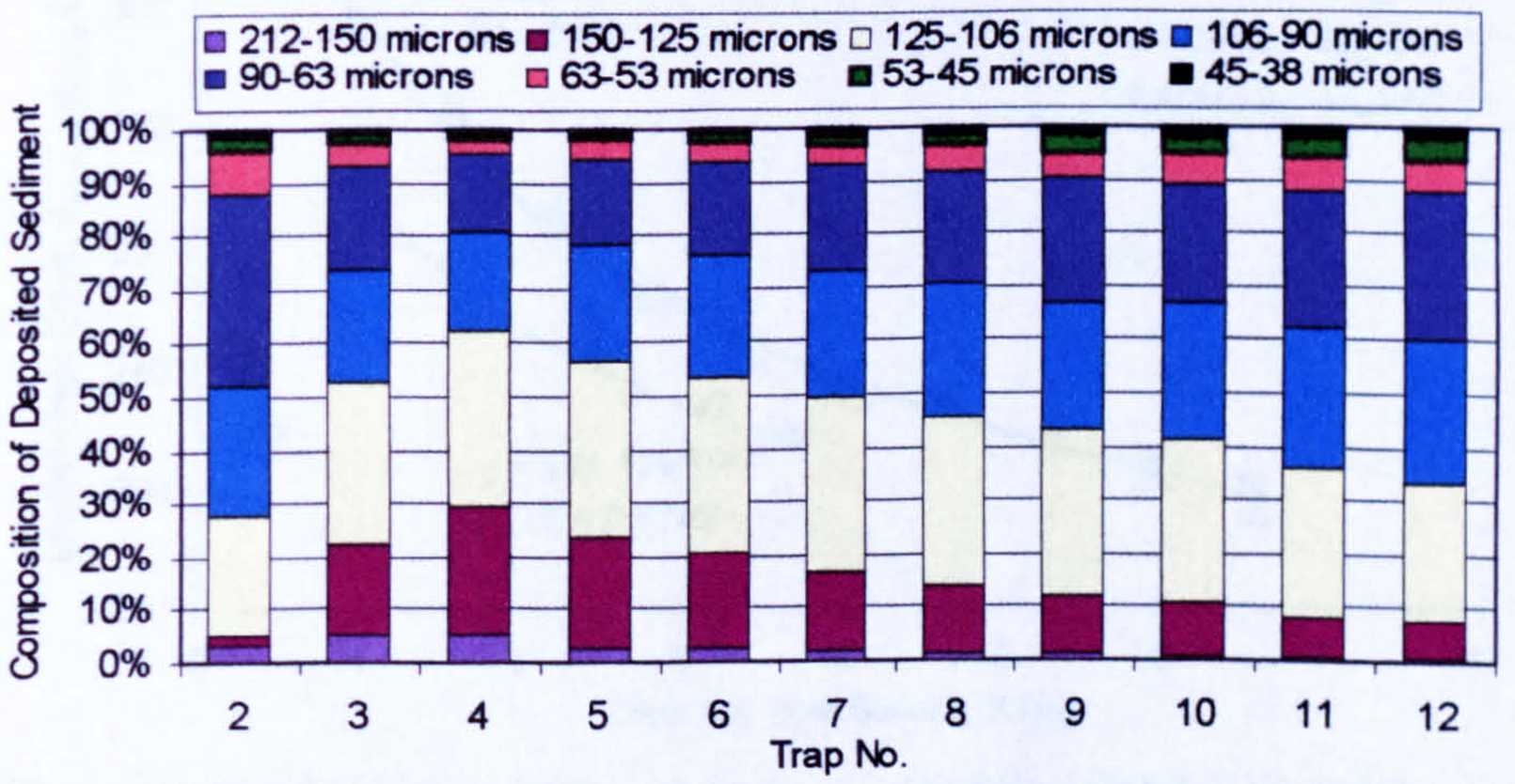

S2_EX11	DB Grade	Trap Number										
		2	3	4	5	6	7	8	9	10	11	12
D_{50} (μm)	97.0	91.4	107.5	113.1	109.8	108.0	105.5	103.3	101.1	100.3	97.5	96.1

Appendix 6.12 Longitudinal Variation in Median Grain Sizes

This appendix presents plots of the longitudinal variation in the median grain sizes calculated from the sieve analysis data for the near-bed sediment concentration samples and the deposited sediment samples in the centreline traps. Experiments with similar prevalent hydraulic conditions have been shown on the same plot for comparison. Negative power functions have been fitted, where appropriate, to both the near-bed concentration and deposited sediment data with good correlation.

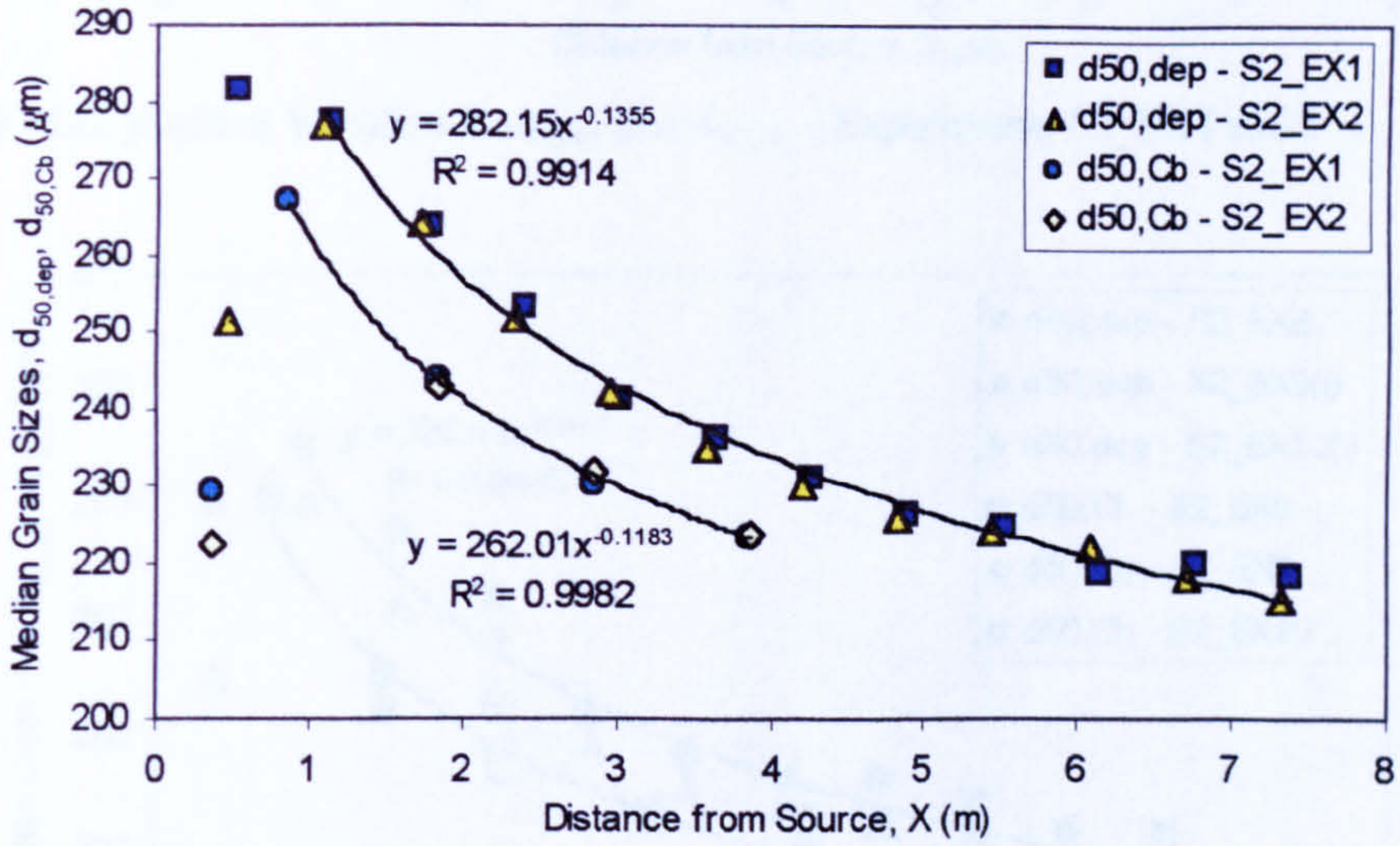

Figure A6.66 - Longitudinal Variation in $d_{50,dep}$ and $d_{50,Cb}$ – Experiments S2_EX1 and 2

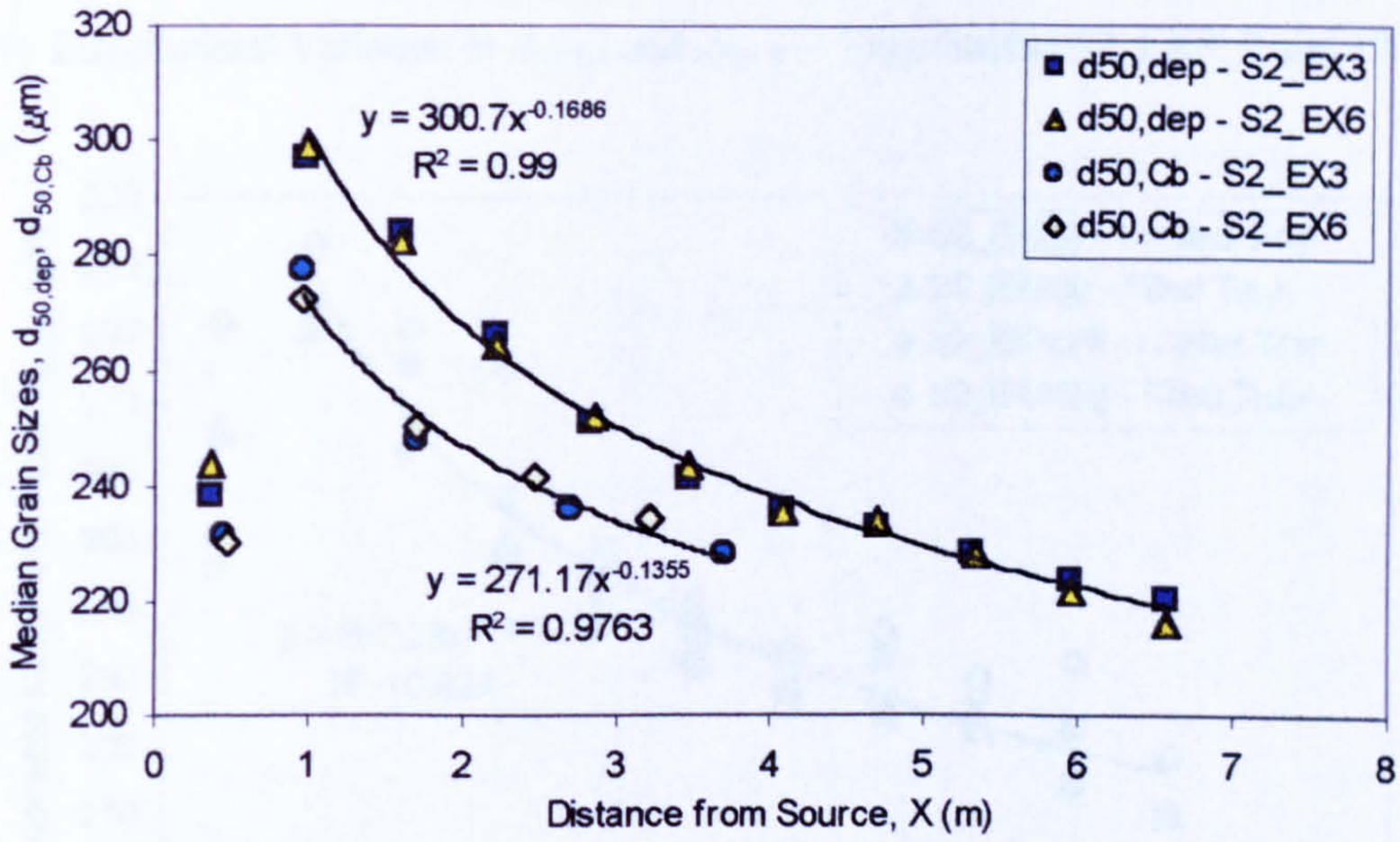

Figure A6.67 - Longitudinal Variation in $d_{50,dep}$ and $d_{50,Cb}$ – Experiments S2_EX3 and 6

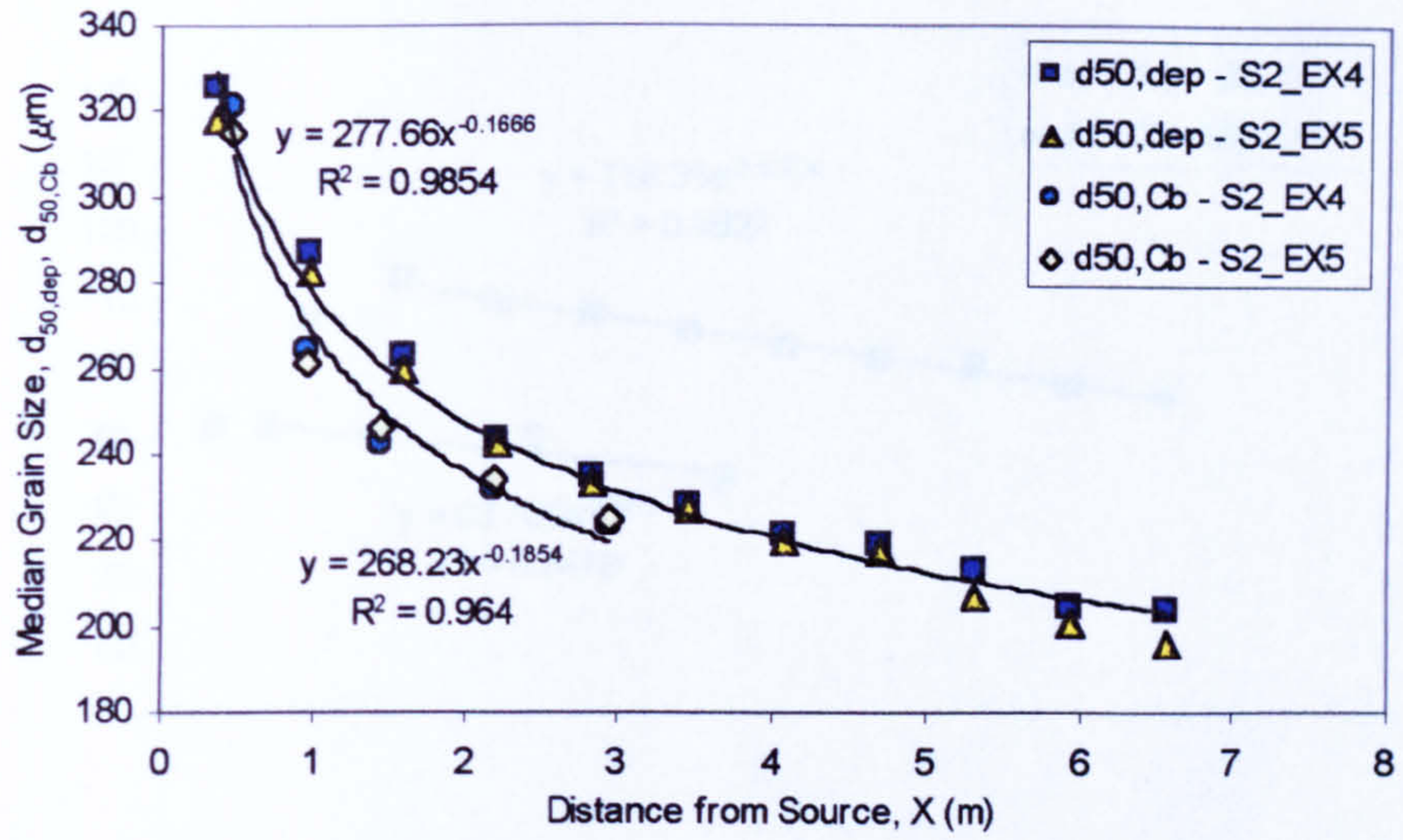

Figure A6.68 - Longitudinal Variation in $d_{50,dep}$ and $d_{50,Cb}$ – Experiments S2_EX4 and 5

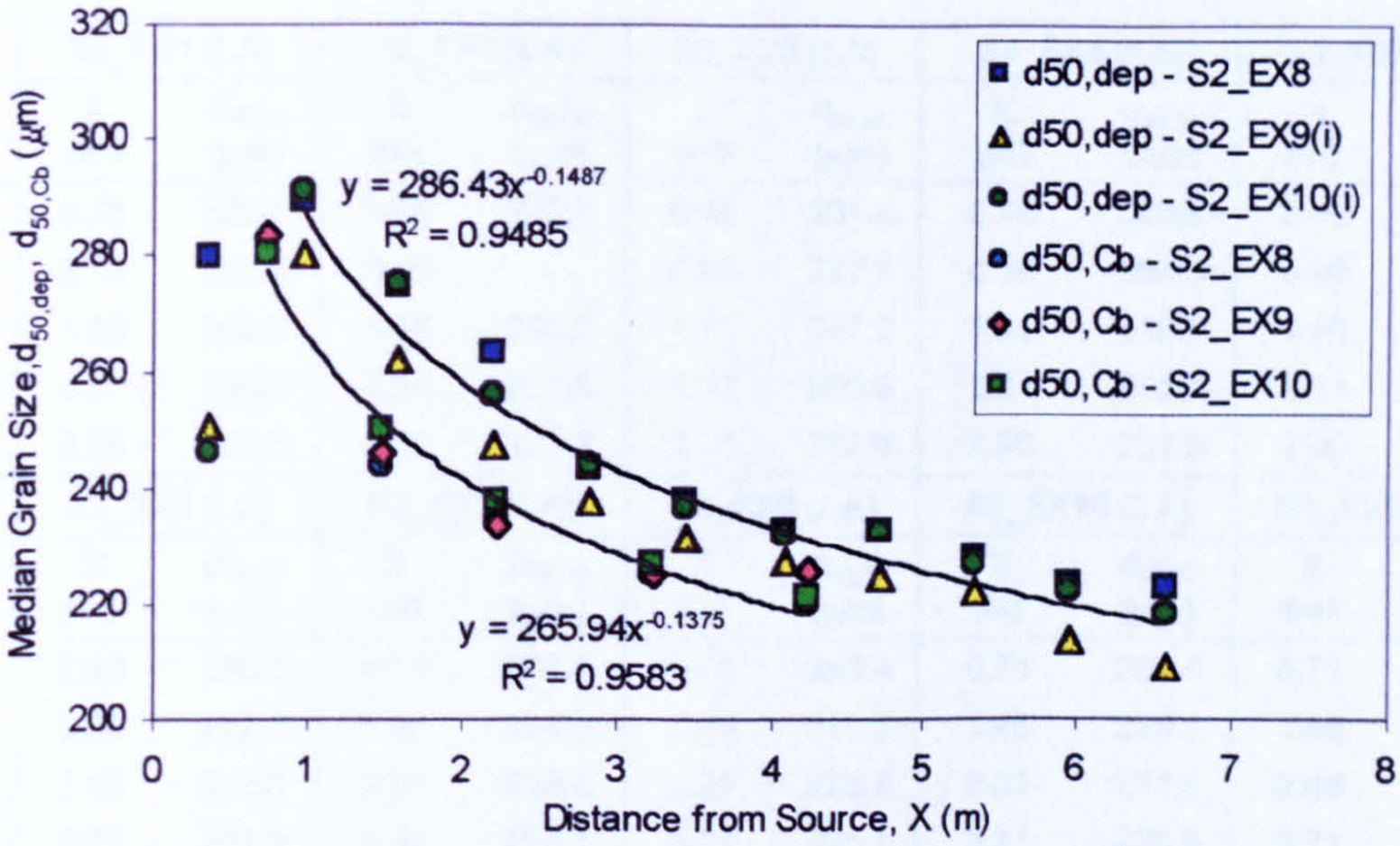

Figure A6.69 - Longitudinal Variation in $d_{50,dep}$ and $d_{50,Cb}$ – Experiments S2_EX8, 9 and 10

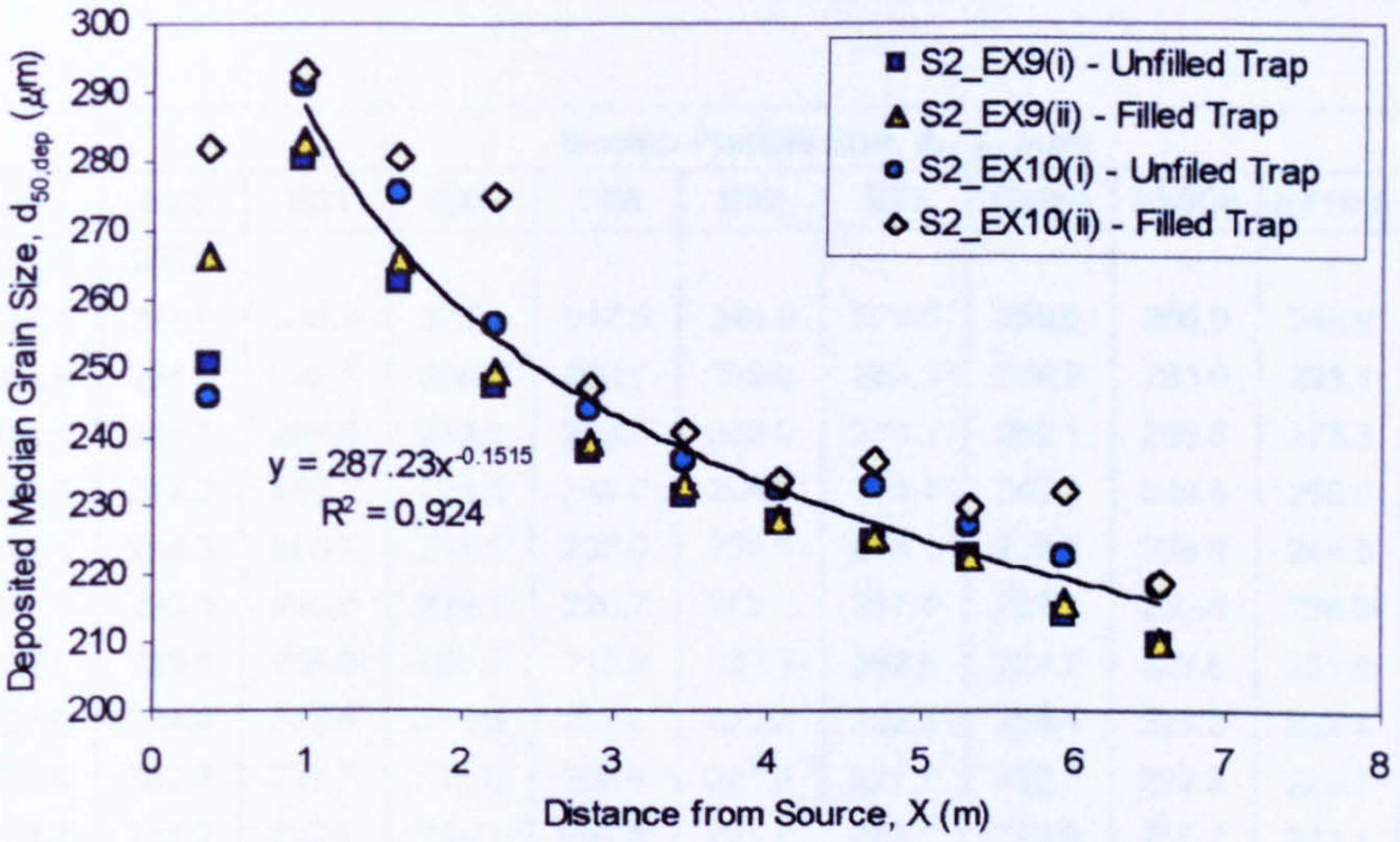

Figure A6.70 - Longitudinal Variation of $d_{50,dep}$ – Experiments S2_EX9(i) and (ii), S2_EX10(i) and (ii)

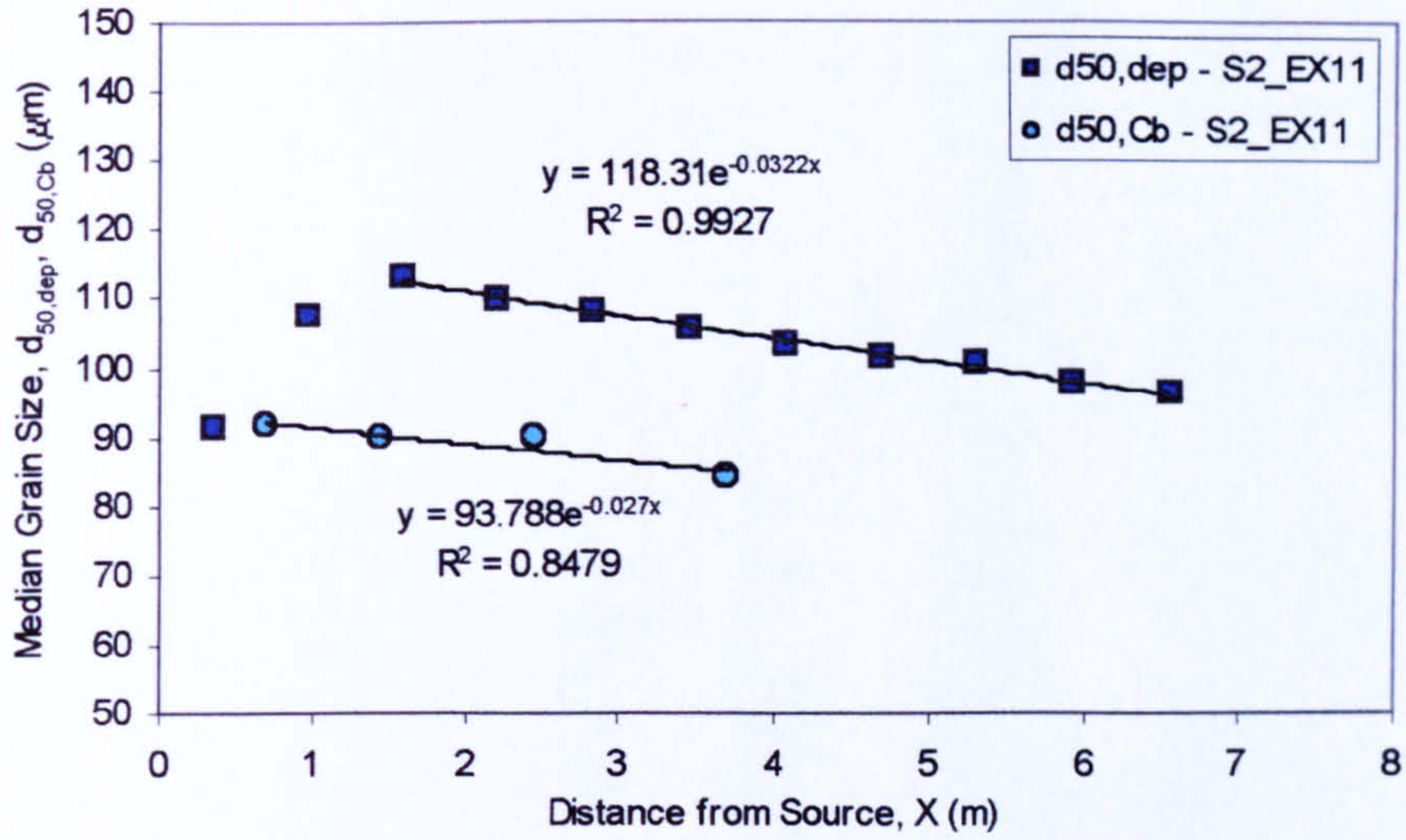

Figure A6.71 - Longitudinal Variation in $d_{50,dep}$ and $d_{50,Cb}$ – Experiments S2_EX11 (DB grade sand)

	S2_EX1 (LA)		S2_EX2 (LA)		S2_EX3 (LA)		S2_EX4 (LA)		S2_EX5 (LA)	
C_b Sample	X (m)	$d_{50,Cb}$ (µm)	X (m)	$d_{50,Cb}$ (µm)	X (m)	$d_{50,Cb}$ (µm)	X (m)	$d_{50,Cb}$ (µm)	X (m)	$d_{50,Cb}$ (µm)
1A	0.36	229.4	0.36	222.7	0.46	231.4	0.46	320.8	0.46	314.7
2A	0.86	267.0	0.86	-	0.96	277.1	0.96	264.3	0.96	261.3
3A	1.86	243.9	1.86	242.9	1.71	247.7	1.46	242.2	1.46	246.0
4A	2.86	230.2	2.86	231.9	2.71	235.6	2.21	231.3	2.21	234.0
5A	3.86	223.5	3.86	223.7	3.71	227.9	2.96	223.3	2.96	225.1
	S2_EX6 (LA)		S2_EX8 (LA)		S2_EX9 (LA)		S2_EX10 (LA)		S2_EX11 (LA)	
C_b Sample	X (m)	$d_{50,Cb}$ (µm)	X (m)	$d_{50,Cb}$ (µm)	X (m)	$d_{50,Cb}$ (µm)	X (m)	$d_{50,Cb}$ (µm)	X (m)	$d_{50,Cb}$ (µm)
1A	0.46	230.4	0.71	282.3	0.71	283.4	0.71	280.4	0.71	91.6
2A	0.96	272.4	1.46	244.0	1.46	245.8	1.46	250.1	1.46	89.6
3A	1.46	249.8	2.21	233.8	2.21	233.7	2.21	237.4	2.46	89.7
4A	2.21	241.3	3.21	225.1	3.21	225.1	3.21	226.5	3.71	83.9
5A	2.96	233.9	4.21	219.9	4.21	225.6	4.21	221.1	-	-

Table A6.11 - Variation of median grain size of near-bed sediment concentration samples ($d_{50,Cb}$)

	Median Particle Size, $d_{50,Dep}$ (µm)											
Trap No	EX1	EX2	EX3	EX4	EX5	EX6	EX8	EX9(i)	EX9(ii)	EX10(i)	EX10(ii)	EX11
1	281.5	251.2	-	-	-	-	-	-	-	-	-	-
2	277.1	277.0	238.1	325.4	317.8	243.9	279.5	250.6	266.0	245.9	281.7	91.4
3	263.6	264.2	296.5	286.7	282.7	299.0	289.5	279.9	283.0	291.1	293.0	107.5
4	253.1	251.7	283.6	262.4	259.6	282.2	274.3	262.1	265.6	275.3	280.3	113.1
5	241.2	242.2	266.0	243.2	241.9	264.4	263.4	247.1	249.6	256.0	274.7	109.8
6	236.1	234.8	250.7	234.4	233.0	251.9	243.1	237.7	238.9	244.0	247.1	108.0
7	231.1	230.3	240.7	228.1	226.7	243.2	237.4	231.2	232.8	236.3	240.4	105.5
8	226.1	225.8	235.0	220.9	219.2	235.3	232.6	227.2	227.6	231.8	233.3	103.3
9	224.6	224.2	232.5	218.9	217.4	233.8	232.5	224.4	225.3	232.4	236.2	101.1
10	218.9	222.2	227.7	212.3	206.4	227.9	227.7	222.3	222.2	226.7	229.3	100.3
11	220.0	218.3	223.2	204.1	200.8	221.7	223.1	213.9	215.7	222.1	232.0	97.5
12	218.3	215.4	219.9	203.3	195.8	216.2	222.8	209.3	210.1	218.0	218.6	96.1

Table A6.12 - Variation of median grain size of deposition samples in centreline traps ($d_{50,Dep}$)

Appendix 6.13

Sediment Deposition Velocity Calculations

EXPERIMENT S2_EX1

Experiment S2_EX1		Near Bed Concentration (C_b) (mg.ℓ^{-1}), Deposition Rate (Δ_b) (g.s^{-1}.m^{-2}) and Deposition Velocity (w_d) (m.s^{-1})											
Sampling Location		Full Mix			500-425 μm			425-355 μm			355-300 μm		
X (m)	Trap No.	C_b (mg.ℓ^{-1})	Δ_{bi} (g.s^{-1}.m^{-2})	w_d (m.s^{-1})	C_{bi} (mg.ℓ^{-1})	Δ_b (g.s^{-1}.m^{-2})	w_{di} (m.s^{-1})	C_{bi} (mg.ℓ^{-1})	Δ_b (g.s^{-1}.m^{-2})	w_{di} (m.s^{-1})	C_{bi} (mg.ℓ^{-1})	Δ_b (g.s^{-1}.m^{-2})	w_{di} (m.s^{-1})
0.36	1A	16.82	1.022	**0.061**	1.01	0.017	**0.017**	1.02	0.048	**0.046**	1.49	0.097	**0.065**
0.86	2A	259.50	10.016	**0.039**	5.43	0.325	**0.060**	17.39	1.107	**0.064**	45.58	2.195	**0.048**
1.86	3B	293.17	8.631	**0.029**	0.98	0.041	**0.042**	5.20	0.290	**0.056**	26.72	1.204	**0.045**
2.86	5A	92.69	3.377	**0.036**	0.15	0.003	**0.020**	0.69	0.031	**0.045**	3.53	0.203	**0.057**
3.86	6C	69.87	1.238	**0.018**	0.10	0.002	**0.016**	0.29	0.004	**0.015**	1.42	0.041	**0.029**

		300-250 μm			250-212 μm			212-150 μm			Σ (500-150 μm)		
X (m)	Trap No.	C_{bi} (mg.ℓ^{-1})	Δ_{bi} (g.s^{-1}.m^{-2})	w_d (m.s^{-1})	C_{bi} (mg.ℓ^{-1})	Δ_b (g.s^{-1}.m^{-2})	w_d (m.s^{-1})	C_{bi} (mg.ℓ^{-1})	Δ_b (g.s^{-1}.m^{-2})	w_d (m.s^{-1})	C_{bi} (mg.ℓ^{-1})	Δ_b (g.s^{-1}.m^{-2})	w_d (m.s^{-1})
0.36	1A	2.87	0.254	**0.089**	4.17	0.315	**0.076**	3.82	0.179	**0.047**	14.38	0.911	**0.063**
0.86	2A	89.56	3.613	**0.040**	75.80	2.031	**0.027**	23.59	0.444	**0.019**	257.35	9.715	**0.038**
1.86	3B	94.21	3.493	**0.037**	116.96	2.783	**0.024**	46.28	0.712	**0.015**	290.36	8.522	**0.029**
2.86	5A	20.78	1.095	**0.053**	39.95	1.416	**0.035**	25.67	0.530	**0.021**	90.78	3.279	**0.036**
3.86	6C	12.11	0.300	**0.025**	29.63	0.544	**0.018**	24.42	0.260	**0.011**	67.98	1.151	**0.017**

Summary of Results - S2_EX1					From Plotted Results		
Size Class	d (μm)	w_{di} (ms^{-1})	w_s (ms^{-1})	w_{di}/w_{si}	Gradient	R^2	w_{di}/w_{si}
Full Mix	250	0.0366	0.0296	**1.24**	0.03320	0.934	**1.12**
500-425 μm	462.5	0.0310	0.0600	**0.52**	0.05790	0.973	**0.97**
425-355 μm	390	0.0452	0.0491	**0.92**	0.06290	0.998	**1.28**
355-300 μm	327.5	0.0490	0.0405	**1.21**	0.04740	0.998	**1.17**
300-250 μm	275	0.0487	0.0322	**1.51**	0.03890	0.984	**1.21**
250-212 μm	231	0.0360	0.0270	**1.33**	0.02530	0.930	**0.94**
212-150 μm	181	0.0225	0.0201	**1.12**	0.01610	0.723	**0.80**

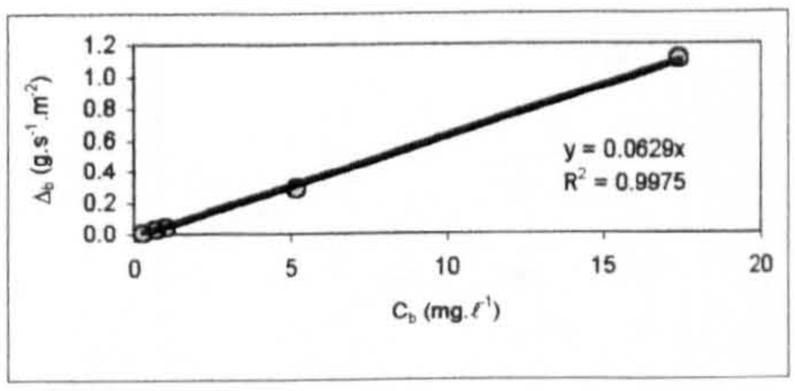

EXPERIMENT S2_EX2

Experiment S2_EX2		Near Bed Concentration (C_b) (mg.ℓ^{-1}), Deposition Rate (Δ_b) (g.s^{-1}.m^{-2}) and Deposition Velocity (w_d) (m.s^{-1})											
Sampling Location		Full Mix			500-425 μm			425-355 μm			355-300 μm		
X (m)	Trap No.	C_b (mg.ℓ^{-1})	Δ_{bi} (g.s^{-1}.m^{-2})	w_d (m.s^{-1})	C_{bi} (mg.ℓ^{-1})	Δ_{bi} (g.s^{-1}.m^{-2})	w_{di} (m.s^{-1})	C_{bi} (mg.ℓ^{-1})	Δ_{bi} (g.s^{-1}.m^{-2})	w_{di} (m.s^{-1})	C_{bi} (mg.ℓ^{-1})	Δ_{bi} (g.s^{-1}.m^{-2})	w_{di} (m.s^{-1})
0.36	1A	11.66	0.637	**0.055**	0.18	0.005	**0.026**	0.37	0.018	**0.048**	0.62	0.041	**0.066**
0.86	2A	-	2.422	-	-	0.089	-	-	0.270	-	-	0.495	-
1.86	3C	73.12	2.511	**0.034**	0.19	0.012	**0.063**	1.47	0.102	**0.069**	6.36	0.341	**0.054**
2.86	5A/B	34.21	1.162	**0.034**	0.00	0.001	-	0.32	0.015	**0.048**	1.50	0.084	**0.056**
3.86	6C	17.27	0.546	**0.032**	0.04	0.000	-	0.10	0.003	**0.027**	0.40	0.019	**0.048**

		300-250 μm			250-212 μm			212-150 μm			Σ (500-150 μm)		
X (m)	Trap No.	C_{bi} (mg.ℓ^{-1})	Δ_{bi} (g.s^{-1}.m^{-2})	w_d (m.s^{-1})	C_{bi} (mg.ℓ^{-1})	Δ_{bi} (g.s^{-1}.m^{-2})	w_d (m.s^{-1})	C_{bi} (mg.ℓ^{-1})	Δ_{bi} (g.s^{-1}.m^{-2})	w_d (m.s^{-1})	C_{bi} (mg.ℓ^{-1})	Δ_{bi} (g.s^{-1}.m^{-2})	w_d (m.s^{-1})
0.36	1A	1.91	0.161	**0.084**	3.83	0.245	**0.064**	3.94	0.137	**0.035**	10.86	0.607	**0.056**
0.86	2A	-	0.810	-	-	0.515	-	-	0.152	-	-	-	-
1.86	3B	22.96	0.986	**0.043**	28.61	0.798	**0.028**	12.32	0.231	**0.019**	71.90	2.470	**0.034**
2.86	5A	8.27	0.372	**0.045**	14.43	0.467	**0.032**	8.74	0.185	**0.021**	33.26	1.124	**0.034**
3.86	6C	3.21	0.133	**0.041**	7.28	0.232	**0.032**	5.71	0.159	**0.028**	16.74	0.546	**0.033**

Summary of Results - S2_EX2					Results from Plots		
Size Class	d (μm)	w_{di} (ms^{-1})	w_s (ms^{-1})	w_{di}/w_{si}	Gradient	R^2	w_{di}/w_{si}
Full Mix	250	0.0386	0.0296	**1.30**	0.03460	0.97660	**1.17**
500-425 μm	462.5	0.0447	0.0600	**0.74**	0.04400	0.67330	**0.73**
425-355 μm	390	0.0480	0.0491	**0.98**	0.06680	0.98170	**1.36**
355-300 μm	327.5	0.0561	0.0405	**1.39**	0.05390	0.99880	**1.33**
300-250 μm	275	0.0534	0.0322	**1.66**	0.04340	0.98640	**1.35**
250-212 μm	231	0.0391	0.0270	**1.45**	0.02940	0.89730	**1.09**
212-150 μm	181	0.0256	0.0201	**1.27**	0.02140	-0.07300	**1.06**

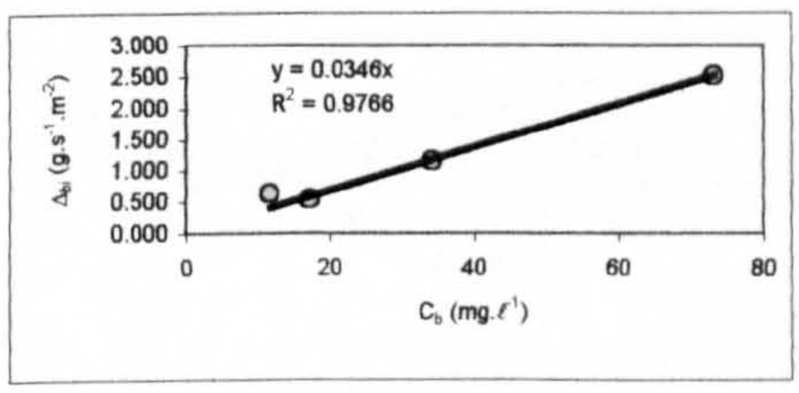

EXPERIMENT S2_EX3

Experiment S2_EX3		Near Bed Concentration (C_b) (mg.ℓ^{-1}), Deposition Rate (Δ_b) (g.s^{-1}.m^{-2}) and Deposition Velocity (w_d) (m.s^{-1})											
Sampling Location		Full Mix			500-425 μm			425-355 μm			355-300 μm		
X (m)	Trap No.	C_b (mg.ℓ^{-1})	Δ_b (g.s^{-1}.m^{-2})	w_d (m.s^{-1})	C_{bi} (mg.ℓ^{-1})	Δ_{bi} (g.s^{-1}.m^{-2})	w_{di} (m.s^{-1})	C_b (mg.ℓ^{-1})	Δ_b (g.s^{-1}.m^{-2})	w_{di} (m.s^{-1})	C_{bi} (mg.ℓ^{-1})	Δ_{bi} (g.s^{-1}.m^{-2})	w_{di} (m.s^{-1})
0.46	2B/C	14.09	0.345	**0.024**	0.34	0.010	**0.030**	0.67	0.020	**0.030**	0.94	0.025	**0.027**
0.96	3B	77.95	4.272	**0.055**	2.36	0.251	**0.106**	8.31	0.708	**0.085**	15.17	1.115	**0.074**
1.71	4C	238.09	6.234	**0.026**	1.24	0.048	**0.039**	7.68	0.404	**0.053**	33.26	1.658	**0.050**
2.71	6A/B	80.13	2.528	**0.032**	0.10	0.004	**0.038**	0.64	0.042	**0.065**	4.27	0.249	**0.058**
3.71	7C	40.83	0.939	**0.023**	0.07	0.001	**0.009**	0.19	0.005	**0.025**	1.21	0.037	**0.031**

		300-250 μm			250-212 μm			212-150 μm			Σ (500-150 μm)		
X (m)	Trap No.	C_{bi} (mg.ℓ^{-1})	Δ_{bi} (g.s^{-1}.m^{-2})	w_d (m.s^{-1})	C_{bi} (mg.ℓ^{-1})	Δ_{bi} (g.s^{-1}.m^{-2})	w_d (m.s^{-1})	C_b (mg.ℓ^{-1})	Δ_b (g.s^{-1}.m^{-2})	w_d (m.s^{-1})	C_{bi} (mg.ℓ^{-1})	Δ_{bi} (g.s^{-1}.m^{-2})	w_d (m.s^{-1})
0.46	2B/C	2.60	0.064	**0.025**	4.38	0.102	**0.023**	4.18	0.067	**0.016**	13.11	0.289	**0.022**
0.96	3B	24.87	1.294	**0.052**	18.30	0.617	**0.034**	6.55	0.123	**0.019**	75.56	4.108	**0.054**
1.71	4C	70.60	2.576	**0.036**	97.57	1.256	**0.013**	26.43	0.246	**0.009**	236.77	6.188	**0.026**
2.71	6A/B	21.67	1.019	**0.047**	35.32	0.931	**0.026**	16.75	0.258	**0.015**	78.77	2.504	**0.032**
3.71	7C	8.18	0.270	**0.033**	18.25	0.430	**0.024**	11.69	0.177	**0.015**	39.59	0.919	**0.023**

Summary of Results - S2_EX3					Results from Plots		
Size Class	d (μm)	w_{di} (ms^{-1})	w_s (ms^{-1})	w_{di}/w_{si}	Gradient	R^2	w_{di}/w_{si}
Full Mix	250	0.0320	0.0296	**1.08**	0.029	0.8042	**0.98**
500-425 μm	462.5	0.0443	0.0600	**0.74**	0.0907	0.8686	**1.51**
425-355 μm	390	0.0515	0.0491	**1.05**	0.0701	0.9112	**1.43**
355-300 μm	327.5	0.0479	0.0405	**1.18**	0.0539	0.9496	**1.33**
300-250 μm	275	0.0387	0.0322	**1.20**	0.0388	0.957	**1.20**
250-212 μm	231	0.0239	0.0270	**0.89**	0.0153	0.5647	**0.57**
212-150 μm	181	0.0149	0.0201	**0.74**	0.0119	0.548	**0.59**

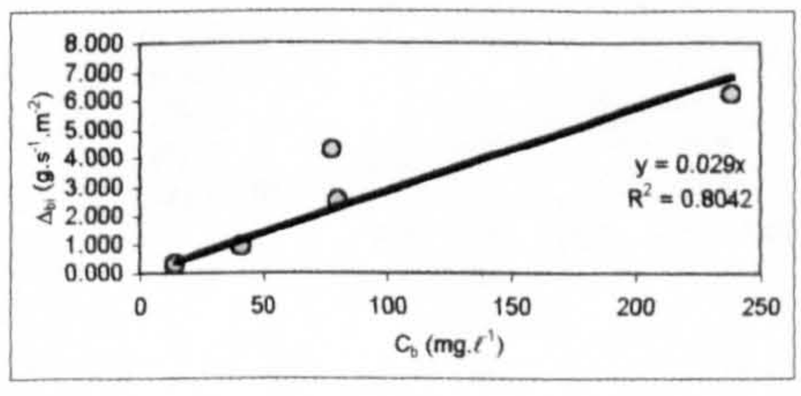

EXPERIMENT S2_EX4

Experiment S2_EX4		Near Bed Concentration (C_b) (mg.ℓ^{-1}), Deposition Rate (Δ_b) (g.s^{-1}.m^{-2}) and Deposition Velocity (w_d) (m.s^{-1})											
Sampling Location		Full Mix			500-425 µm			425-355 µm			355-300 µm		
X (m)	Trap No.	C_b (mg.ℓ^{-1})	Δ_{bi} (g.s^{-1}.m^{-2})	w_d (m.s^{-1})	C_{bi} (mg.ℓ^{-1})	Δ_{bi} (g.s^{-1}.m^{-2})	w_{di} (m.s^{-1})	C_{bi} (mg.ℓ^{-1})	Δ_{bi} (g.s^{-1}.m^{-2})	w_{di} (m.s^{-1})	C_{bi} (mg.ℓ^{-1})	Δ_{bi} (g.s^{-1}.m^{-2})	w_{di} (m.s^{-1})
0.46	2B/C	16.73	0.693	**0.041**	1.65	0.082	**0.050**	2.64	0.145	**0.055**	3.19	0.150	**0.047**
0.96	3B	193.20	7.153	**0.037**	1.62	0.131	**0.081**	9.19	0.736	**0.080**	32.99	1.992	**0.060**
1.46	4A	168.32	4.563	**0.027**	0.27	0.015	**0.055**	2.36	0.141	**0.060**	12.92	0.727	**0.056**
2.21	5B	49.37	1.437	**0.029**	0.06	0.0009	**0.016**	0.19	0.009	**0.049**	1.71	0.084	**0.049**
2.96	6C	31.14	0.500	**0.016**	0.01	0.0004	**0.027**	0.09	0.002	**0.020**	0.58	0.014	**0.024**

		300-250 µm			250-212 µm			212-150 µm			Σ (500-150 µm)		
X (m)	Trap No.	C_{bi} (mg.ℓ^{-1})	Δ_{bi} (g.s^{-1}.m^{-2})	w_d (m.s^{-1})	C_{bi} (mg.ℓ^{-1})	Δ_{bi} (g.s^{-1}.m^{-2})	w_d (m.s^{-1})	C_{bi} (mg.ℓ^{-1})	Δ_{bi} (g.s^{-1}.m^{-2})	w_d (m.s^{-1})	C_{bi} (mg.ℓ^{-1})	Δ_{bi} (g.s^{-1}.m^{-2})	w_d (m.s^{-1})
0.46	2B/C	3.59	0.129	**0.036**	2.05	0.058	**0.028**	1.27	0.027	**0.021**	14.40	0.591	**0.041**
0.96	3B	73.49	2.824	**0.038**	59.87	1.219	**0.020**	15.30	0.199	**0.013**	192.46	7.101	**0.037**
1.46	4A	54.06	2.016	**0.037**	70.26	1.358	**0.019**	27.85	0.288	**0.010**	167.72	4.545	**0.027**
2.21	5B	11.83	0.481	**0.041**	22.02	0.629	**0.029**	13.15	0.218	**0.017**	48.97	1.422	**0.029**
2.96	6C	5.19	0.117	**0.023**	13.65	0.240	**0.018**	11.07	0.115	**0.010**	30.59	0.487	**0.016**

Summary of Results - S2_EX4					Results from Plots		
Size Class	d (µm)	w_{di} (ms^{-1})	w_s (ms^{-1})	w_{di}/w_{si}	Gradient	R^2	w_{di}/w_{si}
Full Mix	250	0.0302	0.0296	**1.02**	0.0324	0.9435	1.09
500-425 µm	462.5	0.0458	0.0600	**0.76**	0.0651	0.903	1.09
425-355 µm	390	0.0528	0.0491	**1.08**	0.0771	0.9839	1.57
355-300 µm	327.5	0.0473	0.0405	**1.17**	0.0597	0.9952	1.47
300-250 µm	275	0.0349	0.0322	**1.09**	0.038	0.9984	1.18
250-212 µm	231	0.0228	0.0270	**0.85**	0.0202	0.9705	0.75
212-150 µm	181	0.0143	0.0201	**0.71**	0.0117	0.8455	0.58

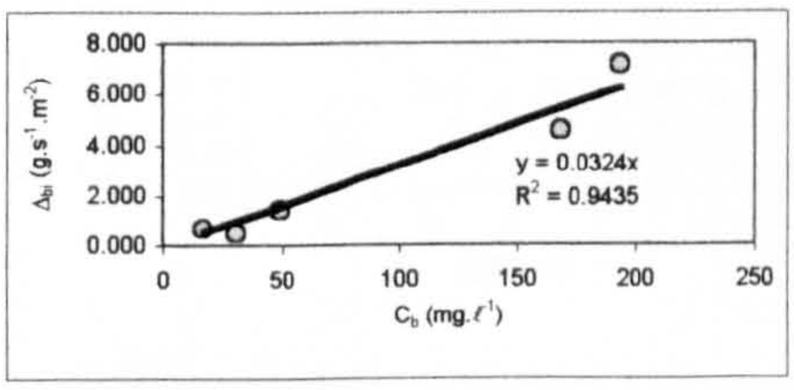

EXPERIMENT S2_EX5

Experiment S2_EX5		Near Bed Concentration (C_b) (mg.ℓ^{-1}), Deposition Rate (Δ_b) (g.s^{-1}.m^{-2}) and Deposition Velocity (w_d) (m.s^{-1})											
Sampling Location		Full Mix			500-425 µm			425-355 µm			355-300 µm		
X (m)	Trap No.	C_b (mg.ℓ^{-1})	Δ_{bi} (g.s^{-1}.m^{-2})	w_d (m.s^{-1})	C_{bi} (mg.ℓ^{-1})	Δ_{bi} (g.s^{-1}.m^{-2})	w_{di} (m.s^{-1})	C_{bi} (mg.ℓ^{-1})	Δ_{bi} (g.s^{-1}.m^{-2})	w_{di} (m.s^{-1})	C_{bi} (mg.ℓ^{-1})	Δ_{bi} (g.s^{-1}.m^{-2})	w_{di} (m.s^{-1})
0.46	2B/C	10.45	0.670	**0.064**	1.02	0.072	**0.071**	1.57	0.133	**0.085**	1.88	0.147	**0.079**
0.96	3B	152.89	7.207	**0.047**	1.21	0.130	**0.107**	6.89	0.673	**0.098**	23.72	1.792	**0.076**
1.46	4A	119.55	5.000	**0.042**	0.31	0.016	**0.051**	2.12	0.150	**0.071**	11.78	0.765	**0.065**
2.21	5B	58.03	1.355	**0.023**	0.07	0.001	**0.014**	0.36	0.009	**0.026**	2.73	0.077	**0.028**
2.96	6C	25.30	0.498	**0.020**	0.04	0.000	-	0.11	0.001	**0.012**	0.59	0.013	**0.023**

		300-250 µm			250-212 µm			212-150 µm			Σ (500-150 µm)		
X (m)	Trap No.	C_{bi} (mg.ℓ^{-1})	Δ_{bi} (g.s^{-1}.m^{-2})	w_d (m.s^{-1})	C_{bi} (mg.ℓ^{-1})	Δ_{bi} (g.s^{-1}.m^{-2})	w_d (m.s^{-1})	C_{bi} (mg.ℓ^{-1})	Δ_{bi} (g.s^{-1}.m^{-2})	w_d (m.s^{-1})	C_{bi} (mg.ℓ^{-1})	Δ_{bi} (g.s^{-1}.m^{-2})	w_d (m.s^{-1})
0.46	2B/C	1.95	0.133	**0.069**	1.62	0.058	**0.036**	1.03	0.039	**0.037**	9.06	0.582	**0.064**
0.96	3B	57.02	2.819	**0.049**	49.01	1.486	**0.030**	14.33	0.256	**0.018**	152.19	7.156	**0.047**
1.46	4A	40.52	2.163	**0.053**	47.52	1.556	**0.033**	16.87	0.332	**0.020**	119.12	4.982	**0.042**
2.21	5B	14.92	0.440	**0.029**	25.88	0.593	**0.023**	13.58	0.220	**0.016**	57.55	1.341	**0.023**
2.96	6C	4.52	0.109	**0.024**	11.13	0.238	**0.021**	8.52	0.123	**0.014**	24.92	0.485	**0.019**

Summary of Results - S2_EX5					Results from Plots		
Size Class	d (µm)	w_{di} (ms^{-1})	w_s (ms^{-1})	w_{di}/w_{si}	Gradient	R^2	w_{di}/w_{si}
Full Mix	250	0.0392	0.0296	**1.32**	0.043	0.9413	1.45
500-425 µm	462.5	0.0605	0.0600	**1.01**	0.0903	0.9207	1.51
425-355 µm	390	0.0581	0.0491	**1.18**	0.0947	0.9871	1.93
355-300 µm	327.5	0.0540	0.0405	**1.33**	0.073	0.9874	1.80
300-250 µm	275	0.0450	0.0322	**1.40**	0.0497	0.9801	1.54
250-212 µm	231	0.0287	0.0270	**1.06**	0.0302	0.9693	1.12
212-150 µm	181	0.0211	0.0201	**1.05**	0.0178	0.9488	0.89

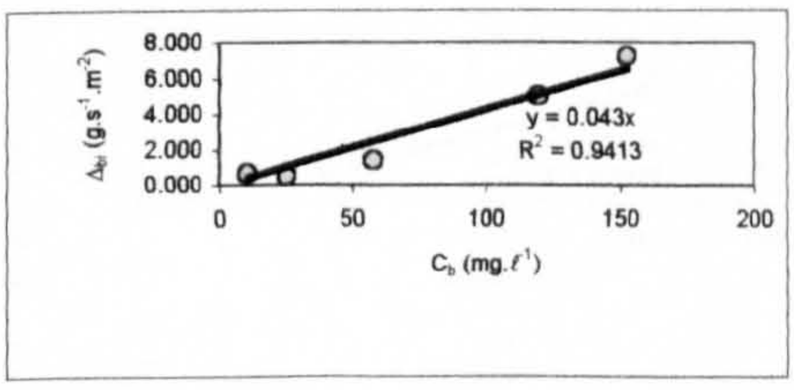

EXPERIMENT S2_EX6

Experiment S2_EX6		Near Bed Concentration (C_b) (mg.ℓ^{-1}), Deposition Rate (Δ_b) (g.s^{-1}.m^{-2}) and Deposition Velocity (w_d) (m.s^{-1})											
Sampling Location		Full Mix			500-425 µm			425-355 µm			355-300 µm		
X (m)	Trap No.	C_b (mg.ℓ^{-1})	Δ_{bi} (g.s^{-1}.m^{-2})	w_d (m.s^{-1})	C_{bi} (mg.ℓ^{-1})	Δ_{bi} (g.s^{-1}.m^{-2})	w_{di} (m.s^{-1})	C_{bi} (mg.ℓ^{-1})	Δ_{bi} (g.s^{-1}.m^{-2})	w_{di} (m.s^{-1})	C_{bi} (mg.ℓ^{-1})	Δ_{bi} (g.s^{-1}.m^{-2})	w_{di} (m.s^{-1})
0.46	2B/C	13.25	0.755	**0.057**	0.38	0.035	**0.092**	0.61	0.063	**0.104**	1.01	0.091	**0.090**
0.96	3B	211.32	11.122	**0.053**	4.80	0.500	**0.104**	18.11	1.626	**0.090**	40.25	3.377	**0.084**
1.46	4A	279.18	15.242	**0.055**	1.10	0.162	**0.147**	7.64	0.953	**0.125**	32.53	3.679	**0.113**
2.21	5B	225.15	7.912	**0.035**	0.39	0.024	**0.062**	2.92	0.219	**0.075**	17.30	1.320	**0.076**
2.96	6C	104.09	3.546	**0.034**	0.11	0.003	**0.031**	0.53	0.038	**0.072**	4.71	0.315	**0.067**

		300-250 µm			250-212 µm			212-150 µm			Σ (500-150 µm)		
X (m)	Trap No.	C_{bi} (mg.ℓ^{-1})	Δ_{bi} (g.s^{-1}.m^{-2})	w_d (m.s^{-1})	C_{bi} (mg.ℓ^{-1})	Δ_{bi} (g.s^{-1}.m^{-2})	w_d (m.s^{-1})	C_{bi} (mg.ℓ^{-1})	Δ_{bi} (g.s^{-1}.m^{-2})	w_d (m.s^{-1})	C_{bi} (mg.ℓ^{-1})	Δ_{bi} (g.s^{-1}.m^{-2})	w_d (m.s^{-1})
0.46	2B/C	2.15	0.164	**0.076**	3.83	0.205	**0.054**	4.27	0.120	**0.028**	12.25	0.679	**0.055**
0.96	3B	71.19	3.516	**0.049**	53.17	1.522	**0.029**	19.45	0.307	**0.016**	206.96	10.848	**0.052**
1.46	4A	97.27	4.762	**0.049**	103.14	2.404	**0.023**	35.98	0.483	**0.013**	277.67	12.443	**0.045**
2.21	5B	69.65	3.288	**0.047**	94.68	2.410	**0.025**	38.65	0.611	**0.016**	223.58	7.872	**0.035**
2.96	6C	26.95	1.366	**0.051**	45.90	1.373	**0.030**	24.40	0.424	**0.017**	102.59	3.519	**0.034**

Summary of Results - S2_EX6					Results from plots		
Size Class	d (µm)	w_{di} (ms^{-1})	w_s (ms^{-1})	w_{di}/w_{si}	Gradient	R^2	w_{di}/w_{si}
Full Mix	250	0.0467	0.0296	**1.58**	0.0476	0.8896	1.61
500-425 µm	462.5	0.0873	0.0600	**1.45**	0.106	0.9853	1.77
425-355 µm	390	0.0933	0.0491	**1.90**	0.0946	0.9668	1.93
355-300 µm	327.5	0.0860	0.0405	**2.12**	0.0933	0.942	2.30
300-250 µm	275	0.0545	0.0322	**1.69**	0.0487	0.9985	1.51
250-212 µm	231	0.0322	0.0270	**1.19**	0.0253	0.9607	0.94
212-150 µm	181	0.0181	0.0201	**0.90**	0.0153	0.9233	0.76

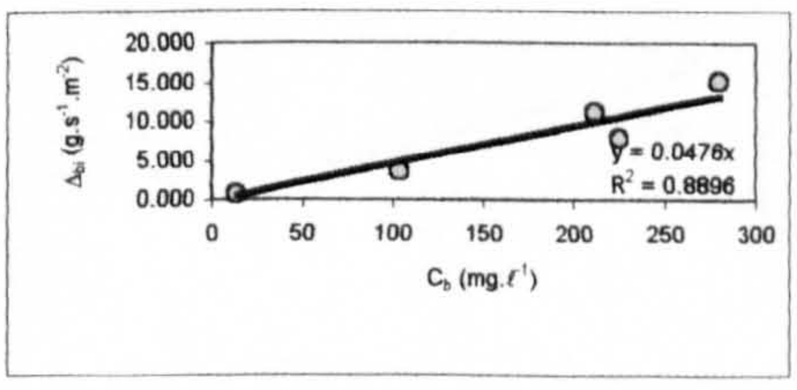

EXPERIMENT S2_EX7

Experiment S2_EX7		Near Bed Concentration (C_b) (mg.ℓ^{-1}), Deposition Rate (Δ_b) (g.s^{-1}.m^{-2}) and Deposition Velocity (w_d) (m.s^{-1})											
Sampling Location		Full Mix			212-150 μm			150-125 μm			125-106 μm		
X (m)	Trap No.	C_b (mg.ℓ^{-1})	Δ_{bi} (g.s^{-1}.m^{-2})	w_d (m.s^{-1})	C_{bi} (mg.ℓ^{-1})	Δ_{bi} (g.s^{-1}.m^{-2})	w_{di} (m.s^{-1})	C_{bi} (mg.ℓ^{-1})	Δ_{bi} (g.s^{-1}.m^{-2})	w_{di} (m.s^{-1})	C_{bi} (mg.ℓ^{-1})	Δ_{bi} (g.s^{-1}.m^{-2})	w_{di} (m.s^{-1})
0.71	3A	76.96	0.687	**0.0089**	1.70	0.066	**0.0387**	1.64	0.008	**0.0047**	7.41	0.062	**0.0084**
1.46	4A	130.51	1.058	**0.0081**	7.76	0.145	**0.0187**	7.89	0.093	**0.0118**	21.08	0.187	**0.0089**
2.21	5B	139.75	0.947	**0.0068**	5.87	0.116	**0.0198**	8.34	0.095	**0.0114**	23.46	0.183	**0.0078**
3.21	7A	147.64	0.853	**0.0058**	4.30	0.069	**0.0160**	7.62	0.089	**0.0116**	23.88	0.209	**0.0088**
4.21	8B/C	139.75	0.679	**0.0049**	3.10	0.046	**0.0149**	6.37	0.082	**0.0129**	21.36	0.146	**0.0068**

		106-90 μm			90-63 μm			Σ (212-63 μm)		
X (m)	Trap No.	C_{bi} (mg.ℓ^{-1})	Δ_{bi} (g.s^{-1}.m^{-2})	w_d (m.s^{-1})	C_{bi} (mg.ℓ^{-1})	Δ_{bi} (g.s^{-1}.m^{-2})	w_d (m.s^{-1})	C_{bi} (mg.ℓ^{-1})	Δ_{bi} (g.s^{-1}.m^{-2})	w_d (m.s^{-1})
0.71	3A	11.19	0.088	**0.0078**	12.51	0.080	**0.0064**	34.45	0.304	**0.009**
1.46	4A	25.41	0.181	**0.0071**	32.37	0.113	**0.0035**	94.51	0.720	**0.008**
2.21	5B	27.71	0.186	**0.0067**	47.80	0.136	**0.0028**	113.17	0.717	**0.006**
3.21	7A	28.93	0.200	**0.0069**	48.75	0.139	**0.0029**	113.48	0.705	**0.006**
4.21	8B/C	29.27	0.162	**0.0055**	42.45	0.116	**0.0027**	102.55	0.553	**0.005**

Summary of Results - S2_EX7					Results from Plots		
Size Class	d (μm)	w_{di} (ms^{-1})	w_s (ms^{-1})	w_{di}/w_{si}	Gradient	R^2	w_{di}/w_{si}
Full Mix	93	0.0069	0.0048	1.45	0.0065	-0.3281	1.36
212-150 μm	181	0.0216	0.0150	1.44	0.0188	0.7767	1.25
150-125 μm	137.5	0.0105	0.0096	1.09	0.0118	0.9643	1.23
125-106 μm	115.5	0.0081	0.0071	1.15	0.0081	0.9028	1.14
106-90 μm	98	0.0068	0.0053	1.30	0.0066	0.8202	1.26
90-63 μm	76.5	0.0037	0.0033	1.11	0.003	-0.0473	0.91

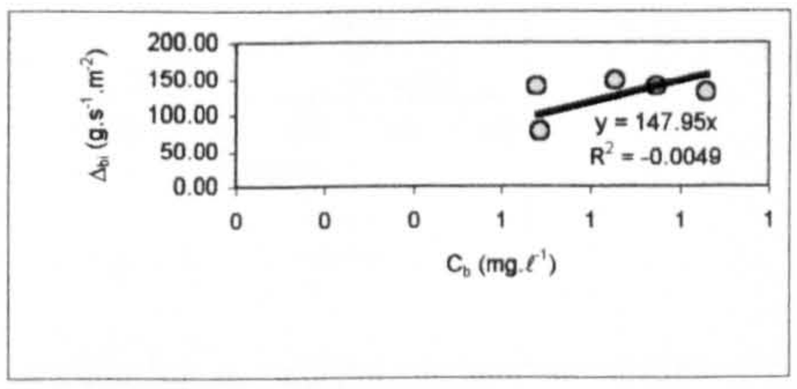

EXPERIMENT S2_EX8

Experiment S2_EX8		Near Bed Concentration (C_b) (mg.ℓ^{-1}), Deposition Rate (Δ_b) (g.s^{-1}.m^{-2}) and Deposition Velocity (w_d) (m.s^{-1})											
Sampling Location		Full Mix			500-425 μm			425-355 μm			355-300 μm		
X (m)	Trap No.	C_b (mg.ℓ^{-1})	Δ_{bi} (g.s^{-1}.m^{-2})	w_d (m.s^{-1})	C_{bi} (mg.ℓ^{-1})	Δ_{bi} (g.s^{-1}.m^{-2})	w_{di} (m.s^{-1})	C_{bi} (mg.ℓ^{-1})	Δ_{bi} (g.s^{-1}.m^{-2})	w_{di} (m.s^{-1})	C_{bi} (mg.ℓ^{-1})	Δ_{bi} (g.s^{-1}.m^{-2})	w_{di} (m.s^{-1})
0.71	3A	39.45	0.873	**0.022**	2.48	0.075	**0.030**	4.56	0.122	**0.027**	6.74	0.181	**0.027**
1.46	4A	157.00	4.107	**0.026**	1.17	0.075	**0.064**	4.67	0.276	**0.059**	16.62	1.016	**0.061**
2.21	5B	126.19	2.569	**0.020**	0.18	0.013	**0.071**	1.48	0.070	**0.047**	7.37	0.412	**0.056**
3.21	7A	53.46	1.189	**0.022**	0.07	0.001	**0.020**	0.29	0.011	**0.038**	1.68	0.072	**0.043**
4.21	8B/C	48.84	0.588	**0.012**	0.04	0.001	**0.015**	0.16	0.002	**0.013**	0.88	0.020	**0.023**

		300-250 μm			250-212 μm			212-150 μm			Σ (500-150 μm)		
X (m)	Trap No.	C_{bi} (mg.ℓ^{-1})	Δ_{bi} (g.s^{-1}.m^{-2})	w_d (m.s^{-1})	C_{bi} (mg.ℓ^{-1})	Δ_{bi} (g.s^{-1}.m^{-2})	w_d (m.s^{-1})	C_{bi} (mg.ℓ^{-1})	Δ_{bi} (g.s^{-1}.m^{-2})	w_d (m.s^{-1})	C_{bi} (mg.ℓ^{-1})	Δ_{bi} (g.s^{-1}.m^{-2})	w_d (m.s^{-1})
0.71	3A	10.69	0.207	**0.019**	8.34	0.129	**0.015**	4.19	0.048	**0.011**	37.00	0.763	**0.021**
1.46	4A	46.39	1.471	**0.032**	59.05	0.952	**0.016**	27.79	0.253	**0.009**	155.68	4.043	**0.026**
2.21	5B	31.90	1.086	**0.034**	51.80	0.724	**0.014**	32.22	0.228	**0.007**	124.94	2.532	**0.020**
3.21	7A	9.83	0.352	**0.036**	22.62	0.492	**0.022**	17.82	0.225	**0.013**	52.30	1.154	**0.022**
4.21	8B/C	7.29	0.134	**0.018**	20.13	0.264	**0.013**	19.09	0.139	**0.007**	47.59	0.560	**0.012**

Summary of Results - S2_EX8					Results from Plots		
Size Class	d (μm)	w_{di} (ms^{-1})	w_s (ms^{-1})	w_{di}/w_{si}	Gradient	R^2	w_{di}/w_{si}
Full Mix	250	0.0206	0.0296	**0.70**	0.0231	0.9249	0.78
500-425 μm	462.5	0.0401	0.0600	**0.67**	0.0367	0.7832	0.61
425-355 μm	390	0.0369	0.0491	**0.75**	0.0435	0.7769	0.89
355-300 μm	327.5	0.0420	0.0405	**1.04**	0.056	0.9285	1.38
300-250 μm	275	0.0279	0.0322	**0.87**	0.0319	0.976	0.99
250-212 μm	231	0.0161	0.0270	**0.60**	0.0155	0.9331	0.57
212-150 μm	181	0.0095	0.0201	**0.47**	0.0085	0.7045	0.42

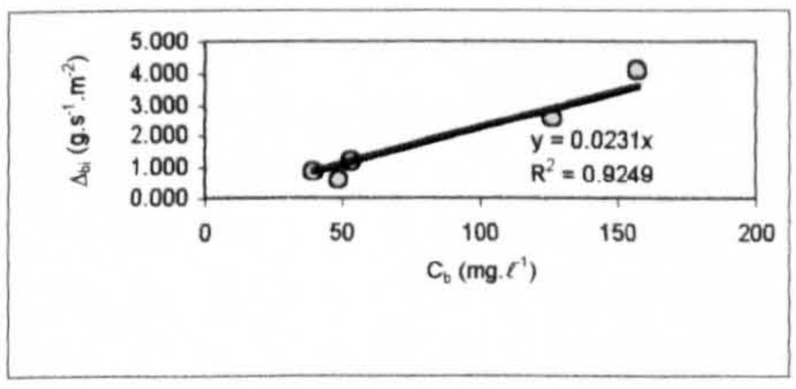

EXPERIMENT S2_EX9(ii)

Experiment S2_EX9(ii)		Near Bed Concentration (C_b) (mg.ℓ^{-1}), Deposition Rate (Δ_b) (g.s^{-1}.m^{-2}) and Deposition Velocity (w_d) (m.s^{-1})											
Sampling Location		Full Mix			500-425 μm			425-355 μm			355-300 μm		
X (m)	Trap No.	C_b (mg.ℓ^{-1})	Δ_{bi} (g.s^{-1}.m^{-2})	w_d (m.s^{-1})	C_{bi} (mg.ℓ^{-1})	Δ_{bi} (g.s^{-1}.m^{-2})	w_{di} (m.s^{-1})	C_{bi} (mg.ℓ^{-1})	Δ_{bi} (g.s^{-1}.m^{-2})	w_{di} (m.s^{-1})	C_{bi} (mg.ℓ^{-1})	Δ_{bi} (g.s^{-1}.m^{-2})	w_{di} (m.s^{-1})
0.71	3A	55.84	1.059	**0.019**	3.17	0.072	**0.023**	6.53	0.150	**0.023**	10.38	0.229	**0.022**
1.46	4A	216.00	4.510	**0.021**	1.57	0.026	**0.016**	7.06	0.155	**0.022**	23.11	0.660	**0.029**
2.21	5B	133.55	3.213	**0.024**	0.20	0.010	**0.050**	1.34	0.059	**0.044**	7.73	0.315	**0.041**
3.21	7A	103.73	1.219	**0.012**	0.15	0.002	**0.011**	0.42	0.008	**0.020**	2.86	0.053	**0.019**
4.21	8B/C	52.89	0.623	**0.012**	0.03	0.001	**0.047**	0.14	0.002	**0.017**	0.78	0.018	**0.023**

		300-250 μm			250-212 μm			212-150 μm			Σ (500-150 μm)		
X (m)	Trap No.	C_{bi} (mg.ℓ^{-1})	Δ_{bi} (g.s^{-1}.m^{-2})	w_d (m.s^{-1})	C_{bi} (mg.ℓ^{-1})	Δ_{bi} (g.s^{-1}.m^{-2})	w_d (m.s^{-1})	C_{bi} (mg.ℓ^{-1})	Δ_{bi} (g.s^{-1}.m^{-2})	w_d (m.s^{-1})	C_{bi} (mg.ℓ^{-1})	Δ_{bi} (g.s^{-1}.m^{-2})	w_d (m.s^{-1})
0.71	3A	15.38	0.278	**0.018**	12.01	0.172	**0.014**	4.85	0.061	**0.013**	52.31	0.962	**0.018**
1.46	4A	67.09	1.740	**0.026**	78.37	1.408	**0.018**	36.92	0.467	**0.013**	214.12	4.456	**0.021**
2.21	5B	33.42	1.192	**0.036**	55.92	1.148	**0.021**	33.30	0.427	**0.013**	131.90	3.151	**0.024**
3.21	7A	19.64	0.309	**0.016**	43.81	0.509	**0.012**	35.08	0.280	**0.008**	101.95	1.162	**0.011**
4.21	8B/C	20.48	0.108	**0.005**	7.47	0.264	**0.035**	22.22	0.185	**0.008**	51.12	0.579	**0.011**

Summary of Results - S2_EX9(ii)					Results from Plots		
Size Class	d (μm)	w_{di} (ms^{-1})	w_s (ms^{-1})	w_{di}/w_{si}	Gradient	R^2	w_{di}/w_{si}
Full Mix	250	0.0175	0.0296	**0.59**	0.02	0.8868	0.68
500-425 μm	462.5	0.0294	0.0600	**0.49**	0.0216	0.9684	0.36
425-355 μm	390	0.0252	0.0491	**0.51**	0.0228	0.9605	0.46
355-300 μm	327.5	0.0265	0.0405	**0.66**	0.0285	0.9463	0.70
300-250 μm	275	0.0201	0.0322	**0.63**	0.0254	0.8313	0.79
250-212 μm	231	0.0200	0.0270	**0.74**	0.0176	0.9045	0.65
212-150 μm	181	0.0109	0.0201	**0.54**	0.0108	0.8058	0.54

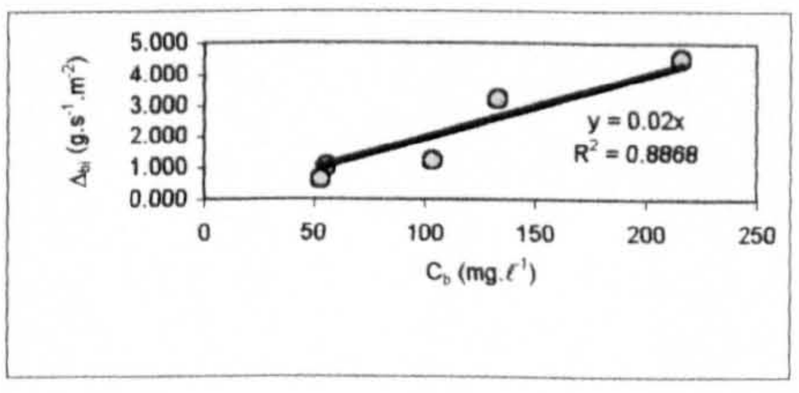

EXPERIMENT S2_EX10(ii)

Experiment S2_EX10(ii)		Near Bed Concentration (C_b) (mg.ℓ^{-1}), Deposition Rate (Δ_b) (g.s^{-1}.m^{-2}) and Deposition Velocity (w_d) (m.s^{-1})											
Sampling Location		Full Mix			500-425 μm			425-355 μm			355-300 μm		
X (m)	Trap No.	C_b (mg.ℓ^{-1})	Δ_{bi} (g.s^{-1}.m^{-2})	w_d (m.s^{-1})	C_{bi} (mg.ℓ^{-1})	Δ_{bi} (g.s^{-1}.m^{-2})	w_{di} (m.s^{-1})	C_{bi} (mg.ℓ^{-1})	Δ_{bi} (g.s^{-1}.m^{-2})	w_{di} (m.s^{-1})	C_{bi} (mg.ℓ^{-1})	Δ_{bi} (g.s^{-1}.m^{-2})	w_{di} (m.s^{-1})
0.71	3A	433.70	4.804	**0.011**	23.17	0.367	**0.016**	47.16	0.691	**0.015**	78.07	1.115	**0.014**
1.46	4A	896.93	12.814	**0.014**	7.85	0.213	**0.027**	31.86	0.917	**0.029**	107.03	3.975	**0.037**
2.21	5B	792.37	14.316	**0.018**	1.81	0.087	**0.048**	11.07	0.488	**0.044**	57.19	4.164	**0.073**
3.21	7A	420.35	5.849	**0.014**	0.22	0.008	**0.034**	1.92	0.051	**0.027**	13.60	0.397	**0.029**
4.21	8B/C	231.07	2.864	**0.012**	0.09	0.002	**0.020**	0.39	0.012	**0.030**	4.51	0.099	**0.022**

		300-250 μm			250-212 μm			212-150 μm			Σ (500-150 μm)		
X (m)	Trap No.	C_{bi} (mg.ℓ^{-1})	Δ_{bi} (g.s^{-1}.m^{-2})	w_{di} (m.s^{-1})	C_{bi} (mg.ℓ^{-1})	Δ_{bi} (g.s^{-1}.m^{-2})	w_{di} (m.s^{-1})	C_{bi} (mg.ℓ^{-1})	Δ_{bi} (g.s^{-1}.m^{-2})	w_{di} (m.s^{-1})	C_{bi} (mg.ℓ^{-1})	Δ_{bi} (g.s^{-1}.m^{-2})	w_{di} (m.s^{-1})
0.71	3A	124.60	1.285	**0.010**	98.84	0.738	**0.007**	39.12	0.246	**0.006**	410.96	4.441	**0.011**
1.46	4A	300.22	4.325	**0.014**	308.16	2.487	**0.008**	133.65	0.761	**0.006**	888.78	12.678	**0.014**
2.21	5B	219.87	4.964	**0.023**	318.43	3.335	**0.010**	175.39	1.154	**0.007**	783.76	14.192	**0.018**
3.21	7A	82.93	2.005	**0.024**	180.31	2.274	**0.013**	133.42	1.016	**0.008**	412.40	5.750	**0.014**
4.21	8B/C	37.33	0.709	**0.019**	96.03	1.223	**0.013**	85.96	0.738	**0.009**	224.31	2.782	**0.012**

Summary of Results - S2_EX10(ii)					Results from Plots		
Size Class	d (μm)	w_{di} (ms^{-1})	w_s (ms^{-1})	w_{di}/w_{si}	Gradient	R^2	w_{di}/w_{si}
Full Mix	250	0.0139	0.0296	**0.47**	0.0152	0.9065	0.51
500-425 μm	462.5	0.0292	0.0600	**0.49**	0.0172	0.894	0.29
425-355 μm	390	0.0288	0.0491	**0.59**	0.02	0.66	0.41
355-300 μm	327.5	0.0351	0.0405	**0.87**	0.036	0.5279	0.89
300-250 μm	275	0.0181	0.0322	**0.56**	0.0169	0.7775	0.52
250-212 μm	231	0.0103	0.0270	**0.38**	0.0098	0.8323	0.36
212-150 μm	181	0.0070	0.0201	**0.35**	0.0068	0.8779	0.34

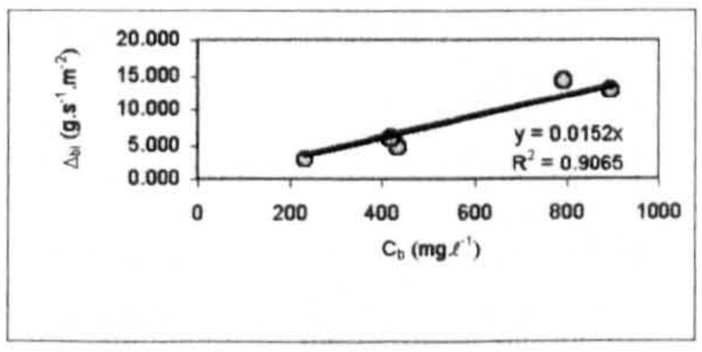

EXPERIMENT S2_EX11

Experiment S2_EX11		Near Bed Concentration (C_b) (mg.l^{-1}), Deposition Rate (Δ_b) (g.s^{-1}.m^{-2}) and Deposition Velocity (w_d) (m.s^{-1})											
		Full Mix			212-150 μm			150-125 μm			125-106 μm			106-90 μm		
X (m)	Trap No.	C_b (mg.ℓ^{-1})	Δ_{bi} (g.s^{-1}.m^{-2})	w_d (m.s^{-1})	C_{bi} (mg.ℓ^{-1})	Δ_{bi} (g.s^{-1}.m^{-2})	w_{di} (m.s^{-1})	C_{bi} (mg.ℓ^{-1})	Δ_{bi} (g.s^{-1}.m^{-2})	w_{di} (m.s^{-1})	C_{bi} (mg.ℓ^{-1})	Δ_{bi} (g.s^{-1}.m^{-2})	w_{di} (m.s^{-1})	C_{bi} (mg.ℓ^{-1})	Δ_{bi} (g.s^{-1}.m^{-2})	w_{di} (m.s^{-1})
0.71	3A	320.72	0.564	**0.0018**	4.74	0.020	**0.0041**	28.73	0.023	**0.0008**	66.63	0.123	**0.0018**	62.27	0.124	**0.002**
1.46	4A	425.77	1.669	**0.0039**	3.88	0.095	**0.0245**	27.88	0.380	**0.0136**	84.62	0.518	**0.0061**	93.72	0.296	**0.003**
2.46	5C	388.11	2.019	**0.0052**	1.60	0.045	**0.0281**	25.85	0.402	**0.0156**	77.69	0.618	**0.0080**	86.96	0.424	**0.005**
3.71	7C	327.92	1.566	**0.0048**	0.94	0.028	**0.0303**	12.83	0.219	**0.0171**	56.98	0.474	**0.0083**	70.44	0.365	**0.005**

		90-63 μm			63-53 μm			53-45 μm			45-38 μm			Σ (212-38 μm)		
X (m)	Trap No.	C_{bi} (mg.ℓ^{-1})	Δ_{bi} (g.s^{-1}.m^{-2})	w_{di} (m.s^{-1})	C_{bi} (mg.ℓ^{-1})	Δ_{bi} (g.s^{-1}.m^{-2})	w_{di} (m.s^{-1})	C_{bi} (mg.ℓ^{-1})	Δ_{bi} (g.s^{-1}.m^{-2})	w_{di} (m.s^{-1})	C_{bi} (mg.ℓ^{-1})	Δ_{bi} (g.s^{-1}.m^{-2})	w_{di} (m.s^{-1})	C_{bi} (mg.ℓ^{-1})	Δ_{bi} (g.s^{-1}.m^{-2})	w_{di} (m.s^{-1})
0.71	3A	77.30	0.146	**0.0019**	26.68	0.035	**0.0013**	23.36	0.028	**0.0012**	13.06	0.015	**0.0011**	302.78	0.471	**0.002**
1.46	4A	114.13	0.220	**0.0019**	31.20	0.048	**0.0015**	30.08	0.030	**0.0010**	17.50	0.014	**0.0008**	403.00	1.282	**0.003**
2.46	5C	111.96	0.339	**0.0030**	23.64	0.063	**0.0027**	25.83	0.048	**0.0019**	16.50	0.025	**0.0015**	370.02	1.543	**0.004**
3.71	7C	95.53	0.304	**0.0032**	34.83	0.062	**0.0018**	25.53	0.047	**0.0019**	13.91	0.022	**0.0016**	310.98	1.156	**0.004**

Summary of Results - S2_EX11					Results from Plots		
Size Class	d (μm)	w_{di} (ms^{-1})	w_s (ms^{-1})	w_{di}/w_{si}	Gradient	R^2	w_{di}/w_{si}
Full Mix	93	0.0039	0.0048	0.82	0.004	0.3167	0.84
212-150 μm	181	0.0218	0.0150	1.45	0.0137	-0.3413	0.91
150-125 μm	137.5	0.0118	0.0096	1.22	0.01	-0.1796	1.04
125-106 μm	115.5	0.0061	0.0071	0.86	0.0061	0.159	0.86
106-90 μm	98	0.0038	0.0053	0.72	0.0039	0.321	0.74
90-63 μm	76.5	0.0025	0.0033	0.76	0.0025	0.3723	0.76
63-53 μm	58	0.0018	0.0019	0.94	0.0018	-0.2132	0.93
53-45 μm	49	0.0015	0.0014	1.06	0.0014	-0.2284	1.00
45-38 μm	41.5	0.0013	0.0010	1.25	0.0012	-0.1241	1.19